Science and Technology Facilities Council

Next Generation XFEL: Conceptual Design

Final Draft - June 2026

xfel.ac.uk

DRAFT

The production team was as follows:

STFC Sponsor: John Collier

Science Lead: Jon Marangos (Imperial College)

Project Manager: Paul Aden

Lead Technical Team: David Dunning, Ed Snedden, Deepa Angal-Kalinin, Jim Clarke

Copyright © 2026 UK Research and Innovation

Foreword

It is my pleasure to introduce these reports examining the Conceptual Design, an Options Analysis, and The Scientific and Technology Case for a transformative Next-Generation XFEL (X-ray Free Electron Laser). The work undertaken to compile these reports is part of the contribution that the expert teams in STFC's research infrastructure, both nationally and through international partnerships, plays as a crucial component of UKRI's mission to advance knowledge, improve lives, and drive economic growth.

The UK is already a partner and shareholder in the European XFEL, with UK researchers currently being one of the largest XFEL users worldwide, so it is natural that we should rigorously evaluate the case for a Next-Generation XFEL. This process follows the 2016 strategic FEL review and the 2020 UK XFEL Science Case. The reports assess various options to enable this, ranging from a new facility in the UK to expansion of an existing international facility to more reactive options.

Since the world's first XFEL began operation in 2009 at Stanford, these machines have rapidly proven to be a transformative new tool for science. Through time-resolved X-ray methods, spectroscopy, imaging and scattering, they offer a unique window into the structural and electronic dynamics of matter at the nanoscale. Providing profound new insights into challenging questions from stellar interiors to protein dynamics and chemical reactions. Recent advances in XFELs, in areas such as: attosecond science, AI integration, dynamic structural biology, imaging techniques, chemical dynamics in batteries and catalysis, carry direct relevance to UK industrial priorities, from more efficient energy storage to the precision materials science underpinning defence and advanced manufacturing. These reports address how, over the coming decades, the technological and scientific opportunities enabled by XFELs will develop and what impact there might be from access to a Next-Generation XFEL.

I wish to express my gratitude to the project's International Advisory Committee, chaired by Massimo Altarelli, for their expert oversight and invaluable advice throughout the project, and for all the help of the international XFEL community. We are indebted to the UK XFEL Leadership Team John Collier (Project Sponsor), Paul Aden (Project Manager), Deepa Angal-Kalinin, Jim Clarke, David Dunning (Technical Lead), Jon Marangos (Science Lead) and Edward Snedden, along with experts from across the STFC, for steering the work on the Conceptual Design over a period of 3 years. The Science and Technology Case was authored by a science team of 40 experts; who refined the opportunities and technical requirements through exchanges with over 500 community members at events including Town Halls in Belfast, Glasgow, Plymouth, Manchester, Sheffield, London, Harwell and Cardiff. The Conceptual Design translated these requirements into a concept machine that is deliverable across a series of options for implementation at existing XFELs or as a new standalone facility.

Together, these documents deliver the evidence the UK needs to make clear, strategic decisions on the future of these innovative light sources.

Professor Michele Dougherty CBE FRS FRAS

Executive Chair, Science and Technology Facilities Council

DRAFT

Contents

1 Executive summary **1**

2 Introduction **4**
2.1 Introduction to XFELs . . . 5
2.1.1 Free-electron lasers . . . 5
2.1.2 XFEL performance strengths . . . 7
2.1.3 XFEL challenges and opportunities . . . 8
2.2 From the next-generation criteria to a facility specification . . . 13
References for Chapter 2 . . . 17

3 Overview of the Next-Generation XFEL Conceptual Design **19**
3.1 Design philosophy and process . . . 19
3.2 Key themes . . . 21
3.3 Theme 1: High repetition rate and high-efficiency, many-user facility . . . 23
3.3.1 High-level facility design choices . . . 23
3.3.2 Low Energy Beamlines: High-brightness electron injectors . . . 25
3.3.3 High Energy Beamline: Accelerator technology and parameters . . . 27
3.3.4 High Energy Beamline: Distribution to many simultaneous experiments . . . 28
3.3.5 Electron beam R&D line . . . 29
3.4 Theme 2: Exceptional X-ray pulse qualities including ‘laser-like’ X-rays . . . 31
3.4.1 Photon energy coverage . . . 31
3.4.2 ‘Laser-like’ or near-transform-limited X-ray pulses . . . 32
3.4.3 FEL-1: extremely high pulse energy and photon energy . . . 34
3.4.4 Widely Separated Two-Colour Pulses . . . 35
3.4.5 Summary of the FEL parameters and beam modes . . . 35
3.4.6 X-ray beamlines and diagnostics . . . 37
3.5 Theme 3: World-class end stations, synchronous sources, data and AI . . . 39
3.5.1 User instrumentation: End stations . . . 39
3.5.2 AI, data, and detectors . . . 42
3.5.3 Synchronous sources . . . 44
3.6 Engineering delivery, environmental sustainability, and project planning . . . 46
3.6.1 Facility layout and engineering . . . 46
3.6.2 Environmental sustainability . . . 48
3.6.3 Importance of site selection . . . 49
3.6.4 Planning, governance, and stakeholder coordination . . . 49
3.6.5 Cost estimates . . . 51
3.6.6 Next steps . . . 51
References for Chapter 3 . . . 52

Theme 1: A high repetition rate and high-efficiency, many-user facility **57**

4 Low energy beam **57**
4.1 Summary . . . 57

DRAFT

4.2 Introduction . . . 57
4.3 Main Discussion, work done for the CDOA . . . 58
4.3.1 Definition of Low Energy Beamline and beam parameter requirements . . . 59
4.3.2 Overview of Current Technology . . . 59
4.3.3 Technology readiness level of CW high brightness electron injectors and gap analysis . . . 62
4.3.4 DC photocathode guns . . . 62
4.3.5 VHF photocathode guns . . . 63
4.3.6 SRF photocathode guns . . . 64
4.3.7 DC-SRF photocathode guns . . . 65
4.3.8 Photocathodes . . . 65
4.3.9 Drive lasers . . . 67
4.3.10 Electron source for UK XFEL . . . 70
4.3.11 Conceptual design options of the Low Energy Beamline . . . 70
4.3.12 VHF gun-based electron injector and required infrastructure . . . 70
4.3.13 L-band SRF gun based electron injector design . . . 82
4.3.14 Comparison of proposed options . . . 87
4.4 Configuration of injector for multiple FEL lines and two-colour operation . . . 88
4.4.1 Merging From Injector . . . 88
4.4.2 Sustainability . . . 92
4.4.3 Summary of technology development areas, R&D needed for future phases to meet specifications . . . 93
4.5 Conclusions . . . 94
References for Chapter 4 . . . 96

5 High energy beam **100**
5.1 Summary . . . 100
5.2 Introduction, scope and assumptions . . . 100
5.3 Radio Frequency Linac . . . 101
5.3.1 SRF Linac: Choice of Technology and Operating Parameters . . . 102
5.3.2 Sustainability . . . 113
5.3.3 Long-Range Wakefields . . . 114
5.3.4 Higher Harmonic Lineariser . . . 121
5.3.5 Low Level RF system . . . 123
5.3.6 Normal Conducting Booster Linac . . . 125
5.4 Compression Schemes . . . 127
5.4.1 Benefits and drawbacks of candidate compression schemes . . . 127
5.4.2 Bunch compressor designs . . . 129
5.4.3 Simulation results . . . 130
5.4.4 Preliminary Microbunching Studies . . . 134
5.5 Fast Beam Distribution & Spreader Design . . . 135
5.5.1 Layout Options . . . 136
5.5.2 Two colour simultaneous FEL pulses at single sample . . . 138
5.5.3 Fast Kickers . . . 139
5.5.4 Design Principles . . . 140
5.5.5 Tracking Studies . . . 140
5.6 Plasma Wakefield Acceleration . . . 142
5.6.1 Start-to-end simulations results of PWFA booster . . . 142
5.6.2 Integration of plasma capabilities into the facility design . . . 144
5.7 Incorporating Microbunching Instability into OCELOT for Fast Tuning . . . 146

DRAFT

5.8 Collimators & Beam Loss Studies . . . 148
5.8.1 Machine Protection Requirements . . . 148
5.8.2 Review of Collimation Schemes . . . 149
5.8.3 Main Issues and Choices . . . 150
5.8.4 Conclusion . . . 150
5.9 Appendix 1: Benchmarking the CST Model for Long-range Wakefields . . . 152
5.10 Appendix 2: Benchmarking ELEGANT and PLACET particle tracking codes for Long Range Wakefields . . . 154
References for Chapter 5 . . . 156

Theme 2: Exceptional X-ray pulse qualities including 'laser-like' x-rays 161

6 FEL and undulators 161
6.1 Outline . . . 161
6.2 Photon Parameter Requirements . . . 162
6.3 Proposed FEL Methods . . . 162
6.3.1 Transform-Limited Pulses . . . 162
6.3.2 Two-colour Pulses . . . 171
6.3.3 FEL-1: High Photon and Pulse Energies for Extreme Environments . . . 173
6.4 FEL Section Design . . . 174
6.4.1 FEL Tuning Ranges . . . 174
6.4.2 FEL Schematic . . . 175
6.4.3 Electron Beam Requirements . . . 175
6.4.4 Parameter Summary . . . 178
6.5 FEL R&D and Performance Studies . . . 178
6.5.1 Optimisation of HB-SASE . . . 178
6.5.2 Comparative Study of Self-Seeding, HB-SASE and Hybrid Scheme . . . 181
6.5.3 HB-SASE in the HXR. . . . 187
6.5.4 Tapering for High Pulse Energy . . . 187
6.5.5 Transform Limited Short Pulses . . . 188
6.5.6 FEL-1 Performance . . . 191
6.5.7 Harmonic Lasing . . . 191
6.6 Summary of Predicted FEL Performance . . . 196
6.6.1 Transform Limited Pulses . . . 196
6.6.2 FEL-1 Pulses . . . 196
6.7 Undulator Technology . . . 199
6.7.1 Undulator Fundamentals . . . 199
6.7.2 Undulator Technologies . . . 199
6.7.3 Choice of UK XFEL Undulator Technology . . . 204
6.8 Summary of Technology Development Requirements . . . 207
6.9 Sustainability Choices and Future Prospects . . . 208
References for Chapter 6 . . . 210

7 X-ray Beamlines and Diagnostics 215
7.1 Summary . . . 215
7.2 Introduction . . . 215
7.3 Source model . . . 216
7.4 Common beamline components . . . 219
7.4.1 X-ray mirrors . . . 219
7.4.2 Focusing optics - Compound refractive lenses . . . 221
7.4.3 Focusing optics – Kirkpatrick-Baez mirror systems . . . 221

DRAFT

7.4.4 Focussing optics - other options . . . 223
7.4.5 Collimating optics . . . 223
7.4.6 Monochromators . . . 224
7.4.7 Beam attenuators . . . 226
7.5 Pulse length effects . . . 230
7.6 Optical design concepts . . . 232
7.6.1 Optical design concept for FEL-5; Attosecond and RIXS end-stations . . . 232
7.6.2 Multi-colour x-ray from FEL-5 and FEL-2 combined . . . 240
7.7 Photon diagnostics . . . 244
7.7.1 Pulse energy by x-ray gas monitors . . . 246
7.7.2 Scintillating intensity and profile monitors . . . 247
7.7.3 Laser power and energy meters . . . 248
7.7.4 Pulse spectrum diagnostics . . . 249
7.7.5 Temporal diagnostics . . . 255
7.7.6 Wavefront diagnostics . . . 257
7.7.7 Commissioning diagnostics . . . 259
7.8 Sustainability . . . 260
7.9 Summary of development areas; R&D needed for future phases to meet specification 261
7.10 Conclusions . . . 262
References for Chapter 7 . . . 263

Theme 3: World-class end stations, synchronous sources, data and AI 268

8 End stations 268
8.1 Introduction . . . 268
8.1.1 Chapter outline . . . 268
8.1.2 Design methodology . . . 268
8.1.3 User and facility engagement process . . . 269
8.2 Overview of end stations for UK XFEL . . . 270
8.2.1 ES1 (AMO) and (ES3) Attosecond . . . 272
8.2.2 ES2, ES5, ES8: Soft X-ray, ambient pressure and hard X-ray PES . . . 275
8.2.3 X-ray spectroscopy and scattering (ES4, ES6 and ES7) . . . 281
8.2.4 ES9 - Hard X-ray Coherent Scattering . . . 287
8.2.5 ES10 - Time-resolved SFX . . . 289
8.2.6 ES11 - Multi-colour end station . . . 292
8.2.7 ES12 and ES13: MEC and Very hard X-ray scattering (FEL-1) . . . 294
8.3 General requirements and support services . . . 299
8.3.1 Control rooms . . . 299
8.3.2 Support laboratories . . . 299
8.3.3 Standarisation of key equipment . . . 299
8.4 Summary and Recommendations . . . 300
References for Chapter 8 . . . 302

9 Synchronous sources 309
9.1 Introduction, scope and assumptions . . . 309
9.2 Motivation . . . 309
9.3 Optical sources . . . 310
9.3.1 Required specifications . . . 311
9.3.2 State of the art . . . 311
9.3.3 Few-Femtosecond Pulses - Resonant Dispersive Wave Sources . . . 316
9.3.4 Attosecond Pulses - High Harmonic Generation . . . 318

DRAFT

9.3.5 Diagnostics . . . 318
9.4 THz . . . 319
9.4.1 Laser based sources . . . 320
9.4.2 Beam-based THz sources . . . 323
9.4.3 Summary . . . 325
9.5 High power and high energy lasers . . . 326
9.5.1 Introduction . . . 326
9.5.2 State-of-the-art . . . 326
9.5.3 Future directions . . . 328
9.6 Sustainability . . . 328
9.7 Summary of technology development areas, R&D needed for future phases to meet spec . . . 329
References for Chapter 9 . . . 330

10 Detectors **333**
10.1 Summary . . . 333
10.2 Introduction . . . 333
10.3 Overview . . . 334
10.4 Large Area X-ray Detectors . . . 334
10.4.1 Sensor Material . . . 337
10.4.2 Low Energy X-ray Sensor Materials (0.05 to 4 keV) . . . 337
10.4.3 Tender X-ray Sensors Materials (4 to 15keV) . . . 341
10.4.4 Hard X-ray Sensors Materials (15 to 40keV) . . . 341
10.4.5 Readout ASICs . . . 344
10.4.6 Interconnect and Arrays . . . 347
10.5 Strip Detectors . . . 349
10.6 Fast and Timing Measurements . . . 350
10.7 X-ray Spectrometers . . . 351
10.8 Electron and Ion Detection . . . 352
10.9 Data Handling in the Detector System . . . 354
10.10 Sustainability of Detector Systems . . . 355
10.11 Operations and Practicalities . . . 356
10.12 Summary and Recommendations . . . 357
References for Chapter 10 . . . 359

11 Synchronisation **363**
11.1 Introduction . . . 363
11.2 Synchronisation architecture . . . 364
11.2.1 Reference oscillator . . . 365
11.2.2 Stabilised clock distribution . . . 366
11.2.3 Client locking . . . 369
11.2.4 Arrival time measurement and control . . . 370
11.2.5 X-ray photon arrival monitors . . . 375
11.2.6 Recommendations . . . 377
11.3 Timing . . . 378
11.4 Sustainability . . . 379
11.5 Summary of R&D recommendations . . . 379
References for Chapter 11 . . . 382

12 Data management and artificial intelligence **385**
12.1 Outline . . . 385

12.2 Introduction . . . 385
12.3 Facility data handling . . . 386
12.3.1 Data rates and pipelines . . . 387
12.3.2 High performance computing and storage . . . 388
12.3.3 Policies and management . . . 389
12.4 Artificial intelligence, machine learning and digital twins . . . 391
12.4.1 Pre-experiment design . . . 392
12.4.2 Optimal beam operations . . . 394
12.4.3 Data reduction and decision-making . . . 396
12.4.4 Post-experiment analysis . . . 396
12.4.5 Implementation challenges and opportunities . . . 397
12.4.6 Connections to AI in the Science and Technology Case . . . 398
12.4.7 Connections to the UK's AI ecosystem . . . 398
12.5 Sustainability . . . 399
12.6 Conclusion . . . 400
References for Chapter 12 . . . 401

Engineering delivery, environmental sustainability, and project planning **403**

13 Facility delivery **404**
13.1 Engineering Delivery – General Layout, Buildings, Infrastructure and Technical Systems . . . 404
13.1.1 Summary . . . 404
13.1.2 Introduction, Scope and Assumptions . . . 404
13.1.3 Comparison of Other Reference Facilities . . . 405
13.2 UK XFEL Conceptual Design Options – Layout, Build & Construction . . . 409
13.2.1 Injector Hall . . . 410
13.2.2 Linac Hall . . . 413
13.2.3 Spreader, FEL Hall & Photon Transports . . . 416
13.2.4 Experimental Halls . . . 421
13.2.5 Site wide infrastructure . . . 425
13.2.6 Radiation safety, shielding and beam dumps . . . 430
13.2.7 Alignment/ Stability and Geotechnical, Land and Environmental Considerations . . . 436
13.2.8 Power and Cooling . . . 441
13.2.9 Engineering Sustainability . . . 446
13.2.10 Summary of technology development areas, R&D needed for future phases to meet specification . . . 446
References for Chapter 13 . . . 448

14 Environmental sustainability analysis **450**
14.1 Introduction . . . 450
14.2 Grid intensity . . . 453
14.3 Operation . . . 454
14.4 Construction . . . 456
14.5 Maintenance . . . 457
14.6 End of life . . . 458
14.7 Conclusions . . . 458
References for Chapter 14 . . . 459

DRAFT

15 Project delivery **460**
15.1 Project Delivery and management 460
15.1.1 Requirements 460
15.1.2 Governance, Approvals, and Funding during Pre-Operations 461
15.1.3 Systems integration 461
15.1.4 Organisational Design and Development 462
15.1.5 Procurement Strategy 463
15.1.6 Risk Management 464
15.1.7 Delivery Planning 464
15.1.8 Technical design phase 465
15.1.9 Site Selection 466
15.2 Construction & phasing strategy 468
15.2.1 Timelines and stages 468
15.2.2 Transition to operations 471
15.3 Conclusions 471
References for Chapter 15 473

DRAFT

1 Executive summary

XFELs are an extraordinary tool for science: the world's most advanced X-ray sources, a billion times brighter than any other, enabling atomic-level imaging and ultrafast time resolution far beyond other methods. This report presents the conceptual design of a 'next-generation' XFEL facility that meets the ambitious requirements of the UK Science and Technology Case. It represents a step-change in capability: a robust and efficient source of 3D-coherent X-rays, and laser-based sources, at unprecedented data-gathering rates for a broad community of simultaneous users.

Since the late-2000s, X-ray free-electron lasers (XFELs) have proven to be a radical technology breakthrough, providing X-rays that are many orders of magnitude brighter than other sources. **XFELs are now ready to enter a new era, characterised by substantial maturation of the technology, which can be leveraged to deliver world-leading, societally-relevant science at scale.** This will enable unprecedented atomic-level structure determination and nanoscale imaging across sectors such as defence, biotechnology, batteries, fusion, solar energy and catalysis. Most importantly, they will give access to the intrinsic timescales of physical, chemical and biological changes in matter, enabling studies of electronic and atomic motion on femtosecond (10^{-15} s) timescales or less, far beyond the nanosecond (10^{-9} s) limit of synchrotrons.

Building on experience from pioneering XFEL facilities, **this report sets out a conceptual design to make a true generational step,** as shown in Figure 1.1 and Figure 1.2. Its defining capabilities manifest throughout the facility and multiple disciplines. They encompass facility layout and operations (parallel operation of many FELs and end stations, MHz data management); X-ray photon output (3D-coherent pulses at femtosecond to attosecond (10^{-18} s) scales, extremes of photon energy and pulse energy, and advanced two-colour modes); and technologies from photoinjectors and linacs to high-power optical lasers, synchronisation systems and detectors.

Figure 1.1: Site visualisation of the next-generation XFEL facility.

A fundamental feature of this project is that, from the outset, the design has been considered through the lens of either creating an entirely new facility or by upgrading existing machines. **The approach has been to think independently of location or infrastructure constraints: setting out a vision for an internationally leading XFEL facility on a 10-15 year outlook, to meet the next-generation specification in the most efficient way possible.** This ensures the conceptual design is relevant to multiple future pathways, including scalable options for a new UK or international facility and substantial upgrades to existing facilities, as outlined in the UK XFEL Options Analysis, with a high level of flexibility to meet emerging priorities.

Next-generation XFELs operating at MHz will be some of the biggest data-generating capabilities on the planet, operating at 100 kHz - 1 MHz and coupling rapid advances in accelerator, laser, detector and end-station technologies with the emergence of AI and exascale computing. The design integrates established MHz-class electron gun technology with a novel injector configuration and dual-injector layout for optimal beam quality, redundancy and advanced double-bunch capabilities. The injectors feed into a high-energy 8 GeV superconducting linear accelerator, in line with other modern projects, to deliver pulse rates 10,000 times higher than the normal-conducting RF technology used in most first-generation XFELs. Coupling XFEL experiments with AI-enabled data pipelines can translate unprecedented data throughput to future discoveries and foundation models across a host of disciplines.

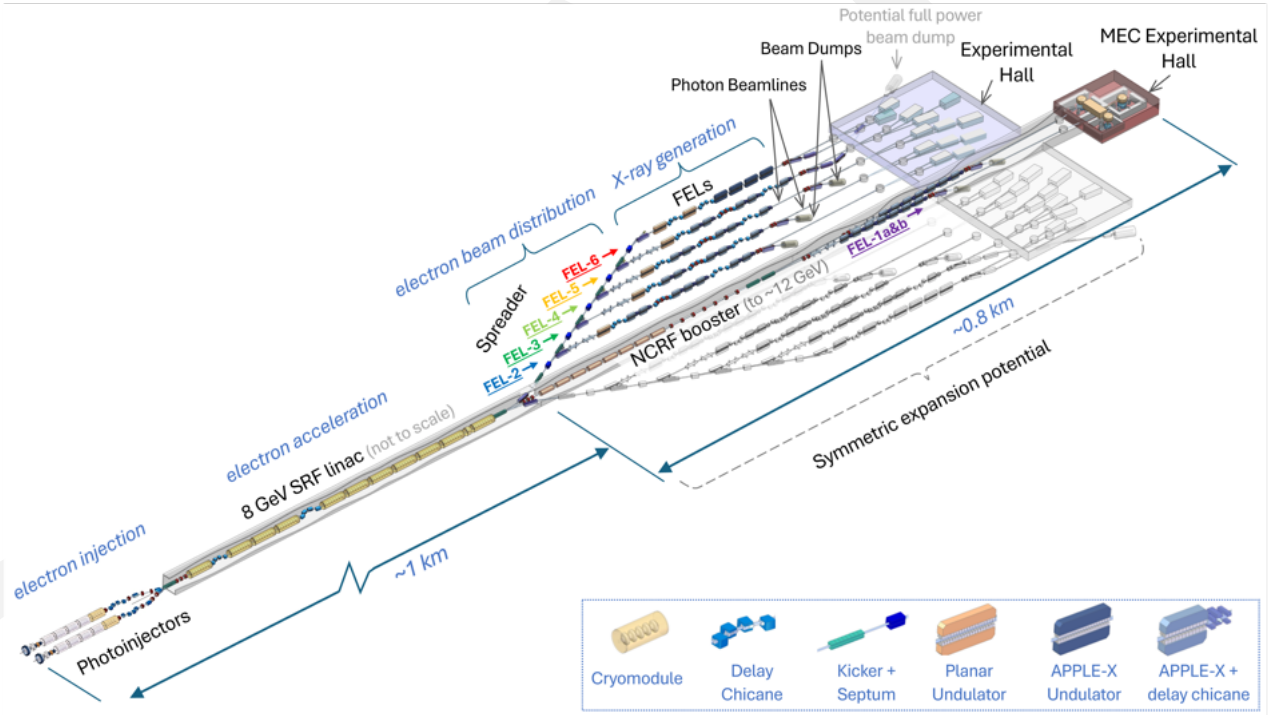

Figure 1.2: An outline of the conceptual design for a next-generation XFEL providing a unique combination of capabilities to meet the requirements of the Science and Technology Case.

To enable rapid progress across many fields, the next-generation XFEL is designed to provide a step-change in throughput and capacity compared to existing machines. Whereas current facilities support only 1-3 simultaneous experiments, this design sets out how to realise the ambition to support 10 or more, and so become more synchrotron-like in terms of throughput. This will significantly shorten the intervals between related experiments, and bring down their cost. To achieve this, the facility design is robust and highly modular in terms of design and civil engineering, with redundancy built in. Since the front end is critical to all later systems, the emphasis is on reliability and high technology readiness level, while the transformative impacts of digital twinning and robotics will be instrumental throughout.

Increased throughput will enable world-class mission-driven and community-driven experimental campaigns, while translating today's state-of-the-art techniques into on-demand measurements for industrial applications. By branching into separate lines and experimental areas, the facility is designed to progressively engender increased specialisation and experimentation. A comprehensive suite of end stations has been developed through an extensive community-guided process - each has been associated with a particular FEL and has its own unique capabilities to deliver world-class science.

Advanced FEL techniques will be used to produce exceptional X-ray pulse qualities, including high quality 'laser-like' 3D-coherent pulses at up to $\sim$100 kHz in up to 10 independently operable FEL lines, as well as a specialised capability for widely separated two-colour pulses (e.g. soft X-ray + hard X-ray). The X-ray pulses will be coupled with **a comprehensive suite of optical lasers and other sources** to initiate and probe a multitude of ultrafast effects. There is also a specialised 'hybrid' aspect to the accelerator design, in that it includes a normal-conducting 'booster' in the straight ahead ('FEL-1') line, to enable extremes of photon energy and energy per pulse for two dedicated stations that combine X-rays and extremely high power and high energy optical lasers. **This will be a cutting-edge platform for studying matter in extreme conditions, for a range of applications.**

An electron beam R&D line will provide a continuous pipeline of novel electron and photon beam enhancements throughout the facility's lifetime. Plasma wakefield acceleration and related techniques offer potential to extend XFEL capability, ensuring a long-term competitive edge beyond the initial design. The design also has potential to re-use the electron beam to expand user reach further into disciplines such as high-energy physics.

Environmental sustainability has been embedded into the project from the outset, maximising the opportunity to secure long-term benefits. Each technical area has identified its most promising sustainability-enhancing technologies and approaches. These are brought together in a holistic study that examines the full lifecycle of the facility, incorporating broader influences such as grid intensity and user travel to assess and reduce the project's overall environmental footprint.

A next-generation XFEL will be a large-scale and long-term project: a £-billion-scale investment, with the new-build option occupying a land footprint of approximately 2 $\times$ 0.25 km. For a facility of this scale and ambition, it is essential, even at this conceptual phase to assess detailed engineering and project planning considerations to ensure successful realisation, and this work is reported.

While this project is a UK initiative, **the aim of realising the next generation of XFELs is a truly international endeavour**, towards which many international collaborators are engaged. This conceptual design is a blueprint for an ambitious new generation of XFEL facilities. Access to such a facility would be transformational to the international light source community, while attracting new generations of users to ultrafast X-ray science for decades to come.

DRAFT

2 Introduction

The advent of X-ray free-electron lasers (XFELs) is one of the defining technological achievements of the 21st century to date, producing X-ray pulses a billion times brighter and over ten thousand times shorter than any other source, unlocking access to the ultrafast world across disciplines. This report describes the Conceptual Design for a Next-Generation XFEL, building on maturing technologies and techniques to chart a route to unprecedented capability. This chapter provides an introduction to the Conceptual Design, to the underlying XFEL principles, and explains how UK user aspirations translate into the specification for a next-generation facility.

In many respects, XFELs are a new class of X-ray source compared to preceding technologies such as synchrotrons, representing far more than an incremental advance. The first light from an XFEL in 2009 [1] is still a relatively recent development, and it has been followed by an extraordinarily pioneering period, marked by rapid advances in XFEL operating modes and entirely new classes of experiment. As existing facilities now look towards future upgrades and key technologies reach maturity, it is an opportune time to assess the future of these facilities and their place in the wider scientific ecosystem, in conjunction with the updated UK XFEL Science and Technology Case.

The starting point for the next-generation XFEL design was defining the capabilities required of such a facility, which was one of the key outcomes from the *2020* Science Case [2]. These criteria inherently emphasise frontier, large-scale XFEL facilities, as the scale offering the most effective route to advancing scientific capability. Concurrent efforts to downsize XFELs could provide a highly complementary type of source.

This first chapter introduces the principles of XFEL operation, which is important to inform some of the decisions described in later sections. It also explores in more detail what is meant by 'next-generation' and outlines how this definition was translated into a machine specification through an extensive consultation process centred on the Science and Technology Case.

The Conceptual Design is then described in depth, starting in Chapter 3 with a facility-wide overview of its main features and the key cross-facility decisions behind them. The detailed conceptual design is then divided into key accelerator, photon and instrument systems in Chapters 4 to 12. Each system component is evaluated against the relevant next-generation design criteria and the current state-of-the-art, in order to identify the development gap to be addressed.

Consideration is given to the most effective and environmentally sustainable technologies which achieve performance targets, and a holistic assessment of sustainability is provided in Section 14.1. Chapter 13 outlines the engineering of the next-generation XFEL, including the major technical systems and their integration, while Chapter 15 describes the project-delivery framework to realise such a facility.

By definition, there is no exact precedent for a next-generation XFEL, and its realisation depends on resolving a broad set of research and development challenges; the key R&D steps are outlined in each chapter. The report also describes potential upgrade paths that can match emerging technologies with evolving priorities throughout the facility's lifetime.

DRAFT

2.1 Introduction to XFELs

The performance of existing XFEL facilities is well-established and well-understood: the remarkable X-ray lasing process results in extraordinary peak brightness and attosecond to femtosecond-scale pulses across an exceptional spectral range, but it presents challenges in terms of capacity and stability compared to other types of large-scale accelerator facility, such as synchrotrons. There are clear routes to resolve these challenges in the next generation of machines, alongside other enhancements, building on the pioneering work at existing XFELs.

Reviews of the XFEL facility landscape, detailing the present status and future plans of existing facilities are provided in both the Science and Technology Case (in Section 2.4) and Options Analysis (in Chapter 5). This section provides a more generic introduction to XFELs, their strengths, and opportunities for improvement in the next generation. Readers are also referred to other reviews on these topics [3, 4, 5, 6, 7] and a comprehensive history of UK contributions to the field [8].

2.1.1 Free-electron lasers

Free-electron lasers (FELs) were first introduced [9] and demonstrated (at optical wavelengths) [10] in the 1970s. Unlike a conventional laser, the electrons in a FEL are not bound in discrete energy levels within the gain medium but are unbound ('free') particles in a relativistic electron beam. Consequently, a FEL is smoothly tunable and *the scaleable physics of the FEL mechanism allows them to be developed at any wavelength from THz to X-ray.*

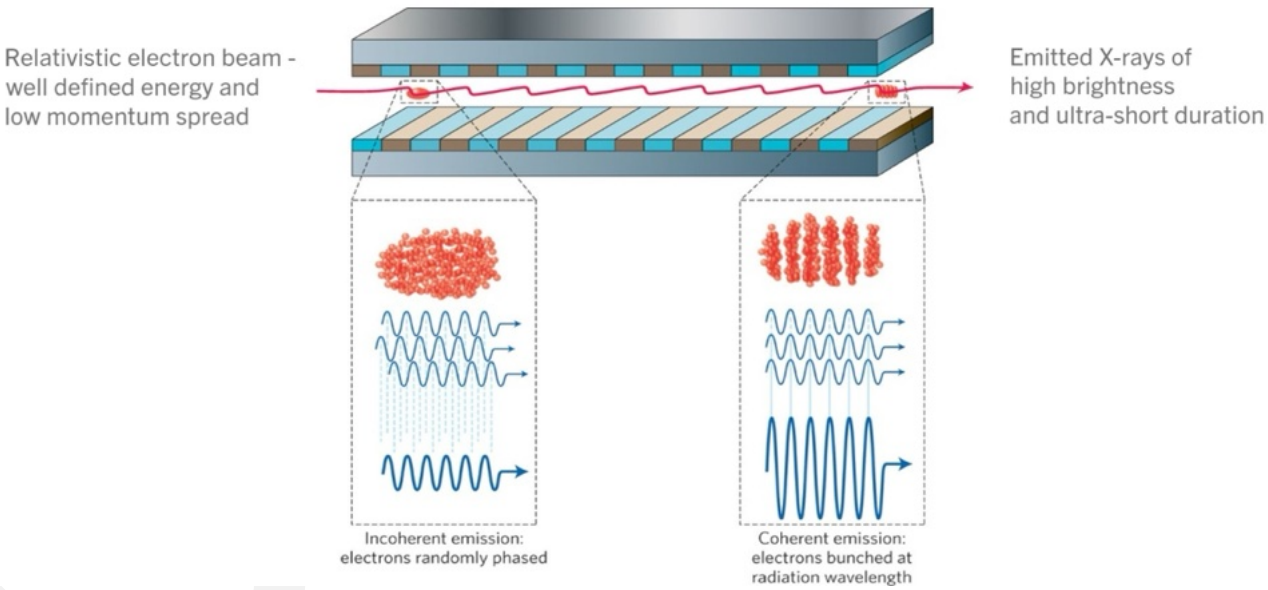

Figure 2.1: Schematic of the FEL mechanism. Bunches of randomly phased relativistic electrons propagate through a long array of alternating polarity dipole magnets (an undulator), which causes them to oscillate transversely and emit radiation. The transverse electric field of the co-propagating radiation couples to the electron transverse velocity allowing an energy exchange. This enables a positive feedback process in which the electrons start to micro-bunch, coherently enhancing their emission, which acts back on the electrons further enhancing the micro-bunching, and so on, giving an exponential growth of the radiation intensity. Figure reproduced from [3].

The key feature that separates FELs from other sources of synchrotron radiation (SR) such as storage rings (synchrotrons) is the *lasing* effect: a positive feedback process in which electrons self-organise and radiation is exponentially amplified. This process is depicted schematically in

Figure 2.1, which shows a high-quality bunch of relativistic electrons propagating through an array of alternating polarity dipole magnets (an undulator).

The undulating changes of direction of the electrons cause emission of electromagnetic radiation, which is highly concentrated around the central axis in the forward direction, due to the relativistic speed of the electrons. The radiation is emitted at a resonant wavelength, $\lambda_r \approx \frac{\lambda_u}{2\gamma^2}$, at which the radiation propagates ahead of the electrons at a rate of one radiation wavelength per undulator period, λ_u. The Lorentz factor of the relativistic electrons is $\gamma = E/mc^2 = E\,[\text{GeV}]/0.511\times10^{-3}$ GeV, such that for typical values of λ_u on the scale of a few centimetres, *electron beam energies on the order of ∼5-10 GeV are required to access hard X-ray wavelengths*.

Except for recent breakthroughs [11], X-ray FELs amplify light in a single pass of a long undulator, with various operating modes, usually based on the effect of *self-amplified spontaneous emission* (SASE) [12]. At the start of the undulator, the electrons (within femtosecond-scale bunches) are randomly distributed at the (attosecond) scale of the emitted radiation wavelength. Their radiation emission is therefore incoherent and its intensity scales linearly with the number of electrons, as is the case for radiation emitted in synchrotrons.

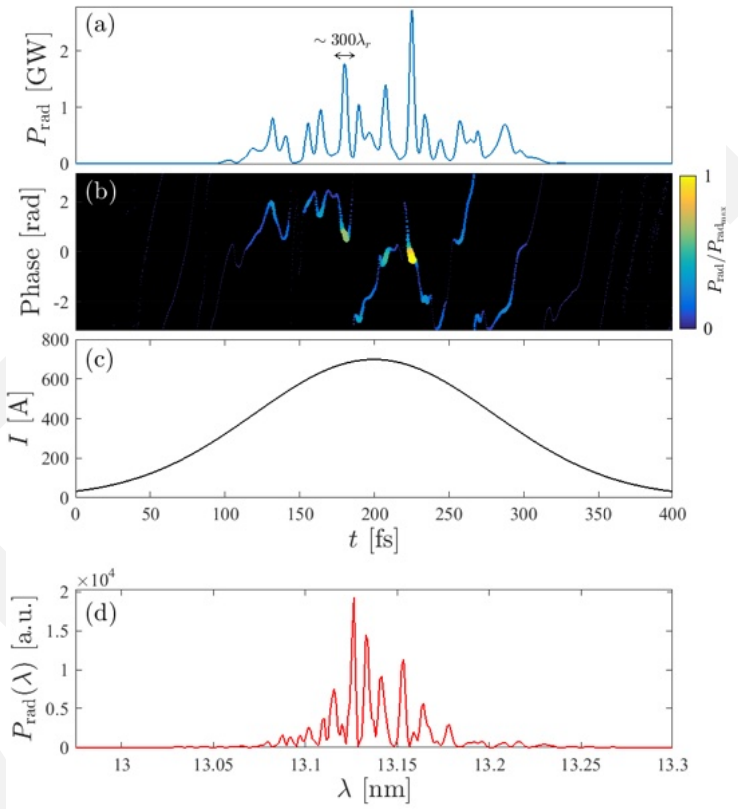

Figure 2.2: Example SASE properties. The figure shows simulation results for a high-gain SASE FEL with parameters similar to FLASH [13]. Results are shown at saturation: (a) radiation temporal profile comprising multiple spikes; (b) radiation phase showing phase correlation within but not between spikes; (c) the idealised Gaussian current profile used in the simulation and (d) the radiation spectrum, also comprising multiple spikes. Figure reproduced from [14].

XFELs differ from synchrotrons in that the emitted radiation interacts with the electrons to modulate their energy at the radiation wavelength, causing the electrons to form into micro-bunches separated at this scale. The emission is then *coherent*, with intensity scaling as N^2, and narrow-bandwidth, with brightness enhanced $\propto N$ compared to the incoherent emission, where N is the number of electrons emitting collectively (typically $\geq 10^6$ for X-ray FELs). The amplification process results in almost full transverse coherence, and because linear accelerators

for FELs deliver bunches with very high peak current, FEL output peak brightness (with units photons/s/mm^2/mrad^2/0.1% bandwidth) can exceed that of synchrotrons by at least eight orders of magnitude.

The disadvantage of SASE is that, by starting from random density variations in the electron bunch, this noisiness can translate into the photon output. Because the radiation propagates forward relative to the electrons, it has a smoothing effect, leading to temporally coherent regions of typically a few hundred radiation wavelengths (e.g. ∼100 attoseconds at hard X-ray). However, the electron bunch is usually longer than this, such that the output pulses comprise a series of random phase-uncorrelated spikes [15, 16]. A simulated typical SASE pulse, and its properties, is illustrated in Figure 2.2. Several methods to improve pulse quality have been demonstrated or proposed, as described in the following sections.

2.1.2 XFEL performance strengths

Because of the X-ray lasing mechanism described above, XFELs have extraordinary output properties. By operating at different electron beam energies and with a range of different undulators, XFELs can deliver coherent radiation across an **exceptional spectral range** (<10 eV to >20 keV), with **narrow bandwidth** (∼0.1% relative to peak photon energy) and **very energetic** (millijoule or ∼10^{12} photons per pulse) **short pulses** (∼1 fs duration), and therefore with **exceptional peak brightness**.

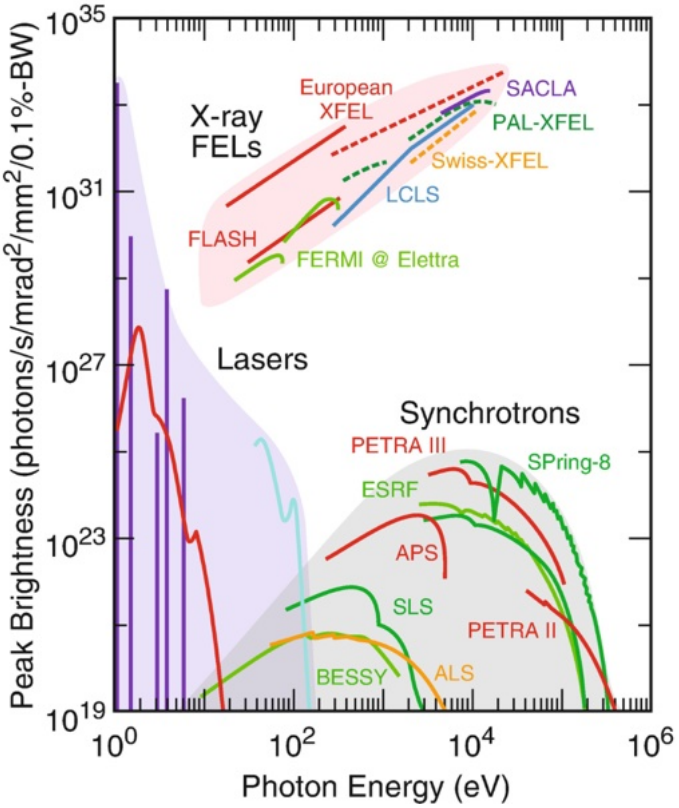

Figure 2.3: Comparison of XFELs, synchrotrons and lasers in terms of peak brightness across their operational photon energy ranges. Figure reproduced from [17].

FELs produce this output at the fundamental (resonant) frequency, and with content at three- and five-times that frequency etc. (i.e. odd harmonics), with the photon number dropping by a factor of around 100 at each odd harmonic step. This is a vastly wider spectral range than that covered

by conventional lasers, and the pulses are typically a hundred thousand times shorter and a billion times brighter than the latest upgraded synchrotron light sources can provide. Figure 2.3 shows a comparison of XFEL peak brightness against that of lasers and synchrotrons, across their operational photon energy ranges.

In addition, enormous progress has been made in developing new FEL techniques for **improved pulse quality** that are continually advancing the scientific reach of XFELs. These include two-colour, two-pulse X-rays; variable polarization states; high spectral purity X-rays; higher brightness X-rays; and attosecond X-ray pulses. Many of these new capabilities go beyond SASE by manipulating the electron bunch (e.g. pre-modulation of its density or controlled spoiling of its quality) prior to it entering the undulator. Even so, this remains an area with opportunity for further development, as described in the following section. Figure 2.4 shows a comparison of experimentally demonstrated isolated attosecond pulses from FELs, showing orders of magnitude enhancements in photon energy and pulse energy compared to HHG sources.

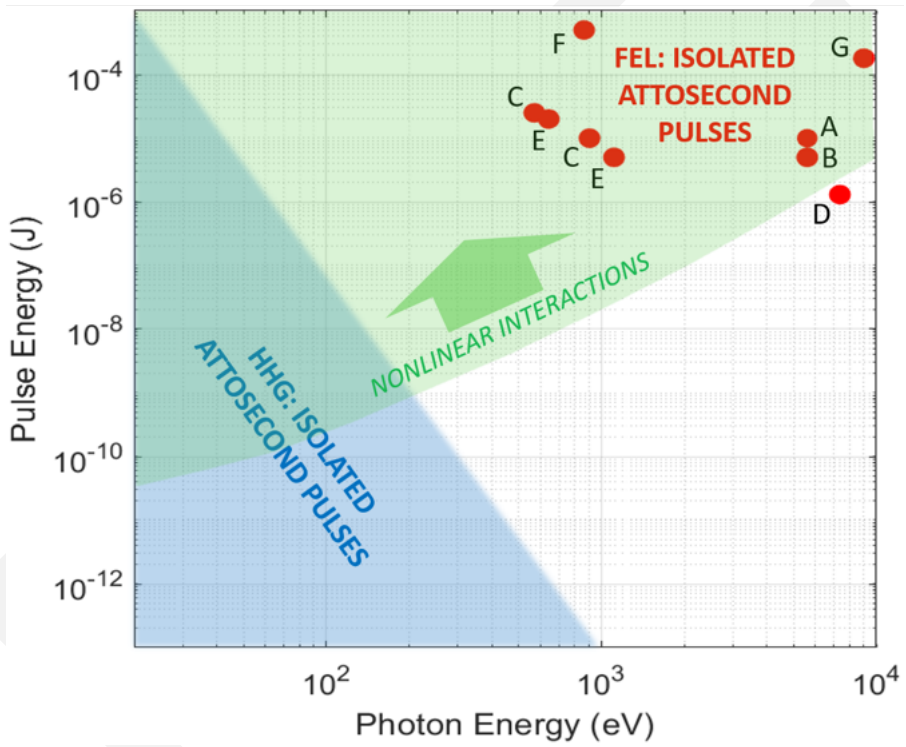

Figure 2.4: Experimentally demonstrated schemes for generating isolated attosecond pulses from XFELs, showing orders of magnitude enhancements in photon energy and pulse energy compared to HHG sources, thus extending access to the study of non-linear interactions for users. Schemes shown are as follows: A [18], B [19], C [20], D [21], E [22], F [23], G [24] Figure adapted from [25].

.

2.1.3 XFEL challenges and opportunities

Some of the main challenges of XFEL operation also arise from the lasing mechanism described above. Because the lasing effect is so intense, it has a major effect upon the emitting electron bunch. As well as a net loss of energy, given to the photon output, there is a significant increase in the spread of energies within the electron bunch. This spoils the electron bunch quality, to the point that it cannot be re-used for lasing. This is a major point of difference to synchrotrons, in which the same electron bunch can emit many times. This difference means that while synchrotrons are based on circular machines (typically 0.5-2 km in circumference), XFELs are based on linear

machines (typically 1-3 km in length). In an XFEL, each electron bunch is single-use (or at most used only a few times in some advanced techniques), i.e. they are generated, accelerated, used for lasing and then dumped. Single-pass operation allows higher beam quality than the equilibrium conditions reached over many passes in a circular machine but it presents a different set of challenges:

2.1.3.1 Capacity

The differences outlined above have implications for the capacity of each type of facility. As shown in Figure 2.5, modern synchrotrons typically have ∼30 X-ray source points (and a corresponding number of simultaneous experiments) operating from circulating electron bunches, whereas present FELs operate with 1-3 X-ray source points (and corresponding experiments). Another reason for this difference in capacity is that synchrotrons are a much more long-established technology (dedicated X-ray facilities have existed since the early 1980s), whereas XFELs have much scope for improvement in this respect. Therefore a next-generation XFEL is specified to provide a step-change in capacity compared to existing machines, as discussed in the following section.

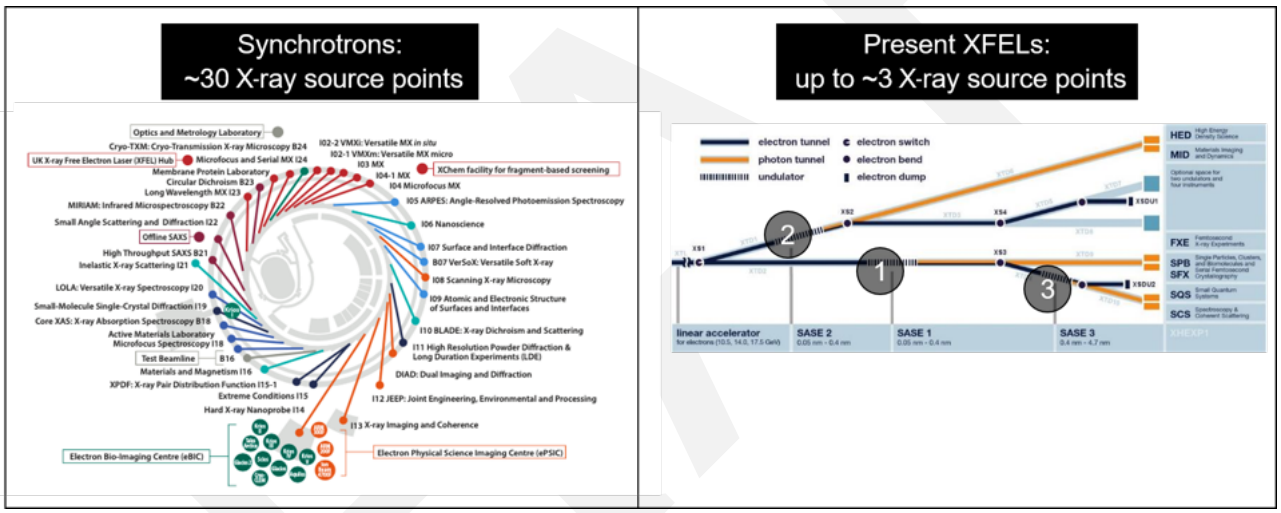

Figure 2.5: Comparison between the capacity of present synchrotron facilities (left, courtesy of Diamond Light Source), and XFELs (right, courtesy of European XFEL).

Over the course of the UK XFEL Conceptual Design and Options Analysis (CDOA) phase of the project, there has been growing international consensus around increasing capacity as an important direction for XFELs, as described in the Options Analysis (Chapter 5). European XFEL [26, 27], while currently operating with three FELs, has tunnel space for five and could potentially add more. LCLS-X, a US concept for a next-generation XFEL [28] envisages ten specialised XFELs (optimised to different science areas) with dozens of end stations to enable multiple parallel experiments.

2.1.3.2 Repetition rate/average brightness

A defining feature of XFEL development for this project is the progression from normal conducting RF (NCRF) linear acceleration (linac) technology (operating at ∼100 Hz) to the increasing usage of superconducting RF (SRF) linac technology. European XFEL is based on SRF linac technology developed through the TESLA collaboration [29], led by DESY – to accelerate trains of up to 2700

electron bunches within one 600 µs-long RF pulse. Using a 10 Hz RF pulse repetition rate, up to 27 000 electron bunches and photon pulses can be produced each second in a burst-mode structure. LCLS-II(+HE) [28] and SHINE [30] are taking this technology to the next step by implementing 1 MHz continuous operation. The implications are immense in terms of scientific

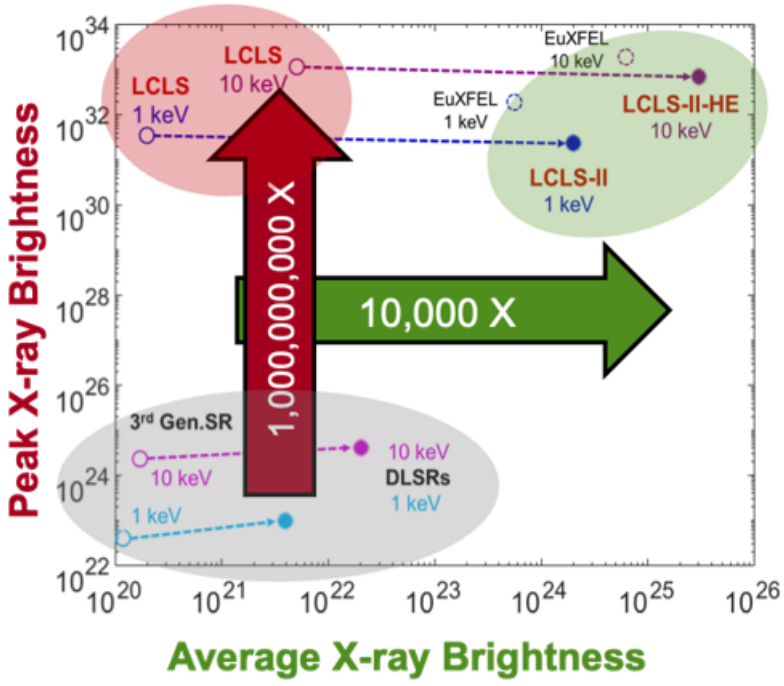

Figure 2.6: The advance of XFELs relative to synchrotrons in terms of peak brightness (already demonstrated) and average brightness - enabled by MHz repetition rate. Figure courtesy of LCLS [31].

opportunity, enabling orders of magnitude increases in data rates and average brightness, as shown in Figure 2.6. There is a similar impact in terms of capacity: MHz repetition rate offers greater scope for multiplexing to many simultaneous experiments with high flux. Many interrelated technical systems must advance in step to realise these benefits, e.g. photoinjectors, kicker magnets, FEL techniques, laser systems, sample delivery systems, detectors, data infrastructure; so it is a common theme throughout this report.

2.1.3.3 X-ray pulse qualities

Despite enormous progress in developing new FEL techniques, one of the the primary challenges for a next-generation XFEL is to generate stable X-ray pulses with full 3D-coherence across a very large parameter space. Most existing XFELs were not designed for this: their original intent was to operate in the default SASE [12] operating mode, which produces pulses that are spatially coherent but are noisy in their temporal and spectral output [15, 16].

Figure 2.7 shows an indicative comparison between the temporal profile of a SASE pulse, which has temporal coherence within its multiple spikes but not between them, and two pulses that are *transform-limited*. This term refers to the Fourier transform between temporal and spectral domains, with a transform-limited pulse representing the minimum possible pulse duration for a given spectral width (and vice versa), i.e. the time-bandwidth product is minimised. Figure 2.8 shows the trade-off between pulse duration and bandwidth (i.e. energy resolution) for transform-limited pulses, compared against typical SASE FEL and synchrotron output.

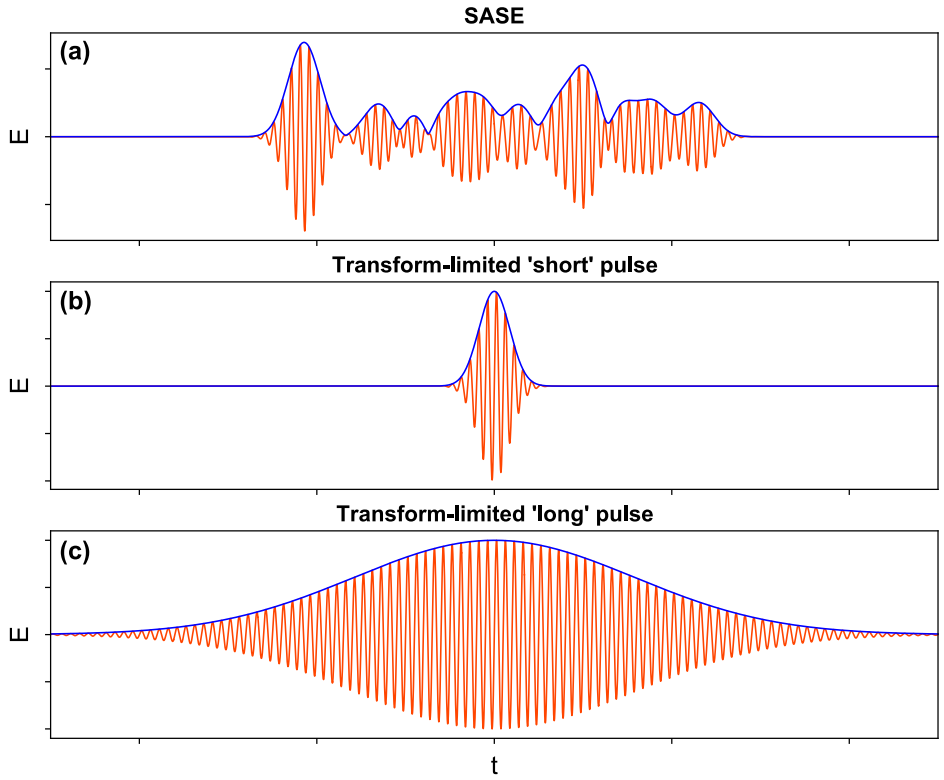

Figure 2.7: Indicative comparison between the temporal profile of (a) a SASE pulse (top) and two pulses that are transform-limited: (b) a 'short' pulse with duration similar to a single SASE spike, and (c) a 'long' pulse with duration similar to the full SASE pulse.

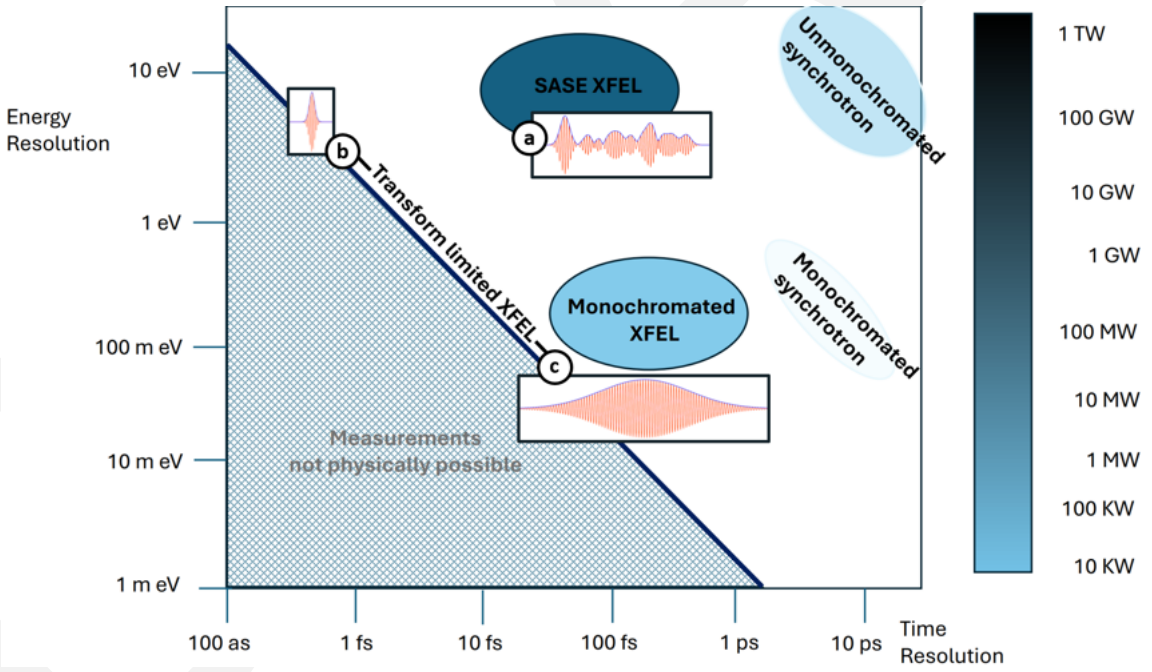

Figure 2.8: Science and Technology Case illustration of the requirement for near-transform-limited FEL operation across the X-ray range, compared to other sources. Indicative temporal profiles are superimposed for a SASE pulse (a), and transform-limited short (b) and long (c) pulses.

Essentially, transform-limited pulses have a smooth Gaussian-like envelope and continuous phase. The 'short' pulse shown in Figure 2.7 (b) represents ultra-short pulses, e.g. down to ∼100 as. The duration of a single SASE spike is typically hundreds of attoseconds at hard X-ray, and up to a few femtoseconds at 100 eV. Therefore coherent ultra-short pulses on these scales can be

realised using FEL techniques that work by selectively enhancing or spoiling the electron bunch to generate just one of these inherent spikes.

The 'long' pulse shown in Figure 2.7 (c) represents pulse durations up to ∼100 fs (tens of meV bandwidth). In this case, phase coherence must be established across the length of many SASE spikes. This is usually achieved through 'seeding' the FEL amplification process with a coherent external laser source or 'self-seeding' by monochromatising the FEL radiation during amplification. This produces much higher power than the post-monochromated FEL shown in Figure 2.8.

The international XFEL community has been extremely innovative in developing new techniques and many such schemes are well-established at international XFELs (described in Section 3.4.2). However, these methods have usually been applied retrospectively and are therefore constrained by existing accelerator infrastructure and initial design choices, whereas new FEL facilities can integrate them optimally from the outset.

In some cases there are significant challenges to operating these techniques at higher repetition rate compared to existing machines, in terms of e.g. laser requirements, detector limitations, and heating of optical components. But high repetition rate also enables more radical cavity-based modes [11], which use oscillator and regenerative amplifier concepts from laser technology and promise to provide unprecedented spectral brightness.

DRAFT

2.2 From the next-generation criteria to a facility specification

Starting with the 2020 Science Case [2], the project has considered all of the potential developments that would advance the science enabled by XFELs, resulting in a definition of the capabilities needed for a next-generation XFEL facility. Multiple rounds of engagement have been undertaken to develop these criteria into a specification, described in this section, upon which the conceptual design is based. These capabilities are described in Sections 2.5.1 and 9.1 of the updated Science and Technology Case, and are as follows:

- Near-transform-limited (TL) operation across the X-ray range
- High efficiency facility, with a step-change in the simultaneous operation of multiple end stations in parallel
- Evenly spaced, high repetition rate pulses to match samples, lasers, and detectors
- New AI approaches for data analysis and interpretation of vast data volumes generated
- Improved synchronisation/timing data with external lasers to <1 fs by harnessing state-of-the-art synchronization strategies and implementing the most advanced timing tools
- Widely separated, multiple colour X-rays to at least one end station by combining the outputs from two FELs
- Full array of synchronised sources including optical lasers + nonlinear optical conversion across the EM spectrum from XUV–THz, charged particle beams, high energy and high power lasers
- Environmentally sustainable facility meeting Net Zero targets

Dedicated rounds of engagement were carried out to establish more specific details for some aspects of the criteria, to form a specification on which to base the conceptual design. For example, the pulse repetition rate requirements for different photon energy ranges are vital for making top-level facility design choices (as described in Chapter 3). A **preliminary consultation** to this effect was carried out during the 2020 Science Case as shown in Figure 2.9. This gave indicative requirements from each science area but was not sufficiently definitive to guide the conceptual design.

To more fully inform the process, consultation with the UK user community took place in the form of a **comprehensive survey**, performed in the initial stages of the UK XFEL CDOA. The aim was to capture more details on the proposals made in the Science Case, plus new ideas, by gathering detailed case studies of ambitious experiments for a next-generation machine. The survey received approximately 70 responses, which provided details on X-ray properties such as repetition rates, photon energies, pulse energies, pulse durations, focusing requirements etc., as well as information about synchronous sources, end stations and detectors, for various scientific areas.

Figure 2.10 shows the mapping of parameters for proposed experiments from the survey (coloured dots) as a function of X-ray photon energy, repetition rate, and pulse energy (which is also an important factor for facility design choices). This information formed the basis for developing key aspects of the specification below.

Furthermore, a **detailed end station engagement process** during the CDOA phase has included focused technical workshops and targeted discussions with international instrument teams to establish a comprehensive initial provision of end stations for a next-generation XFEL, as described in Chapter 8. These have been developed to exploit the cutting-edge capabilities of the facility,

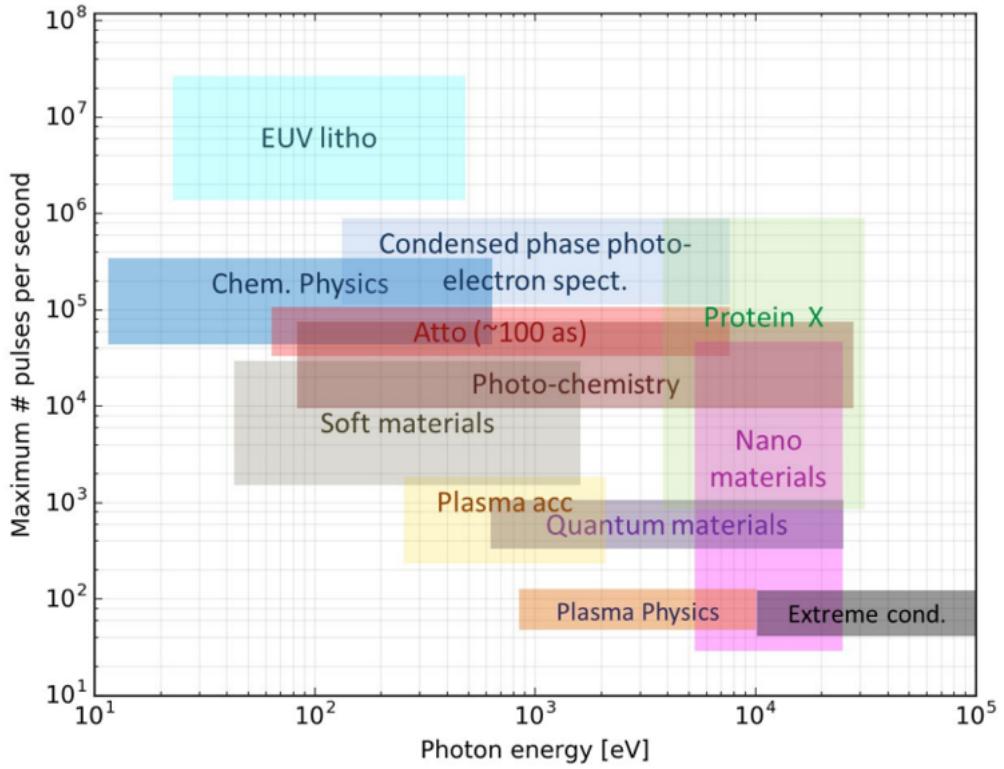

Figure 2.9: Photon energy and repetition rate requirements from the 2020 UK XFEL Science Case.

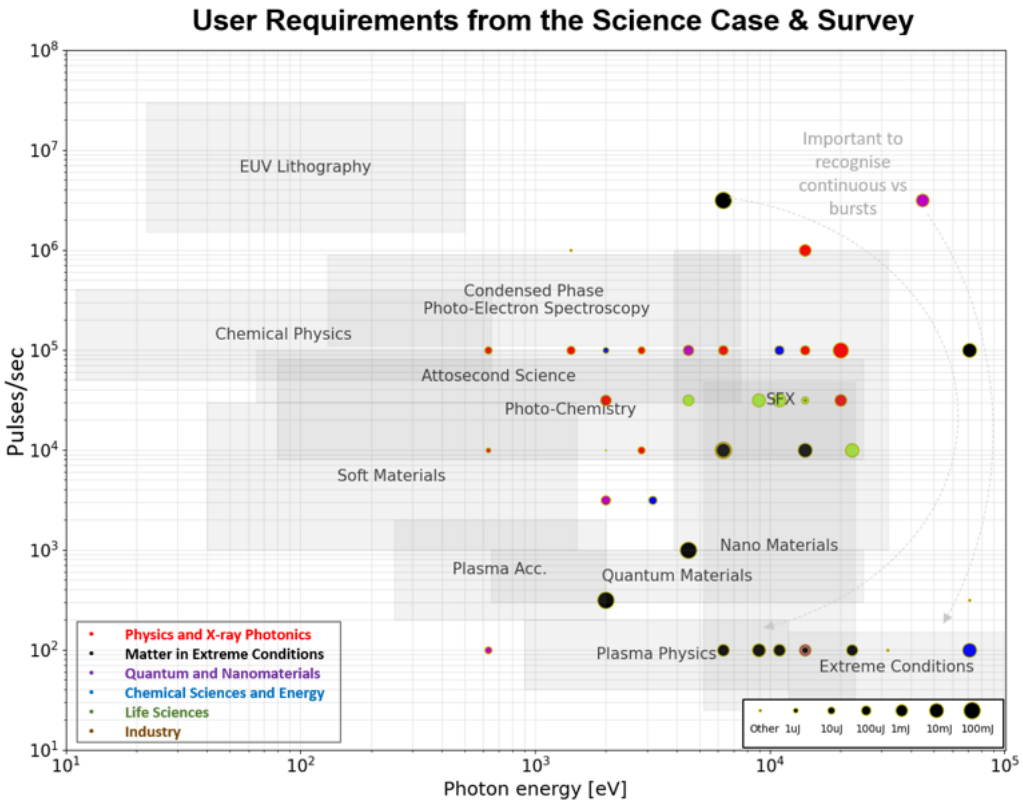

Figure 2.10: Photon energy, repetition rate and pulse energy requirements for the UK XFEL Conceptual Design. Science areas as indicated in the 2020 Science Case are shown as grey boxes; the results of a survey performed in 2022 are shown as coloured dots, with the legend indicating their science area.

with each one associated with a particular FEL design and having their own specific requirements, which have fed back into the conceptual design.

The first key set of factors is the **X-ray pulse repetition rate, pulse energy and pulse quality across different regions of the spectrum**. Based on the Science Case and survey responses, it was identified that the majority of users could be catered for by providing repetition rates up to ∼100 kHz (evenly spaced) per FEL, from ∼100 eV up to ∼20 keV. Most of these cases call for transform-limited pulses from ∼100 as up to ∼100 fs, and for (up to) high but not beyond state-of-the-art pulse energy (up to 1 mJ). The requirement for near transform-limited operation across the X-ray range can therefore be quantified.

Additionally, there is a set of cases that require either higher photon energies (∼20-45 keV) or very high pulse energy (10-100 mJ), e.g. for studies of matter in extreme conditions. These requirements are generally combined with the need for a different pulse timing structure - either low repetition rate (<200 Hz) or very short bursts of pulses (<10 pulses at >1 MHz repetition rate within the burst). *Understanding user requirements for burst modes is crucial to inform facility design choices:* for instance, it can be seen in Figure 2.10, that some experimental proposals specified >1 MHz repetition rate, but this refers to the repetition rate within a short burst, rather than continuous operation, which makes a major difference for the accelerator technology choice. The set of cases described here are also generally combined with a relaxed requirement in terms of pulse quality, i.e. the pulses do not need to be transform-limited.

The requirement for a **'high efficiency facility, with a step-change in the simultaneous operation'**, is more subjective. In the discussion of capacity in the previous section, it was recognised that modern synchrotrons have developed over decades to reach ∼30 X-ray source points (and a corresponding number of simultaneous experiments). Present XFEL facilities operate with 1-3 X-ray source points (i.e. 1-3 FELs), serving a pioneering and relatively small set of experiments (typically a few dozen per facility per year). Access to international XFEL facilities is significantly oversubscribed: established user groups are eager to reduce the waiting time between related experiments, while new communities are seeking timely access with lower barriers to entry. The benefits of reducing the cost per experiment are widely recognised, and a next-generation XFEL would be expected to support many hundreds of experiments each year.

Some capacity increases are likely to be achieved through a combination of increased repetition rates being used to reduce data collection times, improved automation capabilities, and a transition towards some experiment techniques becoming more routine. It could also help to share the photon output from each FEL to multiple end stations simultaneously, however this precludes independent tuning of the X-ray properties (e.g. photon energy) and limits how widely useful this approach can be. The number of independently operable FELs is still likely to be a major factor in defining facility capacity. Therefore the conceptual design targets a step-change in the number of FELs to at least 6, with capacity to reach 10 or more, and >10 end stations to be simultaneously operated.

The requirement for **widely separated, multiple colour X-rays to at least one end station** has been iterated with the Science Team throughout the course of the project. Recognising that two-pulse operation with closely-separated photon energies is already a mature capability, the requirement is for soft X-ray plus hard X-ray combination to at least one end station. It is also desirable to have the potential to add further instances of this capability.

Furthermore, to enable **new AI approaches for data analysis and interpretation of the vast data volumes generated** requires major development of data and computing systems to match the demands of high repetition rate acquisition. Traditional approaches to data acquisition, storage, post-processing, and archival will either need to scale far beyond current practice or

be fundamentally redesigned, while rapid advances in AI must be well-integrated to transform scientific discovery and facility operations.

These details are added to the next-generation criteria to form the **specification for the next-generation facility design:**

- Near-transform-limited operation across the X-ray range
  - Photon energies from ∼100 eV to ∼20 keV, pulse durations from ∼100 as to 100 fs
  - Non-transform-limited operation at ∼5-45 keV, with high pulse energy (10s of mJ at the lower photon energies)
- High efficiency facility, with a step-change in the simultaneous operation of multiple end stations in parallel
  - Target at least 6 FELs, with capacity to reach 10 or more, and >10 end stations to be simultaneously operated
- Evenly spaced, high repetition rate pulses to match samples, lasers, and detectors
  - For TL-pulses: 100 kHz per FEL, with flexibility of repetition rate
  - Non-TL: <200 Hz with a short burst mode (<10 pulses, >1 MHz within the burst)
- New AI approaches for data analysis and interpretation of vast data volumes generated
  - Data and computing systems matched to the demands of high repetition rate acquisition
- Improved synchronisation/timing data with external lasers to <1 fs by harnessing state-of-the-art synchronization strategies and implementing the most advanced timing tools
- Widely separated, multiple colour X-rays to at least one end station by combining the outputs from two FELs
  - Soft X-ray + hard X-ray combination
- Full array of synchronised sources including optical lasers + nonlinear optical conversion across the EM spectrum from XUV – THz, charged particle beams, high energy and high power lasers
- Environmentally sustainable facility meeting Net Zero targets

The specification described above forms the basis of the conceptual design described in this report, with the weighting of emphasis between these factors described in Chapter 3.

The specification for a next-generation XFEL will continue to evolve, so the ability to accommodate emerging priorities must be treated as a core part of the specification itself.

DRAFT

References for Chapter 2

[1] P. Emma et al. “First lasing and operation of an angstrom-wavelength free-electron laser”. In: *Nature Photonics* 4 (2010), p. 641. DOI: 10.1038/nphoton.2010.176.

[2] Jon Marangos et al. *UK XFEL Science Case*. Tech. rep. STFC, 2020. DOI: 10.5286/stfctr.2026008.

[3] B. W. J. McNeil and N. R. Thompson. “X-ray free-electron lasers”. In: *Nature Photonics* 4.12 (Nov. 2010), pp. 814–821. DOI: 10.1038/nphoton.2010.239. URL: https://doi.org/10.1038/nphoton.2010.239.

[4] C. Pellegrini, A. Marinelli, and S. Reiche. “The physics of x-ray free-electron lasers”. In: *Rev. Mod. Phys.* 88 (Mar. 2016), p. 015006. DOI: 10.1103/RevModPhys.88.015006. URL: https://link.aps.org/doi/10.1103/RevModPhys.88.015006.

[5] Peter Schmüser et al. “Free-Electron Lasers in the Ultraviolet and X-Ray Regime”. In: *Springer Tracts in Modern Physics* 258 (2014). ISSN: 00813869.

[6] E A Seddon et al. “Short-wavelength free-electron laser sources and science: a review”. In: *Reports on Progress in Physics* 80.11 (Nov. 2017), p. 115901. ISSN: 0034-4885. DOI: 10.1088/1361-6633/aa7cca.

[7] Kwang-Je Kim, Zhirong Huang, and Ryan Lindberg. *Synchrotron Radiation and Free-Electron Lasers*. 2017. DOI: 10.1017/9781316677377.

[8] E. Seddon and M. Poole. “The origins and development of free-electron lasers in the UK”. In: *Notes Rec.* 78 (2023), pp. 203–251. DOI: 10.1098/rsnr.2022.0038.

[9] John M. J. Madey. “Stimulated Emission of Bremsstrahlung in a Periodic Magnetic Field”. In: *Journal of Applied Physics* 42.5 (Apr. 1971), pp. 1906–1913. ISSN: 0021-8979. DOI: 10.1063/1.1660466. eprint: https://pubs.aip.org/aip/jap/article-pdf/42/5/1906/18357380/1906_1_online.pdf. URL: https://doi.org/10.1063/1.1660466.

[10] Luis R. Elias et al. “Observation of Stimulated Emission of Radiation by Relativistic Electrons in a Spatially Periodic Transverse Magnetic Field”. In: *Phys. Rev. Lett.* 36 (13 Mar. 1976), pp. 717–720. DOI: 10.1103/PhysRevLett.36.717. URL: https://link.aps.org/doi/10.1103/PhysRevLett.36.717.

[11] Patrick Rauer et al. “Lasing of a cavity-based X-ray source”. In: *Nature* 650 (2026), pp. 93–96. DOI: 10.1038/s41586-025-10025-x. URL: https://doi.org/10.1038/s41586-025-10025-x.

[12] R. Bonifacio, C. Pellegrini, and L. M. Narducci. “Collective instabilities and high-gain regime in a free electron laser”. In: *Optics Communications* 50.6 (July 1984), pp. 373–378. ISSN: 0030-4018. DOI: 10.1016/0030-4018(84)90105-6.

[13] W. Ackermann et al. “Operation of a free-electron laser from the extreme ultraviolet to the water window”. In: *Nature Photonics* 1.6 (June 2007), pp. 336–342. ISSN: 1749-4885. DOI: 10.1038/nphoton.2007.76.

[14] David Dunning. “Methods for the generation of ultra-short free-electron laser pulses”. Thesis identifier: T14249. PhD Thesis. University of Strathclyde, 2015. DOI: https://doi.org/10.48730/ztag-j207.

[15] R. Bonifacio et al. “Spectrum, temporal structure, and fluctuations in a high-gain free-electron laser starting from noise”. In: *Physical Review Letters* 73.1 (July 1994), pp. 70–73. ISSN: 0031-9007. DOI: 10.1103/PhysRevLett.73.70.

[16] E. L. Saldin, E. A. Schneidmiller, and M. V. Yurkov. “Statistical and coherence properties of radiation from x-ray free-electron lasers”. In: *New Journal of Physics* 12.3 (Mar. 2010), p. 035010. ISSN: 1367-2630. DOI: 10.1088/1367-2630/12/3/035010. URL: https://iopscience.iop.org/article/10.1088/1367-2630/12/3/035010.

[17] Sébastien Boutet and Makina Yabashi. “X-Ray Free Electron Lasers and Their Applications”. In: *X-ray Free Electron Lasers: A Revolution in Structural Biology*. 2018. DOI: 10.1007/978-3-030-00551-1_1.

[18] S. Huang et al. “Generating Single-Spike Hard X-Ray Pulses with Nonlinear Bunch Compression in Free-Electron Lasers”. In: *Physical Review Letters* 119.15 (Oct. 2017), p. 154801. ISSN: 0031-9007. DOI: 10.1103/PhysRevLett.119.154801.

[19] A. Marinelli et al. “Experimental demonstration of a single-spike hard-X-ray free-electron laser starting from noise”. In: *Applied Physics Letters* 111.15 (Oct. 2017). ISSN: 0003-6951. DOI: 10.1063/1.4990716.

[20] Joseph Duris et al. “Tunable isolated attosecond X-ray pulses with gigawatt peak power from a free-electron laser”. In: *Nature Photonics* 14.1 (Jan. 2020), pp. 30–36. ISSN: 1749-4885. DOI: 10.1038/s41566-019-0549-5.

[21] Alexander Malyzhenkov et al. “Single- and two-color attosecond hard x-ray free-electron laser pulses with nonlinear compression”. In: *Physical Review Research* 2.4 (Oct. 2020), p. 042018. ISSN: 2643-1564. DOI: 10.1103/PhysRevResearch.2.042018.

[22] Eduard Prat et al. “Coherent sub-femtosecond soft x-ray free-electron laser pulses with nonlinear compression”. In: *APL Photonics* 8.11 (Nov. 2023). ISSN: 2378-0967. DOI: 10.1063/5.0164666.

[23] Paris Franz et al. “Terawatt-scale attosecond X-ray pulses from a cascaded superradiant free-electron laser”. In: *Nature Photonics* 18.7 (July 2024), pp. 698–703. ISSN: 17494893. DOI: 10.1038/S41566-024-01427-W. URL: https://www.nature.com/articles/s41566-024-01427-w.

[24] Jiawei Yan et al. “Terawatt-attosecond hard X-ray free-electron laser at high repetition rate”. In: *Nature Photonics 2024 18:12* 18.12 (Nov. 2024), pp. 1293–1298. ISSN: 1749-4893. DOI: 10.1038/s41566-024-01566-0. URL: https://www.nature.com/articles/s41566-024-01566-0.

[25] James P. Cryan et al. “The development of attosecond XFELs for understanding ultrafast electron motion”. In: *Advances in Atomic, Molecular and Optical Physics* 71 (2022). ISSN: 1049250X. DOI: 10.1016/bs.aamop.2022.05.001.

[26] Massimo. Altarelli et al., eds. *XFEL: the European X-ray free-electron laser: technical design report*. DESY XFEL Project Group, 2006, p. 630. ISBN: 9783935702171.

[27] W. Decking et al. “A MHz-repetition-rate hard x-ray free-electron laser driven by a superconducting linear accelerator”. In: *Nat. Photon.* 14.6 (June 2020), pp. 391–397. ISSN: 17494893. DOI: 10.1038/s41566-020-0607-z.

[28] Cynthia M. Friend. *Report on New and Upgraded National User Facilities in Basic Energy Sciences*. Tech. rep. Department of Energy: Basic Energy Sciences, 2024.

[29] B. Aune et al. “Superconducting TESLA cavities”. In: *Physical Review Special Topics - Accelerators and Beams* 3 (9 Sept. 2000), p. 092001. ISSN: 1098-4402. DOI: 10.1103/PhysRevSTAB.3.092001.

[30] Z. Y. Zhu et al. “SCLF: An 8-GEV CW SCRF linac-based x-ray FEL facility in Shanghai”. In: *Proceedings of the 38th International Free-Electron Laser Conference, FEL 2017*. JACoW Publishing, 2017, pp. 182–184. ISBN: 9783954501793. DOI: 10.18429/JACoW-FEL2017-MOP055.

[31] *Cavity-Based X-ray Free-Electron Laser R&D Quarterly Update A Joint ANL-SLAC-SPring8 Collaboration*. https://indico.fnal.gov/event/48495/contributions/212023/attachments/142633/180114/SwapanSympoisum_-_Zhirong_Huang.pdf. Accessed: 2025-09-25.

DRAFT

3 Overview of the Next-Generation XFEL Conceptual Design

This chapter provides an outline of the conceptual design of a 'next-generation' XFEL facility, developed to meet the ambitious requirements of the UK's Science and Technology Case. Such a facility would represent a step-change in capability: a robust and efficient source of 3D fully-coherent X-rays, and laser-based sources, at new extremes of data-gathering rates for a multitude of simultaneous users. The main components of the facility are described, together with the key design choices. The projected output capabilities and the facility parameters are summarised, as well as layout, environmental sustainability, and project delivery aspects.

3.1 Design philosophy and process

A fundamental feature of this project is that, from the outset, the design has been considered through the lens of either creating an entirely new facility or by upgrading existing machines. In general, our approach has been to think independently of constraints from location or existing infrastructure: **We set out the vision for an internationally leading XFEL facility on a 10-15 year outlook, to meet the next-generation specification in the most efficient way possible.** The conceptual design is shown in Figure 3.1 and described throughout this chapter.

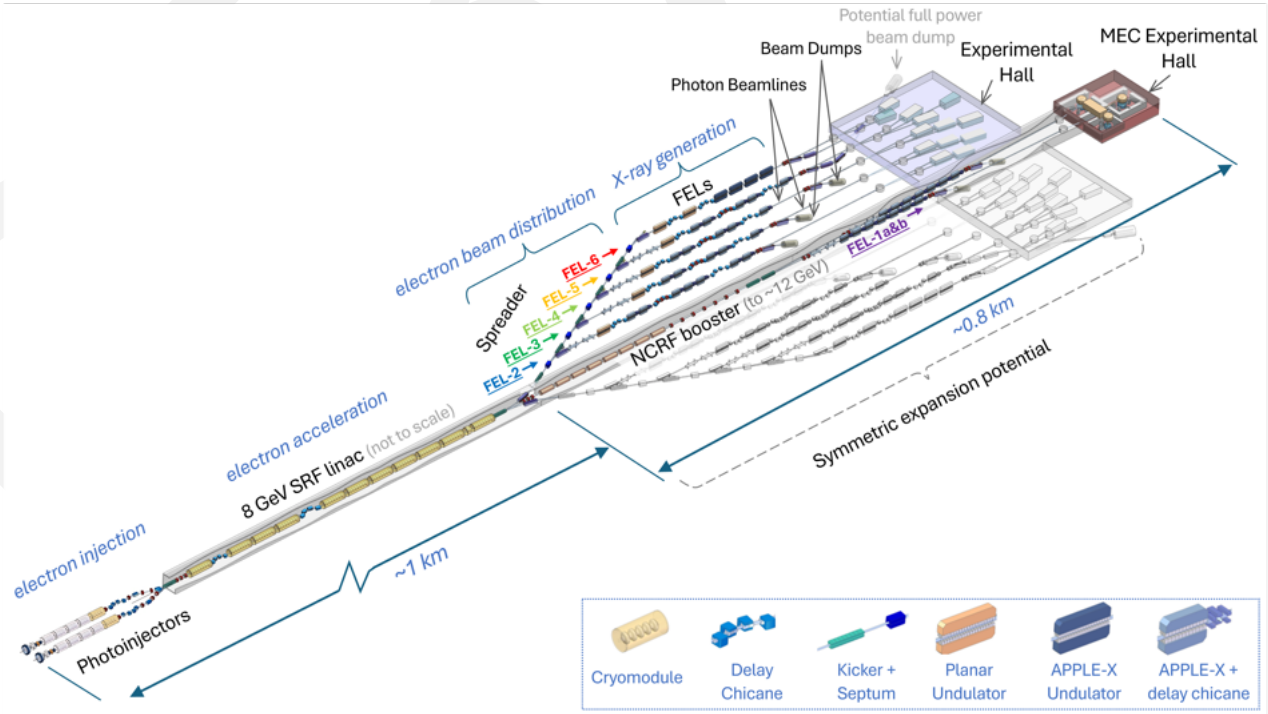

Figure 3.1: An outline of the conceptual design for a next-generation XFEL to meet the requirements of the Science and Technology Case. A repeating section of the SRF linac is omitted for clarity.

In the process, a focus on modularity and scalability of the design make it relevant to multiple future construction options, including a new facility in the UK (or internationally) and to major upgrades to existing facilities, as described in the UK XFEL Options Analysis. This includes **a scaleable set of options for a new-build facility,** that could form the basis of a phased delivery, as shown in Figure 3.2. These are mainly differentiated by the number of FEL lines (and associated cost). Three indicative examples are shown, with 2, 7, and 12 FELs representing 'minimal', 'nominal' and 'full' layouts respectively, with easy scaleability to other variants. The 'nominal' case is used for defining the FELs and user science instrumentation, leaving scope for new or duplicated capabilities in the 'full' layout.

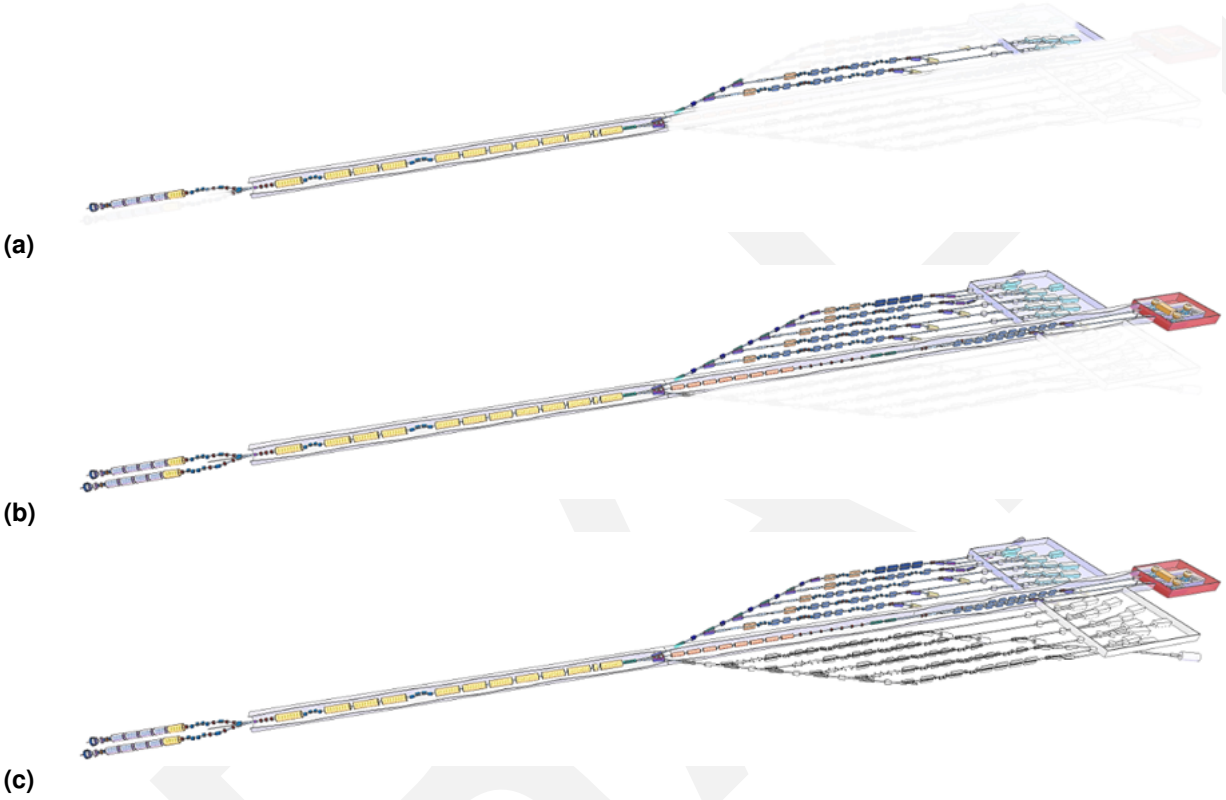

Figure 3.2: Scalable layout of the next-generation XFEL conceptual design, with different versions showing potential for a phased delivery (a) with 2 FELs ('minimal'), (b) with 7 FELs (the 'nominal' case), (c) the 'full' realisation with 12 FELs. A repeating section of the SRF linac is omitted for clarity.

The project's definition of a next-generation XFEL and the community-guided process to develop this into a specification are described in Section 2.2, and are summarised in Figure 3.3. The weighting of emphasis *between* the factors in the specification has developed through iteration with the UK user community over three years as part of this CDOA phase. Design features have been developed and assessed in context with one another, resulting in some being scaled back and others becoming more prominent. These choices and the resulting design are summarised in the following sections.

A key element of the conceptual design is that it is self-consistent: the numerous technical and physical considerations given to different underpinning systems are built on a set of documented common assumptions. Major design choices were informed by input from all relevant technical working groups, and the key decisions are highlighted in this section.

3.2 Key themes

The defining next-generation XFEL capabilities can be encapsulated in three key themes to help structure the conceptual design, as shown in Figure 3.3, and described as follows:

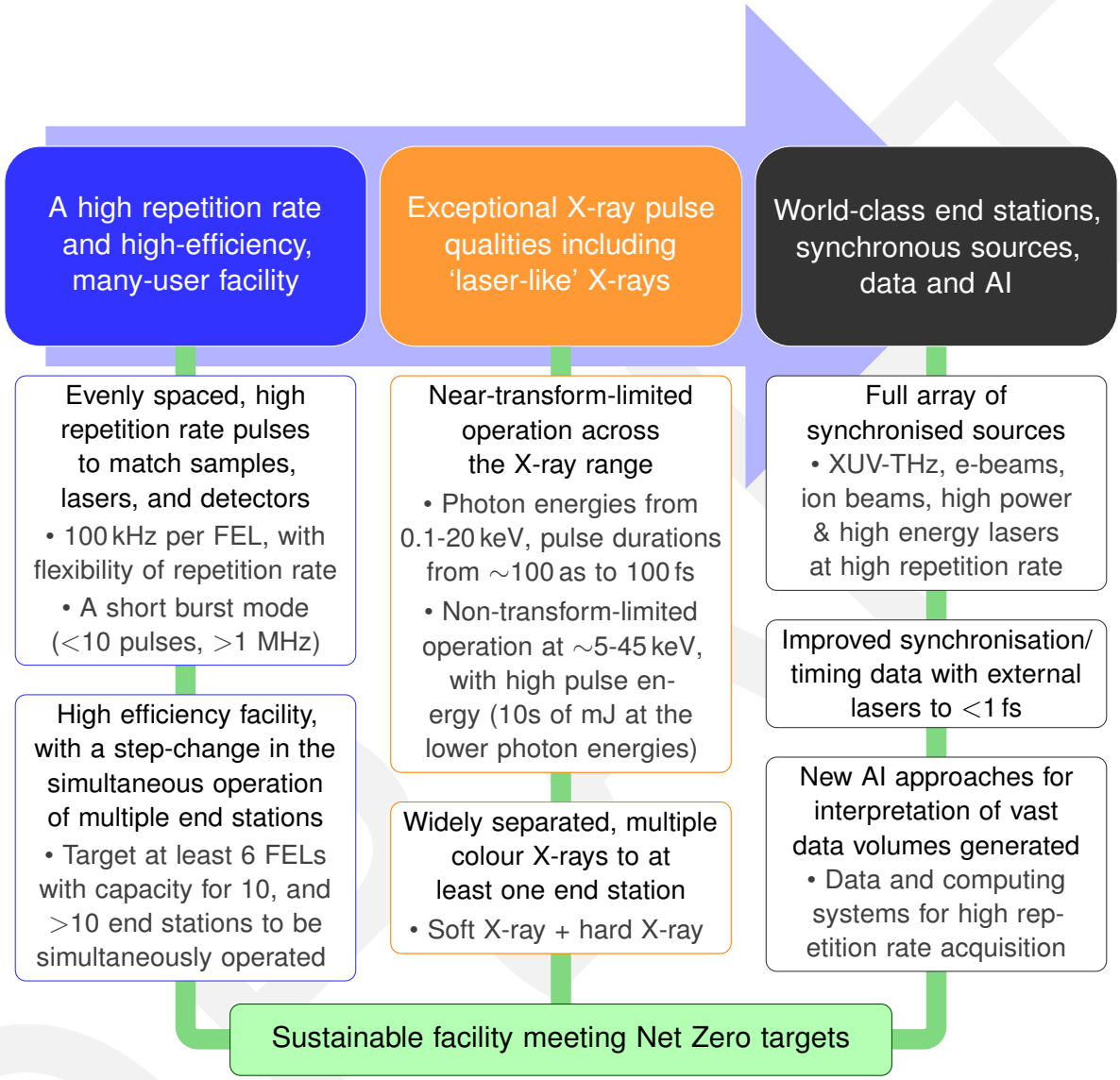

Figure 3.3: Mapping of the next-generation capabilities to the key facility design themes.

1. A next-generation XFEL must be **a high repetition rate and high-efficiency, many-user facility** to enable rapid progress across many fields. At the core of the facility, these capabilities are built upon the accelerator and beam distribution. The photoinjector, linac and spreader must be able to generate and accelerate high-brightness electron bunches at high (∼1 MHz) repetition rate and flexibly multiplex them to many more independent FELs (∼6-10) compared to present facilities (1-3), i.e. towards synchrotron-like operation in terms of throughput. *This theme propagates through all aspects of the facility design.*

2. The second key theme is **exceptional X-ray pulse qualities including 'laser-like' X-rays**. It describes how transformational enhancements of the X-ray pulse qualities can be realised in a next-generation XFEL. These result from the interplay between the accelerator features and the FEL techniques deployed in the undulators. Techniques are selected to deliver high repetition rate and near-transform-limited pulses across a wide range of photon energies and

pulse durations, extremes of photon energy and pulse energy, and multi-colour X-ray pulse combinations, while bespoke photon beamlines optimise the properties for experiments.

3. The third key theme describes how a next-generation XFEL will be defined by its **world-class end stations, synchronous sources, data and AI**. It will feature a suite of cutting-edge and independently operable scientific end stations, including state-of-the-art detectors and auxiliary infrastructure. It will be considered as a laser facility as well as a particle accelerator facility, with exceptional synchronisation between the two. It will leverage transformative impacts of AI and digital twinning and will be one of the largest sources of high-value scientific data in the world, enabling future discoveries and foundation models across a host of disciplines.

A next-generation XFEL is also defined by **including environmental sustainability as part of the decision making throughout the project**, from design, through construction and operation, and finally decommissioning. For each of the key components of the design, potential choices regarding environmental sustainability are highlighted, and these are summarised in Section 14.1.

Engineering delivery of the major technical systems and their integration (Chapter 13) and project-planning frameworks (Chapter 15) have also been assessed for the new-build facility option, where these considerations can be applied most comprehensively from first principles.

DRAFT

3.3 Theme 1: High repetition rate and high-efficiency, many-user facility

This section describes the design choices to realise a high repetition rate and high-efficiency, many-user facility: the critical parameters and accelerator technology selections. It summarises the Low Energy Beamlines, where electron bunches are generated, compressed and accelerated up to a relatively low energy (∼200 MeV); and the subsequent High Energy Beamline: a linear accelerator to high energy (8 GeV), with interleaved bunch compression, and fast distribution to multiple FEL lines. This theme propagates through all aspects of the facility design.

3.3.1 High-level facility design choices

The aim of the facility design is to meet the next-generation specification in the most efficient way possible, enabling rapid progress across many fields. The route to achieving this can be described with the aid of Figure 3.4, which shows how the detailed requirements from the Science Case and Science Team survey translate into high-level facility design choices.

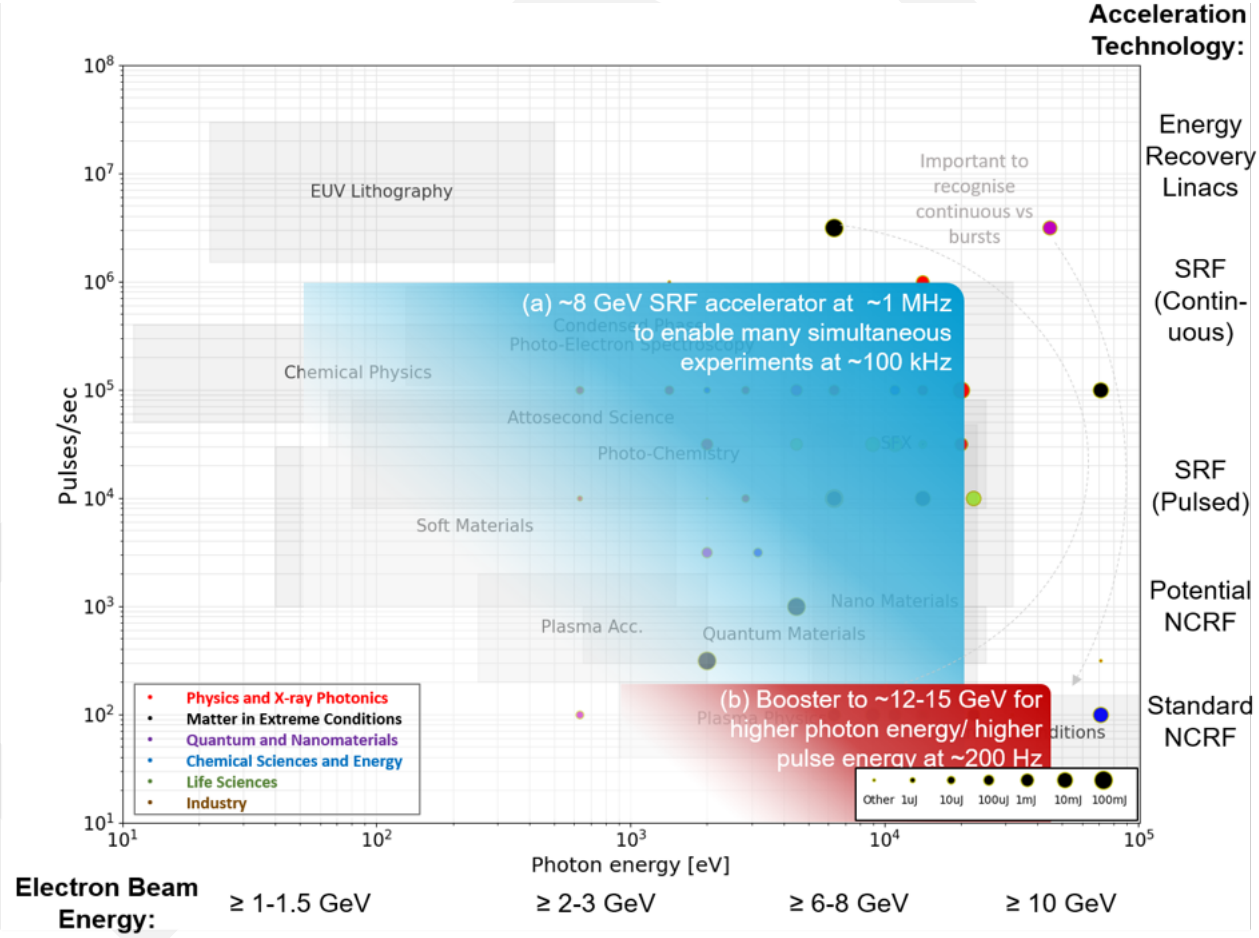

Figure 3.4: User requirements translated to high-level facility design choices for the next-generation XFEL conceptual design: (a) an ∼8 GeV SRF linac operating at ∼1 MHz to enable many simultaneous experiments at ∼100 kHz, and a NCRF booster to 12-15 GeV at ≤200 Hz. An unannotated version of this figure with clearer visibility of the user requirements is given in Figure 2.10

3.3.1.1 Electron beam energy and acceleration technology

The **electron beam energy** is a critical parameter, relevant to photon energy and pulse energy:

- *Photon energy* requirements from the Science and Technology Case can be translated into approximate electron beam energy requirements, following the FEL resonance condition described in Section 2.1. The electron beam energy ranges shown in Figure 3.4 represent the approximate minimum to reach the corresponding photon energy, based on well-established performance of existing facilities and projected advances in undulator technology etc. [1].
- *Energy per pulse* increases with increasing electron beam energy for a given photon energy. So in this respect, it can be advantageous to operate with an electron beam energy substantially higher than the indicated values.

The **pulse repetition rate** depends upon the type of acceleration technology:

- *Normal conducting RF (NCRF)* is the primary technology for the first generation of XFELs, with operation at ∼100 Hz. This technology can support relatively high accelerating gradients (∼20-40 MV/m), with some flexibility to trade off gradient against repetition rate.
- *Superconducting RF (SRF)* is the alternative: European XFEL [2] operates with an SRF linac operating in a 'pulsed' or 'burst' mode of operation, with short bursts of up to 2700 closely-separated (4.5 MHz) pulses delivered at 10 Hz. LCLS-II [3] and SHINE [4] use SRF linacs specified to reach 1 MHz, with evenly spaced pulses. SRF linacs typically operate with a lower accelerating gradient (∼20 MV/m) than NCRF linacs.
- *Energy recovery linacs (ERLs),* reviewed in [5], offer a configuration to re-use the beam energy, and so enable repetition rates $\gg$1 MHz and enhanced efficiency but they require a more complex recirculating accelerator layout. This presents significant challenges in terms of beam quality and multiplexing to many simultaneous experiments.

3.3.1.2 Design choices based on combined parameter sets

Figure 3.4 shows the required parameter space in terms of photon energy, repetition rate, and pulse energy. Potentially, this could be met with a conceptually simple but likely high cost design, e.g. consisting of a single (high repetition rate) acceleration technology with very high electron beam energy. Alternatively, various acceleration technologies could be applied at different photon energy ranges, which could each be efficient in isolation, but likely cost-inefficient overall due to increased complexity.

Ultimately, a hybrid of two technologies is selected as the optimal solution as described below. This encompasses the two largest sets of user requirements, in a way that is easily compartmentalised within the design, and could form part of a phasing route.

- **8 GeV SRF linac:** The majority of users require evenly spaced pulses up to ∼100 kHz, from ∼100 eV-20 keV, and (up to) high but not beyond state-of-the-art pulse energy (up to ∼1 mJ). Therefore **the core accelerating component is an ∼8 GeV linac (to support photon energies up to 20 keV) operating at ∼1 MHz, to enable many simultaneous user experiments to operate at ∼100 kHz.** The choice of an 8 GeV SRF linac is highly compatible with translating aspects of the full design between a new facility and existing ones.

- **NCRF booster:** A large subset of the Science and Technology Case calls for significantly higher photon energies and higher pulse energy, both of which require higher electron beam energy. These applications, e.g. experiments studying matter in extreme conditions (MEC), generally require much lower repetition rate ($\leq$200 Hz) or a short burst mode of $\sim$10 pulses. To meet these requirements, **the design includes a booster to higher electron beam energy (12-15 GeV), for which a normal conducting linac is presently the most appropriate option.**

Both linear and energy recovery/recirculating configurations were considered for the facility layout and a linear layout is selected. At 1 MHz, the beam power is a relatively small fraction of the total facility usage, so the benefits of recirculating the 8 GeV beam for energy recovery are outweighed by the increased complexity. A concept for integrating a 1-2 GeV ERL operating at very high repetition rate ($\sim$10-100 MHz) to deliver unique high-flux EUV and gamma-ray capabilities is outlined in an appendix to the Science and Technology Case. Although not included in the baseline due to integration complexity, many benefits – such as shared infrastructure – could be realised through co-locating a standalone ERL facility.

A simplified schematic plan is shown in Figure 3.5, with key features and components annotated for clarity.

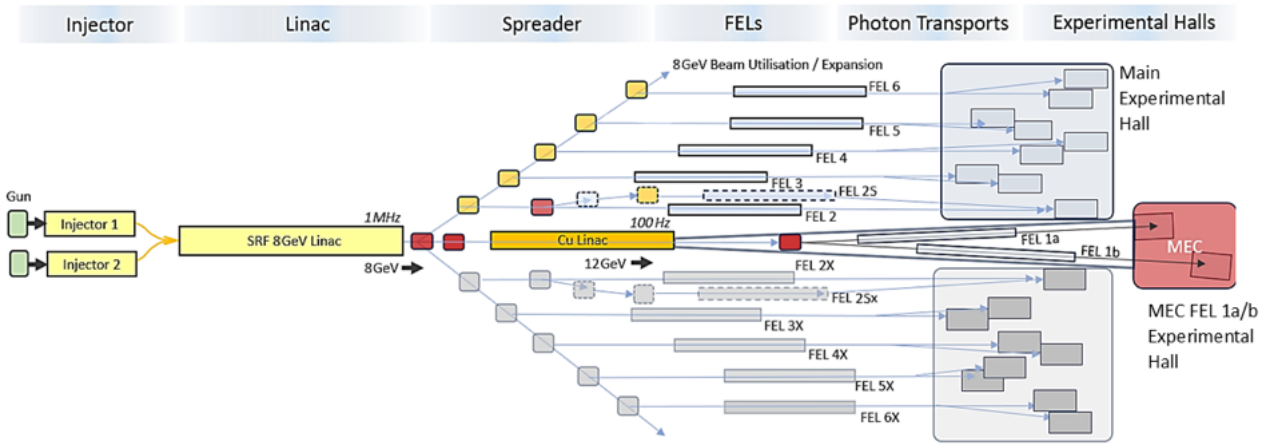

Figure 3.5: Schematic plan of the next-generation XFEL facility.

3.3.2 Low Energy Beamlines: High-brightness electron injectors

The Low Energy Beamlines (LEB), described in Chapter 4, are the first stage of the accelerator and are crucial to XFEL performance: higher quality bunches (i.e. high peak current with low emittance and energy spread) enable higher photon energy X-rays to be generated for a given final beam energy, thereby extending scientific reach or reducing facility size and cost. Supporting a variety of FEL techniques requires bunch quality parameters pushing the state-of-the-art across a range of charge regimes (75, 150, 300 and 600 pC), summarised below in Table 3.1.

Studies have identified two candidate technologies to meet $\sim$1 MHz repetition rate: injectors based on a very high frequency (VHF) gun (as used for LCLS-II [6, 7] and SHINE [8, 9]), and those based on a superconducting L-band gun (as being developed for European XFEL [10]). **The baseline choice for the electron gun is to focus on a normal-conducting VHF option,** which gives most scope for rapid iteration in prototyping, while also collaborating to **support the L-band gun development at European XFEL, which could be adopted at a later phase** if proven to be advantageous. Together these approaches provide a robust route to meeting the requirements.

A VHF gun frequency of 216.67 MHz (as used for SHINE) is selected for its ability to generate higher energy electrons, compared to the 187 MHz APEX design used for LCLS-II [7]. The gun geometry has been refined to maximise accelerating voltage and so to enhance beam quality.

After the electron bunches exit the gun, they must be rapidly accelerated to higher energy to minimise space charge effects, and compressed to shorter duration. Existing injectors based on VHF guns immediately step to 1.3 GHz buncher/booster components, matching the frequency of the subsequent linac. To provide 'next-generation' performance, the UK XFEL project has developed novel designs [11] to better retain beam quality through a progressive increase in RF frequency, using either RF compression (velocity bunching) plus magnetic compression ('Design-I') or two-stage RF compression ('Design-II'). **The injector design based on RF plus magnetic compression is selected as the baseline**, as shown in Figure 3.6: studies indicate higher beam quality through better control of the longitudinal phase space [11]. Simulation study results showing the emittance values for the required range of charge regimes are given in Figure 4.14, and meet the FEL requirements.

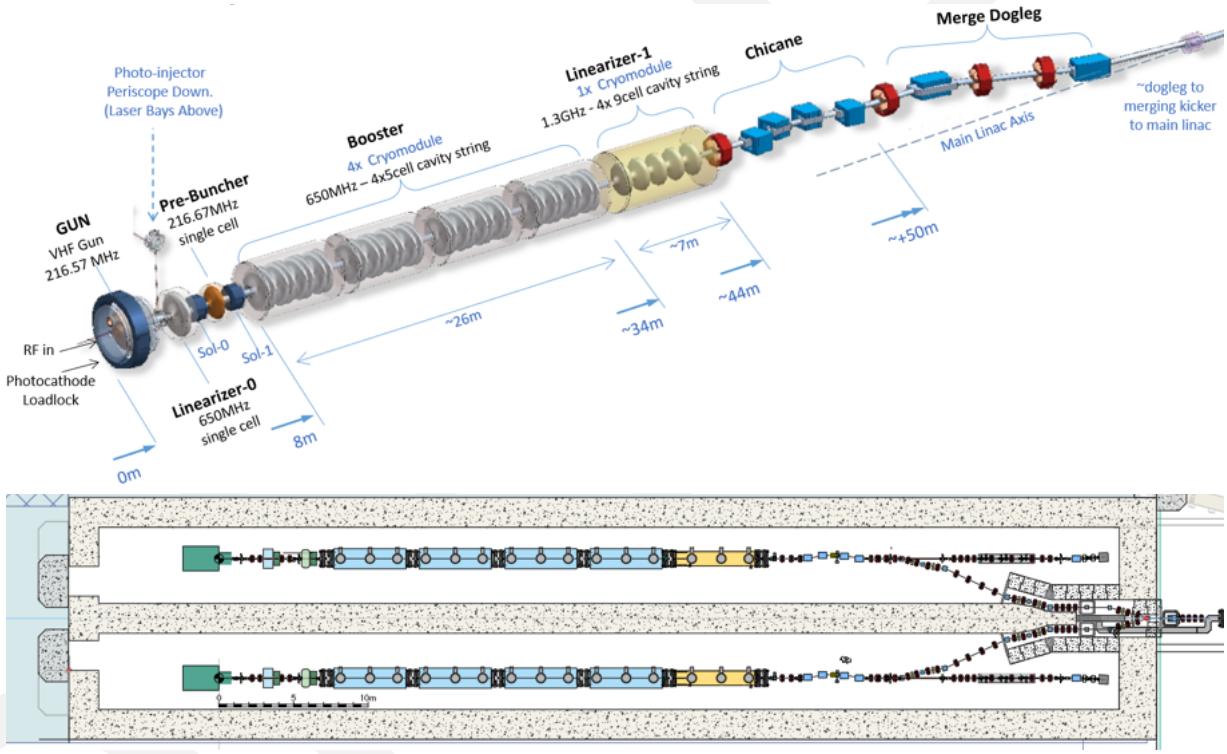

Figure 3.6: Novel injector concept for the Low Energy Beamlines, featuring RF compression (the pre-buncher) and magnetic compression (in the chicane), with a progressive increase in RF frequency for optimal beam quality. The length of the section is ∼50 m. Two identical injectors are envisaged to run in parallel before merging into a single linac.

A further conclusion is that the various beam charge modes can be achieved with the same hardware, but that different tuning will be required for each. To provide flexibility, redundancy and minimised downtime, while focusing on a single technology, **the design includes two injectors, which will be identical in terms of hardware**, as shown in Figure 3.6, with multiple photoinjector lasers per gun for flexibility. Two injectors are also required for the two-colour mode outlined in Section 3.3.4 and Section 3.4.4, which combines two bunches accelerated in adjacent RF cycles by delaying the leading bunch in a chicane. At 216.67 MHz, the required delay (∼5 ns) would require an impractically large chicane, hence the two injector lines can feed adjacent cycles of the 1.3 GHz linac (∼1 ns separation). Two-injector operation presents new challenges in terms of merging, fill patterns, and synchronisation.

Prototyping of the Low Energy Beamlines is expected to be critical for a new facility. Every XFEL constructed to date has undertaken extensive prototyping of their injector and low energy beamline in order to push the limits of performance and operational reliability. In some instances, the prototype was moved outright to the new facility, forming its front end. The proposed design, with its advanced architecture, would be expected to follow this pattern – requiring systematic testing to validate beam dynamics and subsystem integration, as well as developing the requisite experience and processes for efficient operation.

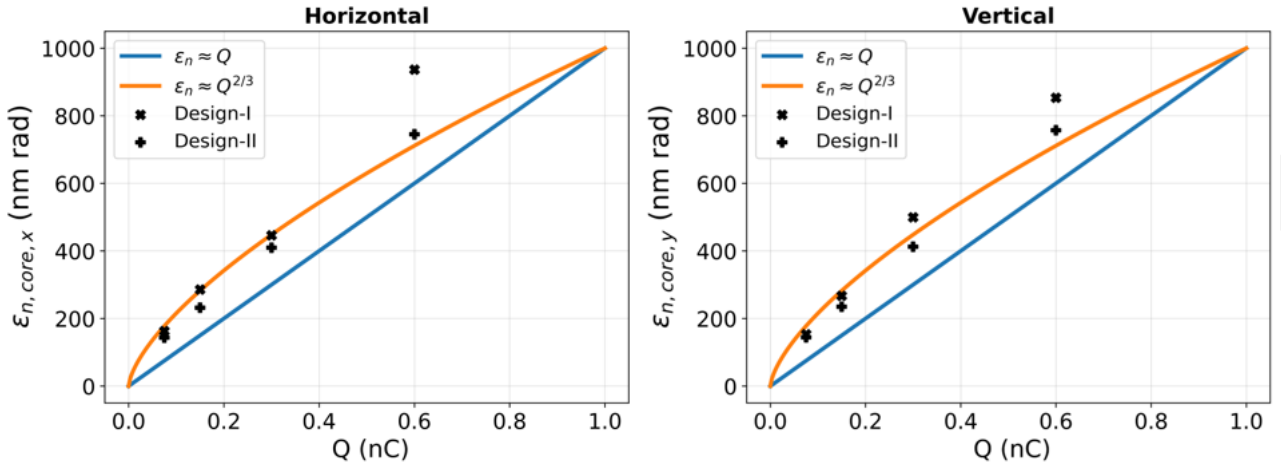

Figure 3.7: Final horizontal and vertical core emittances for the VHF-gun-based injectors Design-I (baseline choice) and Design-II across all simulated bunch charges. Emittance values generally show good agreement with the theoretical scaling law assumed in FEL modelling (orange lines).

3.3.3 High Energy Beamline: Accelerator technology and parameters

3.3.3.1 SRF linac

As outlined in Section 3.3.1, the choice of accelerator technology for the High Energy Beamline (HEB) and its parameters are fundamental to defining the high-level performance parameters of the facility, and these aspects are described fully in Chapter 5. The core accelerating component is an ∼8 GeV linac (for photon energies up to ∼20 keV) operating at ∼1 MHz, to support many simultaneous user experiments at ∼100 kHz. **Niobium SRF cavities operating at 1.3 GHz are the baseline technology choice**, due to their being an established technology, developed over more than 3 decades, based on technology developed through the TESLA collaboration [12], and used at existing XFELs e.g. FLASH, European XFEL, LCLS-II and SHINE.

The SRF linac is one of the largest components of the facility, which impacts its size, cost and energy usage. Section 5.3.1 describes the optimisation of its parameters in order to establish an estimate of capital and recurrent costs and their dependencies. The accelerating gradient is a key parameter: the nominal value is 16 MV/m for LCLS-II [13] and SHINE [4], while for LCLS-II-HE, which incorporates improved cavity processing, the nominal gradient is 20.8 MV/m [14].

The baseline gradient is chosen to be 19.0 MV/m, which is projected to minimise capital build costs, while balancing competing factors: In terms of operational costs (taking into account energy usage and by extension environmental sustainability), the analysis shows it is beneficial to operate at lower gradients: the optimum gradient reduces to 17.6, 15.4 and 14.3 MV/m for 20, 40 and 50 years of operation respectively. On the other hand, technology development can be anticipated to enable moderate gradient increases, such like those demonstrated during

LCLS-II commissioning where upwards of 26 MV/m was seen. Therefore the final value should be determined in a technical design phase.

An alternative approach with the potential to significantly reduce emissions and energy consumption would be to use thin-film SRF cavities [15]. In lieu of a solid niobium cavity, a solid copper cavity is used, coated with a thin film of niobium alloy, e.g. Nb_3Sn. The technology is insufficiently mature to adopt as the baseline but, with suitable R&D, a saving of $\sim$ 70% could be made in electrical costs, enabled by higher critical temperatures of the alloys allowing cryogenics operation at 4.2 K instead of the standard 2 K [15, 16]. **It would be highly advantageous to support R&D into thin-film SRF development at the well-established 1.3 GHz RF frequency** targeting gradients at least matching conventional SRF, for potential adoption at a later stage.

3.3.3.2 NCRF booster

As described in Section 3.3.1, a booster to higher electron beam energy is required for a subset of pulses at a relatively low repetition rate ($\leq$200 Hz) or a short burst mode of $\sim$10 pulses. At these duty cycles, NCRF technology is the most suitable choice due to its higher gradient and increased flexibility compared to SRF, and for its higher technology readiness compared to novel acceleration techniques. **The baseline is assumed to be a 4 GeV booster, to reach a total of 12 GeV, while space is reserved to reach 15 GeV** without having significant impact on the overall facility size. This technology choice and its implementation in a dedicated section provides flexibility to trade off accelerating gradient against repetition rate to best meet experiment requirements.

In order to support burst mode operation, the RF frequency of the booster must be compatible with that of the SRF linac. **For a normal conducting booster, the preferred option is C-band operation at 5.85 GHz**, to provide high gradient acceleration while sharing a common sub-harmonic of 650 MHz with the 1.3 GHz SRF frequency (allowing pulse separations down to 1.5 ns). This non-standard operating frequency is selected for being close to a common commercial high-power klystron frequency (5.712 GHz), which could be adapted with industry support. Development work at CERN along with industry on C-band (and X-band) klystrons are ongoing and likely to prove a viable option for improving the energy consumption of the booster [17].

3.3.4 High Energy Beamline: Distribution to many simultaneous experiments

To enable independent, simultaneous operation of multiple FELs and end stations with high efficiency, **the facility is designed to have a fixed beam energy at 8 GeV (prior to the spreader and booster), such that the FEL photon energy ranges are controlled only by the undulator parameters**.

To support a variety of FEL techniques, the High Energy Beamline must be able to flexibly optimise the longitudinal phase space for various bunch charges, as described in Chapter 5. Following the SHINE design, two bunch compressors are located at electron beam energies of 270 and 2100 MeV. To meet the beam quality requirements outlined in Chapter 6, **alternative designs to the symmetric C-type magnetic chicane are preferred, namely asymmetric 5-dipole chicanes and arc compressors.** To maximise operational flexibility, the proposed lattice enables bunch-by-bunch selection between the two compressor types in parallel, which will require further evaluation in a technical design phase to weigh the benefits against increased complexity.

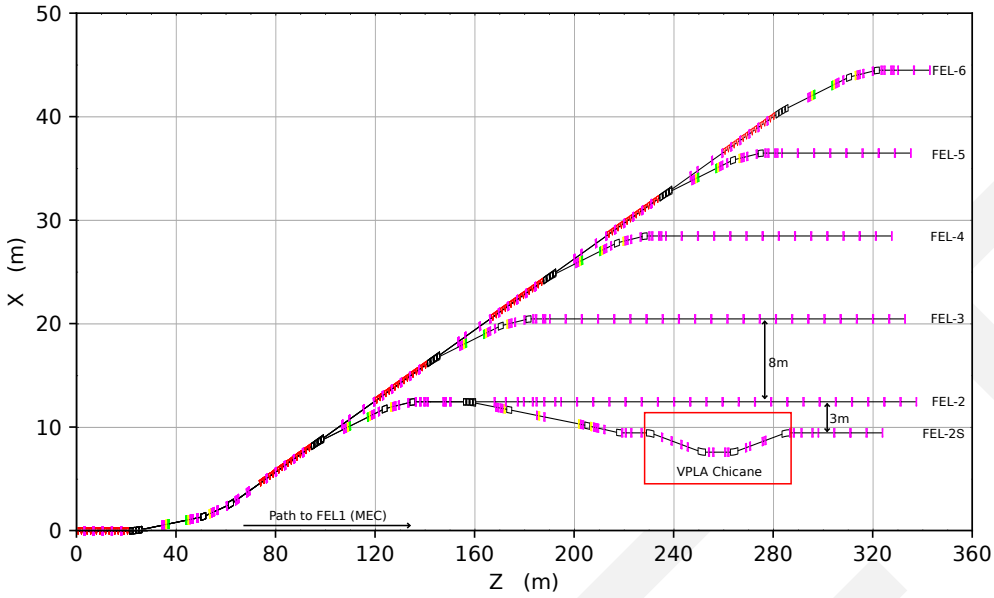

Figure 3.8: Spreader layout for the nominal case. In the full version, this layout is reflected about the z-axis. The FEL-2 line includes an RF deflector to an adjacent undulator line for two-colour operation.

Extensive studies have also been undertaken to quantify long-range transverse wakefield effects in the SRF cavities, in the novel regime of non-uniform bunch-charge patterns.

The facility design distributes the 8 GeV bunches to up to 10 parallel high repetition rate FELs via a beam spreader (switchyard), such that each FEL operates at up to 100 kHz simultaneously. A modular design approach has been developed to assess various combinations of RF-based and pulsed magnetic kickers [18], with the preferred option using magnetic kickers detailed in Figure 3.8. The spreader section angles the beam $\sim 9^{\circ}$ away from the linac straight-on axis and can distribute any electron bunch from the 1 MHz beam to the appropriate downstream FEL undulator lines (via kicker-septum arrays). These lines return the trajectory of the electrons back to the straight-on and have a transverse separation of $\sim$9-10 m to provide suitable space for the end stations, as summarised in Section 3.6.1.

To support widely separated two-colour FEL pulse combinations (as described in following sections), the 'FEL-2' line contains an RF deflector to a variable delay chicane and an adjacent supplementary undulator line 'FEL-2S', with their output combined to a single end station.

A small subset of the bunches, at a much lower repetition rate of $\leq$200 Hz, pass to the straight-on path for acceleration to $\sim$12-15 GeV in the booster. These bunches are directed to one of two adjacent undulators, each leading to an end station.

3.3.5 Electron beam R&D line

As a next-generation XFEL facility, the conceptual design integrates emerging accelerator technologies from the outset, ensuring a long-term competitive edge beyond its initial design. **An electron beam R&D line would be expected to serve as a continuous source of novel electron and photon beam enhancements beyond the initial design.**

For example, plasma-based accelerators offer a transformative pathway to achieving ultra-high accelerating gradients, far beyond the limits of conventional RF technologies. These accelerators can be driven either by high-power, femtosecond-duration infrared laser pulses - known as laser

wakefield acceleration (LWFA) [19] - or by intense particle beams in the case of beam-driven plasma wakefield acceleration (PWFA) [20, 21, 22]. The UK is a world leader in this field [23]. Figure 3.9 shows the proposed inclusion of an electron beam R&D line into the facility layout, e.g. leveraging plasma photocathodes in PWFA to enhance capabilities [24, 25].

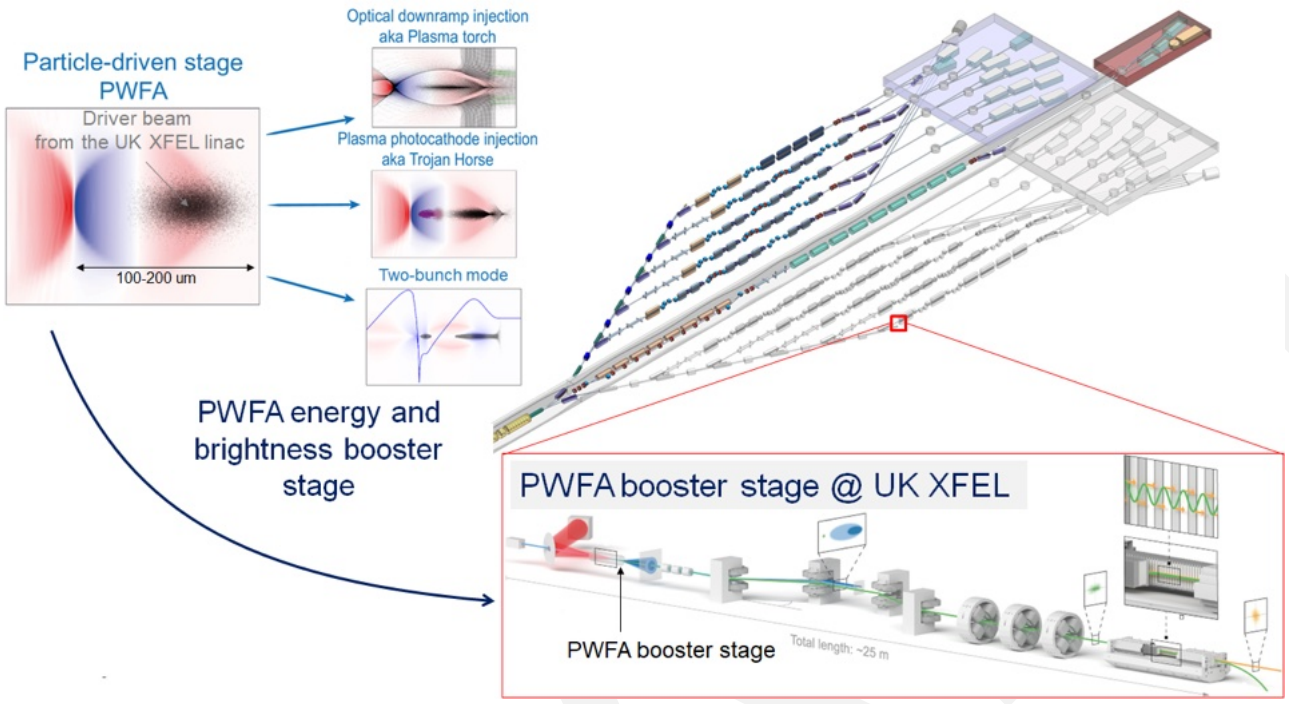

Figure 3.9: Example integration of an electron beam R&D line into the next-generation design, utilising PWFA as an energy and brightness booster stage.

Using PWFA in this way would enable additional capabilities over the lifetime of the facility, including the use of plasma stages to boost the bunch energy (by a factor of two to five), and the use of plasma photocathodes as compact electron brightness afterburners (which could increase brightness by orders of magnitude). Such an energy and brightness plasma booster stage for XFELs would open pathways to higher photon energies and/or sub-femtosecond, higher brilliance photon pulses, and intrinsically synchronised pump-probe multi-colour experiments. A dedicated research station could also be used for related applications, such as high-field science [26, 27] and exploration of PWFA staging physics towards high-energy physics.

Furthermore, there is opportunity to use the high-quality relativistic electron beam to expand user reach further into disciplines such as high-energy physics, e.g. to drive a new generation of kaon science experiments, as described in the Science and Technology Case.

3.4 Theme 2: Exceptional X-ray pulse qualities including ‘laser-like’ X-rays

This section describes how the FEL techniques, undulator technology choices, X-ray beamlines and diagnostics couple with the accelerator features to realise transformational enhancements of the X-ray pulse qualities. Techniques are selected to deliver high repetition rate and near-transform-limited pulses across a wide range of photon energies and pulse durations, extremes of photon energy and pulse energy, and multi-colour X-ray pulse combinations, while bespoke photon beamlines optimise the properties for experiments.

3.4.1 Photon energy coverage

The facility concept is deliberately flexible in terms of the number of FELs, with the aim being to support a step-change in their number, compared to existing facilities (1-3). A ‘full’ layout with up to 12 FELs is shown in Figure 3.1, but a reduced number are defined in the ‘nominal’ case described here, leaving scope to add new or duplicated capabilities in the full layout.

To enable independent operation of multiple high repetition rate FELs, the facility is designed to have the beam energy from the SRF linac fixed at 8 GeV, such that the FEL photon energy ranges are controlled only by the undulator parameters. The required ∼100 eV to 20 keV photon energy range could be covered by a minimum of three FELs, but a more optimal match to **the high repetition rate science requirements can be achieved with five FELs distributed with some overlap as shown in Figure 3.10, i.e. FELs 2 - 6**. Further details are provided in Chapter 6.

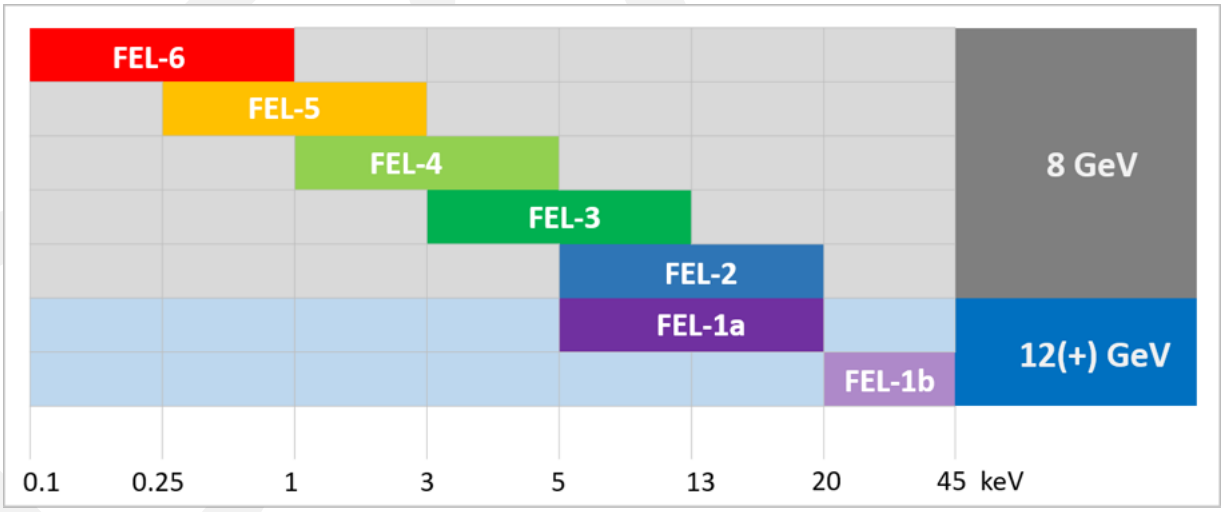

Figure 3.10: FEL tuning ranges.

To meet the requirements for very high pulse energy (10s of mJ at 5-10 keV) and high photon energy (≥40 keV) at relatively low repetition rate (e.g. ≤200 Hz) or as a short (≤10-pulse) burst mode, one of the FEL lines (FEL-1) will include an energy booster to 12-15 GeV as already described. **The low repetition rate FEL-1 line is divided into two adjacent undulators (FEL-1a: high pulse energy and FEL-1b: high photon energy)** leading to separate high-power laser user enclosures.

The FELs outlined here are an indicative set, chosen to demonstrate examples across the photon energy range, with boundaries developed through iteration with the Science Team. It is not meant to represent a priority for even coverage: present end station requirements indicate a preference to implement duplicates of e.g. FEL-2 or FEL-5 ahead of a first instance of FEL-4. In the 'full' case of 12 FEL lines, there could be multiple duplicates. These are decisions for a later phase: a key strength of the concept is that changes like this can be incorporated relatively straightforwardly.

3.4.2 'Laser-like' or near-transform-limited X-ray pulses

The international XFEL community has been extremely innovative in developing new techniques and methods to achieve near-transform-limited pulses have been identified across large regions of the required parameter space, as shown in Figure 3.11. Many such schemes are well-established at international XFELs. However, these methods have usually been applied retrospectively and are therefore constrained by existing accelerator infrastructure and initial design choices. In some cases there are significant challenges to operating the techniques at higher repetition rate compared to existing machines.

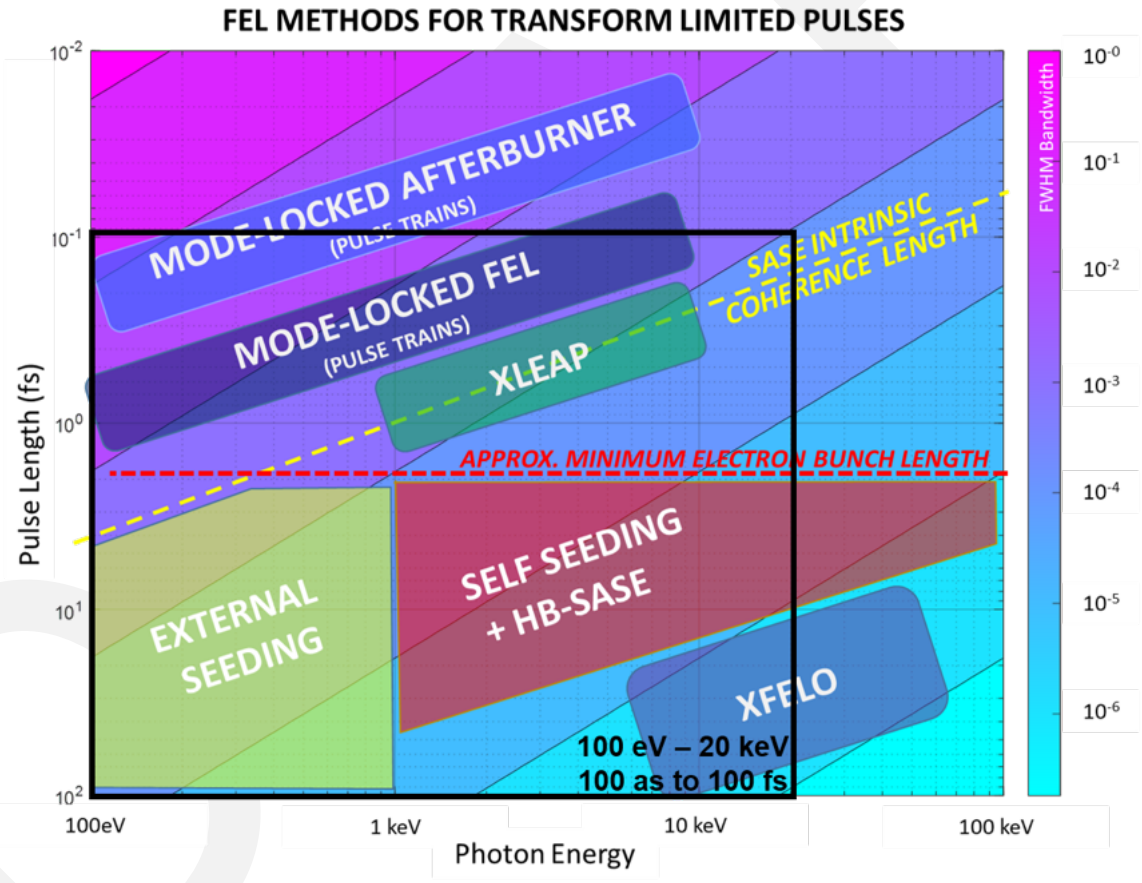

Figure 3.11: The project's aim for near-transform-limited pulses from 0.1 to 20 keV and 100 as to 100 fs is shown by the black box in the photon energy-pulse length parameter space. The contours show the relative bandwidth of a transform-limited pulse within the space and the estimated coverage of some relevant FEL techniques is shown. XLEAP is an example of E-SASE, and XFELO is a cavity-based (CB-XFEL) method.

For longer pulses, there is huge potential to utilise advances in conventional lasers to extend external seeding techniques such as **High-Gain Harmonic Generation (HGHG)**, implemented at e.g. FERMI [28], to much higher repetition rate (∼100 kHz) and to higher photon energy. To realise

such high repetition rate operation calls for very high-average-power laser systems or new variants of seeding techniques to use lower average power seeds [29, 30]. **In terms of photon energy reach, the most advanced seeding and harmonic generation scheme is Echo-Enabled Harmonic Generation (EEHG)** [31] which has been successfully demonstrated [32, 33], and is currently being implemented at a number of facilities [34, 35, 36, 37]. However, this is still only expected to reach up to ∼1 keV, which applies to only FEL-6 and part of FEL-5.

Therefore, much attention has been given to establishing the preferred method for FELs 2-5. **The main candidates are self-seeding** [38, 39, 40], which is established at multiple XFELs **and High-Brightness (HB)-SASE** [41], which has recently been demonstrated at SwissFEL [42]. A detailed comparison concludes that both should be incorporated, with a hybrid of the two potentially providing the best performances. The transformative improvement over SASE is shown in Figure 3.12.

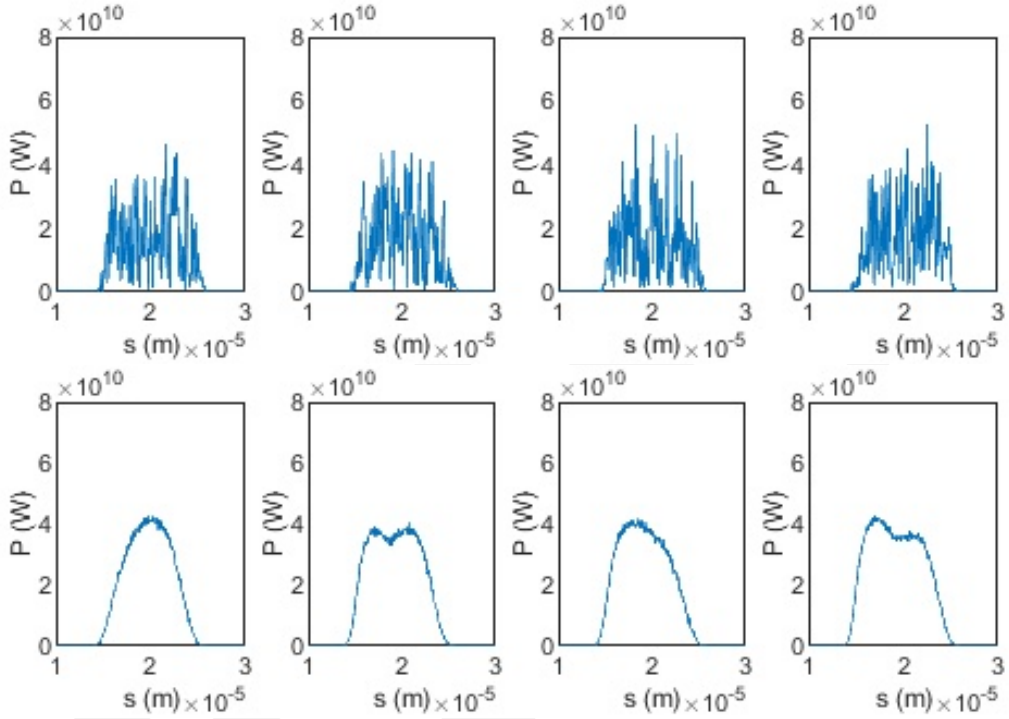

Figure 3.12: Example of the improvement in pulse quality, showing the temporal profile (10^{-5} m ≡ 33.3 fs), between SASE (top row) and advanced (self-seeded + HB-SASE) FEL techniques (bottom row) in the next-generation XFEL design.

Cavity-based (CB-XFEL) techniques promise a further step-change in performance through reflecting the X-rays (using Bragg reflection from diamond crystals) from the exit of the FEL back to the entrance of the undulator to monochromatise and stablise subsequent pulses. These methods, e.g. [43, 44, 45, 46, 47, 48] are under experimental development, including a recent breakthrough at European XFEL demonstrating round trip FEL gain and associated stability and bandwidth reduction [49]. There is potential for widespread application by operating at ∼100 kHz through Q-switching [50]. Tunability to a set of key photon energies could likely be provided by using mirror carousels, however, full tunability of a CB-XFEL is a major challenge, which will require significant further attention in the technical design phase.

Techniques for attosecond pulses will be implemented across the photon energy range (e.g. E-SASE [51], as utilised in the XLEAP demonstration [52]). Several methods are well-established at existing XFELs, as shown in Figure 2.4, and would be included as described in Section 6.3.1.2, with opportunities for enhancement through high repetition rate operation, improved synchronisation, increased tunability and other advanced features.

Chapter 6 describes the selection of the techniques for a next-generation XFEL, as summarised in Table 3.2 and Table 3.3. Schematics of the required hardware for each is shown in Figure 3.13.

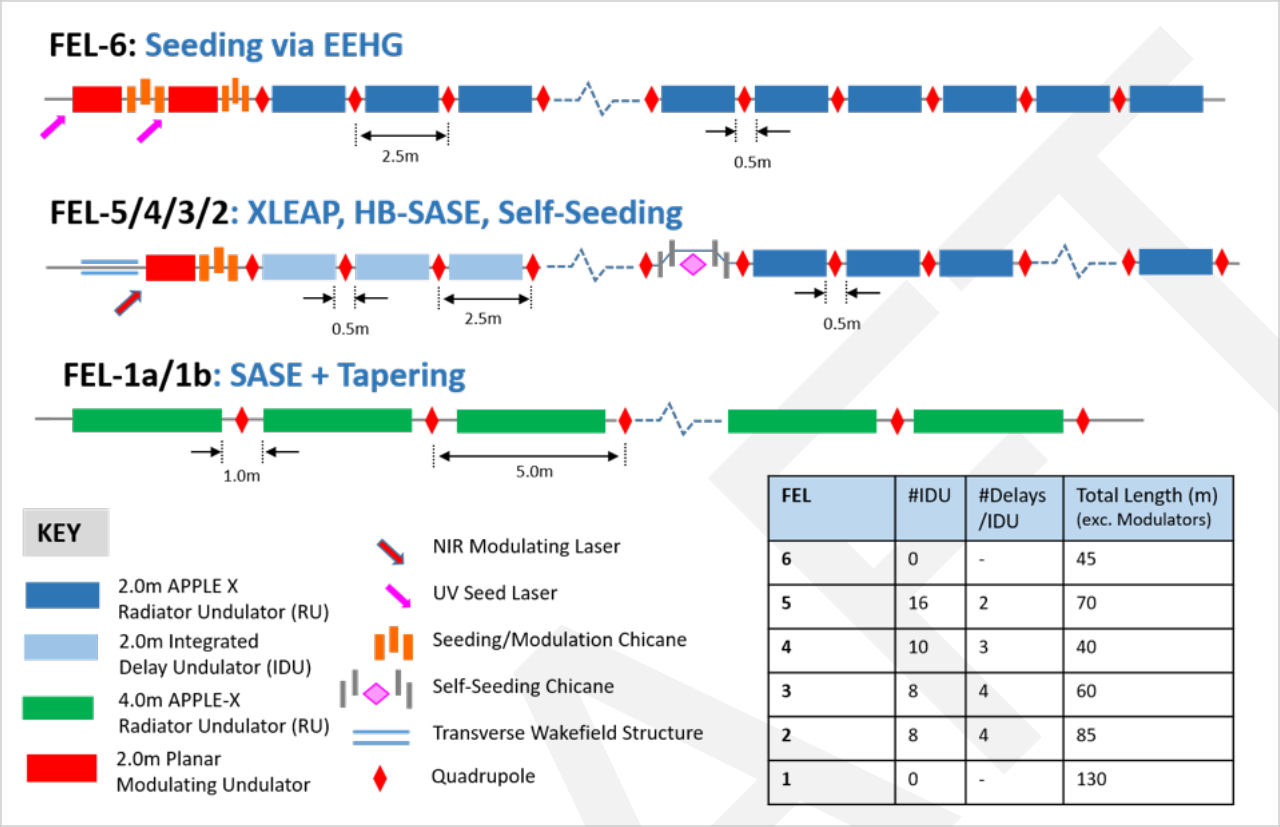

FEL	#IDU	#Delays /IDU	Total Length (m) (exc. Modulators)
6	0	-	45
5	16	2	70
4	10	3	40
3	8	4	60
2	8	4	85
1	0	-	130

Figure 3.13: Schematic of FEL components. FEL-6 features two modulator lasers/undulators to enable EEHG seeding. FELs 2-5 feature relatively short undulator modules with integrated chicane delays to enable HB-SASE, with a chicane for self-seeding, while a modulator laser/undulator enables laser-driven ESASE/XLEAP. FEL-1a/1b have a simple undulator layout for SASE plus tapering for high-power output.

3.4.3 FEL-1: extremely high pulse energy and photon energy

Other transformational enhancements of the X-ray pulse qualities include increasing the energy per pulse and the photon energy. These enhancements arise to a large extent from the accelerator features already outlined, i.e. the NCRF booster. The low repetition rate FEL-1 line is divided into two adjacent undulators (FEL-1a: high pulse energy and FEL-1b: high photon energy). While not included in the baseline due to their early development stage, it is recognised that period length doubling in a superconducting undulator [53] would be highly useful to cover the required photon energy range in a single undulator, and so merits continued investigation.

FEL-1a performance has been assessed in simulations with 300 pC bunches compressed to a peak current of 5 kA (to match the nominal charge for FELs 5 and 6, using the same injector set-up). **FEL-1a is predicted to produce pulse energies from 25 mJ at 5 keV (tapering applied) to 0.5 mJ at 20 keV** (with no tapering: the undulator length is set at 130 m to reach saturation at 20 keV with 50% contingency). FEL-1b will operate at a lower charge of 150 pC in order to achieve the lower emittance requirements at the higher photon energies. **FEL-1b is predicted to produce ∼7 mJ at 20 keV (tapering applied) and 0.15 mJ at 45 keV (with no tapering).**

To produce even higher pulse energies requires **special modes of operation** in which the beam energy is boosted higher (e.g. space is reserved for the NCRF booster to reach 15 GeV) and/or modes to increase the charge (routes to ∼600 pC have been investigated): **pulse energies of 50 mJ at 5 keV and 1 mJ at 40 keV have been reached in simulations.**

Section 5.6 describes alternative, PWFA-based routes to higher photon energies - potentially up to ∼60 keV by energy- and brightness-boosting the 8 GeV beam. Another route to extending the photon energy reach is harmonic lasing [54, 55], which could enable X-ray FELs to access even higher photon energies without requiring significant infrastructure upgrades. A novel split-undulator scheme [56] is proposed and investigated in Section 6.5.7.

3.4.4 Widely Separated Two-Colour Pulses

One of the transformative capabilities to be offered by a next-generation XFEL is a combination of widely separated two-colour X-ray beams at a single end station. Techniques for two-colour pulses are reviewed in Section 6.3.2. To deliver FEL-pump/FEL-probe capability with widely separated photon energies, the most comprehensive output can be delivered from schemes with two electron bunches delivered to two separate (e.g. parallel) undulators. A concept has been developed to achieve this, which builds on that developed for the CompactLight XFEL design [1]: the bunch pattern from the injectors is adjusted such that **two bunches are injected into adjacent RF cycles in the linac (i.e. separated by 0.77 ns), with a GHz subharmonic deflecting cavity in the FEL-2 line used to deflect one bunch onto an adjacent FEL, with path length difference compensating the temporal separation**, as shown in Figure 3.8. The FEL pulses can then be combined, with time of flight matching/scanning using electron delay chicanes.

3.4.5 Summary of the FEL parameters and beam modes

The FEL systems and required electron beam parameters are summarised in Table 3.1. The FEL output capabilities are summarised in Table 3.2 and Table 3.3.

Table 3.1: Main FEL and electron bunch parameters.

FEL	**1a**	**1b**	**2**	**3**	**4**	**5**	**6**
Photon Energy (keV)	5–20	20–45	5–20	3–13	1–5	0.25–3	0.1–1
FEL Modes	SASE + Tapering		ESASE + Self-Seeding + HB-SASE				EEHG
Undulator Period (mm)	28	18	21	24	32	48	82
Minimum Gap (mm)	4	4	4	4	4	5	8
Undulator Technology	APPLE-X		APPLE-X + IDUs				APPLE-X
Electron Energy (GeV)	12(+)		8			8	
Charge (pC)	300	150	75			300	
Bunch duration (fs)	60	30	30			100	
Peak Current (A)	5000	5000	2500			3000	
Emittance (mm-mrad)	0.5	0.3	0.22			0.5	
Slice Energy Spread	3×10^{-4}	3×10^{-4}	1×10^{-4}			1×10^{-4}	

Table 3.2: High repetition rate (≤100 kHz), near-transform-limited pulses from 100 eV to 20 keV.

FEL	Photon Energy [keV]	Mode	Technique	Pulse Duration [fs]	Pulse Energy (tapered)	Bandwidth [eV]
FEL-6	∼0.1 – 1.0	Seeded	EEHG	5 – 100	7 mJ for 100 fs (35 mJ for 100 fs)	0.72 – 0.036
FEL-5	0.25 – 3.0	Long	HB-SASE/ Self-seeding	75 – 30	6 – 1 mJ (30 – 5 mJ)	0.048–0.12
		Short	ESASE	2 – 0.35	160 – 11 µJ	3.6 – 20
FEL-4	1.0 – 5.0	Long	HB-SASE/ Self-seeding	30 – 10	1500 – 300 µJ (7.5 – 1.5 mJ)	0.12–0.36
		Short	ESASE	0.8 – 0.3	40 – 9 µJ	9 – 24
FEL-3	3.0 – 13.0	Long	HB-SASE/ Self-seeding	12 – 7	500 – 90 µJ (2.5 – 0.5 mJ)	0.3 – 0.52
		Short	ESASE	0.4 – 0.2	17 – 2.5 µJ	18 – 36
FEL-2	5.0 – 20.0	Long	HB-SASE/ Self-seeding	10 – 7	300 – 50 µJ (1.5 – 0.25 mJ)	0.36 – 0.52
		Short	ESASE	0.3 – 0.2	10 – 1.5 µJ	24 – 36
	∼10	Cavity	XFELO	∼100	∼10	∼0.035

Harmonics: Potential for parasitic 3rd harmonic emission with few % pulse energy (with appropriate photon transport), or up to 20% pulse energy at 5th harmonic and order of magnitude suppression of fundamental via harmonic lasing split undulator scheme. Not required for FELs 4-6 as already covered by other FELs.
Polarisation: Fully variable polarisation.
Nominal pulse structure: High repetition rate, evenly spaced pulses. Up to 100 kHz per FEL with potential for 200-300 kHz to be assessed.
Burst mode: Option to send pulses at 1 MHz to individual lines in bursts up to 100 ms to be assessed.

Table 3.3: Higher pulse energy and higher photon energies (non transform-limited) at ≤200 Hz or in short bursts.

FEL	Photon Energy [keV]	Mode	Technique	Pulse Duration [fs]	Pulse Energy (example special mode)
FEL-1a	5 – 20	High Power	SASE	∼30	25 – 0.5 mJ (∼50 mJ at 5 keV)
FEL-1b	20 – 45 (with booster)	High Power/ High Energy	SASE	∼30	7 – 0.15 mJ (∼1 mJ at 40 keV)

Harmonics: Potential for parasitic 3rd harmonic emission with few % pulse energy (with appropriate photon transport), or up to 20% pulse energy at 5th harmonic and order of magnitude suppression of fundamental via harmonic lasing split undulator scheme.
Polarisation: Fully variable polarisation.
Nominal pulse structure: Evenly spaced pulses up to 200 Hz
Burst mode: 10 pulses per burst, with >5 ns separation (216.67 MHz). Max. burst length 1 us (100 ns separation/10 MHz)

3.4.6 X-ray beamlines and diagnostics

As described in Chapter 7, the X-ray beamlines deliver the intense FEL pulses to the experimental stations while retaining or adjusting various properties, while photon diagnostics enable optimisation of the FELs and the beamline itself, and provide essential information for users to interpret the data from their experiments. To design an effective beam transport, it is necessary to have detailed and accurate models of the properties (size, divergence etc.) of each FEL source. Such a model must be derived from extensive simulations of the FEL output in each mode of operation, which will not exist until a technical design phase. To facilitate initial beamline concepts, a preliminary generalised model of the sources was developed using a limited set of simulations covering all the FELs.

Two case studies have been developed using this model, including a novel concept for combining X-rays from two different FELs for the two-colour soft X-ray - hard X-ray line as shown in Figure 3.14. Achieving spatial overlap requires deflecting the X-rays horizontally with mirrors to bridge the lateral separation of the FEL undulators. Achieving temporal overlap is more problematic; the majority of the deflection is necessarily done with the soft X-ray beam and this leads to a significant optical path difference between the beamlines. Since broad-band optical delay lines in the X-ray struggle to achieve more than a few picoseconds of delay, the overall timing (nanosecond-scale) synchronisation must be done via manipulation of the timing of the electron bunches through each FEL.

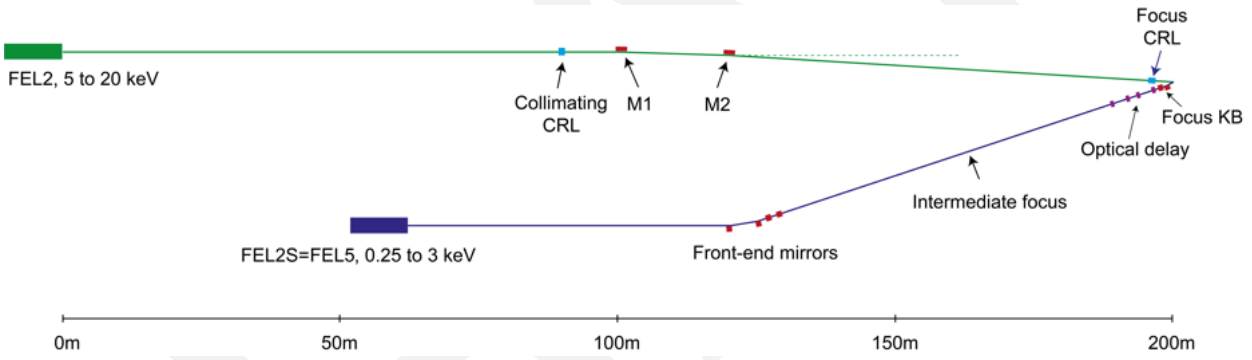

Figure 3.14: Layout of beamlines combining output of FEL-2 (hard X-ray) and its associated soft X-ray FEL (equivalent to FEL-5), separated by 3.2 m to a common interaction point.

With over 20 years of operation of XUV and X-ray FELs, many of the original challenges to effective beamlines and diagnostics that were presented by the unique properties of a FEL source have been addressed. **However, the next-generation FEL presents significant new challenges due to the high repetition-rate CW operation, the near-transform-limited pulses, and the fully flexible polarisation.**

There will be high average power in the photon beams e.g. 10 mJ pulses at 100 kHz repetition rate gives a beam power of 1 kW. The beamline optics will need to not only survive such power levels but also retain their optical quality if the beam on target is not to be degraded. So, although kW-level beams are successfully exploited on synchrotron radiation sources, the extra burden of retaining wavefront on the FEL means additional efforts are required to maintain, for example, the surface form accuracy of the x-ray mirrors. Multi-shot damage also becomes a major concern at high repetition rates; an optic with a lifetime of years at 100 Hz could be damaged in hours at 100 kHz.

The flexible polarisation has consequences for some optics and diagnostics. Bragg crystals, used in monochromators and spectrometers, have zero reflectivity at 45° for the P-polarisation

state and partly depolarise circularly polarised beams. Any beamline designed with a crystal monochromator should have the option for it to be easily removed from the optical path in order to permit circular polarisation on target. Diagnostics that involve measuring the angular distribution of photoemission cannot distinguish circularly polarised and unpolarised beams.

When the pulse duration and bandwidth are related via the transform limit, the need for traditional monochromators must be questioned. In SASE modes, a monochromator can usefully improve spectral resolution and reduce jitter in the central wavelength. For a monochromator to be useful with any single-spike FEL pulse, the central wavelength jitter must be reduced to a small fraction of the monochromator bandpass; larger jitter will reduce or even stop transmission through the monochromator. In general, monochromators will only be useful for improving spectral resolution beyond that offered by the longest transform limited pulses, or if running in SASE mode.

DRAFT

3.5 Theme 3: World-class end stations, synchronous sources, data and AI

This section outlines the suite of world-class and independently operable scientific end stations envisaged for a next-generation XFEL, including state-of-the-art detectors and auxiliary infrastructure. It describes how such a facility will perform as a laser facility as well as a particle accelerator facility, with exceptional synchronisation and timing systems in place throughout. And it outlines the data and AI infrastructure to acquire, process, and realise the transformative impacts of what will be one of the largest sources of high-value scientific data in the world.

3.5.1 User instrumentation: End stations

The conceptual design has been shaped by an extensive, multi-year consultation process involving UK facility users, new scientific communities, and technical experts from leading XFEL facilities worldwide. Through focused technical workshops and targeted discussions with international instrument teams, this process has specified **a comprehensive initial provision of end stations for a next-generation XFEL** that will exploit the cutting-edge capabilities of the facility. They are selected to enable a high throughput of pioneering research in the physical and life sciences, as well as in technological and industrial applications. The resulting end stations are summarised in Figure 3.15 and Table 3.4, with details provided in Chapter 8.

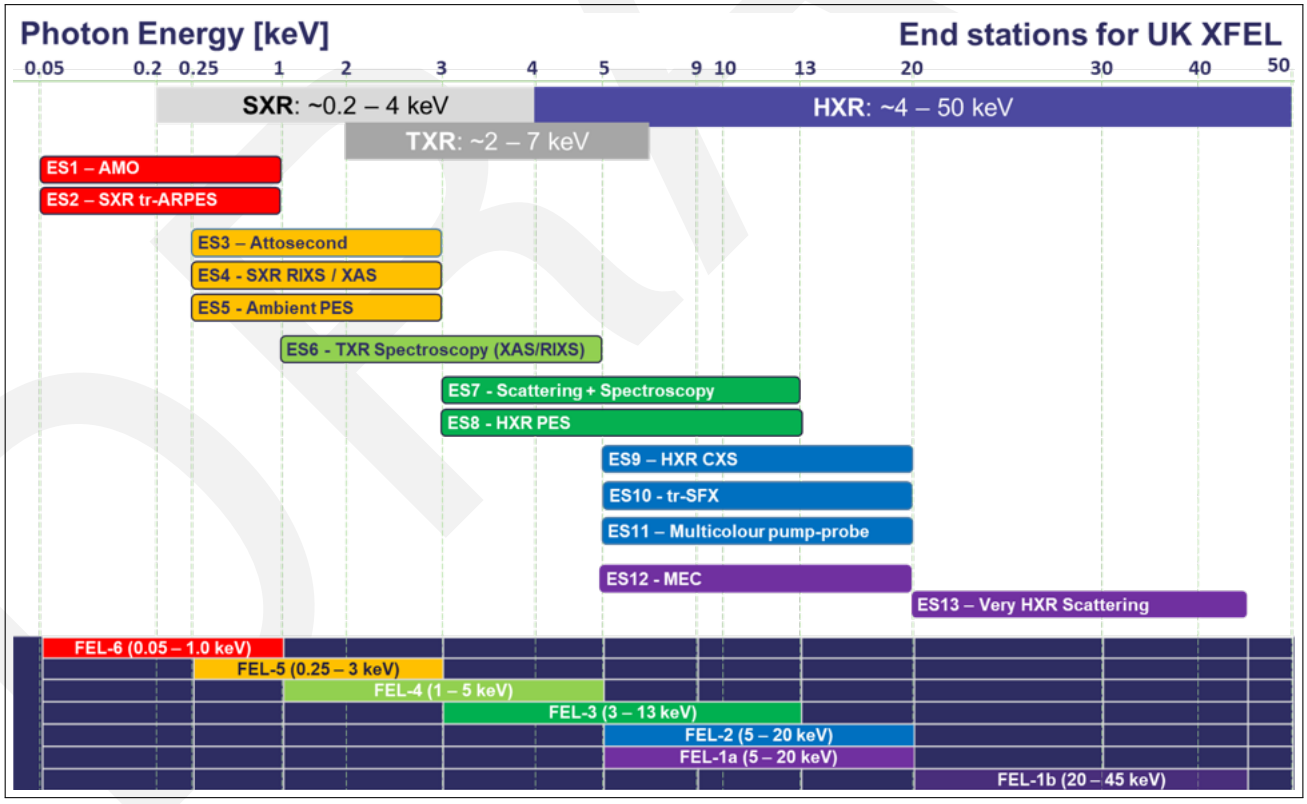

Figure 3.15: Map of proposed end stations across all of the FELs covering the soft X-ray (SXR), tender X-ray (TXR) and hard X-ray (HXR) range.

Table 3.4: Overview of the end station capabilities.

Category	Name	FEL	Description
AMO & attosecond	ES-1	FEL-6	**AMO:** ES-1 will focus on ultra-fast pump-probe atomic, molecular and optical (AMO) experiments primarily in the gas phase, potentially with liquid sample delivery in some circumstances.
	ES-3	FEL-5	**Attosecond AMO:** ES-3 will focus on applying AMO techniques at the very shortest pulse durations, down to 100's attoseconds for X-ray energies between 0.25 – 3 keV. New experiments studying charge migration and its affect on longer-timescale dynamics, with applications across photo-induced processes in chemistry and biology.
ARPES	ES-2	FEL-6	**Soft X-ray tr-ARPES:** Time-resolved ARPES (tr-ARPES) end station on FEL-6 (50-1000 eV) will cater for material sciences, including the studies of ultrafast processes at surfaces and in quantum materials.
	ES-5	FEL-5	**Ambient pressure PES:** Ambient pressure PES (APPES) end station will enable studies of chemical composition by probing both core and valence electron states in a range of sample configurations.
	ES-8	FEL-3	**Hard X-ray PES:** Time-resolved hard X-ray photoelectron spectroscopy (tr-HAXPES). Higher probe energies unlock much greater bulk sensitivity, the option to study samples in operando and the ability to access core energy levels of a much wider range of materials.
Spectroscopy & scattering	ES-4	FEL-5	**RIXS and XAS:** ES-4 will primarily cover resonant inelastic X-ray scattering (RIXS) experiments as well as regular time-resolved X-ray absorption spectroscopy (XAS) and X-ray emission spectroscopy (XES) methods across the 0.25-3 keV tuning range, for two main user communities; those studying quantum materials and those applying RIXS techniques for chemistry.
	ES-6	FEL-4	**Soft-tender X-ray spectroscopy:** The tender X-ray range offers opportunities for time-resolved XAS (tr-XAS), XES and RIXS in chemistry and life sciences, covering elements that play important roles in catalysis, battery research, photovoltaics and environmental science.
	ES-7	FEL-3	**X-ray spectroscopy and scattering:** ES-7 extends these techniques to hard X-rays, up to 13 keV, for time-resolved photochemistry applications. Many experiments will be performed with liquid samples under ambient conditions, often with simultaneous spectroscopy and scattering measurements to study coupled structural and electronic dynamics.
Other	ES-9	FEL-2	**Hard X-ray Coherent Diffraction Imaging (CDI):** ES-9 will specialise in using CDI and time-resolved scattering techniques (WAXS/SAXS) in the hard X-ray range (5-20 keV). Caters for experiments based on transmission and Bragg CDI for both gas phase and solid state samples.
	ES-10	FEL-2	**Time-resolved SFX:** The main end station for time-resolved X-ray serial femtosecond crystallography (tr-SFX) to probe structure and function of biological samples. Supports measurements of crystals down to sub-micron scales under physiological conditions.
	ES-11	FEL-2	**Multi-colour end station:** A transformative capability comprising independently-tuneable soft (approximately 0.25-3 keV) and hard (5-20 keV) X-ray FELs, offering several unique experimental capabilities.
MEC & Very hard X-ray scattering	ES-12	FEL-1a	**MEC end station:** ES-12 will be designed as a flexible experimental area capable of coupling both high intensity, short pulse lasers or high energy, long pulse lasers with FEL-1a (5-20 keV) for X-ray spectroscopy, scattering and imaging.
	ES-13	FEL-1b	**Very hard X-ray scattering and tr-PDF (pair distribution function):** very hard X-rays used to 1) penetrate dense samples and image dynamic processes, and 2) generate scattering patterns covering an extended range of reciprocal space to study local structure for liquids and amorphous samples.

A set of required capabilities has been established for each end station, and each has been associated with a particular FEL from the 'nominal' set of FELs 1-6. **It is assumed that up to 3 end stations could be positioned on each FEL, as shown in Figure 3.16, with the X-ray beam deflected left / right or allowed to propagate straight on.**

A central theme is how the end stations can be designed to minimise set-up periods and facilitate rapid switchover between configurations. Where possible, the priority is placed on providing several semi-permanent experimental set-ups rather than exchanging significant parts of each experiment between runs. As a result, **several end stations feature multiple interaction points** (IPs). Although not able to operate independently, this approach will minimise changeover time between similarly configured experiments and caters for very different sample types, e.g. solid state and liquid jets. A capability must also be maintained to experiment with non-standard set-ups, within the existing end stations or through open ports.

In order to meet the demands of a diverse user community in terms of X-ray beam parameters, FEL-1 is split into two undulators and two beamlines. To maximise the level of parallel operations and minimise extended changeover times between experiment configurations, **two primary end stations are allocated for MEC and related hard X-ray scattering work** (ES12 and ES13 respectively), and a laser-only experimental area is envisaged. The layout is designed to share high-power and high-energy laser capabilities, housed on an upper mezzanine level above the experimental areas.

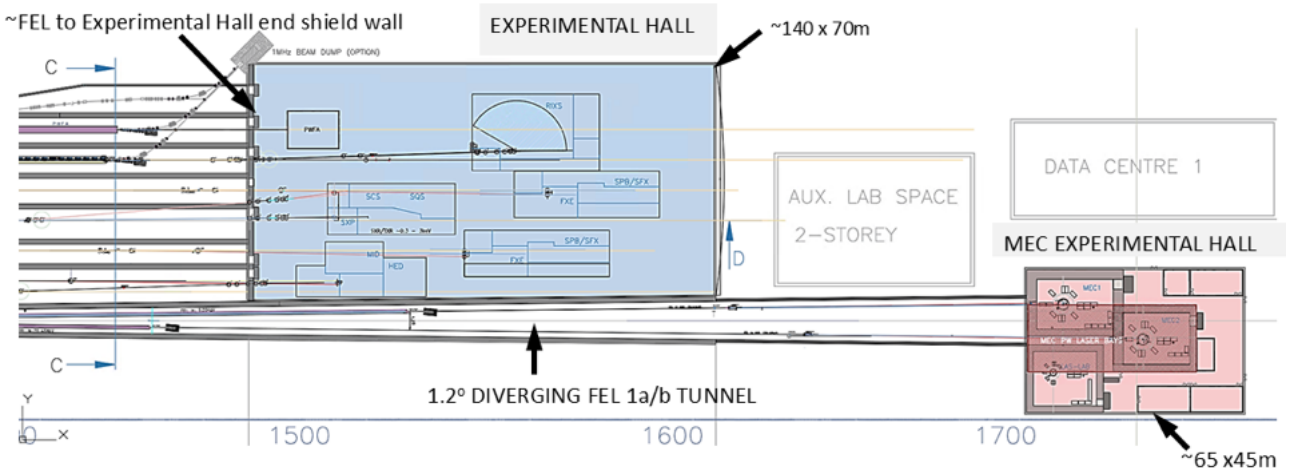

Figure 3.16: Experimental halls layout (spanning from ∼1.4 km to 1.8 km). Three end station hutches can be accommodated per FEL line, with these clusters of end stations staggered relative to each other to minimise the transverse deflection required in the spreader

All end stations share a common requirement for sample preparation and support laboratories. User-provided samples may require extensive characterisation both before and after beamtime. In some cases, particularly where samples are highly sensitive or transport from the home institution is impractical, sample preparation may need to occur entirely on site. To optimise beamtime usage, sample delivery systems could be duplicated in offline settings, allowing for refinement and testing prior to use in the experiment.

3.5.2 AI, data, and detectors

A core feature of the next-generation XFEL concept is the extremely high repetition rate (100 kHz-1 MHz) operation, which couples various accelerator, laser, and end station technologies with the emergence of artificial intelligence. **Next-generation XFELs operating at MHz will be some of the biggest data-generating capabilities on the planet,** supplying vast datasets to underpin foundation models across a host of disciplines.

MHz XFELs will produce data at unprecedented rates (towards TB/s) and scales (PB per data set), requiring a **comprehensive data pipeline that incorporates FAIR data management [57], a dedicated data centre, integration with national exascale computing [58, 59] and AI [60, 61] capabilities,** to enable effective data reduction and analysis, as shown in Figure 3.17. AI-enabled platforms can coordinate mission-driven or community-driven experimental programmes involving multiple user groups and large sample libraries, allowing communities to collectively use XFEL data to accelerate progress across entire scientific areas, as described in Chapter 12.

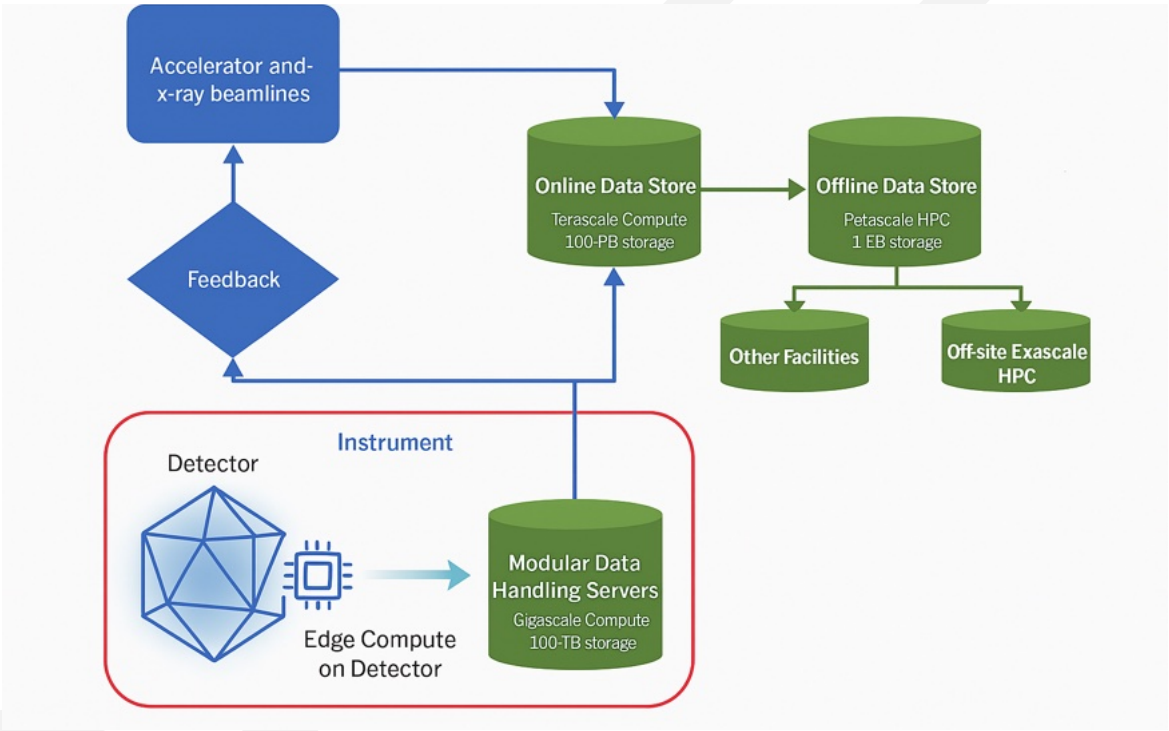

Figure 3.17: Proposed high-level data pipeline for a next-generation XFEL.

Applying AI/machine learning and digital twinning to facility operation will be integral to many-user operation and increased throughput. Present XFELs operate 1-3 FELs simultaneously and rely heavily on expert operators, so increasing automation is important to give operators new capabilities to optimally support many more simultaneous FELs. AI and machine-learning methods for accelerators [62] can provide high-fidelity virtual diagnostics from non-invasive measurements and support early fault detection, while edge- or FPGA-based real-time deployment may be essential for some high-repetition-rate applications.

At the end stations, closed-loop autonomous experiments in which AI models interpret data in real time, make decisions on sample orientation, beam parameters, or instrument configuration, and automatically optimise measurement strategies, will significantly reduce experimental cycle times and unlock scientific studies that would be impractical with traditional manual operations.

Digital twins can unify the real facility and its virtual counterpart into a single, tightly integrated source of truth, combining control-system data with physics and engineering models to support

predictive maintenance, real-time diagnostics, and continuous optimisation. Recent work [63] has demonstrated an auto-generating digital-twin architecture for both existing accelerators and the next-generation XFEL, showing how such systems can prototype software, controls, and experimental procedures even in this conceptual design phase.

Advances in detector technology are required to manage the extreme brightness and high repetition rates of a next-generation XFEL, as described in Chapter 10. Many of these needs can be partially met with existing or developing solutions, but integrating these into fast, continuous-operation detectors remains a challenge. Development goals overlap with other XFELs and scientific facilities, presenting opportunities for collaboration and technology transfer. The wide energy range of proposed FELs and varied experimental techniques require diverse, custom detector technologies. For FELs 4-6, detectors are primarily silicon-based and the main challenges are surface treatments to allow capture of the lower energy X-rays and internal gain mechanisms to amplify the associated low signals. Silicon detectors are well suited for FEL-3 but different sensor materials are required at higher energies for FELs 1-2, as illustrated in Figure 10.3.

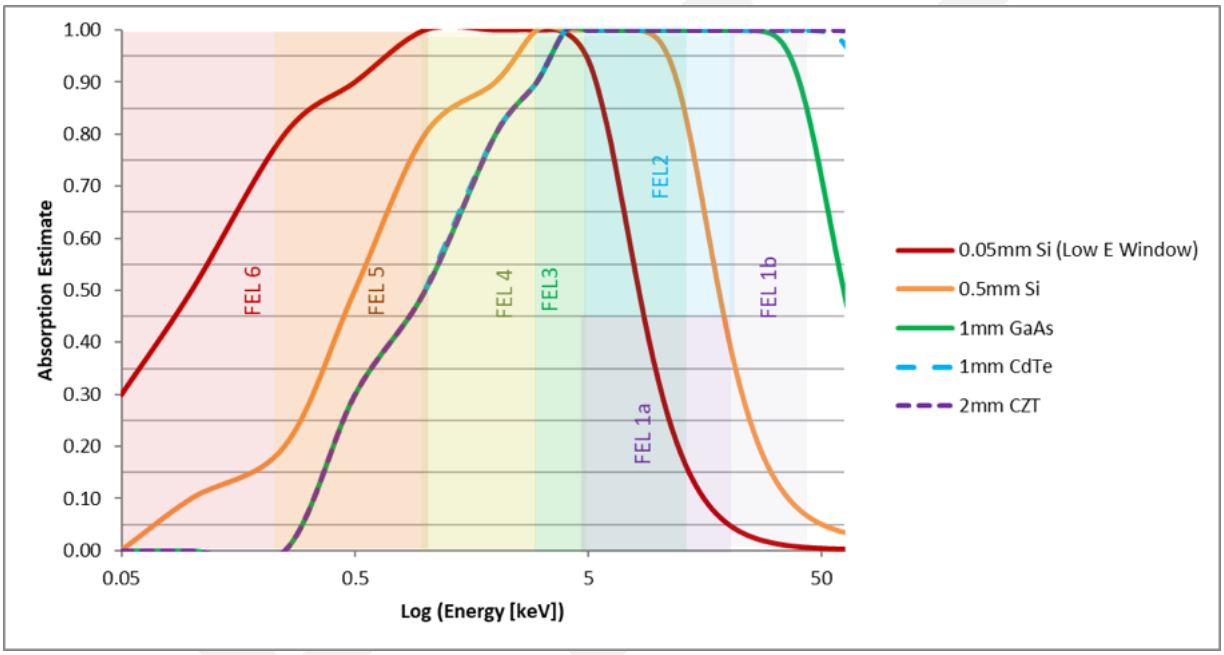

Figure 3.18: Sensor material X-ray stopping power with energy relating to the FEL energies.

The soft X-ray end stations of FEL-6 and 5, such as AMO, have multiple interaction points, requiring a suite of detectors around each location. In general, the primary measurements focus on the electrons and ions emitted from the sample. Whilst hemispherical detectors and magnetic bottles can measure the energy and electronic states of a sample via X-ray Photoelectron Spectroscopy (XPS), more advanced measurements, such as time-resolved ARPES (trARPES) or spin-sensitive detection, require advanced systems such as momentum or reaction microscopes [64].

The tender and hard X-ray end stations primarily conduct X-ray diffraction and scattering measurements across various configurations. The underlying detector requirements generally remain consistent and call for megapixel-scale detectors with a 50–100 µm pixel pitch, high dynamic range, and frame rates in the 10–100 kHz range. The MEC and VHXR end stations, however, focus on imaging and diffraction at MHz or even $>$100 MHz rates in burst mode. Many end stations also require absorption or emission X-ray spectroscopy with energy resolutions at the eV or sub-eV level. Even though various geometries can be used to spatially disperse the different X-ray energies, they all depend on fine pixel or strip detectors capable of high dynamic range measurements.

3.5.3 Synchronous sources

Pump-probe experiments are the cornerstone of ultrafast science at XFELs: they enable samples to be studied by exciting them with one or more ultrafast 'pump' pulses of photons or particles, and interrogating the response with a 'probe' (X-ray) pulse [65]. Therefore, one of the defining features of a next-generation XFEL facility will be timely and dynamic access to a comprehensive suite of synchronous sources, as described in Chapter 9.

Synchronous laser-like optical sources operating at the machine repetition rate (∼100 kHz) will be ubiquitous in a next-generation XFEL. They are required over a wide range of spectral and temporal regimes, and must be highly reliable and straightforward to integrate into experiments. **A core set of laser systems based on a single technology platform will be used to produce energies in the millijoule range at ∼100 kHz, to drive a wide range of cascaded non-linear optical processes. A solution in the form of Ytterbium (Yb)-based lasers and amplifiers [66, 67] is selected,** which has strong commercial development and demonstrated benefits in performance and reliability being realised at LCLS-II and Eu-XFEL.

Each end station will feature a suite of frequency conversion systems, for which there are already several commercial solutions. Bespoke examples of such systems form part of the HiLUX upgrades of ULTRA and Artemis at the Central Laser Facility [68, 69], which will be among the UK's premier ultrafast research facilities. **A modular approach, as used for LCLS-II, will enable rapid deployment by using standard breadboard-mounted optical assemblies.** This further enhances reliability and up-time as the decoupling of the drive laser from the conversion optics allows the drive laser to be swapped over in cases of failure or planned maintenance. This also enables the rapid switching of online optical diagnostics, for both temporal and spatial properties, to provide crucial full characterisation and monitoring of the pulses provided to experiments. A potential configuration for the laser systems in a next-generation XFEL ultrafast science end station, as proposed in [65], is shown in Figure 9.3.

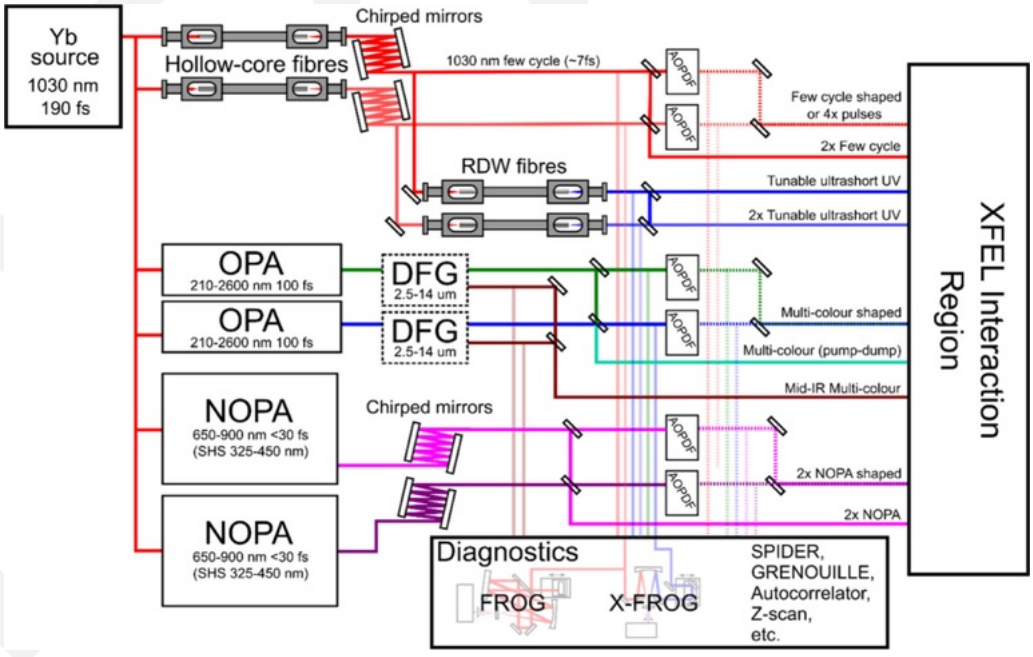

Figure 3.19: Proposed optical arrangement of systems and diagnostics available at an ideal ultrafast XFEL beamline, with an example of an Yb pump laser. Figure reproduced from [65].

For THz sources, laser-based methods [70, 71, 72], including those using organic crystals [73] and spintronics [74, 75, 76, 77, 78], show continued and rapid progress and so are

selected as the baseline, however a stand-alone accelerator-based source [79] could be added behind or to the side of the end stations if required, mitigating impact upon the facility layout.

Specialised high-power and high-energy laser infrastructure [80] is also needed to achieve the high energy density (HED), high field and high pressure environments to enable studies in e.g. fusion energy and laboratory astrophysics/geophysics. It is anticipated that the main laser systems will be underpinned by a next-generation diode-pumped system that can either be operated in a native long pulse mode (ns pulse duration), or used to pump a short pulse (30 fs) high power system. The long pulse driver should deliver energies of at least 500 J per beam at a repetition rate at 10 Hz or above. Two twinned laser systems (500 J + 500 J) would enable more novel experimental configurations such as colliding shocks. These lasers could be used to pump high intensity, short-pulse laser systems to deliver multi-PW (e.g. 10 PW + 10 PW) powers. A next-generation XFEL could draw on the UK's leadership and extensive experience with high repetition rate, high power lasers, notably the Central Laser Facility's design and build of the D100X-DiPOLE laser [81], the recent commercialisation of this technology [82], and the Extreme Photonics Application Centre (EPAC) [83].

Sub-femtosecond timing of X-rays and optical lasers is crucial for a next-generation facility and it is a significant challenge. It requires continuous improvement upon cutting-edge systems, including the advanced hybrid synchronisation architecture which is now routinely demonstrating $<$10 fs levels of performance at European XFEL [84]. Achieving sub-femtosecond experiment resolution requires a step-change in the design and provision of photon arrival monitors (often referred to as 'time tools') which independently measure the X-ray/optical arrival time at each experiment. Advances in material design are required to achieve required performance gains in sensitivity and bandwidth for the wide range of optical and X-ray parameters in a next-generation facility. The design of each photon arrival monitor should be such that it replicates, as far as possible, the configuration of each end station interaction point and samples a common noise environment. This requires fundamental incorporation of timing systems into the broader end station design and engineering process. A proposed synchronisation architecture for the next-generation XFEL concept is shown in Figure 3.20 and is described in Chapter 11.

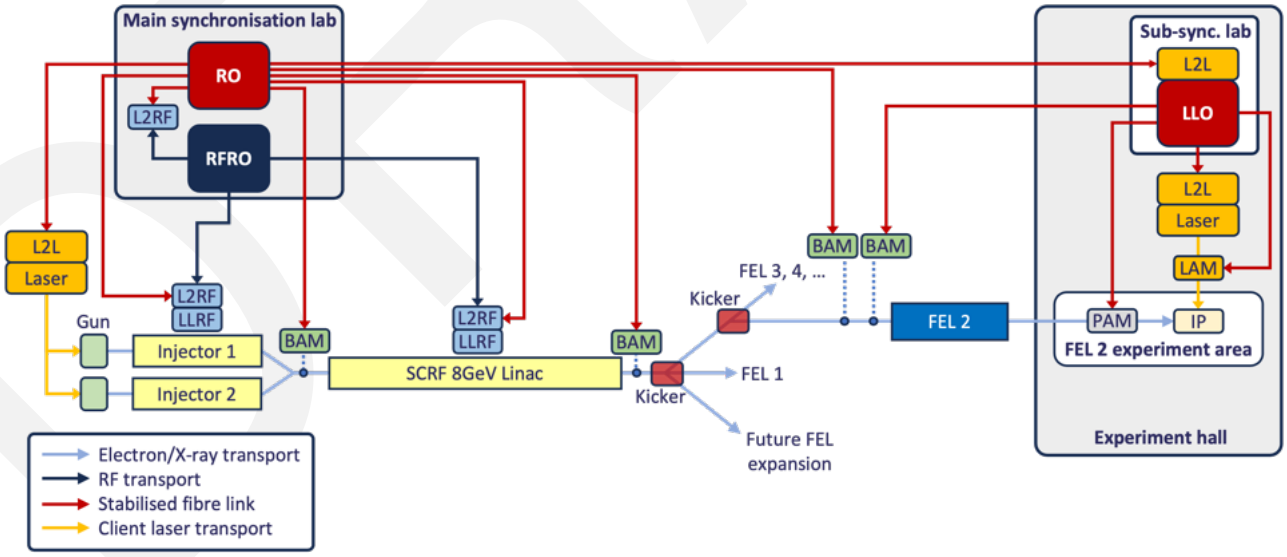

Figure 3.20: Example synchronisation architecture for the next-generation XFEL concept. ORO: Optical Reference Oscillator; RFRO: RF Reference Oscillator; LLO: Local Laser Oscillator; L2L: Laser-to-Laser synchronisation; L2RF: Laser-to-RF synchronisation; BAM: Beam Arrival Monitor; PAM: Photon Arrival Monitor; IP: Interaction point (laser and X-ray).

3.6 Engineering delivery, environmental sustainability, and project planning

This section focuses on the engineering delivery, environmental sustainability principles, and project-planning framework underpinning the new-build facility option, where these considerations can be applied most comprehensively from first principles. It also highlights aspects of the approach that are relevant to upgrades of existing facilities, recognising the constraints imposed by established layouts and infrastructure.

3.6.1 Facility layout and engineering

The engineering design of the next-generation XFEL is driven by the need for a high-throughput, user-focused facility with excellent uptime, efficient operating costs, a relatively compact footprint, and the flexibility to support phased delivery and future upgrades. These aims are realised through the use of established technologies and a ground-level, modular design that simplifies shielding, provides generous experimental space, and allows the facility to expand as scientific needs evolve. Chapter 13 discusses these considerations section by section.

Given the elongated aspect ratio of the site, the version of the layout shown earlier in Figure 3.1 omits a repeating section of the SRF linac for clarity, while Figure 3.21 illustrates the design to scale. **Overall, this version of the facility – with ancillary buildings, a perimeter plus access roads and some allowance for future upgrades would occupy a land footprint of approximately 2 $\times$ 0.25 km**.

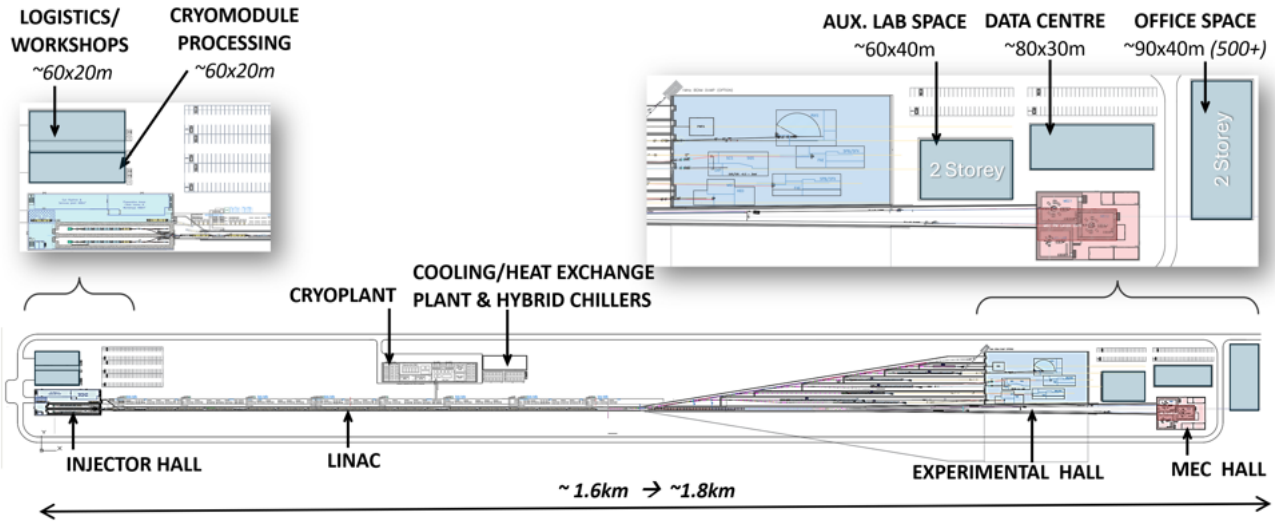

Figure 3.21: Layout of the next-generation XFEL design to scale, including ancillary and auxiliary buildings.

The facility layout has been shaped by user requirements, balancing 'front-to-back' optimisation of spreader beam dynamics against 'back-to-front' requirements for end-station dimensions and spacing. **The experimental hall, shown on the right of Figure 3.21, measures approximately 160 m x 65 m and can accommodate three end station hutches per FEL line.** These clusters of end stations are staggered rather than placed side-by-side to minimise the transverse deflection required in the spreader. They are all located on a single level to simplify equipment access,

laser-room placement, and overall operational logistics. Ensuring that the experimental hall provides generous space and is configured to allow fast, reliable switching between end stations is critical for achieving the high experimental throughput required of a next-generation XFEL.

Working backwards from the end station layout, **the photon transport lines (Chapter 7) and undulators (Chapter 6) are housed in individual halls, separated by modular re-configurable concrete shielding blocks to allow independent maintenance of each FEL line and preserve operational independence.** The resulting spreader design occupies almost 400 m, with the FEL start-points staggered along this length. The spreader deflects the beam by $\sim 9^{\circ}$ from the linac straight-on axis, and can direct any electron bunch from the 1 MHz beam to the appropriate undulator line, enabling distribution up to 100 m off axis in the nominal configuration.

Whilst the width of the spreader is dictated by the end station layout, the overall facility length is primarily set by the electron accelerator. **The linac hall uses a cut and cover design, much like the FEL halls, and extends $\sim$1 km from the photoinjector hall to the FEL spreader.** This allows for a conventional SRF linac to accelerate the beam to 8 GeV, with the length defined by the number of cryomodules and their accelerating gradient, with cost optimisation of the gradient summarised in Section 3.3.3.1. On the straight-ahead linac axis, an additional $\sim$130 m long C-band NCRF booster linac increases the electron energy to 12 GeV, with a further $\sim$100 m drift space reserved for a future energy upgrade. This feeds into the FEL-1 lines that lead to two end stations positioned downstream of the rest, equipped with high-power lasers for MEC and related hard X-ray scattering studies.

A site visualisation, including ancillary and auxiliary facilities, is shown in Figure 3.22.

Figure 3.22: Site visualisation of the next-generation XFEL facility.

A significant remaining design choice is whether to include a dedicated RF hall alongside the linac. Although such a hall could add cost and incurs transmission losses, it offers advantages, including potentially improved uptime and the ability to use either klystrons or solid-state amplifiers (SSAs). Operating without an RF hall is an option only if using SSAs, due to their compact size. A detailed cost–benefit analysis should be carried out during the technical design stage.

One of the more challenging engineering aspects of the build will be the beam dumps: **to simplify the design and to improve operational reliability, each FEL line has its own dedicated beam dump**, as shown in Figure 3.1. The electron beam is diverted downward into a shielded underground pit, where a 300 kW dump will be located inside a removable concrete housing.

Section 13.2.6 details the radiation issues (such as sky-shine and ground water) as well as discussing the space reserved should larger dumps be required.

There will be also be a requirement for additional ancillary buildings and infrastructure, cryoplants, RF galleries, data centres, workshops, logistics buildings, test stands, laboratories and office space etc. During the Town Hall meeting users put significant emphasis on accessible lab space, along with high performance compute access, as such these buildings have been included to ensure efficient sample preparation and effective post experiment data processing. All of the buildings should be well insulated to both improve energy consumption and provide stable temperatures.

A next-generation XFEL should be designed around autonomous operation and robotics from the start, employing infrastructure that supports autonomous inspection, maintenance, and environmental monitoring across the accelerator and experimental halls. Purpose-built robotic systems have the potential to significantly outperform retrofitted capability and can be tightly integrated with facility controls and digital twins. These aspects are described in Chapter 12 and Section 13.2.5.

3.6.2 Environmental sustainability

Large accelerator facilities are among the most complex and resource-intensive of scientific instruments: their construction and operation involve substantial energy consumption, extensive use of materials, and long-term environmental impacts. As such, **environmental sustainability is an essential consideration that must to be integrated into every stage of the facility's lifecycle** - from early design decisions through to decommissioning. This not only aligns with global climate goals but also enhances operational efficiency, reduces costs, and strengthens public support [85, 86, 87].

The greatest opportunities for impact lie in the earliest phases of planning, where strategic choices can lock in long-term environmental benefits. Section 14.1 sets out a framework for embedding sustainability into the design, construction, and operation of the proposed facility. The analysis identifies energy use during operation as the dominant factor in its carbon emissions. During the future operation period of a next-generation XFEL, the carbon intensity of the electrical grid is expected to be significantly lower than that of today in all scenarios [88, 89]. However, it is not zero. A large multi-MW facility like a next-generation XFEL must still strive to reduce its electricity usage as far as possible in order to minimise its environmental impact.

In terms of power consumption, the largest single subsystem is the RF and cryogenic system powering the cavities to accelerate the beam to high energy. This occupies over a third of the estimated total 37 MW. Table 14.1 shows how this figure breaks down across subsystems.

Switching to **thin film cavities** [15] (rather than solid niobium) would enable the operating temperature to be raised to 4 K, reducing the cryogenic power draw by a factor of 3, which would result in a saving of 5.8 MW. Assuming **permanent magnets** [90, 91] could be used for half of all the accelerator magnets gives an approximate saving of 3 MW. Also for **climate control**, depending on facility location, it may be possible to make use of free cooling or ground water cooling to reduce the power consumption of these systems. Additionally, the waste heat generated by the accelerator can be used indirectly to provide heating and hot water for nearby offices and homes.

Computing resources are expected to occupy a significant fraction of the power budget. The **data centre** for a next-generation XFEL would be built to the highest-possible efficiency specifications.

Subsystem	Power consumption [MW]	Annual energy consumption [GW h]	Annual emissions [ktCO$_2$e]	Potential savings [MW]
RF (Section 5.1)	15.2	102	5.00	5.8
Other technical systems	8.12	65.0	3.19	3.0
Services and infrastructure	7.21	57.7	2.83	-
Data centre (Section 12.1)	3.24	14.2	0.70	-
Secondary sources	1.95	9.75	0.48	-
Undulators (Section 6.7)	1.3	10.4	0.51	-
Total	37.0	259	12.7	

Table 3.5: Energy consumption for significant UK XFEL subsystems, and the corresponding annual emissions. The figures for the undulators are based on including SCUs for FEL-1 (which is a potential future upgrade, see Section 6.7.3), and assume that the cryogenic system operates for 8000 hours per year, in line with the assumptions about the RF system (see Section 5.3.2). A grid intensity of 49 gCO$_2$e/kWh is assumed. The major potential savings identified for RF and other technical systems refer to using thin-film SRF and 50% usage of permanent magnets respectively, while others systems should be addressed in a future phase. See also Section 13.2.9 for a detailed breakdown.

Travel of users to a large scientific facility is a large 'hidden' source of carbon emissions, primarily due to the high impact of aviation. This should be a major concern for a future facility, and any siting decision should be made with this in mind, making sure a location is selected with good public transport links, while also pursuing remote operation capabilities. **On-site solar and wind power** will also play a key part and have proven to be effective at other facilities [92].

Although the operation of a large facility over several decades is the dominant factor in its carbon emissions, there is also a significant contribution from the embodied emissions from the materials used in its construction. Sustainable construction practices such as low-carbon concrete [93], modular and reusable shielding blocks, and localised radiation shielding to reduce material volumes. Maintenance and end-of-life considerations are also addressed, with a focus on modularity, recyclability, and minimising activation of components to enable reuse.

3.6.3 Importance of site selection

As indicated above, **for a new-build facility, the site selection process is critical to establishing the final design**, as site characteristics will influence construction style, shielding needs, and environmental impact. A flat, accessible site away from urban centres is preferred to minimise costs and complexity, but should have good proximity to airports, rail, and motorways for global access and logistics. The beam stability will also be dependent upon ground vibration, thermal drift, and long-term settlement, which are all geological considerations. Radiation shielding will to be impacted by the location, however in any case the facility must comply with UK regulations,using advanced shielding models and beam loss monitoring systems to ensure safety for personnel and the environment. This is discussed fully in Chapter 13, and follows a commissioned report by Nuclear Technologies for this project.

3.6.4 Planning, governance, and stakeholder coordination

Delivering a facility of this scale in the UK would constitute a mega-project, reflecting its cost, complexity, and international strategic importance. Such an undertaking demands meticulous

planning, governance, and stakeholder coordination: projects that invest heavily in early-stage definition are much more likely to achieve their intended outcomes later on and display world-class delivery standards [94]. Chapter 13 details the project management and delivery up to operational readiness, covering early appraisal, strategic planning, design, procurement, construction, and commissioning. It draws on decades of scientific infrastructure experience, on UK Government best practices, and on STFC's project management framework. Specifically it refers to the **Green Book** for economic appraisal and strategic alignment, the **Teal Book and Project Routemap** for delivery planning, risk management, and governance, and to the **STFC Project Management Framework** for technical oversight and funding approvals.

Key delivery principles include:

- Phased Construction: Starting with core accelerator infrastructure and expanding based on emerging priorities.
- In-Kind Contributions: Leveraging expertise and resources from UK and international partners.
- Digital Twinning, Model-Based Systems Engineering, and Effects Analysis: to de-risk the build, accelerate delivery and improve integration.
- Stakeholder Engagement: Including public consultation, user input, and coordination with government bodies.

The facility concept has been designed in such a way to allow multiple possible configurations, that could form the basis of a phased delivery. A proposed phasing route is shown in Figure 3.23 and is described in detail in Section 15.2.

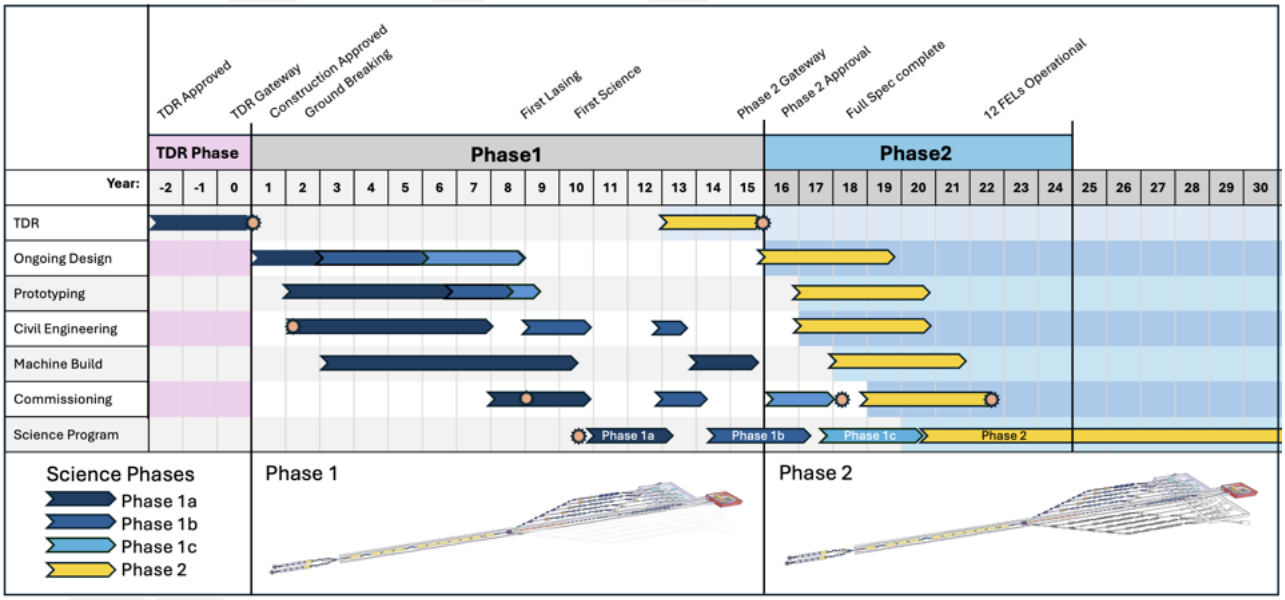

Figure 3.23: Estimated timelines for the proposed phasing route.

Governance will evolve through stages, with oversight from STFC, UKRI, DSIT, and potentially the National Infrastructure and Service Transformation Authority (NISTA) and HM Treasury. It is expected that funding would be released in phases, aligned with technical design reviews and business case development, and the project planning should anticipate this.

3.6.5 Cost estimates

Following the principles described above, a top-level costing has been produced and compared to other reference cases. A next-generation XFEL will be a large-scale and long-term international project, estimated to be a £-billion-scale investment, to be spread over a ∼10-year build phase, projected to begin in the early 2030s. Investment would likely be shared between several countries, with the host nation typically taking a majority share, e.g. European XFEL. Estimated costs are in line with similar facilities, when indexation is taken into account. A final costing must be performed once a technical design is complete and a site chosen. The operational costs are expected to be on par with existing facilities, however there is significant scope to improve on the science per pound cost by designing in more cost- and carbon-efficient processes at the technical design stage.

3.6.6 Next steps

This conceptual design provides a robust and technically feasible blueprint for a new generation of XFEL capabilities. It can underpin a new facility in the UK or internationally, with scalability in performance and a phased construction pathway, while many elements are directly applicable to upgrades of existing XFELs worldwide.

Advancing this work will require a dedicated technical design phase tailored to the chosen option. While many enabling technologies are mature or rapidly advancing, substantial development is still required to meet high-repetition-rate demands across all accelerator, laser, sample-delivery and detector systems, to build advanced data-acquisition and analysis pipelines, and to achieve major environmental sustainability gains. Targeted R&D will be required across these areas, and for a new-build facility an injector test facility is expected to be a critical step in developing and integrating key systems.

The realisation of a next-generation XFEL will be an international endeavour, with collaboration and in-kind contributions playing a central role. An upgrade to an existing facility or a new international facility would enable targeted UK contributions, while a new UK facility would require broader development across key components, acting as a focus for a substantial growth in national capability.

DRAFT

References for Chapter 3

[1] G. D'Auria et al. "The CompactLight Design Study". In: *European Physical Journal: Special Topics* 233.1 (Apr. 2024), pp. 1–208. ISSN: 19516401. DOI: 10.1140/EPJS/S11734-023-01076-0.

[2] Massimo. Altarelli et al., eds. *XFEL: the European X-ray free-electron laser: technical design report*. DESY XFEL Project Group, 2006, p. 630. ISBN: 9783935702171.

[3] Cynthia M. Friend. *Report on New and Upgraded National User Facilities in Basic Energy Sciences*. Tech. rep. Department of Energy: Basic Energy Sciences, 2024.

[4] Z. Y. Zhu et al. "SCLF: An 8-GEV CW SCRF linac-based x-ray FEL facility in Shanghai". In: *Proceedings of the 38th International Free-Electron Laser Conference, FEL 2017*. JACoW Publishing, 2017, pp. 182–184. ISBN: 9783954501793. DOI: 10.18429/JACoW-FEL2017-MOP055.

[5] Andrew Hutton. *Energy-recovery linacs for energy-efficient particle acceleration*. 2023. DOI: 10.1038/s42254-023-00644-6.

[6] F. Sannibale et al. "Advanced photoinjector experiment photogun commissioning results". In: *Phys. Rev. ST Accel. Beams* 15 (10 Oct. 2012), p. 103501. DOI: 10.1103/PhysRevSTAB.15.103501. URL: https://link.aps.org/doi/10.1103/PhysRevSTAB.15.103501.

[7] T. Luo et al. "RF design of APEX2 two cell continuous wave normal conducting photoelectron gun cavity based on multi objective genetic algorithm". In: *Nuclear Instruments and Methods in Physics Research Section A: Accelerators, Spectrometers, Detectors and Associated Equipment* 940 (2019), pp. 12–18. ISSN: 0168 9002. DOI: https://doi.org/10.1016/j.nima.2019.05.079. URL: https://www.sciencedirect.com/science/article/pii/S0168900219307430.

[8] Han Chen et al. "Beam dynamics optimization of very high frequency gun photoinjector". In: *Nuclear Science and Techniques* 33 (Sept. 2022), p. 116. DOI: 10.1007/s41365022201105y.

[9] Lianmin Zheng et al. "Design, fabrication, and beam commissioning of a 216.667 MHz continuous wave photocathode very high frequency electron gun". In: *Physical Review Accelerators and Beams* 26 (10 Oct. 2023). ISSN: 24699888. DOI: 10.1103/PhysRevAccelBeams.26.103402. URL: https://doi.org/10.1103/PhysRevAccelBeams.26.103402.

[10] E. Vogel et al. "High gradients at SRF photoinjector cavities with low RRR copper cathode plug screwed to the cavity back wall". In: (Oct. 2023). URL: http://arxiv.org/abs/2310.02974.

[11] C. Davut et al. "Balance of bunch compression and emittance preservation for high-brightness x-ray free electron laser injectors". In: *Phys. Rev. Accel. Beams* 28 (9 Sept. 2025), p. 091602. DOI: 10.1103/rjns-vqzt. URL: https://link.aps.org/doi/10.1103/rjns-vqzt.

[12] B. Aune et al. "Superconducting TESLA cavities". In: *Physical Review Special Topics - Accelerators and Beams* 3 (9 Sept. 2000), p. 092001. ISSN: 1098-4402. DOI: 10.1103/PhysRevSTAB.3.092001.

[13] LCLS-II Project Team. "LCLS-II Final Design Report". In: (Dec. 2014). URL: https://epp.fnal.gov/DocDB/0016/001646/001/LCLS-II%5C%20Design%5C%20Report.pdf.

[14] M Checchin. "Status of Cavity and Cryomodule Production for LCLS-II-HE". Aug. 2023. URL: https://accelconf.web.cern.ch/srf2023/talks/moiaa06_talk.pdf.

[15] S Posen et al. "Advances in Nb ¡sub¿3¡/sub¿ Sn superconducting radiofrequency cavities towards first practical accelerator applications". In: *Superconductor Science and Technology* 34.2 (Feb. 2021), p. 025007. ISSN: 0953-2048. DOI: 10.1088/1361-6668/abc7f7. URL: https://iopscience.iop.org/article/10.1088/1361-6668/abc7f7.

[16] A. - M. Valente-Feliciano et al. "Next-Generation Superconducting RF Technology based on Advanced Thin Film Technologies and Innovative Materials for Accelerator Enhanced Performance and Energy Reach". In: (Apr. 2022). URL: http://arxiv.org/abs/2204.02536.

[17] Nuria Catalan-Lasheras et al. "High-efficiency klystrons from a dream to a reality". In: *JACoW IPAC* 2024 (2024), FRYD1. DOI: 10.18429/JACoW-IPAC2024-FRYD1. URL: https://cds.cern.ch/record/2930683.

[18] Andrew Potter et al. "Spreader design options for a high-throughput multi-user XFEL". In: presented at the 41st International Free Electron Laser Conf. (FEL'24), Warsaw, Poland, Aug. 2024, paper TUP122-WEB. JACoW Publishing, Geneva, Switzerland.

[19] T. Tajima and J. M. Dawson. "Laser Electron Accelerator". In: *Physical Review Letters* 43.4 (July 1979), pp. 267–270. ISSN: 0031-9007. DOI: 10.1103/PhysRevLett.43.267. URL: https://link.aps.org/doi/10.1103/PhysRevLett.43.267.

[20] Pisin Chen et al. "Acceleration of Electrons by the Interaction of a Bunched electron Beam with a Plasma". en. In: *Phys. Rev. Lett.* 54.7 (Feb. 1985), pp. 693–696. ISSN: 0031-9007. URL: doi:10.1103/PhysRevLett.54.693.

[21] J B Rosenzweig. "Nonlinear plasma dynamics in the plasma wake-field accelerator". In: *Physical Review Letters* 58.6 (Feb. 1987), pp. 555–558. DOI: 10.1103/PhysRevLett.58.555. URL: https://link.aps.org/doi/10.1103/PhysRevLett.58.555.

[22] J B Rosenzweig et al. "Experimental Observation of Plasma Wake-Field Acceleration". In: *Phys. Rev. Lett.* 61.1 (July 1988), pp. 98–101. DOI: 10.1103/PhysRevLett.61.98. URL: https://link.aps.org/doi/10.1103/PhysRevLett.61.98.

[23] Bernhard Hidding et al. *Plasma Wakefield Accelerator Research 2019 - 2040: A community-driven UK roadmap compiled by the Plasma Wakefield Accelerator Steering Committee (PWASC)*. 2019. arXiv: 1904.09205 [physics.acc-ph]. URL: https://arxiv.org/abs/1904.09205.

[24] B Hidding et al. "Ultracold Electron Bunch Generation via Plasma Photocathode Emission and Acceleration in a Beam-Driven Plasma Blowout". In: *Phys. Rev. Lett.* 108 (2012), p. 35001. URL: http://link.aps.org/doi/10.1103/PhysRevLett.108.035001.

[25] A F Habib et al. "Attosecond-Angstrom free-electron-laser towards the cold beam limit". en. In: *Nature Communications* 14.1 (Feb. 2023), p. 1054. ISSN: 2041-1723. DOI: 10.1038/s41467-023-36592-z. URL: https://www.nature.com/articles/s41467-023-36592-z.

[26] "Experimental Signatures of the Quantum Nature of Radiation Reaction in the Field of an Ultraintense Laser". In: *Physical Review X* 8 (3 2018). ISSN: 21603308. DOI: 10.1103/PhysRevX.8.031004.

[27] J. M. Cole et al. "Experimental Evidence of Radiation Reaction in the Collision of a High-Intensity Laser Pulse with a Laser-Wakefield Accelerated Electron Beam". In: *Physical Review X* 8 (1 2018). ISSN: 21603308. DOI: 10.1103/PhysRevX.8.011020.

[28] E. Allaria et al. “Highly coherent and stable pulses from the FERMI seeded free-electron laser in the extreme ultraviolet”. In: *Nature Photonics* 6.10 (Oct. 2012), pp. 699–704. ISSN: 17494885. DOI: 10.1038/NPHOTON.2012.233.

[29] Xiaofan Wang et al. “High-repetition-rate seeded free-electron laser with direct-amplification of an external coherent laser”. In: *New Journal of Physics* 24.3 (Mar. 2022), p. 033013. ISSN: 1367-2630. DOI: 10.1088/1367-2630/AC5492. URL: https://iopscience.iop.org/article/10.1088/1367-2630/ac5492%20https://iopscience.iop.org/article/10.1088/1367-2630/ac5492/meta.

[30] Zheng Qi et al. “First Lasing and Stable Operation of a Direct-Amplification Enabled Harmonic Generation Free-Electron Laser”. In: *Phys. Rev. Lett.* 135 (3 July 2025), p. 035001. DOI: 10.1103/sslg-jjkz. URL: https://link.aps.org/doi/10.1103/sslg-jjkz.

[31] G. Stupakov. “Using the beam-echo effect for generation of short-wavelength radiation”. In: *Physical Review Letters* 102.7 (Feb. 2009), p. 074801. ISSN: 00319007. DOI: 10.1103/PHYSREVLETT.102.074801. URL: https://journals.aps.org/prl/abstract/10.1103/PhysRevLett.102.074801.

[32] E. Hemsing et al. “Highly coherent vacuum ultraviolet radiation at the 15th harmonic with echo-enabled harmonic generation technique”. In: *Physical Review Special Topics - Accelerators and Beams* 17.7 (July 2014). ISSN: 10984402. DOI: 10.1103/PHYSREVSTAB.17.070702.

[33] G. Penn. “Stable, coherent free-electron laser pulses using echo-enabled harmonic generation”. In: *Physical Review Special Topics - Accelerators and Beams* 17.11 (Nov. 2014), p. 110707. ISSN: 10984402. DOI: 10.1103/PHYSREVSTAB.17.110707. URL: https://journals.aps.org/prab/abstract/10.1103/PhysRevSTAB.17.110707.

[34] Primož Rebernik Ribič et al. “Coherent soft X-ray pulses from an echo-enabled harmonic generation free-electron laser”. In: *Nature Photonics 2019 13:8* 13.8 (May 2019), pp. 555–561. ISSN: 1749-4893. DOI: 10.1038/s41566-019-0427-1. URL: https://www.nature.com/articles/s41566-019-0427-1.

[35] P. R. Ribic. “Echo-Enabled Harmonic Generation Lasing of the FERMI FEL in the Soft X-Ray Spectral Region”. In: *Proceedings of the 39th International Free-Electron Laser Conference, FEL 2019*. JACOW Publishing, Geneva, Switzerland, Nov. 2019, pp. 33–37. ISBN: 978-3-95450-210-3. DOI: 10.18429/JACOW-FEL2019-TUB01.

[36] Martin Beye et al. “FLASH and the FLASH2020+ project—current status and upgrades for the free-electron laser in Hamburg at DESY”. In: *The European Physical Journal Plus* 138 (3 Mar. 2023), p. 193. ISSN: 2190-5444. DOI: 10.1140/epjp/s13360-023-03814-8.

[37] Sven Reiche. “Seeding at SwissFEL”. In: *https://doi.org/10.1117/12.2666463* 12581 (June 2023), pp. 16–23. ISSN: 1996756X. DOI: 10.1117/12.2666463.

[38] J. Feldhaus et al. “Possible application of X-ray optical elements for reducing the spectral bandwidth of an X-ray SASE FEL”. In: *Optics Communications* 140.4-6 (Aug. 1997), pp. 341–352. ISSN: 0030-4018. DOI: 10.1016/S0030-4018(97)00163-6.

[39] Gianluca Geloni, Vitali Kocharyan, and Evgeni Saldin. “A novel self-seeding scheme for hard X-ray FELs”. In: *Journal of Modern Optics* 58 (16 2011). ISSN: 09500340. DOI: 10.1080/09500340.2011.586473.

[40] J. Amann et al. “Demonstration of self-seeding in a hard-X-ray free-electron laser”. In: *Nature Photonics* 6.10 (Oct. 2012), pp. 693–698. ISSN: 17494885. DOI: 10.1038/NPHOTON.2012.180.

[41] B. W.J. McNeil, N. R. Thompson, and D. J. Dunning. “Transform-limited x-ray pulse generation from a high-brightness self-amplified spontaneous-emission free-electron laser”. In: *Physical Review Letters* 110.13 (Mar. 2013), p. 134802. ISSN: 00319007. DOI: 10.1103/PHYSREVLETT.110.134802. URL: https://journals.aps.org/prl/abstract/10.1103/PhysRevLett.110.134802.

[42] Eduard Prat et al. “Experimental Demonstration of Mode-Coupled and High-Brightness Self-Amplified Spontaneous Emission in an X-Ray Free-Electron Laser”. In: *Physical Review Letters* 133.20 (Nov. 2024), p. 205001. ISSN: 10797114. DOI: 10.1103/PHYSREVLETT.133.205001. URL: https://journals.aps.org/prl/abstract/10.1103/PhysRevLett.133.205001.

[43] R. Colella and A. Luccio. “Proposal for a free electron laser in the X-ray region”. In: *Optics Communications* 50.1 (May 1984), pp. 41–44. ISSN: 0030-4018. DOI: 10.1016/0030-4018(84)90009-9.

[44] Kwang Je Kim, Yuri Shvyd’ko, and Sven Reiche. “A Proposal for an X-ray free-electron laser oscillator with an energy-recovery linac”. In: *Physical Review Letters* 100.24 (June 2008), p. 244802. ISSN: 00319007. DOI: 10.1103/PHYSREVLETT.100.244802. URL: https://journals.aps.org/prl/abstract/10.1103/PhysRevLett.100.244802.

[45] B. W.J. McNeil. “A simple model of the free-electron-laser oscillator from low into high gain”. In: *Nuclear Instruments and Methods in Physics Research Section A: Accelerators, Spectrometers, Detectors and Associated Equipment* 296.1-3 (Oct. 1990), pp. 388–393. ISSN: 0168-9002. DOI: 10.1016/0168-9002(90)91237-6.

[46] Zhirong Huang and Ronald D. Ruth. “Fully coherent X-ray pulses from a regenerative-amplifier free-electron laser”. In: *Physical Review Letters* 96.14 (2006). ISSN: 00319007. DOI: 10.1103/PHYSREVLETT.96.144801.

[47] Dinh C. Nguyen et al. “First lasing of the regenerative amplifier FEL”. In: *Nuclear Instruments and Methods in Physics Research Section A: Accelerators, Spectrometers, Detectors and Associated Equipment* 429.1-3 (June 1999), pp. 125–130. ISSN: 0168-9002. DOI: 10.1016/S0168-9002(99)00090-X.

[48] D. J. Dunning, B. W.J. McNeil, and N. R. Thompson. “Short wavelength regenerative amplifier free electron lasers”. In: *Nuclear Instruments and Methods in Physics Research Section A: Accelerators, Spectrometers, Detectors and Associated Equipment* 593.1-2 (Aug. 2008), pp. 116–119. ISSN: 0168-9002. DOI: 10.1016/J.NIMA.2008.04.045.

[49] Patrick Rauer et al. “Lasing of a cavity-based X-ray source”. In: *Nature* 650 (2026), pp. 93–96. DOI: 10.1038/s41586-025-10025-x. URL: https://doi.org/10.1038/s41586-025-10025-x.

[50] Jingyi Tang et al. “Active Q-Switched X-Ray Regenerative Amplifier Free-Electron Laser”. In: *Phys. Rev. Lett.* 131 (5 July 2023), p. 055001. DOI: 10.1103/PhysRevLett.131.055001. URL: https://link.aps.org/doi/10.1103/PhysRevLett.131.055001.

[51] Alexander A. Zholents. “Method of an enhanced self-amplified spontaneous emission for x-ray free electron lasers”. In: *Physical Review Special Topics - Accelerators and Beams* 8.4 (Apr. 2005), p. 040701. ISSN: 1098-4402. DOI: 10.1103/PhysRevSTAB.8.040701.

[52] Joseph Duris et al. “Tunable isolated attosecond X-ray pulses with gigawatt peak power from a free-electron laser”. In: *Nature Photonics* 14.1 (Jan. 2020), pp. 30–36. ISSN: 1749-4885. DOI: 10.1038/s41566-019-0549-5.

[53] S. Casalbuoni et al. “Superconducting undulator coils with period length doubling”. In: *Journal of Physics: Conference Series* 1350.1 (Nov. 2019), p. 012024. ISSN: 1742-6596. DOI: 10.1088/1742-6596/1350/1/012024.

[54] B. W. J. McNeil et al. “Harmonic Lasing in a Free-Electron-Laser Amplifier”. In: *Physical Review Letters* 96.8 (Mar. 2006), p. 084801. ISSN: 0031-9007. DOI: 10.1103/PhysRevLett.96.084801.

[55] E. A. Schneidmiller and M. V. Yurkov. “Harmonic lasing in x-ray free electron lasers”. In: *Physical Review Special Topics - Accelerators and Beams* 15.8 (Aug. 2012), p. 080702. ISSN: 1098-4402. DOI: 10.1103/PhysRevSTAB.15.080702.

[56] Alan Mak and Neil Thompson. “Towards gamma-ray free-electron lasers”. In: *Proceedings of the 16th International Particle Accelerator Conference, Taipei, Taiwan*. May 2025, MOPB035.

[57] Mark D. Wilkinson et al. “The FAIR Guiding Principles for scientific data management and stewardship”. In: *Scientific Data* 3.1 (Mar. 2016). ISSN: 2052-4463. DOI: 10.1038/sdata.2016.18. URL: http://dx.doi.org/10.1038/sdata.2016.18.

[58] Johannes P. Blaschke et al. “ExaFEL: extreme-scale real-time data processing for X-ray free electron laser science”. In: *Frontiers in High Performance Computing* Volume 2 - 2024 (2024). ISSN: 2813-7337. DOI: 10.3389/fhpcp.2024.1414569. URL: https://www.frontiersin.org/journals/high-performance-computing/articles/10.3389/fhpcp.2024.1414569.

[59] Mark Wilkinson, Jeremy Yates, and Vassil Alexandrov. *STFC Exascale Requirements*. Version 5.2 - 27th August 2024. 2024.

[60] Thayer, Jana et al. “Massive Scale Data Analytics at LCLS-II”. In: *EPJ Web of Conf.* 295 (2024), p. 13002. DOI: 10.1051/epjconf/202429513002. URL: https://doi.org/10.1051/epjconf/202429513002.

[61] Science and Technology Facilities Council. *AI for Scientific Innovation: STFC AI Strategy*. Produced by Valerie Farr, Mark Wilkinson and Adriano Agnello. 2025. URL: https://www.ukri.org/publications/stfc-artificial-intelligence-strategy/.

[62] Auralee Edelen and Xiaobiao Huang. “Machine Learning for Design and Control of Particle Accelerators: A Look Backward and Forward”. In: *Annual Review of Nuclear and Particle Science* (2024). URL: https://api.semanticscholar.org/CorpusID:272921447.

[63] A. D. Brynes et al. *Closing the Loop: Deploying Auto-Generating Digital Twins for Particle Accelerators*. 2026. arXiv: 2604.19101 [physics.acc-ph]. URL: https://arxiv.org/abs/2604.19101.

[64] Peter Walter et al. “The time-resolved atomic, molecular and optical science instrument at the Linac Coherent Light Source”. In: *Journal of Synchrotron Radiation* 29 (July 2022), pp. 957–968. ISSN: 16005775. DOI: 10.1107/S1600577522004283.

[65] Christopher D M Hutchison, Samuel Perrett, and Jasper J Van Thor. “XFEL Beamline Optical Instrumentation for Ultrafast Science”. In: *J. Phys. Chem. B* 128 (2024), p. 8868. DOI: 10.1021/acs.jpcb.4c01492. URL: https://doi.org/10.1021/acs.jpcb.4c01492.

[66] Clara J. Saraceno et al. “The amazing progress of high-power ultrafast thin-disk lasers”. In: *Journal of the European Optical Society* 15.1 (Dec. 2019), pp. 1–7. ISSN: 19902573. DOI: 10.1186/S41476-019-0108-1/FIGURES/3. URL: https://jeos.springeropen.com/articles/10.1186/s41476-019-0108-1.

[67] Jakub Drs et al. “A Decade of Sub-100-fs Thin-Disk Laser Oscillators”. In: *Laser & Photonics Reviews* 17.8 (Aug. 2023), p. 2200258. ISSN: 1863-8899. DOI: 10.1002/LPOR.202200258. URL: https://onlinelibrary.wiley.com/doi/full/10.1002/lpor.202200258%20https://onlinelibrary.wiley.com/doi/abs/10.1002/lpor.202200258%20https://onlinelibrary.wiley.com/doi/10.1002/lpor.202200258.

[68] *CLF Welcome to HiLUX*. URL: https://www.clf.stfc.ac.uk/Pages/HiLUX-Home.aspx.

[69] Gregory M. Greetham et al. “A 100 kHz time-resolved multiple-probe femtosecond to second infrared absorption spectrometer”. In: *Applied Spectroscopy* 70.4 (Apr. 2016), pp. 645–653. ISSN: 19433530. DOI: 10.1177/0003702816631302.

[70] János Hebling et al. “Velocity matching by pulse front tilting for large-area THz-pulse generation”. In: *Optics Express, Vol. 10, Issue 21, pp. 1161-1166* 10.21 (Oct. 2002), pp. 1161–1166. ISSN: 1094-4087. DOI: 10.1364/OE.10.001161. URL: https://opg.optica.org/viewmedia.cfm?uri=oe-10-21-1161&seq=0&html=true%20https://opg.optica.org/abstract.cfm?uri=oe-10-21-1161%20https://opg.optica.org/oe/abstract.cfm?uri=oe-10-21-1161.

[71] Patrick L. Kramer et al. “Enabling high repetition rate nonlinear THz science with a kilowatt-class sub-100 fs laser source”. In: *Optics Express, Vol. 28, Issue 11, pp. 16951-16967* 28.11 (May 2020), pp. 16951–16967. ISSN: 1094-4087. DOI: 10.1364/OE.389653. URL: https://opg.optica.org/viewmedia.cfm?uri=oe-28-11-16951&seq=0&html=true%20https://opg.optica.org/abstract.cfm?uri=oe-28-11-16951%20https://opg.optica.org/oe/abstract.cfm?uri=oe-28-11-16951.

[72] Hyeongmun Kim et al. “Ionizing terahertz waves with 260 MV/cm from scalable optical rectification”. In: *Light: Science & Applications 2024 13:1* 13.1 (May 2024), pp. 1–13. ISSN: 2047-7538. DOI: 10.1038/s41377-024-01462-w. URL: https://www.nature.com/articles/s41377-024-01462-w.

[73] Meenkyo Seo et al. “High-efficiency near-infrared optical parametric amplifier for intense, narrowband THz pulses tunable in the 4 to 19 THz region”. In: *Scientific Reports 2022 12:1* 12.1 (Sept. 2022), pp. 1–7. ISSN: 2045-2322. DOI: 10.1038/s41598-022-20622-9. URL: https://www.nature.com/articles/s41598-022-20622-9.

[74] T. Seifert et al. “Efficient metallic spintronic emitters of ultrabroadband terahertz radiation”. In: *Nature Photonics* 10.7 (June 2016), pp. 483–488. ISSN: 17494893. DOI: 10.1038/NPHOTON.2016.91;TECHMETA=125,140;SUBJMETA=1130,2798,400,561,624,639,766;KWRD=ELECTRONIC+AND+SPINTRONIC+DEVICES,TERAHERTZ+OPTICS. URL: https://www.nature.com/articles/nphoton.2016.91.

[75] Charlotte Bull et al. “Spintronic terahertz emitters: Status and prospects from a materials perspective”. In: *APL Materials* 9.9 (Sept. 2021), p. 90701. ISSN: 2166532X. DOI: 10.1063/5.0057511/122925. URL: /aip/apm/article/9/9/090701/122925/Spintronic-terahertz-emitters-Status-and-prospects.

[76] Evangelos Th Papaioannou and René Beigang. “THz spintronic emitters: A review on achievements and future challenges”. In: *Nanophotonics* 10.2 (Jan. 2021), pp. 1243–1257. ISSN: 21928614. DOI: 10.1515/NANOPH-2020-0563.

[77] R. Rouzegar et al. “Broadband Spintronic Terahertz Source with Peak Electric Fields Exceeding 1.5 MV/cm”. In: *Physical Review Applied* 19.3 (Mar. 2023). ISSN: 23317019. DOI: 10.1103/PHYSREVAPPLIED.19.034018.

[78] Alkisti Vaitsi et al. “Rotating spintronic terahertz emitter optimized for microjoule pump-pulse energies and megahertz repetition rates”. In: *Applied Physics Letters* 125.7 (Aug. 2024), p. 71107. ISSN: 00036951. DOI: 10.1063/5.0214469/3307900. URL: /aip/apl/article/125/7/071107/3307900/Rotating-spintronic-terahertz-emitter-optimized.

[79] Mikhail Krasilnikov et al. “First high peak and average power single-pass THz free-electron laser in operation”. In: *Physical Review Accelerators and Beams* 28.3 (Mar. 2025), p. 030701. ISSN: 2469-9888. DOI: 10.1103/PhysRevAccelBeams.28.030701. URL: https://journals.aps.org/prab/abstract/10.1103/PhysRevAccelBeams.28.030701.

[80] Colin N. Danson et al. *Petawatt and exawatt class lasers worldwide*. 2019. DOI: 10.1017/hpl.2019.36.

[81] Paul Mason et al. "Development of a 100 J, 10 Hz laser for compression experiments at the High Energy Density instrument at the European XFEL". In: *High Power Laser Science and Engineering* 6 (2018), e65. ISSN: 2095-4719. DOI: 10.1017/HPL.2018.56. URL: https://www.cambridge.org/core/journals/high-power-laser-science-and-engineering/article/development-of-a-100-j-10-hz-laser-for-compression-experiments-at-the-high-energy-density-instrument-at-the-european-xfel/BE9310E57FB3CC7B3BF1F3C87BFB1917.

[82] STFC. *UK laser company launches to target global high-growth industries*. 2026. URL: https://www.clf.stfc.ac.uk/Pages/DiPOLE-Systems-launches.aspx (visited on 04/27/2026).

[83] Luke McHugh et al. "Commissioning a high-energy 10Hz Ti:Sa amplifier for the petawatt laser at the Extreme Photonics Applications Centre". In: *Solid State Lasers XXXIV: Technology and Devices*. Ed. by W. Andrew Clarkson and Ramesh K. Shori. SPIE, Mar. 2025, p. 12. ISBN: 9781510684300. DOI: 10.1117/12.3041937.

[84] Marie Kristin Czwallina, Bjorn Lautenschlager, and Holger Schlarb. *Beam-based Stability Evaluation in the LINAC of European XFEL*. 2024.

[85] SustainableHECAP+ Initiative. *Environmental sustainability in basic research: A perspective from HECAP+*. Tech. rep. 2023. URL: https://hecap.eco/.

[86] Hannah Wakeling et al. "High-level environmental sustainability guidelines for large accelerator facilities". In: (Jan. 2025). URL: https://arxiv.org/abs/2501.14979v1.

[87] Hannah Wakeling et al. "Community-specific guidance for environmental sustainability in particle accelerators". In: *Nature Reviews Physics* (2025). ISSN: 2522-5820. DOI: 10.1038/s42254-025-00878-6.

[88] Department for Energy Security and Net Zero. *Energy and emissions projections 2023 to 2050*. Tech. rep. 2024. URL: https://www.gov.uk/government/publications/energy-and-emissions-projections-2023-to-2050.

[89] *Green Book supplementary guidance: valuation of energy use and greenhouse gas emissions for appraisal*. Tech. rep. Department for Energy Security and Net Zero, Nov. 2023.

[90] C Calzolaio. "Overview of permanent magnet implementations for advanced light sources". English. In: *Proc. IPAC'25*. IPAC'25 - 16th International Particle Accelerator Conference 16. JACoW Publishing, Geneva, Switzerland, July 2025, pp. 42–47. ISBN: 978-3-95450-248-6. DOI: 10.18429/JACoW-IPAC25-MOZN1.

[91] B Shepherd. "Assessing and increasing the sustainability of future accelerator based facilities". English. In: *Proc. IPAC'25*. IPAC'25 - 16th International Particle Accelerator Conference 16. JACoW Publishing, Geneva, Switzerland, July 2025, pp. 1681–1686. ISBN: 978-3-95450-248-6. DOI: 10.18429/JACoW-IPAC25-WEYD1. URL: https://indico.jacow.org/event/81/contributions/6338.

[92] Diamond Light Source. *The big switch on: solar panels fully operational at Diamond*. 2024. URL: https://www.diamond.ac.uk/Home/News/LatestNews/2024/15072024.html (visited on 04/28/2026).

[93] Helen Towrie. *CLF UK's new advanced imaging centre takes shape*. Nov. 2020. URL: https://www.clf.stfc.ac.uk/Pages/UK%E2%80%99s-new-advanced-imaging-centre-takes-shape.aspx.

[94] Infrastructure and Projects Authority and Cabinet Office. *Project and programme management*. Guidance page; first published 24 Aug 2017; last updated 30 Sep 2020. GOV.UK. Sept. 2020. URL: https://www.gov.uk/guidance/project-and-programme-management.

DRAFT

Theme 1:

A high repetition rate and high-efficiency, many-user facility

4 Low energy beam

4.1 Summary

The Low Energy Beamline (LEB) is the first and most critical stage of the UK XFEL drive accelerator. Together with the High Energy Beamline (HEB) described in section Chapter 5, it is crucial to achieving the electron beam parameters necessary for generation of X-rays.

The required electron bunch parameters and beam temporal structure at the end of HEB outlined in Section 3.4.5 necessitates the use of two electron injectors, with the beams combined prior to injection into the main linac. Each injector includes an electron source, if necessary bunch compressors, and a booster to increase the beam energy to the emittance-dominated regime (typically 100+ MeV).

As we will demonstrate, the design requirements for transform-limited operation between 0.1-20 keV (Table 3.2) photon energy, non-transform-limited operation up to 45 keV (Table 3.3), high efficiency operation of multiple undulators in parallel (Table 3.1) requires the design of an ultra-low emittance photoinjector which goes beyond existing technology.

In this section we outline:

- Indicative beam parameters required at the exit of the LEB to achieve transform-limited operation up to 20 keV, and non-transform-limited operation up to 45 keV, across multiple undulators simultaneously
- A review of electron source technologies potentially capable of achieving these parameters at $\sim$1 MHz repetition rate, including developments required to address foreseen technology gaps
- The conceptual design of an injector capable of preserving the source parameters and delivering these to the high energy beamline
- The conceptual design of a beamline which allows multi-undulator and two colour operation

4.2 Introduction

The most critical beam parameter for an XFEL is beam brightness at the undulator which depends on transverse emittance and peak current. The emittance of an XFEL is source limited and will never be better than it is at the cathode. Consequently the injector which sets the minimum emittance in the machine is a key component of any linac driven XFEL like UK XFEL. The beam energy is low at the exit of the injector (100-200 MeV) and the bunch cannot be significantly compressed without emittance degradation. This means that the peak current will still be relatively low and the required 5D brightness will not be achieved without further compression in the HEB (High Energy Beamline). Therefore, during the conceptual design the main effort was

DRAFT

concentrated on the delivering bunches with the lowest possible slice emittance, linear longitudinal phase spaces to allow for effective bunch compression downstream and the bunch length required for injection into the HEB. Various options for the Low Energy Beamline were explored to generate these ultra-low emittance beams.

Typically an electron beam injector for an FEL comprises of: an electron emitter (cathode), an electron source - gun, a bunch compression scheme if necessary and a booster-accelerator. Each component of the injector may contribute to emittance degradation. The goal of this LEB design is to find the injector scheme and beamline components which deliver the lowest possible emittance and linear longitudinal phase space in the required charge regime at MHz repetition rate while allowing the facility to operate in multi-undulator and two colour modes.

4.3 Main Discussion, work done for the CDOA

The requirement that the UK XFEL injector must operate in CW mode while providing low emittance beams with the required temporal structure for injection into the main HEB linac set limits on the injector components which may be used. Current XFEL injector schemes operating in CW mode are not capable of delivering beams which meet the UK XFEL requirements. In this chapter, we summarise our approach and the schemes capable of meeting UK XFEL requirements.

During the CDOA stage our work was concentrated on following steps:

- Defining beam parameters at the exit of LEB
- Analysing performance of existing operational CW electron injectors
- Analysing existing gun technologies to select those which are able to deliver beams with highest brightness and required temporal structure
- Selecting a photocathode which is able to emit the beam with required charge, emittance and temporal structure
- Investigating currently available photoinjector laser technologies.
- Proposing a bunch compression scheme which may compress the bunch to the length required for injection into the main HEB linac while preserving beam emittance
- Selecting a booster-accelerator scheme which is able to accelerate the beam and preserve its emittance
- Performing start to end beam dynamic simulations of the proposed injector schemes and selecting the one most preferable for UK XFEL

The following subsections will review the existing technologies and explain which are preferred for UK XFEL.

4.3.1 Definition of Low Energy Beamline and beam parameter requirements

The main function of the Low Energy Beam Line to deliver electron beams with the lowest possible slice emittance for X-ray generation which can be accelerated to the required XFEL energy by HEB linac. The required bunch charge for UK XFEL varies in the range of 75-600 pC and the repetition rate is 1 MHz. In addition the theoretically required beam emittance is lower than 100 nm rad in the charge range of 75-150 pC.

For injection into the main linac the bunch length should not be longer than 10° of the linac RF period. For L-band 1.3 GHz this sets a limit of 20 ps. To allow for effective bunch compression the longitudinal phase space of the bunches should be as linear as possible. Furthermore, to avoid emittance growth due to space charge effects, the beam should have high enough energy to be in the emittance dominated regime, which is characterised by the laminarity parameter, ρ,

$$\rho = \frac{K_s \sigma^2}{\beta\gamma\varepsilon_{rms}^2} < 1 \tag{4.1}$$

where β is the fraction of the speed of light in a vacuum the bunch is moving at and γ the Lorentz factor of the beam, ε_n is the normalised emittance, σ the rms transverse beam size and $K_s = I/2I_0$ the generalised beam perveance [1], where I is peak bunch current and $I_0 \approx 17$ kA - is Alfvén current. For bunches with a charge of 150 pC and a beam emittance of 300 nm rad this condition may be met at an energy of 150 MeV.

In order to provide multi-undulator operation of the FEL, the LEB should deliver bunches with different charges, alternating with a frequency of 100s kHz. This would require retuning of the injector. However, retuning of magnetic and (S)RF components is not possible at that high a repetition rate. One approach to solve this problem is to build a two injector LEB with a merger that combines the two beams before injection into the main linac. The use of two injectors also simplifies the generation of the beams for two colour experiments. In this case two bunches are injected into the main linac with a delay of one RF linac period. This delay is provided by shifting the timing of one of the injectors as a whole relative to the other.

4.3.2 Overview of Current Technology

The formal requirement of the normalised bunch slice emittance at the entrance to the FEL undulator is defined by the formula:

$$\varepsilon_n = \frac{\beta\gamma\lambda}{4\pi} \tag{4.2}$$

where λ is wavelength of the generated light.

For generation of 20 keV photons this formula provides an emittance requirement of 62 nm rad. Such low emittance has never been demonstrated experimentally for the beams with a charge of 100-150 pC. Table 4.1 shows the values of emittance achieved in existing injectors able to deliver beams on the scale of MHz repetition rate.

Generation of high brightness beam with a repetition rate of 1 MHz and ps scale bunch length is only possible in photocathode guns. In these guns the beam emission is initiated by illumination of a special material, called a photocathode, with a short intense laser pulse. The emitted beam is further accelerated by DC or RF electric field. The emittance of the emitted beam is defined by photocathode Mean Transverse Energy (MTE) and transverse size of the laser pulse. This sets theoretical limit of the emittance available from the injector.

Facility	Technology	Cavity design	Operational frequency [MHz]	Bunch repetition rate [kHz]	Cathode field [MV/m]	Beam emittance [nm rad]	Bunch charge [pC]	Bunch length [ps]	Reference
C-BETA	DC	-	-	-	4.4	300 95% projected	100	3.4	[2]
LCLS-II	NCRF	QW	187.5	50	17.5	520 rms projected	50	?	[3]
SHINE	NCRF	QW	216.7	1000	28	840 95 % slice	100	4.8	[4]
ELBE	SRF	3.5 cell TESLA	1300	250	8	2000 rms projected	200	3	[5]
BNL	SRF	QW	112	78	18	200 rms slice	100	15	[6]

Table 4.1: Beam parameters, achieved by operational CW injectors.

DRAFT

$$\varepsilon_{n,rms} = \sigma_{\perp}\sqrt{\frac{MTE}{mc^2} + \frac{kT}{2mc^2}}, \tag{4.3}$$

where $\sigma_{\perp}$ is the rms transverse beam size.

However the minimum size of the emitted beam is limited by space charge and the electric field on the cathode. The higher the field smaller the beam size. An expression for estimating the minimum achievable beam radius for a bunch in the so called 'cigar' regime where its length is longer than its radius was derived in [7] and [8] using the Child-Langmuir approximation. The expression is:

$$r = \left(\frac{9I}{\sqrt{2}I_0}\right)^{2/3} \frac{mc^2}{eE_{emit}} \propto \frac{I^{2/3}}{E_{emit}} \tag{4.4}$$

where E_{emit} is the cathode field at the emission time.

As may be seen, there are two competing factors which impact minimum beam radius. To achieve a small initial beam radius the emission field should be as high as possible and the emission current as low possible. The emission current is estimated as q/τ where q is bunch charge and τ is emission pulse length. Practically the emission pulse length cannot be longer than 10° of duration of the gun cavity RF period. The maximum value of the cathode RF field is limited by the Kilpatrick criterion [9]. These two conditions give us a limit on the minimum beam radius as follows:

$$\begin{aligned} r &\propto q^{2/3}\frac{f^{2/3}}{E_{emit}} \\ f(MHz) &= 1.64E_{max}(MV/m)^2 \cdot e^{-8.5/E_{max}(MV/m)} \end{aligned} \tag{4.5}$$

where E_{max} is the amplitude of the RF field on the cavity walls. This expression gives us an indication of the theoretical limit on the emittance of the beam delivered by RF guns with an additional Kilpatrick limitation for NCRF guns. For SRF guns situation is more complicated as there are many factors which limit maximum achievable field and its dependence on frequency. There is also another factor which sets a limit on the beam emittance delivered by the gun the emittance growth in the gun due to space charge forces. Unfortunately this factor can be estimated by numerical simulations only. In the following sections the results of the beam dynamic simulation of the emittance growth due to space charge effect will be shown.

The next stage of beam processing is the injection of the beam into booster-accelerator which accelerates the beam to ultra relativistic energies where $\beta \approx 1$. For an L-band gun operating with the frequency of main linac this process is relatively simple as the speed of electrons is close to the speed of light and bunch length may be matched for injection into the booster. Therefore, all that is required is transverse focusing of the beam and emittance compensation [10]. For low energy VHF guns which generate long, 100+ ps bunches, with an energy of less than 1 MeV the process is more complicated. First the bunch should be longitudinally compressed to the required length for injection into the booster. In the existing injectors with VHF guns [3, 4] the length of the bunch generated by the guns is compressed by an L-band RF buncher to a length shorter than 20 ps. However this configuration is not optimal from a beam dynamics point of view and limits the achievable beam brightness.

An alternative approach to VHF gun injectors would be to find the minimum length that the bunch can be compressed to without emittance growth. Then use this length to set the frequency of the buncher and booster-accelerator which do not necessarily need to be the same frequency as the main linac. This approach is discussed in details in Section 4.3.12.

4.3.3 Technology readiness level of CW high brightness electron injectors and gap analysis

Acceleration of the beam with MHz repetition rate may be achieved with either a DC gun or with an RF gun operating in Continuous Wave (CW) mode. The electric field on the cathode in a DC guns is limited to 10-12 MV/m [11, 12]. In normal conducting Very High Frequency (VHF) RF guns the demonstrated field on the cathode is about 27 MV/m [4]. This is the result of a compromise between surface RF power dissipation and RF frequency which is typically in VHF cavities of 200 MHz. More detailed analysis of VHF guns is given in [13] . Higher cathode field may be reached in Superconducting RF (SRF) guns which may operate at a frequency of 1.3 GHz (L-band). Maximum field achieved in an L-band SRF gun cavity is 55 MV/m in Vertical Test [14]. VHF SRF gun options are also under consideration [15].

4.3.4 DC photocathode guns

An option for high repetition rate CW injectors is high voltage DC photoemission guns. These electron guns use a photocathode as the initial source of electrons and a DC potential in the range of 200-500 kV between a cathode and anode electrode to perform the initial acceleration of the electrons. Compared to the other CW electron gun technologies they are the most technically mature. Several injectors have been built and operated using this technology including: the JLAB FEL injector [16], the ALICE ERL injector [17], the Cornell injector [18] and the cERL injector [19].

A number of different DC electron gun geometries have been used. These include back mounted, top mounted and inverted insulator DC electron guns. Back mounted electron guns include the JLAB [16] and ALICE electron guns [20]. This design has the advantage of being axially symmetric; however photocathode exchange is more complicated [20]. Top mounted DC electron guns like the Cornell [21] and KEK electrons guns [12] sacrifice axial symmetry but have much easier photocathode exchange. Inverted insulator electron guns [22] can use simpler insulator designs and are much more compact but are not capable of achieving as high voltages.

The operational voltage of a DC electron gun is limited by charging up and then punch through of the insulator. This happens due to electrons field emitted from the metal high voltage components striking the insulator. The highest operational voltage achieved by a DC electron gun was achieved by the KEK gun and is 500 kV [12]. This was achieved by using a segmented insulator. Inverted insulator guns mitigate the electrons striking the insulator by having less high voltage metal to emit and a geometry where any electrons which are emitted are less likely to strike the insulator. However the highest achieved operational voltage is only 300 kV [23].

DC electron gun based injectors have a number of advantages. These include their technical maturity. Additionally the achievable vacuum levels are very low permitting alkali antimonide photocathodes to be used. These photocathode have low MTEs so high quality beams can be produced and they use green lasers which are easier to work with than UV. Another advantage is that the gun produces no RF non-linearity.

However they also have a number of disadvantages. The main disadvantage is the smaller electric fields that can be produced compared to RF guns. This has two effects. Firstly the electric field on the cathode will be lower than in an RF gun. Therefore larger laser spots need to be used to extract the same charge which means larger initial emittances produced at the cathode. Secondly the beam energy at the exit of the gun will be lower, limited to less than 500 keV compared to

750 keV achieved in VHF guns and several MeV achieved in SRF guns. This means that the space charge forces will be stronger leading to more beam quality degradation. The low electric field on the cathode and beam energy also mean that to achieve a high quality beam an injector with a complicated low energy ballistic bunching section is typically used.

4.3.5 VHF photocathode guns

VHF guns operate continuously, have good vacuum conditions and operational fields of up to 27 MV/m so far [4]. They do not require cryogenics. These attributes make them a desirable option for high repetition rate machines. The downsides are the physical size, and the long RF cycle due to the relatively low frequency ruling out two-colour FEL operation with a single gun.

The design of an NCRF CW VHF gun operating at 187 MHz was first demonstrated at LBNL for the Advanced Photoinjector EXperiment (APEX) [24]. The APEX gun was designed to operate at a voltage of 750 kV with a cathode field of 20 MV/m and an average RF power of 90 kW. Efforts to improve the APEX gun performance continued with a new gun called APEX2, which aimed to improve the cathode field and the beam energy at the gun exit by increasing the number of cells and decreasing the operating frequency to 162.5 MHz [25]. In light of these two studies a VHF gun operating at 216.67 MHz was designed for the SHINE injector, operating at a voltage of 878 kV with a cathode field of 30 MV/m and an average RF power of 95.8 kW [26].

VHF guns have been operated successfully at APEX, LCLS-II and SHINE. The APEX/LCLS-II design is a single re-entrant cell at 185.7 MHz, and has achieved field around 20 MV/m giving an energy of 745 keV[24]. This design has operated at up to 100 pC charge and achieved 500-800 nm rad emittance at 50 pC [3]. This was measured after acceleration to 80 MeV. The higher order energy spread (after the chirp is removed) has been measured at $<$9 keV for a 20 pC bunch at 15 MeV [27] but this is expected to improve.

The SHINE design is similar, but has a higher frequency of 216.7 MHz, enabling a higher field of 27 MV/m, with an output energy of 780 keV. The trade off for this is higher average heating. It has been operated up to 100 pC and has achieved a 95 % projected emittance of 850 nm rad with a bunch length of 1.44 mm [4].

Simulations of the SHINE single cell VHF gun show it should be possible to achieve a field of 30 MV/m, normalised emittance down to 400 nm rad at 300 pC and 150 nm rad at 100 pC, bunch lengths of 1 mm and higher order energy spreads of less than 0.6 keV at 100 pC [26]. A two cell VHF gun has been proposed by APEX2 and this achieves simulated projected emittance of 87 nm rad at 100 pC by accelerating to 1500 keV [25].

In operation, VHF guns suffer from short cathode lifetimes and dark current issues. KCs_2Sb cathodes tested in APEX had only a 3 day lifetime, after investigation it was concluded this may have been due to gun cavity contamination with fluorine [28]. The APEX/LCLS-II gun had 350 nA dark current that was reduced to $\sim$0.1 nA after polishing and dry-ice cleaning of the cavity [29]. Changing from a round to an elliptical cathode opening and introducing stainless steel inserts around the cathode has been employed to limit dark current further for both the LCLS-II spare gun [30] and the ZJLAB/SARI research gun which is also a spare for SHINE [31].The SHINE gun initially had 6 µA of dark current which was reduced to an unmeasurable amount after ultra-pure water rinsing. However this increased to 376 nA after a few days of operation. Possible reasons for this are dust adhesion or cathode material displacement [4].

Both LCLS-II and ZJLAB/SARI have studied the effect of cathode over-insertion as proposed by PITZ [32]. This reduces the dark current emitted from the cavity wall surface around the

cathode plug-hole, which is the main source of dark current. The field on this surface is modestly decreased by cathode over-insertion but the main effect is due to defocusing fields reducing the transport of the dark current. ZJLAB/SARI found a reduction from 275 nA to around 1 nA of dark current with cathode over-insertion [31], and LCLS-II reported a 3 order of magnitude decease in dark current [33].

4.3.6 SRF photocathode guns

The option of an SRF L-band gun has multiple benefits. When compared to a VHF gun, an L-band gun with a copper photocathode has demonstrated fields in vertical tests up to 55 MV/m [34]. The higher accelerating field reduces the amount of time the electron bunch spends at low energies, and so reduces the space charge induced emittance growth. The frequency of the gun also matches that of the booster and main linacs, negating the need for a buncher cavity. However, it imposes restrictions on the choice of cathode material [35]. Currently, CW L-band SRF photoinjectors are being operated or designed for ELBE at HZDR [36], the cERL at KEK [37], SEAlab at HZB [38], and European XFEL at DESY [39].

Since 2018, HZDR's ELBE SRF gun II has routinely delivered 4 MeV CW beam with up to 250 pC charge and 250 kHz repetition rate for user operation. The ELBE gun consists of a liquid helium cooled, 3.5-cell RF fine-grain niobium cavity with a choke cell which leads into the main SRF linac [36]. From 2016, the ELBE SRF gun II operated using normal-conducting high quantum efficiency Mg cathodes which have a QE of 0.1-0.3 %, and then since 2020, have been operating using a Cs_2Te on Cu cathode which gives a QE of $\sim$1 %, but experienced high QE degradation. The measured beam parameters reach up to 300 pC, and have emittances in the range of 200-1500 nm rad using an 8 MeV/m gun accelerating gradient (14.5 MV/m field on the cathode) [40]. The measured dark current was 110 nA, which is mitigated using a fast kicker [41].

The KEK SRF gun was developed for a 3 GeV ERL project. The photoinjector is a 1.5-cell superconducting cavity plus a choke filter and uses a back-side excitation type K_2CsSb photocathode [37]. The first half-cell of the gun is tapered for beam focusing, and the cell shape was optimised for a beam energy of 2 MeV at the exit of the gun. An emittance of $<$1000 nm rad was achieved for a bunch charge of 77 pC at 1.3 GHz repetition-rate [42]. In a vertical test the peak surface electric field was 75 MV/m, but this reduced to 45 MV/m in a horizontal cryostat test, which is thought to be due to particulates entering the cavity during assembly [43, 44].

The injector designed for the SEALab (previously BERLinPro) ERL is a 1.4-cell SRF cavity with a choke cell followed by three 2-cell L-band SRF booster cavities based on a modified Cornell booster. A third cavity is operated in zero-crossing mode to impose an energy chirp onto the bunch for which is used for bunch compression [38]. The gun achieved a peak surface electric field of 57.3 MV/m for up to 2.3 MeV beam energy at the gun exit with variable bunch charge (1 fC to 100 pC), pulse length (1 fs to 6 ps) and spot size (10 to 100s µm), with a projected emittance of $<$500 nm rad for a 77 pC bunch charge [45]. They have recently achieved generation of an electron beam from a multi-alkali (Na-K-Sb) photocathode [46].

The European XFEL SRF gun CW upgrade currently being designed at DESY is a 1.6-cell cavity made of bulk niobium with a copper cathode sealed into the backside of the gun with indium. The achieved gun peak field is 55 MV/m [39]. They are looking into adjusting the position of the cathode in order to provide RF focusing in the cathode vicinity to minimise emittance, with simulations giving $<$100 nm rad emittance for a 100 pC bunch [47].

SRF VHF guns are another type of SRF gun. The CW SRF VHF gun at BNL was designed for the Coherent electron Cooling project at the Relativistic Heavy Ion Collider to produce high brightness, high charge electron beams and has been in routine operation since 2016 [48]. The injector consists of a niobium quarter-wave resonator cavity gun operating at a frequency of 113 MHz followed by a focusing solenoid and a 500 MHz bunching cavity. The VHF gun has achieved maximum field strengths of 18 MV/m giving an energy of 1.25 MeV, 78 kHz repetition rate, and a maximum charge per bunch of 10.7 nC. The room-temperature cathode consists of a CsK_2Sb coated molybdenum puck and had a lifetime of 1-2 months. The cathode position with respect to the cavity nose-cone can be adjusted to apply RF focusing to the beam. The gun has achieved a projected emittance of 300 nm rad for a 50 pC bunch ballistically compressed to 15.3 ps [49, 50]. A second SRF VHF gun project is the gun for the LCLS-II HE low emittance injector [51]. The gun is designed to operate at 185.7 MHz with a cathode field of 30 MV/m and produce bunches with an energy of around 1.6 MeV [52]. It is currently undergoing development and prototyping.

4.3.7 DC-SRF photocathode guns

The DC-SRF photocathode gun, is another gun which is able to operate in CW mode and allows the delivery of high brightness beams with MHz repetition rate. The gun was initially proposed in 2001 [53] by the SRF Accelerator Laboratory of Peking University and its prototype was tested in 2004 [54, 55]. The original design consisted of a 1.3 GHz, 1.5 cell accelerator cavity with a DC photocathode gun serving as a beam emitter. By introducing a separate DC gun based electron emitter, the semiconductor photocathode is moved out from the SRF cavity, which successfully solves the compatibility problem between the photocathode and the SRF cavity. Moreover, the high vacuum which may be achieved in the DC section allows the use of alkali photocathodes, which are able to generate high average current beams.

During the last few decades, further development of DC-SRF guns has continued with different DC emitter designs and structures of the SRF cavity. The final design of the DC-SRF gun was completed in 2021 and described in detail in [56]. The design comprises a 100 kV DC photocathode emitter followed by a 1.5 cell accelerating cavity operated at a acceleration rate of 13-14 MeV/m. The gun was successfully tested in the CW regime with bunch charge of 100 pC and sub mm mrad emittance.

The success in the commissioning of the gun allows to consider it as an injector of CW beams for ERL and IR FEL facilities. The natural limitation on the beam brightness is the low emission field in the DC gun which does not exceed 10 MV/m and therefore limits the emission current density, and, as result, the minimum radius of the emitted beam at given bunch charge and hence the achievable beam emittance. Another limiting factor is the use of of an L-band accelerating cavity that requires a bunch length from the emitter of shorter than 20 ps which limits how low the emission current can be for a given bunch charge. The combination of these two factors does not allow ultra-high brightness beam which are necessary for XFELs to be obtained.

4.3.8 Photocathodes

The choice of which electron gun technology to use leads to limitations on the available photocathodes due to the differences in the achievable vacuum conditions. The most robust photocathodes are metals such as copper which may be used in any type of gun. For example they are used in the high field NCRF S-band guns of pulsed normal conducting XFELs [57, 58, 59]. The performance of metal photocathodes is limited by their relatively low levels of Quantum Efficiency (QE) which

is up to 10^{-4} at best and the requirement that the photoinjector laser must be UV. Therefore the operational repetition rate of injectors with metal photocathodes is limited by the available laser pulse energy and the mirrors used for laser light transportation. Alkali based photocathodes such as Cs_2Te or Cs_3Sb have high QE and are an alternative to low QE metal photocathodes, though unfortunately not all alkali metal photocathodes can operate in high field guns as some types are sensitive to the vacuum conditions.

The baseline design for a UK XFEL calls for a bunch charge of 75-300 pC at a repetition rate of 1 MHz and 600 pC at 100 Hz or more which constitutes a maximum average beam current of 0.3 mA. This places a substantial demand on the photocathode electron source, with a laser pulse energy of 0.15 µJ required to extract this 300 pC bunch charge from a cathode with a QE of 1 % at $\lambda \sim 257$ nm. Due to the need to extract this level of charge on a time scale in the region of 100 ps, space charge is the dominant force acting to increase beam emittance and reduce its brightness. Mean transverse and longitudinal energy are much less important, though photocathode spectral response and in particular high quantum efficiency exceeding 1 % is crucial. QEs of this level are available from alkali and bi-alkali metal photocathodes which confer the added benefit of minimising the heat load on the cathode through the need for only a modest average laser power.

The LCLS-II at the Stanford Linear Accelerator Centre (SLAC) and Shanghai High repetition rate X-ray free electron laser and extreme light facility (SHINE) have both demonstrated operation of high repetition rate photocathode guns designed to deliver bunch charges up to 100 pC at 1 MHz using high QE Cs_2Te photocathodes in their respective projects, and this is close to the design specifications for the UK XFEL. The SLAC design for the LCLS-II [5] which has evolved over nearly two decades from the LBNL APEX gun has gained traction, with the NCRF VHF design also having been applied in multiple variations by Tsinghua University for the SHINE project [4, 60].

Cs_2Te is a robust alkali metal photocathode, and its selection for both the LCLS-II and SHINE facilities is testament to the level of understanding and 'trust' ascribed by the accelerator community to this material as an electron source. Cs_2Te has demonstrated reliable operation with high levels of QE for long periods time, with both DESY and CERN having documented the extended use of Cs_2Te photocathodes, CERN for 2 years at the AWAKE facility [61] and DESY for more than 2 years at FLASH [62] and nearly 4 years at the European XFEL with an integrated charge extraction exceeding 30 C [63]. Furthermore, rejuvenation of Cs_2Te through heating has been shown to restore up to 95 % of the original QE following operational use, and even 60 % of the original QE following exposure to air [61].

Assuming the use of a Yb-based IR laser with a fundamental at $\lambda = 1030$ nm, generation of the 4^{th} harmonic (4H) with $\lambda \sim 257.5$ nm would require a significant but achievable drive laser installation to illuminate a Cs_2Te photocathode with sufficient UV photons to extract a MHz pulse train of 300 pC electron bunches to deliver the required 0.3 mA beam current. It is likely that this would leave little headroom for the inevitable laser system performance (power) deterioration, nor more crucially for the application of transverse and longitudinal laser pulse shaping which are recognised as being essential to minimise detrimental space charge effects and beam emittance to deliver high–brightness electron bunches.

Both the LCLS-II and SHINE plan to test (bi)alkali antimonide photocathodes which photoemit at green wave-lengths with $\lambda \sim 532$ nm, thus reducing the IR power requirement in the drive laser system, and potentially increasing drive laser beam stability due to the need to carry out only a single stage of frequency doubling to access the second harmonic (2H). SLAC have stated that they expect to demonstrate this by 2027, while SHINE have not indicated a target date

at this time (July 2025). A complicating factor in the use of alkali antimonide cathodes is their sensitivity to contamination and the consequent need to operate at good ultra–high vacuum (UHV) or ideally extreme high vacuum (XHV) levels in the 10^{-11} mbar regime. Both SLAC and SHINE acknowledge that an improvement in their respective vacuum conditions is necessary for the successful deployment of this technology.

There are a range of alkali antimonide cathode options, the most common within the accelerator community being Cs_3Sb, CsK_2Sb and NaK_2Sb, this choice having been made on the basis that the avoidance of a Cs-containing photocathode is preferable given its known affinity to react with oxygen–containing compounds and thus alter the photocathode chemistry, potentially impacting the energy spread of the photoemitted electrons (and emittance) and degrading the operational lifetime. Consequently NaK_2Sb is considered to be the most stable bi–alkali photocathode option. HZB have demonstrated their ability to manufacture these photocathodes for their SEALab project [64] while US laboratories are investigating the use of Cs_3Sb as a photocathode electron source [65].

The use of an alkali antimonide photocathode further simplifies the necessary drive laser technology, and creates ample capacity within the drive laser system for the application of sophisticated transverse and longitudinal beam shaping methods, thereby minimising electron beam emittance. Application of this technology also reduces the level of laser pulse amplitude instability introduced through applying two consecutive stages of frequency–doubling to reach the 4^{th} harmonic, and removes the need to work with UV beams and the cumulative damage they cause to what are often expensive and inaccessible optics in the laser beam transport path.

DESY are developing a high field SRF gun based on L-band 1.3 GHz technology with a copper photocathode. The baseline design goal for this gun is to deliver bunches in the 20-100 pC range at a repetition rate between 0.1 and 1 MHz using a single–crystal copper cathode with a QE exceeding 1×10^{-4} at $\lambda = 257$ nm [39, 66], though polycrystalline copper may also be used.

A further technology option which relies on photocathode illumination using the 3^{rd} harmonic (3H) of a Yb-based IR laser with $\lambda \sim 343$ nm is the use of ultra–thin MgO films to reduce the work function of simple metals such as copper and silver [67]. The efficiency of this process to make ‘blue’ photocathodes has been demonstrated, but the technology remains embryonic with a low level of readiness. Further work is required to increase performance consistency, though this technology remains a candidate photocathode solution for operation in high field SRF guns through development on the likely timescale of a UK XFEL.

ASTeC expect to develop the capability to manufacture (bi)alkali antimonide photocathodes operating at visible wavelengths within the next 3 years, possibly augmented through the addition of protective layers to improve cathode lifetime in NCRF guns [68].

In summary, at the current level of technology, Cs_2Te alkali metal photocathodes will allow the generation of the required UK XFEL electron beam based on cathode illumination at UV wavelengths, but with potentially limited headroom for laser pulse shaping. However Cs_2Te is the most viable and arguably safest photocathode choice to meet the UK XFEL electron beam specification operating with a QE around 10 % under UV illumination.

4.3.9 Drive lasers

The delivery of sufficient photons of the correct wavelengths requires a shift from traditional ”work-horse” Ti:Sapphire lasers to Yb:fibre/disk technologies. Fortunately, the development of these technologies is already well underway independent from the need of next generation light

sources [69]. These lasers have been proven at the required energies and pulse rate, and are available from commercial entities such as Trumpf [70] and Light Conversion [71]. LCLS-II and SHINE both implement Yb systems with frequency doubling to green (515 nm), and then doubling again to UV (257.5 nm) wavelengths for compatibility with Cs_2Te cathodes; see Table 4.2 for specifications. Production of 343 nm is also possible by summing the green and fundamental waves. Conversion efficiency from the laser to these "harmonics" has been shown to be 50-65 % for the second (515 nm), and 10-20 % for the fourth (257.5 nm). The third harmonic (343 nm) efficiency lies in between. This indicates that current technology is already capable of providing the pulse energy/rep-rate/wavelength combinations.

Parameter	LCLS-II	SHINE	UK XFEL
Wavelength (nm)	257.5 (4H)	257.5 (4H)	257.5 (4H) 343.3 (3H)
Rep. rate (MHz)	0-0.928	1	1
Energy (µJ)	0-0.3	2	0-0.3
Size (FWHM, mm)	0.2-2	1-3	0.5-1.0
Length (ps)	20-60	30-60	120-130
Temporal profile	Flat top, 2 ps rise/fall	Flat top	Flat top
Spatial profile	Apodised Gaussian or Flat top	Truncated Gaussian	Flat top

Table 4.2: LCLS-II Photo-Injector Laser design specifications for LCLS-II [72] and SHINE [73]

The characteristics of the photo-injector laser pulse play a key role in determining the ultimate electron beam properties [74], and unfortunately the Gaussian temporal and spatial profiles that are most common of ultrashort pulse lasers are not optimal. Many systems to date have targeted "cylindrical" laser pulses. However, more sophisticated pulse shapes have been proposed [75] and demonstrated [76, 77] that are even better at managing the effects of space charge on emittance growth in the gun. These so-called "3D ellipsoidal" pulses are generated from an ultrashort pulse laser using a pair of spatial light modulators situated in the Fourier plane(s) of a zero-dispersion pulse stretcher. The first modulator applies a phase map that has the effect of temporally chirping the pulse. This is relay imaged onto a second modulator which, in combination with a half-wave plate, applies a polarisation rotation. At the exit to the stretcher is a polariser, which then rejects some of the polarised light thereby giving an amplitude modulation. The full set-up is illustrated in Figure 4.1. The use of cylindrical optics and spatial light modulators allows spectral phase to be modified in the dispersion plane of the gratings of the stretcher, and spectrally dependent spatial intensity modulations orthogonally to it. In order to produce a rotationally symmetric profile the pulse must then be image rotated and passed back through the shaper a number of times - twice for rectangular, quasi-ellipsoidal, shaping Figure 4.2, three times for hexagonal, etc. This is lossy and highly sensitive to alignment, but a different solution has been put forward in [78]. Here a 3D volume Bragg grating is implemented that can both chirp and shape the pulse. The principle is to create a chirped grating inside a dielectric material, that also changes in spatial profile at different depths. This results in a spectrally varying spatial reflectance profile in a single reflection, and allows complex shapes to be formed.

Another demonstrated approach to producing flat top beams is to split a short laser pulse into many copies, which are then combined with staggered time delays. This has been shown to be effective in several machines [79, 80], but has also been shown to have negative impact in inducing micro-bunching instabilities [81].

The temporal shaping of a 130 ps pulse is a complex challenge. Transform-limited picosecond

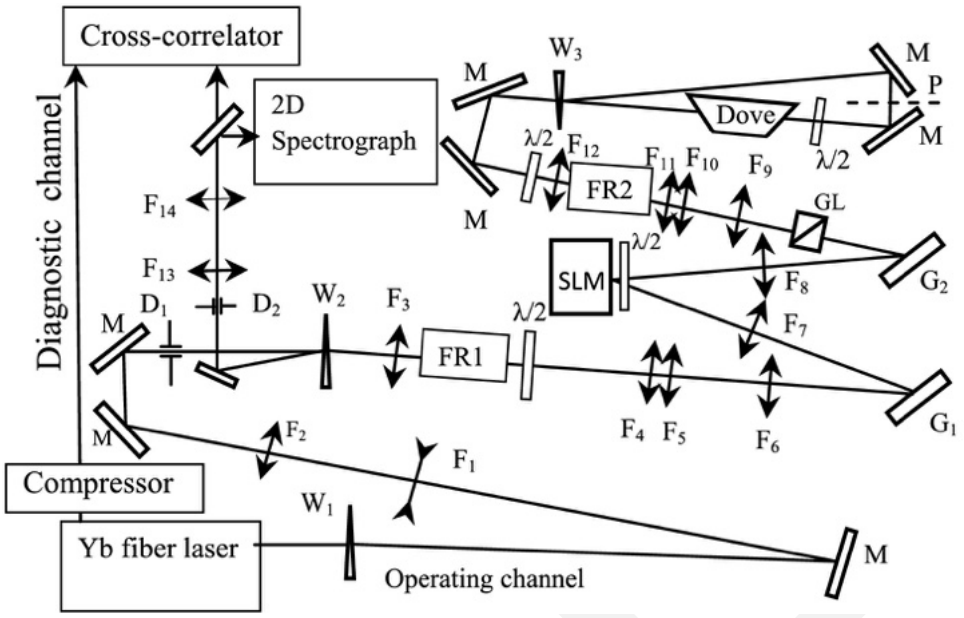

Figure 4.1: Reproduced from [76]. Schematic diagram of experimental setup: M, mirror; G1;2, diffraction gratings; FR1, FR245°, Faraday rotators; SLM, spatial light modulator; GL, Glan prism; W1,2,3, calcite wedges; D1,2, diaphragms; P, plane of image transfer from grating; G2, Fi (I = 1. . . 14) lenses (F1 = –140 mm, F2 = 350 mm, F3 = 400 mm, F4 = 169 mm, F5 = 259 mm, F6 = 369 mm are spherical; F7 = F8 = 405 mm are cylindrical; and F9 = 368 mm, F10 = 174 mm, F11 = 394 mm, F12 = 414 mm, F13 = 160 mm, F14 = 260 mm are spherical).

pulses lack the spectral bandwidth required for conventional femtosecond shaping techniques, while their short duration precludes the use of direct temporal amplitude shaping methods typically applied to nanosecond pulses. An approach championed for LCLS-II is that of dispersion controlled non-linear shaping (DCNS) [82, 83]. Here a close to transform limited, long, laser pulse is generated by the non-collinear sum frequency generation of the more readily shaped, longer wavelength, pulses. It is not a huge stretch to expect that this technique (or the others mentioned here), that is being used to produce tens of ps up to 65 ps pulses, can be extended by a factor of 2, to generate the 130 ps pulses required for UK XFEL.

This technology has been demonstrated, but the stability and power handling (thermal and non-linear optical issues) are points that need investigation and perhaps development. The optimal pulse profile for UK XFEL may not be the one offering the lowest theoretical emittance, but one

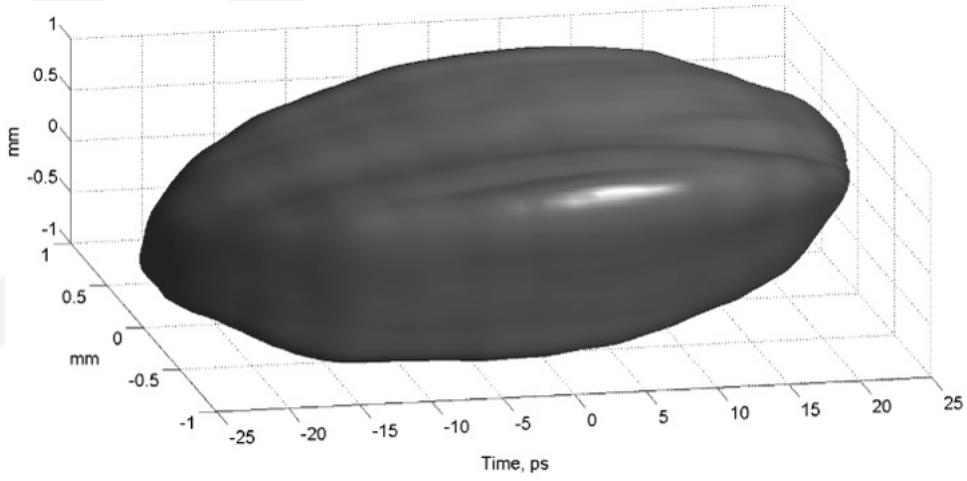

Figure 4.2: Reproduced from [76]. Experimentally measured Quasi-ellipsoidal beam.

that sensibly trades off emittance with stability, reliability, and consistency of performance. Indeed, recent work at LCLS-II [84] using complete, start-to-end simulations, indicates that Gaussian laser pulses can improve electron bunch properties for the FEL.

4.3.10 Electron source for UK XFEL

After reviewing the current state of the art in high repetition rate injectors the decision was made to further investigate normal conducting VHF guns using Cs_2Te photocathodes and L-band SRF guns using Cu photocathodes. Normal conducting VHF guns were chosen as they can provide higher cathode electric fields and exit energies than DC guns while still being technically mature enough to be the technology of choice for current CW XFEL projects such as LCLS-II and SHINE. L-band SRF guns were chosen as they can achieve the highest cathode electric fields (55 MV/m) and exit beam energy (several MeV) while having simpler beam dynamics and RF infrastructure than the other options as they are the same frequency as the main linac.

4.3.11 Conceptual design options of the Low Energy Beamline

Detailed study carried out has shown that CW-compatible injectors can be designed using NCRF guns operating at low frequencies (typically below 250 MHz) with a cathode field of 20-30 MV/m [5, 4]. The primary motivation for using these low RF frequencies is to reduce the RF heating on the cavity walls to manageable levels during CW operation. To achieve minimal transverse emittance, these guns can generate long electron bunches with a relatively low peak current to minimise space charge related emittance growth. However as a consequence, bunch compression becomes necessary to shorten the electron bunches to the required length for further acceleration in the booster. This must be done while maintaining control over the transverse emittance and relative energy spread. On the over hand, L-band (1.3 GHz) SRF gun technology offers higher gun frequency as an alternative to VHF technology, enabling the use of higher cathode fields to produce shorter electron bunches and avoid the need for bunch compression along the low-energy injector beamline [66].

Three preliminary designs for the low-energy beamline have been considered based on the technology choices described above. The first two designs use an NCRF VHF gun but different bunch compression schemes prioritising different design objectives. The third design is based on an SRF L-band gun followed by a booster that operates at the same frequency as the main linac. The components of each beamline design are given below.

- Design-I: VHF Gun (NCRF) + Lineariser (NCRF) + Pre-Buncher (NCRF) + Booster (SRF) + Lineariser (SRF) + C-Shape Chicane
- Design-II: VHF Gun (NCRF) + Pre-Buncher (NCRF) + Buncher (SRF) + Booster (SRF)
- Design-III: L-band Gun (SRF) + Booster (SRF)

4.3.12 VHF gun-based electron injector and required infrastructure

A frequency of 216.67 MHz was chosen for the VHF gun, which is the 6th sub-harmonic of the 1.3 GHz main linac frequency proposed for the UK XFEL. This frequency was chosen over the 7th sub-harmonic as it should allow a higher peak cathode electric field leading to improved gun

performance. Two different VHF gun options were developed and optimised using the methodology outlined in [25]. The first option, termed the traditional geometry, adopts a standard asymmetric re-entrant structure, consistent with earlier VHF gun designs [24, 4], to preserve established performance benchmarks. In this design, the extrusion at the gun's front is restricted to 2 cm beyond the end of the accelerating gap. The second configuration, referred to as the relaxed geometry, removes this limitation, allowing for a more extended extrusion. While this leads to a less compact form factor, it enables a higher RF voltage for a given input power, thereby increasing the bunch energy at the gun exit and offering improved suppression of space charge effects. It is worth noting that this relaxed design approach parallels the single-cell concept explored in the early stages of APEX2 gun development [25], prior to the adoption of a two-cell configuration.

Figure 4.3 shows the gun design optimisation results for both geometries obtained under a set of design constraints including an RF frequency of 216.67 MHz with a tolerance of ± 3 MHz, a maximum allowable surface electric field of 37 MV/m, and a peak power density limit of 35 W/cm^2. The resulting Pareto fronts for both the traditional and relaxed VHF gun geometries are shown in Figure 4.3a, illustrating the trade-offs between RF power and voltage. The corresponding optimised cavity shapes are depicted in Figures 4.3b and 4.3c. Figure 4.3d presents the axial electric field profiles for the two configurations, highlighting the differences in electric field and field extension along the beam axis. An input RF power of 90 kW was adopted for the optimisation (as indicated in Figure 4.3a), reflecting the capabilities demonstrated in existing VHF gun technologies and constrained by current high-power RF transmission infrastructure. Future studies will revisit this power limit to explore the feasibility of higher-power operation, potentially through the implementation of additional input couplers. With this power constraint, the traditional geometry achieves an RF voltage of 826 kV, whereas the relaxed geometry attains a higher value of 1102 kV. While the relaxed geometry benefits from higher final beam energy, further investigation is required to evaluate practical limitations related to the integration of gun solenoids. In addition, neither geometry has been subjected to multipactor analysis; susceptibility to such effects may impose additional design constraints and necessitate the adoption of mitigation strategies, potentially reducing performance. Despite these open considerations, the relaxed geometry was selected for continued injector design studies due to its higher achievable accelerating voltage, lower slice emittance, and enhanced bunch energy at the gun exit.

The performance of the relaxed gun geometry was evaluated in terms of the minimum achievable slice emittance using OPAL [85] simulations with space charge effects enabled. A 150 pC bunch was simulated using 100k macro-particles. Several factors contribute to the slice emittance, including the intrinsic emittance of the photocathode, linear and non-linear space charge forces and aberrations from the gun solenoid. These effects can be balanced by adjusting the laser spot size and pulse length to minimise the overall transverse slice emittance. Figure 4.4 shows how the slice emittance, defined here as the average of the three central slices from nine equal longitudinal divisions of the bunch, depends on the laser parameters for the relaxed geometry. These central slices are used to characterise performance since they typically correspond to the regions of highest current and best transverse quality which is the most relevant region of the bunch for FEL operation. A Cs_2Te photocathode was used in all cases, with flat-top laser profiles in both transverse and longitudinal dimensions. For comparison, the cathode-limited emittance calculated using the approach in [86] is shown with dotted lines. The results show that longer laser pulses reduce the slice emittance by lowering the peak current density and weakening the space charge effects. The smallest emittance was found for a pulse duration of 130 ps, equivalent to 10 degrees of RF phase. Reducing the laser spot size also helps by lowering the cathode emittance contribution, but going below a radius of 0.25 mm causes strong emittance growth due to excessive current density. Overall, the simulations confirm that achieving low slice emittance at the gun favours the use of long laser pulses within practical limits.

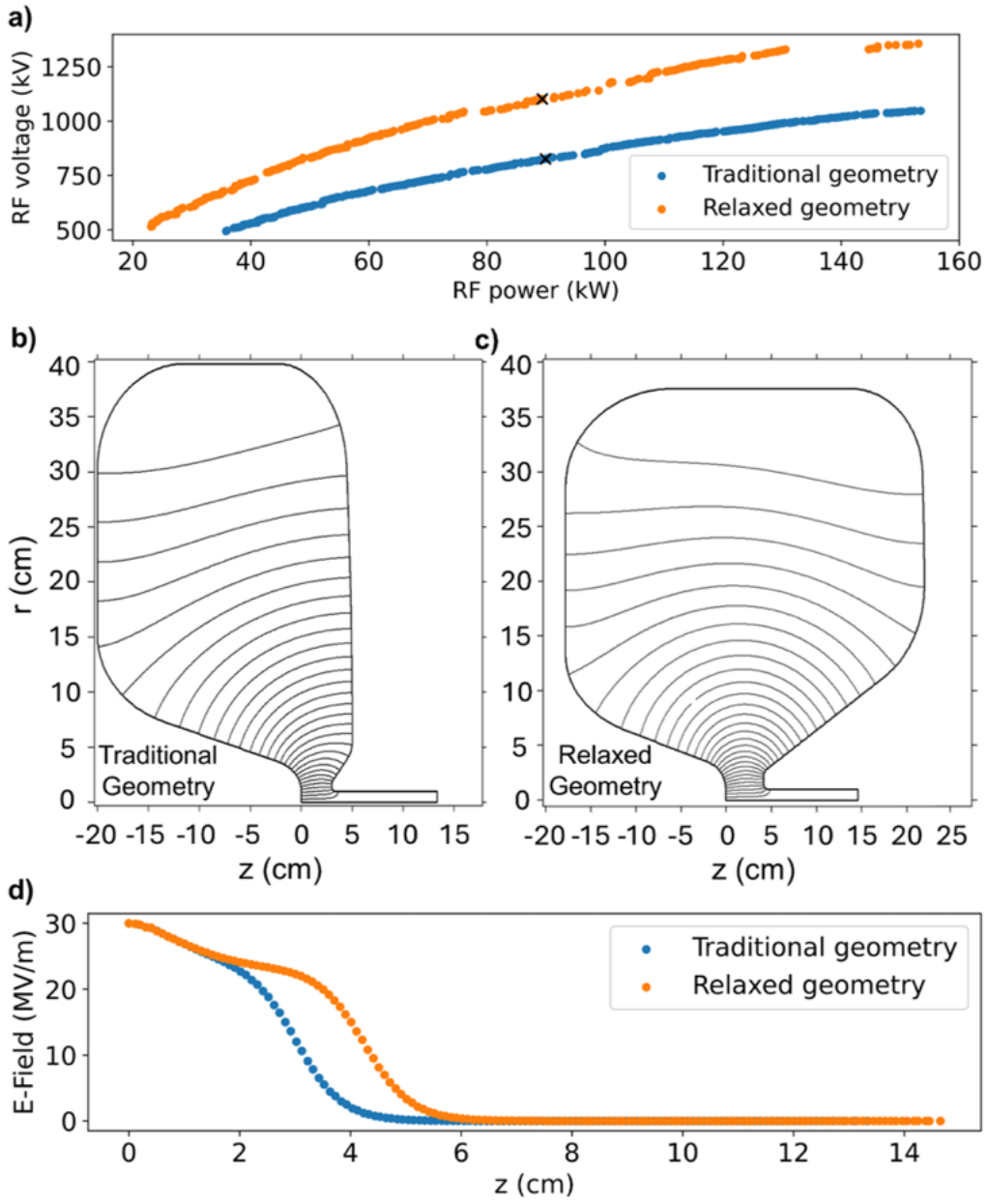

Figure 4.3: (a) Pareto fronts for each gun design. The selected design is marked with a black cross. b) Optimised traditional gun geometry. c) Optimised relaxed gun geometry. d) Peak electric field on axis for each gun design.

Following the VHF gun geometry optimisation and supporting beam dynamics analysis, detailed study of two low-energy injector schemes, referred to as Design-I and Design-II, was undertaken to evaluate their respective advantages and limitations. These designs were considered to investigate alternative strategies for achieving high-brightness beams, with particular emphasis on transverse emittance preservation, controlled bunch compression, and tailoring of the longitudinal phase space. The remainder of this section presents the conceptual layout and optimisation methodology for each configuration in sequence. Detailed simulation results are provided after the design descriptions to enable a thorough comparison of the two approaches. The multi-objective optimisation of alternative low-energy beamline designs employed four key performance metrics—transverse core emittance, skewness of the longitudinal charge distribution, the laminarity parameter, and bunch duration—to evaluate and improve overall injector performance. The requirement of the bunch duration and the importance of the laminarity parameter are described in 4.3.1. In this work, a transverse core emittance is defined as it offers a more representative and

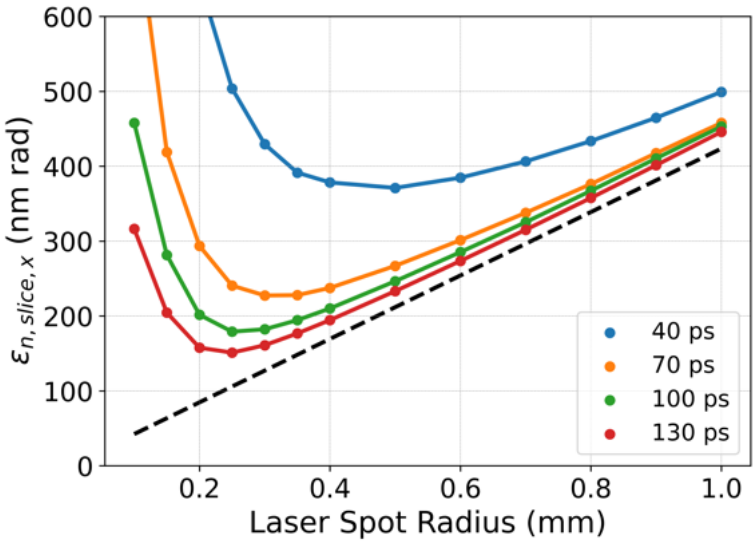

Figure 4.4: Average slice emittance of the three central slices of the 150 pC bunch generated with Cs_2Te photocathode at the emittance compensation point after the gun, shown as a function of laser spot size and pulse duration for the relaxed gun geometry. Dashed line shows theoretical value of the emittance

physically meaningful measure of transverse phase space quality. In general, the core is typically defined to include 95.45% of the total bunch charge. In this work, the Mahalanobis distance-based method [87] is employed to determine the elliptical boundary of the core in transverse phase space and to identify the subset of particles used for emittance evaluation. The approach leverages the full two-dimensional transverse phase space (x,p_x) and explicitly incorporates the beam centroid, assuming an axisymmetric transverse distribution. For each particle, the deviation vector is defined as

$$\Delta \mathbf{x}_i = \begin{pmatrix} x_i - \bar{x} \\ p_{x,i} - \bar{p}_x \end{pmatrix}, \tag{4.6}$$

and its squared Mahalanobis distance is given by

$$D_i^2 = \Delta \mathbf{x}_i^T \, \Sigma_x^{-1} \, \Delta \mathbf{x}_i, \tag{4.7}$$

for

$$\epsilon_{n,core,x} = \sqrt{\det \Sigma_x} = \sqrt{\langle x^2 \rangle \langle p_x^2 \rangle - \langle x p_x \rangle^2}. \tag{4.8}$$

By sorting the particles in order of increasing D_i^2 and accumulating their charge until 95.45% of the total is reached, this approach defines an elliptical core that captures the phase space directionality.

To evaluate the skewness of the longitudinal charge distribution, the charge-weighted centroid of the bunch is defined as:

$$\mu = \frac{\sum_i z_i \, q_i}{\sum_i q_i}, \tag{4.9}$$

where z_i is the longitudinal position of each particle within the bunch and q_i is its corresponding charge weight. The weighted variance σ^2, which measures the spread of particle positions about the centroid, is given by:

$$\sigma^2 = \frac{\sum_i (z_i - \mu)^2 \, q_i}{\sum_i q_i}, \tag{4.10}$$

The weighted third central moment M_3, which quantifies the asymmetry of the distribution about the mean, is defined as:

$$M_3 = \frac{\sum_i (z_i - \mu)^3 \, q_i}{\sum_i q_i}. \tag{4.11}$$

Therefore, the skewness S is then given by:

$$S = \frac{M_3}{\sigma^3}. \tag{4.12}$$

A skewness of zero indicates a perfectly symmetric charge distribution, while non-zero values signify asymmetry. In this work, minimizing the absolute value of skewness was used as a proxy to reduce higher-order energy spread and improve the quality of the longitudinal phase space during the optimisation. One can find a more detailed account of the optimisation process, beam dynamics analysis, and key parameters used such as core emittance, skewness of the longitudinal charge distribution, and the laminarity parameter, as well as descriptions of the NCRF and L-band SRF cavities used in the simulations, is available in [88].

Design-I beamline is developed to maximise the 6D brightness of the electron beam, a critical figure of merit for high-gain XFEL operation. To achieve this, the design process was guided by minimisation of three primary beam quality objectives: core emittance, skewness of the longitudinal charge distribution, and bunch length. The layout of the Design-I low-energy beamline is illustrated in Figure 4.5.

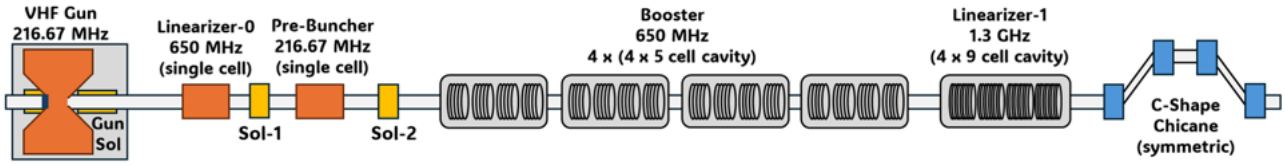

Figure 4.5: Low Energy Beamline layout for Design-I.

The design begins with the optimised relaxed geometry VHF gun using long laser pulse—approximately 10° of the gun RF period—which, as indicated by the beam dynamics simulations above, should lead to low emittance. While this approach improves transverse beam quality, the gun RF introduces 2nd order curvature into the longitudinal phase space of the long bunches. If left uncorrected, this non-linearity degrades the efficiency of the downstream RF and magnetic compression. To address this, a linearising cavity operating at the third harmonic of the gun frequency is placed directly after the VHF gun. This cavity removes the gun RF non-linearity and pre-compensates the T_{566} of the drift, hence significantly improving the quality of the initial RF compression while incurring only a minor reduction in the bunch energy. To implement the RF compression at low energy, a comprehensive series of simulation studies was performed to evaluate the effectiveness of pre-buncher cavities operating at 216.67 MHz, 650 MHz, and 1.3 GHz. The results indicate that a buncher operating at the same frequency as the VHF gun offers the most favourable performance by minimising transverse emittance growth during the initial compression. Figure 4.6 shows the Pareto fronts obtained for all bunch charges after the initial acceleration until the end of the first booster cryomodule shown in Figure 4.5.

As shown above, the RF compression alone is insufficient to compress the bunch to sub 20 ps as required by the main linac while sufficiently preserving the emittance. Consequently, a second magnetic compression stage is used for further compression from 40 ps to 20 ps. The magnetic compression is done at much higher energy in the emittance dominated regime. To bridge the gap between the compression stages, the bunch is accelerated by a subharmonic booster cavity operating at 650 MHz to match the bunch length of 40 ps. A second linearisation stage is introduced to correct the curvature in the longitudinal phase space introduced by the booster linac and to impart the appropriate energy chirp for effective bunch compression by the magnetic compression. To simplify the RF infrastructure and limit the number of operating frequencies, a cryomodule composed of four TESLA-type 9-cell superconducting cavities operating at 1.3 GHz

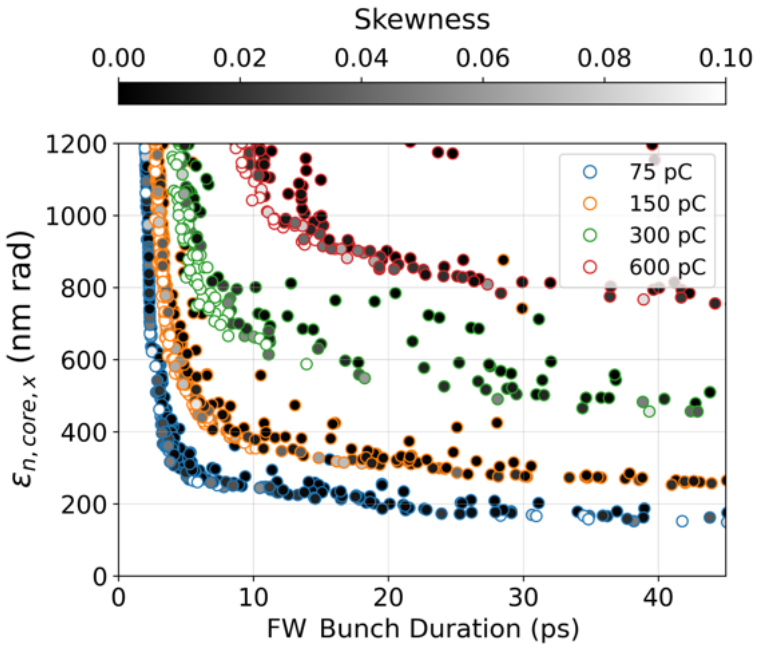

Figure 4.6: Pareto fronts for core emittance and bunch duration obtained for all bunch charges after initial acceleration up to the end of the first booster cryomodule in the Design-I beamline shown in Figure 4.5. The skewness of the longitudinal charge distribution is represented by a colormap ranging from dark to light, explaining the spread in the Pareto front compared to a typical one-dimensional trade-off curve.

is used. The compression itself is achieved using a symmetric C-shaped magnetic chicane, designed to provide a compression factor of at least 2. After the compressor a bunch duration below 20 ps suitable for injection into the main linac is obtained without significant transverse emittance growth.

Design-II beamline is developed as an alternative injector configuration that forgoes early-stage linearisation in favour of a two-stage RF compression scheme. Figure 4.7 illustrates the Design-II low-energy beamline layout.

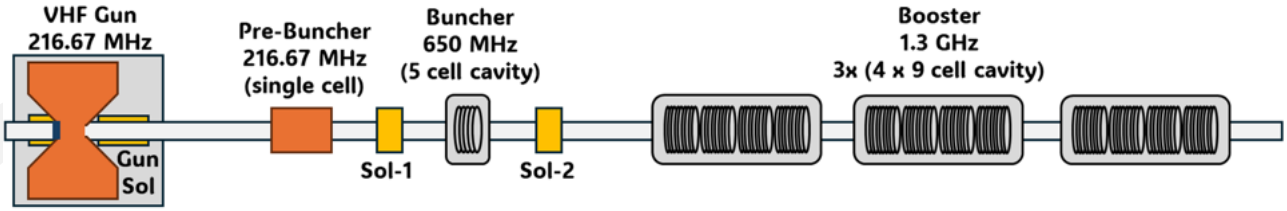

Figure 4.7: Low Energy Beamline layout for Design-II.

Design-II uses velocity bunching scheme, similar to the L-band standing wave option described in [89], which is intrinsically non-linear naturally giving rise to an asymmetric longitudinal charge distribution and a curved longitudinal phase space. This introduces a pronounced trailing tail and high peak current at the head of the bunch. In contrast to Design-I, no linearising cavity is included after the gun. This decision was supported by simulation studies, which examined the potential benefit of a third-harmonic linearisers similar to that used in Design-I. However, the results indicated that such a cavity provided limited improvement in correcting longitudinal asymmetry and led to a noticeable increase in transverse emittance. As a result, the linearisers was excluded in Design-II to preserve beam energy and maintain low transverse emittance, accepting the non-linearity in the longitudinal phase space as a trade-off.

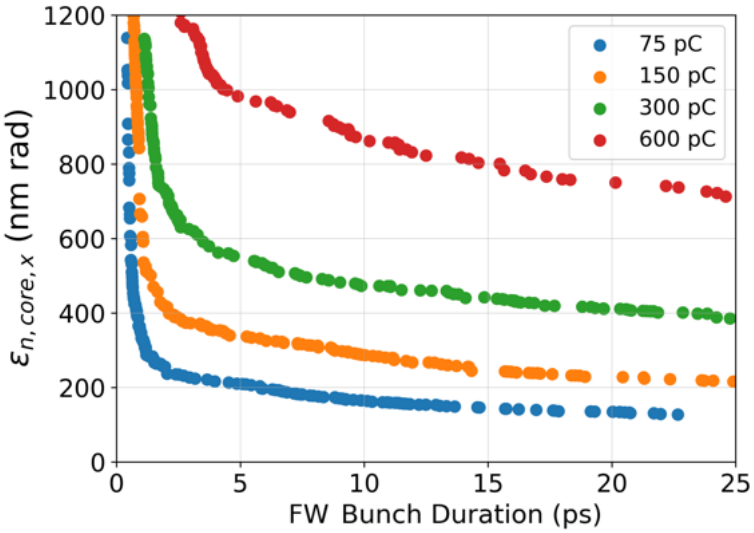

Figure 4.8: Pareto fronts for core emittance and bunch duration obtained for all bunch charges after initial acceleration up to the end of the first booster cryomodule in Design-II beamline shown in Figure 4.7.

Optimisation efforts for Design-II, therefore, focused exclusively on minimising transverse emittance and achieving the desired bunch length. Consistent with findings from Design-I, the same pre-buncher cavity was used to mitigate the transverse emittance growth during early bunching. The primary velocity bunching stage is achieved using a five-cell SRF cavity operating at 650 MHz. This structure compresses the bunch to below 20 ps, which is sufficient for injection into the main linac. The second bunching stage effectively enhances peak current while keeping the emittance within acceptable limits. Following the RF compression stages, the beam is further accelerated by 9-cell TESLA-type superconducting cavities operating at 1.3 GHz combined into 3 cryomodules containing 4 cavities each. This final booster section brings the bunch to higher energy, reduces the influence of space charge, and ensures compatibility with the downstream linac infrastructure. The use of standard TESLA cavities enables a smooth transition to the high-energy beamline and helps maintain beam quality in the emittance-dominated regime. Overall, Design-II offers a compact injector layout, which uses fewer RF frequencies and less total 650 MHz RF than Design-I. The design is capable of producing high peak current, though with a longitudinal tail due to the absence of longitudinal linearisation. Optimisation efforts were focused on minimising core transverse emittance and achieving the target bunch length through start-to-end simulations. Figure 4.8 shows the Pareto fronts obtained for different bunch charges, illustrating the trade-off between core emittance and bunch length for the Design-II configuration.

To assess the performance of the two injector concepts in detail, the following analysis compares the optimised beam dynamics results for a representative bunch charge of 150 pC, focusing on longitudinal and transverse phase space evolution, slice parameters, and beam quality along each injector beamline. Figure 4.9 presents the evolution of key beam parameters along the beamline for both Design-I and Design-II, including normalised projected and core emittances (horizontal and vertical), the bunch duration, and the laminarity parameter. For Design-I, the bunch duration begins at 86.5 ps at the gun exit and is compressed to 16.9 ps by the end of the magnetic chicane, corresponding to a compression factor of 5.1. At the compensation point following the gun, the normalized projected and core emittances are 372 and 257 nm rad, respectively, and transverse symmetry is preserved up to the chicane entrance. There, the projected and core emittances are reduced to 313 and 267 nm rad, respectively. Inside the chicane, the dipole-induced horizontal focusing disrupts the symmetry, leading to a slight increase in horizontal core emittance to 285 nm rad, while the vertical core emittance remains at 268 nm rad. The laminarity parameter is initially above unity, indicating a strong space charge-dominated regime. As the

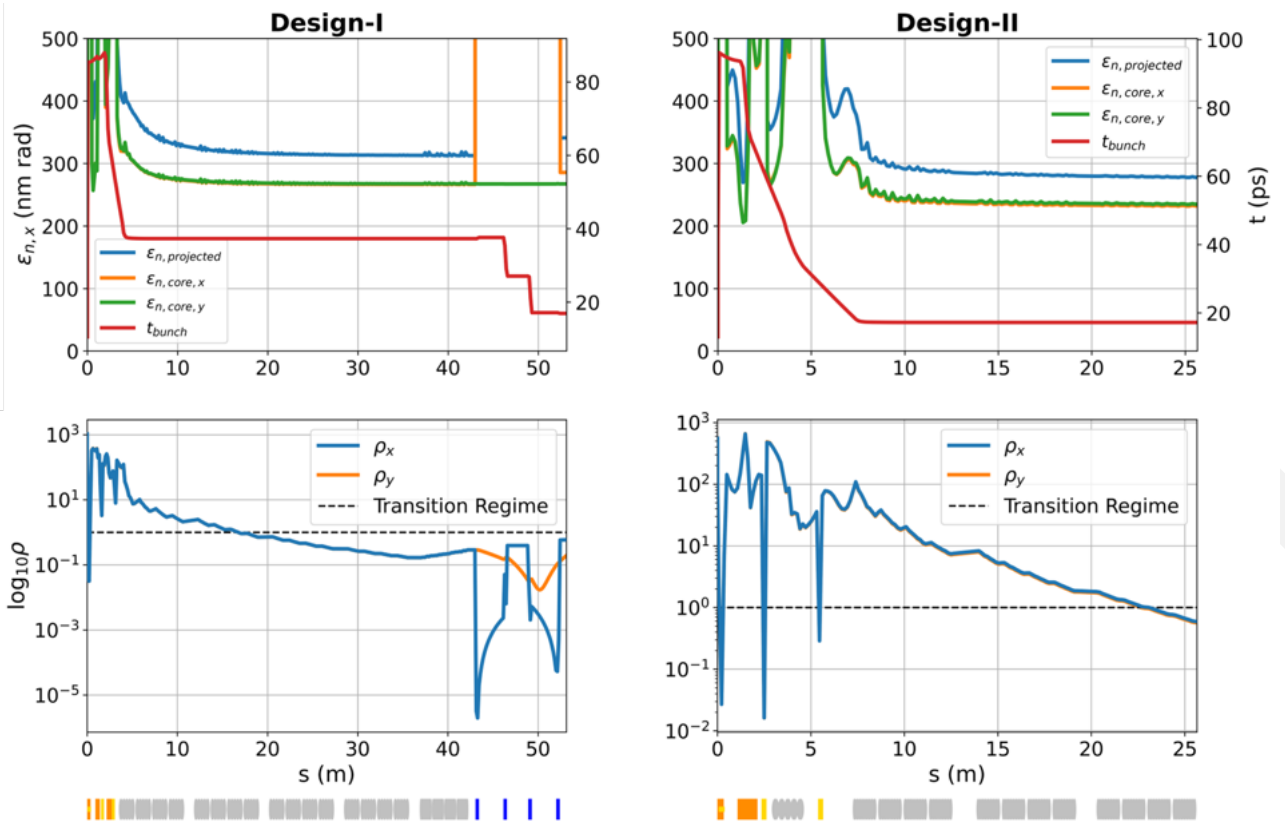

Figure 4.9: Evolution of normalized projected and core emittances (horizontal and vertical), bunch duration, and laminarity parameter along the injector beamline for Design-I and Design-II at 150 pC bunch charge. The plots illustrate compression stages, emittance compensation, and the transition from space charge-dominated to emittance-dominated regimes. The laminarity parameter confirms that both configurations achieve emittance-dominated transport by the injector exit, suitable for main linac injection.

beam is accelerated, particularly through the second cryomodule where the energy reaches ∼80 MeV, space charge effects diminish and the bunch enters the emittance-dominated regime. Minor fluctuations in laminarity are observed in the second linearizer and within the chicane due to localized changes in beam size and energy, but final values remain below unity in both transverse planes, confirming suitability for main linac injection.

For Design-II, the bunch starts at 96.1 ps and is compressed to 17.2 ps by the end of the RF compression stages, giving a compression factor of 5.6. At the compensation point, the projected and core emittances are 423 and 323 nm rad, respectively. These values initially increase at the exits of the pre-buncher and buncher due to RF-induced mismatches, but are effectively reduced to 278 and 233 nm rad after solenoid-based emittance compensation and acceleration through the booster. The laminarity parameter remains above unity for a longer portion of the beamline, indicating stronger space charge effects during the initial compression stages. Only during acceleration in the third cryomodule, as the beam approaches 150 MeV, does the laminarity parameter fall below unity. By the end of the injector, the beam reaches 187 MeV and is clearly in the emittance-dominated regime, with space charge effects rendered negligible.

The evolution of longitudinal phase space and energy spread for both injector configurations is illustrated in Figure 4.10. For Design-I, the longitudinal dynamics are shaped by a combination of RF linearisation and magnetic compression. The (second) lineariser — comprising four 9-cell 1.3 GHz TESLA cavities — operates with a combination of phase settings: near negative on-crest to reduce curvature at the head and tail of the bunch, and slightly off-crest to introduce the required energy–time correlation across the bunch. This configuration provides the necessary

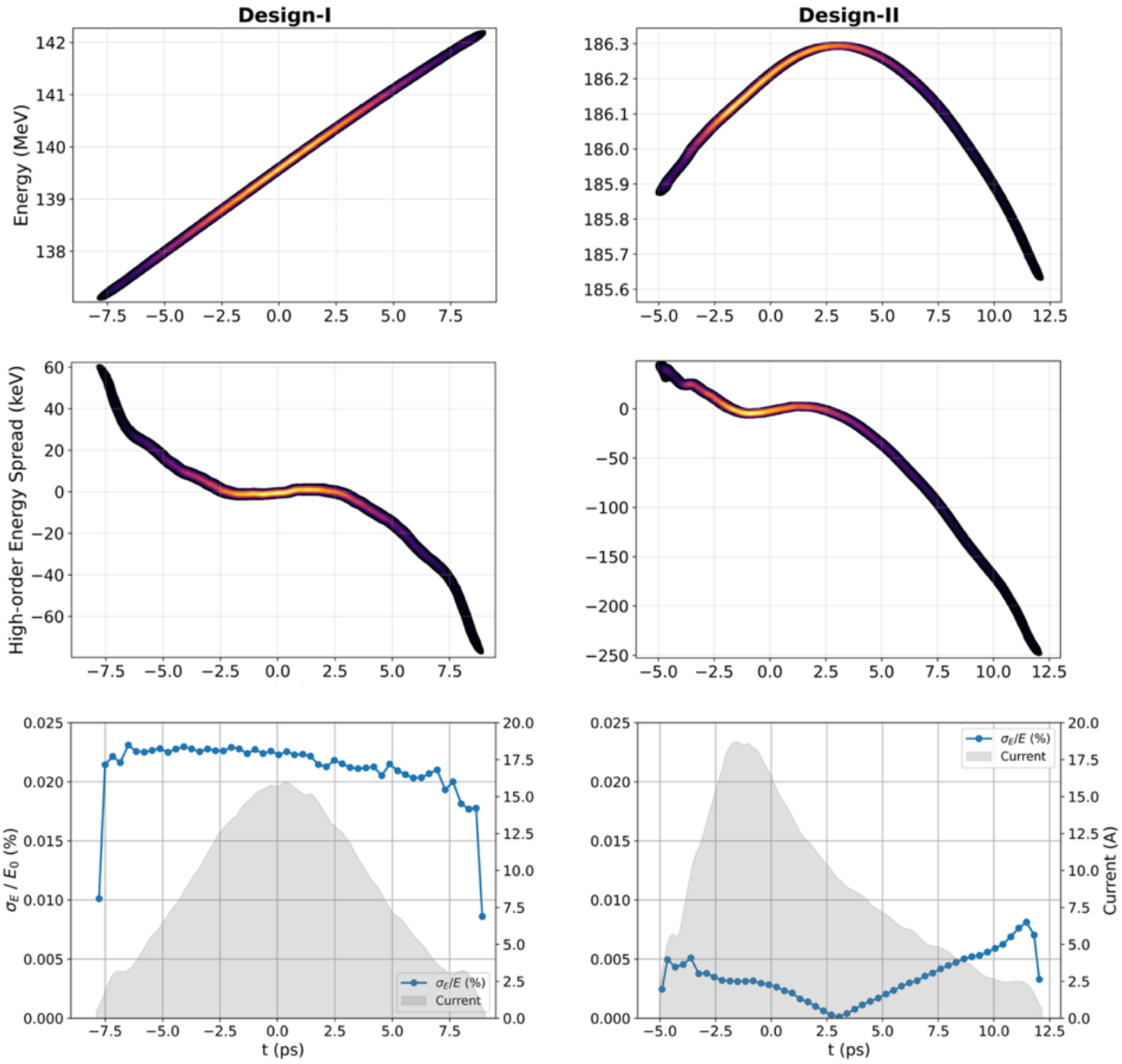

Figure 4.10: Comparison of longitudinal beam dynamics for Design-I and Design-II in terms of bunch energy, high-order energy spread, slice energy spread and current profile.

chirp for compression while preserving the initial RMS higher-order energy spread at 10.2 keV. However, it also results in a noticeable increase — by nearly a factor of five — in the slice energy spread due to the RF curvature. Before the (second) lineariser, the slice energy spread profile exhibits a symmetric V-shaped distribution, with a minimum located at the centre of the bunch distribution, and remains on the same order of magnitude as that of Design-II, as discussed later in the text and shown in the plots. At the entrance of the chicane, the bunch centroid is shifted to –0.66 ps, with a slightly reduced skewness of 0.011 and a bunch duration of 37.2 ps. After compression, the bunch duration is reduced to 16.9 ps, corresponding to a compression factor of 5.1, and the skewness increases modestly to 0.08. The RMS higher-order energy spread increases to 15.3 keV due to the non-linear transport through the chicane, while the mean relative energy spread remains low at 2×10^{-4}. The total energy chirp imparted across the bunch due to the compression process is approximately 4 MeV. The charge distribution is symmetric with a flat energy spread in the central region and a peak current of approximately 16 A.

For Design-II, compression is achieved entirely through RF-based velocity bunching without the

use of a magnetic chicane. The booster cavity operates on-crest, leading to a reverse U-shaped energy profile as second- and higher-order terms dominate the energy gain. This results in a compressed bunch with a high-current front and a trailing tail that cannot be fully preserved during acceleration. At the end of the booster, the RMS higher-order energy spread increases to 50.9 keV. The net energy chirp across the bunch in this case is less than 1 MeV, reflecting the milder longitudinal energy-time correlation typical of RF-based compression. Despite the more curved and asymmetric phase space, the bunch duration is compressed to 17.2 ps, with most of the charge concentrated at the head. The resulting peak current reaches 18.7 A – higher than that of Design-I—and slice analysis indicates that the central region maintains acceptable energy spread and current levels. While the absence of a linearisor and magnetic compressor leads to increased high-order energy spread and phase space asymmetry, Design-II succeeds in delivering a compact, 25 meter long, beamline which is half of the 50 m long Design-I beamline and high-current bunch using a two-stage RF-based bunch compression approach.

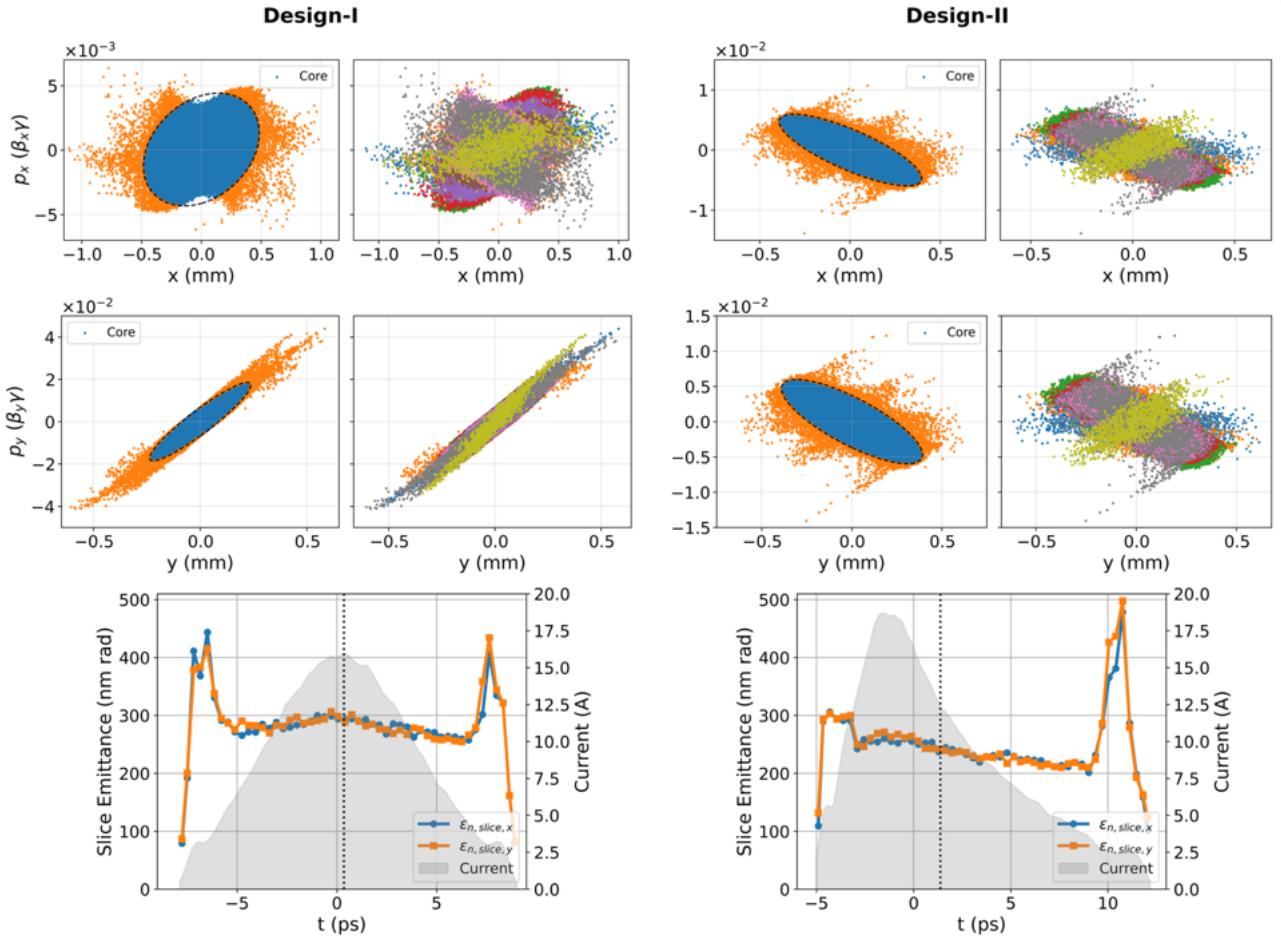

Figure 4.11: Transverse phase space comparison for Design-I and Design-II. Each row shows the full horizontal and vertical phase spaces at the injector exit, followed by 9-slice visualizations along the bunch to illustrate phase space rotation and alignment. The final row shows the horizontal and vertical slice emittance distributions along the bunch, plotted together with the one-dimensional current profile.

Figure 4.11 shows the transverse phase spaces for both Design-I and Design-II at the end of the injector, alongside their corresponding phase space slices divided into nine slices longitudinally, and the final slice emittance and current profile to provide insight into how transverse emittance evolves and how phase space rotations occur across the bunch. For Design-I, the transverse phase space before compression is well aligned in both horizontal and vertical planes. However, after passing through the magnetic chicane, the horizontal phase space shows signs of slice misalignment and rotation, particularly at the bunch extremities. This is attributed to dipole-

induced focusing and residual space charge forces, which introduce phase space distortions. The vertical plane remains largely unaffected due to the absence of vertical dispersion, though slight divergence is observed downstream. The nine-slice visualization reveals that while the central slices retain good alignment, the outer slices exhibit noticeable rotation, especially in the horizontal plane. These distortions contribute to the observed growth in horizontal core emittance, while the vertical emittance remains nearly unchanged. The slice emittance profile further confirms this behaviour: the central portion of the bunch, where most of the charge is concentrated, maintains low emittance, while the head and tail slices show up to 1.5 times higher values due to RF curvature and phase-dependent focusing.

In Design-II, the transverse phase spaces exhibit strong axial symmetry and minimal distortion at the injector exit. The use of axially symmetric RF compression in both stages, without introducing magnetic dispersion, preserves phase space alignment in both planes. The nine-slice views show consistent orientation and size across the bunch, with only minor variations between slices. This results in nearly identical horizontal and vertical core emittances. The slice emittance profile displays small variations-on the order of 50 nm rad-across the central region of the bunch, while a notable increase is observed in the tail due to the extended, low-current region. This long tail, inherent to RF-only compression, causes the charge-weighted mean of the bunch to shift relative to the location of peak current. Nevertheless, the transverse quality of the core is preserved.

To provide a detailed visualization of the longitudinal charge distribution and its correlation with the transverse beam size, the current density projections of the bunch in the horizontal-longitudinal plane are shown in Figure 4.12 for both injector configurations. For Design-I, the

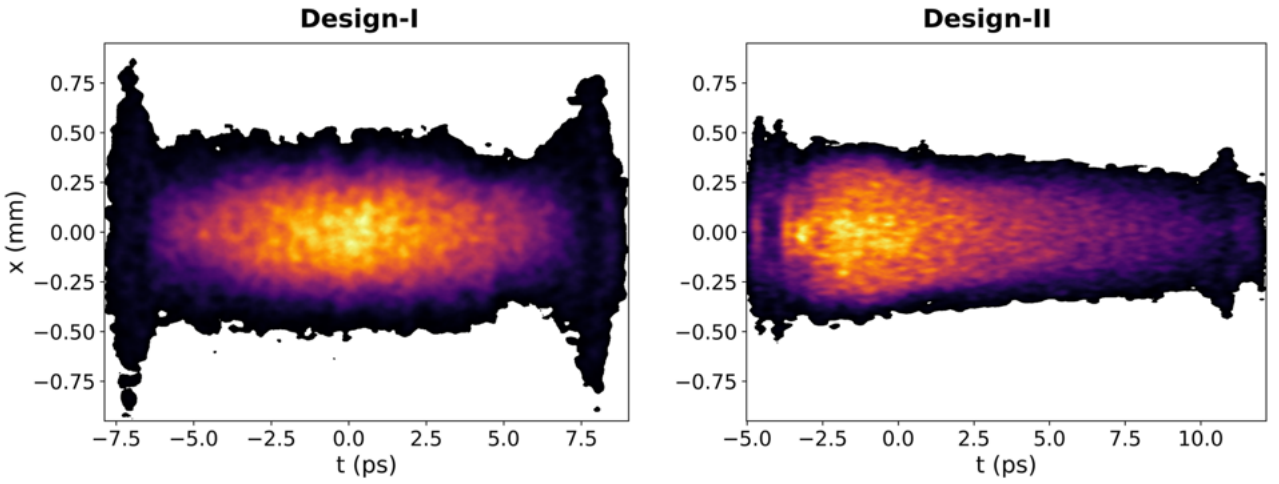

Figure 4.12: Current density projection of the electron bunch in the horizontal-longitudinal plane for Design-I and Design-II.

beam projection reveals a symmetric bunch structure, with peak current density concentrated near the bunch centre. This reflects the effectiveness of the linearisation and compression strategy in maintaining a low-skewness, FEL-compatible longitudinal profile. The head and tail regions display broader transverse spread, which is consistent with the increased slice emittance at the bunch extremities. However, these outer regions contribute minimally to the overall current density. The high-charge-density core remains well localized, confirming that the optimisation approach successfully preserved both longitudinal symmetry and transverse beam quality in the core. In contrast, Design-II exhibits a highly asymmetric longitudinal profile. The highest current density is located near the bunch head, accompanied by a noticeably larger transverse beam size in that region. The tail extends significantly, and while its local charge density is lower, it contributes non-negligibly to the overall current distribution. This behaviour directly results from the non-linear

dynamics of velocity bunching, which lead to a pronounced current skew. Nevertheless, despite the lack of linearisation, the achieved peak current exceeds that of Design-I, reaching 18.7 A with a comparable final bunch duration of approximately 17 ps. This demonstrates that aggressive compression is possible in RF-only configurations, albeit at the cost of longitudinal symmetry.

To further investigate the impact of current distribution and slice emittance together on beam quality, the four-dimensional (4D) beam brightness along the bunch is presented in Figure 4.13 for both Design-I and Design-II at the injector exit.

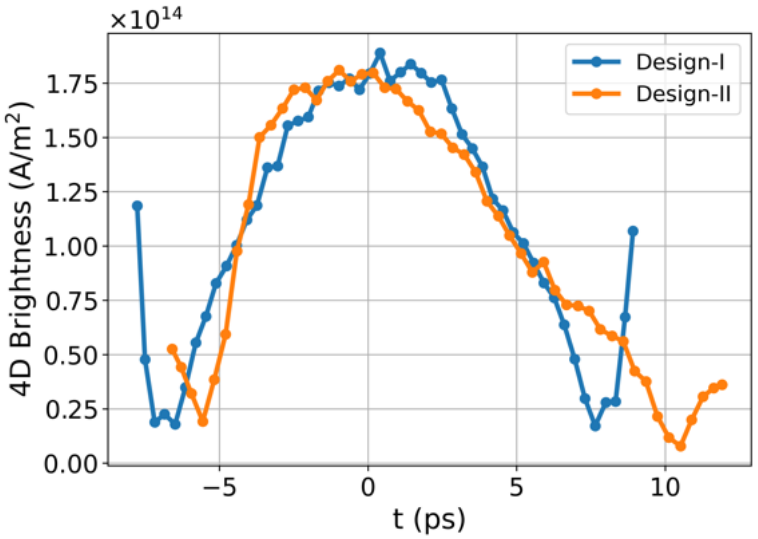

Figure 4.13: 4D beam brightness for Design-I and Design-II at the end of each injector beamline.

The resulting brightness profiles highlight the critical role of balancing the current profile and slice emittance. Although Design-I exhibits higher slice emittance compared to Design-II, as shown in Figure 4.11, its more uniform and symmetric current profile yields a smoother brightness distribution with reduced variation along the bunch. In contrast, Design-II achieves lower transverse emittance but generates a more peaked and asymmetric current profile, limiting the spatial extent of high brightness. This comparison illustrates that low emittance alone does not guarantee optimal beam quality; the current profile plays an equally important role in defining the effective brightness of the beam. While the 4D brightness is a meaningful figure of merit at the injector stage, the full six-dimensional (6D) brightness—accounting for bunch length and energy spread—becomes more critical after final compression in the main linac, where the FEL gain process is directly impacted. One should note that the 6D brightness is not shown at the injector exit, as the energy spread of Design-I is significantly increased by the RF linearisation applied before the chicane, which could lead to misleading conclusions. A fair comparison of the 6D brightness should instead be made after both designs undergo RF linearisation and magnetic compression in the main linac, where the energy spread profiles of the bunches in both Design-I and Design-II are shaped by the linearisation preceding the final compression scheme. Nevertheless, it is worth noting that before the application of RF linearisation, the 6D brightness of Design-I is higher than that of Design-II, reflecting the advantage of its more symmetric current and energy spread profiles at that stage.

Finally, to evaluate the performance of both injector configurations across the full range of operational bunch charges, the final horizontal and vertical core emittances are compared in Figure 4.14 against two transverse emittance scaling laws known in the literature [90]. For both Design-I and Design-II, the core emittance values remain within the expected scaling limits at 75 and 150 pC-the primary operating points considered for UK XFEL operation. At 300 pC, the vertical core emittance of Design-I slightly exceeds the scaling threshold. This excess could be mitigated by including quadrupole magnets around the chicane section to control the beam

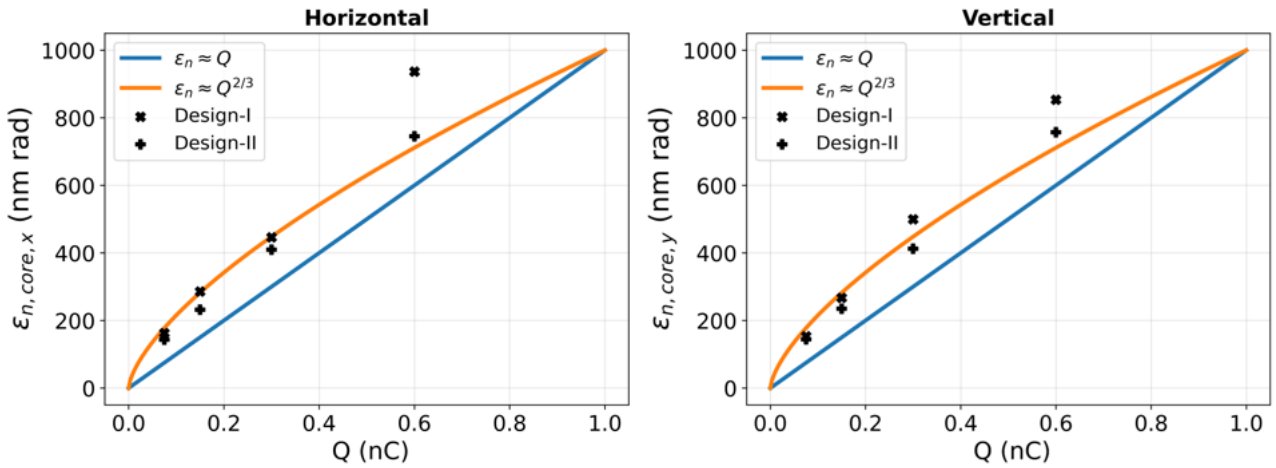

Figure 4.14: Final horizontal and vertical core emittances for Design-I and Design-II across all simulated bunch charges. Emittance values are compared with two theoretical scaling laws (shown as blue and orange lines).

envelope better. At 600 pC, neither design satisfies the scaling criteria, as space charge effects and RF-induced distortions dominate at high bunch charge, indicating that neither layout in its current form is optimised for high-charge operation. Nevertheless, the 6D brightness of the bunch for both designs—being a more comprehensive figure of merit—should ultimately be evaluated at the end of the main linac to avoid premature conclusions based solely on injector-stage emittance scaling and to reflect the beam quality relevant to FEL performance more accurately.

4.3.13 L-band SRF gun based electron injector design

Another attractive CW injector option is a design based on an SRF gun, which would allow for a higher emission field compared to the NCRF VHF option and lower RF power dissipation. For this option the most logical choice is a gun operating at the same frequency as the main linac, which in the case of UKXFEL is 1.3 GHz.

The goals when designing the L-band SRF injector option were to maximise beam brightness and for the beamline to produce a good quality bunch to be injected into the main linac. This requires a bunch with low emittance, and a linear longitudinal phase space. The 1.3 GHz injector provides multiple benefits towards these goals. In addition to being a compact beamline option, the high achievable electric fields on the cathode of 50 MV/m allow for faster acceleration, and so less time for emittance growth due to space charge [91]. The frequency of the gun also matches that of the accompanying booster cavities and main linac, reducing the need for multiple linearisation and compression steps. The design consists of a 1.5-cell, 1.3 GHz photocathode gun, followed by a superconducting solenoid in the same cryostat. The position of the solenoid, defined as the distance from the cathode to the centre of the solenoid field, is varied from a minimum of 0.45 m along the z-axis. This keeps the solenoid close to the gun to optimise transverse emittance, while allowing for geometric constraints within the cryostat, and keeping the solenoid field from interfering with the superconducting state of the cavity [66]. This is followed by a 1.3 GHz booster made of eight 9-cell 1.3 GHz cavities, to accelerate the bunch into the emittance dominated regime. A schematic of this design can be seen in Figure 4.15.

The two options considered for the cathode material are copper and Cs_2Te. Copper has the benefit of a lower thermal emittance which improves the emittance values achievable at the exit of the booster linac, but has not yet demonstrated a repetition rate above the 100 kHz due to the

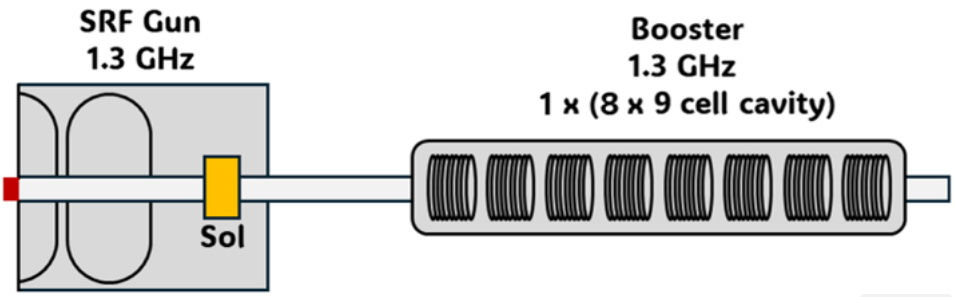

Figure 4.15: Outline schematic of the SRF L-band gun injector beamline.

lower quantum efficiency of metal photocathodes, that required high drive laser power. Cs_2Te would allow a 1 MHz repetition-rate to be more easily achieved, but comes with the disadvantage of a higher cathode emittance. For all simulations of the L-band injector design, a copper cathode was used. Under-inserting the cathode to provide RF focusing or over-inserting to mitigate dark current are both also options of interest [31].

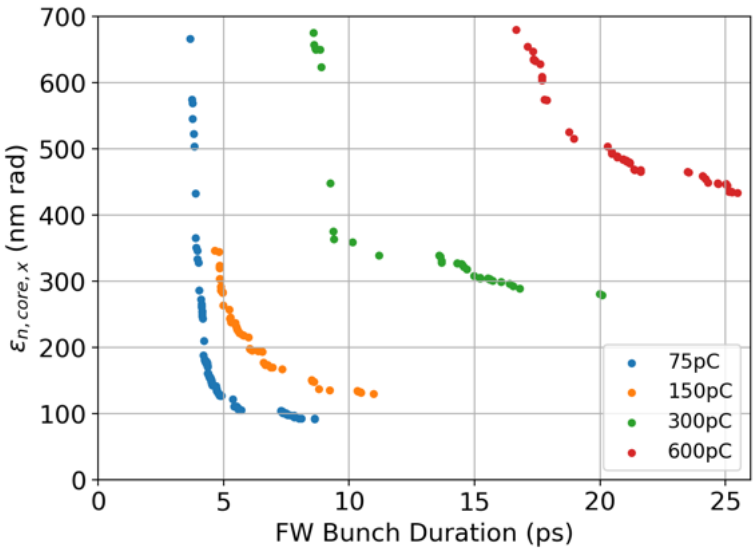

Figure 4.16: Pareto fronts for core emittance and bunch duration obtained for all bunch charges after initial acceleration up to the end of the booster cryomodule for the L-band injector.

ASTRA simulations [92] suggest that in order to produce the maximum beam brightness at the end of the booster, a short, narrow laser pulse should be used to create an initially small bunch. In addition, the first four booster cavities are run at phases far from crest which help reduce bunch length growth, keeping the bunch short enough to be injected into the main linac at a length of less than 10° of RF period. Figure 4.16 shows the achievable bunch length and emittance values at the end of the booster.

The results of beam dynamics simulations of the L-band design for a 150 pC bunch are presented for comparison to Designs I and II in the above section discussing the VHF gun-based electron injector. Figure 4.17 shows on the left column the evolution of key bunch parameters, normalised and core transverse emittance, bunch duration, and laminarity. The right column shows the longitudinal phase space profile in terms of bunch energy, higher-order energy and slice energy spread across the bunch, along with a current profile. The bunch duration starts relatively short due to the higher frequency L-band gun, being 12.3 ps full-width at the cathode. This increases after the gun and then undergoes slight compression due to the off-crest phases used in the L-band booster linac, reaching a full-width duration of 11.1 ps at the end of the injector. Due to the cylindrically symmetrical nature of the L-band design, all properties are transverse-symmetric,

with only small fluctuations. This can be seen in the 95% core emittance, which along with the normalised horizontal emittance, enters the booster with a core emittance value of 362 nm rad, and then follows the well-known double emittance compensation pattern to reach a final core emittance value of 182 nm rad. The laminarity parameter shows there are still improvements to be made to make the bunch optimised for injection into the main linac. While the bunch laminarity reaches a value of 4.33 , close to the transition regime, due to the increase of energy in the booster linac, the bunch remains space charge dominated until the end of the booster linac.

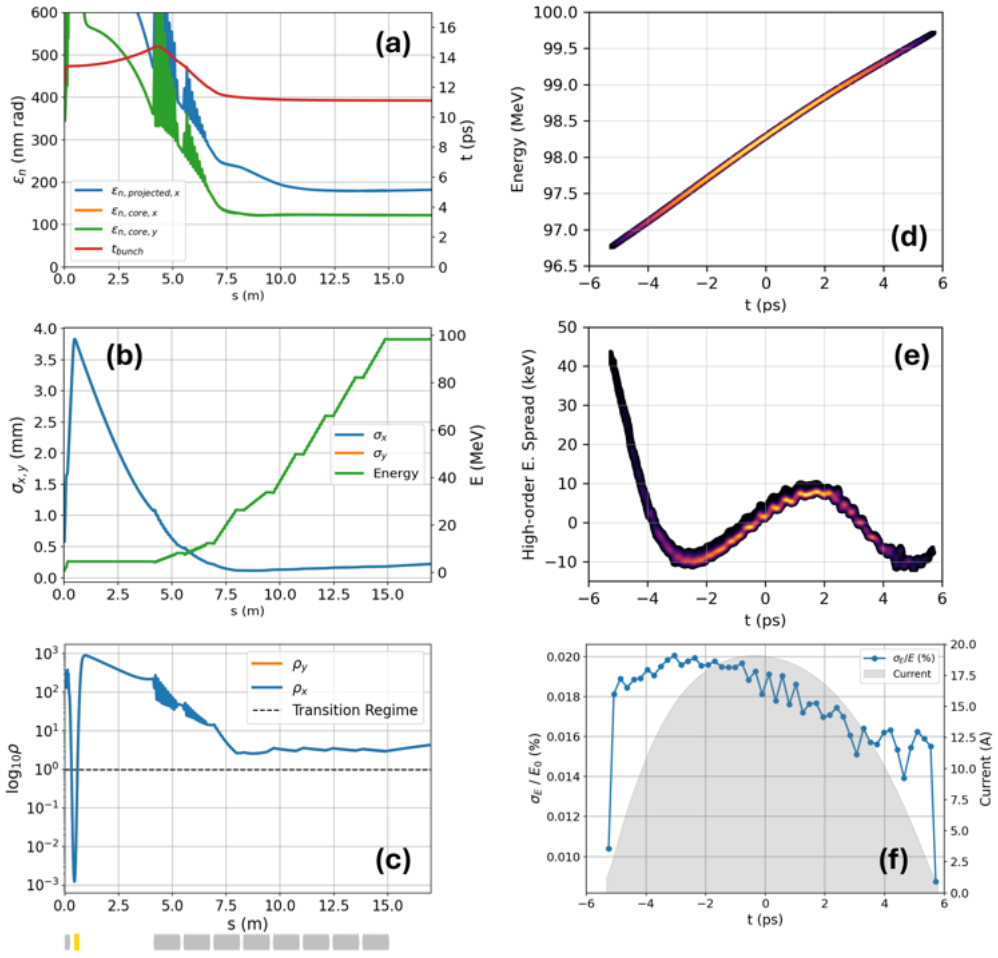

Figure 4.17: Left column: Evolution of beam parameters along the injector beamline for the L-band injector design at 150 pC bunch charge, (a) normalized projected and core emittances (horizontal and vertical) and bunch duration, (b) RMS transverse beam size and mean kinetic energy, (c) laminarity parameter. Right column: Longitudinal beam properties, (d) energy, (e) high-order energy spread, (f) slice energy spread and current profile.

The longitudinal phase spaces are shaped by the RF curvature of the L-band gun and booster cavities being imprinted onto the bunch. Due to the first four cavities of the booster running far from crest the time-energy relationship looks fairly linear, but the higher-order energy terms show a strong curvature. The small amount of RF compression that occurs in the booster cavity leads to a shift of the centre of charge density towards the head of the bunch. The current profile, with a peak current of 19.1 A at the the end of the injector, is largely symmetric along the length of the bunch, again showing a slight skew towards the head which forms in the booster linac due to running far off-crest. This also causes a sharp increase in the relative energy spread of the bunch, which decreases again in the final four booster cavities as the mean bunch energy increases. The slice emittance is quite consistent along the length of bunch, decreasing slightly in the tail which follows the pattern of the charge density.

Further studies into including a higher-harmonic cavity between the booster and the merger to act as a linearisers are still required. The most likely frequency choice for this additional cavity would be 3.9 GHz (third-harmonic of the booster and main linac), similar to the 9-cell cavities being tested at SHINE for linearisation [93]. This would be used to compensate for the longitudinal phase space distortion of the bunch caused by the previous 1.3 GHz RF cavities and reduce longitudinal emittance before the bunch enters the merger, helping to reduce emittance growth.

Figure 4.18 shows the transverse properties of the bunch at the end of the injector, including the transverse phase spaces, slice emittance along the length of the bunch and current density projections in the longitudinal-horizontal plane. Due to the cylindrically symmetric beamline, though only the horizontal phase spaces are shown, these are practically identical to the vertical phase spaces. The phase spaces show that the nine slices along the bunch are well aligned, with only a small rotation between the core, head and tail slices. The charge density projection is not longitudinally symmetric, and shows that the peak current density of the bunch appears towards the head, as also shown by the current profile. These features are all reflected in the slice emittance along the bunch, which shows a small increase at the head, where there is a slight misalignment in the slices and a higher charge density.

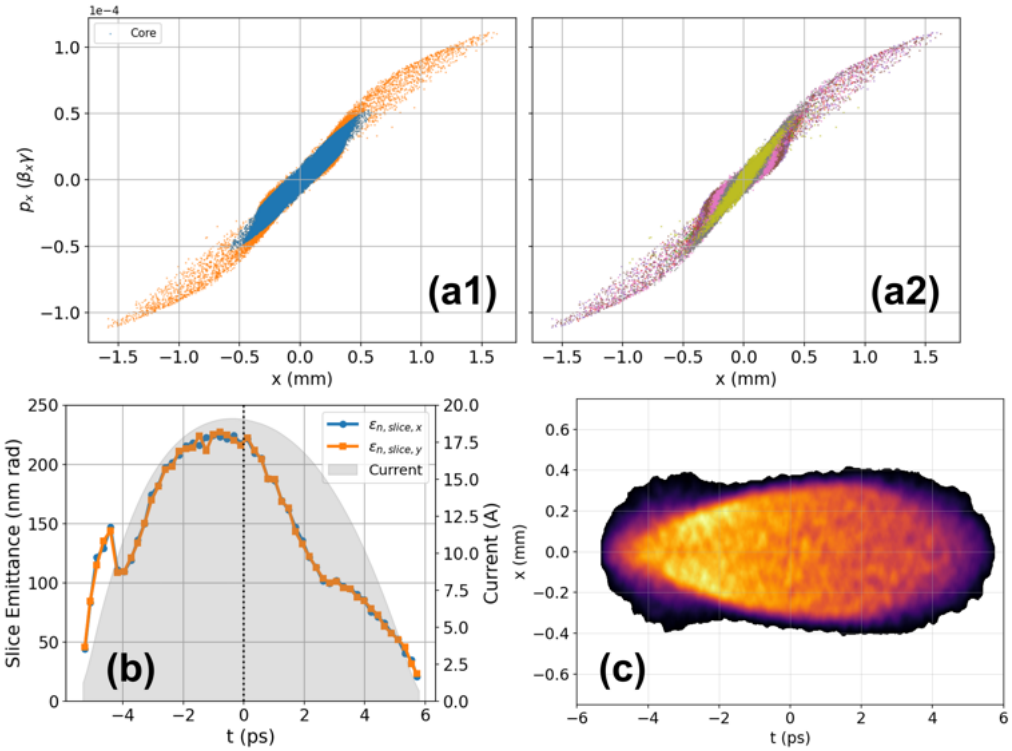

Figure 4.18: Transverse beam properties for the L-band injector design at 150 pC. (a1) The horizontal phase space showing the 95 % core particles, (a2) 9-slice visualizations along the bunch to illustrate phase space rotation and alignment. (c) horizontal and vertical slice emittance distributions along the bunch, plotted together with the one-dimensional current profile. (d) current density projection of the electron bunch in the horizontal-longitudinal plane.

To conclude the injector comparison, Table 4.3 summarises the key beam parameters for Design-I, Design-II and Design-III across all simulated bunch charges at the exit of the low-energy injector. The table includes projected and core transverse emittances, energy spread metrics, bunch duration and size, peak current, and laminarity parameters. For the nominal operating range (75-150 pC), all three designs deliver high-quality beams with preserved transverse core emittance and acceptable energy spreads.

Parameter	Unit	Design-I : Hybrid Compression				Design-II : RF Compression				Design-III : L-band SRF			
		75 pC	150 pC	300 pC	600 pC	75 pC	150 pC	300 pC	600 pC	75 pC	150 pC	300 pC	600 pC
Projected Emittance (Horizontal)	nm rad	191	341	540	1108	177	278	476	851	121	182	404	712
Projected Emittance (Vertical)	nm rad	180	314	633	1014	179	283	480	865	120	181	404	712
Core (95.45%) Emittance (Horizontal)	nm rad	163	286	446	937	144	232	410	745	86	122	279	303
Core (95.45%) Emittance (Vertical)	nm rad	153	267	500	854	144	235	412	757	86	122	279	303
RMS Energy Spread	MeV	0.54	1.1	0.59	0.1	0.16	0.12	0.19	0.17	0.33	0.71	0.64	0.13
RMS High-Order Energy Spread	keV	18.7	15.2	8.1	62.9	37.9	50.9	41.5	17.3	7.1	7.9	12.2	14.6
Mean Relative Energy Spread	ppm	97	200	95	20	30	30	40	40	27	72	60	10
Mean Bunch Energy	MeV	139.7	139.6	177.7	169.3	254.1	186.1	252.1	256.1	121.7	98.25	103.0	103.7
Full-width Bunch Duration	ps	15.5	16.9	14.5	17.2	16.6	17.2	19.8	19.5	8.8	11.1	20.2	23.0
RMS Bunch Size (Horizontal)	mm	0.18	0.2	0.21	0.49	0.19	0.17	0.24	0.28	0.23	0.22	0.46	0.35
RMS Bunch Size (Vertical)	mm	0.17	0.11	0.32	0.45	0.19	0.17	0.24	0.28	0.23	0.22	0.46	0.35
Skewness	-	0.02	0.08	0.02	0.04	0.7	0.7	0.63	0.53	0.04	0.07	-0.001	0.01
Laminarity Parameter (Horizontal)	-	0.72	0.58	0.53	0.99	0.67	0.59	0.46	0.38	0.98	4.31	1.80	0.30
Laminarity Parameter (Vertical)	-	0.76	0.19	0.94	0.97	0.66	0.56	0.45	0.37	0.98	4.33	1.80	0.30
Peak Current	A	7.7	16	42.8	55.6	10.15	18.7	31.7	61.6	24.1	19.1	9.5	8.9
Total Length of the Beamline	m	52.5	53.1	62.0	55.5	31.15	25.65	31.2	31.65	15.13	15.0	14.01	14.89

Table 4.3: Beam parameters for Design-I, Design-II and Design-III at the end of the injector beamline for various bunch charges.

DRAFT

4.3.14 Comparison of proposed options

Three different injector schemes have been analysed in detail. These are:

- Design-I: a NCRF VHF gun with RF and magnetic compression
- Design-II: a NCRF VHF with two stage RF compression
- Design-III: a high field L-band SRF gun without compression

The first two schemes use the same NCRF VHF gun. These guns have a higher technical readiness than high field L-band SRF guns. The current LCLS-II [3] and SHINE [4] injector designs use NCRF VHF guns. However the specific 'relaxed geometry' VHF gun considered in the UK XFEL design study has a lower technical readiness level, than a standard VHF gun, as no VHF gun of this type has been built before. Additionally, it was assumed that a cathode field of 30 MV/m could be achieved; however, the highest experimentally achieved cathode field is 27 MV/m [4]. The relaxed geometry design still has a number of open questions around gun solenoid integration, mechanical design and multipactor which would need to be resolved in the next phase of the project.

Design-I has a number of advantages: better longitudinal phase spaces and current distributions which is beneficial for the downstream compression and lasing and it provides better separation of functions between the two compression stages which should make the easier to operate. However it does have a number of disadvantages: the worst transverse emittance of the three schemes although still acceptable, requires a larger amount of 650 MHz SRF cavities which adds cost and complexity, has complicated beam dynamics and is the physically longest of the three schemes.

Design-II has the following advantages: better transverse emittance than Design-I, and it will likely be cheaper as it is shorter and requires less 650 MHz SRF cavities. The disadvantages of this scheme are: the skewed charge distribution which will cause problems in the downstream compression and lasing, the complicated beam dynamics and limited space for diagnostics which will make it hard to practically operate.

Design-III's advantages are: the best transverse emittance of the three schemes, the simplest beam dynamics, the charge distribution is symmetric, the gun and booster are the same RF frequency as the main linac so the RF systems will be simpler and cheaper, the X-ray pump X-ray probe mode will be relatively simple to implement, and it is the physically shortest of the three schemes. The disadvantages of this scheme are: the low technical readiness level of the gun as beam has not yet been experimentally demonstrated with an SRF gun with 50 MV/m cathode field, and the low QE of the copper photocathode means that the gun will not be able to deliver the required repetition rates for UK XFEL. An SRF gun operating with a copper photocathode and high cathode field is under development at DESY for the CW injector upgrade of EuXFEL [39].

Of the three schemes the preferred option is Design-I despite the fact that it produces the worst transverse emittance of the three options. This is due the fact that the transverse emittance is still acceptable and compared to Design-II the longitudinal properties are better which will lead to better 6D brightness at the FELs and the beam dynamics is simpler. Compared to Design-III the technical readiness level is higher. Design-III, the high field L-band SRF has many desirable characteristics but it is considered too risky to adopt as a baseline for UK XFEL and is unlikely to deliver the required repetition rates. However, progress in the development of this technology should be monitored going forward in case the required performance is experimentally demonstrated. Another technology option continue to observe the development of is SRF VHF guns like the one being considered for the LCLS-II HE low emittance injector [52] and the BNL SRF VHF gun [48].

4.4 Configuration of injector for multiple FEL lines and two-colour operation

One of the key UK XFEL goals is the possibility of simultaneous operation of several FELs to provide X-rays with different wavelengths for different users experiments and to make X-ray pump X-ray probe experiments where the probe X-ray pulse arrives to the sample with small adjustable delay after the pump X-ray pulse. The optimal electron beam parameters such as bunch charge and pulse length, are different for every FEL. As it is impossible to change the tuning of the SRF and magnetic systems of accelerator fast enough to deliver bunches with different parameters, several different accelerators are required, however, that is not practical (see Chapter 3). A possible solution would be to minimise the number of required bunch parameter sets, ideally to two, and design the main accelerator for operation with these bunch parameters. As it is also impossible to retune the photoinjector lasers fast enough it is planned to drive the injectors with two independent lasers synchronised with the machine RF.

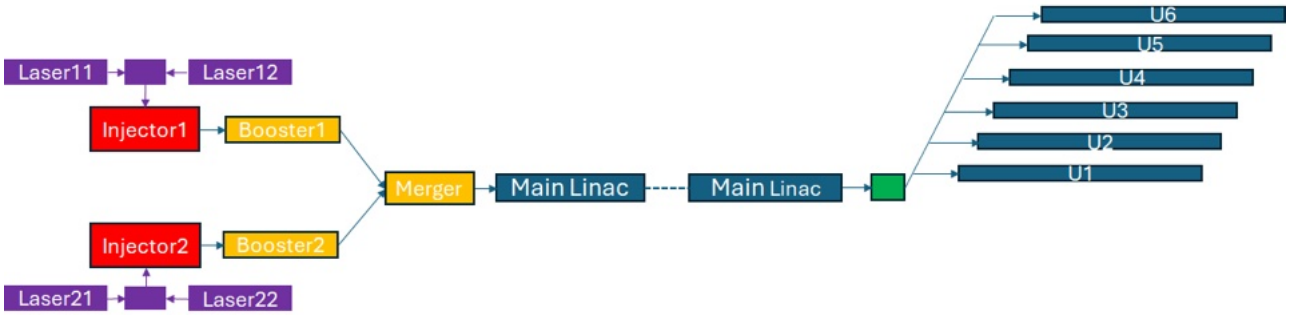

Figure 4.19: Example scheme of the UK XFEL with two injectors and 6 FELs.

Bunches with the required parameters will be provided by two independent injectors operating synchronously with the High Energy Beamline (HEB). Bunches with different charges will be injected into the HEB by an RF merger operating at half the frequency of the main linac. Figure 4.19 shows one of the possible schemes of two injector Low Energy Beamline for operation with L-band main linac. The laser scheme shown in the figure includes two identical laser groups Laser11, Laser12 and Laser21, Laser22 for both injectors to provide operational contingency. An example of the UK XFEL temporal structure for a 6 FEL regime is shown in Figure 4.20.

The two injector scheme also simplifies the operation of the machine in the two colour X-ray pump – X-ray probe mode for an injector based on a sub-harmonic gun. For this mode the electron bunch for generation of pump X-ray pulse is delivered by first injector. The second injector generates the electron bunch for the probe X-ray pulse and operates with delay relative to the first injector. The minimum delay time is one RF period of the HEB linac, which is 0.769 µs for L-band (see Figure 4.21). Further fine tuning of the delay will be provided by X-ray optics.

4.4.1 Merging From Injector

The UK XFEL scheme uses two injectors operating simultaneously. This has two motivations. Firstly, the need to deliver two different bunch charges to the undulators simultaneously. This can be done most effectively with separate injectors which are tuned for their specific bunch charges. Secondly, the need to provide a widely separated two colour X-ray pump X-ray probe mode which is part of the next generation XFEL definition. This requires two electron bunches in adjacent

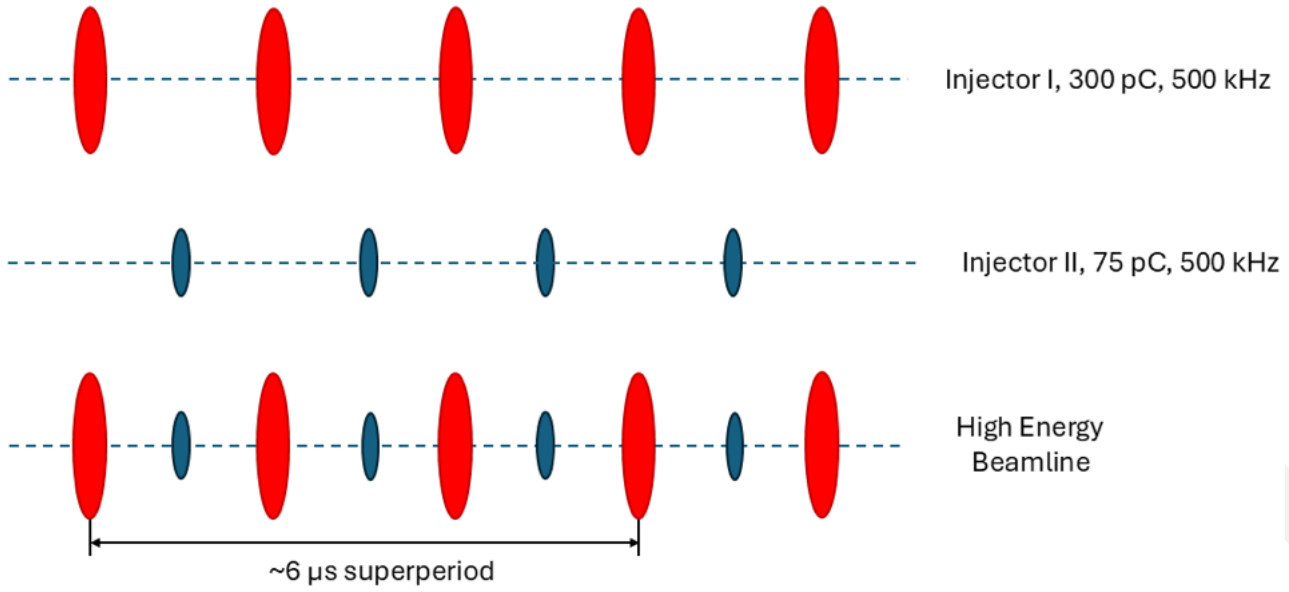

Figure 4.20: Example of two injector LEB operation in 6 FEL mode.

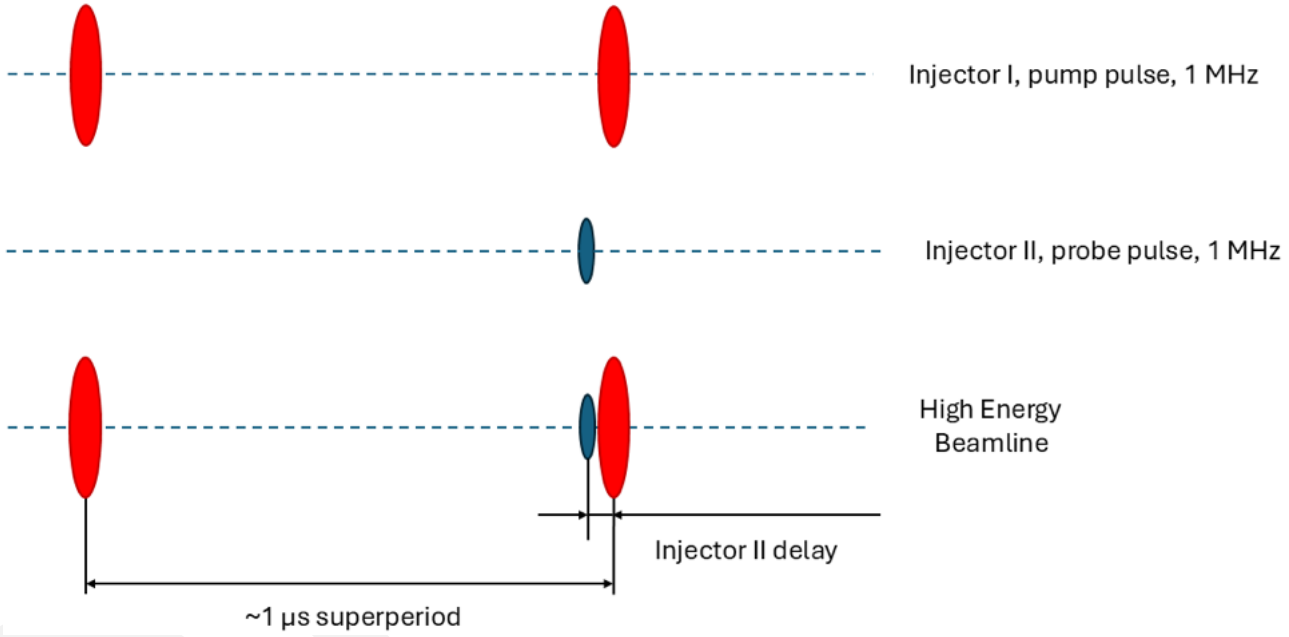

Figure 4.21: Operation of the two injector LEB in two colour mode.

main linac RF buckets. If the injector uses sub-harmonic RF, such as a VHF gun based injector, then two injectors with a timing offset are required to produce bunches with the correct separation. An additional benefit to having two injectors is redundancy. If one of the injectors goes down the machine can, still run albeit with reduced functionality using the other injector.

Having two injectors both feeding into the same main linac means that there needs to be a beamline to merge the bunches from the separate injectors. This beamline has a number of requirements. It will likely operate with energies somewhere between 100-200 MeV, bunch charges between 75-600 pC and FWHM bunch durations of around 20 ps. The full repetition rate of the machine is 1 MHz this means that the merger needs to be able to combine bunches at this repetition rate. However to meet the requirements of two colour X-ray pump X-ray probe it also needs to be able to switch fast enough to inject a bunch from each injector into the adjacent main linac buckets. The RF period of the 1.3 GHz main linac is 769 ps so the switching time needs to be

faster than that. In addition to the switching time, there are a number of other requirements on the beam dynamics of the merger beamline. Firstly, the bunch needs to have minimal positional and angular jitter at the exit of the beamline as the beam needs to traverse the main linac and spreader beamline before it reaches the undulators and shot-by-shot jitter cannot be corrected. Secondly, the steering out of the merger also needs to be very good as any steering difference between the two injectors cannot be corrected downstream. Thirdly, to allow beams with significant chirps to be transported through the merger it is desirable for it to be achromatic and isochronous to second order. A final desirable feature of the merger beamline is to provide sufficient separation between the two injectors that they can be located in separately shielded areas. This will have the operational benefit of allowing one injector and the main linac to operated while the other injector is being accessed for repair or maintenance.

An approach to the merger beamline design is to separate it into two parts. The first is an all magnetic static beamline which does most of the horizontal transport of the beam and has the more complicated optics required for the whole beamline to be achromatic and isochronous to second order. The second is a shorter final combining section containing the final element that combines both beams. Three options for the combining element are: a static magnetic dipole, a kicker or a TDC (Transverse Deflecting Cavity). The advantages of dividing the beamline up in this way are: that it is more modular so the different sections can be designed separately, the optics can be designed to be more easily understood and set-up, and it allows for the final combining section to be designed with a shallower bending angle. The benefit of a shallower bending angle is that the positional and angular jitter out of the merger should be smaller. This is because the final combining element is likely to be less stable than the magnets elsewhere in the merger.

Using a static magnetic dipole as the final combining element has the advantages that static magnets are a very mature technology and it allows for the most flexibility in the timing and bunch sequencing of the beams. The main disadvantage of the scheme is that the beams from the injectors need to be injected into a common dipole at different angles and positions but exit at the same angle and position. This requires that at least part of the merger is asymmetric and the beams from the injectors have different energies. Although the injectors themselves could still be physically identical and just tuned differently. Different beam energies from the injectors would have downstream implications in the HEB bunch compressors and spreader that need further study.

A kicker based combining section uses an element which is capable of rapidly switching on and off as the final combining element of the beamline. There are a range of different technologies that can be used as kickers. For combining evenly spaced (at 1 us separation) 1 MHz beam there are established solutions using kickers. These were developed for LCLS-II [94] and SHINE [95]. However these kickers do not have fast enough rise and fall times to allow bunches from the two different injectors to be placed in adjacent main linac RF buckets for x-ray pump x-ray probe. Fast stripline kickers with ns rise and fall times have been developed [96]. However, the ns rise and fall times are still not fast enough for the X-ray pump X-ray probe. R&D could potentially be done to develop faster kickers of this type.

The final combining section option is to use a transverse deflecting cavity as the final combining element. This cavity would likely need to be superconducting to provide the required kick while operating CW. Superconducting transverse deflecting cavities do exist although they are typically used as crab cavities for machines like the HL-LHC [97]. To allow for injecting bunches from the two separate injectors into adjacent main linac RF buckets as required for widely separated two colour X-ray pump X-ray probe the TDC must operate at 650 MHz. This option has the advantage of having a fast enough switch time for X-ray probe X-ray pump while using an established technology. The disadvantages of this scheme are that although SRF TDC are an established technology they

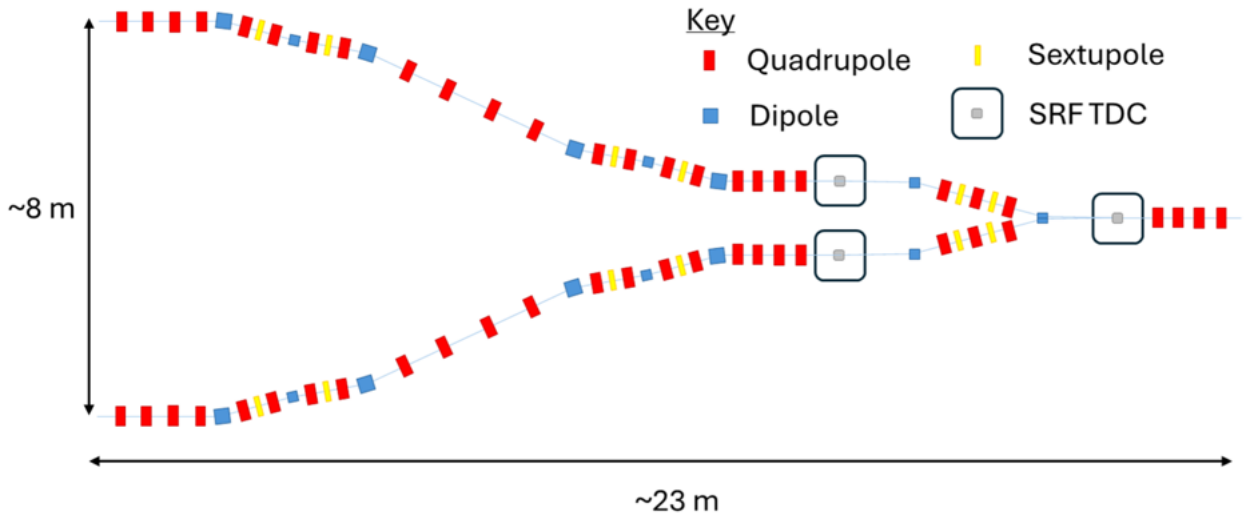

Figure 4.22: A sketch of a potential scheme for combining bunches from two separate injectors into a common main linac. This beamline uses TDCs to do the final combining and should be 2nd order achromatic and isochronous.

are expensive, complicated and significant design effort would be needed. Another disadvantage is that the TDC will have time dependent bending and the bunches are relatively long compared to the RF wavelength. This means that RF curvature will be imprinted on the x-t distribution of the bunch. To avoid this a two SRF TDCs will be needed per injector, a total of three, so that the curvature can be cancelled. This is an additional complication to the beam dynamics.

A sketch of a potential scheme for the merger can be seen in Figure 4.22. This scheme takes the approach of doing the majority of the beam transport with a static magnetic beamline and then doing the final combining with a short shallow bending angle combining section. It uses SRF TDCs to do the final combining with the beam in both legs passing through two TDC so the RF curvature cancels. The final combining section has quads and sextupoles so it can be made achromatic to second order but it will not be isochronous. The upstream translating section consists of a pair of triple bend achromats with a zero dispersion straight between them. These triple bend achromats use shallow reverse bends as the central dipole to keep the total bending angle of the achromat large and to make achieving zero or slightly chicane-like R56 easier. The achromats have quadrupoles and sextupoles so they are achromatic to second order. They will be tuned so that their combined R56 and T566 is opposite to the R56 and T566 of the combining section. This would mean that the whole beamline is isochronous to second order.

The scheme depicted in Figure 4.22 is only conceptual and has not been simulated. Further simulation work will need to be done to develop a complete design. This will include the beam dynamics design of the whole merger and the specification of the magnet parameters. The SRF TDCs will also needed to be designed. These are a key component that will require significant work. SRF TDCs in a similar frequency range have been designed in the past but none at the exact frequency required. Additionally extensive jitter simulation studies will need to be done with tracking through the main linac to confirm that the positional and angular jitter into the main linac are small enough to not degrade machine performance.

4.4.2 Sustainability

The most impact that development in the area of the Low Energy Beamline can make to sustainability is to achieve higher brightness beams, thus lowering the emittance of the beam in the facility. This would allow the same FEL power to be produced with a lower beam energy, and/or saturation length, following the semi-analytical formulae of Ming Xie [98]. A lower emittance beam would thus allow a shorter linac and/or undulator section of the entire facility to be built, saving substantial amounts of energy and carbon emissions in both construction and operation. The exact saving depends on particular linac and FEL design, which is described in other chapters. Two examples are shown here. Firstly for the MEC line at 40 keV photon energy, Figure 4.23 shows the output FEL pulse energy for electron beams of different beam emittances and energies. If a pulse energy of 0.5 mJ is desired, it is seen that halving the emittance from 400 nm rad to 200 nm rad, the beam energy required drops from 12 GeV to 9.5 GeV. This would allow a similar reduction in the length of linac required to reach this beam energy.

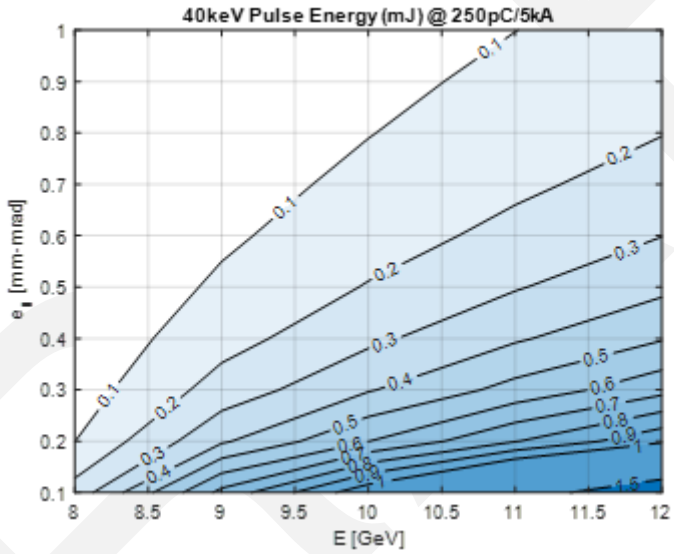

Figure 4.23: Lines of equivalent FEL pulse energy for different beam emittances and energies, for a photon energy of 40 keV.

The second example is of the impact of reducing emittance on reduction in saturation length of the FEL, for the same beam energy. This is shown in Figure 4.24 for a photon energy of 40 keV. Picking a 10 GeV electron beam energy, shows that halving the emittance from 0.4 mm mrad to 0.2 mm mrad drops the saturation length from approx 70 m to approx 30 m, allowing a similar reduction in length of undulators required.

As can be seen from both Figures 4.23 and 4.24, the reduction in beam energy, thus linac length, and/or saturation length, thus undulator length, is highly dependent on the particular FEL setup. However, it is clear that substantial gains can be made by reducing the beam emittance. Consequently, decreasing the emittance by optimising a better electron source, photocathode, and emittance-preserving low energy beam transport and manipulation, is vital to ensuring a small footprint of the facility, and thus lower carbon emissions in construction and operation of the FEL.

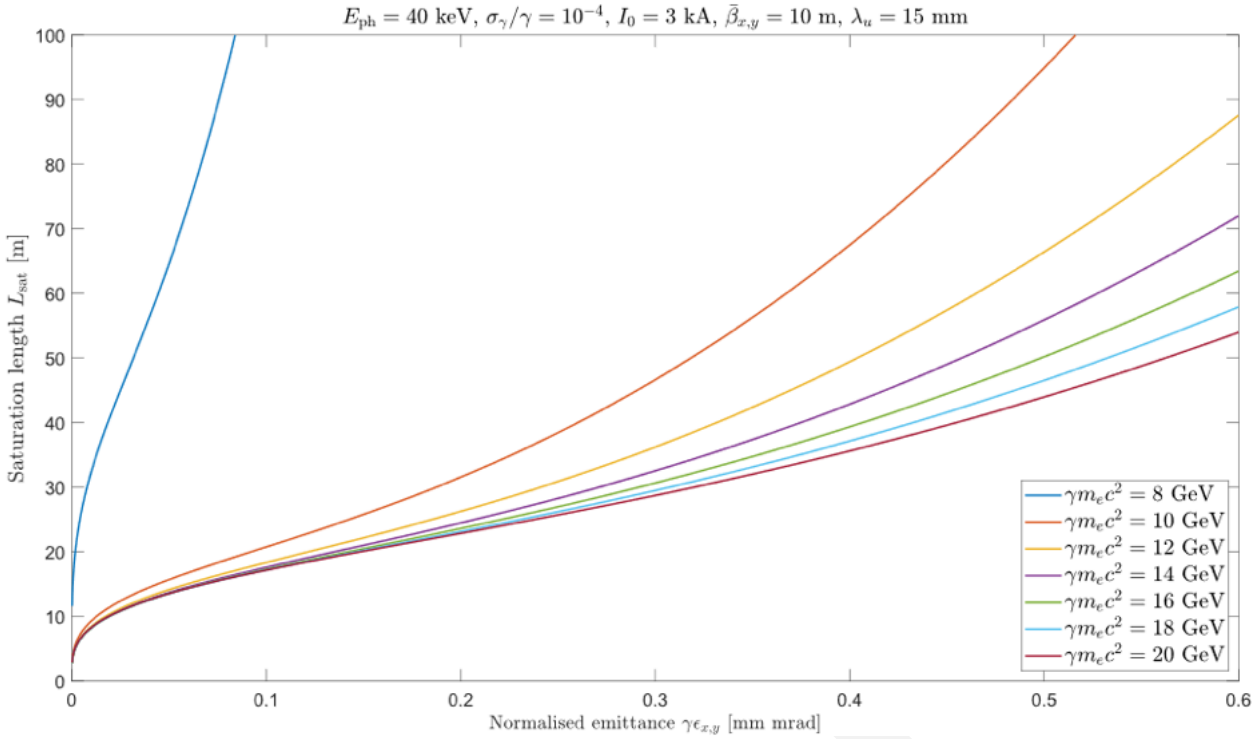

Figure 4.24: Plot of saturation length as a function of beam energy and emittance, for a photon energy of 40 keV.

4.4.3 Summary of technology development areas, R&D needed for future phases to meet specifications

As demonstrated by Section 4.4.2, a reduction in the beam emittance would substantially reduce the length of linac and/or undulators required, and thus greatly improve the environmental sustainability of the facility by reducing tunnel length, amount of accelerator required to be constructed, and operational costs. The complex low energy beamline described in this Chapter to achieve a low emittance beam for the facility is unproven, and thus prototyping is required to prove the technology readiness of the chosen option, and also, to enable decisions to be made about length of linac and undulators required for the full facility. Depending on the option chosen, prototyping of the laser system, photoinjector, bunch compression system, and merger would also be required. Further research and development into these areas would enable lower emittance beams to be produced more reliably which would also benefit the future XFEL facility.

It is clear, that although ideally the full Low Energy Beamline would need to be prototyped, various options are available, in increasing complexity and cost. Although prototyping can apply to all three design options of the Low Energy Beamline, Design-I of:

- VHF Gun (NC) + Linearizer (NC) + Pre-Buncher (NC) + Booster (SRF) + Linearizer (SRF) + C-Shape Chicane + merger

is chosen here as representative. Three options are listed below, Option 1 would test the gun only, Option 2 would test the gun and initial compression stage, and would not require acceleration to higher energies, and Option 3 would test the entire low energy beamline - the gun, both compression stages, and the merger.

- 1 - Barebones - VHF gun
- 2 - Medium - VHF gun, linearizer, pre-buncher, booster

- 3 - Ultimate - VHF gun, linearizer, pre-buncher, booster, linearizer, C-shape chicane, merger

In the above options, when ”VHF gun” is mentioned, it consists of the electron gun, surrounding RF infrastructure, photocathode exchange, and photoinjector laser systems. The gun only options is of limited use, as the beam dynamics properties of the bunch are not yet frozen at the low energy produced from a gun alone.

In all instances, electron beam diagnostics would be required. The level of which can range in scale, ideally up to full 6D phase-space diagnostics, which would allow full characterisation of the beam dynamics presented in this chapter. This diagnostics beamline would include tomographic emittance measurements, an RF transverse deflecting cavity (or THz streaker), and spectrometer.

Ideally the whole prototype would be tested at MHz repetition rates, which would require superconducting RF infrastructure, and R&D into the diagnostics and data infrastructure. Running at kHz repetition rates would be less useful for the full XFEL facility, but available with normal-conducting RF, and existing diagnostic and data technology. A kHz prototype would be substantially cheaper, especially given the lack of cryogenic infrastructure required, and the lower shielding requirements. However, this would not be demonstrative of the full technology required for the facility, and would only demonstrate the beam dynamics.

Only the full Option 3, operating at MHz repetition rates, with a full 6D diagnostics beamline, would fully test the technology readiness level of the Low Energy Beamline to deliver high brightness beams for the UK XFEL. However, the three options could be staged, with each option built upon successful demonstration of the previous stage.

Every other XFEL built worldwide has undergone prototyping of their Low Energy Beamline before construction of the full facility. Moreover, in some instances, the prototype was moved outright to the new facility, forming the Low Energy Beamline of the FEL, and in others, transformed into other facilities. The following lists the type of prototyping performed by existing FEL facilities:

- 1 - Bare-bones - VHF gun only
- 2 - Medium - LCLS-II (APEX [24]), Eu-XFEL (PITZ [99]), SHINE [100], PAL-FEL [101]
- 3 - Full - SwissFEL [58], SACLA (SCSS [102]), Eu-XFEL (FLASH [103])

For the cases of SACLA and Eu-XFEL, the full-scale prototypes were later developed into full FEL facilities in their own right (SCSS [104] and FLASH [103]), operating at the same site, and in parallel to the XFEL, offering further scientific capability to those sites.

4.5 Conclusions

A careful analysis of the possible Low Energy Beamline schemes which could deliver beams with the parameters and temporal structure necessary for the effective operation of UK XFEL and which are based on currently available technology or technology which will be available in the near future has been done. It led to the following conclusions:

To provide beams with different bunch charges and the temporal structure for multi FEL and X-ray pump X-ray probe experiments the Low Energy Beamline should be based on two independently operating injectors with an RF TDC based merger which injects the beams from the two injectors into the High Energy Beamline.

The injectors should be built on the basis of photocathode RF gun which is able to operate in 1 MHz repetition rate. Currently, a normal conducting VHF gun operating with Cs_2Te photocathodes is the only option which has a Technology Readiness Level high enough for use in the UK XFEL. In the near future commissioning of a high Field L-band SRF gun and an SRF VHF gun are scheduled. The results of these commissioning may be included into consideration.

To provide high brightness beams the VHF gun should operate with a bunch length of at least 100 ps, which should be compressed to less than 20 ps for injection into the 1.3 GHz L-band High Energy Beamline. Analysis of the possible compression schemes resulted in the conclusion that two stage compression is required to preserve beam emittance. The first stage is traditional RF compression, while the second stage is either velocity bunching or magnetic compression. Beam dynamics simulation of both schemes has shown that they are able to deliver 150 pC bunches with emittances as low as 300 nm rad. This emittance does not achieve the theoretical optimum value but is still sufficient to produce the require x-ray parameters for UK XFEL. Slightly better emittance is provided by the scheme with a second stage of RF compression and while a better longitudinal phase space is produced by the scheme using second stage magnetic compression. The scheme with magnetic compression is chosen as the baseline.

The effective operation of the two injector Low Energy Beamline to provide a beam with different temporal-space charge structure will be enabled by using a combined magnetic-RF merger. The merger is based on two 3-dipole achromats and two Transverse Deflecting RF cavities in each branch. The complicated structure is necessary so the beamline is an emittance preserving second order isochronous achromat.

In order to demonstrate operational performance of the proposed Low Energy Beamline it should be prototyped, ideally up to sufficient energy to be in the emittance dominated regime and to the end of the bunch compressor.

The analysis lead to the conclusion that the proposed design of the Low Energy Beamline is able to deliver high brightness beams with the necessary bunch charge-temporal structure for UK XFEL and an emittance of about 300 nm rad for 150 pC bunches.

DRAFT

References for Chapter 4

[1] Luca Serafini and James B. Rosenzweig. “Envelope analysis of intense relativistic quasilaminar beams in rf photoinjectors: A theory of emittance compensation”. In: *Phys. Rev. E* 55 (6 June 1997), pp. 7565–7590. DOI: 10.1103/PhysRevE.55.7565. URL: https://link.aps.org/doi/10.1103/PhysRevE.55.7565.

[2] Colwyn Gulliford et al. “Demonstration of cathode emittance dominated high bunch charge beams in a DC gun-based photoinjector”. In: *Applied Physics Letters* 106 (9 Mar. 2015). ISSN: 00036951. DOI: 10.1063/1.4913678.

[3] F. Zhou. “First commissioning of LCLS II injector”. In: *FEL2022*. Talk. Trieste, 2022.

[4] Lianmin Zheng et al. “Design, fabrication, and beam commissioning of a 216.667 MHz continuous wave photocathode very high frequency electron gun”. In: *Physical Review Accelerators and Beams* 26 (10 Oct. 2023). ISSN: 24699888. DOI: 10.1103/PhysRevAccelBeams.26.103402. URL: https://doi.org/10.1103/PhysRevAccelBeams.26.103402.

[5] F. Zhou et al. *Overview of CW electron guns and LCLS-II RF gun performance*. 2023. DOI: 10.3389/fphy.2023.1150809.

[6] Nikhil Bachhawat et al. *CW SRF Gun generating beam parameters sufficient for CW hard-X-ray FEL*. 2025. arXiv: 2511.07620 [physics.acc-ph]. URL: https://arxiv.org/abs/2511.07620.

[7] D. Filippetto et al. “Maximum current density and beam brightness achievable by laser-driven electron sources”. In: *Physical Review Special Topics - Accelerators and Beams* 17 (2 Feb. 2014). ISSN: 10984402. DOI: 10.1103/PhysRevSTAB.17.024201.

[8] Georgii Shamuilov et al. “Child-Langmuir law for photoinjectors”. In: *Applied Physics Letters* 113 (20 Nov. 2018). ISSN: 00036951. DOI: 10.1063/1.5063888.

[9] W. D. Kilpatrick. “Criterion for Vacuum Sparking Designed to Include Both rf and dc”. In: *Review of Scientific Instruments* 28.10 (Oct. 1957), pp. 824–826. ISSN: 0034-6748. DOI: 10.1063/1.1715731. eprint: https://pubs.aip.org/aip/rsi/article-pdf/28/10/824/19301232/824_1_online.pdf. URL: https://doi.org/10.1063/1.1715731.

[10] Bruce E. Carlsten. “Wilson Prize article: Transverse phase-space manipulations in electron accelerators”. In: *Physical Review Accelerators and Beams* 23 (11 Nov. 2020). ISSN: 24699888. DOI: 10.1103/PhysRevAccelBeams.23.114801.

[11] Jared Maxson et al. “Design, conditioning, and performance of a high voltage, high brightness dc photoelectron gun with variable gap”. In: *Review of Scientific Instruments* 85 (9 Sept. 2014). ISSN: 10897623. DOI: 10.1063/1.4895641.

[12] Nobuyuki Nishimori et al. “Operational experience of a 500 kV photoemission gun OPERATIONAL EXPERIENCE of A 500 KV ... NOBUYUKI NISHIMORI et al.” In: *Physical Review Accelerators and Beams* 22 (5 May 2019). ISSN: 24699888. DOI: 10.1103/PhysRevAccelBeams.22.053402.

[13] K. Baptiste et al. “A CW normal-conductive RF gun for free electron laser and energy recovery linac applications”. In: *Nuclear Instruments and Methods in Physics Research, Section A: Accelerators, Spectrometers, Detectors and Associated Equipment* 599 (1 Feb. 2009), pp. 9–14. ISSN: 01689002. DOI: 10.1016/j.nima.2008.10.021.

[14] E. Vogel et al. “High gradients at SRF photoinjector cavities with low RRR copper cathode plug screwed to the cavity back wall”. In: (Oct. 2023). URL: http://arxiv.org/abs/2310.02974.

[15] S Miller et al. *STATUS OF THE SLAC/MSU SRF GUN DEVELOPMENT PROJECT*. Tech. rep. 2023, pp. 0–7. DOI: 10.18429/JACoW-SRF2023-FRIBA07.

[16] T. Siggins et al. “Performance of a DC GaAs photocathode gun for the Jefferson lab FEL”. In: *Nuclear Instruments and Methods in Physics Research Section A: Accelerators, Spectrometers, Detectors and Associated Equipment* 475.1 (2001), pp. 549–553. ISSN: 0168-9002. DOI: https://doi.org/10.1016/S0168-9002(01)01596-0. URL: https://www.sciencedirect.com/science/article/pii/S0168900201015960.

[17] BD Muratori and YM Saveliev. “ALICE (ERLP) injector design”. In: *Proceedings of EPAC08*. 2008.

[18] Colwyn Gulliford et al. “Demonstration of low emittance in the Cornell energy recovery linac injector prototype”. In: *Phys. Rev. ST Accel. Beams* 16 (7 July 2013), p. 073401. DOI: 10.1103/PhysRevSTAB.16.073401. URL: https://link.aps.org/doi/10.1103/PhysRevSTAB.16.073401.

[19] OA Tanaka, Tsukasa Miyajima, Takanori Tanikawa, et al. “Present status of the injector at the compact ERL at KEK”. In: *Proceedings of IPAC2022*. 2022, pp. 2296–2298.

[20] BL Militsyn et al. “Design of an upgrade to the ALICE photocathode electron gun”. In: *EPAC08*. Genoa, Italy, 2008.

[21] K. Smolenski et al. “Design and performance of the Cornell ERL DC photoemission gun”. In: *AIP Conference Proceedings*. Vol. 1149. 1. American Institute of Physics. 2009, pp. 1077–1083.

[22] PA Adderley et al. “Load locked dc high voltage GaAs photogun with an inverted geometry ceramic insulator”. In: *Physical Review Special Topics–Accelerators and Beams* 13.1 (2010), p. 010101.

[23] Erdong Wang et al. “High voltage DC gun for high intensity polarized electron source”. In: *Phys. Rev. Accel. Beams* 25 (3 Mar. 2022), p. 033401. DOI: 10.1103/PhysRevAccelBeams.25.033401. URL: https://link.aps.org/doi/10.1103/PhysRevAccelBeams.25.033401.

[24] F. Sannibale et al. “Advanced photoinjector experiment photogun commissioning results”. In: *Phys. Rev. ST Accel. Beams* 15 (10 Oct. 2012), p. 103501. DOI: 10.1103/PhysRevSTAB.15.103501. URL: https://link.aps.org/doi/10.1103/PhysRevSTAB.15.103501.

[25] T. Luo et al. “RF design of APEX2 two cell continuous wave normal conducting photoelectron gun cavity based on multi objective genetic algorithm”. In: *Nuclear Instruments and Methods in Physics Research Section A: Accelerators, Spectrometers, Detectors and Associated Equipment* 940 (2019), pp. 12–18. ISSN: 0168 9002. DOI: https://doi.org/10.1016/j.nima.2019.05.079. URL: https://www.sciencedirect.com/science/article/pii/S0168900219307430.

[26] Han Chen et al. “Beam dynamics optimization of very high frequency gun photoinjector”. In: *Nuclear Science and Techniques* 33 (Sept. 2022), p. 116. DOI: 10.1007/s41365022011105y.

[27] Fernando Sannibale et al. “APEX Phase II Commissioning Results at the Lawrence Berkeley National Laboratory”. In: *7th International Particle Accelerator Conference*. 2016, TUOCA02. DOI: 10.18429/JACoWIPAC2016TUOCA02.

[28] Zihao Ding et al. “Temperature dependent quantum efficiency degradation of K_2CsSb bialkali antimonide photocathodes grown by a triple element codeposition method”. In: *Phys. Rev. Accel. Beams* 20 (11 Nov. 2017), p. 113401. DOI: 10.1103/PhysRevAccelBeams.20.113401. URL: https://link.aps.org/doi/10.1103/PhysRevAccelBeams.20.113401.

[29] Fernando Sannibale et al. “Status, Plans and Recent Results from the APEX Project at LBNL”. In: *37th International Free Electron Laser Conference*. 2015, MOP024. DOI: 10.18429/JACoWFEL2015MOP024.

[30] Liling Xiao et al. “Spare Gun Multi Physics Analysis for LCLS II”. In: *12th International Particle Accelerator Conference*. Aug. 2021. DOI: 10.18429/JACoWIPAC2021TUPAB127.

[31] X. H. Wang et al. “Experimental demonstration of dark current mitigation by an over inserted plug in a normal conducting VHF gun”. In: *Physical Review Accelerators and Beams* 28 (4 Nov. 2024), p. 043401. ISSN: 24699888. DOI: 10.1103/PhysRevAccelBeams.28.043401. URL: http://arxiv.org/abs/2411.01754.

[32] G. Shu et al. “Dark current studies of an L band normal conducting RF gun”. In: *Nuclear Instruments and Methods in Physics Research Section A: Accelerators, Spectrometers, Detectors and Associated Equipment* 1010 (2021), p. 165546. ISSN: 01689002. DOI: https://doi.org/10.1016/j.nima.2021.165546. URL: https://www.sciencedirect.com/science/article/pii/S0168900221005313.

[33] F. Zhou. “Private communication”. 2025.

[34] E. Vogel et al. “Surface treatment experience of the all superconducting gun cavities”. In: *JACoW* IPAC2023 (2023). DOI: 10.18429/JACOWIPAC2023WEPA145.

[35] Rong Xiang and Jana Schaber. “Review of Recent Progress on Advanced Photocathodes for Superconducting RF Guns”. In: *Micromachines* 13 (8 Aug. 2022), p. 1241. ISSN: 2072 666X. DOI: 10.3390/MI13081241. URL: https://www.mdpi.com/2072-666X/13/8/1241/htm%20https://www.mdpi.com/2072-666X/13/8/1241.

[36] M. Helm et al. “The ELBE infrared and THz facility at Helmholtz Zentrum Dresden Rossendorf”. In: *European Physical Journal Plus* 138 (2 Feb. 2023). ISSN: 21905444. DOI: 10.1140/EPJP/S13360023037202.

[37] T. Konomi et al. “Development of SRF gun applying new cathode idea using a transparent superconducting layer”. In: *Proceedings of ERL 2017, the 59th ICFA Advanced Beam Dynamics Workshop on Energy Recovery Linacs* (Apr. 2018), pp. 1–3. DOI: 10.18429/JACOWERL2017MOIACC002.

[38] A. Neumann et al. “Update on SRF cavity design, production and testing for bERLinPro – Cavity types for bERLinPro”. In: *Proceedings of SRF2015*. Whistler, BC, Canada, 2015. ISBN: 9783954501786.

[39] D. Bazyl. “Development of CW SRF L-band photoinjector for future High Duty Cycle EuXFEL”. In: *UK AI Seminar*. Talk. Daresbury, 2024. URL: https://indico.cern.ch/event/1410360/sessions/555197/attachments/2905672/5098739/Bazyl%202024%20Development%20of%20CW%20SRF%20L-Band%20Photoinjectorss%20for%20Future%20XFELs.pdf.

[40] J. Teichert et al. “Successful user operation of a superconducting radio frequency photoelectron gun with Mg cathodes”. In: *Physical Review Accelerators and Beams* 24 (2021). DOI: 10.1103/PhysRevAccelBeams.24.033401.

[41] R. Xiang. “Operation of Cs_2Te in SRF gun for ELBE”. In: *EWPAA2022*. Talk. Milano, 2022. URL: https://agenda.infn.it/event/29956/contributions/177005/attachments/96738/133309/Xiang_Operation%20of%20Cs2Te%20in%20SRF%20gun%20for%20ELBE.pdf.

[42] T. Konomi. “First high gradient test of KEK SRF gun cavity in horizontal test cryostat”. In: *IHEP KEK meeting 2020*. Talk. Tsukuba, 2020. URL: https://conference-indico.kek.jp/event/130/contributions/2528/attachments/1669/1836/20201206_1st_high_gradient_test_of_KEK_SRF_gun.pdf.

[43] T. Konomi et al. “Horizontal test results of 1.3 GHz superconducting RF gun #2 at KEK”. In: *Proceedings of SRF2023* (2023), pp. 540–544. DOI: 10.18429/JACoWSRF2023TUPTB049.

[44] T. Konomi et al. “Development of High Intensity, High Brightness, CW SRF Gun with Bi Alkali Photocathode”. In: *SRF* (Aug. 2019), pp. 1219–1222. DOI: 10.18429/JACOWSRF2019FRCAB4.

[45] E. Ergenlik. “Overview, status and applications of SEALab (bERLinPro)”. In: *Ankara University Seminar*. Talk. Ankara, 2024. URL: https://hte.ankara.edu.tr/wp-content/uploads/sites/151/2024/06/THE-27-06-24.pdf.

[46] SEALab. *Accelerator Physics: First electron beam in SEALab*. 2025. URL: https://www.helmholtz-berlin.de/pubbin/news_seite?nid=29826&sprache=en&seitenid=1.

[47] Erion Gjonaj and Dmitry Bazyl. “Beam dynamics study of a CW L-band SRF gun for the high duty cycle EuXFEL”. In: *JACoW* IPAC2023 (2023). DOI: 10.18429/JACOWIPAC2023WEPA054.

[48] Igor Pinayev et al. “Performance of CeC PoP Accelerator”. In: *Proc. 10th International Particle Accelerator Conference (IPAC'19), Melbourne, Australia, 19-24 May 2019* (10 June 2019), pp. 559–561. DOI: 10.18429/JACOW-IPAC2019-MOPMP050. URL: http://jacow.org/ipac2019/papers/mopgw128.pdf.

[49] I. Petrushina et al. “High-Brightness Continuous-Wave Electron Beams from Superconducting Radio-Frequency Photoemission Gun”. In: *Physical Review Letters* 124 (24 June 2020). ISSN: 10797114. DOI: 10.1103/PhysRevLett.124.244801.

[50] V. Litvinenko and N. Bachhawat. “CW SRF gun generating beam parameters sufficient for CW hard-X-ray FEL”. English. In: *Proc. 16th International Particle Accelerator Conference* (Taipei, Taiwan). IPAC'25 - 16th International Particle Accelerator Conference 16. JACoW Publishing, Geneva, Switzerland, June 2025, pp. 147–149. ISBN: 978-3-95450-248-6. DOI: 10.18429/JACoW-IPAC25-MOPB041. URL: https://indico.jacow.org/event/81/contributions/7477.

[51] Fuhao Ji et al. “Beam dynamics studies on a low emittance injector for LCLS II HE”. In: 619 (2022).

[52] S. Kim et al. “Design of a 185.7 MHz superconducting RF photo injector quarter wave resonator for the LCLS II HE low emittance injector”. In: 245 (2022).

[53] Kui Zhao et al. *Research on DC RF superconducting photocathode injector for high average power FELs*. Tech. rep. 2001, pp. 564–568.

[54] Rong Xiang et al. “Experimental investigations of DC SC photoinjector at Peking University”. In: *Nuclear Instruments and Methods in Physics Research, Section A: Accelerators, Spectrometers, Detectors and Associated Equipment*. Vol. 528. Aug. 2004, pp. 321–325. DOI: 10.1016/j.nima.2004.04.079.

[55] Jiankui Hao et al. “Primary beam loading tests on DC SC photoinjector at Peking University”. In: *Nuclear Instruments and Methods in Physics Research, Section A: Accelerators, Spectrometers, Detectors and Associated Equipment* 557 (1 Feb. 2006), pp. 138–141. ISSN: 01689002. DOI: 10.1016/j.nima.2005.10.063.

[56] Nan Shun Huang et al. “The MING proposal at SHINE: megahertz cavity enhanced X-ray generation”. In: *Nuclear Science and Techniques* 34 (1 2023). ISSN: 22103147. DOI: 10.1007/s41365-022-01151-6.

[57] R. Akre et al. “Commissioning the Linac Coherent Light Source injector”. In: *Physical Review Special Topics - Accelerators and Beams* 11 (3 Mar. 2008). ISSN: 10984402. DOI: 10.1103/PhysRevSTAB.11.030703.

[58] T. Schietinger et al. *Commissioning experience and beam physics measurements at the SwissFEL Injector Test Facility*. Oct. 2016. DOI: 10.1103/PhysRevAccelBeams.19.100702. URL: https://link.aps.org/doi/10.1103/PhysRevAccelBeams.19.100702.

[59] J Hong et al. *DEVELOPMENT OF PHOTOCATHODE RF-GUN AT PAL*. ISBN: 9783954501267.

[60] Y. Du. "R&D of Very High Frequency (VHF) gun for SHINE project at Tsinghua University". In: *Photocathode Physics for Photoinjectors (P3) Workshop*. BNL. NY, USA, 2023. URL: https://indico.bnl.gov/event/19730/contributions/81330/attachments/50121/85758/R%26D%20of%20Very%20High%20Frequency%20%28VHF%29%20gun%20for%20SHINE%20project%20at%20Tsinghua%20University.pptx.

[61] M. Martinez Calderon et al. "Fabrication and rejuvenation of high quantum efficiency caesium telluride photocathodes for high brightness and high average current photoinjectors". In: *Physical Review Accelerators and Beams* 27 (2 Feb. 2024). ISSN: 24699888. DOI: 10.1103/PhysRevAccelBeams.27.023401.

[62] S. Schreiber et al. "Update on the lifetime of Cs_2Te cathodes opertaed at the FLASH facility". In: *38th International Free Electron Laser Conference*. 2017, WEP003. DOI: 10.18429/JACoW-FEL2017-WEP003.

[63] P. Pavel Juarez-Lopez et al. "Photocathodes update at FLASH and the European XFEL". In: *4th European Workshop on Photocathodes for Accelerator Applications*. 2022. URL: https://agenda.infn.it/event/29956/contributions/178578/attachments/96783/133418/EWPAA'22_PJuarezV2.pdf.

[64] Jonas Dube et al. "Triple Evaporation of Bialkali Antimonide Photocathodes and Photoemission Characterization at the PhoTEx Experiment". In: *submitted* (Mar. 2025). URL: http://arxiv.org/abs/2503.03573.

[65] C.A. Pennington et al. "Ultra thin Cs_3Sb photocathodes with anomolously high quantum efficiency". In: *14th International Particle Accelerator Conference*. 2023, TUPA132. DOI: 10.18429/JACoW-IPAC2023-TUPA132.

[66] Dmitry Bazyl et al. *CW Operation of the European XFEL: SC Gun Injector Optimization, S2E Calculations and SASE Performance*. arXiv: 2111.01756.

[67] C. Benjamin et al. "Photocathode performance characterisation of ultra thin MgO films on polycrystalline copper". In: *Journal of Physics: Conference Series* 2420 (1 2023). ISSN: 17426596. DOI: 10.1088/17426596/2420/1/012032.

[68] E. Isik et al. "Titanium nitride thin films grown by ion beam physical vapor deposition". In: *APL Materials (submitted)* (2025).

[69] Clara J. Saraceno et al. "The amazing progress of high-power ultrafast thin-disk lasers". In: *Journal of the European Optical Society* 15.1 (Dec. 2019), pp. 1–7. ISSN: 19902573. DOI: 10.1186/S41476-019-0108-1/FIGURES/3. URL: https://jeos.springeropen.com/articles/10.1186/s41476-019-0108-1.

[70] *Scientific lasers — TRUMPF*. URL: https://www.trumpf.com/en_GB/products/lasers/scientific-lasers/.

[71] *LIGHT CONVERSION*. URL: https://lightcon.com/.

[72] Sasha Gilevich et al. "The LCLS-II Photo-Injector Drive Laser System". In: *Conference on Lasers and Electro-Optics*. Optica Publishing Group, 2020, SW3E.3. DOI: 10.1364/CLEO{_}SI.2020.SW3E.3. URL: https://opg.optica.org/abstract.cfm?URI=CLEO_SI-2020-SW3E.3.

[73] Zhi Zhao et al. "High-power fiber laser system for the SHINE photo-injector". In: *https://doi.org/10.1117/12.2687142* 12760 (Nov. 2023), pp. 43–45. ISSN: 1996756X. DOI: 10.1117/12.2687142. URL: https://www.spiedigitallibrary.org/conference-proceedings-of-spie/12760/127600B/High-power-fiber-laser-system-for-the-SHINE-photo-injector/10.1117/12.2687142.full%20https://www.spiedigitallibrary.org/conference-proceedings-of-spie/12760/127600B/High-power-fiber-laser-system-for-the-SHINE-photo-injector/10.1117/12.2687142.short.

[74] G. Penco et al. "Experimental demonstration of electron longitudinal-phase-space linearization by shaping the photoinjector laser pulse". In: *Physical Review Letters* 112.4 (Jan. 2014). ISSN: 00319007. DOI: 10.1103/PhysRevLett.112.044801.

[75] Yuelin Li and John W. Lewellen. "Generating a quasiellipsoidal electron beam by 3D laser-pulse shaping". In: *Physical Review Letters* 100.7 (Feb. 2008), p. 074801. ISSN: 00319007. DOI: 10.1103/PHYSREVLETT.100.074801/FIGURES/4/MEDIUM. URL: https://journals.aps.org/prl/abstract/10.1103/PhysRevLett.100.074801.

[76] E. I. Gacheva et al. "Shaping of cylindrical and 3D ellipsoidal beams for electron photoinjector laser drivers". In: *Applied Optics, Vol. 55, Issue 7, pp. 1630-1635* 55.7 (Mar. 2016), pp. 1630–1635. ISSN: 2155-3165. DOI: 10.1364/AO.55.001630. URL: https://opg.optica.org/viewmedia.cfm?uri=ao-55-7-1630&seq=0&html=true%20https://opg.optica.org/abstract.cfm?uri=ao-55-7-1630%20https://opg.optica.org/ao/abstract.cfm?uri=ao-55-7-1630.

[77] M Khojoyan et al. "BEAM DYNAMICS OPTIMIZATION FOR THE HIGH BRIGHTNESS PITZ PHOTO INJECTOR USING 3D ELLIPSOIDAL CATHODE LASER PULSES*". In: *FEL 2013*. New York, 2013, pp. 298–302. ISBN: 9783954501267.

[78] S. Yu Mironov et al. "Generation of 3D ellipsoidal laser beams by means of a profiled volume chirped Bragg grating". In: *Laser Physics Letters* 13.5 (Apr. 2016), p. 055003. ISSN: 1612-202X. DOI: 10.1088/1612-2011/13/5/055003. URL: https://iopscience.iop.org/article/10.1088/1612-2011/13/5/055003%20https://iopscience.iop.org/article/10.1088/1612-2011/13/5/055003/meta.

[79] Ingo Will et al. "Generation of flat-top picosecond pulses by coherent pulse stacking in a multicrystal birefringent filter". In: *Optics Express, Vol. 16, Issue 19, pp. 14922-14937* 16.19 (Sept. 2008), pp. 14922–14937. ISSN: 1094-4087. DOI: 10.1364/OE.16.014922. URL: https://opg.optica.org/viewmedia.cfm?uri=oe-16-19-14922&seq=0&html=true%20https://opg.optica.org/abstract.cfm?uri=oe-16-19-14922%20https://opg.optica.org/oe/abstract.cfm?uri=oe-16-19-14922.

[80] Baichao Zhang et al. "High repetition-rate photoinjector laser system for S 3 FEL". In: (2023). DOI: 10.3389/fphy.2023.1181862.

[81] S Bettoni et al. "Impact of laser stacking and photocathode materials on microbunching stability in photoinjectors". In: (). DOI: 10.1103/PhysRevAccelBeams.23.024401.

[82] Randy Lemons et al. "Temporal shaping of narrow-band picosecond pulses via noncolinear sum-frequency mixing of dispersion-controlled pulses". In: *Physical Review Accelerators and Beams* 25.1 (Jan. 2022), p. 013401. ISSN: 24699888. DOI: 10.1103/PHYSREVACCELBEAMS.25.013401/NON{_}COLINEAR{_}SFG{_}FOR{_}NARROWBAND{_}PULSES{_}FOR{_}PRAB{_}SUPP.PDF. URL: https://journals.aps.org/prab/abstract/10.1103/PhysRevAccelBeams.25.013401.

[83] C. Sauteret et al. “Efficient generation of narrow-bandwidth picosecond pulses by frequency doubling of femtosecond chirped pulses”. In: *Optics Letters, Vol. 23, Issue 14, pp. 1117-1119* 23.14 (July 1998), pp. 1117–1119. ISSN: 1539-4794. DOI: 10.1364/OL.23.001117. URL: https://opg.optica.org/viewmedia.cfm?uri=ol-23-14-1117&seq=0&html=true%20https://opg.optica.org/abstract.cfm?uri=ol-23-14-1117%20https://opg.optica.org/ol/abstract.cfm?uri=ol-23-14-1117.

[84] N Neveu and Y Ding. *LCLS-II Standard Configuration with a Gaussian-Profile Injector Laser*. Tech. rep.

[85] Andreas Adelmann et al. *OPAL a Versatile Tool for Charged Particle Accelerator Simulations*. 2019. arXiv: 1905.06654 [physics.acc-ph]. URL: https://arxiv.org/abs/1905.06654.

[86] K. Flöttmann. *Note on the Thermal Emittance of Electrons Emitted by Cesium Telluride Photocathodes*. Tech. rep. DESY TESLA FEL 97-01. Hamburg, Germany: DESY, 1997.

[87] Prasanta Chandra Mahalanobis. “On the generalized distance in statistics”. In: *Sankhyā: The Indian Journal of Statistics, Series A (2008-)* 80 (2018), S1–S7.

[88] C. Davut et al. “Balance of bunch compression and emittance preservation for high-brightness x-ray free electron laser injectors”. In: *Phys. Rev. Accel. Beams* (Aug. 2025), pp. –. DOI: 10.1103/rjns-vqzt. URL: https://link.aps.org/doi/10.1103/rjns-vqzt.

[89] L. Serafini and M. Ferrario. “Velocity bunching in photoinjectors”. In: *AIP Conference Proceedings* 581.1 (Aug. 2001), pp. 87–106. ISSN: 0094-243X. DOI: 10.1063/1.1401564. eprint: https://pubs.aip.org/aip/acp/article-pdf/581/1/87/11957703/87_1_online.pdf. URL: https://doi.org/10.1063/1.1401564.

[90] James Rosenzweig and Eric Colby. “Charge and wavelength scaling of RF photoinjector designs”. In: *AIP Conference Proceedings*. Vol. 335. 1. American Institute of Physics. 1995, pp. 724–737.

[91] J. Sekutowicz et al. *Cathodes and Shape Modification of Cavity for DESY Superconducting Photoinjector*. 2025. arXiv: 2507.01658 [physics.acc-ph]. URL: https://arxiv.org/abs/2507.01658.

[92] K. Floettmann. *A Space Charge Tracking Algorithm*. URL: https://www.desy.de/~mpyflo/.

[93] X W Wu et al. “Development of 3.9 GHz 9-Cell Cavities at SHINE”. In: *Proc. 21th Int. Conf. RF Supercond. (SRF'23)*. International Conference on RF Superconductivity 21. JACoW Publishing, Geneva, Switzerland, June 2023, pp. 921–924. ISBN: 978-3-95450-234-9. DOI: 10.18429/JACoW-SRF2023-THIAA01. URL: https://jacow.org/srf2023/papers/thiaa01.pdf.

[94] Tony Beukers, Minh Nguyen, and Tao Tang. “Discrete element transmission line beam spreader kickers for LCLS II”. In: *2018 IEEE International Power Modulator and High Voltage Conference (IPMHVC)*. IEEE. 2018, pp. 151–155.

[95] Yong Fang Liu et al. “Development of a high repetition rate lumped inductance kicker magnet prototype for the beam switchyard of SHINE”. In: *Nuclear Science and Techniques* 35.2 (2024), p. 37.

[96] B. I. Grishanov et al. “Very fast kicker with high repetition rate for accelerator applications”. In: *Nuclear Instruments and Methods in Physics Research Section A: Accelerators, Spectrometers, Detectors and Associated Equipment* 396.1 (1997), pp. 28–34. ISSN: 0168-9002. DOI: https://doi.org/10.1016/S0168-9002(97)00739-0. URL: https://www.sciencedirect.com/science/article/pii/S0168900297007390.

[97] R. Calaga et al. “First demonstration of the use of crab cavities on hadron beams”. In: *Phys. Rev. Accel. Beams* 24 (6 June 2021), p. 062001. DOI: 10.1103/PhysRevAccelBeams.24.062001. URL: https://link.aps.org/doi/10.1103/PhysRevAccelBeams.24.062001.

[98] Ming Xie. “Design optimization for an X-ray free electron laser driven by SLAC linac”. In: *Proceedings of the IEEE Particle Accelerator Conference* 1 (1995), pp. 183–185. DOI: 10.1109/PAC.1995.504603.

[99] A Oppelt et al. “Status and first results from the upgraded PITZ facility”. In: *27th International Conference on Free Electron Lasers, FEL2005*. eConf C0508213: THPP043, 2005. Joint Accelerator Conferences Website. 2005, pp. 564–567.

[100] Qiang Gu. “Injector for SHINE”. In: *PITZ Collaboration Meeting December 2018*. Zeuthen, Germany, Dec. 2018. DOI: 10.3204/PUBDB-2018-05592. URL: https://bib-pubdb1.desy.de/record/417400.

[101] JH Han et al. “Beam operation of the PAL XFEL injector test facility”. In: *Proc. of FEL*. 2014.

[102] Tsumoru Shintake et al. “Stable operation of a self amplified spontaneous emission free electron laser in the extremely ultraviolet region”. In: *Phys. Rev. ST Accel. Beams* 12 (7 July 2009), p. 070701. DOI: 10.1103/PhysRevSTAB.12.070701. URL: https://link.aps.org/doi/10.1103/PhysRevSTAB.12.070701.

[103] Siegfried Schreiber and Bart Faatz. “The free electron laser FLASH”. In: *High Power Laser Science and Engineering* 3 (2015), e20. DOI: 10.1017/hpl.2015.16.

[104] Y. Otake. “Relocation and Improvement Status of the SCSS Test Accelerator to Provide Dual FEL Drivers at SACLA”. In: *Proc. 6th International Particle Accelerator Conference (IPAC'15), Richmond, VA, USA, May 3-8, 2015* (Richmond, VA, USA). International Particle Accelerator Conference 6. https://doi.org/10.18429/JACoW-IPAC2015-TUPJE008. Geneva, Switzerland: JACoW, June 2015, pp. 1626–1628. ISBN: 978-3-95450-168-7. DOI: https://doi.org/10.18429/JACoW-IPAC2015-TUPJE008. URL: http://jacow.org/ipac2015/papers/tupje008.pdf.

5 High energy beam

5.1 Summary

The High Energy Beamline (HEB) accelerates bunches at 1 MHz repetition rate from the LEB to 8 GeV; a subset of bunches at $\leq$ 200 Hz rep. rate are then further accelerated to 12 GeV. The 8 GeV bunches are then distributed to up to 10 parallel FELs via a beam spreader, such that each FEL operates at 100 kHz simultaneously. The 12 GeV bunches are directed to one of two available transports each leading to an MEC user station, shown in Figure 4.15. This allows experimental preparation in one whilst the other in in operation. In order to enable parallel operation with high efficiency (Section 2.2), the HEB is designed such that the beam energy prior to the spreader is constant and independent of FEL optimisation.

Acceleration of regularly spaced, high repetition rate pulses of up to $\sim$ 1 MHz up to 8 GeV requires a superconducting RF linac. The linac is a significant fraction of the total facility cost, herewith in Section 5.3.1 we describe the optimisation of its parameters in order to establish an accurate estimate of capital and recurrent costs and their dependencies.

The acceleration of a $\leq$ 200 Hz subset of bunches to 12 GeV requires an additional booster linac. The baseline technology of a high-gradient normal conducting linac for this is described together with reasoning for parameter selection in Section 5.3.6. Additional space is reserved to extend this section to reach 15 GeV, to accommodate upgrade paths and different scenarios for beam quality. An alternative plasma-based scheme is later expounded in Section 5.6.

Optimisation of the longitudinal phase space of the various bunches requires flexibility in the compression during acceleration. This is because each FEL operates over a different photon energy range, and with differing FEL schemes depending on the pulse properties required. In Section 5.4.3 we describe a scheme to achieve this compression flexibility within the confines of simultaneous operation of the FELs.

The layout and bunch transport properties of the 8 GeV beam spreader are described in Section 5.5. The key aim is to achieve simultaneous operation of the FELs without significant degradation of electron bunch brightness.

Integration of a plasma wakefield acceleration (PWFA) based energy and brightness booster stage is explored with start-to-end simulations in Section 5.6.

Operational experience at existing XFEL facilities has shown that care must be taken to minimise and mitigate against beam losses and dark current. This is to preserve component and facility lifetime and availability. We therefore describe options for beam collimation in Section 5.8.

5.2 Introduction, scope and assumptions

In this chapter we outline:

DRAFT

- Selection of an optimised bunch compression scheme capable of providing the required peak current without significant emittance degradation.
- Identification of optimised superconducting RF linac parameters for 8 GeV / 1 MHz operation. Consideration of potential linac upgrades for future-proofing.
- Conceptual design of the HEB, including main linac, bunch compressor and bunch spreader.
- A review of booster technologies compatible with achieving 12 GeV electron beam energy with the required beam brightness, including normal conducting RF and plasma based options.
- Consideration of collimation requirements such that facility lifetime and uptime is maximised.

Diagnostic sections allowing for 6D characterisation of bunch phase space will be allocated space at auspicious points along the high energy beamline. This will include at the injector exit, after each bunch compressor stage, prior to distribution to the FEL lines, and within at least one FEL line. These sections will be defined at a technical design project phase.

5.3 Radio Frequency Linac

The radio frequency (RF) linac consists of two main parts.

The first is the superconducting RF (SRF) linac. This is required to accelerate interleaved electron bunches of typically 150 pC at 500 kHz, and 75 pC at 250 kHz although flexibility will be required. This will be subject to a maximum bunch repetition rate of 1 MHz. The differently charged bunches will originate respectively from two separate injectors as described in Chapter 4. The SRF linac will accelerate these from $\sim$ 150 MeV up to 8 GeV for injection into up to ten free electron lasers (FELs). This SRF linac is made of 3 sections; a low frequency region up to 150 MeV for progressively compressing and linearising long bunches generated in the injectors and accelerating them from the space-charge to emittance dominated regime (described in Chapter 4); a higher-harmonic section to linearise most of the bunches longitudinal phase space, and the main linac at twice the frequency of the initial low frequency section, required for the full acceleration of the beam.

The second linac is normal conducting RF (NCRF). This is designed to accelerate a small subset of bunches, typically single bunches at $\leq$ 200 Hz repetition rate (although short trains are considered), a further 4 GeV to reach 12 GeV final energy to feed two FELs for MEC. In order to accommodate potential upgrade paths and different scenarios for beam quality, space in the layout is reserved to extend the NCRF linac to reach 15 GeV.

Using the criteria above and assuming a combined electron bunches of 200 pC at 1 MHz, to provide some headroom, the proposed RF solutions for the linacs are described below and have been derived from an assessment of the capital and 50 year operational costs, assessing the optimum RF frequencies, cryogenic operating temperature and accelerating gradient along with a review of the available technology in terms of availability, performance and reliability, whilst also assessing potential future developments.

5.3.1 SRF Linac: Choice of Technology and Operating Parameters

Due to the requirement of 1 MHz repetition rate evenly spaced pulses, the automatic choice of technology for the main accelerator is a SRF linac operating in continuous wave (CW). The limitation of normal conducting technology is average power due to the significant resistive heating at high duty cycles. For SRF cavities the extremely low surface resistance when operating at cryogenic temperatures around 2 K means that higher RF powers can be applied with low power dissipation. This enables higher accelerating gradients. Overall, even considering the need for cryogenic cooling and the cost of continually running the cryogenic plant, SRF cavities consume less power in CW operation in comparison to normal conducting cavities, due again to the extremely low surface resistance. This is several nΩ for bulk niobium superconducting cavities compared to several mΩ for bulk copper normal-conducting cavities.

Cavity efficiency can be measured by the quality factor,

$$Q_0 = \frac{W}{P_{loss}}, \tag{5.1}$$

where W is the maximum stored energy and P_{loss} is the RF power loss per cycle. For SRF cavities typically Q_0 of 10^{10} at 2K have been readily achieved, whereas for NCRF cavities this reduces to around $10^4 - 10^5$, which means that the RF power requirements for equivalent accelerating gradients is a factor of around 6 higher for copper cavities. Thus, a significant advantage can be achieved in terms of capital costs for both the length of the linac section and RF power source requirements. While the inclusion of cryogenic cooling systems for SRF cavities introduces additional complexity and increases both capital and operational costs, the overall power consumption for CW operation remains significantly lower than that of normal conducting cavities (by a factor of 200), even when accounting for the energy required to run the cryogenic plant.

5.3.1.1 Frequency Assessment

Superconducting cavities typically range from 400 MHz up to 1.5 GHz and there are numerous factors that influence this frequency choice.

For SRF cavities RF losses are dominated by the BCS surface resistance, which scales as f^2 meaning that higher quality factors can be achieved at low frequencies for the same operating temperature resulting in lower RF power being required to achieve the same accelerating gradient, consequently the cryogenic load increases quadratically with frequency. However, the shunt impedance (R/Q), a measure of efficiency, increases with frequency and at higher frequencies it is possible to obtain larger surface electric fields, meaning that higher accelerating gradients can be achieved, reducing the linac length required to achieve the final beam energy. At low frequencies the cavity size is larger which means that there are lower higher order mode (HOM) power levels, and less emittance growth due to longitudinal and transverse wakefields implying better beam stability. Additionally, the input power couplers are easier to design and have better power handling capabilities. Conversely, for higher frequencies the cavity size is smaller, meaning lower manufacturing costs, and the lower RF power requirements for equivalent external Q, Q_{ext} mean lower operational costs. Over the last decade there have been significant advances in surface treatment processes which has improved Q_0 over and above those achieved using standard buffer chemical polishing (BCP) and electro-polishing (EP). Research into nitrogen doping, nitrogen diffusion, low-T baking, mid-T baking, and 2-step baking has led to a factor of 3 improvement

typically being achieved, as demonstrated by the use of nitrogen doping for 1.3 GHz cavities on LCLS-II and SHINE where the targeted Q_0 of 2.7×10^{10} has been achieved [1, 2].

Thus, the choice of RF frequency for a superconducting accelerator to drive an XFEL is a compromise between all these various factors. To optimise for UK XFEL, an assessment has been performed considering 800 MHz, 1.3 GHz and 1.5 GHz options which concluded that lower capital and operating costs could be gained from higher frequency options. Furthermore, since the technology readiness, in terms of cavities, cryomodules and RF sources is well established for 1.3 GHz, this has been adopted as the preferred choice of frequency for the main SRF linac. This will enable UK XFEL to take advantage of more than 3 decades of proven technology development that has occurred on the TESLA-shape cavity which has already been the cavity of choice for TTF $\rightarrow$ FLASH, EuXFEL, LCLS-II, and SHINE.

5.3.1.2 Operating Gradient

CW operation means that the cost of operating the cryogenic plant to cool the SRF cavities is significant. Cryogenic power per unit length scales as the square of the accelerating gradient therefore a low accelerating gradient per cavity is favoured. At low gradients there is better reliability for the manufacture of cavities, with less likelihood of field emission. However, lower gradients increase the number of cavities required, increasing the length of the linac, and therefore the capital cost of the facility.

The nominal accelerating gradient for LCLS-II and SHINE is 16 MV/m with a Q_0 of 2.7×10^{10}. However for LCLS-II-HE, which incorporates improved cavity processing, the nominal gradient has been increased to 20.8 MV/m with a Q_0 of 2.5×10^{10} [3]. Here for vertical tests an improvement of gradient has been reported from 22.0 ± 3.9 MV/m to 27.2 ± 3.5 MV/m due to tighter quality assurance (QA) control of the processes and the introduction of an additional EP process (including a final cold EP) and a modification of the nitrogen doping process. Due to the number of cavities involved (> 400) the challenge for manufacturing is to have a high production yield that meet the desired specifications. The fabrication and processing within industry of SRF 1.3 GHz cavities for the European XFEL [4] has shown that gradients of $\geq$ 23.6 MV/m (nominal RF pulse width of 1.38 mS at a nominal repetition rate of 10 Hz) with a Q_0 of $\geq 1 \times 10^{10}$ can be achieved for the manufacture of over 800 cavities, demonstrating that high performance through knowledge transfer to industry of the required processing techniques is fundamentally feasible. There have been numerous studies aiming at achieving even higher gradients of 31.5 MV/m at a Q_0 of 1×10^{10} which is required as the baseline of the ILC [5, 6] which is aiming to achieve a production yield of $\geq$ 90%, using EP as the primary processing recipe.

The RF power required to maintain a constant accelerating gradient in a SRF cavity is defined as [7, 8]

$$P_{rf} = \frac{(\beta + 1)L}{4\beta Q_L (r/Q)} \left\{ (E_{acc} + I_b Q_L (r/Q) \cos\theta_b)^2 + \left(2Q_L \frac{\delta f}{f_0} E_{acc} + I_b Q_L (r/Q) \sin\theta_b \right)^2 \right\} \qquad (5.2)$$

where E_{acc} is the accelerating gradient, I_b is the average beam current, (r/Q) is the geometric shunt impedance per unit length (Ω/m), θ_b is the accelerating phase of the beam, f_0 is the operating frequency, δf is the difference between the cavity frequency and the operating frequency, Q_L is the loaded quality factor of the cavity, β is the cavity coupling factor with no beam loading, and L is the length of the cavity (m). In a strongly over-coupled situation where Q_L is much greater

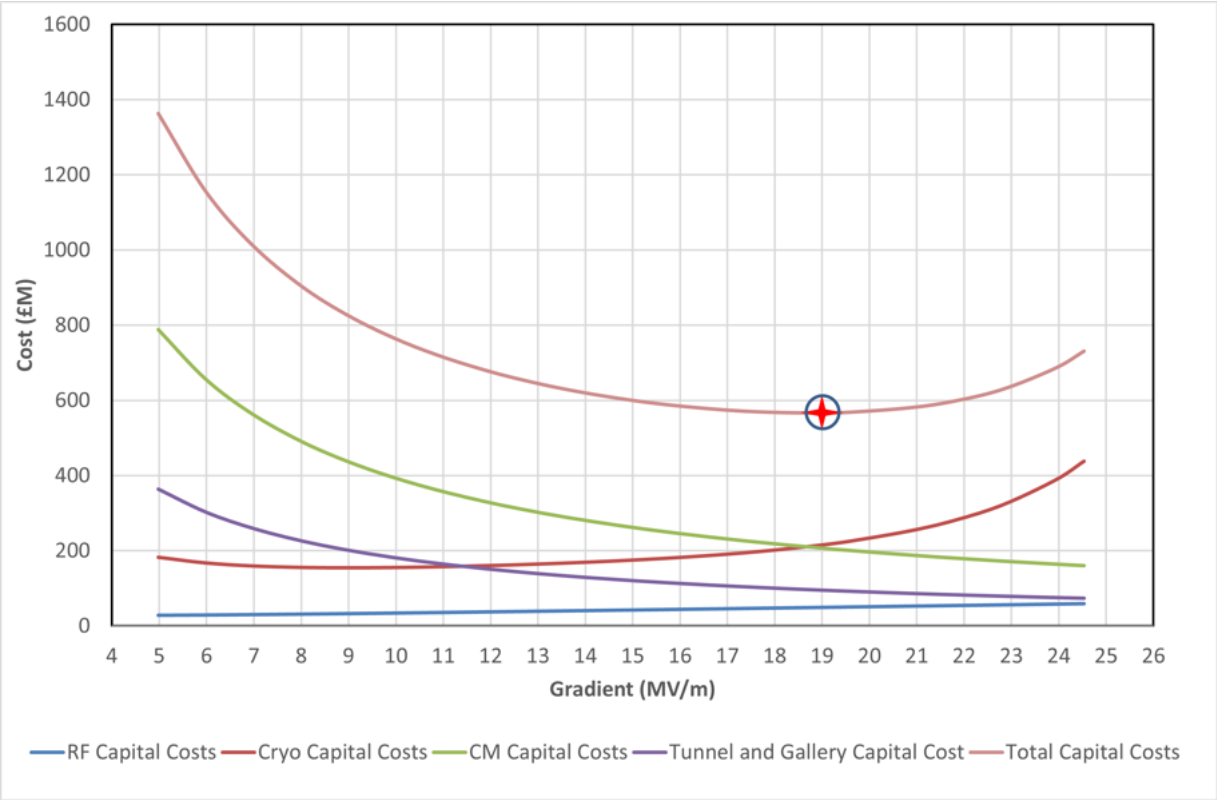

Figure 5.1: Capital costs for the main SRF linac section.

than Q_0 of the cavity then $\beta \gg 1$ ($Q_L \approx Q_{ext}$) and, assuming that the beam is accelerated on the crest of the RF signal, Equation 5.2 simplifies to

$$P_{rf} = \frac{L}{4Q_L(r/Q)} \left\{ (E_{acc} + I_b Q_L (r/q))^2 + \left(2Q_L \frac{\delta f}{f_0} E_{acc} \right)^2 \right\}. \tag{5.3}$$

Assessing these factors and using a cost model to assess optimal gradient with respect to the capital build costs results in 19.0 MV/m being the optimum gradient (Figure 5.1), though when factoring in operational costs for the RF and cryogenic systems the optimised gradient reduces to 17.6, 15.4 and 14.3 MV/m for 20, 40 and 50 years of operation, respectively. This is due to the electrical costs for operation of the cryogenic plant becoming the dominant contributor to overall costs. However, there are large error margins on the projected cost of electricity, particularly with the expected UK move towards carbon net zero.

5.3.1.3 Microphonics

The primary sources of microphonics stem from mechanical vibrations and pressure fluctuations in the cryogenic system. It is necessary to consider the level of microphonics and the consequent effects of detuning of the cavities as this impacts the RF power required to maintain gradient, which needs to be fully understood when defining amplifier requirements. However, it is generally the case that the true source terms are not fully known until the cryomodule design is complete and the accelerator is fully integrated and operational. Reviewing similar facilities, microphonic levels of typically better than 10 Hz have been achieved [9, 10]. Assessing a microphonics level of 10 Hz (Figure 5.2) the RF power per cavity required for a gradient of 19 MV/m is 2.8 kW, which with beam loading effects equates to an RF power requirement of 5.3 kW. However, considering the

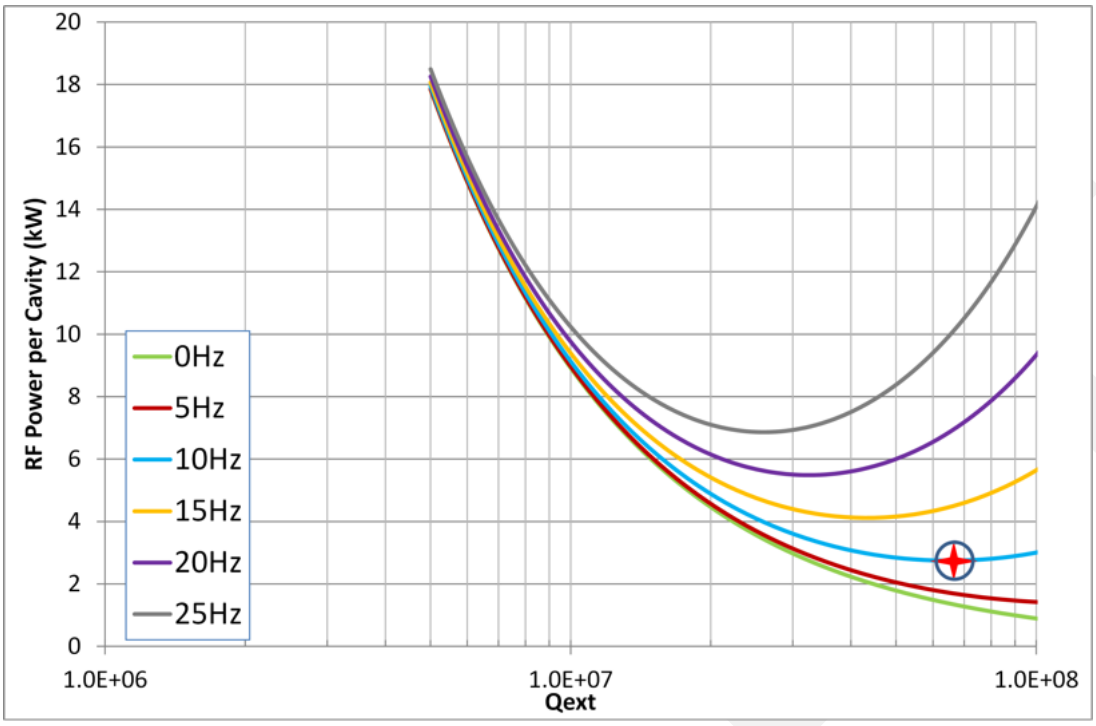

Figure 5.2: Microphonic assessment of 1.3 GHz cavities at gradient 19 MV/m.

possibility that this level of microphonic control may not be achieved on all cavities then for 15 Hz and 20 Hz bandwidths RF powers of 7.4 kW and 10.1 kW, respectively, would be anticipated.

5.3.1.4 Repetition Rate

The baseline for operation of UK XFEL is 1 MHz, however future upgrades to improve the delivery capability of the FELs for user experiments may require increases in the bunch repetition rate, which will influence the RF power requirements due to increased beam loading. A study has been performed to assess the effect of increasing the repetition rate as high as 4.5 MHz (for parity with Eu-XFEL intra-train repetition rate), though for initial upgrades the likely requirement would be to double the repetition rate to 2 MHz. As the repetition rate increases, so does the RF power requirement for each cavity due to increased beam loading. For an increase in the repetition rate to 2 MHz, the RF power required per cavity increases from 5.3 kW to 9.0 kW, and for 4.5 MHz this would increase to 22.9 kW, all for a gradient of 19.0 MV/m. Thus, repetition rate significantly influences the choice for the RF power sources.

5.3.1.5 Thin-Film Cavity Developments

Bulk Nb cavities have been the mainstay of the majority of SRF accelerators for decades and a large amount of development has been performed over this period on the surface treatment, from BCP, EP, Nitrogen doping and infusion, investigations into different ranges of vacuum baking (low, mid and high-T baking). However, these advancements are nearing the limits of what can be achieved with bulk Nb. The next major advancement being pursued is for thin-film SRF cavities, where there are opportunities of combining different materials and improved surfaces that can offer greater performance benefits than bulk Nb. Extensive R&D is ongoing to assess superconducting materials with higher critical temperatures (T_c) such as niobium-tin alloy (Nb_3Sn), niobium nitride

(NbN), and niobium titanium nitride (NbTiN), with the aim of unlocking these opportunities for higher performance capabilities.

For a single-cell cavity it has been demonstrated that when depositing a Nb_3Sn thin film, which has a T_c of 18.3 K, coated on a Nb cavity substrate it is possible to achieve gradients of > 18 MV/m with a $Q_0 > 10^{10}$ at 4.2 K [11, 12], which would reduce the power consumption by nearly a factor of 2. The main area of development is to transfer this technology to copper instead of using Nb as a substrate, to take advantage of improved thermal conductivity, potentially mitigating the risk of quenches, and enabling cheaper material costs. Success of this research would lead to significant savings in terms of operating costs, cryomodule manufacturing [13], and reduced cryogenic plant costs, as well as making the design of the machine more sustainable. Longer-term advancements of Nb_3Sn, alternative high T_c materials and multi-layer materials offer the enhanced potential to push the gradient performance towards 100 MV/m, further reducing accelerator construction and operation costs significantly, though for the study a more moderate gradient of 30 MV/m has been assumed. To assess the cryogenic power savings from predicting material BCS resistance, analysis has been conducted using SRIMP [14] utilising the material properties defined in Table 5.1, based on the referenced literature [15].

Parameter	**Material**		
	Nb	Nb-Cu	Nb_3Sn-Cu
Energy of the SC gap Δ/k_BT_c	1.82 [16]	1.82 [16]	2.20 [17]
SC transition temp. T_c [K]	9.25	9.25	18.00
Coherence length at T=0 K ξ_0 [nm]	39.0	39.0	5.7
RRR	300	10	10
London penetration depth λ_L [nm]	27	27	65
London penetration depth at T=0 K λ_0 [nm]	27.6	42.2	71.5

Table 5.1: Selected parameters for SRIMP for different materials under study.

The BCS resistance, as computed by SRIMP as a function of temperature are shown in Figure 5.3. As the power scales directly with the surface resistance (R – s), highlighting the importance of selecting materials with low surface resistance to minimize power consumption, the dynamic RF power dissipated per cavity can be determined as

$$P_{diss} = \frac{(E_{acc}L)^2}{R_s} = \frac{(E_{acc}L)^2}{R/Q \times Q} = \frac{(E_{acc}L)^2 R_s}{R/Q \times G}. \tag{5.4}$$

Assessing surface resistance behaviour at cryogenic temperatures the cryogenic power demand per cavity can be defined as

$$P_{total} = P_{static} + P_{dynamic} \tag{5.5}$$

Here, $P_{dynamic}$ denotes the power lost within the cavity due to RF fields, and P_{static} encompasses additional losses, such as those in waveguides and transmission lines. The total cryogenic power demand depends on the efficiency of the cryomodule, which varies with operating temperature. The thermodynamic efficiency of an ideal refrigerator approximates the Carnot thermodynamic efficiency

$$\eta_{Carnot} = \frac{T_{cold}}{(T_{hot} - T_{cold})} \tag{5.6}$$

where T_{cold} is the cryogenic operating temperature, and T_{hot} is the ambient temperature. However, real systems fall short of this ideal. To address this, a technical efficiency [18] term, η_r, is introduced

$$\eta_r = 0.318 \tanh\left(\frac{T}{3}\right) \tag{5.7}$$

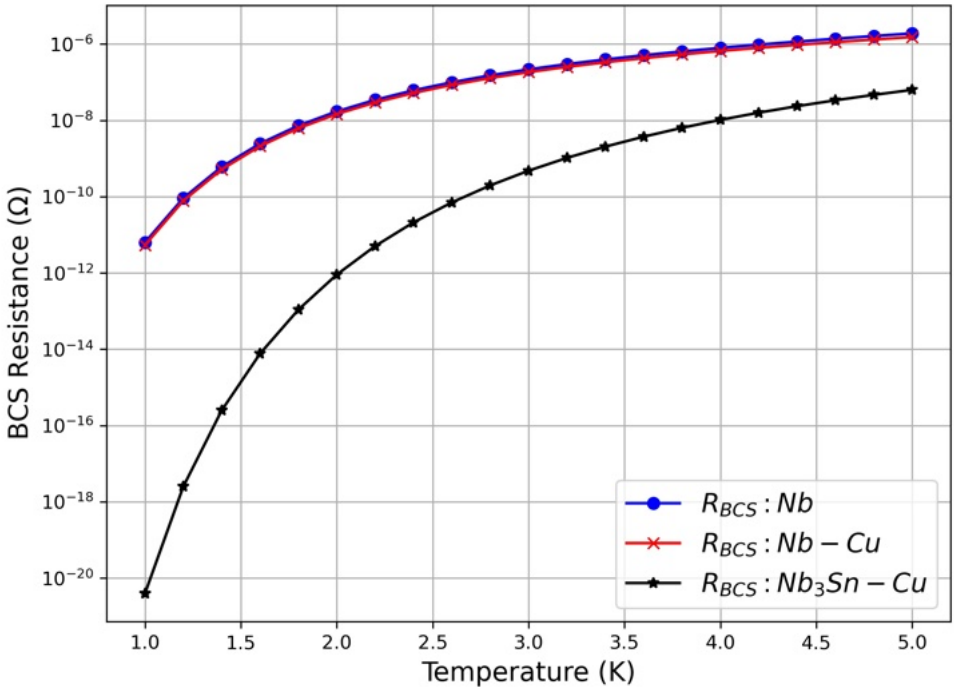

Figure 5.3: BCS resistance of Nb (blue), Nb on Cu (red), and Nb_3Sn on Cu (black) as a function of temperature.

The overall efficiency is then

$$\eta_{\text{Overall}} = \eta_{\text{Carnot}} \times \eta_{\text{r}} \tag{5.8}$$

In cryogenic terms the coefficient of performance (Real COP) quantifies the power needed to remove heat, defined as

$$\text{Real COP} = \frac{1}{\eta_{\text{overall}}} = \frac{1}{\eta_{\text{carnot}} \cdot \eta_{\text{r}}} \tag{5.9}$$

The overall cryogenic power is then

$$P_{\text{cryogenic}} = P_{\text{total}} \times \text{Real COP} \tag{5.10}$$

A summary for Nb, Nb on Cu and Nb_3Sn on Cu operating at a gradient of 19 MV/m is shown in Figures 5.5, 5.6 & 5.7. In summary, a saving of $\sim$ 70% could be made in electrical costs by choosing Nb_3Sn thin-film cavities, shown in Figure 5.4.

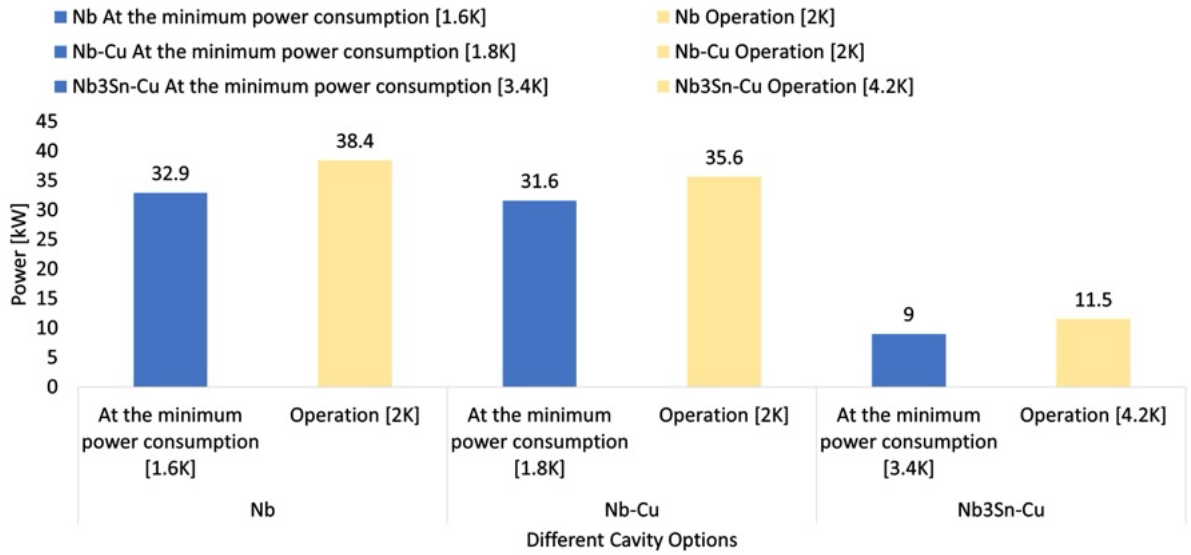

Figure 5.4: Graphical comparison of cryogenic power demand per cavity [kW] for different cavity types, evaluated at the temperature [K] corresponding to the minimum cryogenic load (blue) and at an operationally feasible temperature (yellow).

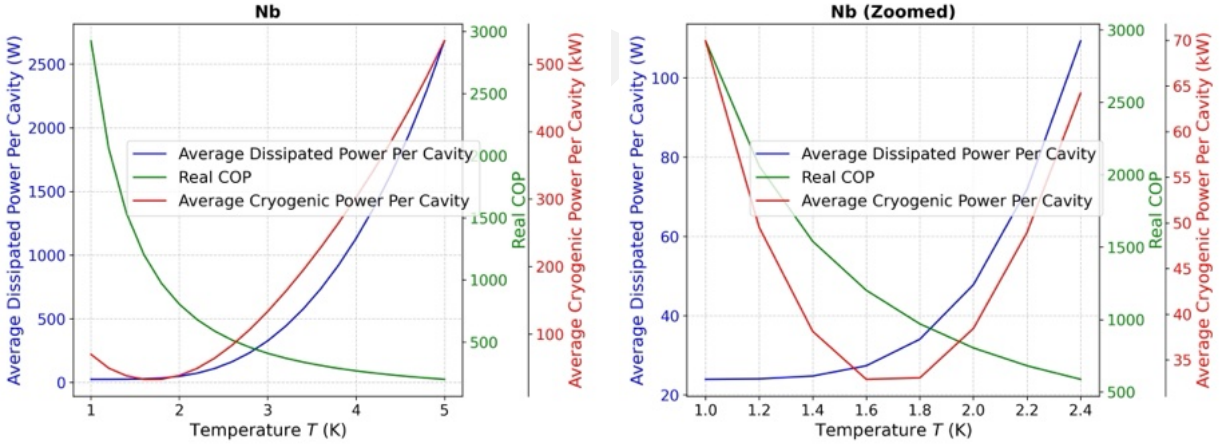

Figure 5.5: Normal-scale (left) and magnified (right) plots as functions of temperature, showing the average dissipated power per cavity (blue), the real coefficient of performance (COP) (green), and the average cryogenic power per cavity (red), for bulk Nb cavities.

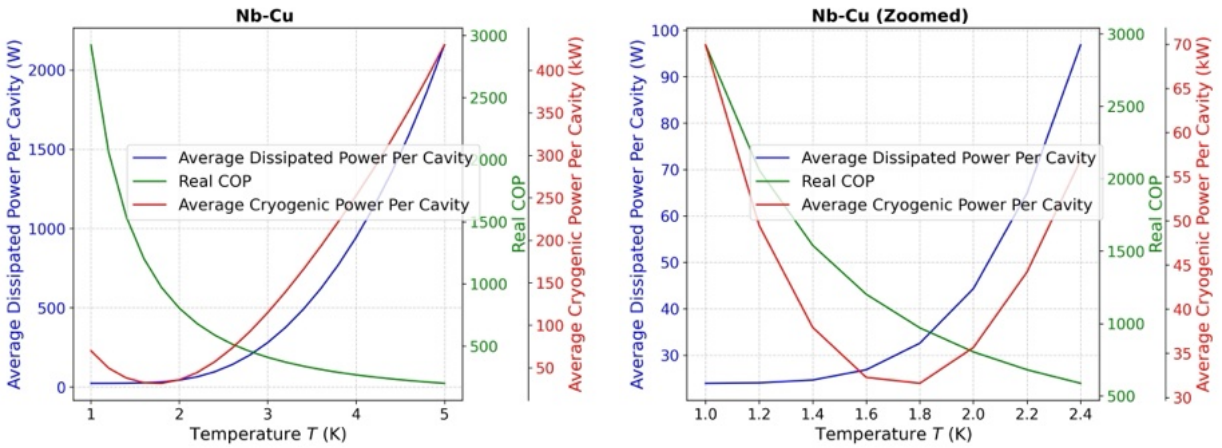

Figure 5.6: Normal-scale (left) and magnified (right) plots as functions of temperature, showing the average dissipated power per cavity (blue), the real coefficient of performance (COP) (green), and the average cryogenic power per cavity (red), for Nb on Cu cavities.

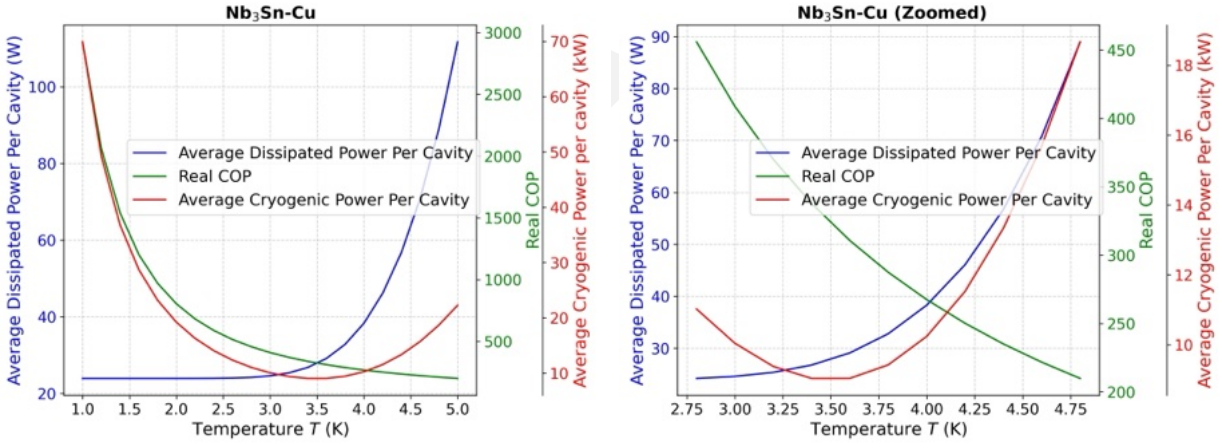

Figure 5.7: Normal-scale (left) and magnified (right) plots as functions of temperature, showing the average dissipated power per cavity (blue), the real coefficient of performance (COP) (green), and the average cryogenic power per cavity (red), for the Nb_3Sn on Cu cavities.

5.3.1.6 RF Parameters

Based on the assessments performed options are shown for the main SRF linac section for nominal parameters for 19 MV/m with a standard Nb cavities and Nb_3Sn coated on cavities, and for 30 MV/m with a Nb_3Sn coated on cavities are summarised in Table 5.2.

Parameter	**Nb (19 MV/m)**	**Nb_3Sn on Cu (19 MV/m)**	**Nb_3Sn on Cu (30 MV/m)**
RF frequency [MHz]	1300	1300	1300
Operating temperature [K]	2	4.2	4.2
Bunch charge [pC]	200	200	200
Repetition rate [MHz]	1	1	1
Beam current [μA]	200	200	200
Gradient [Mv/m]	19	19	30
Q_0	3.0×10^{10}	5.4×10^{10}	5.4×10^{10}
R/Q [Ω]	1036	1036	1036
Cavity length [m]	1.038	1.038	1.038
Number of cavities	416	416	264
Number of cryomodules	52	52	33
Linac length [m]	739	739	469
Q_{ext}	5.2×10^7	5.2×10^7	5.2×10^7
RF Power / cavity [kW]	5.3	5.3	10.6
Total RF Power [MW]	2.2	2.2	2.8
Cavity dynamic load [W]	14.1	6.6	16.3
Total dynamic load [kW]	5.9	2.7	4.3
Cavity static load [W]	2	2	2
Cryomodule static load [W]	8	8	8
Total static load [kW]	1.2	1.2	0.8
Total cryogenic load (+ 50%) [kW]	10.7	6.0	7.6
Total RF power [MW]	4.4	4.4	5.6
Total cryogenic power [MW]	10.7	3.6	4.6
Total power [MW]	15.1	8.0	10.2

Table 5.2: Options for SRF operational parameters for the main SRF linac, baseline is Nb, also shown are Nb_3Sn at two different gradients should thin-film become attractive in the medium term.

5.3.1.7 Amplifier Options

For the RF cavity field, an amplitude stability of better than 0.01% (rms) and phase stability of better than 0.01° (rms) will be required to meet the requirements of the FEL implying individual RF cavity control. For the main section of the SRF linac, the required CW RF power for an average 200 pC electron bunch at 1 MHz, i.e. neglecting short timescale difference in bunch charges required for the difference FELs, with an accelerating gradient of 19 MV/m would be 10.1 kW for each individual 1.3 GHz cavity, assuming a pessimistic microphonics level of 20 Hz. However, at LCLS-II and SHINE microphonic levels of 10 Hz have been achieved which reduces the RF power requirement to 5.3 kW. Additional considerations need to be factored in when considering the RF power source, such as the gradient required is an average of 19 MV/m, with some cavities being run at a higher accelerating gradient to compensate for any poorer performing cavities. Also some

individual cavities may have a higher level of microphonics due to local cavity circumstances, and the cavities Q_0 will potentially degrade over the lifetime of the machine. Thus an RF power of the order of 10.0 kW should be considered for the baseline for standard Nb cavities. For thin-film technology it may be possible to push gradients higher ($>$ 30 MV/m), then a source of 16 kW may be required, though it should be noted that R&D on Fast Reactive Tuners (FRTs) have the potential to reduce this by a factor of 10.

There are currently 2 options to deliver the required RF power, a tube option in the form of an Inductive Output Tube (IOT) or a Solid-State Amplifier. Traditionally, an IOT would be the automatic choice, for which at this frequency there is a commercially available tube capable of delivering up to 30 kW, provided by Microwave Power Products (MPP) - K5-1320W. Over the last few decades there have been advances in solid-state amplifier technology, in particular Gallium Nitride (GaN) transistor development, and it is now possible by combining multiple transistors to achieve commercially up to 30 kW CW. A number of potential suppliers have been identified (Table 5.3).

Table 5.3: Examples of commercially available CW 1.3 GHz Solid State Amplifiers.

RFHIC: RIK1330K-40TG - 30 kW 1.3 GHz CW Solid State Amplifier	**R&K**: A1300BW10-6372R - 16 kW 1.3 GHz CW Solid State Amplifier	**Microwave Amps**: 2 kW CW Solid State Amplifier

5.3.1.8 Couplers

The RF power couplers for TESLA type 1.3 GHz cavities have been extensively studied through the TESLA Technology Collaboration. The coupler used at European XFEL, LCLS-II and SHINE and is shown in Figure 5.8. This coupler (TTF-III) as with the TESLA cavity was designed for pulsed, high peak power operations for the TESLA/ILC colliders. For LCLS-II extensive studies were carried out to modify the coupler to operate with a CW load of 7 kW [19]. UK XFEL will have a Q_{ext} of 2.6×10^7 and an average RF power of 4.7 kW meaning the requirements are similar to LCLS-II and therefore a similarly adapted TTF-III coupler will be suitable. Additional design work will be needed if higher RF power levels are anticipated, as defined above. If thin film technology

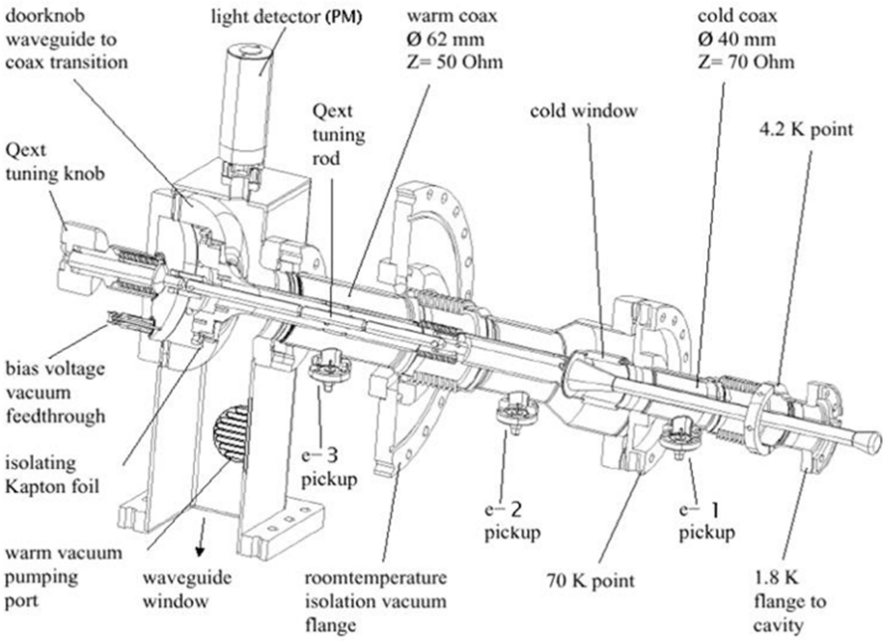

Figure 5.8: TTF-III coupler

is a proven technology by the time of the UK XFEL, the optimal Q_{ext} will be higher, which will necessitate a modification to nominal coupler length to match to the required cavity coupling.

5.3.1.9 Tuner

Several tuner designs from similar projects are evaluated as potential candidates for UK XFEL. Key tuner designs which have been implemented successfully include SACLAY-I/DESY [20], INFN blade type [21], KEK slide-jack type [22], and the two-lever type used in LCLS-II HE [23] which cater for both slow and fast tuning requirements. However, if the thin-film cavity option is taken forward then there is a need to explore alternative methods to perform the mechanical tuning due to the brittle nature of Nb_3Sn and there is also an opportunity to explore alternative methods to deal with the microphonics.

Recently, CERN and Brookhaven National Lab, USA [24, 25, 26, 27] have explored ferroelectric based fast reactive tuner (FE-FRT) designs for SRF cavities for HL-LHC and FCC-ee. The availability of state-of-the-art Barium Strontium Titanate (BST) ferroelectric material [28, 29] with high-speed dielectric switching for an applied high voltage, low loss and high electric breakdown strength enabled this development. The primary benefit of FE-FRT is the absence of mechanically moving parts, allowing the tuner assembly to be placed outside the cryostat at a distance from the cavity and maintained at room temperature. Furthermore, the FE-FRT offers fast (sub-microsecond) and precise frequency tuning, enabling higher sensitivity and resolution in frequency control. This allows for a significant reduction in RF input power required to maintain a given accelerator gradient, making it a more energy-efficient and sustainable option for SRF cavity operation, particularly attractive for large-scale accelerator infrastructures like the UK XFEL [27]. The first ferroelectric based fast reactive tuner (FE-FRT) prototype has been demonstrated for the HL-LHC 400 MHz crab cavity under cryogenic conditions in 2019 [26] as shown in Figure 5.9. CERN has played a leading role in the design improvements of FE-FRT [24, 25] focusing on improved thermal management of thin ferroelectric discs, compatibility with high reactive RF power (kVAR) operation, optimised high-voltage biasing and fast switching systems, effective thermal

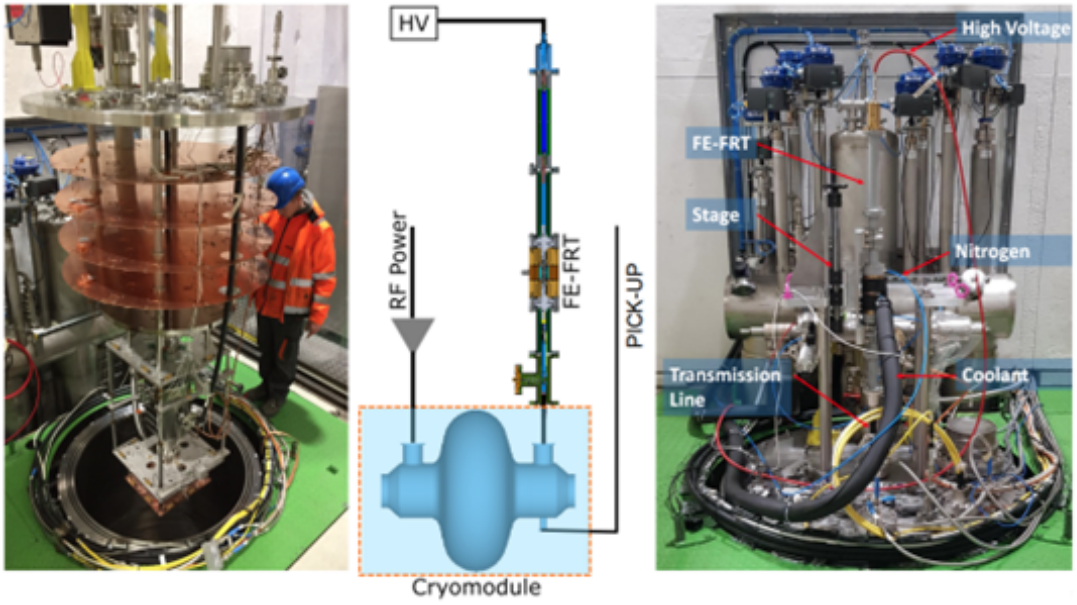

Figure 5.9: Ferroelectric fast reactive tuner under test with 400 MHz HL-LHC prototype crab cavity [26].

stability strategies, enhanced frequency tuning resolution and control, and suppression of RF leakage and high order modes.

For UK XFEL, a decision must be made whether to adopt an existing tuner design or to design a hybrid tuner with mechanical tune-ability for the compensation of static 2K landing frequency and FE-FRT for fast dynamic frequency locking, particularly within the precision and time scale required for microphonics compensation. The ferroelectric-based tuner becomes even more attractive if thin film (e.g. Nb_3Sn) coated multi-cell cavities are used. This approach could drastically reduce the electrical power requirement for the cryogenic plant and operational costs of UK XFEL. UK XFEL stands to benefit both from well-established tuner methodologies and from integrating recent developments in ferroelectric-based tuners for dual-mode (slow and fast) operation.

5.3.2 Sustainability

As with the low energy beam section, the primary sustainability consideration for high energy beamline is to preserve the highest brightness beam possible through the acceleration and distribution sections. In this manner we minimise the beam energy and undulator length required for lasing at a particular FEL resonance and pulse power.

Energy consumption of the RF system represents a large fraction of the total consumption for the machine as a whole. Most of this energy is used by the cryogenic system needed to keep the cavities at the correct temperature for superconducting operation.

An assessment of the power requirements for various different RF frequencies has been performed (Table 5.4). The baseline option for UK XFEL is based on 650 MHz/1300 MHz frequencies; this decision was based on a number of factors as well as energy consumption.

In addition to the carbon emissions associated with electricity usage, there are embodied emissions associated with manufacture of the components needed for the RF system. These embodied emissions are hard to estimate without knowing the full details of the RF system that will be constructed: this is true for all the subsystems of the accelerator. The energy consumption of the

Option	Total RF electrical power [MW]	Total cryogenic system power [MW]	Total annual energy consumption [GWh/year]
400/800 MHz	10.6	15.6	178
650/1300 MHz	6.5	8.7	102
750/1500 MHz	4.4	12.1	119

Table 5.4: Expected power consumption by the RF and cryogenic systems for various options. Annual usage figures assume that the RF system is in use for 5000 hours per year, whilst the cryogenic system is operational for 8000 hours per year.

RF system over an expected operating period of 50 years means that the operational emissions will always be far higher than the construction emissions. This holds even for the lower carbon intensity expected for the UK's energy grid in the next few decades. See Section 14.2 for further details.

From a sustainability point of view, therefore, the critical factor is to reduce the overall power consumption of the RF system, even if this implies a larger number of cavities.

One key technology with the potential to reduce emissions in this area is thin-film SRF cavities. In lieu of a solid niobium cavity, a solid copper cavity is used, coated with a thin film of niobium. This has several advantages, both for sustainability and more generally [13]:

5.3.3 Long-Range Wakefields

Bunches transiting through an RF cavity will induce electro-magnetic (EM) wakefields that will ring out in the structure after the driving bunch has left. These wakes can affect the particles in the same bunch, known as short-range (SR) wakes, or can affect subsequent bunches traversing the cavity, known as long-range (LR) wakes. The voltages experienced by any witness bunches or particles can either be in the longitudinal or transverse directions. Longitudinal kicks are delivered by resonant monopole modes, whereas transverse kicks result from dipole modes. These unwanted kicks can have serious and unintended consequences for the beam and need to be characterised and understood and, if necessary, mitigated to lessen their impact. Here, we concentrate on the LR transverse wakes induced by dipole modes in a TESLA 9-cell elliptical cavity [30] and work to gauge their impact on emittance dilution as the beam propagates through the main accelerating section of UK XFEL.

It should be noted that the summed wakes in the proposed UK XFEL beam are induced by an irregular constituent bunches of differing charges. This has never been investigated previously, and this work therefore represents a novel area of research. Given that, it is appropriate to benchmark the models used against known results, this is discussed in Appendices **??**.

5.3.3.1 Loss Factors, Kick Factors and the Wake Potential

We can ascertain the loss factors for each mode and at given radial offsets by first integrating $E_z(r, \theta, z)$ delivered by CST at that offset to derive the accelerating voltage (V_{acc})

$$V_{acc}(r) = \int_{-L/2}^{L/2} E_z(r, \theta, z) \exp\left(\frac{-i\omega z}{c}\right) dz, \tag{5.11}$$

where c is the speed of light in a vacuum, ω_n is the angular frequency of the n^{th} mode and L is the length or period of the cell or cavity. The longitudinal loss parameter of a mode can be defined as the amount of energy lost by a charged particle traversing a cavity per unit charge squared and is given by

$$k_{\parallel} = \frac{|V_{acc}|^2}{4U}, \tag{5.12}$$

where U is the stored energy. From the offset longitudinal loss factor the kick factor of the mode can be calculated using

$$K = \frac{k_{\parallel} c}{\omega_0 L r^2}, \tag{5.13}$$

where r is the radial coordinate of the longitudinal line integral. This was carried out for all dipole modes in the first six passbands with the results shown in Figure 5.10.

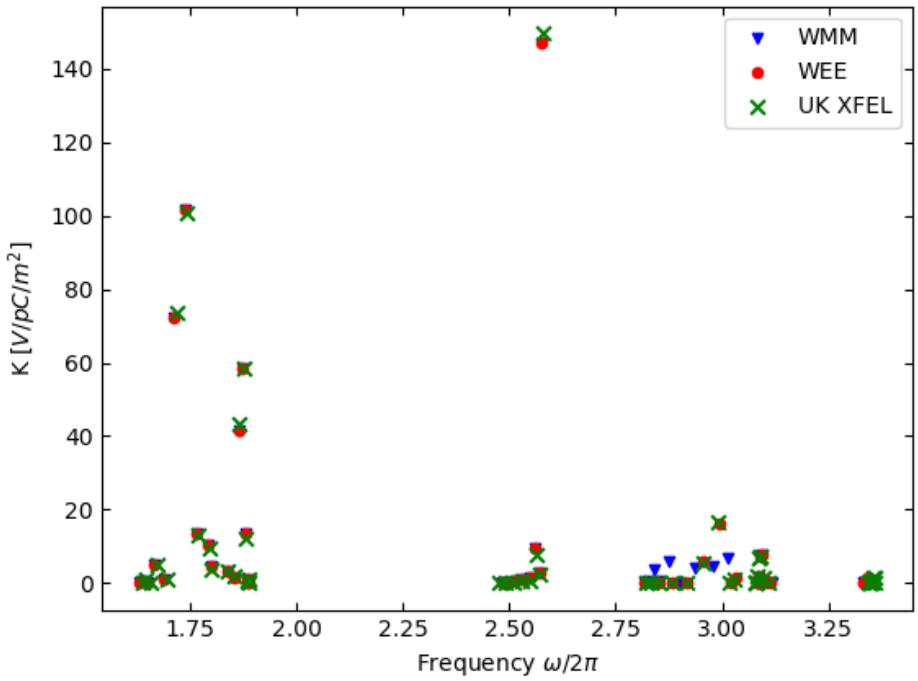

Figure 5.10: Plot comparing the frequencies and kick factors of each mode in the first six dipole passbands to published results [30].

The kick factors can be used to calculate the long-range transverse wake potential [31] via

$$W(s) = 2\mathrm{Im}\left\{ \sum_{n=1}^{N} K_n e^{i\omega_n s/c} e^{-\omega_n s/2Q_n c} \right\} U(s), \tag{5.14}$$

where K_n is the kick factor of the n^{th} mode, ω_n is the angular frequency of the n^{th} mode, s is the longitudinal coordinate, Q_n is the quality factor of the n^{th} mode and U(s) is the unit step function, defined as 1 if $s > 0$ and 0 if $s < 0$. However, since small variations in frequency can result in large variations in the experienced wake, we took the worst-case scenario of the envelope wake potential ($\hat{W}$) as our baseline

$$\hat{W}(s) = 2\left|\sum_{n=1}^{N} K_n e^{i\omega_n s/c} e^{-\omega_n s/2Q_n c}\right| U(s). \tag{5.15}$$

5.3.3.2 The Summed Wake Potential of Constituent and Composite Beams

The proposal is to have two photoinjectors that deliver a combination of any two of the three constituent beams and combine them into a composite beam that is then accelerated, then split between the various FEL to satisfy each photon beam user independently. A typical bunch charges and repetition rate distribution of the three constituent beams are detailed in Table 5.5.

Table 5.5: Baseline definition of the three constituent beams charges, bunch repetition rates, transverse emittance (ϵ_{xy}) and the standard deviations of their transverse Gaussian distribution ($\sigma_\perp$).

Charge [pC]	Rep Rate [kHz]	$\epsilon_{Nx,y}$ [nm rad]	$\sigma_\perp$ [μm]
600	0.1	354	233
150	500	132	142
75	250	82	112

Looking at one TESLA 9-cell cavity, we have a situation where the wake left by an initial drive bunch is still ringing in a cavity when a witness bunch arrives, and in turn, this witness bunch induces a wake of its own and so on until the ringing of the initial bunch dies down to a level we can ignore, a process controlled by the attenuation factor in the decay components of Equations 5.14 and 5.15. At this point, we have reached a steady state in which any new bunches arriving will experience the sum of all the wakes induced by the preceding bunches.
We can illustrate this by plotting the long-range transverse wake potential and the points on that function sampled by one of our constituent beams, the 150 pC beam at a bunch repetition rate of 500 kHz for example, see Figure 5.11.

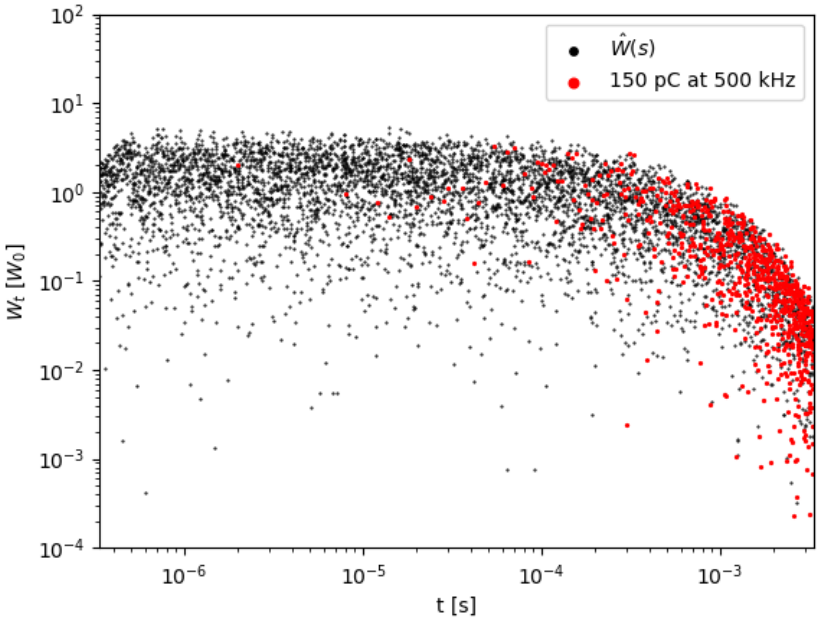

Figure 5.11: Plot showing the transverse envelope wake potential in black normalised to $\hat{W}_0$ = 14.1 V/[pC · m^2] with the 150 pC beam plotted in red with a bunch spacing of 2 ms, or 600 m.

Here we can see that the wake potentials induced by bunches that traversed the cavity around 400 μs previously start to decay to a level at which they can be ignored. The summed envelope wake potential ($\hat{S}$) of this constituent beam is then calculated by simply adding the envelope wake potentials of each bunch of interest.

$$\hat{S} = \sum_{n=1}^{N} \hat{W}_i(s), \tag{5.16}$$

where N is the number of bunches with a wake potential above the cutoff value. For this constituent beam (150 pC at 500 kHz) we have $\hat{S}$ = 6550 V/[pC · m^2]. This analysis can be repeated for each of the other constituent beams.

For each TESLA 9-cell cavity, we can then determine the worst case transverse voltage ($V_\perp$) experienced by a new bunch entering the cavity with steady state wakes ringing out as a function of transverse offset via Equation 5.17.

$$V_\perp = \hat{S} \cdot q_b \cdot L_{CAV} \cdot r_\perp, \tag{5.17}$$

where q_b is the bunch charge, L_{CAV} is the RF length of the TESLA 9-cell cavity, and $r_\perp$ is the radial offset. For the 150 pC beam running at a radial offset of 1σ of its transverse Gaussian bunch profile (142 μm), we have $V_\perp$ = 140 V.

Considering the composite beams, and taking the example of the interleaved 150 & 75 pC constituent bunches, we chose a fill pattern illustrated in Figure 5.12.

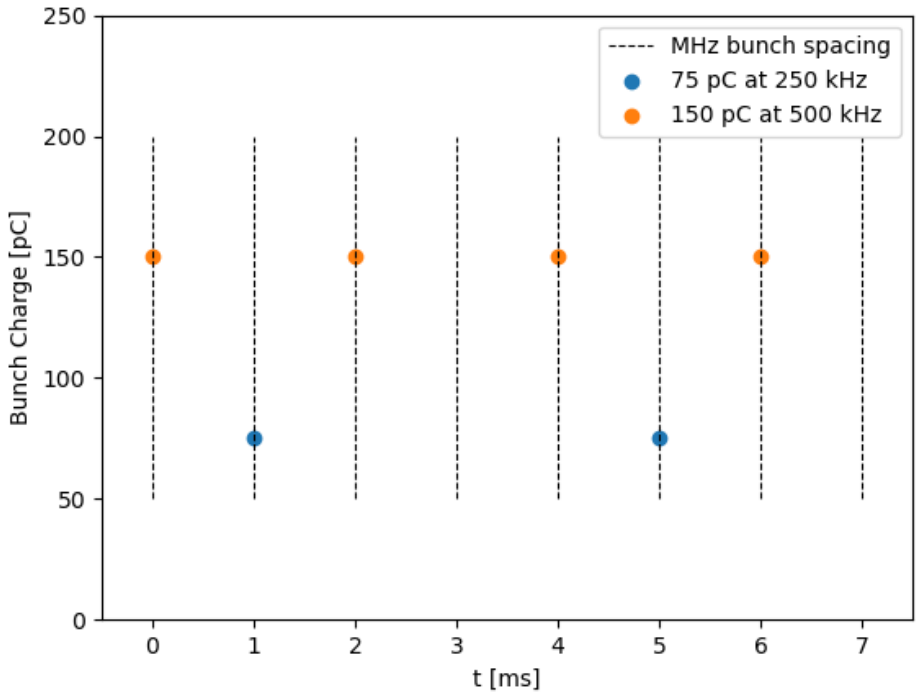

Figure 5.12: The proposed fill pattern of the 150 & 75 pC composite beam with a repeat pattern at 1 MHz of ”150 - 75 - 150 - gap”.

The linear relation of $V_\perp$ as a function of $r_\perp$ for both constituent 150 & 75 pC bunches can the added together to ascertain the $V_\perp$ of the composite bunch for any given radial offset. See

Figure 5.13 for an illustration of the transverse voltage delivered for bunches running at radial offsets of up to half of the TESLA 9-cell cavity's iris radius (35 mm).

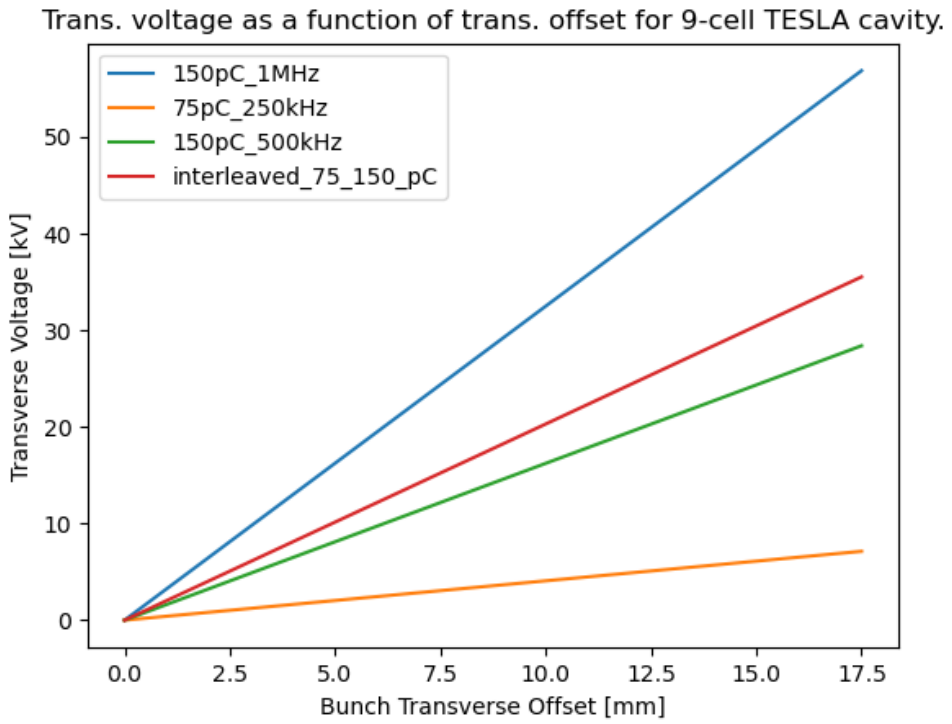

Figure 5.13: The transverse voltage delivered by the constituent 150 & 75 pC bunches as a function of radial offset and the sum of these being the $V_\perp(r_\perp)$ of the composite beam. The case of a 150 pC beam running at a bunch repetition rate of 1 MHz is shown for reference.

5.3.3.3 Comparison of PLACET Long Range Wakes with Analytical Model

To confirm that PLACET is handling LR transverse wakes correctly, a comparison was made to an analytical model outlined in Figure 5.14 [32], where the transverse wake induced by a drive bunch running off-axis is experienced by an on-axis witness bunch causes an angular deflection on the witness defined as

$$\Delta\theta = q_D q_W \frac{L_p}{E_W} W(s) r_D \tag{5.18}$$

where q_D is the charge of the drive bunch, q_W is the charge of the witness bunch, L_p is the length of the structure, E_W is the energy of the witness bunch, W(s) is the wake function induced by the drive bunch at a trailing distance s and r_D is the transverse offset of the drive bunch. This angular deflection was calculated for various values of r_D and simulated using PLACET. The results for 600 pC bunches with a bunch separation of 300 m and various drive bunch offsets are shown in Table 5.6 and plotted in Figure 5.15.

The good agreement between the analytical model and our implementation of LR wakes in PLACET meant that we could proceed with more complicated simulations with confidence.

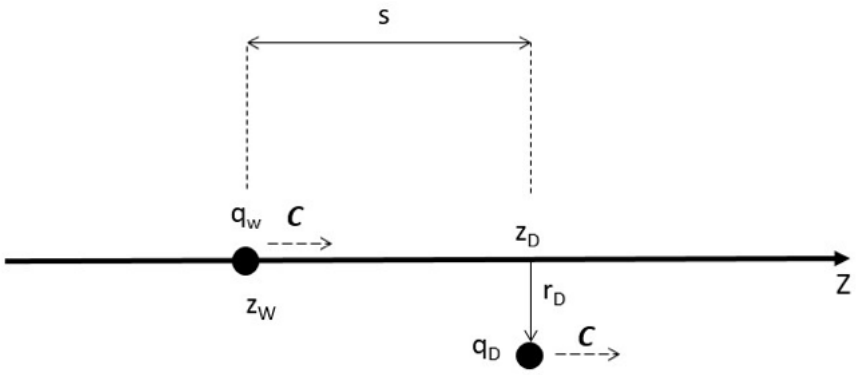

Figure 5.14: An illustration of the situation used to benchmark PLACET's handling of LR transverse wakes to the analytical solution outlined in Equation 5.18.

Table 5.6: Comparison of LR wakes in PLACET to the analytical model outlined in Figure 5.14.

offset [mm]	analytic $\Delta\theta$ [nrad]	PLACET $\Delta\theta$ [nrad]	difference [%]
1	83.9	84.7	–1.0
2	167.8	168.2	–0.3
4	335.5	335.2	0.1
8	671.0	669.1	0.3
16	1342.0	1337.0	0.4
32	2684.0	2672.6	0.4

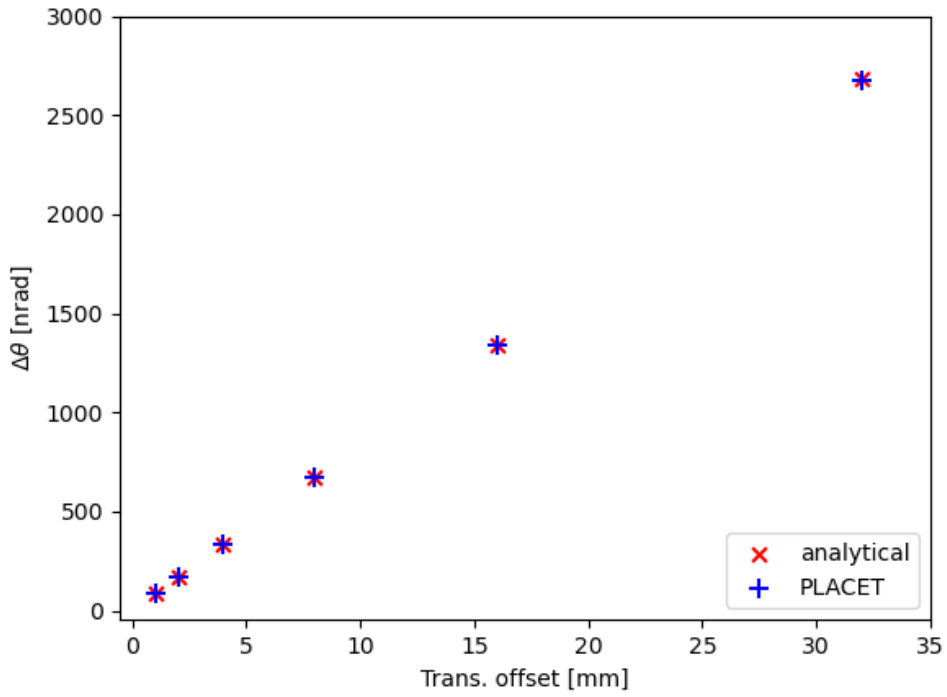

Figure 5.15: Comparison of LR wakes in PLACET to the analytical model outlined in Figure 5.14 and Equation 5.18.

5.3.3.4 Emittance Dilution of Constituent Beams

Emittance dilution ($\Delta\epsilon_N/\epsilon_{N0}$) is defined as the difference between the normalised transverse emittances of the case where there are no LR transverse wakes (ϵ_0) and the case where the LR wakes are applied and the steady-state is reached ($\epsilon_\perp$) (where simulating more bunches does not add to the effect due to the exponential decay term in Equation 5.14) normalised to ϵ_0 and expressed as a percentage thus

$$\Delta\epsilon_N/\epsilon_{N0} = \frac{|\epsilon_0 - \epsilon_\perp|}{\epsilon_0} \times 100\,\%. \tag{5.19}$$

Of the three constituent beams outlined above and detailed in Table 5.5, the 75 pC and 150 pC beams were simulated in PLACET, running at 500 kHz and 250 kHz bunch repetition rates respectively. Both beams were offset by 1σ of their transverse Gaussian distributions and simulations of varying number of bunches were carried out to find the steady state value of the emittance dilution. The results for the 75 pC beam are plotted in Figure 5.16, while the results for the 150 pC beam are shown in Figure 5.17. For the 75 pC beam the results indicate that the unmitigated transverse emittance dilution due to a systematic 1σ transverse offset is 118 %, whereas for the 150 pC beam the effect is slightly less at 106 %. This result is delivered by fitting the simulation data to:

$$\Delta\epsilon_N/\epsilon_{N0} = A(1 - e^{-Bn_B}). \tag{5.20}$$

where n_B is the number of bunches included in each simulation.

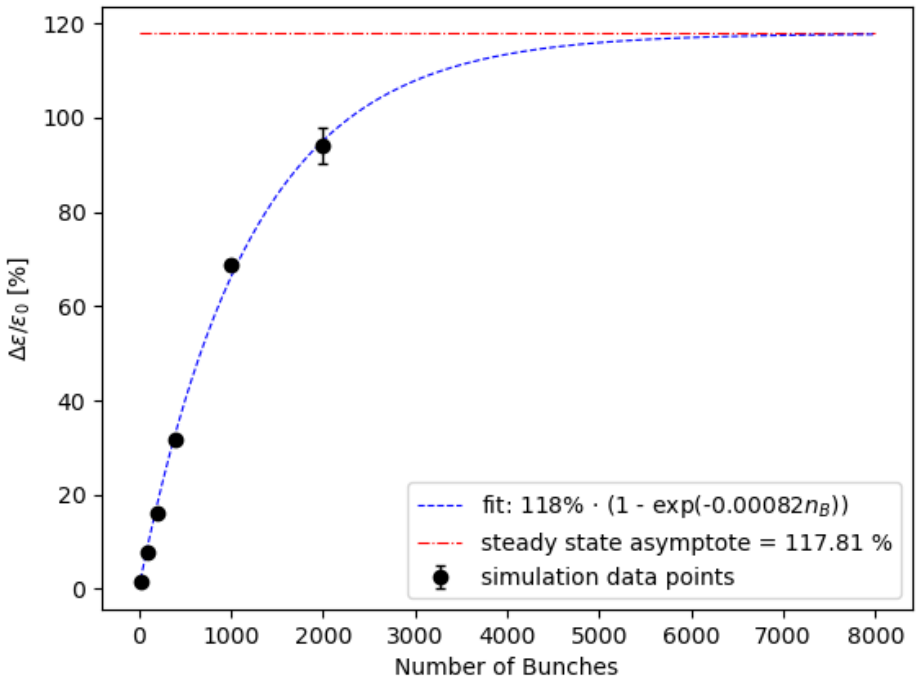

Figure 5.16: Unmitigated transverse emittance dilution due to a systematic 1σ transverse offset of the 75 pC beam returned by multiple PLACET simulations as a function of number of bunches.

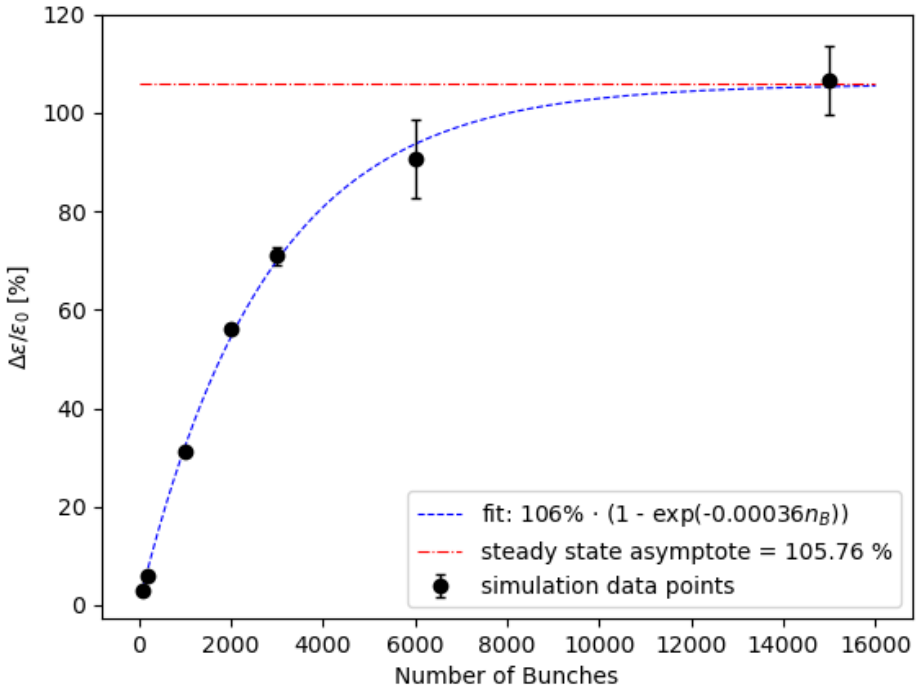

Figure 5.17: Unmitigated transverse emittance dilution due to a systematic 1σ transverse offset of the 150 pC beam returned by multiple PLACET simulations as a function of number of bunches included.

5.3.3.5 Future Work

Further analysis of the composite beam described in Figure 5.12 needs to be carried out to gauge a more realistic effect on the unmitigated transverse emittance dilution, and for different charge filling patterns likely necessary as operational FELs may have differing uptimes.
The LR longitudinal wakes need to be added to assess their effect on the energy spread of the bunch at the end of the main accelerating section.
The results here show the unmitigated effects of the LR transverse wakes, in reality these HOMs will be coupled out and the modal Q_0 values used in the exponential decay term in Equation 5.14 will be reduced down to levels that mean that the effect of the LR transverse wakes on the transverse emittance will be greatly reduced. This scenario needs to be simulated to see how much damping is required for the UK XFEL's main accelerating section in particular.

5.3.4 Higher Harmonic Lineariser

UK XFEL will utilise higher harmonic cavities to linearise the phase space for the C5 compressed bunches (see Section 5.4). There has been extensive research carried out for the development of a third harmonic (3HC), 3.9 GHz, superconducting cavity and cryomodules for FLASH [33], European XFEL [34, 35], LCLS-II [36, 37] and SHINE [38, 39] projects.

LCLS-II 3.9 GHz cavity has demonstrated a maximum accelerating gradient of 19.7 MV/m [34], with quality factor (Q_0) of 2.7×10^9 at 14.9 MV/m. Vertical tests of a prototype at SHINE demonstrated maximum acceleration gradient of 20.3 MV/m, with (Q_0) of 2.9×10^9 at 13.1 MV/m [38] nominal gradient. The original Eu-XFEL 3HC cavity design struggled at higher pulse repetition rate due to the penetration of fundamental mode magnetic field into the higher order mode (HOM)

coupler [40], causing excessive heating and quench. Both LCLS-II [37] and SHINE [39] mitigated this issue by reducing the beam pipe radius, modifying the HOM coupler and end-cell shape. Both have considered microphonics detuning up to 30 Hz and implemented tuning correction using combination of fast piezoelectric and slow motorised tuners, with blade type cavity contact mechanism.

Different machine operation modes for UK XFEL with bunch charge (q_b) ranging from 75 to 300 pC has been considered with composite bunch repetition rate of 1 MHz (the low rep rate 600 pC bunch is not considered here). With high current beam, beam loading dominates the choice of cavity coupling factor and power requirement. The required input RF power P_{RF} to accelerate beam with current I_0 to voltage V_c can be calculated as [7],

$$P_{RF} = \frac{V_c^2}{R_L}\frac{(1+\beta_{opt})}{4\beta_{opt}}\left[\left(1+\frac{I_0 R_L}{V_c}\cos\psi_b\right)^2+\left(\tan\psi_d-\frac{I_0 R_L}{V_c}\sin\psi_b\right)\right], \tag{5.21}$$

where, the optimum cavity coupling factor β_{opt}, can be derived as,

$$\beta_{opt} = \sqrt{(b+1)^2+\left(\frac{2\,\delta f}{\Delta f_0}+b\,\tan\psi_b\right)^2}, \tag{5.22}$$

please refer to [7] for more details and definition of symbols.

Initial beam dynamics simulations indicate a required total beam deceleration voltage of 25.74 MV at 180 degree phase from the crest. The active acceleration length L_c is 0.346 m per nine cell cavity. Depending on number of cavities used, the acceleration voltage V_c and field gradient E_{acc} is derived. Other well demonstrated cavity parameter values such as, R/Q of 758 Ω, intrinsic quality factor Q_0 of 2.0×10^9, total detuning frequency including microphonics δf of 30 Hz are used. The major RF parameters, along with optimum external quality factor (Q_{ext}) and power dissipated in cavity P_d, required to accelerate electron beam consisting average 200 pC bunches at 1 MHz, using different number of cavities are plotted in Figure 5.18 (top). If a cryomodule consisting of six cavities are used then, for 200 pC charge, it will need E_{acc} of 12.4 MV/m, 910 W input RF power (P_{RF}) and will dissipate (P_d) 45.5 W.

With a module containing six cavities, RF parameters required for different bunch charges is plotted in Figure 5.18 (bottom). The system should be designed robust enough to handle a cavity failure. If one of the cavity fails then the rest of the five cavities can compensate it by increasing their gradient to 14.9 MV/m, requiring $P_{RF,1-trip}$ of 3.8 kW, while dissipating $P_{d,1-trip}$ up to 69 W.

The high power RF system will consist of modular solid state amplifiers (SSA), combined to achieve the required RF power. Power will be transported through waveguide network and circulator/isolator will be used to protect the SSA from inherent reflection from the cavity and any breakdown in the cavity or waveguide.

The above parameter values can be achieved using current technologies. Considering timescale of the project, more ambitious values for accelerating gradient, Q_0 and RF power are under consideration. Most of the technology development including thin film based cavity design are focused on the fundamental accelerating cavities at 1.3 GHz, but it will also benefit higher harmonic design. Final design values will be optimised during TDR phase based on technology progress at the time.

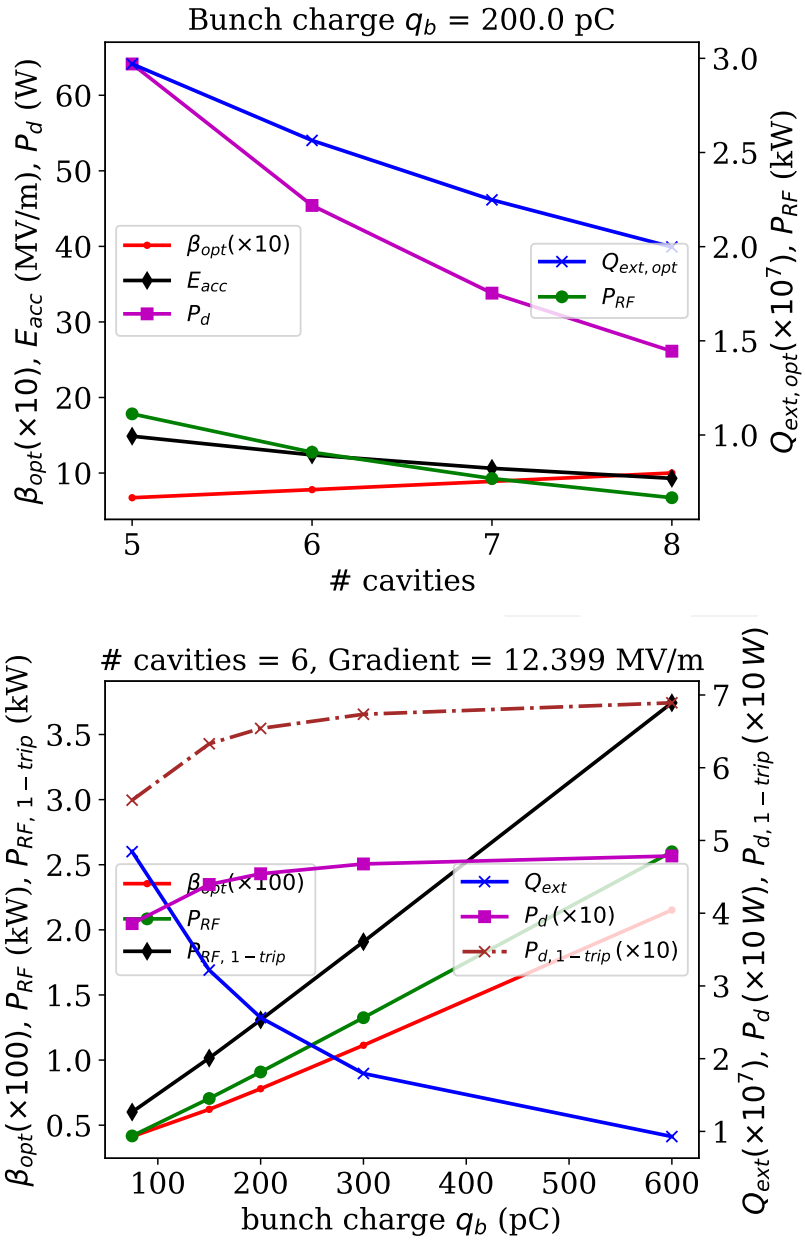

Figure 5.18: RF parameters optimised for different bunch charge and number of cavities, for bunch repetition rate of 1 MHz. Top: For 200 pC bunch, using different number of cavities. Bottom: For different bunch charge using six cavities.

5.3.5 Low Level RF system

The Low-Level Radio Frequency (LLRF) system is responsible for generating highly stable, low-power RF pulses with user-defined amplitude and phase, referenced to a global timing clock. These pulses are subsequently amplified to drive the accelerating structures. In addition to RF generation, the system provides real-time feedback and tuning signals to stabilize the accelerating field within the cavities.

Highly integrated and sophisticated LLRF and control systems have been successfully deployed in existing XFEL facilities, such as the European XFEL [41] and LCLS-II [42].

A stable Laser Master Oscillator (LMO), operating at a sub-harmonic of 1.3 GHz, will be phase-locked to an RF Master Oscillator (MO) to create an ultra-stable hybrid reference signal. This

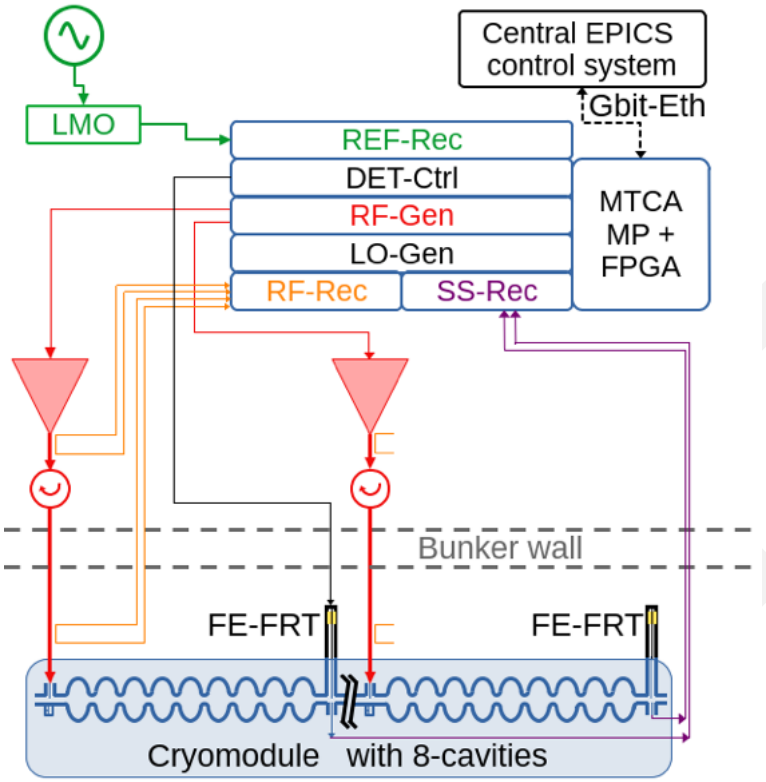

Figure 5.19: Block diagram of proposed unit LLRF system.

reference will be distributed to all RF stations via a high-precision optical synchronization system.

A modular LLRF architecture is proposed for controlling multiple cavities. A block diagram illustrating the submodules of a typical LLRF unit is shown in Figure 5.19. The system is based on the MicroTCA (MTCA) platform, which enables high-speed communication and synchronization among modules.

The Reference Receiver (REF-Rec) module receives the ultra-stable optical reference signal and converts it into RF clock signals using a Sagnac loop and a Mach-Zehnder interferometer-based locking mechanism.

The Local Oscillator Generator (LO-Gen) module generates a local oscillator signal (targeted around 1354 MHz), locked to the reference clock. This signal is used for frequency up/down conversion in the RF Generator (RF-Gen)/RF Receiver (RF-Rec), and Small Signal Receiver (SS-Rec) modules, as well as to generate secondary clock signals (e.g. 216 MHz) for ADCs, DACs, and FPGAs. Stable techniques such as digital direct synthesis (DDS) will be employed to minimize additive phase jitter.

The RF-Gen module synthesizes the actual LLRF signal using a vector modulator (VM) technique. Amplitude and phase control is achieved through local feedback implemented in the MP+FPGA module, complemented by global feedback systems operating over Gigabit Ethernet. The LLRF system must maintain the cavity field amplitude and phase to within 0.01 % and 0.01°, respectively. This will involve generating signals around 54 MHz using a 16-bit DAC operating at 216 MHz. Feedforward amplitude shaping may be used to compensate for beam loading due to non-uniform bunch charge patterns.

Forward and reverse RF signals will be sampled throughout the amplification chain—for example, after the Solid-State Amplifier (SSA) and before the circulator, as well as at the cavity input—via

the RF-Rec module. Probe signals from the cavities will be separately processed in the SS-Rec module to enable precise feedback and cavity field stabilization, ensuring isolation from high-power signals.

The Detuning Control (DET-Ctrl) module generates corrective feedback signals to compensate for cavity detuning caused by factors such as microphonics. The UK XFEL will use Piezo tuners for Nb cavities and proposes to use ferroelectric fast reactive tuners (FE-FRTs) if the thin film cavity option is progressed, which provide a wide frequency tuning range with kHz-level bandwidth.

Advanced Mezzanine Cards (AMCs), integrating microprocessors and FPGAs, will be employed for digital down-conversion and vector modulation processing of RF-Rec and SS-Rec signals. Fast feedback loops for detuning correction will be implemented in the FPGA logic. FPGA cards will communicate with ADCs, DACs, and DET-Ctrl modules via the MTCA backplane. Slower feedback functions, such as beam-based drift correction, will be managed by the microprocessor card and integrated into the central EPICS control system.

The detailed design of the LLRF system will be finalized during the Technical Design Report (TDR) phase, taking into account the evolving state of relevant technologies.

5.3.6 Normal Conducting Booster Linac

A $\leq$200 Hz subset of high charge bunches will be further accelerated on emergence from the SC linac from 8 GeV to 12 GeV, with space reserved to reach 15 GeV to accommodate potential upgrade paths. The defined operating modes are detailed in Table 5.7. The reduced repetition rate and the need to keep the section relatively compact lends itself to a normal-conducting high gradient type linac examples of currently operating / proposed linacs include CLARA, Swiss-FEL or CLIC [43, 44, 45].

Mode	Single Bunch	Burst Mode
Energy Gain [GeV]	4	4
Rep. rate [Hz]	100	$\leq$200
Bunches per train	1	8 - 12
Bunch Frequency [MHz]	N/A	up to 216.67
Bunch Charge [nC]	0.3-1.2	0.3-1.2

Table 5.7: Summary of the booster modes for UK XFEL

These linacs utilise copper cavities at S, C and X-band frequencies respectively with varying implementations of klystron-modulator systems as their RF power sources. The frequency options available are generally limited to those commercially produced high-power klystrons available from suppliers such as Canon, MPP (formerly CPI) and Thales. For a large facility some suppliers have indicated a willingness to develop non-catalogue high-efficiency klystrons.

As a baseline for analysing the options available for the booster section the cavity and RF systems currently in use are used. A summary of four currently used systems are given in Table 5.8.

Each of the options assessed has a different setup for powering the cavities. The options investigated have the following powering schemes:

- S-Band: 45 MW klystron with 4 µs RF pulse going to a pulse compressor, followed by a splitter powering two cavities with 50 MW of RF power with pulse width 1.25 µs.

Parameter	S-Band	C-Band	X-Band-1	X-Band-2
Frequency [MHz]	2998	5712	11998	11998
Gradient [MV/m]	25	35	80	57
Active length required [m]	163.4	115.2	50	70
True length at 70 % fill factor [m]	233	165	72	100
Cavity Length [m]	4.3	1.8	0.5	0.5
Number of required cavities	38	64	104	144

Table 5.8: Summary of headline parameters used as a baseline based on CLARA type S-band, SPring-8 C-Band and CLIC type X-Band cavities

- C-Band: 50 MW klystron with 2.5 µs RF pulse going to a pulse compressor, followed by a splitter powering two cavities with 70 MW of RF power with pulse width 0.5 µs.
- X-Band-1: Two 50 MW klystrons with 1.5 µs RF pulse combined going to a pulse compressor, followed by a splitter cascade powering eight cavities with 80 MW of RF power with pulse width 0.2 µs [45, 46, 47, 48].
- X-Band-2: One 50 MW klystron with 1.5 µs RF pulse going to a pulse compressor, followed by a splitter cascade powering eight cavities with 60 MW RF power with pulse width 0.2 µs [45, 46, 47, 48].

Each of these schemes require varying amounts of equipment which is summarised in Table 5.9.

Components	S-Band	C-Band	X-Band-1	X-Band-2
Modulators	19	32	26	18
Klystrons	19	32	26	18
Pulse Compressors	19	32	13	18
Power Dividers	19	32	104	126
Cavities	38	64	104	144

Table 5.9: Amounts of key RF components required for each frequency option.

As an evaluation of currently available/used technology, these options provide a lot of insight into the parameter space required. The need for a burst mode however changes the frequency requirements for the system. None of the commercially available high-power RF klystrons have a common sub-harmonic frequency with the main RF injector (1300 MHz) above 1 MHz, which is not high enough for burst mode operations. As such a shift in the frequency of the RF to a harmonic of 1300 MHz which would be 3250, 5850 and 11700/12 350 MHz respectively.

The C-band option for the klystron is close to the commercial frequency of 5712 MHz which is easily modifiable to the 9^{th} harmonic of the injector (5850 MHz).

Moreover the option of developing or utilising a high-efficiency klystron is favourable due to the large improvement in the energy consumption. A shift from around 40 % to 60-70 % represents a large energy saving and hence lower carbon footprint. Development work at CERN along with industry on C-band and X-band klystrons are ongoing and likely to prove a viable option for improving the energy consumption of the booster [49].

Due to a combination of keeping the machine length small, the possibility of having klystrons manufactured at the required frequency and high-efficiency being explored, this makes the C-band option the most favoured.

5.4 Compression Schemes

Magnetic bunch compression is the method employed at X-ray FELs to generate kA-level peak currents from electron bunches with an initial peak current on the order of 100 A. All X-ray FEL facilities currently operating use four-dipole C-shape magnetic chicanes placed along the linac (either two or three) to achieve this [50, 51]. Bunch compression is achieved by accelerating the beam with an off-crest RF phase preceding the magnetic chicane, which imparts a correlated energy spread (or 'chirp' along the bunch), with the energy of particles in the bunch increasing from the head to the tail. Given the natural negative longitudinal dispersion (R_{56}) of this arrangement of magnets, the trailing particles in the bunch travel along a shorter path through the chicane, resulting in a reduced bunch length at the exit of the bunch compressor.

This process, however, introduces effects that are deleterious to the operation of a hard X-ray FEL, the most prominent of which are emittance dilution and slice energy spread increase due to coherent synchrotron radiation (CSR) [52]. This effect arises due to the coherent emission of radiation from bunched beams travelling along a curved trajectory, such that trailing particles can give a kick in energy to leading particles. As this occurs when the bunch is experiencing non-zero dispersion, the energy kick leaks into position offset. This spoils the both the slice and projected emittances of the bunch in the bending plane, in other words diluting the bunch brightness [53, 54, 55, 56, 57, 58, 59]. The UK XFEL design will incorporate recently devised techniques that should mitigate, even entirely eliminate, the CSR-driven bunch brightness degradation hitherto inherent in magnetic bunch compression schemes. Although these are as-yet unproven, there is high confidence in their efficacy. It is likely that existing XFELs will incorporate such schemes in order to upgrade performance in the near future. The UK XFEL design ensures that these schemes are fully reducible to the proven four dipole C-type for risk mitigation purposes.

5.4.1 Benefits and drawbacks of candidate compression schemes

Owing to the stringent requirements on the FEL quality outlined in Chapter 6, alternative designs to the symmetric C-type magnetic chicane are proposed, namely an asymmetric 5-dipole chicane (hereby referred to as a 'C5' chicane) and an arc compressor. The feasibility of both of these designs has been investigated for a range of bunch charges and compression factors, in order to determine how well they can deliver the required beam parameters to satisfy all of the FEL lines.

The baseline solution is to implement a flexible compression scheme allowing a bunch-by-bunch choice of arc or chicane compression. This will allow optimal compression for each individual FEL. Two physically separate beam paths will be implemented at each compressor. The expectation is that the majority of bunches will traverse the chicanes, therefore kickers will be implemented to deflect the smaller subset of bunches into the arcs.

5.4.1.1 Arc compression

The natural R_{56} of an arc is positive – the opposite sign to a chicane – and therefore the required energy chirp to compress a beam in an arc is also of the opposite sign. The natural second order longitudinal dispersion (T_{566}) of an arc is such that it compensates for RF-imprinted curvature on the bunch longitudinal phase space. Arc compression therefore does not require the external linearisation usually imparted by a higher-harmonic RF section. As only fundamental RF is utilised,

there is no 'folding over' within the longitudinal phase space of the bunch (for an under-compressed bunch) and caustic current spikes cannot form. It is this feature of arc compression that ensures CSR cannot degrade the bunch, there is no trailing current spike to intensely radiate onto the central lasing portion. It is found that arc compression can produce much higher peak currents without emittance degradation, in comparison with all chicane based schemes, including C5. However, as the longitudinal emittance is preserved, this comes at the expense of increased slice and projected energy spread. This combination of parameters is superior for FEL schemes where higher peak currents (greater than $\sim$ 3 kA) are useful, for example single-spike SASE or to generate particularly high pulse energies (in the mJ range). Conversely it is inferior for FEL schemes requiring relatively low slice and projected energy spread, such as seeded and self-seeded schemes. The further tendency of the geometric wakefields to increase this energy chirp is less important for a SC linac where wakes are relatively weak, nevertheless it is intended to investigate the potential of a plasma dechirper which is in principle capable of mitigating this "wrong" sign chirp [60]. It may therefore be possible to extend the applicability of arc compressed bunches to those FEL schemes requiring small energy chirp.

Arc compression has been applied at the MAX-IV linac short pulse facility (SPF), but to date not to drive a free-electron laser, other than a series of short experiments at Eu-XFEL SASE-2 [61]. The MAX-IV linac employs two arcs [62] to compress bunches for a soft X-ray short pulse facility and planned FEL. RMS bunch lengths on the order of a few fs for a 100 pC beam [63] are routinely provided for SPF users since 2020. The arcs at MAX-IV have fixed R_{56} restricting bunch length control to be only a function of preceding linac phase. Linearisation is controllable through one sextupole pair, although this is at the expense of second order dispersion. As part of the MAX-IV soft X-ray proposal, it is planned to enable R_{56} and T_{566} variability, with second order dispersion cancellation, through additional dipoles and the insertion of an additional sextupole pair and an octupole [64]. R_{56} variability is achieved through trajectory variation through the dipole system, thereby avoiding chromatic degradation. We propose an analogous system for UK XFEL.

5.4.1.2 C5 (asymmetric chicane) compression

Cancellation of CSR kicks through control of the transverse beam optics cannot be achieved with a conventional symmetric 4-dipole chicane (either S-type or C-type). By breaking the symmetry of the chicane geometry, however, CSR cancellation can be achieved in principle. The history of this realisation has its roots in the so-called Zeuthen benchmarking chicane campaign of the early 2000's when CSR effects were not fully understood [65]. Recently attention has increased once more as the limitations of the 4-dipole solution have been exposed at first-generation XFEL facilities [66, 67, 68]. It should be emphasised that unlike arc compression this has not yet been experimentally verified, therefore the proposed UK XFEL implementation will be reducible to the proven 4-dipole case.

A chicane geometry can be designed such that the overall CSR kick to a beam undergoing compression is virtually eliminated. The principle of CSR cancellation through balancing the transverse beam optics along curved trajectories is a well-established method in beam spreader designs [69]. For the UK XFEL design, an asymmetric 5-dipole chicane compression scheme has been studied. A chicane naturally anti-linearises the longitudinal phase space of an under-compressed bunch. Therefore in order to achieve a linear energy chirp, a higher-harmonic RF section is required. In common with existing XFELs we choose the 3rd harmonic of the fundamental linac frequency for this. Furthermore, the C5 chicane must, in general, be longer than a symmetric 4-dipole chicane, in order to achieve CSR cancellation.

5.4.2 Bunch compressor designs

Two bunch compressors are placed along the main UK XFEL linac, designed for electron beam energies of 270 and 2100 MeV. The longitudinal dispersion (R_{56}) values at each compressor are based on those of the SHINE XFEL linac [70]: $\pm$61 mm and $\pm$365 mm, respectively. The two bunch compressor types – arc and C5 – have been designed such that they have equivalent length in the z direction, such that the overall machine design is not impacted by the compressor design. In order to achieve maximum flexibility in the electron beam parameters the lattice contains both bunch compressor types. Figure 5.20 shows the implementation at the first bunch compressor where it is necessary for the arc to bypass the (decelerating) linearising RF structures, and to ensure identical energies on re-entry to the linac a short section of fundamental RF is also bypassed.

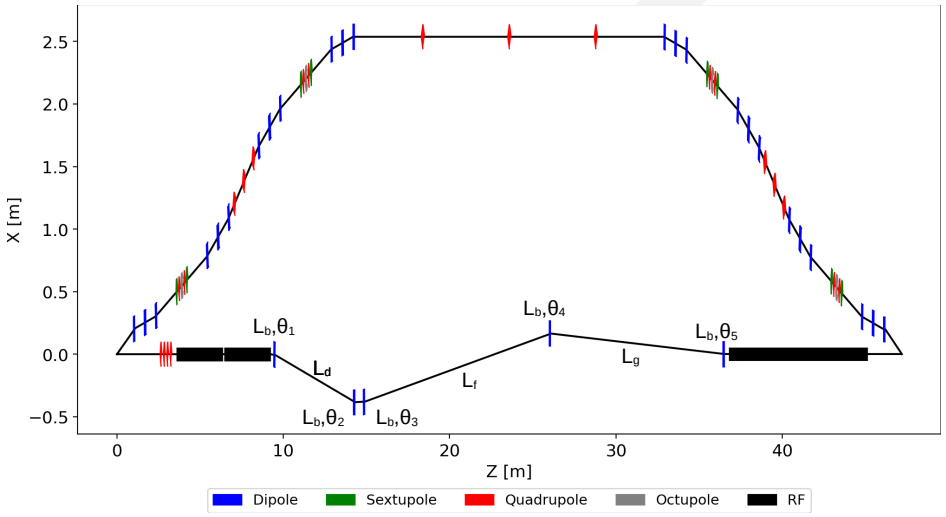

Figure 5.20: Schematic of the first bunch compressor. The beam can be directed onto either the arc (upper beam path) or the C5 chicane (lower beam path) through the use of magnetic or RF kickers.

Bunches can be deflected onto the dispersive path along the arc via magnetic or RF kickers, and brought back onto its original straight path with the same method. This design choice allows either bunch compressor to be selected for compression to deliver bunches with differing longitudinal properties, depending on the requirements of a particular FEL line.

To arrive at an optimal layout, first a regular 4-dipole chicane was considered. The bend angle θ and drift length L_d were optimised to minimise CSR-induced emittance growth in this symmetric chicane. This was used as a starting point for the C5 chicane, a scan was then performed over the additional degrees of freedom, namely the drift lengths between the 4th and 5th dipoles (L_f and L_g, respectively), and the bending angles of the 3rd and 5th dipoles. Firstly, the bend angles θ_3 and θ_5 were scanned, then the drift lengths L_d, L_f and L_g were scanned to achieve the correct R_{56} and to zero the first-order horizontal dispersion R_{16} and its longitudinal derivative R_{26} at the exit of the bunch compressor. The ELEGANT tracking code [71] was used with CSR effects included in both the dipoles and subsequent drift spaces. The bunch compressor length was not constrained to be the same length as the symmetric 4-bend chicane; the assumption being a telescopic matching section can be inserted at will. For both chicanes, the β_x-function decreases along the bunch compressor, reducing the CSR-induced emittance growth as the bunch length decreases. It should be noted during this work an analytic method was proposed to find the optimum parameters without scanning [72]. This greatly simplifies the process of setting the required geometry.

Charge [pC]	75			300		
Scheme	Arc	C5	SC	Arc	C5	SC
L1 phase [°]	+36.5	–33	–31	+36	–32.4	–32.4
L2 phase [°]	+26	–31.1	–31.3	+27.8	–34.8	–34.9
L3 phase [°]	0	0	0	0	0	0

Table 5.10: Linac phasing for different bunch charges and compression schemes. On-crest acceleration is at 0°.

The arc bunch compressors are based on the arc-like variable bunch compressor designed for the MAX-IV linac, presented in [63]. Four achromats are proposed for the UK XFEL arc compressors instead of two as is the case for MAXIV, with the additional achromats mirroring the first two. This means that there is no horizontal translation of the downstream components, and additionally allows cancellation of higher order terms between the two pairs. The drift spaces within the dipole triplets were set to achieve the same absolute R_{56} as the chicanes. The second-order longitudinal dispersion T_{566} was optimised with sextupoles in the achromats to linearise the bunch after compression. The quadrupoles between the achromats were used to reduce the second-order horizontal dispersion, and octupoles in the achromats were used to minimise the horizontal dispersion to third-order. The Twiss parameters were matched at the start of the arc compressors such that they are symmetric around the centre of the bunch compressor, and to provide a phase advance in the bending plane between each achromat that is close to π.

5.4.3 Simulation results

Two bunch modes are presented with charges of 75 pC and 300 pC, compressed to FWHM bunch lengths of 40 fs and 100 fs respectively. Bunch charges of 150 pC and 600 pC were also studied, providing results that followed a similar trend to the results presented below. The linac phase settings for these two bunch modes using the compression schemes considered are shown in Table 5.10. Although the arc compression scheme requires the bunches to be accelerated on the opposite side of crest to chicane compression, this does not preclude the usage of both compressors by subsequent bunches. The timing from the dual injectors (see Chapter 4) can be adjusted such that the bunch will see the correct phase in the section of linac prior to the first compressor, regardless of which compressor is used.

In order to assess the feasibility of each compression scheme for satisfying the stringent demands on the electron beam quality required by all FEL lines (see Chapter 6), scans of the bunch compression factor were performed in linac 2 phase. Figure 5.21 shows the resulting projected normalised emittance and relative energy spread as a function of final bunch length for the 75 pC and 300 pC bunches with three compression schemes considered (arc, C4 & C5). It can be seen clearly in both cases that as the bunch length is decreased the projected emittance grows. This degradation is most significant for the symmetric 4-dipole chicane, which is not able to mitigate the effect of CSR. At the required bunch lengths of 40 fs and 100 fs for the 75 pC and 300 pC bunches respectively, the projected emittance is marginally smallest for the C5 chicane. Similarly, the projected energy spread is smallest for the C5 chicane, although the symmetric chicane reaches similar levels at the required bunch lengths. In the case of the arc, this is larger due to the significant overall energy chirp. As the bunch length decreases further, the C5 projected emittance increases whereas the arc does not. This is because a limit is reached in the (only first order) kick compensation method employed in C5. This is not needed in the arc as there is no trailing spike causing the kick. This scan thus neatly shows the differing physics effects in the choice of compressors.

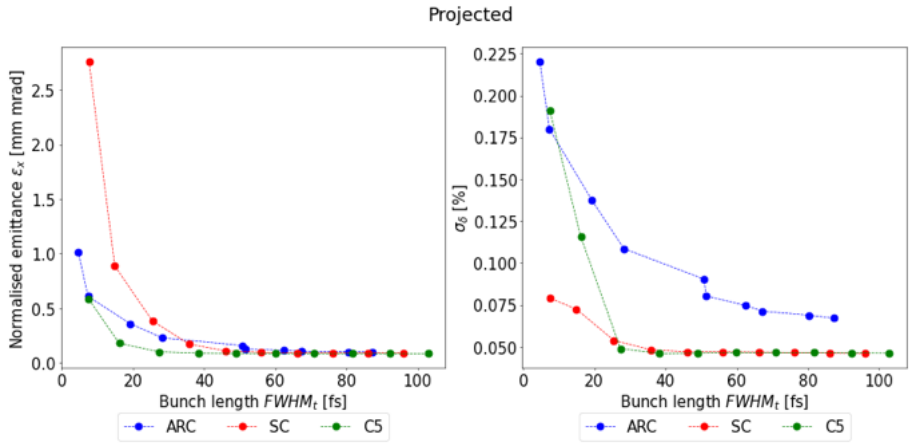

(a) 75 pC

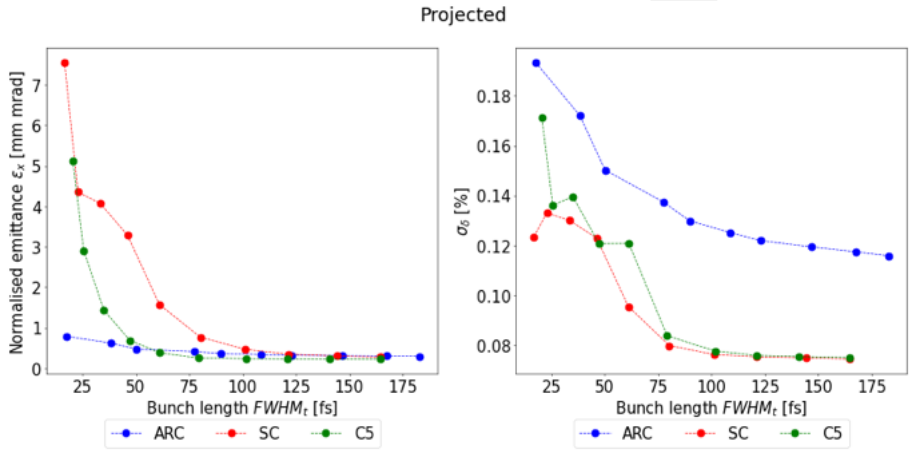

(b) 300 pC

Figure 5.21: Projected bunch properties at the end of the linac as a function of bunch length for the three compression schemes considered at two different bunch charges (above: 75 pC; below: 300 pC). The plots on the left show the projected normalised emittance, and those on the right show the energy spread.

In Figure 5.22 the properties in the core of the bunch at the point of largest peak current are shown. The horizontal normalised emittances in the bunch core are similar for the arc and the C5 chicane at the nominal bunch lengths, while the energy spread in the arc case is of a similar level to that of the C5 case for the 75 pC bunch. The advantage of the arc compressor becomes more evident as the bunch length reduces further for the 300 pC bunch, in the arc neither the normalised emittance nor the energy spread grow significantly, even for highly compressed bunches, while the bunch degrades significantly for both chicanes.

In Figure 5.23 the peak currents are shown as a function of bunch length for the three compression schemes. The peak current is slightly larger for the arc-compressed bunches at the required bunch lengths; this is due to the current profile arising from this compression scheme, in which the core of the bunch forms a central spike, rather than the generally flat current profile with spikes at the head and tail of the bunch, generated by chicane-compressed bunches.

These longitudinal phase space profiles are shown in the top-left of Figures 5.24a and 5.24b. The beams have opposite energy chirps, and, as shown in the bottom-right figures, the bunch currents have different profiles, with the arc-compressed bunch strongly concentrated in the core. The suitability of each of these schemes for the different FEL schemes is further discussed in Chapter 6: essentially seeded FELs require a relatively flat current profile with a smaller energy chirp, and therefore chicane compression is more suitable; conversely short-pulse schemes benefit from the sharp current spike provided by arc compression.

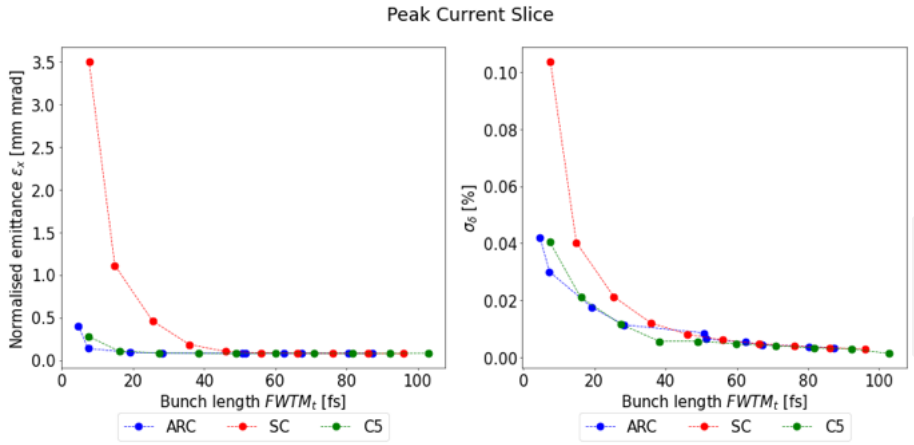

(a) 75 pC

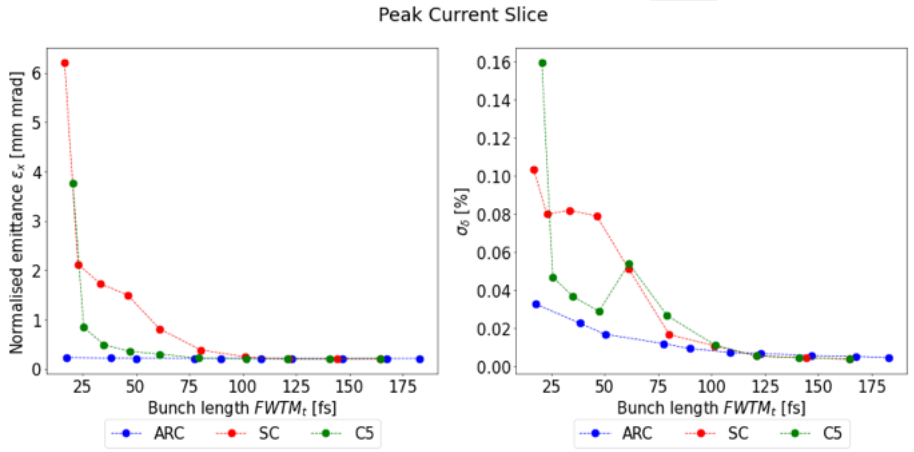

(b) 300 pC

Figure 5.22: Bunch properties in the peak current slice at the end of the linac as a function of bunch length for the three compression schemes considered at two different bunch charges (above: 75 pC; below: 300 pC). The plots on the left show the normalised slice emittance in the bending plane, and those on the right show the slice energy spread.

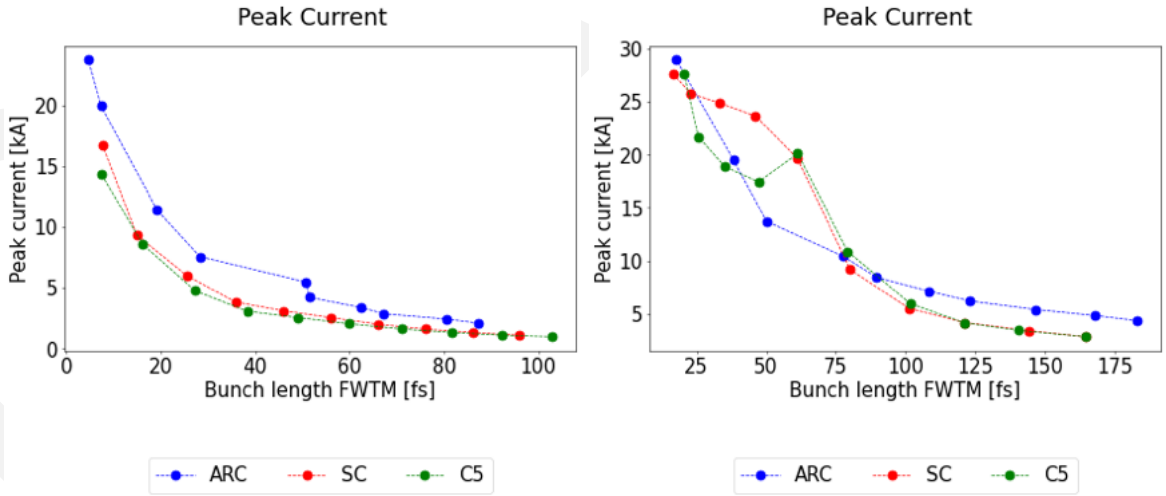

(a) 75 pC **(b)** 300 pC

Figure 5.23: Peak current slice at the end of the linac as a function of bunch length for the three compression schemes considered at two different bunch charges (left: 75 pC; right: 300 pC).

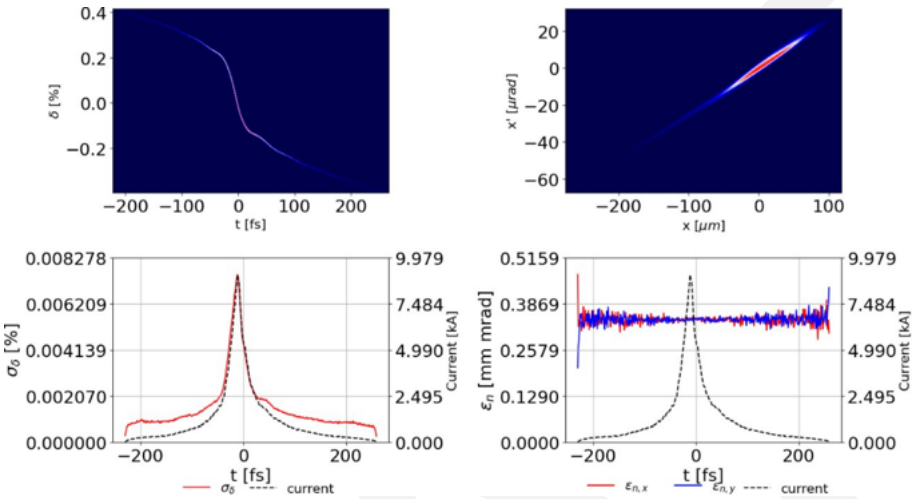

(a) Arc compression

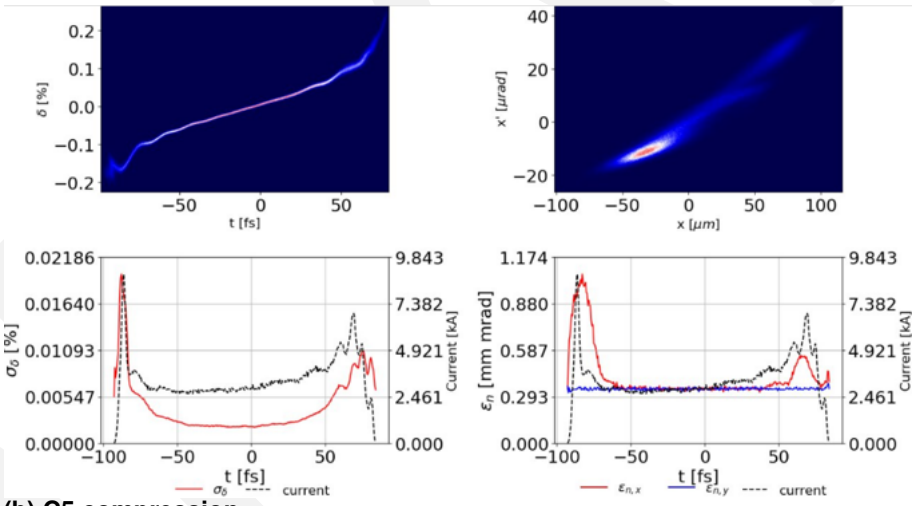

(b) C5 compression

Figure 5.24: Final bunch properties at the exit of the linac for arc (top) and C5 (bottom) 300 pC compressed bunches. Each subfigure contains: Longitudinal phase space; Horizontal phase space; Slice energy spread and peak current; transverse emittances and peak current.

5.4.4 Preliminary Microbunching Studies

Section 5.4.3 focused on comparing the longitudinal beam dynamics, CSR and chromatic effects in each bunch compression compression scheme. While effects that contribute to microbunching instability (MBI) were included in the simulations, microbunching was not directly investigated. The results showed no significant signs of MBI, probably due to very little noise in the initial electron distributions that were generated. Here we show results from preliminary studies comparing MBI in the arc and C5 compression schemes specifically for the 300 pC operating mode.

MBI was studied by performing ELEGANT simulations using electron bunches with artificially added density modulations. Three per scheme were generated, with density modulation wavelengths respectively of 10 µm, 50 µm and 100 µm. In each of these cases, the relative amplitude of density modulation was 0.1 %. These were compared to those with only numerical noise shown in Section 5.4.3. These studies will be extended in a forthcoming publication.

The longitudinal phase space of electron bunches at the exit of linac 3 (entrance of the FEL) from the arc and five dipole chicane compression schemes with different initial density modulations are shown in Figure 5.25. The large energy modulations that are present in the longitudinal phase space distributions are a result of the short range wakefields in linac 3 converting the density modulations to energy modulations [73, 74]. The energy modulations are larger for the cases that had an initial density modulation wavelength of 100 µm. The longitudinal phase space distributions of electron bunches from the five dipole chicane compression scheme have energy and density modulations along the core of the bunch, whilst those from the arc compression scheme are mainly present towards the head and tail and not the core. This is potentially very significant as it is the core of the bunch that partakes in the lasing process.

The slice parameters (current, energy spread and emittance) of electron bunches at the exit of linac 3 (entrance of the FEL) from the arc and five dipole chicane compression schemes with different initial density modulations are shown in Figure 5.26. The current profiles of the electron distributions from the arc and five dipole chicane compression schemes (shown on the left of Figure 5.26) show that density modulations are larger for the cases that had an initial density modulation wavelength of 100 µm. Density modulations are present along the core of an electron bunch from the five dipole chicane compression scheme, while density modulations are mainly present towards the head and tail of an electron distribution from the arc compression scheme. The absence of density modulations in the core of an electron bunch from the arc compression scheme is due to the larger slice energy spread (with the contribution of the chirp to the slice energy spread) in this region, which suppresses micro-bunching gain due to Landau damping [74].

As the head and tail have low currents, these regions of an electron bunch from the arc compression scheme typically have a smaller contribution to the lasing in an FEL than the core of the electron bunch. Therefore, the energy and density modulations at the head and tail of electron bunches from the arc compression scheme may not significantly impact the FEL performance. However, the density and energy modulations that are present along the core of an electron bunch from the five dipole chicane compression scheme, which has a significant contribution to the lasing in an FEL, may lead to worse FEL performance. Although further studies are needed, this indicates less reliance on laser heater suppression of the microbunching instability for the arc compressed case.

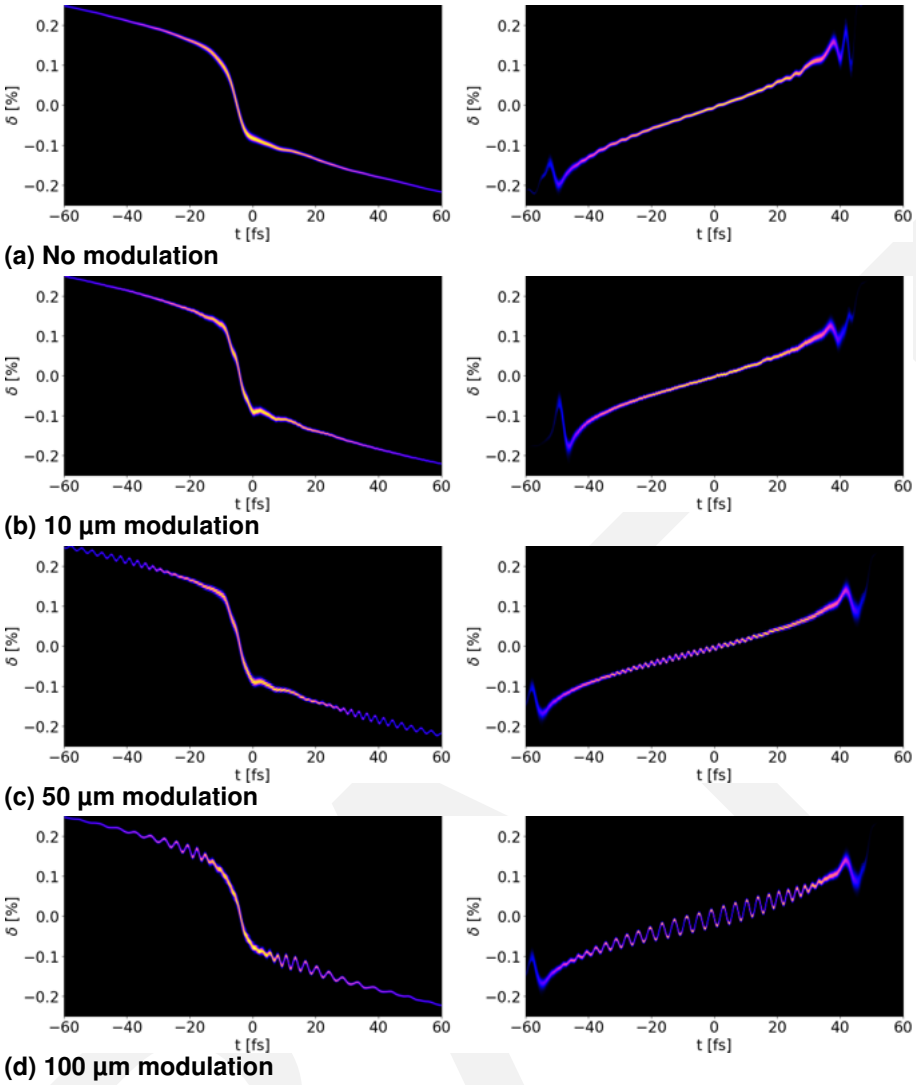

Figure 5.25: Longitudinal phase space of 300 pC electron bunch at the entrance of the FEL compressed by: arc (left) and five dipole chicane (right). The initial electron bunches had no initial density modulation (top/first), 10 µm initial density modulation (second), 50 µm initial density modulation (third), and 100 µm initial density modulation (fourth/bottom).

5.5 Fast Beam Distribution & Spreader Design

The spreader distributes the electron bunches between (up to) ten FEL lines plus a pair of straight-ahead lines for matter in extreme conditions (MEC) user stations. Bunches arrive at the spreader at a maximum 1 MHz rate, each FEL line receives the bunches at a maximum 100 kHz rate. The layout of the spreader is driven by the required layout of the end stations which dictates the transverse separation between the FEL lines of 8 m.

In addition to the 10 main FEL lines and MEC lines, there is an option to build an FEL running in parallel to one of the main FEL lines (double FEL). The separation between these two lines would be 3 m - a reasonable minimum from an engineering and shielding viewpoint. This will be used for ”two colour” experiments, i.e. pulses from two different FEL lines being delivered to the same end station simultaneously.

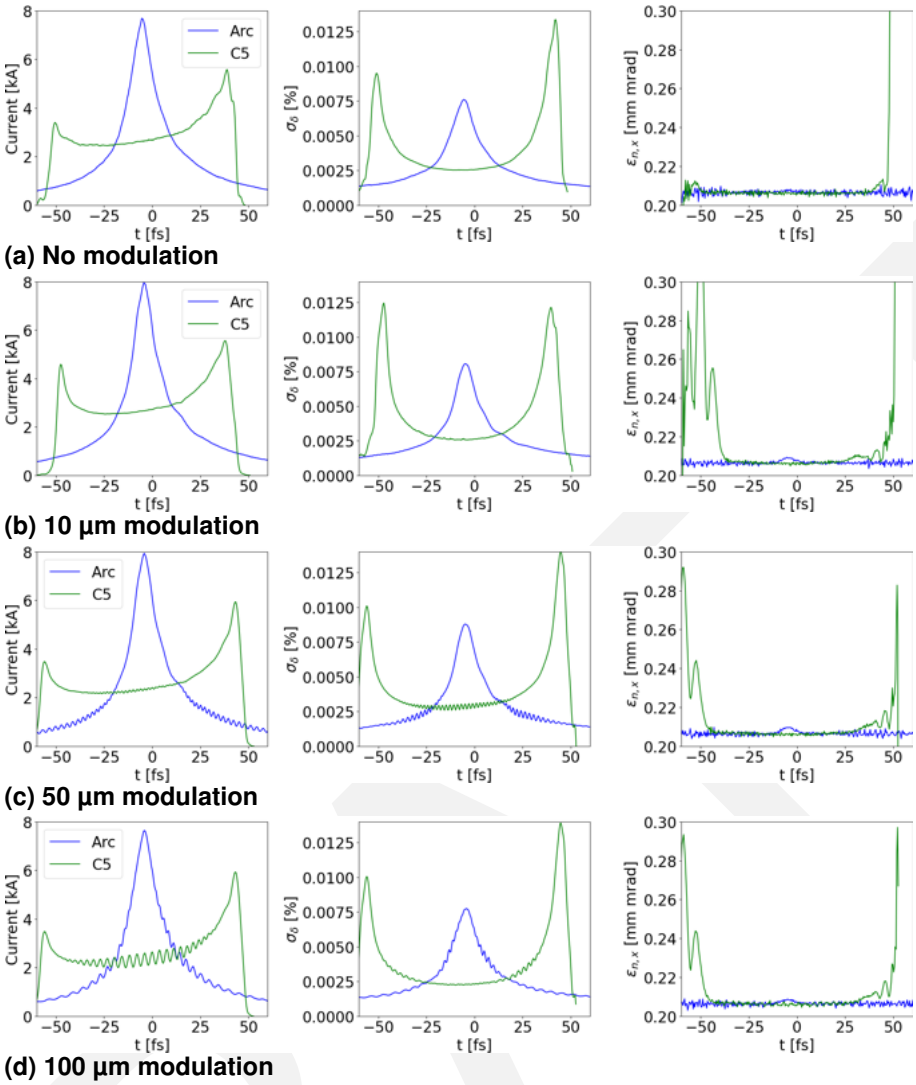

Figure 5.26: Slice current (left), energy spread (middle) and normalised horizontal emittance of the 300 pC electron bunch at the entrance of the FEL from the arc (blue) and five dipole chicane (green) compression schemes. The initial electron bunches had no initial density modulation (top/first), 10 µm initial density modulation (second), 50 µm initial density modulation (third), and 100 µm initial density modulation (fourth/bottom).

5.5.1 Layout Options

A number of layout options were considered. All have benefits and drawbacks in terms of maintaining beam quality and managing the overall footprint of the spreader. An example of a decision dictated by user station requirements is to limit the layout of the spreader to a 2D planar distribution with bending in the horizontal plane. This is due to the difficulty in managing the end stations were they to be staggered both vertically and horizontally. An example of a decision driven by beam dynamic effects is to place the MEC lines straight ahead. This is because bunches driving MEC FELs have the highest charge and energy, therefore are most degraded by CSR .

Two variants of a planar design were considered: a *diagonal wedge* layout and a *trident* layout.

The diagonal wedge shown in Figure 5.27 comprises a single diagonal line diverging from the straight ahead line. From this five FEL lines branch off parallel to straight line. This is mirrored to provide the second five FEL lines. The bunches will be kicked onto the different beamlines using either conventional magnetic kickers or an RF deflecting cavity.

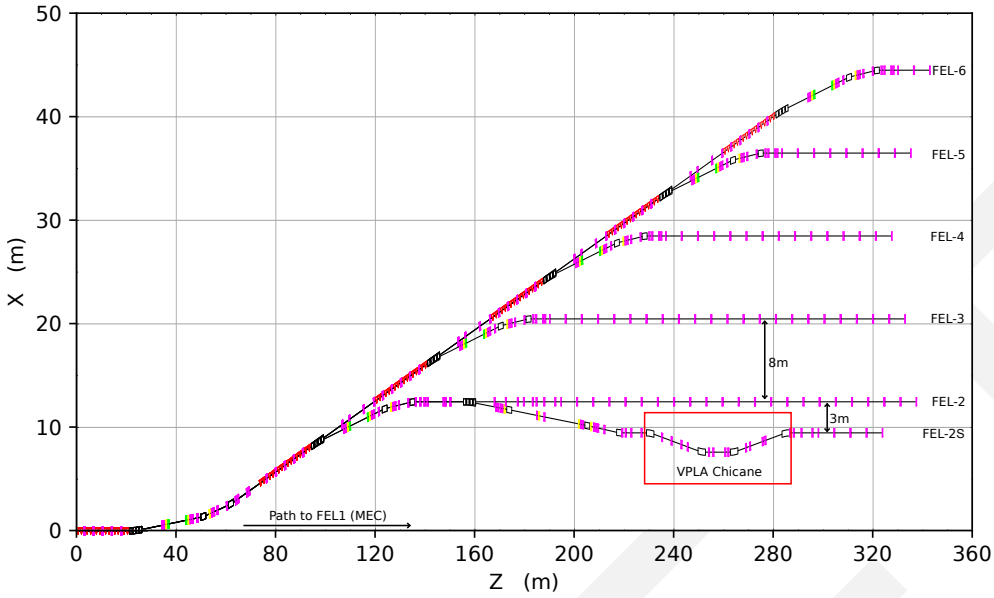

Figure 5.27: Diagonal wedge spreader layout.

The trident differs from this in that only two branches derive from the diagonal line. Both of these branches then separate into 3 more lines in a trident shape as shown in Figure 5.28. The middle two lines in this arrangement would form the double FEL. At the trident points, the beam would be kicked using an RF deflector as current technology for bi-directional magnetic kickers would not achieve the kick strength required at the 1 MHz repetition rate. It is important to note that less optimisation to maintain the beam quality was done on the trident layout than was done on the diagonal wedge layout. Due to this, the footprint of the design shown in Figure 5.28 is probably an underestimate of how big the spreader would be, should this option be used.

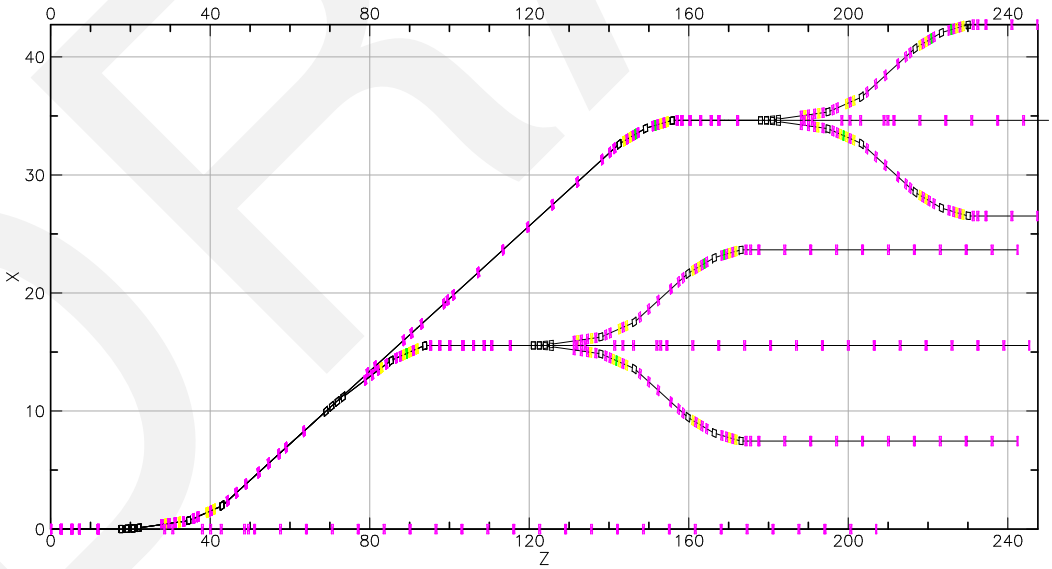

Figure 5.28: Trident spreader layout.

The advantages of the diagonal wedge shape are that the design of one branch can be repeated for all branches. This aids the up-gradability of the facility as adding more beamlines is conceptually trivial due to modularity. The bunches traverse less bends in comparison to the trident to reach the FEL lines, thereby minimising degradation. An advantage of the trident layout is that it significantly

reduces the overall footprint of the spreader.

It was decided to develop the diagonal wedge for the UK XFEL CDOA, however the trident remains an option to explore if the footprint of the facility needs to be reduced.

5.5.2 Two colour simultaneous FEL pulses at single sample

An attractive feature of UK XFEL is to enable two simultaneous pulses onto a single sample with widely separated photon energies. To achieve this, two separate FELs will be placed in the same tunnel with a transverse separation of 3 m. Bunches will be sent down both FELs simultaneously and both FEL pulses will be directed to the same end station by their respective photon transports. Both injectors are required to be in operation to drive the two colour mode. One bunch from each

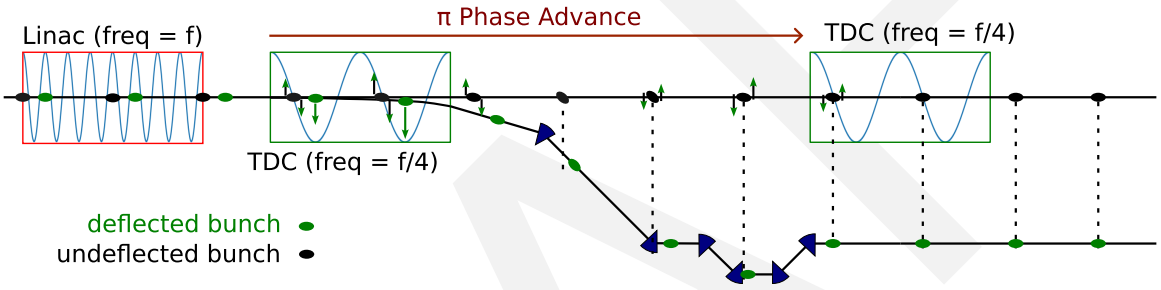

Figure 5.29: The “double bunch” at various point during its passage through the spreader to FELs 2 and 2b. Shown are: the phases that the bunches must enter the linac and the TDC cavities, how a bunch entering the TDC at the zero crossing affects the head tail tilt and how the the transverse offset of the dogleg and VPLA chicane is used to synchronise the two bunches.

injector is placed into the linac separated by an odd number of RF buckets. Upon reaching the spreader this “double bunch” is directed to the tunnel with the double FEL. The double bunch is then separated by an RF deflecting cavity running at the fourth sub-harmonic of the RF frequency. This is illustrated in Figure 5.29. The first of the two bunches will enter at a peak/trough, the second will enter at the zero crossing. The result is that one of the bunches is kicked and will pass through the bending region of a series of septa magnets, and the other will not be kicked and pass through the field free region of the septa. The first bunch will travel along the beamline with the longer path length such that the second bunch catches up. For an ultra-relativistic bunch, the 0.769 ns separation at 1.3 GHz between two bunches in consecutive buckets corresponds to a distance of 23.1 cm, therefore, the path to FEL-2b has to be 23.1 cm longer than the path to FEL-2 for the pulses to be simultaneous. The dogleg subsection of the line to FEL-2b provides 7 cm of the additional required path length. A variable path length adjustment chicane (VPLA) will provide the remaining 16.1 cm when set to its maximum delay. There is a requirement in pump-probe experiments that the timing delay between the pulses be controllable. A larger separation can be achieved by injecting the probe (straight ahead) bunch into a later RF bucket provided that the number of buckets between the pump and probe bunches remains odd. This creates a discrete set of available pump-probe separations in 2 RF bucket (1.52 nm) steps. Continuous control over the pump-probe separation is provided by the VPLA which can delay the pump bunch up to 0.538 ns. The bucket selection and VPLA can be used together to create a range of possible pump-probe separations. The range for the current spreader design is illustrated in Figure 5.30. This could be revisited should further coverage be required experimentally.

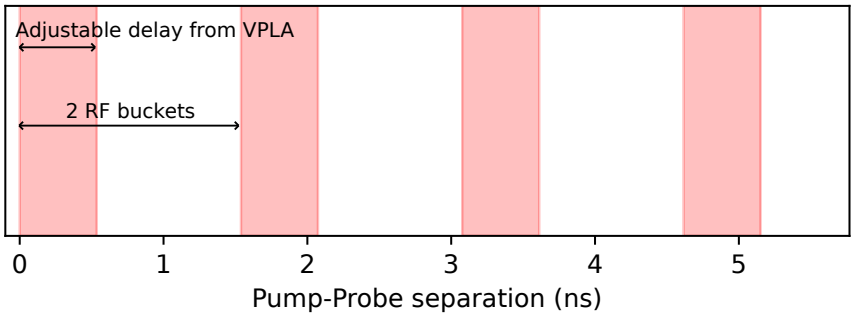

Figure 5.30: The highlighted red regions show the range of possible pump-probe separations that can be provided by the double FEL line using a combination of RF bucket selection and the variable path length adjustment chicane (VPLA).

5.5.3 Fast Kickers

The splits along the beamline are achieved using septa magnets. A kicked beam will pass through the dipole region in the septa and the not-kicked beam will pass through the field free region of the septa. The separation required before entering the septa magnets was assumed to be $\approx$ 15 mm. The kick will be achieved by using either a series of 12 fast magnetic kickers [75] or a single transverse deflecting cavity (TDC). The split in the double FEL has to be achieved using a TDC as explained in the previous section. A decision on whether to use TDC or magnetic kickers for the other splits is postponed to a later project stage after further studies.

The main advantage of using a TDC is that they provide a much stronger kick than the magnetic kickers. The 15 mm kick can be achieved using a single TDC as opposed to a series of 12 magnetic kickers, which together with required gaps and matching quadrupoles totals $\sim$ 18.5 m. This means that using a TDC instead of magnetic kickers could reduce the footprint of the spreader.

The passage of a bunch through a TDC on the zero crossing applies a small head-tail tilt to the bunch. This is corrected using a second TDC. If the TDC was used at every split point, a bunch being directed to FEL-6 would pass through 10 different TDC and be tilted/untilted five times. Although this works well in simulation, there is uncertainty over how difficult this would be to achieve in practice.

Complications arise when using the subsequent TDC in series, as all of the bunches that pass straight ahead through the first TDC have traveled through it at the same phase. At the next TDC, these bunches will need to enter at different phases so that some will be kicked, and some will pass straight ahead. This means that the frequency of each subsequent TDC has to be adjusted so that bunches can be kick/not-kicked. One implication of this is that there would be a lower fraction of RF buckets in the linac that would send each bunch on a specific path through the spreader. The result of this is that the number of highlighted red regions in Figure 5.30 would decrease by a factor of two for each subsequent TDC. For this reason, it is better to use magnetic kickers for the first two split points on the path to FEL 2/2b, and then only use the TDC where it is necessary to, at the point where the paths to FEL 2/2b diverge.

An assessment of the jitter tolerances of kickers will be required in a later project phase.

One final point is to consider the impact that a failure of a component would have on operation. If a single magnetic kicker was to fail, this could be overcome by increasing the strength of the

other 11 kickers to compensate, although this is not ideal, would not cause much disruption to operation. If a TDC was to fail, this would cause more disruption due to there only being 1 before each split. Turning the TDC off would still allow use of the straight ahead path however the FEL on depending on the kick from that TDC would be unusable.

Overall, the first and second split points should use magnetic kickers to provide the kick. The split for the double FEL has to be done using a TDC due to the frequency required. However, for the rest of the splits along the beamline, either magnetic or TDC kickers would work. The use of magnetic kickers is used for this CDOA stage.

5.5.4 Design Principles

The high brightness of bunches supplied to the FEL lines must be preserved during transport, thereby ensuring that maximum photon pulse energy can be generated with minimal undulator transport length. To achieve this, each different path through the spreader must satisfy the following requirements:

- Dispersion and dispersion gradient canceled to third order.
- Isochronous to second order - cumulative R_{56} and T_{566} of zero.
- Lattice functions matched, smooth and bounded throughout (β(s) $\leq$ 120 m).
- Components of adjacent lines cannot overlap.
- Normalised emittance and energy spread growth minimised.

For maximum flexibility in the design process, the spreader was designed in modules. Each module would perform a specific task, for example to bend the beam onto the diagonal line. Each module is self contained and does not rely on surrounding modules to satisfy the beam dynamics requirements listed above. Due to this design decision, the order in which modules are placed in the lattice can be rearranged easily with minimal impact to the beam transport.

The arcs were designed using a standard triple-bend achromat (TBA) lattice as a baseline. A standard TBA could not be used as the initial bending is achieved by a series of kicker and septa magnets which would spoil the exact symmetry required in a TBA. The effect of CSR on the beam was approximated analytically by using a CSR point kick model. This model approximates the effect of CSR as a small kick in x and p_x at the centre of the dipole and is then transported through the rest of the lattice using the transport matrices. Solutions were found such that the total sum of the kicks from all of the dipoles within the lattice cancel at the end of the module. A combination of analytical and numerical techniques were used to find a solution for all of the magnet strengths and drift lengths in each module such that the module satisfies all of the beam dynamics requirements, and the estimates of CSR kicks were cancelled.

5.5.5 Tracking Studies

To verify that the spreader can transport the beam to all of the FEL lines without degradation, tracking studies were performed using BMAD [76]. The initial bunch distributions were taken from tracking simulations through the bunch compressors as shown in Section 5.4.3. The bunches used were from the C5 bunch compressor configuration. The optics was adjusted so that the lattice functions matched what was required at the entrance of the spreader design. The BMAD simulation was setup to include the effects of incoherent (ISR) and coherent (CSR) synchrotron radiation through the dipole magnets. The tracking integration order was set to 6 so that non-linear

dynamics would affect the beam. The results of tracking a 300 pC bunch through to the end of FEL-6 can be seen in Figures 5.31 and 5.32.

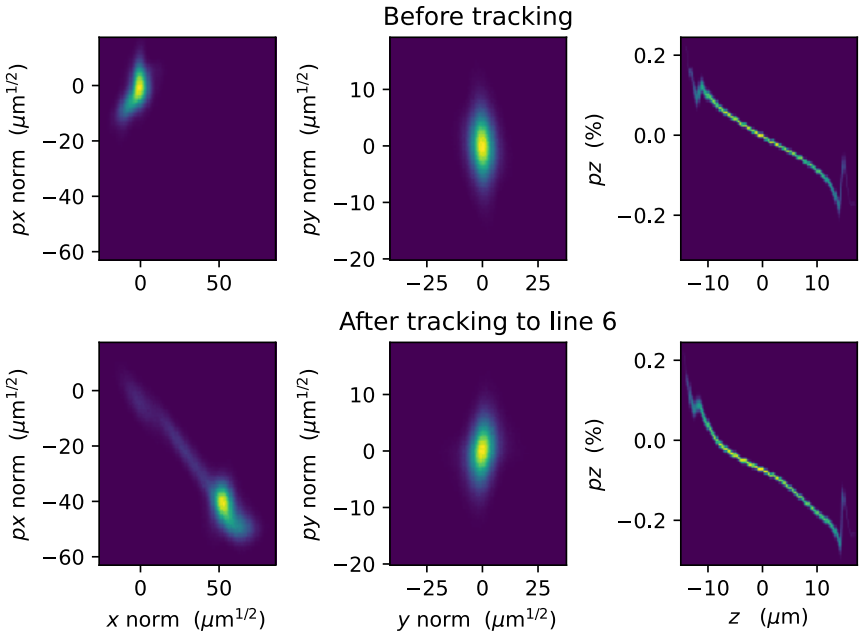

Figure 5.31: The horizontal (left), vertical (centre) and longitudinal (right) phase space of the bunch before (upper) and after (lower) tracking to the end of the spreader line to FEL-6. Horizontal and vertical phase space coordinates have been normalised using the Courant-Snyder parameters to make them invariant through linear beam transport.

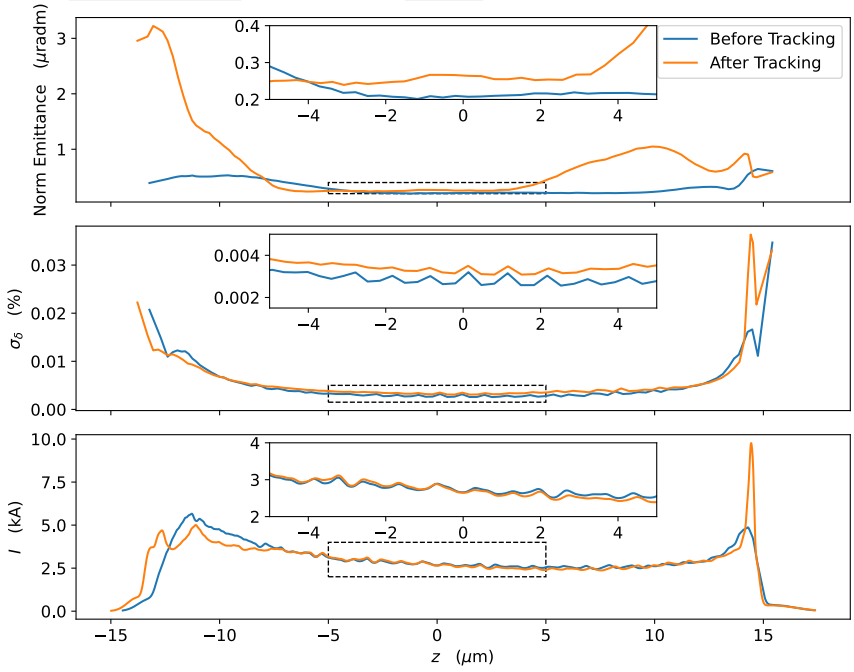

Figure 5.32: The slice normalised horizontal emittance (top), slice energy spread (centre) and current profile (bottom) of the bunch before (blue) and after (orange) tracking to the end of the spreader line to FEL-6. Each plot shows a zoomed-in region to make it easier to read the values at the core of the bunch.

5.6 Plasma Wakefield Acceleration

The UK XFEL project incorporates emerging accelerator concepts within the CDOA as a potential future upgrade pathway, underscoring the project's ambition to develop a next-generation XFEL facility with lasting scientific impact. A plasma-based acceleration stage offers a transformative solution for the next-generation XFEL by serving as a compact, efficient, high-performance energy and brightness booster stage. This section presents how a self-consistent incorporation of advanced accelerator concepts can be realised by uniquely leveraging the capabilities anticipated at the UK XFEL.

5.6.1 Start-to-end simulations results of PWFA booster

We developed a high-fidelity start-to-end simulation chain incorporating realistic electron beams from the UK XFEL linac, optimised as driver beams for the PWFA stage with similar properties presented in Figure 5.24. The PWFA section is modelled with a combination of fully explicit quasi-3D simulations with the Fourier-Bessel Particle-In-Cell (FBPIC) code [77] and simulation tools based on reduced models [78] for computational efficiency. This enables the simulation of metre-scale plasma stages while keeping computational demands manageable. A seamless interface was established between these optimised driver beams and our previously developed high-fidelity PWFA simulation framework [79], which includes both the witness beam transport line and the advanced, unaveraged FEL code Puffin [80] for modelling a plasma-based XFEL. These high-fidelity simulation capabilities allow us to rigorously evaluate how PWFA stages can enhance the performance of the UK XFEL, explore the integration of PWFA technology into the broader facility architecture, and fully leverage the novel capabilities envisioned for the UK XFEL.

We initially investigated the feasibility of a double-bunch PWFA configuration. The UK XFEL linac delivers the driver and witness beam pair at the PWFA stage. Then, the plasma stage facilitates energy transfer from the high-charge driver beam to the low-charge trailing witness beam. Figure 5.33 shows the results of the double-bunch configuration, focusing on boosting the energy of the trailing witness beam. The simulations indicate that the energy of the witness beam can be increased by at least a factor of two, reaching up to 17 GeV. At the same time, the normalised emittance remains at sub-μrad level and the slice (projected) energy spread is at sub-0.1 % scale. The peak slice 6D brightness of the witness beam is $B_{6D} \approx 1.8 \times 10^{17}$ A/m^{2}rad^2/0.1%$\sigma_{W,s}$. Further, with advanced shaping of the driver beam current profile, a high transformer ratio of 4–7 may be achievable [81, 82], opening the potential for near-50 GeV electron beams after a single PWFA stage at the UK XFEL.

Traditionally, such driver–witness pairs are produced using specialised masks [83, 84] placed at the dispersive sections of the linac. However, this method may present significant challenges for machines operating at 100 kHz repetition rates, where radiation levels could become unsustainable. This may also have implications for plasma recovery time [85]. In this context, the unique dual-injector configuration envisioned for the UK XFEL offers a promising alternative (see Chapter 4), enabling direct generation of suitable double bunches for PWFA right at the injector. This capability could be a game-changer for high-repetition-rate PWFA operations in the future.

Next, we optimise the PWFA stage for internal injection study via plasma photocathode injectors for ultra-high brightness witness beam generation [86, 87, 88] in Figure 5.34. We first modelled the injection process using the fully explicit code FBPIC. Then we established a handshake with the quasi-static code Wake-T to simulate the acceleration over a metre-long PWFA stage. Here, only the drive beam from the UK XFEL linac is initially present, setting up a strong blowout regime

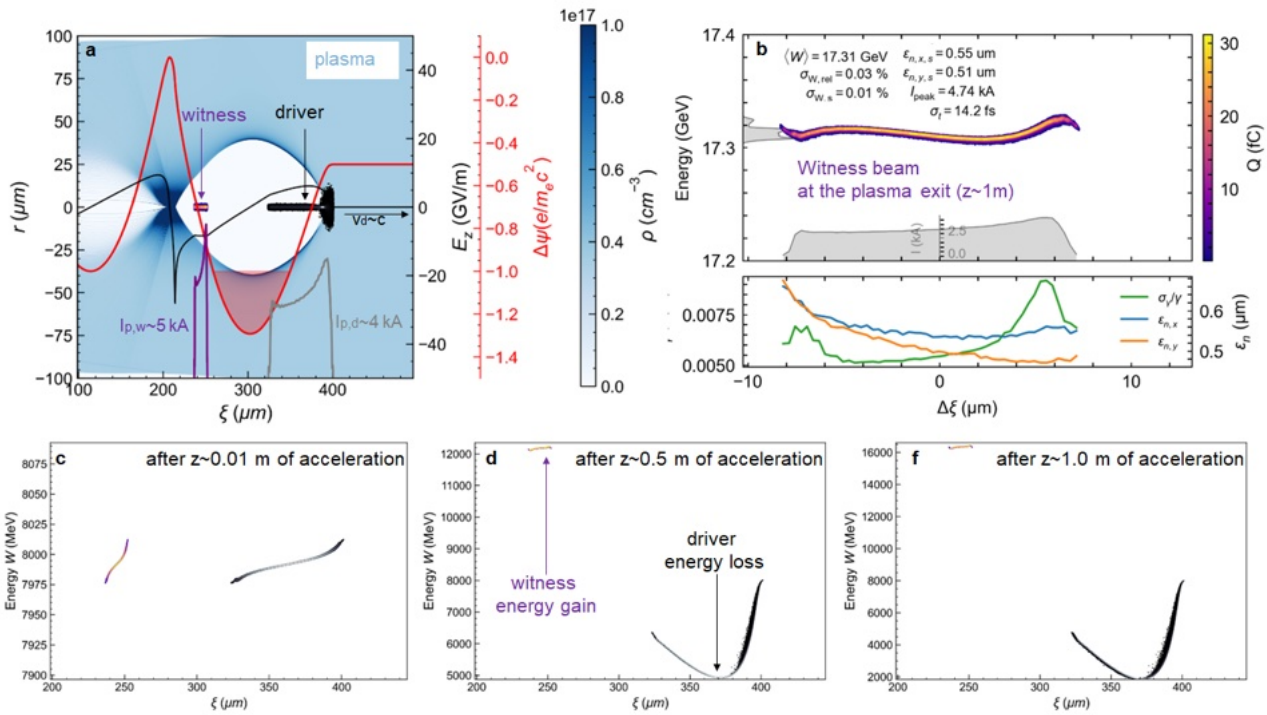

Figure 5.33: Double-bunch PWFA configuration at UK XFEL. (a) An electron driver beam (grey) from the linac propagates through a 1 m long PWFA stage filled with helium plasma (blue), generating a plasma wakefield (solid black line). A trailing witness beam (purple), positioned at the accelerating phase of the wakefield, experiences energy gain. Evolution of the longitudinal phase spaces of both driver and witness beams along the plasma stage length is depicted in the bottom plots (c-f), illustrating the driver beam deceleration and the witness beam acceleration to 17 GeV energy. The resulting witness beam longitudinal phase space and corresponding slice properties at the exit of the plasma stage are shown in panel (b).

in a helium plasma. Then, a sub-mJ class injector laser trailing the driver beam tunnel ionises the helium ions and releases electrons directly inside the blowout (Figure 5.34a). These electrons are rapidly accelerated to relativistic energies, radially and longitudinally compressed in the wakefield (Figure 5.34b). Preliminary simulations suggest that witness beams generated via the plasma photocathode may enable few-femtosecond to sub-femtosecond electron beams with nm-rad normalised emittances and multi-kA peak currents, accelerated to 16.8 GeV beam energies with $\sigma_{W,s} \approx 0.02\%$ slice energy spread. The peak slice 6D brightness of the witness beam is $B_{6D} \approx 5.3 \times 10^{19}$ A/m^{2}rad^2/0.1%$\sigma_{W,s}$ at the exit of the plasma stage (Figure 5.34c-d). This represents an energy boost by a factor of two compared to the initial drive beam and a brightness enhancement by several orders of magnitude compared to the double-bunch scenario. Both electron beams offer excellent prospects for lasing at photon energies $E_{ph} > 20$ keV. As shown in Figure 5.34, a 16 GeV electron beam using a standard undulator (λ_u = 15 mm) can generate photon energies up to E_{ph} = 40 keV. However, the saturation length can vary significantly depending on the normalised emittance of the beam. For instance, our brightness-boosted electron beam could drive an XFEL that reaches saturation within just 10–15 m at E_{ph} = 40 keV.

We employed a beam transport line similar to the configuration developed in Ref. [79] and modelled the witness beam capture and matching using the ELEGANT code. Tracking simulations of the brightness-boosted electron beam revealed that, due to the mm- to cm-scale β-function at the plasma stage exit, the 16.8 GeV witness beam is highly divergent. Focusing gradients on the order of $\simeq$ 3 kT/m are required to capture the beam—beyond the capabilities of high-gradient PMQs. We therefore conclude that plasma-based lenses are necessary for beam capture after the plasma stage, while electromagnetic quadrupoles (EMQs) are sufficient for matching into the

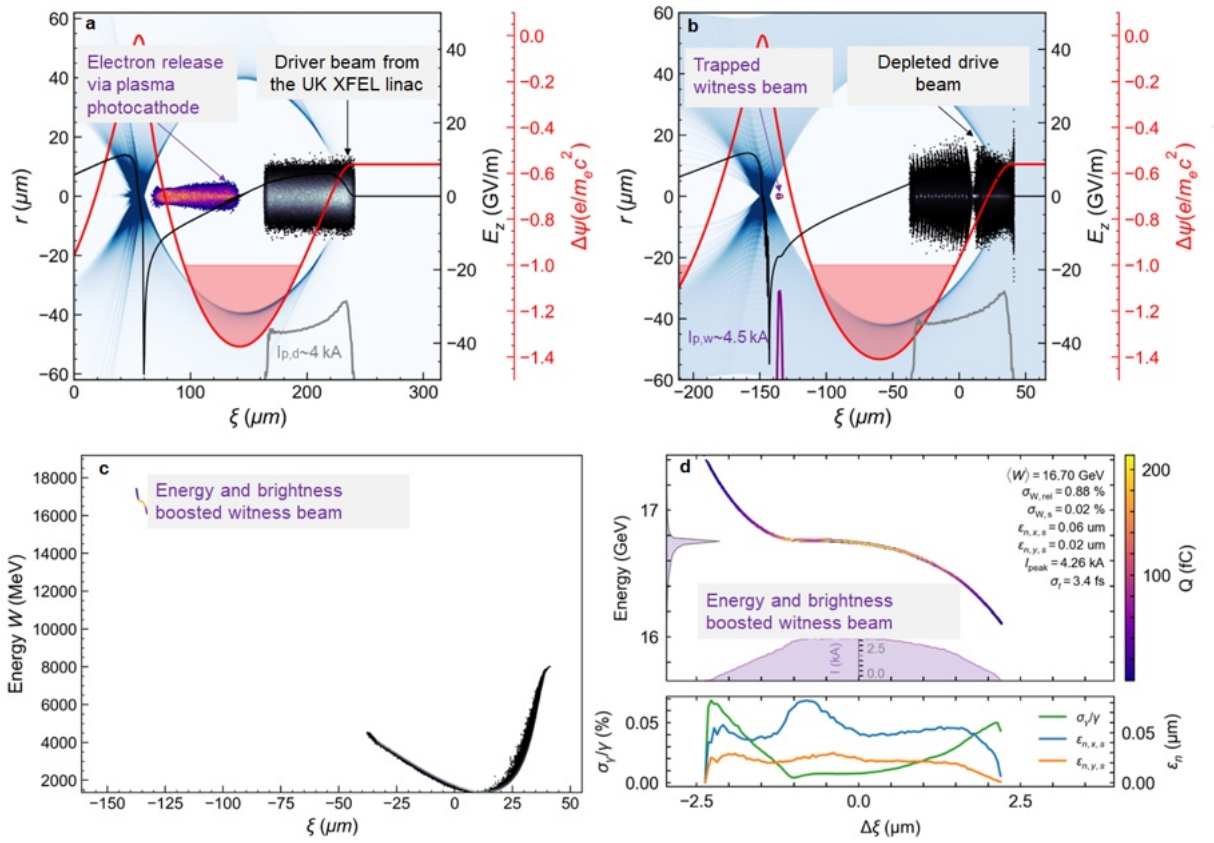

Figure 5.34: Plasma photocathode injection PWFA configuration at UK XFEL. An electron driver beam (grey) from the linac propagates through a one-meter-long PWFA stage filled with helium plasma (blue), generating a plasma wakefield (solid black line). (a) A trailing sub-mJ-class plasma photocathode injector laser pulse releases electrons directly inside the plasma blowout via tunnelling ionisation of helium ions. (b) These released cold electrons form a well-defined witness beam with nm-rad emittance and multi-kA peak current at the back of the wakefield. (c) The witness beam experiences phase-stable acceleration along the PWFA stage and overtakes the driver, reaching multi-GeV beam energy. (d) At the end of the plasma stage, an energy- and brightness-boosted witness beam with exceptional projected and slice beam properties is released into the vacuum.

undulator section. We successfully captured and transported the brightness-boosted witness beam from the plasma stage exit and refocused it into the undulator.

We estimated the XFEL performance of the brightness-boosted witness beam based on Ming Xie theory in Figure 5.35 a-b). We identified prospects for XFEL lasing at photon energies $E_{ph} > 20$ keV. Then, we run a preliminary FEL simulation with the unaveraged code Puffin and verified that potentially lasing at $E_{ph} \approx 60$ keV may be possible. These S2E results are an initial investigation of the prospects of a plasma-based energy and brightness booster stage for the UK XFEL. Future studies will further investigate the novel modalities and capabilities that plasma modules can enable within the TDR phase.

The following Section 5.6.2 will discuss how a plasma-based R&D can be integrated into the wider facility design and what additional research pathways can be expected.

5.6.2 Integration of plasma capabilities into the facility design

The prototyping of crucial components of the plasma booster stages can already be done in the TDR phase of the project. The UK's national accelerator research facilities provide the environment

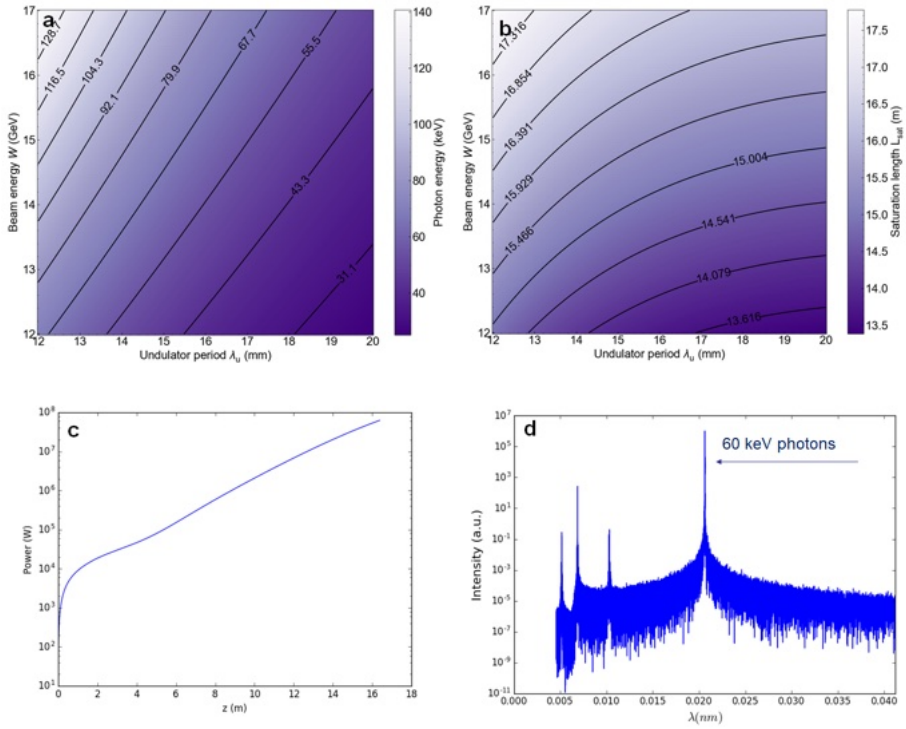

Figure 5.35: Estimation of plasma-XFEL performance and preliminary Puffin XFEL simulation of the brightness-boosted witness beam. (a-b) Estimation of XFEL performances as a function of beam energy and undulator period. (c-d) Preliminary simulation of the plasma-XFEL at E_{ph} = 60 keV.

for systematically advancing plasma components to a high technology readiness level (TRL).

To effectively mature plasma-based acceleration technologies and ensure their seamless incorporation into the main beam lines, we propose a strategic approach centred on a dedicated electron beam line for plasma R&D. An electron beam line enables focused technology development and iterative prototyping under controlled conditions before integration into the core UK XFEL infrastructure. The dedicated electron beam line will serve as a flexible testbed for advanced plasma acceleration experiments, diagnostics, and beam manipulation techniques. By decoupling early-stage R&D from the main user beam lines, we ensure minimal disruption to operational schedules while advancing innovation in areas such as PWFA R&D, injection techniques (e.g., external and internal injection), beam–plasma interaction for real-time monitoring, plasma dechirper [87], and novel beam diagnostics [89].

Further, this R&D beam line will allow the development of prototype components—such as plasma sources, plasma lenses [90], electron–plasma final focusing coupling optics, and staging modules—facilitate rigorous beam-based validation of performance metrics (including emittance preservation, energy gain, and beam stability), enable iterative testing of high-gradient acceleration schemes, and refine beam transport strategies. A key advantage lies in establishing the reliability, reproducibility, and control necessary for transitioning plasma technology into user operational environments.

This strategy ensures that technology transitions only occur once a high TRL has been achieved. By isolating early failures or instabilities, we minimise risk, accumulate valuable operational data, and demonstrate compatibility with FEL-quality beam parameters, such as energy spread below 0.1 % and normalised emittance below 100 nm rad. Ultimately, this approach ensures that only mature, robust plasma technologies are transitioned into the main beam lines, preserving user uptime and performance while enabling cutting-edge advancements in beam physics and light source capabilities.

Alternatively, an afterburner configuration can be considered. For example, after the electron beams have powered the XFEL lines, these spent beams can be recycled for PWFA R&D before being sent to the dump. Such an afterburner PWFA R&D configuration would require minimal investment; however, it would significantly slow progress and limit exploration science compared to a dedicated electron beam line with a programmatic R&D schedule.

Overall, we recommend a dedicated R&D program focusing on developing PWFA booster prototypes and an electron beam line for the UK XFEL in the TDR phase of the project.

5.7 Incorporating Microbunching Instability into OCELOT for Fast Tuning

Coherent synchrotron radiation emission in the bunch compressors and longitudinal space charge effects can lead to an undesirable microbunching instability (MBI) amplifying small perturbations in the longitudinal phase space of the electron bunches. We anticipate that the bunch produced by the injector will not be perfectly smooth due to modulations in the laser intensity profile in the photocathode. MBI in the HEB will then lead to increased slice energy spread. In order to study these effects, simulations of both chicane and arc bunch compressor lattice designs have been compared between Elegant and Ocelot. The latter is used as it provides a convenient testbed for adding additional physics processes which may impact on the MBI.

Figure 5.36 illustrates the high level of agreement for the HEB lattice optics between Elegant and Ocelot implementations. By default the coherent synchrotron radiation effects, longitudinal space charge effects and Wakefield effects leasing to MBI are absent from the Ocelot simulations. To understand the impact of these effects on the longitudinal phase space a series of studies have been carried out to compare the output of the Ocelot simulations, generated using default settings, with Elegant simulations in which each of the effects are systematically switched on and off. Figure 5.37 shows an indicative output for the longitudinal phase space of a standard 4-bend chicane lattice at the end of the HEB. In the case where radiative, space charge and wakefield effects are ignored, the correlation coefficient between Ocelot and Elegant distributions for the spatial longitudinal coordinate is 0.9, and the correlation coefficient for the fractional momentum deviation is consistent with 1.0 within the statistical uncertainty of the simulations. This provides a baseline for the level of agreement allowing the scale of other effects and their subsequent impact on MBI to be evaluated. In the case where synchrotron radiative, space charge and single-bunch geometric wakefield effects are all included in Elegant the correlation coefficient between Ocelot and Elegant for the spatial longitudinal coordinate is –0.2, although the correlation coefficient for the fractional momentum deviation remains within a few percent of 1.0. The level of agreement with the arc lattice is notably lower than with the chicane-based lattices.

Having established the baseline level of agreement, MBI effects can be considered. For these studies the model outlined in [91], which can optionally include intrabeam scattering, has been provisionally implemented in Ocelot. Further studies are ongoing to establish the level of agreement between Ocelot and Elegant, extend to LEB, and compare with experimental data from DESY. Examples of the gain curves from the start to the end of the HEB lattices generated using Elegant are shown in Figure 5.38.

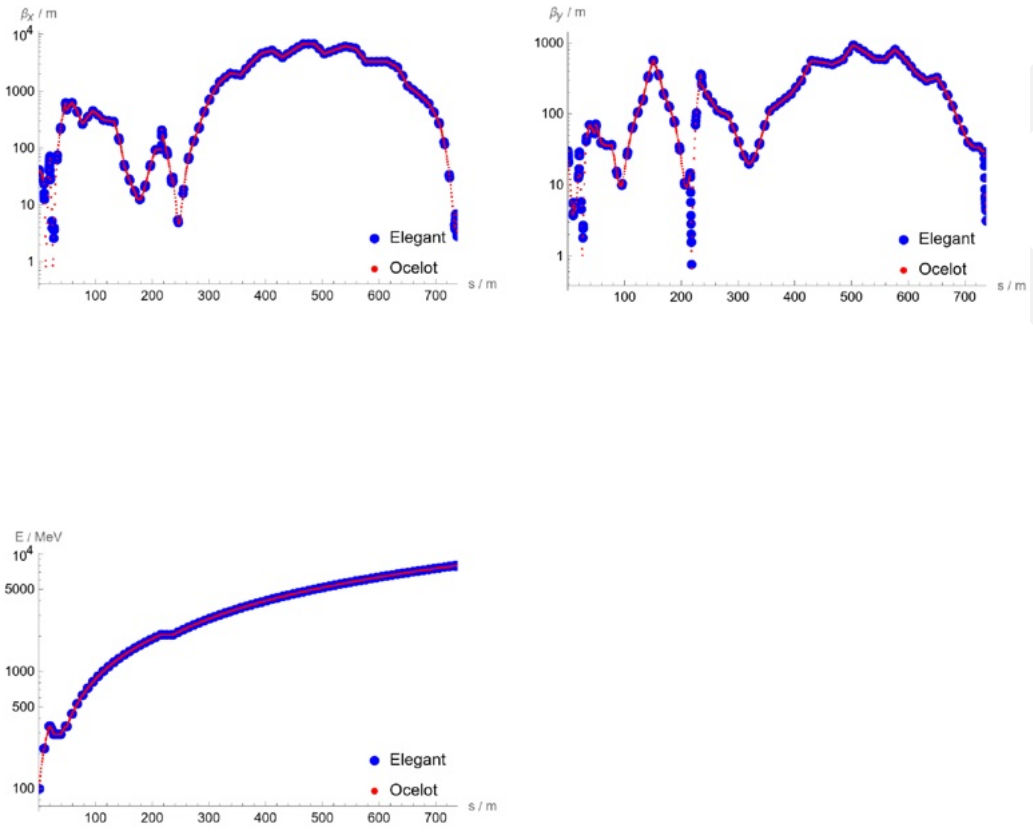

Figure 5.36: The horizontal and vertical beta functions and electron energy for a 4-bend chicane HEB lattice on a logarithmic scale as a function of path length through the lattice showing Elegant (blue) and Ocelot (red).

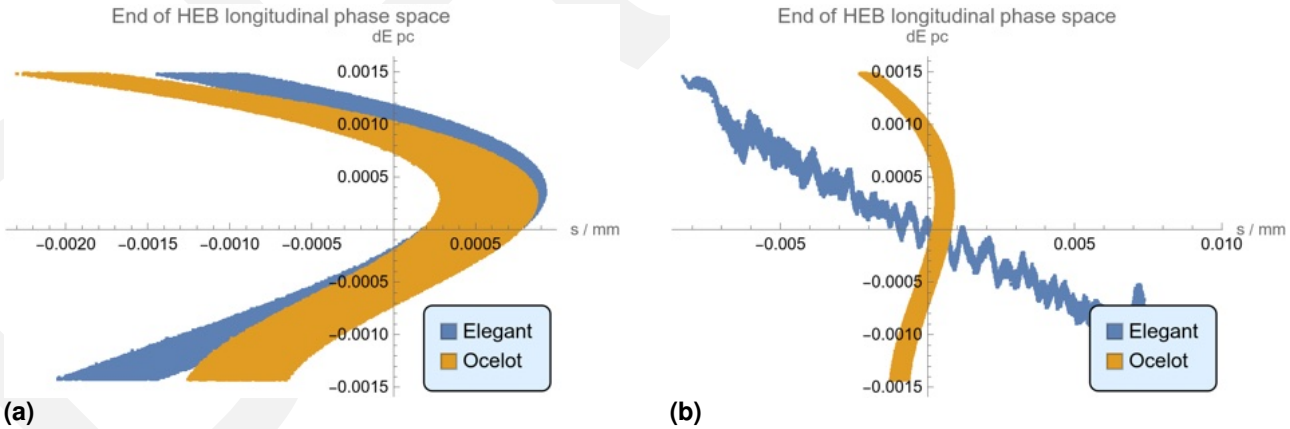

Figure 5.37: Longitudinal phase space distributions at the end of the HEB using a standard 4-bend chicane lattice as simulated using Elegant and Ocelot for a 75 pC bunch. (a) OCELOT compared to an Elegant simulation without synchrotron radiation, longitudinal space charge or wakefield effects. (b) OCELOT compared to an Elegant simulation which includes coherent synchrotron radiation in the dipoles, longitudinal space charge in the drifts and rf cavities, transverse wakefields in the rf cavities and longitudinal wakefields in the rf cavities.

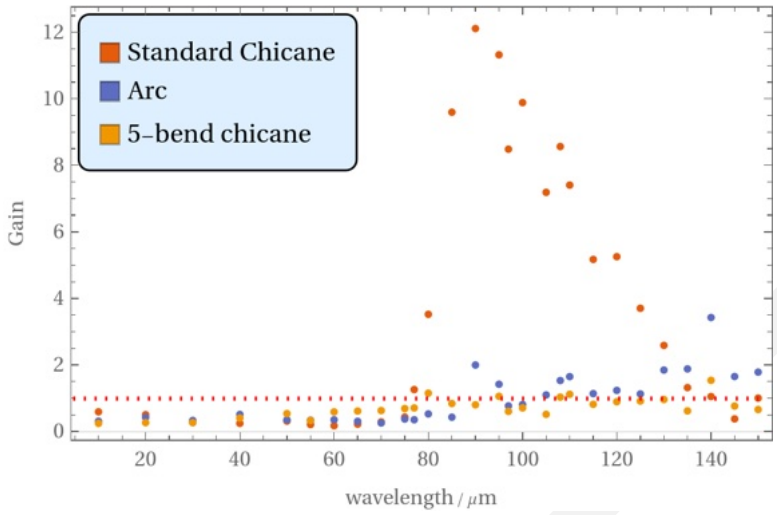

Figure 5.38: The gain as a function of initial density perturbation wavelengths as calculated using Elegant including coherent synchrotron radiation in the dipoles, longitudinal space charge in the drifts and rf cavities, transverse wakefields in the rf cavities and longitudinal wakefields in the rf cavities. Results from a 4-bend chicane lattice are shown in orange, those from an arc lattice are shown in blue, and those from a 5-bend chicane lattice are shown in yellow.

5.8 Collimators & Beam Loss Studies

In the new generation of high average power XFELs, involving transporting thousands of electron bunches per second, a key issue is the beam loss on - and possibly damage to - various accelerator components. Of most concern are the undulator magnets, these are susceptible to demagnetisation from radiation damage which would directly affect FEL performance. The majority of operating FELs (LCLS-I, SwissFEL, PAL, SACLA) are limited to repetition rate around 100 Hz, next generation XFELs, including UK XFEL, propose orders of magnitude higher beam power. Presently operating XFELs relevant here are the European XFEL in recent years and FLASH in recent decades, from which most of the direct practical experience at high power has been gained. The understanding of the damage is an important and rapidly evolving area, and a mitigation concept for beam loss and machine protection is needed as early as possibly in XFEL design. This has been undertaken for new XFELs in Europe, the USA, and China. Approaches vary but typically involve the use of beam collimators. We present here a review of the schemes and some practical experience from beam loss studies, and propose conceptual options for UK XFEL.

5.8.1 Machine Protection Requirements

Undulator demagnetisation caused by radiation damage from beam loss can occur either acutely through direct impact, or chronically from beam halo. Both have been anticipated and observed for many years. Nevertheless, a quantitative understanding and ability to predict accurate dose thresholds to avoid demagnetisation is not complete. Fundamental studies on demagnetisation report a wide range of quantitative results [92]. Limited direct experience has been gained firstly at FLASH [93] and most recently LCLS-I and European XFEL, indicating dose thresholds and effectiveness of mitigation schemes with substantial degree of uncertainty. While collimation system designs often focus on beam halo interception, beam halo is difficult to measure, predict and simulate, and some studies suggest that the issue of single beam loss events in early machine set up is more important than long term beam halo control [94].

In addition to undulator demagnetisation, other beam loss issues (both expected and unexpected) come to light as high power FEL operation becomes a reality. These include, for example at European XFEL, radiation damage to component electronics due to beam-generated synchrotron radiation from undulators, which in a particular case prevented operation of an adjustable undulator [92]. Another example at Eu-XFEL was the damage of X-ray beamstops by the intense X-ray beam which limited the machine repetition rate [95].

5.8.2 Review of Collimation Schemes

The oldest high power short wavelength FEL, FLASH, has a relatively simple scheme where collimators are inserted into the undulator matching section. Whilst dose and demagnetisation has been observed and characterised, the level was low enough that 'it seems that the undulator lifetime is still at least several years' [94]. The fixed gap FLASH undulator has a 'sacrificial' or diagnostic module at its entrance which provides protection and enables periodic measurement of demagnetisation.

European XFEL has a dedicated beam transport section 215 m long performing collimation [96]. Similar to FLASH, each undulator has a diagnostic period at its entrance. Studies of undulator dose, demagnetisation, and collimation performance have been performed [97]. Collimation in the injector, rather than a dedicated high energy collimation section, significantly contributes to overall machine protection. In early beam operation, measured undulator dose and demagnetisation was of concern and dedicated investigations were performed which indicated some of the measured dose arose from undulator synchrotron radiation, which is not demagnetising. In addition, the dose measurements were seen to stabilise after early beam operation [98]. Radiation damage to electronics of the motors of the APPLE-X afterburner undulator was seen during its commissioning which was again found to be due to synchrotron radiation from the upstream main SASE undulator, despite SR absorbers being in place throughout operation; new absorbers with an modified design and extra shielding provided effective mitigation of the radiation.

LCLS-I has been in operation since 2009 at a maximum repetition rate of 120 Hz single bunch. It has a collimation section in the 'dog leg' beam transport from linac to undulator, including several betatron beam collimators within 100 m of the undulator [99]. In 2015 undulator demagnetisation was measured at the level of up to 5% [100], and it was indicated that the collimators near the undulator may generate beam halo via scattering. This was considered in the LCLS-II design [51] which removed existing linac-to-undulator (LTU) collimators, performing collimation further upstream from the undulator(s) in several different locations, with none remaining after the final bend(s) before the undulator.

The SHINE XFEL (whose injector has been commissioned and is due to begin lasing in 2025 [101]) does not have a dedicated collimation section. Collimators are integrated into the beam switchyard section in the high energy beam transport section [102]. Particle tracking simulations have been performed, and the collimation performance for both halo mitigation and machine failure is found to be sufficient. However compared to Eu-XFEL, the collimators are much closer to the FEL and information is limited on whether simulations of undulator damage due to secondary/scattering simulations has been performed.

5.8.3 Main Issues and Choices

The main issue we consider is beam halo removal for undulator protection. The principle of containing the beam halo within a safe region of phase space is well established in methods of lattice design. These methods are implemented in all the schemes mentioned above, and can be relatively easily added to the UK XFEL design (at the cost of increasing the machine length in the case of a dedicated collimation section like European XFEL). However there are several complexities and uncertainties. For example beam halo generation and transport is very difficult to simulate and predict. Thus the specific element of the performance of a given collimation design is difficult to predict in advance, or to benchmark/identify when operational. Eu-XFEL has demonstrated undulator durability over several years and performed simulation/measurement studies of its collimation systems but the precise effectiveness of all the various factors involved is not fully established. The same is true of the only other long-operating high power FEL, FLASH.

One specific element which has been explored in more detail in Eu-XFEL is the scattering effect of collimators. This leads to the characteristic that simply reducing the collimation aperture further and further does not lead to greater and greater protection of the undulators. In a study for a short-pulse XFEL scheme [92] the effect of the collimation system was studied, including this scattering effect, which found that not the smallest but intermediate collimation apertures provided the best undulator protection. In LCLS-I operation it too has been noticed in operation that the original collimation section both generated and reduced beam halo and this influenced the design for the collimation of LCLS-II.

Other specific elements in halo collimation, whose importance has not been isolated / identified include wakefield effects, beam-gas scattering, and contribution of dark current. Indicative observations and simulations exist for all of them but the precise importance of each is not fully understood.

Machine failure is another issue that the collimation design should incorporate, in combination with a machine protection system based on interlocks and beam loss detectors. In the event of failures such as of magnets or kickers, the collimation system should both protect the undulator and should itself survive the failure. The detailed understanding of these kinds of events is lower than that of beam halo, due to their relative infrequency and unpredictability. But Eu-XFEL and SHINE studies mentioned above include this consideration in the design of their collimation.

Finally, other effects not expected may quite reasonably arise, which fall into the general area of machine protection. One example is the damage that synchrotron radiation may cause, which as mentioned above at Eu-XFEL caused significant issues. Close consultation and review of existing machines is essential to identify such effects.

5.8.4 Conclusion

The UK XFEL machine protection system should include:

- Transverse collimation for the high energy beam with adequate phase advances, either existing in dedicated beam transport sections or interleaved with another section.
- Energy collimation in the same manner.
- Diagnostic/sacrificial undulator segments.
- Machine protection provided by beam loss monitoring and interlocks.

Other possibilities, which can be added to any final lattice design, include the use of RF kickers to reduce dark current, and collimation within the injector mergers, depending on cost and ease of integration.

Not all high power XFEL machines have a dedicated collimation section, However Eu-XFEL is the only existing such machine with several years experience of undulator radiation damage and demagnetisation, and does have dedicated collimation. However the necessity of this is still not fully established, with FLASH indicating a simpler collimation scheme can work in an EUV-FEL machine. LCLS-II and SHINE do not have dedicated collimation sections, but their collimation performance has not at time of writing been demonstrated. Ultimately there remains uncertainty in both the advantages and disadvantages of any particular collimation design, and the final choice for UK XFEL should consider factors other than undulator protection, such as machine cost and beam set-up consequences.

DRAFT

5.9 Appendix 1: Benchmarking the CST Model for Long-range Wakefields

The choice of TESLA 9 cell superconducting RF cavities is discussed in Section 5.3. This decision required reliable modelling of the structure and subsequent analysis of the EM fields. To this end, CST [103] was used to benchmark against experimentally validated previous results [30].

The first objective was to tune the geometric parameters to optimise the main accelerating TM_{010} π-mode. Figure 5.39 shows the fundamental accelerating mode rendered in CST (monopole mode 9 in the first passband).

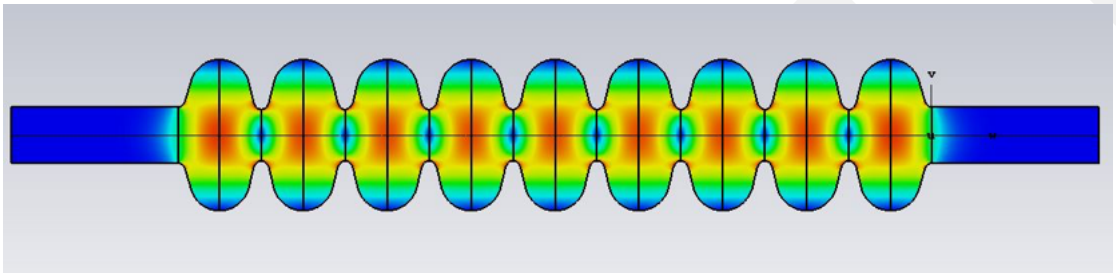

Figure 5.39: The main accelerating TM_{010} π mode of the TESLA 9-cell cavity rendered in CST.

The main feature of this mode is its field flatness (η_{ff}), defined as [104]

$$\eta_{ff} = 1 - \frac{E_{zmax} - E_{zmin}}{\frac{1}{N}\sum_{i=1}^{N} E_{zi}} \cdot 100\,\text{p\%}, \tag{5.23}$$

where E_{zi} is the maximum value of the on-axis z component of the electric field in cell i and E_{zmax} and E_{zmin} are the maximum and minimum value of all E_{zi} respectively.
The field flatness of our CST model is 99.1 %, see Figure 5.40.

With the objective of characterising the transverse and longitudinal long-range wakes, we simulated the first six monopole and dipole passbands and extracted the loss factors, the first step in calculating the long-range wake potentials. Concentrating on the dipole modes and the transverse long-range wakes and in order to be confident of our model, we first chose an offset of 8 mm, approximately $\frac{1}{4}$ if the distance to the iris radius from the axis and sampled the z component of the electric field (E_z) of the dipole modes to extract field profiles, mode frequencies are delivered by CST by default. From the field profiles we could extract the phase advance (ϕ) of each mode by applying the Floquet condition via the following equation,

$$\phi = \cos^{-1}\left(\frac{E_z(r,\theta,z+L) + E_z(r,\theta,z-L)}{2E_z(r,\theta,z)}\right), \tag{5.24}$$

where, $E_z(r,\theta,z)$ is the z component of the electric field of the mode in question at an offset parallel to the axis of r (8 mm in our case) and θ chosen to point at the peak of the dipole field. $E_z(r,\theta,z+L)$ and $E_z(r,\theta,z-L)$ are the equivalent points in the following and previous cells, respectively, L being the longitudinal cell length. Figure 5.41 shows this for the 7^{th} dipole mode, selected for its proximity to the light line (see Figure 5.42), and therefore, relatively large kick factor of 101.5 V/[pC $\cdot$ m^2].

Now we have the frequencies and phase advances for the first 6 dipole passbands, we can plot the dispersion curves and overlay the light line to highlight which modes might affect the beam.

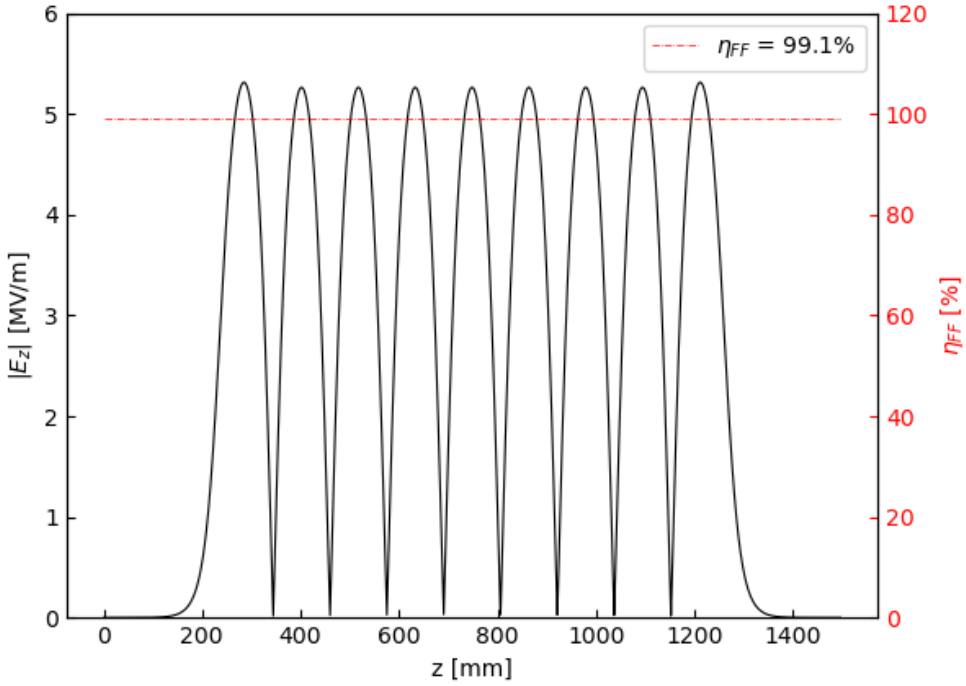

Figure 5.40: The on-axis z component of the electric field of the main accelerating TM_{010} π mode of the TESLA 9-cell cavity, with η_{ff} = 99.1%.

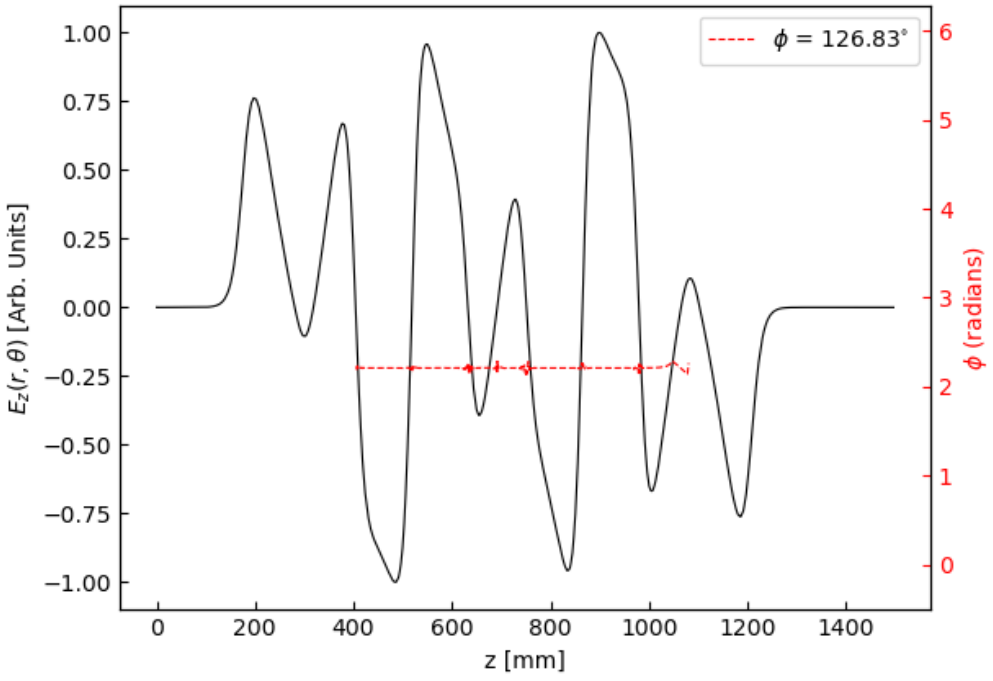

Figure 5.41: The normalised z component of the electric field of the 7th TM_{110} dipole mode of the TESLA 9-cell cavity at a radial offset of 8 mm (black), with the phase advance (ϕ = 126.8°) calculated using Equation 5.24 plotted in red.

Figure 5.42 shows the dispersion curves of the first six dipole passbands calculated by the method outlined above and compared to Wanzenberg's DESY results [30].

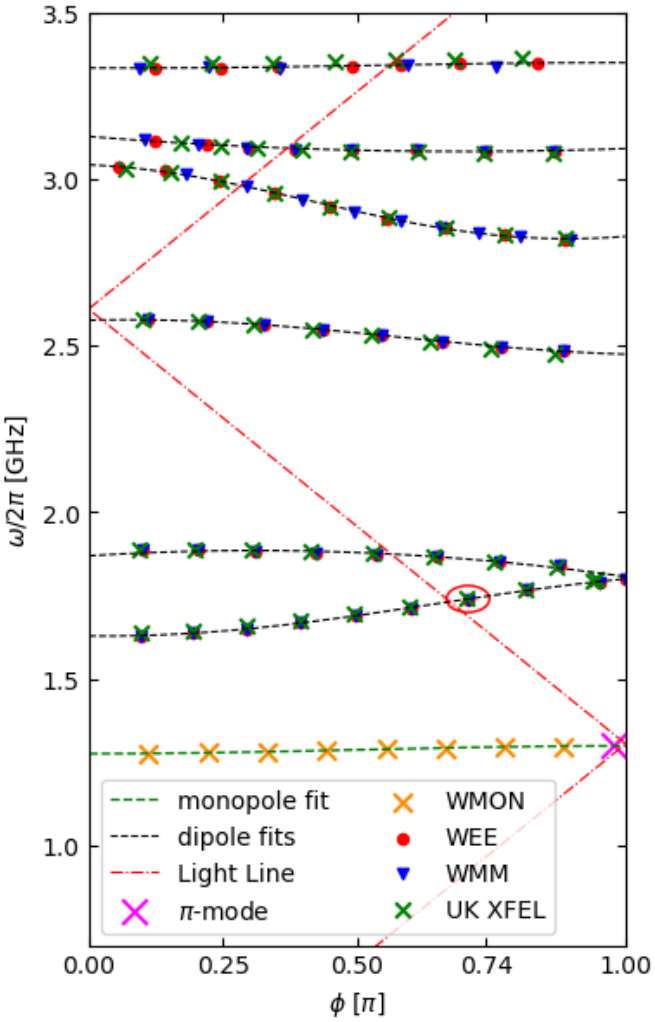

Figure 5.42: The Brillouin diagram showing the dispersion curves of the first six dipole passbands and the equivalent modes from the Wanzenberg DESY study [30]. Here, "WEE" and "WMM" refer to the Wanzenberg study with electric-electric and magnetic-magnetic boundaries in the beampipes, respectively. Also included are the first nine monopole modes (WMON) with the main accelerating π-mode highlights in magenta. The red circle highlights dipole mode 7, the off-axis E_z profile of which is shown in Figure 5.41

5.10 Appendix 2: Benchmarking ELEGANT and PLACET particle tracking codes for Long Range Wakefields

Beam dynamic simulations of UK XFEL team have been conducted using the ELEGANT code [71]. ELEGANT has the capacity to include the effects that short-range wakes have on bunches, but currently does not have the capability to account for the long-range wakes induced by previous bunches. To address this, the CERN-developed code PLACET [105] was used to judge the effect of long-range wakes on key beam parameters such as transverse emittance and energy spread. The first step was to set up the bunch in PLACET using ELEGANT input parameters, see Table 5.11.

The second step was to benchmark each lattice element type, these being:

1. Drift (ensures the bunch is configured correctly)
2. Quadrupole magnet,
3. Dipole magnet,

4. TESLA 9-cell RF cavity,
5. Harmonic RF cavity.

Table 5.11: Table showing the UK XFEL 75 pC bunch characteristics, the input values for ELEGANT and PLACET and the conversion factors from ELEGANT to PLACET

.

Variable name	ELEGANT value	ELEGANT unit	PLACET value	PLACET unit	Conversion factor
E_0	195.7	relativistic γ	0.1	GeV	$m_e \cdot 10^{-9}$
σ_s	10^{-3}	m	10^{-3}	s	1/c (c = 1)
σ_E	10^{-5}	fraction of E	10^{-6}	GeV	E_0
ϵ_{Nx}	82	nm · rad	82	nm · rad	1
ϵ_{Ny}	82	nm · rad	82	nm · rad	1
α_x	–0.1	m	–0.1	m	1
α_y	–0.1	m	–0.1	m	1
β_x	10	m	10	m	1
β_y	10	m	10	m	1

A Python script was written that parses the ELEGANT input files and outputs equivalent PLACET files. Using this method the bunch was characterised after passing through each lattice element. The results for the 3.9 GHz 3rd harmonic cavity are shown in Figure 5.43.

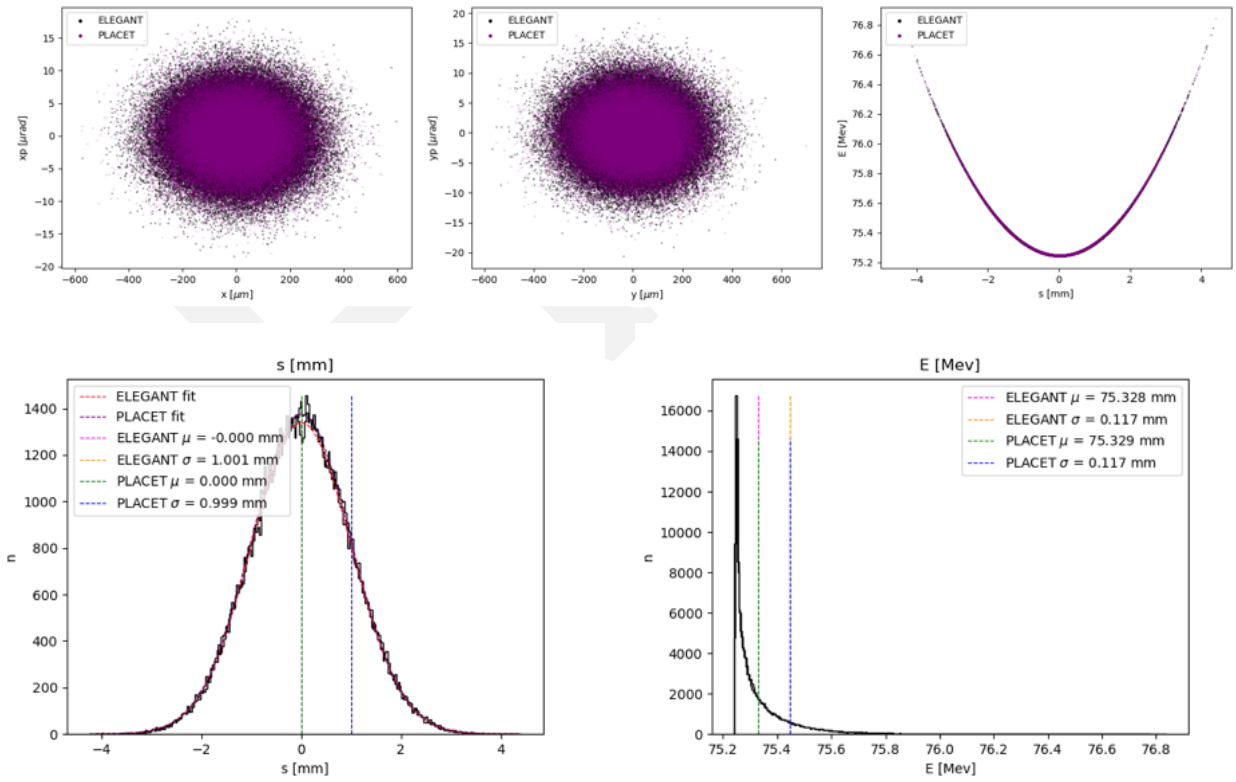

Figure 5.43: The diagnostic plots to verify parity between the ELEGANT and PLACET code bases, with ELEGANT shown in black and PLACET in purple for the 3rd harmonic 3.9 GHz cavity with the bunch coinciding with the trough of the RF phase. **Top left:** Horizontal phase space. **Top middle:** Vertical phase space. **Top right:** Longitudinal phase space. **Bottom left:** Histogram of the longitudinal distribution of the bunch. **Bottom right:** Histogram of the energy distribution of the bunch.

References for Chapter 5

[1] D Gonnella et al. “The LCLS-II HE High Q and Gradient R&D Program”. In: *Proc. SRF'19*. JACoW Publishing, Geneva, Switzerland, 2019, pp. 154–158. DOI: 10.18429/JACoW-SRF2019-MOP045. URL: https://jacow.org/srf2019/papers/MOP045.pdf.

[2] Y. Zong et al. “Realization of Accelerating Gradient Larger than 25 MV/m on High-Q 1.3 GHz 9-Cell Cavities for SHINE”. In: *Proc. SRF'23* (Grand Rapids, MI, USA). International Conference on RF Superconductivity 21. JACoW Publishing, Geneva, Switzerland, Aug. 2023, pp. 658–661. ISBN: 978-3-95-450234-9. DOI: 10.18429/JACoW-SRF2023-WEPWB044.

[3] M Checchin. “Status of Cavity and Cryomodule Production for LCLS-II-HE”. Aug. 2023. URL: https://accelconf.web.cern.ch/srf2023/talks/moiaa06_talk.pdf.

[4] W. Singer et al. “Production of superconducting 1.3-GHz cavities for the European X-ray Free Electron Laser”. In: *Physical Review Accelerators and Beams* 19.9 (Sept. 2016), p. 092001. ISSN: 2469-9888. DOI: 10.1103/PhysRevAccelBeams.19.092001.

[5] D Reschke. “Challenges in ILC SCRF Technology”. In: *Proc. APAC'07*. JACoW Publishing, Geneva, Switzerland, 2007, pp. 26–30. URL: https://jacow.org/a07/papers/MOOPMA01.pdf.

[6] A Yamamoto, M C Ross, and N J Walker. “Advances in SRF Development for ILC”. In: *Proc. SRF'11*. JACoW Publishing, Geneva, Switzerland, 2011, pp. 7–12. URL: https://jacow.org/SRF2011/papers/MOIOA02.pdf.

[7] L Merminga and J Delayen. *On the optimization of Qext under heavy beam loading and in the presence of microphonics*. Tech. rep. 1996. URL: https://www.jlab.org/uspas11/MISC/Beam%20loading%20TN.pdf.

[8] Sam Posen and Matthias Liepe. “Mechanical optimization of superconducting cavities in continuous wave operation”. In: *Physical Review Special Topics - Accelerators and Beams* 15.2 (Feb. 2012), p. 022002. ISSN: 1098-4402. DOI: 10.1103/PhysRevSTAB.15.022002.

[9] R D Porter et al. “Microphonics in the LCLS-II Superconducting Linac”. In: *Proc. SRF'23*. International Conference on RF Superconductivity 21. JACoW Publishing, Geneva, Switzerland, Aug. 2023, pp. 302–305. ISBN: 978-3-95-450234-9. DOI: 10.18429/JACoW-SRF2023-MOPMB081.

[10] Zhen-Yu Ma et al. “High RF power tests of the first 1.3 GHz fundamental power coupler prototypes for the SHINE project”. In: *Nuclear Science and Techniques* 33.1 (Jan. 2022), p. 10. ISSN: 1001-8042. DOI: 10.1007/s41365-022-00984-5.

[11] A. - M. Valente-Feliciano et al. “Next-Generation Superconducting RF Technology based on Advanced Thin Film Technologies and Innovative Materials for Accelerator Enhanced Performance and Energy Reach”. In: (Apr. 2022). URL: http://arxiv.org/abs/2204.02536.

[12] S Posen et al. “Advances in Nb ¡sub¿3¡/sub¿ Sn superconducting radiofrequency cavities towards first practical accelerator applications”. In: *Superconductor Science and Technology* 34.2 (Feb. 2021), p. 025007. ISSN: 0953-2048. DOI: 10.1088/1361-6668/abc7f7. URL: https://iopscience.iop.org/article/10.1088/1361-6668/abc7f7.

[13] C Antoine. “Research and Development in superconducting RF: thin film capabilities as a game changer for future sustainability”. English. In: *Proc. IPAC'23*. IPAC'23 - 14th International Particle Accelerator Conference 14. JACoW Publishing, Geneva, Switzerland, Apr. 2023, pp. 21–26. ISBN: 978-3-95450-231-8. DOI: 10.18429/JACoW-IPAC2023-MOYD3. URL: https://indico.jacow.org/event/41/contributions/618.

[14] J Halbritter. *FORTRAN-PROGRAM FOR THE COMPUTATION OF THE SURFACE IMPEDANCE OF SUPERCONDUCTORS*. Tech. rep. Kernforschungszentrum, Karlsruhe (West Germany). Institut fuer Experimentelle Kernphysik, Aug. 1969. URL: https://www.osti.gov/biblio/4102575.

[15] S Keckert et al. “Critical fields of Nb3Sn prepared for superconducting cavities”. In: *Superconductor Science and Technology* 32.7 (July 2019), p. 075004. ISSN: 0953-2048. DOI: 10.1088/1361-6668/ab119e. URL: https://iopscience.iop.org/article/10.1088/1361-6668/ab119e.

[16] V. Novotny and P. P. M. Meincke. “Single superconducting energy gap in pure niobium”. In: *Journal of Low Temperature Physics* 18.1-2 (Jan. 1975), pp. 147–157. ISSN: 0022-2291. DOI: 10.1007/BF00116976.

[17] Samuel Elliott Posen. “Understanding And Overcoming Limitation Mechanisms In Nb3Sn Superconducting Rf Cavities”. PhD thesis. Cornell U., Cornell U., 2015.

[18] H Safa. “Optimum Operating Temperature of Superconducting Cavities”. In: *Proceedings of the 1998 Linear Accelerator Conference (LINAC'98)*. Chicago, IL, USA: JACoW, Aug. 1998, pp. 289–291. URL: https://accelconf.web.cern.ch/l98/PAPERS/MO4095.PDF.

[19] Marc Ross. *Fundamental Power Coupler Technical Development - Final CRADA Report*. Tech. rep. Menlo Park, CA (United States): SLAC National Accelerator Laboratory (SLAC), June 2018. DOI: 10.2172/1468619.

[20] J Branlard et al. “LLRF Tests of XFEL Cryomodules at AMTF: First Experimental Results”. In: *Proc. SRF'13*. JACoW Publishing, Geneva, Switzerland, 2013, pp. 1132–1134. URL: https://jacow.org/SRF2013/papers/THP087.pdf.

[21] A Bosotti et al. “The Coaxial Tuner for ILCTANML at Fermilab”. In: *Proc. EPAC'08*. European Particle Accelerator Conference 11. JACoW Publishing, Geneva, Switzerland, Sept. 2008, pp. 895–897. URL: https://jacow.org/e08/papers/MOPP146.pdf.

[22] E Kako et al. “Cryomodule Tests of Four Tesla-Like Cavities in the STF Phass-1.0 for ILC”. In: *Proc. PAC'09*. Particle Accelerator Conference 23. JACoW Publishing, Geneva, Switzerland, 2009, pp. 709–713. URL: https://jacow.org/PAC2009/papers/TU3RAI04.pdf.

[23] Y M Pischalnikov et al. “Extended Range SRF Cavity Tuner for LCLS II HE Project”. In: *Proc. SRF'21*. International Conference on RF Superconductivity 20. JACoW Publishing, Geneva, Switzerland, Sept. 2022, p. 203. ISBN: 978-3-95-450233-2. DOI: 10.18429/JACoW-SRF2021-MOPTEV002. URL: https://jacow.org/srf2021/papers/MOPTEV002.pdf.

[24] Ilan Ben-Zvi et al. “Conceptual design of a high reactive-power ferroelectric fast reactive tuner”. In: *Physical Review Accelerators and Beams* 27.5 (May 2024), p. 052001. ISSN: 2469-9888. DOI: 10.1103/PhysRevAccelBeams.27.052001.

[25] Ilan Ben-Zvi, Alick Macpherson, and Samuel Smith. “Detailed Design and Optimization of Ferro-Electric Tuners”. In: (Apr. 2025). URL: http://arxiv.org/abs/2504.19825.

[26] N C Shipman et al. “A Ferroelectric Fast Reactive Tuner (FEFRT) to Combat Microphonics”. In: *Proc. ERL'19*. JACoW Publishing, Geneva, Switzerland, 2019, pp. 42–47. DOI: 10.18429/JACoW-ERL2019-TUCOZBS02. URL: https://jacow.org/erl2019/papers/TUCOZBS02.pdf.

[27] N C Shipman et al. “Ferro-Electric Fast Reactive Tuner Applications for SRF Cavities”. In: *Proc. IPAC'21*. JACoW Publishing, Geneva, Switzerland, 2021, pp. 1305–1310. DOI: 10.18429/JACoW-IPAC2021-TUXC03. URL: https://jacow.org/ipac2021/papers/TUXC03.pdf.

[28] A Kanareykin et al. “Low-Loss Ferroelectric for Accelerator Application”. In: *Proc. PAC'05*. Particle Accelerator Conference 21. JACoW Publishing, Geneva, Switzerland, 2005, pp. 4305–4307. URL: https://jacow.org/p05/papers/WPAT095.pdf.

[29] Ben Freemire. “Measurements of the Dielectric Properties of a Ferroelectric Ceramic for Use in a Fast Reactive Tuner”. In: (2020). URL: http://cds.cern.ch/record/2881905.

[30] M McAshan and R Wanzenberg. “RF design of a transverse mode cavity for kaon separation”. In: *2001*. May (2001). URL: http://www.osti.gov/energycitations/product.biblio.jsp?osti_id=780614.

[31] C. Glasman and R. M. Jones. “Beam dynamics and wake-field simulations for high gradient ILC linacs”. In: (Oct. 2008). URL: http://arxiv.org/abs/0810.2765.

[32] Chris Adolphsen. “Multibunch motion with nearest neighbor wake field coupling”. In: *Int. J. Mod. Phys. Proc. Suppl.* 2, Suppl. 2B.SLAC-PUB-5942 (1993). Ed. by J Rossbach, pp. 867–869. URL: https://inspirehep.net/literature/339083.

[33] I. R. R. Shinton et al. “Higher Order Modes in Third Harmonic Cavities for XFEL and FLASH”. In: (June 2010). URL: http://arxiv.org/abs/1006.0085.

[34] Bozo Richter et al. “Limitations of the EuXFEL 3rd harmonic cryomodule in high duty cycle operation”. In: *JACoW* LINAC2024 (2024), TUPB002. DOI: 10.18429/JACoW-LINAC2024-TUPB002.

[35] P. Pierini et al. “Fabrication and vertical test experience of the European X-ray Free Electron Laser 3.9 GHz superconducting cavities”. In: *Physical Review Accelerators and Beams* 20.4 (Apr. 2017), p. 042006. ISSN: 2469-9888. DOI: 10.1103/PhysRevAccelBeams.20.042006.

[36] Sebastian Aderhold et al. “3.9 GHz SRF Production Cavities for LCLS-II”. In: June 2019. DOI: 10.18429/JACoW-SRF2019-MOP051. URL: https://www.osti.gov/biblio/1843466.

[37] A Lunin et al. “Redesign of the End Group in the 3.9 GHz LCLS-II Cavity”. In: *Proc. of Linear Accelerator Conference (LINAC'16), East Lansing, MI, USA, 25-30 September 2016*. Linear Accelerator Conference 28. Geneva, Switzerland: JACoW, May 2017, pp. 145–148. ISBN: 978-3-95450-169-4. DOI: https://doi.org/10.18429/JACoW-LINAC2016-MOPLR007. URL: http://jacow.org/linac2016/papers/moplr007.pdf.

[38] X W Wu et al. “Development of 3.9 GHz 9-Cell Cavities at SHINE”. In: *Proc. 21th Int. Conf. RF Supercond. (SRF'23)*. International Conference on RF Superconductivity 21. JACoW Publishing, Geneva, Switzerland, June 2023, pp. 921–924. ISBN: 978-3-95450-234-9. DOI: 10.18429/JACoW-SRF2023-THIAA01. URL: https://jacow.org/srf2023/papers/thiaa01.pdf.

[39] Yu-Xin Zhang, Jin-Fang Chen, and Dong Wang. “RF design optimization for the SHINE 3.9 GHz cavity”. In: *Nuclear Science and Techniques* 31.7 (July 2020), p. 73. ISSN: 1001-8042. DOI: 10.1007/s41365-020-00772-z.

[40] P Pierini et al. “Limits for the Operation of the European XFEL 3.9 GHz System in CW Mode”. In: *Proc. of International Particle Accelerator Conference IPAC17*. International Particle Accelerator Conference 8. Geneva, Switzerland: JACoW, May 2017, pp. 1023–1026. ISBN: 978-3-95450-182-3. DOI: https://doi.org/10.18429/JACoW-IPAC2017-MOPVA066. URL: http://jacow.org/ipac2017/papers/mopva066.pdf.

[41] J Branlard et al. “The European XFEL LLRF System”. In: *3rd International Particle Accelerator Conference*. 2012, MOPWI021. URL: https://jacow.org/IPAC2012/papers/MOOAC01.pdf.

[42] Curt Hovater et al. “The LCLS-II LLRF System”. In: *6th International Particle Accelerator Conference*. 2015, MOPWI021. DOI: 10.18429/JACoW-IPAC2015-MOPWI021.

[43] D Angal-Kalinin et al. “Status of CLARA Front End Commissioning”. In: *Proc. 29th Linear Accelerator Conference LINAC'18, Beijing, 16-21 September 2018*. Linear Accelerator Conference 29. Geneva, Switzerland: JACoW Publishing, Jan. 2019, pp. 98–101. ISBN: 978-3-95450-194-6. DOI: doi:10.18429/JACoW-LINAC2018-MOPO035. URL: http://jacow.org/linac2018/papers/mopo035.pdf.

[44] T. Schietinger et al. *Commissioning experience and beam physics measurements at the SwissFEL Injector Test Facility*. 2016. DOI: 10.1103/PhysRevAccelBeams.19.100702.

[45] A Aksoy et al. “Conceptual design of a X-FEL facility using CLIC x-band accelerating structure”. In: (2014). URL: http://accelconf.web.cern.ch/AccelConf/IPAC2014/papers/thpro025.pdf.

[46] T Inagaki. “8-GeV C-Band Accelerator Construction for XFEL/SPring-8”. In: *Proc. LINAC'08*. Linear Accelerator Conference 24. JACoW Publishing, Geneva, Switzerland, 2008, pp. 1090–1094. URL: https://jacow.org/LINAC08/papers/FR101.pdf.

[47] M. Diomede et al. “Preliminary RF design of an X-band linac for the EuPRAXIA@SPARC_LAB project”. In: *Nuclear Instruments and Methods in Physics Research Section A: Accelerators, Spectrometers, Detectors and Associated Equipment* 909 (Nov. 2018), pp. 243–246. ISSN: 01689002. DOI: 10.1016/j.nima.2018.01.032.

[48] Christopher Milne et al. “SwissFEL: The Swiss X-ray Free Electron Laser”. In: *Applied Sciences* 7.7 (July 2017), p. 720. ISSN: 2076-3417. DOI: 10.3390/app7070720.

[49] Nuria Catalan-Lasheras et al. “High-efficiency klystrons from a dream to a reality”. In: *JACoW IPAC* 2024 (2024), FRYD1. DOI: 10.18429/JACoW-IPAC2024-FRYD1. URL: https://cds.cern.ch/record/2930683.

[50] R et. al. Abela. *XFEL: The European X-Ray Free-Electron Laser - Technical Design Report*. Hamburg: DESY, 2006, pp. 1–646. ISBN: 978-3-935702-17-1. DOI: 10.3204/DESY{_}06-097. URL: https://bib-pubdb1.desy.de/record/77248.

[51] LCLS-II Project Team. “LCLS-II Final Design Report”. In: (Dec. 2014). URL: https://epp.fnal.gov/DocDB/0016/001646/001/LCLS-II%5C%20Design%5C%20Report.pdf.

[52] E Saldin. “On the coherent radiation of an electron bunch moving in an arc of a circle”. In: *Nuclear Instruments and Methods in Physics Research Section A: Accelerators, Spectrometers, Detectors and Associated Equipment* 398.2-3 (Oct. 1997), pp. 373–394. ISSN: 01689002. DOI: 10.1016/S0168-9002(97)00822-X. URL: http://dx.doi.org/10.1016/S0168-9002(97)00822-X.

[53] Bruce E. Carlsten and Tor O. Raubenheimer. “Emittance growth of bunched beams in bends”. In: *Physical Review E* 51.2 (Feb. 1995), pp. 1453–1470. ISSN: 1063-651X. DOI: 10.1103/PhysRevE.51.1453.

[54] S. Di Mitri and M. Cornacchia. “Electron beam brightness in linac drivers for free-electron-lasers”. In: *Physics Reports* 539.1 (June 2014), pp. 1–48. ISSN: 03701573. DOI: 10.1016/j.physrep.2014.01.005. URL: http://linkinghub.elsevier.com/retrieve/pii/S0370157314000088.

[55] S. Bettoni et al. “Preservation of low slice emittance in bunch compressors”. In: *Physical Review Accelerators and Beams* 19.3 (2016), p. 034402. ISSN: 2469-9888. DOI: 10.1103/PhysRevAccelBeams.19.034402. URL: http://link.aps.org/doi/10.1103/PhysRevAccelBeams.19.034402.

[56] C. C. Hall et al. “Measurement and simulation of the impact of coherent synchrotron radiation on the Jefferson Laboratory energy recovery linac electron beam”. In: *Physical Review Special Topics - Accelerators and Beams* 18.3 (2015), pp. 1–9. ISSN: 1098-4402. DOI: 10.1103/PhysRevSTAB.18.030706. URL: http://link.aps.org/doi/10.1103/PhysRevSTAB.18.030706.

[57] K. L. F. Bane et al. “Measurements and modeling of coherent synchrotron radiation and its impact on the Linac Coherent Light Source electron beam”. In: *Physical Review Special Topics - Accelerators and Beams* 12.3 (Mar. 2009), p. 030704. ISSN: 1098-4402. DOI: 10.1103/PhysRevSTAB.12.030704.

[58] S. Di Mitri et al. “Transverse emittance preservation during bunch compression in the Fermi free electron laser”. In: *Physical Review Special Topics - Accelerators and Beams* 15.2 (Feb. 2012), pp. 1–9. ISSN: 1098-4402. DOI: 10.1103/PhysRevSTAB.15.020701. URL: http://link.aps.org/doi/10.1103/PhysRevSTAB.15.020701.

[59] A D Brynes et al. “Beyond the limits of 1D coherent synchrotron radiation”. In: *New Journal of Physics* 20.7 (July 2018), p. 073035. ISSN: 1367-2630. DOI: 10.1088/1367-2630/aad21d. URL: http://stacks.iop.org/1367-2630/20/i=7/a=073035?key=crossref.ef51b66c5014c66bcb0439760cd2d06f.

[60] T.H. Pacey et al. “Simulation studies for dielectric wakefield programme at CLARA facility”. In: *Nuclear Instruments and Methods in Physics Research Section A: Accelerators, Spectrometers, Detectors and Associated Equipment* 909 (Nov. 2018), pp. 261–265. ISSN: 01689002. DOI: 10.1016/j.nima.2017.12.038.

[61] Jiawei Yan et al. “Terawatt-attosecond hard X-ray free-electron laser at high repetition rate”. In: *Nature Photonics 2024 18:12* 18.12 (Nov. 2024), pp. 1293–1298. ISSN: 1749-4893. DOI: 10.1038/s41566-024-01566-0. URL: https://www.nature.com/articles/s41566-024-01566-0.

[62] Sara Thorin et al. “The Max IV Linac”. In: *Linac2014* (2014), TUIOA03. URL: http://inspirehep.net/record/1363410/.

[63] Adam Dixon et al. “Reduction of arrival time jitter or energy spread with arc-like variable bunch compressors”. In: *Physical Review Accelerators and Beams* 27.11 (Nov. 2024), p. 110702. ISSN: 2469-9888. DOI: 10.1103/PhysRevAccelBeams.27.110702.

[64] Peter H. Williams et al. “Arclike variable bunch compressors”. In: *Physical Review Accelerators and Beams* 23.10 (Oct. 2020), p. 100701. ISSN: 24699888. DOI: 10.1103/PhysRevAccelBeams.23.100701. URL: https://link.aps.org/doi/10.1103/PhysRevAccelBeams.23.100701.

[65] John Galyda and Joerg Rossbach. “ICFA Beam Dynamics Mini-Workshop on CSR, Zeuthen”. In: 2002. URL: https://www.desy.de/csr/csr_workshop_2002/csr_workshop_2002_index.html.

[66] Donish Z. Khan and Tor O. Raubenheimer. “Novel bunch compressor chicane: The five-bend chicane”. In: *Physical Review Accelerators and Beams* 25.9 (Sept. 2022), p. 090701. ISSN: 2469-9888. DOI: 10.1103/PhysRevAccelBeams.25.090701.

[67] F. Stulle, A. Adelmann, and M. Pedrozzi. “Designing a bunch compressor chicane for a multi TeV linear collider”. In: *Physical Review Special Topics – Accelerators and Beams* 10.3 (Mar. 2007), p. 031001. ISSN: 1098-4402. DOI: 10.1103/PhysRevSTAB.10.031001.

[68] Fancong Zeng et al. “Self-Cancelation of Coherent Synchrotron Radiation Kicks Using a Non-Symmetric S-shape Four-Bend Chicane”. In: (Mar. 2024). URL: http://arxiv.org/abs/2403.06101.

[69] S. Di Mitri, M. Cornacchia, and S. Spampinati. “Cancellation of Coherent Synchrotron Radiation Kicks with Optics Balance”. In: *Physical Review Letters* 110.1 (Jan. 2013), p. 014801. ISSN: 0031-9007. DOI: 10.1103/PhysRevLett.110.014801. URL: http://link.aps.org/doi/10.1103/PhysRevLett.110.014801.

[70] Z T Zhao et al. “SCLF: An 8-GeV CW SCRF Linac-Based X-Ray FEL Facility in Shanghai”. In: *Proc. of International Free Electron Laser Conference (FEL'17), Santa Fe, August 20-25, 2017*. International Free Electron Laser Conference 38. Geneva, Switzerland: JACoW, Feb. 2018, pp. 182–184. ISBN: 978-3-95450-179-3. DOI: https://doi.org/10.18429/JACoW-FEL2017-MOP055. URL: http://jacow.org/fel2017/papers/mop055.pdf.

[71] M Borland. *ELEGANT: A flexible SDDS-compliant code for accelerator simulation*. Tech. rep. Argonne, IL (United States): Argonne National Laboratory (ANL), Aug. 2000. DOI: 10.2172/761286. URL: http://www.osti.gov/servlets/purl/761286/.

[72] Fancong Zeng et al. “Cancelation of coherent synchrotron radiation kicks in chicane bunch compressors”. In: *Physical Review Accelerators and Beams* 28.7 (July 2025), p. 070701. ISSN: 2469-9888. DOI: 10.1103/2vjn-t4qb.

[73] Z Huang et al. “Effects of linac wakefield on CSR microbunching in the Linac Coherent Light Source”. In: *Conf. Proc. C* 030512.SLAC-PUB-9818 (2003), p. 3138. URL: https://cds.cern.ch/record/747416.

[74] Z. Huang et al. “Suppression of microbunching instability in the linac coherent light source”. In: *Physical Review Special Topics - Accelerators and Beams* 7.7 (July 2004), p. 074401. ISSN: 1098-4402. DOI: 10.1103/PhysRevSTAB.7.074401.

[75] K. Marinov et al. *Inductive kickers in the UK XFEL beam spreader*. STFC internal report. 2024.

[76] D Sagan. “Bmad: A relativistic charged particle simulation library”. In: *Nucl. Instrum. Meth.* A558.1 (2006), pp. 356–359. ISSN: 0168-9002. DOI: https://doi.org/10.1016/j.nima.2005.11.001.

[77] Rémi Lehe et al. “A spectral, quasi-cylindrical and dispersion-free Particle-In-Cell algorithm”. In: *Computer Physics Communications* 203 (June 2016), pp. 66–82. ISSN: 00104655. DOI: 10.1016/j.cpc.2016.02.007.

[78] A Ferran Pousa, R Assmann, and A Martinez de la Ossa. “Wake-T: a fast particle tracking code for plasma-based accelerators”. In: *Journal of Physics: Conference Series* 1350.1 (Nov. 2019), p. 012056. ISSN: 1742-6588. DOI: 10.1088/1742-6596/1350/1/012056. URL: https://iopscience.iop.org/article/10.1088/1742-6596/1350/1/012056.

[79] A F Habib et al. “Attosecond-Angstrom free-electron-laser towards the cold beam limit”. en. In: *Nature Communications* 14.1 (Feb. 2023), p. 1054. ISSN: 2041-1723. DOI: 10.1038/s41467-023-36592-z. URL: https://www.nature.com/articles/s41467-023-36592-z.

[80] L T Campbell and B W J McNeil. “Puffin: A three dimensional, unaveraged free electron laser simulation code”. en. In: *Physics of Plasmas* 19.9 (Sept. 2012), p. 93119. ISSN: 1070-664X, 1089-7674. DOI: 10.1063/1.4752743. URL: http://aip.scitation.org/doi/10.1063/1.4752743.

[81] Gregor Loisch et al. “Observation of High Transformer Ratio Plasma Wakefield Acceleration”. In: *Phys. Rev. Lett.* 121.6 (Aug. 2018), p. 64801. DOI: 10.1103/PhysRevLett.121.064801. URL: https://link.aps.org/doi/10.1103/PhysRevLett.121.064801.

[82] R Roussel et al. “Single Shot Characterization of High Transformer Ratio Wakefields in Nonlinear Plasma Acceleration”. In: *Phys. Rev. Lett.* 124.4 (Jan. 2020), p. 44802. DOI: 10.1103/PhysRevLett.124.044802. URL: https://link.aps.org/doi/10.1103/PhysRevLett.124.044802.

[83] C. E. Clayton et al. “Self-mapping the longitudinal field structure of a nonlinear plasma accelerator cavity”. In: *Nature Communications* 7.1 (Aug. 2016), p. 12483. ISSN: 2041-1723. DOI: 10.1038/ncomms12483. URL: https://www.nature.com/articles/ncomms12483.

[84] S. Schröder et al. “High-resolution sampling of beam-driven plasma wakefields”. In: *Nature Communications* 11.1 (Nov. 2020), p. 5984. ISSN: 2041-1723. DOI: 10.1038/s41467-020-19811-9. URL: https://www.nature.com/articles/s41467-020-19811-9.

[85] R. D’Arcy et al. “Recovery time of a plasma-wakefield accelerator”. In: *Nature* 603.7899 (Mar. 2022), pp. 58–62. ISSN: 0028-0836. DOI: 10.1038/s41586-021-04348-8.

[86] B Hidding et al. “Ultracold Electron Bunch Generation via Plasma Photocathode Emission and Acceleration in a Beam-Driven Plasma Blowout”. In: *Phys. Rev. Lett.* 108 (2012), p. 35001. URL: http://link.aps.org/doi/10.1103/PhysRevLett.108.035001.

[87] G. G. Manahan et al. “Single-stage plasma-based correlated energy spread compensation for ultrahigh 6D brightness electron beams”. In: *Nature Communications* 8.1 (June 2017), p. 15705. ISSN: 2041-1723. DOI: 10.1038/ncomms15705. URL: https://www.nature.com/articles/ncomms15705.

[88] Ahmad Fahim Habib et al. “Plasma Photocathodes”. In: *Annalen der Physik* 535.10 (Oct. 2023), p. 2200655. ISSN: 0003-3804. DOI: 10.1002/andp.202200655. URL: https://onlinelibrary.wiley.com/doi/10.1002/andp.202200655.

[89] P Scherkl et al. “Plasma photonic spatiotemporal synchronization of relativistic electron and laser beams”. In: *Phys. Rev. Accel. Beams* 25 (2022), p. 52803. DOI: 10.1103/PhysRevAccelBeams.25.052803. URL: https://link.aps.org/doi/10.1103/PhysRevAccelBeams.25.052803.

[90] S. Kuschel et al. “Demonstration of passive plasma lensing of a laser wakefield accelerated electron bunch”. In: *Physical Review Accelerators and Beams* 19.7 (2016), p. 071301. ISSN: 2469-9888. DOI: 10.1103/PhysRevAccelBeams.19.071301. URL: http://link.aps.org/doi/10.1103/PhysRevAccelBeams.19.071301.

[91] Cheng-Ying Tsai et al. “Theoretical formulation of phase space microbunching instability in the presence of intrabeam scattering for single-pass or recirculation accelerators”. In: *Physical Review Accelerators and Beams* 23.12 (Dec. 2020), p. 124401. ISSN: 2469-9888. DOI: 10.1103/PhysRevAccelBeams.23.124401.

[92] Andrew Potter. “Beam Transport Issues in High Powered X-ray Free Electron Lasers”. PhD thesis. Liverpool: University of Liverpool, Apr. 2024. DOI: 10.17638/03180413. URL: https://livrepository.liverpool.ac.uk/id/eprint/3180413.

[93] J Skupin et al. “Undulator Demagnetization due to Radiation Losses at FLASH”. In: *Proc. EPAC’08*. European Particle Accelerator Conference 11. JACoW Publishing, Geneva, Switzerland, June 2008, pp. 2308–2310. URL: https://jacow.org/e08/papers/WEPC129.pdf.

[94] B Faatz, M Tischer, and P Vagin. “Influence of Radiation Exposure on the FEL Performance at FLASH”. In: *Proc. FEL’19*. Hamburg: JACoW Publishing, Geneva, Switzerland, 2019, pp. 488–491. DOI: 10.18429/JACoW-FEL2019-WEP070. URL: https://jacow.org/fel2019/papers/WEP070.pdf.

[95] W Decking et al. “Status of the European XFEL”. In: *Proc. IPAC’19*. Hamburg: JACoW Publishing, Geneva, Switzerland, 2019, pp. 1721–1723. DOI: 10.18429/JACoW-IPAC2019-TUPRB020. URL: http://accelconf.web.cern.ch/ipac2019/papers/TUPRB020.pdf.

[96] V Balandin et al. “Post-Linac Collimation System for the European XFEL”. In: *Proc. PAC’09*. Particle Accelerator Conference 23. Vancouver: JACoW Publishing, Geneva, Switzerland, 2009, pp. 3763–3765. URL: https://jacow.org/PAC2009/papers/TH6PFP030.pdf.

[97] S Liu, W Decking, and F Wolff-Fabris. “Study of Possible Beam Losses After Post-Linac Collimation at European XFEL”. In: *Proc. IPAC’18*. Vancouver: JACoW Publishing, Geneva, Switzerland, 2018, pp. 4092–4095. DOI: 10.18429/JACoW-IPAC2018-THPMF022. URL: http://accelconf.web.cern.ch/ipac2018/papers/THPMF022.pdf.

[98] Winfried Decking. “European XFEL News”. In: DESY. Zeuthen, Nov. 2019. URL: https://bib-pubdb1.desy.de/record/428836.

[99] J Wu et al. “Linac Coherent Light Source Electron Beam Collimation”. In: *Proc. EPAC’06*. European Particle Accelerator Conference 10. Edinburgh: JACoW Publishing, Geneva, Switzerland, June 2006, pp. 148–150. URL: https://accelconf.web.cern.ch/e06/PAPERS/MOPCH048.PDF.

[100] H.-D. Nuhn et al. “Undulator Radiation Damage Experience at LCLS”. In: *Proc. FEL’14*. Basel: JACoW Publishing, Geneva, Switzerland, 2014, pp. 127–130. URL: https://jacow.org/FEL2014/papers/MOP046.pdf.

[101] Z Zhao and H Ding. “Shanghai hard X-ray FEL facility progress status”. English. In: *Proc. IPAC’24*. IPAC’24 - 15th International Particle Accelerator Conference 15. JACoW Publishing, Geneva, Switzerland, June 2024, pp. 967–972. ISBN: 978-3-95450-247-9. DOI: 10.18429/JACoW-IPAC2024-TUZN1. URL: https://indico.jacow.org/event/63/contributions/3071.

[102] Bingyang Yan et al. “Post-linac beam collimation study of SHINE”. In: *Radiation Detection Technology and Methods* 8.2 (2024), pp. 1286–1297. ISSN: 2509-9930. DOI: 10.1007/s41605-024-00447-y. URL: http://rdtm.ihep.ac.cn/en/article/doi/10.1007/s41605-024-00447-y.

[103] Dassault Systemes. *CST Studio Suite*. www.3ds.com. 2024.

[104] Sun An. “Superconducting RF Cavity Frequency and Field Distribution Sensitivity Simulation”. In: *Proceedings of the 2005 Particle Accelerator Conference*. IEEE, Apr. 2005, pp. 4194–4196. ISBN: 0-7803-8859-3. DOI: 10.1109/PAC.2005.1591762. URL: http://ieeexplore.ieee.org/document/1591762/.

[105] Raul Costa and Andrea Latina. “Tracking Complex Re-Circulating Machines with PLACET2”. In: *JACoW IPAC* 2021 (2021), pp. 4197–4200. DOI: 10.18429/JACoW-IPAC2021-THPAB209. URL: https://cds.cern.ch/record/2809173.

Theme 2:

Exceptional X-ray pulse qualities including ‘laser-like’ x-rays

6 FEL and undulators

6.1 Outline

There are many ‘defining’ features of a next generation XFEL facility. One key feature is the production of ‘laser-like’ **near-transform-limited pulses** across a wide photon energy range. Existing hard x-ray facilities were not designed to deliver transform-limited pulses—their primary aim was to operate in SASE mode which produces pulses which are noisy spectrally and temporally. Other next-generation features are production of **double FEL pulses which are widely separated in photon energy** to enable FEL pump/FEL probe applications, and **pulses at higher photon energies and pulse energies** than currently available. Methods to incorporate such next generation features on existing facilities have been applied retrospectively and are therefore constrained by existing accelerator infrastructure and initial design choices. The inclusion, during the first design phase, of the required concepts and technology for next-generation capability would transform the scientific reach and impact of a new facility.

Achieving the required combination of spectral tuning, bandwidth, and pulse energy for next-generation FEL pulses requires multiple FEL methods and a high quality electron beam—it should have low emittance, low energy spread and minimal energy chirp. By multiplexing a single high repetition rate beam between multiple FELs, undulator lines can be tailored to optimise the photon parameters delivered to their respective instruments.

The outline of this chapter is as follows:

- The target photon parameters, as presented in the Science Case, are presented.
- A review is presented of the potential FEL methods for the production of long and short near-transform-limited pulses, two-colour pulses, and pulses with high pulse energy and photon energy. The methods chosen for each of the multiplex of FELs are then presented and justified.
- The conceptual design of the FELs is presented, and electron beam parameters required by the FELs are given.
- The CDOA research and development outcomes are presented, including optimisation and expansion of the chosen baseline technologies and development of FEL output beyond the baseline performance envelope.
- The expected output performance of the FELs is presented.
- State-of-the-art undulator technologies are reviewed, with discussion of the future potential of emerging technologies, and the chosen technologies are explained.
- Sustainability issues are discussed
- The required research and technology developments to close the gap between the current state-of-the-art and the requirements of UK XFEL are reviewed.

DRAFT

6.2 Photon Parameter Requirements

The key next-generation capabilities identified in the Science Case, and their implications for the design of the facility FELs, are summarised here.

- **Transform-limited operation from 0.1–20 keV with pulse durations 100 as – 100 fs.** This tuning range is unfeasible in a single FEL beamline, so this implies a number of different FELs are required, with each covering a subset of this tuning range. It also implies a variety of FEL techniques are required, each appropriate to the photon energy and required pulse duration.
- **Non-transform-limited operation from 5–45 keV with pulse energies up to tens of mJ.** The pulse energy and tuning range requirement imply that an electron beam energy higher than the nominal 8 GeV is required, with two FELs needed to optimally cover the range.
- **A high-efficiency facility with the simultaneous operation of multiple end stations.** This means a FEL switchyard and fast beam distribution system are required, as well as a robust reliability and fault management strategy.
- **Widely-Separated Two-colour pulses at a single end station for pump-probe experiments.** This means the facility should improve on existing two-colour FEL techniques which are all constrained by the fact they are retro-fitted.
- **Evenly-spaced, high repetition rate pulses to match samples and detectors.** This implies any FEL technique adopted must be suitable for high average beam and photon power.
- **Variable polarisation at all photon energies.** This implies more complex and expensive variably polarising undulators must be used—at least for the final few gain lengths of each FEL.

6.3 Proposed FEL Methods

This section reviews, then selects, state-of-the-art and emerging methods for providing the specified next-generation capabilities.

6.3.1 Transform-Limited Pulses

A key driver is to provide 'laser-like' pulses which are transform limited (time bandwidth product $\Delta\nu\Delta t \leq 1$), diffraction limited ($M^2 \approx 1$) and with shot-to-shot stability in pulse shape, spectrum and pulse energy. A pulse that is transform limited has a coherence length equal to its duration. The coherence length of SASE pulses in short wavelength FELs is typically orders of magnitude less than the pulse duration—hence the pulses comprise a series of random phase-uncorrelated spikes [2, 3]. A simulated typical SASE pulse, and its properties, is illustrated in Figure 6.1. To generate near-transform-limited pulses a number of methods have been demonstrated or proposed—Figure 6.2 shows the approximate photon energy and pulse duration coverage of a number of these methods.

A differentiation is made between **Transform Limited Long Pulses** in which the aim is to extend the coherence length as far beyond the normal SASE limit as possible, and **Transform Limited**

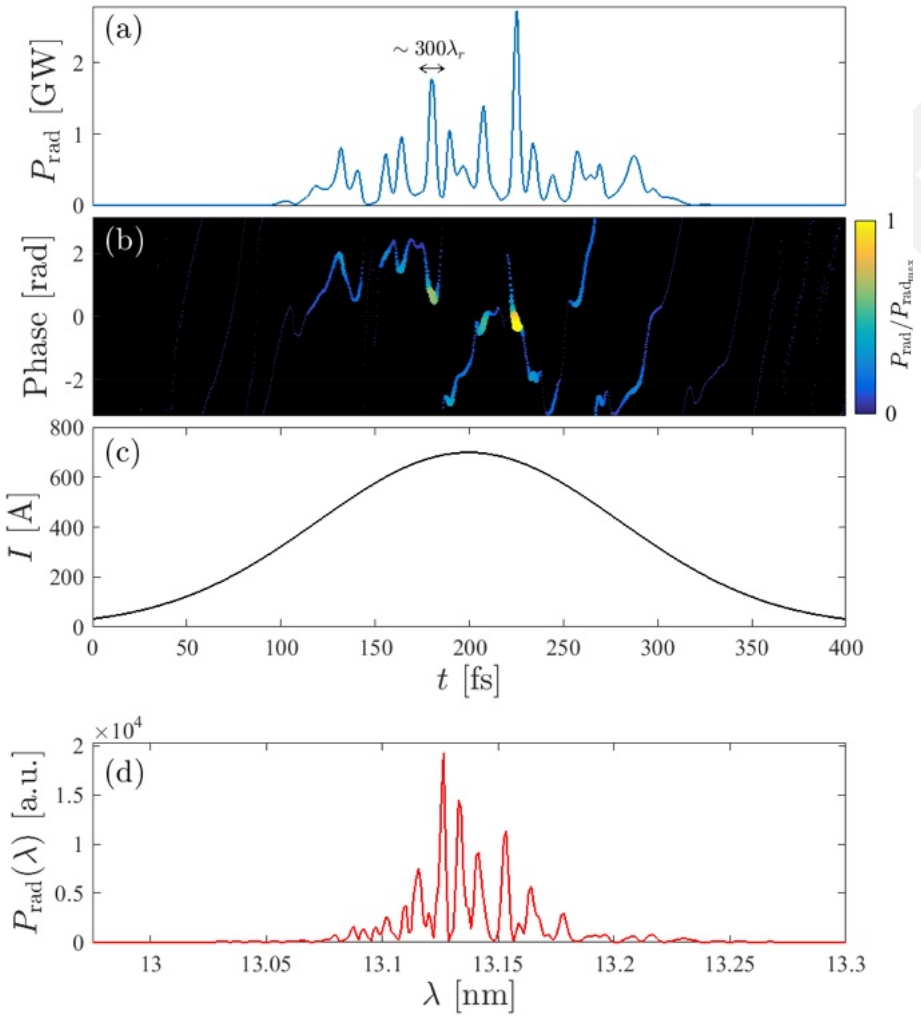

Figure 6.1: Example SASE properties. The figure shows simulation results for a high-gain SASE FEL with parameters similar to FLASH [1]. Results are shown at saturation: (a) radiation temporal profile comprising multiple spikes; (b) radiation phase showing phase correlation within but not between spikes; (c) the idealised Gaussian current profile used in the simulation and (d) the radiation spectrum, also comprising multiple spikes.

Short Pulses in which the output pulse length is of the order of the typical SASE spike length, typically a few hundred attoseconds in the HXR.

6.3.1.1 Transform Limited Long Pulses

For Transform Limited Long Pulses the methods fall into two classes. In the first class the coherence is *imported* from a coherent external source such as a seed laser. If the seed laser power is sufficient to dominate the spontaneous emission generated at the start of the undulator the coherent seed is simply amplified within the FEL. This known as **Direct Seeding**. This technique is only applicable if a seed source of the appropriate wavelength and sufficient power is available, limiting the FEL wavelength to the UV if seeding with a IR-based laser and harmonic generation system, or to the XUV if seeding with a source based on higher harmonics generated

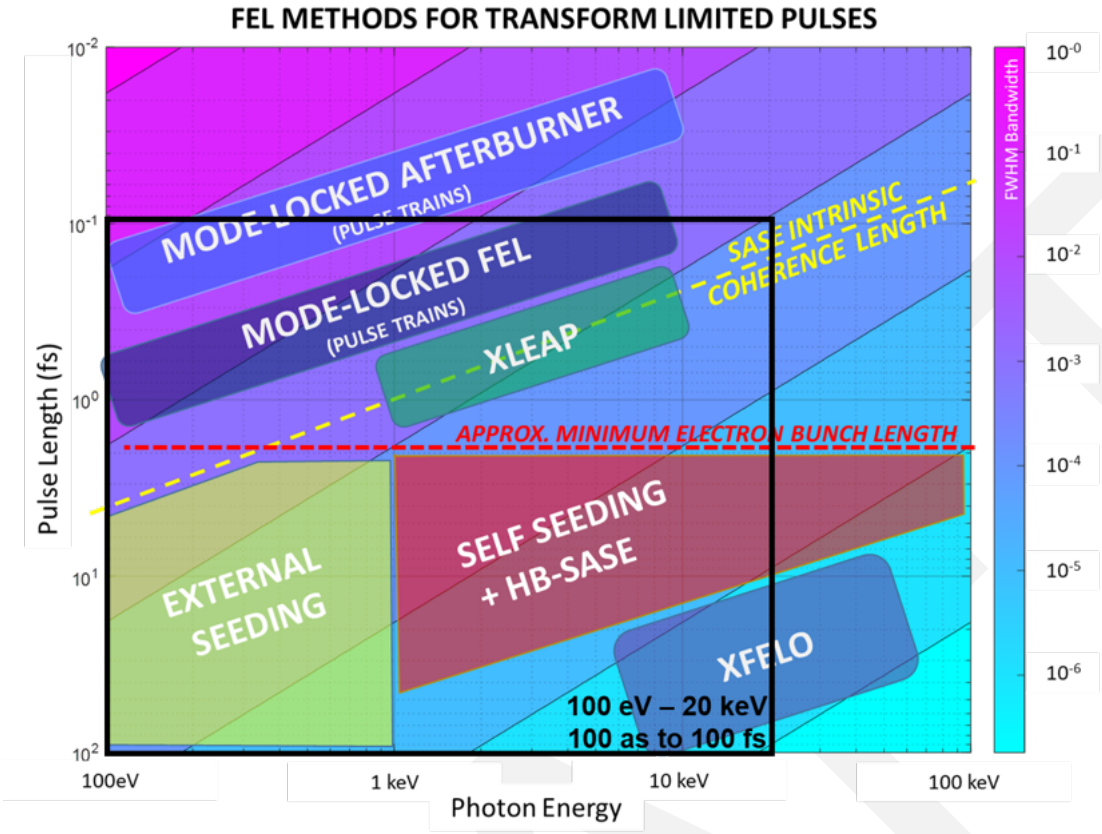

Figure 6.2: The estimated coverage of some relevant FEL techniques for the generation of near-transform-limited pulses. The project's aim for near-transform-limited pulses from 0.1 to 20 keV and 100 as to 100 fs is shown by the black box in the photon energy-pulse length parameter space.

in gases [4, 5], a technique which has been explored at several facilities and has been found to be not competitive with the other techniques referred to later in this section.

To achieve coherent output at higher photon energies higher harmonics of the original seed can be generated within the FEL and amplified to saturation—these harmonics can inherit the coherence of the original seed. The most recent seeding and harmonic generation scheme is known as **Echo-Enabled Harmonic Generation (EEHG)** [7] which has been successfully demonstrated [8, 9], and is currently being implemented at a number of large facilities [6, 10, 11, 12]. A schematic of the system is shown in Figure 6.3. EEHG has some advantages over the earlier harmonic generation FEL scheme known as **High-Gain Harmonic Generation (HGHG)** implemented at FERMI@Elettra [13]: it can produce coherence at higher harmonics; it is more tolerant of electron beam energy spread; and the FEL can sometimes be more compact, depending on required photon energy and beam energy.

However, EEHG also has some disadvantages compared to HGHG: at lower harmonics the achievable bunching factor is lower than in HGHG; tuning and maintaining the operating conditions is more complicated; although less sensitive to beam energy spread it requires a large dispersion chicane which excites microbunching instability (unless this is suppressed by a laser heater in which case it is operated with a larger energy spread, reducing the advantage); harmonics at orders $>$100 are separated by less than 1/100 in frequency—the gain at contiguous harmonics is not negligible and there are spurious signals excited.

In any scheme, however, there is a limit to the harmonic number to which the coherence of the seed laser can be converted due to amplification of phase noise from the original seed [14]. In practice the consensus is that, given current and predicted seed sources, the maximum coherent

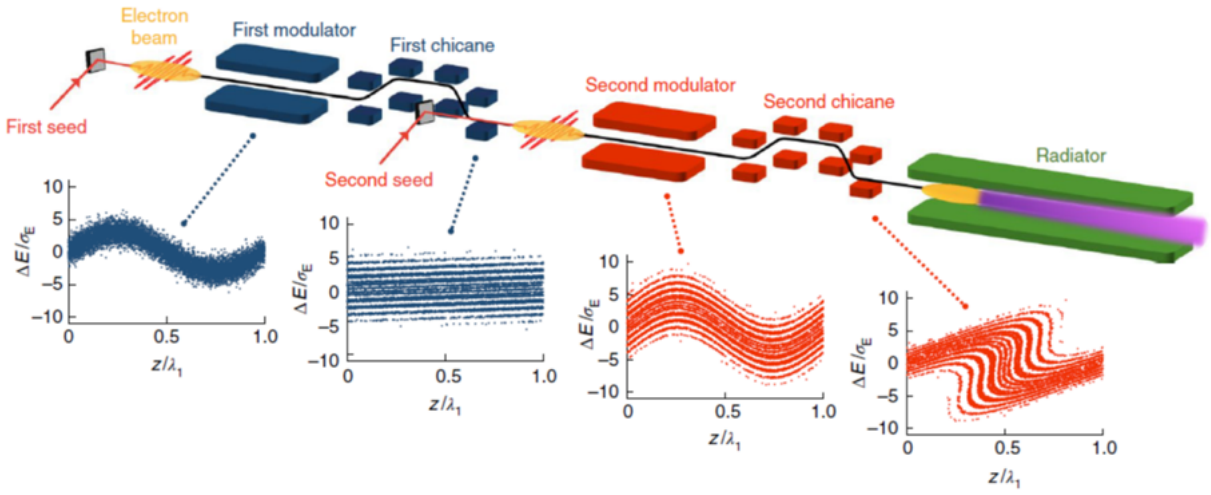

Figure 6.3: Schematic of Echo-Enabled Harmonic Generation (EEHG) scheme. There are two modulator undulators, in which lasers modulate the energy-time phase space of the electron bunch, as shown, to generate microbunching at a high harmonic of the laser. The bunches propagate into a radiator undulator which is tuned to be resonant at this higher harmonic. Figure reproduced from [6].

FEL output photon energy is about 1 keV. To allow for the relative advantages and disadvantages of EEHG and HGHG the lattice proposed for UK XFEL is suitable for both low harmonic number HGHG and also EEHG at higher harmonic number.

To realise the required high repetition rate operation of these externally seeded techniques calls for very high-average-power laser systems or new variants of the methods, designed to use lower average power seeds [15, 16].

The second class of methods for generating Transform Limited Long Pulses involves creating coherence internally within the FEL system. This can be done in a number of ways. In the **Self-Seeding** scheme [17], illustrated schematically in Figure 6.4, the FEL undulator is divided into two sections. Between the two sections is inserted a monochromator (the technology of which is dependent on the FEL wavelength regime) and a magnetic chicane. The spectrally and temporally noisy SASE FEL emission from the first undulator section is filtered by the monochromator to reduce the bandwidth, increasing the coherence. The first undulator section is long enough that the filtered emission has sufficient power to successfully seed the electron bunch in the second undulator section, but short enough that the FEL power does not damage the monochromator optics and has not induced so much energy spread in the electron bunch that exponential gain cannot be achieved in the second undulator section. The electron beam chicane has three functions—to divert the electron bunches around the monochromator optics, to 'smear out' any microbunching that has developed in the first undulator section and finally to provide the appropriate delay such that the electron bunch overlaps temporally with the monochromator output pulse in the second undulator section. Self seeding is in routine use at some FEL facilities [18, 19]. Variations on the scheme which offer potentially enhanced performance have been proposed, but are not directly compatible with a high capacity FEL switchyard facility because they either require a bespoke electron bunch phase space distribution [20] or a double electron bunch [21]. However, the proposed FEL lattice would allow such schemes to be applied in occasional periods of dedicated beam time, and future work will assess their relative performance.

Another option for creating coherence is known as **High-Brightness SASE (HB-SASE)** [22, 23] which takes advantage of the fact that the coherence length in the SASE FEL is determined by the relative slippage distance between electron bunch and co-propagating FEL radiation. Typically

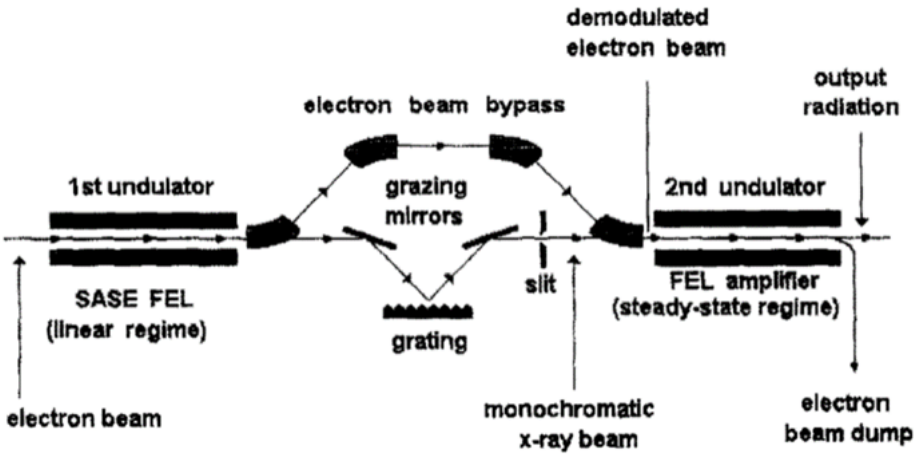

Figure 6.4: Schematic of the original self-seeding concept [17].

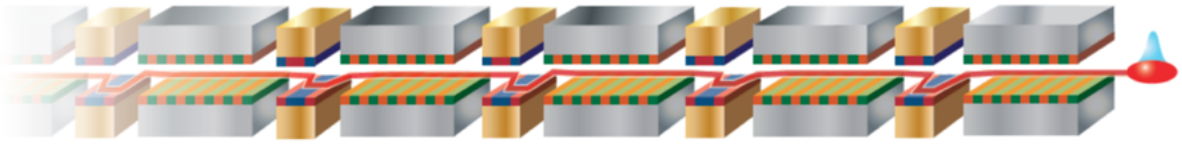

Figure 6.5: Schematic of the HB-SASE concept

in a SASE FEL the coherence length at saturation is $\sqrt{3}$ multiplied by the slippage in one gain length (the distance for an e-fold increase in radiation power). HB-SASE uses electron beam delays inserted between the short undulator modules that comprise the long FEL undulator. See Figure 6.5 for a schematic layout. The electron beam delays increase the slippage and hence increase the coherence length.

However, the delays all need to be different. This can be understood by considering the system in the spectral domain. Here it is seen that if the delays are all equal the result is a wide frequency comb of evenly spaced axial modes. The width of each mode decreases inversely with the number of delays, and the frequency spacing of the modes depends on the magnitude of the delays. Therefore if the delays are all different the axial mode growth is suppressed while the fundamental mode at the resonant frequency continues to grow and narrow. The concept can be thought of as a distributed spectral filtering. The radiation coherence length is seen to grow exponentially. Delays which are isochronous, so that different energy electrons are delayed by the same amount, preserve the growing microbunching within the FEL and can be used to increase the coherence length over SASE by a factor of potentially one hundred. More compact delays which are dispersive, comprising dipoles only, have been shown in simulation studies so far to increase the coherence length by a smaller amount—up to a factor of about thirty-five. HB-SASE is therefore an optics free technique whose efficacy is independent of wavelength and electron bunch repetition rate, and is thus applicable over a broad wavelength range at a high-repetition rate facility such as UK XFEL. The proof of principle was recently demonstrated experimentally on the SXR Athos FEL beamline at SwissFEL [24]. Later in this chapter (Section 6.5.2) a detailed comparative study case of the performance and stability of Self-Seeding and HB-SASE is presented, including further discussion of the parameter optimisation that has been performed for each technique.

A final option for generating Transform Limited Long Pulses in the X-ray (with extremely narrow bandwidths) is to enclose the FEL undulator within an optical cavity. This can be a low loss cavity using Bragg reflection from diamond crystals, which establishes a stable optical mode

that simultaneously recirculates the FEL pulse so that it overlaps the next electron bunch at the same time as monochromatising the FEL pulse, the so called **X-ray FEL Oscillator (XFELO)** [25, 26], or a higher loss, lower feedback cavity in a system termed a **Regenerative Amplifier FEL (RAFEL)** [27, 28, 29, 30] in which the purpose of the cavity is simply to recirculate a seed pulse to the entrance of the undulator. An XFELO should be able to produce extremely stable pulses with linewidths of the order of 10^{-6} and modest pulse energies, whereas a RAFEL is expected to produce less stable, broader bandwidth pulses of higher pulse energy. Both techniques are referred to collectively as **Cavity Based XFELs (CBXFELs)**. LCLS and EuXFEL each have ongoing CBXFEL experiments and initially demonstrated stable cavity round trips [31, 32]. A more recent experiment at EuXFEL demonstrated round trip FEL gain and associated stability and bandwidth reduction [33]. Figure 6.6 shows an illustration of the experimental setup at EuXFEL.

The implementation of a CBXFEL system on one of the UK XFEL beamlines will be studied in a future design phase and via collaboration with other facilities. Collaboration between the UK XFEL team and European XFEL has been well established in this CDOA phase—for example project team members participated in the demonstrator experiment.

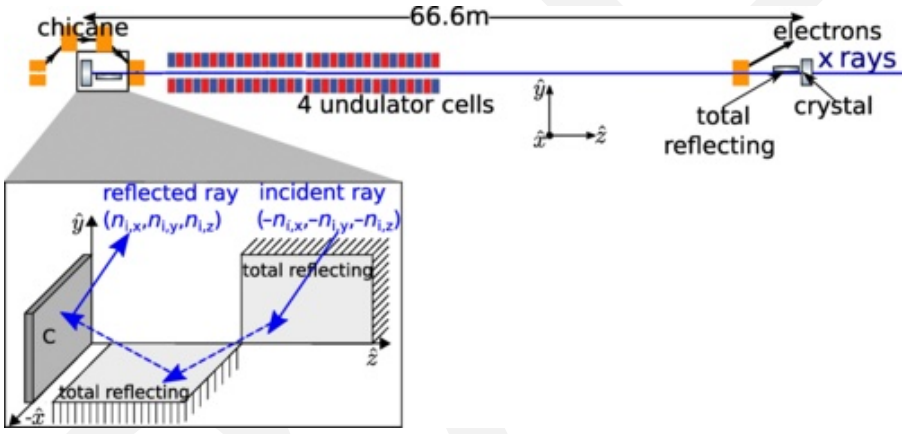

Figure 6.6: Schematic of the proof-of-concept cavity-based x-ray free electron laser (CBXFEL) demonstrator experiment at the European XFEL facility. Figure reproduced from [32].

The available methods for achieving near-transform-limited pulses are dependent on the required FEL photon energy and pulse duration. Therefore, to cover the full photon energy and pulse energy ranges of the facility, a selection of methods are required. It should be noted that achieving **long** transform limited pulses requires the pulse duration to be no longer than the coherence length. Except in the case of external seeding, the pulse duration is given by the electron bunch length, so the design concept for these schemes is to set the electron bunch length at each FEL to the coherence length obtainable with the relevant technique(s) applied on that FEL. More discussion of this is deferred until Section 6.4.3.

At the lower photon energies, at up to 1 keV (1.24 nm), it has been decided to use external seeding. This is employed as the standard mode of operation at FERMI@Elettra and has been proven to generate coherent pulses which are stable in central wavelength and bandwidth. The seed system will be either a frequency tripled Ti:Sa laser or a tunable OPA. The EEHG scheme will be used to generate coherent harmonics in the FEL. EEHG was chosen, rather than HGHG, because the FEL can be more compact, the performance of the method scales more favourably to higher harmonic number, and the requirements on electron beam slice energy spread are less stringent. The pulse length of the output is controlled primarily by the length of the seed laser pulse, so can be varied from a few tens of fs up to 100 fs.

As yet, EEHG has not demonstrated coherent high power output at the maximum photon energy of 1 keV targetted for UK XFEL. However, EEHG is currently being implemented on other facilities

and the current assumption is that lessons learned from these developments, such as fresh-bunch cascaded schemes, in combination with potential improvements in short wavelength (below 266 nm) seed lasers, allow operation at up to 1 keV to be stated now as a reasonable ambition.

At higher photon energies, into the SXR/HXR, the primary options are Self-Seeding or HB-SASE. The focus of the technical work to date has been exploring the performance potential of HB-SASE. This scheme, while more novel than Self-Seeding, which has already been demonstrated and implemented as a user mode at other facilities [18, 19], has some advantages because it is optics-free: there are no limits on repetition rate because there are no optics to be heated; it can access any photon energy because there are no wavelength-dependent material constraints; it is smoothly tunable over a broad range by simply changing undulator field strength. However, the FEL lattices that have been developed for the CDOA also include the components required for self-seeding implementation. As will be demonstrated in Section 6.5.2 there are valid reasons for doing this beyond the need to have a proven fall-back technology. It has been found that the performance and stability characteristics of HB-SASE and self-seeding are different, and that combining the two schemes together into a hybrid self-seeding/HB-SASE system, which is possible with the lattice that has been designed, also offers different output characteristics. Therefore the inclusion of HB-SASE *and* self-seeding widens the flexibility of the output—one scheme may be better suited for some user experiments and another scheme better suited for other experiments.

It should be noted that HB-SASE imposes some constraints on undulator lattice design and required electron beam parameters. These constraints are discussed in detail in Section 6.5.1.

For the longest coherence lengths (up to 100 fs) in the SXR and HXR an optical cavity could be installed on any of the FELs. The facility layout allows this possibility. An important issue to consider with CBXFELs is the tunability of the optical cavity. A fully tunable cavity is extremely challenging. Instead it is anticipated that limited tunability around key photon energies would be provided. As such the geometry of the cavity is more simple, and could include, for example, mirror carousels, in which the optics can be remotely interchanged depending on the required wavelength.

6.3.1.2 Transform Limited Short Pulses

Various methods have been proposed to produce Transform Limited Short Pulses (in the attosecond regime), but only some of these have been experimentally validated as of early 2025.

One method is the **slotted foil scheme**. A slotted metal foil is employed to selectively degrade the transverse emittance of the electron beam. Positioned at the centre of the magnetic chicane upstream of the undulator, the foil preserves a narrow unspoiled beam core while scattering surrounding electrons. This process isolates a short region of good emittance and enhanced current a few femtoseconds long in the longitudinal phase space at the undulator entrance. Lasing is thus confined to this region, producing fully coherent sub-femtosecond photon pulses. The scheme was proposed in 2004 by Emma et al. [34]. It was demonstrated empirically in 2017 at the LCLS [35].

Another method is the chirp and taper scheme which generates a single spike by creating a short modulation in the electron energy along the bunch with a laser then applying an appropriate undulator taper so that only the section of the bunch with the strongest energy chirp can lase. This scheme was proposed by Saldin et al [36] in 2006 then demonstrated for the first time in 2010 at SPARC [37].

A further approach is the **non-linear compression scheme**. Non-linear compression of the electron bunch is achieved using a high-harmonic radio-frequency lineariser. This imparts a non-linear time-energy chirp to a low-charge electron bunch. A magnetic chicane compresses the bunch, over-compressing the head and under-compressing the tail. This forms a curved longitudinal phase space distribution with a sharp current spike of a few femtoseconds and a low-current tail. A reverse undulator taper confines lasing to the spike, yielding transform limited sub-femtosecond photon pulses. The scheme was proposed in 2014 by Huang et al. [38]. It was demonstrated in 2017 at the LCLS [39], in 2020 and 2023 at SwissFEL [40, 41] and at the European XFEL in 2024 [42].

Another important technique is the **enhanced self-amplified spontaneous emission (ESASE) scheme**. It utilises a magnetic chicane between two undulator sections. The first undulator section, combined with an external laser, induces an energy modulation in the electron bunch. The chicane converts this energy modulation into a density modulation, producing a sharp current spike of sub-femtosecond duration. In the second undulator section, the spike radiates, generating a coherent sub-femtosecond photon pulse. The scheme was proposed in 2005 by Zholents et al. [43]. It was demonstrated empirically in 2021 at the LCLS [44]. An extended scheme in which the short FEL pulse is further amplified using a fresh portion of the electron bunch was demonstrated in 2024 [45].

There exists a variant of this approach, known as the **x-ray laser-enhanced attosecond pulse (XLEAP) generation scheme**. It employs coherent infrared radiation emitted by the electron bunch tail in the wiggler to modulate the bunch core, instead of an external infrared laser. This modulation facilitates the generation of a coherent sub-femtosecond photon pulse. It was demonstrated empirically in 2020 at the LCLS [46].

The schemes described above have been able to produce isolated attosecond pulses at photon energies up to an order of magnitude higher, and pulse energies up to two orders of magnitude higher, than pulses produced via High Harmonic Generation in gases. This enables access to the study of nonlinear interactions in the HXR, as shown in Figure 6.7.

Other schemes have been proposed to generate **single-cycle** or coherent **few-cycle** photon pulses, with the aim to achieve the minimum possible pulse duration by decreasing the number of oscillation cycles within the pulse to around unity. Notable examples include the **mode-locked amplifier scheme** [48] which was recently demonstrated at SwissFEL [49], the **mode-locked afterburner** [50], the **compact field-tailored undulator scheme** [51] and the **chirped microbunching scheme** [52]. A comprehensive review of these schemes is provided in Reference [53].

The FEL techniques for generating attosecond pulses having been reviewed, the most suitable options for the UK XFEL are determined below through a process of elimination.

The **mode-locked amplifier scheme** [48, 49] and **mode-locked afterburner** [50] are deemed unsuitable. They produce pulse trains rather than isolated pulses, whereas the UK XFEL Science Case specifies a requirement for isolated pulses. Furthermore, although the afterburner scheme offers the potential to achieve zeptosecond-scale pulse durations, such extremely short pulses exceed current user requirements, which are confined to attosecond pulses.

The **compact field-tailored undulator scheme** [51] is also unsuitable. It requires two single-period undulators with bespoke magnetic field profiles, which conflicts with the overall FEL design outlined in Section 6.4, considering other applications. Furthermore, the photon pulse energy is limited by the number of undulator periods and a single period imposes a fundamental constraint on achievable pulse energy.

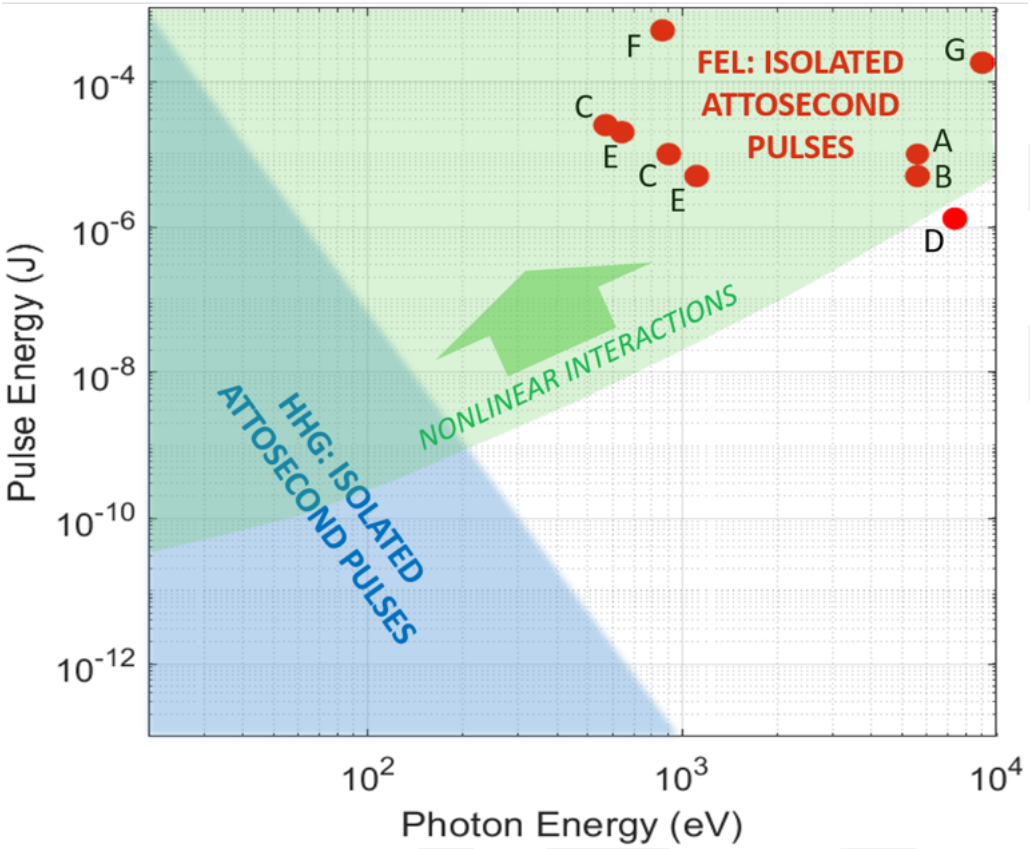

Figure 6.7: Experimentally demonstrated schemes for generating isolated attosecond pulses from FELs, showing orders of magnitude enhancements in photon energy and pulse energy compared to HHG sources, thus enabling access to the study of nonlinear interactions. Schemes shown are as follows: A [39], B [35], C [46], D [40], E [41], F [45], G [42]. Figure adapted from [47] during discussions with the Author.

The **chirped microbunching scheme** [52] is similarly inappropriate. The mechanism for generating the chirped microbunches is relatively complex and requires multiple stages, each necessitating a specialised undulator module or magnetic chicane. This hardware requirement is incompatible with the overall FEL design detailed in Section 6.4, when other applications are considered.

The **slotted foil scheme** [34] is infeasible. The high repetition rate of 1 MHz can induce excessive heat load and damage the foil. Moreover, the foil is positioned upstream of the FEL branch lines and affects the electron bunches delivered to every branch, thus preventing simultaneous operation in varied modes across the soft and hard x-ray regimes. This lack of flexibility renders the scheme incompatible with the facility's multi-line design.

The **non-linear compression scheme** is similarly inappropriate. It requires optimising the voltages and phases of the radio-frequency cavities upstream of all FEL branch lines. However, the optimal settings for one branch may conflict with those needed for others, hindering parallel operation in diverse modes across soft and hard x-ray regimes. This inflexibility renders the scheme incompatible with the facility's multi-line design.

Amongst all the approaches which have been experimentally validated, the only viable options are the **enhanced self-amplified spontaneous emission (ESASE) scheme** [43] and its derivative known as the **x-ray laser-enhanced attosecond pulse (XLEAP) generation scheme** [46]. These schemes avoid upstream hardware modifications, allowing independent tailoring for each FEL branch without affecting others. They are compatible with the repetition rate of 1 MHz and align with the design of individual FEL lines, utilising a short undulator for energy modulation, a magnetic chicane for density modulation and a main undulator for photon pulse production.

ESASE is preferred because it does not require a bunch distribution with a current spike, and is thus compatible a switchyard of FELs supplied with a common electron bunch profile. Additionally, the FEL pulses are naturally synchronised with an external laser system. The simulation study of the ESASE scheme for the UK XFEL is presented in Section 6.5.5.

6.3.2 Two-colour Pulses

Delivering two x-ray pulses with different photon energies to a single experiment is an important next generation feature. In general, the two pulses are also temporally separated, with an adjustable time delay. Two-colour pulses from x-ray FELs are particularly useful in **pump-probe experiments**.

There are two main approaches to generating two-colour pulses.

- The **dual-FEL approach** deploys two independent FEL lines in parallel, each emitting a single x-ray pulse. The resulting pulses are then combined at a common experimental station.
- The **single-FEL approach** produces two x-ray pulses within a single FEL line. There exist a number of FEL schemes in this approach and they generally fall into two categories.
  - The first category involves **undulator tuning**, whereby a single electron bunch traverses a single FEL line comprising two undulator sections in series with different tunings.
  - The second category involves **electron beam manipulation**, whereby two ensembles of electrons with different energies traverse a common undulator.

Amongst the many schemes proposed theoretically, about a dozen have been proven empirically as of early 2025.

In the undulator tuning category within the single-FEL approach, the following schemes have been demonstrated empirically, with years given in brackets. The **undulator splitting scheme** [54] (2013) divides a single undulator into two sections with distinct magnetic field strengths. The **wakefield-based fresh-slice scheme** [55] (2016) utilises a corrugated structure to induce wakefields that transversely displace electron bunch slices, enabling different slices to lase at distinct photon energies in downstream undulator sections. The **matching-based fresh-slice scheme** [56] (2017), adjusts electron beam optics to match different longitudinal slices of the bunch to undulator sections tuned to different resonances. The **dispersion-based fresh-slice scheme** [57] (2018) uses a magnetic chicane to create an energy chirp and transverse dispersion, directing different electron bunch slices to lase at distinct photon energies in the subsequent undulator sections. Finally, the **alternating undulator scheme** [58] (2022) configures a single undulator line with alternating segments of different periods or field strengths, enabling the electron beam to lase at two photon energies simultaneously.

In the electron beam manipulation category within the single-FEL approach, the following schemes have been demonstrated empirically. The **twin bunches scheme** [59] (2015) employs two closely spaced electron bunches with distinct energies and trajectory offsets, each lasing at a different photon energy in the undulator. The **double-slotted foil scheme** [60] (2015) uses a slotted foil to split the electron beam into two beamlets with different time-energy correlations and the two beamlets then radiate at two distinct photon energies. The **wakefield excitation scheme** [61] (2016) utilises a dielectric-lined waveguide to induce wakefields that modulate the electron beam, creating two distinct energy bands that lase at different photon energies. The **two-bucket bunches**

scheme [62] (2017) generates two-colour x-ray pulses by manipulating the electron beam to form two temporally separated bunches within a single RF bucket. The **sextupole scheme** [63] (2020) employs a sextupole magnet to introduce a non-linear correlation in the electron beam's longitudinal phase space, allowing two distinct energy slices to lase at different photon energies. Finally, the **laser emittance spoiler scheme** [64] (2021) uses an external laser to selectively increase (i.e. spoil) the emittance of the central part of the electron beam and allows the two unspoiled segments of the beam (i.e. head and tail) to lase at different photon energies.

Within the single-FEL approach, the **phase shifter scheme** [65] (2023) has also been demonstrated empirically, but it falls into neither the undulator tuning category nor the electron beam manipulation category. The scheme introduces successive phase shifts of π to make the electrons and the radiation out of phase, so that two-colour x-ray pulses can be generated by suppressing the resonant wavelength and amplifying the sidebands in the radiation spectra. In the year 2024, an additional scheme [66] was demonstrated to produce two attosecond pulses at different wavelengths, thus combining the two-colour and attosecond features of a next-generation FEL.

The options for the generation of two-colour pulses are now assessed for suitability for implementation on UK XFEL.

Different techniques are preferred for producing the pump and probe pulses, depending on the required spectral regime combination. For **SXR-SXR** and **HXR-HXR combinations**, the **single-FEL approach** is deemed efficient and appropriate, as it optimises resource use. For **SXR-HXR combinations**, the significant spectral difference between the photon pulses often necessitates the **dual-FEL approach**, where two FELs deliver photon pulses to a single experiment.

The dual-FEL approach, in principle, requires precise coordination to direct photon pulses from separate branches to a single experiment. A more efficient solution involves installing two parallel undulator lines within the same tunnel in one branch. This configuration offers improved synchronisation of the photon pulses due to the parallel alignment of the undulator lines. It also simplifies photon beamline design and enhances operational stability due to the proximity of the source points. Based on the user requirements envisaged in the UK XFEL Science Case, it has been decided to duplicate the SXR undulator line of the FEL-5 branch and place it in the FEL-2 branch tunnel alongside the pre-existing HXR undulator. The relative timing between the electron bunches in each line will be controlled via a combination of placing the bunches in near adjacent RF buckets and use of a magnetic delay chicane.

In the single-FEL approach, the schemes are not always mutually exclusive, as implementing one does not necessarily preclude the others. Rather than committing to a single scheme, the facility design (see Section 6.4) is sufficiently flexible to accommodate multiple schemes in both the **undulator tuning category** and the **electron beam manipulation category**. The capacity to employ multiple schemes improves the stability of two-colour pulse provision and enables more precise tailoring to the specific needs of individual experiments.

However, given that the facility operates at a high repetition rate of 1 MHz, the following schemes are deemed *unsuitable* and excluded for generating two-colour photon pulses.

- The **twin bunches scheme** [59] is unsuitable due to the complexity and potential instability of generating and stabilising two distinct electron bunches at 1 MHz.
- The **double-slotted foil scheme** [60] is unsuitable due to potential foil damage and electron beam quality degradation at high repetition rates.
- The **two-bucket bunches scheme** [62] is unsuitable due to the difficulty of reliably generating and maintaining two electron bunches within a single RF bucket at 1 MHz.

- The **laser emittance spoiler scheme** [64] is unsuitable due to the challenge of providing a stable, high-repetition-rate laser and synchronising it for emittance spoiling at 1 MHz.

The schemes listed above are unsuitable primarily due to challenges in achieving stable operation at the high repetition rate of 1 MHz. Generally speaking, these challenges stem from limitations in laser technology, complex electron beam manipulations or potential hardware damage (e.g. foil).

The **phase shifter scheme** [65] could, in principle, operate at the repetition rate of 1 MHz. However, it is deemed unsuitable due to its limited flexibility in controlling the temporal delay between the pump and probe pulses. It therefore does not fully meet the user requirements outlined in the UK XFEL Science Case. These other schemes are better suited for this purpose: **Undulator splitting scheme** [54], **Wakefield-based fresh-slice** [55], **Matching-based fresh-slice** [56], **Dispersion-based fresh-slice** [57], **Alternating undulator** [58], **Wakefield excitation** [61] and **Sextupole** [63]. In addition, the recently demonstrated scheme [66], which integrates two-colour and attosecond capabilities of a next-generation FEL, merits inclusion for implementation.

Thus far, only schemes empirically validated by early 2025 have been considered, as experimental evidence supports their reliability. The generation of two-colour photon pulses is a rapidly advancing area of research. In the years ahead, more FEL schemes are expected to be experimentally validated. These newly validated schemes can be evaluated in the subsequent phase of the UK XFEL project and integrated into the facility design.

6.3.3 FEL-1: High Photon and Pulse Energies for Extreme Environments

Some user cases, for example Matter in Extreme Conditions (MEC), require a broader range of photon energies, from 5 keV up to 45 keV, and extremely high FEL pulse energies, up to 10's of mJ at the lower photon energies. To cover this broad photon energy range, and to maximise efficiency and throughput, these communities will be served by two FELs, 1a and 1b, covering 5–20 keV and 20–45 keV respectively. To reach the highest photon energies it is necessary to increase the beam energy above 8 GeV, to approximately 12 GeV. This enhanced beam energy also allows enhanced pulse energies from the FELs at all photon energies.

The user case is predominantly experiments combined with high pulse energy optical lasers, which have typically a low repetition rate, so FELs 1a and 1b will operate at a repetition rate matched to these laser sources. This means that the acceleration boost, from 8 GeV to approximately 12 GeV, can be accomplished with a low repetition rate, high gradient, normal conducting linac. There is a requirement for variable polarisation, hence the undulators will be a variably polarising design, but there is no requirement for transform-limited pulses, hence the FEL mode of operation will be SASE, unless future design studies indicate HB-SASE + tapering offers better performance (due to tapering working more efficiently for transform limited pulses than for SASE pulses). At the lower photon energy range of each FEL the saturation lengths are shorter so the spare undulator length can be used for post-saturation tapering. In the absence of advanced FEL modes such as HB-SASE, there is no need for undulator modules to have a maximum length beyond the requirement to be able to obtain a suitable electron beam radius. The preliminary design is therefore based on undulator modules which are 4 m long.

The FEL and electron beam parameters are shown in Table 6.1. FEL-1a will operate predominantly with 300 pC bunches compressed to a peak current of 5000 A. This charge is favoured because it is the nominal charge for FELs 5 and 6 so does not require an independent injector set-up. The results shown in Section 6.5.6 are for this charge, with a beam energy of 12 GeV, and as will

be seen, predicted pulse energies at 5 keV are >20 mJ with the chosen undulator length which allows generous space for post-saturation tapering. To produce pulse energies greater than this will require special modes of operation in which the beam energy is boosted even higher than 12 GeV and the charge is raised as high as 600 pC. This mode of operation will continue to be investigated and studied as user requirements become better defined. FEL-1b will operate at a lower charge of 150 pC in order to achieve the lower emittance requirements at the higher photon energies. Pulse energies will be more modest.

6.4 FEL Section Design

6.4.1 FEL Tuning Ranges

The chosen undulator technology is APPLE-X, as will be discussed in more detail in Section 6.7. Assuming a provisional minimum magnet gap of 4mm, which has been found in initial wakefield assessments to be acceptable, and is comparable to the minimum aperture for other HXR facilities, the complete photon energy range 0.1–20 keV can be covered at a beam energy with 7 FELs. This number of FELs allows full tuning range overlap so that all photon energies from 0.25–20 keV are accessible from two FELs. The tuning ranges for each FEL become progressively narrower as the top photon energy for the FEL increases. For the lower photon energy FELs the chosen beam energy is sufficiently high that the minimum photon energy can be reached with a high undulator a_w parameter, leaving a large variation of a_w to cover a broad range of tuning and good FEL performance due to the high beam energy, compared to other facilities, at these lower photon energies. For the FEL tuned to the highest photon energy the beam energy is only sufficient for a modest maximum a_w, leaving a limited tuning range. The tuning range of each FEL is shown in Figure 6.8. FEL-6 to FEL-2 operate at the nominal electron beam energy of 8 GeV, whereas FELs 1a and 1b require an energy boost to around 12 GeV.

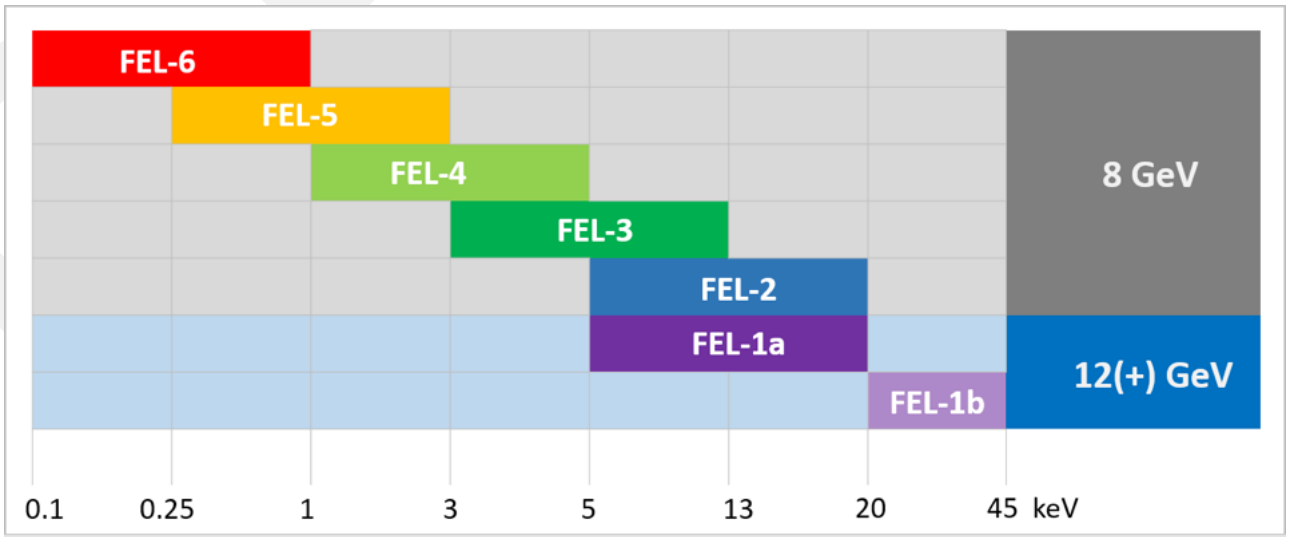

Figure 6.8: FEL Tuning Ranges

6.4.2 FEL Schematic

A schematic of the conceptual design of the facility FELs is shown in Figure 6.9 and is described here. An engineering drawing of the FEL hall is shown, for reference, in Figure 6.10. The process for the determination of the design parameters, including the requirements on the electron beam, are laid out in subsequent sections.

The total undulator lengths are derived from optimised time-dependent SASE simulations. For all FELs (excluding FEL-6 which is seeded), 50 % contingency has been added to the total length. For HB-SASE the delays are integrated into the undulator modules which are termed Integrated Delay Undulators (IDUs). All radiating undulators for FELs 2/3/4/5/6 are APPLE-X to enable polarisation control. All integrated delays are single period PPM undulators and all modulator undulators, required for seeding and/or electron beam modulation for ESASE, are planar permanent magnet devices. The final amplification of the FEL radiation occurs in the radiator undulators where diffraction is minimised because no space is allocated for electron beam delays. For each HB-SASE FEL there are 32 delays, and either 2,3, or 4 delays per IDU, dependent on photon energy. All IDUs and Radiator Undulators (RUs) for FELs 2–6 are 2 m long, with 0.5 m gaps between comprising quadrupole, beam position monitor and vacuum components. The FODO period is 5m, allowing a sufficiently small mean beta function for each FEL. FELs 1a and 1b are SASE only, with radiator module lengths of 4 m, and 1 m gaps in between undulator modules giving a FODO period of 10 m.

6.4.3 Electron Beam Requirements

6.4.3.1 Electron Bunch Length

To achieve near-transform-limited pulses the coherence length must be approximately the photon pulse length. In HB-SASE and Self-Seeding, the photon pulse length is approximately the same as the electron bunch length. Therefore, the electron bunch length at each FEL should be matched to the obtainable coherence lengths from that FEL.

In the limited studies to date, the coherence length increase of HB-SASE over SASE, assuming dipole only chicanes, can be up to a factor of 35. The maximum required electron bunch for each FEL can therefore be estimated from analytic calculations of the SASE coherence length at different photon energies, multiplied by 35. The results of this calculation are shown in Figure 6.11.

The full range of required electron bunch lengths for FELs 2–5 is therefore 7–70 fs. FEL-6 is designed to produce transform limited pulses via external seeding at durations up to 100 fs, therefore the full range requirement is 7–100 fs. This requirement for different bunch lengths at each FEL does not initially appear consistent with the requirement that all FELs are driven by a common electron bunch. The solution to this is to include two injectors producing only two different fixed bunch lengths and to allow some adjustment of ‘effective’ bunch within each FEL line, as described below.

6.4.3.2 Charge and Emittance

The emittance requirement for a FEL depends on the required photon energy. The typical criteria, which is a guide only, is that if the electron beam beta function and gain length are equal the

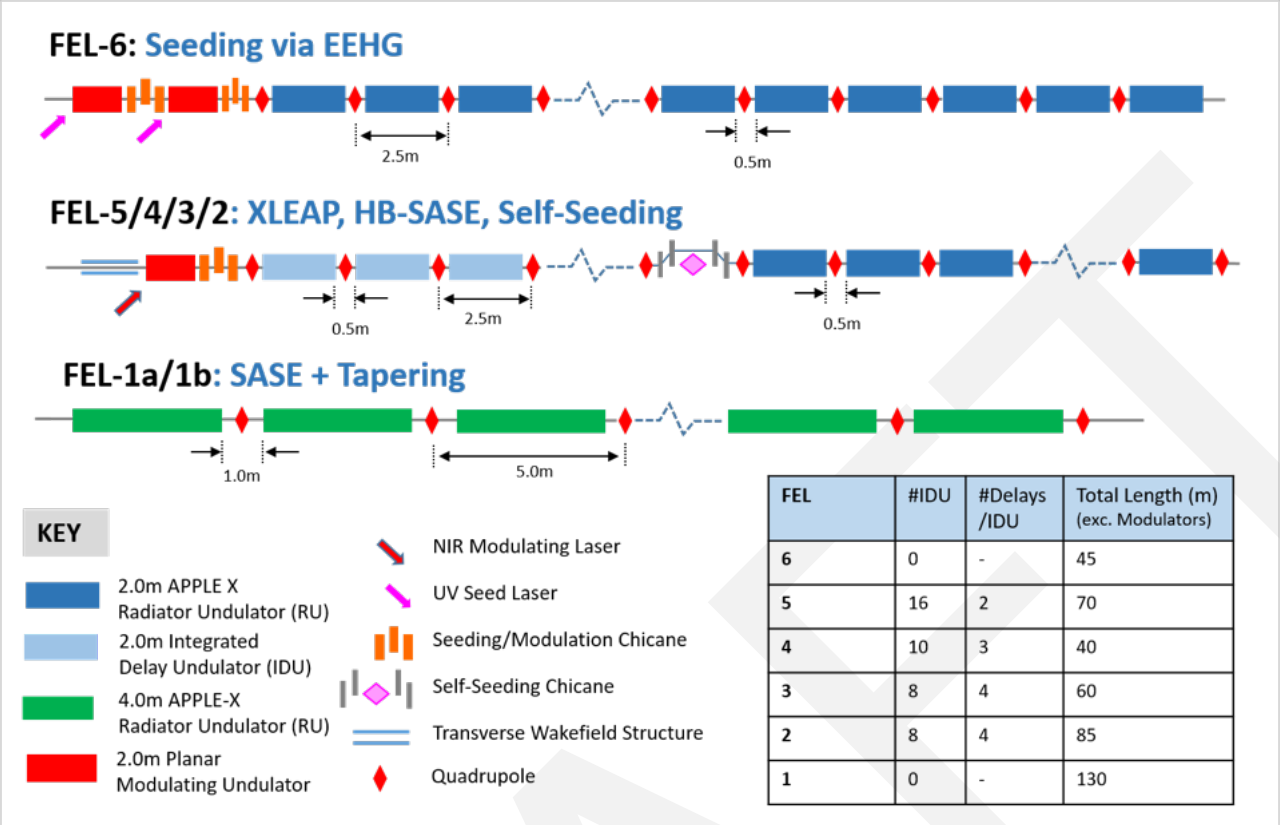

FEL	#IDU	#Delays /IDU	Total Length (m) (exc. Modulators)
6	0	-	45
5	16	2	70
4	10	3	40
3	8	4	60
2	8	4	85
1	0	-	130

Figure 6.9: Schematic of FEL components.

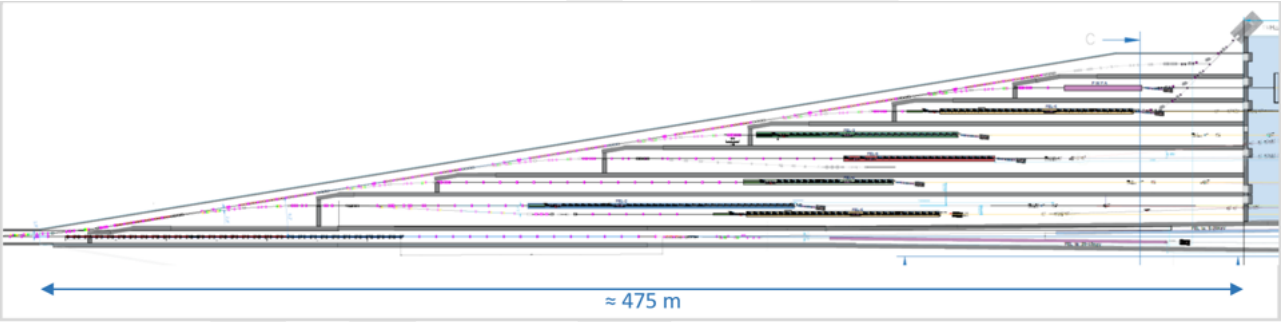

Figure 6.10: Engineering drawing of FEL switchyard

normalised emittance ε_n should satisfy

$$\varepsilon_n \leq \frac{\lambda\gamma}{4\pi} \tag{6.1}$$

with λ the FEL wavelength [67]. The minimum achievable electron beam emittance is a function of the bunch charge, increasing due to space charge forces at the source as the bunch charge increases. Therefore, the optimum bunch charge for each FEL is dependent on its photon energy. This dependence was investigated via a detailed simulation study to determine the optimum bunch charge for each of the two injectors, given the constraint already specified on electron bunch duration.

The concept is to send the lower charge and smaller emittance bunches to the shorter wavelength FELs—these require the smaller emittance and they also need the shorter bunches. Conversely the higher charge and higher emittance bunches are sent to the longer wavelength FELs.

Each FEL line, for FELs 2–5, is equipped with a method for imposing a transverse streak to the tail of the electron bunches. The tail of the bunch is therefore kicked off axis and does not lase in the

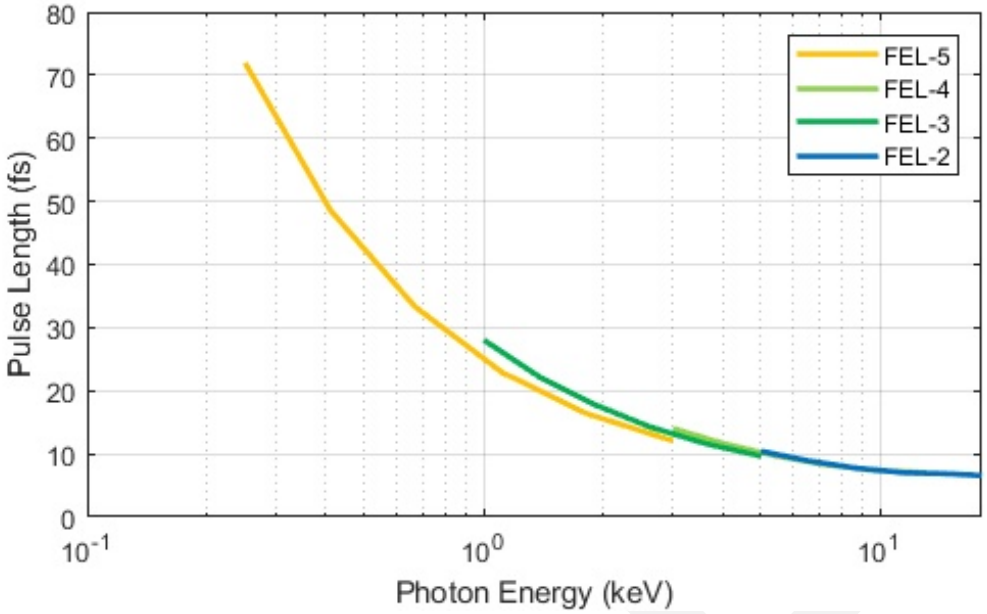

Figure 6.11: Required Electron Bunch Lengths for HB-SASE Transform Limited Operation

FEL, whereas the head of the bunch remains on axis. By adjusting the strength of this transverse kick the effective lasing bunch length can be controlled. The preferred option, for reasons of stability and sustainability, is to use a passive wakefield device to create the transverse kick rather than an RF cavity. A preliminary design indicates that a dielectric device only 1 m long would suffice. The device would be subject to heating due to the power loss in the electron beam. At high repetition rates this power loss would be sufficient to require active cooling and is a topic for future research phases and prototyping. In this way it is possible to send bunches of small enough emittance and appropriate duration to all FELs.

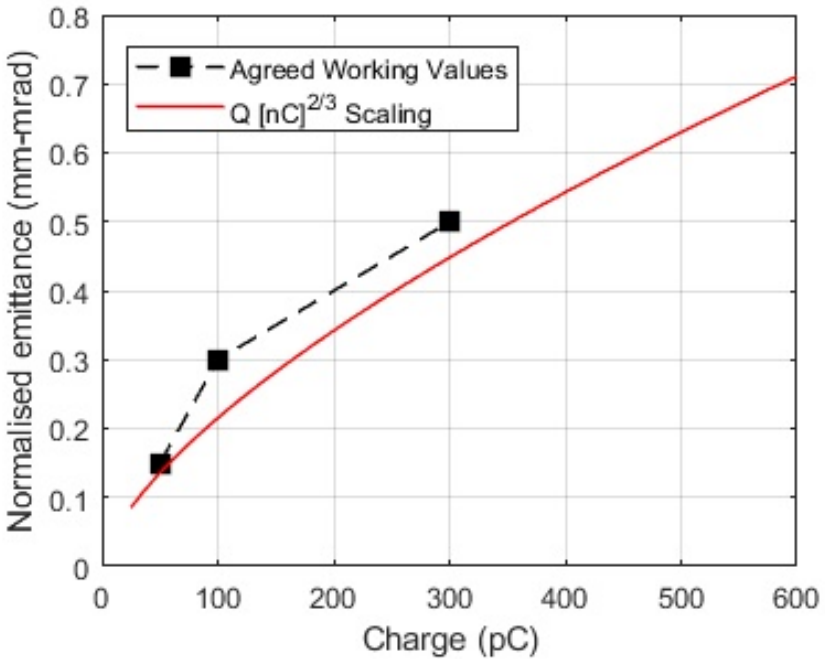

Figure 6.12: Emittance vs Charge scaling.

In the simulation study Injector A produced a flat top electron bunch at the FEL of duration 100fs,

which can be sheared, as described above, to produce an effective duration of 100–30fs. The charge was scanned from 25 pC to 300 pC, with a maximum peak current of 3 kA at 300 pC. For each charge the electron bunch emittance was scaled based on best estimates of emittance at the FEL made at the beginning of the design phase, referred to as Agreed Working Values. These estimates are shown in Figure 6.12 and seen to be conservative compared to the well known scaling law ε_n [mm-mrad] $\simeq$ Q[nC]$^{2/3}$ previously shown in Figure 4.14. Injector B produced a flat top electron bunch of duration 30 fs, which could be sheared to produce effective durations 30–10 fs. The charge was scanned from 25 pC to 150 pC, with the emittance scaled again accordingly. At 150 pC the peak current reaches 5 kA—this was taken as a practical upper limit so 150 pC was the highest charge used.

For this study only, the FEL lattice used a continuous undulator with very closely spaced quads to give a constant electron beam radius. This was to give consistency across all FELs. The use of individual undulator modules and inter-module gaps in a typical FODO lattice gives an oscillating electron beam radius and an extra degree of performance degradation which is not consistent across FELs and beta functions. It was assumed that in practice the minimum beta function is 2 m. This is the smallest that could be obtained in the most tightly compressed undulator lattice that would be considered (0.5 m undulator modules and 0.5 m inter-module gaps) without the minimum beta in the FODO being less than half the mean beta function, at which point FEL performance degrades quickly.

The electron beam beta function was optimised analytically to minimise the gain length using the Ming Xie parameterisation [68]. For each FEL, at its maximum and minimum photon energies, the charge/emittance combination was scanned and the FEL simulated (in SASE) using the code Genesis1.3 (v4) [69, 70] in full time dependent mode. The results are shown in Figure 6.13. From these results it was decided that FELs 2, 3, and 4 should be driven by Injector B operating at a charge of 75 pC—this working point balances maximum brightness with maximum pulse energy. Similarly, FELs 5 and 6 should be driven by Injector A operating at 300pC to maximise brightness and pulse energy and minimise saturation length.

6.4.4 Parameter Summary

The parameters of the FEL systems, and required electron beam parameters, are summarised in Table 6.1.

6.5 FEL R&D and Performance Studies

This section presents some of the FEL R&D work performed as part of the CDOA Project. This work comprises both optimisation and performance studies for the primary FEL methods necessary to fulfill the requirements of the Science Case, and also R&D aiming to extend the performance envelope of the facility, for example towards new efficient methods for harmonic lasing and accessing photon energies higher than the nominal 45 keV.

6.5.1 Optimisation of HB-SASE

HB-SASE has been chosen as one of the FEL methods for generating near-transform-limited pulses. For optimum performance from HB-SASE, there are a number of requirements:

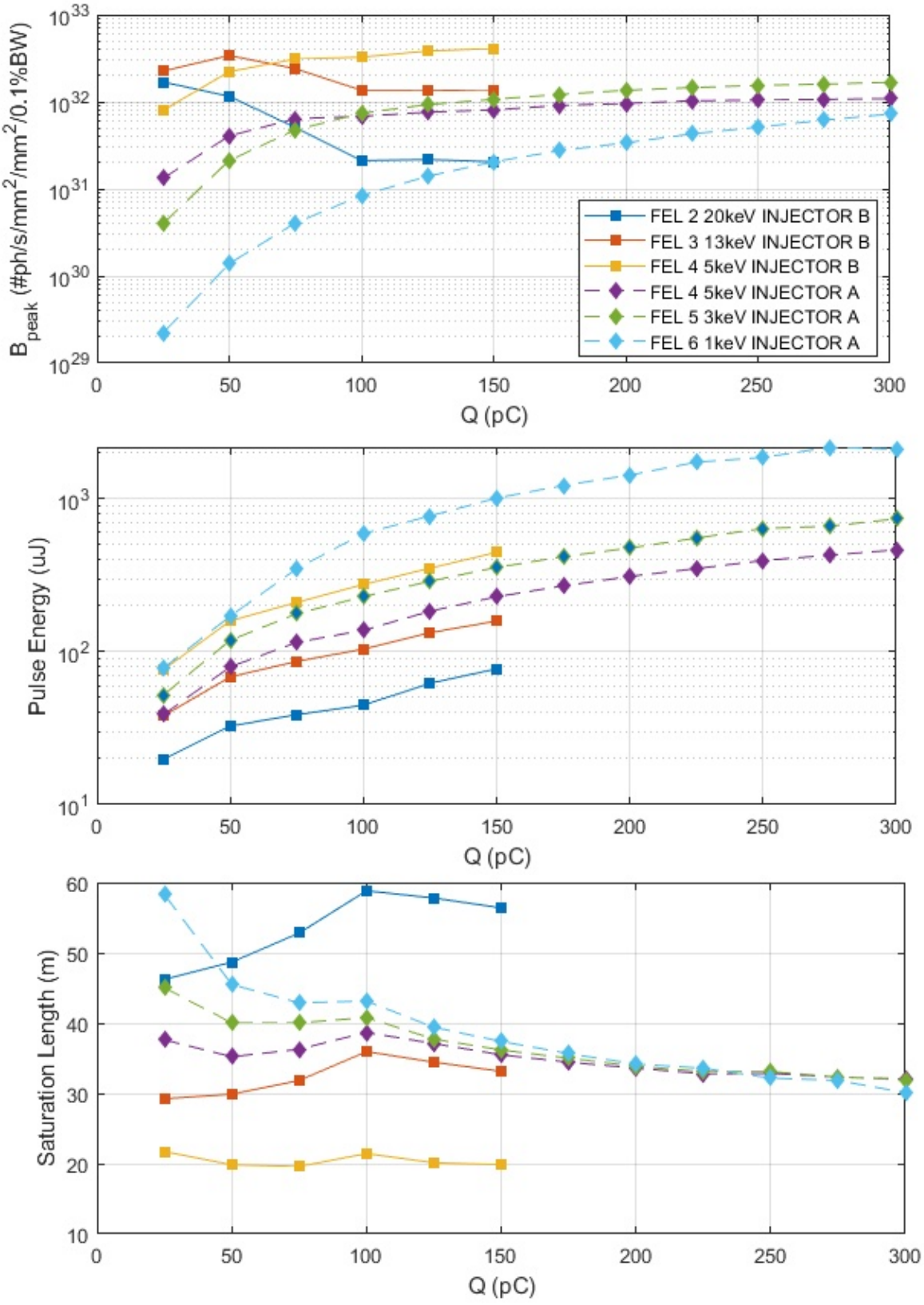

Figure 6.13: Optimisation of Bunch Charge

- **The individual undulator modules must be short**. This is because the technique relies on interference between emission from neighbouring undulator modules, and this interference is more complete if the two signals being interfered have the same amplitude. The outcome,

Table 6.1: Main Parameters

FEL	1a	1b	2	3	4	5	6
Photon Energy (keV)	5–20	20–45	5–20	3–13	1–5	0.25–3	0.1–1
FEL Modes	SASE + Tapering		ESASE + Self-Seeding + HB-SASE				EEHG
Undulator Period (mm)	28	18	21	24	32	48	82
Minimum Gap (mm)	4	4	4	4	4	5	8
Undulator Technology	APPLE-X		APPLE-X + IDUs				APPLE-X
Electron Energy (GeV)	12(+)		8			8	
Charge (pC)	300	150	75			300	
Bunch duration (fs)	60	30	30			100	
Peak Current (A)	5000	5000	2500			3000	
Emittance (mm-mrad)	0.5	0.3	0.22			0.5	
Slice Energy Spread	3×10^{-4}	3×10^{-4}	1×10^{-4}			1×10^{-4}	

which has been validated in simulation studies, is that the shorter the undulator modules, the more effective the technique. Each undulator module should be less than one gain length, or even shorter. The UK XFEL design concept is to integrate several delay sections into the undulator modes in so called Integrated Delay Undulators. As seen in the table in Figure 6.9 each FEL has approximately 30 delays. FEL saturation is typically reached in 20 gain lengths so each undulator module has an effective length of $2L_g/3$, satisfying the criteria.

- **The maximum delay that can be applied to the electron bunch depends on the beam energy spread**. The delay chicanes comprise dipoles only, so the electron delay is energy dependent, and the delays act to smear out the FEL microbunching. For two electrons of energy $E = \pm\sigma_E$, with σ_E the rms beam energy spread, the constraint is imposed that the difference in longitudinal shift is less than half a wavelength to preserve the bunching. An approximate criteria on the maximum delay can then be easily derived as

$$\delta \ll \frac{\lambda}{4(\sigma_E/E)} \tag{6.2}$$

indicating that for large delays the energy spread should be small, and that the delay sequence should start with the largest delays, then reduce as the FEL-induced energy spread increases. For a linearly decreasing delay sequence of 30 delays then the approximate maximum slippage, and hence the maximum possible coherence length (time) depends on photon energy and energy spread as shown in Figure 6.14. This figure shows for example that to be able to delay the electron bunches sufficiently, without smearing out the FEL microbunching, to obtain a coherence time of 10 fs at a photon energy of 20 keV, the beam intrinsic energy spread should satisfy $\sigma_E/E \ll 1 \times 10^{-4}$. This is the required specification of the electron beam. The figure also indicates that longer coherence lengths are obtainable at lower photon energies, as has been proven in extensive simulation studies, and that a route to obtaining coherence lengths longer than 10 fs at 20 keV could be found via further reduction of beam energy spread.

- **The radiation diffraction in the delay chicanes can degrade the normal FEL gain guiding**. Gain guiding in the FEL is responsible for the domination of the fundamental

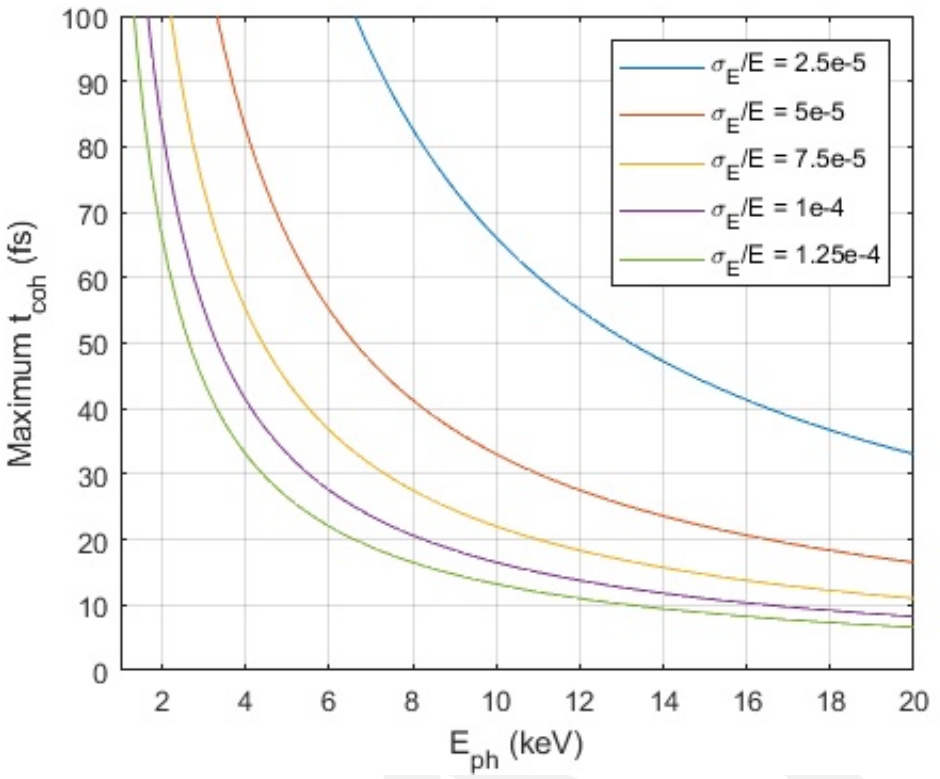

Figure 6.14: Estimate of maximum coherence time vs FEL photon energy, for different beam energy spreads.

Gaussian mode and hence the near diffraction limited FEL output. Introducing extra space for delays degrades this gain guiding. The UK XFEL solution is to divide the undulator lattice into two sections. The first section comprises the IDUs—here the distributed spectral filtering, which is a longitudinal effect, occurs. The second section comprises only radiator undulators, with no delays. Here the filtered FEL radiation is amplified to final saturation and the gain guiding is maximised to enable diffraction limited output. Simulations have shown that the overall 6D brightness of the FEL radiation, which depends on the transverse mode quality, is much improved in this way compared to a lattice in which the delays are applied continually to saturation.

6.5.2 Comparative Study of Self-Seeding, HB-SASE and Hybrid Scheme

A study was done to compare the performance and stability of FEL-3, operating at 1 keV, in four different operating modes: SASE, Self-Seeding, HB-SASE and a Hybrid scheme in which Self-Seeding and HB-SASE are implemented together. The electron beam parameters were

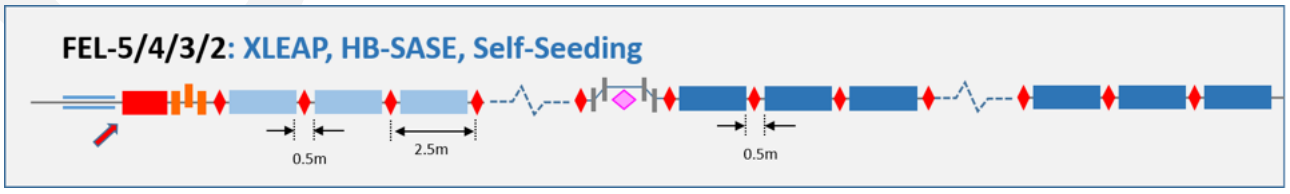

Figure 6.15: Schematic Layout of FELs 2/3/4/5

similar to the nominal parameters, but an earlier iteration. The beam energy was 8 GeV, the peak current was 1600 A, the electron bunch had a flat-top current profile with a short Gaussian roll-off

at each end (a super-Gaussian of order 8), normalised emittance 0.15 mm-mrad and relative RMS energy spread 5×10^{-5}. The FEL lattice was as described in Figure 6.9 and reproduced here in Figure 6.15. In the results presented here the stability was only studied in the presence of electron beam shot noise and neglected jitter in macroscopic electron bunch properties.

For Self-Seeding the monochromator parameters were as follows: bandwidth 0.07 eV, efficiency 5 %, photon delay 200 µm. The same delay, and equivalent longitudinal dispersion (R_{56}) were applied to the electron bunch. The monochromator design was similar to that presented here [71]. The number of undulator modules before the monochromator (with delay chicanes all off, of course) was optimised to provide the maximum final FEL brightness.

For all four schemes simulations were done in `Genesis 1.3 (v4)` with the highest possible resolution: the parameters `one4one=true` and `sample=1` so that the real number of electrons are simulated. For each scheme 24 simulations were done, each with a different random seed for shot noise generation.

6.5.2.1 Results

Figure 6.16, Figure 6.17, Figure 6.18 and Figure 6.19 show, on the same horizontal scale, a randomly chosen 4 examples from the 24 spectra for SASE, Self-Seeding, HB-SASE and the Hybrid Scheme respectively. Figure 6.20, Figure 6.21, Figure 6.22 and Figure 6.23 show, on the same horizontal scale, the corresponding pulse profiles. All of these Figures show spectra and pulses at the median undulator positions, over the 24 individual simulations, of the *maximum brightness*. A qualitative analysis shows the SASE pulses have the expected noisy spectrum and pulse profile. The spectra of the Self-Seeding, HB-SASE and Hybrid schemes are all similarly narrow, often with a single spike. It is also seen that the Hybrid spectra do not sit on a low level 'pedestal' of noise away from the central photon energy. The pulse profiles of Self-Seeding and HB-SASE appear similar—a broad envelope that matched the electron bunch profile—but with some clear noise. The Hybrid pulse profiles however are much cleaner with less noise. The typical pulse duration is 30 fs. In summary, the Hybrid scheme produces qualitatively higher quality pulses, both spectrally and temporally.

A quantitative analysis is summarised in Figure 6.24 which shows the mean brightness over the 24 simulations, vs the relative rms variation over all the simulations. Each point on the plot is data from a different position within the undulator. In this way the available balances between peak brightness and stability are revealed. For example, the maximum brightness for Self-Seeding is seen to be $\langle B \rangle = 3.3 \times 10^{32}$ph/s/mm^2/mrad^2/0.1%bw corresponding to a shot-to-shot stability of 39 %, whereas the best stability is 36 % corresponding to a reduced brightness of $\langle B \rangle = 2.2 \times 10^{32}$ph/s/mm^2/mrad^2/0.1%bw. The data is presented in this way because different user experiments may have different requirements—one experiment may need maximum brightness, whereas another experiment may need maximum stability at the cost of a slightly reduced brightness. A similar analysis was done for for pulse energy. Table 6.2 shows the data summary. The hybrid scheme provides the highest brightness of all the schemes, as well as the best stability in brightness and pulse energy and the narrowest bandwidth. The relative pulse energy fluctuations are as low as 1.1 % at a pulse energy of 1.4 mJ. In addition the pulses are qualitatively higher quality, as discussed above. SASE produces the highest pulse energies, 2.08 mJ, but relies on post-saturation growth which badly degrades the pulse quality. Of the other schemes, HB-SASE produces the highest pulse energies and peak powers.

It is therefore justified that the FEL lattice incorporates the ability to operate in all three modes, of Self-Seeding, HB-SASE and Hybrid, to provide the most flexible performance and highest quality

Table 6.2: Quantitative analysis comparing 1 keV simulation results for SASE, Self-Seeding, HB-SASE and Hybrid schemes.

	SASE	Self-Seeding	HB-SASE	Hybrid
Maximum $\langle B \rangle$ (ph/s/mm^2/mrad^2/0.1%bw)	1.0×10^{31}	3.3×10^{32}	2.7×10^{32}	3.4×10^{32}
$\sigma_B/\langle B \rangle$ (%)	25	39	35	33
Minimum $\sigma_B/\langle B \rangle$ (%)	12	36	34	23
$\langle B \rangle$ (ph/s/mm^2/mrad^2/0.1%bw)	2.8×10^{30}	2.2×10^{32}	2.7×10^{32}	8.8×10^{31}
Maximum Pulse Energy (mJ)	2.08	0.95	2.03	1.45
$\sigma_{PE}/\langle PE \rangle$ (%)	1.8	4.3	3.6	1.5
Minimum $\sigma_{PE}/\langle PE \rangle$ (%)	1.8	2.1	1.4	1.1
Pulse Energy (mJ)	2.08	0.93	1.44	1.40
Mean FWHM bandwidth (at max. $\langle B \rangle$)	2.5×10^{-3}	1.38×10^{-4}	1.42×10^{-4}	1.23×10^{-4}
$\sigma_{BW}/\langle BW \rangle$ (%)	18	35	41	35
Mean Peak Power (GW) (at max. $\langle B \rangle$)	25	27	52	33

pulses. It should be noted that this analysis has been performed at a single photon energy of 1 keV. Future studies can extend this analysis to the HXR where self-seeding would employ a different type of monochromator, based on crystals in transmissive or reflective geometries. These schemes are under investigation on other facilities so it has not been a research priority for this project.

6.5.2.2 Practical Considerations

The study presented here only considered performance in simulations at a single photon energy. It is considered that the ease of wavelength tunability will differ between the schemes, with HB-SASE likely to be the most straightforward to set up at different photon energies or to smoothly scan over a sample resonance, for example. It is also postulated that, due to the lack of direct optical manipulation of the FEL output, HB-SASE is a suitable technique for a high repetition rate facility, avoiding the complications caused by heat load on optical elements, such as physical distortion or wavelength shifting.

It is therefore envisaged that a FEL lattice incorporating all three schemes for the improvement of temporal coherence offers the most flexibility, with different schemes, or combinations of, applicable depending on user requirements for pulse energy, photon energy, brightness, stability, peak field and tunability.

DRAFT

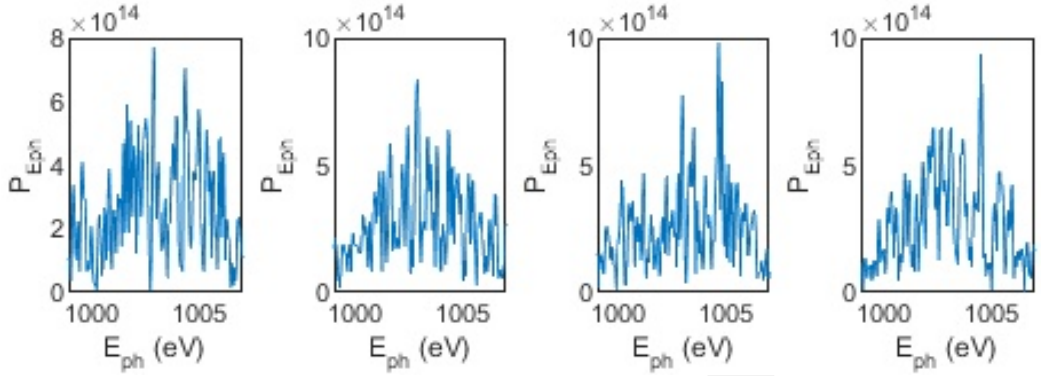

Figure 6.16: SASE Spectra at median position of maximum 6D brightness.

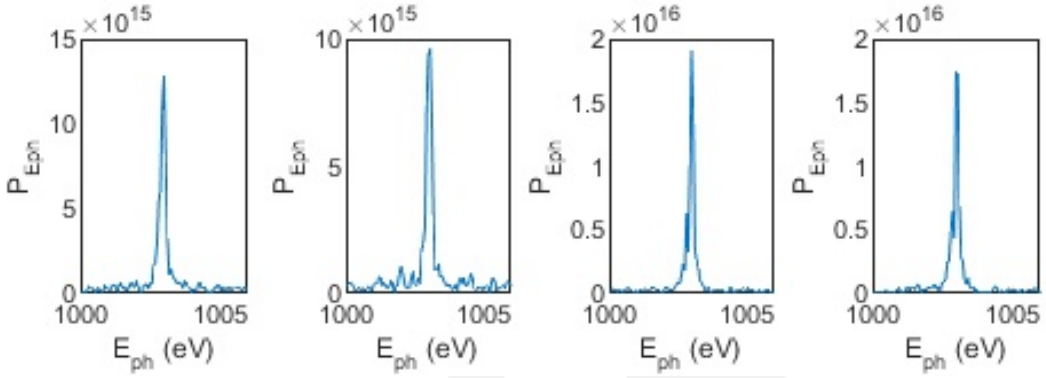

Figure 6.17: Self-Seeding Spectra at median position of maximum 6D brightness.

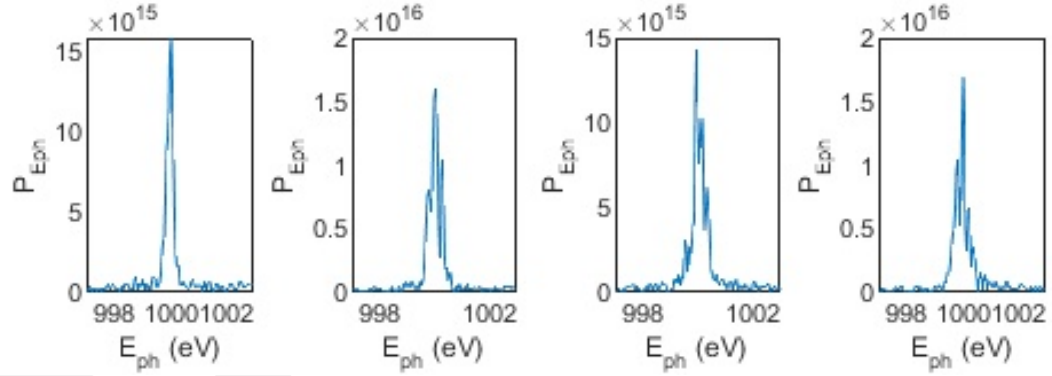

Figure 6.18: HB-SASE Spectra at median position of maximum 6D brightness.

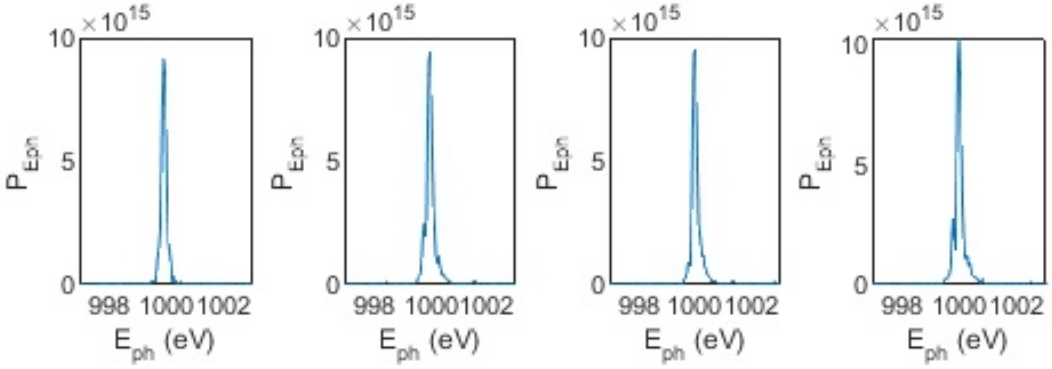

Figure 6.19: Hybrid Self-Seeding/HB-SASE Spectra at median position of maximum 6D brightness.

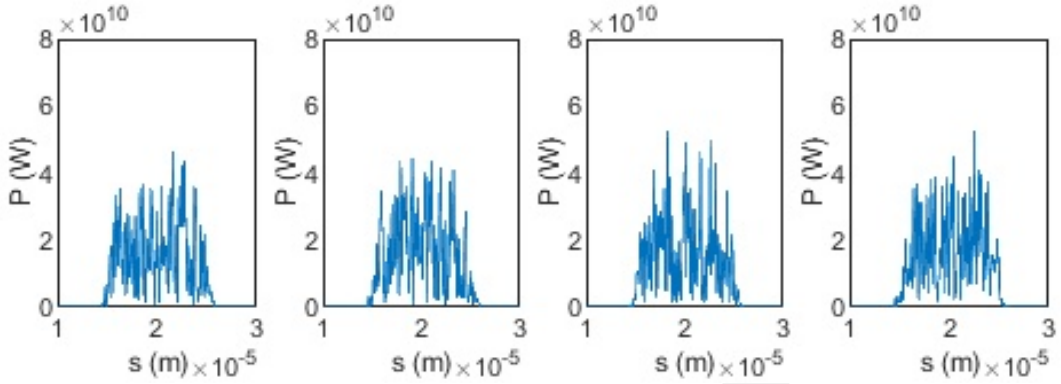

Figure 6.20: SASE pulses at median position of maximum 6D brightness.

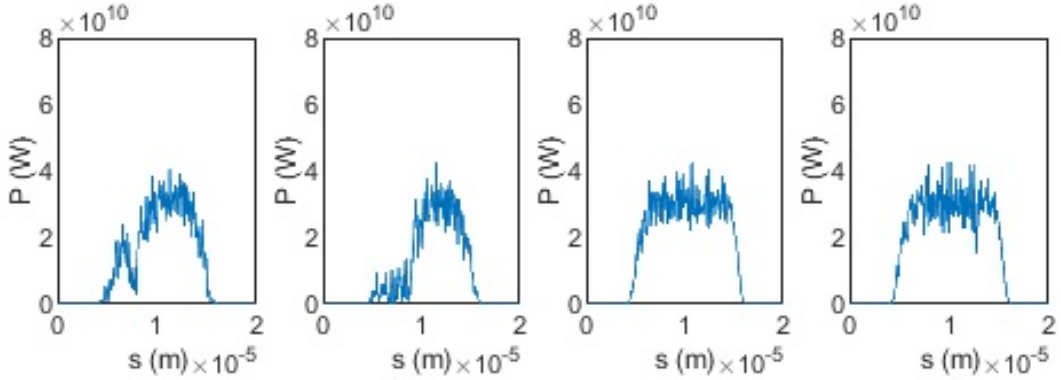

Figure 6.21: Self-Seeding pulses at median position of maximum 6D brightness.

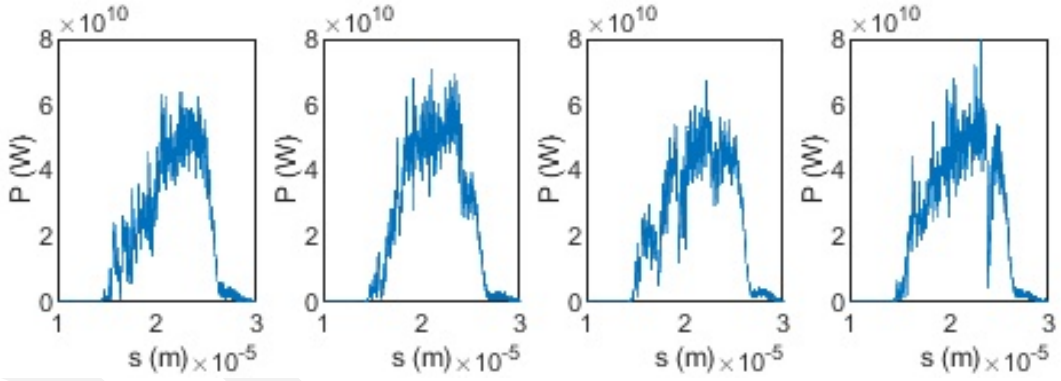

Figure 6.22: HB-SASE pulses at median position of maximum 6D brightness.

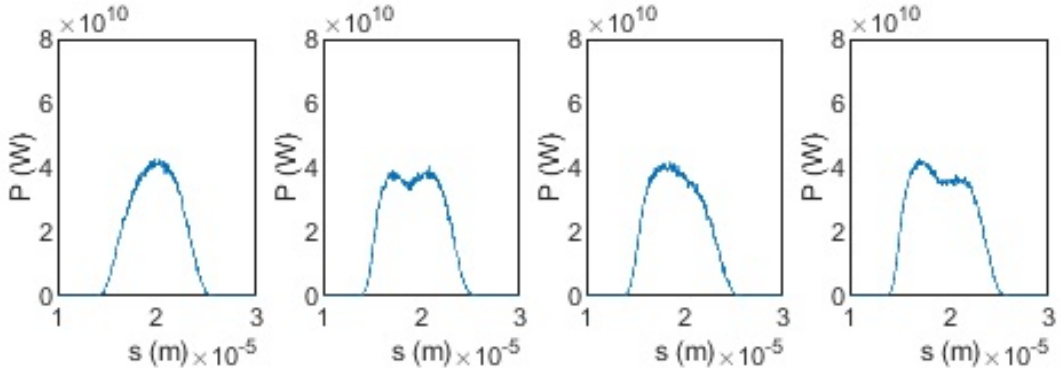

Figure 6.23: Hybrid Self-Seeding/HB-SASE pulses at median position of maximum 6D brightness.

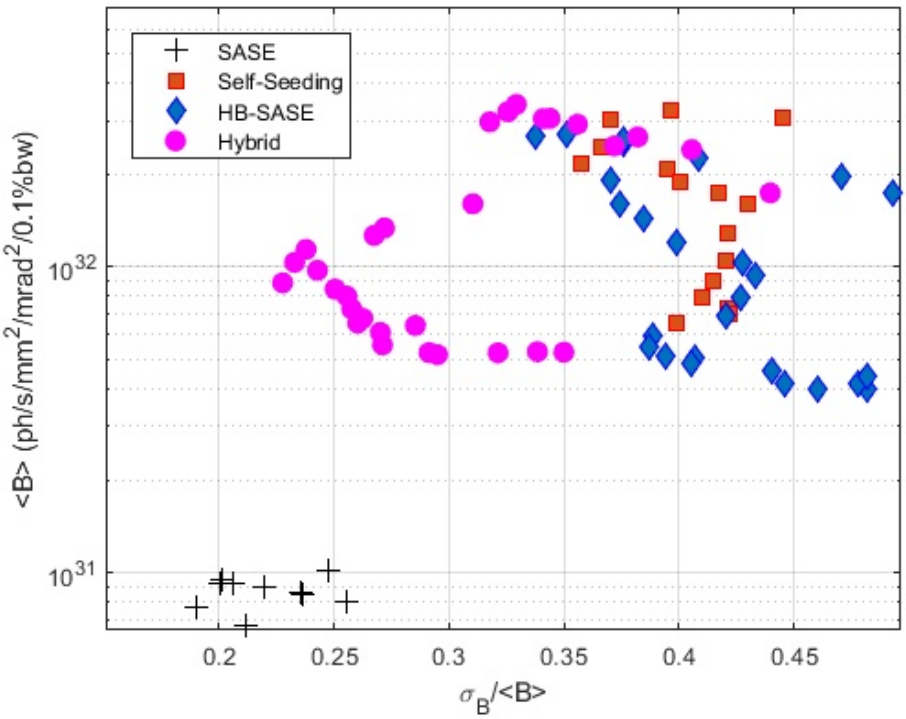

Figure 6.24: Mean Peak Brightness vs rms Brightness variation for the four schemes. Each plot point represents a different distance along the undulator, showing how the balance between brightness and stability changes during the FEL interaction process from start up through exponential growth to post-saturation.

6.5.3 HB-SASE in the HXR.

A full comparative study of the candidate methods for generating transform limited pulses in the HXR has not been completed. However, HB-SASE operation at a photon energy of 20 keV on FEL-2 has been optimised. Example simulation results are shown in Figure 6.25. The pulse energy at the nominal saturation point is 50 μJ, the FWHM pulse duration is 6.5 fs and the FWHM relative bandwidth is 3.4×10^{-5}, giving a time-bandwidth product $\Delta\nu\Delta t = 1.0$. Adding extra undulator length and tapering the field to extract more energy form the electron bunch post-saturation could potentially amplify the pulse energy by a additional factor of up to thirty giving pulse energy up to 1.5 mJ. This possibility is explored further in the next section.

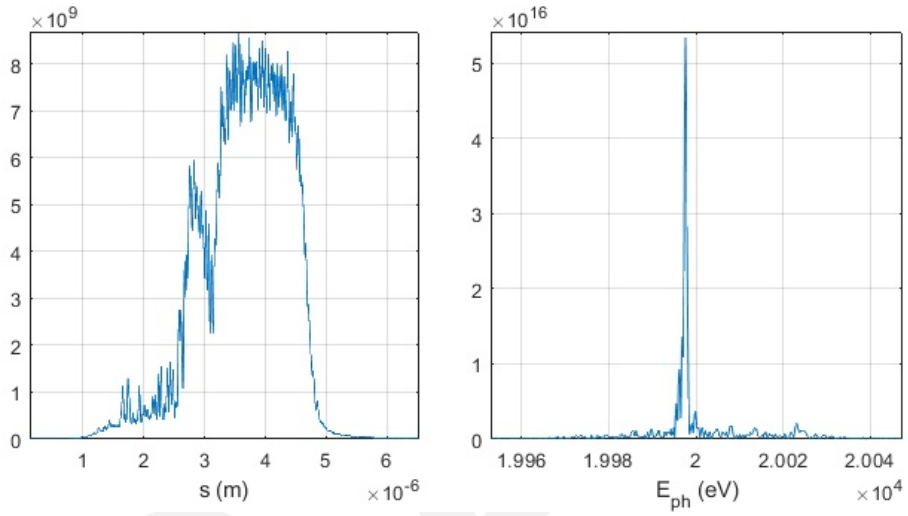

Figure 6.25: HB-SASE output from FEL-2 at 20 keV. Left: pulse profile at position of maximum brightness. Right: the pulse spectrum. The FWHM pulse duration is 6.5 fs and the FWHM relative bandwidth is 3.4×10^{-5}, giving a time-bandwidth product $\Delta\nu\Delta t = 1.0$.

6.5.4 Tapering for High Pulse Energy

An option for the generation of very high pulse energy near-transform-limited HXR pulses is to apply post-saturation tapering to one of the methods. The technique of post-saturation tapering is discussed in detail in References [72] and [73]. An example simulation is shown here of HXR HB-SASE output (at 25 keV) where post-saturation tapering has been applied to increase the pulse energy by a factor of thirty while maintaining good temporal coherence. This example uses an earlier parameter set to that presented in the document as the baseline, but the results are included here as an indicative example of the performance that might be obtained via post-saturation tapering. In this example the undulator length was extended beyond the normal saturation position for a further 80 m.

The results are shown in Figure 6.26. The top row shows the pulse profile, radiation phase and spectrum at the nominal saturation point. The bottom row shows the output after tapering—here the pulse peak power is 700 GW, the pulse energy is 1.6 mJ, the pulse duration is 2.6 fs, the FWHM bandwidth is 1×10^{-4} and the time bandwidth product is $\Delta\nu\Delta t \approx 1.5$.

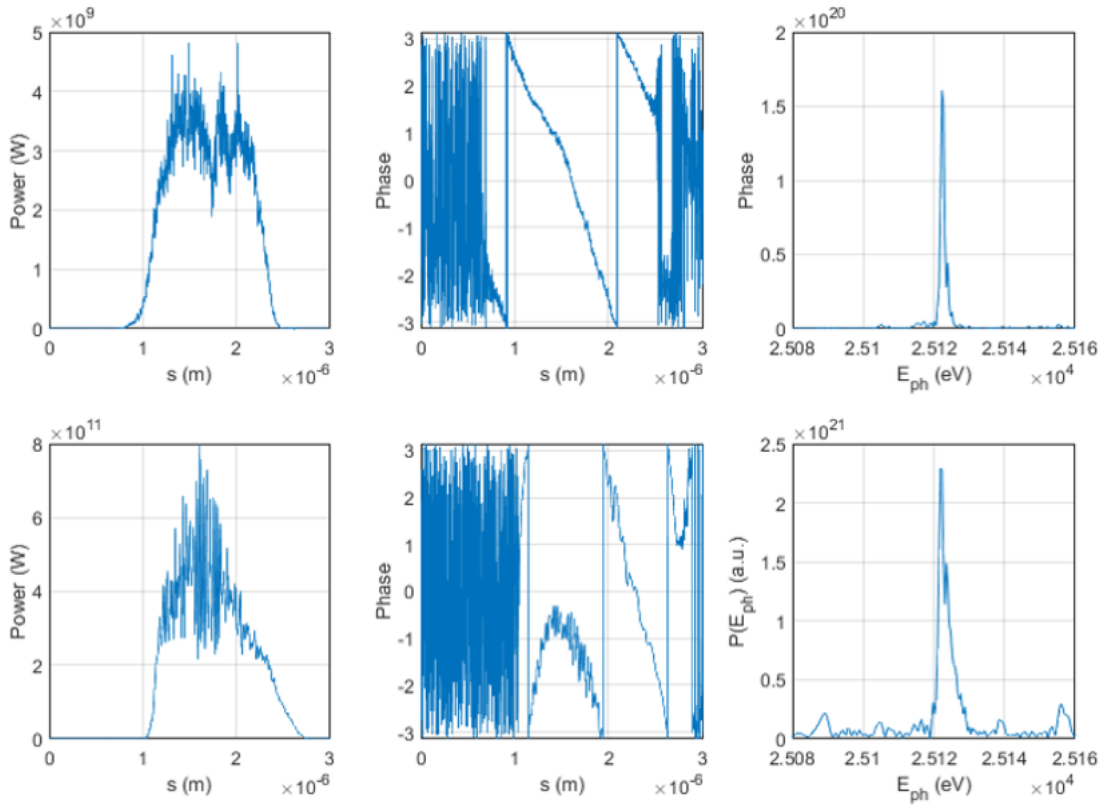

Figure 6.26: Example of HB-SASE at 25 keV (not baseline parameters) where post-saturation tapering has been applied, extending the undulator length by 80 m. Top row: the pulse profile, radiation phase and spectrum at the nominal saturation point. Bottom row: the output after tapering. The pulse peak power is 700 GW, the pulse energy is 1.6 mJ, the pulse duration is 2.6 fs, the FWHM bandwidth is 1×10^{-4} and the time bandwidth product is $\Delta\nu\Delta t \approx 1.5$.

6.5.5 Transform Limited Short Pulses

Different approaches to producing attosecond photon pulses were explored and analysed in Section 6.3.1.2. Following this analysis, the **enhanced self-amplified spontaneous emission (ESASE) scheme** [43] is deemed most appropriate for the UK XFEL. A simulation study is outlined below to assess the efficacy of this method. The simulation is conducted for a case of the UK XFEL with electron parameters shown in Table 6.3. Comparing these parameter values to those in Table 6.1, the simulated case resembles the proposed FEL-2 line in a low-charge operation mode. The photon pulses are to be circularly polarised with a target wavelength of 0.1 nm, which corresponds to a photon energy of 12.4 keV.

Table 6.3: Electron beam parameters in the simulations.

Parameter	Symbol	Value
Beam energy	$\gamma m_e c^2$	8 GeV
Relative energy spread	σ_γ/γ	1×10^{-4}
Peak current	I_0	1.7 kA
Bunch duration	Δt	10 fs
Normalised emittance	$\gamma\epsilon_{x,y}$	0.15 mm mrad
Average radius	$\bar{\sigma}_{x,y}$	10 μm

6.5.5.1 FEL Configuration

The simulated FEL line for the ESASE scheme comprises two undulator sections separated by a magnetic chicane. The first undulator section and the magnetic chicane enable electron beam modulation, whilst the second undulator section produces the photon pulses.

Using the notations defined in Section 6.7.1, the first undulator section has a period length λ_u = 0.5 m and an undulator parameter a_u = 54.2. This section includes a single planar undulator segment of length 2.5 m, with a resonant wavelength λ = 3 μm. An external laser with adjustable power induces the required energy modulation amplitude in the electron beam.

The magnetic chicane, with a total length of 2.5 m, contains four dipole magnets that produce a linear longitudinal dispersion R_{56} = 30 μm.

The second undulator section has λ_u = 20 mm and a_u = 1.20. It comprises ten helical undulator segments, each 2.5 m in length, with a resonant wavelength λ = 0.1 nm. This resonant wavelength matches the target wavelength for attosecond photon pulses.

Throughout the simulated FEL line, the undulator segments and the magnetic chicane are interleaved with drift spaces, each of length 0.5 m and each containing a quadrupole magnet. These quadrupoles form a FODO lattice, providing transverse focusing to maintain the average electron beam radius specified in Table 6.3.

6.5.5.2 Electron Beam Modulation

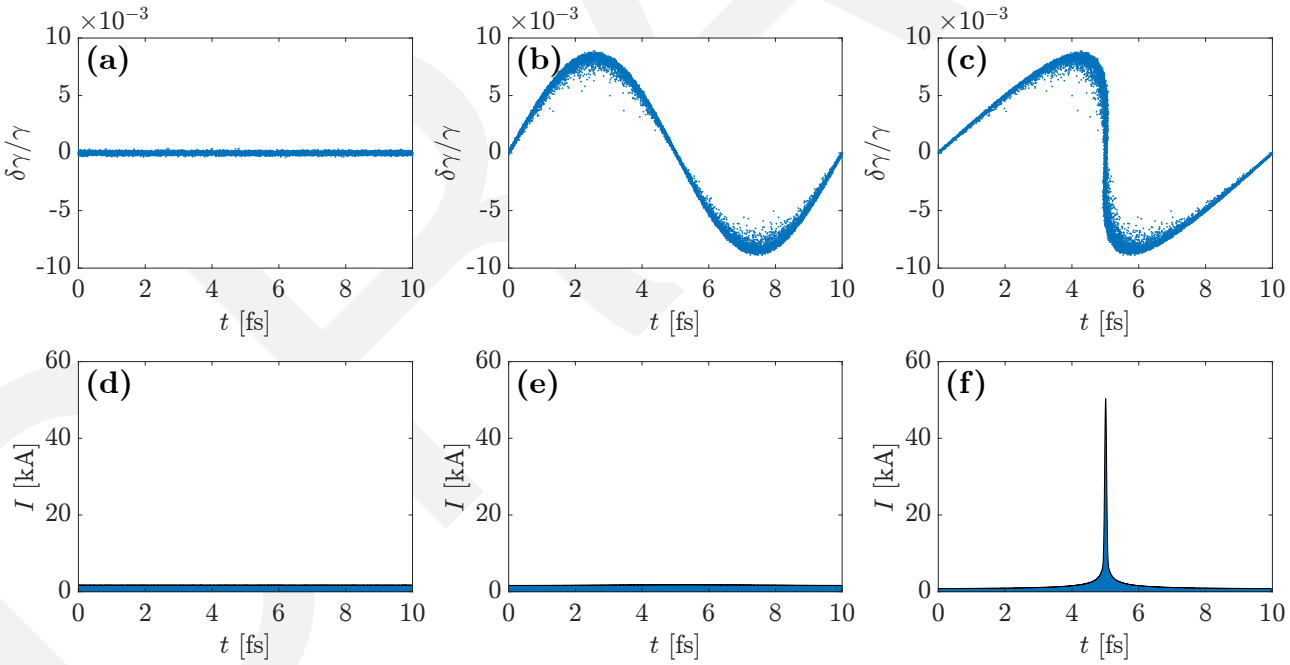

Figure 6.27: Simulation of electron bunch modulation in the ESASE scheme for the selected UK XFEL case. The upper row shows the longitudinal phase space (a) before and (b) after the first undulator section as well as (c) after the magnetic chicane. The lower row shows the corresponding current profiles (d) before and (e) after the first undulator section as well as (f) after the magnetic chicane.

Simulation results for electron bunch modulation using the ESASE technique are presented in Figure 6.27. The upper row illustrates the longitudinal phase space before the first undulator section [see Figure 6.27(a)], after the first undulator section [see Figure 6.27(b)] and after the magnetic chicane [see Figure 6.27(c)]. The lower row displays the corresponding current profiles

before the first undulator section [see Figure 6.27(d)], after the first undulator section [see Figure 6.27(e)] and after the magnetic chicane [see Figure 6.27(f)].

Initially, the electron distributions in the longitudinal phase space [see Figure 6.27(a)] and the current profile [see Figure 6.27(d)] are uniform before the first undulator section.

Following the first undulator section, an energy modulation appears in the electrons, characterised by a sinusoidal distribution with an amplitude of $\delta\gamma/\gamma = 8 \times 10^{-3}$ in the longitudinal phase space [see Figure 6.27(b)]. The current profile remains uniform [see Figure 6.27(e)], indicating the absence of density modulation in the electron bunch.

After passing through the magnetic chicane, the electron bunch exhibits pronounced density modulation, with electrons clustering near the centre of the time window [see Figure 6.27(c)]. This results in a significant enhancement of the peak current, increasing by almost thirtyfold from 1.7 kA to 50 kA [see Figure 6.27(f)].

6

6.5.5.3 Photon Pulse Production

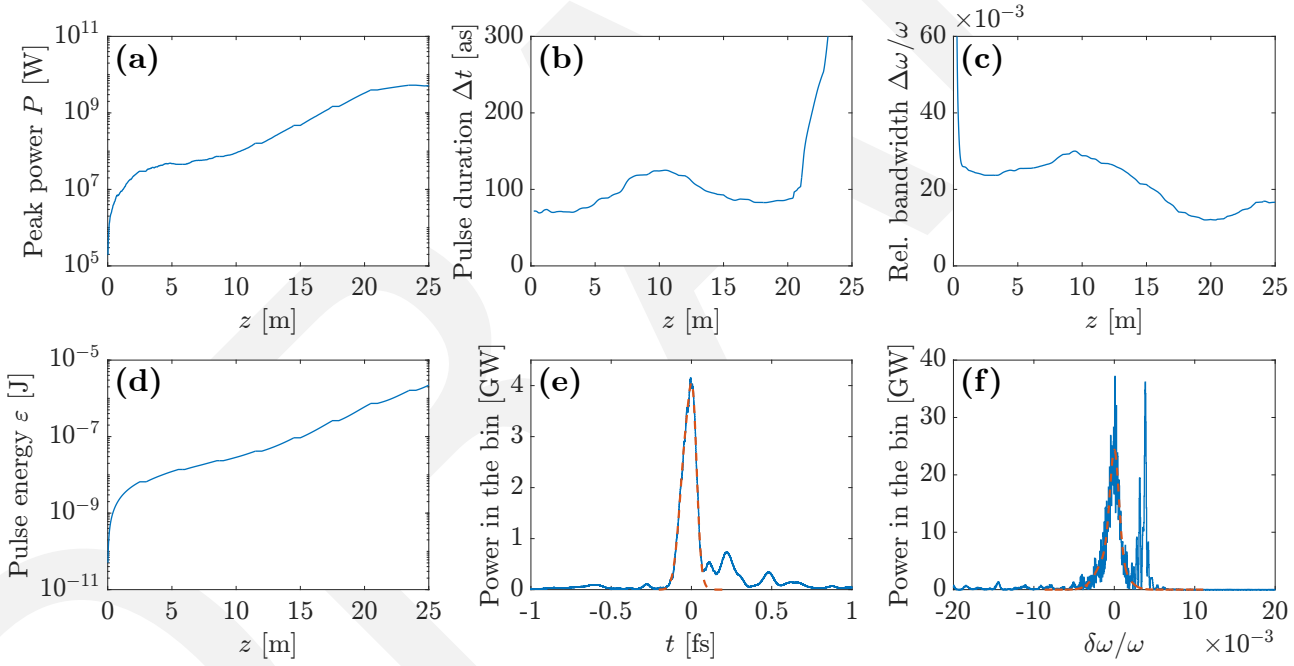

Figure 6.28: Simulation of photon pulse production in the ESASE scheme for the selected UK XFEL case. The (a) peak power, (b) pulse duration, (c) relative bandwidth and (d) pulse energy are shown as functions of the distance z along the second undulator section. Saturation occurs at z = 20 m, for which the (e) temporal and (f) spectral profiles are shown with an additional red dashed curve indicating a Gaussian fit to the principal spike.

The simulation results for photon pulse production are presented in Figure 6.28, plotted as functions of distance z along the second undulator section. Saturation occurs at z = 20 m, where the temporal profile [see Figure 6.28(e)] and spectral profile [see Figure 6.28(f)] are shown, with a red dashed curve indicating a Gaussian fit to the principal spike.

At the saturation point z = 20 m in the second undulator section, the photon beam achieves a peak power of 4 GW, a pulse duration of 90 as, a relative bandwidth $\delta\omega/\omega$ of 1×10^{-2} and a pulse energy of 1 μJ.

Comparing Figure 6.28(a) and (d), the peak power saturates at z = 20 m, whilst the pulse energy continues to increase beyond this point. This behaviour arises from the rapid broadening of the photon pulse due to slippage, as reflected in Figure 6.28(b).

6.5.6 FEL-1 Performance

From Genesis1.3 (v4) simulations FEL-1a will produce pulse energies of 25 mJ at 5 keV (tapering applied) to a more modest 0.5 mJ at 20 keV (no tapering). The required undulator length for saturation at 20 keV is 130 m. At 5 keV saturation is reached at 60 m, leaving a length of 70 m for tapering and an assumed pulse energy enhancement of a factor of 10. FEL-1b will produce approximately 7 mJ at 20 keV (tapering applied) and 0.15 mJ at 45 keV (no tapering). The required undulator length for saturation at 45 keV is 130 m. At 20 keV the normal saturation length is approximately 50 m, leaving 80 m for post-saturation tapering. The undulator lengths stated here include a 50 % contingency.

6.5.7 Harmonic Lasing

To further advance FEL capabilities, harmonic lasing [74, 75] is a promising technique to pursue. By utilising the h^{th} harmonic instead of the fundamental mode of the radiation, this approach scales down the minimum attainable wavelength by a factor of h for a given electron beam energy and undulator tuning range. This allows x-ray FELs to access even shorter wavelengths without requiring significant infrastructure upgrades.

As an added benefit, harmonic lasing holds the potential to extend the spectral reach of FELs into the γ-ray regime, which has wavelengths below 10 picometres (pm) and photon energies above 100 keV.

The efficacy of harmonic lasing can be characterised by two figures of merit: (i) the brightness of the target harmonic and (ii) the signal-to-noise ratio (SNR). In conventional self-amplified spontaneous emission (SASE), the fundamental typically dominates over higher harmonics in both power and brightness, resulting in a suboptimal SNR.

In the scientific literature, a **phase shifter scheme** [74] was previously proposed to suppress the fundamental whilst preserving gain at the target harmonic, thus offering a means to improving the brightness and the SNR. Note that this phase shifter scheme for harmonic lasing is distinct from the phase shifter scheme introduced in Section 6.3.2 for generating two-colour photon pulses, despite sharing the same name.

As part of the research and development (R&D) effort within this phase of the UK XFEL project, a novel **split-undulator scheme** [76] is proposed and investigated. In this scheme, the undulator segments in a FEL line are divided into two sections with different K values, such that the target wavelength corresponds to different harmonic numbers of the resonant wavelengths in the two sections. Typically, the unwanted harmonics of the resonant wavelength from the first section are not amplified in the second section, and those from the second section are not amplified in the first. With the target wavelength amplified in both sections, this scheme offers an avenue to achieving good brightness and SNR.

An alternative technique

The **phase shifter scheme** [74] and the **split-undulator scheme** [76] do not require the target wavelength λ_{tar} to match the fundamental resonant wavelength λ_{res} of the undulator. These

schemes are suited to expanding the spectral range of a FEL towards shorter wavelengths for a given electron beam energy and undulator tuning range.

The phase shifter scheme has been empirically demonstrated [77] through combined use with the HLSS scheme, although its performance is known to be limited [75] in the absence of an external seed laser. Meanwhile, the split-undulator scheme, a novel technique under theoretical development, shows potential to significantly outperform the phase shifter scheme, as indicated by simulation results in Section 6.5.7.3.

The two schemes are not mutually exclusive, as implementing one does not preclude the other. Hence, the phase shifter scheme is adopted as the baseline option for harmonic lasing in the UK XFEL, whilst the split-undulator scheme is included as a second option and shall continue to be developed beyond the current phase of the UK XFEL project.

A simulation study is presented below to examine the performance of the selected schemes. It should be noted that the selected schemes represent a subset of possible options. For example, one promising technique not explored in this study is the harmonic cascade proposed by Giannessi and Musumeci [78].

6.5.7.1 Case Definition

This study aims to compare and contrast the selected schemes using the simulation code GENESIS 1.3 (version 4) [79]. All the simulations are performed for the same case, which is based on the SASE1 line of the European XFEL [80] and has the electron beam parameters shown in Table 6.4.

Table 6.4: Electron beam parameters in the simulations.

Parameter	Symbol	Value
Beam energy	$\gamma m_e c^2$	17.5 GeV
Relative energy spread	σ_γ/γ	2.34×10^{-4}
Peak current	I_0	4.5 kA
Bunch charge	Q	20 pC
Normalised emittance	$\gamma\epsilon_{x,y}$	0.32 mm mrad
Average radius	$\bar{\sigma}_{x,y}$	17 μm

This case is selected for the simulation study for three primary reasons. First, the European XFEL has been in operation since 2017 and its proven success makes it a realistic case for simulation studies. Second, the European XFEL has one of the highest electron beam energies amongst all FEL facilities worldwide, enabling the simulations to demonstrate the furthest spectral reach towards shorter wavelengths. Third, the European XFEL, of which the United Kingdom is a full member and with which UK institutions maintain close collaboration, is considered an overseas investment option for the UK XFEL project.

The simulated FEL line comprises 36 planar undulator segments interleaved with drift spaces. Each segment has length 5 m and each drift space 1.1 m. The K parameters of the segments are independently adjustable, whilst the undulator period λ_u is fixed at 40 mm throughout.

Each drift space incorporates a quadrupole magnet and a phase shifter. The quadrupoles form a FODO lattice that provides the transverse focusing necessary for the electron beam to maintain the average radius shown in Table 6.4.

The target wavelength λ_{tar} is set at 8 pm, corresponding to a photon energy of 155 keV in the γ-ray regime. Recall from Section 6.7.1 that the fundamental resonant wavelength λ_{res} of a FEL can be expressed as [81]

$$\lambda_{res} = \frac{\lambda_u}{2\gamma^2}\left(1 + \frac{K^2}{2}\right).$$

For the given values of γ and λ_u, there is no positive real value of K for which $\lambda_{res} = \lambda_{tar}$, so harmonic lasing is the only way to reach λ_{tar}. Once λ_{res} is set, harmonic lasing enables access to shorter wavelengths of the form λ_{res}/h, where h is a harmonic number. Along the undulator axis, only the odd harmonics $h \in \{1, 3, 5, \dots\}$ are present.

6.5.7.2 FEL Configurations

The three FEL schemes considered here for the purpose of harmonic lasing are (i) conventional SASE, (ii) the phase shifter scheme and (iii) the split-undulator scheme.

For conventional SASE, a constant value of K = 1.64 is used throughout. This value approximates the minimum feasible K for the SASE1 line of the European XFEL [80]. It produces a resonant wavelength of λ_{res} = 40 pm, equivalent to a photon energy of 31 keV in the hard x-ray regime. The target wavelength corresponds to the fifth harmonic of the resonant wavelength, expressed as $\lambda_{tar} = \lambda_{res}/h$ with h = 5. All phase shifters are configured to $\phi = 0$, preserving the phase angle between the electron bunch and the radiation pulse across each drift section.

In the phase shifter scheme, all settings are otherwise identical to those of conventional SASE, except that the phase angle ϕ is set to different integer multiples of $\phi(\lambda_{tar})$ in different drift sections, where $\phi(\lambda_{tar}) = 2\pi \times \lambda_{tar}/\lambda_{res} = 2\pi/5$.

In the split-undulator scheme, the undulator segments are allocated into two sections. The first section is configured identically to conventional SASE. The second section is set to a different K value, resulting in a new resonant wavelength λ'_{res}. Consequently, the same target wavelength λ_{tar} corresponds to a different harmonic number h′ of this new resonant wavelength λ'_{res}, such that $\lambda_{tar} = \lambda_{res}/h = \lambda'_{res}/h'$ with $h' \neq h$. All phase shifters are set to $\phi = 0$.

6.5.7.3 Results

The simulation results are shown in Figure 6.29, with the three columns representing conventional SASE, the phase shifter scheme and the split-undulator schemes, respectively.

The first row depicts the undulator and phase shifter configurations along the FEL line. For the split-undulator scheme [see Figure 6.29(c)], the harmonic number h′ in the second section and the allocation of undulator segments between sections are optimised parameters. Optimal values of $h' = 11$ and an undulator segment ratio of 16 : 20 between the two sections were selected.

The second row presents the brightness B_h as a function of position z for harmonic numbers $h = 1, 3, 5$. For the split-undulator scheme [see Figure 6.29(f)], these harmonic numbers correspond to those for the resonant wavelength λ_{res} of the first section, as opposed to λ'_{res} of the second section. Harmonics higher than the target harmonic (h = 5) are excluded here, as they are found to be orders of magnitude lower in brightness at the end of the FEL line across all three schemes, thus rendering them less significant.

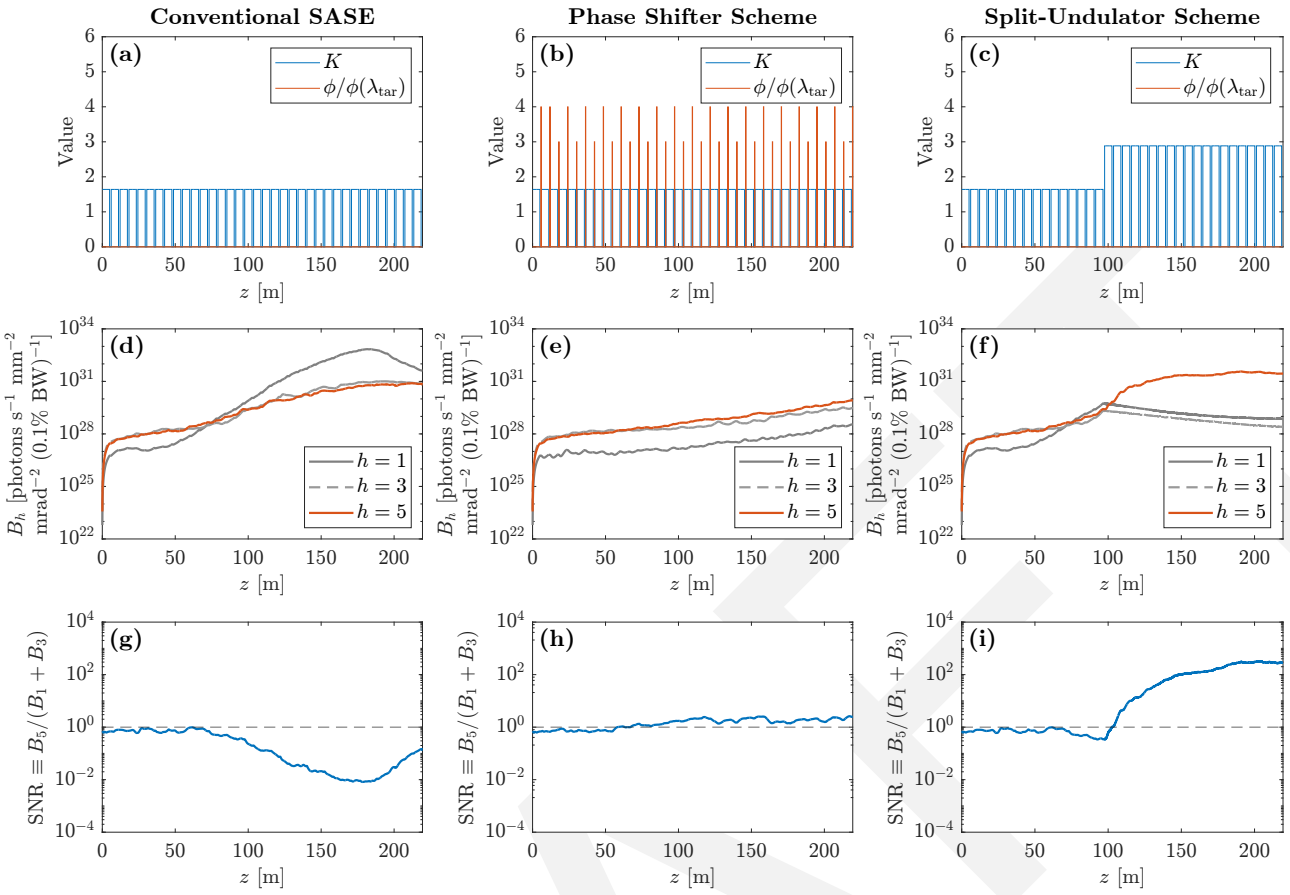

Figure 6.29: Simulation results. The three columns represent the three FEL schemes: conventional SASE (left), the phase shifter scheme (centre) and the split-undulator scheme (right). The top row illustrates the undulator and phase shifter configurations along the FEL line. The middle row displays the brightness B_h as a function of the distance z along the FEL line for harmonic numbers h = 1, 3, 5 of the wavelength λ_{res}. The bottom row shows the SNR as a function of z, defined in this context as $B_5/(B_1 + B_3)$.

In conventional SASE [see Figure 6.29(d)], there is an inverse correlation between harmonic number and maximum brightness, with the fundamental mode (h = 1) being dominant, consistent with expectations. In contrast, the phase shifter scheme [see Figure 6.29(e)] suppresses the unwanted harmonics (h = 1 and h = 3), keeping their brightness below that at the target harmonic (h = 5) over much of the FEL line. However, a comparison of the red curves in Figure 6.29(d) and (e) reveals that the phase shifter scheme delays the growth and saturation of brightness at the target harmonic. Consequently, the phase shifter scheme yields a lower final brightness compared to conventional SASE.

In the split-undulator scheme [see Figure 6.29(f)], the boundary at z = 97.6 m demarcates the two sections. Prior to this point, the brightness curves resemble those of conventional SASE [see Figure 6.29(d)]. Beyond the boundary, the brightness of the unwanted harmonics (h = 1 and h = 3) decreases gradually, due to two combined effects: (i) the radiation power ceases to grow and stays constant; (ii) diffraction widens the beam radius (data not shown). In contrast, the target harmonic (h = 5) exhibits sustained growth and its final brightness exceeds that in both other schemes [see Figure 6.29(d) and (e)].

The bottom row in Figure 6.29 displays the SNR as a function of z, with a horizontal dashed line marking unity for visual guidance. Here, the SNR is defined as $B_5/(B_1 + B_3)$. For conventional SASE, the SNR remains below one throughout the FEL line. The phase shifter scheme marginally enhances performance over conventional SASE, achieving an SNR above unity in the latter section of the FEL line. The split-undulator scheme exhibits a sharp, significant increase in SNR

beyond the boundary at z = 97.6 m, resulting in a substantially higher SNR compared to the other schemes.

From the perspective of the FEL user at the experimental station, the final parameters at the end of the FEL line are critical. These parameters are presented in Table 6.5 and Table 6.6. Regarding the final SNR, the split-undulator scheme outperforms the phase shifter scheme by over a hundredfold and achieves more than a thousandfold improvement over conventional SASE. In terms of the final brightness B_5 at the target harmonic, the phase shifter scheme underperforms compared to conventional SASE, exhibiting a brightness reduction of 3 %. Conversely, the split-undulator scheme surpasses conventional SASE by almost an order of magnitude.

Table 6.5: Simulation results for the end of the FEL line. The top rows show the final brightness B_h in units of photons s^{-1} mm^{-2} $mrad^{-2}$ (0.1 % bandwidth)$^{-1}$ for harmonic numbers h = 1, 3, 5 of the wavelength λ_{res}. The bottom row reports the corresponding SNR at h = 5, defined here as $B_5/(B_1 + B_3)$.

	SASE	Phase Shifter	Split-Undulator
B_1	4.1×10^{31}	3.4×10^{28}	7.2×10^{28}
B_3	7.3×10^{30}	3.0×10^{29}	2.6×10^{28}
B_5	6.6×10^{30}	8.3×10^{29}	2.8×10^{31}
SNR	0.14	2.5	290

Table 6.6: Simulation results for the end of the FEL line. The top rows show the pulse energy U_h in joules for harmonic numbers h = 1, 3, 5 of the wavelength λ_{res}. The bottom row reports the corresponding SNR at h = 5, defined here as $U_5/(U_1 + U_3)$.

	SASE	Phase Shifter	Split-Undulator
U_1	1.7×10^{-6}	8.7×10^{-9}	5.6×10^{-9}
U_3	2.5×10^{-7}	1.4×10^{-8}	3.4×10^{-9}
U_5	7.4×10^{-8}	1.0×10^{-8}	4.1×10^{-7}
SNR	0.037	0.46	46

6.5.7.4 Discussion

The simulation results highlight the excellent performance of the novel split-undulator scheme at the fifth harmonic h = 5, evaluated through the brightness and pulse energy at this target harmonic and the respective SNRs. The brightness (pulse energy) at h = 5 for the split-undulator scheme exceeds that of SASE by a factor of 4.2 (5.5). The improvement in SNR for the split undulator scheme, compared to SASE, is $> 2,000$ for brightness and > 1200 for pulse energy, potentially removing the need for a monochromator on the beamline to remove the unwanted photons at the fundamental wavelength.

The efficacy of the scheme stems from the target wavelength being a harmonic of both λ_{res} and λ'_{res}, enabling its amplification in both sections of the FEL line. In contrast, unwanted harmonics of λ_{res} in the first section are generally not amplified in the second section, allowing energy to be redirected to the target wavelength in accordance with the principle of energy conservation.

However, the simulations have limitations. In the default simulation mode of GENESIS [79], a single reference wavelength applies across the entire FEL line. When simulating the split-undulator scheme, the resonant wavelength λ_{res} of the first section serves as the reference wavelength. Consequently, radiation properties at the resonant wavelength λ'_{res} of the second section and its harmonics are not computed.

In principle, electrons could develop microbunching at intervals of λ'_{res} as they traverse the second section, potentially increasing the brightness at the unwanted harmonics of λ'_{res}. These harmonics contribute to noise, which should be accounted for in the SNR. To address this, further exploration of advanced simulation modes in GENESIS or the use of alternative simulation codes, such as Puffin [82], may be necessary. These investigations shall continue beyond the current phase of the UK XFEL project.

If the unwanted harmonics of λ'_{res} prove to be substantial in brightness, they could be suppressed using appropriate phase shifts, thereby combining the features of the split-undulator and phase shifter schemes. This could be a subject for further exploration.

In conclusion, this study compares the novel split-undulator scheme with the pre-existing phase shifter scheme and conventional SASE. Simulations demonstrate their potential to extend the spectral range of existing FELs into the γ-ray regime through harmonic lasing. The split-undulator scheme outperforms the other schemes substantially in brightness and signal-to-noise ratio. Although limitations in the simulations require further investigation, this study marks a significant step towards integrating γ-ray capabilities into the UK XFEL design.

6.6 Summary of Predicted FEL Performance

6.6.1 Transform Limited Pulses

For the CDR phase detailed simulations have focussed on FEL techniques at specific wavelengths to optimise performance. The simulations have been used to carefully compare different FEL methods against each other. To date, studies have used idealised electron bunch distributions so simulations have not been full start-to-end using fully-modelled bunches which have been tracked all the way from the cathode. These more detailed simulations will be a core component of a future design phase. However, properly optimised simulations of SASE performance have been done for each FEL at either end of their photon energy ranges. These simulations, together with the relative performance of schemes for temporal coherence at 1 keV and 20 keV *compared to SASE*, and the semi-analytic framework produced by Ming Xie, have been used to estimate the performance of all FELs in near-transform-limited modes at each end of their respective tuning ranges. The results are summarised in Table 6.7. The peak and time-averaged FEL brightness for long pulse transform limited mode are shown in Figure 6.30 to Figure 6.31.

6.6.2 FEL-1 Pulses

The estimated output performance and comments are shown in Table 6.8.

Table 6.7: High repetition rate ($\leq$100 kHz), evenly spaced, near-transform-limited pulses from 100 eV–20 keV

FEL	Photon Energy [keV]	Mode	Technique	Pulse Duration [fs]	Pulse Energy (tapered)	Bandwidth [eV]
FEL-6	~0.1 – 1.0	Seeded	EEHG	5 – 100	7 mJ for 100 fs (35 mJ for 100 fs)	0.72 – 0.036
FEL-5	0.25 – 3.0	Long	HB-SASE/ Self-seeding	75 – 30	6 – 1 mJ (30 – 5 mJ)	0.048–0.12
		Short	ESASE	2 – 0.35	160 – 11 µJ	3.6 – 20
FEL-4	1.0 – 5.0	Long	HB-SASE/ Self-seeding	30 – 10	1500 – 300 µJ (7.5 – 1.5 mJ)	0.12–0.36
		Short	ESASE	0.8 – 0.3	40 – 9 µJ	9 – 24
FEL-3	3.0 – 13.0	Long	HB-SASE/ Self-seeding	12 – 7	500 – 90 µJ (2.5 – 0.5 mJ)	0.3 – 0.52
		Short	ESASE	0.4 – 0.2	17 – 2.5 µJ	18 – 36
FEL-2	5.0 – 20.0	Long	HB-SASE/ Self-seeding	10 – 7	300 – 50 µJ (1.5 – 0.25 mJ)	0.36 – 0.52
		Short	ESASE	0.3 – 0.2	10 – 1.5 µJ	24 – 36
	~10	Cavity	XFELO	~100	~10	~0.035

Harmonics: Potential for parasitic 3rd harmonic emission with few % pulse energy (with appropriate photon transport), or up to 20% pulse energy at 5th harmonic and order of magnitude suppression of fundamental via harmonic lasing split undulator scheme. Not required for FELs 4-6 as already covered by other FELs.
Polarisation: Fully variable polarisation.
Nominal pulse structure: High repetition rate, evenly spaced pulses. Up to 100 kHz per FEL with potential for 200-300 kHz to be assessed.
Burst mode: Option to send pulses at 1 MHz to individual lines in bursts up to 100 ms to be assessed.

Table 6.8: Higher pulse energy and higher photon energies (non transform-limited) at $\leq$200 Hz or in short bursts.

FEL	Photon Energy [keV]	Mode	Technique	Pulse Duration [fs]	Pulse Energy (example special mode)
FEL-1a	5 – 20	High Power	SASE	~30	25 – 0.5 mJ (~50 mJ at 5 keV)
FEL-1b	20 – 45 (with booster)	High Power/ High Energy	SASE	~30	7 – 0.15 mJ (~1 mJ at 40 keV)

Harmonics: Potential for parasitic 3rd harmonic emission with few % pulse energy (with appropriate photon transport), or up to 20% pulse energy at 5th harmonic and order of magnitude suppression of fundamental via harmonic lasing split undulator scheme.
Polarisation: Fully variable polarisation.
Nominal pulse structure: Evenly spaced pulses up to 200 Hz
Burst mode: 10 pulses per burst, with >5 ns separation (216.67 MHz). Max. burst length 1 us (100 ns separation/10 MHz)

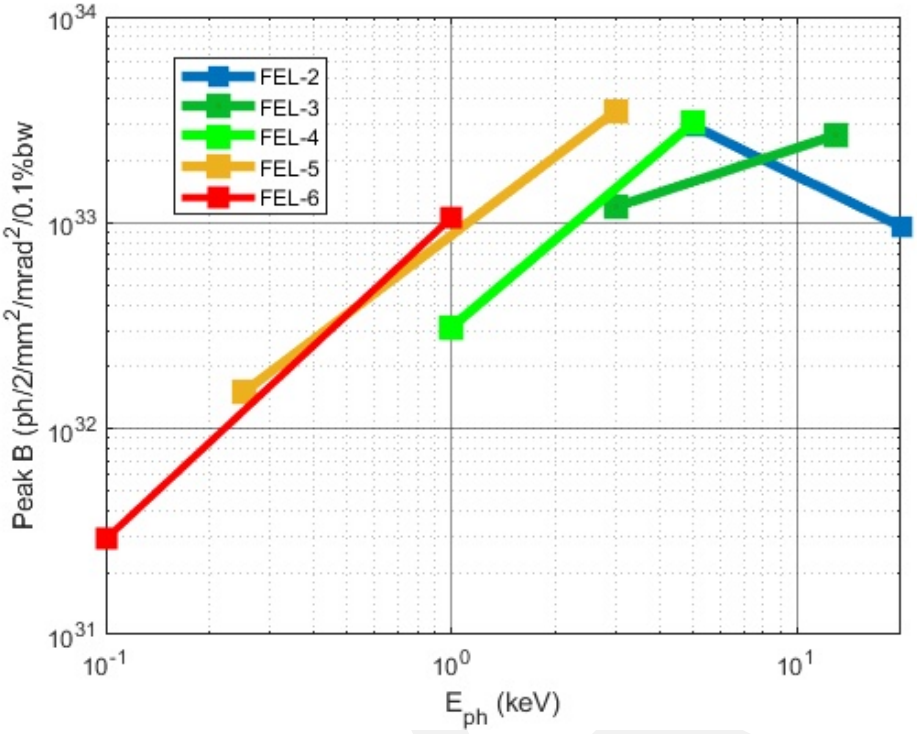

Figure 6.30: Predicted peak brightness in long pulse transform-limited mode.

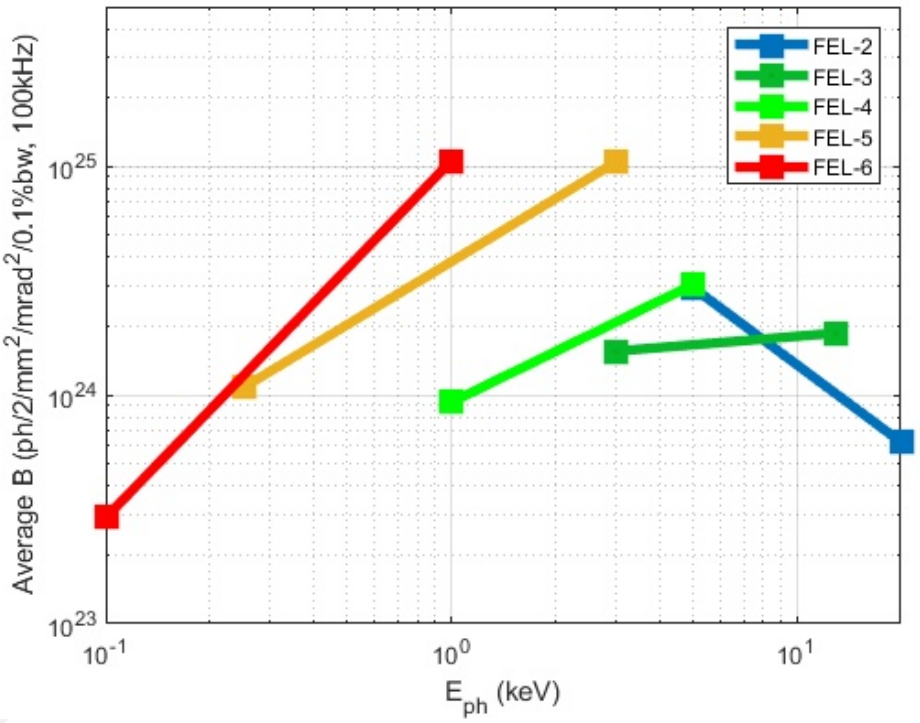

Figure 6.31: Predicted average brightness in long pulse transform-limited mode at a repetition rate of 100 kHz.

6.7 Undulator Technology

A comprehensive survey of undulator technologies for x-ray FELs was undertaken as part of the CompactLight (XLS) project [83, 84]. This was an international collaboration, funded by the European Union, with the aim to design a hard x-ray FEL facility based on X-Band linac technology. STFC was a key partner in the undulator technology analysis, the results of which are summarised here and applied to the requirements of UK XFEL. The requirement is to generate radiation with variable polarization covering the photon energy ranges 0.1–20 keV. Tuning across photon energies will be achieved by undulator scanning rather than electron energy scanning in order to facilitate independent operation of multiple FELs.

6.7.1 Undulator Fundamentals

The performance of undulators is specified by the undulator period λ_u and the deflection strength parameter $K = (e\,B\,\lambda_u)/(2\pi\,m_e\,c)$, where B is the magnetic field strength, e and m_e the electron charge and mass, and c the speed of light. For electrons of energy $E = \gamma\,m_e\,c^2$, with γ being the associated Lorentz factor, the FEL resonant wavelength λ is given by $\lambda = \lambda_u(1 + a_u{}^2)/2\gamma^2$ where $a_u = K/\sqrt{2}$ for planar undulators and $a_u = K$ for helical undulators. The parameters K and λ_u cannot be chosen independently, but they have a given dependency for each undulator technology. Therefore, to reach a specific FEL wavelength the electron beam energy and undulator technology must be specified together. Novel undulator technologies, allowing high on-axis fields with short undulator periods (small λ_u), allow an FEL to reach a given photon energy with a shorter undulator length and a lower electron beam energy, thus reducing the overall dimensions of the FEL facility, but at the expense of peak power and pulse energy.

6.7.2 Undulator Technologies

Available undulator technologies differ in the mechanism for generating the electromagnetic field that produces the oscillation of the electron beam required for the FEL emission process. This section reviews the different undulator technologies available and analyses them in terms of technological readiness.

6.7.2.1 Permanent Magnet Undulators

In permanent magnet (PM) undulators magnetic field is generated by a Halbach-type arrangement of magnet blocks [85], which may include (hybrid design) or not (pure PM design) high permeability material poles in order to concentrate the magnetic flux. These systems usually incorporate a mechanism to modify the distance between the two arrays of magnets forming the Halbach structure—normally referred as the gap of the device, g—allowing tuning of the magnetic field. Although in their simplest form (planar configuration) PM undulators generate radiation with fixed linear polarization, schemes with an increasing degree of sophistication have been developed in order to allow modifying the polarization state of the emitted light. The designs (APPLE-II, APPLE-III, APPLE-X, Delta, Delta-II), which are generically referred as elliptical undulators, are described in Ref. [86]. The most advanced of these designs is the APPLE-X which is used at SwissFEL [87] and is illustrated in Figure 6.32. Here the magnetic fields are orientated radially from the beam axis. To tune the on-axis field strength, and hence the FEL photon energy, the

four arrays move radially in and out together. To tune the field polarisation, from vertical linear, through elliptical, circular, elliptical, then horizontal linear, the arrays move independently along the beam axis in different configurations. The advantage of the APPLE-X, over previous iterations of APPLE devices, is that the resonant photon energy remains constant as the polarisation is changed, simplifying the practical operation of the device.

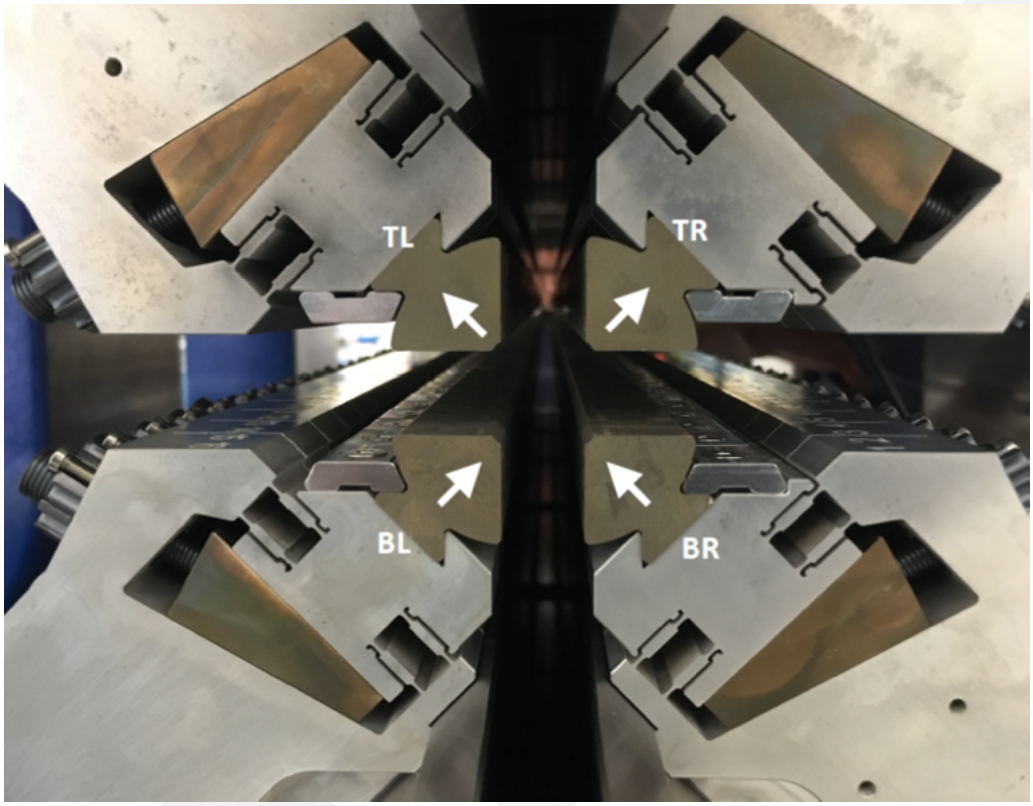

Figure 6.32: View looking along the electron beam axis of an APPLE-X Undulator.

The materials of choice for PMs are rare-earth based compounds: SmCo, NdFeB and PrFeB. The magnetic field delivered by PM undulators is limited by the intrinsic magnetic properties of available materials (remanence and coercivity), which are not expected to improve much further in the future. One option to enhance the magnetic field is to reduce the mechanical gap as much as possible. This led to the development of in-vacuum undulators (IVUs) [88], where the magnet blocks are placed inside the vacuum chamber, and as a consequence the gap is only limited by electron beam aperture and impedance considerations. The IVU design was afterwards adapted to develop cryogenic PM undulators (CPMUs) [89], where magnets are cooled down to cryogenic temperatures by means of either refrigerant channels or cryocoolers. Such operation at low temperature improves the performance of permanent magnets, thanks to an enhancement of their coercivity, which makes them more resistant to demagnetising effects, and to an increase of their remanence, which gives up to 20-30 % higher peak magnetic fields. Most CPMUs in operation make use of (Pr,Nd)FeB or PrFeB magnet grades working close to liquid nitrogen temperature (77 K).

PM undulators have been extensively used in X-ray FELs. For devices with $\lambda_u > 25$ mm, out-of-vacuum solutions are used, corresponding to hard x-ray sources for high energy accelerators (European XFEL with 17.5 GeV or LCLS with 13.6 GeV) or soft x-ray sources for lower energy accelerators (Athos line at SwissFEL with 2.1-3.6 GeV or FERMI@Elettra with 1.5 GeV). For devices with $\lambda_u < 20$ mm, IVUs have also been successfully implemented in FELs, at SACLA, SwissFEL and SXFEL. CPMUs expand the advantages of conventional IVUs at the extra cost of implementing a cryogenic system; this system, however, is much simpler and more relaxed

than the one required for SCUs. Despite the fact that CPMUs have not been yet used in a FEL facility, the experience gained at synchrotron light sources allows the likelihood of a straightforward transfer of this technology to FELs.

PM is the undulator technology with the highest degree of maturity, and it has been extensively used in all existing x-ray FEL facilities. There are many active groups developing and improving the existing solutions, but due to the intrinsic limitations of PM materials the room for further progress is limited. One of its main advantages is the availability of different schemes providing full control on the polarisation of the emitted light. So far such schemes have only been available in out-of-vacuum configurations, but there is an ongoing effort to extend them to IVU and CPMU configurations [90], for example an in-vacuum APPLE-II device under construction at BESSY-II [91] and a cryogenic version in the design phase [92].

Strategies to reduce the cost of PM undulators include reducing the dimensions and complexity of the support structure with force-compensating schemes and/or gravity neutral designs [93], as well as the automation of the assembly and tuning of the devices in order to reduce the manufacturing time and cost [94].

Ultimately, however, all PM technologies are limited by the properties of PM materials, which are not expected to improve in the future. Therefore, for the highest demanding applications they will be eventually superseded by the development of superconducting technology which offers a clear margin in performance.

6.7.2.2 Superconducting Undulators

The basic design of a superconducting undulator (SCU) comprises an array of SC coils, typically wound on a soft iron former or around soft iron poles, or of a high-temperature SC bulk structure including soft iron poles. All SCUs have in common that their magnet assembly forms a cold mass for which cryogenic operation temperatures need to be maintained whilst a high-energy particle beam, and potentially a high-power photon beam, pass through the undulator gap. For storage ring applications the cryostat's insulation vacuum and the beam vacuum are separated, and the beam vacuum chamber is thermally isolated from the coils. As a consequence, the difference between the magnetic gap and the beam-stay-clear is about 1–2.3 mm. For single-pass FELs it has been suggested that removing the beam vacuum chamber might be a feasible option, thus reducing that difference to a mere 0.2 mm and allowing much higher field amplitudes for a given beam-stay-clear.

The two most straightforward SCU configurations are planar and helical undulators. SC planar undulators consist of two opposing periodic arrays of SC coils, either in vertical-racetrack (VR) arrangement, which is the more common one, or in horizontal-racetrack (HR) one. A planar geometry that allows a dual-period device has been demonstrated [95]—the period is changed by altering the current direction in one of the windings. This technology would allow a single device to cover a far broader photon energy range.

SC helical undulators (SCHUs) are typically based on a bifilar helix geometry [96], consisting of two interlocking helical windings with currents flowing in opposite directions. STFC are developing an in-vacuum design [97] comprising a 1 m module with a 13 mm period and a 5 mm gap. The parameters of the design were specified for the CompactLight Project [83, 84] in which the FEL produced photons at 16 keV using a beam energy of 5.5 GeV. Methods for manufacturing the magnet formers and winding the superconducting wire have been advanced to reduce the tolerances in order to achieve the undulator field quality and FEL performance. This was done by constructing a series of 325 mm prototypes—see Figure 6.33—which can be cooled and

measured within a test cryostat [98], shown in Figure 6.34. To date it has not been possible to prove that the prototypes have the stringent field quality required for HXR FEL operation because the Hall sensor is guided by the physical bore of the magnet, rather than the magnetic axis. Further, improved, measurements, are planned.

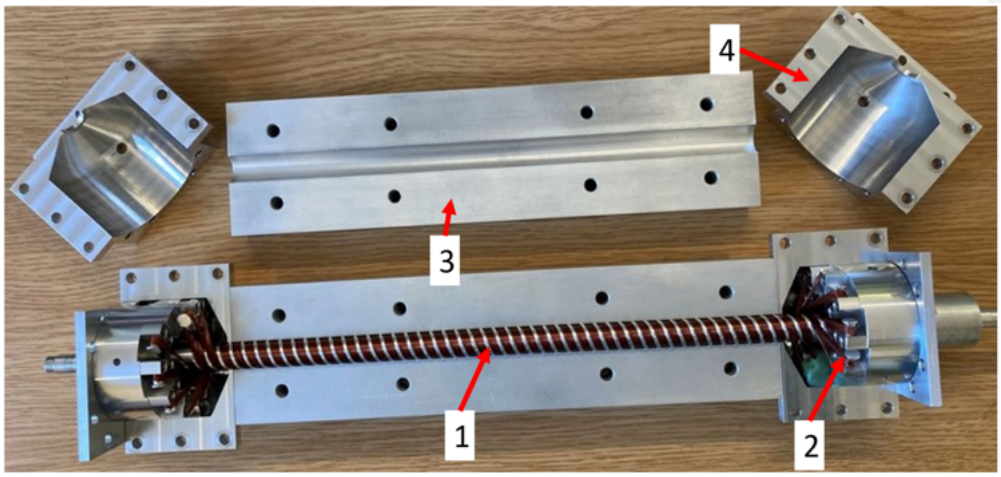

Wound 325 mm HSCU in strong back; 1- Wound HSCU former, 2- Turnaround pins, 3-Potting jig strong back, 4- Potting jig turnaround section.

Figure 6.33: A 325 mm test prototype for the STFC helical SCU.

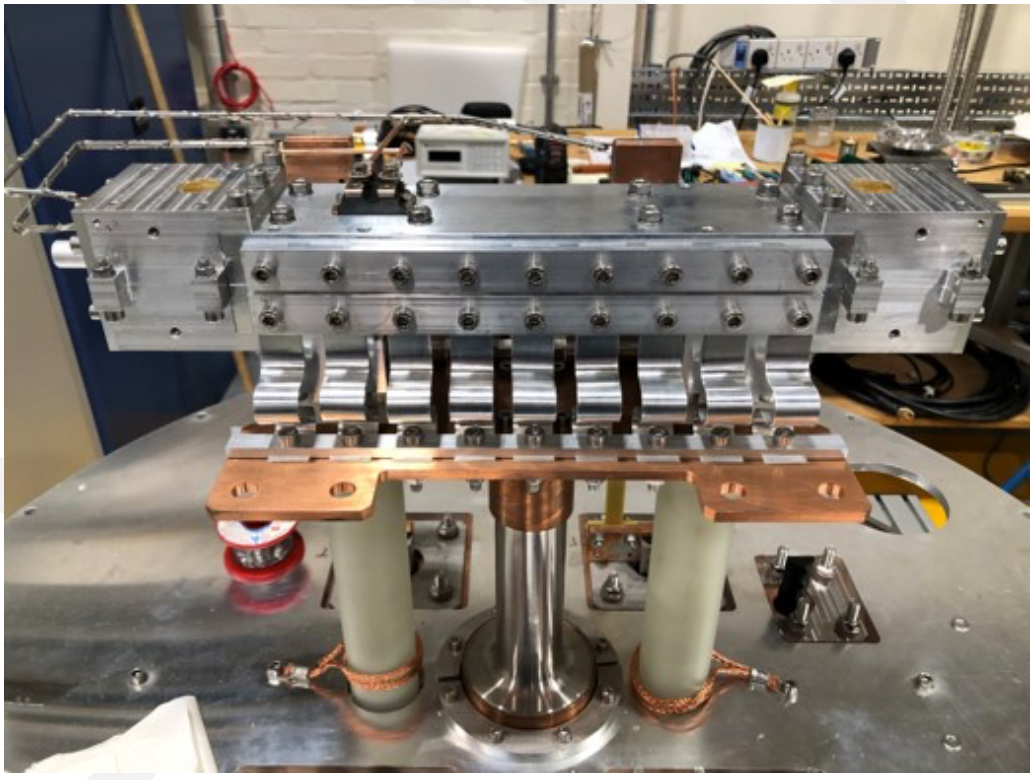

Figure 6.34: Test cryostat for the 325 mm prototype of the STFC helical SCU.

For materials, low-temperature SC (LTS) NbTi wires are the most straight-forward technology. They have been used to develop planar devices for storage ring light sources [99, 100, 101, 102] as well as SCHU devices for both storage rings [103] and for a polarized e^+ source [104]. A short prototype of variably polarising NbTi device has also been manufactured and tested [105]. Therefore NbTi can be considered a mature technology which outperforms PM undulators over a wide range of λ_u values. In principle Nb_3Sn-based SCU technology could offer even higher

performances, but it is much less advanced due to the much more severe technical challenges that it entails [106]. Due to this, so far only short models of Nb_3Sn SCUs have been developed [107]. However, these achievements suggest that the fabrication of a Nb_3Sn SCU, though demanding, is in fact feasible.

A strength common to all low-temperature SCUs is the radiation hardness of SC magnets. The limiting factor for the lifetime of SCUs in a FEL environment is therefore the radiation-induced degradation of insulating material.

High-temperature superconductor (HTS) REBCO tapes have been successfully tested to build short models with VR geometry [108]. Besides planar geometries, helical designs are a possible option, but are limited by the minimum bending radius of coated REBCO tapes, which is not smaller than 5 mm, making gaps smaller than 10 mm unfeasible today. HTS has the advantage compared to LTS that it can be operated at higher temperatures allowing a more cost-efficient and simplified cryogenic system. In principle HTS can offer a significant improvement of the magnetic peak field compared to NbTi technology, up to a factor 2 or 1.5 for HR and VR geometries, respectively.

Another option with HTS is a staggered array undulator using HTS bulks. This geometry consists of a SC solenoid surrounding two rows of HTS bulks staggered half λ_u to shape the homogeneous on axis field into an undulator field [109]. The absence of complex winding simplifies the protection and allows a simple scaling to shorter periods. However, the absence of direct control of the trapped current creates an operation challenge and requires the development of an online measuring system to directly control the undulator field. The best performing ReBCO material is GdBCO ($GdBa_2Cu_3O_{7-\delta}$), where trapped fields as high as 17.6 T have been demonstrated [110]. HTS bulks can be either actual bulks or bulks made with tape stacks, which provide a lower magnetic performance but offer a better mechanical behaviour and overcome inhomogeneity issues. This technology in principle allows the best performance among the family of SCUs, but there are still many open issues to be solved, in particular the lack of reproducibility of the magnetization process.

It can be concluded that already the most conservative SC technology (NbTi) enables a rather aggressive design of a modern x-ray FEL facility in terms of compactness. This is state-of-the-art technology for storage ring light sources and is being further developed and validated for application to FELs in an active R&D program for the upgrade of the LCLS [111].

6.7.2.3 Exotic Undulators

It is very challenging to scale either PM or SC undulators down to ever-decreasing periods.In addition, conventional technologies offer a slow and limited dynamic control of the radiation. To overcome these shortcomings, new ideas such as microwave undulators and laser undulators have been proposed in recent years.

In a microwave undulator (MU) the microwave fields propagating in a waveguide are used to deflect the electron beam trajectory [112]. Potentially this technology may offer several advantages over PM or SC: (1) fast dynamic control of the polarization, (2) easy control of the field strength, (3) determination of λ_u by the wavelength of the electromagnetic wave, and (4) robustness against radiation damage. However little progress has been made since the MU concept was first proposed due to the limited availability of high power microwave sources.

A good candidate to be used as a MU is a corrugated circular waveguide featuring a fundamental HE_{11} mode with a lower loss compared to the TE_{01} mode in a circular waveguide [113]. For the

CompactLight Project such a waveguide cavity operating at 36 GHz was designed as a potential MU [114]. This device, powered with 50 MW, provides $\lambda_u \sim 4.35$ mm and a deflection parameter of K ~ 0.5.

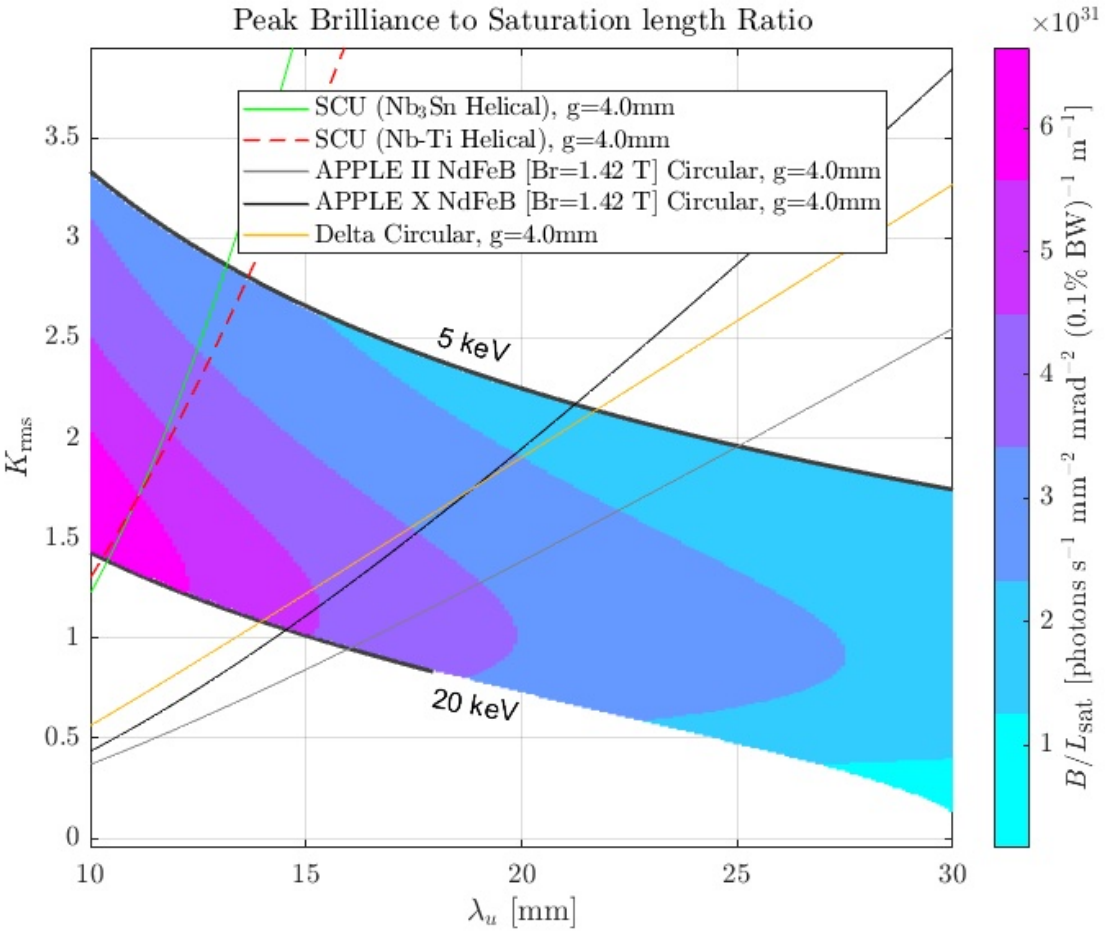

Figure 6.35: Undulator Technology Options for FEL-2

6.7.3 Choice of UK XFEL Undulator Technology

6.7.3.1 Radiator Undulators

A number of undulator technologies have been discussed considered for implementation as the primary radiator undulators for UK XFEL. At this time, the technologies discussed under the label 'exotic' (Section 6.7.2.3) are considered to have a technology readiness level insufficiently high for adoption into a facility design. The requirement that the polarisation of the output is variable further restricts the realistic options.

The high repetition rate has implications for the adoption of SCU technology onto FELs 2–6. The model of [115] was used to calculate the power loss due to resistive wakefields of 300 pC electron bunches with near flat-top profiles of duration 100 fs, propagating with a repetition rate of 1 MHz along the axis of a circular 4 mm diameter aperture cryogenically cooled aluminium pipe. The power loss was found to be 22.5 W/m. It is not currently clear that this level of power deposition is acceptable from a cryogenic perspective. However the much more modest power loss in a low repetition rate FEL such as FEL-1 is likely acceptable. A further risk of using SCU technology is

that the field quality requirements necessary for HXR lasing are extremely stringent and have yet to be demonstrated in practice.

A quantitative comparison was made of the main candidate undulator technologies. The comparison used the parameterisations of the estimated field as a function of undulator period and gap and was based on a combination of the semi-analytical model of Ming Xie [68], which provides an estimation of the saturation power P_{sat} and length L_{sat} of the FEL, together with the analytical theory of Saldin [3], which allows calculation of the FEL longitudinal and transversal coherence, and hence spectral brightness. The chosen figure of merit was the ratio between the FEL peak brightness and the saturation length (B/L_{sat}), which provides a convenient measure of performance *vs* compactness. The figure of merit was analysed for electron beam energies between 7 GeV and 9 GeV using the following set of beam parameters applicable to FEL-2 : peak current I = 1.66 kA, normalized emittance ϵ_n = 0.22 mm · mrad, relative *rms* energy spread $\sigma_\gamma/\gamma_0 = 10^{-4}$ and average β-function $\bar{\beta}$ = 5 m.

Figure 6.35 shows a contour plot of the B/L_{sat} merit function calculated at 8 GeV in the [K, λ_u] parameter space for the FEL-2 photon energy range 5–20 keV. On top is plotted the K_{max} vs λ_u dependencies for the different variable polarisation and helical technologies, assuming a minimum gap of 4 mm. Initial simulations of FEL-2 at 20 keV indicate that the effect of resistive wall wakefields, for a 3 mm internal diameter Cu vacuum pipe, reduces the pulse energy by approximately 20 % at saturation, but that this pulse energy can be recovered fully with a linear undulator taper. The intersection of each undulator curve with the 5 keV line defines the period of that undulator at that beam energy.

The figure shows that a helical SCU would require a period of approximately 13 mm to tune over the photon energy range, an APPLE-X or Delta Circular would require a period of approximately 21 mm, and an APPLE-II would require a period of about 25 mm. The SCU would have the maximum brightness to length ratio, followed by the APPLE-X, the Delta Circular and the APPLE-II. The SCU technology therefore offers the best potential performance in terms of brightness to length ratio and the ability to reach high photon energies due to shorter periods.

However, given the SCU technology readiness level, the lack of a mature design for a variably polarising SCU or in-vacuum device, and the potential implications of wakefield heating complications, **the recommended technology choice is APPLE-X for FELs 1–6 with future SCU development leading to a potential implementation in FEL-1**. The use of in-vacuum undulators is not proposed for the baseline design but this position can be reconsidered in a later design phase as in-vacuum variable polarisation devices become well developed.

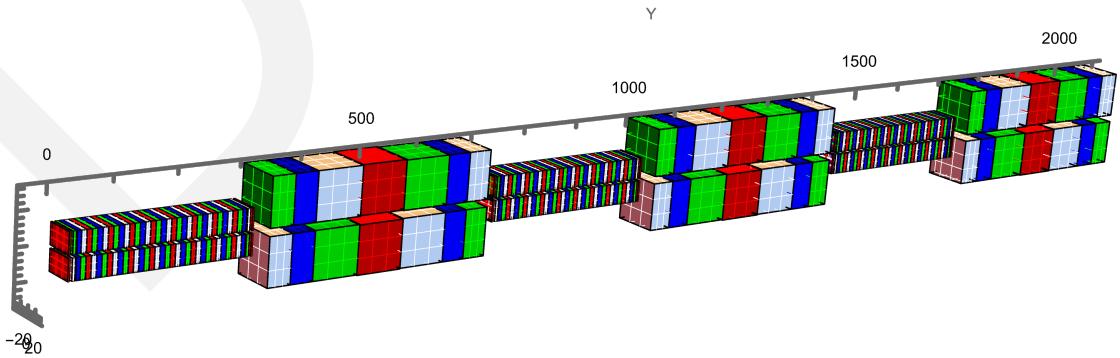

Figure 6.36: RADIA Model of a 2 m long Integrated Delay Undulator

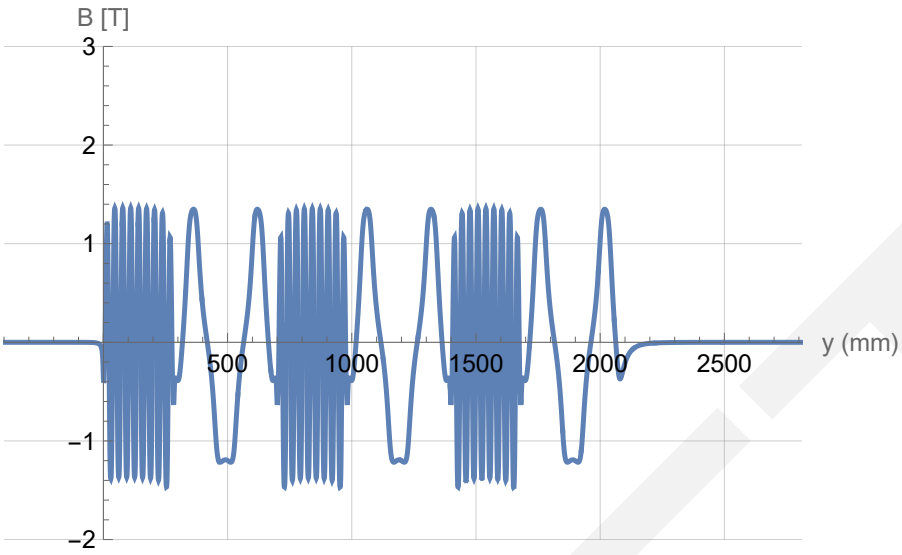

Figure 6.37: Modelled magnetic field of the Integrated Delay Undulator

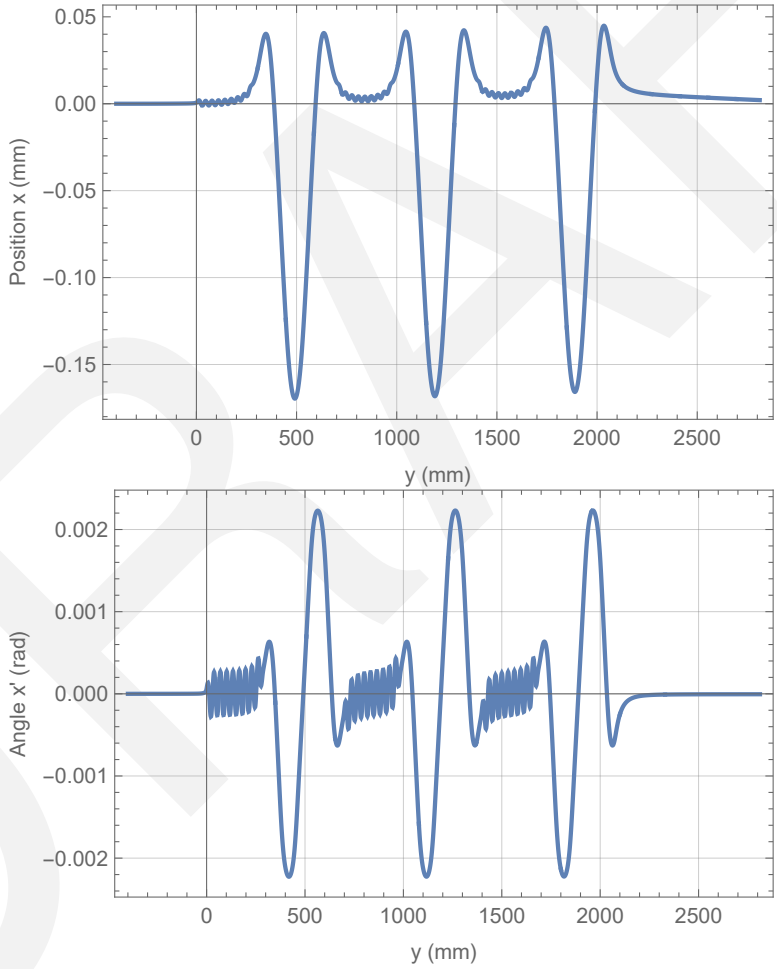

Figure 6.38: Trajectory of an 8 GeV electron: x (mm) (top) and x′ (rad) (bottom).

The K_{rms} of the APPLE-X would be approximately 0.7 at the beam energy of 8 GeV. This is generally considered a realistic practical minimum for reasonable FEL performance—similar plots at lower beam energy show that the minimum K_{rms} would reduce below 0.7, justifying the beam energy choice of 8 GeV as appropriate.

SCUs are seen as a very promising emerging technology for FELs and prototyping the technology

within STFC, and in collaboration with other laboratories, including the implementation of variable polarisation, is a vital programme to ensure a future UK XFEL has world leading performance.

6.7.3.2 Integrated Delay Undulators

A novel feature of the UK XFEL conceptual design is the use of Integrated Delay Undulators (IDUs). In these devices short sections of radiator undulator are interleaved with short single-period undulator sections which are used as electron beam delays. It is proposed that a repeating sequence of these radiator undulators and delay undulators (sub-undulators) are mounted on a common support structure, with independent gap control of each sub-undulator. If the radiator sub-undulators are APPLE-X devices then each of these also requires phase adjustment of individual arrays to control polarisation. A more straightforward initial concept is that the radiator sub-undulators are planar. For such a geometry, FEL simulations have shown that the performance of HB-SASE is very similar and that if the delays are terminated before saturation, and the electron beam then passes into longer polarising undulators for final emission over the last few gain lengths, the saturated FEL output exhibits near perfect polarisation.

A 2 m long planar geometry IDU has been modelled in the code RADIA [116]. The model is shown in Figure 6.36. The magnetic field is shown in Figure 6.37, and the trajectory of an 8 GeV beam in Figure 6.38. The period-averaged trajectory within the radiator sub-undulators deviates by approximately 7μm due to the fringe fields from the delay sections. The current model has no shielding end plates which would be expected to remove this possibly detrimental effect. More study is required.

6.7.3.3 Other Undulators

In addition to the FEL radiator undulators, the lattice design includes modulator undulators required for seeding and short pulse schemes. These are all assumed to be standard planar permanent magnet undulators and as such are well proven technology.

6.8 Summary of Technology Development Requirements

A number of technology development requirements have been identified.

- **In-Vacuum Variably Polarising Undulators**: The baseline design adopts mostly standard undulator technology to enable production of variably polarised FEL output. By adopting in-vacuum technology the undulator minimum gap could be reduced further—this would allow a shorter period and/or a reduced beam energy giving a more compact and/or higher performance facility at the highest photon energies. The technology development required is the further validation of variably polarising in-vacuum undulators, and demonstration that the field quality is sufficiently high for lasing in the HXR.
- **SCU Technology**: this will offer similar advantages, particularly if variable polarising SCUs can be developed further. The progress made with helical prototypes within STFC should also be built upon.

- **Integrated Delay Undulators (IDUs)**: The HB-SASE requirement for short undulator modules led to the concept of the IDU. At the moment this remains a concept whose main challenge is engineering. To have interleaved sub-undulators, of different periods, mounted on a common structure with the ability to independently control the gap of all sub-undulators as well as the phase of the variably polarising sub-undulators, is a novel concept. Full magnetic modelling and a feasible engineering concept are required, followed by prototyping.
- **CBXFELs**: This remains the most feasible concept for production of very stable, very narrow bandwidth, HXR pulses. The technology for such a system is under development at other facilities. UK XFEL has established links with relevant groups and should strengthen collaboration, identifying key areas where significant research contributions can be made.

6.9 Sustainability Choices and Future Prospects

Our recommended technology choice is APPLE-X undulators for FELs 1–6, with the potential for future inclusion of an SCU in FEL-1. This choice is motivated by a number of factors including performance and technology readiness level, as described above. Another factor influencing this choice is sustainability.

PM-based undulators (such as APPLE-X devices) do not use any energy in operation, apart from a small amount for the motors in variable gap or phase devices. This is only required during adjustment and is negligible overall. Cryogenic PM undulators need some energy for refrigeration.

Superconducting undulators require moderate-sized cryogenic systems to keep them at the temperature required for operation (typically 4.2 K). The STFC helical SCU design work has been based on direct cooling using cold heads; the power consumption is dominated by the compressor that drives the cold head. One compressor can cool around 1 m of undulator, and consumes around 10 kW (including water cooling). The power supply for the undulator coils themselves contributes a negligible amount to this, around 200 W. A facility with a total undulator length of 560 m thus has a cryogenic power load of 5.6 MW. At this level, this starts to become comparable to the power requirements of the RF system. If SCUs are only used for FEL-1a and 1b, this power load is reduced to 2.6 MW.

The environmental impact of permanent magnets should be discussed as well. The rare earth materials required for strong PMs must be mined from the ground; currently this is only economically feasible at a small number of locations worldwide, and the vast majority of magnets are ultimately sourced from China. The extraction of rare earth materials has a significant environmental impact, not just in terms of carbon emissions but across a wide range of environmental impact factors [117].

Without a full design being done, it is not possible to make a full assessment of the lifecycle impact of a PM undulator; however, we can estimate it with some reasonable figures. The Athos APPLE-X device at SwissFEL [118] has a PM cross-sectional area of about 900 mm^2. This translates to around 3 t of NdFeB for the 430 m of undulator in FELs 1–6. Estimates of the carbon intensity of PM material vary widely, but the median is around 90 $kgCO_2e/kg$. So the embodied emissions in all the PM material for APPLE-X undulators for FELs 1–6 come to about 270 tCO_2e. The supporting infrastructure adds some embodied emissions to this of course, but this statement is true for any undulator technology.

The current UK electricity grid has emissions of 207 gCO_2e/kWh [119]. Assuming cryogenic system uptime of 8000 hours per year, running the cryogenic system for SCUs for FELs 1–6 would produce emissions of 7.1 $ktCO_2e$. The grid is expected to become 'greener' in the future, but even a figure ten times lower than this is significantly larger than the embodied emissions of PM-based undulators. The conclusion here is that PM technology is significantly better for the environment over the long term than SCU technology, even for a low-carbon electricity grid.

All this is based on like-for-like replacement. In reality, the picture is more complex: the use of SCUs would give the option of a reduced beam energy, the benefit of which would have to be offset against their power requirement.

Relevant future possibilities:

- **Electron Beam Emittance**: research in electron beam production and transport leading to lower emittance at the FEL, compared to current assumptions, would enable improved performance at the highest photon energies, a reduction in the required electron beam energy (with corresponding RF power reduction) or a balance between both of these benefits. Section 5.3.2 has more details on these possibilities.
- **Advanced Undulator Technology**: shorter period high field undulators, such as SCUs or in-vacuum variably polarising undulators, would similarly allow either improved performance, a reduced electron beam energy, or a balance of the two.

DRAFT

References for Chapter 6

[1] W. Ackermann et al. “Operation of a free-electron laser from the extreme ultraviolet to the water window”. In: *Nature Photonics* 1.6 (June 2007), pp. 336–342. ISSN: 1749-4885. DOI: 10.1038/nphoton.2007.76.

[2] R. Bonifacio et al. “Spectrum, temporal structure, and fluctuations in a high-gain free-electron laser starting from noise”. In: *Physical Review Letters* 73.1 (July 1994), pp. 70–73. ISSN: 0031-9007. DOI: 10.1103/PhysRevLett.73.70.

[3] E. L. Saldin, E. A. Schneidmiller, and M. V. Yurkov. “Statistical and coherence properties of radiation from x-ray free-electron lasers”. In: *New Journal of Physics* 12.3 (Mar. 2010), p. 035010. ISSN: 1367-2630. DOI: 10.1088/1367-2630/12/3/035010. URL: https://iopscience.iop.org/article/10.1088/1367-2630/12/3/035010.

[4] B W J Mcneil et al. “An XUV-FEL amplifier seeded using high harmonic generation”. In: *New Journal of Physics* 9 (2007), p. 82. DOI: 10.1088/1367-2630/9/4/082. URL: http://www.njp.org/.

[5] D. J. Dunning, N. R. Thompson, and B. W.J. McNeil. “Design study of an HHG-seeded harmonic cascade free-electron laser”. In: *Journal of Modern Optics* 58.16 (Sept. 2011), pp. 1362–1373. ISSN: 09500340. DOI: 10.1080/09500340.2011.586475. URL: https://www.tandfonline.com/doi/abs/10.1080/09500340.2011.586475.

[6] Primož Rebernik Ribič et al. “Coherent soft X-ray pulses from an echo-enabled harmonic generation free-electron laser”. In: *Nature Photonics 2019 13:8* 13.8 (May 2019), pp. 555–561. ISSN: 1749-4893. DOI: 10.1038/s41566-019-0427-1. URL: https://www.nature.com/articles/s41566-019-0427-1.

[7] G. Stupakov. “Using the beam-echo effect for generation of short-wavelength radiation”. In: *Physical Review Letters* 102.7 (Feb. 2009), p. 074801. ISSN: 00319007. DOI: 10.1103/PHYSREVLETT.102.074801. URL: https://journals.aps.org/prl/abstract/10.1103/PhysRevLett.102.074801.

[8] E. Hemsing et al. “Highly coherent vacuum ultraviolet radiation at the 15th harmonic with echo-enabled harmonic generation technique”. In: *Physical Review Special Topics - Accelerators and Beams* 17.7 (July 2014). ISSN: 10984402. DOI: 10.1103/PHYSREVSTAB.17.070702.

[9] G. Penn. “Stable, coherent free-electron laser pulses using echo-enabled harmonic generation”. In: *Physical Review Special Topics - Accelerators and Beams* 17.11 (Nov. 2014), p. 110707. ISSN: 10984402. DOI: 10.1103/PHYSREVSTAB.17.110707. URL: https://journals.aps.org/prab/abstract/10.1103/PhysRevSTAB.17.110707.

[10] P. R. Ribic. “Echo-Enabled Harmonic Generation Lasing of the FERMI FEL in the Soft X-Ray Spectral Region”. In: *Proceedings of the 39th International Free-Electron Laser Conference, FEL 2019*. JACOW Publishing, Geneva, Switzerland, Nov. 2019, pp. 33–37. ISBN: 978-3-95450-210-3. DOI: 10.18429/JACOW-FEL2019-TUB01.

[11] Martin Beye et al. “FLASH and the FLASH2020+ project—current status and upgrades for the free-electron laser in Hamburg at DESY”. In: *The European Physical Journal Plus* 138 (3 Mar. 2023), p. 193. ISSN: 2190-5444. DOI: 10.1140/epjp/s13360-023-03814-8.

[12] Sven Reiche. “Seeding at SwissFEL”. In: *https://doi.org/10.1117/12.2666463* 12581 (June 2023), pp. 16–23. ISSN: 1996756X. DOI: 10.1117/12.2666463.

[13] E. Allaria et al. “Highly coherent and stable pulses from the FERMI seeded free-electron laser in the extreme ultraviolet”. In: *Nature Photonics* 6.10 (Oct. 2012), pp. 699–704. ISSN: 17494885. DOI: 10.1038/NPHOTON.2012.233.

[14] E. L. Saldin, E. A. Schneidmiller, and M. V. Yurkov. “Study of a noise degradation of amplification process in a multistage HGHG FEL”. In: *Optics Communications* 202.1-3 (Feb. 2002), pp. 169–187. ISSN: 0030-4018. DOI: 10.1016/S0030-4018(02)01091-X.

[15] Xiaofan Wang et al. “High-repetition-rate seeded free-electron laser with direct-amplification of an external coherent laser”. In: *New Journal of Physics* 24.3 (Mar. 2022), p. 033013. ISSN: 1367-2630. DOI: 10.1088/1367-2630/AC5492. URL: https://iopscience.iop.org/article/10.1088/1367-2630/ac5492%20https://iopscience.iop.org/article/10.1088/1367-2630/ac5492/meta.

[16] Zheng Qi et al. “First Lasing and Stable Operation of a Direct-Amplification Enabled Harmonic Generation Free-Electron Laser”. In: *Phys. Rev. Lett.* 135 (3 July 2025), p. 035001. DOI: 10.1103/sslg-jjkz. URL: https://link.aps.org/doi/10.1103/sslg-jjkz.

[17] J. Feldhaus et al. “Possible application of X-ray optical elements for reducing the spectral bandwidth of an X-ray SASE FEL”. In: *Optics Communications* 140.4-6 (Aug. 1997), pp. 341–352. ISSN: 0030-4018. DOI: 10.1016/S0030-4018(97)00163-6.

[18] J. Amann et al. “Demonstration of self-seeding in a hard-X-ray free-electron laser”. In: *Nature Photonics* 6.10 (Oct. 2012), pp. 693–698. ISSN: 17494885. DOI: 10.1038/NPHOTON.2012.180.

[19] Inhyuk Nam et al. “High-brightness self-seeded X-ray free-electron laser covering the 3.5 keV to 14.6 keV range”. In: *Nature Photonics 2021 15:6* 15.6 (Mar. 2021), pp. 435–441. ISSN: 1749-4893. DOI: 10.1038/s41566-021-00777-z. URL: https://www.nature.com/articles/s41566-021-00777-z.

[20] Erik Hemsing, Aliaksei Halavanau, and Zhen Zhang. “Enhanced Self-Seeding with Ultrashort Electron Beams”. In: *Physical Review Letters* 125.4 (July 2020), p. 044801. ISSN: 10797114. DOI: 10.1103/PHYSREVLETT.125.044801. URL: https://journals.aps.org/prl/abstract/10.1103/PhysRevLett.125.044801.

[21] E. Schneidmiller and I. Zagorodnov. “Two-bunch seeding of soft X-ray free electron lasers”. In: *Physical Review Accelerators and Beams* 27.11 (June 2024), p. 110703. ISSN: 24699888. DOI: 10.1103/PHYSREVACCELBEAMS.27.110703. URL: http://arxiv.org/abs/2406.19984.

[22] N R Thompson, D J Dunning, and McNeil B W J. “Improved Temporal Coherence in SASE FELs”. In: *Proceedings of IPAC’10*. 2010. URL: https://accelconf.web.cern.ch/IPAC10/papers/TUPE050.pdf.

[23] B. W.J. McNeil, N. R. Thompson, and D. J. Dunning. “Transform-limited x-ray pulse generation from a high-brightness self-amplified spontaneous-emission free-electron laser”. In: *Physical Review Letters* 110.13 (Mar. 2013), p. 134802. ISSN: 00319007. DOI: 10.1103/PHYSREVLETT.110.134802. URL: https://journals.aps.org/prl/abstract/10.1103/PhysRevLett.110.134802.

[24] Eduard Prat et al. “Experimental Demonstration of Mode-Coupled and High-Brightness Self-Amplified Spontaneous Emission in an X-Ray Free-Electron Laser”. In: *Physical Review Letters* 133.20 (Nov. 2024), p. 205001. ISSN: 10797114. DOI: 10.1103/PHYSREVLETT.133.205001. URL: https://journals.aps.org/prl/abstract/10.1103/PhysRevLett.133.205001.

[25] R. Colella and A. Luccio. “Proposal for a free electron laser in the X-ray region”. In: *Optics Communications* 50.1 (May 1984), pp. 41–44. ISSN: 0030-4018. DOI: 10.1016/0030-4018(84)90009-9.

[26] Kwang Je Kim, Yuri Shvyd’ko, and Sven Reiche. “A Proposal for an X-ray free-electron laser oscillator with an energy-recovery linac”. In: *Physical Review Letters* 100.24 (June 2008), p. 244802. ISSN: 00319007. DOI: 10.1103/PHYSREVLETT.100.244802. URL: https://journals.aps.org/prl/abstract/10.1103/PhysRevLett.100.244802.

[27] B. W.J. McNeil. “A simple model of the free-electron-laser oscillator from low into high gain”. In: *Nuclear Instruments and Methods in Physics Research Section A: Accelerators, Spectrometers, Detectors and Associated Equipment* 296.1-3 (Oct. 1990), pp. 388–393. ISSN: 0168-9002. DOI: 10.1016/0168-9002(90)91237-6.

[28] Zhirong Huang and Ronald D. Ruth. “Fully coherent X-ray pulses from a regenerative-amplifier free-electron laser”. In: *Physical Review Letters* 96.14 (2006). ISSN: 00319007. DOI: 10.1103/PHYSREVLETT.96.144801.

[29] Dinh C. Nguyen et al. “First lasing of the regenerative amplifier FEL”. In: *Nuclear Instruments and Methods in Physics Research Section A: Accelerators, Spectrometers, Detectors and Associated Equipment* 429.1-3 (June 1999), pp. 125–130. ISSN: 0168-9002. DOI: 10.1016/S0168-9002(99)00090-X.

[30] D. J. Dunning, B. W.J. McNeil, and N. R. Thompson. “Short wavelength regenerative amplifier free electron lasers”. In: *Nuclear Instruments and Methods in Physics Research Section A: Accelerators, Spectrometers, Detectors and Associated Equipment* 593.1-2 (Aug. 2008), pp. 116–119. ISSN: 0168-9002. DOI: 10.1016/J.NIMA.2008.04.045.

[31] Rachel Margraf et al. “Low-loss stable storage of 1.2 Å X-ray pulses in a 14 m Bragg cavity”. In: *Nature Photonics 2023 17:10* 17.10 (Aug. 2023), pp. 878–882. ISSN: 1749-4893. DOI: 10.1038/s41566-023-01267-0. URL: https://www.nature.com/articles/s41566-023-01267-0.

[32] Patrick Rauer et al. “Cavity based x-ray free electron laser demonstrator at the European X-ray Free Electron Laser facility”. In: *Physical Review Accelerators and Beams* 26.2 (Feb. 2023), p. 020701. ISSN: 24699888. DOI: 10.1103/PHYSREVACCELBEAMS.26.020701. URL: https://journals.aps.org/prab/abstract/10.1103/PhysRevAccelBeams.26.020701.

[33] Patrick Rauer et al. “Lasing of a cavity-based X-ray source”. In: *Nature* 650 (2026), pp. 93–96. DOI: 10.1038/s41586-025-10025-x. URL: https://doi.org/10.1038/s41586-025-10025-x.

[34] P. Emma et al. “Femtosecond and Subfemtosecond X-Ray Pulses from a Self-Amplified Spontaneous-Emission–Based Free-Electron Laser”. In: *Physical Review Letters* 92.7 (Feb. 2004), p. 074801. ISSN: 0031-9007. DOI: 10.1103/PhysRevLett.92.074801.

[35] A. Marinelli et al. “Experimental demonstration of a single-spike hard-X-ray free-electron laser starting from noise”. In: *Applied Physics Letters* 111.15 (Oct. 2017). ISSN: 0003-6951. DOI: 10.1063/1.4990716.

[36] E. L. Saldin, E. A. Schneidmiller, and M. V. Yurkov. “Self-amplified spontaneous emission FEL with energy-chirped electron beam and its application for generation of attosecond x-ray pulses”. In: *Physical Review Special Topics - Accelerators and Beams* 9.5 (May 2006), p. 050702. ISSN: 10984402. DOI: 10.1103/PhysRevSTAB.9.050702. URL: https://journals.aps.org/prab/abstract/10.1103/PhysRevSTAB.9.050702.

[37] L. Giannessi et al. “Self-Amplified Spontaneous Emission Free-Electron Laser with an Energy-Chirped Electron Beam and Undulator Tapering”. In: *Physical Review Letters* 106.14 (Apr. 2011), p. 144801. ISSN: 00319007. DOI: 10.1103/PhysRevLett.106.144801. URL: https://journals.aps.org/prl/abstract/10.1103/PhysRevLett.106.144801.

[38] Senlin Huang et al. “Generation of stable subfemtosecond hard x-ray pulses with optimized nonlinear bunch compression”. In: *Physical Review Special Topics - Accelerators and Beams* 17.12 (Dec. 2014), p. 120703. ISSN: 1098-4402. DOI: 10.1103/PhysRevSTAB.17.120703.

[39] S. Huang et al. “Generating Single-Spike Hard X-Ray Pulses with Nonlinear Bunch Compression in Free-Electron Lasers”. In: *Physical Review Letters* 119.15 (Oct. 2017), p. 154801. ISSN: 0031-9007. DOI: 10.1103/PhysRevLett.119.154801.

[40] Alexander Malyzhenkov et al. “Single- and two-color attosecond hard x-ray free-electron laser pulses with nonlinear compression”. In: *Physical Review Research* 2.4 (Oct. 2020), p. 042018. ISSN: 2643-1564. DOI: 10.1103/PhysRevResearch.2.042018.

[41] Eduard Prat et al. “Coherent sub-femtosecond soft x-ray free-electron laser pulses with nonlinear compression”. In: *APL Photonics* 8.11 (Nov. 2023). ISSN: 2378-0967. DOI: 10.1063/5.0164666.

[42] Jiawei Yan et al. “Terawatt-attosecond hard X-ray free-electron laser at high repetition rate”. In: *Nature Photonics 2024 18:12* 18.12 (Nov. 2024), pp. 1293–1298. ISSN: 1749-4893. DOI: 10.1038/s41566-024-01566-0. URL: https://www.nature.com/articles/s41566-024-01566-0.

[43] Alexander A. Zholents. “Method of an enhanced self-amplified spontaneous emission for x-ray free electron lasers”. In: *Physical Review Special Topics - Accelerators and Beams* 8.4 (Apr. 2005), p. 040701. ISSN: 1098-4402. DOI: 10.1103/PhysRevSTAB.8.040701.

[44] Joseph P. Duris et al. “Controllable X-Ray Pulse Trains from Enhanced Self-Amplified Spontaneous Emission”. In: *Physical Review Letters* 126.10 (Mar. 2021), p. 104802. ISSN: 0031-9007. DOI: 10.1103/PhysRevLett.126.104802.

[45] Paris Franz et al. “Terawatt-scale attosecond X-ray pulses from a cascaded superradiant free-electron laser”. In: *Nature Photonics* 18.7 (July 2024), pp. 698–703. ISSN: 17494893. DOI: 10.1038/S41566-024-01427-W. URL: https://www.nature.com/articles/s41566-024-01427-w.

[46] Joseph Duris et al. “Tunable isolated attosecond X-ray pulses with gigawatt peak power from a free-electron laser”. In: *Nature Photonics* 14.1 (Jan. 2020), pp. 30–36. ISSN: 1749-4885. DOI: 10.1038/s41566-019-0549-5.

[47] James P. Cryan et al. “The development of attosecond XFELs for understanding ultrafast electron motion”. In: *Advances in Atomic, Molecular and Optical Physics* 71 (2022). ISSN: 1049250X. DOI: 10.1016/bs.aamop.2022.05.001.

[48] N R Thompson and B W J McNeil. “Mode locking in a free-electron laser amplifier”. In: *Physical Review Letters* (2008). ISSN: 00319007. DOI: 10.1103/PhysRevLett.100.203901.

[49] Wenxiang Hu et al. “Demonstration of Mode-Locked Frequency Comb for an X-Ray Free-Electron Laser”. In: *Physical Review Letters* 135.26 (Dec. 2025), p. 265001. ISSN: 10797114. DOI: 10.1103/wn8d-l7sh. URL: https://journals.aps.org/prl/abstract/10.1103/wn8d-l7sh.

[50] D J Dunning, B W J J McNeil, and N R Thompson. “Few-cycle pulse generation in an X-ray free-electron laser”. In: *Physical Review Letters* 110.10 (Dec. 2013), p. 104801. ISSN: 00319007. DOI: 10.1103/PhysRevLett.110.104801. URL: https://link.aps.org/doi/10.1103/PhysRevLett.110.104801.

[51] Z. Tibai et al. “Proposal for Carrier-Envelope-Phase Stable Single-Cycle Attosecond Pulse Generation in the Extreme-Ultraviolet Range”. In: *Physical Review Letters* 113.10 (Sept. 2014), p. 104801. ISSN: 0031-9007. DOI: 10.1103/PhysRevLett.113.104801.

[52] Takashi Tanaka. “Proposal to Generate an Isolated Monocycle X-Ray Pulse by Counteracting the Slippage Effect in Free-Electron Lasers”. In: *Physical Review Letters* 114.4 (Jan. 2015), p. 044801. ISSN: 0031-9007. DOI: 10.1103/PhysRevLett.114.044801.

[53] Alan Mak et al. “Attosecond single-cycle undulator light: a review”. In: *Reports on Progress in Physics* 82.2 (Feb. 2019), p. 025901. ISSN: 0034-4885. DOI: 10.1088/1361-6633/aafa35.

[54] A. A. Lutman et al. “Experimental Demonstration of Femtosecond Two-Color X-Ray Free-Electron Lasers”. In: *Physical Review Letters* 110.13 (Mar. 2013), p. 134801. ISSN: 0031-9007. DOI: 10.1103/PhysRevLett.110.134801.

[55] Alberto A. Lutman et al. “Fresh-slice multicolour X-ray free-electron lasers”. In: *Nature Photonics* 10.11 (Nov. 2016), pp. 745–750. ISSN: 1749-4885. DOI: 10.1038/nphoton.2016.201.

[56] Weilun Qin et al. “Matching-based fresh-slice method for generating two-color x-ray free-electron lasers”. In: *Physical Review Accelerators and Beams* 20.9 (Sept. 2017), p. 090701. ISSN: 2469-9888. DOI: 10.1103/PhysRevAccelBeams.20.090701.

[57] Marc W. Guetg et al. “Dispersion-Based Fresh-Slice Scheme for Free-Electron Lasers”. In: *Physical Review Letters* 120.26 (June 2018), p. 264802. ISSN: 0031-9007. DOI: 10.1103/PhysRevLett.120.264802.

[58] Evgeny Schneidmiller et al. “Two-Color Operation of a Soft X-ray FEL with Alternation of Undulator Tunes”. In: *Applied Sciences* 13.1 (Dec. 2022), p. 67. ISSN: 2076-3417. DOI: 10.3390/app13010067.

[59] A. Marinelli et al. “High-intensity double-pulse X-ray free-electron laser”. In: *Nature Communications* 6.1 (Mar. 2015), p. 6369. ISSN: 2041-1723. DOI: 10.1038/ncomms7369.

[60] Y. Ding et al. “Generating femtosecond X-ray pulses using an emittance-spoiling foil in free-electron lasers”. In: *Applied Physics Letters* 107.19 (Nov. 2015). ISSN: 0003-6951. DOI: 10.1063/1.4935429.

[61] S. Bettoni, E. Prat, and S. Reiche. “Two-color beam generation based on wakefield excitation”. In: *Physical Review Accelerators and Beams* 19.5 (May 2016), p. 050702. ISSN: 2469-9888. DOI: 10.1103/PhysRevAccelBeams.19.050702.

[62] F. J. Decker et al. “Recent developments and plans for two bunch operation with up to 1 μS separation at LCLS”. In: *Proceedings of the 38th International Free-Electron Laser Conference (FEL 2017)*. JACoW Publishing, 2017, pp. 288–291. ISBN: 9783954501793. DOI: 10.18429/JACoW-FEL2017-TUP023.

[63] P. Dijkstal et al. “Demonstration of two-color x-ray free-electron laser pulses with a sextupole magnet”. In: *Physical Review Accelerators and Beams* 23.3 (Mar. 2020), p. 030703. ISSN: 2469-9888. DOI: 10.1103/PhysRevAccelBeams.23.030703.

[64] Carlo Vicario et al. “Two-color x-ray free-electron laser by photocathode laser emittance spoiler”. In: *Physical Review Accelerators and Beams* 24.6 (June 2021), p. 060703. ISSN: 2469-9888. DOI: 10.1103/PhysRevAccelBeams.24.060703. URL: https://link.aps.org/doi/10.1103/PhysRevAccelBeams.24.060703.

[65] Myung-Hoon Cho et al. “Generation of time-synchronized two-color X-ray free-electron laser pulses using phase shifters”. In: *Scientific Reports* 13.1 (Aug. 2023), p. 13786. ISSN: 2045-2322. DOI: 10.1038/s41598-023-39322-z.

[66] Zhaoheng Guo et al. “Experimental demonstration of attosecond pump–probe spectroscopy with an X-ray free-electron laser”. In: *Nature Photonics* 18.7 (July 2024), pp. 691–697. ISSN: 1749-4885. DOI: 10.1038/s41566-024-01419-w.

[67] Zhirong Huang and Kwang Je Kim. “Review of x-ray free-electron laser theory”. In: *Physical Review Special Topics - Accelerators and Beams* 10.3 (Mar. 2007), p. 034801. ISSN: 10984402. DOI: 10.1103/PHYSREVSTAB.10.034801. URL: https://journals.aps.org/prab/abstract/10.1103/PhysRevSTAB.10.034801.

[68] Ming Xie. “Design optimization for an X-ray free electron laser driven by SLAC linac”. In: *Proceedings of the IEEE Particle Accelerator Conference* 1 (1995), pp. 183–185. DOI: 10.1109/PAC.1995.504603.

[69] S. Reiche. “GENESIS 1.3: a fully 3D time-dependent FEL simulation code”. In: *Nuclear Instruments and Methods in Physics Research Section A: Accelerators, Spectrometers, Detectors and Associated Equipment* 429.1-3 (June 1999), pp. 243–248. ISSN: 0168-9002. DOI: 10.1016/S0168-9002(99)00114-X.

[70] S Reiche. “Status of the time-dependent FEL code Genesis 1.3”. In: *15th International Particle Accelerator Conference*. Nashville: jacow.org, 2024, pp. 2631–2634. DOI: 10.18429/JACoW-IPAC2024-WEPR58.

[71] S. Serkez et al. “Grating monochromator for soft X-ray self-seeding the European XFEL”. In: *FEL 2013: Proceedings of the 35th International Free-Electron Laser Conference* (Mar. 2013), pp. 667–674. URL: https://arxiv.org/abs/1303.1392v1.

[72] N. Kroll, P. Morton, and M. Rosenbluth. “Free-electron lasers with variable parameter wigglers”. In: *IEEE Journal of Quantum Electronics* 17.8 (Aug. 1981), pp. 1436–1468. ISSN: 0018-9197. DOI: 10.1109/JQE.1981.1071285.

[73] Alan Mak. “Efficiency Enhancement Techniques for Free-Electron Lasers”. PhD thesis. Lund, Sweden: Lund University, June 2017.

[74] B. W. J. McNeil et al. “Harmonic Lasing in a Free-Electron-Laser Amplifier”. In: *Physical Review Letters* 96.8 (Mar. 2006), p. 084801. ISSN: 0031-9007. DOI: 10.1103/PhysRevLett.96.084801.

[75] E. A. Schneidmiller and M. V. Yurkov. “Harmonic lasing in x-ray free electron lasers”. In: *Physical Review Special Topics - Accelerators and Beams* 15.8 (Aug. 2012), p. 080702. ISSN: 1098-4402. DOI: 10.1103/PhysRevSTAB.15.080702.

[76] Alan Mak and Neil Thompson. “Towards gamma-ray free-electron lasers”. In: *Proceedings of the 16th International Particle Accelerator Conference, Taipei, Taiwan*. May 2025, MOPB035.

[77] Inhyuk Nam et al. “Soft X-ray harmonic lasing self-seeded free electron laser at Pohang Accelerator Laboratory X-ray free electron laser”. In: *Applied Physics Letters* 112.21 (May 2018). ISSN: 0003-6951. DOI: 10.1063/1.5030443.

[78] L. Giannessi and P. Musumeci. “The free-electron laser harmonic cascade”. In: *New Journal of Physics* 8.11 (Nov. 2006), p. 294. ISSN: 13672630. DOI: 10.1088/1367-2630/8/11/294. URL: https://iopscience.iop.org/article/10.1088/1367-2630/8/11/294%20https://iopscience.iop.org/article/10.1088/1367-2630/8/11/294/meta.

[79] S. Reiche. “GENESIS 1.3: a fully 3D time-dependent FEL simulation code”. In: *Nuclear Instruments and Methods in Physics Research Section A: Accelerators, Spectrometers, Detectors and Associated Equipment* 429.1-3 (June 1999), pp. 243–248. ISSN: 01689002. DOI: 10.1016/S0168-9002(99)00114-X.

[80] S. Abeghyan et al. “First operation of the SASE1 undulator system of the European X-ray Free-Electron Laser”. In: *Journal of Synchrotron Radiation* 26.2 (Mar. 2019), pp. 302–310. ISSN: 1600-5775. DOI: 10.1107/S1600577518017125.

[81] Zhirong Huang and Kwang-Je Kim. “Review of x-ray free-electron laser theory”. In: *Physical Review Special Topics - Accelerators and Beams* 10.3 (Mar. 2007), p. 034801. ISSN: 1098-4402. DOI: 10.1103/PhysRevSTAB.10.034801.

[82] L T Campbell and B W J McNeil. “Puffin: A three dimensional, unaveraged free electron laser simulation code”. en. In: *Physics of Plasmas* 19.9 (Sept. 2012), p. 93119. ISSN: 1070-664X, 1089-7674. DOI: 10.1063/1.4752743. URL: http://aip.scitation.org/doi/10.1063/1.4752743.

[83] Gerardo D’Auria et al. “The CompactLight Design Study Project”. In: *Proc. 10th International Particle Accelerator Conference (IPAC’19), Melbourne, Australia, 19-24 May 2019* 10 (June 2019), pp. 1756–1759. DOI: 10.18429/JACOW-IPAC2019-TUPRB032.

[84] G. D’Auria et al. “The CompactLight Design Study”. In: *European Physical Journal: Special Topics* 233.1 (Apr. 2024), pp. 1–208. ISSN: 19516401. DOI: 10.1140/EPJS/S11734-023-01076-0.

[85] Klaus Halbach. “Physical and optical properties of rare earth cobalt magnets”. In: *Nuclear Instruments and Methods in Physics Research* 187.1 (Aug. 1981), pp. 109–117. ISSN: 0167-5087. DOI: 10.1016/0029-554X(81)90477-8.

[86] M. Calvi et al. “Transverse gradient in Apple-type undulators”. In: *urn:issn:1600-5775* 24.3 (Apr. 2017), pp. 600–608. ISSN: 1600-5775. DOI: 10.1107/S1600577517004726. URL: //journals.iucr.org/paper?vv5164.

[87] T. Schmidt and M. Calvi. “APPLE X Undulator for the SwissFEL Soft X-ray Beamline Athos”. In: *Synchrotron Radiation News* 31.3 (May 2018), pp. 35–40. ISSN: 19317344. DOI: 10.1080/08940886.2018.1460174. URL: https://www.tandfonline.com/doi/abs/10.1080/08940886.2018.1460174.

[88] T Tanaka et al. “In-Vacuum Undulators”. In: *27th International Free Electron Laser Conference*. 2005, pp. 370–377. URL: https://accelconf.web.cern.ch/f05/papers/TUOC001.pdf.

[89] Toru Hara et al. “Cryogenic permanent magnet undulators”. In: *Physical Review Special Topics - Accelerators and Beams* 7.5 (May 2004), pp. 13–18. ISSN: 10984402. DOI: 10.1103/PHYSREVSTAB.7.050702. URL: https://journals.aps.org/prab/abstract/10.1103/PhysRevSTAB.7.050702.

[90] Johannes Bahrdt et al. “In-Vacuum APPLE II Undulator”. In: *Proc. 9th International Particle Accelerator Conference (IPAC’18)* (June 2018), pp. 4114–4116. DOI: 10.18429/JACOW-IPAC2018-THPMF031.

[91] J Bahrdt. “Magnet assembly of IVUE32 in-vacuum-APPLE II at BESSY II”. In: *IPAC’25 - the 16th International Particle Accelerator Conference*. 2025. URL: https://indico.jacow.org/event/81/contributions/7580/.

[92] E Rial. “Cryogenic APPLE undulator development at Helmholtz-Zentrum Berlin”. In: *IPAC’25 - the 16th International Particle Accelerator Conference*. 2025. URL: https://indico.jacow.org/event/81/contributions/7537/.

[93] Ryota Kinjo et al. “Lightweight-compact variable-gap undulator with force cancellation system based on multipole monolithic magnets”. In: *The Review of scientific instruments* 88.7 (July 2017). ISSN: 1089-7623. DOI: 10.1063/1.4991652. URL: https://pubmed.ncbi.nlm.nih.gov/28764549/.

[94] M. Calvi et al. “Magnetic assessment and modelling of the Aramis undulator beamline”. In: *urn:issn:1600-5775* 25.3 (Apr. 2018), pp. 686–705. ISSN: 1600-5775. DOI: 10.1107/S1600577518002205. URL: https://journals.iucr.org/paper?xe5025.

[95] S. Casalbuoni et al. “Superconducting undulator coils with period length doubling”. In: *Journal of Physics: Conference Series* 1350.1 (Nov. 2019), p. 012024. ISSN: 1742-6596. DOI: 10.1088/1742-6596/1350/1/012024.

[96] James A. Clarke. “The Science and Technology of Undulators and Wigglers”. In: *The Science and Technology of Undulators and Wigglers* (Sept. 2004). DOI: 10.1093/ACPROF:OSO/9780198508557.001.0001. URL: https://academic.oup.com/book/4976.

[97] A G Hinton et al. “Development of a short period superconducting helical undulator”. In: *Proceedings of IPAC2022* (2022), pp. 2788–2791. DOI: 10.18429/JACoW-IPAC2022-THPOTK010.

[98] A Hinton et al. “Field measurements of a short period helical superconducting undulator”. In: *IPAC*. 2025.

[99] Y. Ivanyushenkov et al. “Development and operating experience of a short-period superconducting undulator at the Advanced Photon Source”. In: *Physical Review Special Topics - Accelerators and Beams* 18.4 (Apr. 2015), p. 040703. ISSN: 10984402. DOI: 10.1103/PHYSREVSTAB.18.040703. URL: https://journals.aps.org/prab/abstract/10.1103/PhysRevSTAB.18.040703.

[100] Y. Ivanyushenkov et al. “Development and operating experience of a 1.1-m-long superconducting undulator at the Advanced Photon Source”. In: *Physical Review Accelerators and Beams* 20.10 (Oct. 2017), p. 100701. ISSN: 24699888. DOI: 10.1103/PHYSREVACCELBEAMS.20.100701. URL: https://journals.aps.org/prab/abstract/10.1103/PhysRevAccelBeams.20.100701.

[101] S. Casalbuoni et al. “Characterization and long term operation of a novel superconducting undulator with 15 mm period length in a synchrotron light source”. In: *Physical Review Accelerators and Beams* 19.11 (Nov. 2016), p. 110702. ISSN: 24699888. URL: https://journals.aps.org/prab/abstract/10.1103/PhysRevAccelBeams.19.110702.

[102] S. Casalbuoni et al. “Superconducting Undulators: From Development towards a Commercial Product”. In: *Synchrotron Radiation News* 31.3 (May 2018), pp. 24–28. ISSN: 19317344. URL: https://www.tandfonline.com/doi/abs/10.1080/08940886.2018.1460171.

[103] Y. Ivanyushenkov et al. “Status of the Development of Superconducting Undulators at the Advanced Photon Source”. In: *Synchrotron Radiation News* 31.3 (May 2018), pp. 29–34. ISSN: 19317344. DOI: 10.1080/08940886.2018.1460172.

[104] D. J. Scott et al. “Demonstration of a high-field short-period superconducting helical undulator suitable for future TeV-scale linear collider positron sources”. In: *Physical Review Letters* 107.17 (Oct. 2011), p. 174803. ISSN: 00319007. DOI: 10.1103/PHYSREVLETT.107.174803. URL: https://journals.aps.org/prl/abstract/10.1103/PhysRevLett.107.174803.

[105] M Kasa. “Measurement results of the first SCAPE prototype”. In: *IPAC 2021, 12th International Particle Accelerator Conference*. jacow.org, 2021, pp. 3872–3874. URL: https://accelconf.web.cern.ch/ipac2021/papers/thpab054.pdf.

[106] Alexander Zlobin et al. “Advantages and Challenges of Nb3Sn Superconducting Undulators”. In: *Proc. 9th International Particle Accelerator Conference (IPAC’18)* (June 2018), pp. 2734–2737. DOI: 10.18429/JACOW-IPAC2018-WEPML025.

[107] Ibrahim Kesgin et al. “Development of Short-Period Nb3Sn Superconducting Planar Undulators”. In: *IEEE Transactions on Applied Superconductivity* 29.5 (Feb. 2019). ISSN: 1051-8223. DOI: 10.1109/TASC.2019.2897645.

[108] Ibrahim Kesgin et al. “High-temperature superconducting undulator magnets”. In: *Superconductor Science and Technology* 30.4 (Feb. 2017), 04LT01. ISSN: 0953-2048. DOI: 10.1088/1361-6668/AA5D48.

[109] Ryota Kinjo et al. “Demonstration of a high-field short-period undulator using bulk high-temperature superconductor”. In: *Applied Physics Express* 6.4 (Apr. 2013), p. 042701. ISSN: 18820778. DOI: 10.7567/APEX.6.042701. URL: https://iopscience.iop.org/article/10.7567/APEX.6.042701.

[110] John H. Durrell et al. “Bulk superconductors: a roadmap to applications”. In: *Superconductor Science and Technology* 31.10 (Sept. 2018), p. 103501. ISSN: 0953-2048. DOI: 10.1088/1361-6668/AAD7CE.

[111] P Emma et al. “A Plan for the Development of Superconducting Undulator Prototypes for LCLS-II and Future FELs”. In: *Proceedings of FEL2014, Basel, Switzerland*. 2014, pp. 649–653. ISBN: 9783954501335. URL: https://accelconf.web.cern.ch/FEL2014/papers/tha03.pdf.

[112] Tsumoru Shintake et al. “Development of Microwave Undulator”. In: *Japanese Journal of Applied Physics, Part 1: Regular Papers & Short Notes* 22.5 (May 1983), pp. 844–851. ISSN: 0021-4922. DOI: 10.1143/JJAP.22.844/XML.

[113] C. Chang et al. “Electron dynamics and transverse-kick elimination in a high-field short-period helical microwave undulator”. In: *Applied Physics Letters* 101.16 (Oct. 2012), p. 161102. ISSN: 00036951. URL: https://pubs.aip.org/aip/apl/article/101/16/161102/23635/Electron-dynamics-and-transverse-kick-elimination.

[114] Liang Zhang et al. “Systematic study of a corrugated waveguide as a microwave undulator”. In: *urn:issn:1600-5775* 26.1 (Jan. 2019), pp. 11–17. ISSN: 1600-5775. DOI: 10.1107/S1600577518014297. URL: https://journals.iucr.org/paper?xe5035%20https://journals.iucr.org/s/issues/2019/01/00/xe5035/.

[115] G. Stupakov et al. “Resistive wall wakefields of short bunches at cryogenic temperatures”. In: *Physical Review Special Topics - Accelerators and Beams* 18.3 (Mar. 2015), p. 034402. ISSN: 10984402. DOI: 10.1103/PHYSREVSTAB.18.034402. URL: https://journals.aps.org/prab/abstract/10.1103/PhysRevSTAB.18.034402.

[116] Oleg Chubar, Pascal Elleaume, and Joel Chavanne. “A three-dimensional magnetostatics computer code for insertion devices”. In: *urn:issn:0909-0495* 5.3 (May 1998), pp. 481–484. ISSN: 0909-0495. DOI: 10.1107/S0909049597013502.

[117] Christina Wulf et al. “Lessons Learned from a Life Cycle Sustainability Assessment of Rare Earth Permanent Magnets”. In: *Journal of Industrial Ecology* 21.6 (Dec. 2017), pp. 1578–1590. ISSN: 15309290. DOI: 10.1111/JIEC.12575.

[118] Xiaoyang Liang et al. “Analysis of the first magnetic results of the PSI APPLE X undulators in elliptical polarisation”. In: *Nuclear Instruments and Methods in Physics Research Section A: Accelerators, Spectrometers, Detectors and Associated Equipment* 987 (Jan. 2021), p. 164741. ISSN: 0168-9002. DOI: 10.1016/J.NIMA.2020.164741.

[119] Department for Energy Security and Net Zero. *Greenhouse gas reporting: conversion factors 2024*. Oct. 2024. URL: https://www.gov.uk/government/publications/greenhouse-gas-reporting-conversion-factors-2024.

DRAFT

7 X-ray Beamlines and Diagnostics

7.1 Summary

This chapter looks at the x-ray beamlines to transport the FEL beams to the user experiments and photon diagnostics for measuring the properties of each FEL pulse. There are three main parts to the chapter. The first part describes a model of the FEL source properties and then a discussion of typical x-ray beamline components and issues that arise in transporting FEL beams in general and UK XFEL beams in particular. The second part describes a couple of preliminary beamline concepts for UK XFEL. The final part is an overview of the more important photon diagnostics that have been developed for x-ray FELs and how well they meet the needs of UK XFEL. The chapter concludes with a short sections on sustainability and future development needs.

7.2 Introduction

X-ray beamlines and diagnostics fulfil two primary objectives:

- Transport the x-rays generated by the FEL source to the experiment whilst modifying or persevering the source properties as appropriate to meet the needs of the experiment. Properties that might be modified include beam size, pulse energy and spectral bandwidth. Properties that might need to be preserved could include pulse duration, transverse coherence, wavefront and polarisation. It is likely to be necessary to modify some properties for some experiments, while preserving them for others, for example, spectral bandwidth.
- Measure essential properties of the x-rays, providing information to users to facilitate data analysis and facility operators to optimally set up the source and the beamline to meet experimental requirements. Typical properties that need to be measured are pulse energy, photon energy and bandwidth, pulse length, polarisation, focal spot size, beam position and profile.

To design an effective beam transport that delivers the required photon properties to the experiment, it is necessary to have an understanding of the basic properties (size, divergence etc.) of the source. At the current stage of the UK XFEL project, there is insufficient modelling data to make an individual source model for each of the FELs proposed. Therefore, a preliminary and generalised model of the source has been developed to facilitate initial beamline concepts. This is described in Section 7.3.

An overview of the most common optical components for x-ray beamlines is described in Section 7.4, with particular reference to usage on FEL sources. A general discussion of the pros and cons of monochromators on FEL beamlines is given in Section 7.4.6. Another issue that will be important to UK XFEL is the effect of optics on femtosecond-duration pulses, and this is discussed in Section 7.5.

DRAFT

Ultimately, each beamline needs to deliver photons to the experiment with a particular set of properties. Within the CDOA phase of UK XFEL, only preliminary work on the optical layouts has been possible. Several beamlines have been looked at and two are described in detail in Section 7.6 as examples of the work undertaken.

Effective photon diagnostics that can measure the properties of every shot from the FEL are an essential part of the facility. They are critical to the proper interpretation of the experimental data. There are many diagnostics already available to determine the key photon properties and these are summarised in Section 7.7. Potential short-falls for UK XFEL are be discussed briefly.

7.3 Source model

It is not possible to design an x-ray beamline without knowledge of at least the size and divergence of the x-ray source. Therefore, a model of the spatial properties of the FEL source has been developed from steady-state simulation of FELs 1 to 6 at the proposed maximum and minimum operating photon energies. The simulations were performed with the Genesis1.3 code. The source is treated as fully transversely coherent and key source parameters (size of the beam waist, its longitudinal position and beam quality factor, M^2) are deduced by performing an M^2 analysis with the aid of the wavefront propagation software FOCUS [1]. The output field file for each FEL as produced in Genesis is propagated forward and backward in free space. The propagation backwards (i.e. to a position within the undulator) shows the beam compress towards the beam waist. This is the apparent beam waist (source) as would be seen by the x-ray transport after the undulator and may be different to the actual beam profile in the undulator, where the radiation can be considered as propagating in a medium with a refractive index due to the interaction of the radiation field with the electrons. However, as far as the x-ray transport is concerned, the waist deduced by the free space propagation is what matters and can be considered as the source for the transport. The assumption here is that the Genesis field file is the field at the end of the undulator (or an undulator module). This is not strictly true, but for the Genesis file to be representative of the actual FEL output, it must be from a position close to the end of the undulator so that any subsequent propagation within the undulator does not significantly modify the radiation field. By the same token therefore, it is acceptable to assume that free-space propagation of the Genesis field file to the end of the undulator and beyond is a valid representation of the field that will propagate down the x-ray transport.

The M2 analysis is made by propagating to a range of distances around the apparent waist and calculating the second moment of the beam profile at each position. M^2 theory states that the second moment of any transversely coherent beam follows a quadratic propagation law. The quadratic function contains the size and position of the beam waist and the beam M^2 value. The validity of using this method to extract the source properties from the FEL simulations is evidenced by the extremely good quadratic fits achieved; see, for example, Figure 7.1, which shows the analysis for FEL-2 at 5 keV. Rayleigh range and far-field divergence can then also be calculated. An additional propagation back to the waist position was also performed so the FWHM waist size could be calculated. The propagated beams were generally not Gaussian, and the FWHM is more useful when considering the optical magnifications needed to give target beam sizes at sample positions. To illustrate the results of the wavefront propagations, Figure 7.2 shows the results for FEL-2 at 5 keV and 20 keV. The beam at the waist position and at a distance of 100 m from the Genesis file, representing the far-field beam profile, are shown.

A universal model applicable to FELs 1 to 6 is achieved by fitting the average of the horizontal and vertical beam parameters with power laws, similar to the approach used by EuXFEL[2, 3].

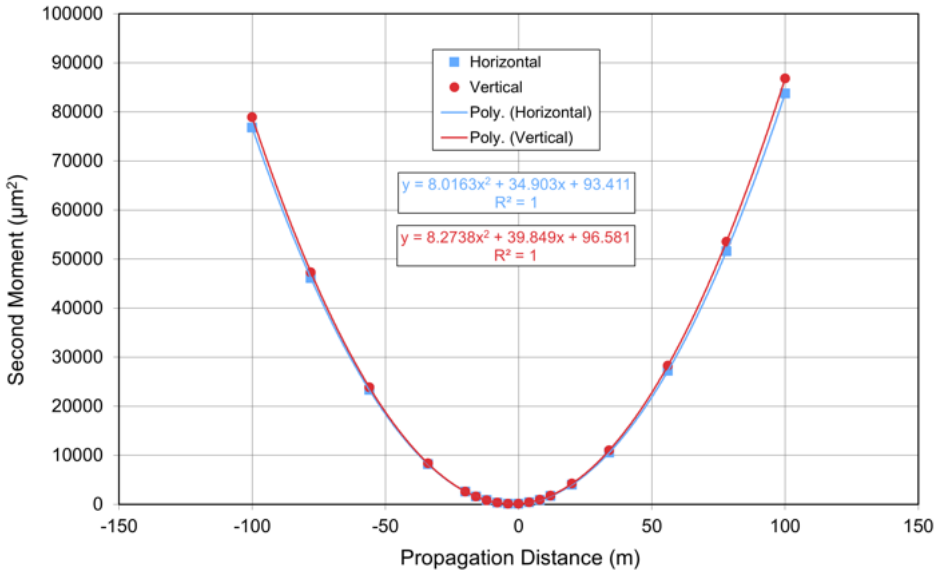

Figure 7.1: M^2 analysis for simulated output of FEL-2 at 5 keV. The abscissa is the propagation distance in metres from the Genesis output file. The ordinate is the second moment of the horizontal and vertical beam profile. Perfect quadratic fits are achieved, confirming the validity of the M^2 theory. The beam is actually close to Gaussian in this case with an average M^2 of 1.04.

Inevitably, the fit is not exact; see Figure 7.3, which shows the average simulation results and the fits to the far-field divergence, RMS and FWHM waist sizes and the M^2. It is not suggested that this model will be completely accurate. In fact, the simulations deviate significantly from it at low photon energies. Partly this is down to the beam deviating significantly from an ideal Gaussian mode at these energies (i.e. large M^2) and there is work to be done in improving the expected FEL performance. Nevertheless, the model serves to allow beamline concepts to be developed, which is critical to inform the overall facility layout. A more thorough study will be required for the technical design phase to create a more robust and FEL-specific model. Such a model is essential for detailed beamline design work to progress but will take a considerable amount of time to develop as simulations for each FEL in every FEL mode will be required.

The empirical source model for photon energy E_{ph} in keV is thus described by four power laws:

- RMS source divergence (μrad), taken as the far-field divergence

$$\sigma_{r'} = 7.0674\ E_{ph}^{-0.663}$$

- RMS source size (μm), taken as the beam waist RMS

$$\sigma_r = 22.357\ E_{ph}^{-0.446}$$

- Beam quality factor M^2

$$M^2 = 1.6015\ E_{ph}^{-0.11}$$

- FWHM source size (μm), taken as the beam waist FWHM

$$\Gamma_r = 44.827\ E_{ph}^{-0.397}$$

Two points to note are that the fitted power laws are consistent with $\sigma_r\sigma_{r'} = M^2\lambda/4\pi$ as expected from M^2 theory (the diffraction limit), and that the fitting becomes non-physical above 72.33 keV when $M^2 < 1$.

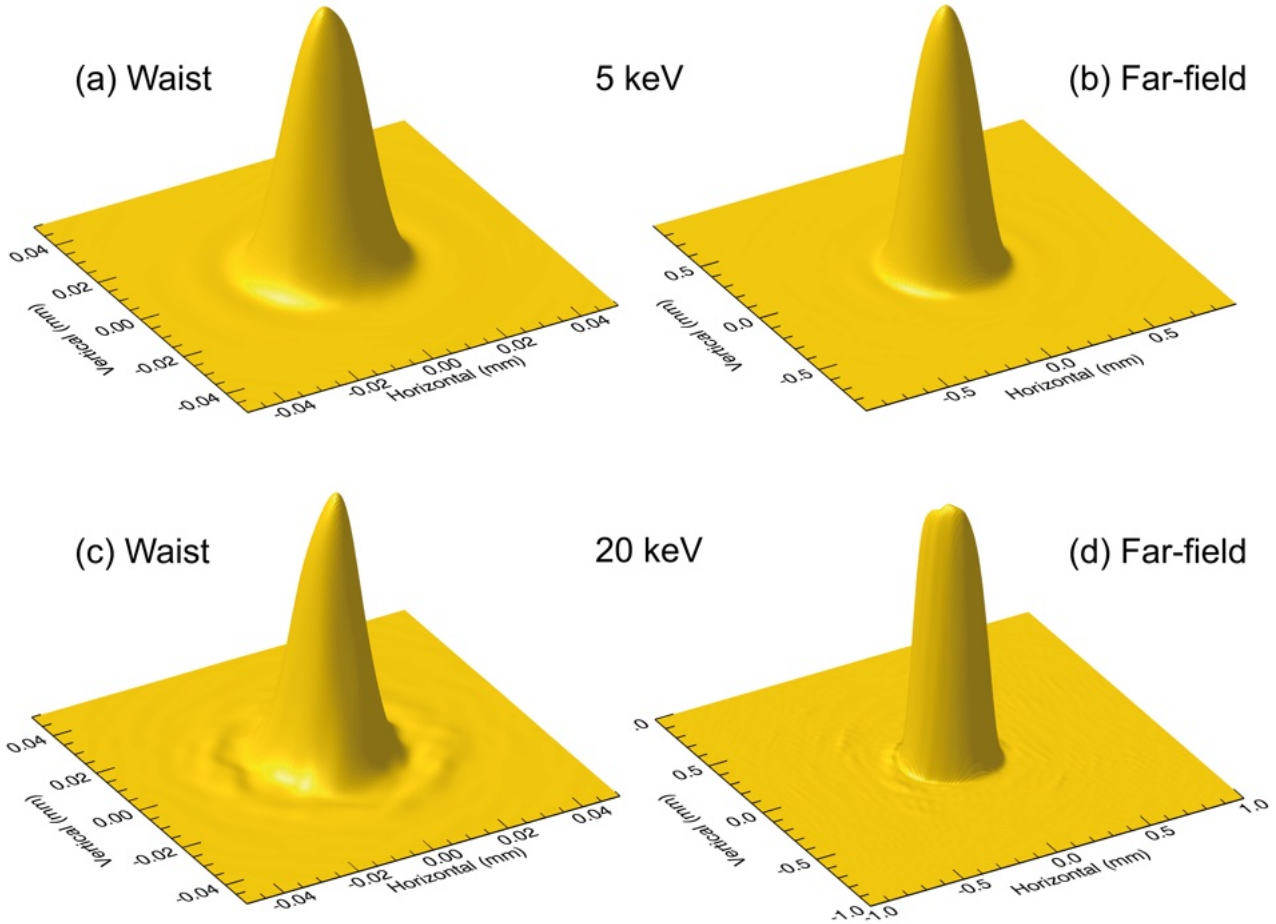

Figure 7.2: Results of the FOCUS wavefront propagations for FEL-2 Genesis simulations at 5 and 20 keV. The 3D plots show the spatial distribution of beam intensity on a linear scale. In (a) and (c) the propagation is back to the average longitudinal position of the horizontal and vertical waists, as determined from the M^2 analysis. We interpret this as the photon source for beamline modelling. In (b) and (d) the propagation is 100 m forward from the location of the Genesis file, representing the far-field beam profile. At 5 keV M^2 = 1.04 and the beam is close to Gaussian. At 20 keV, M^2 = 1.47 and the deviation from Gaussian is obvious.

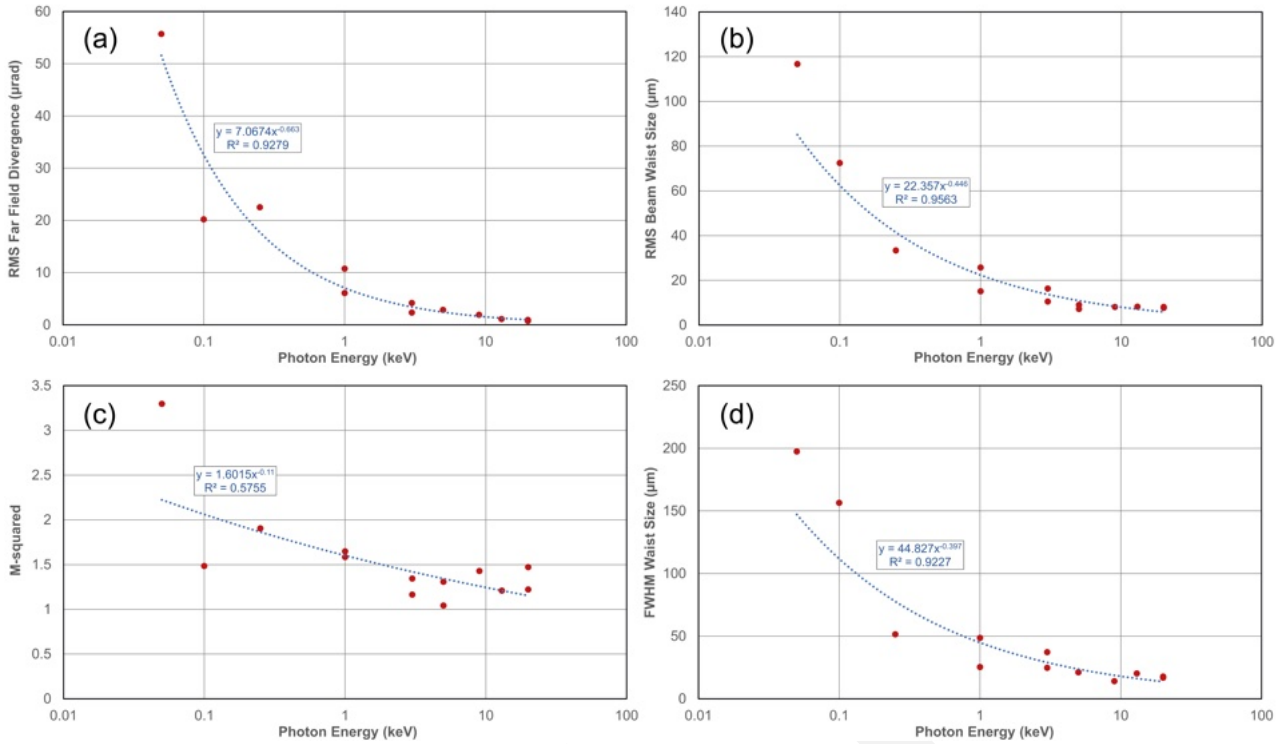

Figure 7.3: The average far-field divergence (a), RMS and FWHM waist sizes (b and d) and the beam quality factor (c), as derived from the M^2 analysis of all the FEL simulations, and the power law fits. When the model was developed it was planned for FEL-6 to operate down to 50 eV. Operation to this energy is now not being considered due to poor beam quality

7.4 Common beamline components

7.4.1 X-ray mirrors

The default optical element in any x-ray transport is the grazing-angle mirror. Mirror length, grazing angle and distance from the source determine the collection aperture of the mirror. As the FEL source has a high degree of transverse coherence, it is important to collect at least 5-sigma, and ideally 6-sigma, of the beam fan to prevent edge-diffraction distorting the beam special profile. Preserving the wavefront quality of the FEL beam requires mirrors with an extremely high surface quality. Typically, the height error from the target profile should not exceed a few nanometres peak-to-valley over the entire optical surface. The longest plane mirrors currently known to be available with this accuracy have a 0.9 m long optical surface [4]. When setting mirror collection apertures, this length has been used.

The limitations on manufacturing mirrors with this level of accuracy also limits the range of mirror shapes that can be employed in the transports for x-ray focusing. A focusing mirror at extreme grazing angles of incidence requires a sagittal radius of curvature in the millimetre to centimetre range but a tangential radius of curvature that is typically hundreds to thousands of metres. Although both are difficult to make accurately, the large tangential radius can be achieved very accurately through bending a precision flat mirror substrate. Aspheric shapes can also be achieved through bending. Strong sagittal curvatures must be polished into the substrates, which makes achieving the required form accuracy difficult. Thus, sagittally focussing elements are not often employed on FEL sources. However, improved manufacturing and metrology in the future could make them practical, especially at the lowest photon energies where larger grazing angles and hence shallower curvatures are possible.

An important consideration for the mirrors in any FEL beamline is the maximum pulse energy that can be allowed without risking ablation damage to the mirror. Under conditions of total external reflection, the penetration of the electromagnetic wave into the coating is very small (nanometers) and so the absorption volume is small despite the spatial dilution from the required grazing angle of incidence. One approach is to calculate the energy absorbed per atom in the mirror coating and limit this to below the threshold dose for material melting. The absorbed energy dose is straightforwardly calculated from the Fresnel equations, giving the reflectivity and hence absorption, and the complex refractive index of the coating material, giving the penetration depth. The challenge is knowing what the melting threshold is. Operational experience and damage measurements at current FEL sources have yielded a body of data that is not always consistent [5, 6, 7, 8, 9]. An important factor is the electron cooling that takes place within the coating. Electrons can transport the absorbed energy deeper into the coating, and so reduce the absorbed dose per atom; the effective absorption volume is substantially larger than the photon absorption volume. An additional complication is that coated mirrors can behave differently to bulk materials [10].

What is known is that boron carbide (B4C) is the most durable of the coatings currently employed and will therefore be used wherever possible. The main disadvantage of B4C is that the critical grazing angle is very small; therefore, it is not a practical coating for operation beyond c. 25 keV. Additionally, it cannot be used below c. 350 eV due to the carbon and boron K-edges (c. 284 and 188 eV respectively). To cover these energy ranges, nickel and platinum coatings are options. Amorphous carbon (a-C) can also be used at photon energies offset from the carbon K-edge. Amorphous carbon has a high single-shot damage threshold, but is known to suffer multi-shot damage, manifesting as graphitisation of the coating, at much lower fluence [11, 12]. With UK XFEL beamlines operating at a continuous 100 kHz (and possibly 1 MHz), multi-shot damage on all coatings could manifest far more quickly than at current x-ray FEL facilities (even EuXFEL). Caution is therefore needed when extrapolating single-shot damage thresholds to safe working fluences at high repetition rates.

Due to these uncertainties, the pulse energy that results in 0.01 eV absorbed per atom in the photon absorption volume of the coating will be presented in this report. This is expected to be a conservative value but can easily be scaled to whatever dose is deemed safe for a given coating. For example, in Chapter 8 of the LCLS-II Conceptual Design Report [13], an absorbed dose of 0.1 eV/atom in B4C is assumed to be safe for even multi-shot damage and thus the pulse energy numbers quoted later in this chapter for B4C mirrors can be multiplied by 10. Scaling factors for other coatings are not known but should be assumed to be smaller, especially for metallic coatings.

High repetition-rate CW operation also results in significant average power loading on the mirrors; 10 mJ at 100 kHz is 1 kW average power. Active cooling will be essential, but these power levels are not uncommon on synchrotron light sources, and so can be handled. However, it should be remembered that the first optics see a lot of power that is not related to the FEL pulse. Large amounts of spontaneous radiation, coherent synchrotron radiation and bremsstrahlung radiation are produced in the machine and co-propagate with the FEL radiation. This spans a much wider spectrum than the FEL pulse itself. A lot of this can be collimated out since the divergence is much larger than the FEL radiation, but the first optics will absorb a lot of the remainder. Thus, power levels on the first optics will need to be carefully calculated and mitigated in the technical design phase.

Even when the total power can be handled without the optics being damaged, it can still be difficult to control the thermally induced distortion of the mirrors to the level required to preserve the wavefront. It is the temperature gradient on the mirror that distorts its shape, and this is driven by the non-uniform power loading and so may remain even with active cooling. EuXFEL uses

a pair of mirrors in the beamline front end, with the second mirror actively bent to correct the thermally induced curvature of the first. LCLS have tested a scheme with active and distributed heating along the mirror surface to generate a region with a minimal temperature gradient [14], but this has not been tested sufficiently to be generally adopted. Thermal modelling will be required to determine the required mitigation measures, but full modelling of the all the output from the undulators (not just the FEL output) is required in the first instance.

7.4.2 Focusing optics - Compound refractive lenses

The main attraction of compound refractive lenses (CRLs) for focusing x-rays is that they are an axial optic and so can be added or removed from the beamline without changing the beam path. Thus, focusing can be changed more simply than with mirror based focusing systems. However, x-ray lenses are strongly chromatic, with the focal length changing as approximately $1/E^2$, where E is the photon energy. Thus, there is a significant challenge in making a CRL give achromatic focusing over the operating range of a given FEL. A standard installation will employ multiple CRLs in a 'transfocator' that can also be translated along the beam path. To focus a particular wavelength, an appropriate combination of CRLs in the transfocator is used that gives the closest match to the required focal length, and translation of the transfocator is used to shift the focus to the required position. The optical magnification does necessarily change, but this effect will be small compared with the natural variation in source size with photon energy. The operating range of the FEL is thus divided into sub-ranges and photon energy scanning requires either adjustment of transfocator translation or accepting some defocus and hence beam enlargement.

CRLs are limited to focusing only hard x-rays due to material absorption. There is no definite cut-off, so a low energy limit of 5 keV has been assumed in this study. This should give reasonable transmission with beryllium, though this will obviously depend on the number and radius of curvature of the individual elements in the CRL stack. In general, CRLs at 5 keV will have few elements with larger radii of curvature. At very high photon energies, more dense materials may be needed (e.g. diamond, silicon or even aluminium) to give stronger refractive power and prevent the number of elements required becoming excessive. If the number of lenses in the stack is too large, then the cumulative losses from both absorption and misalignment of the elements and the total wavefront distortion from the imperfections in the lenses will become unacceptable.

7.4.3 Focusing optics – Kirkpatrick-Baez mirror systems

The Kirkpatrick-Baez system is the most common mirror system for strong focussing of x-ray beams. Using separate, tangentially focussing mirrors to focus in the horizontal and vertical overcomes the limitations in manufacturing mirrors with both sagittal and tangential curvatures. It is also common to have the mirrors in bending mechanisms, so the shape and hence focus position can be adjusted. Benders that achieve highly accurate elliptical profiles are common and give improved quality of focus at high demagnifications compared to cylindrical mirrors. Reflectivity losses of a Kirkpatrick-Baez are twice that of a single mirror. Apart from that, the most significant disadvantage of the KB is that there is a net vertical deflection of the beam, which requires a compensating vertical deflection somewhere in the beamline to give a horizontal beam at the experiment. This may require an additional mirror with its associated loss of beam intensity and quality. Additionally, horizontal and vertical magnifications are different. It is also hard to obtain extremely short working distances because of the length of the mirrors. Very high demagnifications at hard x-rays also require the mirrors to be multilayer coated, since the local angle of incidence

at the most curved end of the mirror will exceed the critical angle of a single-layer coating. This makes the hard x-ray Kirkpatrick-Baez work at a single wavelength only.

For focussing under 5 keV, the Kirkpatrick-Baez mirror is the most widely used technology on FELs, and will be the default option for UK XFEL. For harder x-rays, the choice between Kirkpatrick-Baez and CRL will be made on a case-by-case basis. For example, a Kirkpatrick-Baez will be used where the chromaticism of a CRL is problematic or when higher demagnifications are required, whilst a CRL will be used when the axial optic is advantageous.

Although the Kirkpatrick-Baez with bendable mirrors allows the focal length to be adjusted easily, this only serves to move the beam focus closer to or further away from the mirrors. This is an acceptable method to enlarge the beam at the interaction point for many experiments; however, to produce the highest quality photon beams variable magnification should be employed. Achieving a variable magnification at a fixed position in the beamline would require translating the Kirkpatrick-Baez system along the beam axis. Not only would this involve moving a large and complex mechanical system in a vacuum tank, it would also cause the angle of incidence on the mirror and the beam angle to the interaction point to both change.

A true vari-focal (a.k.a. zoom) system can be constructed with two Kirkpatrick-Baez systems in series. Essentially, the second Kirkpatrick-Baez relays the image formed by the first to the interaction point, and overall magnification can be changed without moving the beam position or angle at the interaction point. This system is proposed for the ATOMIC beamline on the APS upgrade, operating from 5.3 to 30 keV and delivering focal spot sizes from 50 nm to 2 μm [15]. The Zoom-KB can also give equal horizontal and vertical magnifications and can be arranged to give no net angular change in the beam direction, which can be exploited to give a horizontal beam at the experiment. This is at the expense reductions in beam quality and intensity due to the additional reflections.

The Zoom-KB is significantly larger and more complex than a normal Kirkpatrick-Baez. The space between the Kirkpatrick-Baez systems will be significant; in the APS system it is 10 m whilst for UK XFEL beamlines it is likely to be $\sim$30 m or more. Achieving optimal bend on all four mirrors to deliver a high-quality final focus requires in-situ, at-wavelength metrology. Application of AI technology is a potential solution to optimising the mirror bends in a time-efficient manner [16]. One issue that cannot be easily overcome is the consequence of moving the first focus very close to the second Kirkpatrick-Baez when working at low demagnifications. The footprint on the mirrors of the second Kirkpatrick-Baez will become very small and this will greatly reduce the maximum pulse energy that can be safely handled. The range of possible demagnifications or useable pulse energies will therefore need to restricted.

For extreme demagnifications, e.g. to achieve few-nm foci, the traditional Kirkpatrick-Baez has limitations. It is very far from the aplanatic condition required for focussing that is free from coma and spherical aberration. This also makes the output beam position sensitive to the input beam pointing jitter. For extreme focussing, the AKB or 'advanced-KB' has been developed [17, 18, 19, 20]. The AKB can be either a Wolter Type I arrangement (two concave aspheric surfaces) or a Wolter Type III arrangement (convex followed by concave aspheric surfaces), with four mirrors required in total to focus in the horizontal and vertical. Manufacturing and alignment of the mirrors is very challenging. For example, in [20] the mirrors had to be tested at-wavelength with the required multilayer coating applied. Once shape errors had been deduced from the at-wavelength metrology, the coatings had to be stripped, the mirror substrates deterministically refinished, and then recoated with multilayers. This process was only possible with extensive in-house skills and close cooperation with manufacturers, so these systems cannot currently be purchased as a turn-key system.

7.4.4 Focussing optics - other options

Fresnel zone plates (FZPs) are another example of an axial focusing optic that is suitable for x-ray wavelengths. FZPs are essentially transmission diffraction gratings which can focus in two dimensions. They consist of concentric rings of alternating materials which decrease in width with increasing radius. They are most suitable in the soft x-ray region, however, examples of their use up to 50 keV have been experimentally shown with an efficiency of 35% [21].

The focusing properties of the FZP are dictated by the zone plate structure: Δr_N the outermost zone width, and r_N the radius of the outermost zone, and the focal length also depends on the wavelength as:

$$f = \frac{2r_N \Delta r_N}{\lambda}$$

Even though FZPs are less chromatic than CRLs [22], they are less practical for use on XFELs. Stacking of FZPs cannot be used to focus different wavelengths to the same position, only alter the efficiency. FZPs are difficult to manufacture, particularly for hard x-rays where thick structures are required. Multilayer Laue lenses (MLLs), which are linear one-dimensional zone plates, are an alternative to this. These devices often have small aperture sizes, less than 100 μm is common. Typically, MLLs can be produced at much higher quality and with much larger thicknesses than FZPs. This has allowed for an efficiency of 68% at 16.3 keV to be achieved [23]. Either two MLLs are required for two-dimensional focusing, or the MLL is bent to provide focusing in the other direction.

Both MLLs and FZPs are harder to cool than an x-ray mirror because of their complex structure. LCLS found that gold FZPs melted at doses 25% of the expected value [24]. Alternative materials such as iridium filled diamond structures are currently being explored as an alternative that is more appropriate for very high intensity next-generation XFELs. For these reasons, MLLs and FZPs are more suited to specific use cases, for example integration into experimental set-ups, and so have not been considered in the more generalised beamline concepts developed for the UK XFEL CDOA.

7.4.5 Collimating optics

Sometimes it is convenient to collimate the x-ray beam at an early point in the beamline. This allows downstream mirrors to be positioned more freely and still collect all the FEL radiation and can maximise the pulse energy handling of more of the mirrors.

Collimation with a CRL is convenient as there is no net beam deflection, and the collimation in horizontal and vertical planes is achieved simultaneously. Because a CRL is chromatic, several CRLs are required in a transfocator, each covering different parts of the FEL tuning range. Collimation is still only approximate over the FEL range, but relatively few CRLs are needed for the collimation to be effective, e.g. giving at least a factor of 10 reduction in beam divergence. Placing a CRL before the first mirror also adds a useful degree of freedom to the optical design. However, it then sees more beam power from e.g. spontaneous radiation and is at higher risk of melting.

Collimation with mirrors is achromatic but, if only tangentially curved surfaces are used, results in a net vertical deflection. This would need to be corrected with another mirror if a horizontal beam is required at the experiment. Collimation with a sagittally curved mirror could eliminate the vertical deflection but would require improvements in manufacturing capability to make such optics with the precision required to preserve the wavefront.

Rather than collimating and focussing, creating intermediate foci that are relay imaged with downstream focussing elements has the benefit of reducing the impact of beam pointing jitter on the final beam position. However, intermediate foci present a severe hazard to the machine due to the high ablation potential of the beam and so must be carefully planned.

7.4.6 Monochromators

Selecting and varying a specific wavelength and spectral bandwidth from a broad-band source is a basic need for many x-ray experiments. However, a source that generates a truly transform-limited pulse with tunable pulse length would, by definition, also provide a tunable and well-defined pulse bandwidth and therefore should not require a monochromator. The exception would be when the spectral bandwidth of the source needs to be reduced to less than that given by the longest achievable pulse length, for example to support studies at higher spectral resolution. In such a case, it may be still be important that the pulse after the monochromator should remain as close to transform limited as possible, i.e. that the increase in pulse length should be limited to that caused by the reduction in bandwidth. Preserving the pulse duration would be a key difference between monochromators on FEL and SR sources.

The requirement to improve the spectral resolving power will vary with photon energy. For a pulse with Gaussian temporal profile, the FWHM bandwidth and FWHM duration are related by $\Delta E \Delta \tau$ = 1.825 eV.fs. Thus, a 100 fs pulse has a bandwidth of 18.25 meV and a resolving power E/ΔE of circa 5000 at 100 eV but 50000 at 1000 eV. The latter is already a very high resolving power, and thus it seems that the main need for a monochromator would only be at the lowest photon energies covered by FEL-6 and FEL-5.

However, there is still a widespread desire within some user communities to have monochromators. Justifications for a monochromator include:

- Improving spectral resolution as previously discussed, especially if the longer pulses cannot be generated at close to the transform limit and hence with the predicted narrow bandwidth.
- For SASE operation where there will be many random longitudinal modes in the output spectrum and the jitter in the average wavelength can be significant for some experiments. The monochromator defines a constant central wavelength to the pulse at the experiment but at the expense of increased pulse energy jitter. SASE is an operational mode for UK XFEL so this is still relevant.
- In single-spike modes, the actual spectrum of the pulse is unlikely to be Gaussian and could also have a pedestal outside the main pulse bandwidth. The non-gaussian shape can change shot-by-shot, affecting both the bandwidth and average wavelength. Significant energy in a pedestal could further degrade the photon energy resolution for spectroscopies or the temporal resolution in pump-probe studies.
- The monochromator can suppress higher harmonic radiation
- It is easier to tune wavelength with a monochromator than by tuning the source. However, this advantage is not realised with a pseudo-monochromatic source since source and monochromator must be tuned together.

The downsides of using a monochromator include:

- Additional optics in the beamline, increasing cost and degrading beam quality, potentially by a significant margin in both cases.

Crystal	Photon Energy (eV)	Darwin Width (eV)	Resolving Power
Si(111)	5781	0.785	7364
Si(220)	9440	0.557	16947
Si(311)	11069	0.313	35364
C*(111)	8801	0.508	17325
C*(220)	14372	0.284	50607
C*(311)	16853	0.153	110150

Table 7.1: The Darwin widths for S-reflection from perfect silicon (Si) and diamond (C*) crystals at 20° Bragg angle, and the equivalent resolving power. Resolving power is roughly constant with photon energy for a given crystal and cut.

- Grating monochromators are an integrated part of the beamline imaging. For example, the exit slit is imaged to the experiment and so the final image size in the dispersive direction is defined by the slit setting.
- Grating monochromators are generally inefficient in the soft x-ray range ($<$ 20%), and very inefficient above 1000 eV (few %).
- Grating monochromators add pulse front tilt (PFT) to the pulse, increasing the pulse duration beyond the transform limit. This can be mitigated by some designs, but only eliminated by using double-grating schemes that have potentially very low efficiency ($<$ 1%).
- Crystal monochromators using Bragg reflections from perfect crystals have a bandpass determined by the Darwin width of the crystal cut and the beam divergence. The maximum possible resolving power set by the Darwin width is approximately constant with photon energy for a given crystal and cut. Table 7.1 gives the resolving power at 20° Bragg angle based on the Darwin widths calculated for diamond and silicon crystals in various cuts. This shows that an arbitrary choice of resolving power is not possible. High resolving power requires highly perfect crystals operating on high-order cuts and a beam divergence less than the Darwin width.
- Practical implementation of a crystal monochromator requires two crystals reflections (e.g. double crystal or channel cut) to give an output beam parallel to the input beam. High order reflections necessary for high resolving power need the crystals maintained to very high parallelism (sub-μrad). This demands very high mechanical tolerances when scanning in double-crystal designs, whilst differential heating between the two crystal faces in a channel-cut will badly affect the output.
- Crystal monochromators do not preserve any polarisation other than S-polarisation. They are linear polarisers at 45° Bragg angle and partially depolarise circularly polarised light at other angles.
- Monochromators may limit maximum pulse energies since they operate with higher fluence on the optics than fixed angle mirrors elsewhere in the beamline.
- Monochromators are difficult to implement in the ‘tender x-ray’ range, roughly 1 to 5 keV. High efficiency in this range will require multi-layer coated gratings. These are relatively new and the ability to manufacture them on large substrates is not demonstrated. Organic crystals such as potassium acid phthalate could also be used, however damage threshold is a concern [25].

It is evident that the need for a monochromator within the photon beamline transport is strongly dependent on the spectral quality of the FEL output, and the ability to easily tune the FEL pulse

length whilst achieving a pulse that is close to transform limited. Since transform-limited operation is a key goal of UK XFEL, it is valid to assume that monochromators will not be required for at least some, and ideally most, beamlines.

When a beamline does include a monochromator, the way in which it interacts with the source must be considered. With a SASE source, where the average overall spectrum is quite broad, the probability of some part of the source spectrum for any given shot matching the monochromator pass band is high. Thus, the monochromator can usefully reduce both the jitter in the average wavelength and the overall bandwidth at the experiment, but at the expense of increased jitter in the pulse energy, see Figure 7.4(a). Too much jitter will cause a large proportion of shots to contain almost no photons because no longitudinal mode in the source spectrum aligns with the monochromator pass band.

However, if the FEL is operating with the output reduced to a single longitudinal mode, then the output of the monochromator will be determined by the jitter of the central wavelength of the FEL pulse. When the FEL is externally seeded by an optical laser, the central wavelength will be very stable and the monochromator will have little effect on the pulse unless its bandpass is much smaller than the pulse bandwidth. For a FEL seeded in this manner, the monochromator serves little purpose, see Figure 7.4(b). However, other seeding schemes and enhanced SASE modes are likely to result in significant jitter in the central wavelength (driven by jitter in the electron bunch energy). The pulse is also likely to have a spectral pedestal that may be problematic for some experiments. The use of a monochromator may be considered to remove such a pedestal, but the central wavelength jitter will greatly affect the transmitted spectrum and hence pulse duration, see Figure 7.4(c). Some shots may have almost no photons. To successfully operate in this manner, the spectral stability of the source must be a small fraction of the monochromator pass band, and this could be hard to achieve. If the required stability cannot be achieved, the monochromator is likely to do more harm than good.

In a case where a monochromator is required to improve the spectral resolving power, avoiding significant shot-to-shot pulse energy jitter may require the FEL to generate pulses short enough to have a spectrum that significantly over-fills the monochromator pass band. The source then approximates a continuum as far as the monochromator is concerned, and shot-to-shot fluctuations in central wavelength are eliminated and fluctuations in pulse energy much reduced. The downside will be that only a fraction of the pulse bandwidth and hence pulse energy will be transmitted and the rest will be absorbed at the exit slit of a grating monochromator or within the Bragg crystal.

Since a double-crystal mono can be added and bypassed with only a small change in output beam height, it is easy to make provision for them in hard x-ray beamlines. The main consideration would be the need for collimating the beam when working with crystals that have very narrow Darwin widths. On the other hand, grating monochromators for soft and tender x-rays need to be planned as part of the overall beamline layout. The strategy followed at this stage of the project is thus to include a grating monochromator in FEL-6 and FEL-5 beamlines since this is useful to elucidate the constraints and compromises, but to incorporate some form of by-pass in the design that doesn't significantly change the overall imaging of the beamline. An example is described in Section 7.6.1.3.

7.4.7 Beam attenuators

A controllable means of adjusting the pulse energy in the x-ray beam without changing any other properties of the beam is required. Such devices may also be used to suppress unwanted radiation, such as harmonics, in the x-ray beam if they have absorption edges at appropriate

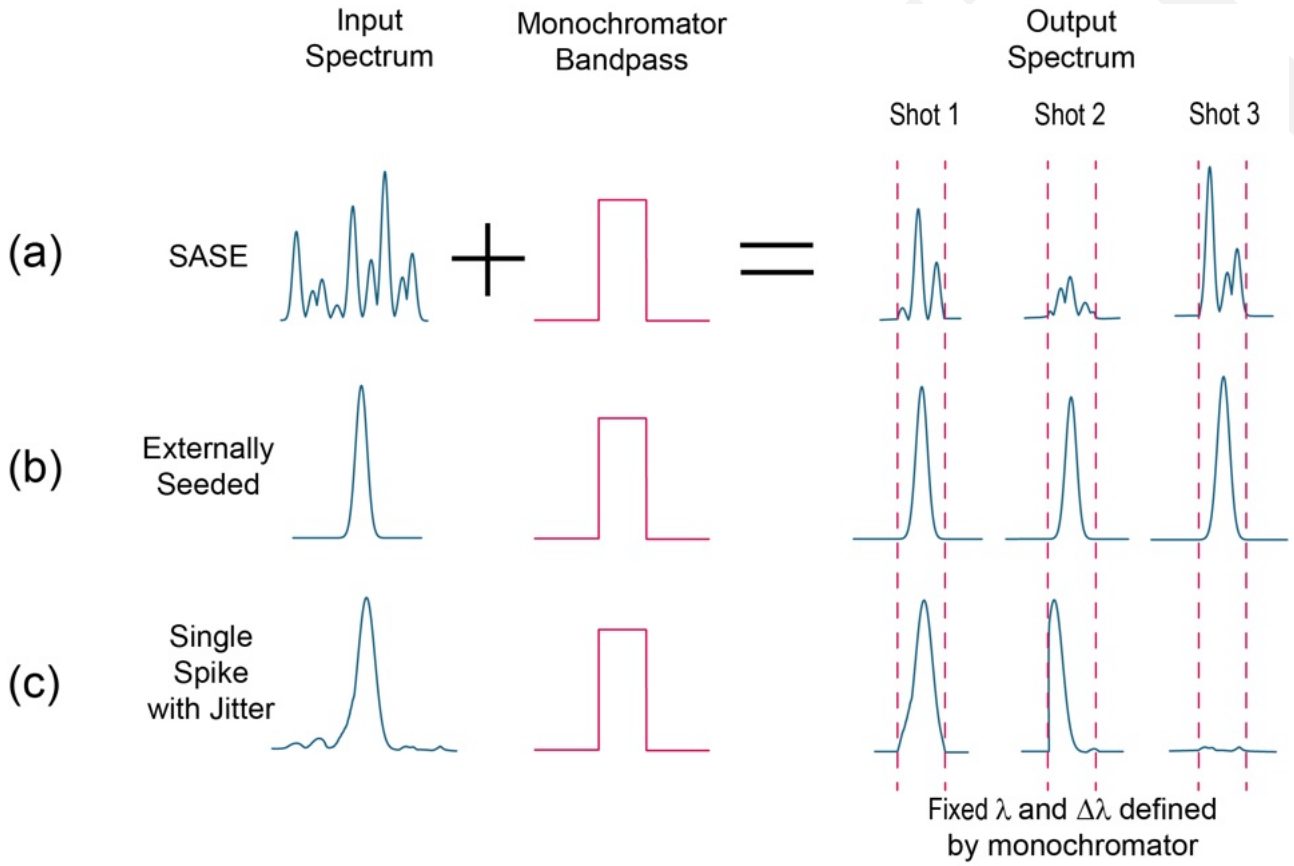

Figure 7.4: How a monochromator can interact with a FEL source. In (a) the source operates in SASE mode; the monochromator will define a narrower spectral range and stabilise the central wavelength at the expense of increased jitter in the pulse energy. In (b) with an externally seeded source, the FEL pulse is stable in both central wavelength and pulse width and the monochromator has no worthwhile effect. In (c) with a single-spike mode, there is jitter in the central wavelength and unwanted spectral contamination. However, the jitter prevents the monochromator from removing the contamination without also modifying the core pulse.

energies. The accuracy of control need be no better than the natural shot-to-shot variation in the FEL output. Beam attenuation is also required during beamline set-up and commissioning to prevent the risk of damage to optics, detectors and other beamline components. Adjustment of pulse energy by altering the lasing in the FEL is possible but risks changing the spatial and temporal properties of the beam and could also affect the source stability (temporal and positional). It is desirable therefore to operate the source at a fixed output and attenuate the beam in the beamline when lower pulse energy is required.

7.4.7.1 Gas attenuators

In the soft x-ray region the standard method for controllable beam attenuation is the gas attenuator. Such devices are used at FERMI [26], FLASH [27], EuXFEL [28], SwissFEL [29], LCLS [30], SACLA [31] and PAL-XFEL [32]. The gas attenuator is essentially a long gas cell through which the x-ray beam passes. The cell is filled with an inert gas such as nitrogen or a noble gas at a controlled pressure. Absorption of the x-rays is nominally determined by the Beer-Lambert Law and thus depends on the gas pressure, total gas column length and the gas used. Since the absorption coefficient of a gas is a function of photon energy, achieving a constant attenuation ratio over the operating range of a FEL requires the gas pressure to be adjusted as the wavelength changes. Different gases are required to avoid large changes in attenuation over the absorption edges. Achievable attenuation ratios are lower at higher photon energies due to weaker absorption, but an attenuation ratio of at least 1000 over the full range of FEL-6 (100 to 1000 eV), FEL-5 (250 to 3000 eV) and FEL-4 (1 to 5 keV) is realistic. Exact performance can only be determined when the available space in the beamline is known and hence the length of the gas cell can been determined; this will be part of the technical design phase.

The gas cell must be coupled to the beamline vacuum without windows and a significant part of the installed length of the gas attenuator is taken up with the differential pumping at each end. For example, the gas attenuator at EuXFEL [28] has a 15 m gas cell length and 22 m total length. It operates with a maximum pressure of 35 mbar of nitrogen. The design used on SwissFEL [29] incorporates a novel manifold that allows the length of the differential pumping section to be reduced, giving a 4 m gas cell in a total attenuator length of 8.8 m. A sophisticated and fully remotely controlled gas delivery system is required that can maintain a very tight control on the pressure in the cell and switch between different gases. Additionally, the use of noble gases like krypton and xenon mandates a gas recovery system due to their extremely high cost.

The operation of gas attenuators with a high repetition rate FEL source raises additional concerns. Studies performed by LCLS [30, 33] point to non-linearity in the response of the gas cell. The basis of the Beer-Lambert law is the assumption of a homogeneous medium through which the x-rays propagate. This breaks down when successive pulses arrive with intervals less than $\sim$millisecond. There is insufficient time for the gas to recover from the absorption of one pulse before the next arrives, so the following pulse does not experience the same gas density and hence absorption. For pulses of equal energy at high repetition rate a steady state will be established with a region of lower gas density where the beam passes (the so-called filament). Thus, the attenuation will be less than expected based on the measured gas pressure in the bulk of the cell. In principle, this can be corrected for by careful characterisation of the actual attenuation under varying beam conditions. However, when there is variation in the shot-to-shot pulse energy, the attenuation of subsequent pulses will vary unpredictably, potentially leading to amplification of the original pulse energy fluctuation [33, 34]. Converting the gas to a plasma has been suggested as a way of overcoming this issue [35]. It is also suggested that these effects will occur in gas-based photon

diagnostics, e.g. XGMDs (Section 7.7.1), which would lead to an increased uncertainty in the shot-by-shot pulse energy measurement.

7.4.7.2 Solid attenuators

Attenuating hard x-rays requires a solid attenuator since gas absorption is insufficient unless heavy gases at high pressures are used. Gas leakage into the rest of the accelerator couldn't be adequately controlled without windows on the cell. Although solid windows on the gas cell to contain the higher gas pressure are more practical, high pressure gases used to give strong absorption would suffer significant density variation. This would result in significant small angle scattering of the beam, which is unacceptable.

For transmission through a solid material, the primary concerns are damage to the attenuator material from ablation and the total absorbed power, and the impact on the transmitted wavefront. It is recommended to make the absorbers larger than the minimum size and build in the ability to move them around in the beam to find the region of minimum wavefront distortion and to move away from any areas that get damaged. Absorbed power gives a thermal distribution over the beam footprint. In extremis, the local temperature could rise sufficiently to result in melting. Even below the onset of melting, the temperature gradient causes a distortion of the surface and induces local stress. If stress exceeds the yield strength, the foil will be permanently damaged (e.g. cracked). Even if not permanently damaged, the distortion to the surface can affect the wavefront.

To minimise these factors, the attenuator material should ideally have a high melting point coupled with a high thermal conductivity and a low thermal expansion coefficient. The material should also be homogeneous to avoid problems with the transversely coherent beam, e.g. generation of speckle in the beam. Achieving relatively low attenuation requires thin sheets of material that need to be flat and uniform to preserve the wavefront. The thin foils also need to be robust enough to be held securely and have good thermal contact with the mounts to facilitate direct cooling.

The most commonly used materials are diamond, silicon and B4C. Typical foil thicknesses range from 100 μm to several millimetres. B4C and diamond have similar attenuation properties and are ineffective for high attenuation ratios above c. 10 keV, where silicon must be used. Diamond, though harder to manufacture and finish, should be better than B4C. It has a higher melting point, higher thermal conductivity and lower thermal expansion. It should also be optically superior since it can be made as single crystal. B4C is only available as a sintered material and inhomogeneity could lead to speckle in the beam. Silicon has poorer thermal properties than diamond and it may be necessary to pre-absorb some of the beam with diamond as described in [13].

Since the attenuator is, by design, absorbing almost the entire beam in some operating modes, the impact of absorbing large amounts of beam power should be calculated. This is particularly important for UK XFEL where several hundred watts of total beam power can be expected on some FELs, and it is prudent to assume $\sim$1 kW handling will be required. Each attenuator foil will need to be effectively cooled. Examples of current water cooled attenuators include the unit made by JJ X-Ray for the MID instrument at EuXFEL [36]. This has only 20 W cooling capacity. The attenuator described for SHINE [37] was modelled for only 10 W absorbed power (i.e. 1 mJ at 10 kHz). These designs are clearly inadequate for UK XFEL. However, the JJ X-Ray attenuator made for LCLS-II can handle 200 W [38].

A simple way to further improve total power handling is to use multiple attenuator units in series, with the absorption of the upstream ones set to not exceed the power handling. To achieve 1 kW handling would require five 200 W units. This will, however, take up more space and the

cumulative impact of multiple foils on the beam wavefront would need to be assessed. Other ways to achieve the higher power handling will become part of the technical design phase.

Solid attenuators are also used for very soft x-ray FEL radiation, for example on FERMI [39], FLASH **??**, and SACLA [31]. In these cases, this is in addition to gas attenuators. The foils (made from elements such as aluminium, palladium, silicon, tin, titanium or zirconium) need to be typically sub-micron in thickness and are inevitably neither flat nor smooth. They therefore have the potential to degrade the beam wavefront quality, most likely through the introduction of speckle.

7.5 Pulse length effects

With a source targeted at producing pulses of femtosecond or even sub-femtosecond duration, the effect of the optical transport on the pulse length must be considered. Dispersion within the optical elements means that the different spectral components within the pulse experience different amplitude and phase responses, so the overall pulse length and shape is modified. Additionally, geometric aberrations from the optical elements impose path length differences spatially within the pulse. Any deviation from perfect point-to-point imaging at the image plane of the transport corresponds to a different path length to the image plane for different parts of the pulse and hence a pulse lengthening.

Geometric path differences caused by aberrations can be assessed through ray-tracing. Careful optical design can all-but eliminate geometric aberrations in the limit of perfect optical components. Slope errors of the optical surfaces become the limiting factor for image quality and hence also for the shortest pulses that can be transported unaffected. The drive to preserve wavefront through the transport would ensure pulse lengths are preserved for pulses down to the order of the radiation period, considerably shorter than any pulse lengths the FEL can generate.

When multilayers are used on mirrors, there are two mechanisms for potential pulse stretch. These are dispersion effects in the multilayer (q.v.), and aberrations that result from local angle and penetration differences in the multilayer on the curved surface [40].

7.5.0.1 Dispersion effects from x-ray mirrors

It is not expected that the dispersion in single-coated mirrors will adversely affect the pulse length even for femtosecond duration pulses. However, the effect should be checked whenever the pulse bandwidth is a large fraction of the central photon energy. Particular care should be taken when the coating has absorption edges near the central photon energy. The operating range of any mirror coating will avoid strong edges because of the reduction in the reflectivity, but sub-femtosecond duration pulses could result in part of the pulse bandwidth spanning the edges. Additionally, high-lying orbitals will only weakly affect reflectivity and are not normally considered a problem, but may impact the pulse duration. For example, the N-edges in platinum span the region 300 to 700 eV and therefore will give varying amounts of anomalous dispersion through this range. Platinum has good reflectivity in this region, but ultra-short pulses could be affected.

7.5.0.2 Dispersion effects from multilayer coatings

Multilayer coated optics will have two main applications in UK XFEL beamlines. Firstly, when mirrors are used at very high demagnifications in the hard x-ray region, the local curvature of the mirror can exceed the critical angle of a single-layer coating and a multilayer is essential to restore reflectivity. Secondly, if diffraction gratings are used in the region ∼2-5 keV), the diffraction efficiency becomes very low but can be hugely improved by coating the grating with a multilayer rather than single-layer metal coating

Multilayers work through constructive and destructive interference in the reflected wave. The layers chosen can be tailored to the desired dispersive properties. Ultrashort pulses have large bandwidths, leading to differences in the amplitude and phase response for wavelengths within the bandwidth. This has the potential to cause pulse stretching. A code using the tool presented in [41] was written to calculate any stretching effect. The initial pulse spectrum is multiplied by the complex reflection coefficients of the multilayer and then Fourier-transformed back to the time domain to reveal and pulse stretch.

In the tender x-ray region, efficiencies peaking at 60% at 3 keV have been reported for a blazed multilayer grating [42]. To understand the magnitude of the temporal stretching effects, the grating presented in [43] has been assessed. This multilayer was used at an angle of incidence of 2.2°, has 35 layers, with 5 nm line spacing and Cr/C ratio of 0.4. This multilayer showed minimal temporal stretch, less than a 6% increase in pulse length for a 100 asec, 2.7 keV pulse. The limited stretching is likely due the bulk of the reflection occurring in the first few layers, leading to minimal path length differences.

At harder x-rays, multilayers may be used to increase the numerical aperture of mirrors. To achieve the 7 nm focusing at 9.1 keV reported in [44], one of the multilayers used was a 30-period, ∼6 nm line spacing, Pt/C multilayer with a thickness ratio of 0.5, operating at 14.1 mrad grazing angle of incidence. This multilayer structure also did not cause any significant pulse stretching effects in simulation because the very small angle of incidence reduces the penetration of the x-ray into the deeper layers. A stretch of less than 0.05% was found for 100 asec pulses at 9.1 keV.

Based on these examples, it is anticipated that the pulse length stretching from multilayer structures will not, in general, be a significant issue for pulses down to at least 100 asec duration. However, whenever the use of multilayers is being considered, the pulse stretching effects should be assessed.

7.5.0.3 Dispersion effects from CRLs

CRLs are transmissive optics and therefore have dispersion. Dispersion affects a short pulse through two mechanisms, namely propagation time difference (PTD) and group velocity dispersion (GVD) [45]. PTD is the result of the difference between the phase and group velocities in the medium. It depends on the first differential of the refractive index with wavelength and is related to chromatic aberration. GVD is where the group velocity depends on wavelength, this depends on the second differential of the refractive index with wavelength. GVD in x-ray lenses is negligible (attosecond level) [46] and can be ignored.

PTD causes the phase and pulse fronts to separate after the lens. Because there is a radial variation in the material thickness in the lens, different parts of the beam travel through different thicknesses of material. In a chromatic lens, the separation of phase and pulse fronts is not constant over the beam section (but is constant along any beam ray). This means that when the

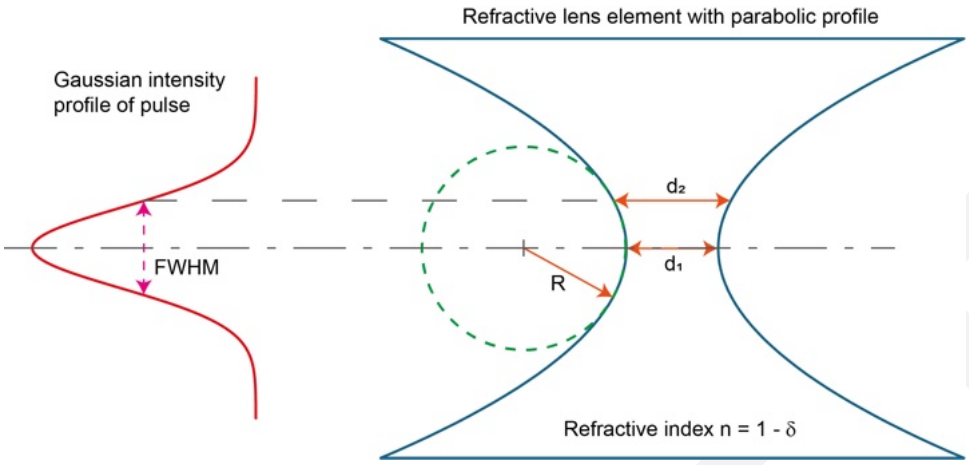

Figure 7.5: Simple model for calculating the thickness of a CRL that contributes to propagation time difference. R is the central radius of curvature of the lens

phase front is flat, the pulse front is still curved. The beam waist is by definition the position of flat phase, so the pulse front is curved at the waist and this amounts to a pulse stretch, though the effect is spatio-temporal.

The PTD as the wave propagates through a medium of refractive index n and thickness l is [45]

$$\Delta\tau = \frac{l}{c}(-\lambda\frac{dn}{d\lambda})$$

Tabulated values of the refractive index decrement for elements [47] allow the PTD to be calculated for a lens material. To estimate the magnitude of the pulse stretch from the PTD for a given CRL, the difference in material thickness over the beam footprint is needed. A simple model of this is presented in Figure 7.5 in which the difference in lens thickness $d_2 - d_1$ over the peak to half-intensity point of the beam footprint is used in calculating the PTD. This needs to be calculated for each lens in the CRL stack, and therefore needs the number of lenses in each stack to be determined. This has been done for a hypothetical beryllium collimating CRL for FEL-2 and shows the PTD is about 20 asec at 5 keV and drops to about 1 asec at 20 keV. A focussing CRL will be worse as there will be more lenses. The PTD per unit thickness of material will also be greater in more dense materials like diamond, though those would only be used at higher energies where the effect gets smaller anyway. Therefore, it is expected that CRLs are not going to stretch pulses of femtosecond duration or longer, whilst the effect on 100 asec or shorter duration pulses will need to be checked, but is only likely to affect the pulse at the lowest photon energies.

7.6 Optical design concepts

In this section, initial concepts for the optical layout of beamlines on FEL-5 and beamlines combining the output of FEL-2 and FEL-5 are presented. The concepts are not fully developed and are not intended to be final. The primary aims are to explore issues around delivering the requirements for the user experiments and to inform the layout of the machine.

7.6.1 Optical design concept for FEL-5; Attosecond and RIXS end-stations

There will be at least two branches on FEL-5 (250 to 3000 eV). One will be a direct beamline (no monochromator) for attosecond science, delivering the shortest possible pulses with the largest

possible pulse energy. Spectral bandwidth will be defined entirely by the source. The other branch will have the option to operate with a monochromator, mainly to ensure very high photon energy resolution is available for RIXS of quantum materials (qRIXS). RIXS for chemistry (ChemRIXS) will also be performed on FEL-5, but doesn't require the high resolving power of qRIXS and therefore doesn't require a monochromator. This is due to the use of a seeded source. ChemRIXS is therefore probably best served by an independent branch on the FEL-5 line because that would avoid the losses associated with running the monochromator in bypass mode. It would also allow the optical design for the qRIXS beamline to be focussed on achieving the high resolving power and the end station area to be optimised for the very large RIXS spectrometer. However, exactly how to include the ChemRIXS end-station hasn't been looked at so far and it is possible they could be served by the same branch with the interaction point for ChemRIXS located after the one for qRIXS. A preliminary optical scheme for the attosecond and qRIXS branches is shown in Figure 7.6.

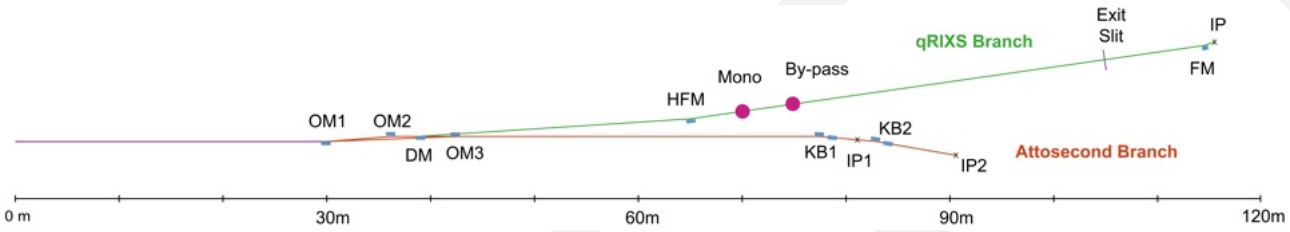

Figure 7.6: Overall optical layout of FEL-5 beamline with separate attosecond and qRIXS branches. OM = Offset mirror; DM = distribuition mirror; HFM = horizontally focusing mirror; KB = Kirkpatrick-Baez mirror; FM = Focussing mirror; IP = interaction point

7.6.1.1 Front-end optics

The first optics will be the mirrors that offset the beamline from the FEL axis for radiation safety. The required offset has not been determined so 50 mm will be assumed. Following the practice of EuXFEL, the second mirror will be bendable to correct for residual curvature in the first, which will absorb the non-reflected power in the beam. This power will come from bremsstrahlung and spontaneous radiation that cannot be collimated out and FEL harmonics above the mirror reflectivity cut-off.

Reflecting over the full FEL-5 tuning range will require at least two mirror coatings. Nickel or platinum coatings can cover the carbon K-edge, whilst boron carbide (B4C) or amorphous carbon (a-C) can be used above the carbon edge and will allow higher pulse energies. B4C and nickel are probably the best choice. Nickel will allow higher pulse energies than platinum, whilst a-C is known to suffer from multi-shot damage. A three-mirror system (Figure 7.7) will allow two grazing angles to be used without changing the output beam direction. The larger grazing angle captures the more divergent radiation at low photon energies, whilst the more grazing angle gives more spatial dilution and hence a larger maximum pulse energy at high photon energies. Mirror 1 thus operates at two different grazing angles whilst Mirror 3 must move out of the beam when Mirror 2 is in use.

Placing the front-end mirrors centred at 33 m from the source means that the maximum grazing angle is 4 mrad for a 0.9 m long mirror to capture 6-sigma of the radiation at 250 eV. The 50 mm offset means the two mirrors are 6.25 m apart. This reduces the collecting aperture of the downstream mirror to 5-sigma at 250 eV, but this acceptable. The upstream mirror determines the maximum pulse energy. The B4C coating has an absorbed dose of 0.01 eV/atom at a pulse energy of 1.0 mJ at 400 eV and 0.34 mJ at 3 keV. The nickel coating absorbs 0.01 eV/atom at a

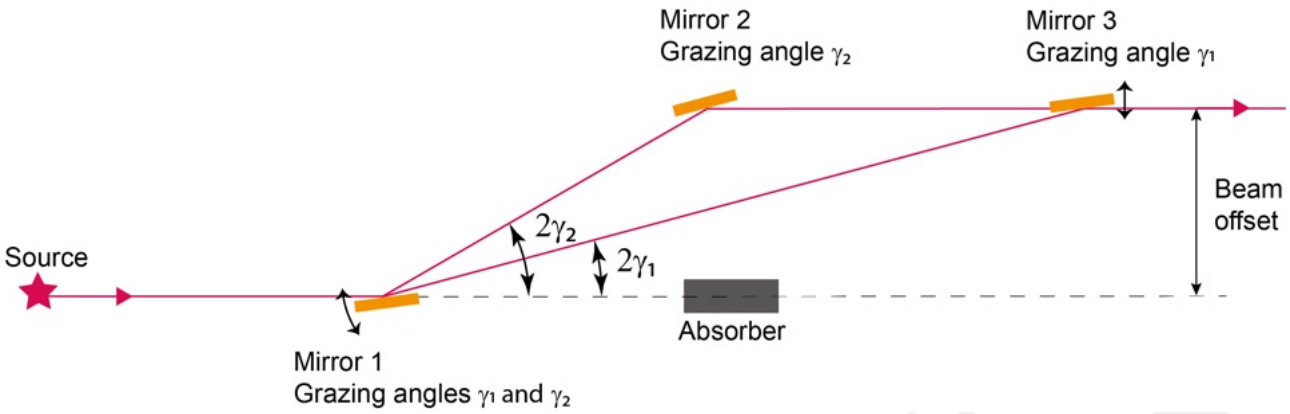

Figure 7.7: Three-mirror system for offset mirrors allowing two grazing angles and a fixed exit beam axis. Mirror 3 moves out of the beam when Mirror 2 is in use.

pulse energy of 6.4 mJ at 250 eV and 1.2 mJ at 800 eV. At 4 mrad grazing angle, B4C will reflect to 7.5 keV.

A third front-end mirror at 2 mrad grazing angle is at 42.375 m from the source. The lowest photon energy at which it collects 5-sigma is 750 eV and 6-sigma is 1000 eV. Only the B4C coating is needed for this mirror. The B4C coating on the first mirror at 2 mrad grazing angle will reflect to 15 keV and has an absorbed dose of 0.01 eV/atom for 2.4 mJ at 750 eV and 1.3 mJ at 3 keV. The lower grazing angle clearly allows the potential for much higher pulse energies.

At least one additional mirror, a distribution mirror, is required to send the beam to one of the branches. A mirror sending the beam in the qRIXS branch whilst keeping the attosecond branch on the straight-ahead position is proposed. Placing the distribution mirror as close as possible to the source and at the largest possible grazing angle gives the maximum lateral separation of the branches. Placing it at 39 m from the source (i.e. between the high- and low-angle second offset mirrors) is one option. At 10 mrad grazing angle, the maximum angle at which B4C will reflect 3 keV, the pulse energies for 0.01 eV absorbed per atom are 1.8 mJ (Ni at 250 eV), 0.35 mJ (Ni at 800 eV), 0.25 mJ (B4C at 400 eV) and 0.1 mJ (B4C at 3 keV). In the energy range 400 to 800 eV, nickel looks to be better than B4C due to the boron and carbon K-edges reducing the reflectivity in B4C. However, the damage threshold in terms of energy absorbed per atom will be larger (and likely a lot larger) in B4C than nickel, and actual maximum pulse energies may therefore be better in B4C. In any case, the optics in the monochromator will be more limiting as the grazing angles will be much larger (few degrees). This will be unavoidable if high spectral resolution is required.

7.6.1.2 High-throughput branch for attosecond science

The attosecond branch requires two interaction points (IPs) for different experiment types with a longitudinal separation of at least 4 m. The beam focus at the first IP should be c. 1-3 μm, whilst the second IP should have a larger beam (up to 50 μm) for liquid jets. The source size varies from 78 μm at 250 eV to 29 μm at 3000 eV, so a demagnification of 26:1 at the first IP will deliver a beam size of 3 to 1 μm at 250 to 3000 eV. Taking the distance from the KB centre to IP to be 3 m (for a good working distance), means a source distance of 78 m is required to give 26:1 average demagnification. At this distance, the 0.9 m long KB mirrors will have to be at a grazing angle of 9 mrad to collect 6-sigma of the beam at 250 eV. B4C coating will reflect to 3.3 keV and nickel coating will be used from 250 to c. 800 eV, but will reflect to 6.2 keV allowing some use of harmonic radiation. At this relatively large grazing angle, the pulse energies for 0.01 eV absorbed per atom are 8.1 mJ (Ni at 250 eV), 1.5 mJ (Ni at 800 eV), 1.3 mJ (B4C at 400 eV) and 0.5 mJ

(B4C at 3 keV). A diagram of the end station layout can be seen within the end stations chapter Figure 8.4.

The simplest system for focussing to the interaction point is to use a single Kirkpatrick-Baez system based on bendable elliptical mirrors allowing the focus to be moved between the two IPs. Adding 4 m to the focus distance for the second IP will reduce the average demagnification to about 11:1, giving a focus size of about 7 to 3 μm (250 to 3000 eV), broadly in line with requirements. However, the experimental requirement is for a focus at both interaction points simultaneously so that the first can used to measure the pulse duration by angular streaking (Section 7.7.5) whilst the actual experiment is conducted at the second. To facilitate this, a second Kirkpatrick-Baez system is required between the interaction points. This will magnify the focus of the first Kirkpatrick-Baez system by a factor of 2 or 3 to give a spot size in the range 3-10 μm. Larger spot sizes will be achieved through defocussing of the beam. The downsides of using two Kirkpatrick-Baez systems are that it is obviously much more complicated, will require a lot more space, and the quality of the second focus is very dependent on the quality of the first.

With a double Kirkpatrick-Baez system, the beam can be arranged to be horizontal at the second IP but will rise (or fall) at the first. If a horizontal beam is important at both IPs, two additional vertically deflecting mirrors will need to be added; this is undesirable due to the extra complexity and beam losses.

7.6.1.3 High resolving power monochromator branch for qRIXS

Even though qRIXS requires very high photon energy resolution, it is not a given that a monochromator will be needed. A transform limited Gaussian pulse of duration 100 fs has a bandwidth of 18 meV, which would be similar to existing RIXS facilities. However, the 2-ID SIX beamline at NSLS (Brookhaven) has an ultra-high resolving power mode delivering 14 meV at 1 keV [48], and the NanaTerasu BL02U beamline reports a World-record total resolution of 16.1 meV, though the photon energy is not stated [49]. Over much of the tuning range of FEL-5 (especially above 1000 eV), 18 meV is a resolution that is hard to achieve with a grazing-angle grating monochromator since the slope errors on the optics limit the ability to achieve extreme resolving powers and contribute proportionally more at higher photon energies. However, the preliminary beamline concept includes a monochromator as contingency against shortfall in source performance. For example, it is unlikely to be possible to achieve perfectly Gaussian and transform limited pulses, and there may also be a spectral pedestal to the pulse that could further degrade the spectral resolution if it is of sufficient intensity. Extensive time-dependent simulations of the FEL output will be needed to assess the likelihood of the source delivering sufficient spectral resolving power without a monochromator. It is also possible that a monochromator will only be required or useful at the lower photon energies of the FEL-5 tuning range, where it will work at its best.

The penalty of using a monochromator is the low efficiency, especially with the high line densities required for high resolving power. The beamline design concept of the qRIXS branch will thus include a monochromator that can be by-passed in some manner whilst retaining a beam focus at the exit slit plane (to ensure downstream optics continue to function correctly). A by-pass working in this way will still compromise beamline performance (through lower transmission and reduced maximum pulse energy) compared to the direct beamline and so is not considered for the attosecond branch. To achieve a very high resolution, a monochromator design that will minimise the number of optical elements that can degrade the resolution due to their slope errors is required. Two designs can be considered, both using a plane grating with varied line spacing (VLS). The Hettrick-Underwood type (HU VLS PGM) operates in converging light generated by a focusing mirror before the grating. The other type (hereafter called dVLS-PGM) operates in diverging light,

with all the focusing done by the VLS grating. However, the dVLS-PGM requires the included angle at the grating to be varied with wavelength to stay in-focus and so requires a plane mirror before the grating. Thus, both options have two optical elements that have a direct impact on the resolution from their tangential slope errors.

The dVLS PGM offers more flexibility in design since it is not constrained to have equal (virtual) entrance and exit arm lengths. Additionally, the nominal C_{ff} value (C_{ff} = cosβ/cosα, where α and β are the incidence and diffraction angles at the grating) can be changed, whereas the Hettrick-Underwood type operates at fixed included angle. C_{ff} for zero defocus in the dVLS PGM is a function of wavelength, but is very nearly constant. Since the monochromator has to work with adjustable C_{ff} anyway, it is possible to increase it to reduce the source and exit slit contributions to the resolution. Hence, the results of a preliminary study of the dVLS PGM are presented here.

Working on the assumption that it is possible to manufacture the grating with the VLS terms sufficiently accurately recorded to reduce defocus, coma and spherical aberrations to negligible levels (and a next-stage model will need to look at the implications of the inevitable errors in the VLS), there are four main contributors to the monochromator resolution. These are the source size and exit slit limiting resolutions and the energy spread from the slope errors of the grating and premirror. It is common (but not strictly accurate) to assume that these contributions add in quadrature. Analytical calculations of the resolution of a dVLS PGM show that aberrations caused by slope errors on the grating contribute significantly to the total resolution and will probably be the limiting factor. The slope errors of the premirror have a weaker effect provided the grating is operated in inside order of diffraction. The source size and exit slit limited resolution can be improved by increasing the entrance arm length, increasing the central grating line density or increasing C_{ff}. The exit slit can also be reduced in size, but needs to remain a practical size at a minimum, e.g. 10 μm. The slope error contributions reduce with higher line densities and C_{ff}, but are not changed by entrance and exit arm lengths. Increasing the line density reduces the required length of the grating (making it easier to make with low slope errors), whilst increasing C_{ff} requires a longer grating. However, higher line density gratings tend to be less efficient and the maximum pulse energy will be lower because the footprint on the grating is smaller. Evidently, a detailed design study will need to be undertaken to find the optimum operating conditions. It is reasonable to propose several gratings with increasing line density to give options to improve resolution at the expense of throughput.

As an example of what might be achievable, Figure 7.8 shows the calculated resolution for the preliminary beamline concept presented here. The results for three grating line densities of 600, 2000 and 4000 l/mm are shown. The 600 l/mm would be a high-efficiency but low resolving power grating for the lower half of the tuning range. The 2000 l/mm would give high RP in the same range but decreasing RP in the upper half. The 4000 l/mm attempts to give high RP in the upper part of the tuning range. Even so, the resolution never betters the RP that would be given by a 100 fs transform limited Gaussian pulse. This is why understanding the temporal properties of the source are critical in deciding whether a monochromator is useful in this application.

7.6.1.4 Pulse duration effects

With a single grating monochromator, the output pulse length can be dominated by the time slew from the pulse front tilt (PFT) caused by the grating rather than the reduction in spectral bandwidth. Since the PFT is one wavelength per illuminated groove on the grating, the time slew is more severe at low photon energies. When very high resolving power is the priority design criterion, minimising the PFT (e.g. by using low line density gratings) is not possible. Therefore, the effective pulse length can be significantly increased over the transform limit corresponding

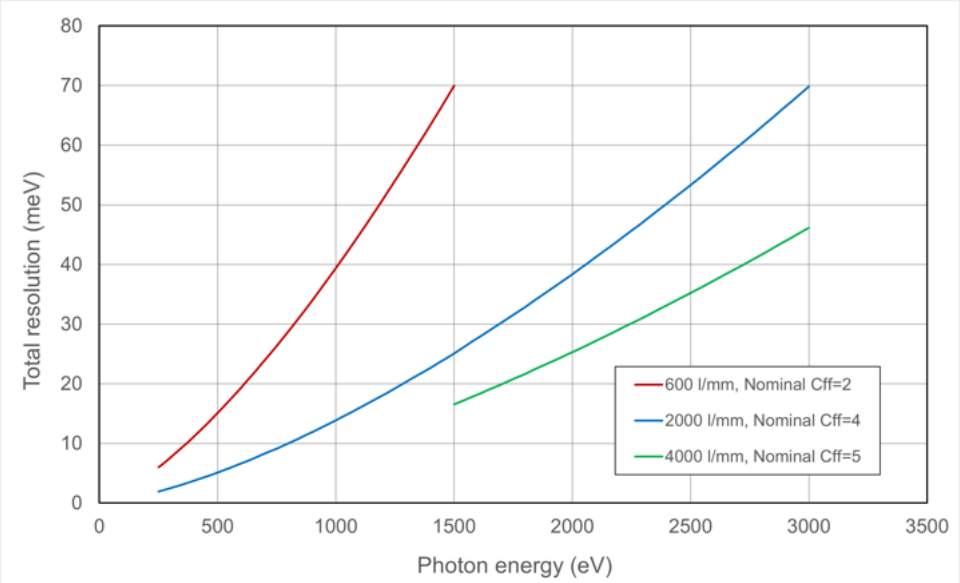

Figure 7.8: Calculated total monochromator resolution for three gratings (600, 2000 and 4000 l/mm) covering the FEL tuning range. The nominal C_{ff} values for each grating are 2, 4 and 5 (note actual C_{ff} changes slightly to keep the monochromator in focus). Grating and premirror slope errors are 100 nrad and 150 nrad RMS respectively. Exit slit is 10 μm. Entrance arm is 70 m and exit arm is 35 m. Resolution is the vector sum of source size, exit slit, and grating and premirror slope error contributions. Defocus, coma and spherical aberration are assumed nulled by the appropriate VLS terms. Any other contribution is ignored.

to the output bandwidth. Figure 7.9 shows the calculated time slew for the three gratings in the resolution calculation. In general, the time slew is not excessive except for the 2000 l/mm grating at very low photon energies, but this grating isn't needed there anyway. The monochromator does compromise temporal resolution compared to a 100 fs pulse though. As previously discussed, a double-grating monochromator can correct the pulse-front tilt, but only at the expense of a significant drop in beamline efficiency. Since qRIXS is a flux-hungry technique, and because it is not definite that a monochromator will be needed on UK XFEL at all, this option was not considered at this stage.

7.6.1.5 Beamline efficiency

Overall beamline efficiency has not been calculated but will be dominated by the reflectivity of the premirror and diffraction efficiency of the grating. These will both be very low, especially at the high photon energy end of the FEL tuning range. The total transport efficiency is unlikely to exceed a few percent when operating at highest resolving power, and will likely be nearer 0.1% above 1500 eV where the grating efficiency will be at the 1% level. Given the inevitable drop in resolving power as photon energy increases (see Figure 7.8), it may be better to run the monochromator in by-pass mode at high photon energies and rely on the temporal properties of the source to define the photon energy resolution.

Diffraction efficiency can be greatly improved by adding multi-layer coatings to the grating [43, 50, 51]. However, this may be problematic in this case. Firstly, staying on the Bragg peak of the multilayer requires a free choice of grating C_{ff} [43] and in the dVLS PGM, C_{ff} is determined by the focussing condition. Exact calculation of the grating efficiency would be needed to see how much enhancement is possible at the in-focus C_{ff} value; it is possible that the enhancement would still be worthwhile. Secondly, and probably more importantly, the slope error on the grating is critical to achieving the very high resolving power, and a very low tangential slope error of below

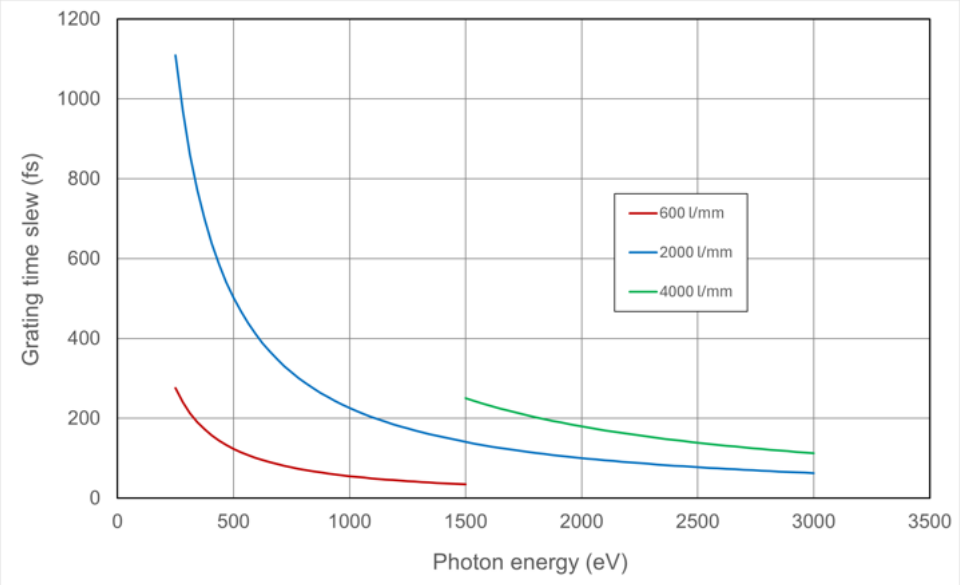

Figure 7.9: Time slew from the pulse front tilt of the RIXS monochromator concept

100 nrad RMS is required. It would need to be demonstrated that this target slope error could be maintained after multilayer coating. A third point is that the multilayer will introduce its own stretch to the pulse, though this is expected to be negligible compared to the PFT induced time slew.

7.6.1.6 Monochromator by-pass

By-passing the monochromator without requiring downstream optics to be reconfigured requires an optical scheme that retains the focus (in the dispersive plane) at the exit slit plane. This could be achieved by changing the grating for a focussing mirror. Modelling would be required to see if a simple spherical surface (sphere or tangential cylinder) would have low enough aberrations, or whether a plane elliptical shape would be required. If an elliptical shape is required, this might be difficult to implement since they are best made by bending a flat or sphere, but the grating mechanism will probably not be compatible with including a bender. This is where the Hettrick-Underwood type of monochromator has an advantage over the dVLS-PGM, since the premirror is doing the focusing and the grating can be simply swapped for a plane mirror.

An alternative approach would be to have a plane mirror and focussing mirror positioned downstream of the monochromator and configured to give the same overall vertical beam offset. They would be at fixed angle of incidence, which would be chosen to give better reflectivity than possible with the grating substitution approach. The focussing mirror could more easily be made an adaptive optic. In by-pass mode, the monochromator is moved out of the beam and the extra mirrors moved into the beam. An engineering study would be required to determine the practicality of this approach. Another advantage would be that the downstream focusing mirror would have higher demagnification, better matching the overall monochromator demagnification, and so the image size at the exit slit plane would change less in by-pass mode. Achieving a similar vertical beam size at the exit plane is important as it defines the source size seen by the RIXS spectrometer via the focusing mirror after the exit slit. If the size of the image at the exit slit is much larger in by-pass mode than in monochromator mode, the spectrometer resolution will be degraded.

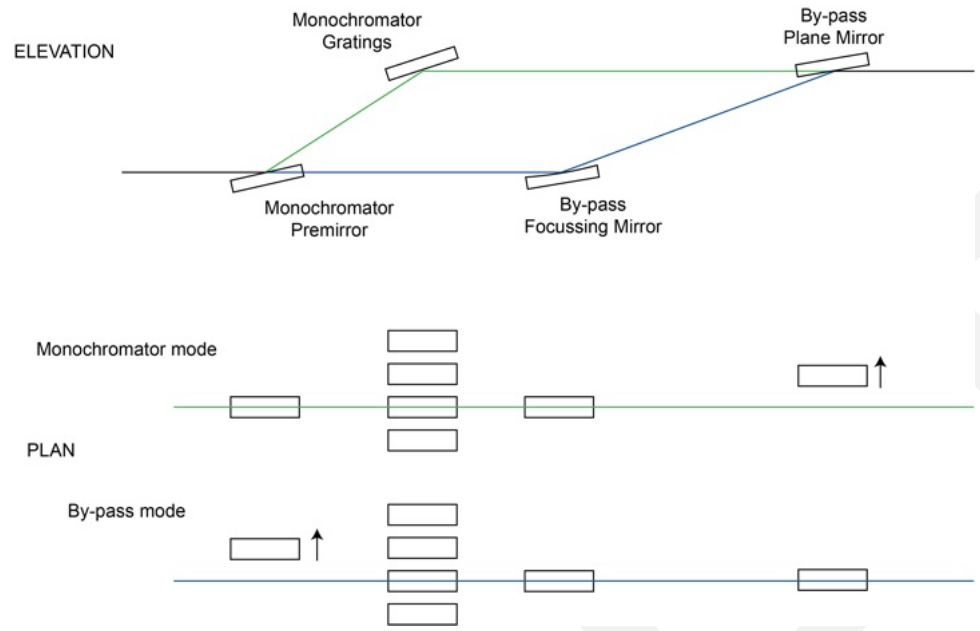

Figure 7.10: Schema showing how a by-pass might be implemented in the qRIXS monochromator. In monochromator mode, the second by-pass mirror is moved out of the beam path. In by-pass mode, the monochromator is moved sideways to allow the beam to pass the premirror.

7.6.1.7 Horizontal and post-exit slit focusing to interaction point

The final beam focus onto the sample is critical and is performed by the mirror(s) after the exit slit. In the vertical (dispersive for both monochromator and spectrometer) direction, the exit slit must be imaged onto the sample. The vertical beam spot on the sample acts as the entrance slit for the qRIXS spectrometer and needs to be at the micron level to deliver the required resolution. With a 10 μm exit slit typical for high monochromator resolution, this means 10:1 demagnification is required from slit to sample, which can be achieved with a 10 m slit to post-focusing mirror (PFM) distance and 1 m from PFM to sample.

The horizontal beam size is less critical, but should fit on the sample at grazing angles to avoid wasting photons. Creating an anastigmatic focus at the exit slit plane is convenient as it allows a single mirror like an ellipsoid to focus onto the sample [52]. However, caution is needed with a FEL source since there is a risk of ablation of the slits. If all the horizontal focussing to the IP were done with the PFM, the demagnification would be excessive, and since the source would be strongly astigmatic, the results would likely be compromised by severe aberrations. Some horizontal focussing therefore has to be done before the slit with an additional mirror somewhere in the beamline. The distribution mirror could be used, focussing either to the exit slit or straight to the sample, but will give an overall small magnification of the source in both cases and hence a beam size that might be too large at the sample. Therefore, an additional, horizontally deflecting and bendable mirror positioned just before the monochromator at 65 m from the source to give a magnification of about 0.6 onto the exit slit is suggested as a starting point for a more detailed design, with the caveat that the ablation risk must be assessed. This mirror can be at a 7.5 mrad grazing angle and thus will not limit the transportable pulse energy.

With this scenario, the post-focussing mirror can then be a horizontally deflecting ellipsoid (i.e. ellipse of revolution) giving a horizontal beam at the sample with size in the range 5 to 2 μm from 250 to 3000 eV and a vertical size of 1 μm for a 10 μm exit slit. This is the solution adopted by the DLS I21 beamline [52]. Although it gives the required horizontal beam at the sample with a single optic, it may not be optimum for UK XFEL. Firstly, using an ellipsoid with two coating

stripes requires a mechanism that can rotate the mirror about the sagittal centre of curvature when moving between the stripes. If this proves too difficult to achieve with the required precision, two separate mirrors (with nickel and B4C coatings) will be needed to cover the FEL tuning range. Secondly, they (DLS) found the quality of the mirror affected the vertical beam size at the sample and hence the spectrometer resolution. Future design optimisation will look into these issues and a better solution may be found.

7.6.1.8 RIXS experimental vessel and spectrometer

These will not be discussed here. It is however notable that the beam at the sample must be very stable in position in order to stay at the centre of the detector arc. According to [52] the beam at the sample needs to be stable to 20 μm. With a total optical path length of about 116 m, the FEL PV pointing stability needs to be better than 170 nrad.

7.6.1.9 Additional beamline branches on FEL-5

Although this has not yet been considered in any detail, a beamline branch for ambient pressure photoemission spectroscopy (APPES) is also required on FEL-5. APPES requires the sample to be in a gas environment at a pressure in the range $\sim$1 to 100 mbar. At these pressures and photon energies, absorption of the photons and emitted electrons is very strong, so the gas path must be kept very short. The x-rays are focussed through a differential pumping system leaving a path in the gas to the sample of typically $\sim$20 mm. The electron path must be even shorter (sub-mm) and a special differentially-pumped electron analyser is required. If a modest spectral resolving power of $\sim$10,000 is sufficient, a monochromator should not be required. A branch on the attosecond line, fed by an additional deflecting mirror located after the offset mirrors, is a possible solution. If a monochromator is wanted, branching the qRIXS line soon after the monochromator bypass maybe be possible. This would require an additional exit slit and complicates the design of the monochromator as additional grating(s) dedicated to the APPES mode will be required. In all cases, final focussing to the sample will be with Kirkpatrick-Baez mirrors.

7.6.2 Multi-colour x-ray from FEL-5 and FEL-2 combined

7.6.2.1 Introduction

To provide x-ray pump and x-ray probe with widely different x-ray wavelengths, there will be beamlines on two different FELs that bring the two x-ray beams to a common interaction point. The FELs chosen are FEL-5 and FEL-2. Note, this will be a duplicate FEL-5, positioned close to FEL-2, and not the same one for the Attosecond and RIXS experiments described above.

Since achieving spatial overlap requires deflecting the x-rays horizontally with mirrors to bridge the lateral separation of the FEL undulators, the majority of the deflection will be done with the FEL-5 beam. Reflecting to 20 keV on FEL-2 with B4C coatings limits the mirror grazing angle to 1.5 mrad. Using many mirrors to achieve a large total defection angle is not acceptable due to the impact on the beam quality (and also the cost and timescale to deliver the mirrors).

Both the soft x-ray and hard x-ray beamlines will be without a monochromator, relying on the superior temporal properties of UK XFEL source to deliver the required spectral bandwidth. For the hard x-ray beam, a 4-bounce crystal monochromator could be added without affecting the

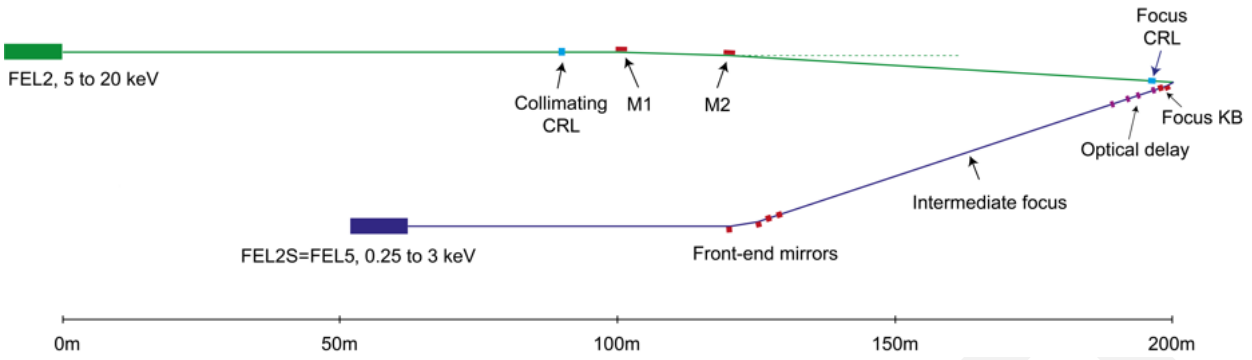

Figure 7.11: Layout of beamlines combining output of FEL-2 and its associated soft x-ray FEL (equivalent to FEL-5) to a common interaction point.

beam position at the interaction point, but would limit operation to linear polarisation. There would also be a wavelength dependent temporal delay added with the monochromator inserted. Adding a grating monochromator to the soft x-ray beamline is non-trivial, which is why it is not considered here.

7.6.2.2 Temporal overlap

Whilst spatial overlap on its own would allow a sample to be probed by a wider range of photon energies in the same experiment, the primary aim is to allow x-ray pump and x-ray probe. Thus, there needs to be a controllable temporal separation of the pulses from the FELs. Optical delay lines in the x-ray region that are tunable in both wavelength and temporal delay are problematic due to the difficulty in achieving variations in optical path lengths giving delays longer than $\sim$10 ps.

For the hard x-ray beamline, it would be necessary to use crystal optics to give any worthwhile path length change, but then wavelength and delay tuning is complicated by the coupling of crystal angle and wavelength. Scanning delay without changing wavelength or scanning wavelength without changing delay requires the crystals to move in two spatial directions and one angle. This requires a complicated mechanism and achieving sufficient precision will be challenging. Possibly more importantly, a crystal-based delay line with large Bragg angles will negatively impact anything other than S-polarised radiation and add some level of pulse stretch affecting femtosecond duration pulses. Thus, the hard x-ray beamline is not equipped with an optical delay line.

For the soft x-ray beamline, grazing angle mirrors must be used for a broad-band delay-line and this severely limits the temporal delay range possible. As described below, the beamline concept presented here (Figure 7.11) incorporates an optical delay line that gives c. 10 ps of delay. This is insufficient to correct for the overall time difference between the hard x-ray and soft x-ray branches that originates from the large difference in optical paths of the two beamlines. The optical paths of the hard x-ray and soft x-ray beamlines as presented here are about 200 m and 142 m respectively. Therefore, most of the temporal synchronisation will have to be achieved by modifying the relative delays between the electron bunches into the FELs. The optical delay may offer better precision of delay within its operating range, but if the e-beam based delay scheme also delivers accurate delay scanning, it may be that the optical delay line is unnecessary.

7.6.2.3 Hard x-ray Beamline on FEL-2

The hard x-ray beamline is kept as simple as possible. The first optical component is a collimating CRL since this gives freedom in positioning downstream optics without overfilling them. The CRL is placed at 90 m from the source, which is the furthest distance that allows the downstream mirrors to collect the target 6-sigma of the 5 keV beam. A further design study will be required to confirm CRLs can withstand the full beam. The next optical components are a pair of mirrors at 1.5 mrad grazing angle of incidence at 100 and 112 m from the source. These are offsetting the beamline axis from the FEL axis for radiation safety. In this case, they deflect in the same direction to increase the overall horizontal deflection angle towards the soft x-ray line. The second mirror can be swapped for a mirror deflecting back onto a line parallel to the FEL axis, giving a fixed offset of 60 mm, feeding an additional beamline on the FEL.

Focussing to the interaction point at about 200 m from the source is with a second CRL transfocator. The aim is to achieve a roughly micron-sized focus at the interaction point. To give achromatic focussing over the FEL tuning range to a roughly constant final beam size and position, it is necessary to use multiple CRLs in the collimating and focussing transfocators, and translate the focussing transfocator along the optical axis. The feasibility was tested with a simple model that calculated the required R/N ratio for the CRLs, where N is the number of individual lenses in the CRL stack, each with central radius of curvature R. The focal length of a CRL made from a material with refractive index decrement δ can be approximated to f = 2δ(R/N).

The model did not consider how many lenses were needed in each stack and how the stacks would be distributed in the transfocator. The modelling did include the photon energy dependent change of both the source waist size and the focal length of both the CRLs. It was done using Gaussian propagation equations rather than assuming geometric optics is valid, with the target being to create a beam waist at the interaction point. This is not strictly the same as a ‘focus’ of the optical system since the planes containing the beam waists are not conjugate planes of the optical system. However, the aim is to minimise the beam size at the interaction point and this corresponds to the achieving a beam waist at the plane of the interaction point. In any case, the difference between modelling with Gaussian or geometric optical propagation is very small.

The modelling showed that achromatic focussing to a nominal 2 μm FWHM beam over the FEL tuning range could be achieved with seven different combinations of collimating and focussing CRLs. However, the focussing CRL needs to translate by 6 m to achieve this. The overall magnification of the CRLs necessarily changes as the transfocator is translated, so the waist size at the interaction point varies from 2 to 2.4 μm FWHM. The shortest focal distance of the CRL was set at 7.5 m to allow space for the substantial bellows and still leave a distance of c. 6 m from the end of the bellows to the interaction point. This should be sufficient for the sample chamber and up-stream diagnostics. The technical design phase will look at the practicality of such a large translation and also whether the CRL R/N ratios are achievable and how the individual CRLs will be distributed inside the transfocator. The modelling required R/N ratios for beryllium CRLs from 2.4 mm for collimating at 5 keV to 23 μm for focussing at 20 keV.

One advantage of using a CRL for the focusing is that it can be easily withdrawn from the beam so the collimated beam can reach the interaction point without any realignment. The collimated beam gives a large beam size at the sample in the range 0.6 to 0.2 mm from 5 to 20 keV. This could be useful for some experiments. There would be a higher transport efficiency without the focusing CRL compared to simply going off-focus to produce a larger beam. A downside would be an increased sensitivity to pointing jitter in the source. Another advantage of using CRLs, and an alternative way of delivering larger beams at the sample, would be that it is simple to add another CRL transfocator further from the interaction point giving lower overall demagnification.

This would not be able to deliver fully achromatic focussing, but that may not matter when larger beam sizes are the target.

7.6.2.4 Soft x-ray beamline of FEL-5

Since CRLs are not an option in the FEL-5 photon energy range, the soft x-ray beamline has to use grazing angle mirrors to achieve spatial overlap with the hard x-ray beamline, for focussing, and for any optical temporal delay.

The first optics are two front-end mirrors, FE-HDM and FE-HFM, deflecting horizontally in the same direction toward the common FEL-2-FEL-5 interaction point. The second mirror is tangentially bendable to make an intermediate horizontal focus that acts as a source for the final focussing Kirkpatrick-Baez mirrors. The front-end mirrors are at 8 mrad grazing angle of incidence, which allows B4C to reflect from about 400 eV to 3.7 keV. A nickel coating stripe will be used to reflect over the carbon K-edge, working from 250 to about 800 eV. With mirrors at 40 and 45 m from the source, the pulse energy that gives 0.01 eV absorbed per atom in B4C is 0.4 mJ at 400 eV and 0.15 mJ at 3 keV. With the nickel coating, the pulse energies are 2.9 mJ at 250 eV and 0.5 mJ at 800 eV.

After the horizontally deflecting mirrors are two vertically deflecting mirrors; FE-VFM is 2 m after FE-HFM and FE-VDM is 2 m after FE-VFM. FE-VFM reflects upwards and FE-VDM reflects downwards so the beam is offset in the vertical direction by about 32 mm. FE-VFM is tangentially bendable to make an intermediate vertical focus that acts as the vertical source for the final focussing Kirkpatrick-Baez mirrors. These mirrors are also at 8 mrad grazing angle of incidence and so have the same reflecting properties and similar pulse energy capability as the horizontally deflecting mirrors.

The intermediate focus can be made anastigmatic, i.e. the horizontal and vertical foci are coincident. However, a more interesting option is to make the intermediate focus astigmatic. This allows the overall horizontal and vertical magnifications of the beamline to be made equal, thus delivering an anastigmatic focus and a round beam at the interaction point. The focus size will still be a function of wavelength because the source size is wavelength dependent. In this concept, with the intermediate focus at roughly unity magnification, the final focussed beam size is 2.5 μm at 250 eV and 1.5 μm at 3 keV in the limit of perfect optics. It is also possible to vary the beamline magnification with wavelength to deliver a fixed spot size at the interaction point, but significant modelling would be required to confirm this would work without causing issues with, for example, small beam footprints on the optics downstream of the front end mirrors.

Before the final focussing Kirkpatrick-Baez is a mirror based optical delay line (ODL) using four mirrors (ODL-M1 to ODL-M4) forming a distorted trapezium shape, see Figure 7.12. For quick and accurate scanning, the mirrors work at fixed angle of incidence and the inner mirrors (ODL-M2 and ODL-M3) translate along the beam path to the outer mirrors. The final mirror in the delay line, ODL-M4, is at a more grazing angle so that the beam from the vertically focussing Kirkpatrick-Baez mirror after the ODL is horizontal, whilst its position is set to correct the height offset of the vertically deflecting front-end mirrors, so the beam is also on the same height at the FEL-2 beam. The need for the ODL to reflect to 3 keV places limits on the achievable range of optical delay by forcing the mirrors to be at very grazing angles. With B4C coatings, the largest grazing angle that will reflect to 3 keV is 10 mrad. This is too shallow to give a good change in path length without making the base length of the ODL excessive. Using a combination of nickel and rhodium coatings allows the grazing angle to be increased to 19 mrad. This increases the temporal delay

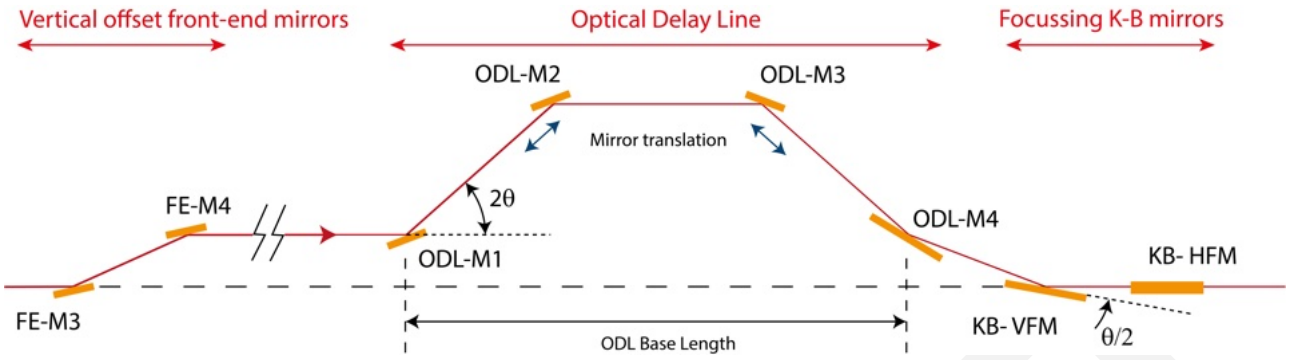

Figure 7.12: Schema showing a 4-mirror optical delay line integrated into the overall scheme for FEL-5 beamline

by a factor of 3.6 to 4.8 psec per metre of mirror travel. The downside will be a more limited maximum pulse energy because of the use of metal coatings and the larger grazing angles.

It is clear that the ODL will have to be very large to give substantial temporal delay. Initial estimates indicate 2 m of mirror travel can be accommodated with a base length of the ODL of 8.2 m, delivering 9.6 psec of temporal delay range. This is with each mirror in its own vacuum vessel coupled by bellows. The mirror vessels can then have air-side translations that will be easier to deliver with the precision and stability needed to deliver fine temporal steps and control temporal jitter. The alternative is to have the ODL mirrors in a single large vacuum vessel and use in-vacuum translations. This will allow the mirrors to be closer together at the extremes of their travel, making the ODL more compact, but an engineering study would be required to see if that actually facilitated more mirror travel. Note the mirrors are moving in the vertical plane since the ODL is being used to give a horizontal beam at the interaction point. Moving the mirrors in the vertical plane is undoubtedly going to be more challenging than in the horizontal plane so an engineering study will be required to access the feasibility of this approach.

The final optics are the Kirkpatrick-Baez focussing mirrors. The vertical focussing mirror is first and deflects upwards to give a horizontal beam. Both mirrors (and the last mirror of the delay line) are at 9.5 mrad grazing angle.

Table 7.2 summarises the mirror grazing angles and coatings required to cover the FEL tuning range. The total S-reflectivity of the beamline is shown in Figure 7.13. The P-reflectivity is only slightly lower and phase shifts are small, so the beamline would preserve the source polarisation extremely well, with a perfectly circularly polarised input beam retaining a degree of circular polarisation $>$0.9996 over the entire range. The transmission above 2.8 keV does drop significantly, but this is unavoidable unless the delay range of the ODL is reduced by lowering the grazing angle on the mirrors.

7.7 Photon diagnostics

The FEL process inherently results in shot-to-shot variation in the properties of the photon pulses. Pulse intensity, spectrum and duration all show variation that can have significant impact on the interpretation of the experimental data. It is well know that SASE results in considerable shot-to-shot variations in pulse properties. However, even when the FEL is operating in seeded or in other enhanced FEL modes, there will be variations that can be sufficiently large that knowledge of each individual pulse is required for experiments where each pulse gives a unique data set. Furthermore, comprehensive diagnostics are essential for setting up and optimising the FEL and the beamlines, including the provision of feedback signals for improving beam stability.

Mirror	Grazing Angle (mrad)	Coating 1 >1200 eV	Coating 2 500 to 2800 eV	Coating 3 <750 eV
FE-HDM	8	B4C	B4C	Ni
FE-HFM	8	B4C	B4C	Ni
FE-VFM	8	B4C	B4C	NI
FE-VFDM	8	B4C	B4C	Ni
ODL-M1	19	Ni	Rh	Ni
ODL-M2	19	Ni	Rh	Ni
ODL-M3	19	Ni	Rh	Ni
ODL-M4	9.5	B4C	B4C	Ni
KB-VFM	9.5	B4C	B4C	Ni
KB-HFM	9.5	B4C	B4C	Ni

Table 7.2: Summary of mirrors for the soft x-ray beamline, grazing angle of incidence and coatings required to cover different parts of the tuning range

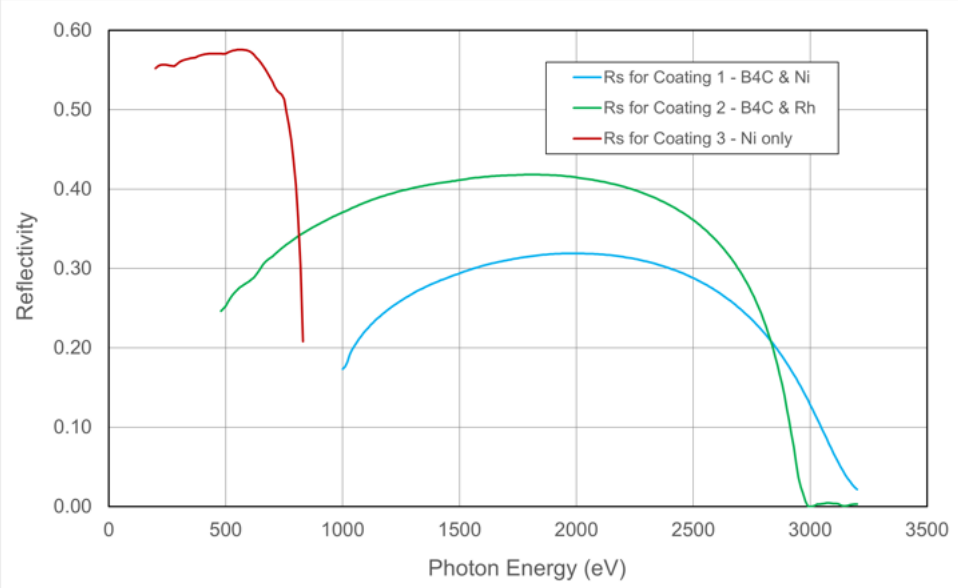

Figure 7.13: Calculated S-reflectivity of the complete soft x-ray beamline from 200 to 3200 eV for different mirror coating combinations

The diagnostics are to be considered an integral part of the overall facility, being essential for the correct running of the machine as well as providing information for the experiments. The data they produce can be analysed and combined with other information from the machine operating diagnostics to form higher-level 'virtual' diagnostics that enable enhanced operation of the machine.

This section is concerned with photon diagnostics that are installed prior to the experiment interaction point and therefore support all experiments. In general, experiments will require additional diagnostics integrated into the experiment or after the interaction point. For example, diagnostics for measuring relative timing between FEL and pump lasers should be performed as close the experiment as possible. These diagnostics will also be a fully integrated part of the machine operation since the information they provide is also essential for optimising the photon properties for the experiment. These diagnostics will be considered in detail in the next phase of the project.

The general principle for the photon diagnostics prior to the interaction point is that they should be, as far as possible, always 'on-line' and therefore non-invasive and should be able to measure every shot in the FEL pulse train. By this means, the end-user experiment can have accurate data on the nature of the FEL pulse that interacted with the sample, sufficient to allow them to analyse and interpret the measured data. This also implies accurate time-stamping of each measurement, but that is not the subject of this chapter.

Non-invasive can be taken to mean transmitting something like 80% or more of the pulse intensity without significantly modifying any of the spatial or temporal properties of the pulse. Obviously, the greater the transmission the better, whilst the term 'significant' might have a different meaning for different experiments. It is also possible, in some circumstances, to exploit the dumped beam e.g. after the interaction point, and this can also be considered to be non-invasive. Invasive diagnostics are acceptable when necessary, for example during commissioning and machine and beamline set-up, or for calibration of other diagnostics. Measurement of every shot on UK XFEL will require diagnostics to measure at 100 kHz for most of the FEL beamlines.

The properties of the photon pulse that should be measured include

- Pulse energy
- Pulse duration (and ideally temporal profile)
- Pulse spectrum
- Wavefront and transverse coherence
- Beam spatial size, shape and centroid location
- Beam divergence
- Polarisation state and degree

7.7.1 Pulse energy by x-ray gas monitors

X-ray gas monitors (XGM) are a key component on XFELs that non-destructively measure pulse energy and position. Following calibration with a radiometer, typically done using a synchrotron source, XGMs can give an absolute measure of the pulse energy.

As these are gas-based devices, they are very radiation hard and can work to high repetition rates so long as the gas column isn't depleted by the radiation, or the ion/electron time of flight

doesn't become longer than the separation of the pulses. EuXFEL has tested their devices up to 2.25 MHz. However, to maintain the linearity of the detector the number of pulses in the train was limited [53]. Literature from LCLS states that in the presence of high pulse energies and repetition rates the local heating of the gas is not dissipated before the next pulse arrives. This results in a local change in gas density and temperature that is not accounted for in the conversion from current to pulse intensity. This effect is more significant with high gas pressures and can be eliminated by careful choice of the gas pressures used. It is also possible to calculate this effect and take it into account after the fact [54]. This phenomenon needs careful consideration when designing such a system. This is also an issue for gas attenuators Section 7.4.7.1.

XGMs are suitable for the whole core energy range of UK XFEL, 100 eV to 20 keV. FLASH pioneered this type of detector and utilises XGMs for the photon energy range 14 to 310 eV [55]. This design needs to be modified to detect hard x-rays because higher photon energies have smaller absorption cross-sections. This is addressed by including two more chambers on the XGM design containing 'huge area open multiplier' (HAMP) detectors that are much more sensitive. The HAMP detector needs a different calibration factor for every multiplier voltage used. This four-chamber arrangement is what is installed on EuXFEL and is operated up to 24 keV [53]. This reference also reports predictions (through simulation) that the HAMPs chambers could detect photon energies up to 50 keV, though with increased uncertainty. Thus, they are still suitable for use on FEL-1 beamlines.

As mentioned above, these devices are routinely used at EuXFEL and FLASH and also at: LCLS [56], SwissFEL [57], SACLA [58] and FERMI [59]. Many, if not all, are based on the EuXFEL/DESY design. PAL are also currently developing their own gas monitors [60]. EuXFEL reports that its devices can measure the intensity of individual femtosecond duration pulses at an absolute accuracy of $<$10% for 10^7 to 10^{15} photons and $<$1% relative accuracy pulse to pulse for pulses with $>10^{10}$ photons. The position of the beam can be determined at an accuracy of $\pm$10 µm within a range of $\pm$1 mm [61].

These partial-pressure gas chambers (10^{-4} to 10^{-2} Pa) [62] are integrated into the beamline by differential pumping to allow windowless operation. The four-chamber EuXFEL design is about 2 m long (not including differential pumping) and has a transmission of approximately 99%. As a result of this, there has been no reported degradation of the wavefront quality from this diagnostic. Typically, an XGM is one of the first devices in the photon beamline, before even the offset mirrors. This is because the XGM is used to monitor the undulator output and is used to tune the undulators during the commissioning period. Another XGM is usually placed just before the experimental end-station to monitor the intensity delivered to the users after the all the beamline optics.

7.7.2 Scintillating intensity and profile monitors

Like the YAG screens used for electron beam diagnostics, scintillating screens are also used as a photon diagnostic. The beam imager consists of the scintillator that can be moved in and out of the beam and a lens and camera system for recording the luminescence. The imaging optics can be implemented in a number of ways depending on the requirements for resolution, accuracy and field of view. For highest accuracy and repeatability, the imaging system should have a fixed focal distance.

Beam imagers are used for position monitoring, relative intensity measurements, and profile imaging. Imagers are placed before and after every optic in a beamline and used for commissioning undulators, monochromators and are critical for alignment of the whole beamline. At the first commissioning, EuXFEL had 25 imagers in total spread across the beamlines [61]. Typically,

screens are destructive ways to image the beam. If a scintillating material is sufficiently thin to give useful transmission, this type of diagnostic can be considered as non-invasive.

Screen-based imagers are suitable for the entire photon energy range of UK XFEL if an appropriate scintillating material and thickness is used to avoid saturation. It is common to have multiple screens available to each imager so that a large photon energy and pulse energy range can be measured. YAG:Ce is the most common material used because of its radiation hardness and the wavelength of light that it emits (visible) which is easily detectable. Diamond is also used. Although YAG:Ce and diamond are known to be radiation hard, it is unlikely that the screens will be able to withstand the full beam. The LCLS-II CDR states attenuation will be needed at photon energies $<$7 keV to reduce the energy deposited in the screen to $<$100 meV/atom [13]. EuXFEL reported that thermal damage is an issue at low photon energies resulting in the number of pulses being limited when imagers are in place, even for diamond scintillators [63].

Both YAG:Ce and diamond can be used for single shot imaging (with a suitably fast camera) because of the fast decay of the luminescence of $\sim$70 ns and a few nanoseconds respectively. The best spatial resolution reported was approximately 2 μm [13]; the resolution is limited by the numerical aperture of the imaging system or the CCD camera pixel size. The position can be accurately determined to 25 μm and once calibrated these images can be used to measure intensity with a relative accuracy of 1% [57].

The field of view and resolution of these types of imagers is tailored to the application. After optics which deflect the beam for example, large fields of view are needed to locate the beam. The imagers designed for LCLS-II have variable fields of view and resolution so that they can be used flexibly [13]. The field of view can be varied from 50 mm to 0.5 mm with resolutions from 100 μm to 2.2 μm so that beam finding and high-resolution measurements can be taken with one device. Compared to XGMs, these devices are very compact.

7.7.3 Laser power and energy meters

Traditional laser diagnostics are also used on XFELs, particularly to measure power and intensity. Photodiodes, thermophiles and pyroelectric sensors can be easily translated into the beam at strategic places for intensity and average power measurements. Although these methods of measuring power and intensity are typically not as accurate as the methods designed specifically for x-rays, they are cheap and compact diagnostics. Laser power/intensity monitors are commonly placed after optics where reflectivity needs optimisation or the Bragg condition needs to be satisfied. These devices intercept the beam and so are only used during commissioning or set-up. For absolute measurements of pulse energy, calibration with an external device is needed as the x-ray wavelength is far outside the range calibrated by the manufacturer.

Pyroelectric sensors have a response time up to k̃Hz and can measure pulse energy and radiant flux. Thermopiles have a slow response so can only be used for radiant flux measurements. The flux measurements can be used for the calibration of other devices. Thermopile cooling schemes are being developed so that the device can withstand the power expected for LCLS-II [13]. Silicon photodiodes can be used to directly measure the beam up to at least 14 keV [64]. They can, however, easily saturate and be damaged when exposed to the full beam, so they are only used to measure spontaneous radiation when aligning undulators before lasing begins or when the beam is attenuated.

Diamond sensors are also used, which are more radiation-hard than silicon. SwissFEL has Si photodiode intensity monitors that can measure photon flux to an accuracy of 20% [57]. Diamond

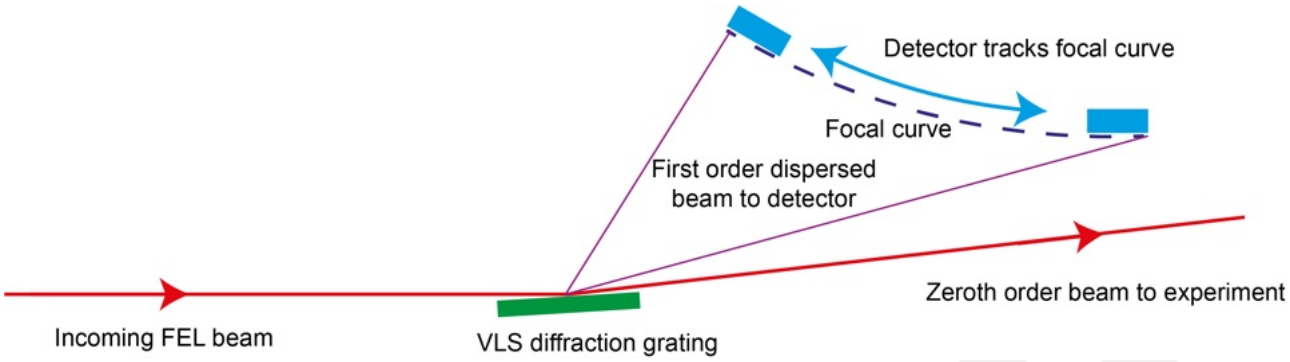

Figure 7.14: Concept of the VLS spectrometer for on-line spectrum measurement in the soft x-ray region

sensors can be made thin enough to be almost transparent to x-rays and can be used as a non-invasive diagnostic. Using pairs of electrodes these devices can also be used as beam position monitors. These devices have been shown at EuXFEL to provide pulse-resolved position measurements at 2.25 MHz with an uncertainty of less than 1% [65]. They are particularly suited for high photon energies and are frequently used at synchrotrons across a wide range of photon energies above the carbon edge up to at least 30 keV.

7.7.4 Pulse spectrum diagnostics

7.7.4.1 Grating spectrometers

On-line measurement of the pulse spectrum at soft x-ray energies (e.g. for FEL-6) can be accomplished with an imaging grating spectrometer. A diffraction grating with varying line spacing (VLS) acts as a dispersing and imaging optic. With the correct choice of VLS terms, the spectrometer can disperse the pulse spectra over a flat field that can be recorded by an imaging detector. The spectral range and resolution that can be measured in one shot are determined by the dispersion of the grating, the size of the flat field in the detector plane, and the detector size and sampling over the flat field. Spectrometers of this type are successfully in use at FLASH [66] and FERMI [67]. The general concept is shown schematically in Figure 7.14

The grating is designed to reflect most of the x-ray energy into the zeroth order, which then carries on down the beamline to the experiment. The grating thus operates at a fixed angle of incidence ($\sim 2°$ grazing angle) and acts as both a beam splitter and a dispersive element. The grating groove profile is optimised to maximise the zeroth order efficiency whilst giving a low first-order diffraction efficiency that is still sufficient for the detectors to give a usable single-shot measurement. Preserving the beam wavefront quality of the specular beam requires gratings of very high surface accuracy. More than one grating will be required to cover the full range of a FEL and it is sensible to allow the grating to be substituted for a mirror to maximise the throughput when the spectrometer is not required. The maximum photon energy at which this type of spectrometer can operate will have to be determined as part of a detailed design study, but there is no inherent reason why the range of FEL-5 (250 to 3000 eV) can't be covered.

The focal plane of the grating can only be considered flat over a narrow spectral region, matched to the pulse spectrum, and the focal length will also change with photon energy. Thus, tuning to different parts of the FEL output range involves moving the detector arm in both angle and distance from the grating to follow the focal curve of the spectrometer. Tilting the detector sensor to be tangent to the focal curve is also necessary to minimise the defocus over the measured

range. The detector thus has a relatively large and complex motion even when several gratings are used.

The maximum measurable repetition rate is determined by the speed at which the detector can be read out. This can be increased by using 1D detectors, such as the GOTTHARD [68]. EuXFEL use the GOTTHARD at 1MHz in burst mode, so we assume 100 kHz CW operation should be possible. The maximum pulse energy will be determined by the damage threshold of the grating, which will be lower than for a mirror at the same angle of incidence. The effect of the high average power on the grating shape also poses a limit on the repetition rate and pulse energy.

7.7.4.2 Crystal spectrometers

For hard x-rays, a spectrometer based on a bent Bragg crystal can be used, [69, 70, 71, 72]. The basic principle is the x-ray beam impinges on a convexly curved Bragg crystal such that each part of the beam strikes the crystal at a different Bragg angle and thus different wavelengths are diffracted at different angles. An imaging detector placed to capture the diffracted beam will thus record a signal where the position on the detector is directly correlated to wavelength.

Since it is necessary to make the spectrometer non-invasive, there needs to be some means of splitting the FEL beam into a small part for the spectrometer and the major part continues on to the experiment. This can be achieved in one of two ways. In the first method, the Bragg crystal itself acts as a beam splitter. [69, 71]. If it is sufficiently thin, most of the beam intensity is transmitted. In the second method, a transmission grating is placed up-stream of the crystal and divides the beam into zeroth- and first-order diffracted beams. [70, 72]. The zeroth order passes to the experiment and one of the first-order beams impinges on the crystal. These two approaches are shown schematically in Figure 7.15 In both cases, the crystal and detector must rotate about a common axis, centred on the point of impingement of the beam on the crystal, in θ-2θ mode as the photon energy is changed. The diffracted beam exits the beamline vacuum through a large beryllium window so the detectors can be in air. The size of the window and the proximity to the crystal determine the accessible range of Bragg angles at the crystal.

It is necessary to have several crystals with different cuts and bend radii to cover the typical tuning range of a FEL. Higher-order reflections from a given crystal can be used to access either higher photon energies or higher spectral resolution. Spectral resolution also depends on the distance from the crystal to the camera and the camera pixel size. The spectral range diffracted from the crystal depends on the footprint of the beam on the crystal and the bending radius. These define the range of Bragg angles on the crystal. The measured spectral range additionally depends on the camera distance and its size in the direction of dispersion. The crystals also need to be very thin (typically 10 μm) even when they are not used in transmission mode because they need to be bent to a small radius of curvature (between 50 and 150 mm is typical).

The two approaches have their own advantages and disadvantages. The transmitting-crystal type typically has lower transmission to the experiment and also a higher minimum photon energy due to the greater absorption. Power handling is also lower as the crystal absorbs a fraction of the direct beam and thermal distortion of the crystal lattice needs to be avoided if the spectrometer is to work as expected. The bending is more difficult as it must be achieved with a 'free-space' mounting of the crystal to allow the transmitted beam to pass onward, whilst a former can be used in the grating-splitter type. The impact of the Bragg reflection on the transmitted beam is also complex, especially when the full bandwidth of the pulse is not Bragg reflected (which could be the case with SASE pulses when operating in high spectral resolution modes). Furthermore, since different wavelengths in the Bragg reflected beam come from different parts of the beam,

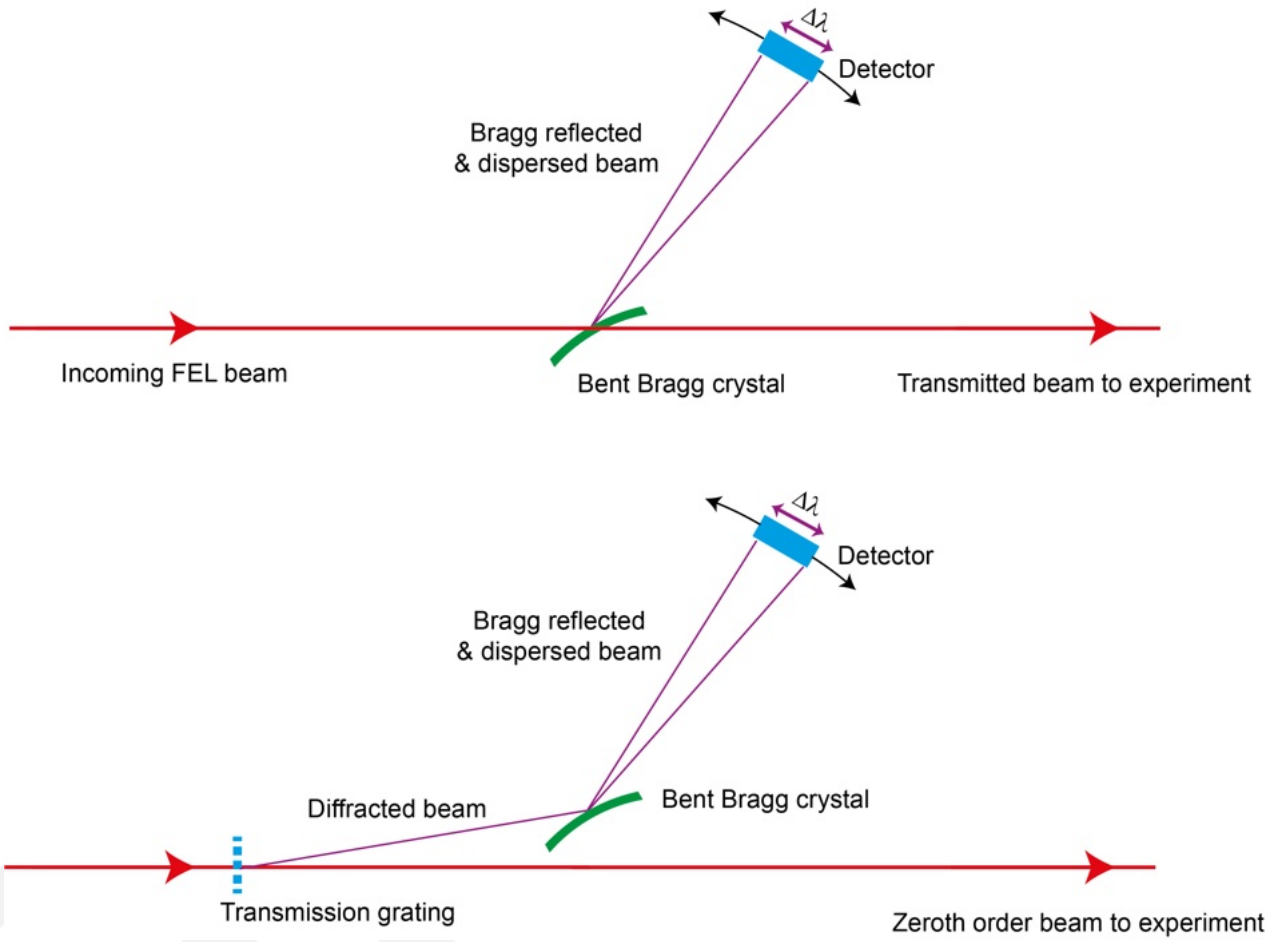

Figure 7.15: Schema showing the operating concepts of the two types of Bragg crystal spectrometers. Top: the crystal is the beam splitter. Bottom: a transmission grating is the beam splitter

there is a spatial dependence on the spectral modification of the transmitted beam. The biggest advantage of the transmitting-crystal type is that it is much more compact since there is no need for the large separation between the grating and crystal that is required to give the necessary spatial separation of the zeroth and first order beams.

It seems, in general, that the transmission grating type is to be preferred. This is the concept of the original HIREX spectrometer on EuXFEL [72]. However, the HIREX has been modified to use a diamond crystal in transmission mode (in addition to the normal silicon crystals used with the grating) because of the reported negative impact of the grating on the beam at the experiments. This is despite previous work [70] not reporting any such effect. Though there should be some spectral modification to the transmitted beam, this has not been reported to be significant.

In any case, for a high repetition rate FEL like UK XFEL, the transmission grating approach may be the only option due to the very high average beam power. Certainly, the only crystal that would withstand the direct beam of UK XFEL at full repetition rate is diamond due to its lower absorption and higher thermal conductivity than silicon, and that would limit the lowest operating energy to c. 3500 eV.

A common issue for any spectrometer using a Bragg crystal is that it requires an S-polarised beam due to the varying Darwin width for P-polarised radiation, which results in no reflectivity at the 45° Bragg angle. Since UK XFEL is expected to deliver flexible polarisation, this suggests both horizontal and vertically dispersing spectrometers will be required. This also points to the grating beam-splitter type being the optimum choice. Firstly, the plus and minus diffraction orders could feed one spectrometer each. Secondly, when circularly polarised radiation is generated, the transmission through the crystal will be modified in a complex manner and the beam will be partially depolarised. When the crystal is acting only as an analyser, this change in polarisation state will not matter.

7.7.4.3 Other optical spectrometers

Another scheme suggested by [73] is to use a transmission grating with curved lines. This is essentially a segment of a Fresnel zone plate and as such has a different focal length at different wavelengths. A detector placed at a grazing angle to diffracted beam can lie along the focal plane and capture a wide range of diffracted wavelengths. The main difficulties with this scheme seem to be the lower damage threshold of the zone plate and limited spectral resolution.

7.7.4.4 Photoionisation-based spectrometers

The described schemes above are all optical spectrometers. An alternative approach is to use photoionisation of gases in conjunction with photoelectron spectroscopy. This approach has the advantage of all gas-based techniques in that it is essentially completely transparent to the beam (due to the low absorption of the low pressures of gas used) and can't be damaged. The lack of moving mechanical components is also an advantage but is offset by the need for complex gas handling systems. It is also possible to use the technique to give other useful information on the beam properties such as polarisation.

Photoionisation is a process in which the absorption of a photon by an atom causes the emission of a photoelectron from a bound state in the atom. To do this, the energy of the photon needs to be above the binding energy of the electron. Any excess of the photon energy E_{phot} above the binding energy E_{bin} is transferred to the kinetic energy of the photoelectron, E_{kin}. Thus $E_{phot} = E_{kin} + E_{bin}$.

The kinetic energy of the electron is measured in a carefully calibrated electron time-of-flight (eTOF) spectrometer, whilst the binding energy is fixed for a given orbital in a given gas and can be found for many gases from the literature. The time of flight is related to the electron kinetic energy (in the non-relativistic limit) by $\tau \sim 1/\sqrt{E_{kin}}$, and so the photon energy can be deduced once it is measured. To make a working diagnostic, the behaviour of the photoionisation process with photon energy and polarisation needs to be understood. Two key aspects are the probability of photoemission, determined by the absorption cross-section, and the angular distribution of the emission about the beam direction.

The production of photoelectrons is a maximum when the photon energy just exceeds the binding energy and rapidly falls when the photon energy is significantly above the binding energy. Achieving a good yield of photoelectrons requires excitation from core-levels in the atom, with the photon energy as close to the core-level binding energy as possible. Therefore, covering a wide photon energy range with good electron yield requires a number of gases to be used. Typically nitrogen and noble gases are used, with heavier gases (i.e. krypton and xenon) being required at high photon energies. Gas pressures are typically in the 10^{-7} mbar range, so total absorption is negligible and the diagnostic is transparent to the transmitted beam.

The angular distribution of the photoelectrons in the plane perpendicular to the beam direction (the azimuthal distribution) depends on the anisotropy parameter β of the gas, which in theory takes values only in the range between -1 and +2. With linearly polarised x-rays, the photo-emission is anisotropic unless β = 0 . When β >0 (which will be the case for any gas likely to be used) the emission is predominately along the direction of the polarisation vector. Only for circularly polarised or unpolarised radiation is the emission always isotropic.

The energy resolution of the electron spectrometer directly determines the achievable photon energy resolution. It is a complex subject that can only be touched on here. Key aspects include the uncertainty in measuring the overall time of flight for a given kinetic energy and the variation in flight times caused by differences in path length from the point of emission to the detector. Because flight time reduces with kinetic energy, the highest resolution is achieved at the lowest kinetic energies. To allow a wide range of photon energies to be measured with each gas, it is normal to apply retarding potentials to the photoelectrons to slow them down. The length of the flight path of the electrons to the detector depends on their point of emission in the gas. A large photon beam size gives a large emission volume and hence a greater variation in flight times for the same kinetic energy, degrading the energy resolution. This can be minimised by focusing the beam into the spectrometer, but for an on-line diagnostic situated prior to the user experiment, this is rarely going to be possible. Thus, ultimate spectral resolution will likely be limited in this type of diagnostic. However, recent work at EuXFEL has shown that the spectral resolution can be improved by the application of machine learning trained on simultaneously-recorded, high-resolution data from an (invasive) optical spectrometer [74].

Transverse movement of the beam relative to the eTOF will also change the flight time, so all instruments use eTOFs in pairs positioned diametrically opposite each other about the photon beam axis to allow beam movements to be corrected. This also adds the potential for the instruments to be used as beam position monitors.

The shape of the measured photoelectron spectrum is a convolution of the photon spectrum, the spectrometer resolution function, and the lineshape of the photoemission peaks. Extraction of the actual photon spectrum would involve deconvolution of these effects. Since p- and d-orbitals are often excited, the photoelectron spectrum will also contain peaks that are very close, complicating the fitting procedure. Although deconvolution is possible, the resolution of the spectrometer is usually too low and the natural linewidth of the photoemission peaks too broad to make extraction

of fine detail (e.g. SASE spikes) in the photon spectrum possible. Therefore, this type of instrument is usually used to give the mean photon energy and spectral envelope of the pulse.

The effect of space charge on the photoelectrons need to be considered at high repetition rates. The ions created in the photoemission process are relatively massive and move with thermal velocities. At high repetition rates, the ions will accumulate in the interaction region and slow down the photoelectrons, making the deduced wavelength become longer. The point at which this effect becomes significant depends on the density of ions and thus depends on the gas pressure and absorption cross-section of the gas in use. Lowering the gas pressure is one way to mitigate the effect. Other techniques are the use of clearing electrodes or the use of a supersonic (rather than effusive) gas jet so the ions have more kinetic energy. It is also possible to use the measured shift in the Auger lines to apply a correction factor to the photoemission lines.

One example of a photoemission-based on-line spectrometer that is currently used is the OPIS instrument developed at DESY for FLASH2, [75, 76]. This has four eTOFs arranged radially in a cross pattern about a common intercept on the FEL beam axis. Each eTOF is angled at 54.7° relative to the horizontal, with two above and two below the beam plane to allow correction of beam movements relative to the tube axis. This is the angle at which photoemission for linearly horizontally polarised radiation does not depend on the anisotropy parameter. It is not clear how suitable the instrument is for use with other linear polarisation states, though it should be fine with circular polarisation.

The primary function of OPIS is as an on-line measurement of the central wavelength of the SASE pulses. As discussed above, the limited kinetic energy resolution and the requirement to deconvolve the natural lineshape and spectrometer resolution functions from the measured photoelectron spectrum make this technique of limited value in measuring the complex spectrum of a SASE pulse. In the case of a pulse that is seeded or otherwise of improved longitudinal coherence, retrieving a useful pulse spectrum may be of greater value. Nevertheless, the on-line measurement of central pulse wavelength by a diagnostic that is essentially completely transparent to the beam and doesn't limit the maximum pulse energy is very valuable. It is useful not only as information to the users but also in controlling the machine operation. For example, it can be integrated into feedback systems that correct for drifts in lasing wavelength.

Arguably the most important diagnostic that uses photoelectron spectroscopy is the Photoelectron Spectrometer (PES), colloquially known as the 'Cookie Box' [77, 78]. This instrument has 16 equispaced eTOFs arranged radially about the beam axis. The underlying principles of operation are the same as with the OPIS, but now the azimuthal distribution of the photoelectrons can be measured. So, not only can the PES measure the wavelength and spectral envelope of the FEL pulse, it can also measure the anisotropy of the photoemission and hence infer the polarisation state of the FEL beam. This can be done shot-by-shot and with complete transparency to the FEL beam. This is absolutely critical to the operation of UK XFEL where delivering flexible polarisation is a key design goal.

The main limitation of the PES for UK XFEL is that it cannot distinguish between circularly polarised and unpolarised radiation, since both generate isotropic photoemission patterns. Therefore, interpretation of the measurement in terms of the degree of circular polarisation involves an assumption as to the fraction of unpolarised light present in the beam. In fact, an assumption like this must be made when interpreting any photoelectron distribution that isn't generated by purely linearly polarised light because any isotropic component cannot be unambiguously ascribed to either circular or unpolarised radiation. Simulations of UK XFEL undulators suggest that the percentage of unpolarised radiation should be ¡1

7.7.5 Temporal diagnostics

This section looks at four methods for measuring the duration or profile of the FEL pulse. The first three use an external laser and can therefore also be used to measure the timing jitter of the FEL pulse and hence give time of arrival information (relative to the laser). More details on time of arrival measurement can be found in Chapter 10, so that aspect is not discussed in depth here.

The so-called 'attoclock' angular streaking technique developed at LCLS is probably the most suitable for femtosecond and sub-femtosecond pulses on UK XFEL [79]. The basic principle of any streaking technique is that the longitudinal profile of the photon pulse is replicated as a distribution of electrons which can then be manipulated by means of an applied field to convert the longitudinal distribution into one that is more easily recorded. For x-rays, it is most convenient to use photoionisation in a low-pressure gas to create the replica of the pulse. Since photoemission occurs on attosecond timescales, the temporal profile of the photoelectrons is an accurate replica of the pulse profile. A laser field can then be used to modulate the momentum of the photoelectrons, with the applied kick dependent on when the emission occurred along the FEL pulse. An assumed knowledge of the size of the kick along the pulse means that a measurement of the energy distribution of the photoelectrons can be converted into the pulse profile. When a linearly polarised laser field is used, timing jitter between it and the FEL pulse leads to an ambiguity in the size of the kick and this limits the accuracy of the retrieved pulse profile. This difficulty is overcome in the attoclock by using a circularly polarised laser, giving a uniform angular streaking of the photoelectrons with the time-base of the pulse projected onto an arc. The energy of the photoelectrons is then measured with the same 'Cookie Box' array of 16 eTOFs described above. The energy-time profiles of the pulse are then extracted using an iterative algorithm.

The period of the laser is the time for the streaking field to make one revolution and therefore sets the maximum pulse duration that can be measured without overlapping of electrons generated from different parts of the pulse. In [79], the laser wavelength was 10.6 μm, giving a period of rotation of $\sim$35 fs. The temporal resolution is given as $\sim$0.4 fs. Shorter pulses can be measured with proportionally higher temporal resolution by using a laser with a shorter wavelength. The technique can also be used to measure the arrival time of the FEL pulse (relative to the streaking laser pulse).

One possible limitation is that in [79] the x-ray beam was focussed in the spectrometer to a spot size of approximately 50 μm. This will improve the energy resolution of the spectrometer and hence the temporal resolution. It is not clear how performance will be affected by using an unfocussed FEL beam. If the FEL beam needs to be focussed to achieve the required temporal resolution for e.g. sub-femtosecond pulses on UK XFEL, then the technique does not fully meet all the requirements for an non-invasive diagnostic since additional optics will be required.

An alternative way to overcome the uncertainty caused by the timing jitter between the FEL and streaking field was described by Juranić et al. for the Photon Arrival and Length Diagnostic (PALM) system at SwissFEL [80]. In this case, two sequential THz streaking systems are used in which the streaking fields are at a relative 90° phase difference. This ensures that the FEL pulse will arrive coincident with a linear part of the streaking field in one of the two systems and the hence the effect of timing jitter can be mitigated. However, later reports [81, 82] show that only one of the systems is streaked and the other records an unstreaked photoemission spectrum. Comparison of the two spectra allows the energy shifts of the streaking field to be uniquely determined, also allowing mitigation of the effect of the timing jitter.

Pulse duration can be measured by monitoring the intensity of sidebands in the photoelectron spectrum generated by the FEL pulse in the presence of a strong IR laser field [83]. Simultaneous

absorption or stimulated emission by the photoelectrons of one or more IR photons results in the production of satellite peaks, the sidebands, around the main photoemission peak. [84]. The *m*th sideband above / below the main photoemission peak corresponds to the absorption / emission of *m* IR photons. The intensity of the *m*th sideband is a function of delay between FEL and IR pulses and the *m*th power of the IR intensity. A time-of-flight electron spectrometer is used to resolve and record the intensity of sidebands. The cross-correlation curve generated by monitoring the intensity of a given sideband as the IR pulse delay is scanned over the FEL pulse can be deconvoluted to give the temporal profile of the FEL pulse. The temporal profile of the IR pulse used in the deconvolution is measured by standard techniques. Temporal jitter between the IR and FEL pulses will broaden the cross-correlation curve and should be small compared to the FEL pulse length. The obvious limitation is that the technique is not single-shot. The sideband technique is only applicable for longer FEL pulses ($>$10 fs) to avoid the pulse bandwidth broadening and blurring of the photoemission and sideband peaks. The IR pulse duration should be short compared with the FEL pulse but also not so short as to cause a broadening of the photoelectron spectrum. Sideband production can be seen as a limit of streaking when the streaking pulse period is short compared to the sample pulse [85].

A single-shot cross-correlation technique exploiting plasma gating has been demonstrated at FLASH [86] and FERMI [83] for the measurement of pulse duration. The technique exploits the transient change in transmission of a material under irradiation of the FEL pulse, the change being probed by a short optical laser pulse. Transient reflectivity or transmission change, in combination with either spectral or spatial encoding of the probe pulse, is also widely exploited as a FEL pulse arrival time monitor; see for example [87, 88, 89, 90]. The FEL pulse impinges on the surface of a thin material (usually a semiconductor e.g. a silicon nitride membrane) at a grazing angle so there is a time to space mapping of the longitudinal profile of the pulse onto the surface. The FEL pulse causes excitation of electrons into the conduction band of the material. If the response is linear with pulse intensity, the excited charge density along the surface is a replica of the longitudinal profile of the pulse. The charge density is probed by looking at the modulated transmission of the IR laser pulse through the material as a function of position along the surface (spatial encoding). The transmitted IR intensity is the cross-correlation of the IR laser pulse profile and plasma gating function. Deconvolution gives the latter, which then gives the temporal profile of the FEL pulse through optical models of the material. If the material is thin enough, there will be good transmission of the FEL pulse and so the measurement can be classed as non-invasive, at least for photon energies away from absorption edges in the material. Fundamental limitations concern the timescale of the photo-excitation processes producing the plasma in the material. These need to be fast compared to the duration of the FEL pulse or the temporal resolution is degraded. At high photon energies where secondary processes dominate, the temporal resolution is reduced to some tens of femtoseconds [86]. The technique is thus mostly suitable for measuring pulse duration rather than profile. Apart from material transmission, practical considerations for UK XFEL include the risk of damage to the material from the FEL pulse, and the need for an IR laser and detector running at the FEL repetition rate to measure every FEL shot.

Recently, a novel technique that requires no external laser was proposed, modelled and then demonstrated on the Shanghai Deep Ultraviolet Free Electron Laser test facility (SDUV-FEL) [91]. The method uses self-referenced spectral interferometry (SRSI) between two x-ray pulses generated from the same electron bunch but with a small temporal delay. It is suggested this method would allow complete spectro-temporal analysis of the FEL pulse in a non-invasive diagnostic with single-shot capability and sub-femtosecond resolution. The principal is that a reference x-ray pulse is generated in a short afterburner undulator with a small temporal delay between it and the main FEL pulse produced by a chicane between the FEL and afterburner. As long as the micro-bunching of electrons is not significantly modified by the chicane, the afterburner

pulse has the same temporal phase as the FEL pulse. Both pulses need an equal frequency shear (which can be produced through 'frequency pulling'). Spatial overlap of the two pulses generates the spectral interferogram which can be analysed to extract the original pulse spectral and temporal profiles. In the test experiment on SDUV-FEL, the pulses were generated at 600 nm so an ordinary optical spectrometer could be used to record the interferogram. For x-ray pulses, spectrometers similar to those described in Section 7.7.4 would be needed. It is not clear how this diagnostic could actually be arranged to be non-invasive; SRSI in optical lasers is an invasive technique. Additionally, aligning the wavefronts of the two pulses with the accuracy required to produce the interferogram will be very challenging at x-ray wavelengths.

7.7.6 Wavefront diagnostics

Measurement of the wavefront of the FEL pulse is important both as an experimental measurement technique and as a diagnostic to aid beamline set-up. The same techniques are used in both cases. The main application for beamline set-up is in optimising the beam focus from e.g. Kirkpatrick-Baez mirror systems, especially when very small foci are required. Additionally, wavefront sensors are used for at-wavelength metrology of beamline optics.

There are methods that can be used to directly measure beam foci, but these have limitations. The focus can be imaged on a scintillating screen, but this must be done with a strongly attenuated beam and is limited to micron spatial resolutions. Knife edge or wire scans are more sensitive but are inherently multi-shot and only accurate if the beam positional jitter is a fraction of the size of the focus. The focus can be measured through assessment of the ablation crater left in a material, however this process requires offline metrology analysis and so is not suitable for routine usage.

A wavefront measurement has the advantage that it is performed remotely from the focus and gives additional information about the beam beyond a simple intensity distribution. Software propagation of the measured wavefront allows the beam profile through the region of focus, and at any other position in the beamline, to be predicted. They can also be used in automated processes for aligning focusing optics [92], which is important for maximising use of limited beamtime resource. The smallest foci achieved on an XFEL was 7 nm; this could only be achieved through wavefront measurement that allowed form errors in the mirrors to be measured and deterministically corrected [20]. Since the best optical metrology is now close to the physical limits of accuracy and resolution, at-wavelength metrology is essential to drive further improvements in the quality of x-ray optics. Wavefront measurements are one way to perform this metrology.

There are several different methods that can be used to characterise the wavefront of a single shot of an XFEL beam. These include: Hartmann wavefront sensors, Talbot grating interferometry (single- and double-grating), and speckle tracking.

Hartmann wavefront sensors are currently used in the XUV / soft x-ray and hard x-ray. The lack of reported use in the tender x-ray region might indicate that further development is required, most likely with the detector. The Hartmann technique involves placing a plate with a grid of pinholes, the Hartmann mask, into the beam. This means the technique is destructive unless an amplitude beam-splitter is used to isolate part of the beam for measurement. An imaging detector behind the mask records the position of the sub-beams from each pinhole, from which the local slope of the wavefront is measured and hence the wavefront reconstructed. FLASH uses Hartmann sensors to measure the wavefront at photon energies from 30 to 310 eV at 10 Hz [93]. The repetition rate is limited by their detector. With the use of a very fast CCD this could be extended to the kilohertz level [94]. However, the need for an imaging detector means that 100 kHz readout is currently not possible. The wavefront at FLASH can be characterised to an accuracy of $\lambda/90$ RMS at 13.5 nm

wavelength [95]. There are commercially available devices from Imagine Optic suitable for the 5 – 25 keV energy range as well as 30 – 300 eV. The hard x-ray sensor has a reduced absolute accuracy of $< \lambda/10$. Either the detector to plate distance or the plate itself needs to be changed to cover large energy ranges for FEL application. Unlike the other methods presented, Hartmann sensors can be used on partially coherent beams and is a commercialised technique.

In single-grating interferometry, a bespoke diffraction grating is positioned in the beam to produce the Talbot pattern, an image of the grating that repeats at regular intervals of the Talbot length from the grating. Unless the measured beam is separated from the main beam with a beam splitter, single grating interferometry will be destructive. The difference between the measured and reference images of the grating can be used to infer the shape of the wavefront. This method can provide measurements with an accuracy of $\lambda/100$ RMS [96]. The Talbot length is photon energy dependent and so the detector or grating will need to move as photon energy is scanned. One grating can cover a bandwidth of about $\pm$10% without translation [97]. Alternatively, multiple gratings can be used to give a consistent Talbot length. In double-grating shearing interferometry, translation of the components isn't required. In this configuration, the second grating is slightly azimuthally rotated with respect to the first. The first order of the first grating interferes with the first order of the second grating forming a Moiré pattern. This pattern can then be used to characterise the wavefront. The zeroth order is unaffected and spatially separated from the interference pattern allowing for a non-invasive measurement.

The double-grating technique is less limited by the detector spatial resolution and can be made more compact [98]. The requirements on the quality of the grating are more stringent in the double-grating interferometer[99]. In single-grating devices, fabrication errors have been shown to not be significant compared to systematic error sources such as misalignment and detector distortion [100]. In both the single- and double-grating configurations, the repetition rate is limited by the detectors and so 100 kHz measurements will not be possible without further detector development. Both types of grating interferometers are suitable for hard x-rays. Single grating interferometry has been achieved up to a photon energy of 183 keV [101]. It has been practically demonstrated down to 8 keV [102]. Double grating interferometry has been demonstrated up to 83 keV [103] and down to 8 keV [104]. These examples are all from synchrotron radiation sources, so transferability to a FEL source is not guaranteed. Development in both grating fabrication and detector technology is currently taking place to extend this technique down to lower photon energies. A suitable grating covering 500 eV to 750 eV has been manufactured [97]. With a suitable grating and high spatial resolution detector, it should be possible to extend the technique down to 100 eV, however further research is required. Achieving this goal will likely be easier for the single grating method than the double.

The speckle tracking method requires an object that produces random scattering, such as sandpaper, to be placed into the beam. The scattered beam will consist of many, randomly distributed, bright spots. By taking an image in two different planes simultaneously and tracking each feature from one image to the other, the wavefront can be reconstructed. This requires two well-aligned, synchronised detectors. The first detector must also be partially transmissive for light to reach the second detector. These images are usually taken with scintillating screens. This method can measure wavefronts to an accuracy of $<$100 nrad [105]. The algorithm used to reconstruct the wavefront is complex; both computation and detector speed currently limit maximum repetition rate and no literature has been found which demonstrates kHz capability. This method is most suited for the hard x-rays due to the need for a transparent speckle mask and first profile monitor. Below 8 keV absorption may prevent the beam from being measured by the second detector [98]. With further research into suitable scattering objects and detectors, it may be possible to extend this technique to higher repetition rates and to tender or even soft x-rays.

Measurement of the wavefront at 100 kHz is not currently possible primarily due to limitations in detector speed; future developments may result in suitable detectors. If single-shot detection is made possible, wavefront sensing could become a crucial part of the data management pipeline. It would allow for quick identification of 'good' and 'bad' pulses, thus saving considerable time in data analysis and resources in data storage. With wavefront sensing, even at less than the machine repetition rate, alignment and optimisation of optics and the accelerator could be automated, streamlining many currently time-consuming and manual procedures. Better quality photon beams and more beamtime delivered to experiments will be a direct consequence of integrating wavefront sensing into machine optimisation procedures.

7.7.7 Commissioning diagnostics

Whilst measuring the photon properties of the pulses delivered to the experiments is a major part of the role of the diagnostic systems, there are additional diagnostics that are required specifically to set the machine up. These are essential for achieving optimal operation of the FEL source itself, but can be invasive systems since they are only required during set-up stages.

A key task is to measure the spectrum of spontaneous radiation from each undulator module. This allows proper tuning of each module and determination of the absolute value of the undulator deflection parameter, K, for a given gap. The undulator spectrum is measured with a photodiode positioned on the output of a removable, channel-cut Bragg crystal monochromator, e.g. Si(111). The energy scale is precisely calibrated against crystal glitches or the absorption edges in foil filters placed in the beam. The Si(333) reflection is used to measure the fundamental or harmonics at higher photon energies. Higher undulator harmonics can be measured when the undulator fundamental falls below the scanning range of the monochromator, though this will likely not be possible if the undulator is set to circular polarisation mode when higher harmonics are all suppressed. Thus, whilst a single monochromator design is able to cover the full range of all the FELs on EuXFEL, a different low-energy monochromator may be required on FEL-6 and FEL-5 of UK XFEL if exact undulator K in circular polarisation mode needs to be determined. Measurement of the spontaneous radiation through the monochromator on a beam imager also allows measurement of the beam pointing at each undulator module and hence determination of the required orbit corrections for optimum lasing [61].

A sensitive intensity monitor, e.g. MCP, is also useful for detecting the on-set of lasing by measuring the total beam intensity over a wide dynamic range. In some circumstances, these can even be used parasitically by detecting the diffuse scatter from the first beamline mirror [61].

Beam imagers as already described are also important for beam alignment through the beamline. Given that the beamline will be inaccessible at any time when there is beam present, a generous provision of imagers with different capabilities (spatial resolution, field of view, sensitivity etc.) along the beamline is essential to study beam position and spatial profile for beam alignment and also for trouble-shooting.

Invasive diagnostics can also be utilised in the calibration of non-invasive diagnostics such as spectrometers and pulse energy monitors. Another example that is important for UK XFEL is in the measurement of the polarisation state of the beam when running in circular polarisation mode. As discussed previously, a photo-electron spectrometer cannot distinguish between circularly polarised and unpolarised radiation. An optical polarimeter such as that described in [106] can determine the exact Stokes vector of the beam but is invasive and requires scanning of both the phase retarder and analyser through 360° of rotation and so is a very time consuming measurement. It will, by its nature, give the average polarisation state over many FEL pulses.

However, it is reasonable to assume the polarisation state of the beam is stable shot-to-shot. Therefore, the optical polarimeter can be used to find the Stokes vector of the beam under known operating conditions and this compared to the PES measurement, allowing an estimation of the unpolarised fraction from the on-line measurements.

7.8 Sustainability

An x-ray beamline in general has very low power consumption during normal operation. They are generally ion-pumped, so electricity consumption for maintaining the vacuum is low except during roughing phase. Bakeout to achieve UHV is also transitory and contributes minimal energy consumption over a year. The optics are mostly passive: mirror alignment motors, Kirkpatrick-Baez benders etc. are very low power and not in continuous use. The greatest power consumption will likely come from:

- Turbo and backing pumps for the gas attenuators and gas-based diagnostics
- Water cooling and cryo-cooling of optics
- Cooling of fast electronics for high repetition rate diagnostics
- Cooling and powering of control racks for the extensive remote control that is an essential part of the beamline operation

The carbon footprint comes mainly from the construction of the beamline itself, i.e. production of the raw materials needed, processing the materials into the finished article and transportation to the site (so-called ‘embodied emissions’). It is therefore important that the beamline design should be correct and that the beamline should meet the needs of the end-user experiments without requiring modification or redesign. For example, if the modelled source properties are far from the actual source properties then significant modifications to the beamline may be required. This could impact beyond simply moving the position of optics if beam tunnels need to be modified and end-stations moved.

Another case is if a beamline is designed with a monochromator that turns out to be unnecessary because the pulse has sufficiently good temporal properties to meet the experimental needs without one. In this example, the considerable resource spent in building a monochromator would be wasted. To mitigate against this, a phased approach to building the beamlines can be adopted (and will be necessary anyway since there is insufficient global production capacity to deliver all beamlines for day-one operation). For example, the ‘attosecond’ beamline on FEL-5 (without monochromator) could be built first and used to measure the spectral properties of the source. Whether a monochromator is needed for the RIXS beamline can then be determined before one is actually built.

Other sustainability issues include:

- Production of high purity gases and other research-grade materials (e.g. as used in XGMD or gas attenuators)
- Consumption of noble gases in gas attenuators and diagnostics (especially krypton and xenon)
- Processing of beryllium for CRLs and windows
- Production of CVD diamond

- Environmental impact of ore mining

7.9 Summary of development areas; R&D needed for future phases to meet specification

An essential next step is to improve the model of the source spatial properties and develop a model of the source temporal properties for each FEL in the facility. This will need to be done for all planned operating modes of the FEL. This will require a large body of simulations of the output of each FEL and an automated process to extract the source terms from the simulations in an efficient manner. Proper design of the x-ray beamlines is not possible without this information.

The requirements for the end-stations also need to be refined so that a definitive set of target beam properties for each of the beamlines is defined. After this, more detailed optical designs of the beamlines can commence. A refined optical design for the beamlines on each FEL will then be followed by a full beamline concept which will include photon diagnostics and beam attenuators. This concept will include detailed analysis of the expected beamline performance and the impact of high peak and average powers.

Technological developments and research studies that will be important include:

- Manufacture of diamond CRLs
- Manufacture of diamond crystals for monochromators and spectrometers
- Manufacture of large diffraction gratings, especially with ultra-low line density, varied line spacings, or very low blaze angles
- Manufacture of multilayer-coated gratings
- Measurement of optic damage thresholds at 100 kHz using existing facilities, especially for metallic coatings like nickel and platinum
- Further modelling of the impact of optics on sub-fs pulses to confirm the conclusions drawn here and extending to Bragg crystals, backed up with actual measurements if possible
- Further studies on the effect of beam transports on the various polarisation states, including exotic states such as orbital angular momentum (OAM)
- Robust simulations of the spectro-temporal profiles of the FEL output to determine the experiments where a spectral filter (monochromator) is required or unnecessary
- The impact of high repetition rate pulses on gas-based components due to localised density reduction and methods to mitigate such effects
- Modelling of non-FEL beam power to understand the total beam power the front-end beamline components must handle and radiation protection requirements, including the size of the beam offset
- Study of systems required for personnel and machine protection, including design of beamstops and protocols for beam alignment and optimisation
- Solid attenuators for kilowatt beams
- Metrology and ion-beam figuring capability to improve and repair optics
- Development of 100 kHz detectors

- Software developments, including machine learning and artificial intelligence, for real-time analysis at high repetition rates of diagnostics data

7.10 Conclusions

In the twenty years since FLASH delivered the first XUV light from a FELto users and the sixteen years since LCLS produced the first hard x-rays, there has been huge development in the beamline technologies required to deliver on the three key requirements of preserving the beam spatial and temporal properties from source to experiment, avoiding optical damage and measuring the beam properties pulse-by-pulse. They have all matured to a point where many of the initial challenges have been successfully addressed. Existing beamlines and diagnostics work to very high levels, and the experience gained with them can be leveraged to make successful photon transports for UK XFEL. A key recommendation for UK XFEL is to establish and maintain close links with existing facilities and suppliers of state-of-the-art optics to ensure beamline designs are sound and can achieve the expected performance.

The new challenges that UK XFEL will present are primarily related to the 100 kHz CW repetition rate, the near-transform limited pulses of controllable duration, and the flexible polarisation.

The high CW repetition rate will result in kilowatt-level average photon beam power from some FELs. Furthermore, the first optics will see a lot of beam power not related to the FEL beam. The recommendation for UK XFEL is for the complete output of the source to be properly modelled and then appropriate mitigation strategies can be devised.

Ultra-short pulses can increase peak power but the major concern for optical damage is from total pulse energies. There is high confidence in the robustness of B4C coatings but less for metallic coatings. In all cases, the move to high repetition-rate CW operation will make multi-shot damage more likely and there is currently limited data on how maximum useable pulse energies will be affected. The recommendation for UK XFEL is to investigate multi-shot damage with existing facilities since the damage limit sets the ultimate pulse energy the beamline can handle.

Flexible polarisation is a key deliverable for UK XFEL but presents new challenges to the beam diagnostics. Photoemission lies at the heart of many diagnostics but is dependent on the beam polarisation. For example, the best diagnostic for polarisation is not able to distinguish between circularly polarised and unpolarised light. Bragg reflection is also polarisation dependent and this will impact crystal-based spectrometers. The recommendation for UK XFEL is to work with existing experts in the field to see how diagnostics can be modified to work with the full range of polarisation states.

The role of monochromators on UK XFEL needs careful consideration. A transform limited pulse with tunable duration should make a monochromator unnecessary in many experiments, and actually unhelpful if the central wavelength jitters by a significant fraction of the bandwidth. Grating monochromators are an integrated part of a beamline design and not easy to retro-fit or remove. The recommendation for UK XFEL is to perform the best simulations possible of the spectral output of the pulses and then to work closely with the user community to clarify the experiments where monochromators will still be considered necessary.

References for Chapter 7

[1] M A Bowler and S P Higgins. *FOCUS - A New Wavefront Propagation Code*. Accessed: June 11 2025. 2009. URL: https://www.esrf.fr/files/live/sites/www/files/events/conferences/2009/SMEXOS/talkBowler.pdf.

[2] Harald Sinn et al. "Design of photon beamlines at the European XFEL". In: *Proc. 32nd Int. Free Electron Laser Conf.(FEL'10)*. 2010, pp. 683–689.

[3] H Sinn et al. "XFEL.EU TR-2011-002 X-ray optics and beam transport". In: *European X-Ray Free-Electron Laser Facility GmbH, Hamburg, Germany* (2011).

[4] JTEC Corporation. *Optical*. Accessed: May 19, 2025. n.d. URL: https://www.j-tec.co.jp/english/optical/optical-products/.

[5] Takahisa Koyama et al. "Damage threshold of coating materials on x-ray mirror for x-ray free electron laser". In: *Review of Scientific Instruments* 87.5 (May 2016), p. 051801. ISSN: 0034-6748. DOI: 10.1063/1.4950723.

[6] Rolf Follath et al. "X-ray induced damage of B_4C-coated bilayer materials under various irradiation conditions". In: *Scientific reports* 9.1 (2019), p. 2029.

[7] Marziyeh Tavakkoly et al. "Comparing single-shot damage thresholds of boron carbide and silicon at the European XFEL". In: *Synchrotron Radiation* 31.5 (2024).

[8] Jacek Krzywinski et al. "Damage threshold of platinum coating used for optics for self-seeding of soft x-ray free electron laser". In: *Opt. Express* 23.5 (Mar. 2015), pp. 5397–5405. DOI: 10.1364/OE.23.005397.

[9] R Soufli et al. "Morphology, microstructure, stress and damage properties of thin film coatings for the LCLS x-ray mirrors". In: *Proc. SPIE 7361*. Vol. 7361. Lawrence Livermore National Lab. (LLNL), Livermore, CA (United States). Apr. 2009. DOI: 10.1117/12.823836. URL: https://www.osti.gov/biblio/953285.

[10] Takahisa Koyama et al. "Investigation of ablation thresholds of optical materials using 1-μm-focusing beam at hard X-ray free electron laser". In: *Optics express* 21.13 (2013), pp. 15382–15388.

[11] J. Chalupský et al. "Damage of amorphous carbon induced by soft x-ray femtosecond pulses above and below the critical angle". In: *Applied Physics Letters* 95.3 (July 2009), p. 031111. ISSN: 0003-6951. DOI: 10.1063/1.3184785.

[12] L. Juha et al. "Radiation damage to amorphous carbon thin films irradiated by multiple 46.9 nm laser shots below the single-shot damage threshold". In: *Journal of Applied Physics* 105.9 (May 2009), p. 093117. ISSN: 0021-8979. DOI: 10.1063/1.3117515.

[13] J Stohr. *Linac Coherent Light Source II (LCLS-II) Conceptual Design Report*. Tech. rep. SLAC National Accelerator Lab., Menlo Park, CA (United States), Nov. 2011. DOI: 10.2172/1029479.

[14] Daniele Cocco et al. "Adaptive shape control of wavefront-preserving X-ray mirrors with active cooling and heating". In: *Opt. Express* 28.13 (June 2020), pp. 19242–19254. DOI: 10.1364/OE.394310.

[15] Thomas E Fornek. *Advanced photon source upgrade project final design report*. Tech. rep. Argonne National Lab.(ANL), Argonne, IL (United States), 2019, pp. 4.1–4.151. URL: https://www.aps.anl.gov/sites/www.aps.anl.gov/files/APS-Uploads/Aps-Upgrade/FDR/Chapter%204%20-%20Experimental%20Facilities.pdf.

[16] Andre Salles and Argonne National Laboratory. *Through the looking glass: How a state-of-the-art optics system will make the APS Upgrade possible*. Accessed: June 11 2025. 2021. URL: https://www.anl.gov/article/through-the-looking-glass-how-a-stateoftheart-optics-system-will-make-the-aps-upgrade-possible.

[17] S Matsuyama et al. "One-dimensional Wolter optics with a sub-50 nm spatial resolution". In: *Opt. Lett.* 35.21 (Nov. 2010), pp. 3583–3585. DOI: 10.1364/OL.35.003583.

[18] R Kodama et al. "Development of an advanced Kirkpatrick–Baez microscope". In: *Opt. Lett.* 21.17 (Sept. 1996), pp. 1321–1323. DOI: 10.1364/OL.21.1321. URL: https://opg.optica.org/ol/abstract.cfm?URI=ol-21-17-1321.

[19] Lei Huang et al. "Manufacturability-based optical design optimization for advanced Kirkpatrick–Baez X-ray focusing mirrors". In: *Opt. Express* 32.15 (July 2024), pp. 25755–25771. DOI: 10.1364/OE.529965.

[20] Jumpei Yamada et al. "Extreme focusing of hard X-ray free-electron laser pulses enables 7 nm focus width and 10^{22} W cm^{-2} intensity". In: *Nature Photonics* 18.7 (2024), pp. 685–690.

[21] Irina Snigireva et al. "Stacked Fresnel Zone Plates for High Energy X–rays". In: *AIP Conference Proceedings* 879.1 (Jan. 2007), pp. 998–1001. ISSN: 0094-243X. DOI: 10.1063/1.2436230.

[22] Ch Morawe and M Osterhoff. "Curved graded multilayers for X-ray nano-focusing optics". In: *Nuclear Instruments and Methods in Physics Research Section A: Accelerators, Spectrometers, Detectors and Associated Equipment* 616.2 (2010). X-Ray Mirror, pp. 98–104. ISSN: 0168-9002. DOI: https://doi.org/10.1016/j.nima.2009.11.064.

[23] Sasa Bajt et al. "X-ray focusing with efficient high-NA multilayer Laue lenses". In: *Light: Science and Applications* 7.3 (2018), pp. 17162–17162.

[24] C David et al. "Nanofocusing of hard X-ray free electron laser pulses using diamond based Fresnel zone plates". In: *Scientific Reports* 1.1 (2011), p. 57.

[25] Ming Wu et al. "Diffraction properties of cylindrically bent KAP crystals in energyrange of 2.3–7.5 keV using synchrotron radiation". In: *Appl. Opt.* 60.3 (Jan. 2021), pp. 558–570. DOI: 10.1364/AO.413678. URL: https://opg.optica.org/ao/abstract.cfm?URI=ao-60-3-558.

[26] L Rumiz et al. "The gas attenuator vacuum system of FERMI@ Elettra". In: *2nd International Particle Accelerator Conference (IPAC)*. JACoW. 2011, p. 1530.

[27] Ulrich Hahn and Kai Tiedtke. "The Gas Attenuator of FLASH at DESY". In: *AIP Conference Proceedings* 879.1 (Jan. 2007), pp. 276–282. ISSN: 0094-243X. DOI: 10.1063/1.2436055.

[28] Raul Villanueva Guerrero. "The Gas Attenuator Instrument for SASE3 Soft X–Ray Beamline at the European XFEL". In: "" POSTER (2014). URL: http://xfel.tind.io/record/1763.

[29] Claude Pradervand et al. "A compact gas attenuator for the SwissFEL ATHOS beamline realized using additive manufacturing". In: *Journal of Synchrotron Radiation* 30.4 (July 2023), pp. 717–722. DOI: 10.1107/S1600577523004241.

[30] D. D. Ryutov et al. *The Physics of the Gas Attenuator for the Linac Coherent Light Source (LCLS)*. Tech. rep. SLAC National Accelerator Lab., Menlo Park, CA (United States), Feb. 2011. DOI: 10.2172/1004930.

[31] Shigeki Owada et al. “A soft X-ray free-electron laser beamline at SACLA: the light source, photon beamline and experimental station”. In: *Journal of Synchrotron Radiation* 25.1 (Jan. 2018), pp. 282–288. DOI: 10.1107/S1600577517015685.

[32] Sang Han Park et al. “PAL-XFEL soft X-ray scientific instruments and X-ray optics: First commissioning results”. In: *Review of Scientific Instruments* 89.5 (May 2018), p. 055105. ISSN: 0034-6748. DOI: 10.1063/1.5023557.

[33] Yiping Feng et al. “Time-dependent simulation of the gas attenuator for the LCLS-II X-ray FEL’s under high beam power operations”. In: *X-Ray Lasers and Coherent X-Ray Sources: Development and Applications XI*. Ed. by Annie Klisnick and Carmen S. Menoni. Vol. 9589. International Society for Optics and Photonics. SPIE, 2015, p. 958910. DOI: 10.1117/12.2186722.

[34] Bo Yang et al. “Fluid dynamics analysis of a gas attenuator for X-ray FELs under high-repetition-rate operation”. In: *Journal of Synchrotron Radiation* 24.3 (May 2017), pp. 547–559. DOI: 10.1107/S1600577517005082.

[35] Alan Fisher et al. “A Plasma Attenuator for Soft X–Rays in LCLS–II”. In: *39th International Free Electron Laser Conference*. 2019, WEP103. DOI: 10.18429/JACoW-FEL2019-WEP103.

[36] Anders Madsen et al. *Technical Design Report: Scientific Instrument MID*. Tech. rep. XFEL.EU TR-2013-005. EuXFEL, 2013, pp. 1–191. DOI: 10.3204/XFEL.EU/TR-2013-005. URL: https://bib-pubdb1.desy.de/record/154260.

[37] Qing Xie et al. “Design and numerical analysis of a solid attenuator for high-repetition-rate X-ray free-electron laser endstation”. In: *Optical Engineering* 63.10 (2024), p. 105102. DOI: 10.1117/1.OE.63.10.105102.

[38] JJ X-Ray. *Attenuator*. Accessed: May 19, 2025. 2025. URL: https://www.jjxray.dk/product/attenuator/.

[39] Marco Malvestuto et al. “The MagneDyn beamline at the FERMI free electron laser”. In: *Review of Scientific Instruments* 93.11 (Nov. 2022), p. 115109. ISSN: 0034-6748. DOI: 10.1063/5.0105261.

[40] JP Guigay et al. “An analytical approach to estimating aberrations in curved multilayer optics for hard x-rays: 1. Derivation of caustic shapes”. In: *Optics Express* 16.16 (2008), pp. 12050–12059.

[41] Steven J. Byrnes. *Multilayer optical calculations*. 2020. URL: https://arxiv.org/abs/1603.02720.

[42] Yeqi Zhuang et al. “Theoretical analysis and development of high efficiency tender x-ray multilayer coated gratings”. In: *Advances in Computational Methods for X-Ray Optics V*. Ed. by Oleg Chubar and Kawal Sawhney. Vol. 11493. International Society for Optics and Photonics. SPIE, 2020, 114930R. DOI: 10.1117/12.2567578.

[43] Andrey Sokolov et al. “Optimized highly efficient multilayer-coated blazed gratings for the tender X-ray region”. In: *Opt. Express* 27.12 (June 2019), pp. 16833–16846. DOI: 10.1364/OE.27.016833.

[44] S Matsuyama et al. “Nanofocusing of X-ray free-electron laser using wavefront-corrected multilayer focusing mirrors”. In: *Scientific reports* 8.1 (2018), p. 17440.

[45] Zsolt Bor, Zoltan Gogolak, and Gabor Szabo. “Femtosecond-resolution pulse-front distortion measurement by time-of-flight interferometry”. In: *Optics letters* 14.16 (1989), pp. 862–864.

[46] Richard H. Pantell et al. “Refractive lenses for coherent x-ray sources”. In: *Appl. Opt.* 40.28 (Oct. 2001), pp. 5100–5105. DOI: 10.1364/AO.40.005100.

[47] Burton L Henke, Eric M Gullikson, and John C Davis. “X-ray interactions: photoabsorption, scattering, transmission, and reflection at E= 50–30,000 eV, Z= 1–92”. In: *Atomic data and nuclear data tables* 54.2 (1993), pp. 181–342.

[48] Brookhaven National Laboratory. *Soft Inelastic X-ray Scattering*. Accessed: May 21, 2025. URL: https://www.bnl.gov/nsls2/beamlines/beamline.php?r=2-ID.

[49] National Institute for Quantum Science and Technology (Japan). *Press Release*. Accessed: May 21, 2025. 2024. URL: https://www.qst.go.jp/site/press/20240918.html.

[50] W Jark. “Enhancement of diffraction grating efficiencies in the soft x-ray region by a multilayer coating”. In: *Optics communications* 60.4 (1986), pp. 201–205.

[51] Shengyou Wen et al. “High efficiency multilayer coated laminar gratings with high line density for tender X-ray region”. In: *Optics & Laser Technology* 168 (2024), p. 109979. ISSN: 0030-3992. DOI: https://doi.org/10.1016/j.optlastec.2023.109979.

[52] K-J Zhou et al. “I21: an advanced high-resolution resonant inelastic X-ray scattering beamline at Diamond Light Source”. In: *Synchrotron Radiation* 29.2 (2022), pp. 563–580.

[53] Theophilos Maltezopoulos et al. “Hard X-ray operation of X-ray gas monitors at the European XFEL”. In: *Journal of Synchrotron Radiation* 31.Pt 4 (2024), p. 681.

[54] Yiping Feng et al. “Time-dependent simulation of the gas attenuator for the LCLS-II X-ray FEL’s under high beam power operations”. In: *X-Ray Lasers and Coherent X-Ray Sources: Development and Applications XI*. Vol. 9589. SPIE. 2015, pp. 125–134.

[55] K Tiedtke et al. “Gas detectors for x-ray lasers”. In: *Journal of Applied Physics* 103.9 (2008).

[56] S Moeller et al. “Photon beamlines and diagnostics at LCLS”. In: *Nuclear Instruments and Methods in Physics Research Section A: Accelerators, Spectrometers, Detectors and Associated Equipment* 635.1, Supplement (2011). PhotonDiag 2010, S6–S11. ISSN: 0168-9002. DOI: https://doi.org/10.1016/j.nima.2010.10.125.

[57] Pavle Juranić et al. “SwissFEL Aramis beamline photon diagnostics”. In: *Journal of Synchrotron Radiation* 25.4 (July 2018), pp. 1238–1248. DOI: 10.1107/S1600577518005775.

[58] Takahiro Tanaka et al. “Absolute laser-intensity measurement and online monitor calibration using a calorimeter at a soft X-ray free-electron laser beamline in SACLA”. In: *Nuclear Instruments and Methods in Physics Research Section A: Accelerators, Spectrometers, Detectors and Associated Equipment* 894 (2018), pp. 107–110. ISSN: 0168-9002. DOI: https://doi.org/10.1016/j.nima.2018.03.045.

[59] M. Zangrando et al. “The photon analysis, delivery, and reduction system at the FERMI@ Elettra free electron laser user facility”. In: *Review of Scientific Instruments* 80.11 (Nov. 2009), p. 113110. ISSN: 0034-6748. DOI: 10.1063/1.3262502.

[60] Seonghan Kim et al. “Development of an X-ray ionization beam position monitor for PAL-XFEL soft X-rays”. In: *Journal of Synchrotron Radiation* 31.5 (Sept. 2024), pp. 1019–1028. DOI: 10.1107/S1600577524006003.

[61] Jan Grünert et al. “X-ray photon diagnostics at the European XFEL”. In: *Journal of Synchrotron Radiation* 26.5 (Sept. 2019), pp. 1422–1431. DOI: 10.1107/S1600577519006611.

[62] Andrey A. Sorokin et al. “An X-ray gas monitor for free-electron lasers”. In: *Journal of Synchrotron Radiation* 26.4 (July 2019), pp. 1092–1100. DOI: 10.1107/S1600577519005174.

[63] Andreas Koch et al. “Design and initial characterisation of X-ray beam diagnostic imagers for the European XFEL”. In: *Proc. SPIE 9512, Advances in Computational Methods for X-Ray Optics VI*. May 2015, 95121R–95121R. DOI: 10.1117/12.2182463.

[64] Pratip Mitra. “A feasibility study on the use of Silicon PIN Diodes for Environmental Gamma Monitoring”. PhD thesis. Unknown, Sept. 2013.

[65] Tuba Çonka Yıldız et al. “Diamond sensors for hard X-ray energy and position resolving measurements at the European XFEL”. In: *Journal of Synchrotron Radiation* 31.5 (Sept. 2024), pp. 1029–1036. DOI: 10.1107/S1600577524006015.

[66] G. Brenner et al. “First results from the online variable line spacing grating spectrometer at FLASH”. In: *Nuclear Instruments and Methods in Physics Research Section A: Accelerators, Spectrometers, Detectors and Associated Equipment* 635.1, Supplement (2011). PhotonDiag 2010, S99–S103. ISSN: 0168-9002. DOI: https://doi.org/10.1016/j.nima.2010.09.134.

[67] Cristian Svetina et al. “PRESTO, the on-line photon energy spectrometer at FERMI: design, features and commissioning results”. In: *Journal of Synchrotron Radiation* 23.1 (Jan. 2016), pp. 35–42. DOI: 10.1107/S1600577515021116.

[68] Paul Scherrer Institute (Switzerland). *GOTTHARD: a Gain Optimizing microsTrip sysTem witH Analog ReaDout*. Accessed: May 21, 2025. 2025. URL: https://www.psi.ch/en/lxn/gotthard.

[69] Diling Zhu et al. “A single-shot transmissive spectrometer for hard x-ray free electron lasers”. In: *Applied Physics Letters* 101.3 (July 2012), p. 034103. ISSN: 0003-6951. DOI: 10.1063/1.4736725.

[70] M. Makita et al. “High-resolution single-shot spectral monitoring of hard x-ray free-electron laser radiation”. In: *Optica* 2.10 (Oct. 2015), pp. 912–916. DOI: 10.1364/OPTICA.2.000912.

[71] David Rich et al. “The LCLS variable-energy hard X-ray single-shot spectrometer”. In: *Journal of Synchrotron Radiation* 23.1 (Jan. 2016), pp. 3–9. DOI: 10.1107/S1600577515022559.

[72] Naresh Kujala et al. “Hard x-ray single-shot spectrometer at the European X-ray Free-Electron Laser”. In: *Review of Scientific Instruments* 91.10 (Oct. 2020), p. 103101. ISSN: 0034-6748. DOI: 10.1063/5.0019935.

[73] Petri Karvinen et al. “Single-shot analysis of hard x-ray laser radiation using a noninvasive grating spectrometer”. In: *Opt. Lett.* 37.24 (Dec. 2012), pp. 5073–5075. DOI: 10.1364/OL.37.005073.

[74] Fady Bishara. *Beamline Automation, Optimization, and Control Activities at the European XFEL*. Presented at PhotonDiag 2025 Conference, Liverpool, UK. 2025. URL: https://indico.stfc.ac.uk/event/1424/page/152-book-of-abstracts.

[75] Markus Braune et al. “A non-invasive online photoionization spectrometer for FLASH2 and present benchmark”. In: *Journal of Synchrotron Radiation* 23.1 (Jan. 2016), pp. 10–20. DOI: 10.1107/S1600577515022675.

[76] Markus Braune et al. “Non-invasive online wavelength measurements at FLASH2 and present benchmark”. In: *Journal of Synchrotron Radiation* 25.1 (Jan. 2018), pp. 3–15. DOI: 10.1107/S1600577517013893.

[77] J. Buck and DESY. “Conceptual Design Report: Online Time-of-Flight Photoemission Spectrometer for X-Ray Photon Diagnostics”. In: *Technical Report* (2012). DOI: 10.3204/XFEL.EU/TR-2012-002. URL: https://bib-pubdb1.desy.de/record/139332.

[78] Joakim Laksman et al. “Commissioning of a photoelectron spectrometer for soft X-ray photon diagnostics at the European XFEL”. In: *Journal of Synchrotron Radiation* 26.4 (July 2019), pp. 1010–1016. DOI: 10.1107/S1600577519003552.

[79] N Hartmann et al. “Attosecond time–energy structure of X-ray free-electron laser pulses”. In: *Nature Photonics* 12.4 (2018), pp. 215–220. URL: https://doi.org/10.1038/s41566-018-0107-6.

[80] P N Juranić et al. “A scheme for a shot-to-shot, femtosecond-resolved pulse length and arrival time measurement of free electron laser x-ray pulses that overcomes the time jitter problem between the FEL and the laser”. In: *Journal of Instrumentation* 9.03 (Mar. 2014), P03006. DOI: 10.1088/1748-0221/9/03/P03006. URL: https://dx.doi.org/10.1088/1748-0221/9/03/P03006.

[81] P. N. Juranić et al. “High-precision x-ray FEL pulse arrival time measurements at SACLA by a THz streak camera with Xe clusters”. In: *Opt. Express* 22.24 (Dec. 2014), pp. 30004–30012. DOI: 10.1364/OE.22.030004. URL: https://opg.optica.org/oe/abstract.cfm?URI=oe-22-24-30004.

[82] Ishkhan Gorgisyan et al. “THz streak camera method for synchronous arrival time measurement of two-color hard X-ray FEL pulses”. In: *Opt. Express* 25.3 (Feb. 2017), pp. 2080–2091. DOI: 10.1364/OE.25.002080. URL: https://opg.optica.org/oe/abstract.cfm?URI=oe-25-3-2080.

[83] Paola Finetti et al. “Pulse Duration of Seeded Free-Electron Lasers”. In: *Phys. Rev. X* 7 (2 June 2017), p. 021043. DOI: 10.1103/PhysRevX.7.021043.

[84] P. Radcliffe et al. “Single-shot characterization of independent femtosecond extreme ultraviolet free electron and infrared laser pulses”. In: *Applied Physics Letters* 90.13 (Mar. 2007), p. 131108. ISSN: 0003-6951. DOI: 10.1063/1.2716360.

[85] Wolfram Helml et al. “Measuring the temporal structure of few-femtosecond free-electron laser X-ray pulses directly in the time domain”. In: *Nature photonics* 8.12 (2014), pp. 950–957.

[86] R Riedel et al. “Single-shot pulse duration monitor for extreme ultraviolet and X-ray free-electron lasers”. In: *Nature communications* 4.1 (2013), p. 1731.

[87] Mina R. Bionta et al. “Spectral encoding of x-ray / optical relative delay”. In: *Opt. Express* 19.22 (Oct. 2011), pp. 21855–21865. DOI: 10.1364/OE.19.021855. URL: https://opg.optica.org/oe/abstract.cfm?URI=oe-19-22-21855.

[88] M. Beye et al. “X-ray pulse preserving single-shot optical cross-correlation method for improved experimental temporal resolution”. In: *Applied Physics Letters* 100.12 (Mar. 2012), p. 121108. ISSN: 0003-6951. DOI: 10.1063/1.3695164. URL: https://doi.org/10.1063/1.3695164.

[89] O. Krupin et al. “Temporal cross-correlation of x-ray free electron and optical lasers using soft x-ray pulse induced transient reflectivity”. In: *Opt. Express* 20.10 (May 2012), pp. 11396–11406. DOI: 10.1364/OE.20.011396. URL: https://opg.optica.org/oe/abstract.cfm?URI=oe-20-10-11396.

[90] Shigeki Owada et al. “Arrival timing diagnostics at a soft X-ray free-electron laser beamline of SACLA BL1”. In: *Journal of Synchrotron Radiation* 26.3 (May 2019), pp. 887–890. DOI: 10.1107/S1600577519002315. URL: https://doi.org/10.1107/S1600577519002315.

[91] Yaozong Xiao et al. “Self-Referenced Spectral Interferometry for Single-Shot Characterization of Ultrashort Free-Electron Laser Pulses”. In: *Phys. Rev. Lett.* 131 (20 Nov. 2023), p. 205002. DOI: 10.1103/PhysRevLett.131.205002.

[92] Pascal Mercère et al. “Automatic alignment of a Kirkpatrick-Baez active optic by use of a soft-x-ray Hartmann wavefront sensor”. In: *Opt. Lett.* 31.2 (Jan. 2006), pp. 199–201. DOI: 10.1364/OL.31.000199.

[93] Barbara Keitel et al. “Hartmann wavefront sensors and their application at FLASH”. In: *Journal of Synchrotron Radiation* 23.1 (Jan. 2016), pp. 43–49. DOI: 10.1107/S1600577515020354.

[94] Azriel Goldschmidt et al. “VeryFastCCD: a high frame rate soft X-ray detector”. In: *Frontiers in Physics* 11 (2023), p. 1285350.

[95] Bernhard Flöter et al. “EUV Hartmann sensor for wavefront measurements at the Free-electron LASer in Hamburg”. In: *New Journal of Physics* 12.8 (2010), p. 083015.

[96] Yanwei Liu et al. “High-accuracy wavefront sensing for x-ray free electron lasers”. In: *Optica* 5.8 (Aug. 2018), pp. 967–975. DOI: 10.1364/OPTICA.5.000967.

[97] Kenneth A. Goldberg, Antoine Wojdyla, and Diane Bryant. “Binary Amplitude Reflection Gratings for X-ray Shearing and Hartmann Wavefront Sensors”. In: *Sensors* 21.2 (2021). ISSN: 1424-8220. DOI: 10.3390/s21020536.

[98] Matthew Seaberg et al. “Wavefront sensing at X-ray free-electron lasers”. In: *Journal of Synchrotron Radiation* 26.4 (July 2019), pp. 1115–1126. DOI: 10.1107/S1600577519005721.

[99] Mikako Makita et al. “Double grating shearing interferometry for X-ray free-electron laser beams”. In: *Optica* 7.5 (May 2020), pp. 404–409. DOI: 10.1364/OPTICA.390601.

[100] Jumpei Yamada et al. “X-Ray Single-Grating Interferometry for Wavefront Measurement and Correction of Hard X-Ray Nanofocusing Mirrors”. In: *Sensors* 20.24 (2020). ISSN: 1424-8220. DOI: 10.3390/s20247356. URL: https://www.mdpi.com/1424-8220/20/24/7356.

[101] M. Ruiz-Yaniz et al. “X-ray grating interferometry at photon energies over 180 keV”. In: *Applied Physics Letters* 106.15 (Apr. 2015), p. 151105. ISSN: 0003-6951. DOI: 10.1063/1.4917293.

[102] Lahsen Assoufid et al. “Development and implementation of a portable grating interferometer system as a standard tool for testing optics at the Advanced Photon Source beamline 1-BM”. In: *Review of Scientific Instruments* 87.5 (May 2016), p. 052004. ISSN: 0034-6748. DOI: 10.1063/1.4950775.

[103] Marian Willner et al. “Quantitative X-ray phase-contrast computed tomography at 82 keV”. In: *Opt. Express* 21.4 (Feb. 2013), pp. 4155–4166. DOI: 10.1364/OE.21.004155.

[104] Gabriel Pérez-Callejo et al. “Phase imaging of irradiated foils at the OMEGA EP facility using phase-stepping X-ray Talbot-Lau deflectometry”. In: *High Power Laser Science and Engineering* 11 (May 2023), pp. 1–11. DOI: 10.1017/hpl.2023.44.

[105] Sebastien Berujon, Eric Ziegler, and Peter Cloetens. “X-ray pulse wavefront metrology using speckle tracking”. In: *Synchrotron Radiation* 22.4 (2015), pp. 886–894.

[106] H. Wang et al. “High-precision soft x-ray polarimeter at Diamond Light Source”. In: *Review of Scientific Instruments* 82.12 (Dec. 2011), p. 123301. ISSN: 0034-6748. DOI: 10.1063/1.3665928. URL: https://doi.org/10.1063/1.3665928.

DRAFT

Theme 3:

World-class end stations, synchronous sources, data and AI

8 End stations

8.1 Introduction

8.1.1 Chapter outline

This chapter outlines an initial provision of end stations for UK XFEL across FELs 1-6 that will exploit the cutting-edge capabilities of the facility to enable a high throughput of pioneering research in the physical and life sciences as well as in technological and industrial applications. The end stations and associated support infrastructure outlined in this chapter are an initial concept that will be revised over coming years as the priorities of the user community evolve and state-of-the-art technology develops at current XFELs. The work presented in this chapter has been delivered with significant input and exchanges with both the user community as well as other closely related work packages in UK XFEL, especially those dealing with FELs and undulators (Chapter 6), photon beams (Chapter 7), synchronous sources (Chapter 9) and detectors (Chapter 10).

This introductory section outlines how the proposed end station provision was arrived at through design choices and extensive consultation. Section 8.2 provides a top-level overview of each of the end-stations. Section 8.3 discusses some of the auxiliary infrastructure required in addition to the experimental hutches themselves to prepare for and deliver efficient operation of user beamtimes.

8.1.2 Design methodology

The end station provision for the facility has been designed primarily around the specific requirements of the UK XFEL Science and Technology Case. A survey of the high demand baseline experimental set-ups at various operating FELs was used to inform design discussions. It is assumed that up to 3 end stations could be positioned on each FEL, with the X-ray beam deflected left / right or allowed to propagate straight on. Not all of these potential end stations have been allocated for a specific capability at this time, however the space will be reserved for future end stations that could be commissioned in future years to suit user demand and respond to national need.

The end stations presented here have been designed to exploit the flagship next-generation UK XFEL parameters including high repetition rates (up to 100 kHz), highly synchronised (and tuneable) secondary sources, transform limited operation and delivery of widely separated multi-colour X-ray pulses to a single end station. However, a particular focus has been the simultaneous operation of multiple end stations, and more broadly the ability to maximise the level of scientific output by focusing on optimisation of user operations.

A large driver for this is the ability to deliver beamtime to up to (initially) 6 end stations simultaneously, thus significantly increasing the level of scientific output compared to many other currently operating XFELs. Staggering beam times could allow most end stations to operate within a typical

week, provided that set-up and operation periods were appropriately coordinated and shared between experiments. In addition, throughout the design process a central theme has been how the end stations can be designed to minimise set-up periods and facilitate rapid switchover between configurations. This could take the form of either multiple interaction points per end station, thus catering for several standardised set-ups, or several roll-in / roll-out chambers that could be configured offline in a neighbouring lab when not in use.

Where possible the priority has been placed on providing several semi-permanent set-ups within an end station rather than rely on exchanging significant parts of each experiment between runs. As a result, several end stations feature multiple interaction points (IPs) in their design. Although not able to operate independently, this approach will minimise changeover time between similarly configured experiments. Having multiple interaction points on several end stations is also motivated by the need to cater for very different sample types, e.g. solid state and liquid jets. While some chambers can accommodate both, many configurations have strict requirements on vacuum and contamination that would not make this possible.

However, a capability must be maintained, either through the existing end stations or through spare open ports, to experiment with non-standard novel set-ups that may require extensive set-up time outside of routine operations. Spare capacity must be maintained (ideally on each FEL) to permit development of new detection techniques, novel X-ray delivery modes or sample delivery in order to future-proof UK XFEL for the many years of operation beyond first light.

Early consideration has been given as to whether parts of the end stations will be core capabilities designed and operated by UK XFEL, and whether some capabilities could be provided by user consortia, either for early operations or as part of future upgrades. While this is ultimately a decision for much later in the design process, ongoing close scientific and technical collaboration with user groups from the UK and abroad will be critical in order to fully realise the potential of UK XFEL, and such a model has proven quite successful with other operating XFELs. Once more is known about which key areas of R&D are required to deliver truly unique techniques for UK XFEL then it will be possible in the technical design stage to clarify how the end stations can be best delivered as a combination of facility and user-led capabilities.

8.1.3 User and facility engagement process

In order to arrive at this point in the conceptual design an extensive consultation process has taken place both with regular users of XFELs (and other facilities) as well as technical experts at existing XFELs around the world. This process started at the beginning of the CDOA with two surveys of the existing XFEL community in the UK to better understand what cutting-edge science each user group wished to see happen in 5-10 years, and what technical requirements would be needed to deliver on this. This first step helped to map out what energies the proposed 6 FEL design would need to cover as a starting point.

Over the next two years UK XFEL organised several themed town hall meetings in order to better understand the main scientific (and industrial) applications for XFELs now, and to identify which user communities (currently not using XFELs) could potentially benefit from applying time-resolved XFEL techniques to their research. This was followed up by a series of smaller online consultations with users focused on particular XFEL detection themes. For example several meetings were held to discuss photoelectron spectroscopy methods spanning energy ranges from 50 eV to 13 keV. These meetings were partly to understand the scientific motivation for using such methods on XFELs (as opposed to synchrotrons or high harmonic sources for example), but also to examine

technical and operational requirements for a future UK XFEL. Common discussion points across all these meetings included:

- What are the growth areas in XFEL science in the UK and internationally?
- What limitations are currently encountered in delivering some potential flagship science experiments on existing XFELs?
- How could UK XFEL overcome some of these limitations through either its unique X-ray or end station capabilities?
- Which successful features of currently operational XFEL end stations should be integrated into the design of the UK XFEL?
- What additional offline support facilities do we need to focus on to ensure successful delivery or beamtime at each end station?
- How can our design and operational decisions help attract new users to XFEL science and lower common barriers to entry?

In 2024 and 2025 two in-person UK XFEL end station away days were held with upwards of 40 members of the user community, together with 10-15 of the UK XFEL design team, to review the overall concept for end stations. These meetings were particularly helpful in identifying where UK XFEL could be unique compared to other operational XFELs, as well research and development priorities that would be required to deliver some of the flagship capabilities that would be expected to be widely available to users in $\sim$10 years' time.

Representatives from XFELs around the world, including end station and instrument leads, were also consulted during the CDOA process, either as part of the wider discussions above or in smaller, targeted discussions where typically 2 or 3 meetings were held for each end station. This part of the consultation process was particularly helpful in understanding how each facility progressed from their conceptual design to the final operational end station. It was also incredibly valuable to learn from the extensive operational experience of expert facility staff to understand where aspects of end station design have posed challenges in practice and how they might approach things differently if starting over with today's knowledge and technological maturity.

8.2 Overview of end stations for UK XFEL

This section will step through each of the proposed end stations for UK XFEL. For the purposes of this conceptual design the scientific context applicable to each end station is briefly presented, followed by any particular opportunities identified that UK XFEL can address with its unique beam and operational modes. The key technical requirements for each end station are then summarised at a high level, including detection methods, X-ray beam parameters, sample delivery, and secondary sources. At the next stage of the design process, each end station will need to be laid out in detail including all aspects of beam delivery and diagnostics, interaction chambers, optical pump lasers, large area detectors and all required mechanical and electrical services.

Figure 8.1 shows an overview and naming scheme for each of the initial end stations for UK XFEL (ES1 - ES13). It should be noted that spare ports are not shown, though should be assumed as an option where each FEL has fewer than 3 occupied end stations. A brief summary of capabilities is as follows:

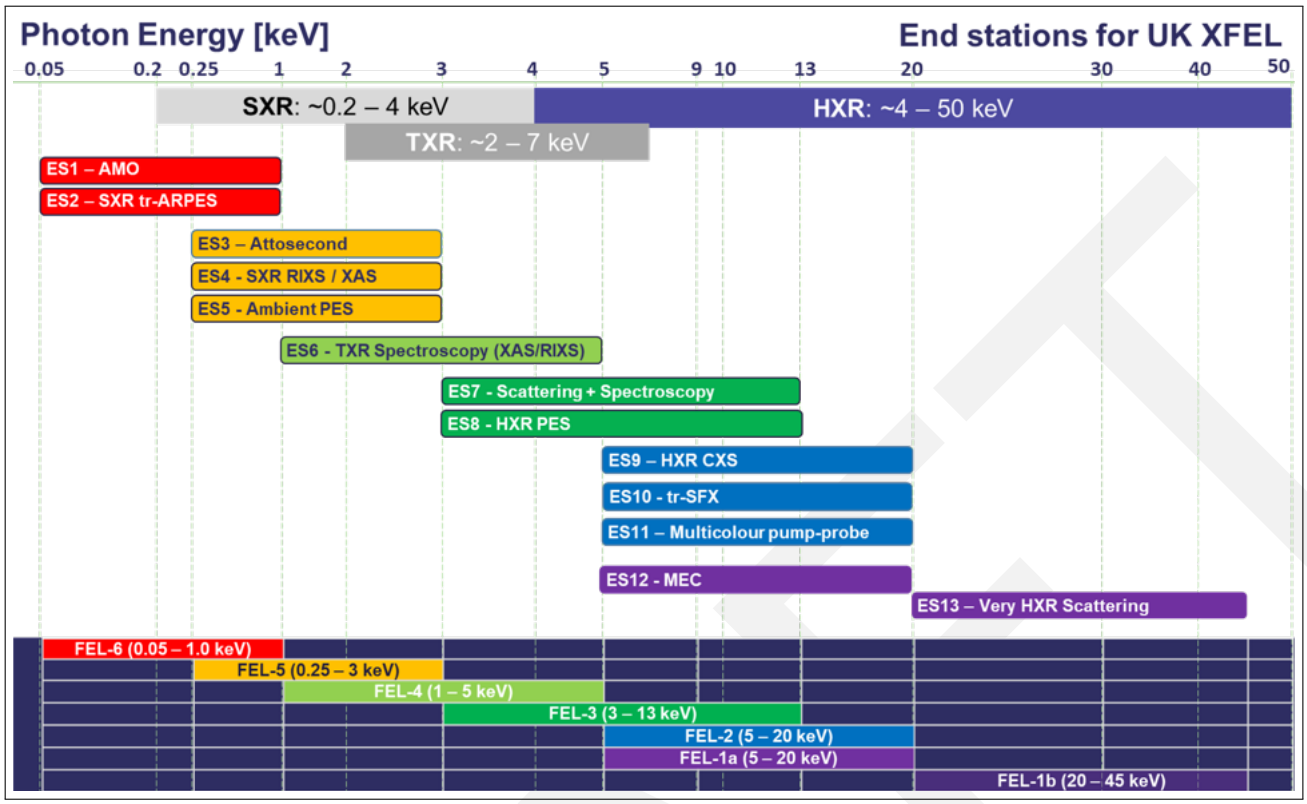

Figure 8.1: Map of proposed end stations for UK XFEL across all of the FELs covering the soft X-ray (SXR), tender X-ray (TXR) and hard X-ray (HXR) range.

- ES1 - AMO - Research in atomic, molecular, and optical (AMO) physics and chemistry aimed at resolving complex single- and multi-photon processes on ultrafast timescales, utilising the combination of high intensity, coherence, and repetition rate of UK XFEL.
- ES2 - SXR tr-ARPES - Angle-resolved photoemission spectroscopy techniques over a broad XUV-SXR range for high throughput studies of ultrafast processes at surfaces and quantum materials.
- ES3 - Attosecond - Very highest X-ray time resolution for studying attosecond electron dynamics for AMO and photo-induced processes in chemistry and biology.
- ES4 - SXR RIXS / XAS - High-resolution, time-resolved RIXS, XAS, and XES methods across 0.25-3 keV for studying ultrafast dynamics in quantum materials and complex chemical systems.
- ES5 - Ambient PES - Application of PES techniques over SXR-TXR range (0.25-3 keV) with complex sample configurations relevant to catalysis, batteries and biomaterials.
- ES6 - TXR Spectroscopy - Flexible platform for time-resolved X-ray spectroscopy (and scattering) bridging the soft to tender X-ray range (1-5 keV), enabling studies of ultrafast catalytic, biological, and magnetic dynamics with high spectral and spatial resolution.
- ES7 - Scattering and Spectroscopy - Ultrafast time-resolved spectroscopy and scattering in the hard X-ray regime (3-13 keV), with flexible sample environments and pump-probe capabilities for studying structural and electronic dynamics.
- ES8 - HXR PES - Hard X-ray photoelectron spectroscopy (HAXPES) for bulk-sensitive chemical analysis of buried interfaces and materials in-operando.

- ES9 - HXR CXS - Application of coherent X-ray scattering (CXS) techniques to investigate nanoscale materials and dynamic processes in complex systems, enabled by flexible detector and sample setups for a wide-range of experimental configurations.
- ES10 - tr-SFX - Time-resolved X-ray serial femtosecond crystallography (tr-SFX) at high repetition rates to study macromolecules and small chemical systems with the very highest spatial and temporal resolutions.
- ES11 - Multi-colour pump-probe - Flexible experimental platform for advanced dual-colour X-ray experiments with widely separated, independent soft and hard X-rays for pump-probe or sequential probing of transient states.
- ES12 - MEC - Cutting-edge platform for studying materials under extreme conditions (MEC), driven primarily by high-power lasers for the application hard X-ray spectroscopy and scattering techniques supporting research in laboratory astrophysics, ICF and materials under dynamic compression.
- ES13 - Very HXR Scattering - Dedicated platform for imaging and time-resolved scattering at very hard X-ray energies (20-45 keV), enabling studies of high-density materials under dynamic compression or in-operando conditions, as well as high-resolution, time-resolved pair distribution function (PDF) measurements.

8.2.1 ES1 (AMO) and (ES3) Attosecond

Atomic, molecular, and optical (AMO) physics and chemistry is a field ideally suited to X-ray free-electron lasers (XFELs). Their ultra-short pulse durations, from the femtosecond to attosecond regime, combined with high X-ray intensities and a high degree of coherence, provide optimal conditions for studying single- or multi-photon-induced processes on the fastest timescales [1, 2, 3]. These experiments typically involve the focusing of an XFEL probe beam to a gas, cluster or liquid phase sample, which has been pumped by either a highly synchronised optical pulse, or by an X-ray pulse that has been split from the main beam. Experiments centre around electron and ion spectroscopy where analysis of all the fragments of the reaction are used to characterise the complex ionisation, recombination and charge redistribution processes. Current end stations in operation with a strong focus on these types of experiments include TMO at LCLS-II, SQS at European XFEL, FL26 at FLASH, Maloja at SwissFEL and LDM at FERMI. FEL-5 and FEL-6 on UK XFEL are particularly well placed to cater for these end stations and provide some unique capabilities not available at other operating XFEL facilities:

- X-ray energies from 50–1000 eV on FEL-6 and 250–3000 eV on FEL-5 cover the range required to directly excite not only valence but also the core electrons of many important elements.
- Ability to deliver high pulse energies across this range at high repetition rates (up to 100 kHz initially).
- Ability to access both ultra-short pulse durations for the very highest temporal resolution (sub-femtosecond) or the narrowest spectral bandwidths (10's of meV) where longitudinal coherence is a priority.
- Availability of highly tuneable optical sources or multiple X-rays via split and delay techniques, both with a high degree of spatial and temporal synchronisation.

Since there are extensive overlaps between the sample and detection requirements of ES1 and ES3, every effort will be made to ensure consistent design in mounting systems, flanges etc. to enable exchange of systems between end stations if required.

8.2.1.1 ES1 - AMO (FEL-6 0.05-1keV)

ES1 (FEL-1) will focus on ultra-fast pump-probe AMO experiments primarily in the gas phase, although provision could be made for liquid sample delivery in some circumstances. ES1 will feature two interaction points (IP1 and IP2), separated by several metres to allow sufficient space for differential pumping as well as independent beam diagnostics, optical pump beam injection and synchronisation systems. Many of these experiments require the highest X-ray intensities so spot sizes on the order of 1-3 μm must be achievable as well as high pulse energies at both interaction points. In order to achieve this, it is likely that two, independent sets of KB mirrors will be used in a configuration as below:

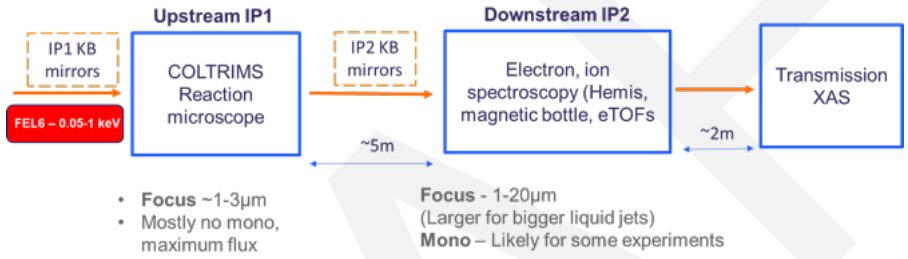

Figure 8.2: Planned configuration for ES1 for AMO experiments on FEL-6 using soft X-ray energies (0.05 - 1 keV)

The first (IP1 - upstream) will feature a cold-target recoil-ion momentum spectrometer (COLTRIMS) capable of measuring the momenta of charged reaction fragments in coincidence [4]. This would be exclusive to gas phase experiments (due to stringent vacuum requirements) and be of particular interest for Coulomb Explosion Imaging (CEI) and electron-ion coincidence experiments for resolving ultrafast electronic processes in molecules [5, 6, 7]. The matching repetition rate of UK XFEL and optical pump systems will permit the acquisition of large data sets required by such methods. A molecular gas-jet sample delivery system will be required to provide shaped jets as well as tuneable pressures and temperatures at such a repetition rate. Full polarisation control possible on FEL-6 will also extend such techniques to study the effects of chirality under different conditions.

IP2 will need to cater for various sample systems including atomic or molecular gases [8], clusters/nanoparticles [9] as well as particles and biomolecules in droplets and liquid jets. The X-ray beam will be required to be focused to a range of 1-20 μm, typically matched to the size of pump beams and/or sample jet size. Liquid experiments may require slightly larger spots. The IP2 chamber will have to operate under a range of vacuum conditions, the most stringent of which will require ultra-high conditions ($<10^{-10}$ mbar) to minimise background signal. If liquid samples are required on IP2 for some experiments (likely in a run of configured access), it may be a requirement to implement a version of a roll-in / roll-out sample chamber in order to minimise the risk of persistent contamination that could occur for subsequent gas-phase campaigns.

A comprehensive set of high-resolution electron and ion analysers will be essential to ensure complete coverage of options on kinetic energy and angular resolution, as well as to maximise collection efficiency. High-resolution electron spectroscopy via multiple electron time of flight (TOF) detectors placed at various angles around the interaction will provide high energy and angular resolution. For higher angular resolution (but lower energy resolution) and chiral measurements a

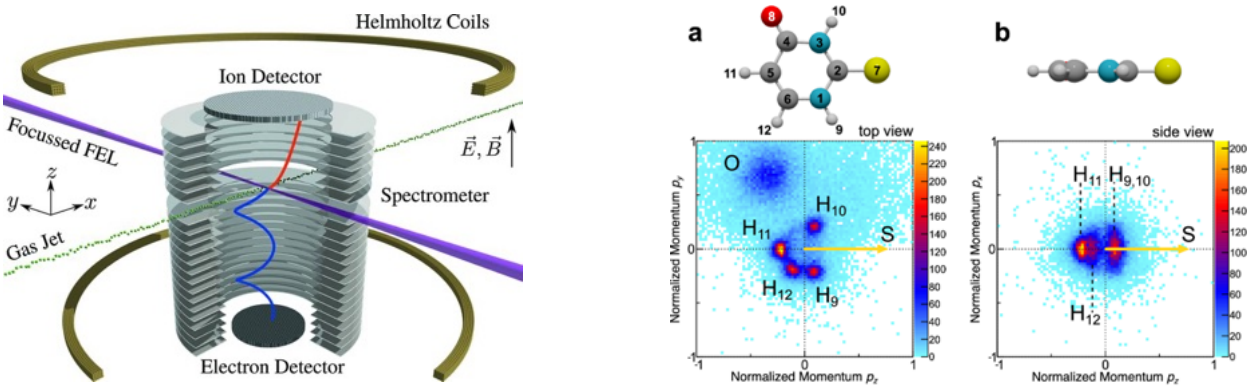

Figure 8.3: (Left) - Principle of operation of a reaction microscope. Reproduced from G. Schmid *et al.* J. Synchrotron Rad. **26**, 854-867 2953 (2019) (Right) - Coulomb explosion momentum-space images of 2-thiouracil obtained from the COLTRIMS reaction microscope at SQS on European XFEL. (a) Top view projection of the measured momentum-space data of the oxygen ions and the protons (b) "Side view" projection of the measured proton momenta. Figure adapted from T. Jahnke *et al.* Nat Comms. **16** 2074 (2025).

Velocity Map Imager (VMI) could be used either for electrons, or for ion fragments. A magnetic bottle spectrometer (MBES) set-up will likely be required by users to achieve high (kinetic energy) resolution measurements of higher energy electrons. MBES typically feature high collection efficiency although their implementation can require an spatial offset in interaction point compared to other diagnostics. Alternatively, two or more pre-configured set-ups for IP2 could be offered to ensure minimal set-up time between similar experiments.

A dispersive spectrometer will sit at the end of the beamline (after IP2). This would primarily be used for accurate recording of X-ray spectra but could be used to measure XAS.

Optical pumping from the UV (down to ∼200 nm) up to the Mid-IR (∼20 μm) is envisioned for ES1 via synchronised, femtosecond laser pulses. Further design will be required to specify exact coupling-in points along the beamline for each interaction point as well as well as the array of optical diagnostics required in the end station. The optical pump beam(s) should be able to match the maximum operating rate of the XFEL (up to 100 kHz initially) and be synchronised to better than ∼20 fs (for most experiments).

8.2.1.2 ES3 - Attosecond (FEL-5 0.25-3 keV)

ES3 (FEL-5) will focus on experiments at the very shortest pulse durations, down to 100's attoseconds for X-ray energies between 0.25 - 3 keV. Such short pulses will permit the tracking of electrons on their natural time scale and open up new experiments studying charge migration and its effect on longer-timescale dynamics, with applications across photo-induced processes in chemistry and biology [10, 11, 12]. XFEL sources are now able to produce tuneable, broadband attosecond X-ray pulses at high peak powers [13]. With pulse energies many orders of magnitude brighter than laser-based sources, and the ability to scale to significantly higher X-ray energies, there are a range of new types of experiments across AMO, materials science and condensed matter physics that need to be catered for on UK XFEL.

It should be noted that attosecond pulse durations will not be exclusive to FEL-5, but FEL-5 (and ES3) will be the first to implement this mode for user beamtime. In addition, it will also be possible to field longer pulse experiments on ES3 (from few fs to ∼100 fs), where very similar experiments to ES-1 can be implemented at higher fundamental X-ray energies.

ES3 will feature two interaction points in a similar mode to ES1. The first (IP1) will be modelled on the successful demonstration of ”MRCOFFEE” on LCLSII at the TMO end station [14], an angularly resolving array of electron TOF detectors. IP1 will serve two purposes - the first is high resolution photoelectron spectroscopy for high intensity, non-linear processes, the second is temporal characterisation of attosecond pulses produced on FEL-5.

Figure 8.4: Planned configuration for ES3 for experiments on FEL-5 for ultra-short pulse (attosecond) soft x-ray experiments

When operating in a short-pulse mode it is planned for IP1 and IP2 to be used simultaneously to permit accurate pulse length measurement (and synchronisation) in IP1 before the main interaction in IP2. Focal spots from 1 μm upwards will be required in IP1 and IP2, along with an ability to host a range of sample types in a similar fashion to ES1 IP2 covering gas to condensed phase. All sample delivery systems (along with detectors) will need to be matched to required XFEL repetition rates, sometimes up to 100 kHz, although often (especially in early operations) at much lower repetition rates.

A lot of experimental techniques will be common across ES1 and ES3 (e.g magnetic bottle, VMI, electron time-of-flight), albeit adapted to study slightly higher X-ray energy interactions. In terms of photon techniques, the ability to do XAS on ES3 is highly desirable, and there may also be applications for X-ray scattering measurements, enabling the collection of simultaneous structure and electron dynamics for inhomogeneous samples such as clusters.

Although conventional optical pump, X-ray probe will be a core capability for ES3 (across a similar UV- mid-IR range as ES-1), a large fraction of beamtime on ES3 is anticipated to involve X-ray pump-probe measurements [15]. Multi-colour pump-probe pulses would be possible within the tuning range of FEL-5 (0.25-3 keV).

8.2.2 ES2, ES5, ES8: Soft X-ray, ambient pressure and hard X-ray PES

Early in the CDOA process, it was identified that there was a broad user need for applying angle-resolved (and integrated) photoelectron spectroscopy (PES) techniques across a range of X-ray energies and sample environments. In order to cater for these quite distinct user communities, a decision was made to include in the concept three end stations (ES2, ES5 and ES8 across FELs 6, 5 and 3, respectively).

Fundamentally, PES involves detecting photoelectrons emitted from a sample following irradiation by UV/X-rays via the photoelectric effect. By detecting the emitted electrons with a high degree of energy and angular (momentum) resolution, it is possible to map out the electronic band structure and explore aspects of chemical bonding through the analysis of core state spectra. Time-resolved (and angle-resolved) PES (ARPES) adds a capability for characterisation of non-equilibrium properties by pre-pumping the sample with an optical pump pulse prior to the arrival of the short pulse UV / X-ray probe beam.

Most PES (and tr-PES) research over the last 20 years has focused on low-energy photoelectron spectroscopy, typically using HHG sources, where the technique has made significant advances in different families of quantum materials [16]. There continues to be a thriving community in soft X-ray ARPES that crosses over between HHG sources, synchrotrons and XFELs that must be catered for on UK XFEL (see ES2).

There has been increasing interest in applying PES techniques to areas including catalysis research, environmental science and biomaterials, where sample environments must operate at higher pressures (i.e. non-UHV) to perform in-situ experiments under relevant conditions. This group of experiments is commonly referred to as ambient pressure PES (or APPES). The elevated pressures required for the sample environments and higher maximum X-ray probe energies typically required drove the decision to add a dedicated end station for this type of work on FEL-5 (see ES5).

Hard X-ray photoelectron spectroscopy (HAXPES) uses harder X-rays (from a FEL or a Synchrotron) for greater bulk sensitivity and to extend element specificity to higher atomic numbers. Time-resolved HAXPES (tr-HAXPES) can study interface science of transient bulk electron structure dynamics (including under working conditions) via similar pump-probe schemes to softer X-ray techniques. HAXPES covers samples of interest relevant to energy materials, batteries, opto-electronic devices, as well as fundamental condensed matter physics [17]. While catered for on synchrotrons, having a dedicated tr-HAXPES end station on UK XFEL would provide a truly unique capability with an operating parameter space not currently available elsewhere.

8.2.2.1 ES2 (Soft X-ray tr-ARPES) (FEL-6 0.05-1keV)

A time-resolved ARPES (tr-ARPES) end station on FEL-6 (50 - 1000 eV) will cater for a range of opportunities in material science. These will include the studies of ultrafast processes at surfaces and in quantum materials [18, 19, 20, 21], including the fundamental physics in light-matter interactions in highly correlated many-body quantum states. In addition, a large application area is expected to be the development of new paradigms in relation to data processing, ultrafast switching and data storage [22, 23, 24]. Surface chemistry also represents a growing part of the potential user base, especially those studying photocatalytic processes, which are highly relevant for industry and for atmospheric and environmental sciences [25, 26, 27].

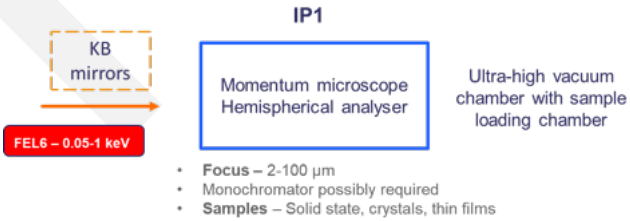

Figure 8.5: ES2 end station - FEL-6's fully tuneable operating range of 50 - 1000 eV would provide flexibility for studying different interfaces and photoelectron escape depth

FEL-6's fully tuneable operating range of 50 - 1000 eV would provide flexibility for studying different interfaces and photoelectron escape depths [28], and for probing core-level electronic states [29, 30] as well as dispersing valence and conduction-band states [31]. Through seeded operation on FEL-6 a facility like UK XFEL would offer stable, narrow bandwidth operation across this range for the highest energy resolution (∼10's meV), a critical factor for distinguishing complex physical and chemical processes occurring at similar energy scales. Full polarisation control would yield insight into the orbital character of electronic states; granting access, for example, to

technologically important phenomena such as spin-orbit coupling in solids. The option to include a monochromator on FEL-6 is planned in order to accommodate certain experiments where the narrowest bandwidths are required beyond what seeding may be able to achieve. On the opposite end of operations, where higher temporal resolution is required (down to a few fs) this bandwidth would by necessity increase to $\sim$1 eV.

Whilst space charge is a significant issue for the typical high pulse energies from a FEL [32, 33, 34], pulse energies could be reduced and the high repetition rate (up to 100 kHz initially) utilised to maximise average count rates per second. Such a high repetition rate capability would also help to reduce the time typically required for a user experiment, thus increasing the availability for what is currently high-demand beam time.

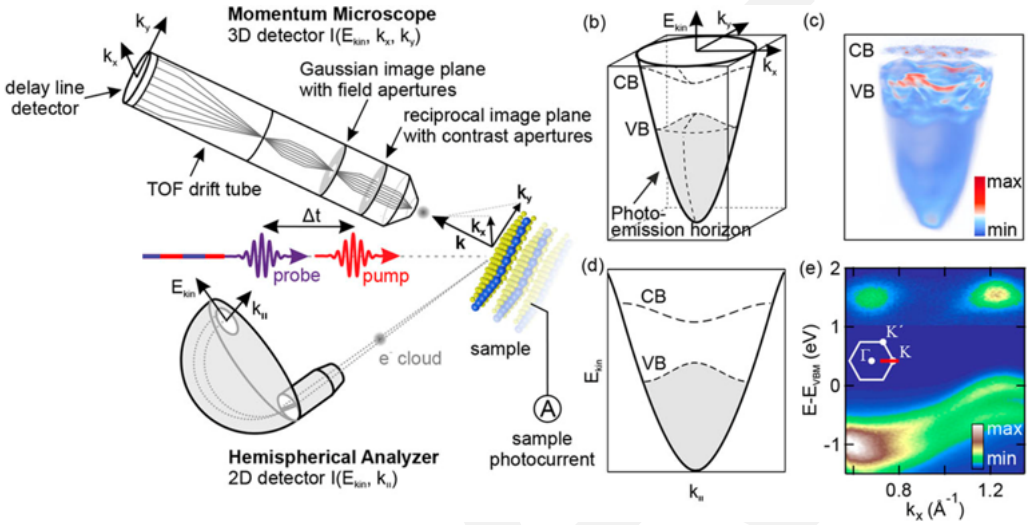

Figure 8.6: Schematic of two common detection techniques for trARPES measurements - the hemispherical analyser and the momemntum microscope - illustrated here for a sample of bulk tungsten diselenide. Adapted from J. Maklar *et al.* Rev. Sci. Instrum. 91, 123112 (2020).

The ES2 end station, in terms of sample chamber and detection techniques, would not look radically different from those already operating on synchrotrons, HHG sources or at some XFELs [35]. Soft X-ray ARPES measurements would be made inside a single interaction chamber with a very high vacuum ($<10^{-10}$ mbar), to minimise the risk of contamination to the prepared sample surfaces. It will be required to have a sample preparation and insertion chamber adjacent to the X-ray interaction chamber where the sample can be subjected to various preparations including baking, cleaving, sputtering or annealing. Sample characterisation may also be required in this chamber, including techniques such as low-energy electron diffraction (LEED) and scanning tunnelling microscopy (STM). Once loaded (onto a high accuracy hexapod mount) a capability will be required to cool and heat the sample in situ depending on the needs of the experiment.

Tr-ARPES will be implemented using a tuneable pump laser that will need to operate from UV wavelengths to mid IR (and possibly out to THz also). Appropriate synchronisation down to the few fs will be required. The minimum expected X-ray spot size is 2-3 μm (especially for 2D materials), although operation in the range of 10-100 μm would be more typical. This would be achieved via defocusing of the beam with the deformable KB optics in the end station. Hemispherical analysers have been the standard instrument for most ARPES work regardless of the probe light source. As a flexible detector capable of high energy and angular resolution they will be required for many experiments on UK XFEL ES2. Momentum microscopes [36, 37] have grown in popularity in recent years owing to their very high collection efficiency and ability to operate in either spatial or momentum-imaging modes. As the technology develops it is likely that momentum microscopes could be the default detector for most tr-ARPES experiments, although an ability to

field conventional hemispherical analysers should be retained for maximum flexibility in terms of sample set-ups [38].

8.2.2.2 ES5 (Ambient pressure PES) (FEL-5 0.25-3keV)

The ambient pressure PES (APPES) end station on FEL-5 (ES5) would serve to provide measurements of chemical composition by probing both core and valence electron states in a range of complex sample configurations. (Near) ambient pressure operation (up to 10s mbar) opens up opportunities to study solid-gas, liquid-gas, and solid-liquid interfaces, commonplace in catalysis, batteries, biomaterials, and environmental chemistry research. Aside from avoiding contamination of quantum material experiments that would otherwise share a chamber, this dedicated end station would cover a higher X-ray range, a crucial capability to avoid both the X-rays and subsequent photoelectrons interacting too strongly with the surrounding gaseous environment [39].

Understanding the dynamics of photon-initiated processes, including photocatalysis, photovoltaics, and photobiology, requires ultrafast pump-probe spectroscopy, with photoelectron spectroscopy being a powerful example. Some of these processes occur at solid-gas interfaces, but many involve solid-liquid (mainly aqueous) interfaces. The dynamics of thermal processes can be initiated with terahertz or optical pulses, with electron dynamics studied on the fs range [40] and slower processes on the ps-ns scale accessible using time-resolved synchrotron sources.

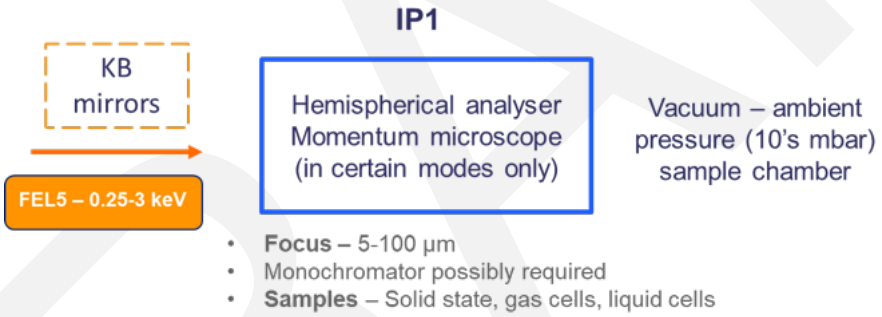

Figure 8.7: Configuration for ES5 end station for time-resolved APPES on FEL-5

At present, there are no tr-APPES facilities available in either regime. There have so far only been static PES studies of solid-liquid interfaces associated with photo-electrocatalysis, which show the potential for electrochemical control of the interface, which could be interrogated with operando tr-APPES to examine reactive intermediates [41]. Related to photovoltaics, there have been tr-PES of an N3 dye on TiO2 using a HHG laser source which provided a view of the charge transfer process from the dye to the electron collector [42]. UK XFEL's fully tuneable energy range on FEL-5 (over the fundamental and higher energies via harmonics if required) will permit time-resolved spectroscopic studies over an extended depth range in many samples.

To cater for a range of different sample environments, a single flexible interaction point is envisioned for ES5 that would primarily cater for near-ambient pressure samples. A highly controllable gas environment is necessary, permitting mixing of different gases, including hazardous gases and the control of humidity levels in complex gas mixtures. UHV operation in ES5 is not precluded, but this would likely require the sample chamber to be exchanged for an extended period of operation.

In order to protect the X-ray beamline, a differentially pumped beam entrance would be required at the X-ray beam input. An adjacent load-lock chamber for sample preparation would still be required, as per the soft X-ray ARPES (ES2) end station with similar characterisation diagnostics. A hexapod, or other multi-axis manipulator would hold the sample, with cooling and heating

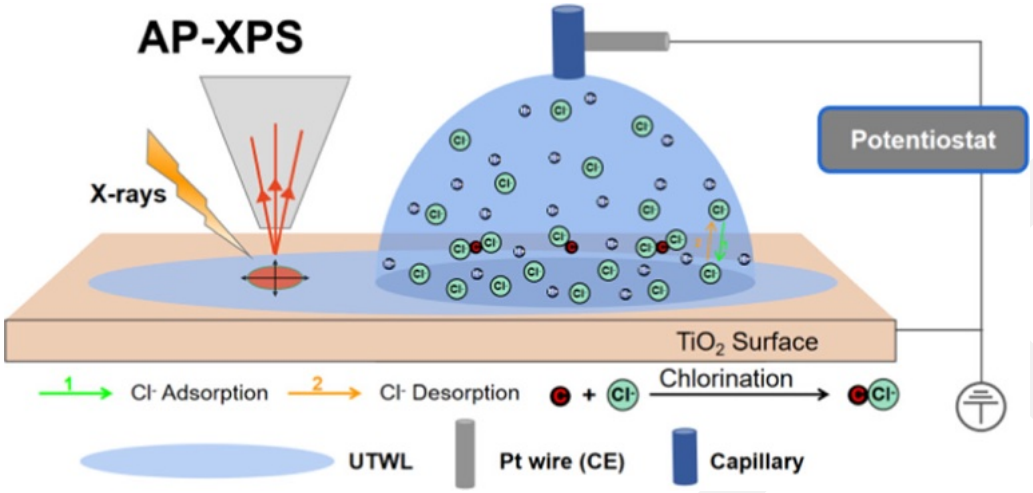

Figure 8.8: Experimental set-up for ambient pressure X-ray PES to investigate the effect of applied potential on the interface of TiO_2(110) with 0.1 M HCl, as performed on the VerSoX end-station at B07 on the Diamond Light Source. Ambient pressure operation (13 mbar) with in-operando electrochemical characterisation, enabled real-time monitoring and analysis of electrochemical processes. Figure reproduced from J. Yu *et al.* J. Phys. Chem. C **128**, 49, 20933-20939 (2024).

available as standard. X-ray focal spots would be in the range of 5-100 μm, matched to optical pump beam diameters. Excitation sources from the THz to the UV would be required, ideally continuously tuneable from NIR to energies around 4 eV.

The electron analyser would also require differential pumping in order to operate under high-voltage conditions. While it may be possible to operate a momentum microscope under certain conditions in future on ES5, currently it is anticipated that only a differentially pumped hemispherical analyser can be used. Here the repetition rate and high flux of UK XFEL will be beneficial as compensating for the reduced photoelectron collection rate in a differentially pumped configuration. Enclosed sample or ”virtual pressure cells” [43] may also offer a route to higher-pressure operation.

8.2.2.3 ES8 (Hard X-ray PES) (FEL-3 3-13keV)

Completing the trilogy of PES end stations is ES8 for time-resolved hard X-ray photoelectron spectroscopy (tr-HAXPES). HAXPES techniques [44] have steadily developed at synchrotrons and more recently on laboratory-based sources, covering energy ranges of approximately 2-15 keV, although some sources can extend significantly above this (whilst the photoelectron energy possible to detect is usually limited to 15 keV by hemispherical analysers) [17]. The higher probe energies unlock much greater bulk sensitivity, the option to look at samples in operando, and the ability to access deeper core states of a much wider range of elements. Furthermore, tunability of the photon energy across this range coupled with a high degree of polarisation control allows for the select discrimination of specific orbitals in order to disentangle degenerate contributions to semi-core and valence states and obtain a clearer understanding of orbital character. There are several expected main applications for a HAXPES end station on UK XFEL.

Much higher X-ray energies possible on FEL-3 (up to 13 keV in the fundamental, and even higher in 3rd harmonic) create much larger photoelectron inelastic mean free paths (IMFPs). This coupled with the time resolution unlocks studying of dynamic processes in buried layers and interfaces, with the energy of the XFEL used to scan depth within the sample (the ”information depth”) and extending the probing depth possible at the SX-ARPES endstation ES2. When coupled with angular-resolved measurements this provides unparalleled information depth selection. This can

be achieved by slicing of wide acceptance angle analysers or stepwise changing of the sample angle for small acceptance angle analysers. For in-situ measurements where analysis is required of samples operating under real-world conditions without the requirement for UHV preparation, e.g. similar to the actual conditions expected for a particular catalytic reaction or operation of a battery cell, HAXPES at the UK XFEL will provide the necessary probing depth to see through any surface overlayers and probe the bulk of the materials. In addition, chamber pressures around a sample can be significantly greater than those on the ambient pressure end station on FEL-5. Similar to the other PES end stations, the high repetition rate of UK XFEL will be required in order to overcome the limitations of space charge effects and provide sufficient average photon (and electron) flux. To date, only SACLA has been used for initial HAXPES measurements on an XFEL, albeit at a repetition rate of just 30 Hz [45].

The availability of a synchronised, tuneable optical pump laser on ES8, capable of scaling to 100 kHz (and beyond in future) will allow pump-probe tr-HAXPES experiments with probe delays from femto- to picoseconds and beyond, covering slower phase transitions to the fastest carrier and magnetisation dynamics with element specificity and chemical sensitivity. The full polarisation control on FEL-3 for UK XFEL will also be very important for measurements ranging from quantum materials to femto-chemistry.

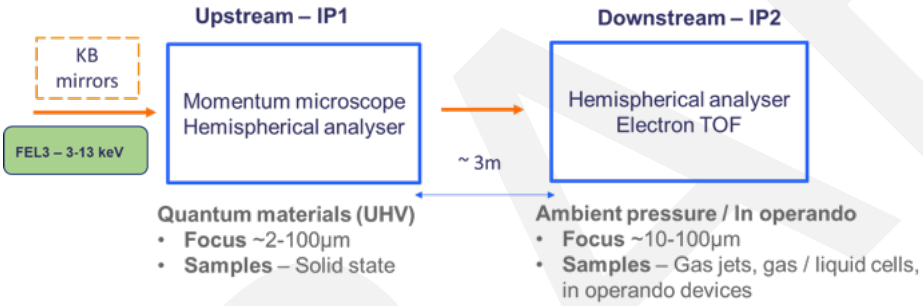

Figure 8.9: The ES8 (HAXPES) end station configuration on FEL-3 with two interaction points for differing sample environments.

For ES8 there will be a need to cater for several configurations of tr-HAXPES experiments, from gas phase and UHV condensed matter to ambient pressure / in operando work. As a result, it is planned that ES8 will have two separate interaction points (and sample chambers).

The first (IP 1) would be limited to samples that require high vacuum in a similar mode to soft X-ray ARPES on ES2. This would include a wide range of opto-electronic and quantum materials. The set-up would consist of a small sample chamber for manipulating the solid-state sample and cryo-cooling (and heating) over a temperature range to be determined at a later date. A neighbouring preparation chamber would be available with capabilities similar to the SX-ARPES endstation. The X-ray beam would be focused down to $\sim$5 μm minimum on the sample, with the usual option to defocus beyond this. The primary diagnostic technique for this IP would be a momentum microscope, although other hemispherical or electron ToF analysers would also be compatible. This end-station will also include the option of sample biasing to allow for operando characterisation of heterostructures and interfaces key in optoelectronic devices [46].

At a second interaction point downstream (IP2) a more flexible sample chamber would serve to perform experiments in a similar way to that on ES5 for near ambient pressure work on FEL-5. In this chamber (differentially pumped so as not to contaminate IP1 or any HV analyser), a range of samples could be interrogated, including those relevant to catalytic and electrochemical processes [47]. Careful design of a range of insertable sample environments will be required so that liquid/solid and gas/solid interfaces can be fielded along with electrochemical devices in

operando. For these more complex sample environments, it is expected that more conventional hemispherical analysers or electron ToF diagnostics would be routinely used owing to the complex vacuum and contamination issues. X-ray focusing requirements at IP2 will be more relaxed, operating in the range from $\sim$10 μm upwards, but typically closer to 50-100 μm.

On FEL-3 the expected bandwidth when operating in HB-SASE mode is expected to vary according to X-ray energy. Within the operating range of 3-13 keV the typical bandwidth is estimated to be 180-360 meV. It is anticipated that both sample chambers will require optical pump lasers, typically operating in the IR regime, although this still be tuneable to shorter (UV) wavelengths, or to longer wavelengths (THz) if required.

8.2.3 X-ray spectroscopy and scattering (ES4, ES6 and ES7)

X-ray spectroscopy covers a broad range of techniques and is applicable in almost every area of research on FELs. The application of spectroscopy methods (including EXAFS, XANES, XES and RIXS) can yield information on electronic structure, local atomic environment, materials dynamics and other phenomena including magnetisation, all with elemental specificity according to the X-ray pulse energy. Several X-ray photoelectron spectroscopy (XPS) techniques are covered by other end stations already discussed, namely those applying (AR)PES detection as well as those set-up to study AMO phenomena. However, there is also a need to apply photon-based spectroscopy techniques across a wide X-ray energy range and for multiple sample environments. A common requirement in particular is to apply spectroscopy techniques across solid state and liquid phase samples, two types of experiments that cannot be easily combined with one interaction chamber per end station.

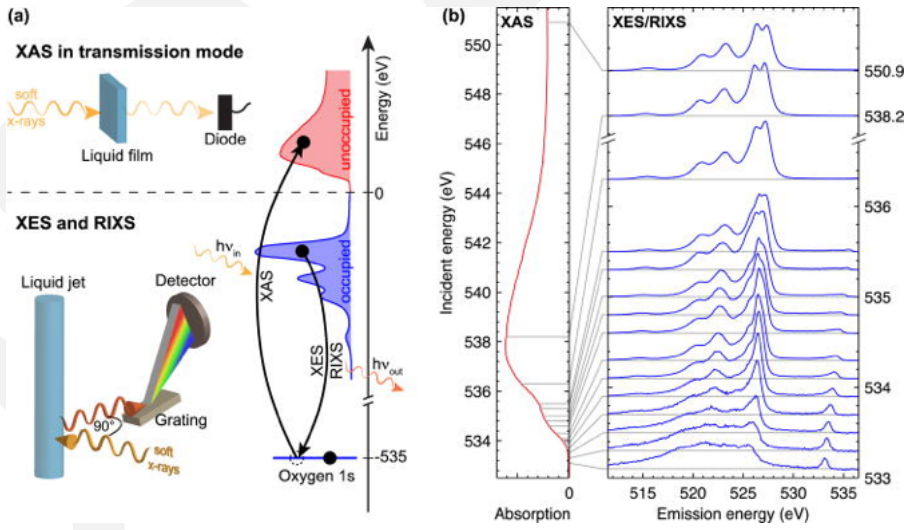

Figure 8.10: Illustration of X-ray absorption and emission methods along with RIXS, in this example for liquid methanol. (a) Schematic of transmission XAS geometry and XES/RIXS with a grating spectrometer. (b) Experimental data of XAS spectrum and RIXS spectra for excitation energies tuned through the X-ray absorption resonance. Figure adapted from S. Schreck *et al.* Struct. Dyn. **1**, 054901 (2014).

For XFELs especially, where time-resolved spectroscopic techniques can be applied with synchronised pump lasers, there is often a trade-off between temporal and spectral resolution. Each application will balance these factors differently so flexibility in the X-ray beam properties of UK XFEL, in terms of pulse duration and bandwidth) will be highly desirable for many user groups. A high degree of X-ray longitudinal coherence will be a common requirement across spectroscopy end stations. Currently for many SASE-based FELs, monochromators are required to reduce the

bandwidth to an acceptable level, albeit with significantly reduced X-ray transmission and often a stretched pulse [48].

ES4, operating on FEL-5 will focus on inelastic X-ray spectroscopy techniques at the lower end of the energy spectrum (0.25 - 3 keV). Such an energy range covers K-edges from carbon to chlorine, as well as L-edges for many transition metals. Resonant inelastic X-ray scattering (RIXS) combines aspects of XAS and XES to study a broad range of energy transfers to specific excitations from the meV - keV scale depending on the science of interest. High resolution measurement of the energy (and sometimes momentum) shift between incoming and outgoing X-ray photons can reveal information on lattice vibrations, magnons, orbital excitations and local lattice structure. ES4 will apply RIXS techniques across quantum materials and photochemistry as well as more conventional XAS measurements if required. ES6 will primarily focus on complementary time-resolved XAS and XES techniques over the FEL-4 tender X-ray energy range. Where useful, X-ray scattering methods could be applied simultaneously, for example with liquid phase samples where bulk structural information is of interest for solutes and solvents. ES4 should also be seen as a flexible end station for other X-ray detection techniques in this energy range, including coherent diffraction imaging (CDI) and X-ray photon correlation spectroscopy (XPCS). ES7 will operate in a similar manner to ES6, offering ultrafast pump-probe spectroscopy and scattering techniques but in the hard X-ray range from 3-13 keV (in the fundamental) where most experiments can be conducted at atmospheric pressure.

8.2.3.1 ES4 (RIXS and XAS) (FEL-5 0.25-3 keV)

ES4 will primarily cover RIXS experiments as well as regular tr-XAS and XES methods across the 0.25-3 keV tuning range. Within this energy range there are two main user communities; those studying quantum materials and those applying RIXS techniques for chemistry. As with other end stations the X-ray, sample and detector requirements are slightly different even if the technique is shared.

RIXS is especially demanding as a spectroscopy technique in terms of bandwidth and flux. RIXS requires a high resolving power both from the beam onto the sample, as well as on the spectral analyser acquiring the signal. RIXS is extremely photon hungry and therefore requires high repetition rate and high pulse energies, and also requires precise tunability of the photon energy. UK XFEL is designed to meet all of these challenges.

For some solid state samples there is great demand to use time-resolved RIXS to study ultra-fast transient states, studying how energy and charge flow in materials is coupled to, and directed by, a manifold of transient states where spin, vibrational and electronic degrees of freedom are intrinsically coupled. With sufficiently accurate measurement of the change of X-ray energy and momentum it is possible to infer the nature of different material excitations [49]. While RIXS end stations are increasingly commonplace on synchrotrons, tr-RIXS is of increasing interest as the technique can benefit not only from the short probe durations but also from the large increase in spectral brightness [50, 51, 52].

For chemistry, RIXS is increasingly being used as a powerful technique to probe occupied and unoccupied orbitals with element- and chemical-site specificity [53, 54], attracting many users who commonly use laser-based UV-Visible spectroscopy techniques to address the mechanism of redox reactions in for example, battery cycles, photo- or electrocatalysis, and metalloenzymes. The time-resolved nature of XFEL probing allows reaction dynamics to be resolved, increasingly in dilute samples as the range of pulse energies, tuneability of the X-ray sources, and sample delivery technology improves [55].

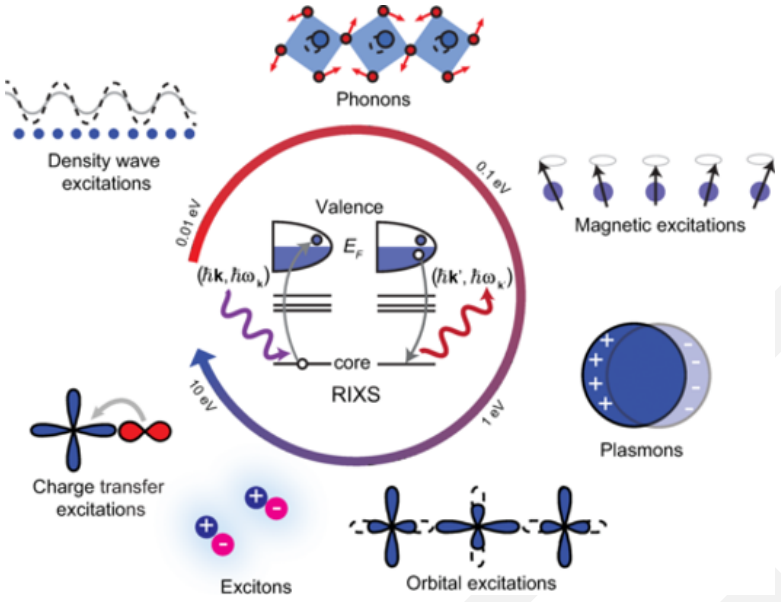

Figure 8.11: The Kramers-Heisenberg process for resonant inelastic x-ray scattering (RIXS) and the different excitations that it can probe. Image adapted from M. Mitrano *et al.*, Phys. Rev. X 14, 040501 (2024).

The high repetition rate of UK XFEL will also be highly beneficial for cutting-edge experiments in chemistry on ES4 and other similar end stations. The ability to acquire much larger data sets will not only support the use of lower concentration samples, but also help to achieve the signal quality required to help deconvolve complex chemical dynamics and resolve small chemical shifts. The much greater throughput will also help to support more exploratory campaigns as opposed to experiments more limited to targeting a single problem.

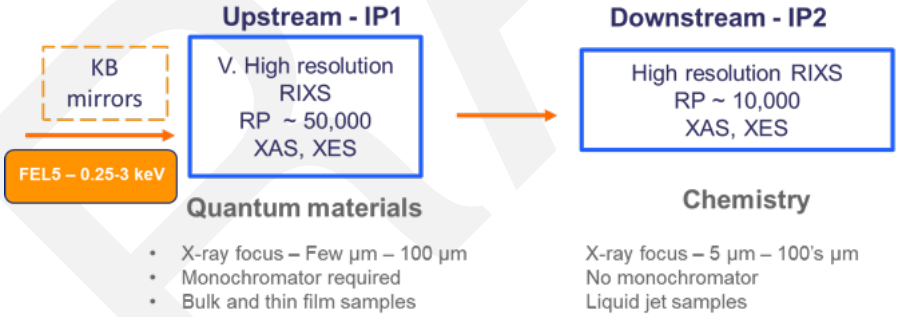

Figure 8.12: ES4 for RIXS and other photon spectroscopy methods on FEL-5. Note - these two interaction points may require splitting into two hutches due to the differing requirements for monochromation

Conceptually the ES4 end station will be split into two interaction environments; the first for quantum materials, the second for time-resolved chemistry. For the purposes of this CDOA the two interaction points for ES4 are shown in series, similar to LCLS II's qRIXs and ChemRIXS instruments [56]. How this is delivered in practice will be decided as the design for UK XFEL evolves, but it would clearly be beneficial to completely split ES4 into two separate hutches (one on a mono branch, one not) to maximise parallel set-up work and greater throughput.

For quantum materials (IP 1) it will be a requirement to implement a monochromator in the beamline in order to achieve resolving powers on the order of 50,000. If possible UK XFEL should aim for resolving powers beyond this (stretching the pulse to 100's fs), although this would place very stringent requirements on both the X-ray optics and detector specifications (as well as the size of the experimental hutch). The RIXS instrument itself would consist of collection optics, a high resolving power diffraction grating and a 2D detector several metres from the interaction

point. Since scanning in momentum is required, a swing arm with angular range of at least 150 degrees would be desirable. APDs will also be available for XAS in Total Fluorescence Yield mode if there is no requirement to measure a 2D spectrum. For IP1 focal spots down to a few μm will be required although a vertical line focus is typically used for RIXS. Samples (bulk and thin film) will typically be held on a multi-axis diffractometer with sample cooling available.

For chemistry experiments (on IP2) the X-ray and detection requirements for RIXS measurements are slightly more relaxed. As the energy transition modes of interest are naturally higher in energy, the resolving power required is lower, on the order of 10,000 at 1keV. For UK XFEL this presents an opportunity to operate with a long pulse mode on FEL-5 without the need for a monochromator and hence at least 3 orders of magnitude more flux. This will unlock the use of RIXS for low concentration samples that currently cannot yield enough signal on most FEL beamlines. The reduced resolving power requirements and lack of momentum resolution means that the swing arm (and hence whole footprint) for IP2 can be considerably smaller. An alternative approach could also be implemented on ES3 whereby the broad bandwidth nature of attosecond pulses can be used to recover sub-bandwidth resolution for transient absorption spectroscopy with the ”ghost imaging” technique [57].

Sample delivery will be critical to maximising the capabilities of RIXS for Chemistry. Liquid jet diameters down to 5 μm (matched with X-ray and laser spot sizes) will not only increase flux but minimise the use of precious samples. Some flat jets (down to 100’s nm thickness) will be needed where transmission XAS can be employed also. For time-resolved XAS it would be beneficial to operate using a system of on-shot normalisation, as recently deployed by SCS at European XFEL using X-ray zone plates [58].

8.2.3.2 ES6 (Soft-tender X-ray spectroscopy) (FEL-4 1-5 keV)

The tender X-ray range (broadly defined as 2-7 keV) offers opportunities for time-resolved XAS (tr-XAS), XES and RIXS in chemistry and life sciences, covering elements that play important roles in catalysis, battery research, photovoltaics and environmental science. One of the largest applications for time-resolved XAS in this range is the study of catalytic processes over extended timescales to better understand reaction mechanism and ultimately design improved catalysts for many applications [59, 60]. Many existing studies are limited on signal-to-noise (SNR) ratio, so UK XFEL’s high repetition rate (together with the high brightness source) will improve the SNR ratio considerably whilst permitting the use of precious samples more effectively.

From 1-5 keV there are opportunities to probe L-edges of 4d transition metals including rhodium, palladium and silver. Some of these metals have a critical role in cleaving carbon-hydrogen bonds, with a recent study demonstrating the power of ultrafast X-ray spectroscopy to reveal new insights to this process [61]. The K-edges of lighter elements, including sulphur and phosphorous, are of particular importance: these elements form part of many industrial catalysts, have important roles in biology (proteins, DNA, drug design) and environmental science (atmospheric chemistry, aerosol formation, air pollution, antibiotic resistance) as well as many technologically advanced areas including battery technologies and organic optoelectronics. However, the tender X-ray regime is challenging to operate in as relatively low X-ray energies prevent most experiments from being conducted at ambient pressures, necessitating the use of helium atmospheres or sophisticated gas cell techniques.

It should be noted at this stage that while the energy range of FEL-4 is currently defined as 1-5 keV, from some of our consultation with the user community there was clear interest to extend this range to the upper end of the tender X-ray range (for example 2-9 keV). While this would

create greater overlap with FEL-3, it would open up significantly more elements for analysis using a single, flexible experimental chamber sample environment. As the UK XFEL project proceeds to its next steps the energy range of FEL-4 may be revised to explore this opportunity.

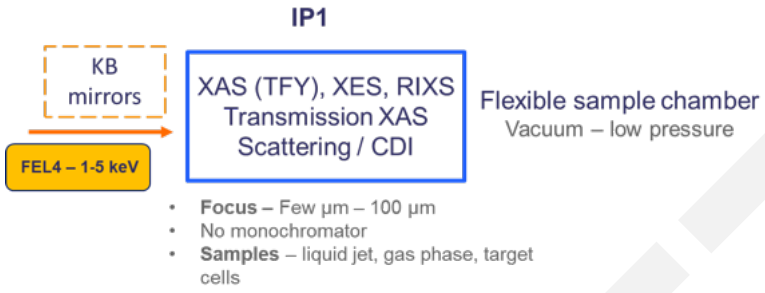

Figure 8.13: Configuration for ES6 featuring soft-tender X-ray photon spectroscopy methods.

To accommodate these diverse sample types relevant to the tender X-ray range, ES6 will consist of a single, flexible interaction chamber, capable of operating either in vacuum or at low ambient (10's mbar) gas pressures and helium environments. Experimental cells would also be an option for studying some higher pressure in-situ catalytic reactions or in-operando gas sensors. Within this chamber will be X-ray spectrometers as well as an area imager for scattering techniques. Spectroscopy techniques will be similar to the chemistry RIXS set-up on ES4, with either Johann or Von Hamos spectrometers available depending on energy resolution and collection efficiency required for the technique. Scanning XAS (and RIXS) would be possible using the tuneable energy range of the FEL (without the need for a monochromator). The high repetition rate of UK XFEL, coupled with high flux in long pulse mode, would be applicable for many liquid sample types that aren't currently viable due to the concentration barrier. These features also enable the photon-hungry (time-resolved) RIXS method for many more sample types, which will be crucial for many research areas.

Aside from spectroscopy, ES6 will be a platform for applying scattering and coherent imaging techniques at soft and tender X-ray energies to study spatial dynamics of ultrafast processes down to nanometre length scales. One particularly relevant example in this tender X-ray energy range is scattering and holography techniques to resolve structure and dynamics of ultrafast magnetism. Recent experiments at similar energies on SCS revealed detailed information on magnetic domain evolution and formation of spin-wave solitons highly relevant to research into state-of-the-art magnetic storage [62, 63, 64]. Other research into ultra-fast antiferromagnetic (AFM) dynamics at nanoscales will naturally fit on XFELs where time-resolved scattering (and spectroscopy techniques) can resolve the natural AFM dynamics timescales of 10 fs - 100 ps [65]. For many of these research areas it will be essential for ES6 (and other similar end stations) to provide static magnetic fields (up to $\sim$1 T) at the sample position, with tunable direction and magnitude.

8.2.3.3 ES7 (X-ray spectroscopy and scattering) (FEL-3 3-13 keV)

ES7 will extend spectroscopy and scattering techniques to the hard X-ray regime, up to 13 keV in the fundamental with main applications for time-resolved photochemistry experiments. Many experiments will be performed with liquid samples under ambient conditions, often with simultaneous spectroscopy and scattering measurements to study coupled structural and electronic dynamics [66]. For ES7, UK XFEL's high degree of longitudinal coherence (and repetition rate) will enable new solution phase spectroscopy measurements with low concentration solutions and

for low probability transitions. The energy range of ES7 (3-13 keV) is essential to follow transition metal complexes - the key components in quantum computing and information storage, photonic materials, photocatalysis, and metallo-enzymes.

Recent developments in ultrafast magnetism have resulted in photo-magnetic recording in materials which has the distinct advantage of faster sequential switching rates due to the non-thermal mechanism [67]. The capability of fs X-ray spectroscopy will facilitate unprecedented new insights into the mechanism of emerging photo-magnetic materials, such as the trinuclear SMM [MnIII3O(Et-sao)3(β-pic)3(ClO4) [68] as performed for light-induced excited spin-state trapping (LIESST) systems [69].

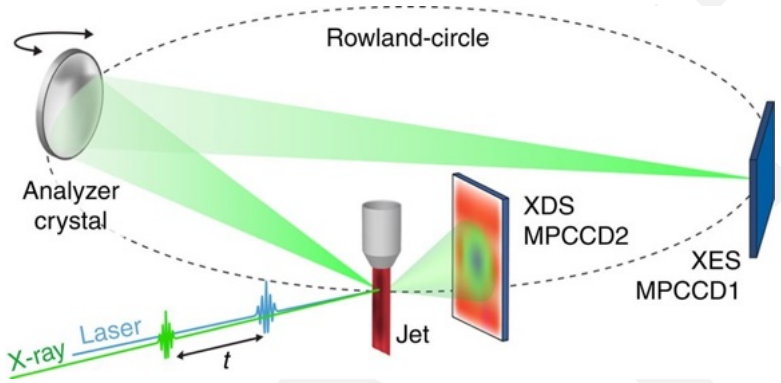

Figure 8.14: An example of a pump-probe set-up accommodating simultaneous XES and X-ray scattering from BL3 on SACLA for measurement of coupled electronic and structural dynamics following photoinduced electron transfer. Figure reproduced from S.E. Canton *et al.* Nat. Comms. 6 6359 (2015).

The ability to probe the electronic (XAS, XES), structural (XAS) and spin (XES) dynamics of these complex materials and related analogues on the timescale upon which they operate, i.e. femtoseconds, will enable fine control of the magnetic properties and coherence times of these materials, and provide crucial new insights urgently required to develop to new storage materials. Examples of such materials include all period 3 transition metal complexes, where K-edge energies range from 5465 eV (V), progressively increasing through Cr, Mn, Fe, Co, Ni to Cu (8979 eV). [70]

Another area of high relevance for ES7 is of photocatalysis, where current catalysts combine one or more 3rd, 4th or 5th transition metals with organic ligands containing C, N, S and P atoms. Since 4d- and 5d metals have K-edges at very high energies (e.g. $\sim$80 keV for gold), the experiments are preferable at their L-edges. Those range from $\sim$3224 eV for ruthenium (also a key component in solar cells) to gold ($\sim$11919/13734/14353 eV). Thus covering the range from 3 keV to 13 keV is absolutely essential in order to understand the full mechanism of the catalytic cycles involving both molecular catalysts, and plasmonic materials (primarily based on platinum or gold structures). This range will also be highly applicable to metalloenzyme research where transition metal complexes (typically including Fe, Cu and Mo) have a crucial role [71, 72, 73].

In all of the above, the essential information regarding coupled electronic, structural and spin dynamics can only be obtained from a combination of time-resolved (down to femtoseconds) XAS, XES methods, coupled with RIXS. These studies mostly need to be performed in solution, often at low concentrations and with limited precious samples. However samples can also include complex interfaces (heterogeneous catalysis), or be in solid state (e.g. battery materials). ES7 will cover a large number of spectroscopy techniques. Firstly XAS (XANES and XAFS) to probe valence states with targeted sensitivity to local chemical environment and oxidation states. XES will be applied to study charge states and occupied molecular orbitals (mostly a multi-crystal Von Hamos design), with the technique extended to high resolution RIXS for revealing low energy transfer

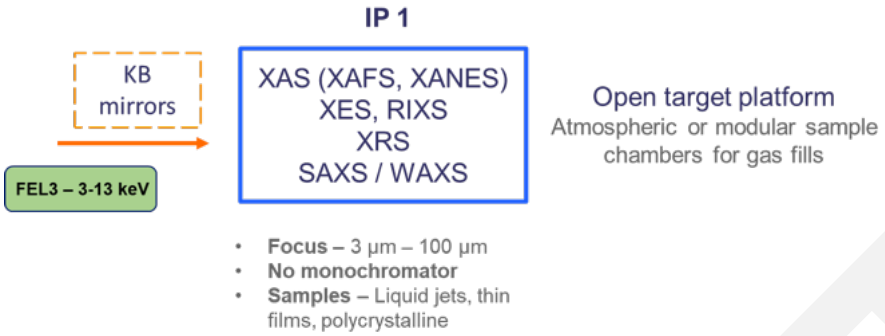

Figure 8.15: ES7 end station for tender-hard X-ray spectroscopy and scattering

processes. X-ray Raman spectroscopy (XRS) can also be used to probe bulk samples whilst targeting absorption edges of low-Z elements (e.g. carbon, nitrogen and oxygen).

Hard X-ray scattering techniques (WAXS and SAXS) and be applied to reveal structural dynamics on various spatial scales. For harder energy X-rays the detection platforms can operate in air, aiding flexible configurations. However for X-rays down to the tender X-ray range ($<$7 keV) it may be a requirement to couple some detectors under vacuum / low pressure helium fill. Further design revisions as UK XFEL enters the technical design phase may advise FEL-3 energies increasing to enable all experiments to operate in air.

An ambient platform for ES7 will allow a range of sample stages, operating either at atmospheric pressure, or under vacuum or helium gas fill with the use of small, exchangeable sample chambers. These can be pre-configured offline prior to beamtime, including user-supplied platforms. It is anticipated that most experiments will field liquid jets (flat or cylindrical) with diameters from $\sim$5-50 μm but solid state samples (e.g. thin films, small crystals and polycrystalline structures) should be catered for.

8.2.4 ES9 - Hard X-ray Coherent Scattering

ES9 will specialise in using Coherent Diffraction Imaging (CDI) and other ultra-fast coherent scattering techniques, including X-ray photon correlation spectroscopy (XPCS), in the hard X-ray range (5-20 keV). CDI covers a range of different lensless imaging techniques that enables structural analysis for non-crystalline, and nano-scale crystalline, materials, utilising the ”diffraction before destruction” concept. XPCS is increasingly used as a powerful tool on XFELs to study nanometres-scale dynamics of materials over many timescales (femtoseconds to microseconds) and is relevant to the study nanoparticles, biology and soft matter physics.

For applications on ES9 there are two main types of coherent X-ray scattering experiments. Firstly transmission ultra-fast coherent X-ray scattering (UXS) where the forward scattering signal is recorded on a large area detector, typically using gas or liquid phase samples and can often include biological samples (See ES10 also). Secondly Bragg CDI where a (nano) crystalline sample is irradiated with coherent X-rays and the scattered light collected in a Bragg geometry [74]. Iterative phase-retrieval methods are used to reconstruct the 3D electron distribution and phase, which can then be used to reveal the strain field for crystalline samples.

UXS has become a widely used tool in photochemistry, offering detailed insights into the time evolution of molecular structures during often complex reactions. Its high temporal resolution, combined with access to a wide Q-range, has enabled the investigation of numerous molecules that undergo structural transformations upon excitation by an optical pump laser [75, 76]. This

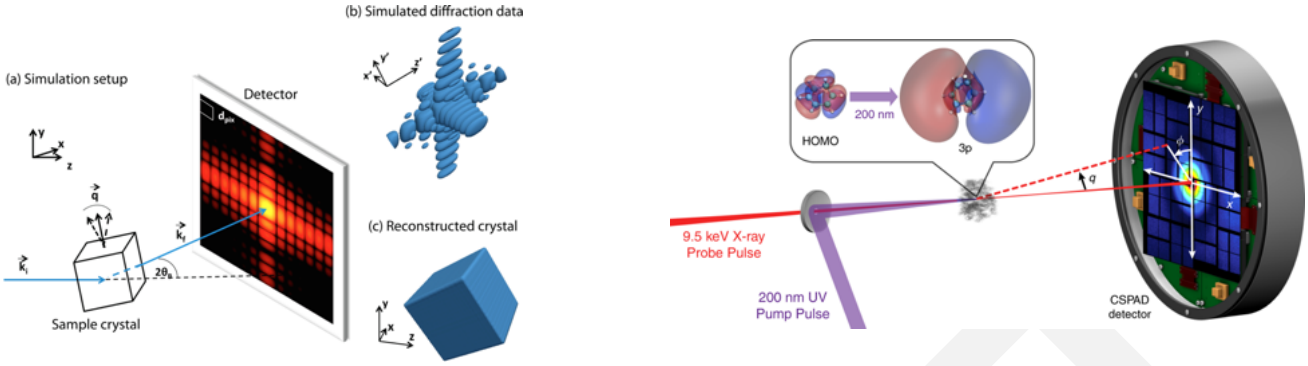

Figure 8.16: The two main experimental geometries for ES9. Left - Schematic of a Bragg CDI geometry. Adapted from H Ozturk *et al.* New J. Phys. **19** 103001 (2017). Right - Schematic of ultrafast, time-resolved X-ray scattering with a gas sample of 1,3-cyclohexadiene (CHD). Adapted from H Yong *et al.* Nat Comms. **11**, 2157 (2020).

technique is particularly valuable for the optimised design of catalytic systems. The recent development of more advanced measurement and analysis techniques has also enabled the simultaneous tracking of electron dynamics [77], as well as observation of photochemistry in real space and time [78]. For gas-phase measurements, the UK XFEL's high repetition rate, along with its high brightness and narrow bandwidth operation, would significantly broaden the range of samples that can be studied using these cutting-edge methods.

Nano-scale crystals and structures have many applications in the development of next-generation materials owing to their unique properties that often differ from that of the bulk form. XFELs offer a unique platform to study transient phenomena in quantum materials on the nanoscale with the potential to impact many cutting-edge areas of science and technology. For example the study of battery materials under in-operando conditions [79, 80], domain structure of materials with ferroic properties [81, 82], or ultrafast lattice dynamics in nanocrystals [83, 84]. UK XFEL's exceptional brightness coupled with high degree of temporal and spatial coherence will be critical to supporting a wide range of ultra-fast pump-probe CDI experiments.

XPCS can be applied over a range of temporal and spatial scales [85, 86] depending on the system of interest. For slowly evolving systems on larger spatial scales (10s nm), temporal correlations between pulses of ms-μs can be analysed using data from SAXS (with a sample-detector distance of typically $>$5 m). With a MHz repetition rate, UK XFEL would be able to perform XPCS at these rates, with data quality greatly benefiting from a high degree of coherence and high beam brilliance for weakly scattering samples. Pushing to higher temporal resolution (sub-nanosecond) requires double-pulse XPCS where a sum of two speckle patterns is collected for each detector frame [87, 88]. In this mode it is important to minimise pulse-to-pulse fluctuations, especially in intensity, and maintain mutual coherence between pulses.

For CDI techniques (as well as XPCS and other coherent scattering methods) a high degree of coherence will be required in order to perform image reconstruction or high contrast speckle analysis. These analysis methods will be greatly supported by the near-transform limited operation across the energy range on UK XFEL. Care will also need to be taken to maintain a consistent wavefront quality following each X-ray optic. Many previous experiments have been limited to operating at lower X-ray energies due to wavefront quality limitations (and detector efficiency issues). ES9 will aim to increase the useable range of hard X-rays for CDI techniques, permitting stable measurement at higher Q values and thus higher spatial resolutions.

A number of standard detector configurations will be required depending on the technique in question. An ability to translate detectors both in scattering angle, and distance from target will be

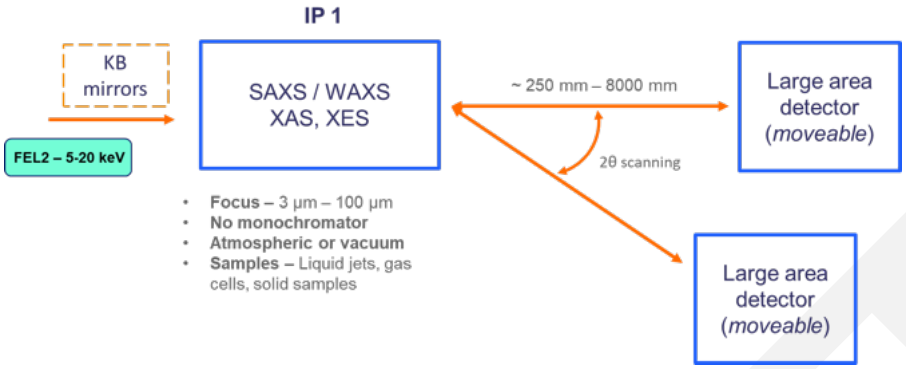

Figure 8.17: ES9 end station for coherent scattering techniques

important, similar to capabilities currently available at similar end stations at LCLS and European XFEL. For transmission CDI, any large area detector will need to have the capability be mounted directly behind the sample ($\sim$100 mm) in the interaction chamber, so as to maximise the field of view and hence maximum Q. Alternative CDI configurations will see the primary large area detector placed outside the interaction chamber, with initial gross adjustment up to $\sim$8000 mm and fine control of $\sim$500 mm during the experiment. For Bragg CDI (BCDI), the large area detector would operate in a horizontal swing-arm WAXS configuration for large Q measurements (2θ of $\sim$50°), with similar levels of sample-detector distance. However if pixel sizes can be reduced on the detector this would enable a reduction in sample-detector distance and permit lower fluxes when using delicate samples. An option to field a XAS/XES diagnostic would also be made available.

Differing requirements in pixel size, detector area and operating distance will require careful consideration in order to suit most high demand use cases. For transmission CDI data close to the direct transmitted beam (low 2θ) is lost as a beam stop (or hole in the detector) is required. One configuration to be considered will be operating with a primary detector operating close to the sample for high Q values (WAXS), while a second detector can operate several metres downstream to help collect some of these low-Q values (SAXS).

For BCDI set-ups a flexible solid sample positioning system is required, with a multi-axis kappa goniometer to enable precise and rapid alignment of crystal samples to the X-ray beam. For transmission set-ups for CDI or XPCS, several sample environments need to be available including gas cells, liquid jets and capillaries. Provision for sample cooling, heating will need to be planned for along with other capabilities such as external magnetic fields. A pulsed magnetic field set-up (on the order of 10s T) should be designed that could be added to study ultrafast magnetic dynamics in condensed matter systems using the scattering capabilities on ES9. Typical X-ray spot sizes on the sample will range from $\sim$3-100 μm although the option to install nano-focusing optics should not be precluded.

Pumping of samples will be required over the UV-IR range, with continuous scanning over certain ranges where possible without sacrificing pulse durations. For many CDI applications especially, there could be high demand for synchronised THz sources, either laser-based on FEL-based.

8.2.5 ES10 - Time-resolved SFX

ES10 will be the main end station on UK XFEL for time-resolved X-ray serial femtosecond crystallography (tr-SFX) to probe structure and visualise molecular dynamics. tr-SFX is now a widely applied technique across hard X-ray FELS due to the ability to use the high brightness and

temporal resolution properties of XFELs to study macromolecules and small chemical systems during reactions and, significantly, under near-physiological conditions [89, 90, 91]. These reactions can be triggered by a chemical process or by exciting the sample with a pulse of light, with the reaction dynamics being tracked over various timescales. Pump-probe methods using synchronised pump lasers [92] are particularly well-suited to XFELs to study high-profile light-responsive systems such as rhodopsin proteins [93] or photosystem II [94]. Novel methods such as photocaging [95] now offer a way to perform high repetition-rate, time-resolved structural biology studies on the majority of samples that aren't naturally photoactivable.

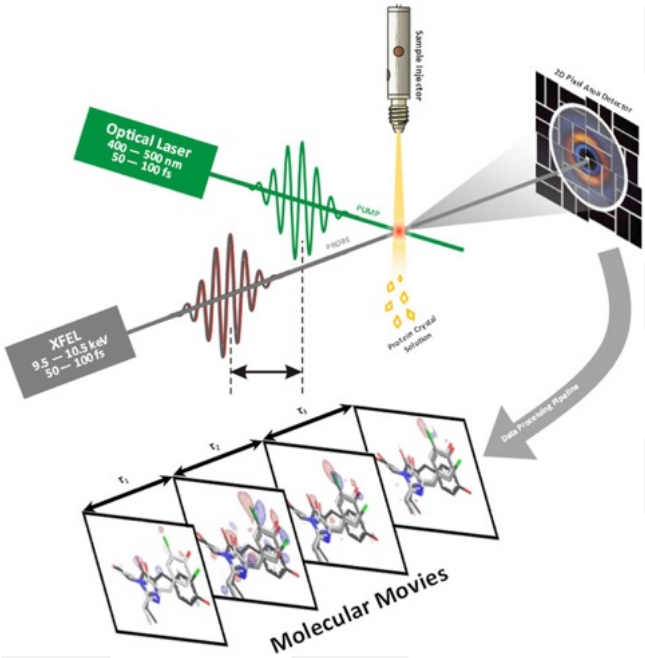

Figure 8.18: Schematic of a time-resolved Serial Femtosecond Crystallography (tr-SFX) experiment, enabling the production of ultrafast molecular movies. Reproduced from S. Perrett et al. J. Chem. Phys. 160, 100901 (2024)

For tr-SFX studies, the ability to obtain useable data from smaller, micro-crystals is critical. For many proteins it can be hard to crystallise large samples. In addition, the use of protein microcrystals allows uniform reaction initiation, in the case of reactions triggered by chemical mixing and photoactivation. UK XFEL's high brilliance across the 5-20 keV range for FEL-2, coupled with an ability to focus down to the μm scale, will make it an ideal platform to provide sufficient signal strength from nano and micro-crystalline samples. Although equal effort should also be made to reduce sources of noise where possible to maximise the signal to noise ratio. Being able to routinely perform tr-SFX at the harder end of FEL-2's tuning range will also help to obtain near-atomic resolution [96], especially when coupled with next-generation large area detectors that can offer $>$1 Mpixels with high dynamic range. Finally, ultra-short pulse durations ranging from attoseconds to 10s fs will provide dynamics information through reaction processes including short-lived intermediate states. A broad bandwidth mode, similar to that available at SwissFEL [97], could also open up the possibility of pushing crystallography to ultra-fast, sub-femtosecond timescales with application of chirped Laue diffraction [98, 99].

Reliably performing tr-SFX at higher repetition rates, and with little sample waste, will significantly increase throughput for such experiments on UK XFEL and attract many more user groups through lowering barriers to entry. More than most end-stations on UK XFEL, the ability to perform tr-SFX at high repetition rates will be limited by sample preparation and delivery. To accurately determine the structure of a sample using tr-SFX, it is a requirement that the sample be replenished at a repetition rate matching the X-ray beam to present a fresh crystal for each exposure. For UK

XFEL several sample delivery methods will be required, including fixed target and jet methods widely used elsewhere [100]. Liquid-phase injectors can reach the highest repetition rates, with gas dynamic virtual nozzle (GDVN) or double flow focusing nozzle (DFFN) commonly used for repetition rates of >100 Hz. However recent results at kHz repetition rates using ”droplet-on-demand” injection point the way towards increasing tr-SFX data rates whilst also optimising sample efficiency [101]. Other delivery methods such as fixed target arrays and aerosol injectors will also need to be made available. Although offline sample preparation labs will be important to many end stations, these will be particularly critical for supporting user operations in ES10.

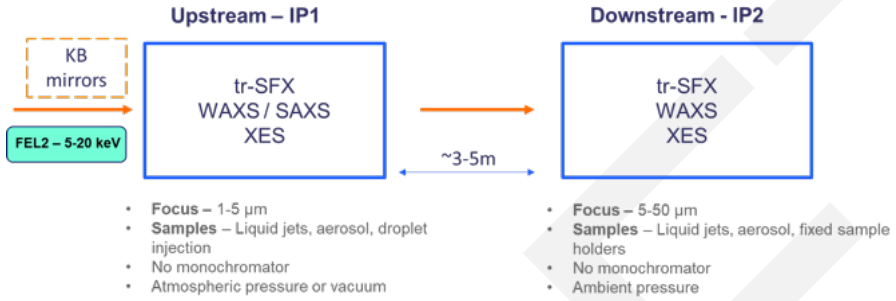

Figure 8.19: ES10 end station for application of tr-SFX techniques

In order to accommodate a range of sample systems, and experimental configurations, on ES10 the end station should ideally have two interaction points that could be set-up independently. This could take the form of providing one interaction point for fixed configurations (for higher scientific throughput), whilst a second interaction point emphasises flexibility and the ability to field novel set-ups (see Figure 8.19). The two interaction points would also likely be differentiated based on focusing, with one set-up for $\sim$1 μm focus for maximum fluence, the other for $>$ 5 μm. CRL nano-focusing could be an option for even smaller foci, but only at certain operating energies owing to the chromatic focusing. A high quality, and stable, wavefront and intensity will be critical for both IPs. Similar configurations with an upsteam and downstream interaction point have been successfully implemented with MicroMAX at MAXIV, CXI at LCLS II and SPB/SFX at the European XFEL. If possible the two interaction points should be sufficiently separated (and shielded) to allow IP1 to operate while IP2 is being configured for a later experiment. This would be a similar mode of operation to T-REXX at beamline P14 on PETRA III. It will be critical that sufficient space is available around both IPs in order to facilitate the exchange of sample delivery systems. Sample and detector systems would naturally be designed to be exchanged between IPs as required.

One or more large area detectors will be required for ES10, with at least one able to be positioned as close to the sample as possible to maximise accessible q range. A combination of short sample -detector distance combined with vacuum operation would be highly desirable for single particle imaging experiments where background signal needs to be minimised. There will sometimes be a requirement for larger crystals (or for SAXS measurements) to operate the detector further back, and this should be accommodated for in a similar fashion to other coherent scattering set-ups on ES9. Although large area detectors will be the primary source of data for almost all experiments, the ability to perform element-selective XES in parallel will be of interest for some user groups especially concerning studies of metallo-enzymes [102].

Almost all tr-SFX experiments will involve optical lasers, mainly for pumping of samples prior to arrival of the X-ray pulse but also for more novel configurations including ”pump and dump” schemes [103]. Pulse durations of the optical lasers will vary from a few femtoseconds to many picoseconds, and naturally the repetition rate will need to match that of the probe beam. Multiple colour pulses will also be required for novel multiple-pulse optical schemes. Synchronisation and arrival time diagnostics will be key, enabled by high resolution timing tools and thoughtful optical

design to minimise jitter and drift. Aspects of the optical layout will need to be duplicated for each IP to minimise changeover between experimental set-ups. If possible, optical pump beams should be made available in advance of user beamtime (ideally in conjunction with sample delivery) in order to test and optimise sample response and thus optimise efficient data collection during the run.

8.2.6 ES11 - Multi-colour end station

One of the main transformative capabilities to be offered by UK XFEL is a combination of widely separated colour X-ray beams at a single end station. Two-colour operation is currently possible at other XFELs [104, 105, 106, 107, 108], but not with widely separated energy ranges. On all the FELs of UK XFEL, a similar two-colour operation over the photon energy range of that FEL will be available by default.

Early in the CDOA process the UK user community was consulted to gather use cases for multi-colour X-ray experiments. This was to determine if one pre-existing end station could be identified as a candidate for adding an additional X-ray beamline to enable additional classes of experiments. However, it was decided that due to the additional complexity of performing multi-colour experiments (in terms of spatial and temporal synchronisation and detector requirements), it would be prudent to allocate a dedicated end station for this purpose. This would allow the extended set-up and operation for cutting-edge dual-colour experiments, whilst not impacting the high scientific throughput with more standardised set-ups planned for all other end stations.

A combination of independently-tuneable soft (approximately 0.25-3 keV) and hard (5-20 keV) X-ray FELs offers several unique experimental capabilities. The main class of experiments will be pumping of samples with a soft-tender X-ray beam to induce a novel transient state that can then be probed using a hard X-ray beam. The second class is for samples that can still be pumped with an optical laser, but then simultaneously probed at two X-ray energies. This could be applicable to some systems where performing two experiments on neighbouring beamlines (at different probe energies) would be extremely difficult due to very limited sample availability or for particularly inhomogeneous samples where reproducibility of the sample structure / composition is challenging.

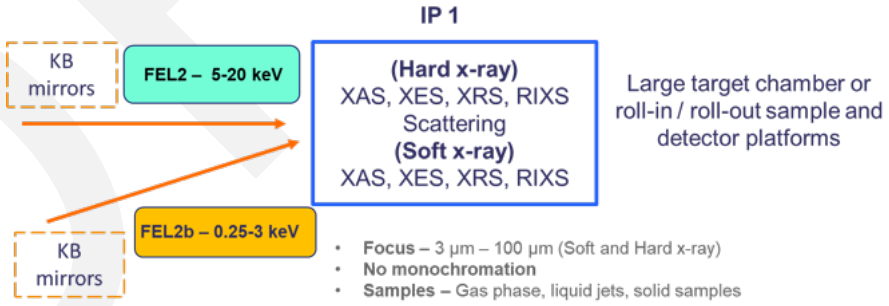

Figure 8.20: The ES11 end station for multi-colour X-ray experiments. Note - Since this needs to be a very flexible end station many detection techniques beyond those few listed here will need to be catered for at some stage.

One potential high impact use case is in time-resolved serial femtosecond crystallography (tr-SFX) where typically protein microcrystals are probed following a reaction initiated normally by either light or chemical reaction. However since a large number of reactions are driven by electrons in biology, being able to use a low-energy X-ray pulse to initiate these through the photoelectric effect with fs-timing accuracy would be a significant new approach to tr-SFX. By pumping with a

soft X-ray beam (above the oxygen K-edge) a large number of electrons can be produced quickly from water molecules [109] whilst minimising damage to the main target. This can then be safely probed with a separate (fs) hard X-ray beam to study changes in the atomic structure over many orders of magnitude of timing between the two pulses (ps - 100 ms) [110, 111].

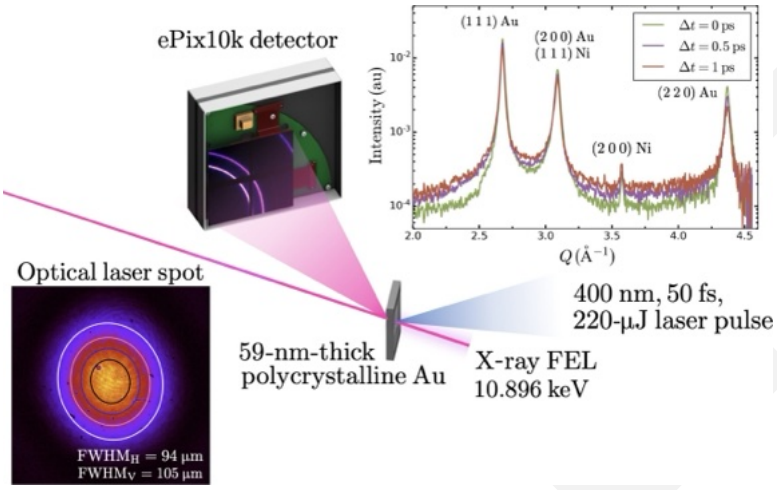

Figure 8.21: Schematic of the experimental setup used to measure the temporal evolution of the diffraction pattern from laser-heated, thin (50 nm) Au foils at the LCLS. High energy, soft X-ray pumping could open up many more experiments where the electrons in bulk samples are near-instantaneously heated. Figure courtesy of A. Descamps *et al.* Sci. Adv. 10 eadh5272 (2024)

A second case study for ES11 is the field of warm dense matter (WDM), where there is a desire to develop accurate models of high temperature, solid density conditions relevant to inertial confinement fusion (ICF), planetary interiors and shocked materials. XFELs have the unique ability to create homogeneous WDM conditions on femtosecond timescales, significantly faster than other methods such as laser-driven shock [112, 113]. A multi-colour SXR + HXR capability on UK XFEL will allow high energy (>mJ) soft X-ray pumping of bulk samples to high temperatures that can then be probed with a hard X-ray beam, either with X-ray spectroscopy or scattering methods for non-equilibrium structural transitions. This unique capability could be used to study effects such as phonon hardening, where metals are predicted to behave very differently from semiconductors by exhibiting stiffening of interatomic potentials when the electrons are near-instantaneously heated while the lattice remains cold [114, 115].

The layout for ES11 will require significant design effort owing to the complex multi-beam geometry and requirement to cater for a broad range of samples and detection techniques. It is currently planned that the two beams will intersect at a single point with a modest angle between the two beams similar to that planned for TXI at LCLS II. Focal spots (soft and hard X-ray) would range from a few μm to 100 μm depending on the experiment, with an emphasis on ensuring spatial overlap of X-ray beams (and any additional optical pump beams).

At the interaction point there will need to either be a single, larger flexible chamber that can house various sample systems and detectors, or a capability to exchange roll-in / roll-out set-ups should this be more practical operationally. Forward scattering for the hard X-ray beam will be a primary diagnostic, along with XAS, XES, RIXS and other photon spectroscopy methods. Care will be needed to avoid cross-talk between detectors when operating with very shot pump-pulse offsets.

8.2.7 ES12 and ES13: MEC and Very hard X-ray scattering (FEL-1)

Together ES12 and ES13 are being designed to cater for users studying Matter in Extreme Conditions (MEC) as well as communities who require the very highest X-ray energies (>20 keV) for advanced X-ray scattering and imaging techniques. The combination of XFEL with techniques to drive high energy density (HED) states creates the opportunity to probe extreme states and high-rate material response with a spatial and temporal resolution that can't easily be replicated elsewhere. HED states cover a very broad range of densities and temperatures covering warm dense matter all the way up to hot dense matter and quantum plasmas. Areas of scientific interest cover planetary and stellar interiors [116, 117, 118] conditions relevant to ICF [119] materials under static and dynamic shock compression [120] as well as fundamental plasma physics where high temperatures and densities lead to complex combinations of classical and quantum physics [121]. Studying how materials behave when under high strain rate and shock with X-rays is a distinct growth area, where material responses from the microscopic to the bulk scale need to be resolved over a range of time scales, often in situ or in operando [122, 123, 124].

Combinations of high-power lasers together with hard X-ray probing capability are in high demand at LCLS, SACLA and European XFEL. Other techniques to drive HED states across longer timescales, including pulsed power systems and gas guns are also routinely used with many potential applications when coupled ultra-fast, hard x-ray probing. UK XFEL will provide a unique, cutting-edge platform for HED science, not only to address specific flagship experiments from the UK XFEL Science and Technology Case, but to support a broad range of high-profile innovative science for years to come.

Applications for very hard X-ray scattering and imaging also include imaging of additive manufacturing or the production of 2D functional materials [125] where complex interactions can take place in liquid and solid states of matter over various spatial and temporal scales. For small scale studies of materials with poor structural coherence, e.g. nanoparticles, Pair Distribution Function (PDF) measurements using X-rays is seen as a powerful tool to reveal quantitative structural information [126]. There is a large community of users who use PDF techniques on synchrotrons and spallation sources who are keen to apply time resolved measurements that XFELs provided that high energy X-rays (ideally ∼40 keV or greater) can be matched to large area, fast area detection.

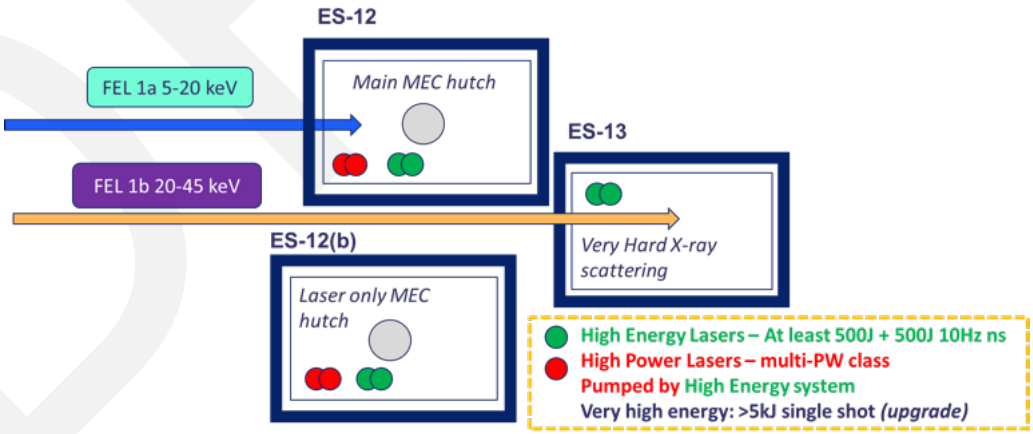

Figure 8.22: End station layout for FEL-1 featuring ES12 for a broad range of MEC experiments (including a separate hutch for laser-only experiments), and ES13 for very hard X-ray scattering measurements for materials under high static and dynamic load as well as time-resolved PDF (tr-PDF).

A consistent challenge for ES12 (and FEL-1 generally) was how to meet the demands of a diverse user community in terms of X-ray beam parameters. Simultaneously there have been requests

for high X-ray pulse energies (multi-mJ) to create WDM conditions, a wide tuning range for X-ray spectroscopy, very hard X-ray scattering to penetrate high density samples, as well as a desire to operate in multi-pulse modes for imaging of single shot, dynamic events. A decision was made during the CDOA process to split FEL-1 into two undulators and two beamlines in order to meet these demands. The first (FEL-1a) would cover ∼5-20 keV, the second (FEL-1b) ∼20-45 keV.

While there was consideration of creating a multi-colour MEC end station, the drive to maximise the level of parallel operations for UK XFEL and minimise extended changeover times between experiment configurations meant that a decision was made to also create two primary end stations for MEC and related hard X-ray scattering work (ES12 and ES13 respectively).

8.2.7.1 HED drivers for ES12 and ES13

The two main end stations will share the high-power laser capabilities, housed on an upper mezzanine level above the experimental areas. It is not possible at this stage to exactly define the high-power laser parameters as developments in this field are moving rapidly, and the final decision will depend heavily on available resource. However, it is anticipated that the main laser systems will be underpinned by a next-generation diode-pumped system that can either be operated in a native long pulse mode (ns pulse duration), or used to pump a short pulse (30 fs) high power system.

The long pulse driver should deliver energies of at least 500J per beam at a repetition rate at 10Hz or above. Two twinned laser systems (500J + 500J) would enable more novel experimental configurations such as colliding shocks, or merely the ability to drive higher pressure shocks with overlapping beams. In the alternative mode these lasers could be used to pump high intensity, short-pulse laser systems to deliver multi-PW (e.g. 10 PW + 10 PW) powers at matched repetition rates. UK XFEL will naturally draw on the UK's leadership and extensive experience with high repetition rate, high power lasers, notably the Central Laser Facility's design and build of the D100X laser [127] and soon to be commissioned Extreme Photonics Application Centre (EPAC).

Other systems to drive HED states will also need to be considered alongside high power laser drivers. Compact pulsed-power drivers would offer the ability to investigate hydrodynamic phenomena over microsecond timescales, relevant to astrophysical phenomena and ICF especially [128]. Pulsed-power systems together with other dynamic drivers would be a key requirement for Flagship Science and Technology Programmes VI and VII (See section 9.4 in the UK XFEL Science and Technology Case). Provision of a portable system capable of currents of 1MA or greater would allow users to access unique pressure regimes over much larger spatial scales. At even greater timescales, gas guns could be used to drive samples on the millisecond timescales, relevant to studying how materials respond during high energy impacts [129]. Even if not part of initial operations, the design of both ES12 and ES13 should permit the option of deploying such systems in future, possibly as part of user consortia. Even if low repetition rate by nature (although not necessarily at lower currents [130], both pulsed power and gas gun drivers would greatly expand the parameter space that could be studied using an XFEL and attract users from many fields who currently struggle to deploy similar systems on existing FELs.

During the CDOA consultation process with the MEC community, some users requested higher laser pulse energies (at multi-kJ) level, albeit at a much slower shot rate (e.g. 1 shot every 30 minutes). This would permit not only access to more extreme states, but also allow the study of more modest pressures at larger scales, allowing access to the mesoscale regime [131]. While this could be an important additional capability for UK XFEL, it is likely that prioritisation will be given to higher repetition rate laser-drivers in order to optimise use of the XFEL beam. Additional

discussions have involved lower-power, high repetition rate systems, e.g. 1 PW short pulse operating at 100 Hz. These together with the core laser requirements will be revisited during the subsequent technical design process.

8.2.7.2 ES12 - MEC

ES12 will be designed as a flexible experimental area capable of coupling both high intensity, short pulse lasers or high energy, long pulse lasers with FEL-1a (5-20 keV) for X-ray spectroscopy, scattering and imaging. The area itself will have to have a footprint of approximately 20 m by 12 m in order to house a large (vacuum) interaction chamber together with X-ray and high power laser beam transport. Sufficient space needs to be allocated to not only allow several standard configurations, but also to support efficient set-up, safe operations (including significant shielding) and room for additional laser and other system upgrades in the future. ES12 experiments will mostly be split into three categories based on the primary pump source; high energy X-ray pulse, high energy long pulse (nanosecond) laser or high intensity, short pulse (femtosecond) laser. An additional category may use static (and dynamic) compression from Diamond Anvil Cells (DAC) or other MEC drivers.

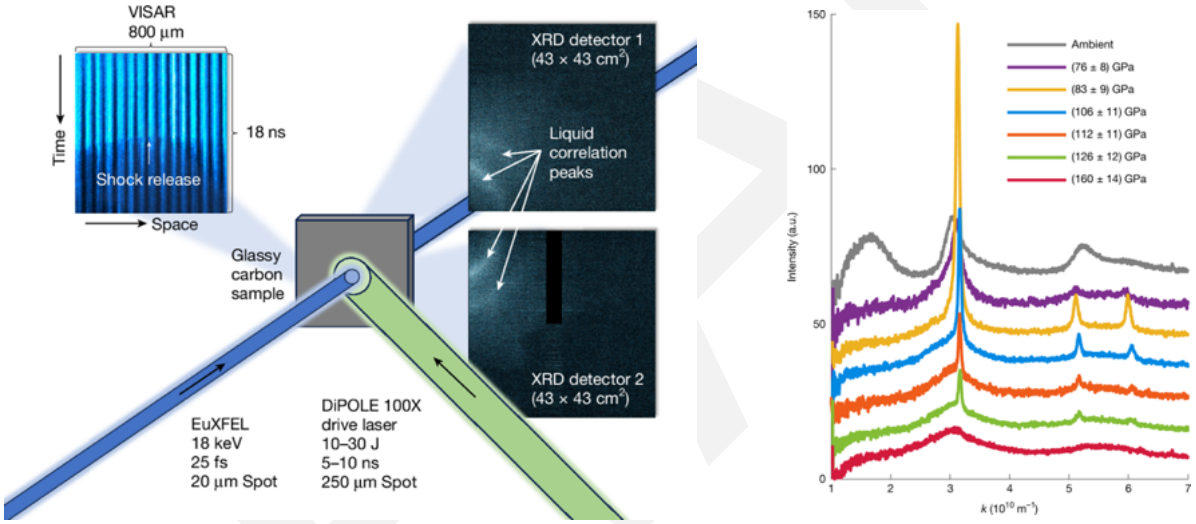

Figure 8.23: (Left) - X-ray diffraction of laser-shocked glassy carbon samples. (Right) - X-ray diffraction patterns for varying drive pressures. The transition from amorphous carbon structure to a liquid carbon state is observed as the pressure increases. Figures adapted from D. Kraus *et al.* Nature **642** 351-355 (2025)

Many experiments will require X-ray spectroscopy techniques such as XES, EXAFS, RIXS or XRS with shielded spectrometers positioned in the large interaction chamber at various positions depending on the main pumping system. X-ray energies in the full range from 5-20 keV to cover a broad spectrum of K- and L-edges of interest. The ability to probe electronic structure with high resolution [132] whilst maintaining high pulse energies (without the need for monochromation) would create a platform for studying phase transitions in much greater detail. This would be especially relevant to strongly-correlated systems where both electronic and structural transitions can be triggered by intense pressures and temperature [133]. An ability to realise the very highest spectral resolution in future (down to 10s meV over 5-20 keV) could unlock powerful inelastic X-ray scattering techniques for directly measuring temperature of viscosity in materials under extreme conditions [134].

Vacuum-compatible area detectors will also be required for SAXS and WAXS measurements, with some detectors having to operate as close to the target as possible in order to maximise 2θ

coverage. Lower power lasers will also be required for optical probing techniques common for laser-shock experiments such as VISAR (Velocity Interferometer System for Any Reflector).

Samples for ES12 will take many forms including gas phase (gas jets, gas cells), liquid jet (including cryogenic liquids) and solid state (tape drives or target arrays). Experiments using these samples will naturally be limited to the repetition rate of the high-power laser systems, which is expected to be in the range of 10 Hz to 100 Hz. X-ray probing under such extreme conditions will be challenging due to substantial background X-ray noise from laser-created plasma, EMP as well as the risk of debris from targetry that can damage high value optics.

There is increasing interest in applying secondary radiation sources generated by compact laser-plasma accelerators for both fundamental science as well as applications in medicine and industry [135]. Gaseous targets (typically gas cells or gas jets) can be used to generate multi-GeV electron beams [136] along with multi-keV betatron radiation or very hard (MeV) X-rays from Compton scattering or Bremsstrahlung processes. Higher density (liquid or solid) targets can be used to generate ultra-short pulses of multi-MeV ion beams [137] which not only have their own multi-disciplinary applications but can also be used as a method of neutron production. ES12 will harness the latest advances in laser accelerators to provide a broad range of secondary sources, enabling cutting-edge pump-probe experiments alongside the primary X-ray beam.

Should sufficient resource be available it would be highly desirable to also include a laser-only experimental area adjacent to ES12 that was served only by the high-power laser systems (and other MEC drivers) and not the XFEL beam. This would extend the idea of parallel operations of UK XFEL to make full use of what would be several world-class laser systems for HED science. This area could also be de-risk more complex experiments in advance of fielding in ES12 or ES13 with X-ray probing.

8.2.7.3 ES13 - Very Hard X-ray scattering and tr-PDF

With the availability of high energy, very hard (>20 keV) X-ray pulses from UK XFEL, there is an opportunity to perform many types of experiments that are currently not possible at other XFELs. The first broad category includes applications where very hard X-rays are required to penetrate dense samples and image dynamic processes. The second category is where energies into the 30-45 keV range can generate scattering patterns covering an extended range of reciprocal space to study local structure for liquids and amorphous samples both ex situ and in situ. ES13 will have to be flexible experimental platform for the application hard X-ray techniques using a range of dynamic loading methods and sample types. As a result, ES13 is currently envisioned as being more similar to an open port in that many aspects of the beamline may have to be reconfigured depending on the scale and complexity of the experiment. As UK XFEL develops, and demand dictates, it may be possible to extend ES13 to field multiple interaction points, similar in fashion to the DCS at APS [138].

There are a diverse range of applications for studying materials under non-equilibrium or high-rate conditions for many sectors of materials science and engineering. For each there is a requirement to study materials and processes in realistic environments and often over spatial scales from microscopic to macroscopic. One example is for additive manufacturing (AM) where there is a lack of understanding of the relevant physics involved during the AM process and hence a desire to use hard X-rays to probe inside bulk materials as they are made using AM. This requires a high flux of hard X-rays to penetrate the materials in question as well as ultra-high speed gating to resolve the relevant dynamics [139]. A second example is for materials compressed to extreme conditions, often using high-energy laser pulses to drive irreversible material deformations and

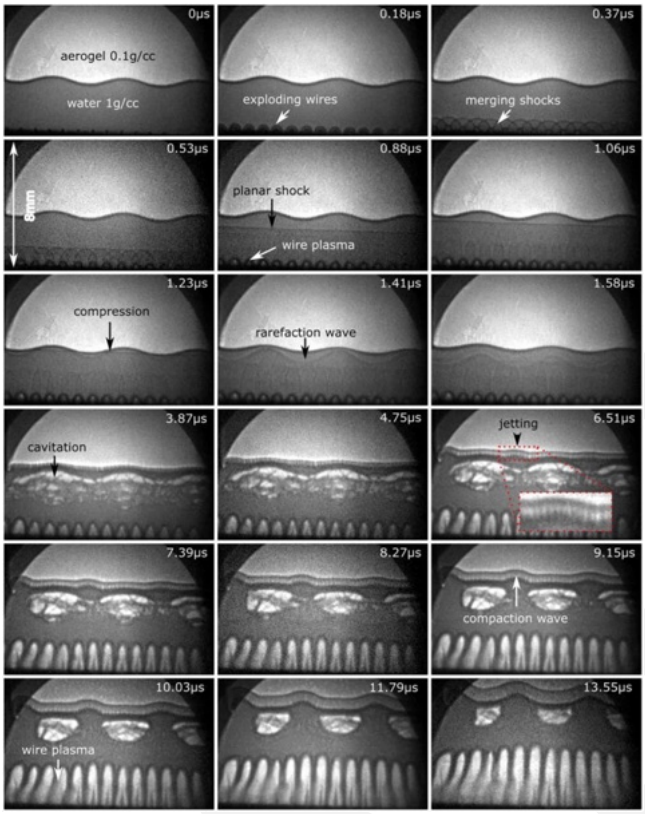

Figure 8.24: Multi-frame hard X-ray ($\bar{E}$ ∼30 keV) radiography showing a Richtmyer-Meshkov instability driven by exploding wire arrays, conducted on ID19 at the ESRF. Figure adapted from J. Strucka *et al.* Physics of Fluids **35** 044108 (2023)

failures [140, 141]. Full-field X-ray phase-contrast imaging (XPCI) has recently been tested at MHz acquisition rates on European XFEL and shows great promise for a range of academic and industrial applications [142].

The unique parameters of UK XFEL offer the chance to extend hard x-ray scattering imaging modes to study many additional types of dynamic events over varying spatial and temporal scales. The possibility to use UK XFEL in a burst mode, where approximately 10 X-ray pulses can probe the sample with >5 ns separation, would be highly applicable for studies of single dynamic events on 10s to 100 ns time scales, with the MHz repetition rate covering effective frame times of 1 μs or greater. Extending UK XFEL's fundamental energy to 40-45 keV would also enable in-situ or in-operando imaging of dynamics in high density materials [143].

For atomic pair distribution function (PDF) measurements there is a desire to obtain scattering measurements to a high q-max (scattering vector) value in order to map both long and very short range order with high structural resolution in real space. UK XFEL's ability to increasing the maximum X-ray probe energy to ∼45 keV would be transformative in this area, especially when coupled with an ability to perform time-resolved measurements in a manner that is currently not possible on synchrotrons where the bulk of PDF measurements are currently made. Early demonstrations of tr-PDF on XFELs to study fs-ps dynamics are now emerging [144], with the prospect of high X-ray energies and improved data analysis promising many more applications across nano materials, life sciences and energy storage.

8.3 General requirements and support services

8.3.1 Control rooms

For most end stations, a single control room will typically be sufficient to support both staff and visiting users in overseeing experiment setup and operation. From inside the control room, data acquisition and processing can be performed, along with operation of the control system to adjust optics or sample settings inside the experimental area. Each control room should be located adjacent to its respective experimental area to ensure convenient access and should be adequately sized to accommodate the often large teams currently required for XFEL beamtime operations. To supplement this, additional flexible office space and conference facilities should be provided elsewhere within the facility to support user groups and visiting scientists.

The MEC end station will require at least three dedicated control rooms: one each for ES12 and ES13, and one for the high-power laser systems. A fourth control room may also be necessary to support the laser-only area, should this component be included in the project scope.

8.3.2 Support laboratories

All end stations share a common requirement for sample preparation and support laboratories. These facilities will enable users to prepare for beamtime, develop and test new instrumentation, and modify or repair experimental setups during an active campaign. To ensure efficiency, these laboratories should be located as close as possible to their respective end stations.

User-provided samples may require extensive characterisation both before and after beamtime. In some cases, particularly where samples are highly sensitive or transport from the home institution is impractical, sample preparation may need to occur entirely on site. To further optimise beamtime usage, certain sample delivery systems could be duplicated in offline settings, allowing for refinement and testing prior to use in the experiment. Expanding the availability of preparation and support laboratories would substantially lower barriers to XFEL access by reducing the need for users to have extensive resources or specialised expertise for preparing complex samples and experimental setups at their home institutions.

Where appropriate, multi-purpose laboratories may be shared between end stations. However, dedicated laboratory space will be provided for applications in both biology and chemistry, reflecting the specialised needs of these user communities. As with the end stations, the role of these laboratories will naturally evolve alongside the facility's scientific priorities and applications, adapting to user needs and supporting the most effective use of available beamtime.

8.3.3 Standarisation of key equipment

Where feasible, end station equipment should be standardised to streamline both design and operational processes. A consistent design approach across end stations facilitates the efficient provision of critical spares throughout the facility and enables the flexible deployment of beamline diagnostics, detector systems, and sample delivery components for testing novel configurations. This standardisation should encompass mechanical, electrical and control systems; including kinematic mounting systems, vacuum infrastructure and motion control platforms. While it is

recognised that certain end stations will require bespoke solutions due to specialised scientific requirements, standardisation should be adopted as the default strategy wherever possible.

Many existing XFEL facilities have established centralised support groups responsible for key capabilities such as sample delivery, optical lasers, and detector development. These groups provide expert technical support across multiple end stations, enhancing both operational efficiency, minimising downtime and improving the pace of technical development. Facility-led support for commonly used end station equipment also lowers the barrier to entry for new users, reducing the need for them to supply and operate their own experimental systems.

8.4 Summary and Recommendations

This chapter has outlined an initial concept for a suite of end stations at the UK XFEL, designed to harness the facility's next-generation X-ray capabilities to enable groundbreaking, high-impact science across the user base. From the initial stages of the user consultation it was clear that a diverse range of end stations would be required in order to address the breadth of flagship experiments covered in the UK XFEL Science and Technology Case.

Some of the proposed end station concepts reflect those already in operation at other soft and hard X-ray XFELs - a result of strong demand and level of scientific output at these instruments. For UK XFEL, even where capabilities nominally overlap with other facilities, there is a clear focus on how its unique X-ray source can be leveraged to explore novel parameter spaces. This must be supported by world-leading secondary sources, advanced detectors and cutting-edge sample delivery. End stations with capabilities not found at other XFELs present a key opportunity to attract new users transitioning from other light sources, offering the appeal of time-resolved measurements with a highly tuneable, high-brightness X-ray beam. It should also be emphasised that substantial impact could be achieved by exploiting the strong complementarities between a UK XFEL and other large-scale national user facilities, such as Diamond-II and the Central Laser Facility, particularly in regimes where multimodal or correlative measurements can be performed across extended ranges of X-ray energies, pulse structures, and sample environments. Such coordinated use of complementary techniques would enable a more complete understanding of the underlying physical, chemical or biological processes of interest.

The strength of UK XFEL will lie not just with the breadth of end stations proposed and its technical capabilities, but its ability to perform as a high efficiency facility. Unlike synchrotrons, XFELs are often constrained by the limited number of end stations that can run simultaneously, which can significantly impact the volume of science, and therefore overall efficiency, delivered each year. In addition to high-repetition-rate operation, UK XFEL will address this challenge by supporting concurrent operation of six or more end stations. Furthermore, through careful design choices, each station will be capable of running in multiple configurations, minimising changeover times between experiments and maximising scientific throughput.

As UK XFEL progresses past the CDOA, the design of the end station provision will develop in several aspects. Firstly, consultations with the user community and other facility experts will continue, to both follow the latest areas of scientific interest, as well as highlight where key design decisions may have to be reviewed. This could for example include changes to the X-ray parameters required to address priority science areas, or the need to add additional detection capabilities onto certain end stations. All of this would be continued in parallel with design work in other work packages to ensure a consistent design across the facility. A more clearly defined

operating regime will be also be produced for each main configuration to understand the usable parameter space beyond the broad specifications outlined here.

Once the key operating parameters and top-level specifications are confirmed for each end station then more detailed technical design work can begin. This will include comprehensive layouts for each end station including all X-ray optics, sample environments, diagnostic and detector systems, timing systems, pump lasers as well as engineering and data acquisition services. Planning will also extend to the timing and logistics of installation and commissioning to further clarify the timeline from design to operation. This will also encompass staffing requirements for installation, commissioning, and ongoing operations. Prioritising this aspect is essential to establish a pipeline for developing the significant number of skilled personnel with the necessary expertise in XFEL science and technology who will be critical to the successful delivery and long-term operation of the UK XFEL.

DRAFT

References for Chapter 8

[1] J. Feldhaus et al. “AMO science at the FLASH and European XFEL free-electron laser facilities”. In: *Journal of Physics B: Atomic, Molecular and Optical Physics* 46 (16 2013). ISSN: 09534075. DOI: 10.1088/0953-4075/46/16/164002.

[2] Linda Young et al. *Roadmap of ultrafast x-ray atomic and molecular physics*. 2018. DOI: 10.1088/1361-6455/aa9735.

[3] Carlo Callegari et al. *Atomic, molecular and optical physics applications of longitudinally coherent and narrow bandwidth Free-Electron Lasers*. 2021. DOI: 10.1016/j.physrep.2020.12.002.

[4] Peter Walter et al. “The DREAM Endstation at the Linac Coherent Light Source”. In: *Applied Sciences (Switzerland)* 12 (20 2022). ISSN: 20763417. DOI: 10.3390/app122010534.

[5] Till Jahnke et al. “Direct observation of ultrafast symmetry reduction during internal conversion of 2-thiouracil using Coulomb explosion imaging”. In: *Nature Communications* 16 (1 2025), p. 2074. ISSN: 2041-1723. DOI: 10.1038/s41467-025-57083-3. URL: https://doi.org/10.1038/s41467-025-57083-3.

[6] Rebecca Boll et al. “X-ray multiphoton-induced Coulomb explosion images complex single molecules”. In: *Nature Physics* 18 (4 2022). ISSN: 17452481. DOI: 10.1038/s41567-022-01507-0.

[7] X. Li et al. “Coulomb explosion imaging of small polyatomic molecules with ultrashort x-ray pulses”. In: *Physical Review Research* 4 (1 2022). ISSN: 26431564. DOI: 10.1103/PhysRevResearch.4.013029.

[8] Daniel Rolles. *Time-resolved experiments on gas-phase atoms and molecules with XUV and X-ray free-electron lasers*. 2023. DOI: 10.1080/23746149.2022.2132182.

[9] Yoshiaki Kumagai et al. “Radiation-Induced Chemical Dynamics in Ar Clusters Exposed to Strong X-Ray Pulses”. In: *Physical Review Letters* 120 (22 2018). ISSN: 10797114. DOI: 10.1103/PhysRevLett.120.223201.

[10] Zhaoheng Guo et al. “Experimental demonstration of attosecond pump–probe spectroscopy with an X-ray free-electron laser”. In: *Nature Photonics* 18 (7 2024), pp. 691–697. ISSN: 1749-4893. DOI: 10.1038/s41566-024-01419-w. URL: https://doi.org/10.1038/s41566-024-01419-w.

[11] Siqi Li et al. “Attosecond coherent electron motion in Auger-Meitner decay”. In: *Science* 375 (6578 Jan. 2022). doi: 10.1126/science.abj2096, pp. 285–290. DOI: 10.1126/science.abj2096. URL: https://doi.org/10.1126/science.abj2096.

[12] Taran Driver et al. “Attosecond delays in X-ray molecular ionization”. In: *Nature* 632 (8026 2024), pp. 762–767. ISSN: 1476-4687. DOI: 10.1038/s41586-024-07771-9. URL: https://doi.org/10.1038/s41586-024-07771-9.

[13] Joseph Duris et al. “Tunable isolated attosecond X-ray pulses with gigawatt peak power from a free-electron laser”. In: *Nature Photonics* 14 (1 2020), pp. 30–36. ISSN: 1749-4893. DOI: 10.1038/s41566-019-0549-5. URL: https://doi.org/10.1038/s41566-019-0549-5.

[14] Peter Walter et al. “Multi-resolution electron spectrometer array for future free-electron laser experiments”. In: *Journal of Synchrotron Radiation* 28 (5 Sept. 2021), pp. 1364–1376. DOI: 10.1107/S1600577521007700. URL: https://doi.org/10.1107/S1600577521007700.

[15] Shuai Li et al. “Attosecond-pump attosecond-probe x-ray spectroscopy of liquid water”. In: *Science* 383 (6687 Mar. 2024). doi: 10.1126/science.adn6059, pp. 1118–1122. DOI: 10.1126/science.adn6059. URL: https://doi.org/10.1126/science.adn6059.

[16] Jonathan A Sobota, Yu He, and Zhi-Xun Shen. “Angle-resolved photoemission studies of quantum materials”. In: *Reviews of Modern Physics* 93 (2 May 2021), p. 25006. DOI: 10.1103/RevModPhys.93.025006. URL: https://link.aps.org/doi/10.1103/RevModPhys.93.025006.

[17] Curran Kalha et al. “Hard x-ray photoelectron spectroscopy: a snapshot of the state-of-the-art in 2020”. In: *Journal of Physics: Condensed Matter* 33 (23 May 2021), p. 233001. DOI: 10.1088/1361-648X/abeacd. URL: https://dx.doi.org/10.1088/1361-648X/abeacd.

[18] Fabio Boschini, Marta Zonno, and Andrea Damascelli. “Time-resolved ARPES studies of quantum materials”. In: *Reviews of Modern Physics* 96 (1 Jan. 2024), p. 015003. ISSN: 15390756. DOI: 10.1103/REVMODPHYS.96.015003/FIGURES/29/MEDIUM. URL: https://journals.aps.org/rmp/abstract/10.1103/RevModPhys.96.015003.

[19] Chan young Lim et al. “Recent technical advancements in ARPES: Unveiling quantum materials”. In: *Current Applied Physics* 60 (Apr. 2024), pp. 43–56. ISSN: 1567-1739. DOI: 10.1016/J.CAP.2024.01.010. URL: https://www.sciencedirect.com/science/article/pii/S156717392400018X.

[20] Martin Aeschlimann et al. “Time-resolved photoelectron spectroscopy at surfaces”. In: *Surface Science* 753 (Mar. 2025), p. 122631. ISSN: 0039-6028. DOI: 10.1016/J.SUSC.2024.122631. URL: https://www.sciencedirect.com/science/article/pii/S0039602824001821?via%3Dihub.

[21] Vishal Shokeen et al. “Real-time observation of non-equilibrium phonon-electron energy and angular momentum flow in laser-heated nickel”. In: *Science Advances* 10 (5 Feb. 2024), p. 31. ISSN: 23752548. DOI: 10.1126/SCIADV.ADJ2407/SUPPL_FILE/SCIADV.ADJ2407_SM.PDF. URL: /doi/pdf/10.1126/sciadv.adj2407?download=true.

[22] Kin Fai Mak and Jie Shan. “Photonics and optoelectronics of 2D semiconductor transition metal dichalcogenides”. In: *Nature Photonics* 10 (4 Apr. 2016), pp. 216–226. ISSN: 17494893. DOI: 10.1038/NPHOTON.2015.282;SUBJMETA=1019,1021,1054,301,399,624,639,918;KWRD=NANOPHOTONICS+AND+PLASMONICS,OPTICAL+PROPERTIES+AND+DEVICES. URL: https://www.nature.com/articles/nphoton.2015.282.

[23] Ethan C. Ahn. “2D materials for spintronic devices”. In: *npj 2D Materials and Applications 2020 4:1* 4 (1 June 2020), pp. 1–14. ISSN: 2397-7132. DOI: 10.1038/s41699-020-0152-0. URL: https://www.nature.com/articles/s41699-020-0152-0.

[24] John R. Schaibley et al. “Valleytronics in 2D materials”. In: *Nature Reviews Materials 2016 1:11* 1 (11 Aug. 2016), pp. 1–15. ISSN: 2058-8437. DOI: 10.1038/natrevmats.2016.55. URL: https://www.nature.com/articles/natrevmats201655.

[25] Neeraj Kumar, Rashi Gusain, and Suprakas Sinha Ray, eds. *Two-Dimensional Materials for Environmental Applications*. Vol. 332. Springer International Publishing, 2023. ISBN: 978-3-031-28755-8. DOI: 10.1007/978-3-031-28756-5. URL: https://link.springer.com/10.1007/978-3-031-28756-5.

[26] “2D Nanomaterials for Energy and Environmental Sustainability”. In: (2022). Ed. by Zeba Khanam, Neelam Gogoi, and Divesh Narayan Srivastava. DOI: 10.1007/978-981-16-8538-5. URL: https://link.springer.com/10.1007/978-981-16-8538-5.

[27] Alexander Neef et al. “Orbital-resolved observation of singlet fission”. In: *Nature 2023 616:7956* 616 (7956 Apr. 2023), pp. 275–279. ISSN: 1476-4687. DOI: 10.1038/s41586-023-05814-1. URL: https://www.nature.com/articles/s41586-023-05814-1.

[28] Tianlun Yu et al. “Momentum-resolved electronic structure and band offsets in an epitaxial NbN/GaN superconductor/ semiconductor heterojunction”. In: *Science Advances* 7 (52 Dec. 2021), p. 5833. ISSN: 23752548. DOI: 10.1126/SCIADV.ABI5833/SUPPL_FILE/SCIADV.ABI5833_SM.PDF. URL: /doi/pdf/10.1126/sciadv.abi5833?download=true.

[29] Davide Curcio et al. “Ultrafast electronic linewidth broadening in the C core level of graphene”. In: *Physical Review B* 104 (16 Oct. 2021), p. L161104. ISSN: 24699969. DOI: 10.1103/PHYSREVB.104.L161104/SUPPLEMENTARY.PDF. URL: https://journals.aps.org/prb/abstract/10.1103/PhysRevB.104.L161104.

[30] Davide Curcio et al. “Tracking the surface atomic motion in a coherent phonon oscillation”. In: *Physical Review B* 106 (20 Nov. 2022), p. L201409. ISSN: 24699969. DOI: 10.1103/PHYSREVB.106.L201409/PHONON_XPD_SM_2.PDF. URL: https://journals.aps.org/prb/abstract/10.1103/PhysRevB.106.L201409.

[31] D. Kutnyakhov et al. “Time- And momentum-resolved photoemission studies using time-of-flight momentum microscopy at a free-electron laser”. In: *Review of Scientific Instruments* 91 (1 Jan. 2020), p. 13109. ISSN: 10897623. DOI: 10.1063/1.5118777/1018655. URL: /aip/rsi/article/91/1/013109/1018655/Time-and-momentum-resolved-photoemission-studies.

[32] Kai Rossnagel. “Pushing the space-charge limit in electron momentum microscopy”. In: *New Journal of Physics* 20 (2 Feb. 2018), p. 021001. ISSN: 1367-2630. DOI: 10.1088/1367-2630/AAAC6B. URL: https://iopscience.iop.org/article/10.1088/1367-2630/aaac6b%20https://iopscience.iop.org/article/10.1088/1367-2630/aaac6b/meta.

[33] J. Graf et al. “Vacuum space charge effect in laser-based solid-state photoemission spectroscopy”. In: *Journal of Applied Physics* 107 (1 Jan. 2010), p. 31. ISSN: 00218979. DOI: 10.1063/1.3273487/287315. URL: /aip/jap/article/107/1/014912/287315/Vacuum-space-charge-effect-in-laser-based-solid.

[34] S. Hellmann et al. “Vacuum space-charge effects in solid-state photoemission”. In: *Physical Review B - Condensed Matter and Materials Physics* 79 (3 Jan. 2009), p. 035402. ISSN: 10980121. DOI: 10.1103/PHYSREVB.79.035402/FIGURES/7/MEDIUM. URL: https://journals.aps.org/prb/abstract/10.1103/PhysRevB.79.035402.

[35] P. Grychtol et al. “The SXP instrument at the European XFEL”. In: *Journal of Physics: Conference Series* 2380 (1 Dec. 2022), p. 012043. ISSN: 1742-6596. DOI: 10.1088/1742-6596/2380/1/012043. URL: https://iopscience.iop.org/article/10.1088/1742-6596/2380/1/012043%20https://iopscience.iop.org/article/10.1088/1742-6596/2380/1/012043/meta.

[36] G. Schönhense et al. “Time-of-flight photoemission electron microscopy – a new way to chemical surface analysis”. In: *Surface Science* 480 (3 June 2001), pp. 180–187. ISSN: 0039-6028. DOI: 10.1016/S0039-6028(01)00833-0. URL: https://www.sciencedirect.com/science/article/pii/S0039602801008330?via%3Dihub.

[37] Christian Tusche et al. “From Photoemission Microscopy to an “All-in-One” Photoemission Experiment”. In: *e-Journal of Surface Science and Nanotechnology* 18 (Feb. 2020), pp. 48–56. ISSN: 1348-0391. DOI: 10.1380/EJSSNT.2020.48.

[38] J. Maklar et al. “A quantitative comparison of time-of-flight momentum microscopes and hemispherical analyzers for time- And angle-resolved photoemission spectroscopy experiments”. In: *Review of Scientific Instruments* 91 (12 Dec. 2020), p. 123112. ISSN: 10897623. DOI: 10.1063/5.0024493/1018565. URL: /aip/rsi/article/91/12/123112/1018565/A-quantitative-comparison-of-time-of-flight.

[39] Jin Qian et al. “Addressing the sensitivity of signals from solid/liquid ambient pressure XPS (APXPS) measurement”. In: *Journal of Chemical Physics* 153 (4 July 2020), p. 16. ISSN: 10897690. DOI: 10.1063/5.0006242/19758207/044709_1_ACCEPTED_MANUSCRIPT.PDF. URL: /aip/jcp/article/153/4/044709/1065036/Addressing-the-sensitivity-of-signals-from-solid.

[40] Michael Wagstaffe et al. “Ultrafast Real-Time Dynamics of CO Oxidation over an Oxide Photocatalyst”. In: *ACS Catalysis* 10 (22 Nov. 2020), pp. 13650–13658. ISSN: 21555435. DOI: 10.1021/ACSCATAL.0C04098/ASSET/IMAGES/LARGE/CS0C04098_0003.JPEG. URL: /doi/pdf/10.1021/acscatal.0c04098?ref=article_openPDF.

[41] Jiangdong Yu et al. “Operando Characterization of Electrochemistry at the Rutile TiO2(110)/0.1 M HCl Interface Using Ambient Pressure XPS”. In: *Journal of Physical Chemistry C* 128 (49 Dec. 2024), pp. 20933–20939. ISSN: 19327455. DOI: 10.1021/ACS.JPCC.4C07173/ASSET/IMAGES/LARGE/JP4C07173_0009.JPEG. URL: /doi/pdf/10.1021/acs.jpcc.4c07173?ref=article_openPDF.

[42] Mario Borgwardt et al. “Charge Transfer Dynamics at Dye-Sensitized ZnO and TiO2 Interfaces Studied by Ultrafast XUV Photoelectron Spectroscopy”. In: *Scientific Reports* 6 (1 Apr. 2016), pp. 1–7. ISSN: 20452322. DOI: 10.1038/SREP24422;SUBJMETA=4062,4072,4077,440,638,639;KWRD=DEVICES+FOR+ENERGY+HARVESTING,PHYSICAL+CHEMISTRY. URL: https://www.nature.com/articles/srep24422.

[43] David Degerman et al. “Operando X-ray Photoelectron Spectroscopy for High-Pressure Catalysis Research Using the POLARIS Endstation”. In: *Synchrotron Radiation News* 35 (3 2022), pp. 11–18. ISSN: 19317344. DOI: 10.1080/08940886.2022.2078580;PAGE:STRING:ARTICLE/CHAPTER. URL: https://www.tandfonline.com/doi/pdf/10.1080/08940886.2022.2078580.

[44] Joseph Woicik, ed. *Hard X-ray Photoelectron Spectroscopy (HAXPES)*. Vol. 59. Springer International Publishing, 2016. ISBN: 978-3-319-24041-1. DOI: 10.1007/978-3-319-24043-5. URL: http://link.springer.com/10.1007/978-3-319-24043-5.

[45] L. P. Oloff et al. “Time-resolved HAXPES at SACLA: probe and pump pulse-induced space-charge effects”. In: *New Journal of Physics* 16 (12 Dec. 2014), p. 123045. ISSN: 1367-2630. DOI: 10.1088/1367-2630/16/12/123045. URL: https://iopscience.iop.org/article/10.1088/1367-2630/16/12/123045%20https://iopscience.iop.org/article/10.1088/1367-2630/16/12/123045/meta.

[46] Anthony Boucly et al. “Bias dependent band alignment in Ga2O3 ferroelectric interface by operando HAXPES”. In: *Scientific Reports* 15 (1 Dec. 2025), pp. 1–10. ISSN: 20452322. DOI: 10.1038/S41598-025-90555-6;SUBJMETA=1005,1007,301,639;KWRD=ELECTRONIC+DEVICES,MATERIALS+FOR+DEVICES,MATERIALS+SCIENCE. URL: https://www.nature.com/articles/s41598-025-90555-6.

[47] Takahiro Nakamura et al. “Quick Operando Ambient Pressure Hard X-ray Photoelectron Spectroscopy for Reaction Kinetic Measurements of Polymer Electrolyte Fuel Cells”. In: *Journal of Physical Chemistry C* 124 (32 Aug. 2020), pp. 17520–17527. ISSN: 19327455. DOI: 10.1021/ACS.JPCC.0C04871/ASSET/IMAGES/LARGE/JP0C04871_0006.JPEG. URL: /doi/pdf/10.1021/acs.jpcc.0c04871?ref=article_openPDF.

[48] N. Gerasimova et al. “The soft X-ray monochromator at the SASE3 beamline of the European XFEL: from design to operation”. In: *urn:issn:1600-5775* 29 (5 Aug. 2022), pp. 1299–1308. ISSN: 1600-5775. DOI: 10.1107/S1600577522007627. URL: https://journals.iucr.org/paper?ok5074%20https://journals.iucr.org/s/issues/2022/05/00/ok5074/.

[49] M. Mitrano et al. “Exploring Quantum Materials with Resonant Inelastic X-Ray Scattering”. In: *Physical Review X* 14 (4 Oct. 2024), p. 040501. ISSN: 21603308. DOI: 10.1103/PHYSREVX.14.040501/FIGURES/6/MEDIUM. URL: https://journals.aps.org/prx/abstract/10.1103/PhysRevX.14.040501.

[50] Matteo Mitrano and Yao Wang. “Probing light-driven quantum materials with ultrafast resonant inelastic X-ray scattering”. In: *Communications Physics 2020 3:1* 3 (1 Oct. 2020), pp. 1–9. ISSN: 2399-3650. DOI: 10.1038/s42005-020-00447-6. URL: https://www.nature.com/articles/s42005-020-00447-6.

[51] Y. Cao et al. “Ultrafast dynamics of spin and orbital correlations in quantum materials: an energy- and momentum-resolved perspective”. In: *Philosophical Transactions of the Royal Society A* 377 (2145 May 2019), p. 20170480. ISSN: 1364503X. DOI: 10.1098/RSTA.2017.0480. URL: /doi/pdf/10.1098/rsta.2017.0480.

[52] Matteo Mitrano et al. “Ultrafast time-resolved x-ray scattering reveals diffusive charge order dynamics in La2-xBaxCuO4”. In: *Science Advances* 5 (8 Aug. 2019). ISSN: 23752548. DOI: 10.1126/SCIADV.AAX3346/SUPPL_FILE/AAX3346_SM.PDF. URL: /doi/pdf/10.1126/sciadv.aax3346?download=true.

[53] Marcus Lundberg and Philippe Wernet. “Resonant Inelastic X-ray Scattering (RIXS) Studies in Chemistry: Present and Future”. In: *Synchrotron Light Sources and Free-Electron Lasers: Accelerator Physics, Instrumentation and Science Applications* (Jan. 2020), pp. 2315–2366. DOI: 10.1007/978-3-030-23201-6_74. URL: https://link.springer.com/rwe/10.1007/978-3-030-23201-6_74.

[54] Faris Gel’Mukhanov et al. “Dynamics of resonant x-ray and Auger scattering”. In: *Reviews of Modern Physics* 93 (3 Sept. 2021), p. 035001. ISSN: 15390756. DOI: 10.1103/REVMODPHYS.93.035001/FIGURES/17/MEDIUM. URL: https://journals.aps.org/rmp/abstract/10.1103/RevModPhys.93.035001.

[55] Raphael M. Jay et al. “Capturing Atom-Specific Electronic Structural Dynamics of Transition-Metal Complexes with Ultrafast Soft X-Ray Spectroscopy”. In: *Annual Review of Physical Chemistry* 73 (Volume 73, 2022 Apr. 2022), pp. 187–208. ISSN: 15451593. DOI: 10.1146/ANNUREV-PHYSCHEM-082820-020236/CITE/REFWORKS. URL: https://www.annualreviews.org/content/journals/10.1146/annurev-physchem-082820-020236.

[56] *https://lcls.slac.stanford.edu/instruments*.

[57] Taran Driver et al. “Attosecond transient absorption spooktroscopy: a ghost imaging approach to ultrafast absorption spectroscopy”. In: *Physical Chemistry Chemical Physics* 22 (5 Feb. 2020), pp. 2704–2712. ISSN: 1463-9084. DOI: 10.1039/C9CP03951A. URL: https://pubs.rsc.org/en/content/articlehtml/2020/cp/c9cp03951a%20https://pubs.rsc.org/en/content/articlelanding/2020/cp/c9cp03951a.

[58] Loïc Le Guyader et al. “Photon-shot-noise-limited transient absorption soft X-ray spectroscopy at the European XFEL”. In: *Journal of Synchrotron Radiation* 30 (Pt 2 Feb. 2023), pp. 284–300. ISSN: 16005775. DOI: 10.1107/S1600577523000619/HTTPS://JOURNALS.IUCR.ORG/SERVICES/RSS.HTML. URL: https://journals.iucr.org/paper?ok5086%20https://journals.iucr.org/s/issues/2023/02/00/ok5086/.

[59] George E. Cutsail and Serena DeBeer. “Challenges and Opportunities for Applications of Advanced X-ray Spectroscopy in Catalysis Research”. In: *ACS Catalysis* 12 (10 May 2022), pp. 5864–5886. ISSN: 21555435. DOI: 10.1021/ACSCATAL.2C01016/ASSET/IMAGES/LARGE/CS2C01016_0006.JPEG. URL: /doi/pdf/10.1021/acscatal.2c01016?ref=article_openPDF.

[60] Zachary Mathe et al. “Coupling experiment and theory to push the state-of-the-art in X-ray spectroscopy”. In: *Nature Reviews Chemistry 2025 9:7* 9 (7 May 2025), pp. 436–453. ISSN: 2397-3358. DOI: 10.1038/s41570-025-00718-2. URL: https://www.nature.com/articles/s41570-025-00718-2.

[61] Raphael M. Jay et al. “Tracking C–H activation with orbital resolution”. In: *Science* 380 (6648 June 2023), pp. 955–960. ISSN: 10959203. DOI: 10.1126/SCIENCE.ADF8042/SUPPL_FILE/SCIENCE.ADF8042_MOVIES_S1_TO_S4.ZIP. URL: /doi/pdf/10.1126/science.adf8042?download=true.

[62] Nanna Zhou Hagström et al. “Megahertz-rate ultrafast X-ray scattering and holographic imaging at the European XFEL”. In: *Journal of Synchrotron Radiation* 29 (6 Sept. 2022), pp. 1454–1464. ISSN: 16005775. DOI: 10.1107/S1600577522008414/AY5598SUP1.PDF. URL: https://journals.iucr.org/paper?ay5598%20https://journals.iucr.org/s/issues/2022/06/00/ay5598/.

[63] R. Plumley et al. “On ultrafast x-ray scattering methods for magnetism”. In: *Advances in Physics: X* 9 (1 Dec. 2024). ISSN: 23746149. DOI: 10.1080/23746149.2024.2423935. URL: https://www.tandfonline.com/doi/pdf/10.1080/23746149.2024.2423935.

[64] Diego Turenne et al. “Nonequilibrium sub–10 nm spin-wave soliton formation in FePt nanoparticles”. In: *Science Advances* 8 (13 Apr. 2022), p. 523. ISSN: 23752548. DOI: 10.1126/SCIADV.ABN0523/SUPPL_FILE/SCIADV.ABN0523_MOVIE_S1.ZIP. URL: /doi/pdf/10.1126/sciadv.abn0523?download=true.

[65] Hariom Jani et al. “Antiferromagnetic half-skyrmions and bimerons at room temperature”. In: *Nature 2021 590:7844* 590 (7844 Feb. 2021), pp. 74–79. ISSN: 1476-4687. DOI: 10.1038/s41586-021-03219-6. URL: https://www.nature.com/articles/s41586-021-03219-6.

[66] Sophie E. Canton et al. “Visualizing the non-equilibrium dynamics of photoinduced intramolecular electron transfer with femtosecond X-ray pulses”. In: *Nature Communications* 6 (1 Mar. 2015), pp. 1–10. ISSN: 20411723. DOI: 10.1038/NCOMMS7359;TECHMETA=140;SUBJMETA=119,301,440,638,639,77,886,947;KWRD=CONDENSED-MATTER+PHYSICS,ELECTROCATALYSIS,ELECTRON+TRANSFER. URL: https://www.nature.com/articles/ncomms7359.

[67] A. Stupakiewicz et al. “Ultrafast nonthermal photo-magnetic recording in a transparent medium”. In: *Nature 2017 542:7639* 542 (7639 Jan. 2017), pp. 71–74. ISSN: 1476-4687. DOI: 10.1038/nature20807. URL: https://www.nature.com/articles/nature20807.

[68] Daniel Ortiz et al. “Electrolytes Ageing in Lithium-ion Batteries: A Mechanistic Study from Picosecond to Long Timescales”. In: *ChemSusChem* 8 (21 Nov. 2015), pp. 3605–3616. ISSN: 1864-564X. DOI: 10.1002/CSSC.201500641. URL: /doi/pdf/10.1002/cssc.201500641%20https://onlinelibrary.wiley.com/doi/abs/10.1002/cssc.201500641%20https://chemistry-europe.onlinelibrary.wiley.com/doi/full/10.1002/cssc.201500641.

[69] Gerald Auböck and Majed Chergui. “Sub-50-fs photoinduced spin crossover in [Fe(bpy)3]2+”. In: *Nature Chemistry 2015 7:8* 7 (8 July 2015), pp. 629–633. ISSN: 1755-4349. DOI: 10.1038/nchem.2305. URL: https://www.nature.com/articles/nchem.2305.

[70] Simon Wall et al. “Ultrafast disordering of vanadium dimers in photoexcited VO2”. In: *Science* 362 (6414 Nov. 2018), pp. 572–576. ISSN: 10959203. DOI: 10.1126/SCIENCE.AAU3873/SUPPL_FILE/AAU3873S2.MP4. URL: /doi/pdf/10.1126/science.aau3873?download=true.

[71] Asmit Bhowmick et al. “Structural evidence for intermediates during O2 formation in photosystem II”. In: *Nature 2023 617:7961* 617 (7961 May 2023), pp. 629–636. ISSN: 1476-4687. DOI: 10.1038/s41586-023-06038-z. URL: https://www.nature.com/articles/s41586-023-06038-z.

[72] Thomas Gruhl et al. “Ultrafast structural changes direct the first molecular events of vision”. In: *Nature 2023 615:7954* 615 (7954 Mar. 2023), pp. 939–944. ISSN: 1476-4687. DOI: 10.1038/s41586-023-05863-6. URL: https://www.nature.com/articles/s41586-023-05863-6.

[73] Lin X. Chen and Junko Yano. “Deciphering Photoinduced Catalytic Reaction Mechanisms in Natural and Artificial Photosynthetic Systems on Multiple Temporal and Spatial Scales Using X-ray Probes”. In: *Chemical Reviews* 124 (9 May 2024), pp. 5421–5469. ISSN: 15206890. DOI: 10.1021/ACS.CHEMREV.3C00560/ASSET/IMAGES/MEDIUM/CR3C00560_0044.GIF. URL: /doi/pdf/10.1021/acs.chemrev.3c00560?ref=article_openPDF.

[74] Ian Robinson, Jesse Clark, and Ross Harder. “Materials science in the time domain using Bragg coherent diffraction imaging”. In: *Journal of Optics* 18 (5 Mar. 2016), p. 054007. ISSN: 2040-8986. DOI: 10.1088/2040-8978/18/5/054007. URL: https://iopscience.iop.org/article/10.1088/2040-8978/18/5/054007%20https://iopscience.iop.org/article/10.1088/2040-8978/18/5/054007/meta.

[75] M. P. Minitti et al. “Imaging Molecular Motion: Femtosecond X-Ray Scattering of an Electrocyclic Chemical Reaction”. In: *Physical Review Letters* 114 (25 June 2015), p. 255501. ISSN: 10797114. DOI: 10.1103/PHYSREVLETT.114.255501/SMFIG4.EPS. URL: https://journals.aps.org/prl/abstract/10.1103/PhysRevLett.114.255501.

[76] Brian Stankus et al. “Ultrafast X-ray scattering reveals vibrational coherence following Rydberg excitation”. In: *Nature Chemistry* 11 (8 Aug. 2019), pp. 716–721. ISSN: 17554349. DOI: 10.1038/S41557-019-0291-0;SUBJMETA=440,638,639,94,949,950;KWRD=CHEMICAL+PHYSICS,EXCITED+STATES,REACTION+KINETICS+AND+DYNAMICS. URL: https://www.nature.com/articles/s41557-019-0291-0.

[77] Haiwang Yong et al. “Observation of the molecular response to light upon photoexcitation”. In: *Nature Communications 2020 11:1* 11 (1 May 2020), pp. 1–6. ISSN: 2041-1723. DOI: 10.1038/s41467-020-15680-4. URL: https://www.nature.com/articles/s41467-020-15680-4.

[78] Aviad Schori et al. “Real-space observation of the dissociation of a transition metal complex and its concurrent energy redistribution”. In: *Nature Communications* 16 (1 Dec. 2025), pp. 1–9. ISSN: 20411723. DOI: 10.1038/S41467-025-60009-8;SUBJMETA=439,440,563,638,639,949,981;KWRD=EXCITED+STATES,MOLECULAR+DYNAMICS,PHOTOCHEMISTRY. URL: https://www.nature.com/articles/s41467-025-60009-8.

[79] David Serban et al. “Imaging in-operando LiCoO2 nanocrystallites with Bragg coherent X-ray diffraction”. In: *Communications Chemistry 2024 7:1* 7 (1 Oct. 2024), pp. 1–9. ISSN: 2399-3669. DOI: 10.1038/s42004-024-01331-y. URL: https://www.nature.com/articles/s42004-024-01331-y.

[80] Yifei Sun et al. “Operando real-space imaging of a structural phase transformation in the high-voltage electrode LixNi0.5Mn1.5O4”. In: *Nature Communications* 15 (1 Dec. 2024), pp. 1–8. ISSN: 20411723. DOI: 10.1038/S41467-024-55010-6;TECHMETA=123,128,145;SUBJMETA=12,299,301,639,891,930;KWRD=BATTERIES,CHARACTERIZATION+AND+ANALYTICAL+TECHNIQUES. URL: https://www.nature.com/articles/s41467-024-55010-6.

[81] Jialun Liu et al. “Electric field driven domain wall dynamics in BaTiO3 nanoparticles”. In: *Physical Review B* 111 (5 Feb. 2025), p. 054101. ISSN: 24699969. DOI: 10.1103/PHYSREVB.111.054101/FIGURES/8/MEDIUM. URL: https://journals.aps.org/prb/abstract/10.1103/PhysRevB.111.054101.

[82] Mansoor A. Najeeb et al. “Three-dimensional imaging of topologically protected strings in a multiferroic nanocrystal”. In: *Communications Materials 2025 6:1* 6 (1 Jan. 2025), pp. 1–8. ISSN: 2662-4443. DOI: 10.1038/s43246-025-00738-x. URL: https://www.nature.com/articles/s43246-025-00738-x.

[83] J. N. Clark et al. “Ultrafast three-dimensional imaging of lattice dynamics in individual gold nanocrystals”. In: *Science* 341 (6141 July 2013), pp. 56–59. ISSN: 10959203. DOI: 10.1126/SCIENCE.1236034/SUPPL_FILE/CLARK.SM.PDF. URL: /doi/pdf/10.1126/science.1236034?download=true.

[84] Jesse N. Clark et al. “Imaging transient melting of a nanocrystal using an X-ray laser”. In: *Proceedings of the National Academy of Sciences of the United States of America* 112 (24 June 2015), pp. 7444–7448. ISSN: 10916490. DOI: 10.1073/PNAS.1417678112/SUPPL_FILE/PNAS.1417678112.SM03.AVI. URL: /doi/pdf/10.1073/pnas.1417678112?download=true.

[85] Felix Lehmkühler, Wojciech Roseker, and Gerhard Grübel. “From Femtoseconds to Hours—Measuring Dynamics over 18 Orders of Magnitude with Coherent X-rays”. In: *Applied Sciences 2021, Vol. 11, Page 6179* 11 (13 July 2021), p. 6179. ISSN: 2076-3417. DOI: 10.3390/APP11136179. URL: https://www.mdpi.com/2076-3417/11/13/6179/htm%20https://www.mdpi.com/2076-3417/11/13/6179.

[86] Francesco Dallari et al. “Real-time swelling-collapse kinetics of nanogels driven by XFEL pulses”. In: *Science Advances* 10 (16 Apr. 2024), p. 7876. ISSN: 23752548. DOI: 10.1126/SCIADV.ADM7876/SUPPL_FILE/SCIADV.ADM7876_SM.PDF. URL: /doi/pdf/10.1126/sciadv.adm7876?download=true.

[87] Claudia Goy et al. “Speckle contrast from the split-and-delay unit with seeded X-ray pulses of the MID instrument at European XFEL”. In: *Journal of Physics: Conference Series* 3010 (1 May 2025), p. 012173. ISSN: 1742-6596. DOI: 10.1088/1742-6596/3010/1/012173. URL: https://iopscience.iop.org/article/10.1088/1742-6596/3010/1/012173%20https://iopscience.iop.org/article/10.1088/1742-6596/3010/1/012173/meta.

[88] W. Roseker et al. “Towards ultrafast dynamics with split-pulse X-ray photon correlation spectroscopy at free electron laser sources”. In: *Nature Communications 2018 9:1* 9 (1 Apr. 2018), pp. 1–6. ISSN: 2041-1723. DOI: 10.1038/s41467-018-04178-9. URL: https://www.nature.com/articles/s41467-018-04178-9.

[89] Allen M. Orville. “Recent results in time resolved serial femtosecond crystallography at XFELs”. In: *Current Opinion in Structural Biology* 65 (Dec. 2020), pp. 193–208. ISSN: 0959-440X. DOI: 10.1016/J.SBI.2020.08.011. URL: https://www.sciencedirect.com/science/article/pii/S0959440X20301482.

[90] Raphaël de Wijn et al. “Potential of Time-Resolved Serial Femtosecond Crystallography Using High Repetition Rate XFEL Sources”. In: *Applied Sciences 2022, Vol. 12, Page 2551* 12 (5 Feb. 2022), p. 2551. ISSN: 2076-3417. DOI: 10.3390/APP12052551. URL: https://www.mdpi.com/2076-3417/12/5/2551/htm%20https://www.mdpi.com/2076-3417/12/5/2551.

[91] Nicolas Caramello and Antoine Royant. “From femtoseconds to minutes: time-resolved macromolecular crystallography at XFELs and synchrotrons”. In: *urn:issn:2059-7983* 80 (2 Jan. 2024), pp. 60–79. ISSN: 2059-7983. DOI: 10.1107/S2059798323011002. URL: https://journals.iucr.org/paper?qu5005%20https://journals.iucr.org/d/issues/2024/02/00/qu5005/.

[92] Marie Luise Grünbein et al. “Illumination guidelines for ultrafast pump–probe experiments by serial femtosecond crystallography”. In: *Nature Methods* 17 (7 July 2020), pp. 681–684. ISSN: 15487105. DOI: 10.1038/S41592-020-0847-3;SUBJMETA=1265,1266,1647,2258,527,57,631;KWRD=BIOPHYSICS,NANOCRYSTALLOGRAPHY,OPTICAL+SPECTROSCOPY. URL: https://www.nature.com/articles/s41592-020-0847-3.

[93] Ji Hye Yun et al. “Early-stage dynamics of chloride ion–pumping rhodopsin revealed by a femtosecond X-ray laser”. In: *Proceedings of the National Academy of Sciences of the United States of America* 118 (13 Mar. 2021), e2020486118. ISSN: 10916490. DOI: 10.1073/PNAS.2020486118/SUPPL_FILE/PNAS.2020486118.SM01.MP4. URL: /doi/pdf/10.1073/pnas.2020486118?download=true.

[94] Hongjie Li et al. “Oxygen-evolving photosystem II structures during S1–S2–S3 transitions”. In: *Nature* 626 (7999 Feb. 2024), pp. 670–677. ISSN: 14764687. DOI: 10.1038/S41586-023-06987-5;TECHMETA=101,28,82,9;SUBJMETA=1464,1734,2076,449,57,631;KWRD=BIOENERGETICS,PHOTOSYSTEM+II. URL: https://www.nature.com/articles/s41586-023-06987-5.

[95] Diana C.F. Monteiro et al. “Using photocaging for fast time-resolved structural biology studies”. In: *urn:issn:2059-7983* 77 (10 Sept. 2021), pp. 1218–1232. ISSN: 2059-7983. DOI: 10.1107/S2059798321008809. URL: https://journals.iucr.org/paper?qn5001%20https://journals.iucr.org/d/issues/2021/10/00/qn5001/.

[96] Christopher D.M. Hutchison et al. “Optical control of ultrafast structural dynamics in a fluorescent protein”. In: *Nature Chemistry 2023 15:11* 15 (11 Aug. 2023), pp. 1607–1615. ISSN: 1755-4349. DOI: 10.1038/s41557-023-01275-1. URL: https://www.nature.com/articles/s41557-023-01275-1.

[97] Rafael Abela et al. “Perspective: Opportunities for ultrafast science at SwissFEL”. In: *Structural Dynamics* 4 (6 Nov. 2017), p. 45. ISSN: 23297778. DOI: 10.1063/1.4997222/365912. URL: /aca/sdy/article/4/6/061602/365912/Perspective-Opportunities-for-ultrafast-science-at.

[98] Jasper J. Van Thor. “Advances and opportunities in ultrafast X-ray crystallography and ultrafast structural optical crystallography of nuclear and electronic protein dynamics”. In: *Structural Dynamics* 6 (5 Sept. 2019), p. 50901. ISSN: 23297778. DOI: 10.1063/1.5110685/804249. URL: /aca/sdy/article/6/5/050901/804249/Advances-and-opportunities-in-ultrafast-X-ray.

[99] Alisia Fadini et al. “Applications and Limits of Time-to-Energy Mapping of Protein Crystal Diffraction Using Energy-Chirped Polychromatic XFEL Pulses”. In: *Applied Sciences 2020, Vol. 10, Page 2599* 10 (7 Apr. 2020), p. 2599. ISSN: 2076-3417. DOI: 10.3390/APP10072599. URL: https://www.mdpi.com/2076-3417/10/7/2599/htm%20https://www.mdpi.com/2076-3417/10/7/2599.

[100] Marie Luise Grünbein and Gabriela Nass Kovacs. “Sample delivery for serial crystallography at free-electron lasers and synchrotrons”. In: *urn:issn:2059-7983* 75 (2 Jan. 2019), pp. 178–191. ISSN: 2059-7983. DOI: 10.1107/S205979831801567X. URL: https://journals.iucr.org/paper?ba5295%20https://journals.iucr.org/d/issues/2019/02/00/ba5295/.

[101] Samuel Perrett et al. “Kilohertz droplet-on-demand serial femtosecond crystallography at the European XFEL station FXE”. In: *Structural Dynamics* 11 (2 Mar. 2024). ISSN: 23297778. DOI: 10.1063/4.0000248/3283113. URL: /aca/sdy/article/11/2/024310/3283113/Kilohertz-droplet-on-demand-serial-femtosecond.

[102] Jan Kern, Vittal K. Yachandra, and Junko Yano. “Metalloprotein structures at ambient conditions and in real-time: biological crystallography and spectroscopy using X-ray free electron lasers”. In: *Current Opinion in Structural Biology* 34 (Oct. 2015), pp. 87–98. ISSN: 0959-440X. DOI: 10.1016/J.SBI.2015.07.014. URL: https://www.sciencedirect.com/science/article/pii/S0959440X15001128.

[103] Christopher D.M. Hutchison, Samuel Perrett, and Jasper J. van Thor. “XFEL Beamline Optical Instrumentation for Ultrafast Science”. In: *Journal of Physical Chemistry B* 128 (37 Sept. 2024), pp. 8855–8868. ISSN: 15205207. DOI: 10.1021/ACS.JPCB.4C01492/ASSET/IMAGES/LARGE/JP4C01492_0003.JPEG. URL: /doi/pdf/10.1021/acs.jpcb.4c01492?ref=article_openPDF.

[104] Karol Nass et al. “Structural dynamics in proteins induced by and probed with X-ray free-electron laser pulses”. In: *Nature Communications 2020 11:1* 11 (1 Apr. 2020), pp. 1–9. ISSN: 2041-1723. DOI: 10.1038/s41467-020-15610-4. URL: https://www.nature.com/articles/s41467-020-15610-4.

[105] Ken R. Ferguson et al. “Transient lattice contraction in the solid-to-plasma transition”. In: *Science Advances* 2 (1 Jan. 2016). ISSN: 23752548. DOI: 10.1126/SCIADV.1500837/SUPPL_FILE/1500837_SM.PDF. URL: /doi/pdf/10.1126/sciadv.1500837?download=true.

[106] W. Lu et al. “Development of a hard X-ray split-and-delay line and performance simulations for two-color pump-probe experiments at the European XFEL”. In: *Review of Scientific Instruments* 89 (6 June 2018), p. 63121. ISSN: 10897623. DOI: 10.1063/1.5027071/362561. URL: /aip/rsi/article/89/6/063121/362561/Development-of-a-hard-X-ray-split-and-delay-line.

[107] Haoyuan Li et al. “Generation of highly mutually coherent hard-x-ray pulse pairs with an amplitude-splitting delay line”. In: *Physical Review Research* 3 (4 Dec. 2021), p. 043050. ISSN: 26431564. DOI: 10.1103/PHYSREVRESEARCH.3.043050/SUPPLEMENT.MP4. URL: https://journals.aps.org/prresearch/abstract/10.1103/PhysRevResearch.3.043050.

[108] Svitozar Serkez et al. “Opportunities for Two-Color Experiments in the Soft X-ray Regime at the European XFEL”. In: *Applied Sciences 2020, Vol. 10, Page 2728* 10 (8 Apr. 2020), p. 2728. ISSN: 2076-3417. DOI: 10.3390/APP10082728. URL: https://www.mdpi.com/2076-3417/10/8/2728/htm%20https://www.mdpi.com/2076-3417/10/8/2728.

[109] Graham N. George et al. “X-ray-induced photo-chemistry and X-ray absorption spectroscopy of biological samples”. In: *urn:issn:0909-0495* 19 (6 Oct. 2012), pp. 875–886. ISSN: 0909-0495. DOI: 10.1107/S090904951203943X. URL: https://journals.iucr.org/paper?wa5040%20https://journals.iucr.org/s/issues/2012/06/00/wa5040/.

[110] Colin Nave et al. “Imperfection and radiation damage in protein crystals studied with coherent radiation”. In: *urn:issn:1600-5775* 23 (1 Jan. 2016), pp. 228–237. ISSN: 1600-5775. DOI: 10.1107/S1600577515019700. URL: //journals.iucr.org/paper?tz5075.

[111] Ruslan Sanishvili et al. “Radiation damage in protein crystals is reduced with a micron-sized X-ray beam”. In: *Proceedings of the National Academy of Sciences of the United States of America* 108 (15 Apr. 2011), pp. 6127–6132. ISSN: 10916490. DOI: 10.1073/PNAS.1017701108/SUPPL_FILE/PNAS.1017701108_SI.PDF. URL: /doi/pdf/10.1073/pnas.1017701108?download=true.

[112] S. M. Vinko et al. “Creation and diagnosis of a solid-density plasma with an X-ray free-electron laser”. In: *Nature* 482 (7383 Feb. 2012), pp. 59–62. ISSN: 00280836. DOI: 10.1038/NATURE10746;SUBJMETA=33,400,525,639,766;KWRD=OPTICAL+PHYSICS,SPACE+PHYSICS. URL: https://www.nature.com/articles/nature10746.

[113] A Lévy et al. “The creation of large-volume, gradient-free warm dense matter with an x-ray free-electron laser”. In: *Physics of Plasmas* 22 (3 Mar. 2015), p. 40. ISSN: 1070-664X. DOI: 10.1063/1.4916103. URL: /aip/pop/article/22/3/030703/929084/The-creation-of-large-volume-gradient-free-warm.

[114] Adrien Descamps et al. “Evidence for phonon hardening in laser-excited gold using x-ray diffraction at a hard x-ray free electron laser”. In: *Science Advances* 10 (6 Feb. 2024), p. 5272. ISSN: 23752548. DOI: 10.1126/SCIADV.ADH5272/SUPPL_FILE/SCIADV.ADH5272_SM.PDF. URL: /doi/pdf/10.1126/sciadv.adh5272?download=true.

[115] Sam Azadi, Justin S. Wark, and Sam M. Vinko. “Lattice stability of ultrafast-heated gold”. In: *Scientific Reports* 15 (1 Dec. 2025), pp. 1–10. ISSN: 20452322. DOI: 10.1038/S41598-025-89470-7;SUBJMETA=1135,119,1960,2795,639,766;KWRD=LASER-PRODUCED+PLASMAS,PHASE+TRANSITIONS+AND+CRITICAL+PHENOMENA. URL: https://www.nature.com/articles/s41598-025-89470-7.

[116] Thomas G. White et al. “Speed of sound in methane under conditions of planetary interiors”. In: *Physical Review Research* 6 (2 Apr. 2024), p. L022029. ISSN: 26431564. DOI: 10.1103/PHYSREVRESEARCH.6.L022029/SUPPLEMENTRYINFORMATION.PDF. URL: https://journals.aps.org/prresearch/abstract/10.1103/PhysRevResearch.6.L022029.

[117] Guillaume Morard et al. “In situ X-ray diffraction of silicate liquids and glasses under dynamic and static compression to megabar pressures”. In: *Proceedings of the National Academy of Sciences of the United States of America* 117 (22 June 2020), pp. 11981–11986. ISSN: 10916490. DOI: 10.1073/PNAS.1920470117/SUPPL_FILE/PNAS.1920470117.SAPP.PDF. URL: /doi/pdf/10.1073/pnas.1920470117?download=true.

[118] D. Kraus et al. “The structure of liquid carbon elucidated by in situ X-ray diffraction”. In: *Nature* (June 2025). ISSN: 14764687. DOI: 10.1038/S41586-025-09035-6.

[119] David S. Montgomery. “Invited article: X-ray phase contrast imaging in inertial confinement fusion and high energy density research”. In: *Review of Scientific Instruments* 94 (2 Feb. 2023), p. 21103. ISSN: 10897623. DOI: 10.1063/5.0127497/2869156. URL: /aip/rsi/article/94/2/021103/2869156/Invited-article-X-ray-phase-contrast-imaging-in.

[120] Justin S. Wark, Malcolm I. McMahon, and Jon H. Eggert. “Femtosecond diffraction and dynamic high pressure science”. In: *Journal of Applied Physics* 132 (8 Aug. 2022), p. 80902. ISSN: 10897550. DOI: 10.1063/5.0089388/20035345/080902_1_5.0089388.AM.PDF. URL: /aip/jap/article/132/8/080902/2837271/Femtosecond-diffraction-and-dynamic-high-pressure.

[121] Shenyuan Ren et al. “Non-thermal evolution of dense plasmas driven by intense x-ray fields”. In: *Communications Physics 2023 6:1* 6 (1 May 2023), pp. 1–10. ISSN: 2399-3650. DOI: 10.1038/s42005-023-01216-x. URL: https://www.nature.com/articles/s42005-023-01216-x.

[122] D. Broege et al. “The Dynamic Compression Sector laser: A 100-J UV laser for dynamic compression research”. In: *Review of Scientific Instruments* 90 (5 May 2019), p. 53001. ISSN: 10897623. DOI: 10.1063/1.5088049/10028641/053001_1_ACCEPTED_MANUSCRIPT.PDF. URL: /aip/rsi/article/90/5/053001/361202/The-Dynamic-Compression-Sector-laser-A-100-J-UV.

[123] A. Rack et al. “Dynamic loading platforms coupled to ultra-high speed X-ray imaging at beamline ID19 of the European Synchrotron ESRF”. In: *High Pressure Research* 44 (3 July 2024), pp. 400–417. ISSN: 14772299. DOI: 10.1080/08957959.2024.2370369;WEBSITE:WEBSITE:TFOPB;PAGEGROUP:STRING:PUBLICATION. URL: https://www.tandfonline.com/doi/abs/10.1080/08957959.2024.2370369.

[124] Rajmund Mokso et al. “Megahertz x-ray microscopy at x-ray free-electron laser and synchrotron sources”. In: *Optica, Vol. 6, Issue 9, pp. 1106-1109* 6 (9 Sept. 2019), pp. 1106–1109. ISSN: 2334-2536. DOI: 10.1364/OPTICA.6.001106. URL: https://opg.optica.org/viewmedia.cfm?uri=optica-6-9-1106&seq=0&html=true%20https://opg.optica.org/abstract.cfm?uri=optica-6-9-1106%20https://opg.optica.org/optica/abstract.cfm?uri=optica-6-9-1106.

[125] Kang Xiang et al. “Ultrasound cavitation and exfoliation dynamics of 2D materials re-vealed in operando by X-ray free electron laser megahertz imaging”. In: (May 2023). URL: https://arxiv.org/pdf/2305.08538.

[126] Simon J.L. Billinge. “The rise of the X-ray atomic pair distribution function method: A series of fortunate events”. In: *Philosophical Transactions of the Royal Society A: Mathematical, Physical and Engineering Sciences* 377 (2147 June 2019). ISSN: 1364503X. DOI: 10.1098/RSTA.2018.0413;WEBSITE:WEBSITE:RSJ-SITE;WGROUP:STRING:PUBLICATION. URL: /doi/pdf/10.1098/rsta.2018.0413.

[127] Paul Mason et al. “Development of a 100 J, 10 Hz laser for compression experiments at the High Energy Density instrument at the European XFEL”. In: *High Power Laser Science and Engineering* 6 (2018), e65. ISSN: 2095-4719. DOI: 10.1017/HPL.2018.56. URL: https://www.cambridge.org/core/journals/high-power-laser-science-and-engineering/article/development-of-a-100-j-10-hz-laser-for-compression-experiments-at-the-high-energy-density-instrument-at-the-european-xfel/BE9310E57FB3CC7B3BF1F3C87BFB1917.

[128] J. Strucka et al. “Synchrotron radiography of Richtmyer-Meshkov instability driven by exploding wire arrays”. In: *Physics of Fluids* 35 (4 Apr. 2023), p. 44108. ISSN: 10897666. DOI: 10.1063/5.0144839/17994121/044108_1_5.0144839.AM.PDF. URL: /aip/pof/article/35/4/044108/2883072/Synchrotron-radiography-of-Richtmyer-Meshkov.

[129] Vatsa Gandhi et al. “Real-time characterization of dislocation slip and twinning of shock-compressed molybdenum single crystals”. In: *Physical Review Materials* 7 (7 July 2023), p. 073601. ISSN: 24759953. DOI: 10.1103/PHYSREVMATERIALS.7.073601/MOLYSUPPLEMENTARY_V5.PDF. URL: https://journals.aps.org/prmaterials/abstract/10.1103/PhysRevMaterials.7.073601.

[130] Christopher S. Campbell et al. “Data-driven picosecond X-ray imaging for quantitative plasma-induced shock characterization”. In: *Communications Physics* 8 (1 Dec. 2025), pp. 1–9. ISSN: 23993650. DOI: 10.1038/S42005-025-02021-4;SUBJMETA=1106,1960,400,639,766;KWRD=PLASMA+PHYSICS,X-RAYS. URL: https://www.nature.com/articles/s42005-025-02021-4.

[131] John L. Barber et al. “Diffractive imaging at large Fresnel number: Challenge of dynamic mesoscale imaging with hard x rays”. In: *Physical Review B - Condensed Matter and Materials Physics* 89 (18 May 2014), p. 184105. ISSN: 1550235X. DOI: 10.1103/PHYSREVB.89.184105/FIGURES/8/MEDIUM. URL: https://journals.aps.org/prb/abstract/10.1103/PhysRevB.89.184105.

[132] Alessandro Forte et al. “Resonant inelastic x-ray scattering in warm-dense Fe compounds beyond the SASE FEL resolution limit”. In: *Communications Physics* 7 (1 Dec. 2024), pp. 1–9. ISSN: 23993650. DOI: 10.1038/S42005-024-01752-0;SUBJMETA=1020,1087,1135,1960,624,639,766;KWRD=FREE-ELECTRON+LASERS,LASER-PRODUCED+PLASMAS. URL: https://www.nature.com/articles/s42005-024-01752-0.

[133] A. Amouretti et al. “Isostructural Phase Transition of Fe2 O3 under Laser Shock Compression”. In: *Physical Review Letters* 134 (17 May 2025), p. 176102. ISSN: 10797114. DOI: 10.1103/PHYSREVLETT.134.176102/FIGURES/5/MEDIUM. URL: https://journals.aps.org/prl/abstract/10.1103/PhysRevLett.134.176102.

[134] A. Descamps et al. “Towards performing high-resolution inelastic X-ray scattering measurements at hard X-ray free-electron lasers coupled with energetic laser drivers”. In: *Journal of Synchrotron Radiation* 29 (4 July 2022), pp. 931–938. ISSN: 16005775. DOI: 10.1107/S1600577522004453/HTTPS://JOURNALS.IUCR.ORG/SERVICES/RSS.HTML. URL: https://journals.iucr.org/paper?ok5069%20https://journals.iucr.org/s/issues/2022/04/00/ok5069/.

[135] Félicie Albert et al. “2020 roadmap on plasma accelerators”. In: *New Journal of Physics* 23 (3 Mar. 2021), p. 031101. ISSN: 1367-2630. DOI: 10.1088/1367-2630/ABCC62. URL: https://iopscience.iop.org/article/10.1088/1367-2630/abcc62%20https://iopscience.iop.org/article/10.1088/1367-2630/abcc62/meta.

[136] A. Picksley et al. “Matched Guiding and Controlled Injection in Dark-Current-Free, 10-GeV-Class, Channel-Guided Laser-Plasma Accelerators”. In: *Physical Review Letters* 133 (25 Dec. 2024), p. 255001. ISSN: 10797114. DOI: 10.1103/PhysRevLett.133.255001. URL: https://journals.aps.org/prl/abstract/10.1103/PhysRevLett.133.255001.

[137] Tim Ziegler et al. “Laser-driven high-energy proton beams from cascaded acceleration regimes”. In: *Nature Physics* 20 (7 July 2024), pp. 1211–1216. ISSN: 17452481. DOI: 10.1038/S41567-024-02505-0;TECHMETA. URL: https://www.nature.com/articles/s41567-024-02505-0.

[138] D. Capatina et al. “DCS - A high flux beamline for time resolved dynamic compression science - Design highlights”. In: *AIP Conference Proceedings* 1741 (1 July 2016), p. 33. ISSN: 15517616. DOI: 10.1063/1.4952859/821249. URL: /aip/acp/article/1741/1/030036/821249/DCS-A-high-flux-beamline-for-time-resolved-dynamic.

[139] Ross Cunningham et al. “Keyhole threshold and morphology in laser melting revealed by ultrahigh-speed x-ray imaging”. In: *Science* 363 (6429 Feb. 2019), pp. 849–852. ISSN: 10959203. DOI: 10.1126/SCIENCE.AAV4687/SUPPL_FILE/AAV4687S9.MOV. URL: /doi/pdf/10.1126/science.aav4687?download=true.

[140] Vinay Rastogi et al. “Application of ultrafast x-ray lasers in studying the material structure under shock compression”. In: *Journal of Applied Physics* 137 (7 Feb. 2025), p. 70702. ISSN: 10897550. DOI: 10.1063/5.0239330/3336616. URL: /aip/jap/article/137/7/070702/3336616/Application-of-ultrafast-x-ray-lasers-in-studying.

[141] James Coakley et al. “Femtosecond quantification of void evolution during rapid material failure”. In: *Science Advances* 6 (51 Dec. 2020), pp. 4434–4450. ISSN: 23752548. DOI: 10.1126/SCIADV.ABB4434/SUPPL_FILE/ABB4434_SM.PDF. URL: /doi/pdf/10.1126/sciadv.abb4434?download=true.

[142] Jayanath C.P. Koliyadu et al. “Development of MHz X-ray phase contrast imaging at the European XFEL”. In: *Journal of Synchrotron Radiation* 32 (1 Jan. 2025), pp. 17–28. ISSN: 16005775. DOI: 10.1107/S160057752400986X/YI5159SUP2.MP4. URL: https://journals.iucr.org/paper?yi5159%20https://journals.iucr.org/s/issues/2025/01/00/yi5159/.

[143] Chu Lun Alex Leung et al. “In situ X-ray imaging of defect and molten pool dynamics in laser additive manufacturing”. In: *Nature Communications* 9 (1 Dec. 2018), pp. 1–9. ISSN: 20411723. DOI: 10.1038/S41467-018-03734-7;TECHMETA=123,135,147;SUBJMETA=1023,1026,1032,2735,301,639,930;KWRD=DESIGN. URL: https://www.nature.com/articles/s41467-018-03734-7.

[144] Jack Griffiths et al. “Resolving length-scale-dependent transient disorder through an ultrafast phase transition”. In: *Nature Materials 2024 23:8* 23 (8 June 2024), pp. 1041–1047. ISSN: 1476-4660. DOI: 10.1038/s41563-024-01927-8. URL: https://www.nature.com/articles/s41563-024-01927-8.

DRAFT

9 Synchronous sources

9.1 Introduction, scope and assumptions

One of the defining features of a Next Generation XFEL facility is timely and dynamic access to a broad array of synchronous sources. These sources must be overlapped with the X-ray pulses in time and space, cover an extended range of electromagnetic and particle beam options, be readily available, and come with a comprehensive suite of shot-by-shot diagnostics. They should be, where possible, matched to the X-ray repetition rate to maximise the utility of the XFEL source.

The UK XFEL Science and Technology Case has identified a broad range of synchronous sources to satisfy experimental needs. They consist of optical-laser-like pulses spanning UV to THz wavelengths, and bunches of particles spanning electrons, protons, and other ions.

This chapter will assess the technological readiness of the sources required to meet these needs, identify potential research and development partners where further work is required, and comment on factors such as source location and beam transport that inform the overall facility design.

9.2 Motivation

Pump-probe experiments are the cornerstone of ultrafast science, enabling the investigation of dynamic processes on femtosecond and attosecond timescales. In these experiments, a sample is excited by one or more ultrafast pulses (the “pump”) and subsequently interrogated by an another pulse (the “probe”). By varying the delay between the pump and probe pulses, researchers can construct a time-resolved picture of structural, electronic, or magnetic changes in a sample of interest. Further discussion of the techniques that can be implemented at facilities such as a UK XFEL can be found in the updated Science and Technology Case and in the literature [1].

A user survey was performed at the start of the conceptual design process to narrow down user requirements for the XFEL outputs, with the opportunity taken to ask synchronous source requirements. There were 64 responses in total, 40 of which identified 1 or more synchronous sources. Of those, 36 required at least one optical laser-driven source. A summary of responses is presented in Figure 9.1. Discussions with laser specialists from the European XFEL and LCLS facilities uncovered similar statistics at their facilities. As such this chapter will primarily focus on laser systems as the primary synchronous source of interest.

Anticipating the long-term needs of a diverse range of scientific fields presents inherent challenges, particularly given the evolving nature of research priorities and methodologies. The varied approaches taken by survey contributors in articulating their requirements further underscored the complexity of distilling a unified set of specifications. To address this, continued engagement with the broader scientific community was prioritised through town hall meetings, focused workshops, and in-depth discussions with members of the science team, fostering a collaborative path toward refining the technical requirements.

DRAFT

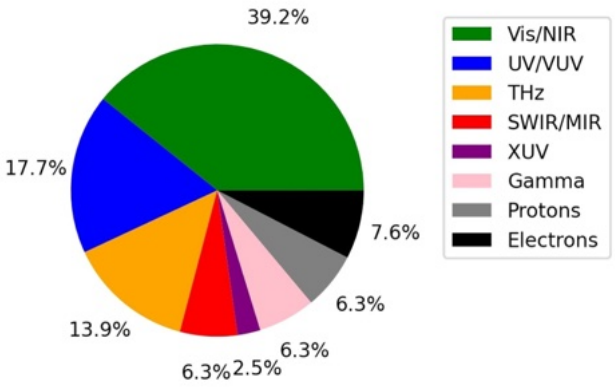

Figure 9.1: Summary of the synchronous source requests derived from user survey responses.

9.3 Optical sources

Discrete laser sources are available throughout much of the infrared to ultraviolet, but gaps remain in spectral coverage, power capability, and technological maturity. This problem is overcome by combining one or more powerful and stable 'workhorse' lasers with a suite of non-linear optical processes including: harmonic generators, widely tuneable optical parametric amplifiers, and difference- and sum- frequency generators. More exotic non-linear optical techniques such as optical rectification, resonant dispersive wave generation, and high harmonic generation methods are available to extend the accessible range far into the terahertz and XUV respectively.

Initial investigation has been directed towards $\sim$100 kHz laser systems with pulse energies in the millijoule range. These are required to match the X-ray pulse repetition rate and are capable of driving a wide range of cascaded non-linear optical processes. Ti:Sapphire laser technology as used on several XFEL facilities and does not scale to this parameter regime, but there is already a developing solution in Yb based lasers and amplifiers [2, 3]. This type of laser is already in use (e.g.) at LCLS and European XFEL, and has the following characteristics:

- lower quantum defect – brings reduction in thermal load and benefits in efficiency
- gain medium in disk lasers can be thin allowing rapid removal of heat
- disc gain media can be grown larger transversely for power scaling
- fundamental bandwidth is much lower than Ti:Sapphire - 3 level vs 4 level laser, manifold
- improving maturity of the field with an increasing number of annual sales
- spectral broadening techniques (hollow fibres and multipass Heriott cells) demonstrated

There are a number of commercial solutions that include integrated and customisable optical parametric and sum and difference frequency mixing stages, as well as super-continuum generation. A number of bespoke Light Conversion [4] high average power systems have been developed as part of the HiLUX upgrades of ULTRA and Artemis at the Central Laser Facility (CLF) [5, 6], which will be among the UK's premier ultrafast research facilities.

9.3.1 Required specifications

A treatise on the optical instrumentation required for modern and future applications on XFELs has been published which covers the majority of the experimental techniques required for spectroscopy and scattering experiments [1]. The authors propose the following capabilities should be available at XFEL facilities:

1. pulse compression and shaping (full spectral phase and amplitude)
2. multipulse single-/two-colour pulse trains and combinations, with cross-correlation and timing of the final pulse train
3. detailed characterisation of spectral phase and amplitude of all possible outputs
4. a rapid z-scan capability to optimise interactions

These capabilities are important not only to perform the experiments required, but also enable the duplication of experimental studies already performed at (e.g.) university facilities, or as at other facilities.

The types of multiple pulse trains and their applications are illustrated in Figure 9.2. There are many experimental techniques where multiple optical pulses are required; this includes optical properties which would allow for simple beam splitting and delaying of pulses, but also experiments involving different colours. This latter scheme may require parallel frequency conversion systems pumped by the same laser. A schematic covering the processes that could be implemented to meet these needs is shown in Figure 9.3.

9.3.2 State of the art

9.3.2.1 European XFEL

European XFEL employs high repetition rate laser systems to support ultrafast experiments across several of its scientific instruments, notably FXE, SXP, and SPB/SFX. The XFEL pulse structure consists of 10 Hz bursts of 4.5 MHz pulses. Matching this in the laser system is a challenge that has required pushing the limits of available laser technologies [7]. There are three laser systems servicing the end stations at each of the SASE 1-3 beamlines, as shown in Figure 9.4.

The fundamental laser system, shown in Figure 9.5, consists of a commercial Yb:fibre laser oscillator, which passes through a fibre-based amplification, and then two further Innoslab amplifiers. This beam is then either transported as-is, or used to pump non-collinear optical parametric amplifiers to produce a broadband, 800 nm Ti:Sapphire-like output. The operational set points of this laser are listed in Table 9.1. This beam can then be used in the experimental area to pump commercial OPAs (TOPAS) or pump other non-linear optical processes based around Ti:Sapphire technologies. This approach was decided upon before the proliferation of commercial direct Yb-pumped OPA solutions.

Each end station includes several commercial frequency conversion systems (TOPAS optical parametric oscillators). These can be used to provide an extremely wide range of pump-probe wavelengths to the user experiments. An example of the tuning range is shown in Figure 9.6. In addition, terahertz radiation via optical rectification of the 1030 nm laser in lithium niobate can be provided with pulse energies up to 70 µJ. This source is only suitable for a small subset of the nonresonant experimental needs, and is pumped close to the thermal dissipation limit of the lithium niobate system [9, 10].

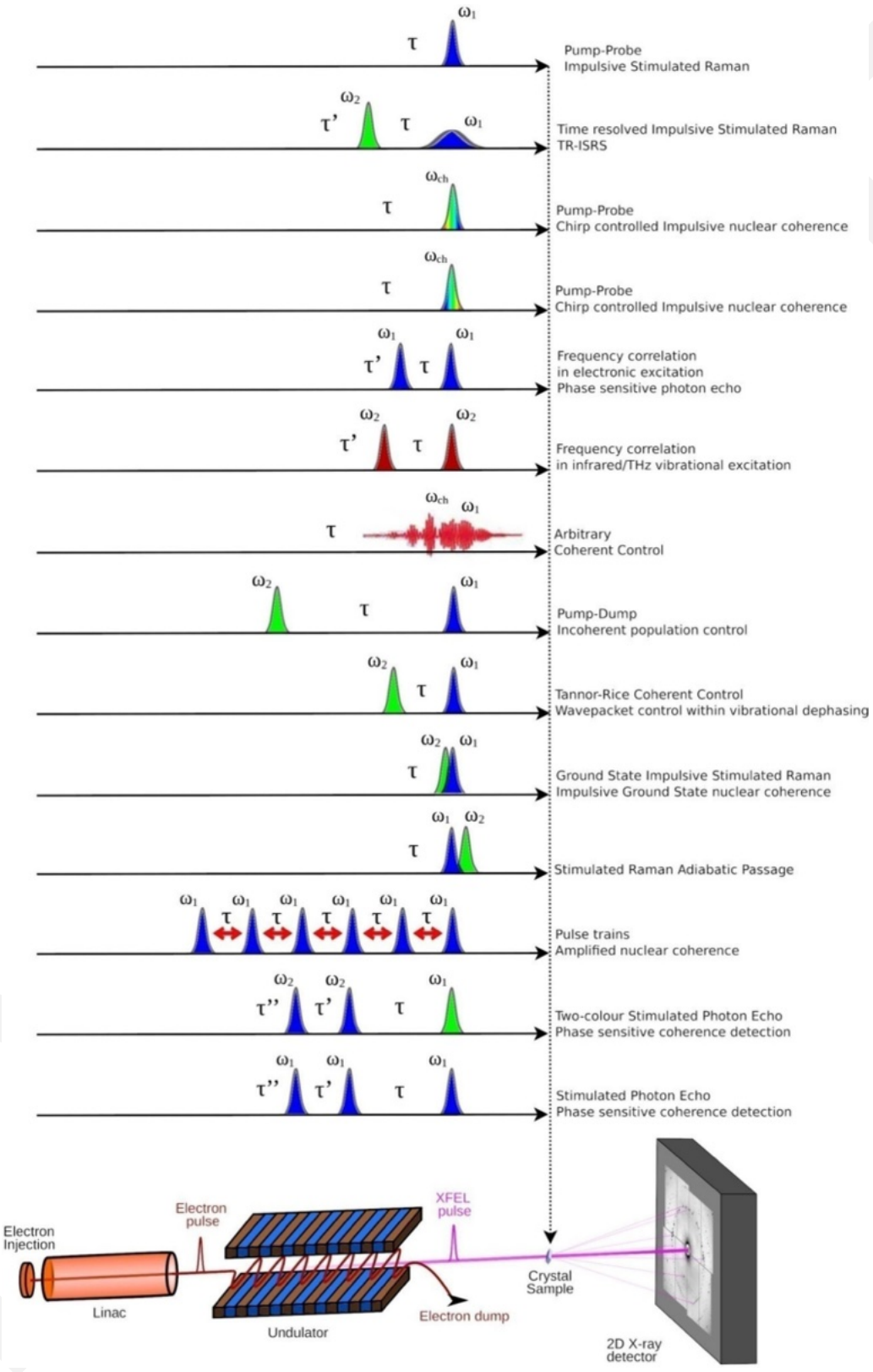

Figure 9.2: Overview of proposed pulse schemes for ultrafast hard X-ray diffraction. Taken from [1]

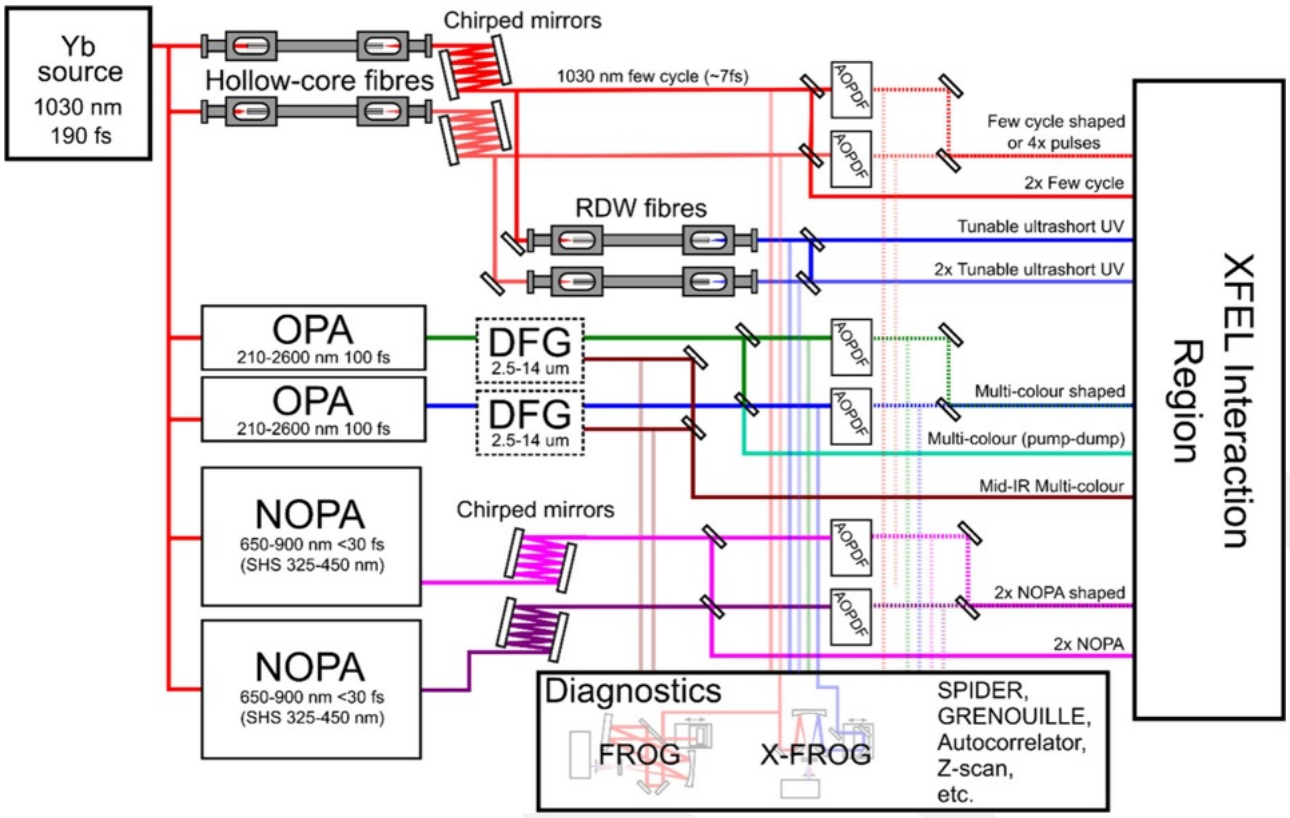

Figure 9.3: Proposed optical arrangement of systems and diagnostics available at an ideal ultrafast XFEL beamline, shown here with an example of an Yb pump laser. Operation at MHz repetition rates would add further design considerations. The figure is representative of possible systems that could be present at a beamline, and it is not the expectation that a single fundamental pump would supply all systems pictured simultaneously but rather different combinations thereof, depending on the desired optical excitation scheme. Figure and caption taken from [1]

The SXP instrument is also equipped with an Yb-fiber laser system delivering 250 fs, 200 µJ laser pulses at ~300 kHz. This laser can be spectrally broadened and temporally compressed via a Herriott multi-pass cell [11] which is then used to generate XUV pulses via high-harmonic generation (HHG) [12].

9.3.2.2 LCLS

The Linac Coherent Light Source (LCLS) supports a diverse scientific portfolio encompassing chemistry, atomic, molecular and optical (AMO) physics, materials science, and biology. Approximately 75 % of LCLS experiments require the use of a pump laser, with the majority of pump-probe investigations focused on ultrafast dynamics occurring on femtosecond to picosecond timescales. To meet the needs of future studies, LCLS are developing optical sources with the following requirements:

- They should be capable of delivering pulse durations shorter than 10 fs, along with a precise control over delay timing, including synchronization and time-of-arrival.
- The excitation wavelengths should span a broad spectral range, from ultraviolet through to terahertz, with typical pulse energies in the range of 1-100 µJ.
- The laser systems must exhibit robust, stable, and highly reliable performance.

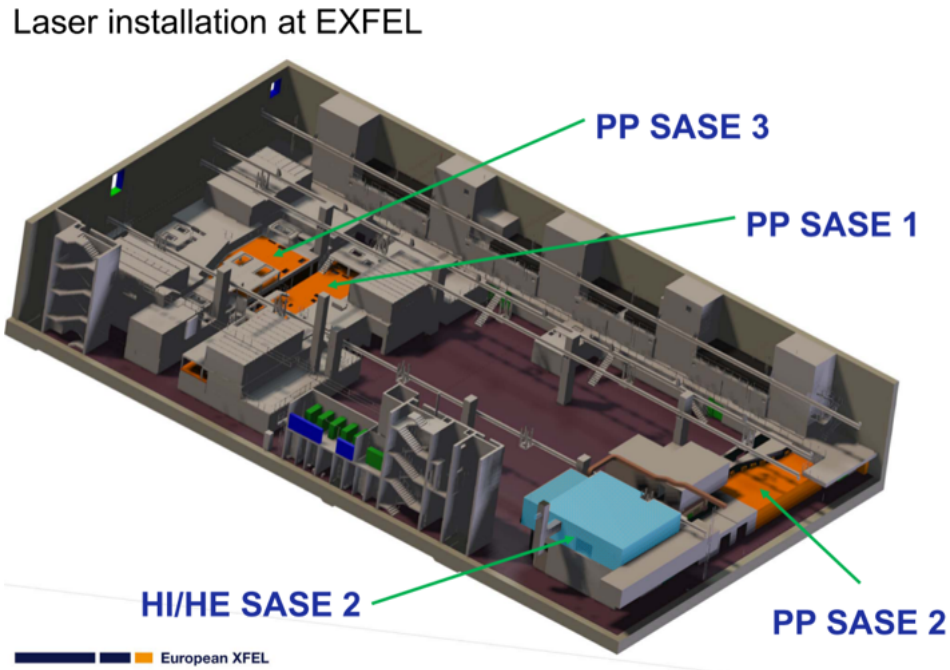

Figure 9.4: Location of the pump-probe laser systems at European XFEL [8]

Mode	F_{rep} (MHz)	Δ t (ns)	F_{eff} (Hz)	800 nm E_{pulse} (mJ)	1030 nm E_{pulse} (mJ)
1	4.5	222	27000	0.05	1
2	1.13	886	6000	0.2	4
3	0.103	9750	600	2	40
Pulse duration				15-300 fs	0.8 ps or 400 ps

Table 9.1: European XFEL pump-probe laser set-points from [9].

9

Historically, LCLS used amplified Ti:Sapphire laser technology at 120 Hz (linked to the repetition rate of the LCLS Cu linac), but, as at European XFEL, they have developed a system based around Yb lasers that produced a high rep-rate, high energy laser at 800 nm, emulating what a Ti:Sapphire laser would be if the technology scaled. This allowed the use of OPAs with standard designs. After further advancements of Yb laser technology, it has now been decided to use an Yb laser to directly, with OPAs designed to work with the 1030 nm pump wavelength. In order to achieve short pulses from the system the pump pulses will be spectrally broadened in gas filled hollow core fibres or Herriott cells.

Initial specification for the LCLS pump laser systems are shown in table Table 9.2.

Rather than situate the laser systems adjacent to the end-stations, LCLS locates the multiple pump lasers in two central halls, one for each of the near and far experimental halls (NEH and FEH). Each laser is coupled to a vacuum-based beam transport “switch-yard”, allowing different

Parameter	Quantity	Comment
wavelength	1030 nm	
repetition rate	40 kHz	later scaling to 96 kHz
pulse duration	25-300 fs	tunable via broadening - potentially sub 10 fs
pulse energy	2 mJ	

Table 9.2: Target laser parameters for next generation of LCLS synchronous source pump laser.

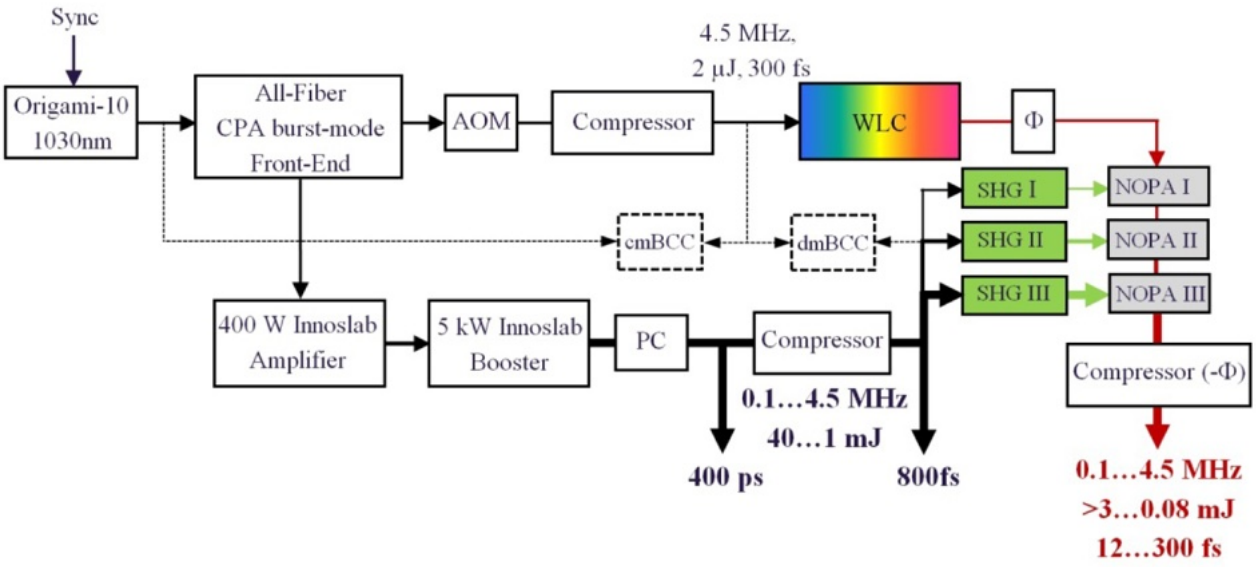

Figure 9.5: Schematic of the PP-laser prototype: AOM (Acousto-Optical Modulator), PC (Pockels cell), SHG (Second Harmonic Generation), Φ (dispersion management with multi-bounce chirped mirrors and/or material), cmBCC (common mode Balanced Cross Correlator), dmBCC (differential mode Balanced Cross Correlator), NOPA (Non-collinear Optical Parametric Amplifier). Seed and pump beams are controlled by beam pointing stabilization systems. Replicated from [7].

laser systems to be coupled into the transport lines to each experimental hutch. This centralisation simplifies and potentially improves the energy efficiency of the environmental controls. The switch-yard provides versatility in pump laser parameters and provides some redundancy preventing service/repair activities causing down time. In addition, locating the laser systems in one (or two) places may simplify the timing synchronisation systems, removing disparate timing connections to different rooms and simplifying maintenance. However, the lasers are transported many tens of meters to the experimental hutches, which is then not corrected for by the laser synchronisation. LCLS mitigate this with vacuum transport lines and laser arrival time monitors at the hutches (thereby requiring a timing link to the hutch in any case).

This system works where there are two clusters of quite closely packed hutches, but may not work as well if the stations were separated further (as they are in this Next Generation concept). LCLS believes the longest transport line they can operationally manage is 30 m. User feedback from town-hall meetings and workshops has been that they would prefer to have the lasers local to the end-stations, as the feeling is that timing and synchronicity are likely to be superior. There are also a challenges in aligning long transport lines, engineering the image relaying optics required (which is not trivial for broadband laser pulses) and in the conditioning the beam of each laser to match the transport lines properly (size, divergence, pointing).

At the experimental hutches LCLS plan to utilise so-called Modular Optical Delivery Systems (MODS). The MODS is a framework to deliver laser beams to experimental stations using a system of interchangeable optics. This system enhances flexibility and maintainability by allowing components to be easily installed, removed, or reconfigured based on experimental requirements. The modular components are referred to as TILEs (Tabletop Integrated Laser Elements). These are breadboard-mounted optical assemblies that can be quickly deployed or removed, enabling rapid adaptation. Specific TILEs include:

- An Injection TILE is for initial beam conditioning, with a layout tailored to the beam's entry geometry
- An ejection TILE delivers the laser to the instrument and includes diagnostics

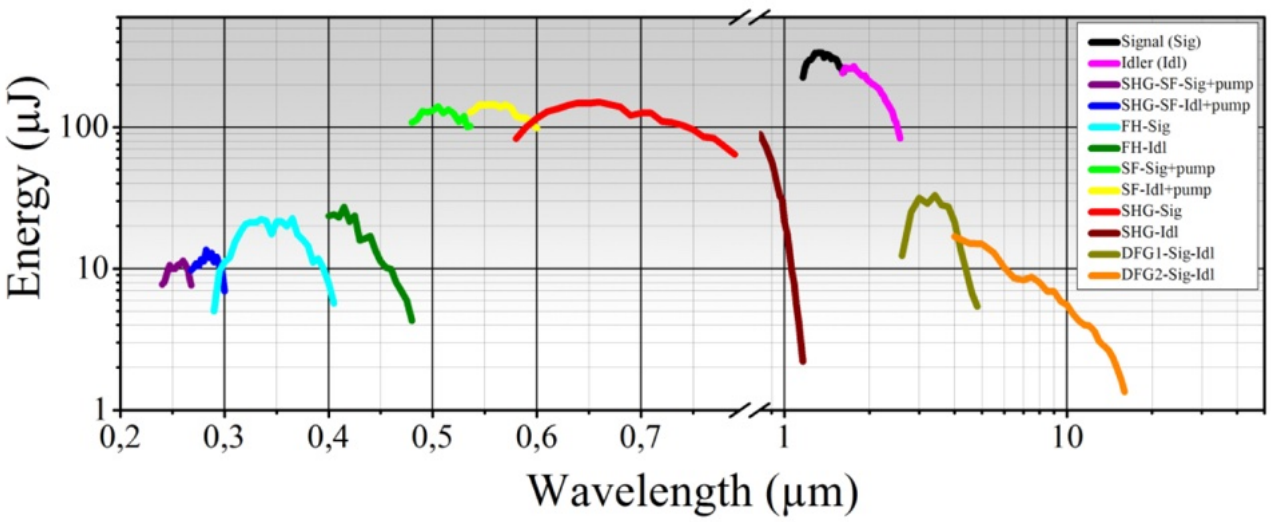

Figure 9.6: Illustrative tuning range from a TOPAS system pumped at 800 nm.[7]

- An ATM TILE which directs pulses to the Arrival Time Monitor, for synchronisation purposes
- Standard TILEs, such as those for harmonic generation or pulse compression, are built to a common design and can be transferred between hutches as needed.

This modular approach is very appealing, and is recommended as part of the Next Generation concept, independent of the location of the laser systems (either central, or deployed at each station). It allows the system to be highly versatile, even customisable per experiment, without adding greatly to the footprint and complexity, and provides a solution to the need for different mirror coatings and optics for widely varying optical pulse parameters. This is particularly true for the extremes – XUV and THz pulses – where efficient optics and long distance transport are very difficult.

9.3.3 Few-Femtosecond Pulses - Resonant Dispersive Wave Sources

Resonant dispersive wave (RDW) emission in gas-filled hollow-core waveguides offers a powerful method for generating tuneable, few-femtosecond pulses spanning from the vacuum ultraviolet to the near infrared [13, 14, 15, 16, 17, 18] The process relies on resonant energy transfer to a phase-matched spectral region during soliton-driven self-compression of an intense laser pulse [19, 20].

RDW sources can be driven from the pump lasers mentioned in the previous sections, and importantly, when driven above saturation, can provide pulses which are more intensity stable than the driving laser and maintain sub-femtosecond timing stability [13]. The temporal profiles of these pulses tend to have long pedestals which are not obviously communicated via the headline FWHM values [18], and the spectra, which necessarily will be very wide, have longer wavelength components, as discussed in Figure 9.9. The extent to which this is an issue will vary by experiment, but it is a factor that should be further improved on. The UK currently has world-leading expertise at Heriot-Watt University and the technique should be included in the optical laser provision for a next generation XFEL.

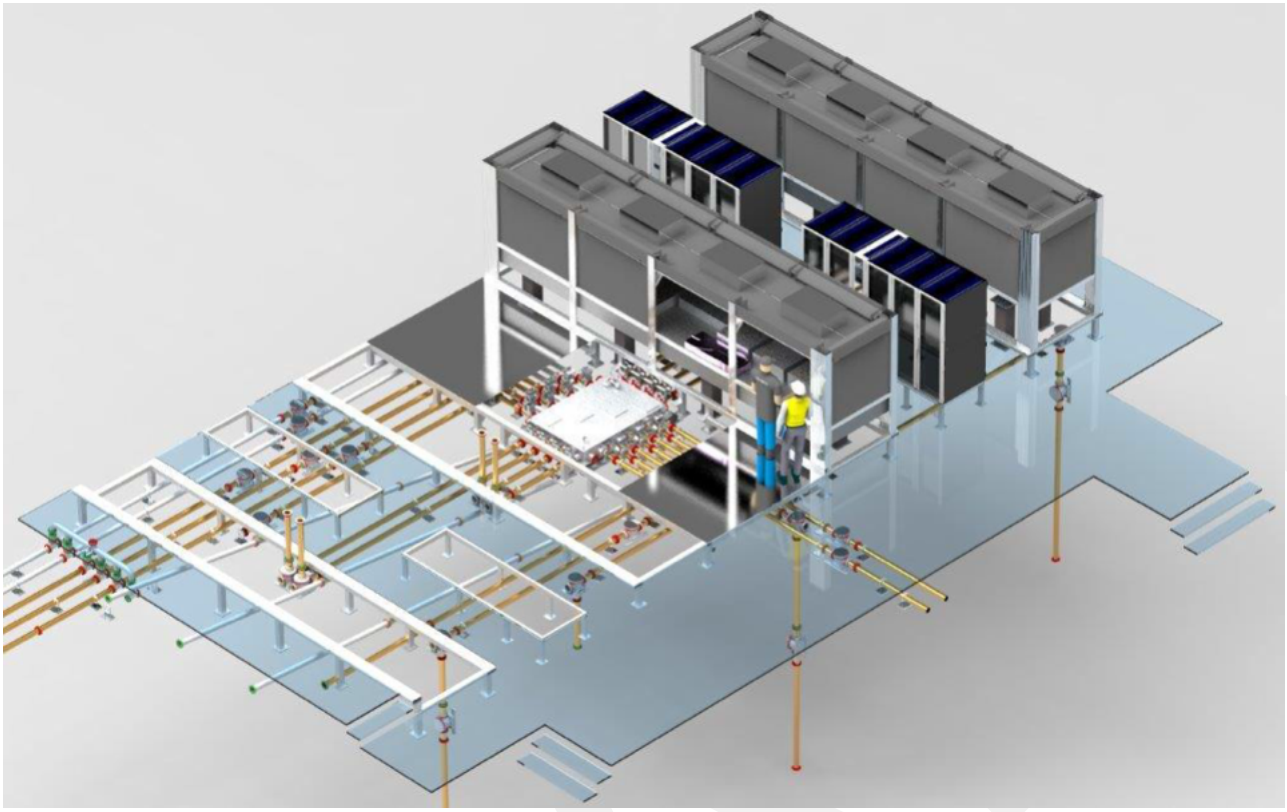

Figure 9.7: LCLS NEH laser hall and switch yard. The hall is a class 10000 clean room, with laser bays achieving class 100. The transport pipes and the central reconfigurable switchbox lie underneath the floor.

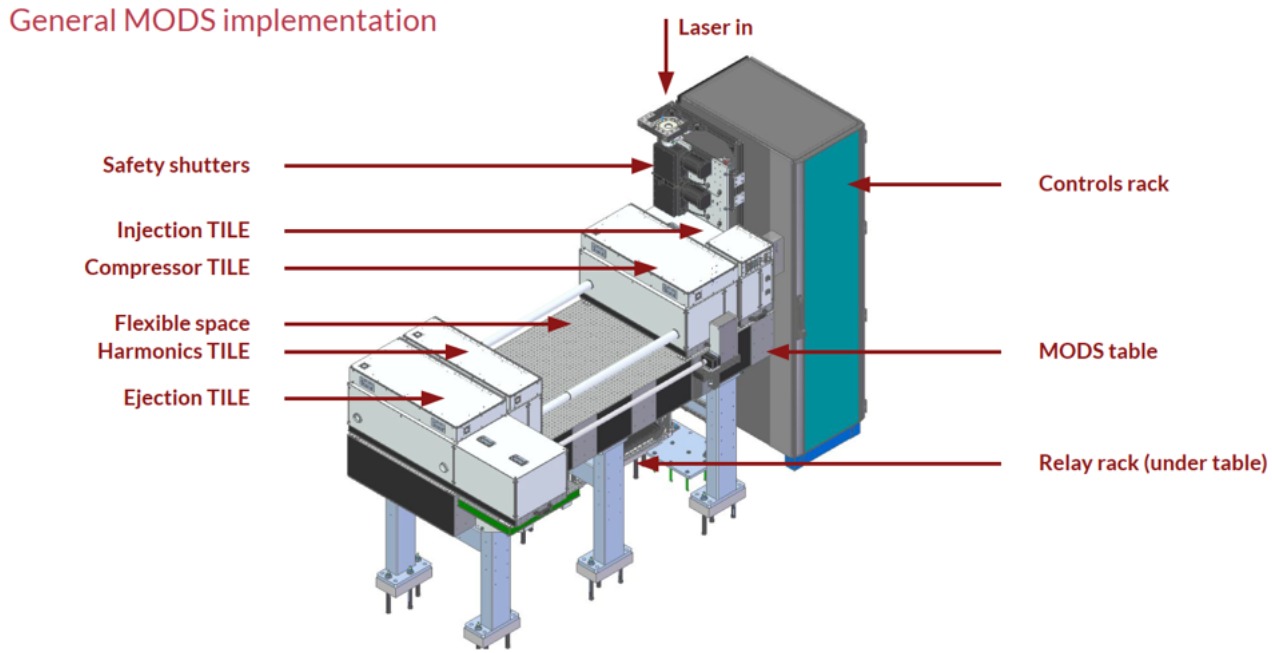

Figure 9.8: MODS system at LCLS showing and example implementation of the reconfigurable TILE layout.

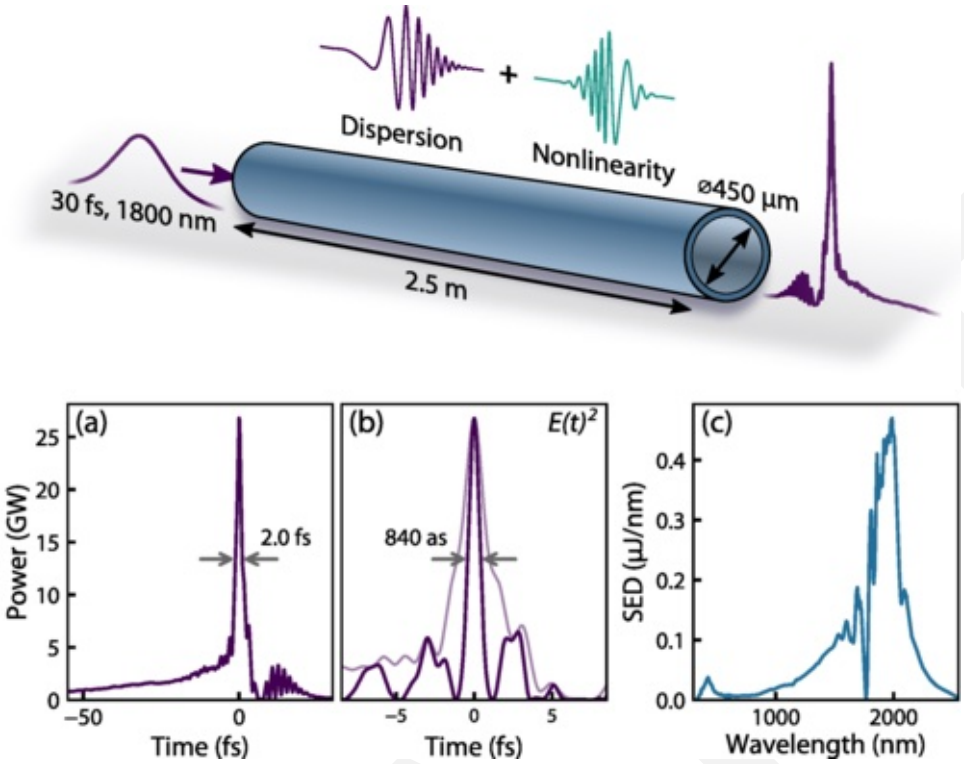

Figure 9.9: Example RDW pulse replicated from [18]. Self-compression to infrared attosecond pulses. Laser pulses at 1800 nm central wavelength with a duration of 30 fs at FWHM are coupled into a 2.5 m long gas-filled HCF with an inner diameter of 450 µm. In the HCF, the combination of anomalous dispersion arising from the waveguide and positive nonlinearity provided by the gas leads to self-compression of the pulses. With an argon pressure of 470 mbar and an initial pulse energy of 289 µJ, the pulse at the HCF exit has an envelope duration of 2 fs at FWHM (a), which corresponds to an 840 as field transient (b). The spectrum of this pulse extends from the ultraviolet (400 nm) to the mid-infrared (2550 nm) (c).

9.3.4 Attosecond Pulses - High Harmonic Generation

[21] Lasers can be used to generate attosecond light pulses via the process of high harmonic generation (HHG). High repetition rate HHG was demonstrated at 600 kHz by Krebs et al. [22] in 2013, using a CEP stable OPCPA source pumped by Yb laser technology. The HHG pumping pulses were centred at 918 nm, 6.6 fs long, with only 14 µJ. The resulting flux was estimated to be 5.8×10^9 photons/s in the range of 62-72 eV. More recently, isolated attosecond pulses have been demonstrated at 100 kHz by Witting et al. [21]. Using a CEP stable 3.3 fs pulse centred at 760 nm with 95 µJ of energy, a flux of 1×10^{11} photons/s was produced in sub 140 as pulses Figure 9.10. The pulse was generated from Yb laser pumped OPCPA seeded by a Ti:Sa oscillator, broadened in a 1 m long neon-filled hollow-core fibre and compressed using chirped dielectric mirrors.

This type of source is realisable with the Yb systems mentioned previously, but there will be significant development required to produce a few-cycle, CEP stabilised source that is synchronised with the X-ray pulses, which is also fully characterised and time stamped. The UK is establishing capability in 100 kHz HHG via Artemis at the CLF, and so is well positioned to address this challenge.

9.3.5 Diagnostics

An integral part of any provision is characterisation of the pulses provided. This will ideally be at the repetition rate of the machine, with some level of live monitoring during an experiment to

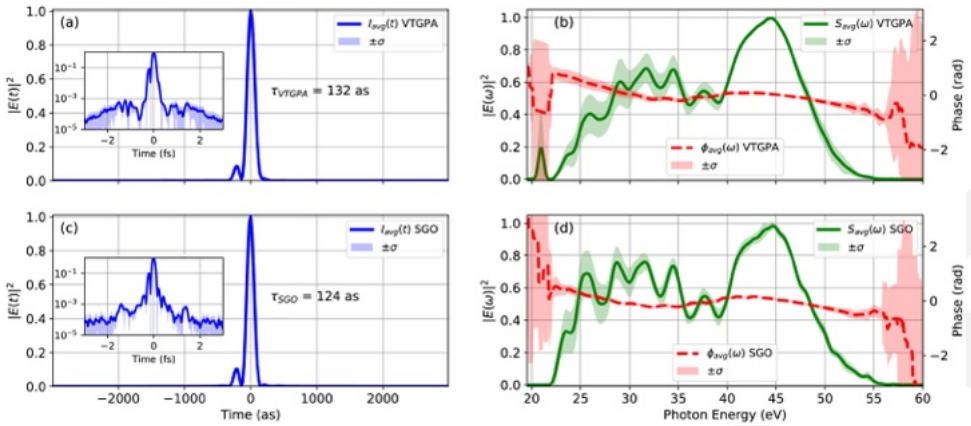

Figure 9.10: Example of an HHG attosecond pulse replicated from [21]. Retrieval of the XUV isolated attosecond pulses. (a) Retrieved XUV pulse intensity envelope normalized to its maximum value. The blue line corresponds to the average over all Volkov-transform generalized projection algorithm retrievals, and the shaded area corresponds to one standard deviation around the mean (not visible on the linear scale). The inset shows the intensity envelope on a logarithmic scale. (b) Retrieved average spectrum (green) and spectral phase (red dashed line) corresponding to the pulse in (a). The shaded areas correspond to one standard deviation around the means. (c) and (d) show the corresponding results found with the streaking global optimisation retrievals.

monitor for issues. LCLS have tested a range of Frequency Resolved Optical Gating systems based on second harmonic generation and self diffraction to recover the full temporal profiles of pulses. These need customised optics and nonlinear materials for the widely varying pulse properties and so will need to be modularly switched in according to experimental needs.

The most challenging part will be the data rates required for single-shot FROG measurements, which consist of two-dimensional spectrograms captured using camera based systems. Technical solutions for this are already being developed as 100 kHz systems are becoming more available. This issue is beyond the scope of this chapter, but will need addressing for data capture both for the UK XFEL and within the end stations.

9.4 THz

Terahertz sources are the second most requested source in the user survey. It has been several decades since the identification of the so-called “THz gap” and THz source development has been the subject of significant research. Now there are many source technologies available, although it is still a very challenging are of the spectrum to work in.

In this region of the electromagnetic spectrum the period of the waves is of the order of 100 fs, so it makes little sense to talk of femtosecond pulse durations. However, femtosecond phase stability is of high importance to many of the scientific use cases (SFX, CDI, ARPES, and others). Consultation with the community and science team identified interest in a THz FEL, either driven by the spent XFEL beam or a distinct machine. This resulted in a set of requirements that were presented to and accepted by the wider community, summarised in Table 9.3.

Source Parameter	Value
Tunability	0.5->20 THz
Bandwidth	<500 GHz
Peak E-field	semiconductors 100 kV/cm chemistry 10 MV/cm biological 10 V/Å
Phase stability	≪1 ps
Repetition rate	100 kHz (machine rate)
Polarisation	Full control desired

Table 9.3: Desired THz pulse parameters

9.4.1 Laser based sources

As all end stations will have at least one laser system available, a laser based THz source would be highly advantageous. The state-of-the-art does not yet cover all the requirements listed previously, but – as described below – this is a very active field and there are many sources currently achieving some of them, and upcoming technologies that show great promise.

9.4.1.1 Lithium niobate

The generation of THz radiation using the so-called Cherenkov phase-matching scheme in lithium niobate [23] is well established, and what much of the work to date has utilised. These sources typically use an amplified Ti:Sapphire laser which is shaped by imaging the reflection from a diffraction grating into a specially cut lithium niobate crystal to both achieve efficient phase-matching and avoid THz absorption in the crystal. The grating, shaping optics, and THz absorption, have peak energy and average fluence limitations. There have been attempts to improve this via cryogenic cooling of the lithium niobate, but this adds complexity without achieving orders-of-magnitude increase in efficiency.

An optimised and thermally managed design has been demonstrated by [24] that is capable of matching state of the art lithium niobate source pulse energies(1.44 µJ) but at 100 kHz pulse rates. This system, see Figure 9.11, is based on Yb:YAG laser technology to provide high rep rate, powerful pump pulses, which are then broadened to optimally match the phase-matching condition in the lithium niobate crystal. The pump wavelength of 1030 nm also has lower levels of nonlinear absorption, allowing higher powers to be reached. A peak field of 150 kV/cm was demonstrated. Although this does not extend the frequency range, it would boost signal to noise ratio and throughput, thereby providing a step change in capability.

Lithium niobate sources to date have have been limited to the lower THz frequencies because the many phonon absorption lines [25], however it has been demonstrated that operation in certain transmission windows above 3 THz are possible. 260 MV/m has been demonstrated at 15 THz [26]. This demonstration was at 5 Hz and used a 150 TW Ti:Sapphire laser, so is limited in applicability to end stations which already have high power lasers available.

9.4.1.2 Organic emitters

Organic crystals are candidates for THz generation. They potentially offer much higher efficiencies and very broad band tuning ranges. Unfortunately the materials can be hard to grow, can have low

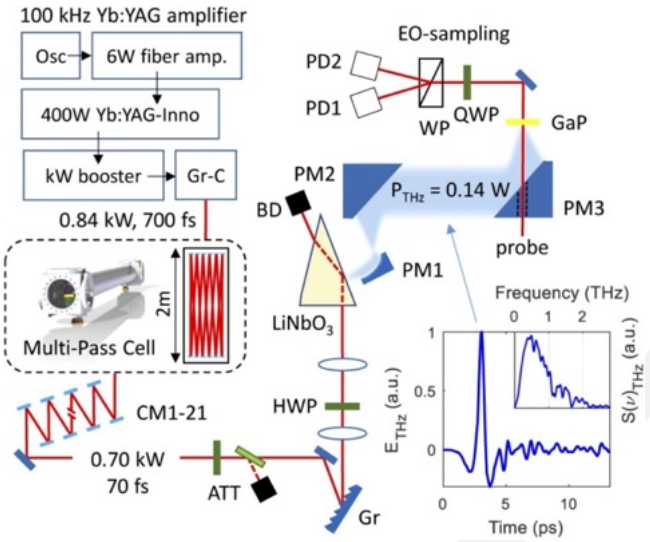

Figure 9.11: THz generation using lithium niobate at high repetition rate, as demonstrated (and reproduced from) [24].

optical quality, and have poor thermal, mechanical, and radiation, resistance. Despite these draw backs recent work is promising [27]: via the careful management of thermal build-up, achieved by mounting the crystal directly on a diamond substrate, considerably higher average powers were accessed before/without material failure. The spatial profile is very close to Gaussian, allowing efficient transport and a tight 75 µm focus with up to 6.7 MV/cm.

The THz pulses were CEP stable, and controllable via the phase of the optical pumps. With a tuning range of 4-19 THz and 0.5 THz, this source does meet some needs of the UK XFEL Science and Technology case.

9.4.1.3 Two-colour gas plasma

The THz radiation generated from laser plasma typically has a broad spectrum, 1-40 THz [28] The THz radiation generated by a two-colour plasma filament has a conical emission pattern, a feature characteristic especially for long filaments. This is caused by the off-axis phase matching, and results in typical opening angles in the range of 2-10° [29]. The polarisation is also radial, and spatial profile is a ring. These factors limit its scalability, transportability, and ultimately field at focus. The pulses are very broad band and so do not satisfy the selectivity requirement for UK XFEL.

9.4.1.4 Spintronics

Spintronic THz emitters are compact, broadband sources of THz radiation that utilize ultrafast spin-to-charge conversion in magnetic heterostructures [30]. These devices typically consist of a bilayer structure composed of a ferromagnetic (FM) layer and a non-magnetic (NM) layer with strong spin-orbit coupling. When excited by a femtosecond laser pulse, the FM layer generates a non-equilibrium distribution of spin-polarised hot electrons. These electrons diffuse into the adjacent NM layer, producing a transient spin current.

In the NM layer, the spin current is converted into a transverse charge current via the inverse spin Hall effect, a process enabled by the strong spin-orbit interaction in materials such as platinum, tungsten, or tantalum. The resulting ultrafast charge current emits a broadband THz pulse into

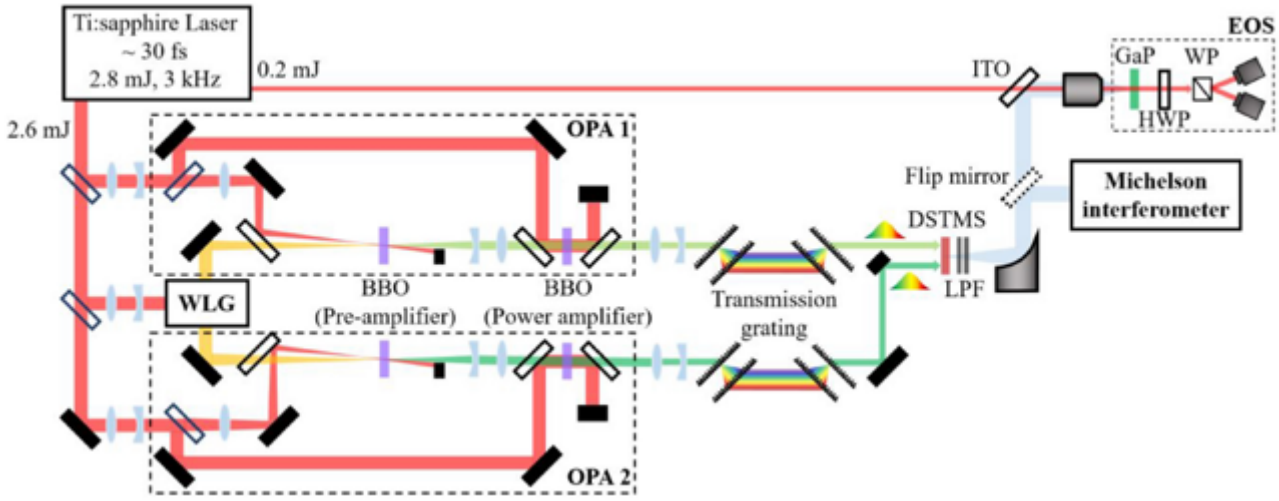

Figure 9.12: Schematic of a high efficiency terahertz source based on an organic-crystal difference system, from [27] "Experimental setup for generating narrowband, strong THz fields, composed of two high-efficiency OPAs. A laser pulse with 2.8 mJ is separated to pump two identical two-stage OPAs seeded by the same white light generation (WLG) system, and to probe for electro-optic sampling (EOS). Each separated beam is down-collimated by a Galilean telescope. The signal output from each OPA is chirped by a pair of high-efficiency transmission gratings and utilized for the DFG process in a DSTMS crystal. The generated THz pulses are extracted by a pair of low pass filters (LPF) and characterized by either interferometric autocorrelation or EOS in a GaP crystal. The EOS setup consists of a half-wave plate (HWP), a Wollaston prism (WP), and two fast photodiodes in a balanced detecting configuration."

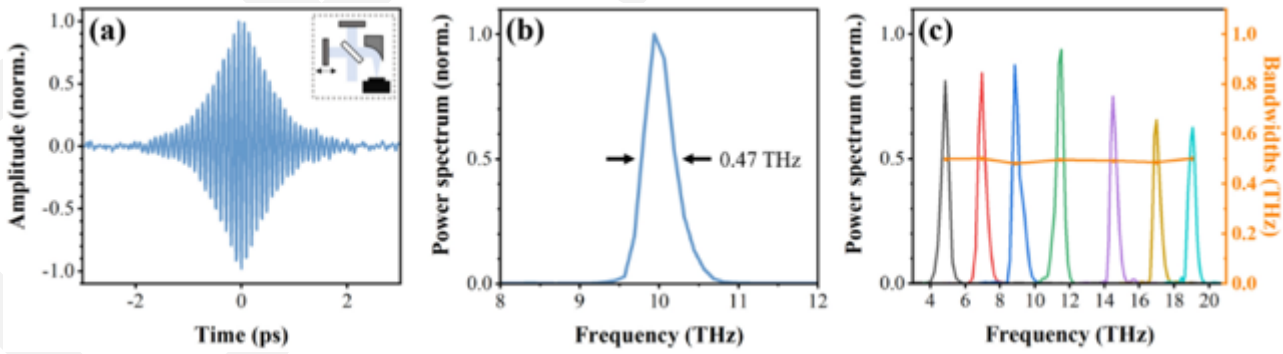

Figure 9.13: Properties of THz generated from DFG THz source based on an organic crystal, from [27] "(a) Energy of signal pulse (left axis) in the pre-amplifier along with the internal conversion efficiency (right axis). (b) Output signal energy as a function of the input signal and pump energy in the power amplifier. (c) Spectra of output signals at different wavelengths. (d) The total output energy (signal plus idler pulse) (red dots) and the corresponding conversion efficiency (blue squares) for a total pump energy of 1.3 mJ."

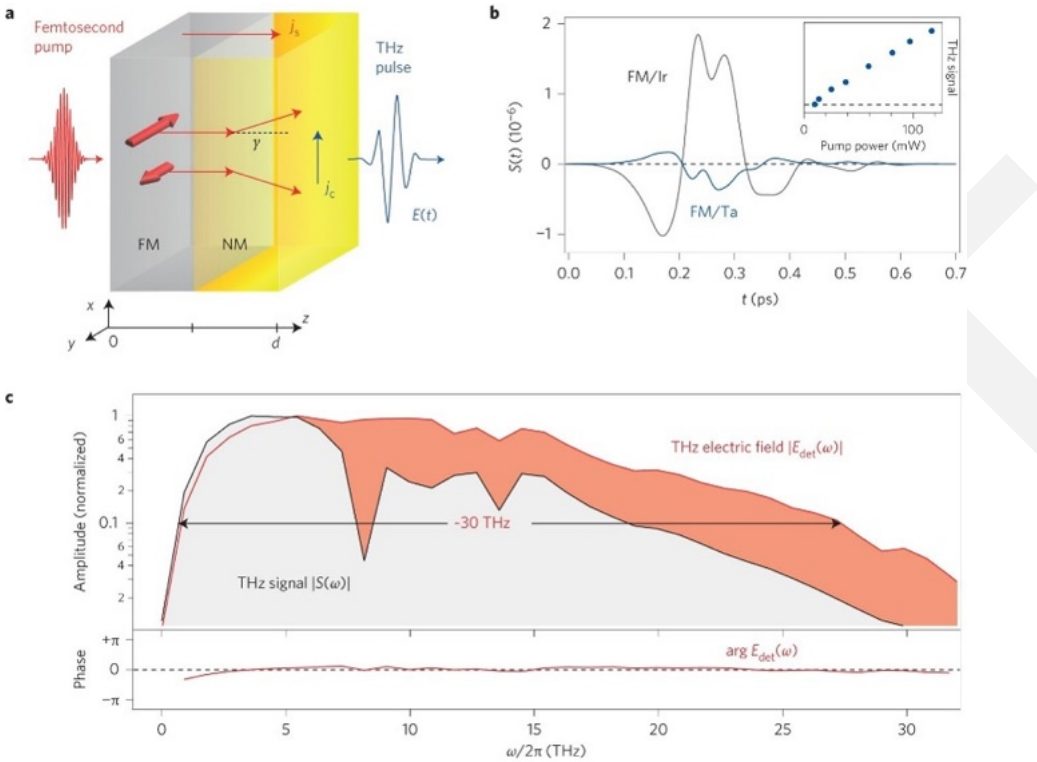

Figure 9.14: Replicated from [30]. "Metallic spintronic terahertz emitter. a, Principle of operation. A femtosecond laser pulse excites electrons in the metal stack, thereby changing their band velocity and launching a current along the z direction. Because in the FM layer the mobility of spin-up (majority) electrons is significantly higher than that of spin-down (minority) electrons, the z current is spin-polarized. In the NM layer, spin-orbit interaction deflects spin-up and spin-down electrons in opposite directions and transforms the spin current j_s into an ultrafast transverse charge current $j_c = \gamma j_s$, leading to the emission of a terahertz electromagnetic transient. b, Typical electrooptic signal S(t) of terahertz pulses obtained from photoexcited Ta- and Ir-capped $Co_{20}Fe_{60}B_{20}$ thin films and detected by a 50-μm-thick GaP crystal. Inset: Terahertz signal amplitude as a function of incident pump power. c, Fourier spectra of terahertz signal S(t) and the extracted transient terahertz electric field $E_{det}(t)$ incident on the electrooptic detector. Both spectra are normalized to peak amplitude 1. The double-headed arrow illustrates the 30 THz large bandwidth of the emitter. The flat spectral phase indicates that the terahertz pulse is Fourier-limited."

free space. The emitted radiation is typically linearly polarised and spans a spectral range of 0.1-30 THz, depending on the material system and excitation conditions. See Figure 9.14 for details. Spintronic THz emitters offer several advantages, including broadband emission without phase-matching constraints, a compact and scalable thin-film design, and tunability through material and structural optimisation. [31, 32, 33, 34]

High repetition rate operation [34], and tunable narrow-bandwidth outputs [35], have been demonstrated. This technology is rapidly advancing and is likely to find application in a next generation XFEL.

9.4.2 Beam-based THz sources

A way to optimise temporal synchronisation is to generate THz using the same electron bunches that generate the x-rays. Timing jitter in the electrons then becomes a common mode between the beams and cancels out to first order.

There are however a number of issues with this approach. As the THz is generated after the x-rays, the x-rays will always arrive first making a THz pump very difficult to realise. This is exacerbated by

the THz transport, which, because of the long wavelengths, requires relay imaging, and because of the many octave tuning range/bandwidth, requires reflective optics extending the length further. These optics will also be metallic, and so power absorption and thermal deformation would need to be managed. The technique also does not aid in synchronising to other laser pumps that may be needed in the experiment. Spatial mode quality is very important for achieving high fields and efficient delivery to the sample, and sources based on transition radiation processes tend to have poor transverse profile [36], as shown in Figure 9.15.

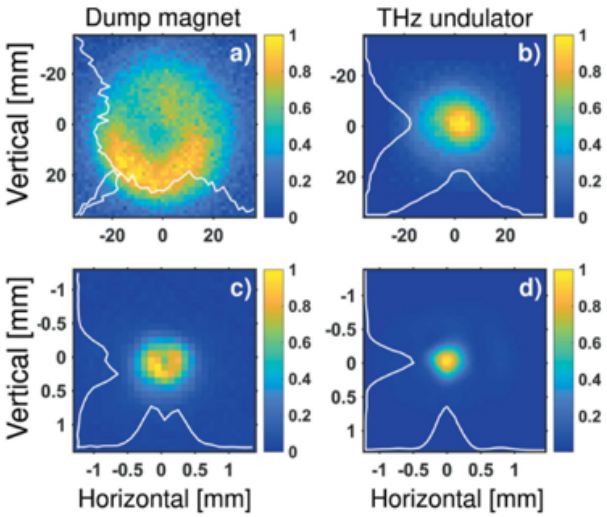

Figure 9.15: Replicated from [36]. (Top) THz transverse beam profiles at FLASH. (a) Dump magnet (the THz undulator is off), and (b) THz undulator tuned to 88 mm (3.4 THz), unfocused beam profiles measured in the THz hutch; beam position imaged 10 m from the virtual source. Note that the undulator profile is padded with zeros to fill in the same image size. (Bottom) The same beams focused. (c) Dump magnet beam (600 mm FWHM), and (d) THz undulator beam (350 mm).

9

9.4.2.1 Afterburner FEL

Wide-bandwidth sources can be achieved using coherent transition radiation, diffraction radiation, or radiation from bending magnets. For narrow-band THz, sources based on undulators are needed. These require electron bunches shorter than the THz radiation wavelength. A commonly considered approach is the “afterburner” concept, which utilizes short electron beams that have already emitted radiation at shorter wavelengths. To produce high THz pulse energy a high charge at moderate beam energy is needed. However, the generation of short pulses is constrained by the longitudinal space-charge effect. This puts it at odds with the electron bunch requirements for x-ray generation. An “afterburner” THz FEL using the spent XFEL beam would have a much better spatial profile than broadband sources, but still has the inherent delay behind the x-ray pulses. Additionally, the spent beam is far from ideal for this purpose: the high energy of the bunch requires a single period of the FEL to be of the order of 1.5 m long to provide the required phase slippage, and to get a bandwidth of better than 500 GHz this would require a FEL hundreds of meters long.

We quote a useful summary from [37]: *“FEL facilities around the world, including LCLS-II, FLASH ,European-XFEL and Swiss-FEL have adopted an afterburner to compress the duration of the electron beam into one THz period to obtain high-power X-ray and intense THz with a broad spectral bandwidth of about* 10 %*, a pulse energy up to* 200 µJ *and a great synchronization performance. However, generating THz radiation with a frequency above* 10 THz *requires the*

suppression of the pulse duration of the electron beam below 100 fs*, which is still a challenge for most of the existing FEL facilities."*

9.4.2.2 Stand-alone THz FEL

A prototype high-power, tunable, accelerator-based THz source for pump-probe experiments is being developed at the Photo Injector Test Facility at DESY in Zeuthen (PITZ) [38]. The primary drive is to supply the European XFEL with a pulse structure matching THz source. The requirements of the facility are a tuning range of 0.1-30 THz, a bandwidth of only 1-2 %, and a pulse energy across the tuning range 10 µJ. The FEL is based on Self Amplified Spontaneous Emission (SASE) in order to overcome the charge limits of short, low energy, bunches, and provide a relatively (on the order of 100 m long) compact and high power THz source. First-light was

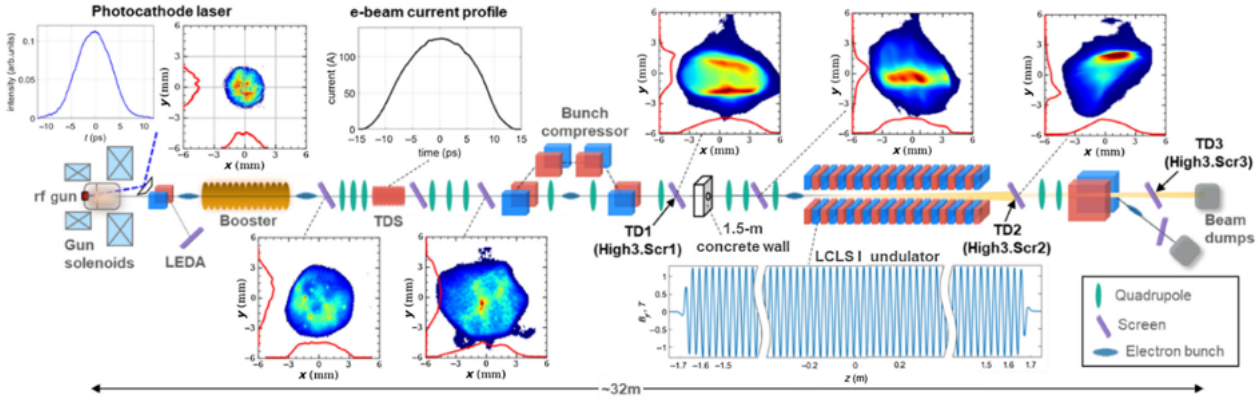

Figure 9.16: Replicated from [38]: PITZ machine layout (not to scale). The beam travels from the rf gun through the booster, electron beam transport beamline, bunch compressor, the LCLS-I undulator, and THz diagnostic sections. The photocathode laser, electron beam transverse distributions, and temporal profiles measured along the beamline are shown as insets close to locations of measurement. The measured magnetic field of the LCLS-I undulator is shown as well.

recently demonstrated, producing 65 µJ pulses at 3 THz, from a 10 ps, 2.4 nC electron bunch with an energy of only 17 MeV. Their predictions are that the pulse energy can be increased by over an order of magnitude, and smooth tunabilty via bunch energy optimisation can be achieved.

This source is very promising when considering the claimed pulse parameters, but the associated running costs, complexity of synchronisation and transport lines, and footprint, mean it may not be the optimal choice for every end station.

9.4.3 Summary

There currently is no THz solution that satisfies all requirements, but there is continued and rapid progress in laser based THz sources, and the research effort by DESY/PITZ will continue. The best route seems to be to plan for laser based sources at all end stations, and reserve the option to have an independent FEL source located near the end stations with the clearest experimental need. This FEL can be located behind, or to the side of the end stations, mitigating the impact on the x-ray transport and facility design.

9.5 High power and high energy lasers

9.5.1 Introduction

A key component of the UK XFEL Science and Technology Case is the investigation of matter in extreme conditions (MEC). The FEL-1 MEC beamline requires specialised infrastructure to achieve the high energy density (HED), high field and high pressure environments to enable studies in (e.g.) fusion energy, weapons research, and laboratory astrophysics/geophysics.

High performance laser systems are key components in accessing these extreme states of matter. We will refer to two technology classes which come under this heading:

High peak power, 'short-pulse' lasers: petawatt-class systems, with typical pulse durations of the order 10-100 fs and pulse energies of 100-1000 J

High energy, 'long-pulse' lasers: delivering pulse energies $>$1 kJ in ns duration pulses

As outlined in the science case, short-pulse lasers are exploited for laser-matter interaction and strong-field science, while long-pulse lasers can be used as shock drivers for warm dense matter experiments.

These systems are large-scale facilities in their own right, being sufficient complex and expensive to demand specialised infrastructure and operational support. There are many such dedicated laser facilities in Europe and beyond, with UK capability delivered through STFC's Central Laser Facility (CLF). There is a parallel between these facilities and XFELs, which typically have the scale, funding and skill-base to take up the installation of high-power laser infrastructure.

XFELs with a dedicated programme committed to high performance laser development and operation include the HED end station at European XFEL [39], the MEC station [40] (and associated upgrade project MEC-U [41]) at LCLS, and the planned Station of Extreme Light (SEL) at SHINE [42]. These installations are typically delivered through extensive collaboration between the XFEL facility and external partners. Exploitation is focussed on the combination of short-pulse and long-pulse laser light with hard X-rays, which have the penetrating power to investigate high density states of matter.

9.5.2 State-of-the-art

A comprehensive summary of high performance laser infrastructure worldwide is available in [43], and an accompanying summary of worldwide high performance laser infrastructure is given in Table 9.4.

The UK has two major new high performance laser facilities under construction. The Extreme Photonics Applications Centre (EPAC) will provide a 1 PW (30 J in 30 fs), 10 Hz Ti:Sapphire laser to two experimental areas [44]. The laser utilises CLF's proprietary D100X-DiPOLE technology as a pump source [45] capable of delivering 100 J pulses at 100 Hz using diode-pumped, cryogenic gas-cooled Yb:YAG multi-slab technology. DiPOLE is also an ideal platform for experimental use, featuring pulse shaping, variable pulse duration and the option for efficient second harmonic generation.

Vulcan 20-20 is a significant upgrade of the existing Vulcan facility, which will deliver a 20 PW (400 J in 20 fs) using OPCPA technology. The laser will be pumped by 2 $\times$ 1 kJ 527 nm Nd:Glass disc amplifiers, which will incorporate active cooling to allow a repetition rate of one shot every

five minutes [46]. Three large-aperture opto-parametric amplifiers (OPAs) will deliver 800 J before compression, which requires large-diameter DKDP crystals. The Vulcan 20 PW laser expects to be the world's most intense laser source once fully operational.

The Vulcan upgrade will also increase the pulse energy of its six long-pulse beams lines to 10 kJ (collectively) at 1054 nm. Combined with the pump lasers, the facility will collectively deliver approximately 20 kJ of long-pulse energy, which combined with the 20 PW, gives Vulcan '20-20' its name [47].

The CLF has supplied DiPOLE systems to several other European facilities, including HiLASE in the Czech Republic. This includes a 145 J, 10 Hz (>1 kW average power) system ('Bivoj') [48], and more recently a 10 J, 100 Hz system ('Kazi') delivered 2023 [49]. Both systems were delivered with HiLASE via the Widespread collaboration. A further DiPOLE system (DiPOLE 100-X) achieving 78 J at 10 Hz was provided to the HED end station at European XFEL, via the HIBEF collaboration [39]. Comparable average power performance has been achieved using Total Reflection Active Mirror (TRAM) technology, at the GENBU3 system (Osaka University: 10 J, 100 Hz) [50].

The High Energy Density (HED) instrument at European XFEL, operated together with the HIBEF user consortium (HED-HIBEF), is a dedicated platform for combining hard X-ray XFEL pulses with matter under extreme conditions (temperature, pressure, electric field). The instruments includes multiple mechanisms for generating these states of matter, including pulsed magnets, diamond anvil cells, the XFEL itself, and two high performance laser systems.

In addition to a DIPOLE 100-X laser (as above), the HED instrument has access to a 6 J (nominal) at 5 Hz, 23 fs Ti:Sapphire laser system ('ReLaX') designed and built by Amplitude [39], in collaboration with HZDR. The laser incorporates a probe pick-off which is used to seed a photon arrival monitor upstream of the instrument for time-of-arrival measurement of X-rays with respect to the main pulse. The laser oscillator is optically synchronised to the European XFEL pulsed timing distribution with <10-100 fs timing jitter. The relative timing of the laser can be moved with respect to the XFEL pulses using a combination of phase shifters (high range, increased jitter) and optical delay stage (low range, reduced jitter).

Laser	Host institute	Location	Pulse energy [J]	Pulse duration [fs]	Peak power [PW]	Frequency [Hz]	Average power [W]
L1: Allegra	ELI-BL	Czech Republic	0.1	20	5×10^{-3}	1000	100
L2: Duha	ELI-BL	Czech Republic	2	25	8×10^{-2}	50	100
ReLaX	European XFEL	Germany	6	30	0.2	5	30
NIF	LLNL	US	2×10^{6}	3.6×10^{6}	0.6	Single-shot	-
EPAC	CLF	UK	30	30	1	10	300
ORION	AWE	UK	500	500	1	Single-shot	-
L3: HAPLS	ELI-BL	Czech Republic	30	30	1	10	300
BELLA	LBNL	US	40	40	1	1	40
OMEGA-EP	LLE	US	1000	1000	1	Single-shot	-
HFLS	ELI-ALPS	Hungary	50	25	2	10	500
Apollon*	Saclay	France	180	18	10	Single-shot	-
L4: Aton	ELI-BL	Czech Republic	1500	150	10	2×10^{-2}	30
HPLS	ELI-NP	Romania	220	22	10	2×10^{-2}	4.4
Vulcan 20-20*	CLF	UK	400	20	20	Single-shot	-
DiPOLE100-X	European XFEL	Germany	100	2×10^{6}	-	10	1000
DiPOLE 'Kazi'	HiLASE	Czech Republic	10	2×10^{6}	-	100	1000
GENBU	Osaka	Japan	10	1×10^{7}	-	100	1000

Table 9.4: Summary of selected high performance laser systems, based on [43] and [51]. Entries sorted by peak power. Systems marked with (*) are, at the time of writing, either undergoing commissioning or construction, and may not have met the listed parameters.

9.5.3 Future directions

A Next Generation XFEL should look to exploit developments in laser technology to deliver higher pulse energies at higher repetition rates. There are additional challenges from the implementation of this technology around the specific constraints of an XFEL facility.

Fully exploiting these advances in laser technology will also require related developments linked to experimentation, including target systems (e.g., those capable of sustained high repetition rate operation), target debris management, laser and X-ray diagnostics, and laser control systems (potentially incorporating artificial intelligence for improved reliability, repeatability and optimisation). These subjects are currently out-of-scope for this work, however would be key components of a future design phase.

Although examples linked to XFEL facilities are presented, many of these laser source developments are driven by independent roadmaps, and the technology as a whole is expected to progress accordingly. The challenge for a next generation XFEL will be to maintain fully connected with this field as it progresses, build the relevant collaborations (e.g., UK laser technology contributing to an international facility, or vice-versa), and generate the project activity which would deliver the infrastructure on the timescale required.

For all of the above, the world-leading expertise in high performance laser infrastructure provided by the CLF should be utilised. The UK is clearly well-positioned through the CLF to contribute to the provision of advanced short and long-pulse laser technology for a Next Generation XFEL, along with other technical elements underpinning their scientific exploitation, and should be expected to lead technical design contributions in this area.

Achieving high average power together with high pulse energy (long-pulse) and high peak intensity (short-pulse) is linked to increasing the repetition rate of the laser technology. Increasing average power requires specialised schemes for managing the higher (potential) thermal load on both optical components and the laser gain media. Use of diode pumping, as used ELI HAPLS, over a much narrower bandwidth within the absorption spectrum is more efficient, with remaining heating limited to the quantum defect. Gas cooling offers increased performance over more common water cooling. The DiPOLE 100 system utilises cryogenic cooling to remove heat from multiple thin Yb:YAG ceramic slabs mounted in series. The high surface area of each slab ensures efficient heat removal and the geometry helps to suppress amplified spontaneous emission losses [52].

Beyond the gain medium, advances in optical systems are required to allow performance to be maintained under higher thermal loading. For example, heat deposited into the diffraction gratings used in vacuum laser compressors can lead to local surface deformation and wavefront distortion; this impacts the peak intensity which can be achieved through focussing and introduce spatiotemporal distortions into the ultrashort pulses. The EPAC facility is investigating multiple solutions to this problem, including active water cooling of the grating substrate.

9.6 Sustainability

One of the most obvious improvements is the move to a more efficient laser technology than Ti:Sapphire. It has only been in the last 10 years that Yb laser technology has reached a maturity level where commercially available systems are starting to replace them. Not only is it more energy efficient, indications are that it may also be more reliable and consistent. This will bring

about an additional, and perhaps more impactful, benefit in increased source up-time, thereby enabling a more efficient use of a next generation XFEL.

Utilising modular designs where possible, for example MODS at LCLS, will minimise replication of laser systems, reduce the footprint and of the source (and therefore also reduce the room size and it's associated environmental controls), and enable up-grading without replacing/reworking the whole system.

As the laser systems will be available at all end-stations, it would be preferable to derive all sources from them, such as THz radiation, where possible and it does not significantly degrade the scientific capability.

9.7 Summary of technology development areas, R&D needed for future phases to meet spec

For the optical sources provision, the repetition rate, tuning range, and pulse energy that is currently available from commercial laser system suppliers would already provide an adequate solution for many applications. In general, the scientific and commercial community is continually pushing the development of optical sources, so this situation will only improve. To meet the aspiration of single femtosecond (or better) science, further development to drive down the pulse duration to something close to single-cycle across the whole wavelength range would be of benefit. RDW sources can provide this for shorter wavelengths, but even then their spectral selectivity could be improved. The UK also has world leading departments in this field which a future design phase should seek to collaborate with.

Timing stability in HHG sources is an area needing attention, possibly via the application of RDW pulse pumping which is also something being developed in the UK. Particle sources do not have a clear user requirement, this should be monitored and further effort could go into generation of a proposal. There is the potential for laser-derived sources (e.g. TNSA) at kHz rates driven by high power lasers, but this would not available at all end stations.

Current THz sources do not yet meet all of the required specification, but progress is being made with both electron beam based solutions and laser based technologies. It seems clear that a laser based technology that could be pumped by the optical-source drive-laser would be much more efficient and lower impact to the facility design. Emerging laser-based THz-source technology is where collaboration should be sought – with the many UK Universities that are already actively developing it (e.g. Spintronic sources at the University of Manchester). A future design phase should also accelerator-based sources (such as that under development at PITZ) to mitigate risk of the laser sources not delivering, and to gain understanding and perhaps have input into the specifications of a machine.

References for Chapter 9

[1] Christopher D M Hutchison, Samuel Perrett, and Jasper J Van Thor. “XFEL Beamline Optical Instrumentation for Ultrafast Science”. In: *J. Phys. Chem. B* 128 (2024), p. 8868. DOI: 10.1021/acs.jpcb.4c01492. URL: https://doi.org/10.1021/acs.jpcb.4c01492.

[2] Clara J. Saraceno et al. “The amazing progress of high-power ultrafast thin-disk lasers”. In: *Journal of the European Optical Society* 15.1 (Dec. 2019), pp. 1–7. ISSN: 19902573. DOI: 10.1186/S41476-019-0108-1/FIGURES/3. URL: https://jeos.springeropen.com/articles/10.1186/s41476-019-0108-1.

[3] Jakub Drs et al. “A Decade of Sub-100-fs Thin-Disk Laser Oscillators”. In: *Laser & Photonics Reviews* 17.8 (Aug. 2023), p. 2200258. ISSN: 1863-8899. DOI: 10.1002/LPOR.202200258. URL: https://onlinelibrary.wiley.com/doi/full/10.1002/lpor.202200258%20https://onlinelibrary.wiley.com/doi/abs/10.1002/lpor.202200258%20https://onlinelibrary.wiley.com/doi/10.1002/lpor.202200258.

[4] *LIGHT CONVERSION*. URL: https://lightcon.com/.

[5] *CLF Welcome to HiLUX*. URL: https://www.clf.stfc.ac.uk/Pages/HiLUX-Home.aspx.

[6] Gregory M. Greetham et al. “A 100 kHz time-resolved multiple-probe femtosecond to second infrared absorption spectrometer”. In: *Applied Spectroscopy* 70.4 (Apr. 2016), pp. 645–653. ISSN: 19433530. DOI: 10.1177/0003702816631302.

[7] M. Pergament et al. “Versatile optical laser system for experiments at the European X-ray free-electron laser facility”. In: *Optics Express* 24.26 (Dec. 2016), p. 29349. ISSN: 10944087. DOI: 10.1364/oe.24.029349.

[8] Maximilian Lederer. *Laser systems for science instruments*. 2017. URL: https://xfel.tind.io/record/2924.

[9] Peter Zalden et al. *Terahertz Science at European XFEL*. 2018. URL: https://xfel.tind.io/record/1564.

[10] P. Grychtol et al. “The SXP instrument at the European XFEL”. In: *Journal of Physics: Conference Series* 2380 (1 Dec. 2022), p. 012043. ISSN: 1742-6596. DOI: 10.1088/1742-6596/2380/1/012043. URL: https://iopscience.iop.org/article/10.1088/1742-6596/2380/1/012043%20https://iopscience.iop.org/article/10.1088/1742-6596/2380/1/012043/meta.

[11] Anne-Lise Viotti et al. “Multi-pass cells for post-compression of ultrashort laser pulses”. In: *Optica, Vol. 9, Issue 2, pp. 197-216* 9.2 (Feb. 2022), pp. 197–216. ISSN: 2334-2536. DOI: 10.1364/OPTICA.449225. URL: https://opg.optica.org/viewmedia.cfm?uri=optica-9-2-197&seq=0&html=true%20https://opg.optica.org/abstract.cfm?uri=optica-9-2-197%20https://opg.optica.org/optica/abstract.cfm?uri=optica-9-2-197.

[12] Christina Möller et al. “Ultrafast element-resolved magneto-optics using a fiber-laser-driven extreme ultraviolet light source”. In: *Review of Scientific Instruments* 92.6 (June 2021), p. 65107. ISSN: 10897623. DOI: 10.1063/5.0050883/992880. URL: /aip/rsi/article/92/6/065107/992880/Ultrafast-element-resolved-magneto-optics-using-a.

[13] Christian Brahms and John C. Travers. “Timing and energy stability of resonant dispersive wave emission in gas-filled hollow-core waveguides”. In: *Journal of Physics: Photonics* 3.2 (Apr. 2021), p. 025004. ISSN: 2515-7647. DOI: 10.1088/2515-7647/ABF238. URL: https://iopscience.iop.org/article/10.1088/2515-7647/abf238%20https://iopscience.iop.org/article/10.1088/2515-7647/abf238/meta.

[14] N. Y. Joly et al. “Bright spatially coherent wavelength-tunable deep-UV laser source using an Ar-filled photonic crystal fiber”. In: *Phys. Rev. Lett.* 106.20 (May 2011), p. 203901. ISSN: 00319007. DOI: 10.1103/physrevlett.106.203901.

[15] Ka Fai Mak et al. “Tunable vacuum-UV to visible ultrafast pulse source based on gas-filled Kagome-PCF”. In: *Opt. Express* 21.9 (May 2013), p. 10942. ISSN: 10944087. DOI: 10.1364/oe.21.010942.

[16] A. Ermolov et al. “Supercontinuum generation in the vacuum ultraviolet through dispersive-wave and soliton-plasma interaction in a noble-gas-filled hollow-core photonic crystal fiber”. In: *Phys. Rev. A* 92.3 (Sept. 2015), p. 033821. ISSN: 10941622. DOI: 10.1103/physreva.92.033821.

[17] John C. Travers et al. “High-energy pulse self-compression and ultraviolet generation through soliton dynamics in hollow capillary fibres”. In: *Nat. Photon.* 13.8 (Aug. 2019), p. 547. ISSN: 17494893. DOI: 10.1038/s41566-019-0416-4.

[18] Christian Brahms, Federico Belli, and John C. Travers. “Infrared attosecond field transients and UV to IR few-femtosecond pulses generated by high-energy soliton self-compression”. In: *Phys. Rev. Res.* 2.4 (Oct. 2020), p. 043037. ISSN: 26431564. DOI: 10.1103/physrevresearch.2.043037.

[19] M. Erkintalo et al. “Cascaded phase matching and nonlinear symmetry breaking in fiber frequency combs”. In: *Phys. Rev. Lett.* 109.22 (Nov. 2012), p. 223904. ISSN: 00319007. DOI: 10.1103/physrevlett.109.223904.

[20] Nail Akhmediev and Magnus Karlsson. “Cherenkov radiation emitted by solitons in optical fibers”. In: *Phys. Rev. A* 51.3 (1995), p. 2602. ISSN: 10502947. DOI: 10.1103/physreva.51.2602.

[21] Tobias Witting et al. “Generation and characterization of isolated attosecond pulses at 100 kHz repetition rate”. In: *Optica, Vol. 9, Issue 2, pp. 145-151* 9.2 (Feb. 2022), pp. 145–151. ISSN: 2334-2536. DOI: 10.1364/OPTICA.443521. URL: https://opg.optica.org/viewmedia.cfm?uri=optica-9-2-145&seq=0&html=true%20https://opg.optica.org/abstract.cfm?uri=optica-9-2-145%20https://opg.optica.org/optica/abstract.cfm?uri=optica-9-2-145.

[22] Manuel Krebs et al. “Towards isolated attosecond pulses at megahertz repetition rates”. In: *Nature Photonics* 7.7 (July 2013), pp. 555–559. ISSN: 17494885. DOI: 10.1038/NPHOTON.2013.131;SUBJMETA=2796,36,385,400,584,624,639,766;KWRD=ATTOSECOND+SCIENCE,NONLINEAR+OPTICS,ULTRAFAST+PHOTONICS. URL: https://www.nature.com/articles/nphoton.2013.131.

[23] János Hebling et al. “Velocity matching by pulse front tilting for large-area THz-pulse generation”. In: *Optics Express, Vol. 10, Issue 21, pp. 1161-1166* 10.21 (Oct. 2002), pp. 1161–1166. ISSN: 1094-4087. DOI: 10.1364/OE.10.001161. URL: https://opg.optica.org/viewmedia.cfm?uri=oe-10-21-1161&seq=0&html=true%20https://opg.optica.org/abstract.cfm?uri=oe-10-21-1161%20https://opg.optica.org/oe/abstract.cfm?uri=oe-10-21-1161.

[24] Patrick L. Kramer et al. “Enabling high repetition rate nonlinear THz science with a kilowatt-class sub-100 fs laser source”. In: *Optics Express, Vol. 28, Issue 11, pp. 16951-16967* 28.11 (May 2020), pp. 16951–16967. ISSN: 1094-4087. DOI: 10.1364/OE.389653. URL: https://opg.optica.org/viewmedia.cfm?uri=oe-28-11-16951&seq=0&html=true%20https://opg.optica.org/abstract.cfm?uri=oe-28-11-16951%20https://opg.optica.org/oe/abstract.cfm?uri=oe-28-11-16951.

[25] Aizitiaili Abulikemu, Takumi Fukuda, and Muneaki Hase. "Ultrafast dynamics of coherent phonons and phonon-polaritons in lithium niobate crystals". In: *Applied Physics Express* 15.9 (Sept. 2022), p. 092005. ISSN: 1882-0778. DOI: 10.35848/1882-0786/ac871c. URL: https://iopscience.iop.org/article/10.35848/1882-0786/ac871c.

[26] Hyeongmun Kim et al. "Ionizing terahertz waves with 260 MV/cm from scalable optical rectification". In: *Light: Science & Applications 2024 13:1* 13.1 (May 2024), pp. 1–13. ISSN: 2047-7538. DOI: 10.1038/s41377-024-01462-w. URL: https://www.nature.com/articles/s41377-024-01462-w.

[27] Meenkyo Seo et al. "High-efficiency near-infrared optical parametric amplifier for intense, narrowband THz pulses tunable in the 4 to 19 THz region". In: *Scientific Reports 2022 12:1* 12.1 (Sept. 2022), pp. 1–7. ISSN: 2045-2322. DOI: 10.1038/s41598-022-20622-9. URL: https://www.nature.com/articles/s41598-022-20622-9.

[28] George Rodriguez et al. "Scaling behavior of ultrafast two-color terahertz generation in plasma gas targets: energy and pressure dependence". In: *Optics Express, Vol. 18, Issue 14, pp. 15130-15143* 18.14 (July 2010), pp. 15130–15143. ISSN: 1094-4087. DOI: 10.1364/OE.18.015130. URL: https://opg.optica.org/viewmedia.cfm?uri=oe-18-14-15130&seq=0&html=true%20https://opg.optica.org/abstract.cfm?uri=oe-18-14-15130%20https://opg.optica.org/oe/abstract.cfm?uri=oe-18-14-15130.

[29] Andrei Gorodetsky et al. "Physics of the conical broadband terahertz emission from two-color laser-induced plasma filaments". In: *Physical Review A - Atomic, Molecular, and Optical Physics* 89.3 (Mar. 2014), p. 033838. ISSN: 10502947. DOI: 10.1103/PHYSREVA.89.033838/FIGURES/5/MEDIUM. URL: https://journals.aps.org/pra/abstract/10.1103/PhysRevA.89.033838.

[30] T. Seifert et al. "Efficient metallic spintronic emitters of ultrabroadband terahertz radiation". In: *Nature Photonics* 10.7 (June 2016), pp. 483–488. ISSN: 17494893. DOI: 10.1038/NPHOTON.2016.91;TECHMETA=125,140;SUBJMETA=1130,2798,400,561,624,639,766;KWRD=ELECTRONIC+AND+SPINTRONIC+DEVICES,TERAHERTZ+OPTICS. URL: https://www.nature.com/articles/nphoton.2016.91.

[31] Charlotte Bull et al. "Spintronic terahertz emitters: Status and prospects from a materials perspective". In: *APL Materials* 9.9 (Sept. 2021), p. 90701. ISSN: 2166532X. DOI: 10.1063/5.0057511/122925. URL: /aip/apm/article/9/9/090701/122925/Spintronic-terahertz-emitters-Status-and-prospects.

[32] Evangelos Th Papaioannou and René Beigang. "THz spintronic emitters: A review on achievements and future challenges". In: *Nanophotonics* 10.2 (Jan. 2021), pp. 1243–1257. ISSN: 21928614. DOI: 10.1515/NANOPH-2020-0563.

[33] R. Rouzegar et al. "Broadband Spintronic Terahertz Source with Peak Electric Fields Exceeding 1.5 MV/cm". In: *Physical Review Applied* 19.3 (Mar. 2023). ISSN: 23317019. DOI: 10.1103/PHYSREVAPPLIED.19.034018.

[34] Alkisti Vaitsi et al. "Rotating spintronic terahertz emitter optimized for microjoule pump-pulse energies and megahertz repetition rates". In: *Applied Physics Letters* 125.7 (Aug. 2024), p. 71107. ISSN: 00036951. DOI: 10.1063/5.0214469/3307900. URL: /aip/apl/article/125/7/071107/3307900/Rotating-spintronic-terahertz-emitter-optimized.

[35] R. Ji et al. "Tunable multi-cycle terahertz pulse generation from a spintronic emitter". In: *Applied Physics Letters* 123.21 (Nov. 2023), p. 212402. ISSN: 00036951. DOI: 10.1063/5.0176314/2922358. URL: /aip/apl/article/123/21/212402/2922358/Tunable-multi-cycle-terahertz-pulse-generation.

[36] Rui Pan et al. "Photon diagnostics at the FLASH THz beamline". In: *Journal of Synchrotron Radiation* 26.3 (May 2019), pp. 700–707. ISSN: 1600-5775. DOI: 10.1107/S1600577519003412. URL: https://journals.iucr.org/s/issues/2019/03/00/yi5073/.

[37] Yin Kang et al. "Generating High-Power, Frequency Tunable Coherent THz Pulse in an X-ray Free-Electron Laser for THz Pump and X-ray Probe Experiments". In: *Photonics* 10.2 (Feb. 2023). ISSN: 23046732. DOI: 10.3390/PHOTONICS10020133. URL: https://www.researchgate.net/publication/367524740_Generating_High-Power_Frequency_Tunable_Coherent_THz_Pulse_in_an_X-ray_Free-Electron_Laser_for_THz_Pump_and_X-ray_Probe_Experiments.

[38] Mikhail Krasilnikov et al. "First high peak and average power single-pass THz free-electron laser in operation". In: *Physical Review Accelerators and Beams* 28.3 (Mar. 2025), p. 030701. ISSN: 2469-9888. DOI: 10.1103/PhysRevAccelBeams.28.030701. URL: https://journals.aps.org/prab/abstract/10.1103/PhysRevAccelBeams.28.030701.

[39] Ulf Zastrau et al. "The High Energy Density Scientific Instrument at the European XFEL". In: *Journal of Synchrotron Radiation* 28.5 (Sept. 2021), pp. 1393–1416. ISSN: 1600-5775. DOI: 10.1107/S1600577521007335.

[40] Bob Nagler et al. "The Matter in Extreme Conditions instrument at the Linac Coherent Light Source". In: *Journal of Synchrotron Radiation* 22.3 (May 2015), pp. 520–525. ISSN: 1600-5775. DOI: 10.1107/S1600577515004865.

[41] Gilliss Dyer and Alan Fry. *Matter in Extreme Conditions Upgrade (Conceptual Design Report)*. Tech. rep. SLAC National Accelerator Laboratory (SLAC), Oct. 2021. DOI: 10.2172/1866100.

[42] Xinliang Wang et al. "13.4 fs, 0.1 Hz OPCPA Front End for the 100 PW-Class Laser Facility". In: *Ultrafast Science* 2022 (Jan. 2022). ISSN: 2765-8791. DOI: 10.34133/2022/9894358.

[43] Colin N. Danson et al. *Petawatt and exawatt class lasers worldwide*. 2019. DOI: 10.1017/hpl.2019.36.

[44] Luke McHugh et al. "Commissioning a high-energy 10Hz Ti:Sa amplifier for the petawatt laser at the Extreme Photonics Applications Centre". In: *Solid State Lasers XXXIV: Technology and Devices*. Ed. by W. Andrew Clarkson and Ramesh K. Shori. SPIE, Mar. 2025, p. 12. ISBN: 9781510684300. DOI: 10.1117/12.3041937.

[45] Paul Mason et al. "Development of a 100 J, 10 Hz laser for compression experiments at the High Energy Density instrument at the European XFEL". In: *High Power Laser Science and Engineering* 6 (2018), e65. ISSN: 2095-4719. DOI: 10.1017/HPL.2018.56. URL: https://www.cambridge.org/core/journals/high-power-laser-science-and-engineering/article/development-of-a-100-j-10-hz-laser-for-compression-experiments-at-the-high-energy-density-instrument-at-the-european-xfel/BE9310E57FB3CC7B3BF1F3C87BFB1917.

[46] Samuel Buck et al. "A Review of Optical Parametric Amplification at the Vulcan Laser Facility". In: *Photonics* 11.6 (May 2024), p. 495. ISSN: 2304-6732. DOI: 10.3390/photonics11060495.

[47] Cristina Hernandez-Gomez. *Vulcan 20-20 Upgrade*. 2025. URL: https://www.clf.stfc.ac.uk/Pages/Vulcan-2020.aspx.

[48] Petr Navratil et al. "Characterization of Bivoj/DiPOLE 100: HiLASE 100-J/10-Hz diode pumped solid state laser". In: *Solid State Lasers XXVII: Technology and Devices*. Ed. by W. Andrew Clarkson and Ramesh K. Shori. SPIE, Feb. 2018, p. 33. ISBN: 9781510615076. DOI: 10.1117/12.2290290.

[49] Helen Towrie. *New Record for CLF's DiPOLE Technology*. Nov. 2023. URL: https://www.clf.stfc.ac.uk/Pages/New-Record-for-CLF%E2%80%99s-DiPOLE-Technology.aspx.

[50] Ryo YASUHARA et al. “1J x 100 Hz Cryogenic Yb:YAG Laser Development for Feasibility Demonstration of GENBU Main Laser”. In: *The Review of Laser Engineering* 36.APLS (2008), pp. 1092–1093. ISSN: 0387-0200. DOI: 10.2184/lsj.36.1092.

[51] STFC. *A strategic vision for the UK's large-scale light source user facilities*. Tech. rep. https://www.ukri.org/publications/stfc-light-sources-vison-report-2021-to-2022/. STFC, 2021.

[52] Paul Mason et al. “Development of a 100 J, 10 Hz laser for compression experiments at the High Energy Density instrument at the European XFEL”. In: *High Power Laser Science and Engineering* 6 (2018). ISSN: 20523289. DOI: 10.1017/hpl.2018.56.

DRAFT

10 Detectors

10.1 Summary

This chapter reviews the detector demands for continuous, high-throughput experiments at next-generation XFELs. The wide energy range of proposed FELs and varied experimental techniques require diverse, custom detector technologies. While many needs can be partially met with existing or developing solutions, integrating these into fast, continuous-operation detectors remains a challenge. Embedding data processing within detectors is key for rapid feedback and managing overwhelming data volumes. Development goals overlap with other XFELs and scientific facilities, presenting opportunities for collaboration and technology transfer. With targeted investment, these efforts will support the efficient, high-throughput discoveries enabled by future XFEL advancements.

10.2 Introduction

To achieve the scientific goals of a next-generation XFEL, it is essential to procure or develop and deliver detector technology capable of capturing and measuring photons and particles across the diverse range of planned experiments. Advancements in x-ray beam delivery require corresponding advancements in detector technology to manage the extreme brightness and high repetition rates of a next-generation XFEL.

The Detectors work package has collaborated closely with the End Stations work package to identify the experimental techniques and measurements that detectors must perform at a next-generation XFEL. A diverse array of complementary detector technologies will be essential to address the wide-ranging and demanding requirements for the suite of end stations, including:

- Covering a range of photon energies from 50eV to $>$ 40keV
- Measuring the energy and momentum of emitted electrons and ions
- Resolving emitted and transmitted photon energies at the 1eV resolution range
- Handle high fluxes of $\sim 10^4$ photons/pixel simultaneously as resolving single photons
- Operating at sustained frame rates of 100 kHz with burst mode operation at up to GHz rates

The scope of the CDOA is to evaluate and capture the detector needs; evaluate against the current state of the art and known development; identify where the next generation XFEL detectors are feasible and what developments would be required. This spans the different sensor materials required to operate over the energy ranges of the End Stations; readout ASICs with the necessary dynamic range, noise and frame rates; the bonding technology to assemble detectors with the necessary pixel size and with minimal dead space; and the different configuration of pixel detectors, strip detectors, energy resolving configurations and sensors, specialised high speed detectors and a variety of electron/ion energy and momentum measuring systems.

DRAFT

An unavoidable consequence of a next generation XFEL is the tremendous volumes of raw data that will be generated from the range of detectors across the many end stations. The Data work package will summarise strategies for handling, processing, evaluating, storing,archiving and accessing the experimental data. However, as will be discussed here, the data volumes of TB/Mpixel/s are unmanageable and data reduction, compression and vetoing schemes must become part of the detector system architecture.

10.3 Overview

A summary of the main detector requirements is provided in Table 10.1. This is not an exhaustive list of all possible experimental configurations and does not extend to the need for secondary detectors, such as intensity diodes, beam monitoring, or sample observations via microscopes or electron microscope (EM) columns, which scientists have requested.

The soft X-ray energy End Stations of FEL6 and 5, such as AMO, have multiple interaction points that require a suite of detectors around each location. In general, the primary measurements focus on the electrons and ions emitted from the sample. Whilst hemispherical detectors and magnetic bottles can measure the energy and electronic states of a sample via X-ray Photoelectron Spectroscopy (XPS), more advanced measurements, such as time-resolved ARPES (trARPES) or spin-sensitive detection, require advanced systems such as momentum or reaction microscopes [1].

The tender and hard X-ray End Stations primarily conduct X-ray diffraction and scattering measurements across various configurations and geometries. The underlying detector requirements generally remain consistent (apart from differences in energy range) and call for megapixel-scale detectors with a 50–100 µm pixel pitch, high dynamic range, and frame rates in the 10–100 kHz range. The MEC and VXHR End Stations, however, focus on imaging and diffraction at MHz or even $>$100 MHz rates in burst mode.

Many of the End Stations also require absorption or emission X-ray spectroscopy with energy resolutions at the eV or sub-eV level. Even though various geometries are used to spatially disperse the different X-ray energies, they all depend on fine pixel or strip detectors capable of high dynamic range measurements.

The various detector types are discussed in detail below, along with a comparison of their requirements to the current state of the art, and an analysis of the prospects and challenges associated with developing new detectors. The vast raw data rates present a challenge in terms of the practicality and sustainability of a next generation XFEL and methods to reduce the raw data in the detector system are explored. While the detector requirements of a next-generation XFEL surpass the current state of the art, advancements driven by 4th generation synchrotrons and the first high-rate continuous wave XFELs are paving the way for new detector technologies to meet these demands of a next generation facility.

10.4 Large Area X-ray Detectors

A large fraction of end stations require large-area pixelated detectors for diffraction and scattering measurements. From consultation with the science community and with reference to the Next

End Station	FEL	X-ray Energy [kev]	Rate [kHz]	Primary Detectors
AMO	6	0.05 - 1	100	Reaction Microscope Electron & Ion Spectrometers Absorption Spectrometer
SXR ARPES	6	0.05 - 1	100+	Momentum Microscope
Atto	5	0.25 - 3	10 - 100	Angular Streaking Camera Electron & Ion Spectrometers Absorption Spectrometer
hRIXs	5	0.25 - 3	10 - 100	Large area XRD Detector Absorption Spectrometer
tr SFX S	5	0.25 - 3	10 - 100	Large area XRD Detector Absorption Spectrometer
Spectroscopy	4	1 - 5	10 - 100	X-ray Emission Spectrometer Large area XRD Detector Absorption Spectrometer
Scattering & Spectroscopy	3	3 - 13	10 - 100	Large area XRD Detector Absorption Spectrometer
HX AR PES	3	3 - 13	10 - 100	Momentum Microscope Electron & Ion Spectrometers
tr SFX H	2	5 - 20	10 - 100	Large area XRD Detector Absorption Spectrometer
CDI	2	5 - 20	10 - 100	Large area XRD Detector Absorption Spectrometer
2 Colour	2 , 5	1-5 & 5-20	MHz Burst	Large area XRD Detector
MEC	1	5 - 40+	GHs burst	Large area XRD Detector GHz Imaging Detector AbsorptionSpectrometer
VHX trXRD/PDF	1	20 - 40	100+	Very large area XRD Detecot

Table 10.1: Summary of Primary Detector Requirements

Generation XFEL beam parameters and experimental techniques, the main requirements of the large-area detectors for diffraction and scattering measurements were:

- The detectors must have single photon sensitivity and simultaneously be able to measure 100-10,000 photons per XFEL pulse
- Pixel sizes of 50 – 100μm to match the diffraction spot sizes
- Have areas of Mpixel to 20Mpixel sizes
- Operate at 10-100kHz continuous with some beamlines requesting burst modes into MHz or GHz regimes
- Have a high efficiency at the energy range of interest

Figure 10.1 shows these values as a radar plot. The range of requirements for a next generation XFEL cover the blue shaded area with the solid blue and green lines indicating the limited. The red dashes line shows the current state-of-the-art and is an illustration that some minimum requirements can be met but significant developments needed to meet the full requirements. As discussed in detail below, the high and low energy ranges are a specific challenge as is operating at continuous 100 kHz frame rates.

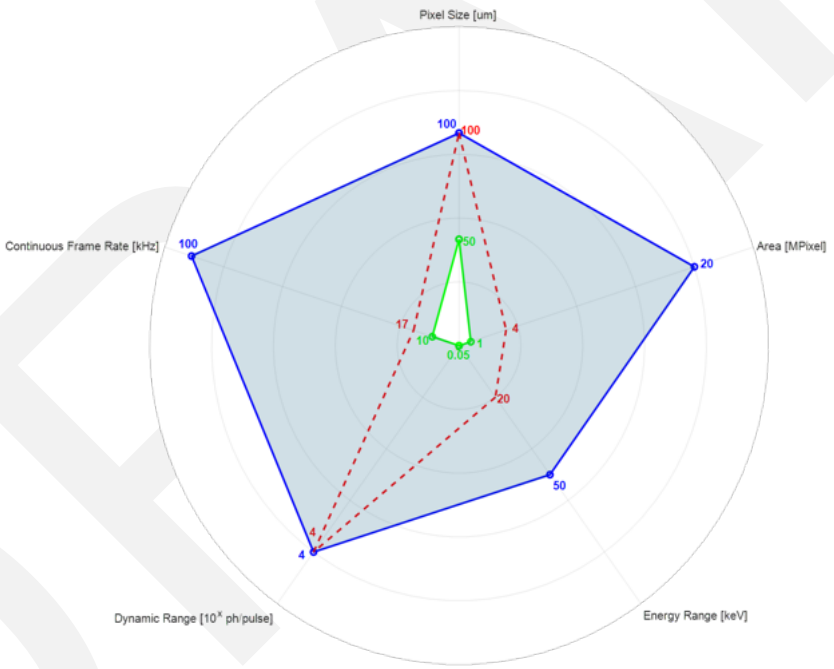

Figure 10.1: Summary of some detector key detector requirements for a next generation XFEL. Blue and green show the ranges for a next generation XFEL and the red dashed line is an indication of the current state of the art.

To address these demanding requirements, hybrid pixel detectors present the most viable solution due to their adaptable sensor material and the density of readout electronics that can be included to make measurements at high rates. Here, the sensor material can be selected to match the energy range of the end station and the charge carriers generated from the X-ray capture process are amplified, measured and digitised by a readout application specific integrated circuit (ASIC). Typically, the sensor material is bump bonded to the readout ASIC and many detector modules

(made from a sensor + ASIC hybrid) are tiled together, as shown in Figure 10.2, although some monolithic detectors would be viable for the soft X-ray regime. Each part of the large area detector system is discussed in turn.

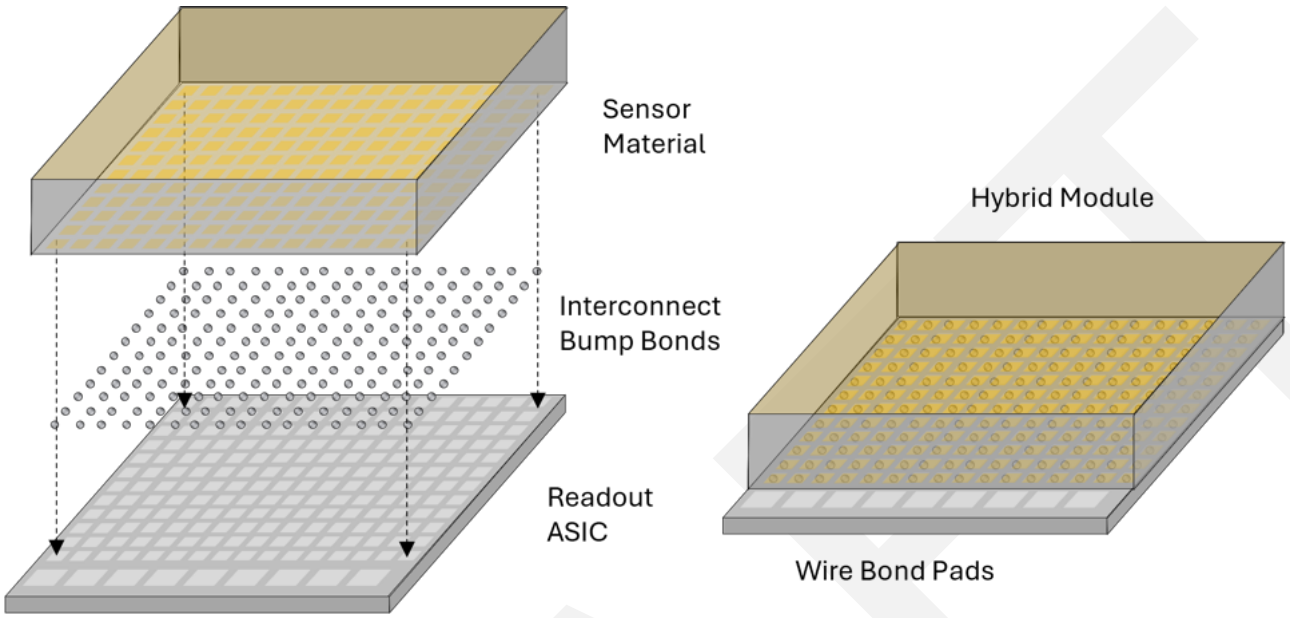

Figure 10.2: Illustration of a hybrid detector module.

10.4.1 Sensor Material

The need to operate across the soft, tender, and hard X-ray regimes necessitates the use of different sensor materials. In the soft X-ray regime, spanning 0.05 – 4 keV as provided in FELs 4–6, the primary technical challenge lies in capturing low-energy X-rays within the bulk of the detector material. This involves addressing issues such as penetration through metal contacts and low electric fields at the metal-semiconductor interface.

Conversely, at the higher end of the energy range, above 15 keV, as delivered by FEL1 and FEL2, silicon, the most commonly used sensor material for light sources becomes transparent at the detector thicknesses available. To address this limitation, ”high-Z” semiconductors, such as CdZnTe, CdTe, and GaAs, are required for efficient detection.

In the intermediate X-ray range of 4–15 keV, as in FEL3, silicon detectors are well-suited to the energy requirements. However, the high radiation doses received at a 100 kHz repetition rate XFEL may result in radiation damage to the material, posing additional challenges.

Figure 10.3 illustrates the X-ray absorption properties of various detector materials matched to the operational ranges of the Next Generation XFEL's End Stations.

10.4.2 Low Energy X-ray Sensor Materials (0.05 to 4 keV)

Low-energy X-ray sensor materials pose a significant technical challenge. The sensor entrance window must be thin and transparent to X-ray photons, while also maintaining a defect-free and conductive surface that prevents surface leakage currents entering the detector bulk. This ensures the generation of an electric field at the interface and into the bulk of the sensor material, enabling charge carriers from shallow interaction depths to drift efficiently toward the collecting pixels.

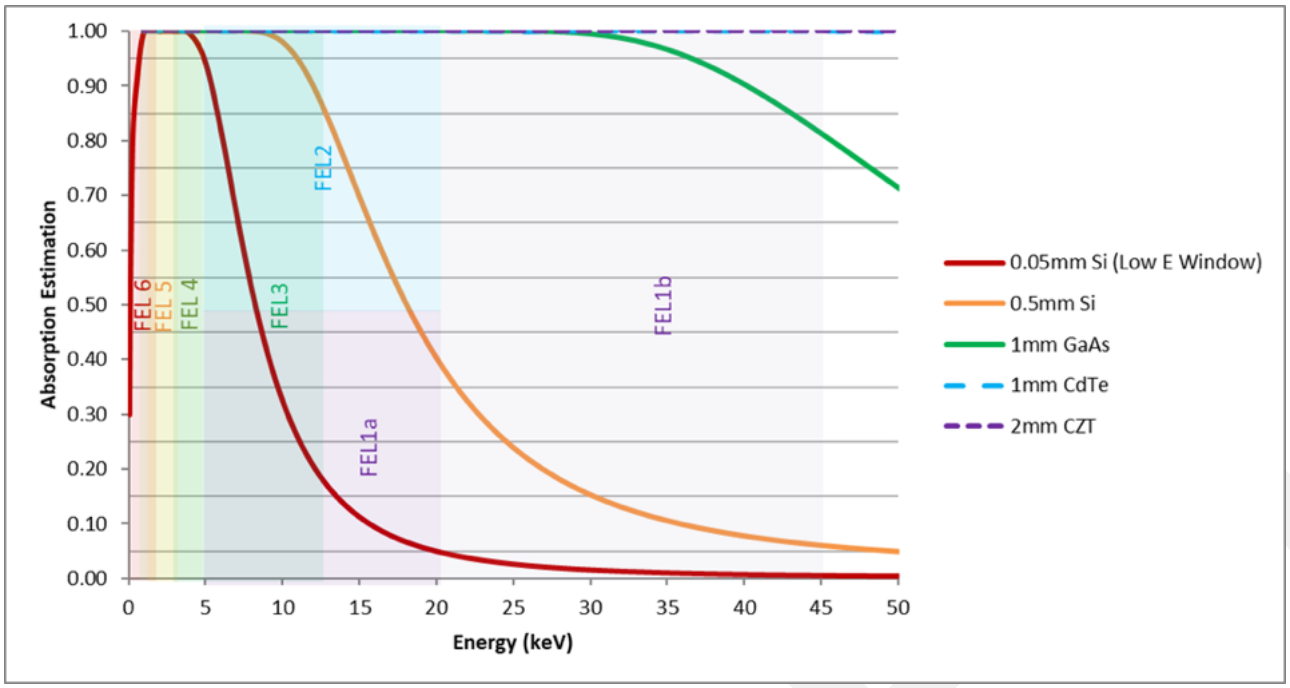

Figure 10.3: Sensor material X-ray stopping power with energy relating to the FEL energies.

Monolithic Active Pixel Sensors (MAPS) and similar devices fabricated directly in a silicon CMOS process can achieve the required active layer thickness for the 0.05–4 keV energy range. These sensors typically operate in a backside illumination geometry and require back-thinning with surface processing to effectively detect the lowest energy X-rays.

CCD technology, originally developed for low-energy X-ray applications such as astronomy, has been successfully adapted for use in XFELs [2]. These detectors offer the necessary efficiency and pixel size and are widely available from stable suppliers with broad customer bases, although they are limited in frame rates compared to the needs of a Next Generation XFEL. Specialised technologies, such as pnCCDs, can provide lower noise performance and frame rates up 1-10 kHz depending on the array size and pixel binning [3].

MAPS created using conventional CMOS image sensor foundry processes can feature active epitaxial layers with thicknesses ranging from 10–50μm. Alternatively, they can be fabricated on high-resistivity substrates that can be depleted to achieve thicknesses of 50–300μm [4]. For low energy X-ray and XUV detection, these sensors are typically back-illuminated to ensure a uniform and low-absorption entrance window. However, traditional back side illumination (BSI) treatments provided by CMOS foundries are optimised for optical light capture rather than low-energy X-ray absorption, necessitating separate post-processing to thin, dope, and protect the backside of the CMOS wafer.

Amptek's patented "C2" entrance window, based on a Si_3N_4 coating for silicon drift detectors, achieves 29% efficiency at the Li K line energy of 54.3 eV [5]. Delta doping, developed by NASA's Jet Propulsion Laboratory for the Hubble Space Telescope UV imagers, employs a single atomic layer of boron deposited via molecular beam epitaxy (MBE), with a native oxide layer only a few nanometers thick added to the backside of the sensor. Originally applied to CCDs, this technique can also be extended to MAPS, achieving close to 100% quantum efficiency [6]. LBNL have optimised their fast CCD with 10nm deep doping and 0.55nm of Al contact on the back surface to achieve 75% QE at 200 eV [7]. SLAC employ a low energy implant and microwave annealing to provide a very shallow implant of dopants at the surface and is a relatively low cost technique [8]. The Soleil synchrotron have worked with the sCMOS company, GPixel, to develop a BSI

process that demonstrated measurements down to 100 eV [9]. While these additional processes allow detection at lower X-ray energies, they are reliant on specialist providers and are not widely accessible.

The PERCIVAL MAPS sensor utilizes CMOS stitching technology, enabling the creation of large-area detectors in single tiles at 120 Hz frame rate [10]. However, this approach involves trade-offs: reading out pixel data, transferring electrical signals across large areas, and digitizing these signals, particularly when digitisation is performed at the periphery, limits the achievable frame rates to $\leq$ 10kHz. PERCIVAL achieves high dynamic range in the pixel by adding lateral overflow capacitors to a traditional 3T pixel that can store the charge when the photodiode becomes saturated, and such a design could be used to provide the necessary dynamic range of a next generation XFEL.

Many research groups are leveraging the advantages of thin CMOS Monolithic Active Pixel Sensors (MAPS), integrating them with readout ASICs to enhance performance. At SLAC, back-illuminated CMOS sensors are bump-bonded to the ePix ASIC (ePix-M), enabling their use as low-energy X-ray detectors at LCLS-II [11]. This approach offers the benefit of being able to include active circuitry in the MAPS sensing layer and using the ASIC layer for additional processing. A cross section image of the sensor is shown in Figure 10.4. At RIKEN, the CITIUS detector was developed in partnership with Sony, utilising a stitched version of a back illuminated Sony MAPS sensor optimised for X-rays and utilising “Zibond”, a proprietary oxide-oxide bonding process, to connect to the readout ASIC [12]. The MAPS sensor layer uses a 3T pixel with lateral overflow to provide high dynamic range and gain in the sensor material and, as discussed in the ASIC section below, the ASIC provides digitisation and fast readout to achieve higher frame rates than an individual MAPS sensor.

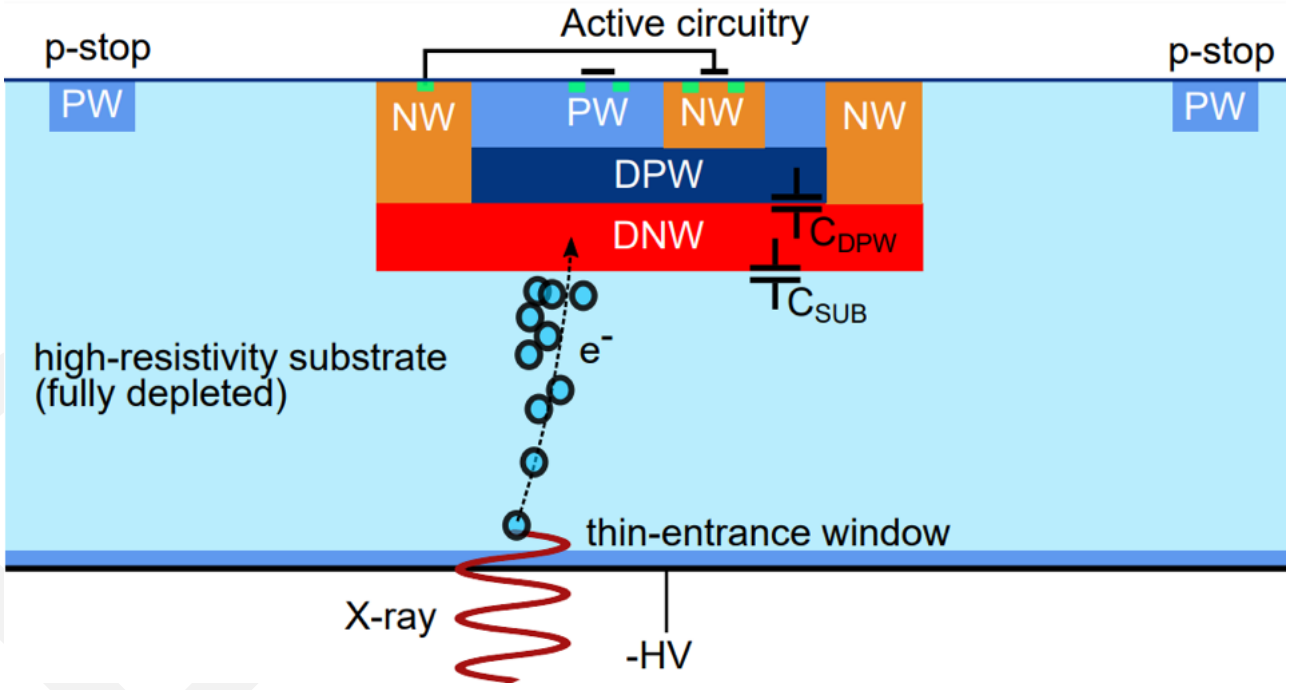

Figure 10.4: Cross section of ePix-M. Credit: L. Rota

Measuring single photons from low-energy X-ray sources presents a challenge due to the relatively small number of charge carriers generated. The first version of the DSSC detector at EuXFEL [13] tackled this issue by employing silicon drift detectors, which feature small pixel collection contacts with low capacitance. This design reduces readout noise in the ASIC, enabling single-photon resolution measurements. A further enhancement came with the deployment of DSSC detectors

incorporating DEPFET sensors [14]. These sensors integrate an in-built pFET within each pixel, offering low capacitance and minimized noise. Additionally, they provide internal and non-linear gain that can be tuned to accommodate large signal levels from XFEL sources [15].

The concept of internal gain within detector materials is a growing field in low-energy X-ray detection. Various low-gain avalanche detector (LGAD) designs have been explored, initially targeting fast timing measurements in particle physics experiments. LGADs are silicon-based detectors with highly doped regions that enhance local electric fields, allowing charge carriers to achieve sufficient velocity for impact ionization and the generation of additional charge carriers. By tuning the doping, researchers have achieved cascade effects with gains of 5 to 40 times, avoiding the full avalanche regimes seen in highly doped and high-field devices such as SiPMs and SPADs. Conventional LGADs rely on high-gain structures near the charge-collecting pixels but require inter-pixel isolation via p-stop doping, which creates regions devoid of gain between pixels. The inverted LGAD (iLGAD) design addresses this limitation by placing the gain region beneath the planar contact at the sensor entrance window. PSI and FBK have successfully demonstrated iLGAD devices operating down to 250 eV [16] with studies into different implantations to optimsed the low energy entrance window [17]. This is an active field with LGAD devices made by commercial suppliers such as Hamamatsu and Sintef as well as large research institutions like Brookhaven National Laboratory for light source applications [18], [19].

Similar gain-enhancing technologies could be developed using higher-Z materials. Notably, an Italian collaboration has demonstrated staircase avalanche gain sensors, utilizing epitaxially grown GaAs and InGaAs layers atop thicker GaAs wafers that serve as sensing layers [20]. Although not initially optimised for low-energy applications, these designs may hold future promise for thinner sensors, where shorter drift lengths and high electric fields facilitate faster operation.

The essential material requirements for soft X-ray sensors in a Next Generation XFEL have been individually demonstrated across various detectors. Capabilities such as fluxes of 10,000 photons per frame, frame rates exceeding the MHz range, and pixel sizes as small as tens of microns have been successfully validated. The challenge lies in integrating all of these individual features into a unified detector system.

Achieving the necessary signal-to-noise ratio for single-photon detection requires strategies such as small, low-capacitance collection nodes with minimal noise or sensor materials incorporating internal gain. Specialized technologies like iLGADs and DEPFETs, available through lower-volume specialist foundries, offer optimisation potential but currently come at high costs or lower yields.

For more commercially scalable solutions, CMOS MAPS present an attractive option due to their lower cost and higher production volumes, particularly relevant if radiation hardness limits detector lifespan. While intrinsically radiation-hard materials offer promising alternatives, they are not yet widely available or fully validated for low-energy applications.

A significant challenge remains in optimising entrance windows for the lowest energy ranges, as commercial foundries do not typically offer end-of-line processing for such enhancements. However, a specialized market continues to support these needs, driven by EUV and low-energy X-ray instrumentation.

Overall, the soft X-ray sensor material requirements for a Next Generation XFEL could be met with existing technologies, and specific detector systems could be developed today. Future advancements would be utilised by improving radiation hardness and finding cost-effective ways to enhance sensitivity to low-energy X-rays.

Figure 10.5: Summary of the status of the soft X-ray sensor material requirements.

10.4.3 Tender X-ray Sensors Materials (4 to 15keV)

The tender X-ray energy range of 4–15 keV is the primary operating range for current large XFEL and synchrotron facilities. Silicon hybrid detectors are widely used, and various integrating detectors (see Section 10.4.5) have demonstrated the necessary pixel sizes (50–100 µm), frame rates (10–100 kHz), and dynamic ranges (1–10,000 photons) required for a Next Generation XFEL, although never all combined in one detector. Silicon sensors are readily available from commercial suppliers like Hamamatsu and Micron Semiconductors, typically produced on 6-inch wafers. These sensors offer advantages such as large-area monolithic detector modules, which can be assembled into megapixel-scale arrays (see Section 10.4.6).

A Next Generation XFEL will push the limits of silicon detectors, particularly in managing the total ionising dose resulting from high continuous frame rates and extensive operational time at the End Stations. Silicon detectors experience surface radiation damage due to X-ray exposure, where charge carriers become trapped at Si-SiO_2 interfaces. This degrades internal electric fields, leading to increased dark currents and reduced charge collection efficiency.

Figure 10.6 shows an example from colleagues at LCLS II where an array of ePix detectors are used to measure diffraction patterns. The bad pixel map on the right shows that radiation damaged pixels lin up with the repeated high-flux exposure from water diffraction rings. This degradation occurs independently of direct beam exposure or ice crystal diffraction peaks, which pose risks for all detectors. Whilst it is possible to attempt to design some additional radiation tolerance into the design of the sensor doping, particularly in the case of MAPS devices, there is an inherent radiation damage limitation of such silicon detectors.

While higher-Z semiconductor materials have numerous disadvantages compared to silicon detectors, they offer one significant advantage: they do not suffer radiation damage from X-rays. This characteristic may make them a viable alternative for handling the high total ionisation dose in Next Generation XFELs, even within the tender X-ray energy range

10.4.4 Hard X-ray Sensors Materials (15 to 40keV)

Hard X-ray sensor materials are widely utilized in fields such as medical imaging, security screening, and non-destructive testing. These areas have traditionally relied on scintillator-based detectors, which typically lack the single-photon sensitivity and speed required for advanced applications like Next Generation XFELs. However, the development of photon-counting CT (PCCT) in the medical industry has driven significant advancements in CdTe and CdZnTe detector

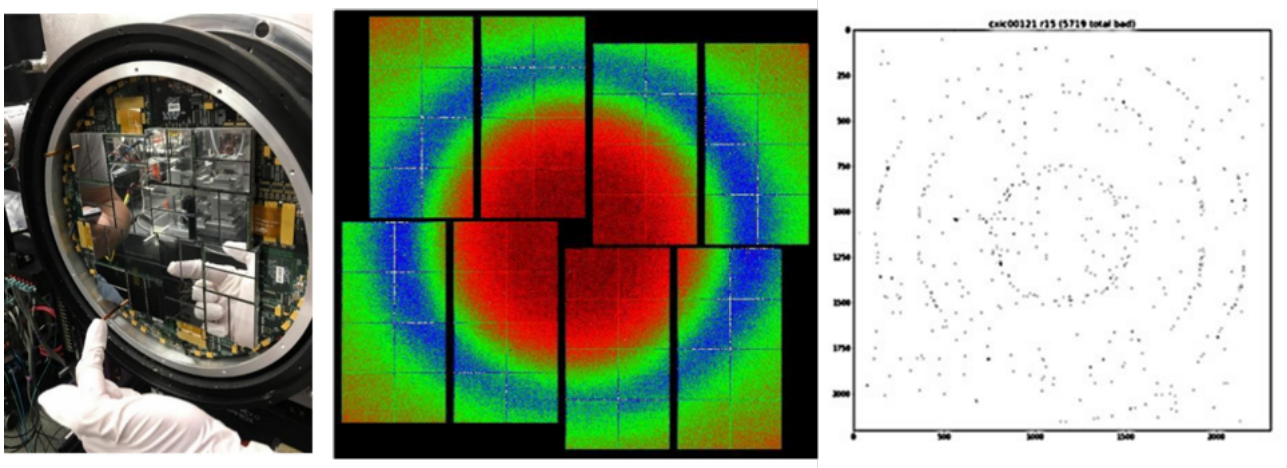

Figure 10.6: An ePix10k2M detector array (left), a typical diffraction pattern with water ring features (middle), and a map of bad pixels on a Jungfrau 4M detector due to radiation damage with the pattern corresponding to the water ring pattern. Credit: Conny Hansson

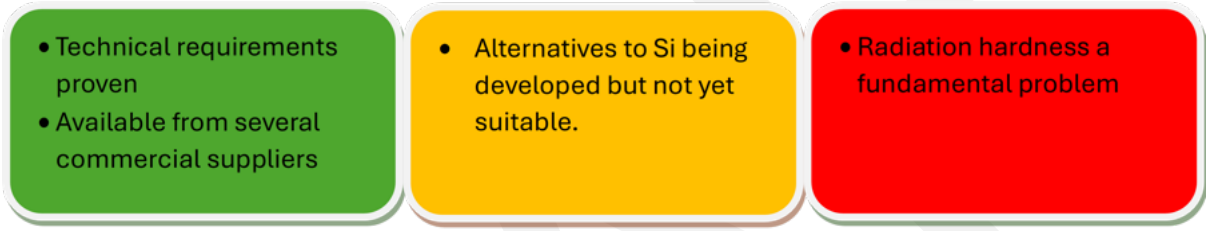

Figure 10.7: Summary of the status of the tender X-ray energy sensor material requirements.

technologies. These materials enable continuous high flux, single photon measurements at hard X-ray energies.

CdTe and CdZnTe are grown from the melt in Bridgman or Travelling Heater Methods, which limits the size of wafers to 3 inch diameter, with single detectors sizes limited to 45 x 45 mm and with better yields and lower costs if made in smaller 20x20mm size sensor die. CdTe is available from Acrorad (Japan), who are 50% owned by Siemens, and Siemens are using the material for their first to market, Naeotom PCCT scanner. CdZnTe is available from Redlen Technologies Inc (Canada) who are wholly owned by Canon Medical. Both companies are currently supplying sensors to the scientific community but there is a risk in the supply of these materials as they will prioritize supply for their own medical scanner products.

CdTe is already widely used in synchrotron instruments [21] that use photon counting readout ASICs with 75μm pixels and operate at $> 10^8$ph/s/mm^2 in the 8 - 100 keV range. CdTe and CdZnTe have poor hole transport properties that have historically limited the flux at which they can operate. At high flux, the trapped holes would build up in the detector and cause the electric field strength to reduce, resulting in a runaway process of slower transport and more trapping, eventually resulting in the electric field collapsing and the detector becoming polarised [22]. In the case of CdZnTe, Redlen developed a high-flux version with improved hole lifetimes so that they can escape the bulk [23]. The high flux CdZnTe material is being investigated for use at synchrotrons and XFELs [24], [25], [26] and have demonstrated high flux operation to 10^{12}ph/s/mm^2 and MHz rate performance in small prototype devices. The integrating readout ASICs needed at a pulse source like a Next Generation FEL and 4th generation synchrotrons would be exposed to large or unstable leakage currents and are currently subject to investigation [27], [28] with different metal contacts being tested. The leakage currents are linked to the surface preparation and metal contacts used. Whilst the metallisation is not as mature as CMOS or Si detector foundry,

50 – 100μm pitch pixels can be readily achieved and meet the needs of a Next Generation XFEL. The charge cloud size, and therefore the point-spread function (PSF) of CdZnTe is in the region of 50 – 100μm, depending on the energy and the drift length of the charge carriers [29]. As CdZnTe is currently only supplied in thicknesses as low as 1.5 mm (due to the brittleness of the material) there is significant charge sharing in small pixel detectors, which means the readout electronics must be sufficiently low noise to measure a resolve a fraction of a photon energy or lower. It is also worth noting that at energies above the k-edge of Cd (26.7 keV) there is a large detector self-fluorescence yield, and a mean free path of the Cd k_α at 23 keV fluorescence photon is $>$ 100μm, further complicating the charge sharing. In comparison, the Si fluorescence energy is 1.7keV and has a mean free path of 0.3μm. As such, alternative high-Z detector materials may be beneficial for some specific energy ranges.

GaAs has been a longstanding candidate semiconductor X-ray sensor material [30] but suffered from defects in thicker devices that limited the charge transport. Doping wafers with Cr to compensate the traps has been developed as way to produce detectors in the range of 0.5 to 1mm in thickness that would be suitable for the energy range of a Next Generation XFEL. High flux performance has been demonstrated [31], [32] but the supply of detectors is not yet fully commercialised, although vendors in the EU are beginning to supply sensor material.

An area of rapid X-ray sensor material development is in the area of Perovskite detectors. Perovskite materials such as $CsPbBr_3$ have been developed initially as photovoltaic devices but have rapidly expanded into other areas such as LEDs and, because of their high-Z, X-ray detectors. There is a rapidly increasing variety of Perovskite or Perovskite-inspired materials being developed and tested. The Perovskite semiconductors are typically grown from solution, with cm^3 scale single crystals grown from solution on timescales of hours and days. There is the potential to grow such materials directly onto CMOS as it is a low temperature process but there are additional challenges in metallisation compatibility, process control and achieving large area single crystals with the desired charge transport properties to get single photon resolution and to operate at high frame rates. Northwestern University have demonstrated both solution based growth and melt based growth of $CsPbBr_3$ with the X-ray operation of pad detectors grown by both methods demonstrating the high fluxes suitable for a next generation XFEL [33], [34]. Perovskites have been reported to have lower charge carrier mobility than Si and CdZnTe based detectors that may limit high speed performance but they do have long lifetimes so the charge trapping that causes polarisation in CdZnTe should be avoided. $FAPbBr_3$from Cambridge has shown signal rise times of $<$ 1μs and single photon resolution [35]. This is a rapidly growing research community where the fast turnaround in growth (solution based in hours to days vs melt grown over several days to weeks) is facilitating a route to market, although technical challenges in volume production and lifetime operation are still to be overcome. Actina Ltd have started to commercialise the Northwestern University $CsPbBr_3$ melt grown crystals and Clarity Sensor Ltd has formed from the $FAPbBr_3$ from Cambridge. As with the CdTe and CdZnTe detectors, the market forces driving this innovation and investment are in areas such as medical imaging and nuclear security. However, the needs of a future light sources are closely matched to those in the most advance medical scanners and the technology could reach the needs of a Next Generation XFEL.

There is an ongoing effort explore high-Z materials and others for 4th generation synchrotron and existing XFELs as they have similar requirements to a Next Generation XFEL. Whilst results are promising and prototypes are being made, CdTe and CdZnTe are not yet a fully proven technology for a Next Generation XFEL. Alternative detector materials are at a lower TRL but are developing quickly and could become an option for hard X-ray detection.

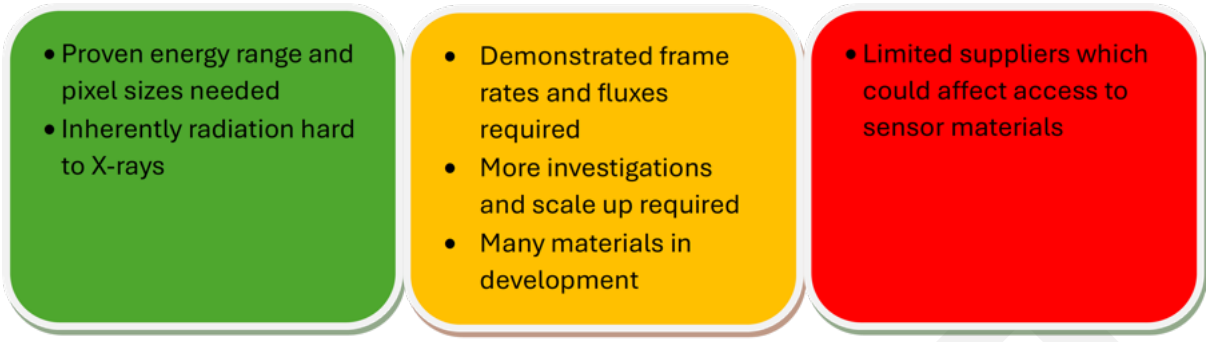

Figure 10.8: Summary of the status of the hard X-ray energy sensor material requirements.

10.4.5 Readout ASICs

The introduction of the first-generation XFEL facilities created a demand for novel integrating readout ASICs capable of handling high dynamic ranges of instantaneous flux, spanning from 1 to 10,000 photons per pixel. Achieving this dynamic range with a single gain stage proved challenging due to limitations in operating voltage and electronic noise, prompting the development of selective, adaptive and parallel gain systems. At LCLS, this led to the development of the CSPad [36] and the ePix ASIC family [37], while EuXFEL supported the creation of the AGIPD [38], [39], DSSC [13], [14], and LPD ASICs [40]. Each detector employed distinct designs to address the dynamic range challenge: CSPad and ePix utilized two-stage adaptive gain architectures, AGIPD implemented a three-stage adaptive gain system, LPD adopted parallel gain stages, and DSSC combined the aforementioned DEPFET sensor gain with selectable ASIC gain. More recently, the CITIUS detector [12] developed by RIKEN for Spring8 and SACLA, in partnership with Sony, utilises MAPS sensors with lateral overflow integration capacitors in the sensor pixels to achieve the high dynamic range measurements. These innovations have demonstrated the feasibility of capturing the dynamic range required for Next Generation XFELs. Among these designs, LPD's fixed and parallel gain stages offer a straightforward approach but occupy considerable pixel space, making it unsuitable for the required pixel pitches of 50–100μm in Next Generation XFELs. In contrast, adaptive gain architectures such as ePix, with pixel pitches of 50 µm and 100 µm and Jungfrau, a 75 µm pixel pitch detector developed by PSI built upon the AGIPD front-end concepts [41], have proven capable of meeting dynamic range requirements while maintaining compact pixel sizes suitable for applications at XFEL End Stations.

The development of XFEL detectors has predominantly been tailored to meet the specific requirements of individual facilities. For instance, the CSPad detector was designed to operate at the 120 Hz repetition rate characteristic of the Linac Coherent Light Source (LCLS), utilizing continuous digitization and constant readout of all pixel data. In contrast, the European XFEL (EuXFEL) posed a significantly greater challenge due to its bunch structure, which consists of trains of up to 2700 pulses per train at a repetition rate of 4.5 MHz, albeit with an overall train rate of 10 Hz. Digitising and reading out data at 4.5 MHz was unfeasible; consequently, the ASICs were developed to implement in-pixel analogue storage, with the number of storage cells based on pixel size constraints. The digitisation and readout was implemented in the more relaxed time interval between pulse trains. The "ePixUHR" family of detectors at LCLS has iteratively developed ever higher performing versions of their detectors, achieving a frame rate of 35 kHz [42], which demonstrates the baseline capability required for Next Generation XFELs. Future designs targeting rates of up to 100 kHz [43] are anticipated to align with the operational demands of most Next Generation XFEL end stations. The SparkPix varients build upon the ePix architecture with SparkPixS using sparse readout to achieve up to 1 MHz frames rates [43]. The widely adopted Jungfrau detector initially supported a continuous frame rate of 1 kHz, with burst capability up

to 2.2 kHz. Its successor, the planned Jungfrau II, aims to achieve frame rates as high as 10 kHz. The CITIUS detector employs one Analog-to-Digital Converter (ADC) for every eight pixels to increase data throughput and achieved a continuous frame rate of 17.4 kHz, meeting some of the minimum requirements of a Next Generation XFEL.

Fourth-generation synchrotron facilities are capable of producing photon fluxes up to 100 times higher than those of current third-generation facilities [44]. Consequently, traditional photon-counting detectors are insufficient for the highest dynamic range measurements, necessitating the development of a new generation of integrating detectors with performance specifications akin to those required for Next Generation XFELs. While the first XFELs had highly specific requirements that necessitated facility-sponsored detector development, there is now greater potential for collaboration in new detector developments or adaptation and customisation based on existing designs. Such collaborative efforts can accelerate development timelines, especially when compared to the first XFEL specific detectors discussed above, that took over a decade to go from concept to delivering science. Even where there are no ASICs to meet all of the requirements of a Next Generation XFEL there is the potential to mitigate risk and reduce development time by reusing proven design blocks from other ASICs. The need to collaborate is even greater for any new development needed for a Next Generation XFEL as the performance requirements, particularly speed of operation, mean that the ASICs will need to be on more advance CMOS nodes (65nm or even 28nm) which come with factors of 5-10 increase in mask costs compared to the designs conducted to date on 110nm and 180nm processes.

One notable new project is the CORDIA detector, currently under initial developments at DESY [45], intended for the PETRA IV synchrotron upgrade. The CORDIA detector incorporates adaptive gain pixels capable of measuring up to 1000 photons per integration, in-pixel ADCs, and 10 Gbps data serializers to achieve a sustained readout rate of 130 kHz. It is designed in 65 nm CMOS technology to facilitate compact circuitry within a 100 µm pixel while supporting high-speed clocking necessary for high bandwidth data outputs. The HYLITE range of ASICs are in development at SHINE for the STARLIGHT detector systems and employ a similar adaptive gain pixel in a 130nm process [46]. A continuous frame rate of 1 kHz with 200μm pixels has been demonstrated and a development path to 10 kHz continuous operation and 100μm pixels is planned [47]. The MMPad detectors developed at Cornell [48] for the CHESS synchrotron utilize an alternative method to reach high dynamic range imaging by use of charge-cancellation circuitry to iteratively capture and remove predefined charge packets, thereby enhancing dynamic range. The latest iteration, MMPad2.1 [49], [50], when operated at a reduced spatial resolution, with frame rates up to 9 kHz. Whilst this frame rate falls short of Next Generation XFEL requirements, its adaptive gain pre-amplifier is an example of how charge-cancellation techniques could be adapted for high instantaneous flux at pulsed radiation sources. Following the charge cancellation design is XIDyn, a fourth-generation synchrotron detector being jointly developed by STFC, the University of Heidelberg, ESRF, EuXFEL and Diamond. XIDyn employs a two-stage charge-cancellation mechanism within 110 µm pitch pixels, enabling measurements of hundreds of photons at 5.7 MHz integration rates or thousands of photons at 100 kHz integration rates. Its directly digitises with single-photon resolution and in-pixel RAM allows the storage of up to 256 integrations. Six 14.1 Gbps serializers constrain its sustained frame rate to 178 kHz, while the RAM facilitates faster burst captures with a subsequent readout that has a short deadtime. This architecture aligns with FEL1 End Station requirements, where bursts of MHz-rate pulses are requested. LCLS are developing a continuous MHz rate detector in SparkPixS [43] optimised for XPCS type measurements. The relatively low counts and occupancy of the technique are an advantage in utilising a sparse readout on the ASIC. Continuous MHz full frame rate X-ray detectors have been demonstrated with the HEXITEC-MHz detector [28] but with a relatively low dynamic range of 300keV per pixel.

Figure 10.9 highlights the performance of two of the most challenging parameters for a next generation XFEL detector, with the requirements highlighed in purple. It is notable that the X-ray flux (in numbers of 12 keV photons per XFEL pulse) is achievable and that developments are pushing to increase the sustained frame rates. whilst this parameter is of importance for a next generation CW facility the burst mode MHz operation ASIC such as LPD, AGIPD and DSSC could still have a major role to play in many techniques. As demonstrated by the SparkPix ASICs, the use on chip memory for burst capture and selective readout is a data efficient approach for some instruments. Other critical parameters, such as pixel size, energy range, and noise floor, are equally important but not detailed here but have also been shown to be possible across this sample of ASICs. This highlights that, on the timescales of a Next Generation XFEL, that there will be, or at least an advanced starting point to develop, an ASIC to meet the scientific needs of a future facility.

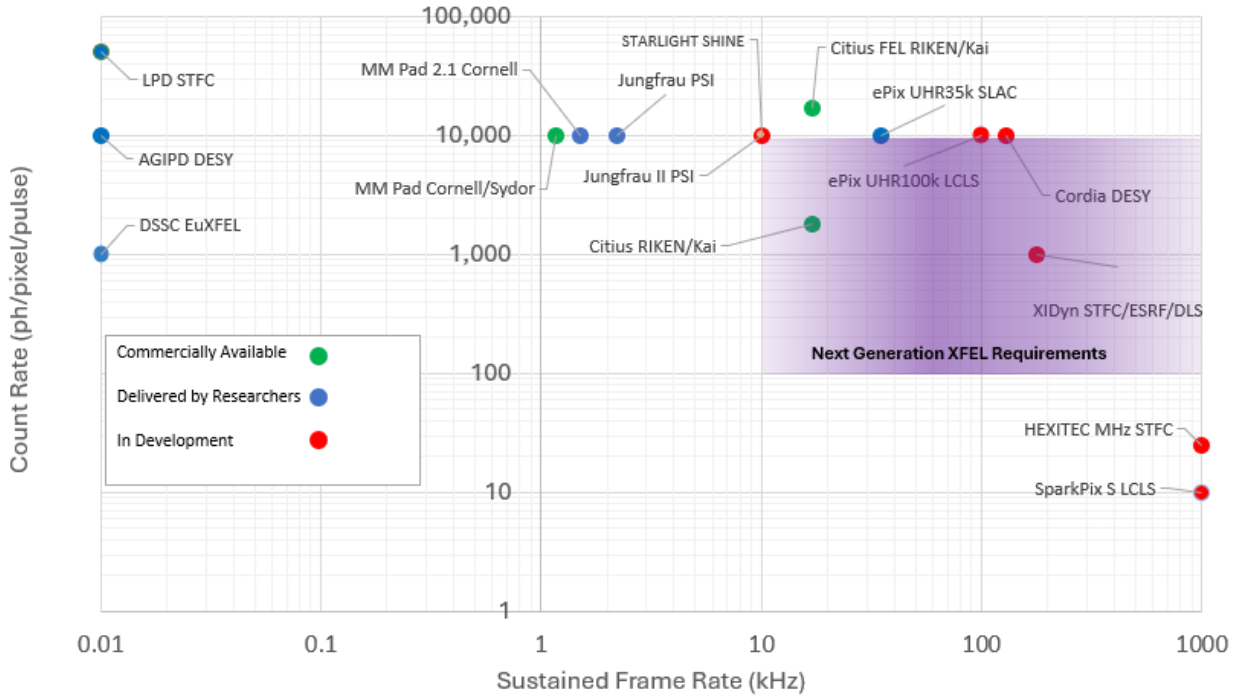

Figure 10.9: Summary of the integrating X-ray detector readout ASICs with commercially available (green), fully developed detector systems (blue) and new ASIC in development (red). **Any ASIC developments not included here is not an indication of their merit or importance, but this variety was most easily accessible to the authors.*

In summary, numerous existing readout ASICs have proven their suitability for large-area detectors at Next Generation XFELs. Ongoing developments on advanced CMOS processes are enhancing frame rates to 100 kHz and beyond. However, few integrating detectors are commercially available as off-the-shelf products. As the requirements of diffraction-limited synchrotrons converge with those of XFELs, opportunities for collaboration and combining efforts to create a larger markets for commercial suppliers are emerging. From an operational perspective, integrating and supporting fewer detector types offers significant benefits, with the ePix model of common interfaces exemplifying a pathway for optimising specific detector designs for specific End Stations without necessitating complete ASIC and DAQ redevelopment. It is also important to acknowledge that most ASIC developments take a decade or more to transition from conceptual design to operational End Station instrumentation, underscoring the need for significant time and investment in ASIC and detector system in any development phases of a Next Generation XFEL facilities.

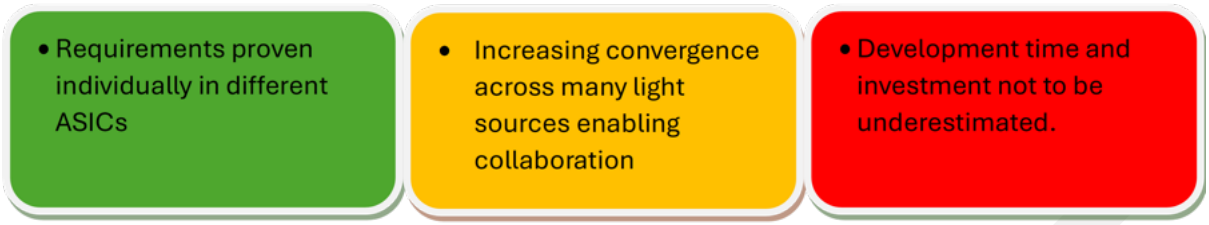

Figure 10.10: Summary of readout ASIC technology compared to the Next Generation XFEL requirements.

10.4.6 Interconnect and Arrays

As discussed above, the Mpixel scale detectors required at a Next Generation XFEL will be assembled from tiles of sensor material hybridised to readout ASICs in one form or another. The hybrid modules can be made with single or multiple ASICs per sensor, depending on the sizes available. At least one edge would have wire bonds to get the signals in and data out of the readout ASIC which results in a dead space around the edge of a hybrid tile. The hybrid module mechanics has to include mounting and handling points, route electrical signals in and out and help to manage the thermal. Figure 10.11 shows the example of the AGIPD detector developed by DESY. A detector module has 16 ASICs per Si sensor which are tiled, in this case, into a 1 M pixel array.

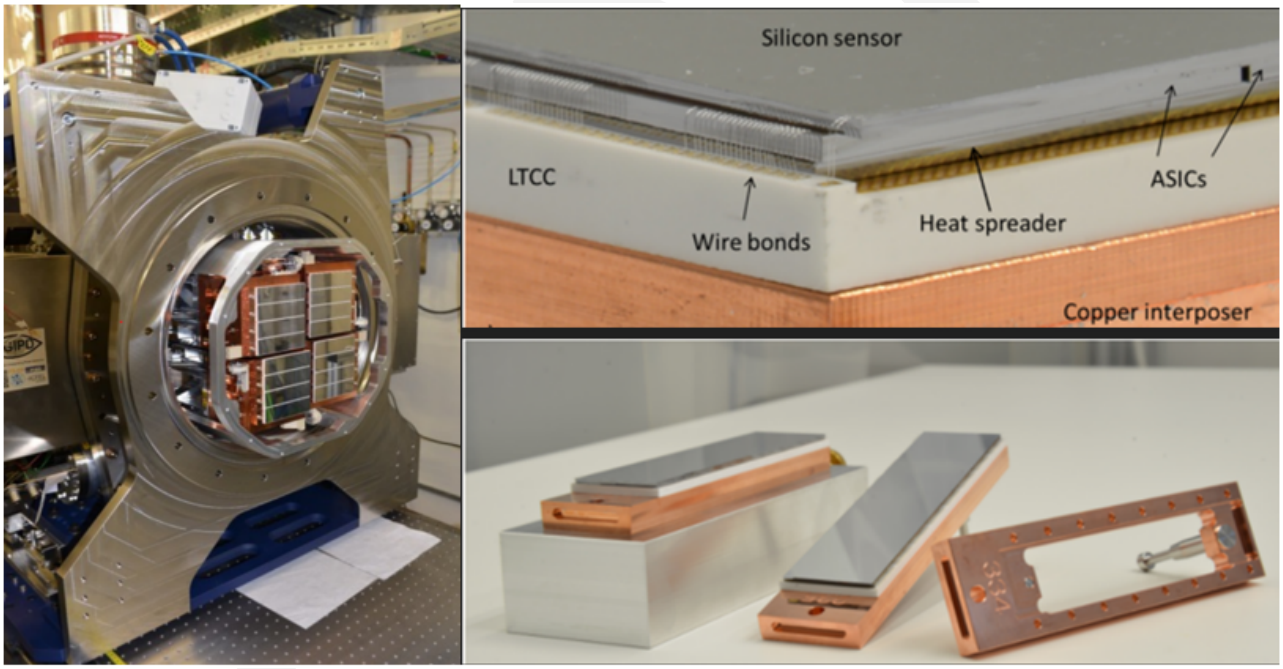

Figure 10.11: Example of the AGIPD detector module and array at the European XFEL. Credit: Heinz Graasfma

Typical readout ASIC reticle sizes are up to 25 x 25 mm^2, so that an ASIC might be 256 x 256 pixels at 100μm pitch or 512 x 512 at 50μm pitch. Silicon or MAPS sensor material could be bonded directly to multiple ASIC. A typical array would be 2x3 ASICs of such reticle sized dimensions to form a single detector tiles of 400 k pixels at 100μm pitch or 1.6 M pixels at 50μm pitch. Where CITIUS has wafer to wafer assemblies provided directly to the foundry, most other detector systems would require die to wafer or die to die assembly outside of the CMOS foundry. The assembly processes for the pitches needed for a Next Generation XFEL are widely available from industry and at research institutes via solder or indium bump bonding processes. The industry standard C4 solder bump process requires heating above 200^{0}C to reflow the bumps whilst indium can be bonded at room temperature but with a higher force applied. High-Z materials,

as required for the FEL1 and FEL2 End Stations, are reported to be sensitive to temperatures above 120^0C and can be brittle. A low temperature and low force option is silver epoxy that is screen printed onto the sensor material and has been demonstrated at 100μm pitch level [REF]. Investigations into solder alloy and pure indium bonding at lower temperature and force are being explored for alternative processes to reach the finer pitches. A complication for CdTe and CdZnTe is that they are only supplied as single die up to 45 x 45 mm, but at present it is more economical and with higher yields to work with 25 x 25mm single die. This makes spin coating resist materials and lithographical process more demanding and limits the number of pixels per single hybrid tile to 65 k pixels at 100μm or 262 k pixels at 50μm for a 25.6 x 25.6 mm^2 CdZnTe sensor.

The XFEL detectors are typicall 1-20M pixels and are made up of many detector modules with an inactive dead-space of a several pixels between modules. Feedback from the scientific user community has been that gaps between tiled modules can be problematic and, whilst currently tolerated, it would be an area for improvement for a Next Generation XFEL. The dead area around a detector module consists of the sensor material guard ring on all 4 sides and is typically of the order of 100 – 200μm depending on the sensor material. In high-Z detector materials it is possible, although not common, to conduct edge wall treatments to reduce leakage currents and the need for guard rings. The mechanical tolerance of the hybrid assembly can typically be made at 10 – 20μm, but the space required for access and insertion is then typically of the order of 100μm or more. The dominant dead space factor is from the periphery of the ASIC that would have some circuitry that does not fit in the pixels (control logic, power and clock generation, serialisers for data output) and in most cases, pads for the wire bonds. Additionally, the wire bonds are out onto a PCB where signals most be routed and minimum size vias cause additional dead space. In total, this dead space on one edge can be on the mm scale.

A “roof tile” or “stepped” tiling geometry of neighboring sensors is placed over the inactive readout edges of the ASIC as demonstrated with CdTe [51] and with the CITIUS 20M detector [12]. The downside of the stepped geometry is that there is no longer a flat imaging plane, but this can be mathematically corrected. An alternative is to use an interposer and pitch adapter as was applied in the LPD detector developed at STFC. As shown in Figure 10.12, LPD used a sensor with larger pixels and an interposer to route the connection to a finer pitch on the ASIC and give space for wire bonds behind the active sensor area. To adopt a similar method at the $< 100\mu$m pixel pitches required at a next generation XFEL a new interposer technology would be required with finer tracks and smaller vias. Although there is no proven method or provider of this service, there are similar methodologies of assembling chiplets and packages of ASICs in industry. The difficulty is to access these advanced processes on the budget and volumes associated with scientific facilities. Similarly, thru-Si-vias (TSVs) are an established process in CMOS foundries to route signals to the back side of ASICs and negate the need for wire bonds. This is typically only available from the foundry for the most advanced processes and requires investments and volumes beyond that of a science facility. Adding TSVs on the wafer level after production has been explored by different groups and initiatives in the detector community. The difficulty has been in developing and maintaining a capability with sufficient throughput to give service providers such as CEA Leti and Fraunhofer IZM a viable business model. The latest development of the Timepix 4 ASIC is designed specifically to include TSVs and promising results with other vendors suggest that these TSV processes could be available on the timescales of a next generation XFEL.

In summary, and as listed below in Figure 10.13. The bonding technology for a Next Generation XFEL are widely accessible. The high-Z detector materials have limit sensor sizes that will require more tiles/Mpixel an increase the dead space percentage compared to silicon-based sensors. The use of TSVs to make 4-side buttable devices is an attractive option but requires further development and a continuous volume of production to become a standardised process.

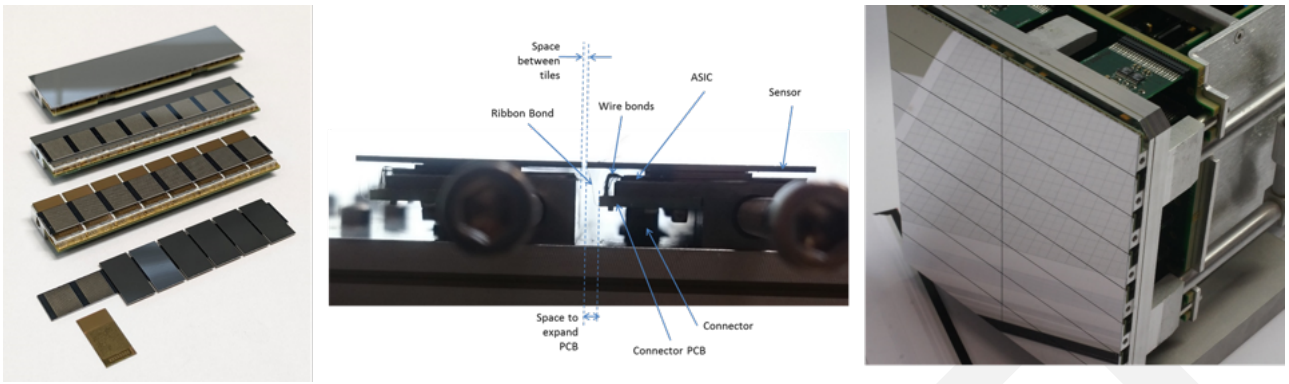

Figure 10.12: The LPD tile with interposer parts (left), side view of the tiled modules (middle) and a tiled arrray (right). Credit: Matthew Hart

Figure 10.13: Summary of status of the interconnect technology and prospect of detector module production.

10.5 Strip Detectors

Strip detectors for a Next Generation XFEL have similar flux, dynamic range and energy requirements as the large area detectors (Section 10.4). They are typically assembled with wire bonds between the sensor material strips and the readout ASIC. The bond pads for the wire bonds can limit the pitch of strips on the sensor material, typically 50μm. Having bonds on both sides can half the strip pitch. Strip detectors are predominantly used in spectrometer arrangements (see Section 10.7) where the strip pitch determines the energy resolution. They are also used for X-ray beam monitoring to give a 1D profile of beam intensity.

The state of the art for XFEL applications is the Gotthard-II detector which utilises the adaptive gain front end of Jungfrau to provide a dynamic range up to 10^4 photons/pulse [52]. It can operate at 410 kHz in continuous readout, more than sufficient for the majority of Next Generation XFEL experiments and has a burst mode capture at 4.5 MHz and 2700 memory cells, to match the EuXFEL beam structure, that could be useful for $>$MHz experiments at the FEL1 End Stations. The ASIC has a 50μm wire bond pitch and 25μm detectors have been assembled with ASICs on both sides of the sensor material with interleaving strips. The ASIC is optimised for the energy range of 5-20 keV and utilises Si detector material with an active detector width of 64 mm providing 1280 strips at 50μm or 2560 strips at 100μm. A hard X-ray version with CdZnTe or other materials would be limited in continuous area and the lithography to develop strips below 50μm pitch is not currently offered from vendors. Soft X-ray versions for FEL 1 and FEL 2 would be possible with some of the MAPS and LGAD detector materials discussed in Section 10.4.2, but an ASIC optimised for those signal levels would be required. A summary of the status of the technology and it's suitability for a Next Generation XFEL are show in Figure 10.14.

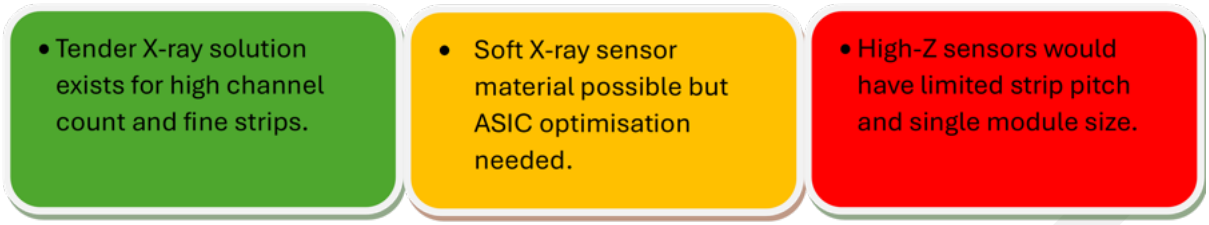

Figure 10.14: Summary of status of strip detector technology.

10.6 Fast and Timing Measurements

High speed detectors cover a wider variety of different detector technologies that would be required at a Next Generation XFEL. This covers the MHz into GHz burst rate imaging requested for FEL1 and the angular streaking techniques to get into the atto-second regimes on FEL6. Each detector type is considered below.

As discussed above, large area hybrid pixel detectors can operate in burst modes at 1-10 MHz rates to conduct diffraction and scattering measurements. Similarly, the strip detectors in burst mode can reach similar rates for X-ray emission or absorption spectroscopy. The request to reach into 100s of MHz or GHz imaging require different technologies. Micro-channel plate (MCP) detectors can provide high speed imaging solutions with 10-100ps timing resolution [53] but can only operate at low instantaneous flux rates and are useful for reaction and time of flight microscopes as discussed below in Section 10.8. For the high instantaneous flux and dynamic range required at a Next Generation XFEL they would not be suitable. To overcome these instantaneous dynamic range limitations, Sandia National Laboratory have the Ultra-Fast Digital X-ray Imager (UXI) development for a wide range of applications including the National Ignition Facility (NIF) [54], but have direct applications at XFELs and have been demonstrated for XCS [55]. Their Daedalus detector operates with a time gated ASIC to reach 1ns integration windows and hybridised CMOS sensors with a large full well of 1.5x10^6 e- in a 25μm pixel [56]. The 1024x512 pixels can capture 3 successive frames or be interlaced to, for example, capture 6 frames at 512x512 pixels. The direct detection sensor material is typically 25μm thick Si that ensures a short drift time and high timing resolution but has limited efficiency at tender and hard X-ray energies. Alternatives such as the fore mentioned LGAD technology (Section 10.4.2) could help to increase the timing resolution of thicker sensor materials but this has limited benefits for the $>$ 20keV energies that are requested GHz measurements at a Next Generation XFEL. Other sensor materials such as GaAs have been investigated [57] but the requirement to be thin for short drift lengths and fast timing limits the sensor. The GaAs staircase avalanche detectors discussed in Section 10.4.2 could have a cross-over to this high-speed imaging technology too. The alternative of optically or directly coupling a fast scintillator is one option for reaching higher energies. Any scintillator would have to be have the usual properties of high-Z and a fast decay to keep any afterglow lower than the frame rate. YAG:Ce is a scintillator that is commonly used for X-ray beam monitoring a light source but has an afterglow time constant of 70 ns. There are many scintillator materials in development and new materials such as GAGG:Ce could improve performance [58]. Structuring scintillator materials on the same spatial scale as optical wavelength to gain enhancements through nanophotonic effects could also lead to improved light output [59] and faster emissions [60] . It is worth noting that the UXI detector programme is focused around the Sandia National Laboratories own 0.35μm CMOS process which has been optimised for radiation hardness. There are ongoing developments with the Tantalus detector is in progress and will aim for 500 ps integration times [ref - Quinn talk]. There is also the possibility of adopting commercial CMOS processes that could go to finer process nodes and potentially improve the

timing or offer smaller memory cells to be able to capture more frames in the pixel.

Streaking cameras are available as commercial off the shelf products with applications at XFELs for electron and beam monitoring. Commercial cameras offer $\sim$ 100fs timing resolution but do not meet the requirements to move into the atto-second regime required at the FEL5 end stations. Angular streaking cameras, first demonstrated at LCLS [61] use an X-ray absorbing gas to generate a short duration bunches of photoelectrons that are streaked by a circularly polarised laser synchronised with the X-ray pulse. The streaked photoelectrons are measured by a ring of 16 time of flight detectors at 90 degrees to the X-ray beam direction. The angular distribution of the circularly streaked photoelectrons gives a measurements of the timing to a 300 atto-second resolution and the time-of-flight measurement provides additional photoelectron energy and intensity information. This technique is reported to be suitable for 100 kHz frame rates and the demonstrated energy ranges meet the needs of the FEL2 End Station. The limitation in the timing resolution comes from the wavelength of the streaking laser (time for one rotation of its polarisation which is related to the wavelength, currently 10.6μm, equates to 35 fs) and the number of angular samples (16 in this case, which give 2.2fs per ToF detector) and the reconstruction of the photoelectron position to a sub-detector resolution. Whilst current technology would meet the baseline requirements of a next generation XFEL there are further developments in reconstruction [62] and corrections methods [63] that could improve timing resolution further.

In summary, there are a number of specialised systems that can provide the high-speed detection on the nanosecond and attosecond timescales required for a Next-Generation XFEL. The GHz rate imaging has the potential to move to higher frame rates or frame depths but will always have an efficiency limit due to the sensor material and thickness. . The angular streaking detectors are a specialised piece of new equipment with the necessary timing resolution but a higher TRL would benefit a continually operating and high uptime facility like a Next Generation XFEL.

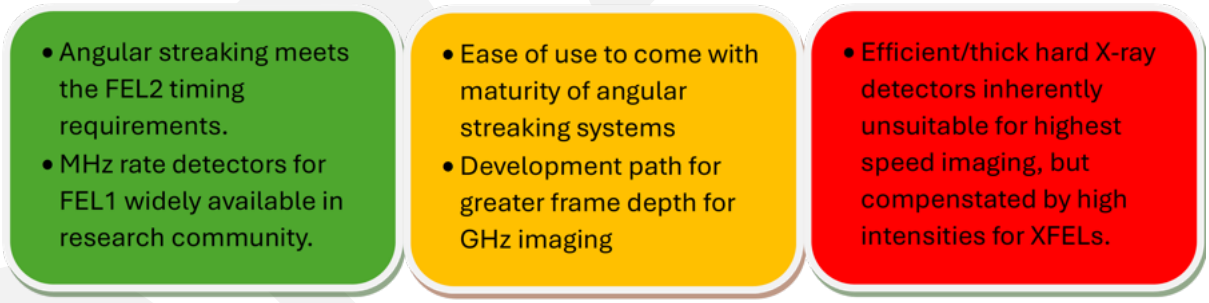

Figure 10.15: Summary of nanosecond and attosecond detector technology.

10.7 X-ray Spectrometers

Energy resolving detectors are required for several End Stations in X-ray absorption and emission arrangements including the hRIXS End Station on FEL2. The energy resolution requirements of 10s of meV resolution is beyond the current capability of direct measurements and reflection or diffraction based analysers are typically used in many FEL and synchrotron facilities to spatially separate the different energies [64]. There are several methods to distribute the X-ray beam including KB-mirror arrangements [65] the Fresnel Zone Plates [66], Von Hamos geometries [67] and Laue spectrometers [68]. As with the sensor materials, they have different advantages and are chosen for their specific energy ranges.

Pixel and strip detectors are used to measure the spatially distributed energies, with the pixel/strip pitch becoming a dominant factor in the energy resolution and the number of pixels or strips determining the energy range. As previously discussed (Section 10.5), the Gotthard II strip detector would meet the needs of the Next Generation XFEL in a spectrometer geometry.

Direct measurements of the energy with eV levels of energy resolution is achievable with transition edge sensors. The most prominent developments from NIST, Boulder [69], with a system at SPring8 reporting 2-5 eV energy resolution at 6 keV and resolution as low as 1 eV energy resolution at 500eV [70]. The TES pixel array sizes are typically in the 100-1000s of pixels which results in instantaneous count rates of 100s of photons per X-ray pulse. The absorbing pixel materal can be optimised for harder X-ray energies with the use of Au and Bi sensor pixel pads of different thickness but are limited to $\sim$ 10μm thicknesses. Whilst the technology does not currently meet the needs of all XAS and XES measurements at a Next Generation XFEL they could still have applications at a Next Generation XFEL and are consistently improving in terms of energy resolution and number of pixels.

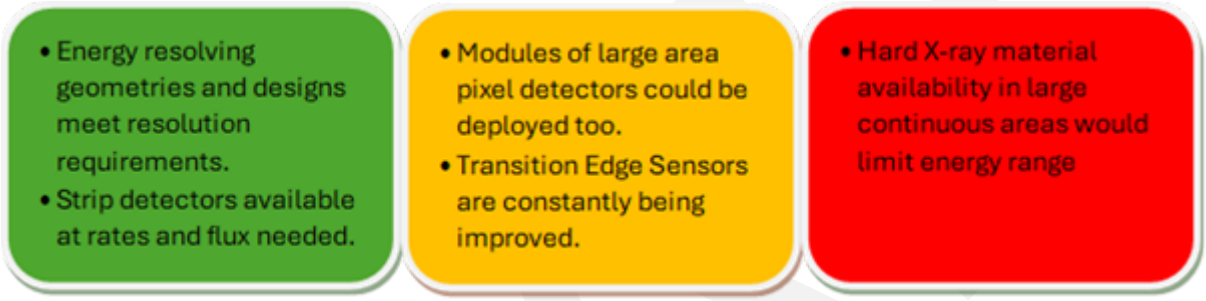

Figure 10.16: Summary of nanosecond and attosecond detector technology.

10.8 Electron and Ion Detection

Several End Stations rely upon measuring the energy and momentum of the electron and ions emitted from the samples at rep rates up to 100 kHz, dependent on sample delivery and stimulation. There are several different options for these measurements, from hemispherical detectors, to so-called magnetic bottles and more advanced momentum microscopes and COLTRIMS. The instruments are used widely in surface science measurements and at high power laser facilities which has helped to build up a set of commercial suppliers for the different technologies.

Hemispherical detectors are widely used in photoelectron spectroscopy (XPS) and angle-resolved photoemission spectroscopy (ARPES) and the commercially available devices meet the needs for many experiments, such as at the second interaction point at the AMO End Station on FEL 6 or for the HX ARPES End Station on FEL 3 [71]. The hemispheres are available from vendors such as SPECS [72], scienta omicron [73], Thermo Fisher [74], and more. They are available with different sensor options of 2D CMOS, 1D strip, MCPs and Delay Line Detectors, which give different count rate capabilities of the order of 100-1000kcps, although the instantaneous flux rates as required at a Next Generation XFEL, are not easily found. Compared to the other instruments in this section, they have the advantage of being 'plug and play' solutions and are relatively inexpensive in price.

Magnetic Bottle Spectrometers are typically more custom developments and utilise a magnetic field shaped like a bottle to collect the electrons or ions emitted from a sample. A retardation field is applied to slow and separate the collected charge carriers which are then sent down a flight

tube with their time of arrival measured by an MCP sensor [75] and the total intensity with time is recorded as a charge carrier energy spectrum. When two opposing Magnetic Bottle Spectrometers are used to collect electrons and ions in coincidence [76],this geometry is sometimes referred to as a Reaction Microscope . Similarly, magnetic bottles can be positions in different positions to collect electrons of different spin. As with Hemispherical detectors, Magnetic Bottle Spectrometers are commonly used with MCPs and Delay Line Detectors that have demonstrated the ability to operate at 4.5MHz at the EuXFEL but have limited instantaneous hit rates. The use of Timepix 3 with an MCP time of arrival on the 1 ns timescale and 2D energy resolved images has helped enable velocity mapping at the FLASH and EuXFEL [77]. Despite the faster detectors, the limiting factor in the repetition rate comes from the fundamental limit in the time of flight of the electrons (1 MHz) and ions (250 kHz) [78] , which is still faster than the majority of repetition rates planned at a Next Generation XFEL.

Momentum Microscopes are more advanced instruments that measures the distribution of electronic states in k-space and can be adapted to make spin-resolved measurements. Standard products offered by SPECS utilise CCD or CMOS detectors as the sensing elements, whereas the faster ToF Momentum Microscopes (TOFMM) use the delay line detectors to measure the time of arrival and position of the collected electrons. The ToFMM is currently limited to 50kHz repetition rate and a maximum rate of 5M cnts/s which would be suitable for most applications at a Next Generation XFEL. Whilst the MCP + Delay Line Detectors can reach timing resolution of $<$ 100ps [79] they are limited in instantaneous flux (or occupancy per frame). New ASICs such as the SprakPix-T device from SLAC[80],[81] and Timepix 4 from CERN [82] offer similar timing resolution to a delay line detector, but the 2D pixel arrays allow higher instantaneous hit rates. There are such developments planned for LCLS II to reach 1MHz repetition rates with SparkPix which would bring the performance inline and beyond the needs of a Next Generation XFEL [43]. In conversations with XFEL scientists there were concerns that the high performance of the momentum microscopes came with a complication of tuning the parameters of up to 60 parameters for the collection and distribution of the charged particle. Whilst this can be a daunting task for a high up time and high throughput facility as envisioned for a Next Generation XFEL, it is this type of automated optimisation where AI could be developed and deployed to improved beamtime scientific efficiency.

In summary, there are a variety of electron and ion measuring instruments and configurations that are provided by commercial vendors, and the state of the art is continually being pushed forward by laser and X-ray facilities. There were no obvious technical limitations in the instrumentation that would prohibit the planned experiments at a Next Generation XFEL and the potential of more advanced sensor and automated operation will only serve to increase throughput and scientific uptime in the future.

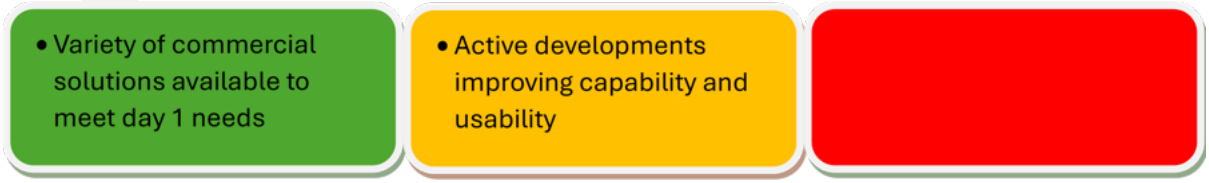

Figure 10.17: Summary of status of the electron and ion spectrometers and ToF instrumentation.

10.9 Data Handling in the Detector System

The continuous and parallel operation of multiple end stations with typical frame rates of 100kHz will result in vast amounts of raw data generation. A simple estimation of 16b per pixel operating at 100 kHz would be that this is 1.6 Tbps/Mpixel detector. Across the initial 13 end stations at a Next Generation XFEL there would be a variety of 1-16 Mpixel scale detectors with a resulting estimation of the total maximum raw data rate of $\sim$ 20 PBps when all experiments are operating. For comparison, the LHC experiment at CERN generates 1PB/s before triggering, which demonstrates the scale of the data processing challenge at a Next Generation XFEL. Whilst Chapter 7 discusses the facility wide approach to data handling, there is a clear need to reduce the raw data rates at the detectors themselves.

There are many different approaches to reducing the data in the detector system. Some examples and possibilities are listed below, moving through the detector system from the experimental technique, the ASIC output and onto data reduction and compression in the DAQ system.

- **Experimental Technique:** Some experimental methods like Coherent Diffraction Imaging operate by conducting multiple measurements scanning different parameters or scanning over surfaces to build up information. Work at the APS demonstrated the use of AI with edge processing at the detectors to optimise the scanning over a 2D sample to estimate the most interesting subset points to sample and the most efficient way to scan them. Interpolation techniques used over just 25pc of full area scan recovered the ground truth image which increased sample throughput and reduced data volumes [83]. Similar techniques could be employed on any experimental method where parameters are scanned and could help reduce data volumes from the outset.

- **ASIC Level:** The ASIC is the source of generating the raw data and there are many examples of reducing the data volume on chip rather than outputting all values from all pixels for all frames. Simple thresholding and outputting data with a pixel address can reduce data volumes for sparse data, which can be the case for many diffraction techniques. The SparkPix-S [43] from LCLS employ a sparse readout for frames to be evaluated in a local FPGA and a decision made whether to readout or discard the data, so only interesting data is saved. There are several ASIC developments, in photon science, particle physics and beyond, that are often using advanced CMOS nodes at 65-28 nm to retain benefits of analogue circuitry but include more processing or programmable logic in the ASIC periphery and in-pixels. One simple implementation is on-chip pixel centroiding [84] which when used with threshold based readout reduces the number of pixels output. In ASIC data compression, as proposed for SparkPix-RT [85] is another method to reduce the data rate at source. Programmable NN circuitry in the detector are being developed in custom ASICs for science with examples applied to pulse shape filtering and analysis [86] and for identifying and extracting specific particle tracks for future particle physics colliders [87].

- **FPGA or Edge Level:** The detector systems typically have at least one layer of FGPAs to receive and package the data from the ASIC for transfer to the facility data storage and computing systems. This additional level where data can be selected, vetoed, compared to simulated results, rare events identified, accumulated, or compressed. The choice of processing is experiment dependent and the FPGAs (or other processors such as GPUs) are readily programmable to have this flexibility. For example, the CITIUS 20M detector generates 107GBps of raw data that is compressed to 15GB/s after a first level of processing and a lossless compression in edge servers reduces this further to 2.5GBps. These more

manageable data volumes can be sent to centralised or off site high power computing infrastructure for further processing and down selection.

It is evident that the raw data rates from a Next Generation XFEL are not manageable or sustainable. However, there are many rapidly developing methods in the photon science field and beyond to apply smarter data collection and edge processing into the detector systems. A key addition to the technical developments will be to change user practices and expectations of storing all raw data. This problem is not unique to a Next Generation XFEL and it is anticipated that on the timescales of a new facility that the majority of existing XFELs and 4th generation synchrotrons will have similar edge processing, and that verified and proven data reduction schemes will be accepted by users.

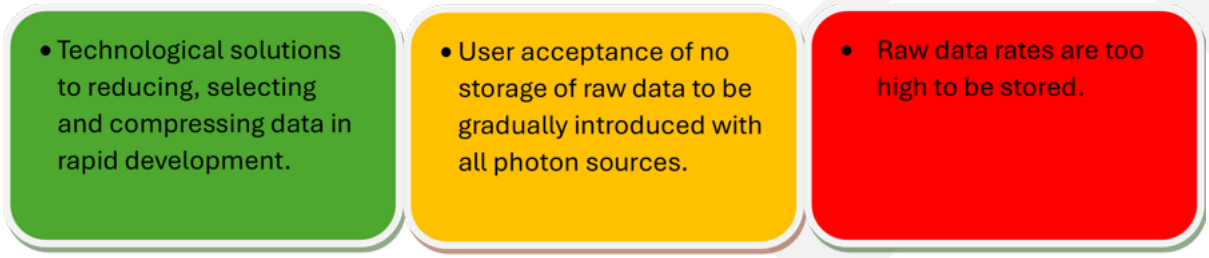

Figure 10.18: Summary of status and outlook of the data management within the detector system.

10.10 Sustainability of Detector Systems

The sustainability of detector systems for a Next Generation XFEL can be categorised into the life-cycle of the detector system based on the production or supply of the detector system, the energy usage during the operation of the detectors and considerations of the lifetime and disposal of the detectors themselves.

The microelectronics in the ASICs, CMOS devices and readout components in a detector system are procured from large foundries and suppliers with specific design rules and processes. Whilst it is not possible for a Next Generation XFEL to change these processes they should not be ignored. IMEC [88] estimate that for a 28 nm CMOS node , a realistic technology for a Next Generation XFEL, consumes $\sim$ 400kWh per wafer, equivalent to $\sim$ 2000 miles in an electric vehicle. The use of greenhouse gases in the CMOS production has an environmental impact equivalent to $\sim$ 120kgCO2/wafer, equivalent to one passenger on a short haul flight. As the total number of wafers for development and production for a Next Generation XFEL would only reach the order of $\sim$ 100 wafers this is a relatively small environmental impact compared to the overall facility. The use of rare earth and purified metals and the impact of mining and processing those materials is less well reported and is likely to be a significant factor not considered here. The production of just the silicon for CMOS process via the Czochralski method consumes around 1MWh per ingot, which typically provides $\sim$ 500 wafers. It is worth noting that the detector housings and experimental chambers manufactured from steel ($\sim$ 65 – 95kWh per kg from ore) or aluminium ($\sim$ 65 – 95kWh per kg from ore) could be several hundred kg or even tonnes in weight and could dominate the energy usage to produce a detector system.

The energy use of operating a detector system is estimated to be in the region of 1500kWh/year per Mpixel based on a 256x256 pixel ASICs consuming $\sim$ 10 W each and the readout boards of a 1M pixel detector consuming 300 MW. With an up time of 33% throughout the year this would be in the region of 200 MWh/year for the detector front ends for the entire Next Generation XFEL

facility. The detector system back end with high power computing and further data processing could dominate this number with 3kW per high power server. Whilst this is a large fraction of the energy consumption of operating a detector system, it is evident that putting more data processing and data reduction at the detector system level reduces the demand and scale of the centralised data systems.

The lifetime of the detectors at light source facilities is typically in the 5-year time frame. However, as discussed above, the radiation hardness of the detector materials at a Next-Generation XFEL may greatly reduce this lifetime which would have an economic and environmental impact. The more radiation tolerant and high-Z materials such as CdZnTe or Perovskites like $CsPbBr_3$ may have longer lifetimes but have hazardous materials in Cd and Pb. Whilst there are no alternative high-Z detector materials at present, there is an effort to look at more environmentally friendly detector materials via Pb-free Perovskites, but they do not currently provide the required detector performance. The disposal and recycling of such hazardous materials, alongside the waste electrical and electronic equipment, would be a consideration of any new facility.

Whilst there is little influence that a Next Generation XFEL could have on the production methods and materials used for CMOS, detector material or readout electronics, there is a responsibility and desire to adopt sustainable engineering via design and decision making. Finding the least energy intensive methods of data handling and developing modular and repairable detector systems to reduce waste are just two examples where the best practical solutions come hand in hand with the least environmentally damaging options. Such practices are not unique to a Next Generation XFEL and there will be many sustainable science and engineering best practices that a future facility can adopt in its detectors programmes.

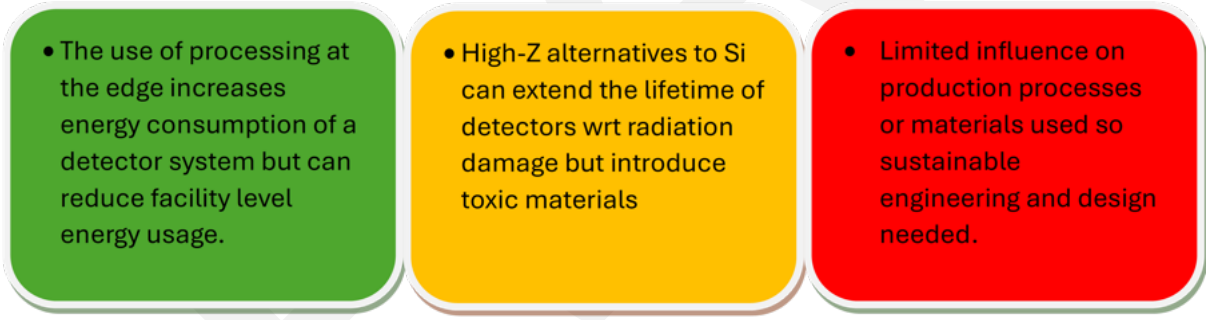

Figure 10.19: Summary of status of the sustainability of detector systems.

10.11 Operations and Practicalities

The suite of next generation XFEL detectors will have to operate in hostile environments and present operational challenges beyond the radiation damage mentioned above. The detectors must be integrated physically, with the data pipelines and be characterised and calibrated to provide the best possible scientific data. A short summary touching on some of the operational challenges are listed below:

- The detectors and readout systems will have to be integrated in a manner to protect against electromagnet pulses and interference from the experimental set-ups and pump sources.
- The detectors have to operate in vacuum and have to be kept at a constant and often relatively low temperature that requires cooling considerations. The latest higher power

detectors at LCLC II, for example, are moving to CO_2 cooling which required additional beamline infrastructure and mechanical design constraints.

- In applications like TMO the detectors will operate in high electrical fields and need to be electrically floating to avoid disturbing the experiment but still connect to conventional data acquisition hardware.
- Hosting a variety of instruments will necessitate that a variety of detector types will be needed and these will have different data interfaces that complicate installation and operational support. Where possible, standardising on interfaces, data acquisition and formats makes installation and integration into data pipelines more efficient.
- All detectors must be calibrated before they can become operational instruments. Whilst efficient and automated calibration routines should be included in new detector technology, any new facility must include the infrastructure and schedule beam access to enable detector calibration.

10.12 Summary and Recommendations

The continuous high repetition rates, suite of experiment techniques and range of energies at a next generation XFEL will push the boundaries of detector technology and presents a grand challenge in data handling and processing. As summarised in this chapter, there are already some commercially available detector systems that will meet the needs of some experiments, ongoing developments that show that the majority of requirements are feasible, and that other areas require more research to be robust and user-friendly detector systems.

By definition, a next generation XFEL will be breaking new ground in detector requirements. The experience of other facilities such as the EuXFEL is that the development of completely new and custom detector systems can take 10+ year and cost £5-10M. However, the next generation XFEL has commonalities with other XFELs, synchrotrons, laser-driven light sources and other areas of science. As such, there is an opportunity to work collaboratively, share development costs and speed up development times. Whilst it is unlikely that there will be one detector that can meet the needs of multiple collaborating facilities or experiments, it is likely that developing a common design architecture in the ASIC and DAQ, sharing and re-using specific IP blocks and standardising on pixel array sizes would prevent duplication of effort and give common platform technologies that are easier to integrate and support at the facility. It is worthwhile noting that whilst any next generation XFEL detector development would not be starting from scratch, it will require more advanced CMOS processes that come at an increased cost and multi-million pound investments are needed to develop and scale up the detector technology. Similarly, these developments do take years of development so investment is needed well before any next generation XFEL begins construction.

At this early stage of a next generation XFEL concept there are still some fundamental detector technology areas that require attention. The priority areas for research and development would be:

- **Radiation Hard Sensors:** Conventional Si detectors will not survive the continuous high-flux operation of a next generation XFEL. High-Z sensor materials outlined for hard X-ray measurements may provide a solution for lower energy end stations but are not fully proven, have limited suppliers and currently have relatively small monolithic areas. Evaluating, improving

and developing new radiation hard sensors would be a valuable area of development for a next generation XFEL.

- **Low Energy Sensors:** Measuring the lowest energies at FEL6 and FEL5 is particularly challenging and requires specialised entrance windows and processing on CMOS and Si sensors that are not easily accessible. A next generation XFEL would require access to a proven and stable process to make sensor material sensitive to the lowest energy ranges.
- **Edge Processing:** Perhaps the largest detector challenge for a next generation XFEL is how to convert the vast amounts of raw data into scientific impact. Workflows to convert data into results in a timely fashion and reduce data into manageable volumes for storage is a fundamental to the facility. Investment in edge processing in the ASIC and readout system is not only needed for data management and efficient operation but is essential to take advantage of frontier developments such as AI driven experiments.

In summary, the next generation XFEL is pushing the boundaries of detector technology and data handling beyond the current state of the art. Whilst there are several development areas that should be recognised as risks for the facility, the UK and wider detector research communities have demonstrated that the required step changes in detector performance are feasible and could be delivered to help enable the pioneering science at a next generation XFEL.

DRAFT

References for Chapter 10

[1] Peter Walter et al. “The DREAM Endstation at the Linac Coherent Light Source”. In: *Applied Sciences (Switzerland)* 12 (20 Oct. 2022). ISSN: 20763417. DOI: 10.3390/app122010534.

[2] Takashi Kameshima et al. “Development of an X-ray pixel detector with multi-port charge-coupled device for X-ray free-electron laser experiments”. In: *Review of Scientific Instruments* 85 (3 Mar. 2014), p. 033110. ISSN: 0034-6748. DOI: 10.1063/1.4867668. URL: https://doi.org/10.1063/1.4867668.

[3] Norbert Meidinger et al. “pnCCD for photon detection from near-infrared to X–rays”. In: *Nuclear Instruments and Methods in Physics Research Section A: Accelerators, Spectrometers, Detectors and Associated Equipment* 565 (1 2006), pp. 251–257. ISSN: 0168-9002. DOI: https://doi.org/10.1016/j.nima.2006.05.006. URL: https://www.sciencedirect.com/science/article/pii/S0168900206007662.

[4] Lucio Pancheri et al. “Fully Depleted MAPS in 110-nm CMOS Process with 100-300-μm Active Substrate”. In: *IEEE Transactions on Electron Devices* 67 (6 June 2020), pp. 2393–2399. ISSN: 15579646. DOI: 10.1109/TED.2020.2985639.

[5] Inc Amptek. *Patented C-Series Low Energy X-Ray Windows*. https://www.amptek.com/products/x-ray-detectors/fastsdd-x-ray-detectors-for-xrf-eds/c-series-low-energy-x-ray-windows]. 2025.

[6] Michael E. Hoenk et al. “Delta-doped back-illuminated CMOS imaging arrays: progress and prospects”. In: *Infrared Systems and Photoelectronic Technology IV*. Vol. 7419. SPIE, Aug. 2009, 74190T. ISBN: 9780819477095. DOI: 10.1117/12.832326.

[7] Azriel Goldschmidt et al. “VeryFastCCD: a high frame rate soft X-ray detector”. In: *Frontiers in Physics* 11 (2023). ISSN: 2296424X. DOI: 10.3389/fphy.2023.1285350.

[8] Julie Segal et al. “Thin-Entrance Window Process for Soft X-Ray Sensors”. In: *Frontiers in Physics* 9 (Mar. 2021). ISSN: 2296424X. DOI: 10.3389/fphy.2021.618390.

[9] Kewin Desjardins et al. “Backside-illuminated scientific CMOS detector for soft X-ray resonant scattering and ptychography”. In: *Journal of Synchrotron Radiation* 27 (Nov. 2020), pp. 1577–1589. ISSN: 16005775. DOI: 10.1107/S160057752001262X.

[10] Alessandro Marras et al. “Characterization of the Percival detector with soft X-rays”. In: *Journal of Synchrotron Radiation* 28 (Jan. 2021), pp. 131–145. ISSN: 16005775. DOI: 10.1107/S1600577520013958.

[11] L. Rota et al. “Design of ePixM, a fully-depleted monolithic CMOS active pixel sensor for soft X-ray experiments at LCLS-II”. In: vol. 14. 12. Dec. 2019, p. C12014. DOI: 10.1088/1748-0221/14/12/C12014. URL: https://dx.doi.org/10.1088/1748-0221/14/12/C12014.

[12] Michael Grimes et al. “Bragg coherent diffraction imaging with the CITIUS charge-integrating detector”. In: *Journal of Applied Crystallography* 56 (June 2023), pp. 1032–1037. ISSN: 16005767. DOI: 10.1107/S1600576723004314.

[13] M. Donato et al. “First functionality tests of a 64 $\times$ 64 pixel DSSC sensor module connected to the complete ladder readout”. In: *Journal of Instrumentation*. Vol. 12. Institute of Physics Publishing, Mar. 2017. DOI: 10.1088/1748-0221/12/03/C03025.

[14] Stefano Maffessanti et al. “A 64k pixel CMOS-DEPFET module for the soft X–rays DSSC imager operating at MHz–frame rates”. In: *Scientific Reports* 13 (1 Dec. 2023). ISSN: 20452322. DOI: 10.1038/s41598-023-38508-9.

[15] A. Castoldi et al. “Assessment of the Non-Linear Response of DEPFET Sensors with Signal Compression”. In: *2020 IEEE Nuclear Science Symposium and Medical Imaging Conference, NSS/MIC 2020*. Institute of Electrical and Electronics Engineers Inc., 2020. ISBN: 9781728176932. DOI: 10.1109/NSS/MIC42677.2020.9508034.

[16] V. Hinger et al. “Advancing the JUNGFRAU detector toward low-energy X-ray applications”. In: *Journal of Instrumentation*. Vol. 17. Institute of Physics, Sept. 2022. DOI: 10.1088/1748-0221/17/09/C09027.

[17] J. Zhang et al. “Development of LGAD sensors with a thin entrance window for soft X-ray detection”. In: *Journal of Instrumentation* 17 (11 Nov. 2022). ISSN: 17480221. DOI: 10.1088/1748-0221/17/11/C11011.

[18] S M Mazza et al. “Synchrotron light source X-ray detection with Low-Gain Avalanche Diodes”. In: *Journal of Instrumentation* 18 (10 Oct. 2023). ISSN: 17480221. DOI: 10.1088/1748-0221/18/10/P10006.

[19] Julie Segal et al. “Design, fabrication, and preliminary test results of a new inverse-LGAD for soft X-ray detection”. In: *Nuclear Instruments and Methods in Physics Research, Section A: Accelerators, Spectrometers, Detectors and Associated Equipment* 1065 (Aug. 2024). ISSN: 01689002. DOI: 10.1016/j.nima.2024.169467.

[20] Matija Colja et al. “Experimental Characterization of Separate Absorption–Multiplication GaAs Staircase Avalanche Photodiodes under Continuous Laser Light Reveals Periodic Oscillations at High Gains”. In: *Photonics* 10 (8 Aug. 2023). ISSN: 23046732. DOI: 10.3390/photonics10080933.

[21] Tilman Donath et al. “EIGER2 hybrid-photon-counting X-ray detectors for advanced synchrotron diffraction experiments”. In: *Journal of Synchrotron Radiation* 30 (June 2023), pp. 723–738. ISSN: 16005775. DOI: 10.1107/S160057752300454X.

[22] Derek S. Bale and Csaba Szeles. “Nature of polarization in wide-bandgap semiconductor detectors under high-flux irradiation: Application to semi-insulating Cd_{1-x} Zn_x Te”. In: *Physical Review B - Condensed Matter and Materials Physics* 77 (3 Jan. 2008). ISSN: 10980121. DOI: 10.1103/PhysRevB.77.035205.

[23] B. Thomas et al. “Characterisation of Redlen high-flux CdZnTe”. In: *Journal of Instrumentation*. Vol. 12. Institute of Physics Publishing, Dec. 2017. DOI: 10.1088/1748-0221/12/12/C12045.

[24] M C Veale et al. “Cadmium zinc telluride pixel detectors for high-intensity x-ray imaging at free electron lasers”. In: *Journal of Physics D: Applied Physics* 52 (8 Feb. 2019). ISSN: 13616463. DOI: 10.1088/1361-6463/aaf556.

[25] Marin Collonge et al. “Probing the potential of CdZnTe for high-energy high-flux 2D X-ray detection using the XIDer incremental digital integrating readout”. In: *Frontiers in Physics* 12 (2024). ISSN: 2296424X. DOI: 10.3389/fphy.2024.1304570.

[26] D. Greiffenberg et al. “Signal stability of high-Z sensors at synchrotron light sources”. In: *Journal of Instrumentation* 20 (1 Jan. 2025). ISSN: 17480221. DOI: 10.1088/1748-0221/20/01/P01031.

[27] O. Baussens et al. “Characterization of High-Flux CdZnTe with optimized electrodes for 4th generation synchrotrons”. In: *Journal of Instrumentation* 17 (11 Nov. 2022). ISSN: 17480221. DOI: 10.1088/1748-0221/17/11/C11008.

[28] B D Cline et al. “Characterisation of HEXITECMHz - A 1 MHz continuous frame rate spectroscopic X-ray imaging detector system”. In: *Nuclear Instruments and Methods in Physics Research Section A: Accelerators, Spectrometers, Detectors and Associated Equipment* 1057 (2023), p. 168718. ISSN: 0168-9002. DOI: https://doi.org/10.1016/j.nima.2023.168718. URL: https://www.sciencedirect.com/science/article/pii/S016890022300709X.

[29] Kjell A.L. Koch-Mehrin et al. “Charge sharing and charge loss in high-flux capable pixelated CdZnTe detectors”. In: *Sensors* 21 (9 May 2021). ISSN: 14248220. DOI: 10.3390/s21093260.

[30] Alan Owens and A. Peacock. “Compound semiconductor radiation detectors”. In: *Nuclear Instruments and Methods in Physics Research, Section A: Accelerators, Spectrometers, Detectors and Associated Equipment*. Vol. 531. Sept. 2004, pp. 18–37. DOI: 10.1016/j.nima.2004.05.071.

[31] M C Veale et al. “Investigating the suitability of GaAs:Cr material for high flux X-ray imaging”. In: *Journal of Instrumentation*. Vol. 9. Institute of Physics Publishing, Dec. 2014. DOI: 10.1088/1748-0221/9/12/C12047.

[32] D. Greiffenberg et al. “Characterization of GaAs:Cr sensors using the charge-integrating JUNGFRAU readout chip”. In: *Journal of Instrumentation* 14 (5 May 2019). ISSN: 17480221. DOI: 10.1088/1748-0221/14/05/P05020.

[33] Lei Pan et al. “Perovskite $CsPbBr_3$ Single-Crystal Detector Operating at 10^{10} Photons s^{-1} mm^{-2} for Ultra-High Flux X-ray Detection”. In: *Advanced Optical Materials* 11 (7 Apr. 2023). ISSN: 21951071. DOI: 10.1002/adom.202202946.

[34] Lei Pan et al. “Ultrahigh-Flux X-ray Detection by a Solution-Grown Perovskite $CsPbBr_3$ Single-Crystal Semiconductor Detector”. In: *Advanced Materials* 35 (25 June 2023). ISSN: 15214095. DOI: 10.1002/adma.202211840.

[35] Tumen-Ulziia Ganbaatar et al. “Photon-counting FAPbBr3 radiation detector performance enhanced by additive assisted crystal growth and electronic passivation”. In: *Nature Photonics* (2025). Submitted for publication. Manuscript ID: NPHOT-2025-08-01722.

[36] Sven Herrmann et al. “CSPAD-140k: A versatile detector for LCLS experiments”. In: *Nuclear Instruments and Methods in Physics Research, Section A: Accelerators, Spectrometers, Detectors and Associated Equipment* 718 (2013), pp. 550–553. ISSN: 01689002. DOI: 10.1016/j.nima.2013.01.057.

[37] Gabriel Blaj et al. “X-ray detectors at the Linac Coherent Light Source”. In: *Journal of Synchrotron Radiation* 22 (May 2015), pp. 577–583. ISSN: 16005775. DOI: 10.1107/S1600577515005317.

[38] A. Allahgholi et al. “AGIPD, a high dynamic range fast detector for the European XFEL”. In: *Journal of Instrumentation*. Vol. 10. Institute of Physics Publishing, Jan. 2015. DOI: 10.1088/1748-0221/10/01/C01023.

[39] Aschkan Allahgholi et al. “The Adaptive Gain Integrating Pixel Detector at the European XFEL”. In: *Journal of Synchrotron Radiation* 26 (1 Jan. 2019), pp. 74–82. ISSN: 16005775. DOI: 10.1107/S1600577518016077.

[40] M.C. Veale et al. “Characterisation of the high dynamic range Large Pixel Detector (LPD) and its use at X-ray free electron laser sources”. In: *Journal of Instrumentation* 12 (12 Dec. 2017), P12003–P12003. ISSN: 1748-0221. DOI: 10.1088/1748-0221/12/12/P12003. URL: https://iopscience.iop.org/article/10.1088/1748-0221/12/12/P12003.

[41] A. Mozzanica et al. “Characterization results of the JUNGFRAU full scale readout ASIC”. In: *Journal of Instrumentation*. Vol. 11. Institute of Physics Publishing, Feb. 2016. DOI: 10.1088/1748-0221/11/02/C02047.

[42] P King et al. “Characterization of ePixUHR-35kHz: a 13.8 Gb/s full-frame X-ray imaging readout ASIC for the LCLS-II upgrade”. In: *2023 IEEE Nuclear Science Symposium, Medical Imaging Conference and International Symposium on Room-Temperature Semiconductor Detectors (NSS MIC RTSD)*. 2023, p. 1. DOI: 10.1109/NSSMICRTSD49126.2023.10338013.

[43] L. Rota et al. “The SparkPix-S ASIC for the sparsified readout of 1 MHz frame-rate X-ray cameras at LCLS-II: pixel design and simulation results”. In: *Journal of Instrumentation* 19 (1 Jan. 2024). ISSN: 17480221. DOI: 10.1088/1748-0221/19/01/C01010.

[44] Gianluigi A. Botton et al. “An Innovative Update and Expansion Programme to the UK’s National Synchrotron”. In: *Synchrotron Radiation News* 37 (1 2024), pp. 33–38. ISSN: 19317344. DOI: 10.1080/08940886.2024.2312066.

[45] A. Marras et al. “Development of CoRDIA: An Imaging Detector for next-generation Synchrotron Rings and Free Electron Lasers”. In: *Journal of Physics: Conference Series*. Vol. 2380. Institute of Physics, 2022. DOI: 10.1088/1742-6596/2380/1/012093.

[46] X. Li et al. “Coulomb explosion imaging of small polyatomic molecules with ultrashort x-ray pulses”. In: *Physical Review Research* 4 (1 2022). ISSN: 26431564. DOI: 10.1103/PhysRevResearch.4.013029.

[47] X. Jia et al. “Characterization results of the first full-scale readout HYLITE chip for STARLIGHT”. In: *Journal of Instrumentation* 20 (2 Feb. 2025). ISSN: 17480221. DOI: 10.1088/1748-0221/20/02/C02019.

[48] Hugh T. Philipp et al. “High dynamic range CdTe mixed-mode pixel array detector (MM-PAD) for kilohertz imaging of hard x-rays”. In: (Apr. 2020). DOI: 10.1088/1748-0221/15/06/P06025. URL: http://arxiv.org/abs/2004.03421%20http://dx.doi.org/10.1088/1748-0221/15/06/P06025.

[49] D. Gadkari et al. “Characterization of 128 × 128 MM-PAD-2.1 ASIC: A fast framing hard x-ray detector with high dynamic range”. In: *Journal of Instrumentation* 17 (3 Mar. 2022). ISSN: 17480221. DOI: 10.1088/1748-0221/17/03/P03003.

[50] Katherine S. Shanks et al. “The MM-PAD-2.1: A Wide-Dynamic-Range Detector for High-Energy X-ray Imaging”. In: *2020 IEEE Nuclear Science Symposium and Medical Imaging Conference, NSS/MIC 2020*. Institute of Electrical and Electronics Engineers Inc., 2020. ISBN: 9781728176932. DOI: 10.1109/NSS/MIC42677.2020.9507923.

[51] M. D. Wilson et al. “A 10 cm × 10 cm CdTe Spectroscopic Imaging Detector based on the HEXITEC ASIC”. In: *Journal of Instrumentation* 10 (10 Oct. 2015). ISSN: 17480221. DOI: 10.1088/1748-0221/10/10/P10011.

[52] Marco Ramilli et al. “Integration and first operation of the Gotthard-II detector at European XFEL”. In: *Nuclear Instruments and Methods in Physics Research, Section A: Accelerators, Spectrometers, Detectors and Associated Equipment* 1058 (Jan. 2024). ISSN: 01689002. DOI: 10.1016/j.nima.2023.168796.

[53] A S Tremsin and J V Vallerga. *Unique capabilities and applications of Microchannel Plate (MCP) detectors with Medipix/Timepix readout*. Jan. 2020. DOI: 10.1016/j.radmeas.2019.106228.

[54] L. Clause et al. “Design and characterization of a novel 1-ns multi-frame imager for the Ultra-Fast X-ray Imager (UXI) program at Sandia National Laboratories”. In: (Sept. 2018), p. 21. ISSN: 1996756X. DOI: 10.1117/12.2319856.

[55] Philip A. Hart et al. “First x-ray test of the Icarus nanosecond-gated camera”. In: SPIE-Intl Soc Optical Eng, Apr. 2019, p. 27. ISBN: 9781510627420. DOI: 10.1117/12.2520974.

[56] Quinn Looker et al. “Optical and x-ray characterization of the Daedalus ultrafast x-ray imager”. In: *Review of Scientific Instruments* 94 (11 Nov. 2023). ISSN: 10897623. DOI: 10.1063/5.0171222.

[57] Quinn Looker et al. “GaAs X-ray detectors with sub-nanosecond temporal response”. In: *Review of Scientific Instruments* 90 (11 Nov. 2019). ISSN: 10897623. DOI: 10.1063/1.5127294.

[58] Amandine Baillard et al. “Terbium-doped gadolinium garnet thin films grown by liquid phase epitaxy for scintillation detectors”. In: *RSC Advances* 15 (24 2025), pp. 18802–18813. ISSN: 2046-2069. DOI: 10.1039/D5RA01784J. URL: https://xlink.rsc.org/?DOI=D5RA01784J.

[59] Louis Martin-Monier et al. “Large-scale self-assembled nanophotonic scintillators for X-ray imaging”. In: (Oct. 2024). URL: http://arxiv.org/abs/2410.07141.

[60] Michal Makowski et al. “Scaling Up Purcell-Enhanced Self-Assembled Nanoplasmonic Perovskite Scintillators into the Bulk Regime”. In: (Nov. 2024). ISSN: 15214095. DOI: 10.1002/adma.202417874. URL: http://arxiv.org/abs/2411.18477.

[61] N Hartmann et al. “Attosecond time–energy structure of X-ray free-electron laser pulses”. In: *Nature Photonics* 12.4 (2018), pp. 215–220. URL: https://doi.org/10.1038/s41566-018-0107-6.

[62] David Meier et al. “Reconstructing Time-of-Flight Detector Values of Angular Streaking Using Machine Learning”. In: (Jan. 2025). URL: http://arxiv.org/abs/2501.08966.

[63] Xiaokai Li et al. “Coulomb focusing in attosecond angular streaking”. In: *Light: Science and Applications* 13 (1 Dec. 2024). ISSN: 20477538. DOI: 10.1038/s41377-024-01600-4.

[64] Frank M.F. de Groot et al. “Resonant inelastic X-ray scattering”. In: *Nature Reviews Methods Primers* 4 (1 Dec. 2024). ISSN: 26628449. DOI: 10.1038/s43586-024-00322-6.

[65] Yi De Chuang et al. “A design of resonant inelastic X-ray scattering (RIXS) spectrometer for spatial- and time-resolved spectroscopy”. In: *Journal of Synchrotron Radiation* 27 (May 2020), pp. 695–707. ISSN: 16005775. DOI: 10.1107/S1600577520004440.

[66] Florian Döring et al. “A zone-plate-based two-color spectrometer for indirect X-ray absorption spectroscopy”. In: *Journal of Synchrotron Radiation* 26 (July 2019), pp. 1266–1271. ISSN: 16005775. DOI: 10.1107/S1600577519003898.

[67] Aleksandr Kalinko et al. “A von Hamos-type hard X-ray spectrometer at the PETRA III beamline P64 Kalinko Aleksandr”. In: *Journal of Synchrotron Radiation* 27 (Jan. 2020), pp. 31–36. ISSN: 16005775. DOI: 10.1107/S1600577519013638.

[68] X Huang et al. “A high-energy Laue X-ray emission spectrometer at the FXE instrument at the European XFEL”. In: *Journal of Synchrotron Radiation* 32 (3 May 2025), pp. 506–523. DOI: 10.1107/S1600577525001389. URL: https://doi.org/10.1107/S1600577525001389.

[69] Joel N. Ullom and Douglas A. Bennett. *Review of superconducting transition-edge sensors for x-ray and gamma-ray spectroscopy*. Aug. 2015. DOI: 10.1088/0953-2048/28/8/084003.

[70] Shinya Yamada et al. “Broadband high-energy resolution hard x-ray spectroscopy using transition edge sensors at SPring-8”. In: *Review of Scientific Instruments* 92 (1 Jan. 2021), p. 013103. ISSN: 0034-6748. DOI: 10.1063/5.0020642. URL: https://doi.org/10.1063/5.0020642.

[71] Yang Wang and Maciej Dendzik. *Recent progress in angle-resolved photoemission spectroscopy*. Apr. 2024. DOI: 10.1088/1361-6501/ad1915.

[72] Specs Group. *SPECS spectroscopy*. https://www.specs-group.com/specs/products/spectroscopy/. 2025.

[73] Scienta Omicron. *Scienta Omicron*. https://scientaomicron.com/en. 2025.

[74] Thermo Fisher Scientific. *X-Ray Photoelectron Spectroscopy*. https://www.thermofisher.com/uk/en/home/electron-microscopy/products/xps-instruments.html?SID=srch-srp-IQLAADGAAFFAFLMAMC. 2025.

[75] “Design and characterization of a magnetic bottle electron spectrometer for time-resolved extreme UV and X-ray photoemission spectroscopy of liquid microjets”. In: *Structural Dynamics* 8 (3 May 2021). ISSN: 23297778. DOI: 10.1063/4.0000107.

[76] I. Ismail et al. “A modified magnetic bottle electron spectrometer for the detection of multiply charged ions in coincidence with all correlated electrons: decay pathways to Xe^{3+} above xenon-4d ionization threshold”. In: *Physical Chemistry Chemical Physics* 24 (34 Aug. 2022), pp. 20219–20227. ISSN: 14639076. DOI: 10.1039/d2cp02930h.

[77] Merlin Fisher-Levine et al. “Time-resolved ion imaging at free-electron lasers using TimepixCam”. In: *Journal of Synchrotron Radiation* 25 (2 Mar. 2018), pp. 336–345. ISSN: 16005775. DOI: 10.1107/S1600577517018306.

[78] Hubertus Bromberger et al. “Shot-by-shot 250 kHz 3D ion and MHz photoelectron imaging using Timepix3”. In: *Journal of Physics B: Atomic, Molecular and Optical Physics* 55 (14 July 2022). ISSN: 13616455. DOI: 10.1088/1361-6455/ac6b6b.

[79] Anton S. Tremsin et al. “Photon-counting MCP/Timepix detectors for soft X-ray imaging and spectroscopic applications”. In: *Journal of Synchrotron Radiation* 28 (July 2021), pp. 1069–1080. ISSN: 16005775. DOI: 10.1107/S1600577521003908.

[80] B. Markovic et al. “Design and characterization of the tPix prototype: A spatial and time resolving front-end ASIC for electron and ion spectroscopy experiments at LCLS”. In: *2016 IEEE Nuclear Science Symposium, Medical Imaging Conference and Room-Temperature Semiconductor Detector Workshop (NSS/MIC/RTSD)*. 2016, pp. 1–4. DOI: 10.1109/NSSMIC.2016.8069725.

[81] Peter Walter et al. “The time-resolved atomic, molecular and optical science instrument at the Linac Coherent Light Source”. In: *Journal of Synchrotron Radiation* 29 (July 2022), pp. 957–968. ISSN: 16005775. DOI: 10.1107/S1600577522004283.

[82] X. Llopart et al. “Timepix4, a large area pixel detector readout chip which can be tiled on 4 sides providing sub-200 ps timestamp binning”. In: *Journal of Instrumentation*. Vol. 17. IOP Publishing Ltd, Jan. 2022. DOI: 10.1088/1748-0221/17/01/C01044.

[83] “Demonstration of an AI-driven workflow for autonomous high-resolution scanning microscopy”. In: *Nature Communications* 14 (1 Dec. 2023). ISSN: 20411723. DOI: 10.1038/s41467-023-40339-1.

[84] Piotr Otfinowski, Grzegorz W. Deptuch, and Piotr Maj. “Asynchronous Approximation of a Center of Gravity for Pixel Detectors’ Readout Circuits”. In: *IEEE Journal of Solid-State Circuits* 53 (5 May 2018), pp. 1550–1558. ISSN: 00189200. DOI: 10.1109/JSSC.2018.2793530.

[85] A Gupta et al. “SparkPix-RT2: The design of a 192 $\times$ 168 pixel detector ASIC with on-chip data processing for ultra-fast photon science”. In: *2024 IEEE Nuclear Science Symposium (NSS), Medical Imaging Conference (MIC) and Room Temperature Semiconductor Detector Conference (RTSD)*. 2024, p. 1. DOI: 10.1109/NSS/MIC/RTSD57108.2024.10657530.

[86] A. Koziol et al. “Artificial neural network on-chip and in-pixel implementation towards pulse amplitude measurement”. In: *Journal of Instrumentation*. Vol. 18. Institute of Physics, Feb. 2023. DOI: 10.1088/1748-0221/18/02/C02048.

[87] Anthony Badea et al. *Intelligent pixel detectors: towards a radiation hard ASIC with on-chip machine learning in 28 nm CMOS*. Tech. rep. 2024, pp. 18–24. URL: https://pos.sissa.it/.

[88] M. Garcia Bardon et al. “DTCO including Sustainability: Power-performance-area-cost-environmental score (PPACE) analysis for logic technologies”. In: *Technical Digest - International Electron Devices Meeting, IEDM*. Vol. 2020-December. Institute of Electrical and Electronics Engineers Inc., Dec. 2020, pp. 41.4.1–41.4.4. ISBN: 9781728188881. DOI: 10.1109/IEDM13553.2020.9372004.

DRAFT

11 Synchronisation

11.1 Introduction

XFEL instruments combine pulses of ultrashort X-rays with an external source, most commonly an optical laser, in a 'pump-probe' configuration. The temporal resolution $\Delta\tau_{\text{res}}$ is given by:

$$\Delta\tau_{\text{res, rms}} = \sqrt{\Delta\tau^2_{\text{pump, rms}} + \Delta\tau^2_{\text{probe, rms}} + \Delta\tau^2_{\text{pp jitter, rms}} + \Delta\tau^2_{\text{pp drift, rms}}} \tag{11.1}$$

where $\Delta\tau_{\text{pump}}$ and $\Delta\tau_{\text{probe}}$ are the pump and probe durations and $\Delta\tau_{\text{pp}}$ is the variation due to noise in the relative pump-probe (pp) time.

Noise can conceptually be separated into 'jitter' and 'drift'. Jitter is typically defined as noise at frequencies greater than or equal to the bunch repetition rate ($f \geq f_{\text{rep}}$); drift is typically defined as noise at frequencies lower than the bunch repetition rate ($f < f_{\text{rep}}$) and has the potential to be monitored and actively corrected. Alternatively, jitter and drift may be defined with respect to a fixed frequency (f =10 Hz).

As seen from Equation 11.1, in order to maximise the utility of the ultrashort pulses delivered by an XFEL, any noise in pump-probe relative timing should ideally be better than the X-ray pulse width. For advanced XFEL schemes, such as those to be delivered by UK XFEL, the X-ray pulse width could be of the order of single femtoseconds (1×10^{-15} s) or shorter. The effective temporal resolution of an experiment can be improved if an independent measurement of the pump-probe time with suitable resolution is available shot-by-shot, which can be used to sort data in post-processing.

The timing of X-rays is primarily determined by the arrival time of high energy electrons at the undulators. This is a complex function of multiple and distinct accelerator sub-systems including the linac, bunch compressors, and the photoinjector, all of which must be temporally synchronised to achieve the required bunch parameters. The amplitude and phase stability of the photoinjector and linac RF systems are critical in determining the energy and energy spread of the electron beam; for example, a requirement for 0.01° phase stability for a 1.3 GHz cavity is equivalent to $\sim$20 fs in timing phase. The timing of optical laser pulses may be influenced by systems distributed across a path of $\sim$10-100 m connecting laser oscillator to X-ray interaction point.

Collectively, these accelerator and laser systems must be synchronised across a km-scale facility. At the speed of light, single-femtosecond synchronisation is equivalent to controlling path length variation (in air/vacuum) to 3 µm. This level of control in the face of numerous physical perturbations is an intense technology and engineering challenge.

The design approach to synchronisation, as used at current XFELs and to be employed on UK XFEL, can be conceptually split into:

- Passive stabilisation and isolation of noise sources from critical systems, as far as possible, via appropriate engineering.

DRAFT

- Active stabilisation of systems using a common high-precision timing reference - referred herein as Reference Oscillator (RO). Multiple systems (e.g., lasers, RF) are synchronised to the RO and are therefore synchronised to each other. This is complicated by the frequency bandwidth of the active stabilisation, which often varies between systems and leads to relative jitter.

- Compensation of any remaining remaining drift via active feedback and/or feed-forward.

- Direct and independent measurement of any residual variation in pump-probe delay time allowing data sorting to be performed.

In Section 11.2 we break down the XFEL synchronisation architecture into key systems, making reference to the current state-of-the-art and identifying where a gap to UK XFEL requirements exist. We outline the related requirements for event timing in Section 11.3, which interfaces with many of the same facility systems as the synchronisation architecture. Consideration to environmental sustainability is made in Section 11.4. Finally, we outline R&D priorities for UK XFEL to achieve its performance targets in Section 11.5.

11.2 Synchronisation architecture

The principle components of an XFEL synchronisation architecture are shown in Figure 11.1 and described below.

- An ultralow noise RO, which serves as the facility's reference clock

- Distribution of the clock (either directly or via locking of local oscillators) to client systems, with low additive noise and stabilised against environment drift

- Client locking with low additive noise

- Feedback on the electron beam and optical laser time-of-arrival via direct measurement using arrival monitor systems

- X-ray arrival time measurement at each instrument relative to either the clock and/or optical laser system, with the potential for time-sorting

At each level of the architecture, design and technology choices are informed by balancing the need for high availability and performance against local constraints (e.g., budget, environment, facility length, target up-time, complexity, etc.) [1].

As will be discussed, the combination of single-femtosecond stable clock distribution and client locking, with sub-femtosecond resolution arrival time measurement (both of the electron beam, and X-ray photons), is currently the most viable route to achieving the Next Generation synchronisation requirements.

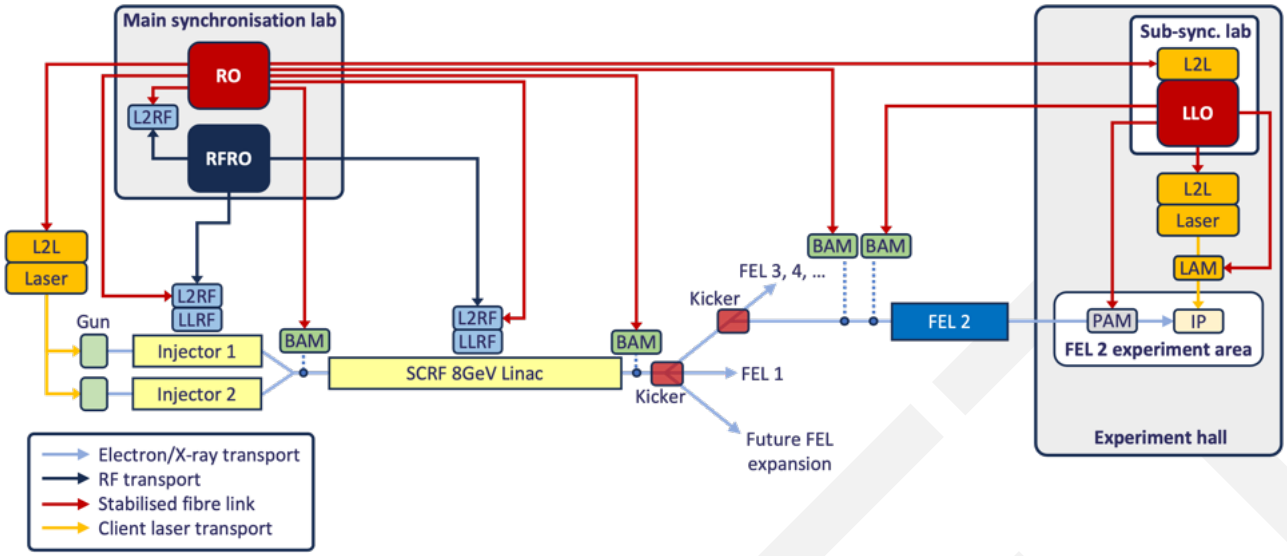

Figure 11.1: Example XFEL synchronisation architecture, as applied to the UK XFEL concept. This figure is for illustrative purposes only and does not reflect a final design decision. ORO: Optical Reference Oscillator; RFRO: RF Reference Oscillator; LLO: Local Laser Oscillator; L2L: Laser-to-Laser synchronisation; L2RF: Laser-to-RF synchronisation; BAM: Beam Arrival Monitor; PAM: Photon Arrival Monitor; IP: Interaction point (laser and X-ray).

11.2.1 Reference oscillator

The RO is the facility's primary timing reference and generates a continuous wave RF signal. All facility subsystems must operate at either a harmonic or sub-harmonic of the RO frequency (and therefore each other) to remain continuously synchronised.

The quality of the RO as described by its phase noise is key in determining the overall synchronisation performance of the facility. Each client system within the synchronisation architecture locks to the RO either directly or via the output of a link. Within the locking bandwidth the client system is typically capable of following the clock with high precision, whereas 'out-of-loop' the noise of the client and clock are uncorrelated. This locking bandwidth varies by client system.

For single-femtosecond synchronisation, it is advantageous to minimise the phase noise of the RO, as it minimises in turn:

- The absolute noise of the client systems following the clock within their locking bandwidth
- The residual noise of client systems with respect to the clock out-of-loop
- Following from the points above, the relative noise of client systems via varying relative locking bandwidth

Long-term phase drifts of the RO such as those induced by imperfect environment control leading to increased phase noise at low offset frequencies ($<$1 Hz) can be mitigated by locking the crystal oscillator to a Rubidium or GPS-disciplined signal.

RF Reference Oscillators (RFROs) are highly reliable, capable of operating 24/7 for prolonged periods of time without maintenance. Alternatively, an optical reference oscillator (ORO) can be used as a clock reference, which is achieved by locking a laser oscillator to the RFRO at a harmonic of the RO frequency. OROs are commercially available with high reliability but have a finite lifetime ($\sim$10 000 hours) before major intervention is required. The ORO will follow the phase noise of the RFRO within its locking bandwidth.

The absolute phase noise of the ORO is important for the same reasons as outlined above for the RFRO. Fibre lasers based on soliton mode-locking are used to maximise the stability of the ORO output, particularly at high offset frequencies ($>$100 kHz to 10 MHz). The performance in this regime dictates the accuracy of several clock stabilisation schemes as described in Section 11.2.2 via the relative timing jitter between successive laser pulses in the pulse train. Timing drifts of the ORO can be mitigated by locking the ORO to an RFRO, which has improved performance at low offset frequencies.

The European XFEL 1.3 GHz RO is derived from a GPS-synchronised oven-controlled 9 MHz crystal oscillator [2]. Disciplining the oscillator to the GPS clock improves the stability of the oscillator at very low frequencies. Improvements made over the last decade have reduced the integrated timing phase jitter of the oscillator to $<$2 fs (integrated, 100 Hz to 10 MHz). This technology was developed in cooperation between DESY and the Warsaw University of Technology (WUT) and is available commercially via KVG [3]. The LCLS-II phase reference line (PRL) [4] RO is based on a Wenzel 162.5 MHz RFRO disciplined by a Rubidium standard, multiplied to 1.3 GHz and achieving 12.3 fs integrated timing phase jitter (10 Hz to 10 MHz) [5].

The European XFEL ORO is based on a commercial fibre laser oscillator provided by Menhir, generating 1550 nm pulses at $\sim$200 MHz and $\sim$10 fs integrated (10 Hz to 10 MHz) phase noise [6]. Multiple OROs are used simultaneously to provide redundancy in operation and improve overall system up-time.

11.2.1.1 Recommendations

The European XFEL RFRO and ORO configuration is state-of-the-art; for facility synchronisation to approach sub-fs precision, further improvements (e.g., lower overall integrated phase noise) could be explored during a technical design phase, including engagement with relevant commercial suppliers (KVG, Menhir) along with experts from other XFEL facilities.

11.2.2 Stabilised clock distribution

Client systems can be well over 1 km from the RO. Distribution of the clock to these systems requires special consideration in order to preserve the quality of the clock and maintain synchronisation of systems across the facility.

There are three principal methods for clock distribution, each with varying performance and cost factors:

1. RF over coaxial distribution
2. RF over optical fibre distribution
3. Pulsed optical fibre distribution

11.2.2.1 RF over coaxial distribution

Distribution of the (RF) clock over coaxial cable is simple, robust and inexpensive compared to other techniques listed below. Signals are subject to attenuation during distribution and must be restored prior to application. A local oscillator (LO) can be locked with high precision via phase-locked loop (PLL) to the distributed clock. This must be performed carefully as to not add significant noise to the LO. The LO may be at a harmonic/sub-harmonic of the clock depending on the client.

The principle disadvantage of coaxial distribution is the sensitivity to changes in environment. Coaxial cable designed for high thermal stability can still generate temporal phase drift of ∼10-100 fs/°C/m [7]. Minimising drift for cable distributions in excess of 100 m requires precise control of the environment along the full length of coaxial distribution.

PAL XFEL utilises a specially designed cable distribution system in which the coaxial cable is transported along a foam insulated, water-cooled conduit. This provides damping to vibrations and utilising feedback on the temperature of the water circuit. The daily peak-to-peak temperature variation of these RF links has been measured to be 0.08 °C in the 100 m long SX undulator section, and 0.01 °C in the 90 m SX experimental hall [8]. PAL XFEL has demonstrated <20 fs rms timing jitter (measured over 3 minutes at 10 Hz) [9] and 1 ps PTP drift over 24 hours between X-ray and optical laser sources [7].

11.2.2.2 RF over fibre distribution

An alternative approach to coaxial cable is to use optical fibre to distribute the clock signal. So-called RF-over-fibre (RFoF) utilises amplitude and frequency modulation of a CW laser to encode the RF clock into an optical signal, delivered through optical fibre. Optical fibre at telecommunications wavelength (∼1550 nm) is both low loss and demonstrates higher thermal rigidity (40 fs/m/K), making it less sensitive to environmental changes.

Additive jitter of the order 10 fs is possible (as a function of link length) [10], although drift compensation at this level requires special techniques. RFoF has the advantage of being robust, with relatively low cost (compared to pulsed optical fibre distribution) and ease of operation.

RFoF is supplied commercially by vendors including Cycle Lasers [11] and Instrumentation Technologies (iTech) [12]. Cycle originated as a technology spin-off from DESY. The iTech Sync3 systems were developed in collaboration with the Paul Scherrer Institute (PSI) [10] and have a maximum link length of 1.5 km; longer links are possible but require environmental stabilisation.

SwissFEL (operated by PSI) uses iTech RFoF to provide the RF reference to the linac systems, achieving 23 fs peak-to-peak drift over 24 hours, and 3.8 fs rms (10 Hz to 10 MHz) timing jitter [13].

LCLS currently uses Cycle RFoF to transport the RO over 3 km from the photoinjector to the experiment halls where laser systems are located [5]. The measured additive jitter of the Cycle RFoF link has been measured to be 100 fs rms (1 Hz to 10 MHz) [14]. Due to the long accelerator length (3 km) and large temperature changes during the diurnal cycle which can approach ∼20 °C, the temporal phase drift of LCLS is ∼800 ps; this phase variation is beyond the performance capability of the Cycle system and recent efforts to address this have been made [14]. Pulsed distribution (see below) delivered by Cycle is used for distributing the RO locally within the experiment halls.

11.2.2.3 Pulsed optical fibre distribution

The highest performance clock distribution is achieved using optical pulses delivered along optical fibre. This requires an ORO (Section 11.2.1) and compared to previous methods, a comb of multiple frequencies is transported, with each harmonic of the comb locked to the other via mode-locking. A pulsed link can therefore be used to supply multiple sub-harmonic client systems simultaneously without the need for frequency conversion.

The length of each fibre can be actively stabilised by sampling and correcting for changes in transit time using non-linear optics, with sub-fs accuracy possible [15].

The round trip time for a $\sim$1 km long fibre is of µs in duration, meaning the return pulse cannot be compared with a direct copy of that which entered the fibre. As a result, any pulse-to-pulse timing jitter over the time range of interest will couple into the measurement of round trip time. This is one reason why the absolute noise of the ORO must be minimised, particularly at high offset frequencies (1 µs$\rightarrow$1 MHz offset frequency).

Depending on the link length and coupling losses, maintaining sufficient intensity may require dispersion compensation (possible at 1550 nm) and re-amplification. For optimum performance and enhanced modularity, it is preferable to use a constant length for all fibres throughout the facility; this fixes the round-trip time and therefore the bandwidth of the link stabilisation.

The disadvantage of pulsed distribution is increased cost and complexity in operation of the associated equipment, and specialised skills to perform maintenance.

Pulsed distribution has been developed and refined by DESY with applications on FLASH and later European XFEL. In-loop integrated timing jitter of 2 fs (10 Hz to $\sim$100 kHz) for a 3 km link has been demonstrated [16], with the residual noise between two consecutive link outputs measured to be as low as 700 as [1]. Cycle Lasers [11] offer solutions for full pulsed optical distributions, including ORO, pulsed links and client locking.

11.2.2.4 Hybrid approaches

It is common for an XFEL facility to deploy a combination of multiple distribution systems based individual system requirements and local operational requirements.

European XFEL combines both pulsed optical and RF over coaxial distribution to provide clock signals to the superconducting linac. The coaxial distribution is used to seed the low-level RF (LLRF) directly, ensuring high reliability of operation. To address phase drift, the output of the coaxial is re-synchronised to the output of a stabilised pulsed link [17]. These systems combine to provide a high reliability, high stability distribution. Should the pulsed optical link fail, the corresponding RF station will continue to operate from the coaxial distribution, albeit with increased temporal drift (500 fs during operation) [1].

PAL-XFEL use a combination of a temperature stabilised RF coaxial distribution for the normal conducting linac, with RFoF for laser clients. Photon arrival monitors (Section 11.2.5, below) are used to compensate for variation in x-ray arrival time with respect to instrument optical lasers, achieving 21.5 fs rms arrival time stability measured over three hours [18].

SwissFEL use a combination of pulsed optical distribution and RFoF. Pulsed distribution is used to seed BAMs, lasers and an X-band RF station on the linac; RFoF is used to seed the normal conducting S-band linac. This provides a combination of high performance (to the systems that need it most), high availability matched to resource constraints [13].

11.2.2.5 Recommendations

A hybrid distribution incorporating pulsed distribution and combined with coaxial distribution for RF systems – as currently deployed at European XFEL – is recommended. Improvements as compared to the state-of-the-art should be explored to achieve attosecond performance, including those listed in Ref. [19]. This includes gains in ORO performance (overall lower absolute phase noise) and increased sensitivity (and therefore improved temporal resolution) in cross-correlation techniques for round-trip-time measurement. The experience of European XFEL (and projected forward by a decade) demonstrates that this technology is suitably robust and reliable to support facility operations.

Engineering improvements could include transporting cable (both optical and coaxial) in temperature and vibration-insulated trunking, similar to as used on PAL XFEL; this would minimise external perturbations, potentially allowing high resolution locking via reduced range. It is critical that environmental stabilisation is applied along the full length of distribution; this includes both local distribution on small length scales within racks and rooms, to distribution over long lengths including the main linac. Even a small length of cable (fibre or otherwise) which is out-of-loop has the potential to compromise the performance of the network.

11.2.3 Client locking

Different client systems (lasers, RF) can be locked to the distributed (stabilised) clock with femtosecond precision. The technique used is a function of the clock type (RFRO, ORO) and client system.

11.2.3.1 Laser-to-RF locking

Laser-to-RF (L2RF) locking is required for client locking of optical lasers to an RF clock, and client locking of low-level RF (LLRF) systems to an optical clock. Direct conversion of signals from the optical to the RF domain using a photodiode and bandpass is conceptually simple, but effects such as amplitude-modulation-to-phase-modulation [20] and the sensitivity of coaxial cables and RF components to changes in environment (300 fs/K) [21, 22] limit performance. Highest performance levels are achieved by measuring the relative laser-RF phase information in the optical domain as part of a phase-locked loop (PLL) with a local voltage controlled oscillator. This can be achieved using an electro-optic intensity modulator (EOM) based on lithium niobate ($LiNbO_3$) EOM [23].

L2RF locking is used at PAL XFEL to synchronise Ti:Sapphire oscillators used for multiple laser systems to an RF clock, including the injector and experiment lasers, with residual jitter of 14 fs over the bandwidth 1 Hz-100 kHz [7].

EOM devices are used in optical reference modules (REFM-OPT) that synchronise the 1.3 GHz RF clock to the 1550 nm optical clock signal at European XFEL and other experiments at DESY [24]. An integrated in-loop jitter of 4.1 fs over the bandwidth 1 Hz-125 kHz has been achieved [17]. Electro-optic phase detection is also used at European XFEL to directly synchronise the ORO to the RFRO, with an out-of-loop RMS jitter of 2.7 fs (10 Hz-100 kHz) achieved.

11.2.3.2 Laser-to-laser locking

Laser systems are locked to a facility's ORO using either direct conversion or all-optical techniques. The highest performance laser-to-laser (L2L) locking is achieved through balanced optical cross-correlation (BOXC). Sensitivity to timing fluctuations on the order of 1 mV/fs has been demonstrated, three orders of magnitude greater than direct conversion techniques [25] and readily-capable of achieving single-fs performance [16, 26].

One-colour BOXCs (where the optical clock and laser subsystem pulses have the same wavelength) are used in European XFEL to synchronise the local laser oscillator (LLO) with an integrated rms timing jitter of 1.25 fs over the bandwidth of 10 Hz - 10 MHz [27]. One-colour fully fibre-coupled BOXCs have been developed and tested at DESY. A sensitivity of 16.72 mV/fs has been achieved, over 100 times more sensitive than a comparable free-space coupled BOXC with an integrated noise floor of around 20 as over the bandwidth 1 Hz-4 MHz [28].

Two-colour BOXCs are used to lock laser systems of different wavelength and can achieve a sensitivity of 6.31 mV/fs [29]. Systems developed for SHINE for locking the injector laser to the ORO have demonstrated 8.7 fs rms timing jitter (1 Hz-10 MHz) and 1.2 fs drift [30]. A two-colour BOXC is used to monitor drifts of the photocathode laser pulses after the pre-amplifier with respect to the ORO [31].

11.2.3.3 Recommendations

For femtosecond-level synchronisation at a Next Generation XFEL facility, optical techniques for L2RF and L2L locking are recommended. This technology is available commercially (Menlo, Cycle), although many facilities currently use in-house for their lower costs, easier maintenance, and potentially greater performance particularly when concerning possible upgrade pathways. As such, as part of a future technical design phase, it is recommended to assess the status of commercial technology at that time and perform a cost-benefit analysis. In addition, as a path to potential sub-fs performance, fully fibre-coupled optical techniques for L2L locking should be explored, as well as methods for mitigating environmental fluctuations to minimise sources of timing jitter and drift.

11.2.4 Arrival time measurement and control

Arrival monitors are timing diagnostics used to measure the arrival time of the electron bunches and laser pulses with respect to the facility RO or ORO. Data from arrival monitors can be used to both monitor and actively stabilise the arrival time at different points in an XFEL facility.

11.2.4.1 Bunch arrival monitors (BAM)

Bunch Arrival Monitors (BAMs, also referred to as Beam Arrival Monitors) are used to detect the passage of a charged particle beam with respect to the facility RO or ORO. For simplicity, we focus on BAMs which which utilise an ORO due to improved performance levels.

A pulsed electronic signal generated from the passage of a particle beam is generated using a high-bandwidth RF pickup; the relative time of this pulsed signal is then compared against the ORO reference using an electro-optic modulator.

To maximise the sensitivity of the BAM, the gradient of the RF pulse generated by the pick-up should be as large as possible for the operating charge of interest. The RF design of the pick-up is a critical factor and should maximise the sensitivity to the pick-up at the target charge while retaining as high bandwidth as possible. This may present complications to this facility concept, in which successive bunches in the linac could originate from different injectors, with different charges.

ASTeC has explored different pick-up designs as part of BAM systems implemented on the CLARA accelerator [32], with a solution developed and provided by DESY based on a cone-shaped pick-up finally implemented [33]. This device has a 40 GHz bandwidth, which (together with the electro-optic modulator scheme as described in Ref. [23] is capable of achieving 3 fs single-shot arrival-time resolution at 250 pC and 6 fs resolution at 100 pC [34].

DESY, in collaboration with THM, KIT and HZDR, are working on the design of a high sensitive, high bandwidth RF pick-up theoretically capable of achieving 1 fs resolution at 1 pC [35]. Tests of this device at the future RUEDI electron diffraction instrument at STFC Daresbury Laboratory have been proposed; RUEDI diffraction will routinely operate at sub-pC charges and seeks to achieve 10 fs pump-probe resolution in combined laser-electron experiments [36].

Within the high energy beam transport, combining sections of dispersion (e.g., bunch compression) with a BAM allows the possibility of using feedback to stabilise variation in arrival time [37]. The linac low-level RF can be controlled to adjust the beam energy and therefore arrival time. The bandwidth of the controller and relative location of the BAM and RF station are key factors influencing feedback performance.

European XFEL and FLASH have combined the DESY BAM architecture with high-bandwidth (25 kHz) feedback capable of modulating the LLRF of the superconducting linac *within* the $\sim$1 ms burst, stabilising the arrival time after the second bunch compressor. This intratrain feedback requires 10 µs to stabilise (20 bunches within the burst) - the remainder of the bunch train can be delivered in a stable configuration to different undulators. With the feedback operational, European XFEL has achieved a record 3.3 fs beam stability, with 4-5 fs observed daily [34].

The electron beam arrival time influences the X-ray photon arrival time, as the generation of photons is linked to the passage of an electron bunch through an undulator. BAM can therefore provide some - but not complete - information on the estimated arrival time of X-ray photons at an instrument.

The combination of high precision clock distribution, beam arrival measurement, and arrival time stability, has allowed European XFEL to identify the influence of seismic activity which changes the arrival time of X-ray photons. X-rays are delivered to instruments over 3 km from the point of bunch stabilisation (bunch compressor 2); the physical distance between these locations can stretch and compress due to body waves within the earth, such as those generated from ocean waves [38]. This has been identified using systematic studies of BAM and photon arrival monitor systems, relying on the $<$1 fs stability of the stabilised clock distribution, and (in the case of ocean waves) results in 23 fs peak-to-peak drift of the X-ray instruments compared to the BAM used to stabilise the linac. European XFEL are investigating if feedforward control can be used to compensate for this variation, which requires suitable modelling work to be performed and the effect to remain predictable.

11.2.4.2 Laser arrival monitors (LAM)

Laser-to-laser (L2L) locking methods can allow for femtosecond-level synchronisation of an external laser oscillator to the stabilised ORO signal. However, the pulses from the oscillator will likely have to undergo several stages of chirped pulse amplification and frequency conversion to reach the desired pulse intensity and wavelength before being transported. This requires optical transport in air of the order of 10 m; this may increase to 100 m accounting for connections between the laser system and XFEL instrument. Subsequent timing drift can be measured using laser arrival monitors (LAMs), which measure the arrival time of pulses with respect to either the ORO or the source laser oscillator.

Laser pulses propagating in air are subject to timing drift with variation in environment properties including temperature (3 fs/K/m), pressure (0.9 fs/mbar/m) and humidity (0.3 fs/RH%/m) [39]. Laser propagation in air cannot be fully avoided, therefore necessitating careful control of the local environment in laser areas, although noting only temperature and humidity can be actively controlled.

Although independent of environmental factors, laser transport in vacuum is still subject to pointing-based variation in arrival time via changes in total path length. Measurements on FERMI have demonstrated this can be reduced to 4 fs rms through suitable engineering design, including transverse beam stabilisation [40]. The functionality of vacuum laser transport is however more limited due restrictions on the type of equipment which can be installed in vacuum, and increases maintenance complexity.

SwissFEL uses a one-colour BOXC as a LAM to stabilise drifts in the arrival time of the Yb:CaF_2 photocathode laser pulses. With the feedback from the LAM active, the rms jitter of the amplifier with respect to the seeding oscillator is measured to be 4.5 fs over the frequency bandwidth 2 mHz-100 Hz, and the rms jitter of the whole laser relative to the SwissFEL reference oscillator is 11 fs over the same bandwidth [41].

Laser arrival monitors for experimental lasers are currently being implemented at European XFEL and FLASH. A LAM based upon two-colour BOXC is used to compare the arrival time of the FLASH pump-probe laser pulses with the stabilised optical clock signal. With the LAM feedback active, the in-loop rms jitter and drift of the pump-probe laser pulse arrival time over 12 hours is measured to be 10 fs and $<$1 fs respectively, compared to 500 fs drift peak-to-peak without the LAM feedback [42].

Although standard two-colour BOXCs provide a sensitive measurement of relative arrival time, the phase-matching conditions of the non-linear crystal used in the BOXC limits the range of optical wavelengths that can be cross-correlated with the stabilised optical clock signal. For facilities such as UK XFEL that will utilise synchronous sources over a wide spectral range (from UV to mid-IR) for experiments, a large number of LAMs with different non-linear crystals would be required to measure the arrival time of the different wavelength external laser pulses. This would introduce additional complexity in either diverting the external laser pulse to the correct LAM based on its wavelength or swapping LAMs based upon the experiment.

DESY are currently developing non-collinear, two-crystal BOXCs as shown in Figure 11.2 where each non-linear crystal is housed on a rotation mount. This utilises non-collinear phase-matching to achieve conversion over a much wider range of wavelengths [43]. The UK XFEL team have been assisting in the initial prototyping of these devices at FLASH.

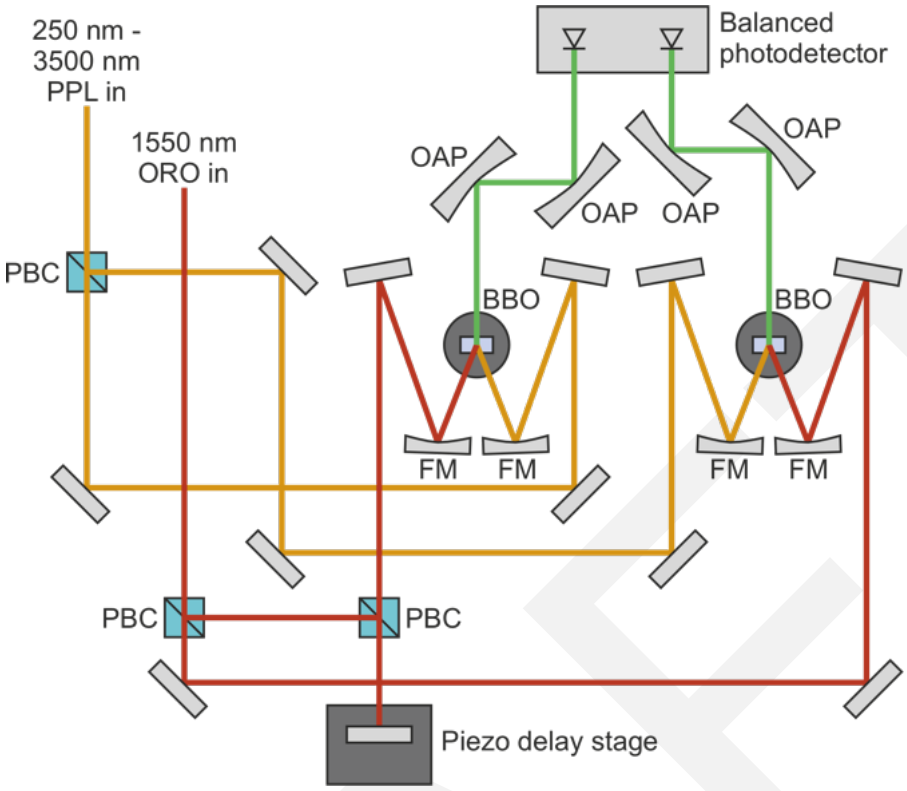

Figure 11.2: Layout of the non-collinear, two-crystal BOXC being developed at DESY for use as an all-colour LAM. PPL: Pump-probe laser; ORO: Optical reference oscillator; PBC: Polarising beamsplitter cube; FM: Focusing mirror; BBO: Barium borate non-linear crystal; OAP: Off-axis parabolic mirror. Figure printed with DESY permission.

11.2.4.3 Recommendations

Arrival monitors will be essential systems on a Next Generation XFEL. As discussed above, even with excellent engineering the influence of timing drift cannot be fully mitigated, particularly at the femtosecond level. Arrival monitors employed as part of a control loop are required to achieve single-femtosecond stability and meet performance requirements for both particle beam and laser systems.

The excellent result of beam-based stabilisation on European XFEL is based, in part, on the burst mode structure (4.5 MHz in ∼1 ms long bursts). The implication of continuous-wave (CW) stabilisation, at potentially lower frequencies (∼100 kHz) is one of several topics under investigation as part of the European XFEL High Duty Cycle Upgrade; we recommend UK XFEL monitors the outcome of that process closely, and is ideally integrated into both early discussions and R&D activities to transfer learning to UK XFEL.

For particle beam stabilisation, there are two major complications to this originating with the Next Generation concept, which should be explicitly addressed in a future technical design phase:

1. The baseline concept is based on two photoinjectors, each operating at ∼500 kHz and interleaved to generate a ∼1 MHz CW bunch pattern.
2. Each photoinjector will be configured to meet the requirements of specific FELs, and therefore may operate in different parameter regimes (e.g. charge, which may different by a factor of two: 75 pC/150 pC, etc.).

Regarding (1), even if identically designed and utilising the same technology, the two injectors will be subject to independent physical perturbations, resulting in non-common noise between

interleaved bunch 'trains'. The injector includes some temporal compression, as part of the merge of the injector into the main high energy linac; this presents the possibility of using a BAM to stabilise each 500 kHz bunch train independently prior to recombination.

Additional control systems would be required to compensate for noise in the 1 MHz beam on the high energy linac, and could utilise BAM systems situated after each of the three bunch compressors. Detailed study is required to evaluate associated performance factors. A complete beam jitter tolerance study will be required, including the performance requirements of the linac (amplitude, phase stability) and FEL modes.

Bunch parameter regimes for each photoinjector as described in (2) can only be confirmed in a final design phase. A final solution could either require a compromise in the performance of a single BAM (e.g., optimised at one charge point only, and therefore degraded at the other), or multiple BAM systems at the same location, separately optimised to the beam parameters of each injector, with logic to isolate the relevant signals of interest. This would again require dedicated R&D.

BAM systems located on each undulator line, in conjunction with PAM systems (Section 11.2.5), could be used to monitor drift (e.g., that associated with environment or seismic effects) on each individual FEL, with compensation implemented though control of the relative delay of synchronous sources, e.g. using feedforward methods. It is critical that as much of the facility is brought 'in loop' as possible, and it is recommended that BAM systems are placed as close to the undulators as possible. For the same reason, PAM systems should be placed as close to each instrument interaction point as possible.

Likewise, R&D into advanced LAM system should be prioritised. This includes the availability of the LAM at multiple user wavelengths (as opposed one-colour configuration, which is typically implemented at the exit of the laser amplifier), continuing to work in collaboration with DESY on all-colour BOXC technology. It also includes close integration into the design of the XFEL instruments, such that the laser arrival time can be measured as close to the instrument's interaction point as possible.

This could incorporate developments as pursued at LCLS, including the 'DART' concept [44] in which X-ray photon arrival monitors based on a fixed-wavelength are compared against the an optical laser of varying wavelength using an all-colour LAM – see Figure 11.3.

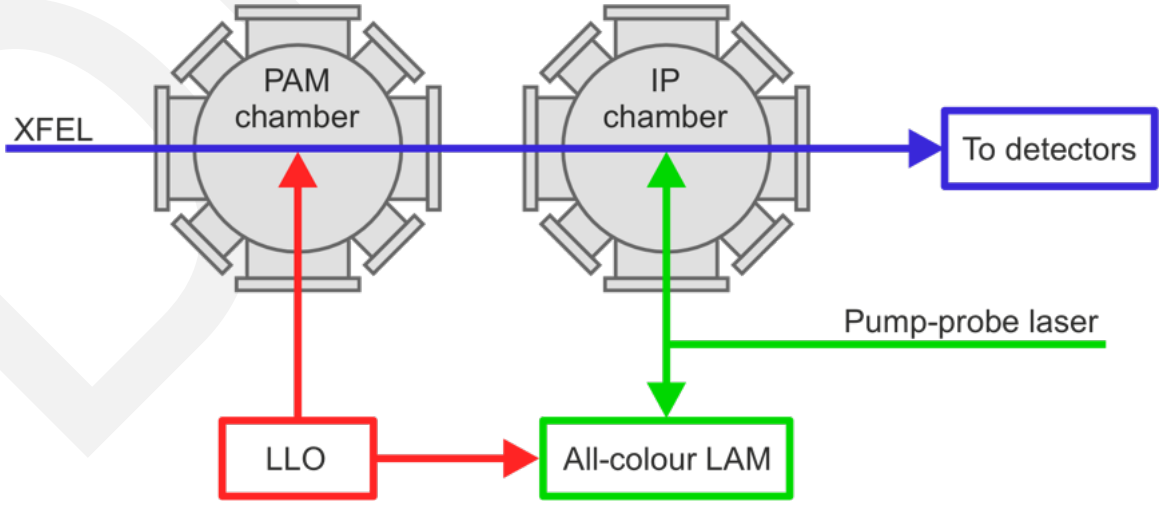

Figure 11.3: Hold: DART concept [44], employing an all-colour LAM as close to the interaction point as possible. LLO: Local laser oscillator; LAM: Laser Arrival Monitor; PAM: Photon Arrival Monitor; IP: interaction point.

11.2.5 X-ray photon arrival monitors

The most direct measurements of the arrival time of X-ray beams are made by Photon Arrival Monitors (PAMs). PAMs compare the X-ray beam delivered to an instrument to an optical reference to derive a signal dependent on relative arrival time. This allows data from a pump-probe experiment to be sorted by expected arrival time, removing the impact of timing drifts and improving the effective temporal resolution of the instrument [45].

The reference utilises an optical laser, which could either be a pick-off of the experiment's pump laser, or optical clock reference (e.g., LLO, as shown in Figure 11.1). The X-ray and optical parameters, and the location at which they are measured, should be as close as possible to the instrument IP in order for the measurement and associated time-sorting to most accurately reflect the condition of the experiment. This is non-trivial to achieve in practice; for example, it may not be possible for the PAM to operate at all optical wavelengths as delivered to the instrument. It is also not possible for the PAM to share the same physical location as the experiment, and therefore non-common elements (e.g., optical transport to a down- or up-stream location) may introduce spurious timing noise. An illustration of an instrument including a PAM and experiment chamber (IP) is shown in Figure 11.3.

PAM systems must operate shot-by-shot and multiple techniques have been demonstrated on existing XFEL facilities including LCLS and European XFEL. Detail on notable PAM methodologies is provided below.

11.2.5.1 Spectral encoding

Spectral encoding utilises a chirped optical reference with a know time-frequency correlation [46]. The optical reference and X-rays are combined in an nominally optically transparent sample; the X-rays induce a change in complex refractive index, which in turn modulates in the optical spectrum which is then measured shot-by-shot. Knowledge of the time-frequency correlation can be used to extract the relative arrival time of the X-rays; the chirp rate can be adjusted to change the temporal range and resolution.

Spectral encoding is used as a standard diagnostic on LCLS [47] and European XFEL [48, 49]. Data published from European XFEL has demonstrated time-sorting on the SQS instrument using gas (Neon) as a mixing medium, demonstrating a typical sorting accuracy of 15 fs [49]. Spectral decoding has also been used to measure megahertz-rate timing jitter of (24.0 ± 12.4) fs using solid (Ce:YAG) samples on the SPB/SFX instrument [50]. The SPB/SFX utilises both 800 nm and 1030 nm for optical pumping [51], although it is unclear which was used as a reference in [50].

11.2.5.2 Spatial encoding

For spatial encoding, either the reference light or the X-ray beam is directed at an angle relative to the sample [52]. As shown in Figure 11.5, the time-of-arrival of the optical reference relative to the incident X-rays is a function of transverse position and set by the incident angle. Similar to as discussed in spectral decoding, the modulation in complex index induced by the X-ray beam results in a modification of the optical reference, e.g. an intensity modulation, which can be detected using a camera.

In [52] spatial encoding was used to measure the time-of-arrival of the LCLS beam and improve the pump-probe experiment resolution from 280 fs (FWHM) to 130 fs (FWHM). As shown in

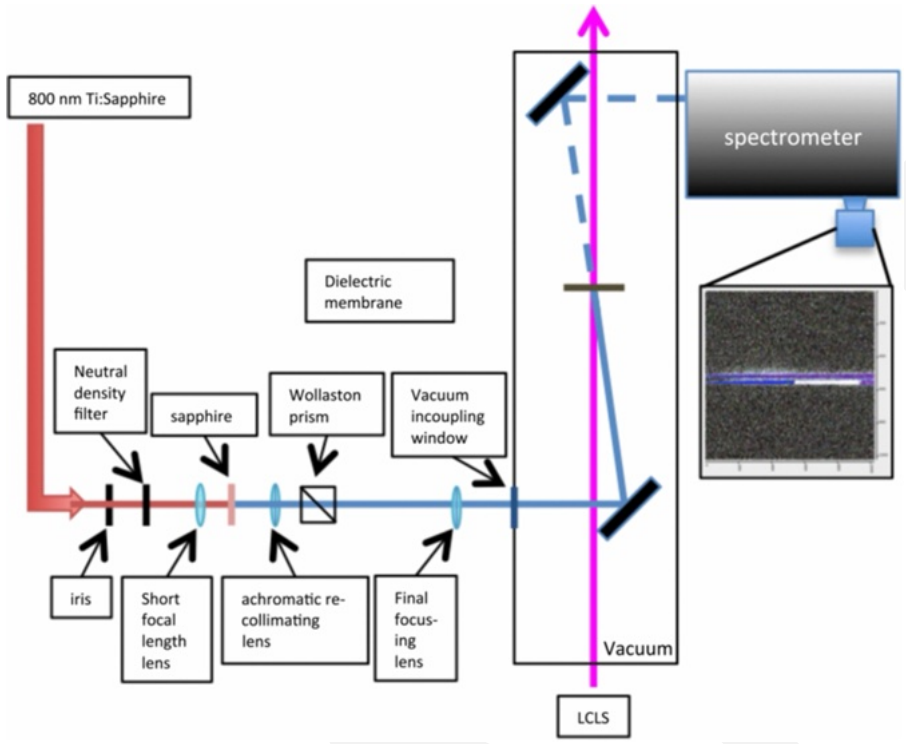

Figure 11.4: Experimental geometry of spectral decoding used at LCLS, as presented in [47]. A broadband chirped optical super-continuum is mixed with the LCLS X-ray beam in a semiconductor membrane and the spectrum measured using a spectrometer with CCD camera.

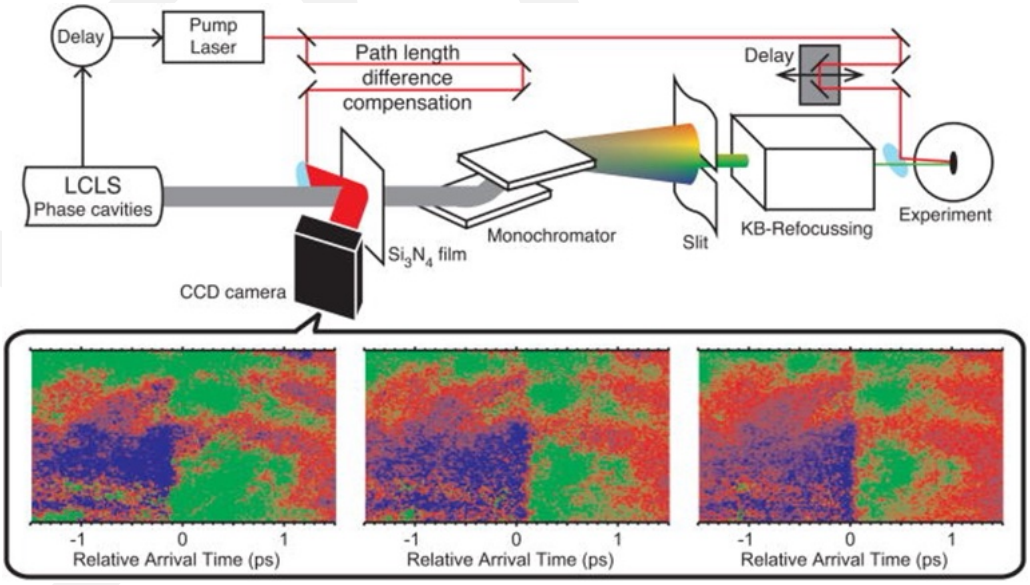

Figure 11.5: Experimental setup of spatial encoding at LCLS, as presented in [52]. The LCLS beam (grey) impinges on a thin Si_3N_4 film prior to travelling through the monochromator. An optical reference was derived using a pick-off of the laser pulse directed to the experiment IP, with suitable path length matching. Typical camera images of the optical laser reflected from the film after background subtraction are shown at the bottom. The relative arrival time jitter is mapped onto a spatial coordinate on the camera (here already converted to time).

Figure 11.5, the arrival monitor was located upstream of the experiment IP and utilised a 200 nm-thick Si_3N_4 film with 80 % transmission. This was located prior to the monochromator used in the experiment, which subsequently attenuated the X-ray beam intensity by two-to-three orders of magnitude.

The X-ray intensity, subsequent transmission to the experiment IP, and non-common elements between the monitor and the IP are all key factors to be considered in the design and implementation of an X-ray arrival time diagnostic, and such consideration should be merged into the overall instrument design.

Research has been performed at SLAC into novel materials and detection schemes which could improve the temporal resolution of encoding techniques towards sub-10 fs. Droste *et al.* [53] reports the application of interferometric detection in a spatial encoding scheme, combined with a multi-layer (etalon) structure. This structure was designed to enhance the reflectivity change at the optical reference wavelength (1550 nm). This technique allows for detection of extremely weak X-rays, or equivalently a significant improvement in temporal resolution: an estimated temporal resolution of 2.8 fs was achieved for 1.6 mJ/cm^2 soft X-rays (530 eV).

11.2.5.3 Electron streaking

Electron streaking exploits X-ray photoionisation of gas molecules and the subsequent interaction of ionised electrons with the electromagnetic field of an optical (or THz-frequency) reference [54]. Depending on the amplitude and phase of the optical reference, the photoelectrons are either accelerated or decelerated, with the momentum change measured using a time-of-flight (TOF) detector.

In common streaking applications, the optical field is linearly polarised, and the X-ray pulse is set to be coincident with the greatest gradient in the field to maximise temporal resolution (at the field zero-crossing position). This results in an approximately linear correlation between momentum and time-of-arrival, allowing both temporal information (duration, etc.) of the X-rays to be measured via the width of the momentum distribution, and the time-of-arrival via the centroid.

If the phase of the field relative to the X-rays varies outside of the zero-crossing regime, the linear correlation is lost and resolution degraded. This is a particular challenge when the relative temporal jitter is high. To address this, LCLS have developed a so-called ‘attoclock’ in which a circularly polarised streaking field is used [55]. This has the advantage of combining high temporal resolution with long temporal range, with the electrons deflected over a range of angles which can be mapped to time. Resolving the momentum changes is performed using bank of TOF detectors in a clock arrangement, allowing both the temporal profile and arrival time to be reconstructed from the data acquired. Using a 10.6 μm optical field, Hartmann *et al.* measure an arrival time jitter of 51 fs FWHM (15 minute period) with an estimated arrival time resolution of 2.5 fs.

11.2.6 Recommendations

As demonstrated in results such as [55] and [53], the current state of the art timing resolution for PAMs is of the order 1 fs, which is a factor of ten above the Next Generation performance target of synchronisation/timing of external lasers to $<$1 fs. Furthermore, these results represent only a snap-shot of possible experiment requirements, which may individually constrain the selection of external laser, X-ray photon energies and intensities; UK XFEL could need to review and consider this performance target across a broad range of configurations, adding additional complexity.

Before entering this process, the PAM requirements for each instrument should be identified, as it is not expected that every instrument will require the same target temporal resolution, and therefore (as above) the range of X-ray and optical parameters (as relevant to $\leq$1 fs timing may be more specific.

Future R&D activities along three broad tracks are recommended:

1. Increasing the compatibility of PAM systems with a broad range of optical laser sources, as matched to experiment requirements. This could consider both efforts to develop compatibility of a single PAM device with a wide range of optical synchronous sources at different wavelengths, or – as part the Direct Arrival Time (DART) concept under investigation by LCLS [44] – development of a fixed optical reference wavelength PAM, with comparison of that wavelength to the synchronous source via optical cross-correlation.
2. Improving the sensitivity of PAM sources via design of cross-correlation samples, utilising multi-layer structures as described in [53] and optimised to a wide range of experiment configurations. This research should also take into account compatibility of the samples with the high repetition rate and high average power of the UK XFEL concept.
3. Integrating PAM design into the design of the UK XFEL instruments, such that the placement and function of the device are as closely matched to the experiment IP as possible, and sources of non-common noise (impacting the X-ray and optical sources) between the PAM and IP are minimised as far as possible.

This is a specialised platform of work which will require STFC to collaborate closely with existing expertise. This includes UK researchers who are users of existing XFELs, on both instrument design and X-ray/optical interactions, and existing international X-ray facilities, including LCLS-II, European XFEL and DLS.

11.3 Timing

'Timing' is the provision of signals responsible for initiating or recording events across the accelerator facility. This includes:

- Triggering responsible for initiating different client systems at different times, including RF (e.g., signals to begin filling a cavity) and lasers (e.g., opening of a fast shutter)
- Generation of signals from accelerator systems based on pre-defined criteria or detected events (e.g., generation of a beam diagnostic signal)
- Distribution of interlock signals
- Clock distribution, as to be used in the digitisation of signals throughout the facility

The performance requirement for timing is less demanding than synchronisation, with picosecond and nanosecond precision suitable for applications.

An event timing system consists of a reference timing source distributed to multiple receivers using fan-out modules. The timing reference is driven by a divisor of the facility RO, and is capable of passing this clock to downstream devices. The timing reference can also be phase locked to the mains frequency, allowing the complete timing system to drift with variation in the mains frequency. This improves the stability of all systems which may be sensitive in changes in mains voltage.

Events are converted into square-wave electronic timing signals with variable delays and pulse widths and distributed to receiver clients. Event receivers are capable using these to initiate additional signals, generating further delay and changes in pulse width as required. They are also capable of comparing the information received from the timing reference to local events, such as those associated with beam diagnostics. This allows the output of multiple systems and accelerator settings associated with a single 'shot' to be compared and correlated in post-processing.

State-of-the-art event timing is based on micro-TCA (mTCA) industrial computing architecture, with relevant examples present at FLASH, European XFEL and CLARA. Commercial solutions based on this architecture are available from Micro-Research Finland and Safran. These systems can interface with established accelerator control systems including EPICS and TANGO. Transmitted and receiver units pass signals via optical fibre, and the units can employ link stabilisation to improve the temporal performance.

11.4 Sustainability

The overall goal of synchronisation systems, as described in Section 11.1, is to increase the precision of pump-probe experiments via passive and active mitigation of errors in timing. This potentially allows experiments to be performed more efficiently; more XFEL shots are 'on target' (in timing), and therefore less overall time is required to accurately map dynamical behaviour. This could improve overall facility efficiency (e.g., numbers of successful experiments performed for each day of operation).

This impact on experiment time is however small compared to the impact of overall machine repetition rate, and therefore the environmental factors associated with facility efficiency are expected to be driven by the systems linked to repetition rate (principally, the superconducting linac).

At the system level, we have not identified any design features or choices within the synchronisation system that could be influenced by sustainability concerns. In most cases, achieving the required level of performance dictates design choices to a narrow range, and choices within this range do not vary by environmental impact. For example: the choice of clock distribution, whether RFoF or pulsed, involves the use of similar fibre-doped laser oscillators and other fibre optic materials.

Achieving $\sim$1 fs synchronisation places requirements on the environmental control of areas housing electronic and optical systems, e.g. lasers room, instrument areas, electrical rack storage, etc. Although such control is typically associated with elevated power consumption requirements, it is not immediately clear what the impact associated with higher levels of performance specification will be, e.g. 0.1 K temperature control as compared with 1.0 K control, and the presence of active humidity control. Although the requirement remains, further analysis could be performed in a technical design phase to explore the most sustainable engineering solutions to support the required environment control. This should be merged into the responsibilities of an associated infrastructure work package during a technical design phase.

11.5 Summary of R&D recommendations

In order to meet the requirements of a Next Generation XFEL facility and meet the next generation requirement "Improved synchronization/timing data with external lasers to $<$1 fs", we propose the

following synchronisation architecture:

- A hybrid clock network (e.g., as utilised on European XFEL) incorporating both optical and RF distribution for laser and low-level RF clients respectively, with attosecond-precision stabilisation of the distribution via a pulsed network. With continuous technology improvement, (described below) this network should – as currently demonstrated [34] – be capable of routinely achieving single-femtosecond arrival time jitter performance.
- Active stabilisation of electron beam and laser time of arrival drift, using a network of BAMs and all-colour LAMs. These diagnostics should be placed as close to the instrument interaction points as possible, such that as many accelerator and laser systems are brought in-loop as possible. This is required to achieve single-femtosecond X-ray arrival time drift performance.
- PAM systems installed on each end station, providing a direct measurement of X-ray arrival time with respect to optical lasers used in experiments. Their design should be fully integrated into instrument design, with consideration given to target time resolution and the range of optical excitation conditions. This should be combined with BAM systems (installed as close to the undulators as possible) to explore a non-invasive diagnostic capable of providing measurement and feedback *if* a PAM is not compatible with a particular experiment.

As outlined through Section 11.2, further technology improvements are required within the architecture above. This includes improvements in the phase noise performance of RF and optical reference oscillators; engineering solutions for improved environment control across multiple levels (within equipment, rooms and cable conduits); improved sensitivity in laser client locking; high resolution, high sensitivity beam arrival monitors; and all-colour cross-correlation for laser arrival monitors.

A significant component should be reserved for control systems to stabilise timing drift, both for electron beam and laser systems. As to be evaluated in a future phase, this could be key in generating the $\sim$1 MHz linac electron beam through interleaving of two $\sim$500 kHz injectors, as proposed for the UK XFEL concept. The development of beam-based control for time-of-arrival stabilisation can draw concepts demonstrated successfully on European XFEL, but will need to take into account both the CW operation of each source and the lower (relative) frequency range as compared to the burst-mode currently deployed.

Synchronisation technology is increasingly available commercially; in particular, suppliers such as Cycle can be contracted to provide large fractions of the architecture described above, including reference oscillators, clock distribution and client locking. Based on discussions during this project, this approach is not currently recommended, although could be reconsidered in a future phase as the technology continues to mature. This is based on feedback from existing facilities, who have found it difficult to implement performance improvements, within a commercially supplied architecture. With dedicated and reserved development time, synchronisation teams of sufficient scale should have the scope to analyse and develop solutions to problems with greater freedom.

Accessing sub-femtosecond resolution fundamentally requires significant developments in PAMs to allow time-sorting of data. This is one of the larger research gaps identified in this conceptual design and should be prioritised accordingly. It requires advances in a range of fields, including materials research for high sensitivity X-ray/optical interactions, compatibility with a range of optical and X-ray parameters, and integration of PAM design explicitly into instrument engineering such that that diagnostic is as close as possible (both physically and in terms of experiment parameters) to the instrument interaction point as possible. This is key as any non-common optical

or X-ray path (including interaction) is likely to be subject to environment-induced temporal drift, which is very difficult to manage at a sub-femtosecond (sub-micron) level. This is a body of work which would benefit from the participation of the UK X-ray community, including existing XFEL users.

We highly recommend to continue collaborative activities with the relevant teams at DESY and LCLS who have been positively engaged through this project. The architecture proposed above largely follows that developed for European XFEL and FLASH, and as those facilities continue to operate we expect further improvements to be established. Activities performed as part of the European XFEL High Duty Cycle Upgrade investigation will be particularly relevant to UK XFEL, including beam stabilisation at $\sim$100 kHz continuous operation. Expertise at LCLS in the development of PAM systems ('time-tools') should be explored, including lessons learned from the operation of these devices on LCLS-II (and LCLS-II-HE) at CW high repetition rate.

Furthermore, we recommend broader collaboration with other facility synchronisation teams, as the challenge of achieving single-femtosecond performance is often dictated by unforeseen practical factors which can only be identified through experiments at working facilities. In addition to technology improvements, this level of practical skills development would be critical in any future facility achieving its performance targets.

DRAFT

References for Chapter 11

[1] Marie Kristin Czwalinna. *An Overview: Reference Distribution and Synchronization Systems, from Sub-picoseconds to Sub-femtoseconds Stability*. 2024.

[2] Bartosz Gacsowski et al. "Concept of Master Oscillator Upgrade for FLASH". In: *2020 23rd International Microwave and Radar Conference (MIKON)*. 2020, pp. 165–168. DOI: 10.23919/MIKON48703.2020.9253858.

[3] KVG. *KVG GmbH*. 2025. URL: https://kvg-gmbh.de.

[4] Shreeharshini Dharanesh Murthy et al. "Installation, Commissioning and Performance of Phase Reference Line for LCLS-II". 2022. URL: https://arxiv.org/abs/2210.05441.

[5] Bo Hong et al. "Phase reference line synchronization for LCLS-I and LCLS-II at SLAC". In: *Proc. 14th International Particle Accelerator Conference (IPAC'17), Venice, Italy*. Vol. IPAC2023. JACoW, Geneva, Switzerland, 2023, THPA069. DOI: 10.18429/JACoW-IPAC2023-THPA069.

[6] Menhir Photonics AG. *Menhir 1550 GHz*. https://menhir-photonics.com/menhir-1550/. Accessed 23.06.25.

[7] C.-K. Min et al. "RF Timing Distribution and Laser Synchronization Commissioning of PAL-XFEL". In: *Proc. 7th International Particle Accelerator Conference (IPAC'16), Busan, Korea*. International Particle Accelerator Conference 7. JACoW, Geneva, Switzerland, June 2016, pp. 4234–4236. ISBN: 978-3-95450-147-2. DOI: doi:10.18429/JACoW-IPAC2016-THPOY057. URL: http://jacow.org/ipac2016/papers/thpoy057.pdf.

[8] Minseok Kim, Chang-Ki Min, and Intae Eom. "Laser systems for time-resolved experiments at the Pohang Accelerator Laboratory X-ray Free-Electron Laser beamlines". In: *Journal of Synchrotron Radiation* 26.3 (May 2019), pp. 868–873. DOI: 10.1107/S1600577519003515. URL: https://doi.org/10.1107/S1600577519003515.

[9] Heung Sik Kang et al. "Hard X-ray free-electron laser with femtosecond-scale timing jitter". In: *Nature Photonics* 11.11 (Nov. 2017), pp. 708–713. ISSN: 17494893. DOI: 10.1038/s41566-017-0029-8.

[10] Instrumentation Technologies. *Libera Sync 3 Clock Distribution System*. 2025. URL: https://www.i-tech.si/wp-content/uploads/2023/07/it029_Libera_Sync_3_compressed.pdf.

[11] Cycle GmbH. *Cycle Lasers*. https://www.cyclelasers.com. Accessed 23.05.25.

[12] Instrumentation Technologies. *Instrumentation Technologies*. https://www.i-tech.si/. Accessed 23.06.25.

[13] S Hunziker et al. "Reference Distribution and Synchronization System for SwissFEL: Concept and First Results". In: *Proc. 3rd International Beam Instrumentation Conference (IBIC2014), Monterey, CA, USA*. JACoW Publishing, Geneva, Switzerland, 2014, pp. 29–33. URL: https://jacow.org/IBIC2014/papers/MOCZB2.pdf.

[14] C Xu. "LCLS II Precision Timing System". In: *2024 LLRF Topical Workshop, INFN-LNF*. 2024.

[15] Ming Xin et al. "Attosecond precision multi-kilometer laser-microwave network". In: *Light: Science & Applications* 6.1 (2017), e16187. ISSN: 2047-7538. DOI: 10.1038/lsa.2016.187. URL: https://bib-pubdb1.desy.de/record/317221.

[16] S. Schulz et al. "Few-femtosecond facility-wide synchronization of the European XFEL". In: *Proc. 39th International Free Electron Laser Conference (FEL2019), Hamburg, Germany*. JACo, Geneva, Switzerland, 2019, pp. 318–321. ISBN: 9783954502103. DOI: 10.18429/JACoW-FEL2019-WEB04.

[17] T Lamb et al. "Large-Scale Optical Synchronization System of the European XFEL with Femtosecond Precision". In: *Proc. 10th International Particle Accelerator Conference (IPAC'19), Melbourne, Australia, 19-24 May 2019*. International Particle Accelerator Conference 10. JACo, Geneva, Switzerland, June 2019, pp. 3835–3838. ISBN: 978-3-95450-208-0. DOI: doi:10.18429/JACoW-IPAC2019-THPRB018. URL: http://jacow.org/ipac2019/papers/thprb018.pdf.

[18] H Heo et al. "XFEL Performance Achieved at PAL-XFEL". In: *Proc. 10th International Particle Accelerator Conference (IPAC'19), Melbourne, Australia*. International Particle Accelerator Conference 10. JACo, Geneva, Switzerland, June 2019, pp. 1182–1184. ISBN: 978-3-95450-208-0. DOI: doi:10.18429/JACoW-IPAC2019-TUYPLM1. URL: http://jacow.org/ipac2019/papers/tuyplm1.pdf.

[19] F X Kärtner, K Shafak, and M Xin. "Attosecond Timing". In: *Proc. 60th ICFA Advanced Beam Dynamics Workshop (FLS'18), Shanghai, China*. ICFA Advanced Beam Dynamics Workshop 60. JACoW, Geneva, Switzerland, June 2018, pp. 79–84. ISBN: 978-3-95450-206-6. DOI: doi:10.18429/JACoW-FLS2018-WEA1PL03. URL: http://jacow.org/fls2018/papers/wea1pl03.pdf.

[20] M Currie and I Vurgaftman. "Microwave phase retardation in saturated InGaAs photodetectors". In: *IEEE Photonics Technology Letters* 18.13 (2006), pp. 1433–1435. ISSN: 1041-1135. DOI: 10.1109/lpt.2006.877552.

[21] C. Hoffman. *Temperature Dependence of Coaxial Cable Delay*. https://scipp.ucsc.edu/milagro/memos/hoffman052101.pdf. May 2001. URL: https://scipp.ucsc.edu/milagro/memos/hoffman052101.pdf.

[22] B Lorbeer et al. "Noise and drift characterization of direct laser to RF conversion scheme for the laser based synchronization system for FLASH at DESY". In: *2007 IEEE Particle Accelerator Conference (PAC)*. 2007, pp. 182–184. DOI: 10.1109/PAC.2007.4440152.

[23] Thorsten Lamb. "Laser-to-RF Phase Detection with Femtosecond Precision for Remote Reference Phase Stabilization in Particle Accelerators". PhD thesis. Hamburg: Technische Universität Hamburg Harburg, 2017, p. 174. DOI: 10.3204/PUBDB-2017-02117. URL: https://bib-pubdb1.desy.de/record/320841.

[24] T Lamb et al. "Design and Operation of the Integrated 1.3 GHz Optical Reference Module with Femtosecond Precision". In: *Proc. 8th International Particle Accelerator Conference (IPAC'17), Copenhagen, Denmark*. International Particle Accelerator Conference 8. JACoW, Geneva, Switzerland, May 2017, pp. 3963–3965. ISBN: 978-3-95450-182-3. DOI: https://doi.org/10.18429/JACoW-IPAC2017-THPAB105. URL: http://jacow.org/ipac2017/papers/thpab105.pdf.

[25] Kemal Shafak and F. Kärtner. "Large-scale laser-microwave synchronization for attosecond photon science facilities". PhD thesis. Hamburg: Universität Hamburg, 2017, p. 134. DOI: 10.3204/PUBDB-2017-01934. URL: https://bib-pubdb1.desy.de/record/320657.

[26] J Kim et al. "Long-Term Femtosecond Timing Link Stabilization Using a Single-Crystal Balanced Cross-Correlator". In: *Optics Letters* 32.9 (2007), p. 1044. ISSN: 0146-9592. DOI: 10.1364/ol.32.001044.

[27] J M Müller et al. “Large-Scale Optical Synchronization System of the European XFEL”. In: *Proc. 29th Linear Accelerator Conference (LINAC'18), Beijing, China, 16-21 September 2018*. Linear Accelerator Conference 29. Geneva, Switzerland: JACo, Geneva, Switzerland, Jan. 2019, pp. 253–256. ISBN: 978-3-95450-194-6. DOI: doi:10.18429/JACoW-LINAC2018-MOPO121. URL: http://jacow.org/linac2018/papers/mopo121.pdf.

[28] Kemal Şafak et al. “Extreme-Timing-Resolution with Waveguide-Based Balanced Optical Cross-Correlators”. In: *Conference on Lasers and Electro-Optics*. Optica Publishing Group, 2022. DOI: 10.1364/CLEO{_}SI.2022.STh5N.3. URL: https://opg.optica.org/abstract.cfm?URI=CLEO_SI-2022-STh5N.3.

[29] C L Li et al. “Two Color Balanced Optical Cross Correlator to Synchronize Distributed Lasers for SHINE Project”. In: *Proc. 11th International Beam Instrumentation Conference (IBIC'21), Seoul, Korea*. International Beam Instrumentation Conference 10. JACoW, Geneva, Switzerland, Nov. 2021, pp. 370–372. ISBN: 978-3-95-450230-1. DOI: 10.18429/JACoW-IBIC2021-WEPP05. URL: https://jacow.org/ibic2021/papers/WEPP05.pdf.

[30] B Liu et al. “Progress of Shanghai HIgh repetitioN rate XFEL and Extreme light facility (SHINE)”. In: *Proc. 31st International Linear Accelerator Conference (LINAC'22), Liverpool, UK*. International Linear Accelerator Conference 31. JACoW, Geneva, Switzerland, Sept. 2022.

[31] L Winkelmann et al. “The European XFEL Photocathode Laser”. In: *Proc. 39th International Free Electron Laser Conference (FEL2019), Hamburg, Germany*. Free Electron Laser Conference 39. JACoW Publishing, Geneva, Switzerland, Nov. 2019, pp. 423–426. ISBN: 978-3-95450-210-3. DOI: 10.18429/JACoW-FEL2019-WEP046. URL: http://jacow.org/fel2019/papers/wep046.pdf.

[32] A Kalinin, T Thakker, and S Jamison. “Design and Simulation Studies of the novel beam Arrival Monitor Pickup at Daresbury Laboratory”. In: *Proc. 7th International Particle Accelerator Conference (IPAC2016), Busan, Korea*. JACoW, Geneva, Switzerland, 2016. ISBN: 9783954501472. URL: https://www.cst.com/.

[33] Aleksandar Angelovski et al. “Evaluation of the cone shaped pickup performance for low-charge sub 10 fs arrival time measurements at free electron laser facilities”. In: *Physical Review Special Topics – Accelerators and Beams* 18.1 (Jan. 2015), p. 012801. ISSN: 1098-4402. DOI: 10.1103/PhysRevSTAB.18.012801.

[34] Marie Kristin Czwallina, Bjorn Lautenschlager, and Holger Schlarb. *Beam-based Stability Evaluation in the LINAC of European XFEL*. 2024.

[35] B. E. J. Scheible et al. “Pickup development for short low-charge bunches in x-ray free electron lasers”. In: *Physical Review Accelerators and Beams* 24.7 (July 2021), p. 072803. ISSN: 2469-9888. DOI: 10.1103/PhysRevAccelBeams.24.072803.

[36] J W McKenzie et al. “Establishing a Relativistic Ultrafast Electron Diffraction & Imaging. (RUEDI) UK National Facility”. In: *Proc. 4th International Particle Accelerator Conference (IPAC'17), Venice, Italy*. JACoW, Geneva, Switzerland, 2022. ISBN: 9783954502318. DOI: 10.18429/JACoW-IPAC2023-TUPL144.

[37] C Schmidt et al. “Feedback Strategies for Bunch Arrival Time Stabilisation at FLASH Towards 10 fs”. In: *Proc. 33rd International Free Electron Laser Conference (FEL2011), Shanghai, China*. JACoW, Geneva, Switzerland, 2011. ISBN: 9783954501175.

[38] E. Genthe, C. Burmeister, and H. Schlarb. “Impact of ocean-generated microseism on the European X-ray Free Electron Laser”. PhD thesis. Hamburg: DESY, 2024.

[39] Marta Csatari Divall et al. “Timing jitter studies of the SwissFEL Test Injector drive laser”. In: *Nuclear Instruments and Methods in Physics Research Section A: Accelerators, Spectrometers, Detectors and Associated Equipment* 735 (Jan. 2014), pp. 471–479. ISSN: 01689002. DOI: 10.1016/j.nima.2013.09.067.

[40] P. Cinquegrana et al. “Optical beam transport to a remote location for low-jitter pump-probe experiments with a free electron laser”. In: *Physical Review Special Topics – Accelerators and Beams* 17.4 (Apr. 2014), p. 040702. ISSN: 1098-4402. DOI: 10.1103/PhysRevSTAB.17.040702.

[41] Andreas Dax et al. “Arrival time fluctuation of the SwissFEL photocathode laser: characterization by a single color balanced cross correlator”. In: *Optics Express* 30.9 (Apr. 2022), pp. 15495–15511. DOI: 10.1364/OE.444679. URL: https://opg.optica.org/oe/abstract.cfm?URI=oe-30-9-15495.

[42] Atia-tul-noor et al. “Sub-50 fs temporal resolution in an FEL-optical laser pump-probe experiment at FLASH2”. In: *Optics Express* 32.4 (Feb. 2024), pp. 6597–6608. DOI: 10.1364/OE.513714. URL: https://opg.optica.org/oe/abstract.cfm?URI=oe-32-4-6597.

[43] Anne-Laure Calendron. “Development of a versatile arrival-time monitor for Laser-to-FEL stabilization in the FLASH2020+ project”. Apr. 2022. URL: https://events.hifis.net/event/318/.

[44] Mina Bionta et al. *LCLS II Experiment Timing Development - Improving FEL Experiment Resolution*. Presented at FEL 2024 - 41st International Free Electron Laser Conference, Warsaw, Poland.

[45] James M. Glownia et al. “Pump–probe experimental methodology at the Linac Coherent Light Source”. In: *Journal of Synchrotron Radiation* 26.3 (May 2019), pp. 685–691. DOI: 10.1107/S160057751900225X. URL: https://doi.org/10.1107/S160057751900225X.

[46] Mina R. Bionta et al. “Spectral encoding of x-ray/optical relative delay”. In: *Opt. Express* 19.22 (Oct. 2011), pp. 21855–21865. DOI: 10.1364/OE.19.021855. URL: https://opg.optica.org/oe/abstract.cfm?URI=oe-19-22-21855.

[47] M. R. Bionta et al. “Spectral encoding method for measuring the relative arrival time between x-ray/optical pulses”. In: *Review of Scientific Instruments* 85.8 (Aug. 2014), p. 083116. ISSN: 0034-6748. DOI: 10.1063/1.4893657. eprint: https://pubs.aip.org/aip/rsi/article-pdf/doi/10.1063/1.4893657/13493099/083116_1_online.pdf. URL: https://doi.org/10.1063/1.4893657.

[48] Henry J. Kirkwood et al. “Initial observations of the femtosecond timing jitter at the European XFEL”. In: *Opt. Lett.* 44.7 (Apr. 2019), pp. 1650–1653. DOI: 10.1364/OL.44.001650. URL: https://opg.optica.org/ol/abstract.cfm?URI=ol-44-7-1650.

[49] Patrik Grychtol et al. “Timing and X-ray pulse characterization at the Small Quantum Systems instrument of the European X-ray Free Electron Laser”. In: *Opt. Express* 29.23 (Nov. 2021), pp. 37429–37442. DOI: 10.1364/OE.440718. URL: https://opg.optica.org/oe/abstract.cfm?URI=oe-29-23-37429.

[50] Tokushi Sato et al. “Femtosecond timing synchronization at megahertz repetition rates for an x-ray free-electron laser”. In: *Optica* 7.6 (June 2020), pp. 716–717. DOI: 10.1364/OPTICA.396728. URL: https://opg.optica.org/optica/abstract.cfm?URI=optica-7-6-716.

[51] Adrian P. Mancuso et al. “The Single Particles, Clusters and Biomolecules and Serial Femtosecond Crystallography instrument of the European XFEL: initial installation”. In: *Journal of Synchrotron Radiation* 26.3 (May 2019), pp. 660–676. DOI: 10.1107/S1600577519003308. URL: https://doi.org/10.1107/S1600577519003308.

[52] M. Beye et al. “X-ray pulse preserving single-shot optical cross-correlation method for improved experimental temporal resolution”. In: *Applied Physics Letters* 100.12 (Mar. 2012), p. 121108. ISSN: 0003-6951. DOI: 10.1063/1.3695164. eprint: https://pubs.aip.org/aip/apl/article-pdf/doi/10.1063/1.3695164/14242352/121108_1_online.pdf. URL: https://doi.org/10.1063/1.3695164.

[53] Stefan Droste et al. “High-sensitivity x-ray/optical cross-correlator for next generation free-electron lasers”. In: *Opt. Express* 28.16 (Aug. 2020), pp. 23545–23553. DOI: 10.1364/OE.398048. URL: https://opg.optica.org/oe/abstract.cfm?URI=oe-28-16-23545.

[54] S Düsterer et al. “Femtosecond x-ray pulse length characterization at the Linac Coherent Light Source free-electron laser”. In: *New Journal of Physics* 13.9 (Sept. 2011), p. 093024. DOI: 10.1088/1367-2630/13/9/093024. URL: https://dx.doi.org/10.1088/1367-2630/13/9/093024.

[55] N. Hartmann et al. “Attosecond time–energy structure of X-ray free-electron laser pulses”. In: *Nature Photonics* 12.4 (Apr. 2018), pp. 215–220. ISSN: 1749-4893. DOI: 10.1038/s41566-018-0107-6. URL: https://doi.org/10.1038/s41566-018-0107-6.

DRAFT

12 Data management and artificial intelligence

12.1 Outline

A next-generation XFEL will generate extreme data volumes at rates that will challenge the capabilities of traditional acquisition, networking, and storage models. To remain scientifically competitive and operationally efficient, and based on current approaches, the facility must leverage fast, localised reduction at the instrument; scalable second-stage processing within a dedicated data centre or federated national compute resources; and value-driven long-term curation policies consistent with FAIR principles. At the same time, advances in AI and ML will potentially reshape these requirements and create an opportunity to transform how data is processed, interpreted, and used for real-time decision-making, enabling adaptive experiments and dramatically shortening time to publication. This section will outline the scale of the challenge, the principles that will guide the design of the facility, and the areas where future design efforts should take advantage of current and future developments in technology to meet these challenges.

12.2 Introduction

A defining capability of the next-generation XFEL facility will be its ability to acquire, process, and exploit the unprecedented data volumes generated by a high-repetition-rate X-ray free-electron laser. Handling these data rates represents a major technical and operational challenge. Traditional approaches to data acquisition, storage, post-processing, and archival will either need to scale far beyond current practice or be fundamentally redesigned.

At the same time, rapid advances in artificial intelligence (AI) and machine learning (ML) are transforming scientific discovery and facility operations. When integrated effectively, AI has the potential to impact all aspects of next-generation XFEL operation: improving accelerator efficiency and reliability, enabling automated and adaptive experiments, reducing the time from experiment to publication, and extracting scientific insight from individual or combined datasets that would otherwise be impractical to analyse.

The pace of evolution in both AI methods and computing hardware makes it difficult to predict precisely what the optimal computing architecture for a next-generation XFEL will look like in five to ten years. Advanced AI models may dramatically accelerate data reduction and curation, support real-time experimental decision-making, and enable new classes of data-driven discovery. To remain effective over its operational lifetime, a next-generation XFEL must therefore be designed to accommodate continual advances in computing technologies and analysis paradigms, rather than optimised around a fixed snapshot of current capability.

The scale of the data produced by a next-generation XFEL also raises fundamental questions about data value, retention, and reuse. The volumes expected may make it impractical for most

users to store or process raw data outside the facility, placing increased responsibility on the facility to provide reliable fast-feedback, validated reduction pipelines, and simple-to-use analysis tools that allow users to transition from data to scientific output efficiently. Where reduction approaches are validated and demonstrably reliable, it may not be necessary—or affordable—to retain all raw data indefinitely. Instead, informed approaches to data vetoing, reduction, curation, and selective retention will be essential to balance scientific value against financial and environmental cost.

These challenges must be understood within a broader strategic context. The UK government has identified science, technology, and AI as key drivers of economic growth, placing significant emphasis on developing and deploying critical technologies and investing in world-class national scientific infrastructure. In alignment with this, the STFC has articulated a vision centred on maximising the value of data generated by its facilities through responsible AI, modern data technologies, and high-performance computing. A next-generation XFEL strongly integrates with these priorities: it will both depend on and enable advances in AI-enabled data processing pipelines, digital twins of facilities, autonomous operational tools, and AI surrogate models to accelerate scientific computing.

Comparable facilities worldwide, including the European XFEL and LCLS-II, are already experiencing significant challenges related to rapid data acquisition, high-throughput analysis, and user expectations for fast, accessible scientific output. Their experience reinforces the need for a next-generation XFEL to adopt fast, edge-based processing close to detectors; scalable compression and data vetoing strategies; integrated metadata capture; and a well-designed approach to high-performance computing for both in-experiment and post-experiment analysis. These capabilities are essential not only for enabling world-leading single-experiment science, but also for enabling cross-experiment insight in support of critical UK missions such as clean energy, advanced materials, biology, and drug discovery.

This section outlines the scale of the data and computing challenge posed by a next-generation XFEL, the principles that should guide the design of its data and AI infrastructure, and the areas where future facility design should deliberately take advantage of emerging developments in AI, computing hardware, and data management. Related material on future autonomous integration, e.g. robotics, is included in Section 13.2.5.

12.3 Facility data handling

A next-generation XFEL will generate substantial amounts of data, both from the accelerator itself and from the detectors in the end stations. Handling this data represents a significant challenge in the design of the facility; in terms of acquisition, storage and analysis. The European XFEL held around 115 PB of raw scientific data by the end of 2023 [1], and is pursuing a number of methods to reduce this data, both during experiments and after the fact [2]. A next-generation XFEL has the potential, even with data reduction, to generate that much data in a single day, which will present a significant challenge to the facility's data handling systems. The STFC as a whole holds around 500 PB of scientific data [3], so a next-generation XFEL would represent a significant step change in the amount of data held by STFC, comparable to the equally large-scale Square Kilometer Array [4].

12.3.1 Data rates and pipelines

Estimating the total data rate of the facility is difficult at this early stage, but some examples for raw data rates are given in Table 12.1. While accelerator data can generally be reduced by storing only scalar values (e.g. beam size and position, rather than full images), scientific data from imaging detectors at the end station must generally be stored for at least some time before processing.

Table 12.1: Estimated data rates for various facility components.

Component	Potential Numbers	Data	Data Rate
Scalar diagnostics	Dozens	16bit@1MHz	16 Mbps
Beam position monitors	Hundreds	2x16bit@1MHz	32 Mbps
Beam imaging screen	Dozens	1024x1024x12bit@100Hz	1.25 Gbps
Imaging X-ray detectors	10	1–16MP, 16bits@100kHz	1600–25,600 Gbps

A reasonable worst-case estimate for the data rates of the facility's end stations is around 64 Tbps [10 detectors at 4 MPx@100 kHz]. State-of-the-art lossless compression [5] can achieve around 50–70× compression of images, which still gives a total facility scientific data rate of over 100 PB/day. To achieve this level of compression, it is proposed to deploy modular data handling servers close to the detectors, requiring around 800 CPU cores per end station, along with the necessary storage. The data handling servers would also interface with automatic facility feedback (fast feedback) and slow feedback to users and operators for experiment verification, with data only stored for minutes. These systems would take advantage of advancements in edge computing, including AI at the Edge, as well as expansible data acquisition systems such as the microTCA.4 standard [6]. An example data pipeline for one instrument is shown in Figure 12.1.

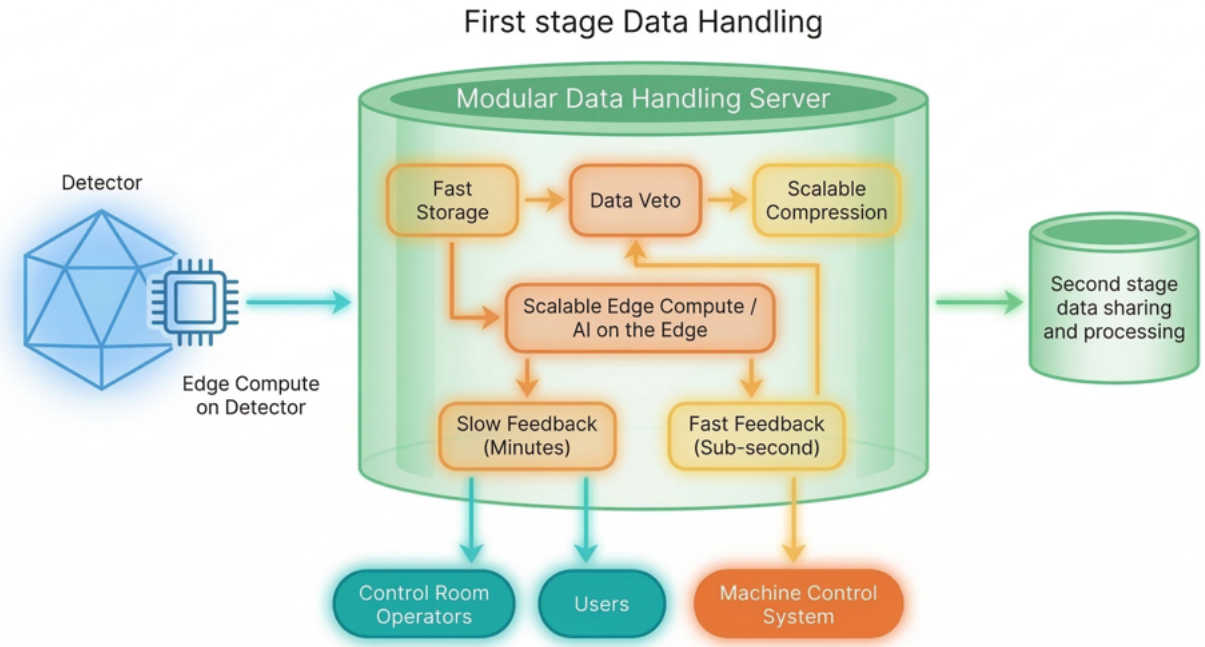

Figure 12.1: Example first stage pipeline for one instrument.

Even this 100 PB/day data rate is unsustainable for long term storage and must be further reduced. Data vetoing coupled to automatic fast analysis would enable shots that contain no data, for example due to missing the sample, or repeating data, due to random orientations in samples, to

be discarded. The facility would have to enforce data vetoing for experiments (another area where AI can help), requiring users to set parameters for when to discard shots, which would take place in the end station data handling servers.

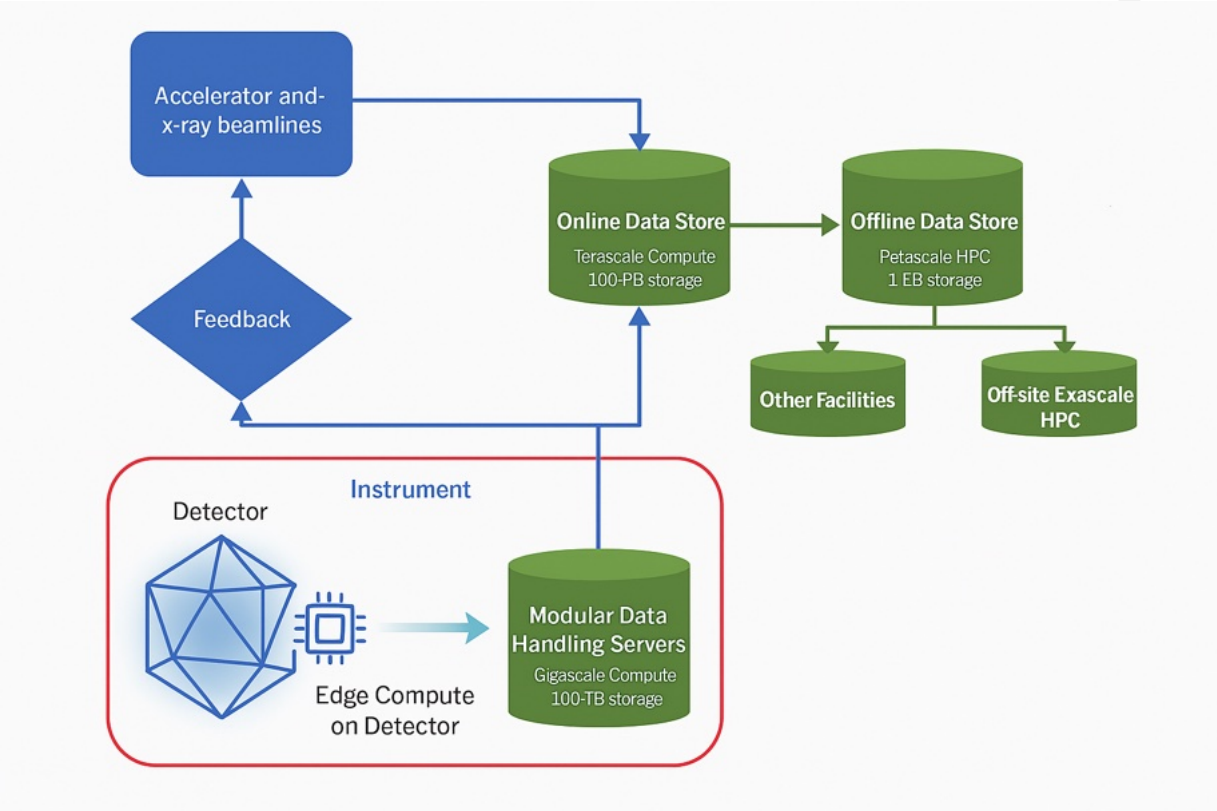

Figure 12.2: Proposed high-level data pipeline for the next-generation XFEL.

From the end stations, a Terascale HPC capability is envisioned to further reduce the data, for example by more effective compression algorithms or analysis to tag more data for deletion. This data centre would also be linked to the accelerator data systems, to enable tagging of the scientific output with the necessary metadata for future analysis. It would be expected that data would be stored here for a matter of days, being processed during experiments. It is then proposed to transmit the reduced data to an Online Data Store where second stage processing can take place in a dedicated data centre with a local petascale HPC system or through national compute resources. The proposed high-level data pipeline for the next-generation XFEL is shown in Figure 12.2.

12.3.2 High performance computing and storage

Comparable facilities, such as LCLS-II [7], expect that over half their user experiments will require more than 1 PFLOP of analysis computing power, with 10% requiring more than 100 PFLOPs. Figure 12.3 shows how the most powerful supercomputers in the world have developed over the last decade. To ensure the facility can meet its next generation requirements, it is proposed that the facility provides this HPC capability as part of beam time allocations. Combined with an offering of standard analysis routines for common types of experiments, this would enable a rapid pipeline from experiment to publication, which is key to both minimizing the cost of data storage and to fulfil the facility's Next Generation Capabilities.

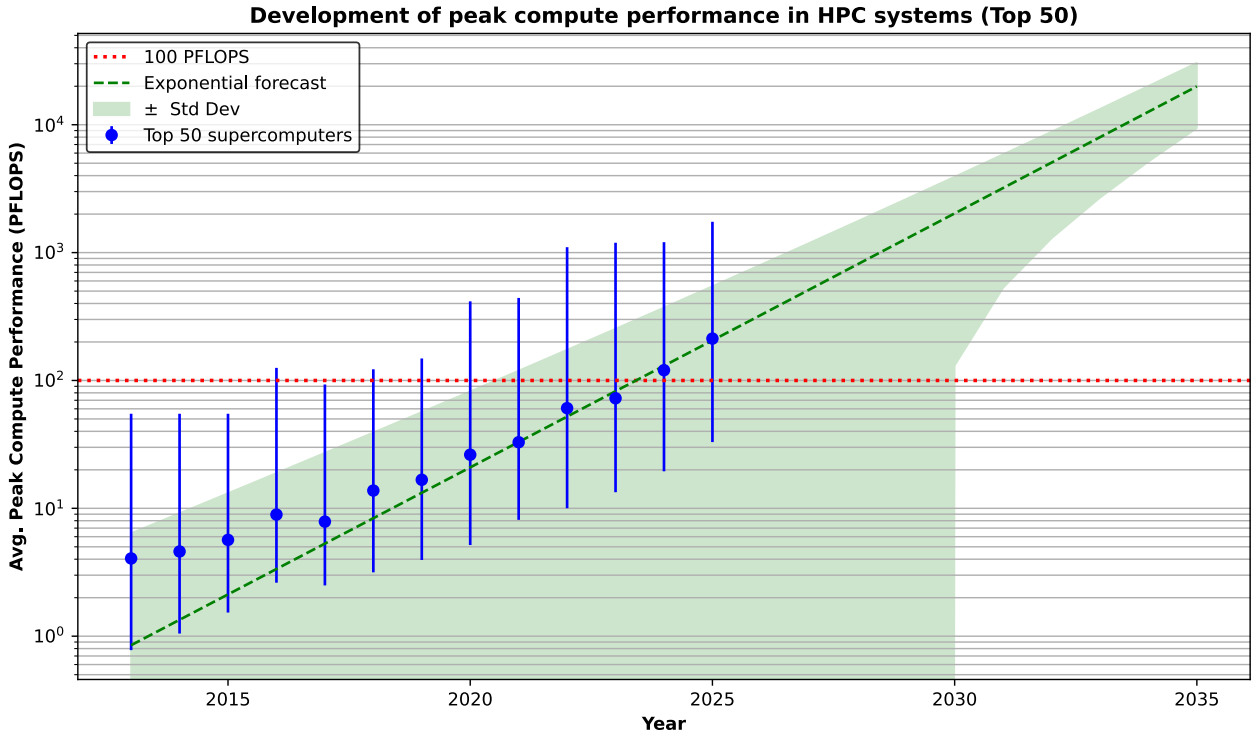

Figure 12.3: Nominal 100 PFLOP HPC facility compared to Top 500 HPC rankings.

This Petascale HPC capability would be provided in a dedicated data centre, combined with an extabyte-scale offline storage system. This would enable users to carry out offline analysis after their experiments, with the intention that the facility provides standardized tools and workflows for common types of analysis, which would accelerate the time to publication. To take advantage of wider UKRI Digital Research Infrastructure, such as the AI Research Resource and National Computing Resources (NCR's), the facility should host dedicated links to the UK's national research and education network (JANET).

The facility should also engage with UK-wide processes on Exascale computing to support those experiments requiring more than 100 PFLOPs of computing power, for example the planned exascale expansion of the AI Research Resource [8], as well as international efforts such as the ExaFEL program at SLAC [9]. The STFC has already identified that there is a significant need for Exascale computing in the UK [10], and a next-generation XFEL should be designed to take advantage of this capability, for example by providing dedicated links to Exascale computing facilities.

A nominal specification for a 100 PFLOP HPC facility is shown in Table 12.2, which would provide sufficient computing power for the facility's next generation capabilities. While this represents a significant investment, it is likely to be an important component in delivering the required performance and capacity. As shown in Figure 12.3, a 100 PFLOP supercomputer would be comparable to the most powerful supercomputers in the world today, but would be much less of an outlier by the time a next-generation XFEL is operational.

12.3.3 Policies and management

The scientific community increasingly recognises the importance of open and FAIR data [11], and this principle forms a key component of the STFC's AI Strategy [3]. UKRI's Data Policy [12] further

Table 12.2: Specifications for a nominal 100 PFLOP HPC facility.

Parameter	Value
Compute performance	100 PFLOPs
Number of CPU cores	40,000
Number of GPUs	1,112
Cost	£100m
Energy consumption	14,200 kWh/yr

requires that outputs from UKRI-funded research are managed in accordance with FAIR data principles, while explicitly recognising that data retention and access must be balanced against reasonable financial and environmental costs.

The data volumes expected from a next-generation XFEL will make it impractical for most non-specialist facilities or individual users to store, retrieve, and process raw data at scale outside the facility's computing environment. It is therefore essential to consider not only how data are stored, but how they will be used. Raw per-shot data may be primarily valuable for the development, validation, and continual improvement of reduction and analysis methods, whereas much of the long-term scientific impact is likely to come from the sharing and re-use of reduced or processed data products. Establishing appropriate data-handling policies will require close consultation with the user community and the development of trust in automated and AI-assisted data reduction pipelines, particularly where such pipelines determine which data are retained or discarded.

In evaluating the cost-value balance of data retention, it is important to recognise that for some experiment types it may be more practical—and more cost-effective—to repeat a measurement than to store all raw data indefinitely. At the repetition rates expected for a next-generation XFEL, and in cases where samples are readily available and conditions can be reproduced reliably, the scientific cost of reacquiring specific datasets may be far lower than the financial and environmental cost of long-term storage. This possibility adds a further dimension to the facility's data-value model: retention decisions must consider not only scientific utility and future reuse, but also the relative ease and fidelity of re-measurement. In turn, efficient repeatability may drive greater automation, higher throughput, and more streamlined operations, helping to manage storage pressures without compromising scientific flexibility or quality. Any policies built around this principle will need to be developed transparently with the user community, acknowledging discipline-specific expectations regarding reproducibility, sample uniqueness, and what constitutes a "repeatable" measurement under varied experimental conditions. Ultimately, the repeat-versus-retain question should be part of an evidence-based assessment that aligns with UKRI data policy and FAIR principles, while remaining flexible enough to support mission-driven science at extreme scale.

In this context, the next-generation XFEL should aim to adopt a data policy that is as open and FAIR as possible, in order to maximise the scientific and societal impact of the data generated by the facility. Open data refers to data that are accessible, exploitable, editable, and shareable by anyone for any purpose, typically under an open licence. *FAIR data* refers to a set of guiding principles for scientific data management designed to enhance data accessibility and reuse. Specifically, data should be:

- **Findable:** Data are assigned a unique and persistent identifier, such as a DOI, are described with rich metadata, and indexed in a searchable resource such as a repository.

- **Accessible:** Once the data is found, it can be accessed in a defined, easily implementable way. This does not necessarily mean free access, but that it is accessible with proper authentication using open, free, and universal protocols.
- **Interoperable:** Data is stored in a format that allows integration with other data or workflows.
- **Reusable:** Data must be well-described with metadata, have a clearly defined reuse license, and adhere to relevant standards and best practices.

By ensuring that the data generated by a next-generation XFEL is FAIR, the facility will enable researchers to access and use the data in a wide range of applications, from basic research to applied science and engineering. This will not only enhance the impact of the facility's scientific output, but also drive further advancements in AI and ML technologies, for example by enabling development of new foundation models in areas such as pharmaceutical research and materials science, which could lead to new discoveries and applications. Other comparable facilities, such as the European XFEL [1], have already adopted FAIR data policies.

Significant expertise in these areas already exists within STFC, particularly within the Ada Lovelace Centre (ALC) [13], which provides specialist capability in scientific software, research software engineering, data management, and AI-enabled analysis, with the aim of maximising the scientific impact of STFC's national facilities. A next-generation XFEL should collaborate closely with the ALC and other data-intensive facilities to align standards, share tools, and leverage existing expertise. As part of this, the facility should evaluate and adopt data formats that are not only FAIR but AI-ready, such as Croissant [14] or equivalent structured, machine-interpretable representations that support modern AI/ML workflows. While FAIR principles remain a critical foundation, the facility's data policy may need to be adapted to reflect realistic cost-value trade-offs at extreme scale. This may include prioritising formats, metadata structures, and retention strategies that accelerate facility operations or support mission-driven scientific objectives, while still maintaining a transparent and community-endorsed approach to openness, curation, and reuse.

12.4 Artificial intelligence, machine learning and digital twins

The application of AI, ML, and digital twins spans the full experimental lifecycle and can be broadly grouped into four stages, which are described in detail in this section:

- Pre-experiment design
- Optimal beam delivery and instrument operation
- Data processing and experimental decision-making
- Post-experiment analysis

Each stage places different demands on models, compute hardware, experiment-control systems, and operational workflows. While these stages can be considered individually, their combined, end-to-end integration is what enables a step-change in capability for facilities such as XFELs. Instead of waiting for post-experiment analysis to interpret results, AI-driven pipelines enable rapid reconstruction, analysis, and interpretation during data collection itself. This supports faster iteration cycles in materials research, chemistry, structural biology, and dynamics studies—directly impacting fields such as advanced manufacturing, drug discovery, and pharmaceuticals across both academia and industry. In particular, this integration enables two transformational modes of operation:

Closed-loop autonomous experiments: Experiments in which AI models interpret data in real time, make decisions on sample orientation, beam parameters, or instrument configuration, and automatically optimise measurement strategies. These experiments may run with minimal or no human intervention and are supported by:

- high-throughput data reduction at the instrument,
- high-throughput data reduction at the instrument,
- low-latency channels to decision models,
- robotic sample-handling systems,
- and digital twins that simulate experiment outcomes.

Such workflows significantly reduce experimental cycle times and unlock scientific studies that would be impractical with traditional manual operations.

Mission or collective community driven experiments: AI-supported platforms can coordinate complex experimental programmes that involve multiple user groups, large sample libraries, or sequential experiments driven by shared scientific goals. These campaigns allow communities—such as materials discovery consortia, pharmaceutical groups, or energy-research networks—to collectively use XFEL data to accelerate progress across an entire scientific area.

Together, these developments illustrate how the integration of AI, robotics, high-rate data handling, and advanced control systems can fundamentally transform the scientific productivity and operational efficiency of a next-generation XFEL.

12.4.1 Pre-experiment design

Pre-experiment design will be central to maximising the scientific return of the UK XFEL. For complex experiments, digital twins of the accelerator, beamlines, and instruments allow scientists to explore optimal configurations prior to proposal submission and long before beamtime begins. AI and ML are key to delivering the speed and accuracy required to maximise the utility of digital twins of the accelerator, beamlines, and instruments.

12.4.1.1 Facility design

The design of the facility itself can be optimised with machine learning methods, which can find regimes of operation not previously attainable with human-only design. By augmenting the speed of simulations with machine learning (for example, using surrogate models to approximate numerically complex physics), lattice configurations can be searched orders of magnitude faster. Such research has been applied not only to the lattice, but to the individual design elements from magnets [15] to cavities. Tools which leverage these advancements have been created by the community [16, 17, 18, 19] as well as bespoke solutions relying on established techniques such as genetic algorithms and Bayesian optimisation.

12.4.1.2 Digital twins

Digital twins are expected to be a foundational element of a next-generation XFEL. A digital twin [20] is a virtual representation of a physical system, which can be used to simulate and predict the behaviour of the system in real-time and which accesses real-time data to carry out verification, validation and uncertainty quantification [21]. Digital twinning for a next-generation XFEL would be expected to comprise virtual replicas of the many components that make up the facility. They can be used throughout the facility lifecycle—from design and commissioning through to daily operations—to improve efficiency, reliability, and scientific productivity. Recent work [22] has demonstrated an auto-generating digital-twin architecture for both existing accelerators and the next-generation XFEL, showing how such systems can prototype software, controls, and experimental procedures even in this conceptual design phase.

Digital twins can be used to:

- Optimise facility performance by predicting accelerator and instrument behaviour and informing control settings,
- Support condition-based maintenance by anticipating faults and scheduling interventions,
- Help user communities understand expected data characteristics and experimental constraints in advance,
- Guide experimental design choices such as sample preparation, concentration, and exposure strategy.

By reducing simulation latency, these approaches enable near-real-time optimisation and monitoring rather than purely offline analysis.

Before and during construction, digital twins will be used to plan and optimise aspects of the facility by integrating data from various sources and sharing it between different groups, to test scenarios, anticipate issues, and make informed decisions. They can be a cost-efficient way to identify risks early and avoid expensive mistakes. Digital twinning will provide an in-silico testing ground to optimise the performance of the facility throughout its lifetime, providing an environment where operators and users can use physical simulators and statistical emulators to enhance the understanding of real-world results and act as a test-bed for future activities. Time on the physical machine is extremely valuable and in-demand, so digital twins are of enormous value for prototyping software applications and experimental procedures,

Figure 12.4 gives a schematic representation of digital twinning for the accelerator: a virtual replica runs alongside the physical machine and is calibrated to it, to provide additional insights, e.g. virtual diagnostics. Simulations with a range of computational complexity and fidelity can be included to meet the needs of different applications. AI/ML techniques can be used to accelerate the digital twin, e.g. by using surrogate models to replace expensive simulations, to enable high-fidelity and near-real-time optimisation and monitoring. With a continuously updated model of the facility, advanced control algorithms can safely explore operational parameter space, adapt to changing conditions, and optimise performance in real time. This promises to lower barriers for new users, improve reproducibility, and support more complex experimental protocols, including remote and automated operation.

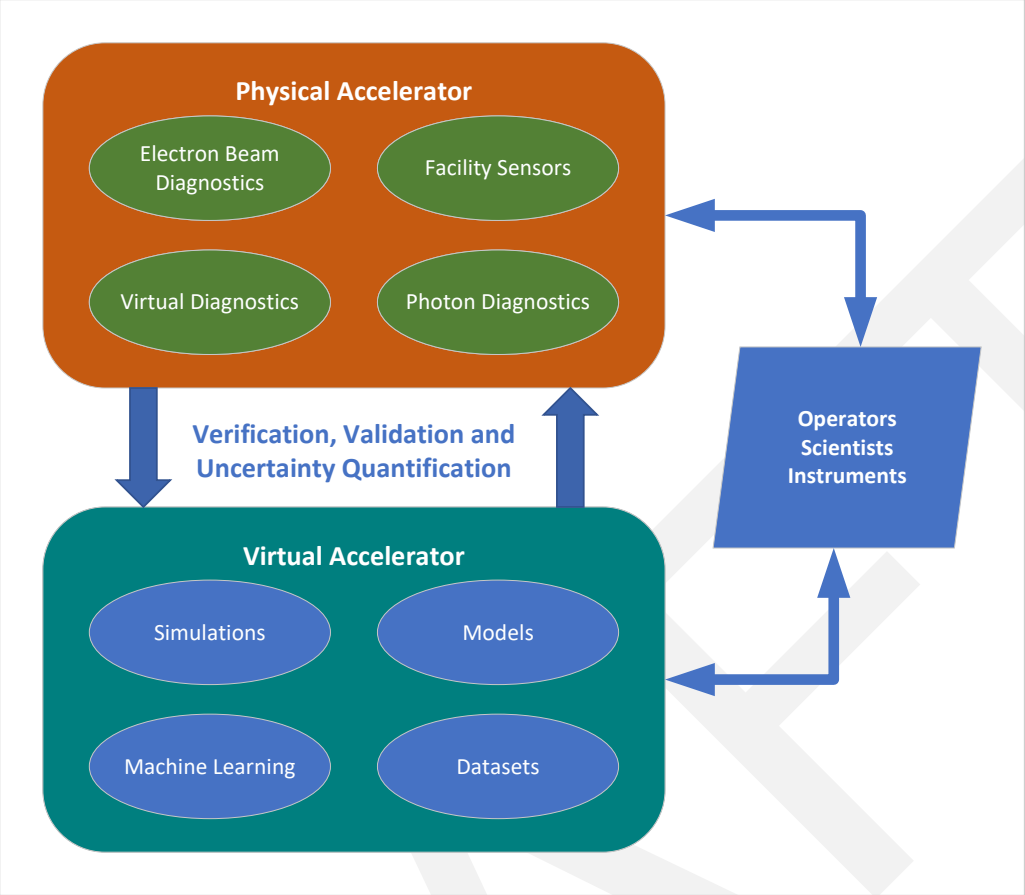

Figure 12.4: Schematic of a Digital Twin.

12.4.1.3 Software frameworks

A critical enabler for digital twins in a next-generation XFEL is the development of robust software frameworks that can integrate real-time data, physics-based simulations, and control systems into a unified environment [23, 24]. These frameworks provide the backbone for interoperability across diverse hardware and software components, ensuring that accelerator models, beamline diagnostics, and experimental stations can all be mirrored accurately. Modern frameworks are designed to be modular and scalable, supporting high-performance computing for simulation, advanced data management pipelines, and secure interfaces for both human operators and AI-driven agents. By standardising data formats and communication protocols, they allow multidisciplinary teams to collaborate effectively and ensure that digital twins can evolve alongside advances in instrumentation and computational methods.

Broader developments in AI also point towards new modes of scientific support. For example, progress towards AI-assisted or “co-scientist” systems has demonstrated the potential for generating hypotheses, experimental strategies, and research proposals to augment human expertise.

12.4.2 Optimal beam operations

Developments in the field of applied machine learning for accelerators have been significant in recent years [25], with many specialised communities and conferences being formed and performing advanced research. These advances have demonstrated the potential for AI and

machine learning (ML) to support a wide range of critical applications, from accelerator lattice design and optimisation, through predictive maintenance and fault detection, to increasingly autonomous facility operation.

The next-generation XFEL design is well positioned to leverage these capabilities. To fully exploit current advances and enable future developments, the facility must be designed from the outset with advanced data acquisition, metadata capture, and control systems that can interface cleanly with both present-day and next-generation AI models. This requires AI to be treated as an integral part of the facility architecture, rather than an add-on.

Machine learning has already demonstrated value in accelerator optimisation, including the identification of operating regimes that may be difficult to discover through traditional human-driven tuning alone. Learning-based anomaly detection and fault prediction can further support predictive maintenance, helping to reduce unplanned downtime and minimise disruption to user experiments.

At the instrument level, AI techniques can support:

- Optimisation of beam shape and delivery,
- Real-time identification of particle size, shape, and orientation from diagnostic images,
- Selection and adaptation of experimental parameters during beam time, and
- Hybrid approaches combining physics-based models with ML to improve robustness and interpretability.

Rapidly setting the beam properties to user's desired specifications is vital because active beam time is always at a premium. This can be achieved by the application of online optimisation systems using techniques such as Bayesian optimisation[26], reinforcement learning [27, 28], and by augmenting the abilities of operators with the use of virtual diagnostics which can be used to predict difficult-to-observe measures, including fully predicting the 6D phase space of the beam at multiple points [29, 30]

Machine learning can also unlock new capabilities by allowing the exploitation of existing technologies in new ways. ML-based control of acousto-optic laser shapers has been implemented at the CLARA facility to enable bespoke electron bunch shaping [31]. Similar techniques have been used to optimise the X-ray output of the LCLS-II XFEL [32], and may be used in future to explore new regimes in FELs such as multi-colour Echo-Enabled-Harmonic Generation [31]. Controlling acousto-optic shapers algorithmically and shot-per-shot is not currently possible with non-machine-learning based techniques.

With ML-based anomaly detection and fault prediction, predictive maintenance can be scheduled to prevent unexpected beam time loss and prevent costly and disruptive delays to user experiments. ML-based techniques for anomaly detection have been explored at a number of labs for detection, prediction [33], and classification [34] of breakdowns in RF cavities. At the LHC, unsupervised ML systems are used to detect failures in beam position monitors [35], as well as in analysing particle tracking data to identify new physics [36]. For anomaly detection at high-repetition rates in non-trivial signal processing scenarios (i.e., where a simple threshold test is not sufficient), ML is practically essential as the rapid inference speed and strong function approximation of feed forward networks allows the complex analysis of signals where traditional numerical analysis would be slow or difficult to implement.

Large language models (LLMs) also offer new interaction paradigms, acting as interfaces to operational and experimental systems by generating plots, executing analysis tasks, and lowering barriers to entry for non-expert users, while retaining appropriate safeguards and human oversight.

12.4.3 Data reduction and decision-making

To answer even basic experimental questions - such as whether sufficient data have been collected, whether a sample has changed state, or whether key transitions have been observed - raw data must be reduced and interpreted rapidly.

AI can automate and accelerate data reduction through:

- Extraction of experimental intent from proposals or metadata using LLMs,
- ML-assisted identification of peaks, features, or spots to seed conventional reconstruction and fitting algorithms,
- Sorting, classification, and de-noising of detector images, and
- Identification of redundant or uninformative data for vetoing or down-sampling.

Based on reduced data products and uncertainty estimates, AI-assisted systems can support decisions on experimental progression, such as whether to continue, adapt parameters, or terminate data collection.

12.4.4 Post-experiment analysis

Post-experiment analysis in many XFEL science cases relies on computationally intensive methods, such as electronic structure calculations and large-scale simulations of material dynamics. AI offers several routes to accelerating this stage.

Recent large-scale reference datasets, such as Meta's OMol25 dataset [37] of high-accuracy density functional theory (DFT) calculations, enable the development of surrogate models or the enhancement of foundation models such as MACE [38], which can reproduce DFT-level accuracy at a fraction of the computational cost. More broadly, AI techniques are increasingly being applied at the interface of mathematics and physics, for example through learned or hybrid solvers for partial differential equations, further accelerating traditionally expensive computational workflows.

Across experiments, AI has also demonstrated strong capability in extracting trends and correlations across large, heterogeneous datasets, enabling cross-experiment insight that would be difficult to obtain using manual or single-experiment analysis alone.

12.4.4.1 Conventional Analysis

Despite rapid progress in AI, the majority of analysis and optimisation workflows currently used in accelerator and photon science remain based on established CPU- and GPU-based codes. In many cases, AI is likely to complement rather than replace these tools.

Hybrid approaches, in which AI guides users through conventional analysis workflows, generates input configurations, or accelerates specific computational components, are expected to dominate over the medium term. Conventional physics-based modelling will remain essential where maximum accuracy, interpretability, and traceability are required. Delivering these capabilities will require flexible interfaces, including virtual machines, web-based environments, visualisation services, and access to HPC resources, likely deployed through a combination of on-premise and cloud infrastructure.

12.4.5 Implementation challenges and opportunities

Deploying AI at a next-generation XFEL brings significant technical and organisational challenges. Tackling them is essential to unlocking the facility's benefits and, more broadly, to delivering the high-tech ecosystem that depends on major research infrastructure:

12.4.5.1 Real-time inference and feedback

The next-generation XFEL will operate at extremely high repetition rates, and any machine-learning models used for live data assessment or control must operate in real time. At present, field-programmable gate arrays (FPGAs) represent the only viable solution for sub-microsecond inference, requiring specialised hardware and significant expertise. While successful deployments exist - such as FPGA-based ML inference in high-energy physics experiments [39] - this requires specialised skills, which are highly sought after by industry, such that recruitment and retention of staff with these skills remains challenging.

For near-experiment or sub-second feedback, inference can instead be performed on specialised accelerator-adjacent systems, such as GPU-based servers (e.g. NVIDIA DGX), with correspondingly relaxed latency constraints.

12.4.5.2 Model development and MLOps

Developing, validating, and maintaining large AI models requires specialised skills and substantial computing resources, often involving large GPU clusters with capital costs in the hundreds of millions of pounds. Although future trends are uncertain, current trajectories suggest increasing compute demands as models and datasets grow.

AI models are not static artefacts. They require ongoing validation, monitoring, retraining, and versioning as data and experimental regimes evolve. Assuming that AI will be widely deployed across the next-generation XFEL, the compute and staffing requirements for continual model improvement must be factored into long-term planning.

12.4.5.3 Trust, explainability, and uncertainty

Explainability remains a key challenge for many ML models. While some deployed systems will inevitably function as partial 'black boxes', trust can be established through extensive validation, robust uncertainty quantification, and conservative deployment strategies. Conversely, interpretable models have already demonstrated their ability to uncover unexpected causal relationships [40], occasionally revealing new physical insight rather than obscuring it.

12.4.6 Connections to AI in the Science and Technology Case

AI is already revolutionising science and technology, as evidenced by award of the 2024 Nobel Prize in Chemistry to Hassibis and Jumper (Google Deep Mind, London) 'for protein structure prediction' (AlphaFold [41]) and Baker (University of Washington) 'for computational protein design'. AI needs data: e.g. AlphaFold is built upon data from around 200,000 protein structures that were determined by experiments at synchrotrons and other facilities, analysed by collaborative computing projects, and compiled into a worldwide archive - the Protein Data Bank (PDB). There is potential for a similarly synergistic relationship between XFELs and AI to explore ultrafast dynamics across many fields.

Examples of the importance of AI are evident throughout the Science and Technology Case. Section 10 maps next-generation XFEL capabilities to the UK's Five Critical Technologies (AI, engineering biology, advanced connectivity, semiconductors, quantum). The combination of next-generation XFELs and AI is envisaged as not only a scientific tool but a strategic driver, connecting these priority areas. Many of the Flagship Programmes described in Section 9.4 rely on the analysis of extremely large datasets, for example the case of 'Probing exciton and spin dynamics in optoelectronic materials' relies on many hundreds or thousands of repeat measurements to understand the relevant exciton and spin dynamics. Elsewhere, Section 3.4.2 describes data-driven approaches to structural dynamics, in which large datasets and advanced data-sorting algorithms are essential for reconstructing rare events.

New opportunities enabled by AI are likely to revolutionise how next-generation XFEL experiments are conducted. Section 9.2.7 highlights the importance of data infrastructure and AI, using SFX experiments as an example. Such experiments are expected to 'tax computational resources by generating very large datasets, which may require varying degrees of image triage, and will need to be merged rapidly, so that users can make the most effective use of XFEL beamtime'. AI is likely to form part of on-chip data reduction (feature extraction, vetos, and multi-event identification) using FPGAs integrated to the front-end detectors. Fast AI-aided online analysis will be needed to assess the quality of data collected during experimental runs and help predict the most effective next steps. Automation of end-station setups using AI tools is already being developed and is likely to accelerate experiment set-up times and help facility staff to support more concurrent experiments.

12.4.7 Connections to the UK's AI ecosystem

Significant expertise in these areas exists within STFC, particularly within the Ada Lovelace Centre (ALC), Scientific Computing Department and the Hartree National Centre for Digital Innovation, which provide specialist capability in scientific software, research software engineering, data management, and AI-enabled analysis. Furthermore, the STFC's AI Strategy identifies a number of institutes that are already working on developing the UK's AI ecosystem, including the AI

Safety Institute, Alan Turing Institute, Responsible AI UK and Innovate UK's Bridge AI. The UK Government has also invested significant funds in compute resources for AI, such as the Isambard-AI and Dawn facilities, which are part of the AI Research Resource. These programs are already demonstrating the impact AI can have on scientific research.

Other actors are also demonstrating how AI can be used to accelerate scientific research. Deepmind, a leading UK-based AI research company has demonstrated progress across many fronts in addition to AlphaFold [41], including an AI co-scientist [42], which can assist researchers by generating hypotheses and formulating research proposals.

The OpenBind consortium, based at the Diamond Light Source, will use foundation models such as AlphaFold, to accelerate drug discovery using synchrotron light [43], and similar initiatives would be expected to be integral to experiments at a next-generation XFEL.

12.5 Sustainability

A significant part of the facility's power consumption would come from the proposed HPC facility, along with the edge computing associated with the accelerator and end stations.

The most efficient supercomputer as of June 2025 produces 72.7 GFLOPs/W [44]. At this efficiency level, a 100 PFLOP supercomputer would consume 1.4 MW, costing almost £4 million per year at current industrial electricity prices [45]. By 2030 the UK government aims to reduce the carbon intensity of UK generation to "well below 50 gCO_2e/kWh" [46], from 171 gCO_2e/kWh in 2023, but even this would represent around 700 $kgCO_2e$ per year, or around 160 cars. Therefore any further technical design must take advantage of new forms of technology that could reduce the energy consumption, and the facility must include measures to offset any residual emissions.

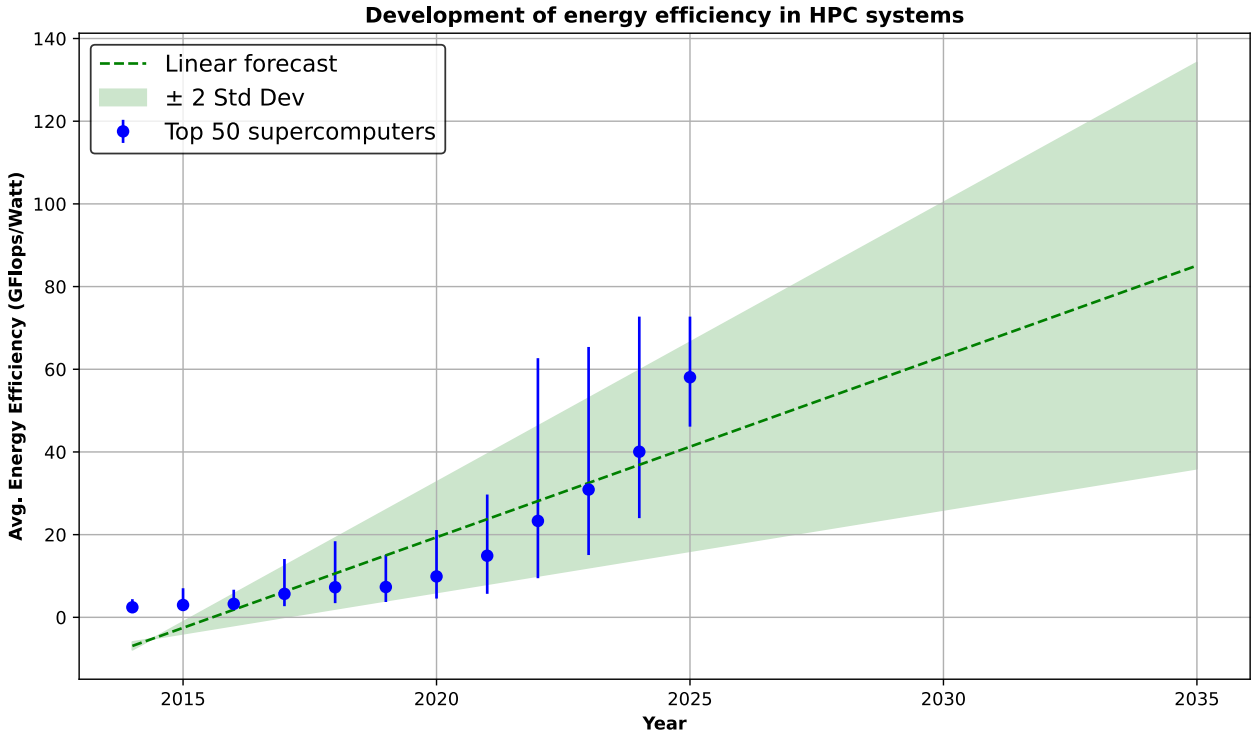

Figure 12.5: Development of the Green 500 ranking of supercomputer energy efficiency.

The good news is that technology in this area is advancing at a rapid rate, as shown in terms of supercomputer energy efficiency in Figure 12.5. In June 2025, the average energy efficiency for the top 30 most powerful supercomputers in the world was 42.5 GFLOPs/W [44]. In June 2015 that was 1.73 GFLOPs/W, meaning that in ten years energy efficiency has improved by almost a factor of 25, while the computing power of the most powerful computer has improved by a factor of 50 [47]. This reflects improvements in transistor density, low voltage transistors, interconnect efficiency, improved ways of cooling data centres and other areas. DOE's next generation of supercomputer, Doudna, will deliver ten times the compute power of its predecessor, Perlmutter, with only 2-3 times the power consumption [48] using no novel computing technology.

In addition there is research ongoing into other areas of computing technology, for example using optical signals to run computations rather than electronic signals. These have the potential to drive step changes in energy efficiency, especially in the types of calculations used in machine learning, such as matrix multiplication. [49] The UK's Advanced Research and Innovation Agency (ARIA) also has a research programme aimed at Scaling Compute, with a stated goal of reducing the cost of compute by up to 1000x, for example by designing compute technologies that minic how nature computes [50].

12.6 Conclusion

Handling and storing the immense data rates produced by a next-generation XFEL is a major technical challenge, but also creates opportunities to take advantage of advances in AI and ML. These technologies can improve facility efficiency, accelerate user discoveries, and reveal scientific features that would otherwise remain hidden. To realise this potential, the facility must be designed from the outset to leverage current and emerging AI and ML capabilities. This includes provision of a petascale HPC environment, an exabyte-scale offline storage system, and a comprehensive digital twin of the facility, all delivered within a sustainable infrastructure that mitigates residual emissions.

A number of areas remain for further development, including developing specifications for the control system, edge computing, high performance computing, data storage, high speed data acquisition and sustainable data centres. Targeted R&D is also needed in areas such as XFEL-specific data reduction, optimisation of experimental setups, and ML-driven accelerator operations. Additional opportunities exist to develop facility-specific technologies, including accelerated ML models for FPGAs, FPGA-based compression pipelines, and the use of computer-vision accelerators for beamline and accelerator diagnostics.

Maximising the facility's use of AI and ML is essential both for delivering next-generation capability and for aligning with STFC's AI Strategy and the UK Government's broader science and technology ambitions. The UK XFEL project should continue to strengthen its connections with the many groups already advancing these technologies across STFC, UKRI, and the wider national and international communities. This includes deepening engagement with international facilities such as the European XFEL and LCLS-II, as well as wider AI initiatives for accelerator facilities in Europe (ARTIFACT) and the US (Genesis Mission and Multi-Office particle Accelerator Team). Ongoing developments at UK accelerator facilities such as CLARA, Diamond, and ISIS will also provide valuable experience and expertise.

References for Chapter 12

[1] Krzysztof Wrona. *Scientific Data Policy of the European XFEL (Presentation at European XFEL User Meeting 2024)*. 2024. URL: https://www.xfel.eu/sites/sites_custom/site_xfel/content/e51499/e60513/e63558/e215369/e218977/e218989/e236047/xfel_file236058/SDP-Dataworkshop-UserMeeting2024_KW1_eng.pdf.

[2] Egor Sobolev et al. "Data reduction activities at European XFEL: early results". In: *Frontiers in Physics* Volume 12 - 2024 (2024). ISSN: 2296-424X. DOI: 10.3389/fphy.2024.1331329. URL: https://www.frontiersin.org/journals/physics/articles/10.3389/fphy.2024.1331329.

[3] Science and Technology Facilities Council. *AI for Scientific Innovation: STFC AI Strategy*. Produced by Valerie Farr, Mark Wilkinson and Adriano Agnello. 2025. URL: https://www.ukri.org/publications/stfc-artificial-intelligence-strategy/.

[4] Square Kilometer Array Observatory. *SKA Data*. 2025. URL: https://www.skao.int/en/explore/big-data/.

[5] Yann Collet and Murray Kucherawy. *Zstandard Compression and the 'application/zstd' Media Type*. RFC 8878. Feb. 2021. DOI: 10.17487/RFC8878. URL: https://www.rfc-editor.org/info/rfc8878.

[6] PICMG. *MicroTCA.4 Specification*. 2024. URL: https://www.picmg.org/openstandards/microtca/.

[7] Thayer, Jana et al. "Massive Scale Data Analytics at LCLS-II". In: *EPJ Web of Conf.* 295 (2024), p. 13002. DOI: 10.1051/epjconf/202429513002. URL: https://doi.org/10.1051/epjconf/202429513002.

[8] UK Government. *Scotland to host UK's national supercomputer as Chancellor confirms £750 million investment*. 2025. URL: https://www.gov.uk/government/news/scotland-to-host-uks-national-supercomputer-as-chancellor-confirms-750-million-investment/.

[9] Johannes P. Blaschke et al. "ExaFEL: extreme-scale real-time data processing for X-ray free electron laser science". In: *Frontiers in High Performance Computing* Volume 2 - 2024 (2024). ISSN: 2813-7337. DOI: 10.3389/fhpcp.2024.1414569. URL: https://www.frontiersin.org/journals/high-performance-computing/articles/10.3389/fhpcp.2024.1414569.

[10] Mark Wilkinson, Jeremy Yates, and Vassil Alexandrov. *STFC Exascale Requirements*. Version 5.2 - 27th August 2024. 2024.

[11] Mark D. Wilkinson et al. "The FAIR Guiding Principles for scientific data management and stewardship". In: *Scientific Data* 3.1 (Mar. 2016). ISSN: 2052-4463. DOI: 10.1038/sdata.2016.18. URL: http://dx.doi.org/10.1038/sdata.2016.18.

[12] UK Research and Innovation. *UKRI Draft Data Policy*. 2025. URL: https://engagementhub.ukri.org/ukri-openresearch/developing-ukris-research-data-policy/user_uploads/draft-ukri-research-data-policy-for-consultation_published-09-april-2025.pdf.

[13] Ada Lovelace Centre. *Ada Lovelace Centre*. 2025. URL: https://adalovelacecentre.ac.uk/.

[14] Mubashara Akhtar et al. "Croissant: A Metadata Format for ML-Ready Datasets". In: *Proceedings of the Eighth Workshop on Data Management for End-to-End Machine Learning*. DEEM '24. Santiago, AA, Chile: Association for Computing Machinery, 2024, pp. 1–6. ISBN: 9798400706110. DOI: 10.1145/3650203.3663326. URL: https://doi.org/10.1145/3650203.3663326.

[15] David Cajander et al. "Using supervised machine learning in power converters design for particle accelerators–Application to magnetic components design". In: *Journal of Physics: Conference Series*. Vol. 2687. 8. IOP Publishing. 2024, p. 082019.

[16] Axel Huebl et al. "Next generation computational tools for the modeling and design of particle accelerators at exascale". In: *arXiv preprint arXiv:2208.02382* (2022).

[17] Asif Iqbal, John Verboncoeur, and Peng Zhang. "A Supervised Machine Learning Framework for Multipactor Breakdown Prediction in High-Power Radio Frequency Devices and Accelerator Components: A Case Study in Planar Geometry". In: *arXiv preprint arXiv:2507.17881* (2025).

[18] Jan Kaiser et al. "Bridging the gap between machine learning and particle accelerator physics with high-speed, differentiable simulations". In: *Phys. Rev. Accel. Beams* 27 (5 May 2024), p. 054601. DOI: 10.1103/PhysRevAccelBeams.27.054601. URL: https://link.aps.org/doi/10.1103/PhysRevAccelBeams.27.054601.

[19] Oliver Stein, Jan Kaiser, and Annika Eichler. "Accelerating Linear Beam Dynamics Simulations for Machine Learning Applications". In: *Proceedings of the 13th International Particle Accelerator Conference*. 2022.

[20] Fei Tao et al. "Digital twin modeling". In: *Journal of Manufacturing Systems* 64 (2022), pp. 372–389.

[21] Kishansingh Rajput et al. "Outlook towards deployable continual learning for particle accelerators". In: *Machine Learning: Science and Technology* 6.3 (July 2025), p. 031001. DOI: 10.1088/2632-2153/adeb45. URL: https://doi.org/10.1088/2632-2153/adeb45.

[22] A. D. Brynes et al. *Closing the Loop: Deploying Auto-Generating Digital Twins for Particle Accelerators*. 2026. arXiv: 2604.19101 [physics.acc-ph]. URL: https://arxiv.org/abs/2604.19101.

[23] D. J. Scott, A. D. Brynes, and M. P. King. "High Level Software Development Framework and Activities on VELA/CLARA". In: *Proc. IPAC'19* (Melbourne, Australia, May 2019). JACoW Publishing, Geneva, Switzerland, pp. 1855–1858. DOI: 10.18429/JACoW-IPAC2019-TUPRB084. URL: http://accelconf.web.cern.ch/ipac2019/papers/TUPRB084.pdf.

[24] M. King et al. *Controls Abstraction Towards Accelerator Physics: A Middle Layer Python Package for Particle Accelerator Control*. 2025. arXiv: 2509.19794 [physics.acc-ph]. URL: https://arxiv.org/abs/2509.19794.

[25] Auralee Edelen and Xiaobiao Huang. "Machine Learning for Design and Control of Particle Accelerators: A Look Backward and Forward". In: *Annual Review of Nuclear and Particle Science* (2024). URL: https://api.semanticscholar.org/CorpusID:272921447.

[26] Ryan Roussel, Adi Hanuka, and Auralee Edelen. "Multiobjective Bayesian optimization for online accelerator tuning". In: *Phys. Rev. Accel. Beams* 24 (6 June 2021), p. 062801. DOI: 10.1103/PhysRevAccelBeams.24.062801.

[27] Jan Kaiser et al. "Reinforcement learning-trained optimisers and Bayesian optimisation for online particle accelerator tuning". In: *Scientific reports* 14.1 (2024), p. 15733.

[28] C. Xu et al. "Beam trajectory control with lattice-agnostic reinforcement learning". In: *Proc. IPAC'23* (Venice, Italy). International Particle Accelerator Conference 14. JACoW Publishing, Geneva, Switzerland, Sept. 2023, pp. 4487–4490. ISBN: 978-3-95-450231-8. DOI: 10.18429/JACoW-IPAC2023-THPL029.

[29] Ryan Roussel et al. “Efficient six-dimensional phase space reconstructions from experimental measurements using generative machine learning”. In: *Phys. Rev. Accel. Beams* 27 (9 Sept. 2024), p. 094601. DOI: 10.1103/PhysRevAccelBeams.27.094601. URL: https://link.aps.org/doi/10.1103/PhysRevAccelBeams.27.094601.

[30] A. Wolski et al. “Transverse phase space tomography in an accelerator test facility using image compression and machine learning”. In: *Phys. Rev. Accel. Beams* 25 (12 Dec. 2022), p. 122803. DOI: 10.1103/PhysRevAccelBeams.25.122803. URL: https://link.aps.org/doi/10.1103/PhysRevAccelBeams.25.122803.

[31] A. Pollard et al. “Machine learning for laser pulse shaping”. In: *Proc. IPAC'23* (Venice, Italy). International Particle Accelerator Conference 14. JACoW Publishing, Geneva, Switzerland, Sept. 2023, pp. 4495–4498. ISBN: 978-3-95-450231-8. DOI: 10.18429/JACoW-IPAC2023-THPL034.

[32] J. Hirschman et al. “Leveraging the capabilities of LCLS-II: linking adaptable photoinjector laser shaping to x-ray diagnostics through start-to-end simulation” (Taipei, Taiwan, Jun. 2025). presented at IPAC'25, Taipei, Taiwan, Jun. 2025, paper MOPB040, unpublished.

[33] A. E. Pollard, D. J. Dunning, and A. J. Gilfellon. “Machine Learning for RF Breakdown Detection at CLARA”. In: *Proc. LINAC'22* (Liverpool, UK). International Linear Accelerator Conference 31. JACoW Publishing, Geneva, Switzerland, Oct. 2022, pp. 858–862. ISBN: 978-3-95-450215-8. DOI: 10.18429/JACoW-LINAC2022-THPORI16.

[34] Chris Tennant et al. “Superconducting radio-frequency cavity fault classification using machine learning at Jefferson Laboratory”. In: *Physical Review Accelerators and Beams* 23.11 (2020), p. 114601. DOI: 10.1103/PhysRevAccelBeams.23.114601.

[35] Elena Fol et al. “Detection of faulty beam position monitors using unsupervised learning”. In: *Physical Review Accelerators and Beams* 23.10 (2020), p. 102805. DOI: 10.1103/PhysRevAccelBeams.23.102805.

[36] Vasilis Belis et al. “Quantum anomaly detection in the latent space of proton collision events at the LHC”. In: *Communications Physics* 7.1 (2024), p. 334.

[37] Daniel S. Levine et al. *The Open Molecules 2025 (OMol25) Dataset, Evaluations, and Models*. 2026. arXiv: 2505.08762 [physics.chem-ph]. URL: https://arxiv.org/abs/2505.08762.

[38] Ilyes Batatia et al. “A foundation model for atomistic materials chemistry”. In: *The Journal of Chemical Physics* 163.18 (Nov. 2025), p. 184110. ISSN: 0021-9606. DOI: 10.1063/5.0297006. eprint: https://pubs.aip.org/aip/jcp/article-pdf/doi/10.1063/5.0297006/20801246/184110_1_5.0297006.pdf. URL: https://doi.org/10.1063/5.0297006.

[39] Zhixing Jiang et al. “Machine learning evaluation in the Global Event Processor FPGA for the ATLAS trigger upgrade”. In: *Journal of Instrumentation* 19.05 (2024), P05031.

[40] Christoph Obermair et al. “Explainable machine learning for breakdown prediction in high gradient RF cavities”. In: *Physical Review Accelerators and Beams* 25.10 (2022), p. 104601. DOI: 10.1103/PhysRevAccelBeams.25.104601.

[41] John Jumper et al. “Highly accurate protein structure prediction with AlphaFold”. In: *Nature* 596.7873 (July 2021), pp. 583–589. ISSN: 1476-4687. DOI: 10.1038/s41586-021-03819-2. URL: http://dx.doi.org/10.1038/s41586-021-03819-2.

[42] Juraj Gottweis et al. *Towards an AI co-scientist*. 2025. DOI: 10.48550/ARXIV.2502.18864. URL: https://arxiv.org/abs/2502.18864.

[43] Innovation Department for Science and Technology. *UK to become world leader in drug discovery as Technology Secretary heads for London Tech Week*. 2025. URL: https://www.gov.uk/government/news/uk-to-become-world-leader-in-drug-discovery-as-technology-secretary-heads-for-london-tech-week/.

[44] Top500. *Green500 List*. 2025. URL: https://www.top500.org/green500/.

[45] Department for Energy Security and Net Zero. *Quarterly Energy Prices*. 2025. URL: https://assets.publishing.service.gov.uk/media/67e3d1f9148bef6fa4cfdb6c/quarterly-energy-prices-march-2025.pdf.

[46] Department for Energy Security and Net Zero. *Clean Power 2030 Action Plan*. 2025. URL: https://www.gov.uk/government/publications/clean-power-2030-action-plan/clean-power-2030-action-plan-a-new-era-of-clean-electricity-main-report.

[47] Top500. *Top500 List*. 2025. URL: https://www.top500.org/top500/.

[48] NVIDIA. *The Supercomputer Designed to Accelerate Nobel-Worthy Science*. 2025. URL: https://blogs.nvidia.com/blog/dell-nvidia-berkeley-doudna/.

[49] Sufi R. Ahmed et al. “Universal photonic artificial intelligence acceleration”. In: *Nature* 640.8058 (Apr. 2025), pp. 368–374. ISSN: 1476-4687. DOI: 10.1038/s41586-025-08854-x. URL: http://dx.doi.org/10.1038/s41586-025-08854-x.

[50] Suraj Bramhavar. *Unlocking AI compute hardware at 1/1000th the cost*. 2023. URL: https://www.aria.org.uk/media/1dqpf505/aria-unlocking-ai-compute-hardware.pdf.

Engineering delivery, environmental sustainability, and project planning

DRAFT

13 Facility delivery

13.1 Engineering Delivery – General Layout, Buildings, Infrastructure and Technical Systems

13.1.1 Summary

For the option of a Next-Generation UK-based XFEL of the proposed size, scope, and cost, it is critical, even at the conceptual stage, to outline practical and efficient strategies for achieving the scientific and technological goals while managing technical engineering, business, and administrative risks. This section presents a potential facility layout, compares it to similar international facilities, and outlines key risks and management strategies to support successful project delivery.

13.1.2 Introduction, Scope and Assumptions

There are limited but prominent global examples of X-ray FELs operating at the high repetition rates envisioned for UK XFEL, such as European XFEL, LCLS and SHINE (see Section 13.1.3), limiting opportunities to draw on established best practices. Relevant documentation has been reviewed and, where possible, direct engagement with key personnel has provided additional insight, as many critical factors influencing design and cost decisions are not clearly documented or publicly available.

In addition to lessons from these reference projects, this assessment draws on core engineering and physics principles, expert advisory input, and decades of UK research council experience in delivering large-scale scientific facilities (electron accelerators, spallation sources, etc.) which are of comparable cost and scope.

Engineering and Practical Considerations: The technical design, accelerator engineering, and scientific objectives of an XFEL are highly interdependent. These relationships strongly affect cost, performance, and usability, making early evaluation essential.

Examples include:

- Beam spreader layout: Strongly determines FEL separation and experimental hall access but is also constrained by available magnet and kicker cavity technologies as well as lattice design beam physics.
- Beam dump design: Accessibility of high power beam dumps, with their corresponding large amounts of surrounding shielding and handling procedures and provision for redundancy, along with many other factors influences whether dumps can or should be co-located with FEL lines, dispersed, or shared, which in turn can affect maximum allowable pulse energies and repetition rates into the FELs.

DRAFT

- Photon optics: Overall lengths depend on source distance and divergence which must match with aberration-free fill limits and optic manufacturability and size constraints, whilst optic ablation damage thresholds limit maximum photon flux - all of which influence upstream and downstream layout of the FEL and Experimental Halls.
- Novel two-colour, synchronised-pulse techniques proposed for the UK XFEL CDOA introduce further constraints on spreader layout, FEL separation, and photon transport lengths and angles.
- RF Amplifier technology will considerably alter the buildings shape and size, and as such early decisions on type and location need to be decided early in the design process.
- The chosen 'phasing philosophy' will often dictate the technology choice, as particular options may constrain certain parameters.

This set of parameters illustrates how tightly coupled design choices are: each can significantly influence the engineering approach to layout and construction and act as a major driver of overall facility costs—emphasizing the need for a robust, realistic concept to manage risks and avoid costly revisions.

Overall, this engineering review is limited to a UK-based XFEL, without a specific constraint on location in the UK. This is the only option developed in sufficient detail to date, as broader collaborative or international options remain too preliminary for any meaningful evaluation. Focusing on a single, well-defined conceptual (yet feasible) design provides a realistic costing framework for a UK facility and a robust basis for any future, more detailed comparisons, including potential international collaborations.

The proposed facility layout is shown as a proportionally scaled schematic plan view in Figure 13.1, indicating the principal macro-scale elements of the XFEL (beam direction left to right). An isometric 3D representation of the site layout is also provided in Figure 13.2, highlighting the arrangement of the main buildings and supporting infrastructure.

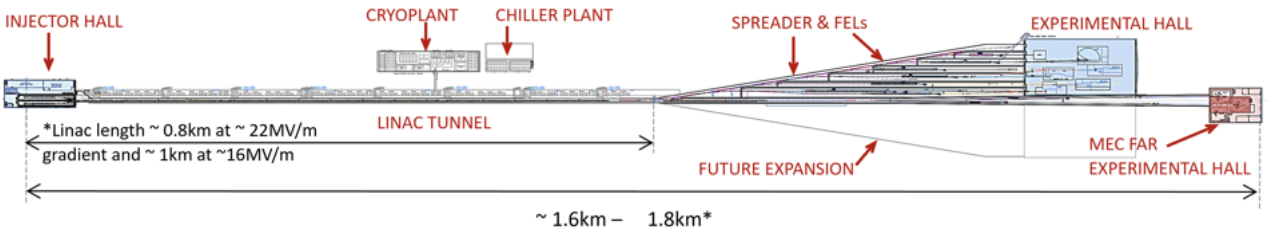

Figure 13.1: Scaled Plan View Full Layout of UK XFEL concept

Due to the extreme aspect ratio of the facility ($\sim$ 1.8 km in length), it is not practical to present meaningful detail in a single proportionally scaled overview layout within this report format. As a result, a simplified schematic plan (Figure 13.3) and an isometric 3D view (Figure 13.5) are provided, with key features and components annotated for clarity. Subsequent sections present an end-to-end walkthrough of the facility, offering more detailed views of major systems and infrastructure. The facility layout has been shaped by scientific requirements and optimised around current and anticipated technology developments envisioned for the UK XFEL concept, targeting a ten year build phase.

13.1.3 Comparison of Other Reference Facilities

In order to provide context to the UK XFEL design detailed in this chapter we will first compare against key reference facilities, selected due to their similarity in machine parameters and/or scale,

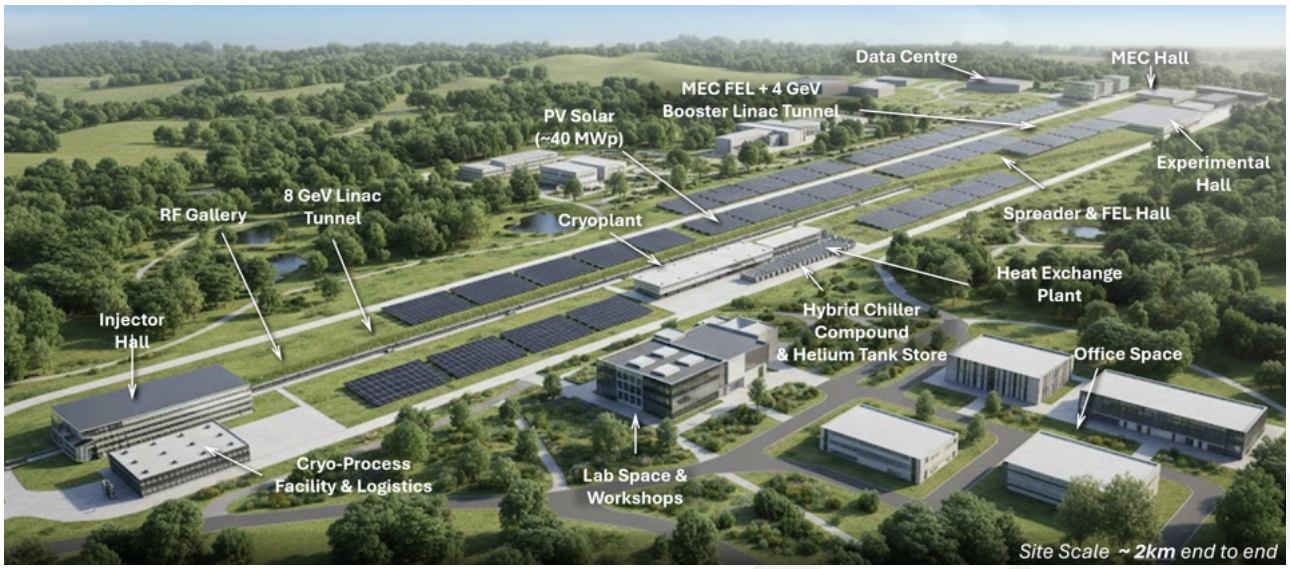

Figure 13.2: Scaled 3D CAD View of Site Layout of UK XFEL concept with key infrastructure and buildings

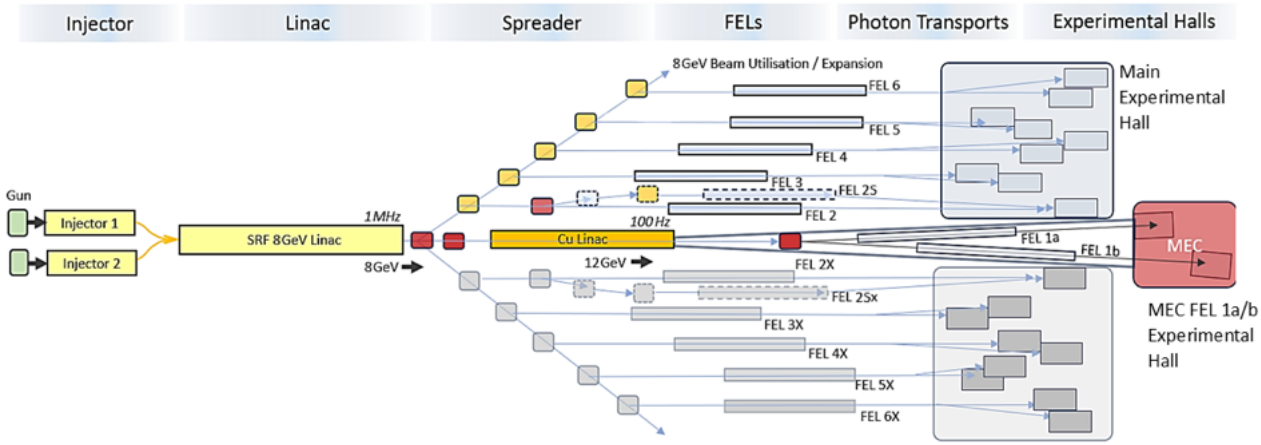

Figure 13.3: Schematic illustration of UK XFEL key elements

they include:

- European XFEL (Eu-XFEL) at DESY site, Hamburg, Germany [1]
- LCLS-II-HE, SLAC, Menlo Park, California, USA [2]
- SHINE (Shanghai High Repetition Rate X-ray FEL), CAS, China [3]

A common feature among all the XFELs referenced is the use of tunnel bores and deep excavations, this is not primarily driven by shielding requirements, but rather by the necessity of integrating with existing infrastructure in densely populated areas. In such settings, surface-level linear layouts extending several kilometres are often unfeasible, necessitating these costlier subsurface solutions. By contrast, UK XFEL, which currently has no fixed site, is assumed to adopt a near-surface “cut and cover” construction approach as its baseline, significantly reducing civil engineering costs, and allows for earthworks to be used as part of the radiation shielding. This is particularly viable given that the UK XFEL design as proposed is significantly shorter than many of its peers (see Figure 13.4), this is in part due to not being bound by geographic or historic constraints and the accelerator design itself.

This assumption underscores the critical need for early site selection. Delaying this decision could significantly constrain design options and lead to higher costs if deeper construction becomes necessary. While a subsurface configuration is technically feasible, it would likely require a

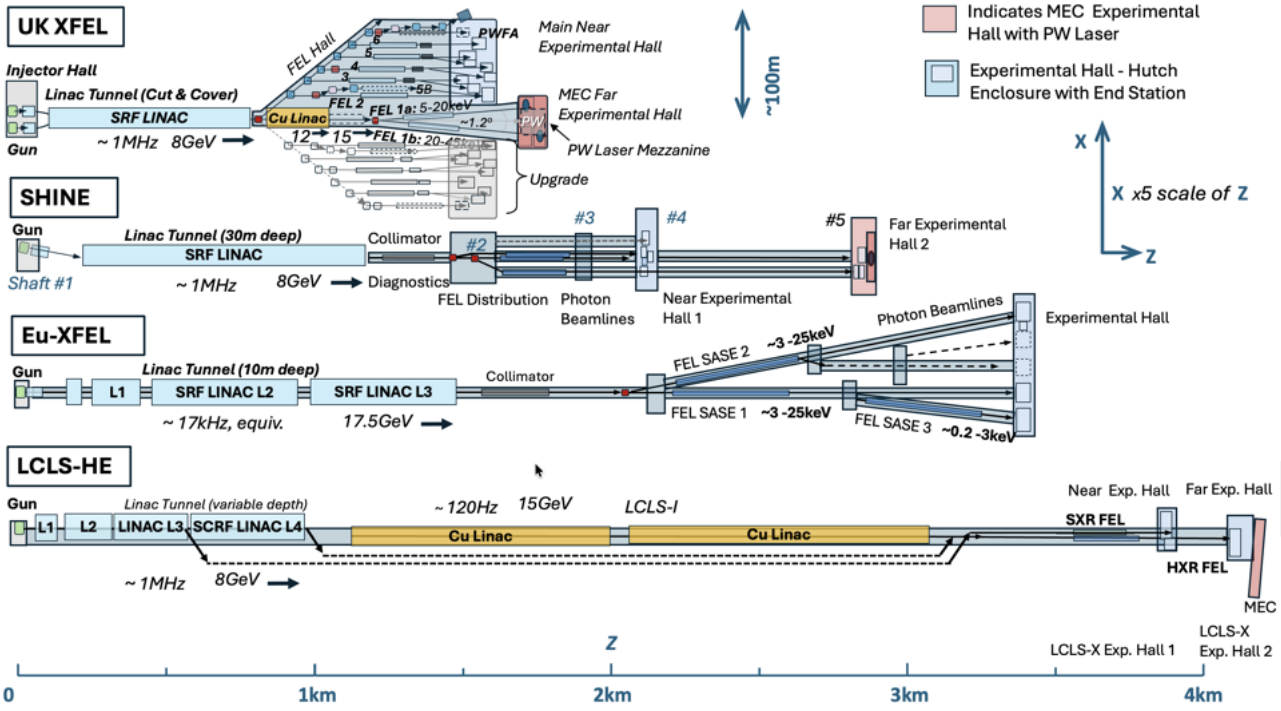

Figure 13.4: Approximately proportionally scaled schematic of UK XFEL in context of other Reference Facilities (with exaggerated $\times 5$ scaling in X to highlight features)

reconfiguration of the planned FEL hall and spreader volumes, making early agreement on site and construction approach essential.

SHINE also presents similar machine parameters to UK XFEL and plans for 6 end stations at launch, supported by adjacent tunnels with capacity for future FEL expansion. It begins operation with two 'Day 1' FELs. Notably, the photon transport systems at SHINE, and even more so at the European XFEL, are significantly longer than those planned for UK XFEL. The rationale for this is discussed in later sections concerning FEL halls and photon transport layout. These differences result in a UK XFEL design that is relatively compact along the beam axis (Z-direction), but wider transversely (X-direction), favouring a shared FEL hall with greater separation between beamlines over discrete tunnels. This configuration is more feasible and cost-effective under a near-surface construction scenario.

Extensive and ongoing collaboration with the Eu-XFEL team and the UK XFEL Conceptual Design and Options Analysis (CDOA) group has informed and improved multiple aspects of the UK XFEL's accelerator, FEL, and photon transport designs, as well as feeding into Eu-XFELs own plans.

Distinctive features of the UK XFEL include the ability to host at least seven distinct FELs in phase 1, including two MEC class (Material Extreme Conditions) high-energy X-ray FELs with high pulse energy across energy ranges 5-20 keV and 20-45 keV matched into Petawatt high power lasers at $\sim$100 Hz. A further five FELs: 2, 3, 4, 5, 6 will cover energy ranges from hard to tender and soft X-ray ranges; 5-20, 3-13, 1-5, 0.25–3 and $\sim$0.1-1 keV respectively, at hundreds of kHz repetition rate up to potentially 1 MHz (see Figure 6.8).

Space is also allocated for a experimental accelerator test line. In addition, provision is made for potential multiple synchronised two-colour FELs positioned adjacent to the main FELs within the FEL Hall, as explained in later sections. Other configurations are also envisaged for matched synchronous sources, such as accelerator-based THz or other high-power laser systems, feeding into the experimental stations.

UK XFEL's layout and site boundary will facilitate easy future upgrades that could nearly double FEL capacity without modifying the original structure or significantly interrupting operations. In fact, continued expansion well beyond the nominal symmetric plan is plausible, contingent only on site boundary constraints. This flexibility and expandability will enable significantly more end stations than what is available at current XFELs, really pushing capacity towards that of synchrotron facilities.

DRAFT

13.2 UK XFEL Conceptual Design Options – Layout, Build & Construction

General Accelerator & FEL Layout:

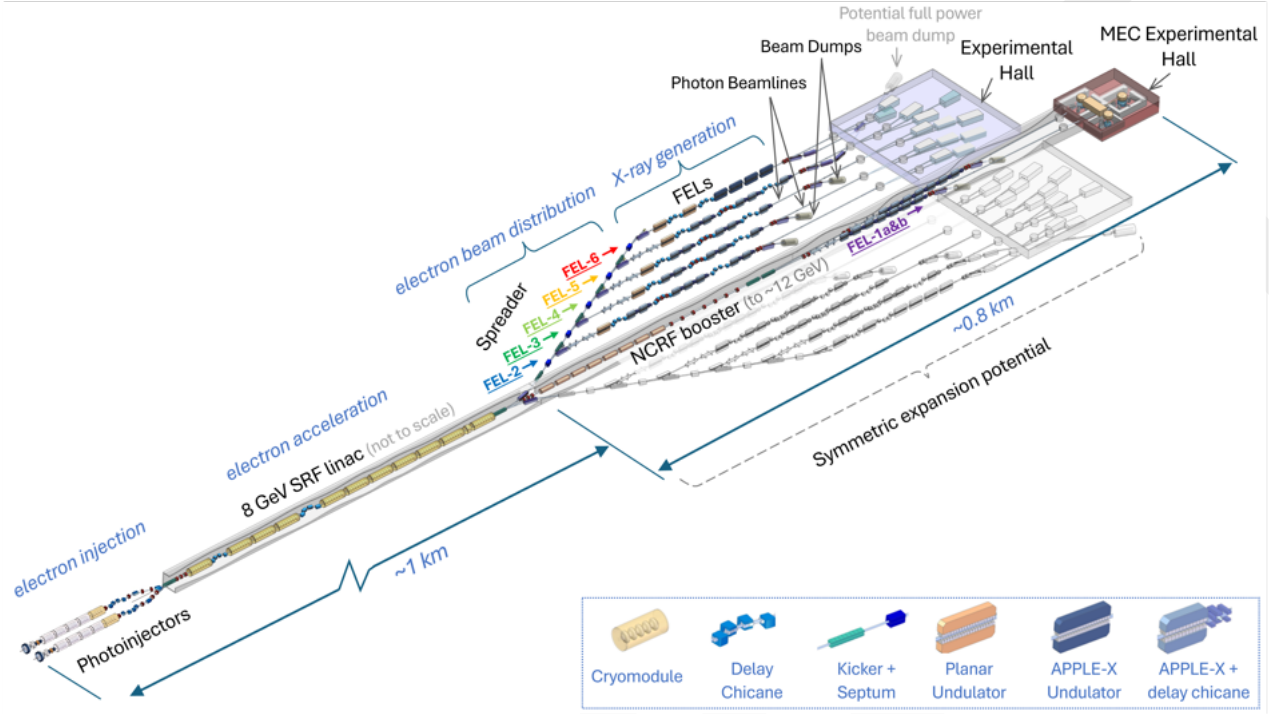

Figure 13.5: Illustrative 3D Schematic CAD Layout

Overview of Key Machine Elements The accelerator complex extends from the dual Photoinjector source through the 8 GeV superconducting RF (SRF) linac, covering nearly 1 km in length. Following the linac, the spreader section occupies an additional ∼400 m. This section bends the beam by approximately 9° away from the main linac axis and enables distribution of individual electron bunches to multiple downstream FEL undulator lines using cavity and kicker-septum magnet arrays. The FEL lines maintain a parallel transverse separation of approximately 9 m. The photon pulses that emerge within the FEL lines are then transported downstream, pass through an end shield wall that marks a boundary of the FEL Hall, and on into multiple experimental end stations housed within a common Experimental Hall.

Adjacent to the spreader and FEL lines, on the straight-ahead linac axis, an additional ∼130 m long C-band (normal conducting) booster linac is installed to increase the electron energy to 12 GeV, with a further ∼100 m drift space reserved for a future energy upgrade. The booster linac operates at a lower repetition rate (∼100 Hz), comparable to high-peak-power lasers used in Matter at Extreme Conditions (MEC) experimental stations. A kicker-septum array diverts beam pulses into two separate high energy X-ray FEL beamlines (1a & 1b). With a modest angular separation of ∼1.2°, the configuration provides sufficient spatial divergence to support two independently operated FELs. This separation is also wide enough to accommodate large, shielded experimental stations within the Far MEC Experimental Hall, while remaining shallow enough to avoid excessive intrusion into the main experimental hall footprint.

A critical consideration from the outset is that both the construction strategy and associated costs for a UK XFEL are highly dependent on the characteristics of the selected site. The estimates and methodology outlined here are based on the assumption of a near-ideal but realistic

location: a relatively flat area consisting of a continuous strip of surface-accessible land situated away from densely populated or urbanised zones. This avoids the need for deep tunnelling or costly compulsory land acquisition, both of which could significantly escalate project costs. By contrast, peer facilities such as SHINE, LCLS-II-HE, and the European XFEL are based on bored tunnel construction with substantial excavation works at either end to accommodate Photoinjector infrastructure and experimental halls lying many metres below the surface. These approaches reflect different site constraints and illustrate how location can drive construction complexity and cost. Altogether, site selection has the potential to impact capital expenditure by up to ∼20%, representing a possible increase of several hundred million pounds in a multi-billion-pound project. It may also necessitate a significantly different construction approach or technical layout, particularly for components like the spreader and FEL hall, compared to the baseline assumptions presented here. While the current baseline assumes a favourable site for initial design and costing purposes, it is recognised that final site selection for large national flagship facilities may not be based solely on optimal technical or cost-efficiency grounds. Strategic, socio-economic, or co-location considerations may ultimately favour sites that require sub-surface construction or more complex delivery methods.

This proposed layout of the facility has been designed with future flexibility in mind, ensuring a range of future upgrade possibilities. Overall, the facility – with ancillary buildings plus access roads, along with some allowance for future upgrade space will occupy a perimetered fence land footprint of approximately 2 × 0.25 km.

13.2.1 Injector Hall

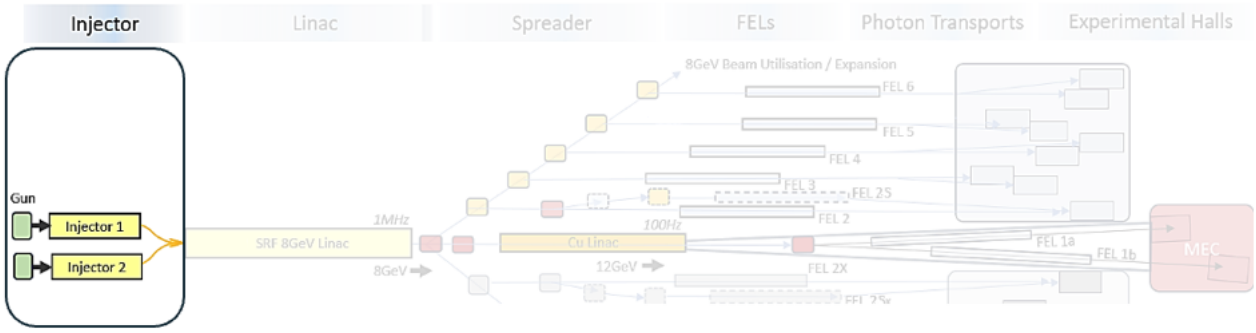

Achieving the machine design beam parameters, particularly in terms of supporting beam mode types (e.g. simultaneous operation of several FELs as well as two colour operation) along with redundancy requirements, necessitates the use of dual Photoinjectors, merging into the main linac. A key driver for the design of the shielding enclosures in the injector hall is the requirement that each Photoinjector area remains accessible while the other is operational. This design provision ensures that operations can continue running even if one injector beam line is offline for maintenance or repair.

This presents a challenging shielding arrangement, as the dual injector beams must converge through a merge section at a common point just upstream of the main linac. In addition, large-aperture cryo-pipes (greater than 600 mm in diameter) must pass from the high-radiation environment of the Linac Hall to the nearby, and potentially occupied, Photoinjector areas. To address this, a close-packed composite shielding structure is envisaged around the merging section, incorporating dense high-Z materials (such as barytes concrete). Large double-bend labyrinths are also proposed for the cryo-pipes, in order to reduce scatter dose rates to acceptable levels

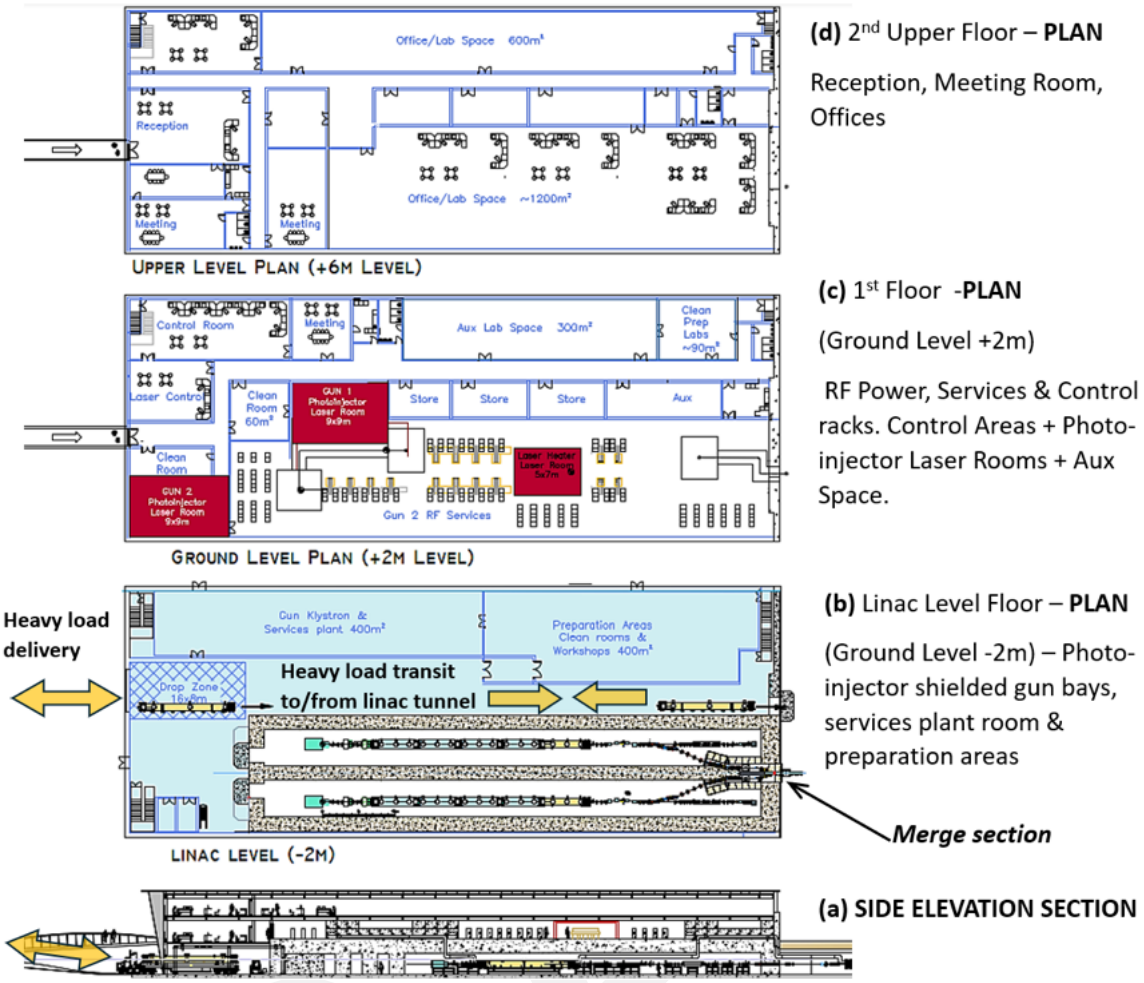

Figure 13.6: Photoinjector Hall showing 90 × 35 m plan of 3 levels plus side elevation view

on the cold side and within adjacent injector areas. Given the complex geometry and access requirements around the injector hall, an all-concrete shielding construction contained within the building, rather than the predominantly earth berm approach used elsewhere in the facility, is preferred. This also has an advantage in that the thick concrete roof can serve as a stable platform for RF infrastructure and photo-cathode laser systems placed directly above.

A closer view of the proposed injector is illustrated in Figure 13.6 with the gun areas shown in plan and side elevation view at the bottom tier, at the Linac Hall level, and two floors of the proposed building above shown in plan view. Essential injector infrastructure and control rooms will sit on the first floor, while above is envisaged for optional reception and office space. The RF power infrastructure for this sector will sit directly above the injector bays as will the Photoinjector lasers and feed waveguide and laser transports which feed directly down to the injector areas through back-shielded and/or labyrinth routes so that this key area above can also remain accessible whilst the XFEL is running (for the UK option as either a IRR17 radiation controlled or supervised area).

Overall, even though beam losses can be typically higher here, the electron energy in the injector areas are lower and ∼2 m concrete shielding thickness has provisionally been assumed as sufficient (although this must be validated by later analysis). Barytes concrete or other higher density materials could likely be used to maintain adequate shielding where geometric space constraints exist, such as through the converging merge points of the injector to the linac.

The injector hall is constructed in an excavated depression with the lowest point level with the

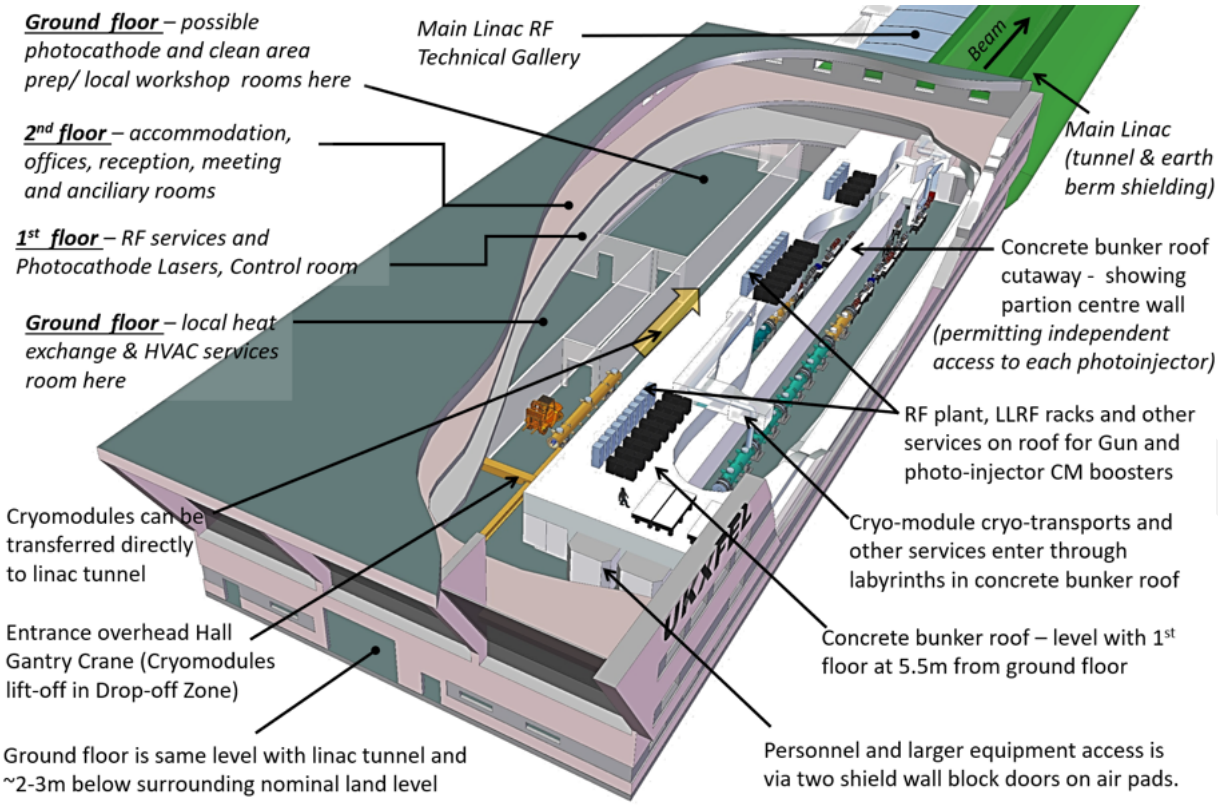

Figure 13.7: Injector Hall Building - 3D cutaway view with floors and shielding bunker cut to show dual Photoinjectors

Linac Hall floor, approximately 1 to 2 m below nominal ground level as indicated in side elevation (a) Figure 13.6. Personnel and light equipment access to the two gun areas is via air skate shield doors, whilst large equipment (e.g. cryomodules) access is via large shield block doors, again on air skates, as indicated in (b). Adequate space for truck delivery of accelerator Cryomodules to a drop zone / gantry crane access point toward the front of the building and once lifted off the transport, the accelerator modules will be fitted with air skates and moved either into position in the injector rooms or down the Linac Hall along the arrow marked pathways as indicated in the same figure (b). A further view of the Injector Hall, showing 3D isometric cutaway can be seen in Figure 13.7.

DRAFT

13.2.2 Linac Hall

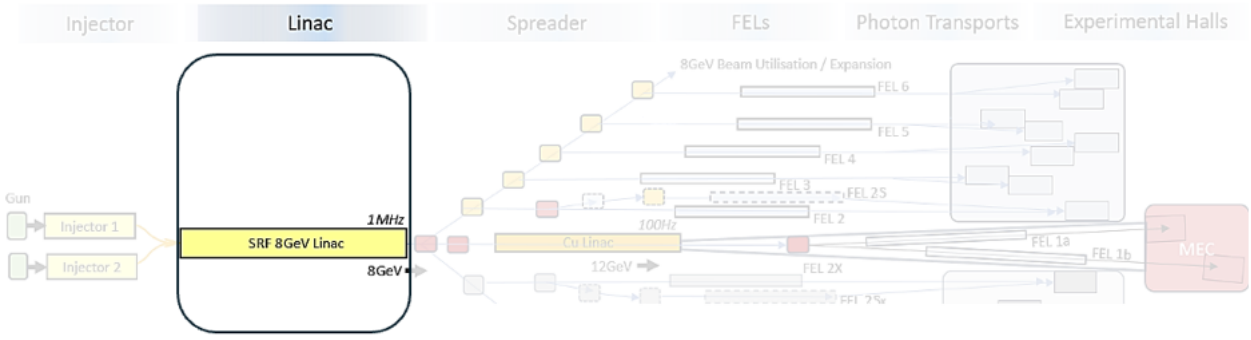

The Linac Hall, approximately between ∼0.8 to 1 km in length (dependent on final selection of linac gradient) houses approximately 60+ of the accelerator cryomodules which, along with associated beam transport systems (bunch compressors, collimators, etc.), comprise the linear accelerator.

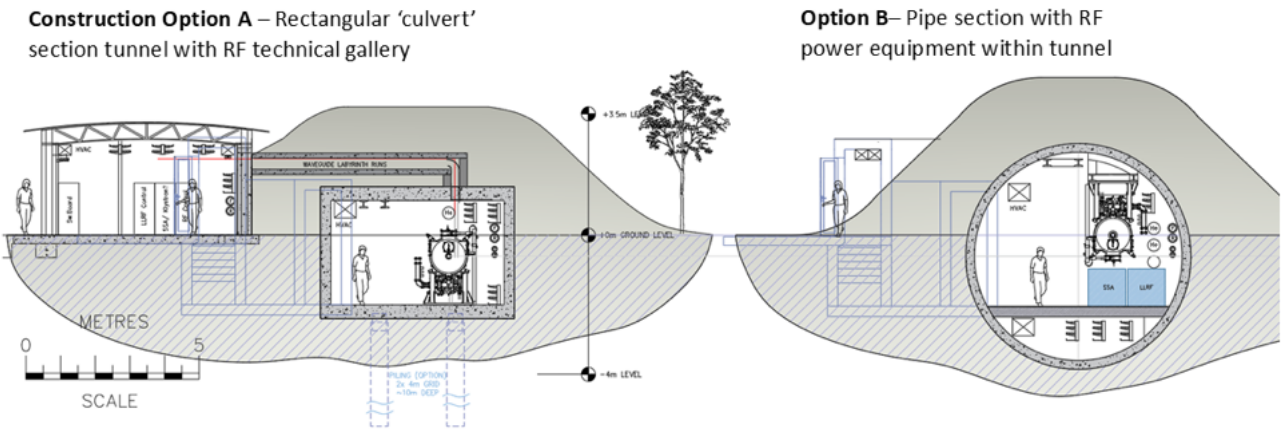

Figure 13.8: Cross section for cut and cover construction options for Linac Hall

Two possible cross section options of the Linac Hall are shown in Figure 13.8. In the left hand view, option A, a 'box culvert-like' concrete tunnel housing the linac accelerator is shown buried somewhat lower than the nominal surrounding land level. The tunnel is covered with 1.5 -2m of compacted earth to act as radiation shielding and insulation. The earth shielding here is repurposed from foundation excavations of this tunnel and hall buildings elsewhere. The depth of the tunnel floor below the land level (which globally defines the nominal beam centre of the whole facility) will depend on the lay of the surrounding land, bulk shielding earth thickness and depth of foundations required elsewhere. It is intended that the overall balance between additionally required and excess spoils of earth is neutral and a 1 to 2m depth is estimated as reasonable range in this regard.

An RF Technical Gallery runs alongside the full length of the tunnel housing the RF infrastructure and other services. RF equipment will consist of numerous Low Level RF Systems (LLRF), control racks and either solid state amplifiers (SSA) or much larger klystron modulators, dependent on final selections. Waveguide labyrinth penetrations will intermittently span over from the gallery at ∼30m+ intervals to fan out and feed into (typically) ∼4 cryomodules. The electrical and cooling service runs are mounted on the wall adjacent to the RF coupler side of the cyromodules. The Heating/Ventilation/Air Con (HVAC) and other services run at high level on the labyrinth egress side

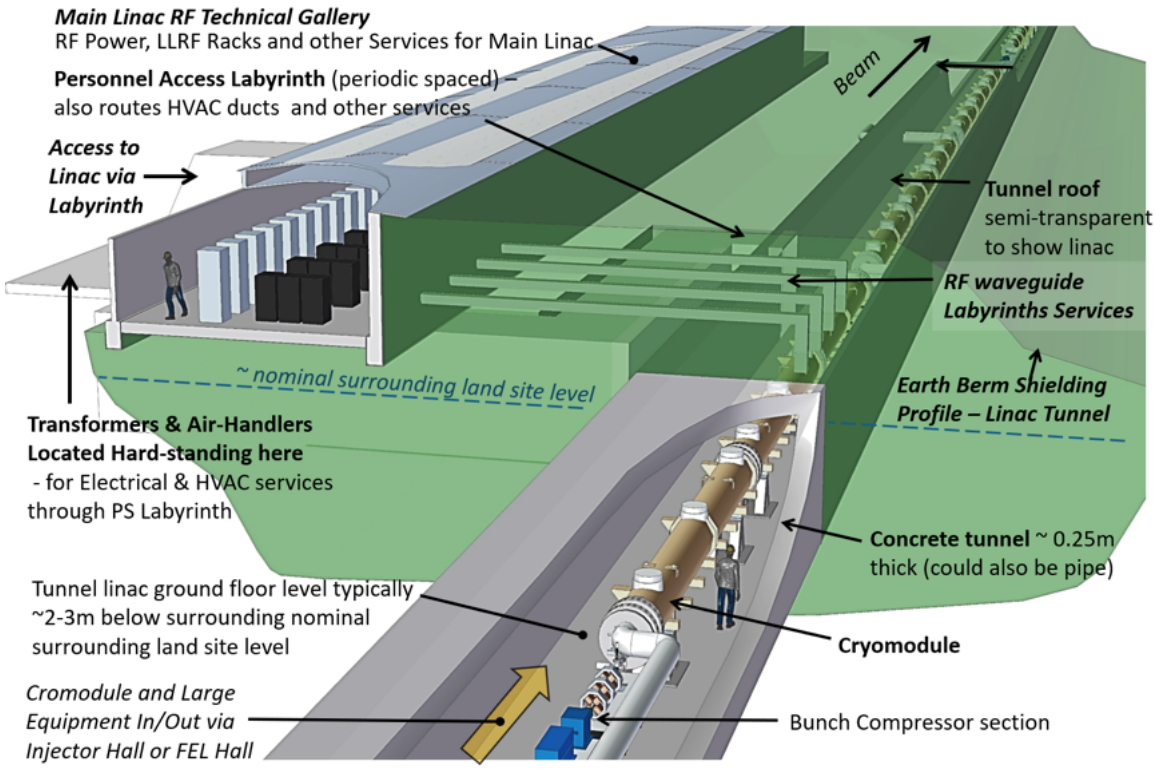

Figure 13.9: Linac Tunnel & RF services gallery – 3D cutaway visualisation of option A

of the tunnel - keeping the floor unobstructed. Interconnections between strings of cryomodule require that the cryo services run in a large diameter pipes. This is also depicted at the upper right hand corner of the tunnel cross section of Figure 13.8. Whilst the 3D visualisation in Figure 13.9 shows a conceptual cut out view of the cryomodules situated in the tunnel.

Personnel access and emergency exits for the tunnel will be provided via stairwell labyrinths. These could be spaced at maximum intervals of approximately 80-90 meters to meet emergency regulations but greater spacing may be permitted to reduce number and costs, provided that suitable alternative escape routes or safe shelters are implemented. High-level routes within these labyrinths will accommodate large radiation aperture services, such as HVAC ducts, connecting to external air handling units. Adjacent to the labyrinths would be a goods lifts capable of handling light equipment. For larger and heavier equipment (such as the 8000 Kg linac Cryomodules), entry and exit will occur exclusively at the injector hall end of the tunnel. Such equipment will be transported along the access side of the tunnel using skates or air pads. To facilitate this, one side of the tunnel must always remain unobstructed and free of services. It is expected that the tunnel will also house infrastructure needed for inspection robots and remote handling systems to reduce the need for human intervention in the accelerator.

Option B of Figure 13.8 depicts an alternative section without an RF technical gallery that is an option only available for RF power based on Solid State Amplifiers (SSA) and is described next.

RF & Technical Gallery: RF power equipment, whether klystron modulators or SSAs, along with their associated Low-Level RF (LLRF) control racks, should ideally be located as close as possible to the accelerating cavities. A Personnel Safety (PS) accessible RF technical gallery, with radiation dose rates low enough to permit controlled access to the RF racks and power plant during operation, is highly desirable for monitoring and serviceability purposes. Both LCLS [4] and European XFEL [5] have the majority of their RF infrastructure located in a separate RF services space following this philosophy. In order to facilitate this approach, there must be some level of bulk shielding and labyrinth of services between the operational linac and RF services. This tends

to lengthen waveguide runs and introduces the drawback of higher RF power losses along with higher costs of more complex services construction. To mitigate the long waveguide runs, the RF technical gallery could potentially be positioned directly above the tunnel on a concrete shielded roof as at the SwissFEL linac. However, this approach would necessitate over 150,000 Tonnes of additional concrete, which is both costlier and conflicts with sustainability goals and is thus not pursued further.

Constructing such an RF gallery, extending parallel to the entire 1 km tunnel length at ground level, (as shown in cross-sectional view option A in Figure 13.8) could increase overall civil construction costs of the linac section by up to 10-20%. Alternatively, Solid State RF Amplifiers (SSA), while somewhat less efficient, are more reliable than klystron-modulator systems and are compact enough to be installed *within* the Linac Hall, close to the cryomodules. This minimizes waveguide losses and is the approach adopted by the SHINE facility, depicted as option B in Figure 13.8. Implementing this option would likely require slight tunnel enlargement and additional in-situ high-Z shielding enclosing the SSAs, with the drawback that the linac must be turned off to directly access and maintain and of the RF infrastructure. For UK XFEL, preliminary cost estimates will include ballpark figures for both options. However, conducting a detailed cost-benefit analysis of the critical RF power equipment configurations, Option A vs. Option B, will be a key decision in the next phase of planning, with current preference being for Option A.

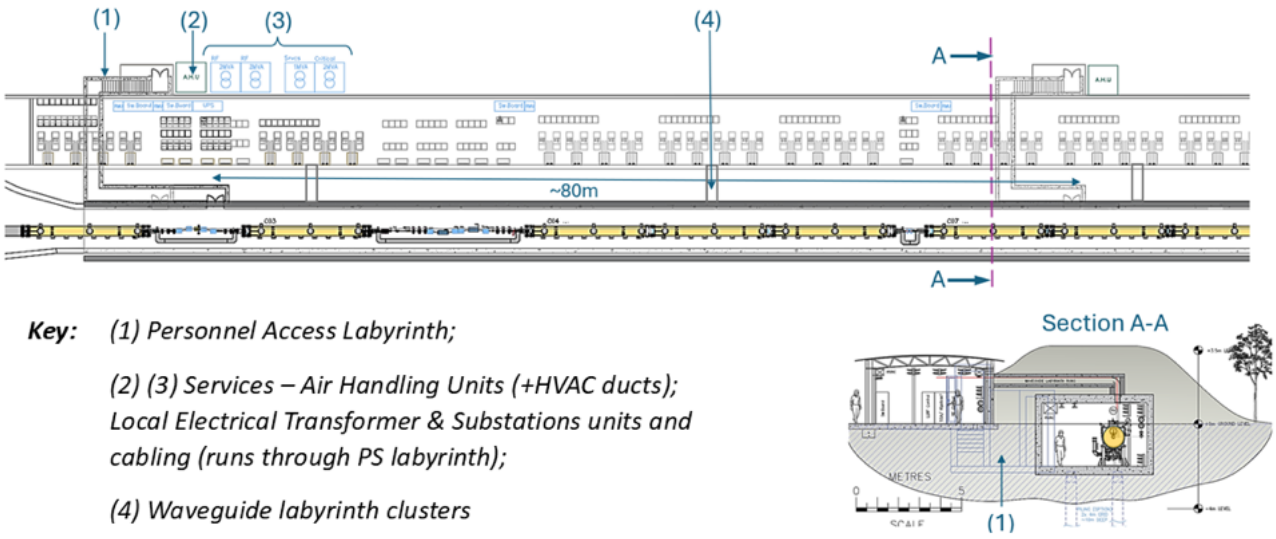

Figure 13.10: Portion of Linac Hall & RF services gallery – Plan view option A & Section.

13.2.3 Spreader, FEL Hall & Photon Transports

The Photoinjectors feed into the low energy beamline of the accelerator, the construction of which was addressed in previous Figure 13.2.2. At the end of the ∼1 km linac section a length of ∼20 m is nominally reserved for collimators and diagnostics. This is comparatively shorter than other facilities and may need to increase in size subject to further study.

Downstream of the linac is a spreader section which distributes any required bunch pattern from the linac train along any of the separate FEL undulator lines. This complex array of interconnected and interdependent systems are described below.

Spreader:

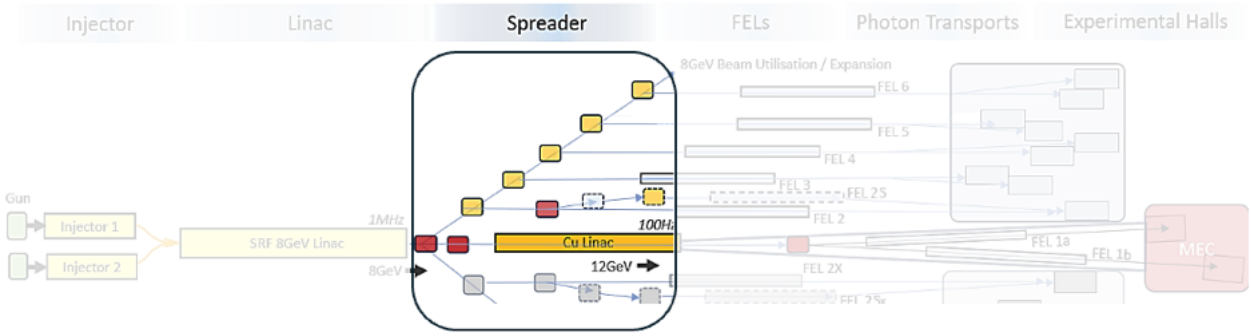

Several spreader configurations have been evaluated, including branching tridents, angled and parallel geometries, and diverging arrays. Based on beam physics, practical implementation, future expandability and site geometric layout considerations, a wedge-shaped fan and parallel line configuration (Figure 13.11) was ultimately selected.

The spreader starts at ∼1 km (from the photocathode source point (SP)), immediately downstream of the linac. Here most of the beam is deflected at ∼2.8° using a ∼25 m span array of fast kicker-septum magnets. Downstream bending magnets increases the deflection to ∼9.2°, followed by a second kicker-septum array that brings the beam back to a parallel trajectory—forming FEL2 which is offset ∼12 m from the straight-on linac axis. (see Figure 13.11 - close-up (b)). This allows enough space for the diverging MEC lines downstream to bypass the FEL2 experimental hall. This 9.2° diagonal continues through the spreader, with repeated reverse kicker-septum arrays generating five additional parallel FEL lines, each offset ∼9.1 m from the next. The kicker system operates at up to ∼1 MHz, enabling single-pulse switching with microsecond spacing.

As shown in Figure 13.11(a), some FEL lines include branching beamlines that then run parallel and spaced 3 m out from the main FEL (as example see FEL-2 and FEL-2S). On demand, the Photoinjectors can deliver a double electron pulse with an adjacent RF-cycle timing offset of ∼1 ns within any microsecond-scale MHz pulse train along the spreader. An RF deflecting cavity on the FEL line diverts the first of these two pulses at an angle of ∼2.7°, directing it into a branchline that is ultimately offset by ∼3 m from the main FEL. This clearance is sufficient to accommodate a full, conventional second FEL line parallel to the main straight.

The geometry of this branchline, together with the typical length and angular divergence of the downstream photon transport, enables two FEL pulses of different energies to become synchronised and reach a single experimental sample either simultaneously or with a controlled sub-nanosecond delay, facilitating pump–probe experiments. This configuration provides the basis for a synchronised two-colour capability on UK XFEL, positioning the facility uniquely

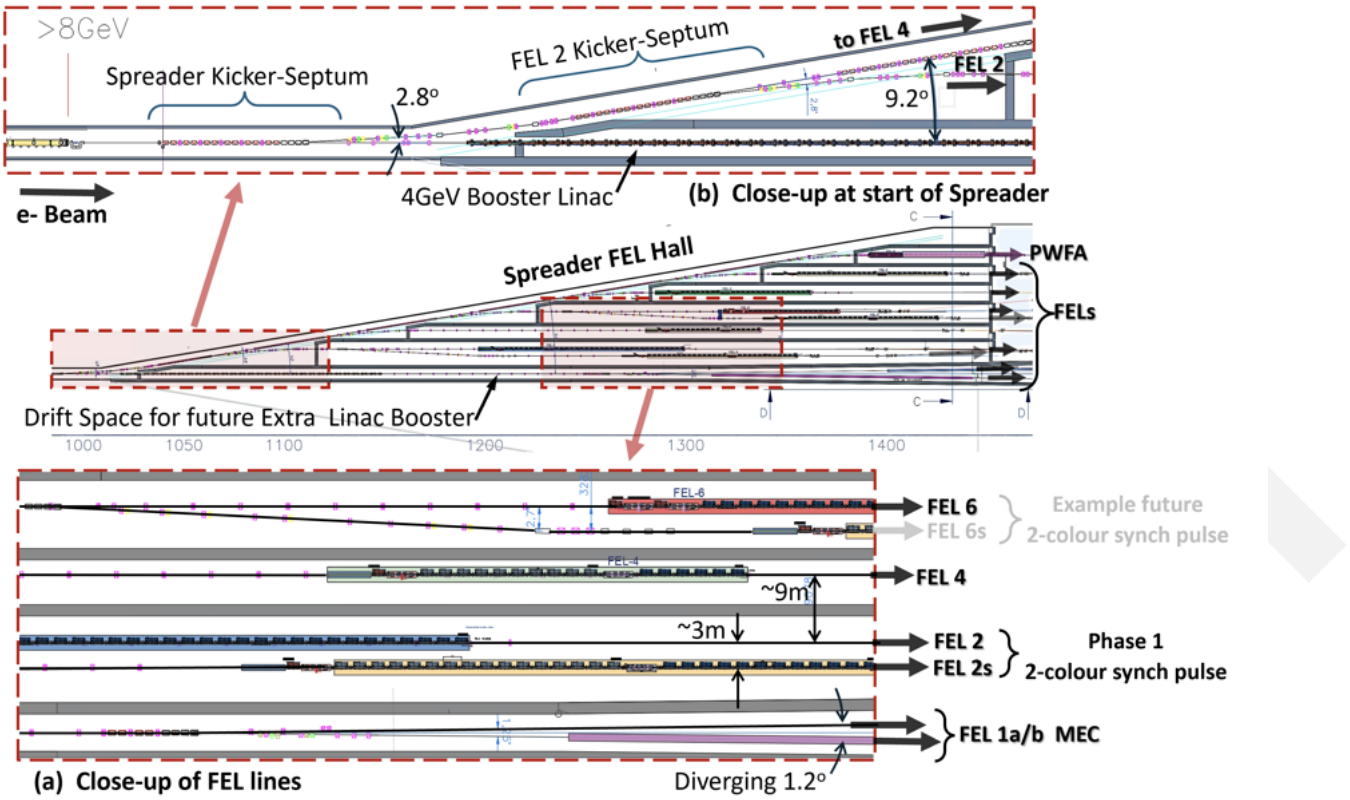

Figure 13.11: 2D Plan View of the Spreader and FEL Hall

for novel XFEL science. Although not shown here, the branching lines could also incorporate variable-magnet chicanes to introduce additional, small tunable timing delays.

DRAFT

FEL Hall:

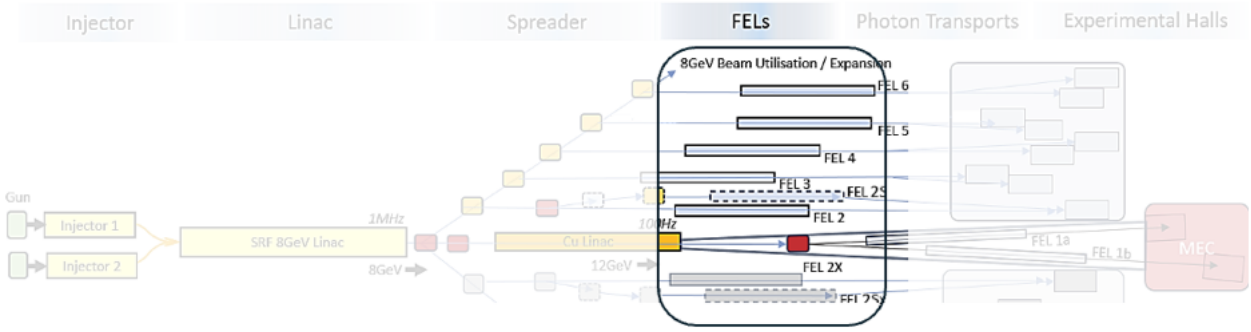

The chosen lattice separation of $\geq$ 9 m offers a high degree of adaptability and can be scaled up or down with relative ease. The resulting parallel FEL beamlines extend downstream into the photon transport system and experimental hall, providing good clearance and access around end station hutches.

To optimise space use while preserving cost-effectiveness, the design adopts a staggered layout in which FEL lines and associated photon transports are offset longitudinally (i.e. along beam Z axis). This staggered arrangement results in alternate experimental hutches having effective separations comparable to those at the European XFEL, thereby enhancing accessibility and operational flexibility. User community consultations have consistently highlighted the importance of generous and accessible experimental space as a key factor in maximising the scientific output of the facility.

The FEL line separation in this design is substantially greater than that planned for SHINE, where FEL-1 and FEL-2 are spaced at 3.3 m and FEL-1 to FEL-3 at approximately 7.5 m. It also exceeds the separations envisaged for LCLS-X (2.5m in tri-clusters with 4.5m spacing). Nonetheless, the UK XFEL configuration remains just over half that of the European XFEL, where slightly diverging photon transport lines enter the experimental hall with separations of $\sim$16–21 m.

The chosen configuration represents a balanced approach, offering wide access, future upgrade potential, and control of FEL hall civil construction costs. The FEL lines will be housed within a single, wide and diverging box-culvert-style concrete enclosure, with internal array of concrete or steel stanchions designed to support the load of the compacted earth berm above, which provides bulk radiation shielding (as in the Linac Hall); see Figure 13.12, Section C–C. This common, shared-hall approach is expected to be more cost-effective than constructing multiple separate tunnels and offers greater flexibility for future installations, such as an cavity XFELs, dual-colour synchronised FEL operation, or extended timing chicanes.

In order to optimised the simultaneous operation of the FEL lines, the internal shielding between FELs will consist of modular reconfigurable $\sim$1.5 m thick concrete walls. This internal modular design will not only allow repositioning of the walls, via air skate bogeys, but will also ensure that during modifications, maintenance or repairs to any given FEL line will not impact the operation of other lines, minimising facility downtime.

The current design accommodates up to ten undulator lines within the hall, with minimum 7 FELs independently operable (see Figure 13.12 and Figure 13.11). This includes the two central low-repetition-rate high energy MEC FELs (1a and 1b), five FELs covering remaining lower energy ranges, space for up to two FELs configured for dual-colour synchronised pulse operation and a shorter line towards the top of the plan view reserved for a dedicated test beamline. In practice, this allows for a similar number of experimental stations to operate simultaneously.

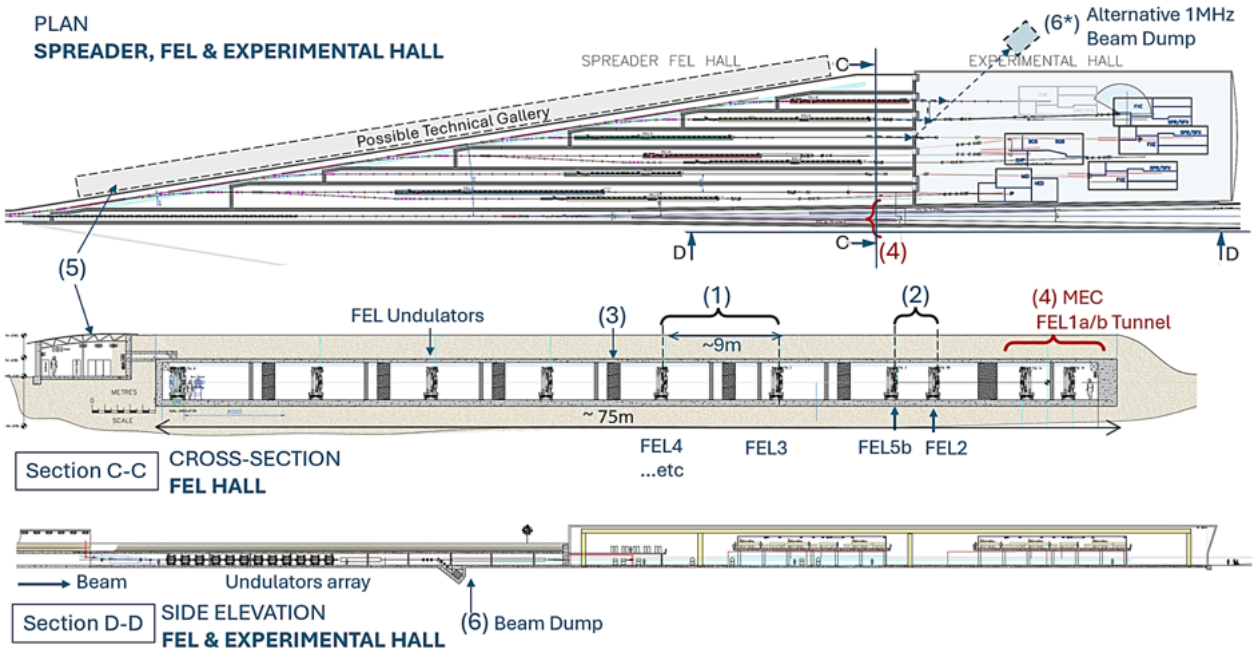

Key **(1)** Typical separation of FEL lines ~ 9m; **(2)** Synchronised two colour FELs (2 & 5) ~3m separation; **(3)** Partion block shielding allows independent FEL access with some flexibility in positioning; **(4)** Diverging HXR FEL section to MEC; **(5)** FEL technical services (motor controls, magnet PS) can be inside FEL hall or option for adjacent gallery indicated; **(6)** Beam dump section – see also later section.

Figure 13.12: Spreader, FEL & Experimental Hall in Plan (Spanning from 1 to 1.6km S.P.) with Cross-section C-C (along beam) of FEL Hall and Side Elevation D-D of FEL & Exp. Halls.

While the total number of FELs could in principle be reduced or increased, the present design provides sufficient space to realise the expected next-generation requirements through a phased build approach. Both the FEL hall and the experimental hall have scope to expand further if required. Reducing the footprint at the outset would lower initial costs, but assuming a long-term target of 10 or more FELs, the proposed layout offers the greatest flexibility. This includes potential for symmetric expansion about the central axis that could nearly double the capacity.

At present, the FEL hall terminates in a straight shielding wall, with the first optics and beam stops positioned primarily upstream within the FEL tunnel. Any downstream protrusions into the experimental hall would therefore necessitate dedicated local shielding enclosures. As FEL and photon transport concepts evolve, the stacking sequence may require re-optimisation. While a straight shielding wall simplifies construction, a staggered arrangement could be adopted in future to better accommodate photon transport geometries.

DRAFT

Photon Transports:

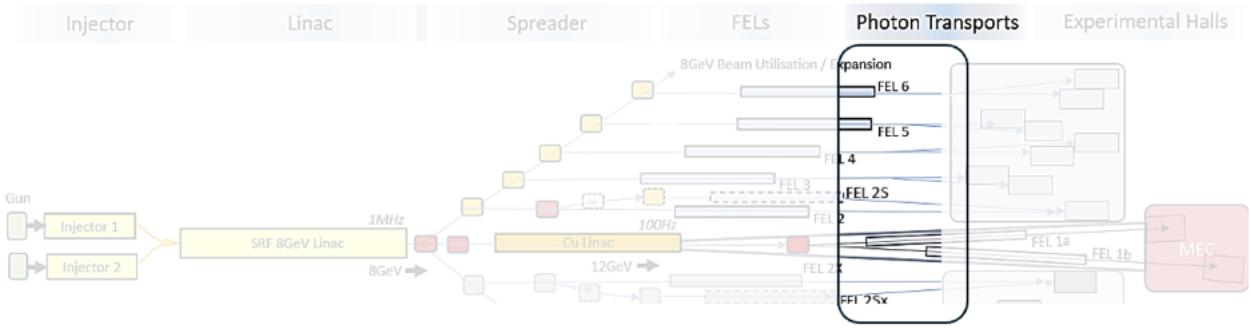

X-ray beamline photon transport lines have been added to the scaled 2D CAD layouts, consistent with the reference designs in Section 7.1. A notable feature of the UK XFEL concept is that proposed overall photon transport lengths are significantly shorter than those at other peer facilities (i.e. LCLS, SHINE and Eu-XFEL). This reduction arises from experience at other XFELs showing that collection of at least 5-6σ beam divergence onto the first optics is essential to avoid diffraction-limited distortions. At 6σ, the projection of this divergence onto a grazing incidence mirror determines the minimum distance from source to first optic. Current mirror fabrication technology limits their usable maximum lengths to $\sim$0.9 m, which directly then constrains the transport geometry to the layouts as depicted here. As a result of the optimal stacking and a desire to minimise building footprints (and costs), several photon transport sections are part located within the FEL hall tunnels, whilst also extending out into the experimental hall.

Because the beamline optics are positioned relatively close to the FEL source, the shorter transport distances will impose stricter lower limits on allowable photon flux onto the mirrors, as governed by ablation-damage thresholds, when compared with other XFELs. This compromise is driven by current manufacturing constraints on mirror length and the requirement to maintain a minimum 6σ angular acceptance. Should longer, high-quality mirrors become commercially feasible, or if FEL source parameters evolve during the design process, the transport lengths could potentially be increased signficantly. Such an adjustment would enable higher overall photon fluxes while still ensuring full 6σ beam capture. However, the current hall's wide span means that any additional extension to the transport lines lengthwise would add considerable cost. This remains an important consideration for future studies, where alternative hall geometries or layouts (e.g. FEL and photon transport discrete tunnels instead of a shared hall) might prove more cost-effective for accommodating significantly longer beamlines.

13.2.4 Experimental Halls

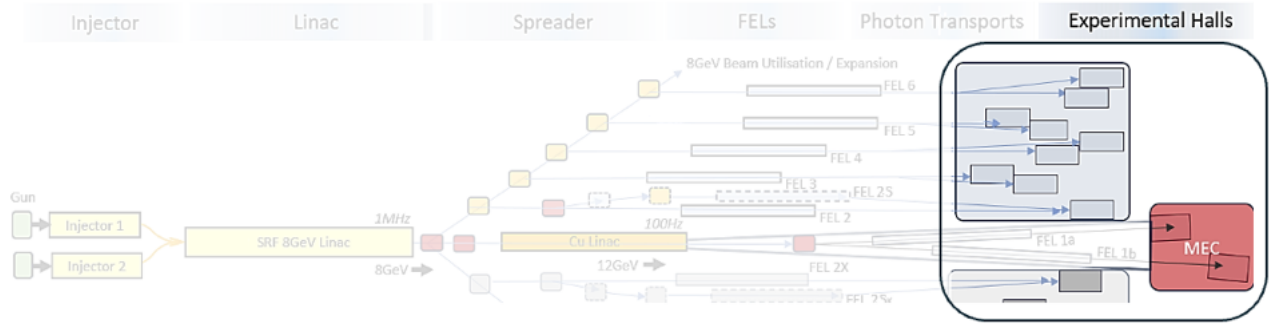

Main Experimental Hall:

As described earlier, the experimental hutches are in a staggered arrangement contained within a conventional unshielded building construction insulated to highest standards[1]. Individual hutch complexes or end station enclosures within hutches may be shielded, depending on requirements and subject to X-ray dose rate analyses in later studies. This will be achieved through a mix of concrete and/or local composite high-Z type shielding where space is a premium and costs allow.

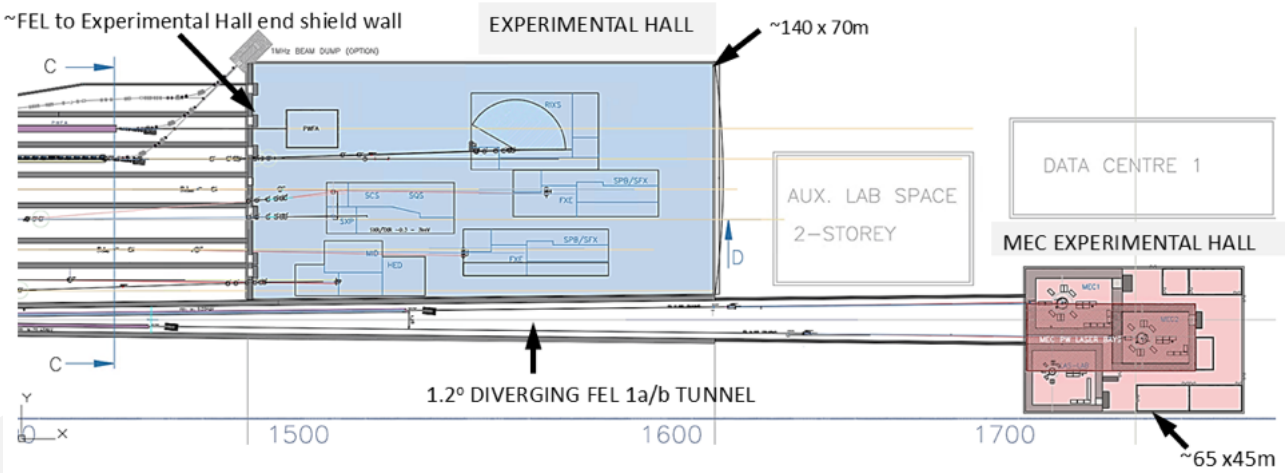

Figure 13.13: Experimental Halls in Plan (Spanning from 1.4km to 1.8km S.P.)

The experimental hutch areas are shown within the main Experimental Hall in Figure 13.13. The layout of the hutches are consistent with size allocations used at the European XFEL, with an additional 20% overhead margin (Figure 13.15). The overall hall footprint occupies ∼140 m × 70 m (∼10,000 m^2), almost double that of the European XFEL hall. The UK XFEL design therefore provides a generous margin to accommodate six or more hutch complexes with multiple end-stations as well as offering a degree of future-proofing from the outset.

Furthermore, because the hall is located at near ground level—rather than in 10 m deep excavations—future extensions would be relatively much easier than at other deeper sub-surface

[1] Insulating standards compliant with RIBA 2023/ ISO 14001 and 52000 series will apply to all buildings not covered by earth berm construction

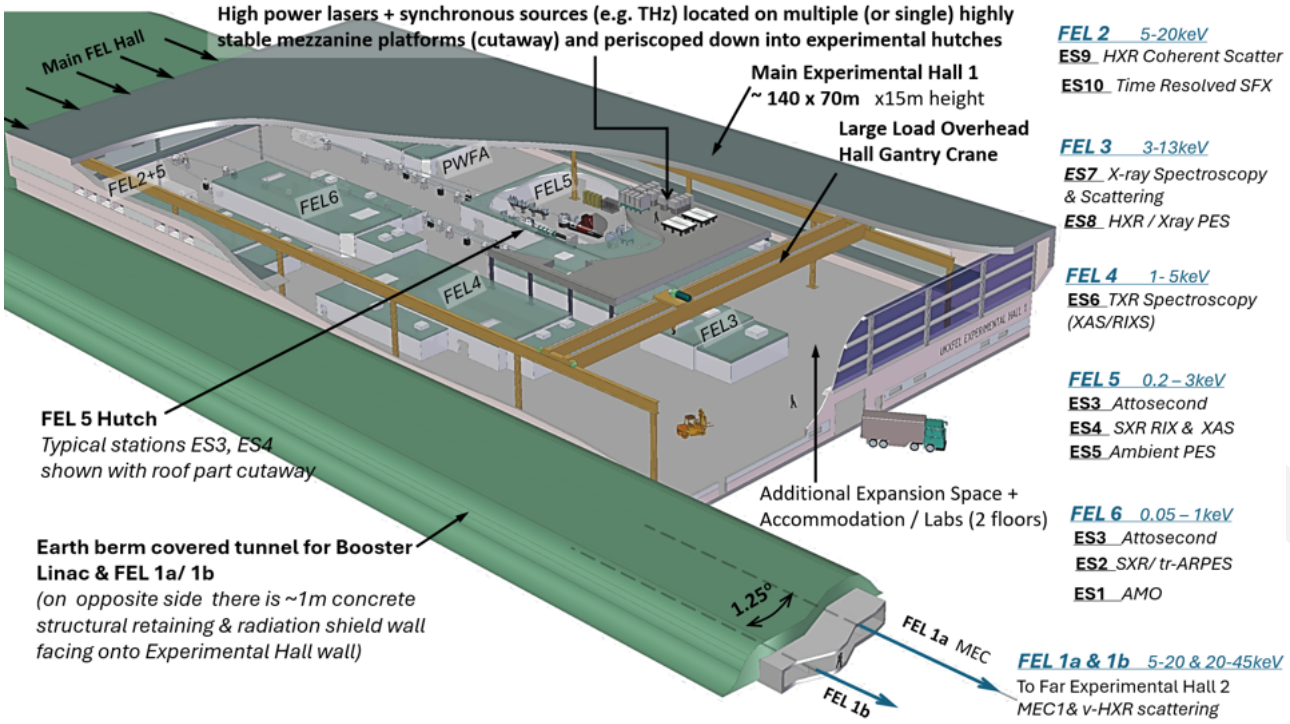

Figure 13.14: 3D Isometric Elevation & Cutaway of Main Experimental Hall

facilities. Nevertheless, designing for a larger footprint at the outset should minimise the likelihood of requiring subsequent expansion.

Additionally, the Experimental Hall will be equipped with a large mezzanine-level platforms covering up to an equivalent significant proportion of the ground-floor area. These structures will provide adjacent overhead space above the hutches for the installation of laser systems, secondary radiation sources, and associated ancillary equipment. Beamlines and utility services can be routed directly downward from the mezzanine to the experimental areas below. Strategically positioned large hatches will permit vertical transfer of equipment from the mezzanine using a double-gantry crane system with full coverage of the hall. This arrangement is illustrated in the isometric cutaway shown in Figure 13.14.

Together with the Far MEC experimental hall, the total planned experimental area of the UK XFEL would rank among the largest of any contemporary facility. This directly addresses one of the most frequently cited themes in user feedback at other sites: the need for maximised experimental space. The comparative schematic of end stations in Figure 13.15 illustrates this advantage. At other facilities, experimental areas are often constrained by site limitations, an issue which can be mitigated through careful site selection during the future phases.

MEC (Matter at Extreme Conditions) Hall:

The extended booster linac and the diverging geometry of the MEC FELs 1a and 1b (each with inherently longer high-energy X-ray transport paths) necessitate locating the MEC Experimental Hall considerably further downstream. Consequently, the MEC Hall will be housed in a separate building, positioned beyond the main experimental complex.

This standalone facility, approximately 65 × 45 m, is a conventional, well-insulated two-storey structure, constructed similarly to the main Experimental Hall. It will house three radiation-shielded hutches, each around 25 × 15 m, enclosed by 2–3 m thick concrete walls and roofs with sliding shield-block doors. Two hutches will be dedicated to FEL 1a & b high-energy X-ray experiments

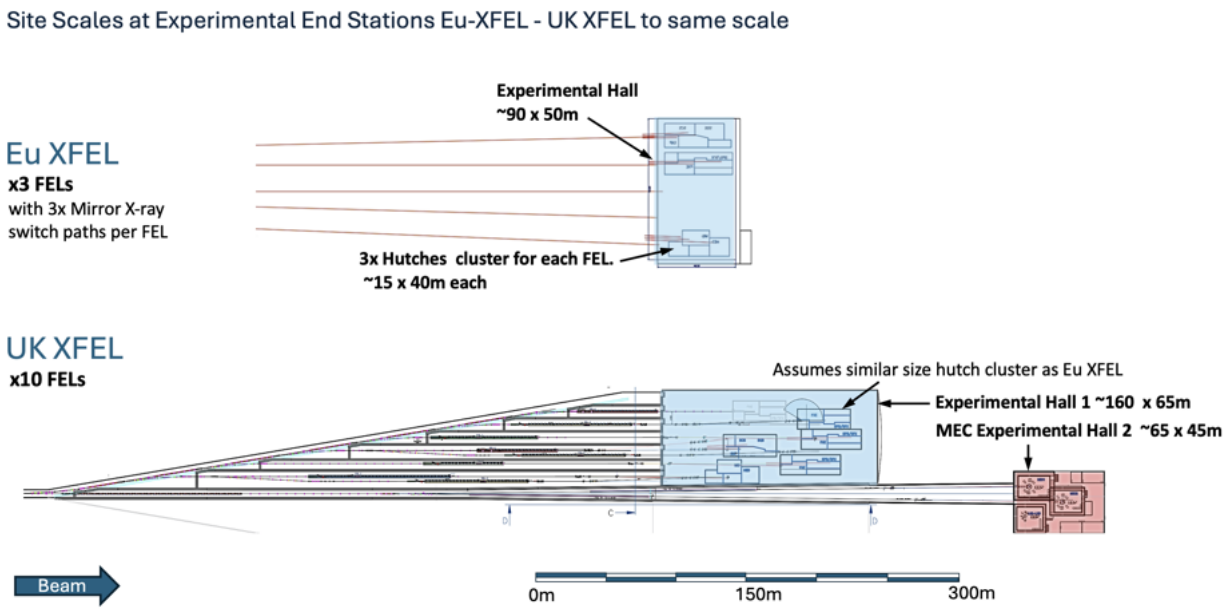

Figure 13.15: Comparison of Main Experimental Halls: European XFEL and UK XFEL

that also support simultaneous high repetition rate (e.g. ∼100 Hz) Petawatt-class high-power laser (HPL) operations, whilst the third will be dedicated to HPL only.

MEC type experiments using high repetition Petawatt lasers produce significantly higher radiation dose rates than the X-ray pulses in the main Experimental Hall, so significantly extra shielding will be required in this hall. The shielding enclosures will be constructed from either cast concrete or modular interlocking concrete blocks with equivalent roof protection. The roof structure will also serve as a mezzanine platform for the HPL system infrastructure. Wide HPL beams will be directed vertically down via shielded periscope transports into the hutch space below, minimizing beam transport distances. The building will be equipped with an overhead gantry crane covering most of the floor and hutch roof area and will include some local (unshielded) laboratory and office space. The hutch layout and shielding can be reconfigured with minimal disruption, enabling future upgrades such as direct downstream beamline extensions, an option to be evaluated in subsequent design phases.

The MEC Far Experimental Hall arrangement is illustrated in both simplified schematic plan view in Figure 13.16 and as a 3D isometric cutaway shown in Figure 13.17.

DRAFT

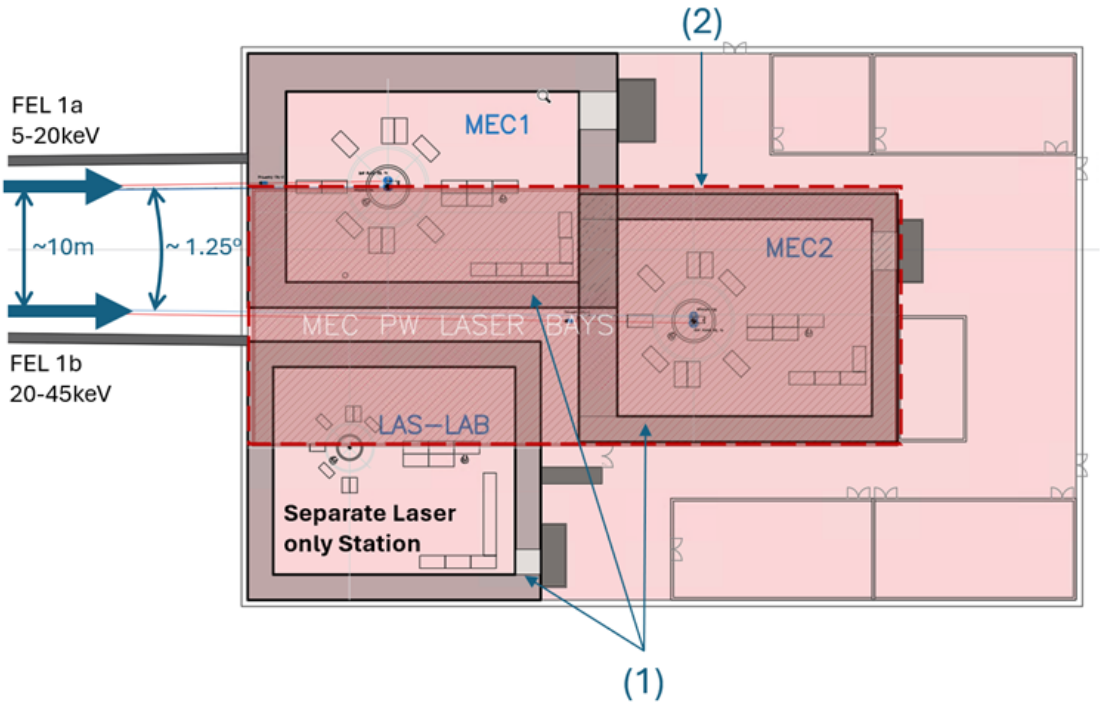

Figure 13.16: MEC Experimental Hall , showing (1) Concrete shielded 2x MEC interaction experimental areas with 1 ancillary laser only and (2) Petawatt high power lasers to be mounted above on stable concrete hutch roof with a short run periscope down to the experimental areas.

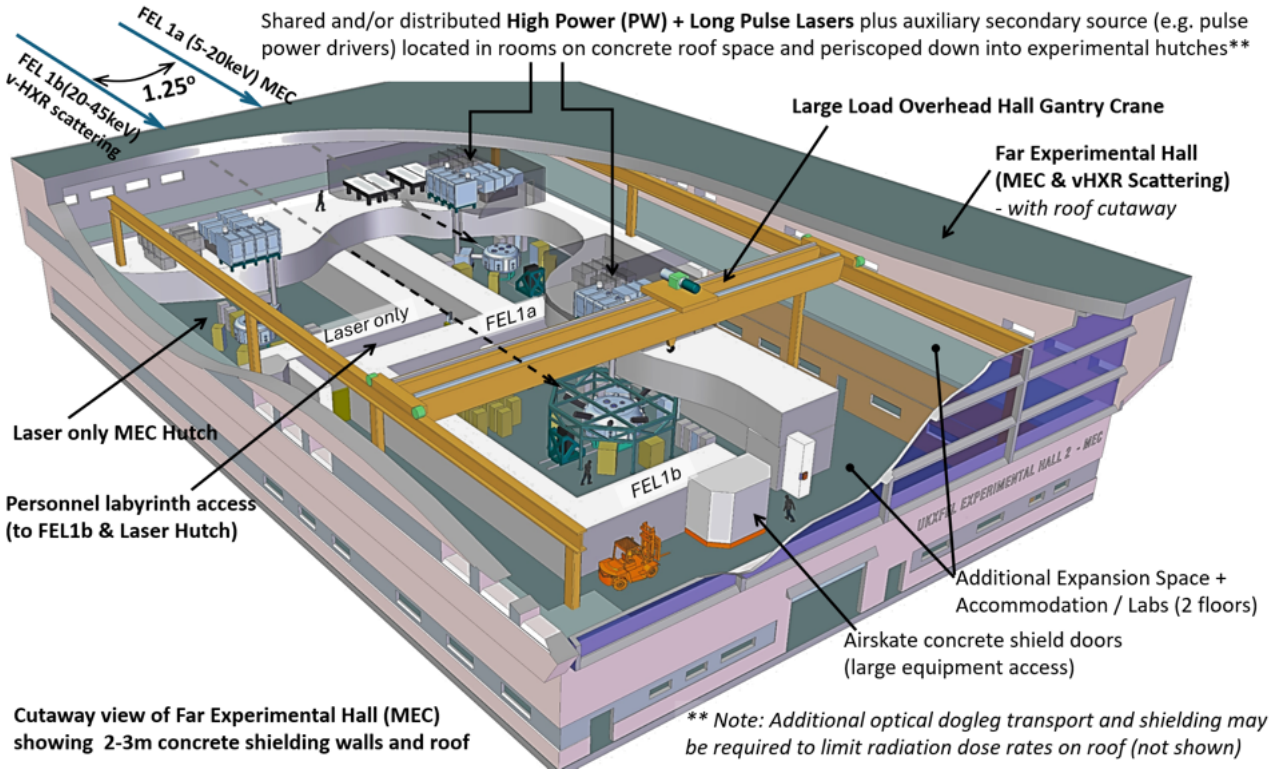

Figure 13.17: 3D Isometric Elevation and Cutaway of MEC Far Experimental Hall

13.2.5 Site wide infrastructure

Cryoplant: The cryoplant site is assumed to occupy a single building footprint of approximately 90 × 25 m, based on the Linde concept developed for the NLS (2010) [6]. To reduce the overall footprint, a two-storey design is proposed—similar to the recent dual 4 kW cryoplant installation at LCLS-II-HE (which has a footprint of 75 × 25 m and 10 m height). The cryoplant must be carefully designed to mitigate ground vibration noise to the XFEL from the large multi-MW power compressor pumps. Accordingly, the plant should be located at a sufficient distance from the Linac Hall to minimize vibration transmission, while remaining close enough to avoid excessive distribution pipe lengths, which would increase both cost and cryogenic losses. Operational data and experience from many existing facilities are now available to inform and support an ultimate optimised site selection and design strategy [7] [8].

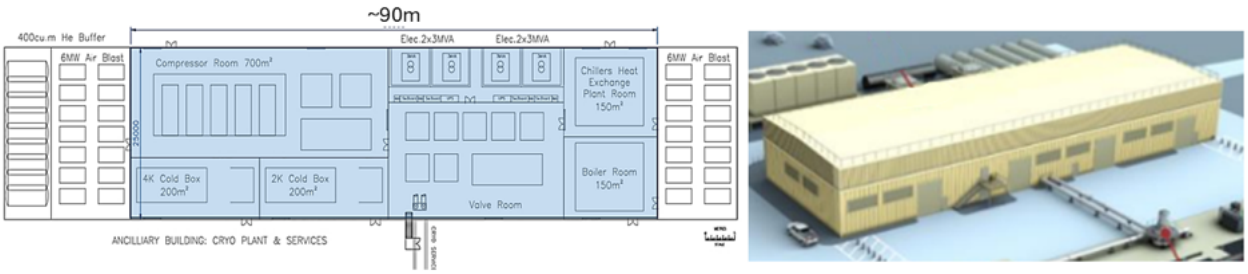

Figure 13.18: 90 × 25 m Cryoplant Plan (left) vs Recent LCLS-II-HE install 75 × 25 m (right)

The ancillary and auxiliary facilities are shown schematically in the site plan (Figure 13.19) and are outlined descriptively below, more detailed engineering assessments will be undertaken in subsequent project phases. These buildings are not expected to present significant engineering challenges, location-specific constraints, or long-lead procurement risks, and generally do not represent schedule-critical paths in the same way as the core systems and primary buildings of the XFEL.

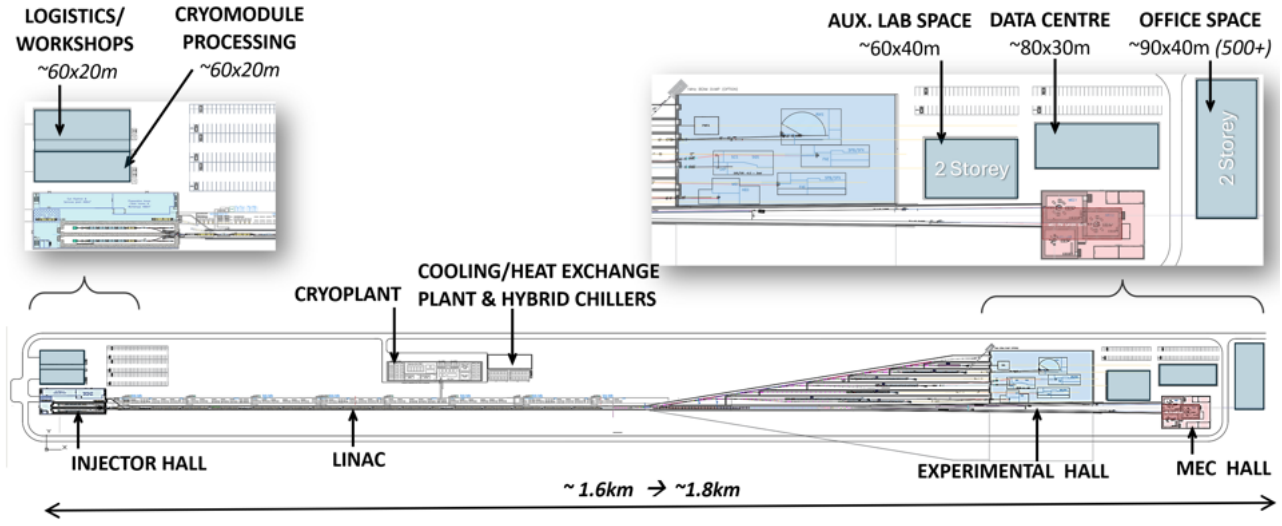

Figure 13.19: Showing Entire ∼2 Km site with ancillary buildings highlighted

Data Centre:

To meet anticipated data requirements, the facility must incorporate a dedicated high performance data centre. Data centres are increasingly very significant contributors to the costs and

infrastructure of accelerator-based science research facilities. Over the past decade, earlier predictions of exponential growth [9] in data centre scaling and energy demand have aligned well with the installed reality. Consequently, a degree of future-proofing must be embedded in even at conceptual design stage. Current planning therefore assumes a baseline specification of computing power of approximately ∼100 PFLOPS and electrical utility power approximately ∼3–4 MW, with provision for future expansion of on-site power supply to ∼6 MW and beyond.

The planned data centre will occupy a footprint of 80 × 30 m (an approximate scaling based on recent data centre installation at LCLS-II [10]). It is planned to be located as close as possible to the Experimental Hall, ensuring proximity to the primary data sources and thereby minimising network latency and potential transfer bottlenecks. An additional area should be reserved for future expansion, recognising that storage and compute demands are expected to grow significantly over the facility's operational lifetime. Post processing of data could be carried out elsewhere if needed.

Laboratory and Workshop Space:

Comprehensive on-site laboratory and workshop capabilities are critical to supporting the multi-disciplinary research enabled by the UK XFEL. This feedback was received over multiple town halls, where in some instances the lack of certain sample preparation laboratories at existing facilities meant samples went missing, got damaged in the post, which in extreme cases delayed the experimental work. These functions will be concentrated in a dedicated multi-storey building (∼60 × 40 m) and include:

Chemistry, Biochemistry & Sample Preparation Laboratories:

This area will include both wet and dry laboratories:

- **Wet Labs**: Designed for handling biological samples, chemical reagents, nanomaterials, and hazardous substances (COSHH-compliant).
- **Dry Labs**: Tailored for solid-state sample preparation (powders, crystals and thin films...etc).

Additional specialized facilities in this building will include:

- **Cryogenic Laboratories**: For the preparation and storage of cryo-sensitive samples.
- **Clean Rooms**: Supporting experiments requiring particulate-free environments, particularly in materials science and nanofabrication.

Elsewhere on site, a 60 × 20 metre workshop and laboratory space is reserved at the far end of the facility, adjacent to the Photoinjector hall. This area will support specialist technical activities, including:

- Electronics and detector development, calibration and test.
- Mechanical engineering and fabrication.
- Radiation monitoring.
- General beamline and facility support services (e.g. optics test, vacuum services)

Logistics:

The logistics building will be crucial early milestone in the build phase of the project, allowing components to be received and in-kind contributions stored. It is important, given the amount of equipment that will be brought onto site during the first years of the build, that this is one of the first buildings completed, along with an appropriate asset management system to ensure that all incoming items are tracked, verified, and stored efficiently. This will support the smooth

coordination of deliveries, reduce the risk of loss or damage, and enable timely access to critical components when needed. The logistics building and asset management system together will form the backbone of early site operations, underpinning the project's ability to scale up construction activities and maintain control over a complex and evolving inventory.

Cryomodule Processing & Handling:

There will be need for a dedicated Cryomodule processing and test area. This should be a highly automated facility capable of warm and cold tests (2K) as well as being able to supply full RF load and be equipped with low level RF. It is currently expected that a significant proportion of the Cryomodules will be manufactured off site and as such will need site acceptance testing upon arrival. To ensure that there are no bottlenecks during testing, the facility should be equipped with two test areas. However, it should be designed in so that once all testing has been complete the space can be reconfigured to adapt to the day to day operations of the facility. This area should be linked to both the workshop and the injector hall so any Cryomodules can be easily moved between the test area, tunnel and workshop should repairs or maintenance need to be carried out.

Office Accommodation

A conventional two storey office building, with an approximate footprint of 90 $\times$ 40 m, is proposed to be located near the Experimental Hall. It will be able to accommodate over 500 people and, combined with the 100+ spaces available in the Photoinjector hall and other ancillary and workshop buildings, will provide facilities comparable to other XFEL facilities. While the operational demands will increase with the addition of further FEL beamlines, the expected rise in on-site personnel will be moderated by the increasing use of automated and remote-controlled experimental procedures, including off-site sample handling and experimental management, lessening need for a physical on site presence.

Future Autonomous Integrations:

Building a next-generation facility, presents many opportunities to integrate modern technologies into both the build and operations. From a facility design point of view it is important that the design philosophy should allow flexibility to ensure future innovation that is unavailable now can be integrated into the build at a later date. It also means there is the opportunity to incorporate new developments such as autonomous operations, maintenance, safety and inspections systems, which could improve safety, reduce downtime, and increase efficiency. Building these features in at the design stage will produce a more effective and robust system capable of doing much more than what a retro fitted system could do.

Currently robots that are deployed at similar facilities (such as TIM at CERN and MARWIN at Eu-XFEL [11] [12]) are used for; remote inspection, preventative maintenance, environmental monitoring and quality assurance. Robotic systems often include high speed high resolution cameras, lidar, radiation sensors, O_2 depletion monitors, gas leaks detection system and magnetic field sensors, allowing for early failure detection and long term monitoring. They can also be deployed as rapid search and rescue systems. However most current robotic systems are retrofitted, and as such always have some level of compromise or additional complexity. A new Next-Generation XFEL facility should adopt a **robot centric facility design**; whilst humans will still be a critical part of maintenance and inspection, a robot centric design could improve safety, reduce downtime, and increase efficiency. An example of robot centric design can be seen at the European Spallation Source which has a fully remotely operated waste processing facility [13] drawing on advances made in remote handling techniques and technology from the nuclear sector.

The system comprises of dual-crane handling systems, size reduction of activated components using fully remotely operated and remotely maintained wire saws, and remote packing and storage of the activated waste ready for export off-site. These systems were designed and manufactured by UKAEA, STFC and UK Industry specifically for the ESS, and once fully operational should prove to be an prime example of what could be achieved facility wide, in a next-generation XFEL.

Similarly ESS have also able to employ remote vacuum clamps in spaces of the accelerator where it would be to hazardous to work, using these technologies across all areas the machine could allow for repair and maintenance work without long shut down periods. Building on this for a Next-Generation, whole systems should be built with modularity in mind (magnets, vacuum pumps, diagnostic sensors, etc.) and consist of modular cassettes allowing rapid exchange. Another example of a robotic system is CERN's LESS [14] robot, whilst this has been designed to modify the internal surface of the LHC's beampipes. It proves the concept of a internal inspection robot, a significant upgrade from Felicia [15], and could pave the way for integration of these robots inside the accelerator at the design stage. Whilst CERN's RF cavity inspection camera [16] is currently a pre-installation inception machine, providing this sort of capability in situ would allow monitoring of cavities for degradation or damage, alerting the accelerators AI systems of these alterations.

It is expected that once the build of the facility commences, autonomous robotics will be significantly more mature, and the examples above could move from remotely operated to semi (or even fully) autonomous. Even now, autonomous robots like Boston Dynamics Spot are becoming common place on many building sites and harsh environments, with JET recently completing a successful trial period of Spot at it's Fusion Reactor for regular scheduled monitoring [17].

When adopting a robot-centric facility design approach, UK XFEL should ensure to embed this across multiple systems by using a *standardised robotic interface*, this would make it easier to provide modular systems across the whole facility allowing for a wider range of robot tasks with a more simplistic architecture.

The tunnels and experimental halls should be designed to provide unobstructed robotic movement (be it for wheeled, quadrupeds or drone style robotics) as well as embedded monorail systems to allow rapid deployment of specialised tools and safety equipment. Tunnels should contain docking stations to provide radiation shelter and power to robotics as well as robotic 'airlocks' to allow robots to swap hardware or even exit the building without shutting the machine down. By unifying designs and adopting modular approaches to experimental systems, the experimental halls could adopt robots similar to Amazons Hercules and Proteus [18] allowing transfer of experimental setups into place ahead of experimental runs, permitting offline setup of experimental system- as well as providing more autonomous, and remote user access.

Further to mobile robotics throughout the facility, the buildings themselves could form part of the feedback control system. By embedding environmental data systems into the design direct feedback between the accelerators AI systems and the building sensors (humidity, energy, vibration, acoustic monitors, air flow, etc.) would allow real time beam corrections, and a deeper understanding of how the machine operates. Ensuring this data is captured alongside experimental and machine data would give a greater level of machine reproducibility and stability between experimental runs Section 12.1. These systems could also be extended to energy efficiency; by producing a smart campus, facility-wide energy consumption and requirements can be tuned and automated throughout the year, aligning with the national grid to consume more energy when possible and dialling it back when needed. These systems will also enable monitoring of the buildings' condition over time, allowing for evaluation of cracks, leaks and defects, which again could be fed back into the accelerator's operation.

All this should be mirrored in a digital twin, which should be developed alongside the initial facility design, providing models and scenario exploration as the build develops and moves into operations Section 12.1. Whilst many of these systems currently exist individually, there is no, to the author knowledge, fully integrated facility as described above. As such careful planning at the design stage should include; future proofing, prioritisation and phased testing. To ensure that these ancillary systems will operate smoothly and not at the cost of overall machine performance over the lifetime of the facility.

A National Lab

These additional spaces inbuilt up-gradability, will help elevate the facility to be truly Next-Generational, as well as ensuring it's scientific output is maximised. Getting these ancillary building and services right could allow the UK XFEL to become the heart of a new national laboratory, clustering skills and talent in and around the area which it is built. However, co-location with an existing facility could be beneficial by sharing resources already built (for example, additional test facilities, acceptance testing, vacuum, electrical, data etc.), ensuring that the facility does not become shackled by the constraints of existing locations should remain paramount to ensure successful delivery of a truly revolutionary next-generation XFEL.

DRAFT

13.2.6 Radiation safety, shielding and beam dumps

13.2.6.1 Radiation Protection Overview

This section outlines the key principles governing radiation protection. Design strategies, shielding, beam dumps, and cost implications are addressed in subsequent sections.

Regulatory Compliance

A UK facility would need to comply with the Ionising Radiations Regulations 2017 (IRR17), enforced by the Health and Safety Executive (HSE). Design will be informed by best practices from UK facilities such as the Diamond Light Source and ISIS Neutron and Muon Source. A suitable, certificated Radiation Protection Adviser (RPA) will be involved throughout design and operation and formal Radiation Risk Assessments (RRA) will guide radiation zoning, engineering controls, procedural safeguards, and the development of local rules and a Radiation safety management system, as required under IRR17.

Designation of Radiation Areas and Shielding

The approach to designating facility areas must consider the prompt radiation hazard presented when the beam is on, in addition to the residual hazard from the activation of machine components. It must also note that some areas may not have permanent designations but may change whilst the machine is in different configurations.

Shielding design will use validated methods from existing light sources and ensure exposures remain well below legal limits, consistent with ALARP (As Low As Reasonably Practicable) principles. It will also consider groundwater contamination, and the amount of shielding required to remain below out of scope (OoS) concentrations.

Induced Activity and Environmental Protection

Structural activation near beam dumps, collimators, and high-flux areas will be minimised through material selection and layout optimisation.

Radioactive waste modelling will be required to forecast the production of activated air within the accelerator hall, activated water (e.g. in cooling circuits) and activation within accelerator components. The results of these assessments can be interpreted by an RPA and Radioactive Waste Adviser (RWA) to estimate worker doses from such hazards and inform any requirement for a radioactive substances environmental permit under the devolved environmental permitting regulations enforceable by the relevant Environment Agency.[2]

Typically, a permit would be required to discharge activated air and water and accumulate and dispose of accelerator components, though there may be some exemptions from the full permitting process that can be used, depending on the outcome of assessments.

Methods of control: A suitable and sufficient RRA completed in consultation with an RPA is imperative in optimising exposures and achieving legal compliance. Methods of controlling worker doses are likely to involve:

- Engineered controls as a priority; a combination of interlocks, search and lock devices and emergency stops to prevent access to high dose rate areas.
- Real-time surveillance to protect staff from unintended fault scenarios, e.g. beam mis-steer.
- Special procedures that trained staff are required to follow to protect them from any residual risks after engineered methods have been proportionately exhausted.

[2] In England and Wales, these are the Environmental Permitting Regulations 2016 as amended (EPR16)

- A programme of personal and area radiation monitoring

Design Integration:

Radiation protection requirements will directly inform facility architecture. Shielding structures—using concrete, lead, polyethylene, or equivalent—will be dimensioned via Monte Carlo simulations (e.g. FLUKA, GEANT4). Major elements (beam dumps, collimators, labyrinths) will influence layout, structural loading, and cooling systems. Early integration is critical to avoid costly rework or delays.

13.2.6.2 Prompt Radiation: Bulk Shielding

Defining the bulk shielding strategy for an XFEL facility is essential for the facility layout, building design, civil engineering planning, and cost estimation, particularly along key infrastructure such as the linac and FEL tunnels. Even during early conceptual phases, a preliminary assessment of shielding requirements is critical, as these decisions significantly influence machine layout and construction feasibility.

For cost-effectiveness and to support sustainability, the primary shielding material will be compacted earth. However, practical upper limits must be set: excessive earth volumes can necessitate larger concrete support structures and extensive excavation, both of which escalate costs and compromise environmental goals.

Shielding Requirements

The concept has targeted electron beam parameters (e.g., 300 pC, 8 GeV, up to 1 MHz) that could potential yield up to 2.4 MW beam power, exceeding any existing XFEL. Accordingly, bounding the shielding envelope has been a design priority from the outset. Shielding references from other XFELs, such as LCLS and SHINE, are limited in applicability. These facilities are typically tunnel-based, with up to $\sim$10 m or more of earth cover—a byproduct of site-specific construction conditions, not necessarily due to shielding requirements.

For cut-and-cover linac configurations, SwissFEL provides a more relevant precedent. SwissFEL adopted a nominal beam loss assumption of 0.1 W from a 560 W beam ($\sim 2 \times 10^{-4}$ loss), consistent with standard practice for non-SRF linacs [19]. Shielding design focused on dark current and expected localized losses (e.g., at bunch compressors and collimators). For a 10 W average loss scenario, a shielding depth of 1.5 m concrete plus 1 m compacted earth was sufficient, equivalent to $\sim$3 m of earth-only shielding.

The 2010 NLS Conceptual Design Report [6] addressed similar SRF parameters (200 pC, 2.25 GeV, 1 MHz, 450 kW beam power) with a 10^{-4} loss rate assumption, yielding 45 W of loss. Using SHIELD11 and independent validation [6], this scenario required 0.5 m concrete plus 4.3 m compacted earth ($\sim$5 m earth-only equivalent) to maintain external dose rates below 0.5 µSv/hr.[3]

Early design CDOA planning assumed similar conservative beam loss of 10^{-4}, requiring significant shielding of $>$6 m of earth-equivalent material. However, empirical measurements at the European XFEL, the only high repetition rate SRF linac in operation, demonstrate actual loss rates several orders of magnitude lower. Measurements from commissioning and early user operation,

[3] Which is the UKRI/STFC workplace environment limit, set to ensure that even with high occupancy - e.g., 2,000 hours/year - an individual's dose would remain around 1 mSv, aligning with the legal limit for a member of the public in the UK.

particularly in high-loss regions such as FEL undulators, reported average beam losses closer to 10^{-8} or less [20]. Mobile dosimetry within the linac and injector systems further corroborated these findings, benefiting from large SRF aperture geometries. Discussions with European XFEL experts [21] concluded that a 10^{-8} beam loss assumption is realistic for a Next-Generation design, and not unreasonably optimistic. At this level, continuous beam loss for UK XFEL (2.4 MW$\times 10^{-8}$) is only 0.024 W, orders of magnitude below prior conservative values, yet consistent with empirical data from the European XFEL operating facility. Under such scenarios, the recommended bulk shielding is nominally around 1 m thick equivalent of compacted earth, sufficient to meet regulatory dose rate limits on the external side; typically below 0.1 µSv/hr. However, to maintain a conservative approach and enhance thermal insulation, current planning assumes 1.5 to 2 m of compacted earth mass shielding bulk equivalent. In certain specific areas, such as beam dumps, significantly greater shielding will be required locally and is addressed later in this section.

Transient Beam Loss During Fault Conditions:

For a worse case scenario, such as mis-steering or faults, full beam loss may occur locally for brief periods before protection systems intervene. The critical factor is the total dose accumulated during this short interval. At European XFEL, beam shut-off is achieved in $<$1 µs. However, at $\sim$1 km linac length, signal propagation delays dominate. Assuming $\sim$2/3c transmission velocity, shut-off via Photoinjector intervention is expected within $\sim$5 µs. With detector and system response contingencies, a conservative 10 µs total shutdown latency is assumed. In this time, 10 bunches (10 pulses at 1 MHz) may be delivered, corresponding to 24 J (10 $\times$ 2.4 J). Averaged over an hour, this equates to only $\sim$0.0067 W - which is far below the continuous loss case. Therefore, such transient losses remain within the acceptable shielding envelope, provided they occur infrequently (e.g. typically less than once per hour). For dual-colour FEL operation with adjacent pulses $\sim$1 ns apart, the energy deposition may increase, but still remain well below prompt loss conditions when time-averaged.

Beam Loss Monitoring and Protection Systems:

The design will incorporate advanced commercial and custom systems to ensure microsecond-scale beam termination during loss or mis-steering events:

- Beam Loss Monitors(BLMs): detect abnormal radiation levels using scintillators or ionization chambers.
- Cavity Beam Position Monitors (CBPMs): track beam trajectories and detect deviations using algorithmic analysis.
- Beam Halo Monitors identify peripheral beam losses indicative of misalignment or instability.

These will be integrated via:

- Fast Signal Processing & Interlocks: real-time anomaly detection with rapid shutdown protocols.
- Active Feedback Loops: preventative beam control to mitigate loss scenarios.

Systems will comply with Safety Integrity Level (SIL) standards (IEC 61508), ensuring robust, high-reliability operation. Similar systems have proven safe and effective at European XFEL and LCLS-II.

Simulation Study and Preliminary Shielding Model:

A prompt radiation shielding assessment was conducted using the FLUKA Monte Carlo code by TÜV SÜD Nuclear Technologies [22]. The simulation assumed an 8 GeV electron beam operating at 0.2 MHz (one-fifth of the nominal repetition rate, as the beam will be spread over multiple FELs) with a fractional beam loss of 10^{-8}, transported in a 4 m diameter FEL tunnel. Adjacent tunnels were modelled with a 6 m undulator spacing and approximately 2 m of intervening earth shielding, conservatively represented as shale. The resulting combined dose rate distribution is presented as a contour plot in Figure 13.20. Predicted dose rates in the adjacent tunnel are below 10^{-2} µSv h^{-1}, which is well below the STFC design target of 0.5 µSv h^{-1} and several orders of magnitude lower than applicable regulatory dose limits. The adjacent tunnel is therefore radiologically independent of the operational tunnel and may be considered accessible.

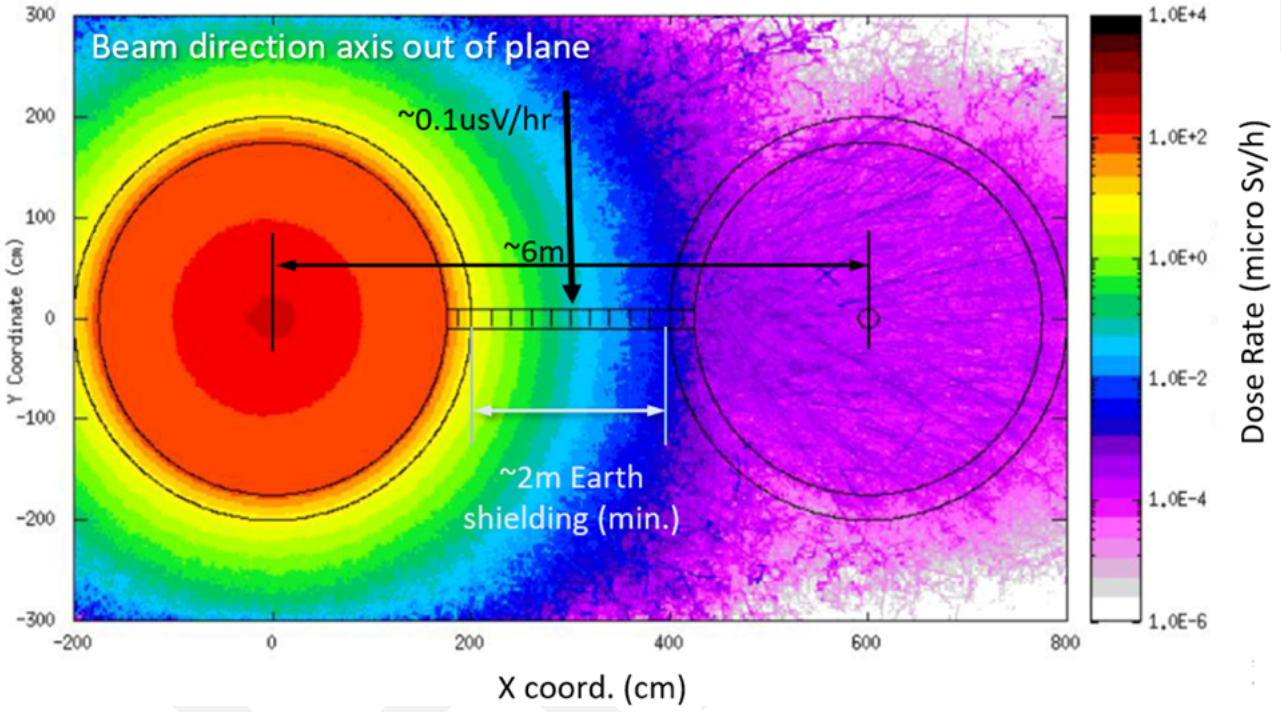

Figure 13.20: FLUKA Simulation Plot Radiation Dose Rates Concept Option FEL Tunnels

Subsequent developments in design have placed undulators further apart in a shared FEL hall, separated by 1–1.5 m concrete walls, rather than in discrete tunnels. At the current CDOA phase, this simulation is considered equivalent and valid for shielding purposes, and no further simulation is necessary until future design stages.

13.2.6.3 Location-Specific Shielding Considerations:

Injector and Gun Region:

Dark current at the injector is a known concern, but is expected to be manageable and comparable to European XFEL and LCLS-II-HE. The injector will be enclosed in a concrete structure with thickness $\geq$2 m, upgradable to 3 m of heavy concrete (e.g., haematite, barytes) if necessary.

Gas Bremsstrahlung:

Gas Bremsstrahlung arises from high-energy electrons that interact with residual gas, particularly at the downstream ends of long accelerator straights ($>$900 m). Dose rates can reach several

Gy/hr. Effective mitigation requires localized high-Z shielding (e.g. tungsten, steel, lead), especially at:

- Bunch compressors.
- Collimators.
- Linac terminus (spreader/kicker).
- FEL undulator ends and photon lines.

As Bremsstrahlung radiation is emitted with a very narrow angular divergence (proportional to 1/E) and typically $<$0.1 mrad, it remains tightly collimated along the beam direction. As a result, the use of localized shielding with high-Z, high-density materials such as tungsten, steel, or lead is significantly more effective and efficient than increasing bulk shielding throughout the entire enclosure. This is especially relevant in the photon transport sections, where line-of-sight radiation is otherwise limited.

Dedicated Gas Bremsstrahlung stops will be located within the FEL Hall shielding containment, upstream of the Experimental Hall, to intercept both primary Bremsstrahlung and any secondary scattered radiation. Provided that the first optical mirrors (which define the photon angular acceptance) are also contained within the FEL Hall, the resulting photon transport will be angularly displaced from the FEL beam axis. Consequently, any residual radiation that propagates along the photon beamlines will consist primarily of low-level ambient scatter. This scatter will be largely confined within the FEL Hall, thereby reducing the radiation burden at the FEL/Experimental Hall interface and allowing effective shielding at this boundary.

Synchrotron Radiation in FEL Undulators:

Synchrotron radiation generated within the FEL undulators, explicitly modelled using worst-case 1.6 T undulator fields, results in local dose rates orders of magnitude higher than the general electron beam loss. See Figure 13.21. However, due to the low ($\sim$keV) photon energy, as compared with GeV electron losses, the shielding attenuation is highly efficient so that $<$0.5 m earth is typically sufficient.

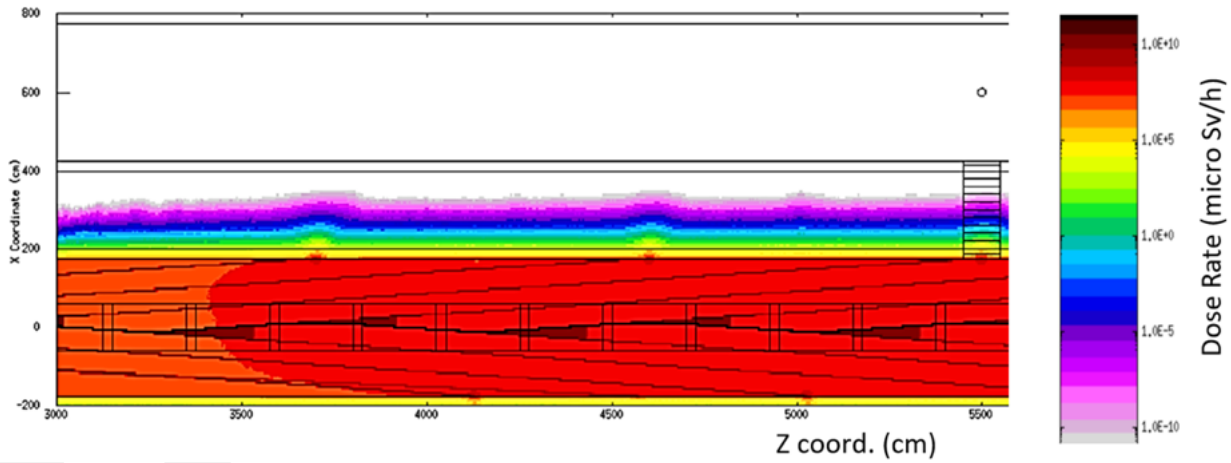

Figure 13.21: Plan view dose rates contour plot during normal operation from Synchrotron Radiation.

13

13.2.6.4 Beam Dumps and Associated Shielding

Unlike distributed beam losses ($\sim 10^{-8}$), beam dumps, by definition, must be designed to absorb the full beam load and, as such, require very substantial localized shielding. This potentially can

involve, depending on the dump's location, type, and operational repetition rate, relatively major civil engineering works to accommodate the shielding required. For this reason it is important to define an approach for beam dump design, location and distribution, even at the conceptual stage.

Beam Dump Concepts and Layouts:

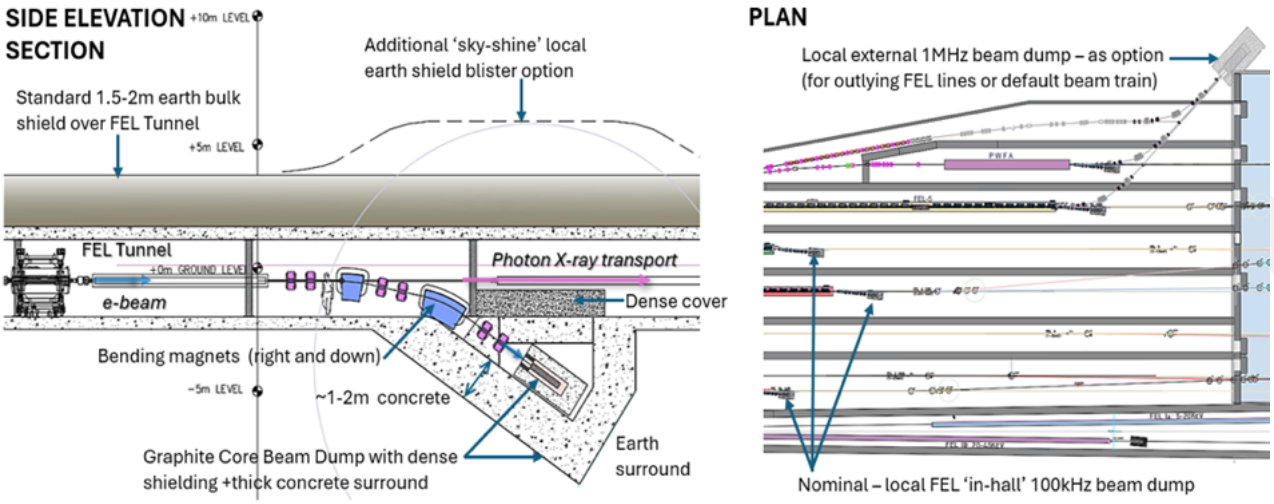

Figure 13.22: Beam dump concepts - Left: illustrates a side elevation of a local $<$250 kW beam dump within the FEL hall. Right: shows a conceptual layout for a shared high-power ($\sim$1 MHz, $>$2 MW) beam dump located outside the FEL hall, with associated beam transport lines.

The CDOA proposal for the UK XFEL adopts a design in which each FEL line has an independent beam dump positioned immediately downstream of its respective undulator. The electron beam is directed downward beneath the photon transport line into a shielded underground pit, utilizing earth mass for far-field radiation attenuation. Surrounding shielding consists of several metres of concrete and other optimised materials, see Figure 13.22.

While this configuration minimizes overhead shielding requirements, a heavy concrete slab or equivalent structure will still be required above the pit to suppress prompt radiation and mitigate residual dose from activation products during shutdown periods. Additional surface shielding—such as earth berms, indicated by dashed lines in Figure 13.22 may be necessary, along with restricted access during operation. Further assessment of secondary radiation (sky-shine) at the site boundary will be required in the technical design phase.

Baseline Beam Dump Parameters:

It is estimated that the baseline dump design (for each FEL line at around 100 kHz), will allow for beam powers of up to 250–300 kW, within the capability of established technologies, such as the graphite-cored, copper-jacketed design operating at European XFEL or the aluminium-based LCLS-II-HE dump [23].

Due to the physical separation between FEL lines, maintenance and potential extraction of individual dumps at this power scale should remain feasible. To ensure unobstructed access, it will be necessary to cant the dump slightly to the side, in addition to the downward angle.

High-Power Dump Option:

Early CDOA-phase designs anticipated individual FEL lines operating at repetition rates up to 1 MHz, necessitating beam dumps exceeding 2 MW. While no longer a baseline requirement,

high-repetition operation (>100 kHz) remains a possible scenario. Integrating such high-power beam dumps within individual FEL lines in the FEL hall was deemed impractical. Consequently, a designated area outside the hall has been reserved for a potential shared high-power dump (See Figure 13.22, right side figure). One or two FEL lines, positioned near the hall's periphery, could direct high-repetition electron trains to this external dump via relatively short beamlines. However extending this capability to all FEL lines was evaluated as prohibitively complex and costly.

Additionally, during periods when electron bunches are produced but not used (e.g., FEL maintenance or downtime), machine stability may be compromised. One mitigation strategy is to maintain a stable pulse train and divert unused pulses to a common dump. Retaining at least a viable option for high power dump for the two reasons outlined above is therefore considered prudent at this stage.

Existing beam dump designs from contemporary facilities (e.g., SHINE, European XFEL, and LCLS-II) are not rated for the required average power (2 MW at 1 MHz), falling short by nearly an order of magnitude. Alternative concepts, such as CEBAF-style beam dumps [24], offer significantly higher power handling capability but are optimized for substantially different beam energies. A detailed feasibility study will be carried out in the next project phase to evaluate whether a dedicated high-power beam dump is required and, if so, to identify a viable technical solution.

This approach substantially reduces project risk, both by minimizing the need for novel high-power hardware development and by improving operational robustness and reliability.

Groundwater Activation and Induced Radioactivity:

The LCLS-II BSY dump design includes extensive shielding to limit groundwater activation (primarily from tritium) to below 40 Bq/L, in compliance with US regulatory limits [22]. The design incorporates substantial concrete mass surrounding the dump to meet this constraint. Although UK regulatory thresholds permit higher activation levels, local site-specific factors such as groundwater depth and geotechnical conditions differ significantly from those at LCLS. In the UK, water tables can vary from a few metres to several tens of metres below ground. At shallow water table sites, additional shielding and/or localized groundwater pumping may be required. This underscores the importance of finalizing the UK XFEL site location, as meaningful analysis of groundwater activation risks depends critically on specific geotechnical data. More detailed modelling can be undertaken during the technical design phase, preferably when a candidate site, or selected range of sites, is known.

13.2.7 Alignment/ Stability and Geotechnical, Land and Environmental Considerations

13.2.7.1 Stability

The successful operation requires electron and photon beam positions to remain stable within a few microns. A strategic approach is critical to ensure both mechanical and thermal stability, addressing long-term and short-term perturbations (ranging from years to seconds) as well as high-frequency motion. Active feedback systems depend on a quiet passive noise environment, necessitating exceptional stability in the floor of the accelerating complex and photon transport pathways.

Ground Vibration:

Figure 13.23 illustrates typical ground vibration power spectral densities (PSD) observed at various accelerator sites globally [24].

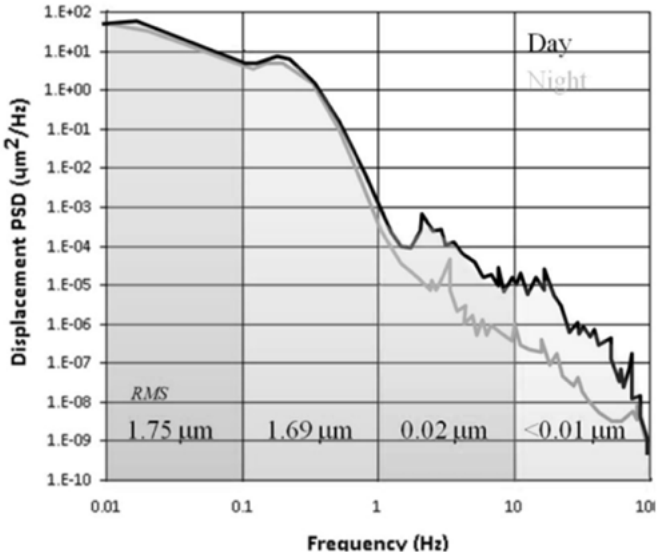

Site Location	Year	Av. RMS (nm)	σ (nm)	Max RMS (nm)	Min. RMS (nm)
DESY HERA, Hamburg	2007	53.3	18.9	77	34.8
DESY XFEL, Schenefeld	2007	41.1	16.6	70	35.1
ESRF, Grenoble	2003	74	34.9	137	40.2
SLAC, Menlo Park	2003	4.9	1.2	7.4	4.1
Spring-8, Harima	2004	2	0.4	2.5	1.8

Figure 13.23: (a) Left, Generic ground noise spectrum of a typical quiet site. (b) Right, RMS ground vibration results for f $>$ 1 Hz at various sites, [24]

Ground Vibration Analysis:

Integration of the ground-motion power spectral density (PSD) indicates that more than 99 % of ground displacement occurs at frequencies below 1 Hz, dominated by natural sources such as continental-scale motion ($\gg$ 0.01 Hz) and ocean-wave-driven microseisms ($\sim$0.1–0.3 Hz). At these low frequencies, seismic wavelengths are on order of many kilometres and generally produce correlated, near in-phase motion over local spatial scales, resulting in negligible relative displacement between nearby components.

Over site-wide baselines of several kilometres, finite coherence lengths and phase gradients in the ground motion lead to residual differential motion between spatially separated accelerator and beamline subsystems. This motion couples into the machine primarily through RF phase and energy sensitivity and through effective optical path-length variations, giving rise to pulse arrival-time jitter at the level of tens of femtoseconds (1 fs $\approx$ 3 μm at the speed of light in free space, *c*). Such effects have been observed at the European XFEL, where ocean-generated microseisms have been associated with arrival-time jitter exceeding 20 fs [25].

While this low-frequency ground motion cannot be eliminated mechanically, its effects are predictable and can be effectively beam-based feedback and feed-forward techniques, enabling correction at the few-femtosecond level. The magnitude of the residual timing jitter is strongly site dependent.

Above 1 Hz, ground motion becomes increasingly influenced by local soil properties and structural dimensions comparable to beamline and experimental scales, potentially affecting source-to-experiment synchronization. Motions below 1 Hz are not considered further here pending confirmation of site-specific geotechnical data.

The vibration PSD decreases approximately as $\sim 1/f^4$, making 100 Hz a practical upper bound for higher-frequency analysis. Within the 1–100 Hz band, vibration is dominated by cultural noise

from anthropogenic sources such as road traffic (∼10 Hz), pumps, and compressors. Table (b) in the referenced comparison provides representative RMS vibration levels measured at other accelerator facilities. [26].

Random ground vibration can be mitigated through passive isolation using low-amplification support structures or through active damping systems. Priority should be given to eliminating vibration at source via careful engineering design, including anti-vibration isolation for major plant equipment (e.g., turbo-pumps in vacuum, cryogenic, and HVAC systems) and, where practical, attenuation by distance separation.

Electron Beam Transport:

Ground vibrations primarily impact the alignment of quadrupole magnet centres throughout the machine, causing angular 'kicks' in the electron beam trajectory. The extent of this effect depends on the quadrupole strengths and local beam optical functions. To address this, mechanical movement of the quadrupoles will be minimized through well-designed support stands and structures, such as those routinely designed by STFC. A dynamic feedback system has not proved necessary at similar XFEL facilities but could be implemented, should site selection require it. While detailed simulations and measurements will be conducted, experience from similar setups suggests no significant challenges in maintaining trajectory within acceptable limits. Notably, the FEL facilities at DESY, despite operating in a relatively noisy environment, have not reported major electron stability issues caused by ground motion (although with tweaking Taylor Swift was detectable at European XFEL [27]).

Accelerating Cavities:

Studies indicate that ground motion as small as 1 nm in certain frequency bands can induce cavity motion sufficient to affect their operation. Given the anticipated detuning sensitivity of ∼0.3 Hz/nm for the cavities (similar to comparable systems), RMS floor motion of 10 nm, coupled with amplified motion in the support structures of over 100 nm, could potentially lead to RF frequency shifts exceeding 30 Hz. Such shifts would surpass the typical cavity bandpass budget of 20–30 Hz. To mitigate this, closed-loop feedback Piezo actuation tuners, already demonstrated successfully at other facilities, will be implemented to counter microphonics, effectively reducing mechanical noise by several magnitudes. FLASH and European XFEL facilities at DESY Hamburg have shown that operating a FEL based on SRF accelerator modules is feasible at noisy sites. However, studies do confirm a direct link between mechanical noise and RF phase jitter, with much of the microphonics attributed to the cryogenic systems. Since this design aims to achieve strict jitter stability, it will adopt the latest developments from similar facilities. Special emphasis will be placed on refining piezo tuner designs, accelerator module supports, and cryogenic delivery systems, including optimal siting and design of the cryoplant. These aspects will undergo a detailed review in upcoming design phases.

Diffuse Motion & Settlement:

Over long periods, ground displacement behaves diffusively, following the ATL Shiltsev law [28], and could exceed mm at the UK XFEL site over decades. Early systematic motion, such as concrete shrinkage and ground settlement, arises from initial excavation, re-compaction, and groundwater variations. To mitigate these effects, proven construction methods like heavy vibro-compaction, substantial piling, and monolithic concrete structures (if feasible) must be employed, during the construction phase. Long-term displacements, typically hundreds of micrometers, are considered alignment rather than stability issues which are addressed more in the following sections.

Thermal Stability

Thermally induced displacement occurs over months to hours. The earth bank shielding offers high thermal inertia ($\sim$several months time constant), minimizing diurnal and seasonal temperature variations. Super-insulative panels will be used for the injector and experimental hall to replicate these effects. However, localized heat sources in the tunnel and service areas may cause temperature gradients, controlled by a well-designed HVAC system. Temperature stability of ±0.5℃ should be sufficient for electron beam transport in the linac and spreader, as trajectory feedback will handle minor induced displacements in quadrupole magnets and BPMs. Within the tunnel and service areas themselves various localized heat sources (mostly from equipment such as vacuum pumps, magnets, certain instrumentation racks etc.) will give rise to temperature gradients unless adequately controlled. This control is achieved through the use of a distributed heating, air-conditioning and ventilation system.

FELs:

In addition to trajectory variations caused by quadrupole and BPM displacements, FEL undulators experience specific effects, including:

- Alterations in magnet gap, influencing undulator field strength.
- Variations in undulator field strength due to the temperature dependence of permanent magnet materials.

Typically electron beam trajectory must remain straight within 10% of the beam size ($<\sim$3 µm of the $<\sim$30 µm FEL beam size of UK XFEL) in order to maintain FEL performance at 10% of peak power. This presents significant alignment and thermal stability challenges. However, incoherent ground vibrations (RMS $\sim$20–30 nm above 1 Hz) are unlikely to cause such displacements if support mounts are adequately designed.

Photon Transport & Experimental Area:

Using best practices in beamline design, such as decoupling optics from vacuum systems, ensuring precise temperature control, and employing noise-dampening thermal mounts, photon transport systems should meet the stability requirements for most experimental applications.

The required temperature stability is tied to the FEL gain parameter (ρ) and, indirectly, to the operating wavelength. For XFEL at 0.1 nm ($\rho = 3\times10^{-4}$), a stability of $<$±0.1℃ is ideal and at $\sim$1 nm ($\rho = 2\times10^{-3}$), the equivalent requirement is around ±0.7℃. A temperature stability of ±0.5℃, as planned for the experimental area, should be adequate as a general target with some additional attention given to control in the HXR FELs. A more detailed analysis will be conducted in later phases to verify this requirement. General stability aspects, including thermal stability, were previously discussed under ground vibration. Temperature control across the experimental hall is expected to achieve perhaps significantly less than ±0.25℃, aligning with best practices at comparable facilities.

Direct cooling of optics to counter beam absorption depends on the specific optic and its position in the beamline. At repetition rates of several hundred kHz, active cooling of beryllium compound lenses is almost certainly essential, and will likely also be required for certain mirrors and gratings. Where the average absorbed power is low enough not to cause excessive temperature rise, passive radiative cooling may be preferable, as it avoids strong localised gradients that can distort the optic surface. Fortunately, this challenge has been addressed with focused solutions developed for synchrotrons and applied at other XFELs, albeit with varying success. The topic will

be revisited in the next phase of development, once beam parameters are more quantitatively defined in terms of absorbed power.

Beyond the well-established aspects of beam stability, recent advances in X-ray wavefront sensing techniques have demonstrated significant improvements in compensating for drift and focus aberrations [29, 30, 31]. Applying these methods should make it considerably easier to enhance the facility's optical performance, provided that the fundamental requirements for thermal and vibration control are maintained within previously established norms.

13.2.7.2 Alignment

The alignment of an accelerator requires consideration of a number of stages, as illustrated in Figure 13.24 below.

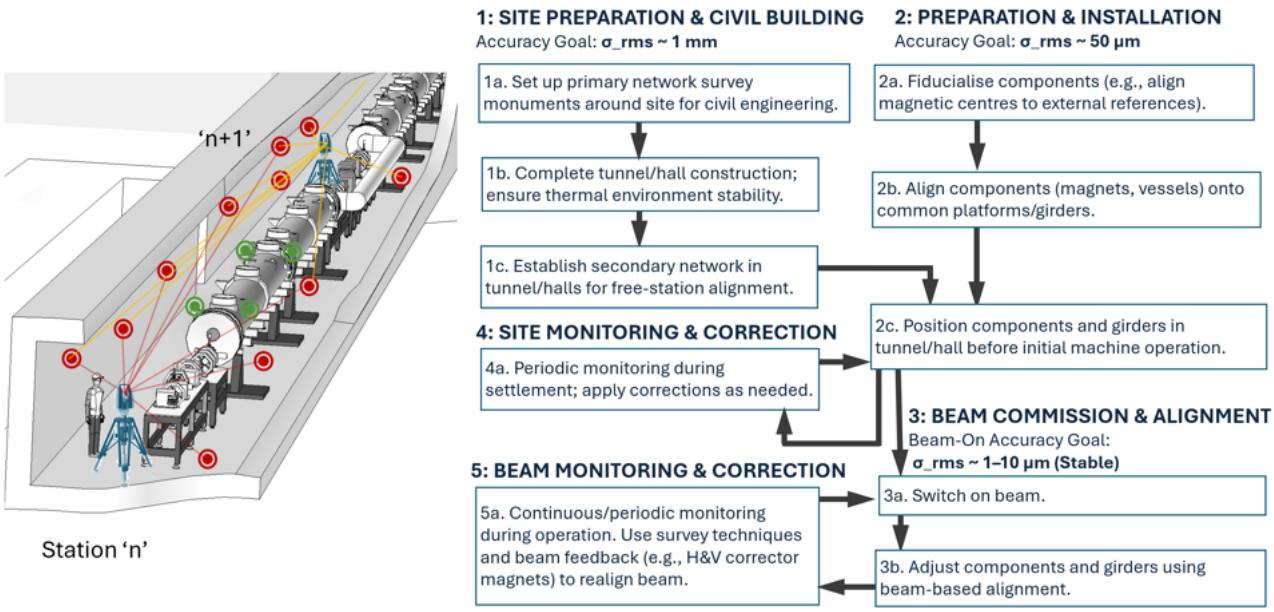

Figure 13.24: *Left:* Establishing a typical laser tracker survey network & *Right:* Flow chart for alignment operations

Survey equipment for these stages falls into two categories: generic and integral. Generic tools like laser trackers, total stations, and digital levels are adaptable across the facility without impacting machine design. Their accuracy varies by application, for example, high-end laser trackers achieve ∼10 µm positioning accuracy per metre, while Trimble DiNi levels provide 1 µ rad angular precision with 10 µm height resolution. Integral systems, such as stretch wire and hydrostatic levelling, are tailored to fixed machine points for position monitoring. Though their reference accuracy is limited to ∼100 µm, they offer sub-µm resolution and repeatability, making them highly effective for tracking beam shifts in alignment and control systems.

Primary and Secondary Network:

The primary survey network for construction relies on pillars anchored to bedrock outside the building area. These allow precise force-centring of instruments, ensuring millimetre-level accuracy over hundreds of metres.

The secondary network, established inside the accelerator tunnel and experimental hall post-construction, references the primary network to monitor settlement but primarily serves precision machine alignment. A 3D free-stationing approach using laser trackers and total stations will replace traditional force-centring methods. Precision-machined nests fixed in the tunnel serve as reference points, ensuring sub-µm repeatability. A double-run levelling procedure will improve vertical accuracy, while the tunnel network will be integrated with service and experimental area networks to enhance stability. Periodic remeasurements will detect motion and ensure long-term reliability. Advanced software will identify and discard misaligned points.

Fiducialisation and Alignment in the Tunnel:

The fiducialisation process is used to determine where the survey reference points lie with respect to the critical datum of any component. For instance, measured quadrupole magnetic centres can be transferred to laser tracker fidcucial targets within $\sim$20–30 µm accuracy using coordinate measuring machines during the production phase. This fiducial target can then be aligned with the established machine network using laser trackers or collimators to similar precision – to achieve an ultimate alignment precision between magnetic field and ideal machine centres in a range 30–50 µm. Components like magnets and BPMs will be pre-assembled on common platforms for stability. Final alignment in the tunnel involves coarse positioning followed by fine-tuning using manual or motorized adjustment. The accelerator's beam steering system ensures optimal placement within several tens of microns.

Longer Term Drift:

Alignment drift from thermal changes and settlement will necessitate periodic beam-based re-alignments, likely every few months, with an estimated day-long downtime per iteration. While accelerator and photon transport alignment follows established best practices, FEL alignment demands higher precision and frequent corrections. Lessons from LCLS underscore the need for meticulous alignment strategies and quality assurance to ensure operational success.

Beam Based FEL Alignment:

For FEL alignment, initial mechanical accuracy ($\sim$50 µm) is insufficient for optimal FEL gain ($\sim$3 µm). Beam-based alignment techniques will compensate for errors using feedback mechanisms.

13.2.8 Power and Cooling

Electrical infrastructure and equipment locations have been assessed early in the conceptual building design phase and power consumption for the facility calculated with critical and sensitive loads identified.

The electrical distribution system can be separated into two zones; (1) Ancillary– which will serve cryoplant, heating and ventilation plant and other ancillary services buildings, etc. and (2) XFEL machine. The ancillary building should be fed from a dedicated 11 kV ring to ensure that the point of common coupling for the critical magnet loads and heavy plant equipment is at 11 kV, minimising disturbances caused by load variations and power quality issues. The main XFEL power should have two dedicated 11 kV rings. One should provide the necessary power to support the critical and power converter loads of the injector, accelerator, FEL Hall, and Experimental Hall with the other supporting the general loads and lighting, plus anything else that has load variations and can affect the facility operating stability. This can be the same ring main as that used for the ancillary power.

The table in Figure 13.25 shows the breakdown of estimated electrical power supply requirements of the site by system - which totals to $\sim$ 35 MW. This is for peak power requirements with all services pushed simultaneously to maximum (e.g. during vacuum pump and cryo-cool down as well as RF commissioning). Within most line entries there are contingencies assumed (10 to 50%) along with some future proofing. Therefore, a reasonable expectation is that in operation the nominal power consumption could be considerably lower than this peak figure, perhaps below the 30 MW range. Of recent note is that during the energy cost crisis of 2022, changing schedules and RF modulator operations, European XFEL saved several GWh per year [32], demonstrating there is always scope for ongoing savings in power consumption – and this focus is of course critical in terms of sustainability and target to net zero.

However, as stated in the table (Figure 13.25), the power consumption indicated for RF and cryoplant operations is a dominant contribution and is assumed to be at a lower linac acceleration gradient of 16 MV/m. At higher gradients e.g. 19 MV/m (which will shorten the linac by $\sim$100 m+) the power consumption will *increase* for RF and Cryo-plant by approximately 1 and 3 MW respectively. For 22 MV/m power consumption will be higher still, which again must be set against a further reduction of the total length, around 100 m of savings in terms of capital build costs. This suggests that whilst this headline power figure is not unrealistic it is still subject to significant change as the design matures and decisions made, and could increase as well as decrease.

DRAFT

System	kW	Qty	Power kW	Sub-tot. kW	Notes
RF					
8GeV SCRF accelerator RF electrical power	6,000	1	**6,000**		from main RF estimates - assumes 16MV/m gradient with SSA
SCRF Cryo-plant electrical	8,000	1	**8,000**		working at 2K - with ~ 50% overhead added
4GeV Booster RF copper cavity	1,440	1	**1,440**		Estimated for 4GeV C-Band at 25MV/m
				15,440	**System Sub-tot (kW)**
ACCELERATOR & FEL TECHNICAL SYSTEMS					
Magnet Power Convertors	12	350	**4,200**		~350 racks for ~ 600 quads, 60 dipoles (+ sextupoles, kickers)
Gun	2	600	**1,200**		2x photo-injectors 60 racks
Vacuum	3	120	**360**		120 racks
Personnel Safety	2	18	**36**		~ 20 racks
Network Control	2	56	**112**		~ 56 racks
Diagnostics	2	48	**96**		~50 racks
Cryo N2 systems	3	30	**90**		~30 racks
Undulators - controls & aux.	2	100	**200**		~ 200 undulators (8 FELs x 25 undulators) - 2 controls per rack
RF controls & aux.	1	540	**540**		1kW per cavity, 60CMs (60x9 cavities)
Motion control	2	30	**60**		30 racks
6 branch transport beamlines	20	6	**120**		
18 hutch end stations	20	18	**360**		
3x Seeding Laser	50	3	**150**		E-XFEL & LCLS-II-HE benchmark
				7,524	**System Sub-tot (kW)**
SERVICES & INFRASTRUCTURE					
Lighting	40	1	**40**		Assumes average ~5 lumen/m2 ~ 1W/m2
Climate Control HVAC	500	1	**500**		Assumes buildings at highest standards RIBA 2030/ ISO52000
Water circulation pumps	300	1	**300**		Typical for around ~5MW cooling capacity
Compressed Air Systems	100	1	**100**		Chamber dry air let up and few pneumatic actuators
Office Laboratories	120	1	**150**		Offices for between 300 - 500 people on site
Chiller System (Magnets, Cryo, RF)	4,478	1	**4,478**		Ref ~90% electrical power - hybrid cooling at CoP ~5 - 7
				5,568	**System Sub-tot (kW)**
SECONDARY SOURCES					
3x HPR Laser	100	3	**300**		E-XFEL diode and CLF EPAC reference baselines
MEC 10Hz Petawatt laser	1,500	1	**1,500**		Guide from Ref: LCLS-II with contingency
				1,800	**System Sub-tot (kW)**
ANCILIARY / AUXILIARY SYSTEMS					
Data Centre	4,000	1	**4,000**		Based on 100PFLOPS and Stanford LCLS-II (& future proofed)
					capacity to increase site supply to be >6kW+
				4,000	**System Sub-tot (kW)**
				34,332	**Site total (kW)**

Figure 13.25: Estimated UK XFEL Peak Power Consumption Table (RF and cryoplant based on lower 16 MV/m gradient, which will increase for higher gradients).

Electrical distribution scheme:

The main transformer locations are shown in very basic schematic form in Figure 13.26. The distribution scheme provisionally follows an upscaled approach of the NLS concept of 2010 [6] in having vectored transformers with redundancy built into infrastructure throughout to minimize site down-time and separation of 11kV ring supplies for ancillary, critical, and main heavy loads.

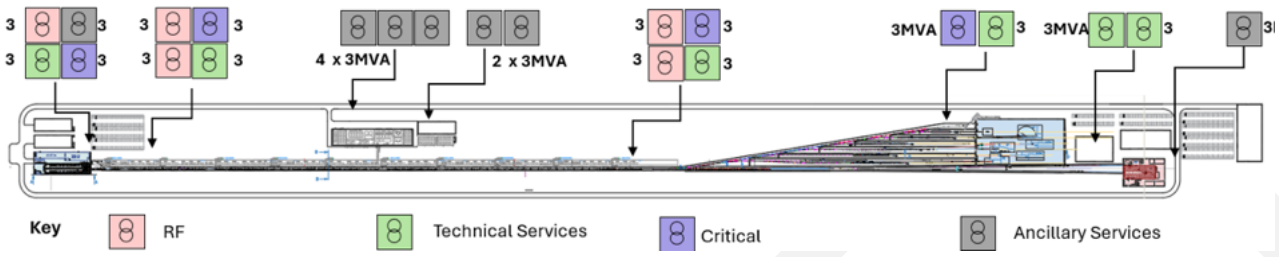

Figure 13.26: Electrical distribution scheme: Transformer locations and type

Site supply assumes a typical load factor ∼0.8- 0.9 and for costing and planning purposes at concept phase is recommended to comprise at least three 11 kV step-down transformers rated at 25 MVA. This allows the site to follow N+1 redundancy strategy, nominally permitting operation in the event of a single point transformer failure and allows for essential maintenance without site disruption, whilst also incorporating some measure of contingency for future site upgrades.

Power consumption is obviously critically important as regards sustainability. The facility will be categorised as a very large load (VLL) which may require a dedicated substation at EHV (132 kV). The grid connections to achieve net zero objectives – or near net zero as possible will have to be strategically planned in at the very earliest opportunity. National Energy System Operator (NESO) National grid guide-lines now suggest 8 to 10 years planning lead times for VLL facilities, as a minimum [33]. Such planning cannot realistically progress far without defining a site location or at the very least a selection of candidate sites. This decision, even as of 2026, is likely to become a critical path item in the project plan timeline.

Sustainability and net zero planning is further discussed in Section 13.2.9 and Section 14.1 - which may prove to be one the most challenging aspects of delivering a UK XFEL facility.

Cooling

Conventional (non-cryogenic) cooling constitutes a critical infrastructure system for UK XFEL, providing thermal stabilisation for the accelerator complex, FEL systems, experimental halls, and associated technical services. Cooling demand is governed primarily by total electrical power consumption, since the majority of installed equipment must operate within narrow temperature tolerances (typically $<1\,^{\circ}\mathrm{C}$). Heat generated within sensitive subsystems is removed locally by forced liquid convection and transported via heat-exchange networks to a central cooling plant. Final heat rejection is achieved through high-efficiency chiller and cooling tower installations, with provision for partial energy recovery where feasible. Comparable large-scale research facilities, including CERN and the European Spallation Source, have demonstrated district heating recovery schemes capable of reutilising up to approximately 50% of consumed electrical energy [34]. Lower grade heat can be re-used on site for heating and there should be a very large surplus (tens of MW) that can potentially be re-used as local district heating supply. CERN is already utilising waste heat from its Data Centres in local district heating [35] and has similar expanded plans for it's prospective Future Circular Collider (FCC). A similar scheme for UK XFEL would be entirely dependent on it's location.

Process water cooling performance requirements are stringent. Magnet circuits in the beam transport system require temperature stability of order ±0.2 ℃, while RF gun cavity cooling may demand stability approaching ±0.1 ℃ under heat loads of up to 10's kW. Such specifications are achievable using modern industrial chiller technology integrated with distributed fibre-optic temperature sensing and high-bandwidth feedback control. Equivalent performance is already routinely achieved at existing STFC accelerator installations, including the CLARA facility at Daresbury Laboratory. Primary chilled-water systems will supply building HVAC loads and feed secondary de-ionised process water loops. Secondary circuits will incorporate fine filtration (10 µm), oxygen removal to mitigate corrosion, and strict control of water chemistry, with conductivity maintained at $<$0.1 µS/cm in accordance with established accelerator standards.

The overall cooling architecture will likely closely follow established European XFEL design principles, with enhanced emphasis on lifecycle energy efficiency and environmental sustainability [36]. Hybrid evaporative/dry cooling towers are selected as the baseline technology due to their reduced water consumption and favourable seasonal coefficients of performance under UK climatic conditions. For a peak site electrical load exceeding approximately 35 MW, the associated cooling power demand is therefore expected to be in the range 4–5 MW. Recent advances in high-density data-centre thermal management demonstrate the feasibility of substantially higher effective efficiencies; published case studies report power usage effectiveness (PUE) values as low as $\sim$1.06 [37], corresponding to an effective CoP greater than 16. Continued technological progress in this very active sector therefore provides a credible pathway to further reductions in operational cooling energy.

Subject to environmental permitting and hydrogeological suitability, natural water resources such as river abstraction or deep aquifer exchange may provide partial or full free-cooling capability. Integration of such systems could significantly reduce mechanical chiller operation and associated energy consumption - potentially by several MW. Once again, this very much depends on suitable site selection criteria.

Environmental Heating, Ventilation and Air Conditioning (HVAC)

The linac hall will be constructed with 1.5–2 m of earth overburden, providing substantial passive thermal inertia and environmental isolation. For a representative UK annual ambient variation of ±6 ℃, passive attenuation is expected to limit intrinsic tunnel temperature drift to below half this value without active intervention. Short-term external excursions of up to 10 ℃ are similarly anticipated to translate to internal variations significantly below 1 ℃. Above-ground structures, including injector and experimental halls, will be designed to high thermal-efficiency standards consistent with RIBA 2030 targets and ISO 52000 / 50001 / 16813 frameworks for sustainable building performance.

Heat removal from technical equipment is dominated by closed-loop water cooling, and residual thermal leakage into conditioned spaces via convective or radiative pathways is expected to be small. Consequently, HVAC heating and cooling loads represent only a very minor fraction of the total facility thermal budget ($<<$1 MW).

A dedicated cooling plant building with an approximate footprint of 60 m $\times$ 20 m, together with an adjacent hardstanding area of comparable size for hybrid cooling towers, will house the principal heat-exchange and chiller infrastructure. The plant will likely be co-located with the cryogenic installation to consolidate high-capacity utility services, while maintaining sufficient physical separation from accelerator tunnels to minimise vibration transmission. All major rotating equipment will be installed on anti-vibration mountings consistent with accelerator stability requirements.

13.2.9 Engineering Sustainability

Provisional UK XFEL carbon budget (indicative) Assuming best-practice, low-carbon construction methodologies based on a 2025 baseline (RIBA 2030), and conservative projections for electricity carbon intensity from 2035 to 2065 (BEIS/DESNZ [38]), the overall 30-year life-cycle carbon footprint of the XFEL is predicted to be approximately $\sim$**300 ktCO_2e** split roughly **50**/**50** between embodied and operational emissions. No single "silver bullet" dominates; achieving reductions will require a combination of multiple measures and incremental gains.

Embodied carbon covers the greenhouse gas emissions tied to materials and construction, from raw material extraction, manufacturing, and transport, through to on-site build and eventual demolition. For a UK XFEL, this spans everything from structural concrete and steel to accelerator components and radiation shielding. Whereas operational carbon covers emissions generated by running the facility over its lifetime, principally through energy use. A UK XFEL carries large operational energy demands (Figure 13.25), such as magnet systems, cryogenics, RF systems, cooling infrastructure, and user travel, meaning operational carbon will likely dominate any whole-life assessment. In the UK context, this figure is tied to the grid carbon factor, which is projected to fall significantly over coming decades, so whole-life assessments must account for grid decarbonisation trajectories across the facility's full operational lifespan - something that should be taken into account at the next stage of this projects design.

A breakdown of the carbon estimated accounting for the current design can be found in Section 14.1. Embedded carbon emissions are largely fixed at the design and procurement stage, and unlike operational carbon can not be altered after construction, however ensuring that the design process contains the relevant steps to include options to reduce operational costs (such as remote operating systems, carbon conscious coding etc.) makes early stage carbon assessments essential. Striving for an environmentally sustainable machine facility will produce a more efficient machine, which in turn will deliver on improving the science throughput of XFELs.

13.2.10 Summary of technology development areas, R&D needed for future phases to meet specification

The UK XFEL conceptual design establishes a credible technical baseline, but several areas of targeted R&D and technology development will be essential to refine specifications and ensure the facility can be delivered to performance, cost, and sustainability requirements.

Beam dumps represent a priority. Detailed simulation and modelling are needed to validate shielding requirements for lower-power ($\sim$300 kW) dumps, including provisions for safe access, radiation control, and groundwater containment. In parallel, the design envelope for a potential high-power common dump, capable of accepting a significant fraction of the 1 MHz pulse train, must be explored in consultation with beam physicists and experimenters.

Site-dependent design options also require attention. If site selection is not resolved before detailed design, costed alternatives for deeper sub-surface construction—similar to the European XFEL—should be evaluated alongside cut-and-cover concepts. In addition, opportunities for international collaboration in key technical areas should be considered as part of the optimisation.

Synchronous sources offer further scope for development. In addition to high power laser sources, work is needed to define the feasibility, scale, and cost envelope for additional accelerator-based sources such as THz, which could be integrated to enhance experimental capability.

Finally, **costing and sustainability studies** must be advanced. This includes robust capex and opex models, evaluation of low-carbon construction options, and alignment with net-zero power grid supply projections. Benchmarking against a range of potential UK sites will be critical if location remains undetermined at the time of the technical design phase.

Collectively, these development areas form a provisional forward look development programme from the standpoint of engineering delivery, reducing uncertainty and ensuring that the UK XFEL design matures into a deliverable, future-proof facility.

DRAFT

References for Chapter 13

[1] DESY. *European XFEL*. DESY facility overview (accessed 2026-01-29). URL: https://www.desy.de/research/facilities__projects/european_xfel/index_eng.html.

[2] Axel Brachmann. "Commissioning of LCLS-II". In: *Proceedings of LINAC2024*. Paper THZA001. Oct. 2024. DOI: 10.18429/JACoW-LINAC2024-THZA001. URL: https://proceedings.jacow.org/linac2024/pdf/THZA001.pdf.

[3] S. Chen et al. "Design of the Beam Distribution System of SHINE". In: *Proc. IPAC'21*. International Particle Accelerator Conference 12. 2021, pp. 1562–1565. DOI: 10.18429/JACoW-IPAC2021-TUPAB081. URL: https://jacow.org/ipac2021/papers/tupab081.pdf.

[4] S. Choroba. "The High Power RF System for the European XFEL". In: *Proc. 29th Linear Accelerator Conference (LINAC'18)*. Beijing, China, 2019, pp. 601–604. DOI: 10.18429/JACoW-LINAC2018-WE1A04. URL: https://proceedings.jacow.org/linac2018/papers/we1a04.pdf.

[5] A. D. Yeremian et al. *LCLS-II High Power RF System Overview and Progress*. Tech. rep. SLAC-PUB-16408. SLAC National Accelerator Laboratory, 2015. URL: https://www.slac.stanford.edu/pubs/slacpubs/16250/slac-pub-16408.pdf.

[6] STFC. *NLS Project: Science Case and Outline Facility Design*. Tech. rep. Science and Technology Facilities Council (STFC), 2009. URL: https://www.researchgate.net/publication/235765405_NLS_Project_Science_Case_and_Outline_Facility_Design.

[7] Ramila Amirikas et al. "Effects of the Cryogenic Operational Conditions on the Mechanical Stability of the FLASH Linear Accelerator Modules". In: *Proceedings of EPAC08*. Genoa, Italy, 2008, WEPP075. URL: https://proceedings.jacow.org/e08/papers/wepp075.pdf.

[8] E. Fauve et al. "First-Year Operation Overview of the SLAC LCLS-II Cryoplant". In: *IOP Conference Series: Materials Science and Engineering* 1327 (2025), p. 012005. DOI: 10.1088/1757-899X/1327/1/012005. URL: https://iopscience.iop.org/article/10.1088/1757-899X/1327/1/012005/pdf.

[9] Nicola Jones. "How to stop data centres from gobbling up the world's electricity". In: *Nature* 561.7722 (2018), pp. 163–166. DOI: 10.1038/d41586-018-06610-y. URL: https://www.nature.com/articles/d41586-018-06610-y.

[10] Manuel Gnida. *SLAC expands and centralizes computing infrastructure to prepare for data challenges of the future*. SLAC News (27 July 2022). URL: https://www6.slac.stanford.edu/news/2022-07-27-slac-expands-and-centralizes-computing-infrastructure-prepare-data-challenges.

[11] CERN. *LHC Train Inspection Monorail*. Sept. 2016. URL: https://home.cern/news/news/accelerators/meet-tim-lhc-tunnels-robot.

[12] N. Möller A. Dehne T. Hermes. *A MOBILE AUTONOMOUS ROBOT FOR MAINTENANCE AND INSPECTION*. Oct. 2017. URL: https://home.cern/news/news/accelerators/meet-tim-lhc-tunnels-robot.

[13] J.Davies. *Fully remotely operated waste processing in the European Spallation Source Active Cells Facility*. Mar. 2023. URL: https://scientific-publications.ukaea.uk/wp-content/uploads/UKAEA-RACE-CP2201.PDF.

[14] M. Sitko et al. "Towards Implementation of Laser Engineered Surface Structures for Electron Cloud Mitigation". In: *Proceedings of IPAC2018*. May 2018. ISBN: 978-3-95450-184-7. DOI: 10.18429/JACoW-IPAC2018-TUZGBE3. URL: https://jacow.org/ipac2018/papers/tuzgbe3.pdf.

[15] Frank Beck. *Felicia helps out*. Fermilab feature article describing the historical use of a ferret to help diagnose accelerator issues. Fermilab. Oct. 2016. URL: https://news.fnal.gov/2016/10/felicia-helps-out/.

[16] A Macpherson. *Taskforce on Robotics needs: SY-RF Input*. Nov. 2025. URL: https://indico.cern.ch/event/1610133/contributions/6784998/attachments/3176865/5649941/LongTermStrategy__Robotics_PreliminaryInfoCollection_SY_RF.pdf.

[17] UK Atomic Energy Authority. *Autonomous robot paves the way for future fusion maintenance*. Press release detailing first-ever autonomous robot deployment inside a fusion energy facility. GOV.UK. Sept. 2024. URL: https://www.gov.uk/government/news/autonomous-robot-paves-the-way-for-future-fusion-maintenance.

[18] Amazon Staff. *4 cool facts about Hercules, the small-but-mighty robot in Amazon's fulfillment centers*. Operations news article featuring technical and operational details of the Hercules robot. About Amazon. Sept. 2023. URL: https://www.aboutamazon.com/news/operations/amazon-hercules-robot.

[19] *SwissFEL Concept Design Report*. Tech. rep. PSI Bericht 10-04. See Section 6.2.1.3 SwissFEL Shielding. Paul Scherrer Institut, Apr. 2012. URL: https://www.psi.ch/sites/default/files/import/swissfel_old/CurrentSwissFELPublicationsEN/SwissFEL_CDR_V20_23.04.12_small.pdf.

[20] F. Wolff-Fabris et al. "Absorbed Radiation Doses on the European XFEL Undulator Systems During Early User Experiments". In: *Proceedings of FEL2019*. Hamburg, Germany, 2019. DOI: 10.18429/JACoW-FEL2019-WED02. URL: https://accelconf.web.cern.ch/fel2019/papers/wed02.pdf.

[21] Albrecht Leuschner. *Meeting notes and email communications with Albrecht Leuschner (RPA) at European XFEL, including Winni Decking and Harold Sinn*. Internal communication. Logged in internal UKXFEL Project Design Note WP11-dsn-0012-02. 2025.

[22] A. Adrych-Brunning and D. Holt. *UK XFEL FEL Seperation Study*. Tech. rep. TUV SUD Nuclear Technologies, May 2024.

[23] M. Santana-Leitner et al. "Beam Dumps of the New LCLS-II". In: *Proceedings of IPAC2014*. Dresden, Germany, 2014. DOI: 10.18429/JACoW-IPAC2014-THPRI086. URL: https://accelconf.web.cern.ch/ipac2014/papers/thpri086.pdf.

[24] M. Wiseman et al. "High power electron beam dumps at CEBAF". In: *Proceedings of the 1997 Particle Accelerator Conference*. Vol. 3. 1997. DOI: 10.1109/PAC.1997.753410. URL: https://www.researchgate.net/publication/224276738_High_power_electron_beam_dumps_at_CEBAF.

[25] Erik et al. Genthe. "Seismic noise contributions to European X-ray free-electron laser bunch arrival time jitter from ocean-generated microseism". In: *High Power Laser Science and Engineering* 13 (2025), e52. DOI: 10.1017/hpl.2025.40. URL: https://www.researching.cn/ArticlePdf/m00068/2025/13/4/04000e52.pdf.

[26] DESY. *Ground Vibrations: Compilation of ground motion by DESY*. Website. Accessed 2026-01-29. URL: https://vibration.desy.de/overview/.

[27] Eu-XFEL. 2024. URL: https://www.xfel.eu/news_and_events/news/index_eng.html.

[28] Vladimir Shiltsev. *Space-Time Ground Diffusion: The ATL Law for Accelerators*. Tech. rep. DESY-MPY, 1995. URL: https://www.slac.stanford.edu/econf/C951114/papers/036.PDF.

[29] Yanwei Liu and Matthew et al. Seaberg. “High-accuracy wavefront sensing for x-ray free electron lasers”. In: *Optica* 5.8 (2018), pp. 967–975. DOI: 10.1364/OPTICA.5.000967.

[30] Xianbo et al. Shi. “Development of X-ray Wavefront Sensing Techniques for Adaptive Optics Control at the Advanced Photon Sources”. In: *Synchrotron Radiation News* 35.1 (2022), pp. 1–6. DOI: 10.1080/08940886.2022.2066440.

[31] Daniele et al. Cocco. “Adaptive shape control of wavefront-preserving X-ray mirrors with active cooling and heating”. In: *Opt. Express* 28.13 (2020), pp. 19242–19254. DOI: 10.1364/OE.394310.

[32] J. et al. Branlard. “RF-BASED ENERGY SAVINGS AT THE FLASH AND EUROPEAN XFEL LINACS”. In: *LINAC2024*. 2024. DOI: 10.18429/JACoW-LINAC2024-THZA003.

[33] National Energy System Operator. *The Electricity Ten Year Statement (ETYS)*. URL: https://www.neso.energy/publications/electricity-ten-year-statement-etys.

[34] Anders Sunesson. “Experiences from ESS on Green Facilities”. In: *Workshop on Sustainability in Future Accelerators*. 2023.

[35] CERN. 2023. URL: https://ntnuopen.ntnu.no/ntnu-xmlui/handle/11250/3100356.

[36] Jens-Peter Jensen, Andreas Block, and Sylke Feuker. “EUROPEAN XFEL COOLING AND VENTILATION SYSTEMS”. In: *LINAC 2018*. 2018. DOI: 10.18429/JACoW-LINAC2018-MOPO122.

[37] Munters. *Oasis indirect evaporative cooling treats 10MW at DigiPlex*. 2021. URL: https://www.munters.com/en-us/knowledge-bank/case-studies/casestudy-2498/.

[38] UK Department for Energy Security and Net Zero. *Energy and emissions projections 2023 to 2050*. 2024. URL: https://www.gov.uk/government/collections/energy-and-emissions-projections.

DRAFT

14 Environmental sustainability analysis

14.1 Introduction

As the world faces the escalating impacts of climate change, the scientific community has a critical role to play —- not only in advancing knowledge but also in modelling responsible environmental stewardship. The Intergovernmental Panel on Climate Change (IPCC) has made it clear that urgent action is needed to reduce greenhouse gas emissions and limit global warming to 1.5 °C above pre-industrial levels [**ipcc˙sr15**]. This global imperative places a renewed focus on the sustainability of all sectors, including large-scale research infrastructure. Scientific facilities, particularly particle accelerators and other energy-intensive installations, must rise to the challenge by minimising their environmental footprint while continuing to drive innovation and discovery.

Large accelerator facilities are among the most complex and resource-intensive scientific instruments ever built. Their construction and operation involve substantial energy consumption, extensive use of materials, and long-term environmental impacts. As such, embedding sustainability into every phase —- from design and construction to operation and decommissioning -— is essential. This not only aligns with global climate goals but also enhances operational efficiency, reduces costs, and strengthens public support. By adopting renewable energy sources, optimising energy use, reducing waste, and promoting circular economy principles, big science can lead by example —- demonstrating that scientific excellence and environmental responsibility are not mutually exclusive, but mutually reinforcing.

In recent years, researchers across different fields within big science have been investigating the best approaches to attack this problem, both in general terms and specific to particular fields of study. The HECAP+ initiative has produced a general overview of guidelines and best practices across a wide range of projects and facility types [1]. Additionally, a UK-based group has produced guidelines specifically aimed at accelerator facilities [2]. Some relevant points drawn from these documents include:

- **Research infrastructure and technology**
  - Engage with industrial partners who exemplify best practice and sustainable approaches.
  - Appoint a dedicated sustainability officer to oversee project development, and institute regular meetings with a focus on environmental sustainability.
  - Critically assess the environmental impact of materials, construction and the operational life cycle as an integral part of the design phase for all new infrastructure.
  - Ensure that environmental sustainability is an essential consideration at all stages of projects, from initial proposal, design, review and approval, to assembly, commissioning, operation, maintenance, decommissioning and removal, using life cycle assessment and related tools.
- **Construction**

  - Utilise lower carbon construction materials: alternatives to steel and other high-impact materials, and low-carbon concrete.
  - Develop precise modelling of anticipated beam loss points and radiation levels to optimise the shielding thickness required for safety, as a function of location within the machine.
  - Evaluate possibility of performing the same science with a more compact accelerator, e.g. with higher gradient and larger magnetic fields.

- **Component design**
  - Design with specific intention of reuse/recyclability/proper disposal of products (in that order), e.g. modularity, type of coating.
  - Reduce gross material use through efficient and optimised design and machining techniques.
  - Optimise/minimise the number of spare parts through designing modular equipment with the same spare parts, through accurate simulation of use and lifetime and through designing for longevity.

- **Energy**
  - Ensure that energy efficiency is a major focus in experimental design, and prioritise technologies that minimise consumption and maximise energy recovery.
  - Ensure that energy efficiency is a major factor in the design and construction of new infrastructure.
  - Prioritise moving to sustainable and renewable energy sources via both local generation, and energy import and export.
  - Investigate operation modes and implement demand shifting with consideration of greener power generation (e.g. seasonal and daily fluctuations, operation for optimal PV, boosting with battery power, etc.).
  - Explore less environmentally impactful operational cooling, e.g. optimise the absolute temperature of the accelerator tunnel, cooling water and user area; change the accepted ranges of temperature stability; and implement other cooling methods, e.g. free cooling.
  - Design with waste reduction efforts implemented from the start e.g. waste thermal energy used for district heating, gas recovery systems etc.

- **Resources and waste**
  - Prioritise suppliers instituting sustainable sourcing and operating policies, with a particular focus on the raw materials processing stage and with the aim of creating demand for recycled (secondary) raw materials.
  - Assess waste generation and management for the design, operation and decommissioning of IT and infrastructure projects by right-sizing needs, establishing specific treatment channels for all waste categories, and setting recycling targets that include the recycling of all construction waste.

- **Travel**

  - Implement remote/hybrid user access in relevant areas of the facility, e.g. to minimise the need for large groups of users to visit the facility to carry out an experiment and therefore encourage reduction in travel, and to provide additional (international) staff time for different types of facility shifts or projects over all time zones.
  - Re-assess needs for in-person meetings, and prioritise formats that minimise travel emissions and diversify participation by making use of hybrid, virtual or local hub participation, and optimising the meeting location(s).

- **Location.** Choose site location considering lowering long-term environmental impact, e.g. siting near abundant renewable energy sources, co-locating with existing support and scientific infrastructure, near a railway station to enable user access, or near a town or city with district heating that utilises waste heat.
- **Computing.** Ensure that environmental sustainability is a core consideration when designing and choosing sites for large computing infrastructure, such as data centres, including, e.g., the availability of renewables, the efficiency of cooling systems and the reuse of waste heat.

Building an environmentally sustainable facility is one of the key themes of the UK XFEL project. There are many facets to sustainability; the main goal of any effort in this area should be to ensure environmental impact is factored in for every decision that is made on the project. It will be a key factor, but not always the overriding one – our primary aim is to ensure we can build a world-leading next-generation facility, and the aim of the sustainability work package is to ensure that the facility is delivered in the most efficient way possible. The most impactful opportunities to reduce overall emissions are early on in the project lifecycle: a failure to grasp those early opportunities may lead to additional long-term financial costs and reduce the impact of any carbon savings.

Some important aspects of sustainability relevant to UK XFEL include:

- **Construction** – including materials required to build the components and subsystems (concrete, steel, copper, aluminium), as well as manufacturing and delivery to site
- **Operation** – energy use for the linac, magnets, and beamlines, as well as data processing and storage
- **Travel** of staff, contractors, and users
- **Maintenance** – consumables, spare parts, and upgrades for subsystems
- **Decommissioning** – reuse and recycling of regularly-changed parts, as well as the whole facility at the end of its life

With limited resources available, we need to concentrate efforts on those aspects where (a) we have some influence, and (b) there is potentially a large impact. This will hopefully result in a facility design with an intrinsically low environmental impact. Of course, this does not mean that other areas are neglected: everything with a potential impact should be given due consideration, and effort should be prioritised accordingly.

The most critical areas for sustainability are listed here in priority order.

1. **Energy use** during operation, particularly in the RF system and data centres
2. **Embodied carbon** of construction materials, particularly concrete for shielding

Ongoing maintenance and decommissioning are both important areas. As far as possible, components and subsystems should be designed to be modular and easily replaceable, and be made from easily recyclable materials. These principles will be embedded at the technical design stage.

14.2 Grid intensity

For a facility with a lifetime measured in decades, the largest contribution to overall lifecycle carbon emissions will be the emissions during the operation phase. This in turn will be dominated by emissions associated with grid electricity.

Since the turn of the century, the UK has made great strides in decarbonising its electricity supply; all of its coal-fired power stations have now been shut down, and there has been a substantial effort to install new wind and solar farms. Thanks to this continued effort, the average emissions produced by 1 kW h of electricity has decreased from a steady value of around 500 gCO_2e in the years 2000-2010, to around 200 gCO_2e in 2024. This is expected to decrease further as more low-carbon generation comes online. Projecting the carbon intensity of the electricity supply into the future is obviously more difficult, since it depends on policies implemented by future governments. The UK government publishes annual energy and emissions projections (EEP) [**eep˙23˙50**] looking forward to 2050. These are a baseline set of projections, taking into account policies which are implemented or almost ready to implement, and therefore we could expect them to be somewhat conservative. The UK government also produces a document called the Green Book [3] which provides a model for grid emissions going forward to 2050 and beyond. In the decade 2030-40, the average grid intensity is 49 gCO_2e/kWh for the EEP model, and 34 gCO_2e/kWh for the Green Book model. Figure 14.1 shows these projections in more detail. In the estimates below, we have used the more conservative EEP intensity figures.

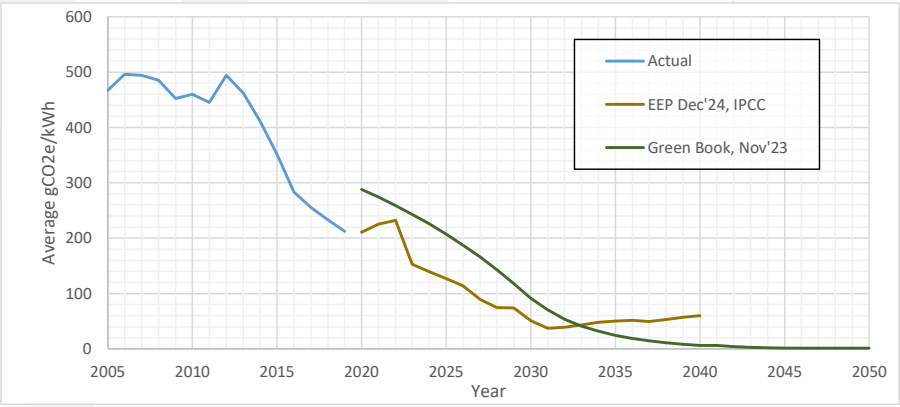

Figure 14.1: Carbon intensity of electricity generation, in gCO_2e/kWh, for the period 2005-2050. The blue line shows the actual intensity up to 2019; the green and brown lines are projections from the UK government's Green Book and EEP documents respectively.

During the future operation period of UK XFEL, the grid intensity in all scenarios is expected to be significantly lower than that of today. However, it is not zero. A large multi-MW facility like UK XFEL must still strive to reduce its electricity usage as far as possible in order to minimise its environmental impact.

14.3 Operation

In terms of power consumption, the largest single subsystem is the RF powering the cavities to accelerate the beam to high energy. This occupies over a third of the estimated total 37 MW. Table 14.1 shows how this figure breaks down across subsystems.

Subsystem	Power consumption [MW]	Annual energy consumption [GW h]	Annual emissions [ktCO$_2$e]	Potential savings [MW]
RF (Section 5.1)	15.2	102	5.00	5.8
Other technical systems	8.12	65.0	3.19	3.0
Services and infrastructure	7.21	57.7	2.83	
Data centre (Section 12.1)	3.24	14.2	0.70	
Secondary sources	1.95	9.75	0.48	
Undulators (Section 6.7)	1.3	10.4	0.51	
Total	37.0	259	12.7	

Table 14.1: Energy consumption for significant UK XFEL subsystems, and the corresponding annual emissions. The figures for the undulators are based on including SCUs for FEL-1 (which is a potential future upgrade, see Section 6.7.3), and assume that the cryogenic system operates for 8000 hours per year, in line with the assumptions about the RF system (see Section 5.3.2). A grid intensity of 49 gCO$_2$e/kWh is assumed. See also Section 13.2.9 for a detailed breakdown. Note that the figures reported in that section are similar, but not identical, to the figures reported here, due to differing assumptions.

In many of these areas, there is ongoing active technology development aiming to increase efficiency and reduce power demand whilst maintaining the same or improved performance. Some examples are briefly listed here, along with their potential impact on UK XFEL consumption.

- **Thin film superconducting RF.** The RF cavities must be cooled to around 2 K in order to provide the required accelerating gradient. To reach this temperature requires a large electrical power load; the efficiency of cooling has a strong dependence on the laws of thermodynamics. Switching to thin film cavities (rather than solid niobium) would enable the temperature to be raised to 4 K, reducing the cryogenic power draw by a factor of 3, which would result in a saving of 5.8 MW. Thin film technology is not yet ready for deployment on a user facility, but this is a highly active area of R&D and a great deal of progress is expected over the next decade.
- **RF power delivery.** In the normal-conducting (i.e. higher than 8 GeV) section, there is potential for installing high-efficiency klystrons with an efficiency of 50-55 % compared to the 'standard' efficiency of around 43 %. This would have a reasonable impact on the power requirements for the RF system as a whole, with potential reductions from a baseline of 11.5 GW h to a reduced level of 9-10 GW h.
- **Magnets.** Around half of the total under 'other technical systems' in Table 14.1 is taken up by power converters for beamline magnets. Electromagnets are the default option for beam manipulation due to straightforward and relatively rapid tuneability. However, in recent years many light source facilities have been switching to permanent magnet (PM) systems in instances where no tuning is required [4, 5]. There are solutions for highly-tuneable PM systems based on moving parts as well. There is potential for some of the beam transport magnets to be replaced with PM-based devices, depending on the field level and required adjustment range. This would also reduce the water cooling load. Assuming half the magnets could be PM-based, this could result in an approximate saving of 3 MW.

Figure 14.2: Progression of the energy efficiency of supercomputers on the Green500 list between 2007-23, measured in MFLOPs/W [6].

- **Climate control.** The environment of the accelerator hall must be carefully controlled for temperature and humidity, with subsystems having a variety of different requirements. Every watt of electrical power used ends up as heat eventually; as a rule of thumb, a 35 % overhead can be added to take this heat away either by air or water cooling. Depending on facility location, it may be possible to make use of free cooling or ground water cooling to reduce the power consumption of these systems. Additionally, the waste heat generated by the accelerator can be used indirectly to provide heating and hot water for nearby offices and homes. This is only possible if the outlet temperature is high enough, so systems must be designed with this in mind from the outset. Making use of waste heat does not have a direct impact on the facility, but will help reduce the emissions of the surrounding buildings.

- **Computing.** As described in Section 12.1, computing resources are expected to occupy a significant fraction of the UK XFEL power budget. A data centre for UK XFEL would be built to the highest-possible efficiency specifications. Efficiency for supercomputers has been steadily improving over the past few decades (Figure 14.2), and the most efficient supercomputers have now improved to over 10 GFLOPs/W, having doubled in efficiency roughly every two years. As ever, there needs to be care taken regarding the Jevons paradox [**jevons˙wiki**]: greater efficiency often leads to greater usage, meaning overall power consumption does not necessarily decrease. Efficiency improvements need to be coupled with 'green algorithms' and careful management of compute resources. Computing power can help drive improvements in efficiency as well: machine learning techniques can help us to optimise accelerator operation much quicker than a traditional operator-based approach. This could help to reduce setup time, increasing the number of science hours delivered by a facility, as well as helping to diagnose issues and increase power efficiency.

Efficiency gains such as those mentioned here do not usually come with zero cost. In some cases (RF and magnets), some technology R&D is required before newer and more efficient technologies can be adopted on a large user facility. This means investing in a long-term research effort to ensure that UK XFEL is well-positioned to take advantage of the technological advances that STFC's staff are pushing forward. In other cases (climate control and computing), the technology already exists to reduce operating emissions, but using it will come with a higher upfront financial cost. These higher upfront costs are more than balanced out by reduced operating costs over the lifetime of a large facility, which is typically measured in decades. Care needs to be taken that

more efficient technologies are not ‘value-engineered’ out of the design, and that investment in greener accelerator technologies is prioritised at an early stage.

Travel of users to a large scientific facility is a large ‘hidden’ source of carbon emissions, primarily due to the high impact of aviation. This should be a major concern for a future facility, and any siting decision should be made with this in mind, making sure a location is selected with good public transport links. As detailed in Section 15.1.9, the design is site-agnostic at the moment, and so this is primarily a concern for a later stage of the project. It’s important to ensure that in-person access for users is supplemented by a strong capability for ‘sample-by-post’ operation, especially for routine and/or technically straightforward experiment modalities. This remote operation capability will reduce carbon emissions as well as financial costs for researchers, making the facility more attractive overall and opening up access to a wider pool of potential users.

Another factor which affects a siting decision is grid connectivity, and specifically availability of low-carbon electricity generated from renewables. As mentioned above, the UK has made great progress installing renewable capacity over the last couple of decades. However, this is not the full story – there is a strong North-South divide, with a high concentration of wind farms in northern latitudes. The further south a large facility is located within the UK, the greater its emissions will be. Figure 14.3 illustrates this: during the first eight months of 2025, the average carbon intensity for South Scotland was 23 gCO_2e/kWh, compared to 256 gCO_2e/kWh for South Wales - an order of magnitude difference.

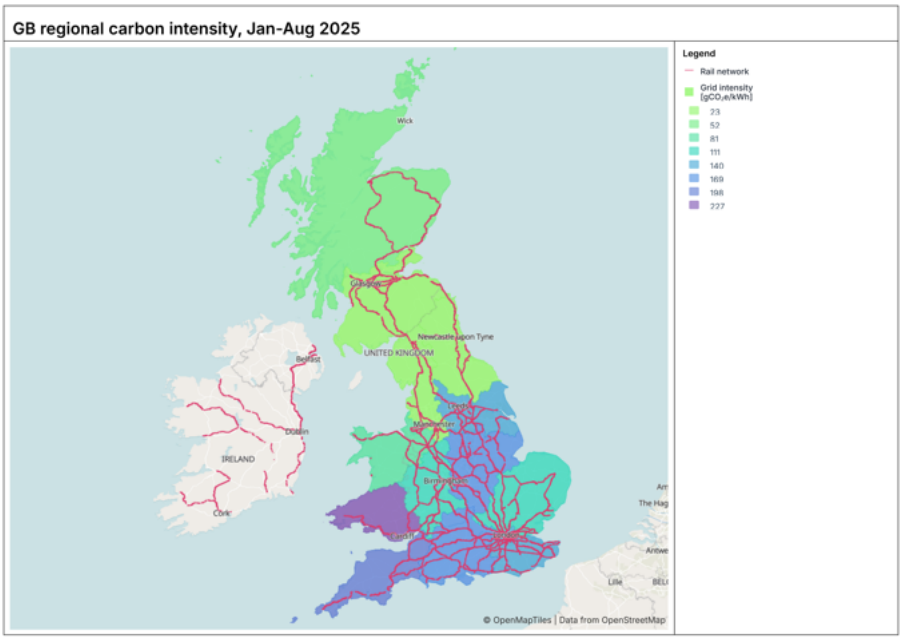

Figure 14.3: Carbon intensity for each of the 14 Distribution Network Operators (DNOs) in Great Britain, averaged over the period January-August 2025 and measured in gCO_2e/kWh. The data was sourced from the Carbon Intensity API [7] and the map was generated using Atlas. Rail lines are superimposed to highlight places with good public transport links. Data is not available for Northern Ireland.

14.4 Construction

Although the operation of a large facility over several decades is the dominant factor in its carbon emissions, there is a significant contribution from the embodied emissions from the materials used in its construction. Additionally, the construction of a new facility has a high level of visibility

in the public eye. Efforts to improve environmental sustainability credentials in this area will have a disproportionate impact on the public perception of the project, and hence affect UKRI's 'license to operate'.

Recently, STFC carried out a study looking at the lifetime emissions of a planned mid-range facility, RUEDI [**ruedi˙sus**]. Of the estimated 1.7 ktCO_2e generated by the project over ten years, 137 tCO_2e are attributed to the concrete used for shielding. This illustrates the relatively large contribution for a single one-off item, even for a small project.

Concrete is an excellent shielding material, absorbing neutrons and gamma rays very well. It is easy to manufacture, highly durable, and can be used as a supporting structural element, often playing the role of floor, wall and ceiling in addition to its shielding properties. Unfortunately, it is highly carbon-intensive primarily due to the high temperatures used during cement production.

The durability of concrete can be turned into an advantage for sustainability: the lifetime of the shielding is likely to be greater than the lifetime of the facility, enabling easy re-use of modular concrete blocks. Reusing blocks from previous projects means that less material is required to be newly manufactured, as well as reducing the volume of waste disposal. There are potential extra costs for assessing and refurbishing damaged blocks, as well as costs for storing blocks between projects. Additionally, shielding enclosures made using standardised blocks may be bulkier and less flexible than custom-built enclosures made from poured concrete. Nevertheless, this approach has been employed by many accelerator institutes for many years, and there are numerous examples of modern accelerators housed within enclosures built for facilities several decades ago.

One way of reducing the overall volume of concrete is to employ **local shielding** closer to any sources of ionising radiation. This leads to a smaller shielding requirement within the outer walls of enclosures. This could be implemented by, for instance, building a small lead or concrete enclosure around a beam dump.

It is possible to reduce the environmental impact of concrete without impacting its shielding or structural properties. Most accelerator shielding uses concrete made from ordinary Portland cement (OPC); however, this can be partly replaced with other materials. In a recent example, the EPAC project used 75 % Ground Granulated Blast-furnace Slag (GGBS) in its cement [8], resulting in the embodied greenhouse gas emissions being reduced by half compared to standard concrete, at only a slightly higher cost.

Combining the low-carbon concrete approach with the use of standardised, reusable (and reused) blocks, as well as implementing local shielding wherever applicable, will result in significant carbon savings for the construction phase of the project.

14.5 Maintenance

Wherever possible, subsystems should be designed to be modular, using common and readily-available parts, especially for subsystems with a high likelihood of needing regular maintenance or replacement of parts. Wherever parts are likely to be regularly replaced, these parts should be easily recyclable. Materials should be stamped with material grades and issued with material 'passports' as an identification aid for reuse and recycling.

14.6 End of life

As above, components used in the construction of UK XFEL should be able to be disassembled into raw materials ready for recycling at the end of their useful lives. The UK XFEL beam is composed of electrons, which means that we expect a low level of activation for beamline equipment (in contrast to proton or neutron accelerators, for instance). Nevertheless, we should seek to minimise the amount of activation required, as this will complicate and lengthen the recycling process. This can be achieved through careful planning of component locations, and local shielding where necessary.

14.7 Conclusions

In seeking to build a next-generation XFEL facility, one of our key aims is to ensure that such a facility is built and operated in the most resource-efficient way possible, at the same time ensuring that our science goals are met. To do this, we must embed environmental considerations into every decision made throughout the project, and particularly at the beginning when key strategic choices are being made. This chapter has summarised the considerations that need to go into those decisions, outlined a few of the major factors affecting sustainability, and highlighted where there is a need for improved technology in the future.

DRAFT

References for Appendix 14

[1] SustainableHECAP+ Initiative. *Environmental sustainability in basic research: A perspective from HECAP+*. Tech. rep. 2023. URL: https://hecap.eco/.

[2] Hannah Wakeling et al. "High-level environmental sustainability guidelines for large accelerator facilities". In: (Jan. 2025). URL: https://arxiv.org/abs/2501.14979v1.

[3] *Green Book supplementary guidance: valuation of energy use and greenhouse gas emissions for appraisal*. Tech. rep. Department for Energy Security and Net Zero, Nov. 2023.

[4] C Calzolaio. "Overview of permanent magnet implementations for advanced light sources". English. In: *Proc. IPAC'25*. IPAC'25 - 16th International Particle Accelerator Conference 16. JACoW Publishing, Geneva, Switzerland, July 2025, pp. 42–47. ISBN: 978-3-95450-248-6. DOI: 10.18429/JACoW-IPAC25-MOZN1. URL: https://indico.jacow.org/event/81/contributions/6337.

[5] B Shepherd. "Assessing and increasing the sustainability of future accelerator based facilities". English. In: *Proc. IPAC'25*. IPAC'25 - 16th International Particle Accelerator Conference 16. JACoW Publishing, Geneva, Switzerland, July 2025, pp. 1681–1686. ISBN: 978-3-95450-248-6. DOI: 10.18429/JACoW-IPAC25-WEYD1. URL: https://indico.jacow.org/event/81/contributions/6338.

[6] Vignesh Adhinarayanan and Wu Chun Feng. "Looking Back to Look Forward: 15 Years of the Green500". In: *Computer* 58.1 (2025), pp. 76–86. ISSN: 15580814. DOI: 10.1109/MC.2023.3333316.

[7] Lyndon Ruff. *Carbon Intensity API*. URL: https://carbon-intensity.github.io/api-definitions/.

[8] Helen Towrie. *CLF UK's new advanced imaging centre takes shape*. Nov. 2020. URL: https://www.clf.stfc.ac.uk/Pages/UK%E2%80%99s-new-advanced-imaging-centre-takes-shape.aspx.

DRAFT

15 Project delivery

15.1 Project Delivery and management

A next-generation XFEL would be a transformative mega-project for the UK, delivering against UKRI's core missions; advancing knowledge, improving lives, and driving growth. Its scale and complexity demand extensive early-stage planning; projects that invest here are far more likely to achieve intended outcomes [**IPAhandbook**, 1]. Techniques like Digital Twinning, Model-Based Systems Engineering, and Effects Analysis can de-risk delivery and provide flexibility if scientific objectives shift. This chapter covers project management from early appraisal through to operational readiness, while noting that operations, benefits realisation, and decommissioning must also be considered during technical design and business case stages.

The UK has a strong track record delivering both domestic mega-projects (Crossrail, Thames Tideway, Heathrow expansion) and major international facilities (ESS, CERN, Eu-XFEL, SKA), providing a wealth of relevant guidance and lessons learned. Key frameworks include NISTA's Teal Book (project and portfolio management) [2], HM Treasury's Green Book (appraisal and strategic viability) [3], the Orange Book (risk management) [4], and the Magenta Book (evaluation) [5]. The 2022 Project Routemap handbook [6] a support tool for novel, complex major projects — structures delivery around eight key areas: Requirements, Governance, Systems Integration, Organisational Design, Procurement, Risk Management, Asset Management, and Delivery Planning. These, alongside the APM Body of Knowledge [7] and STFC's project management framework [8], form the basis for the UK XFEL delivery approach outlined below.

15.1.1 Requirements

The requirements for a Next Generation XFEL have been clearly defined and have subsequently been translated to the necessary machine parameters to meet these demands **??**. This current phase of the project has been focused on ensuring that the mechanism to deliver these requirements has been properly shortlisted and studied thoroughly by adding an Options Analysis to the Conceptual Design. The result of which is that this stage is effectively an expanded version of the Green Books shortlist process [3]. As can be seen in the Options Analysis this shortlist aligns with the Green Book's 'Do Minimum' (meeting only essential needs), 'Preferred Way Forward' (appearing most likely to achieve SMART objectives), and more/less ambitious alternatives. Following this process through the CDOA will require a Shortlist Appraisal, whereby the work presented is reviewed, recommendations analysed an option selected and a preferred way forward approved. Following the CDOA appraisal it is expected that, as per UK Government guidance, the following stage should be detailed technical design and prototyping stage. However, the timescale of this process for UK XFEL is not yet defined.

15.1.2 Governance, Approvals, and Funding during Pre-Operations

A well planned governance framework established early will provide oversight, ensure accountability, and facilitate timely decision-making throughout the project lifecycle, however it is useful to maintain continuity as the project evolves. The governance structure will evolve as the project ramps up and down through various stages. STFC's project management framework states that *As the Business Case matures and approaches significant funding gates, formal Project Boards and/or Oversight Committees will need to be established to direct and oversee the work* [8], and that: *major projects (£20M+ value), independent representation on these boards is mandatory* [8]. Given the reputational value and impact that the CDOA has, along with the eventual scale of a Next Generation XFEL, the CDOA team has already been implementing this approach by installing a project board, and an International Advisory Committee. The project has also been reporting to STFC's Project Review Committee as well as the UKRI Infrastructure Fund (the funding body during this phase) all of which have been overseeing the progress and delivery of the work todate. Following the CDOA, the governance structure in place would remain similar whilst prototyping and technical design reviews take place. It is expected that once the project progresses technical design and into prototyping it would also be overseen by NIST (National Infrastructure and Service Transformation Authority) amongst other government bodies, such as, the Government Major Projects Portfolio [9], which tracks major national projects ($\sim$ 227 projects as of 2025, including $\sim$68 infrastructure and construction schemes).

Approval for funding and progression should be granted at defined decision gates, the 2020 science case established the mission need for a Next Generation XFEL, following this the next major phase would be a technical design review (TDR) which would provide a detailed proposed design, site selection, in depth business case and other material required to make the final decision on release of funding. For a project of this scale [1], approvals will be required from multiple bodies, likely including UKRI Investment Advisory Working Group (IAWG), UKRI Executive Committee (ExCo), DSIT InvestCo, and HM Treasury etc. These approvals will be subject to rigorous scrutiny, ensuring the project remains strategically aligned, economically justified, financially affordable, and managerially deliverable. Budgeting strategies during this phase must account for the phased nature of approvals. It is expected that funding for technical design stages and early prototyping is distinct from funding for the main construction, and that the final construction build would itself be phased. Transparency regarding the sources of funds and how they align with project costs is essential [3].

15.1.3 Systems integration

There are two elements to ensuring that a systems integration methodology is correctly applied during later stages of the project: internal and external. Internally, a Next Generation XFEL will comprise highly specialised and interdependent subsystems, including accelerator infrastructure, experimental end stations, computing, autonomous systems, controls, safety systems, utility services etc. all of which must function as a cohesive, reliable whole. STFC has plenty of experience on these type of large-scale complex systems both in operating and delivering equipment to work within this environment. However, a Next Generation XFEL would need to more tightly integrate these specialist subsystems to achieve it's AI ambitions. Early identification and definition of critical interfaces, responsibilities, and integration risks would enable proactive coordination across disciplines. Appointing a dedicated systems integrator would help manage

[1] Assuming that the outcome of review of the Options Analysis is to either build a UK facility or proceed significantly increased investing in a existing generation XFEL

these interfaces, especially given the lessons learnt from in-kind contribution models, by embedding elements of this function in delivery partners it would strength the collaboration between host and contributor, whilst ensuring robust systems could be implemented. This approach of embedding the systems integrator role was successful in the delivery of the Heathrows Terminal 5 project [10] (a public/private £4.5bn mega project).

Externally, a Next Generation XFEL facility must be integrated into the broader UK, and international, science and innovation landscape, as demonstrated in the science case [11]. This includes aligning with national science priorities, complementing existing large-scale infrastructure (e.g. Diamond II, ISIS, CLF), and ensuring interoperability with global XFEL facilities to avoid duplication and foster collaboration. A broader integration will also support whole-life value creation: enabling shared data systems, coordinated access policies, and programme-level outcomes that link to the UK's net zero, health, and technology missions. In this way, the facility is positioned not as an isolated asset but as a vital, interconnected node in the UK's science strategy.

The next phase of UK XFEL should undertake a deeper landscape analysis, along with: clarifying stakeholders, engaging potential users, funders and regulators, mapping dependencies across policy, digital infrastructure, and skills pipelines, etc. By expanding this work early in the development phase the project will increase the chances of early benefits realisation.

15.1.4 Organisational Design and Development

It is important to note that the creation of a Next Generation XFEL should also establish a new organisational structure, and one which will need to change as the project moves from construction to operations, ensuring that the organisational structure is setup for change will be an important part of the planning.

Assuming that a UK XFEL would employ a common delivery model such as in-kind contribution, it is expected that academic, industrial, and institutional partners both across the UK and internationally would need to operate under a coordinated system. However managing this sort of system, where contribution partners hold both the budget and the risk can be extremely challenging, it can also lead to a 'supplier - customer' style relationship which has proven to present it's own set of challenges. Designing a organisational model which offers a more integrated contributor relationship will result in improved performance and delivery of the project. It is important to note that the organisational model must accommodate contributions through clear governance, robust interface management, and contractual clarity, ensuring that all parties understand how their inputs align with the project's objectives and delivery timeline, whilst maintaining a collaborative relationship.

Internally within the project delivery there should be an understanding that thousands of people will end up working on 'UK XFEL'; engineers, lawyers, executives, surveyors, fitters, accountants, welders, landscapers, technicians, cooks, scientists, painters etc. these people will come from many backgrounds across multiple organisations but all must have the same goal: *building a 'UK XFEL'*. Particular attention must be paid to defining roles that span scientific leadership, technical integration, project delivery, and long-term asset stewardship. The UK Governments Project Routemap [6] supports planning for workforce development, succession, and behaviours — all essential for building a high-performing, collaborative team capable of navigating complexity and change.

Effective stakeholder management is essential to the successful delivery of a complex infrastructure project like the UK XFEL. With a wide range of interested parties (including government

departments, funding agencies, research institutions, industry partners, local authorities, international institutions, existing XFELs, international governments and future users) a proactive and structured engagement ensures that expectations are aligned, roles are clearly defined, and potential conflicts are addressed early. Managing these relationships through consistent communication, clear governance structures, and inclusive decision-making processes reduces the risk of delays, scope changes, and misaligned objectives. Moreover, strong stakeholder coordination enhances collaboration (especially with in-kind contribution models), secures long-term support, and ensures that the facility delivers maximum value across its scientific, economic, and societal goals.

Thus public engagement at the early stages of a national facility, such as the UK XFEL, is not only a matter of transparency, but a critical factor in building long-term legitimacy, trust, and public value. As a project driven by public funding (with the assumption that private sector partnerships will be required), it is essential that citizens understand the purpose, benefits, and impacts of the investment. Early engagement allows communities to contribute to shaping the project, helps identify and address concerns before they escalate, and fosters a sense of shared ownership. Moreover, it lays the foundation for inclusive access to the facility's future scientific, educational, and economic opportunities. Meaningful public engagement is therefore a strategic enabler of successful delivery, social licence to operate, and lasting impact.

15.1.5 Procurement Strategy

A detailed procurement strategy should be developed during the technical design phase (often referred to as the 'Define' phase) and be informed by strategic sourcing analysis [8], [7]. This strategy outlines how goods, services, and intellectual property will be acquired, considering the complexity of the supply chain, the capabilities of potential suppliers, and the desired risk allocation between the public sector and contractors. For major procurements (over £10m), external assurance and Cabinet Office/HMT approvals are required before tender launch [8]. Contractual arrangements will be designed to motivate performance, manage risks [7], and reflect the chosen delivery models (linear vs. iterative).

The UK Government's Project Routemap [6] emphasises the need for procurement to be strategically aligned with the overall delivery model, beginning in the early planning phases rather than as a downstream function. For an XFEL, this means designing a procurement approach that supports phased delivery, accommodates in-kind contributions from domestic and international partners, and ensures seamless systems integration across critical technical components such as accelerators, undulators, experimental end stations, and data systems. Early engagement with potential suppliers and research institutions will be key to understanding market capacity, fostering innovation, and securing the specialist capabilities required, such as systems integrators and advanced photon instrumentation providers. Given the technology readiness levels of some systems, some suppliers may require significant input from the design team, stressing the importance of early engagement.

The Routemap also advocates outcome-oriented procurement models that incentivise performance, collaboration, and delivery certainty, principles that are highly relevant, when scientific output and reliability are paramount. Rather than traditional input-based contracts, alliance-style models or framework agreements may offer the flexibility and risk-sharing structures needed to integrate diverse contributors, including those providing in-kind hardware, software, or expertise. Furthermore, procurement decisions must be informed by a well-articulated commercial strategy that clearly defines risk allocation, interface responsibilities, and lifecycle value. This will ensure

that the XFEL's procurement function is not only a mechanism for buying goods and services but a strategic lever to build capability, manage complexity, and enable whole-life value across the facility's scientific mission. An example of this can be seen during ESS's vacuum procurement framework, where ESS leveraged their buying power allowing in-kind contributors to effectively purchase through ESS, this reduced both cost and risk of critical infrastructure.

15.1.6 Risk Management

Effective risk management will be central to the successful delivery of this scale, given its technical complexity, long delivery timescales, and significant public investment. Whilst technically a Next Generation XFEL is a unique facility delivering cutting-edge scientific benefits, it is after all a large scale infrastructure project and has many similar projects within the same classification (large 'mega-projects') having been delivered over the past couple of decades [12] (such as Crossrail, HS2 Tideway Sewer System, Hinkley Point C, Heathrow Terminal 5 etc.) The UK has also been involved in a number of International Scientific mega-projects, more closely akin to a stand alone Next Generation XFEL, such as the European Spallation Source, the Square Kilometre Array, ESRF, LHC (and its associated upgrades/experiments), Eu-XFEL, ITER etc. All of these projects faced the same scale of issues as a new national facility would, long time scales leading to long open risk windows multiple collaborators with a significant number of interfaces and significant impact to the local area.

The UK Government's Project Routemap [6] stresses that risk management must go beyond passive monitoring to become an active, embedded process that drives informed decision-making and strengthens delivery capability. For a national laboratory of this scale, this involves identifying and addressing risk across multiple dimensions — technical (e.g. accelerator reliability, cryogenic systems), programme (e.g. interface delays, supply chain constraints), strategic (e.g. changing policy or funding landscape), and operational (e.g. future readiness of data systems and user access models). The Routemap also highlights the need for a culture where risk is openly discussed and constructively challenged across stakeholders, from sponsors and clients to delivery partners and contributors of in-kind elements.

In the context of an XFEL project, the Routemap advises that risks should be allocated on the basis of capability rather than convenience — ensuring, for example, that complex technical risks rest with those organisations best equipped to manage them. It also supports dynamic risk identification across life cycle transitions, particularly where project scope evolves or interfaces between subsystems and partners intensify. The use of integrated risk registers, linked to programme governance and assurance frameworks, along with project schedules, stakeholder maps, is recommended to ensure risks are tracked, escalated, and mitigated effectively. Where in-kind contributions are involved, additional care must be taken to assess and manage interface and delivery risks associated with distributed responsibility.

15.1.7 Delivery Planning

Delivery Planning, as set out in the UK Government's Project Routemap, is vital to ensuring that the new Next Generation XFEL facility transitions smoothly from concept to operational reality. This module emphasises readiness for delivery, not just in terms of timelines and budgets, but in having the right delivery model, sequencing, capabilities, and assurance mechanisms in place. For an XFEL, this means mapping out a realistic and robust delivery schedule that accounts for the interdependencies of technical systems (such as the accelerator, undulator, and experimental

stations), interfaces with in-kind contributors, and commissioning milestones. It also requires early clarity on delivery responsibilities between the sponsor, client, supply chains, identification of key decision points, constraints, and delivery risks, etc. A well-structured delivery plan will need to be dynamic and regularly updated, ensuring that the project remains responsive to change while maintaining momentum and strategic alignment.

The Routemap's guidance also recognises the importance of delivery planning as a coordination tool — particularly for complex, multi-partner projects with novel elements. Delivery planning must incorporate mechanisms for integrating in-kind contributions, synchronising them with site readiness, installation schedules, and system integration activities. Furthermore, the plan must build in time for iterative testing, safety validation, and phased handover, including early science operations. The delivery plan should link explicitly to the project's business case, ensuring that early decisions around procurement, asset management, and governance remain aligned with end outcomes. Finally, the Routemap highlights the value of embedding assurance and performance tracking into the plan — allowing stakeholders to monitor progress, address emerging risks, and ensure the project remains on track to deliver a world-class facility that meets the needs of its scientific users and funders alike.

At this conceptual stage the delivery planning has still to be detailed as there are multiple options available, however the following section gives some rough outlines of expected stages and timescales.

15.1.8 Technical design phase

A technical design phase forms part of the rigorous planning process required on a mega project like this. This is the phase of the project where detail is provided around the machine design and activities such as digital twinning, systems engineering and prototyping should take place. As well as developing a technical design for one of the recommended Next Generation options, the Technical Design Phase should also include the robust planning needed to execute the design, including;

- *Detailed Schedule*: Developed using critical path or critical chain analysis, defining activities, durations, dependencies, and key milestones for the build [7].
- *Resource Plan*: Identifying the required human (scientists, engineers, project managers, technicians) and non-human (materials, equipment) resources, balancing demand with availability [7].
- *Cost Plan*: Translating the resource plan and schedule into a time-phased cost profile (BCWS), detailing fixed and variable costs, and aligning with funding releases [7].
- *Risk Register*: Documenting all identified risks for the build, their analysis, planned responses, and allocated risk owners, integrated with contingency planning [7].
- *Quality Plan*: Defining the standards, processes, and acceptance criteria for all outputs and deliverables during construction [7], [8].
- *Stakeholder Engagement & Communication Plan*: Detailing how stakeholders will be informed, consulted, and involved throughout the build [7].
- *Configuration Management Plan*: Establishing processes for managing the technical and administrative aspects of the evolving design and build, ensuring traceability and control of changes [8].

Given the complexity of an XFEL, the design phase will likely adopt a multi threaded approach. Foundational civil and conventional infrastructure (buildings, utilities) may follow more linear,

predictive design processes. However, the design of the core accelerator technology, experimental stations, and complex control software will likely require iterative or agile approaches, allowing for learning, prototyping, and refinement as technical challenges are addressed and user requirements evolve [8].

15.1.9 Site Selection

It is expected that as a site selection would be a major strategic and political decision it would require a dedicated appraisal process that rigorously evaluates potential sites against technical, logistical, environmental, social, and economic criteria. This is not something that this phase of the design has evaluated, however, in order to produce a technical design the location *must* be considered, as multiple physical parameters (geology, geography, environment) will impact the design and therefore the both machine design and costing. This is an example of place-based analysis influencing design, considering impacts on local infrastructure, employment, and communities [3]. It's important to note that one of the major benefits to building a new facility based around a Next Generation XFEL is removing limitations which existing XFELs currently experience, for historical reasons, as such benchmarking against site selection processes for other large facilities (e.g., Eu-XFEL, LCLS, ESS, CERN, SKA) at the define phase, is crucial.

As can be seen from the conceptual design, a Next Generation XFEL would be a substantial build, and could form a new National Laboratory. This would necessitate the acquisition and preparation of a substantial plot of land. The facility (including external support infrastructure) would minimum footprint of approximately 2.5 km in length and 250 m in widthFigure 8.20, the location of which will require careful consideration based upon specific requirements a number of which are discussed in this section.

Transportation and Accessibility

As an international facility with 1000's of expected users per year operational and logistical efficiency (both during the build phase and operations phase) demands robust transportation infrastructure. Candidate sites should be able to deliver multimodal connectivity, allowing for sustainable transport modes (including cycle infrastructure and mass transit) to align with Net Zero objectives and reduce the operational carbon cost of the facility [13].

The following criteria is recommended:

- Air transport: Accessibility to an international airport within 60 minutes' travel time to accommodate global scientific access.
- Rail infrastructure: Integration with high-speed and regional rail services for staff, visiting researchers, and freight logistics.
- Road access: Direct connectivity to the national motorway network to support construction-phase logistics and long-term operations.

Utilities and power requirements

Whilst covered in more detail in Chapter 13, high-energy accelerator facilities such as XFELs require robust and scalable electrical infrastructure. Candidate sites must be located within viable proximity to high-voltage electrical substations capable of providing up tot 30 MW load capacity. Provision for future energy demand growth—potentially, should be factored into the site masterplan. Given the size of the site required and the electricity consumption, it would make financial sense to install a substantial solar plant onsite (at current capital and electricity costs a

50MW plant, similar in size to Deeside's Shotwell site would cost around £50m, paying for itself in around 7 years and saving over £200m over a 30 year life span).

In addition to electrical supply, high-throughput data infrastructure and availability of process water, are also critical baseline requirements.

Environmental and Ecological Constraints

Site selection should take into account environmental constraints ensuring the site is not located within any Special Scientific Interest (SSSIs), Special Protection Areas (SPAs), or other designated conservation zones. Or if it is that a comprehensive environmental due diligence is carried out to minimise the environmental footprint of a new facility. And where unavoidable, environmental impacts should be mitigated through biodiversity net gain commitments and landscape restoration, in line with statutory planning policy.

Land Availability and Planning Policy Alignment

The facility's design and linear geometry necessitates the acquisition of a long, thin and uninterrupted parcel of land. Site candidates must be assessed for:

- Land ownership and tenure (private, public, Crown Estate).
- Compatibility with local development plans and zoning frameworks.
- Land value and cost-efficiency, inclusive of acquisition, clearance, and remediation (if brownfield).
- Planning risk and potential public opposition, particularly where agricultural, heritage, or green belt land is implicated.
- Were feasible, engagement with local authorities to identify allocated land for science and innovation may streamline the planning process.

Alignment with UK Government Missions

Site selection must actively contribute to national policy priorities, which as of 2026 include:

Ensuring global visibility, access to UK facilities, and integration with international research infrastructure networks [14]. Minimising the facility's operational carbon footprint through sustainable design, efficient systems, and access to green energy infrastructure. Prioritising regions of economic underinvestment to deliver inclusive growth through high-skilled job creation and regional innovation capacity. By strategically locating the XFEL in a region targeted for uplift, the facility can serve as a catalyst for high-tech clustering and skills development, aligned with UKRI's place-based research investment strategy.

Campus Development

To maximise scientific return and support knowledge exchange, a facility sited in proximity to established research institutions, science parks, and/or industrial innovation clusters will foster collaborations, facilitate workforce development, and support cross-sectoral utilisation of XFEL capabilities. Campuses built around these models are also able to take advantage of public and private investment, both Harwell and Sci-Tech Daresbury have demonstrated this to significant effect over the years, growing their campuses around the existing facilities and operating as joint pubic private ventures to maximise economic impact. [15]. These successful campus models should be built in from the outset of any new national laboratory, with a focus on the Next Generation XFELs key scientific outputs to capitalise on synergistic collaborations. This approach aligns with the UKRIs strategic goal of enhancing place-based innovation ecosystem: "We want

to grow capacity to perform R&I across the country, recognising that growth is strongest when the focus is on agglomeration, clustering and comparative strengths." [14]

Summary

As can be seen, the site selection process for a UK XFEL facility must balance rigorous technical requirements with strategic and policy alignment. Therefore a land acquisition strategy should adopt a multidisciplinary framework, integrating land use planning, infrastructure engineering, environmental sustainability, and socio-economic uplift. A successful site will meet both the technical imperatives of a high-energy light source and contribute substantively to national goals in science, sustainability, and inclusive economic development. The site selection process should be formalised through a structured, multi-criteria assessment incorporating stakeholder consultation, spatial data analysis, and infrastructure feasibility studies. It is important to establish the site selection process early on in the project, as this will impact the final design and cost of the facility depending upon location constraints and preparatory work required. This work should engage with local councils early so they can understand future requirements, assess the impact of any new facility and advise on use of brownfield availability. Land acquisition may not require purchase of the land, as the government already owns many long narrow stretches of land in disused airfields and railway lines, which should be considered during the process. Reaching out to places like the MoD, the crown estate and local councils could help identify potential cost effective areas suitable for construction of a new national facility. Finally, it will be important that any site selection should learn from the lessons of existing facilities as not to constrain future upgrades.

15.2 Construction & phasing strategy

It is not expected that a Next Generation XFEL would be built in a single phase. In order to ensure early benefits realisation, flexibility to adapt to changes over the long term and cost smoothing, multiple build phases of a Next Generation XFEL should be explored. The Options Analysis report details possible entry point options for each stage, whilst ensuring that no early phase prevents capability expansion up to the full feature set. This roadmap would allow construction of the Accelerator, and then build end stations based on expected scientific demand. In addition to this a phased approach may also favour in-kind contribution agreements allowing more flexibility in delivery of contributions. Combining this with modular designs and off-site fabrication will improve safety, predictability, and speed of delivery.

15.2.1 Timelines and stages

Executing the build plan involves managing numerous complex activities, ensuring compliance with design specifications, quality standards, health and safety regulations [8], and sustainability commitments. Continuous learning and improvement are embedded practices [8]. Lessons from previous projects, both within STFC/UKRI and from other large international facilities, will be actively sought and integrated into planning and processes from the start. Regular project reviews, supported by monitoring against the baselined plan [8] [7], provide essential feedback for decision-making and adaptation.

The delivery of the facility shown in **??** would be an ambitious project, with the start of technical design to first science taking around a decade. During this period new capabilities may arise at

existing facilities, and national priorities may evolve in response to technological advances and changes in government policy.

To deliver sustained impact, it is essential that the scope of the proposed facility can evolve in response to such external factors. This can be achieved by spreading the delivery over a series of phases. The facility concept has been designed in such a way to allow multiple possible configurations: an example of one possible approach is presented below.

Phase 1a

To enable early science, Phase 1a consists of a single photoinjector with two FEL beamlines supporting Soft X-ray and Hard X-ray (up to ∼8 keV photon delivery). The linac energy would be set at 8 GeV, as the anticipated cost/time savings of a lower energy linac are expected to be outweighed by reconfiguration downtime, disruption to operations, and integration costs.

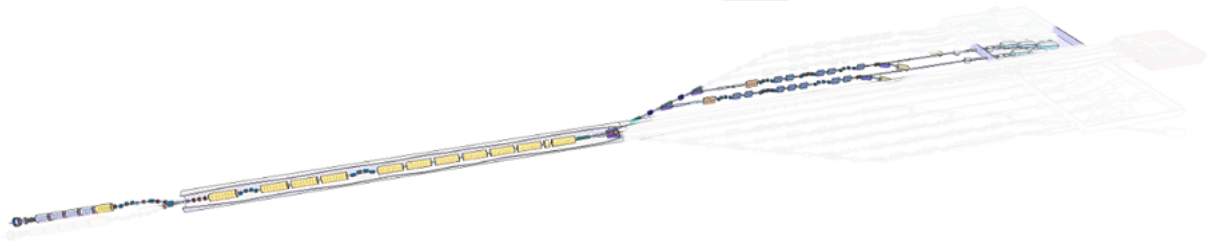

Figure 15.1: Phase 1a, consisting of a 8 GeV superconducting linac driven by a single photoinjector, and 2 FEL beamlines (SXR/HXR).

Phase 1b

Once operational, Phase 1a could be expanded to include the interleaved dual photoinjector, and MEC infrastructure including normal conducting booster, dual FEL beamline, and hall including target areas and high power/high energy laser infrastructure.

Figure 15.2: Phase 1b, including dual photoinjector, normal conducting booster, and MEC hall including beamlines and laser infrastructure.

Phase 1c

This would see completion of all FEL beamlines covering (continuously) a nominal photon energy range of ∼100 eV to 20 keV, supplying up to 18 end stations. This configuration represents the ‘nominal’ facility concept outlined in the UK XFEL Conceptual Design.

Upgrade

Following scientific exploitation, a second fan of beamlines could be installed on the opposite side of the linac. This array could combine FEL and electron-only beamlines, and represent the maximum utilisation of the 1 MHz linac. The specific beamlines installed would account for the

Figure 15.3: Phase 1c, representing the 'nominal' configuration based on 7 FELs supplying up to 18 end stations.

usage of beamlines as experienced in Phase 1 as well as accounting for new/emerging areas of interest.

Figure 15.4: Maximum utilisation of the superconducting linac, with FELs supplying up to 30 end stations, which could be delivered as an upgrade to Phase 1.

A phased approach has the following advantages:

- An initial reduced-scope phase would allow the UK to establish a firm foundation in XFEL construction and operation, deliver early scientific outcomes, while mitigating overall project risk.
- The total investment for full realisation can be distributed over an extended timeline. This allows for controlled budgetary profiling through the strategic scheduling of upgrade activities.
- A phased approach supports adjustment of both capability and cost in response to external factors, as described above.

Disadvantages in a phased approach include the total time to establish full capability, overall increased cost (as compared to a single-phase build), skills retention, and impact on user operations which would be disrupted by upgrade periods. Recommissioning of components may be required. A single phase build would be financially more efficient, but would not be the quickest way to realise early benefits.

Figure 15.5 assumes that a greenfield site is selected during a Technical Design Report (TDR) phase, that there is no delay between a TDR and the start of the build process, and that there would be suitable delays between phases to assess user requirements. It does not show any processes for re-evaulating these parameters, showing only the top level work breakdown. As such it is simplified, and detailed breakdown of the phases is not shown. On a timeline such as this, new facility would achieve first science within 10 years of project approval, building out to the nominal configuration within 18 years (allowing for delays to assess user requirements). Due to the modular nature of the FEL design, every stage other than commissioning can progress without the requirement of beam downtime, this improves up gradability and access to early science significantly, as well as providing options to expedite the build process should it be required.

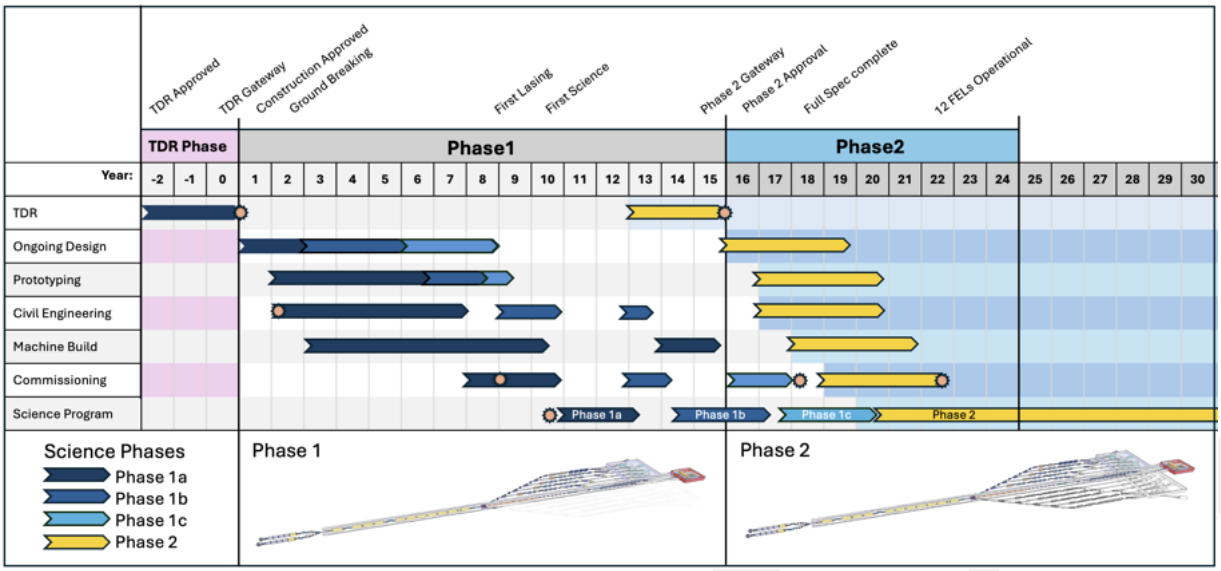

Figure 15.5: Estimated timelines for design and build of the two main phases of the project.

15.2.2 Transition to operations

The successful completion of this extensive pre-operations phase is marked by formal closure of the construction project, rigorous commissioning and testing of the facility, and a formal handover to the dedicated operational team [8] [7]. This transition period ensures the operational team is ready, the facility performs as intended, and accountability for future operations and benefits realisation is clearly established.

The transition phase marks the crucial handover from the construction project team to the operational organisation [8] [7]. This is not merely a physical transfer but a deliberate process to ensure the facility's engineered outputs are transformed into realised outcomes for users and stakeholders [3].

Key activities during this phase include: Commissioning and Testing, Business Readiness and Adoption, Formal Handover and Acceptance, Benefits Management, Monitoring and Evaluation, Ongoing Governance, Operations and Maintenance, Sustainability [8] [7].

A Next Generation XFEL has an expected operational life measured in decades; the management framework must therefore incorporate a view towards the facility's long-term evolution, potential upgrades, and eventual decommissioning [3]. Lessons learned from the operational phase, including the actual benefits realised, should be captured and fed back into organisational knowledge and used to inform future investments [8] [7]. The formal closure of the facility at the end of its useful life will require dedicated planning and execution, addressing technical, environmental, and financial aspects in a responsible and compliant manner.

15.3 Conclusions

The successful delivery of a Next Generation XFEL demands an approach that reflects both the scale and complexity of the project, as well as the lessons learned from past mega-projects. This chapter has outlined the critical delivery and management considerations required to transition from conceptual design to operational readiness, underpinned by government best practice

guidance, particularly the Green Book, the Project Routemap, and the STFC project management framework.

Several overarching themes emerge. First, early and comprehensive front end planning is paramount. Time invested upfront in defining requirements, validating options, and establishing governance, integration, and risk management structures will yield significant returns in reduced delays, cost certainty, and delivery resilience. Rushed starts or optimism bias, common failures in major infrastructure projects, must be actively mitigated through prototyping, digital twinning, and independent assurance processes.

Second, project delivery must be strategically aligned and adaptive. The project should remain focused on its core scientific mission while evolving to accommodate new discoveries, stakeholder needs, and external pressures. Phased development, robust procurement strategies, and a flexible organisational structure will support this adaptability and enhance resilience. In-kind contributions, if used, must be tightly managed through embedded systems integration and clear risk allocation mechanisms.

Third, successful delivery is not limited to construction. Asset management, operational readiness, and benefit realisation must be embedded from the outset. The XFEL's long lifespan requires whole-life planning, scalable infrastructure, and proactive transition to operations strategies to ensure sustained performance and value creation. Continuous monitoring and evaluation should be used not only to demonstrate impact but to inform future upgrades and strategy.

Finally, delivery success will depend on people. Building a high-performing, multidisciplinary team with shared objectives and domain expertise is crucial. This includes not just technical experts, but skilled project managers, user advocates, and operational leaders. The XFEL will be delivered by a diverse community; fostering alignment, collaboration (along with engagement to with general public), and capability across that community is one of the project's most important tasks.

DRAFT

References for Chapter 15

[1] Bent Flyvbjerg and Dan Gardner. *How Big Things Get Done: The Surprising Factors Behind Every Successful Project, from Home Renovations to Space Exploration*. London: Macmillan, 2023. ISBN: 9781035018950.

[2] Government Project Delivery. *The Teal Book — Project delivery in government*. Version 2.0. Apr. 2025. URL: https://projectdelivery.gov.uk/teal-book/home/.

[3] *Green Book supplementary guidance: valuation of energy use and greenhouse gas emissions for appraisal*. Tech. rep. Department for Energy Security and Net Zero, Nov. 2023.

[4] HM Treasury and Government Finance Function. *The Orange Book: Management of Risk – Principles and Concepts*. UK Government risk management guidance, latest revision. June 2025. URL: https://www.gov.uk/government/publications/orange-book.

[5] HM Treasury and Evaluation Task Force. *The Magenta Book: Central Government Guidance on Evaluation*. UK Government guidance on evaluation design, conduct, use and dissemination. July 2025. URL: https://www.gov.uk/government/publications/the-magenta-book.

[6] Infrastructure and Projects Authority. *Project Routemap — Setting up projects for success*. Feb. 2022. URL: https://www.gov.uk/government/publications/improving-infrastructure-delivery-project-initiation-routemap.

[7] Association for Project Management. *APM Body of Knowledge*. Ed. by Michael Bourne. 8th ed. Buckinghamshire, UK: Association for Project Management, 2025. ISBN: 978-1-913305-39-0. URL: https://www.apm.org.uk/book-shop/apm-body-of-knowledge-8th-edition/.

[8] *The STFC Project Management Framework*. Tech. rep. Version 6. UK Research, Innovation, Science, and Technology Facilities Council (STFC), Sept. 2021. URL: https://www.ukri.org/wp-content/uploads/2022/12/STFC-191222-FundingOpp-GridPP7Operations-ProjectManagementFramework.pdf.

[9] National Infrastructure and Service Transformation Authority, Cabinet Office, and HM Treasury. *Major projects data*. GOV.UK. Aug. 2025. URL: https://www.gov.uk/government/collections/major-projects-data.

[10] Uzor Onyia et al. "Evaluation of Integrated Teamworking Approach in Project Management: A Case Study of Heathrow Terminal 5 Project". In: *International Research Journal of Engineering and Technology (IRJET)* 8.10 (2021). URL: https://www.irjet.net/archives/V8/i10/IRJET-V8I1025.pdf.

[11] et. al Jon Marangos. *UK XFEL Science Case*. 2020.

[12] Infrastructure and Projects Authority and Cabinet Office. *Project and programme management*. Guidance page; first published 24 Aug 2017; last updated 30 Sep 2020. GOV.UK. Sept. 2020. URL: https://www.gov.uk/guidance/project-and-programme-management.

[13] *Future Energy Scenarios 2025: Pathways to Net Zero*. National Energy System Operator (NESO), Nov. 2025. URL: https://www.neso.energy/document/364541/download.

[14] UK Gov. *Government Functional Standard GovS 002: Project Delivery*. Sept. 2025. URL: https://www.gov.uk/government/publications/project-delivery-functional-standard.

[15] STFC BID. *Business and Innovation Directorate Impact Highlights 23-24*. 2025.

DRAFT

The UK XFEL team would like to thank the UK XFEL International Advisory Board, for providing peer review, scrutiny and challenge over the course of this work:

Massimo Altarelli, Winni Decking, Markus Guehr, Daniel Gonnella, Simona Bettoni, Richard Catlow, Linda Young, Luca Giannessi.

A Special Thanks to those who contributed to Chapter 8 as contributors, advisors and additional authors:

Pierre Aller, Shakil Awan, Camila Bacellar, Darren Batey, Simon Bland, Mark Brouard, Andrew Burnett, Cephise Cacho, Stephen Carr, Philip Chater, Andrew Comley, Mark Dean, Andrien Descamps, Sanjeet Dhesi, Sofia Diaz-Moreno, David Dye, Helen Fielding, Andrew Goodwin, Alice Green, Samar Hasnain, Georg Held, Andrew Higginbotham, Philip Hinchliffe, Christopher Hutchison, Rebecca Ingle, Evans John, Gabril Karras, David Keen, Adam Kirrander, Hanna Kwon, Tien-Lin Lee, Frederico Lima, Alice Llewellyn, Adrian Mancuso, Jon Marangos, Stephen Marshall, Emma McBride, David McGonegle, Malcolm McMahon, Christopher Milne, Russell Minns, Peter Moody, Marcus Newton, Matthew Oliver, Allen Orville, Robin Owen, Charlotte Palmer, Giancarlo Panaccione, Raj Pandya, Thomas Penfold, Tommaso Pincelli, Louis Piper, Patrick Rabe, Anna Regoutz, Patrick Robertson, Ian Robinson, Charlotte Sanders, Christoph Schlueter, Gerd Schönhense, Sven Schroeder, Robbie Scott, Elaine Seddon, Khalid Siddiqui, Jergus Strucka, Penfold Thomas, Andrew Thomas, James Thompson, Geoff Thornton, Claire Vallance, Benjamin Van Kuiken, Jasper van Thor, Sam Vinko, Tiffany Walmsley, Ryan Wang, Robert Weatherup, Bruce Weaver, Julia Weinstein, Philippe Wernet, Nigel Woolsey, Briony Yorke, Amelle Zaïr, Yu Zhang,

We would also like to thank UKRIs internal bodies:

The Project Board, Infrastructure Fund, Facilities Strategic Advisory Group, Projects Review Committee.

This work was a cross council project and included input from multiple external institutions: BBSRC, ERSC, EPSRC, NERC, Innovate UK, Department for Science, Innovation and Technology, Ministry of Defence, Imperial College, Diamond Light Source, Brookhaven National Laboratory, Newcastle University, University of Leeds, AWE, University of York, Rolls-Royce, The Cockcroft Insitute, John Adams Insitutue, Univeristy of Plymouth, University of Edinburgh, University of Oxford, University of Strathclyde, Queens University Belfast, University of Southampton, University of Sheffield, ICFO, Oxford Brooks University, The Productivity Insitute.

Without support of the other facilities this endevour would not have been possible, as such we woould like to extand our gratitude to everyone who took time out to give tours, discussions, design and strategic philosophies, and constructive feedback, we very much enjoyed everyone's hospitality at:

European XFEL, LCLS, SwissFEL, SHINE, PAL XFEL, SACLA, PSI,

Finally: To all of the XFEL community, and the 1000+ people who have taken the time out to come to our townhalls, presentations, conferences and online meetings. Thank you.

DRAFT

Science and Technology Facilities Council
Polaris House
North Star Avenue
Swindon
SN2 1SZ

stfc.ukri.org

xfel.ac.uk